*pmd*CRC*

Project I7 Final Report
April 2005 – July 2008

Mineral system analysis of the Mt Isa–McArthur region, Northern Australia

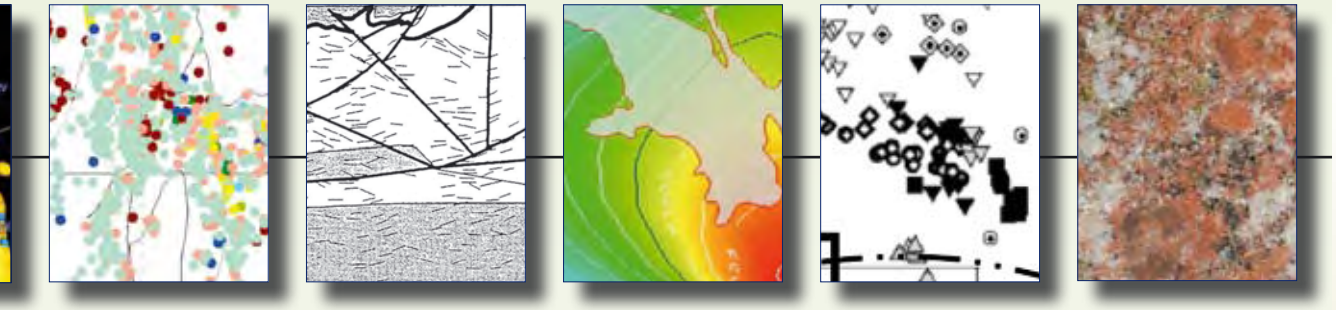

Compiled by the I7 Project Team

*pmd*CRC*

Project I7 Final Report
April 2005 – July 2008

Mineral system analysis of the Mt Isa–McArthur region, Northern Australia

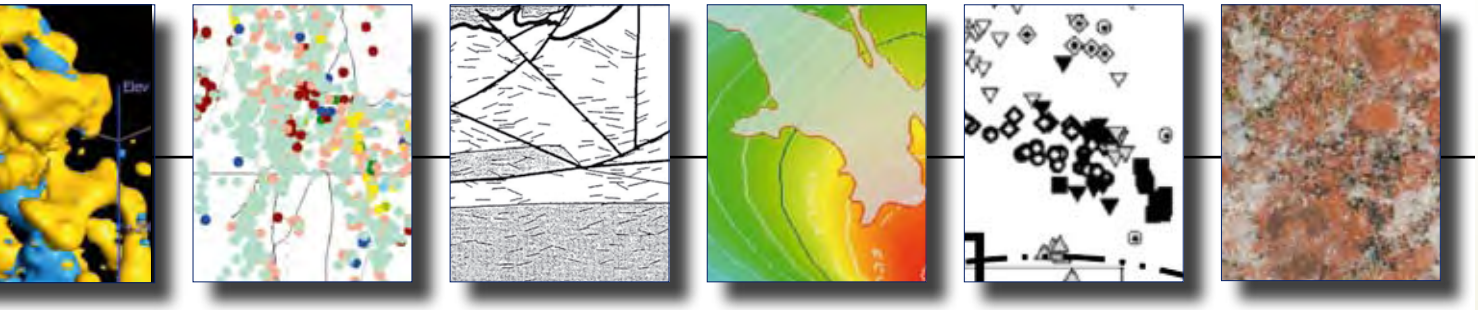

Compiled by the I7 Project Team

pmd*CRC

Core Partners

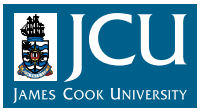

Sponsors

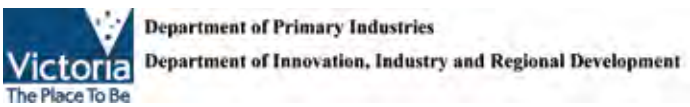

RESEARCH COLLABORATORS

Barry Murphy (Project Leader), Mark Kendrick, Roland Maas, David Phillips: The University of Melbourne.

Ben Jupp, Laurent Ailleres, Bruce Schaefer, Geordie Mark, Andy Wilde: Monash University.

John McLellan, Mike Rubenach, Carsten Laukamp, Nick Oliver, Arianne Ford, Louise Fisher, Damien Keys, Rowena Duckworth, Gustav Nortje, Jim Austin, Mark Edmiston, Piter Lepong, Tom Blenkinsop, Damien Foster: James Cook University.

Indrajit Roy, Narelle Neumann, George Gibson, Matilda Thomas, Peter Southgate: Geoscience Australia.

Klaus Gessner, Frank Bierlein, John Miller: The University of Western Australia.

John Walshe, James Cleverley, Alison Ord: CSIRO.

Laurie Hutton: Geological Survey of Queensland.

CONTENTS

Part V: the data supporting the science

This section will be hosted on a removable usb hard drive. It is anticipated company data will only be included with permission.

Metadata and read.me files

Regional scale datasets

- Geophysics
  - Magnetics (incl worms)
  - Gravity (incl worms)
  - DTM
  - Tomography
- Geology
  - Interpretative layers and maps, 2D and 3D map and GIS (will include line work eg faults, boundaries etc, cross-sections, images, inversions, forward model tests
- Mineral Deposits

District scale datasets

- Geophysics
  - Aster imagery
  - Seismic
  - Magneto-Telluric
  - Interpretative layers and maps
    - *Terrane scale 3D map (will include line work eg faults, boundaries etc, cross-sections, images, inversions, forward model tests)*
- Metamorphism
  - Metamorphic map
  - Metamorphic whole rock analyses
  - Metamorphic mineral analyses
  - Quantitative PT data and field gradients
  - Photomicrographs
  - Petrology, pseudosections and P-T-t evolutions
- Geochemistry
  - Whole rock
- Geochronology
- Geology point datasets
  - structural geology
  - rock properties
- Geology (GIS)
  - Interpretative layers
    - *maps*
    - *time-space event charts*

Prospect and Deposit scale datasets

- Geophysics
  - *Aster imagery*
  - *Hymap*
  - *PIMA*
  - *Interpretative layers and maps*
- Geochemistry
  - *Whole rock*
  - *FLINCS*
- Geochronology
- Geology point datasets (incl drilling)
  - *structural geology*
  - *lithology*
- Geology (GIS)
  - *Interpretative layers*
  - *maps*
  - *Regional 3D map*

PART I: EXECUTIVE SUMMARY AND THE 'FIVE ANSWERS'

Executive Summary

An holistic approach to the hydrothermal mineral system in the Mt Isa and McArthur River regions involves an analysis of the "5 Questions" (Geodynamics, Architecture, Sources, Pathways, Deposition) as a means to predicting locations of new deposits in the region. This is a multi-scale and multi-disciplinary approach that builds on earlier research by the ***pmd****CRC in the region and seeks to provide an integrated analysis that leads to more cost effective exploration.

The rich Pb-Zn-Ag, Cu and Cu-Au metal endowment of the region, an area of >200,000 km^2, is analysed across a range of scales, from the lithospheric architecture to the fluid compositions deemed responsible for mineralisation. The Western and Eastern Fold Belts (or Successions) at Mt Isa have, traditionally, been distinguished on their contrasting lithology, metamorphic grade, structural complexity, magmatic history and mineral deposits. Rather, the similarities of these two regions, separated by the Kalkadoon-Leichhardt Belt, are emphasised here and suggest a shared geodynamic and metallogenic history. The Mt Isa Inlier is somewhat unique in the North Australian Craton as the dominant structural grain is north-south and there are contrasts in evolution which suggest some de-coupling of the Mt Isa geology from that in the Northern Territory to the west, and from the Georgetown Block to the east. At Mt Isa, a series of mainly extensional Superbasins, magmatic episodes and shortening events occurred between 1870 Ma and 1480 Ma. The early formed Kalkadoon-Leichhardt Belt is interpreted as an elongate basement-cored magmatic and volcanic arc (Cover Sequence 1) related to subduction processes (towards the west?) and it exerted a strong control on subsequent evolution of the Eastern and Western Fold Belts. The distribution of major geological units and faults is modelled here in 3D maps of the region. Rifting led to the formation of the north-south trending Leichhardt River Fault Trough within which the Leichhardt Superbasin was focussed during ENE-WSW extension, followed by the Calvert Superbasin which developed (almost orthogonally) during NNE-SSW extension. The ensuing Isa Superbasin has a widespread distribution with its development and preservation largely being a function of the evolving Isan Orogeny. This orogeny has accentuated the tectonic grain to varying degrees in different areas and caused widespread re-activation of the extensional fault architecture.

There is no compelling evidence for large scale, lateral accretion of distinct terranes in the region. Extension, elevated heat flow and protracted magmatic activity characterise much of the history. This suggests mantle plume activity and/or a distal back-arc setting during extension. Felsic magmatic rocks enriched in radioactive elements, and mafic bodies emplaced at different crustal levels, both contributed to the thermal regime. Rifting of the lithosphere is modelled numerically as a thin elastic upper crust, with virtually every other lithospheric layer being weak or plastic. Ductile flow in the middle crust, magmatic accretion and basin formation in the upper crust appear to be associated with emplacement of granite-cored metamorphic core complexes in the Eastern (Wonga Granite, 1745-1725 Ma) and Western Fold Belts (Sybella Granite, 1650 Ma). Doming is a feature of the architecture at various times resulting in topographic effects that could have impacted on fluid flow regimes. Depositional changes in sedimentary environments have been related to deformation events, in extension and compression, and such events are apparently matched by hairpin bends in the 5000 km long Apparent Polar Wander Path. Large shifts in global position must have involved the entire lithospheric plate, by slab pull or ridge push, in tandem with strong vertical accretion. Combinations of these processes are the far-field drivers of the mineral system.

Crustal thicknesses during rifting and later contraction remain difficult to constrain. While there is a trend towards thinner crust and deeper depositional environments in the Eastern Fold Belt, this is also where the Isan Orogeny generated greatest crustal thickening. Crustal addition was from suites of granites intruded during, or following, late stages of contraction and oscillating extension. Orogeny resulted in shortening, uplift and a crustal thickness of up to *ca.* 55 km beneath the Mt Isa region and shallowing to 45 km below the McArthur River region. The reason for the emplacement of mafic magma into mid-crustal levels of the Eastern Fold Belt, which triggered the intrusion of the youngest suite of magmatic rocks, remains unclear but

convective removal of thickened lithospheric mantle is a possible process. Regionally significant high temperature-low pressure metamorphism can be related, in large part, to magmatic activity, perhaps driven by deeper level mafic magmas. The metal endowment may be determined by the availability of steep fluid pathways, such as along major faults, connecting different fluid reservoirs during a protracted period of vertical accretion and high heat flow.

As is manifest by fault control on deposit location, at a range of scales, the regional faults are numerically modelled (in FLAC) as fluid pathways which, in extension, draw down fluids and, in compression, the convective cells breakdown and fluids are expelled upwards, typically ponding in permeable hanging wall positions or (less often perhaps) at the sea floor. Discrete element modelling (UDEC) at the district to deposit scales indicates that stress anomalies associated with a particular compression direction during D4 deformation played a critical role in the localisation copper deposits in both the Eastern and Western Fold Belts. Fault bends, jogs and intersections are regarded as key localisation features.

The mineral system(s) operated, depositionally, during the last 100 Ma of the 400 Ma history. Importantly, the pre-existing Leichhardt and Calvert Superbasins provided permeable aquifers and fluid reservoirs for many of the metals that are hosted by the Isan Superbasin, or deposited during the Isan Orogeny. In addition to sedimentary formation waters in the Superbasins, the origins of fluids are potentially diverse, with volatiles from magmatic, metamorphic (basinal and basement units), meteoric and possibly mantle sources. Combinations of fluids in different proportions across gradients in salinity, temperature and pressure are important controls on ore deposition. For example, the generation of CO_2-rich fluids in IOCG-related hydrothermal breccias in the Eastern Fold Belt and the carbon enrichment at the Mt Isa Copper deposit in the west both attest to mixing of different fluid sources as a mineralising process.

The application of these understandings, spatially, to area selection in the exploration realm is attempted from a range of scales for Cu (-Au) and Pb-Zn-Ag deposits. All of the known major base metal mines are hosted in Isa Superbasin rocks; note that deposits hosted in earlier Superbasins, such as Mammoth Cu, formed during the Isan Orogeny where competency contrasts were an important control. The implication is that conditions for mineralisation (e.g. extensional and thermal events) did not lead to ore deposition during the Leichhardt and Calvert Superbasin episodes. Rather, these Superbasins were key fluid reservoirs and source regions for later mineralising events. Their preservation and distribution in 3D space are therefore important to constrain. Steep penetrative faults appear to be the most effective mechanism for accessing such fluids, and thus become a focus for regional to district scale area selection.

A key prospectivity indicator at the regional scale is the strike length of faults and related potential field gradients as, being a loose proxy for fault depth, the longer faults tap deeper into potential fluid reservoirs and may distort the thermal gradient. In the strike extensive regions buried under shallow cover, such fault structures can be manifest as long wavelength gravity and aeromagnetic gradients. At a more local scale, areas of geological complexity, fault intersections and jogs, can be used to prioritise targets. Aspects of alteration footprints at the deposit scale are evaluated through the application of new remote sensing data in the exploration tool kit.

Project Introduction

Acknowledgements

Industry Sponsors: X Strata, Zinifex, Copper Co, Barrick Gold, Qld Mines Dept, NTGS

List of Abbreviations

APWP – Apparent Polar Wander Path
CSB – Calvert Superbasin
ECV – Eastern Creek Volcanics
EFB – Eastern Fold Belt
FLAC – Fast Lagrangian Analysis of Continua
IOCG – Iron Oxide Copper Gold
ISB – Isa Superbasin
HFS – High Field Strength elements
HHPG – High Heat Producing Granites
HTLP – High Temperature Low Pressure Metamorphism
KLB – Kalkadoon-Leichhardt Belt
LHP – Lawn Hill Platform
LRFT – Leichhardt River Fault Trough
LSB – Leichhardt Superbasin
MKFB – Mary Kathleen Fold Belt
MORB – Mid-Ocean Ridge Basalt

NAC – North Australian Craton

RSB – Roper Superbasin

SCG – Soldiers Cap Group

TSR – Thermochemical Sulphate Reduction

UDEC – Universal Distinct Element Code

WFB – Western Fold Belt

Aims and Scope

The aim is to synthesise the across-scale elements of the geological evolution and their relationship to mineralisation in the region (Figure 1). The research seeks to deliver a comprehensive analysis of crustal to district and deposit scale characterisations of the controls on mineralisation. Major advances being sought are *knowledge-based* – through a better understanding of geology and mineral systems in 2D, 3D and 4D, building on existing models and concepts, testing and developing new ideas and models, *technology-based* – by developing an "exploration toolkit", with a focus on tangible, observable criteria, and *economic-based* – to help reduce the time and cost to discovery. Key project deliverables are:

- Better constrained tectono-magmatic history and role of crust/mantle processes
- Better constrained tectono-thermal and metasomatic history and a regional thermal model
- Coupled deformation-thermal-fluid flow modelling of a range of scenarios and scales
- Revised time-space correlation of Eastern and Western Fold Belts (or Successions)
- 3D geological maps of the outcropping region and its undercover geology
- Characterisation of structural controls on the localisation of Cu, Cu-Au and Pb-Zn-Ag deposits
- Fingerprinting fluid pathways related to mineralisation and alteration, using across scale remote sensed techniques
- Comprehensive geoscientific database
- Prospectivity analysis using 2D and 3D geological models, deriving empirical criteria and employing numerical simulations to test a range of coupled deformation/thermal transport/fluid flow modelling scenarios
- An investigation of the permeability architecture at times of mineralisation, evaluating the role of faults, seals and potential aquifers
- Exploration "toolkit", from regional to deposit scale studies that will allow prioritisation in project generation decisions.

Figure 1: Project area and major domains (from G. Gibson, presented at 17 project meeting).

Datasets used

The project involves constructing 3D maps and incorporating a range of diverse elements in the investigation of the mineral system. The project brings together, and builds on, the outcomes of the Eastern (I1) and Western (I2/3) Isa projects in relation to architecture and evolution, and integrates results from the 1:1 projects in the Isa Valley (I4) and Lawn Hill (G14) regions. It seeks to extend this coverage to incorporate results from the McArthur River region (I5). Methods involve data compilation, processing, interpretation and modelling of geophysical, geological and geochemical data. New data acquisition includes bulk rock and mineral chemistry using direct and remote detection techniques, field campaigns, isotopic dating and fingerprinting of fluid systems. The research is framed around five key questions (Geodynamics, Architecture, Sources, Pathways, Deposition) and these were subset, initially, into a series of modules, most of which were completed, and are reported on here:

Q1: What is the Geodynamic setting?

- There remains considerable uncertainty regarding the geodynamic setting and far-field factors controlling the evolution of the inlier. A synthesis of observations is presented here
- Constrain the tectono-magmatic history and role of crust/mantle processes in magma generation, with an emphasis on the WFB in the first instance, using geological mapping, isotopic dating and radiogenic isotope analysis. This research follows 3 themes on:
  a) The nature of pre-Barramundi crustal elements,
  b) Source regions of potassic "A-type" granites and
  c) Tectono-magmatic evolution
- Constrain the tectono-thermal and metasomatic evolution, with an initial focus on the WFB, though structural and microstructural studies, isotopic dating, P-T-t paths and development of a regional thermal model of the inlier
- Constrain the time-space correlation through a targeted sampling campaign, using isotopic dating and sequence stratigraphic concepts.

Q2: What is the architecture of the system?

- Develop 2D and 3D maps of the region, incorporating existing coverage, and blending with models in new areas
- Examine the camp scale structural controls on deposit clustering
- Determine the nature of structural controls on copper deposits.

Q3: What are the fluids, their sources and reservoirs?

- Compile a database of isotopic and geochronological data
- Examine potential fluid source regions using noble gas and halogen tracers.

Q4: What are the fluid flow drivers and pathways?

- Undertake coupled deformation-thermal-fluid flow numerical simulations in relation to scenarios from the Mt Isa Inlier, with a focus on geodynamic history, fluid flow pathways and drivers, thermal modelling, and controls on Cu deposits in the WFB. Simulations of the architecture at the time(s) of mineralisation will be made, based on an understanding of the permeability structure, mineralisation ages and fluid flow histories
- Examine potential role of hydrocarbons and the broad scale permeability stucture of the WFB during Zn-Pb-Ag mineralisation
- Investigate the potential fluid pathways and alteration signals from detailed analysis of key localities, geochemical modelling and relate to regional scale features
- Characterise Cu-Au-U deposits, and develop guidelines for exploration targeting
- Characterise the alteration footprints of mineralised systems using across scale remote sensing techniques with an initial focus in the Mt Isa Valley.

Q5: What are the metal transport and deposition processes?

- Examine a range of possible geochemical models that may be applicable to the mineralising systems of interest
- Develop reactive transport and permeability models related to Zn-Pb-Ag (e.g. Century), Cu (Isa), and Cu-Au (Ernest Henry) deposits.

Structure of the Final Report: Parts I, II, III, IV, V

Part I presents the essential framework for the research project, summarises the main outcomes and offers "answers" to the five questions asked of the Isan mineral system. Part II develops some exploration targeting criteria at a range of scales, with predictions derived from 2D, 3D and 4D modelling described in the project deliverables. Part III summarises the science behind the five answers, with reviews of each of the questions in turn. Part IV (Appendix 1) contains the main project deliverables as a series of stand-alone reports which serve to support the analysis in Parts II and III. Part V is a compendium of mainly digital data sets related to the project deliverables.

The Mineral System's 'Five Answers'

"Answers" outlined here derive from the five questions asked in Part III and from the supporting material in Parts IV and V of this report.

Geodynamics

Combinations of vertical and lateral accretion are the driving forces. Interpreted far-field plate geometries suggest an intra-continental rift through to a distal back arc basin or, perhaps, evolving to a passive margin setting. Extension was accommodated by sedimentary basin development (Leichhardt, Calvert and Isa Superbasins), volcanism and magmatism, with input to the high thermal gradient from both radiogenic felsic rocks and mafic bodies emplaced in the mid to upper crust. The region is modelled in extension as a thin, brittle upper crust above a thermally weakened lithosphere, where connectivity between the two vertically stacked domains appears to be largely along steep crustal scale faults. The Isa Superbasin (ISB) is regarded as a composite of early rift-sag to later foreland basin. The Isan Orogeny is associated with early north-south shortening that overlapped with Isa Superbasin (ISB) sedimentation. The latter is mostly preserved in the Lawn Hill Platform (LHP) and Western Fold Belt (WFB) and in parts of the Eastern Fold Belt (EFB). The major period of deformation was an east-west shortening and crustal thickening which was most pronounced in the EFB.

Architecture

Across the WFB and EFB, Superbasin development is interpreted to be interspersed with extensional core complex development and emplacement of syntectonic granites (Wonga, Sybella), and the generation of fault-controlled buttress-like geometries and doming. The rift architecture was founded on a faulted basement substrate which had undergone crustal addition in a volcanic/magmatic arc that focussed along the Kalkadoon-Leichhardt Belt (KLB). Repeated extension occurred during the Leichhardt (LSB) and Calvert Superbasins (CSB). Uncertainty surrounds whether there was an intervening compressional event. The "Cover Sequence 2/3" unconformity is cited as a compressional event in the literature (Betts et al. 2006), but it may instead be related to extension on crustal scale detachments (Gibson and Hitchman 2005). Although the Isan Orogeny has generated complex structuring in places, the regional Superbasin architecture can be modelled in 3D as a sheet-like geometry with relatively flat enveloping surfaces disrupted by a series of mainly steeply dipping faults. These faults were generated during the Isan Orogeny or were re-activated from earlier extensional events. Regions of high temperature-low pressure metamorphism appear to be largely related to magmatic input.

Fluid Sources and Reservoirs

Sedimentary formation waters, magmatic, metamorphic, surficial, and mantle fluids make up the diverse sources. Most of the ore deposits and regional alteration have mixed geochemical signals indicating the involvement of at least two of the fluid end-members. Where basins are thickly developed, as in the Leichhardt River Fault Trough (LRFT), heterolithic proximal facies sediments are identified as diagenetic aquifers for storage of sedimentary formation waters. These were important fluid sources both for earlier formed Pb-Zn-Ag deposits and the later Cu deposits.

In the EFB, recent noble gas and halogen data suggests a lesser role for magmatic fluids regionally than previously thought and strong evidence for the involvement of such fluids has only been obtained for the Ernest Henry IOCG deposit. At other IOCG deposits, halogen data indicates multiple sources of salinity in the ore forming fluids with end member compositions being a halite dissolution fluid and a bittern brine fluid. Noble gas data is compatible with sedimentary formation waters or locally derived metamorphic fluids being significant fluid sources at Osborne, and contrast with the additional

external magmatic fluid component identified at Ernest Henry. As Ernest Henry is the largest IOCG deposit in the district, this may indicate the presence of magmatic fluid components is required to form the richest deposit. Magmatic volatiles have been identified in isolated un-mineralised parts of the Mary Kathleen Fold Belt and there is, as yet, no evidence for the involvement of magmatic fluids in any of the deposits in the WFB.

The Mt Isa Cu deposit is the best example of a hydrothermal system with a large component of basement-derived metamorphic fluids. In particular, high $^{40}Ar/^{36}Ar$ values, together with rare CO_2-rich fluid inclusions, suggest devolatilisation of the Eastern Creek Volcanics (ECV), and mixing with either bittern brines or halite dissolution waters. In the EFB, metamorphic fluids from metasedimentary rocks, such as the Corella Formation, were an important potential source of CO_2, SO_4 and Cl. The high abundance of CO_2 fluid inclusions in IOCG deposits that formed close to the metamorphic peak (Osborne, Eloise and Starra) is most likely to have had a metamorphic origin.

Fluid Pathways and Drivers

The metal endowment may be determined by the availability of steep fluid pathways, such as along major faults, connecting different fluid reservoirs. This is manifest by fault control on deposit location at a range of scales. The regional scale faults of the Leichhardt River Fault Trough are modelled numerically (in FLAC) as fluid pathways that, in extension, tend to draw down fluids and perturb relatively stable convection cells. Storage of such fluids in diagenetic aquifers for ten's of millions of years is a key consideration, as such aquifers may be re-charged by lateral flow and disturbed by topographic and structural influences. In compression, the convection cells breakdown quickly and fluids are expelled upwards, typically ponding in permeable hanging wall positions or (perhaps) at the sea floor.

Discrete element modelling (UDEC) at the district to deposit scales indicates complex zoning of stress anomalies in response to the partitioning of stress across fault blocks, and the interaction between rock units of different competencies. A far field ESE stress orientation provides the best correlation with known deposits and suggests regional a D4 stress regime may have been responsible for both Cu and Cu-Au mineralisation in the Eastern and Western Fold Belts. Fault bends, jogs and intersections are regarded as key localisation features. Tools for rapid analysis of remote sensed data, combined with on-going calibration with geology, provide great promise for discriminating mineralisation-related alteration footprints.

Depositional Mechanisms

Depositionally, the mineral system was only active in the latter parts of the evolution. Extension and thermal input during early Superbasin development did not result in the formation of mineral deposits but rather were the storage compartments for fluids drawn down into the system.

Fluid mixing and dilation are key ingredients to the hydrothermal deposits studied. In particular, at the Mt Isa Cu and IOCG deposits (Ernest Henry, Osborne), brecciation is classically developed in and peripheral to the ore zone. An analysis of apatite compositions provides some insights to the fluid compositions at the time of mineralisation at Ernest Henry. The apatites record evidence for PO_4-HF-SO_2-CO_2 fluids that carry $As(^{6+})$ and/or SO_4 and that have little or no Cl or H_2O. An evolution from SO_4 to As could be related to mixing of external fluids at that time or an in-situ change in the redox state of the carrier fluid. Overgrowth of apatite by titanate might record the transition from volatile CO_2-rich fluids to brine-rich liquids. The extreme nature of the chemistry of the Ernest Henry apatites relative to the regional rocks indicates that there are processes that existed within the deposit that did not occur in structurally similar barren rocks.

At the Mt Isa Cu deposit, ore-related brecciation is represented by a "once-off" fluid mixing event. Arguably, the sulphide deposition process was by *in-situ* Thermochemical Sulphate Reduction. The range of $\delta^{34}S_{sulfide}$ (~15 to 30 ‰) is consistent with high temperature inorganic reduction of marine sulphate, implying either bittern brines or halite dissolution waters. A geochemical mixing model is developed to explain the enriched C isotopes in carbonates and suggests the introduction of H_2 as a strong reductant with possible mantle affinity.

PART II: EXPLORATION TARGETING

(Main contributors: Murphy, Oliver, Laukamp, McLellan)

Introduction

The explorationist's role is to target new ore deposits. Criteria on which area selections are made are scale dependant, determined by conceptual models that are applied and limited by the available and appropriate data sets. They are invariably driven by a narrow range of criteria, peppered with varying degrees of subjectivity. Narrowing the search area from regional to prospect and ore body scales is a process of eliminating areas deemed less prospective. The success of this process may be measured from the rate of discovery which, over the past decade, has been low. That there are undiscovered ore bodies remaining in the Mt Isa and McArthur River regions is virtually certain, especially in the strike extensive under cover areas where we are challenged in constraining a geological framework. The objective here is to outline key criteria for predicting new ore systems, using empirical observations and process understanding of the mineral system. In addition, acquisition of the appropriate data sets at various scales, their costs and the relevant bodies who would collect and provide such data are indicated and tabulated below (Tables 1 and 2).

The variety of deposits can be regarded as belonging to two general types, traditionally related to separate mineral systems: 1) the generally older (?1660-1595 Ma) Pb-Zn-Ag sediment hosted massive sulphides which may be of gigantic proportions (e.g Mt Isa, Century, McArthur River), and 2) the generally younger (1600-1500 Ma) Cu +/-Au (+/- U) deposits which encompass Isa Cu and Mammoth Cu deposits in the WFB and the IOCG Cu-Au deposits in the EFB (e.g. Earnest Henry, Osborne). Broken Hill-type Pb-Zn-Ag deposits (e.g. Cannington) and Au-only deposits (e.g. Tick Hill) are not evaluated in this analysis. In a broad view, similar processes drive the mineralising system, with a commonality in source regions and brine compositions across large regions and over time. For example, isotopic characteristics of brine fluids in the McArthur River Pb-Zn-Ag deposit are indistinguishable from those related to the U mineralisation in the Murphy inlier (Polito et al. 2006b). Also, the source of copper from the EVC at Mt Isa at around 1520 Ma (Wilson et al. 1985; Wyborn 1987; Heinrich et al. 1995; Matthai et al. 2004) is within the same Supersequence that contains the diagenetic aquifers from which base metal brines were sourced for the Pb-Zn orebodies (~1660 Ma if a syngenetic model is accepted; Polito et al. 2006a). This commonality suggests availability and/or stripping of different metals from similar source regions at different times during the last 100 Ma of the 400 Ma evolution. Ultimately, gradients in temperature, pressure and salinity are the drivers for ore deposition, and these gradients can arise from far field effects, such as mantle plumes, core complex development and orogeny, operating in tandem with more local scale controls, such as areas of dilation, competency contrasts, increased fluid flux and availability to fluid reservoirs.

Mineralising processes operated throughout the region, as seen from the distributions of its contained deposits (Figure 2). Remarkably, all of the major base metal mines are hosted in upper level rocks: perhaps from as old as ~1680 Ma (although this age for Cannington host rock is not well constrained and could be younger (Foster and Austin 2007)), the WFB deposits (Mt Isa, Hilton, ~1655-1640 Ma host), up to 1595 Ma (Century host) and demonstrably later deposits formed during the D2 Isan orogeny at ~1570 Ma (e.g. Silver King on the LHP). The implication is that conditions for mineralisation did not operate or combine in a focussed way until late in the history, and that major deposits did not form during the LSB and CSB episodes *per se*. The extensional and thermal events that characterise the LSB and CSB do not appear to be a driver for mineralisation in these Superbasins, yet they form the foundation for the subsequent metallogenic events and, without these as a substrate and fluid source region, it is less likely that the ISB-hosted mineralisation would ever be world class. Note that deposits hosted within earlier Superbasins, such as the Mammoth Cu system, were formed during the Isan Orogeny where competency contrasts were an important control (Miller, McLellan(b); Appendix 1).

Hydrothermal mineralization requires metal-bearing fluids to flow across gradients of pressure, temperature, chemical concentration, or a combination of these gradients

Table 1: Targeting table for Pb-Zn-Ag deposits

Pb-Zn-Ag SHMS	Key Criteria (inc rankling)	Necessary Data	Min Data Density	Acquisition Costs	Responsibility
Regional Analysis (Province)	Precambrian Rift-fill sediments Regional scale faults	Terrain Chron Gravity Aeromagnetics Regional geology	100km^2 catchments 10km stations 5km flight line 1:500k, 1:250k maps	$ millions to tens of millions	Federal Agencies (GA)
District Analysis (60x60km)	Major (basin margin) Faults Hanging wall positions Supersequence boundaries Late Basin Seds (Isa SG) Extension and Compression..! Geological Complexity	Gravity Aeromagnetics Geology maps Seismic AEM 3D Map	3km stations 1km flight line 1:250k, 1:100k maps Reflection/Refraction	$ tens of millions	State (and large company)
Prospect Analysis (5x5km)	Carbonaceous shale Fault intersections, Cross Faults Growth Faulting/Depocenter? Alteration halo	Detailed geophysics AEM Petrophysics Remote sensing WR geochem 3D Map	500 m stations 200m flight line Magnetotellurics Aster, Hymap, Hyperion, PIMA	$ hundreds of thousands to millions	Company
Ore System Definition	Fluid focussing Multiple fluids/mixing Alteration halo	Drill core Field/Lab integration WR geochem	500m stations 50m flight line or ground based	$ millions	Company
Ore Deposit Identification	Alteration gradients	Drill core Microscopy	1km drill spacing	$ millions	Company
Ore Deposit Delineation	Ore continuity and grade	Drilling DHEM	Infill drilling 500m	$tens of millions to hundreds of millions	Company

Table 2: Targeting table for Cu and Cu-Au (IOCG) deposits

IOCG Cu Au Cu	Key Criteria (inc ranking)	Necessary Data	Min Data Density	Acquisition Costs	Responsibility
Regional Analysis (Province)	Carbonate Sequences/Evaporites Granites (esp A-types) Mafic rocks Basin Inversion (compression) Regional scale faults	Terrain Chron Regional geophysics Regional geology	10km gravity 5km aeromag 1;500k, 1:250k geol maps	$ millions to tens of millions	Federal Agencies (GA)
District Analysis (60x60km)	Geological Complexity Stress partitioning and dilation Strike slip/transpression Corella/SCG boundary Regional alteration patterns	• as above, more detailed • fault architectural map Remote sensing	1:250k, 1:100k geol maps 5km gravity ASTER and HyMap	$ tens of millions	State (and large company)
Prospect Analysis (5x5km)	Magnetic highs/Gravity highs Fluid focussing and dilation Host rock rheology/permeability Fault intersections, jogs, bends Magnetite depletion Lithogeochemical haloes	Detailed geophysics Petrophysics Fault fills Remote sensing 1:100k, 1:50k geol maps AEM	2km gravity 200m aeromag	$ hundreds of thousands to millions	Company
Ore System Definition	Multiple fluids, Alteration Halo & Nob Gases, high $^{40/36}$Ar (Isa), Magmatic (at EH). Bittern brines	Drill core Field/Lab integration Petrophysics	500m gravity 50m aeromag or ground mag	$ millions	Company
Ore Deposit Identification	MS in inclusions (IOCG) Alteration gradients	Drill core Microscopy	1km drill spacing	$ millions	Company
Ore Deposit Delineation	Ore continuity and grade	Drilling	500m centres	$ tens of millions to hundreds of millions	Company

(Phillips 1991). The existence of vertical or steeply dipping aquifers within the architecture of a mineralising system can be of great significance, because they provide a higher potential for fluid to flow across gradients of temperature and pressure than horizontal, or shallowly dipping aquifers. A steep aquifer is also more likely to favour free thermal convection (Mullis, 1995), which is a highly effective fluid flow driving process in hydrothermal systems. In addition to the presence of inclined and steeply dipping aquifers, the overall high thermal gradient would have further favoured free thermal convection over conductive heat transfer (Turcotte and Schubert, 2002) in areas with high permeability (Appendix 1, McLellan (a)). The likelihood of free thermal convection to occur is therefore significantly increased by the steepening of stratigraphy and deformation fabrics in the upper crust by progressive deformation in the 'vice tectonics' mode (Cruden et al. 2004). Overall, 'vice-style' tectonics (Cruden et al. 2004) in a high geothermal gradient will lead to a number of mechanical, structural and thermal consequences, which greatly increase mineral prospectivity. Furthermore, the steep structural grain in the upper crust leads to a high degree of mechanical anisotropy at high angles to the tectonic shortening direction, which tends to favour the elongation of the shear zone and the formation of strike slip fault zones (e.g. Teyssier and Tikoff, 1999).

Pb-Zn-Ag Deposits

Examples are: Mt Isa, Hilton-George Fisher, Lady Loretta, Century, McArthur River.

These deposits are characterised by stratiform massive sulphide lenses in carbonaceous shales and siltstones at varying stratigraphic levels within the Isa Superbasin (Table 1). There is an apparent strong fault control on the location of deposits, in particular with long strike length features (Figure 3). The age and timing of mineralisation remains a source of considerable debate, from early, shallow burial sub-seafloor replacement (e.g. McArthur River) to later, deeper burial, syn-inversion replacement (e.g. Century). There is increasing consensus that ore deposition at the sediment-water interface is a less important process than sub-seafloor replacement (Huston et al. 2006). However, Feltrin et al. (2007) used geometric and numerical models in their model of primary syngenetic mineralization for Century with a protracted history of reworking.

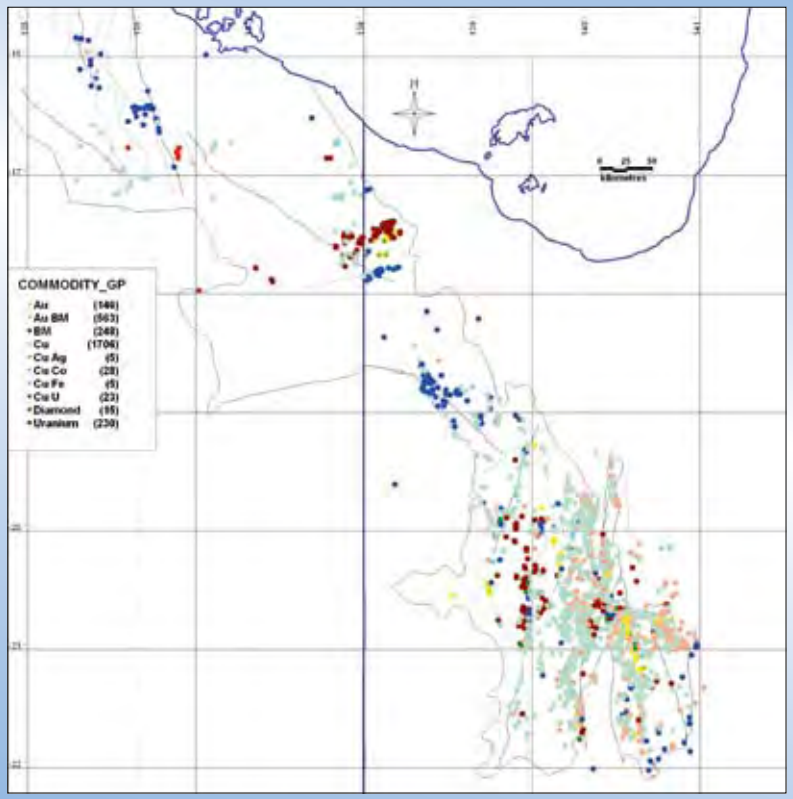

Figure 2: Deposit distributions according to major commodity groups.

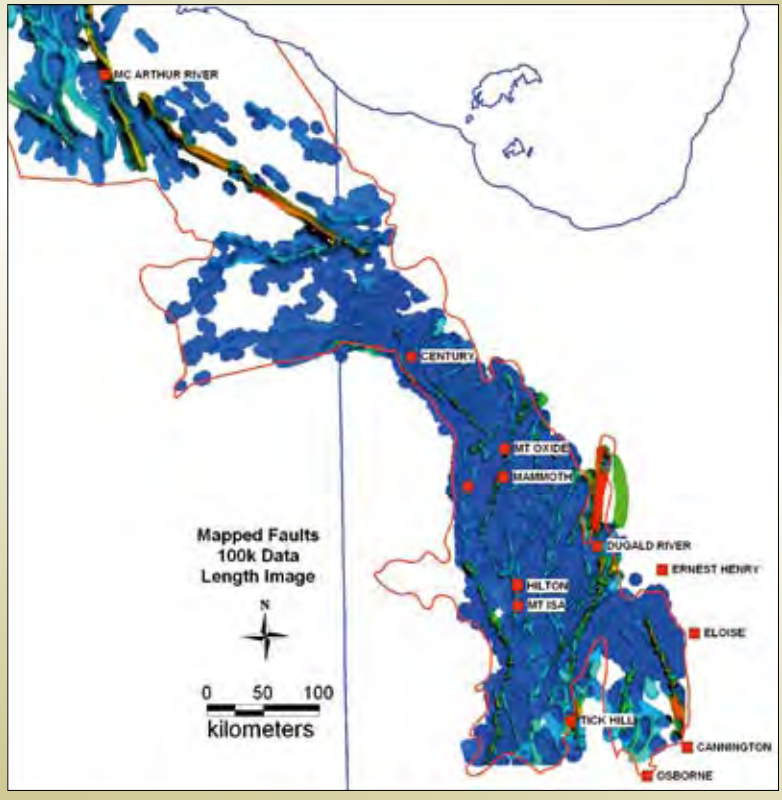

Figure 3: Image of mapped fault length and locations of major deposits.

Scale 1: Regional Analysis

As the explorationist undertakes project generation at a terrane scale in other parts of the world for regions with similar characteristics as the Mt Isa terrane, some distinguishing features are, in approximate order of importance:

- Plumbing system that taps deep into the crust (maybe even mantle?), as evidenced by:
  - Linear, strike extensive gravity anomalies with strong gradients within an overall high gravity response. The sources of the high gravity responses are varied (Wellman, 1987) but an association with abundant mafic rocks at depth is implied. Sampling on at least 5 km station spacing is needed to determine this and, typically, such data is available from Government organisations
  - Aeromagnetic response, though more influenced by shallower level responses, with evidence of long wavelength gradients. These typically have a similar fault-related nature as the gravity responses, and an integration of these two data sets provides essential information relating to the terrane scale architecture
  - Complex pattern of faulting and major, laterally continuous, large dimension faults. This is not unique to the Isa region, as other terranes with similar features are far less mineralised. In outcropping terranes, mapped geology and TM, in the first instance, would determine this, otherwise, in under cover regions, determined from available regional geophysics. Sources of such data generally reside with Geological Survey organisations.
- Mesoproterozoic age – metal abundance varies in a non-systematic pattern over Earth history with the Mesoproterozoic being a particularly fertile period and a major contribution to this global abundance is from the Mt Isa and Broken Hill regions of Australia (Huston et al. 2006). Stream sediment sampling of detrital zircons to determine age spectra maybe an appropriate technology (e.g. Terranechron) to gain a rapid, first pass assessment of this history, in catchments of ~ 100 km^2 and is a cost effective strategy
- Intracratonic rift or distal back arc environment, abundant mafic and felsic rocks, and a thick sediment pile. A history of repeated extension and inversion, perhaps observable from geological maps (at a

minimum, 1:250 000 scale) and regional geophysical signatures, particularly the magnetic expression of rift-related mafic sequences

- High geothermal gradient and regional high temperature/low pressure metamorphism. Nor is this unique to the region, as there other less mineralised terranes with similar features. Such information, however, requires detailed analysis and is generally not determinable from remote data sets
- Existing deposits and occurrences ("smoke") are a clear signal of fertility.

Scale 2: District Analysis

Having determined the terrain of interest, the following criteria can be indicative of mineral camps, in approximate order of importance:

- Evidence of potential source rocks (rift-related volcanics) and diagenetic aquifers in lower parts of stratigraphic pile, comprising thick proximal clastic sequences with potential to be buried to 5-10 km depth at times of mineralisation, e.g. LSB sediments and volcanics (e.g. Polito et al. 2006a, b and c)
- Evidence of carbonaceous, argillaceous host rocks in upper levels of youngest (pre-orogenic) basin, e.g. ISB sediments
- Faulting – evidence for long strike length faults (Figure 3), commonly associated with significant gradients in potential field data, indicative of penetrative, crustal scale faulting. In addition to mapped geology, critical data sets are:
  - Seismic data is an important contribution to this, and is generally acquired by State organisations in collaboration with exploration companies
  - Gravity – minimum 3 km spacing, typically acquired by Geological Surveys
  - Aeromagnetics – minimum 400 m line spacing, 100 m height, acquired by Geological Surveys and/or exploration companies
  - Geostatistical approaches to the clustering of vein-style Pb-Zn deposits which should show strong correlations between faults and mineral occurrences.
- Evidence of extension and growth faulting – potential driver of fluids by underpressure, dilation and downward excavating convective flow
- Evidence of inversion, compressional folding and faulting – potential driver of fluids by upward expulsion from breached reservoirs
- Evidence of saline brines, evaporates or remnants thereof in deeper parts of sediment pile
- Alteration – possibly seen from geophysical (magnetite depletion?) or remote sensed data (TM, ASTER). This would particularly include the common occurrence of primary and diagenetic carbonates such as siderite or dolomite that should be distinctive from regional stratigraphic signals irrespective of the specific genetic model
- Clustering of existing deposits and occurrences ("smoke")
- Stream sediment sampling – in catchments of 10 km^2. Geological Surveys and/or exploration companies.

An undercover example and how to explore in this space

In the under cover regions, the 3D map and potential field data are key resources. The "brine factories" are areas that contain substantial thickness of potential source rocks and diagenetic aquifers. These can be outlined in an approximate way, based on extrapolation our interpretation from the outcropping regions and interpretation of potential field responses. Areas of thick accumulations of LSB and CSB rocks that were buried to 5-10 km by the time ISB was been deposited are key. Also critical is the preservation of the ISB as a host rock. The outcropping distribution of the ISB (red regions) is superimposed on an interpreted fault architecture derived from potential field gradients (Appendix 1, Murphy et al.). Warmer colours in the image reflect longer strike length elements. Blue lines are first and second order faults and green lines are interpreted extensions of faults under cover. This highlights large domains (Figure 4) which can be included or excluded accordingly, such as:

- Excluded regions are:
  - areas to the west of Mt Isa, that is to the west of the Barramundi breakaway structure and beneath the Georgina Basin, are excluded. This is because the LSB and CSB are thin or absent, with shallow depth to basement, and such regions are less likely to have generated substantial fluids. However, lateral fluid flow from the deeper, thicker LRFT westwards

onto this platform may be possible, nut not as likely to have seen as much fluid as the hanging wall sediments

  - the southward extension of the LRFT is mostly excluded because the level of erosion is generally to the LSB and basement levels, and ISB host sequences seem to be only preserved in narrow fold/fault keels
  - Areas of deep cover (refer to NWQMPR 2000).

- Included areas, the "brine factories", are:
  - northward continuation of the LRFT has the best potential for preserving both the source aquifers and the ISB host rocks
  - the LHP preserves the ISB host sequences of interest, and the under cover extensions of the LHP eastwards are considered to have good potential. There are regions of the LHP where the LSB may be too deeply buried, such that secondary porosity gets occluded, and the CSB may be an alternative source (Polito et al. 2006c). This is particularly the case in the northern hanging wall of the Little Range Fault, and perhaps the eastern hanging wall of the Riversleigh Lineament
  - undercover extensions of the ISB northwards and southwards in the EFB
  - numerical modelling of fluid flow in the LRFT shows an asymmetry whereby the most concentrated flow occurs along the western side of the trough and is more dispersed in the east (Appendix 1, McLellan (a)). This asymmetry is most likely due to the thickening sediment wedge to the east and the underlying basement detachment zone geometry. As a result of this dilation, shear strain and fluid flux is concentrated proximal to the western margin fault. The hanging wall areas have higher dilation and cumulative fluid fluxes than the footwall (Appendix 1, McLellan (a)).

An analysis of the sensitivity of deposit location relative to potential field gradients (Appendix 1, Murphy et al.) shows that proximity to long wavelength features, i.e. deep tapping faults, holds greater prospectivity (Figure 5). Using buffers of varying width in relation to fault-related gravity features of varying strike length, this demonstrates that the bulk of metal is contained in corridors defined by the major gradients. Hence, applying a buffer in the area selection routine (e.g. the 80,000 km^2 buffer area in Figure 5 as a cutoff) results in a much more focussed outcome (Figure 6).

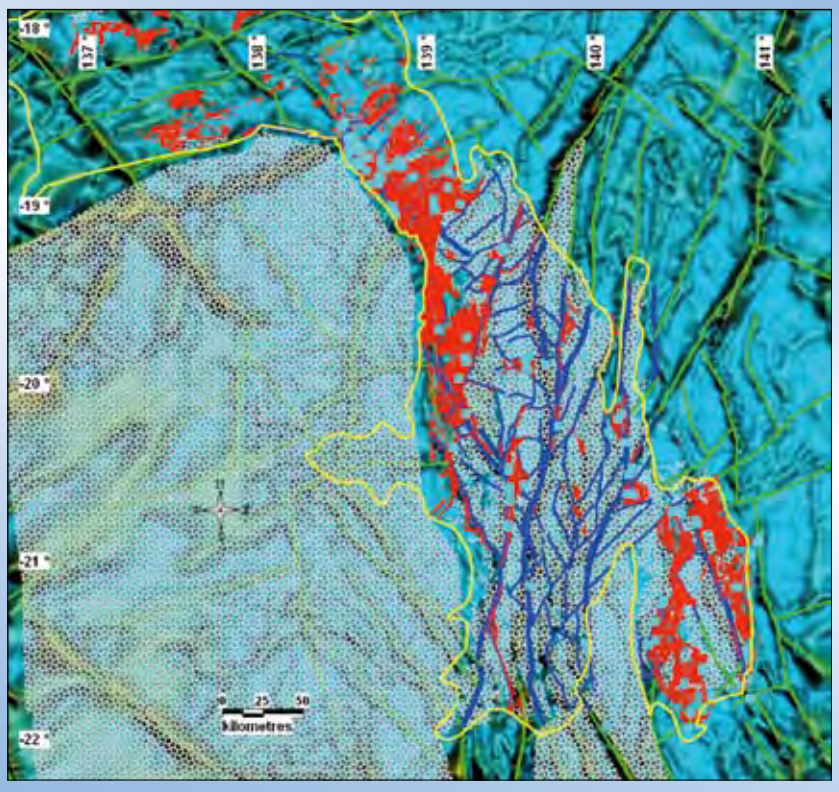

Figure 4: Base Metal potential and edge length image with superimposed ISB outcrop (red) with excluded areas in stipple. Blue dots are base metal occurrences.

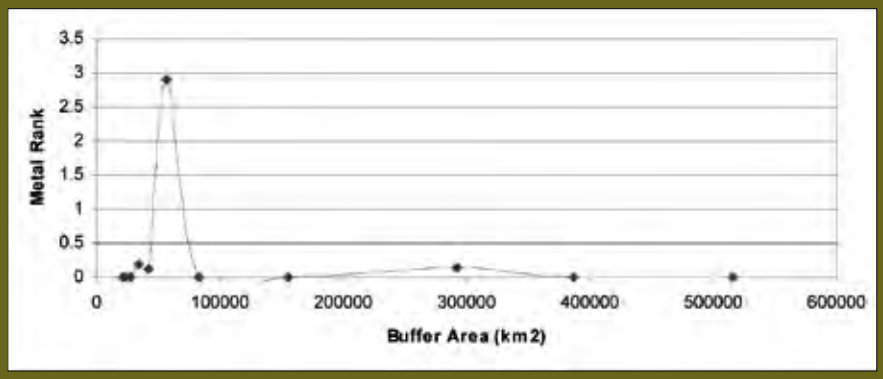

Figure 5: Plot of metal rank per unit area with increasing distance from fault-related gravity gradients using length weighted buffers (Appendix 1, Murphy et al.).

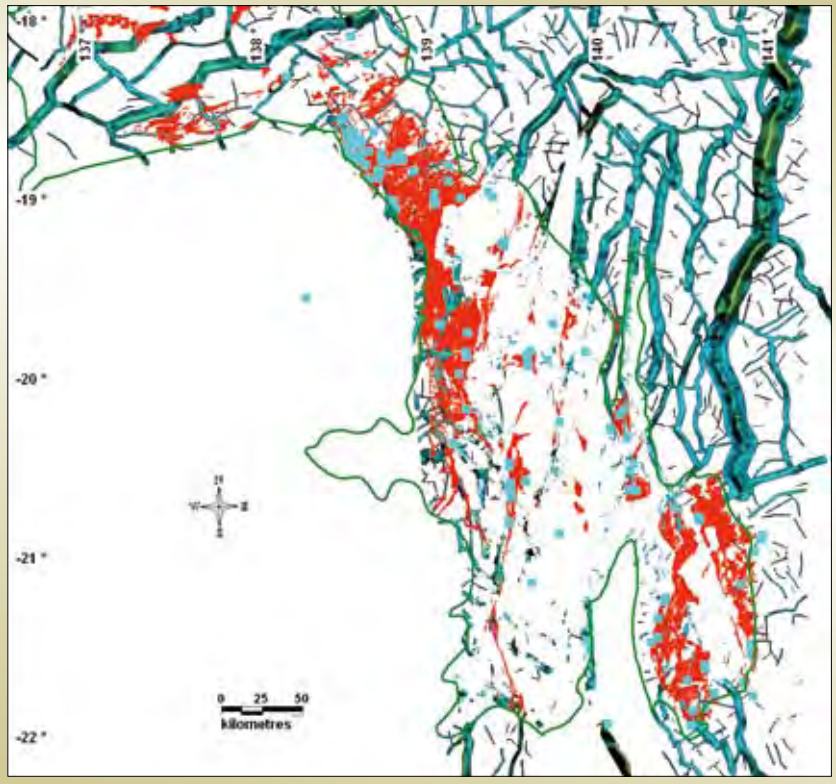

Figure 6: Base Metal potential and edge length image with superimposed ISB outcrop and buffer area cutoff applied to gravity gradients (Appendix 1, Murphy et al.).

Scale 3: Prospect Analysis

Within a mineral camp, key features to evaluate are:

- Host rock – presence of carbonaceous argillite
- Fault architecture – fault intersections, dilational jogs; complexity. Existence of penetrative faults, supported by potential field data: detailed gravity, minimum 500m station spacing, and aeromagnetics, minimum 200m flight line spacing
- Local depocentres – growth faulting, hanging wall positions? May be determined from mapping, and/or magnetotelluric and seismic data
- Alteration footprints
  - lithogeochemical haloes up to 15 km from McArthur River deposit (Large et al. 2000; enriched Zn, Pb, Cu, Ag, Tl, Hg and Mn)
  - Illite xtalinity halo at Century – (Wilde 2006)
  - carbonate (siderite), pyrite.
- Stream sediment and rock chip sampling
- AEM
- Drilling.

An undercover example and how to explore in this space

This has not been a particular focus in the I7 project. However, application of fault intersections on the LHP coupled with fluid flow modelling have been investigated under the G14 project with Zinifex (Murphy et al. 2007; Zhang et al. 2007).

Scale 4: Ore System Definition

At this scale, an advanced mineralised prospect has been outlined and further work in delineating its potential lies in:

- Drilling
- Determining the size and tenor of the alteration footprint – within halos:
  - Hylogger characteristics need to be determined.
  - PIMA at Mt Isa does not show diagnostic signals (Appendix 1, Duckworth)
  - Mn halo, C-O isotope halo as per Large et al. (2000), Zn to Pb to Mn zonation and vectors related to that.
- Constraining fault architecture, through mapping and 3D modelling
- Constraining stratigraphy to look for parts of the package with alternating shale/siltstone and stratigraphic variations that could be interpreted as growth faulting
- Constraining fluid compositions and isotopes. See above, these have pretty good isotope haloes. Fluid inclusions next to useless due to fine grain size and questionable relationship of veins to mineralization (except for Silver King style)
- Ground based EM
- DHEM.

Cu (-Au) Deposits

Examples are: Mt Isa Cu, Mt Gordon, Gunpowder Ernest Henry, Osborne, Mt Elliott, Eloise.

These deposits are characterised by a distinctive epigenetic association, very strong structural controls (breccias, fault bends and intersections, rock competence contrasts), and modest to high copper grades with highly variable gold (Table 2). The spectrum of deposits ranges from almost pure copper-rich and Au-absent (e.g. Mt Isa and Mt Gordon in the WFB) to Cu-Au deposits of the iron-oxide-Cu-Au (IOCG) association which carry a diverse and complex additional element enrichment (U, REE, Co, Ba being the most common). The deposits are mostly of the low sulphidation variety being dominated by chalcopyrite and iron oxides. The timing of these deposits is dominated by geochronology centred on 1530 Ma, the same timing as emplacement of many intrusions of the Williams Batholith, and several lines of evidence point to a magmatic origin for some of the fluids at least in the EFB. In the WFB, where granitoids of this age are unknown, and for older IOCGs in the EFB, basinal fluid sources are likely. Much of the ~1530 Ma mineralisation appears to have formed by the initiation of strike-slip faulting and granite emplacement during the final stages of cratonisation.

Scale 1: Regional Analysis

- Thick volcano-sedimentary packages lying on rifted continental margin, actual arc rocks obscure or absent
- Widespread intrusions of likely same age as mineralisation
- Paleo- to Mesoproterozoic
- Continent-scale anomalous magnetism and gravity (big gradients, worms).

Scale 2: District Analysis

- Intense strike-slip fault networks in which it can be demonstrated that some were active during mineralisation
- Intensity of sodic-calcic alteration (for IOCGs) or chlorite-hematite+/- carbonate +/-talc alteration (for Mt Isa-Mt Gordon-style Cu). HyMap and ASTER data can be used to detect regional metasomatic alteration systems (e.g. sodic-calcic alteration in the Snake Creek Anticline: “white mica composition”, “white mica abundance”) or hydrothermal alteration along major fault zones (e.g. Mt Dore fault zone in the Selwyn Corridor: “white mica abundance”, “white mica composition”, “white mica relative water”)
- Strong rock property contrasts in association with fault offsets. Stress partitioning, stress anomalies and failure seem to be regionally important guides (Appendix 1, McLellan (b))

- For IOCG style – abundant granite intrusion into sediments or metasediments containing diverse rock suites (carbonates, pelites, mafic volcanics)
- For Mt Isa copper style – large contrasts in gravity, magnetics, rock property contrasts at this scale (e.g. Sybella Block vs Mt Isa valley)
- Multi-layer prospectivity analysis. Blenkinsop et al. (2005) work in the I2 project appears particularly effective both at this scale and at Prospect Scale (Figure 7)
- Broad-scale geomechanical analysis of fault arrays (Appendix 1, Ford and Blenkinsop; Ford et al. 2007).

Scale 3: Prospect Analysis

- Geostatistical and/or numerical analysis of parts of the fault arrays most favourable for failure in tension or extensional shear failure (weights of evidence, UDEC, FLAC), using 2D and 3D prospect data from 1:100 000 to 1:10 000 scales
- Trace element analysis of iron oxides for which transition elements should reveal distinctive signals in haloes, at least in the EFB
- Core or edges of aeromagnetic anomalies in conjunction with gradients in radiometrics and/or gravity, particularly in the context of a prospectivity analysis and geomechanical models
- Abundance of veins and potassic alteration overprinting earlier sodic-calcic alteration (for IOCGs) or dolomite-silica+/- hematite-chlorite (for Mt Isa – Mt Gordon style Cu)
- Hyperspectral mineral maps, alone or in combination with other geophysical data (e.g. magnetics, radiometric) can be used to detect not only possible host rocks, but also alteration assemblages and their spatial distribution. A good knowledge of the mineralisation-related alteration assemblage and its spatial distribution in combination with a good knowledge of the geology (calibration) of the investigated area is required
  - Amphibolites are host rocks for some of the IOCGs in the EFB (e.g. Mt Elliott, Selwyn Corridor) and can be separated from other mafic units (e.g. gabbros, dolerites) using mineral maps derived from hyperspectral data ("MgOH content", "MgOH composition", "amphibole/chlorite" and "Fe^{2+} ass. with MgOH")

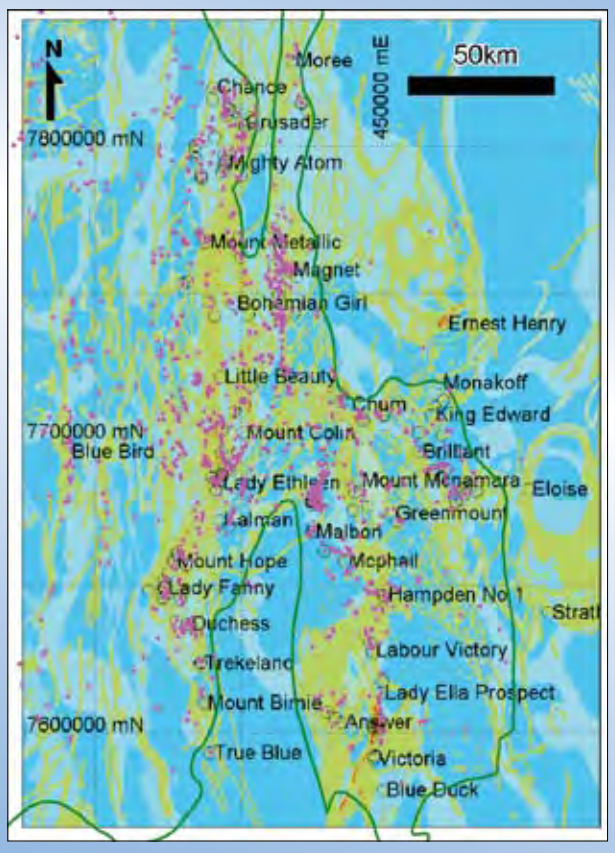

Figure 7: Prospectivity model for IOCG deposits in EFB, 9 layer model (from Blenkinsop et al. 2005).

- Spatial relationships of sodic-calcic and potassic alteration are important for the recognition of IOCGs in the EFB and can be detected with mineral maps derived from hyperspectral data (Na(-Ca)-alteration: e.g. "white mica composition", "white mica abundance"; K-alteration in mafics: "MgOH content", "MgOH composition", "amphibole/chlorite" and "Fe^{2+} ass. with MgOH" combined with "white mica composition" and "white mica abundance")
- The combination of magnetic, radiometric and hyperspectral data can be used to detect sodic-calcic alteration (integration of ASTER band 8 data with magnetic and K-radiometric data).

An undercover example and how to explore in this space

The northern extensions of the LRFT are considered highly prospective, from a district scale assessment. We have explored this space by employing discrete element modelling, using UDEC (Appendix 1 McLellan et al.) where particular fault intersections and an imposed stress field appear to be an effective tool in predicting the locations of existing deposits. Using criteria described in McLellan et al. (see Appendix 1), a series of UDEC outputs were exported to a GIS environment (Figure 8) of the interpreted fault architecture in this northern undercover region, an area of 150 x 150 km. These outputs show a range of parameters of maximum principal stress (σ_1), minimum principal stress (σ_3), differential stress ($\Delta\sigma$) and failure state (plasticity). This tool appears to be a good first pass tool in defining 10 x 10 km prospect areas.

Scale 4: Ore System Definition

- Detailed aeromagnetics with backup ground magnetics
- IP and/or other electrical methods
- Geochemical zonation studies from drill chips or core (Ernest Henry shows good 'radial' zonation) focussing on Cu, Fe, As, Mn, Co, As, K, Na, Ca
- Stress inversion studies on veins, faults etc to determine likely stress field during mineralisation
- Detailed structural mapping and/or interpretation of dilatant fault, fault-bend, fault/rock properties
- Numerical modelling using stress inversion results to impose far-field stresses on known fault or shear arrays.

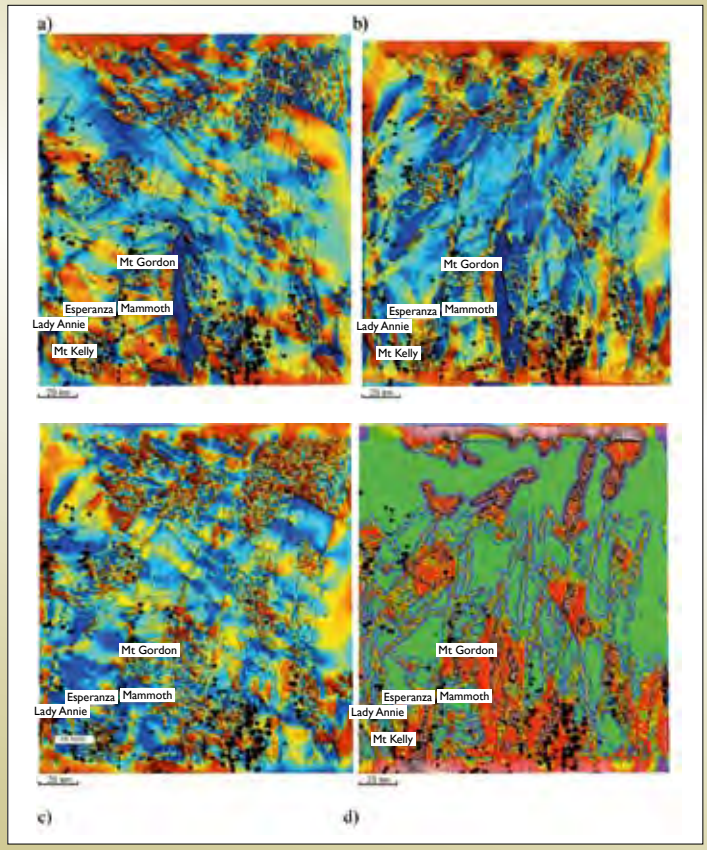

Figure 8: Discrete element UDEC modeling in the undercover northern extends of the Mount Isa region, a) maximum principal stress (σ_1), red colours indicating highest values of compressive stress, b) minimum principal stress (σ_3), red colours indicating minimum values of least compressive stress, highlighting areas of most likely fluid focussing, c) differential stress ($\Delta\sigma$), red colours indicating highest values, and d) plasticity or failure state, with red values indicating most intense failure. Cu occurrences shown as black stars.

PART III: THE SCIENCE BEHIND THE ANSWERS: THE 'FIVE QUESTIONS'

Q1: What is the Geodynamic Setting?

(Major Contributors: Murphy, Gessner, Bierlein, Hutton)

Introduction

Why is the Mt Isa-McArthur region so well endowed in world class deposits of different commodity groups (Pb-Zn-Ag, Cu, Cu-Au)? The answer is, in large part, determined by the geodynamic setting, involving far field and deep seated effects which are not well constrained but lead to a limited number of possible solutions. We are concerned here with the evolution of the lithosphere, that is, mechanically, the outer more rigid region of the Earth compared to the underlying asthenosphere, which flows during flexing of the lithosphere (Muirhead and Drummond 1991; O'Reilly et al. 2001). Broadly, there are two competing processes that impact on lithospheric strength and thickness (e.g. Pearson 1999): *vertical accretion* through asthenosphere-driven processes (e.g. plumes) that cool the interior of the Earth leading to lithospheric growth by mafic underplating and partial melting in an intra-continental setting (Etheridge et al. 1987), and *lateral accretion* through plate margin processes, allowing heat loss at the surface, with growth of the lithosphere through subduction/accretion and collision. Combinations of these processes over time are the likely drivers for the large metal endowment of the North Australian Craton (NAC; Giles et al. 2002; McLaren et al. 2005).

Crustal thickness and heat flow are key considerations. Heterogeneity of the deep lithosphere in Australia is evidenced by mantle xenoliths (O'Rielly et al. 2001), while thickness variations are determined from acoustic/elastic measurements (seismic reflection, refraction and tomographic data; e.g. Drummond et al. 1988; Simons et al. 1999) and from electromagnetic (MT) data (e.g. Heinson et al. 2006). The crustal thickness of the NAC, that is the Mt Isa, McArthur, Tennant Creek and Arunta regions, is up to 55 km compared to an Australian Proterozoic average of 45 km (Figure 9; Chevrot and van der Hilst 2000). The Moho depth (from tomographic data) actually varies significantly within the project region, from *ca.* 55 km in the south to *ca.* 40 km in the north. The elevated thermal regime in the NAC is related by McLaren et al. (2005) to the heterogeneous distribution of high heat producing granites (HHPG) in the upper 5-10 km of the crust. A high geothermal gradient at Mt Isa (Cull and Denham 1979) has been linked to widespread high-temperature-low-pressure (HTLP) metamorphism (Wyborn 1988). Additional thermal input is related to the

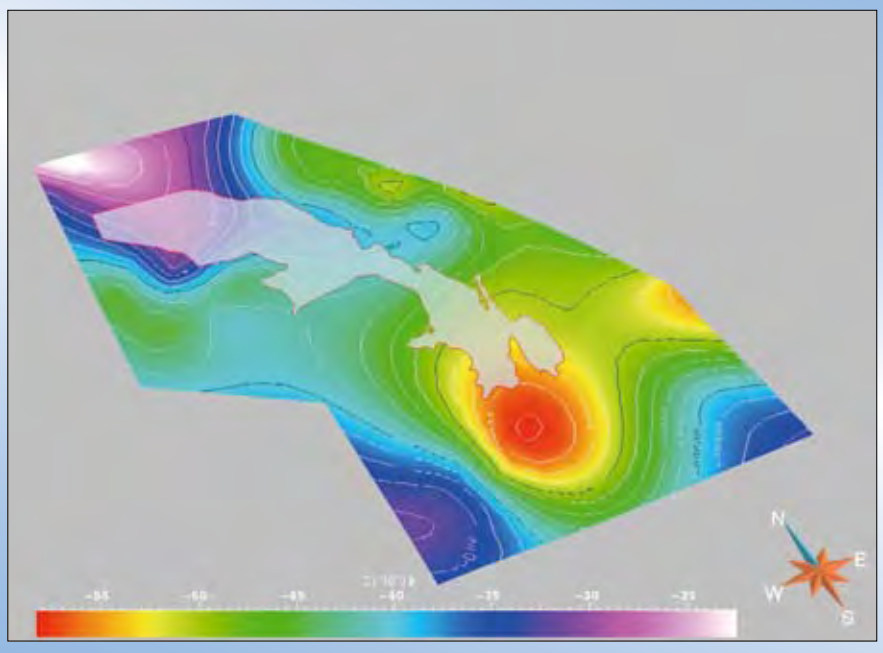

Figure 9: Depth to Moho surface and outline of Proterozoic inlier.

emplacement of mafic rocks, and high seismic velocities at depth in the NAC have been interpreted as underplated mafic rocks (Drummond and Collins 1986; Goncharov et al. 1996; MacCready et al. 1998).

Without direct evidence of a preserved plate boundary in the immediate environs of the inlier, the plate tectonic setting has to be inferred from internal units and their perceived relationships with other Proterozoic provinces in Australia. Much depends on reconstructing geometry in relation to the Curmanona Craton, the Gawler, Arunta and Georgetown regions, and involves post-Isan Orogeny rotations and translations (Figure 10; Giles et al. 2002). A feature of the Australian Proterozoic is the correlation of lithostratigraphic assemblages, together with similarities in deformation and tectonomagmatic histories amongst spatially distinct terrains (Giles et al. 2004). Some of the more remarkable features that require geodynamic explanation are:

- Tectonic switching, oscillating extension and contraction, which culminated in the Isan Orogeny at *ca.* 1600 Ma. There is apparent synchronicity between changes in depositional environment (Southgate et al. 1997), regional deformation events (Rubenach, Appendix 1), and changes in the Apparent Polar Wander Path (APWP), with hairpin bends in the ~50,000 km long trajectory (Indrum 2000)
- The inlier is unique in the overall architecture of the NAC by the dominance of north-south trends. There may be decoupling of the history at Mt Isa from that of the more inboard craton to the west and with outboard regions to the east (towards Georgetown). The major north-south trending rift at Mt Isa (LSB) only correlates with minor volcanism elsewhere in the NAC. Also, the extension-related volcanics in the overlying CSB appear to postdate the main felsic volcanism in the Northern Territory by about 10 Ma. The dominant north-south grain of the Mt Isa region is discordant to the northwest-southeast trending fabric to the west, interpreted as likely extensions of the stratigraphy in the Northern Territory, and to the east-west fabric to the east of the inlier. Although exploited by the Isan Orogeny D2 deformation, the north-south grain is regarded as a pre-existing architecture that ultimately relates to KLB. If this belt originated as a volcanic arc, it most likely parallels a north-south trending (west dipping?) subduction zone.

Extension and thermal input dominate the history. The tectonic environments to which this may be ascribed are: intra-continental rifts, core complex development, backarc basins, passive continental margins and volcano-magmatic arcs. Fore-arc, trench environments and ophiolites are not encountered, nor are large lateral terrane-scale translations

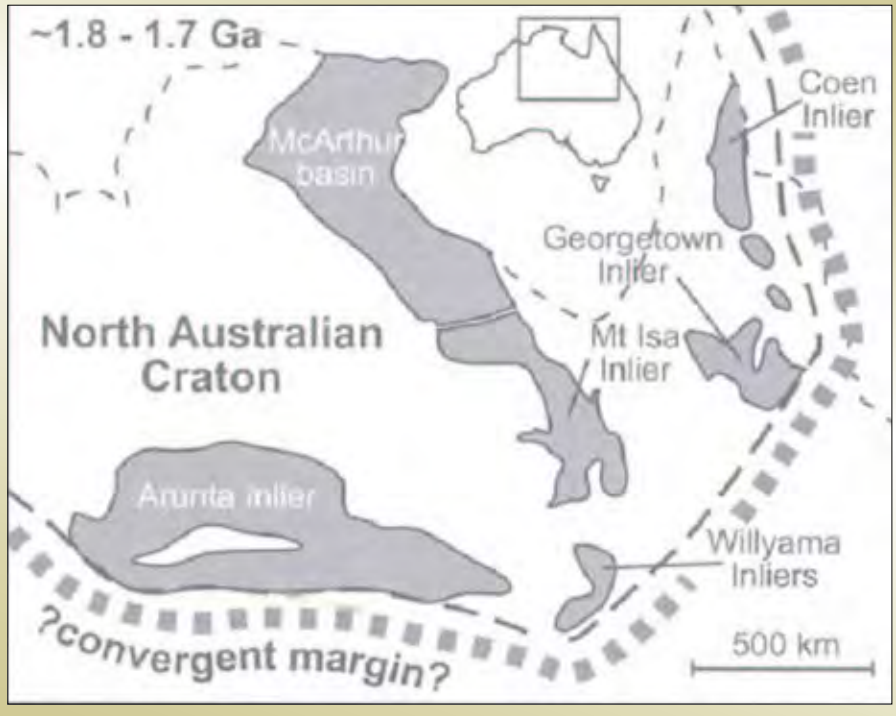

Figure 10: North Australian Craton (Giles et al. 2002).

required to explain the juxtaposition of different crustal components (Betts and Lister 2001). Vertical accretion via a mantle plume is not easily reconciled with the palaeomagnetic evidence of the widely varying location over time, unless more than one plume is implicated. There are some contrasting interpretations in the EFB and WFB – a backarc basin in the EFB (Giles et al. 2002; Butera et al. 2005), and an intra-continental rift in the WFB that transformed into a passive margin (Gibson et al. 2006). However, there is now compelling evidence that the inlier evolved as a coherent entity, with a shared history in the EFB and WFB. A distal continental backarc setting of the NAC advanced by Giles et al. (2002) has wide appeal (Figure 10), while noting uncertainty in the perceived northward polarity of subduction and distance from the subduction zone. A foreland basin during the upper parts of the Isa Superbasin is interpreted in the evolving Isan Orogen.

Discriminating a passive rifted margin from the inboard side of a continental backarc basin is, however, problematical (Bill Collins *pers. comm.*). The time and length scales of such systems can be considerable. For example, in modern analogues, the current eastern Australian setting is commonly called a passive margin, but in a broader context it actually developed because of Pacific slab retreat, and thus is the cratonic edge (upper plate) of a backarc basin. Mafic rocks provide insights to the tectonic environment, source regions and depth of melting. However, interpretations of tectonic environments using discrimination diagrams based on basalts are of limited use, as the inferred settings were defined in the 1970s, prior to modern backarc basin basalt chemistry research. Commonly, these rocks are transitional between arc basalt and MORB, as backarcs form by splitting of arcs and evolve to genuine seafloor given sufficient time. Most mafic rocks in the inlier (volcanics, dolerites 1670-1690, syn-D2 dolerites, 1520-1550 Ma dolerites synchronous with the Williams Batholith) show very similar results on Spider diagrams normalized to N-MORB's (Butera et al. 2005), i.e. flat and MORB-like for most of the High Field Strength (HFS) elements, but strongly sloping and spiky for the Large Ion Lithophiles and most incompatible HFS elements, which is typical of a subducted slab component (strong positive Pb anomaly, negative Nb anomaly, etc). The spider plots are very similar to basaltic rocks from back arcs.

Geological Evolution

The history of Mt Isa spans almost 400 Ma of the Proterozoic, and is broadly divided here into three time periods (Figures 11 and 12):

- >1900-1840 Ma: basement, Barramundi Orogeny, Cover Sequence 1 and Kalkadoon Leichhardt Belt (KLB) magmatism
- 1800-1640 Ma: Basin formation, volcanism, sedimentation and magmatism, encompassing three Superbasins (Leichhardt, Calvert, lower part Isa). Note that, in this analysis, we have distinguished two elements of the ISB, a pre-1640 Ma sequence from a post-1640 Ma sequence
- 1640-1570 Ma: Foreland basin (upper part ISB), Isan Orogeny and late stage magmatism.

>1900-1840 Ma: Basement, Barramundi Orogeny, KLB and Cover Sequence 1

The basement comprises supracrustal sediments and igneous rocks that were deformed and metamorphosed to amphibolite facies during the *ca.* 1870 Ma Barramundi Orogeny (Etheridge et al. 1987). In the centrally located KLB (Figure 11), the Kalkadoon Granite Suite (1.88-1.82 Ga) shows magmatic arc-type affinities that is the most likely be related to subduction (Wilson, 1978). Large scale volcano-magmatic input to the crust (the Kalkadoon Suite and Cover Sequence 1) suggests a magmatic arc above a thickened lithosphere. This may have formed inboard of an attenuated marginal basin to the east of the Pilgrim Fault. This fault might separate different basement elements (see Q2-Architecture), and is perhaps a fossil subduction zone (Figure 13). Subsequent thinning of lithosphere towards the east may be due to mafic underplating, as reflected in the high gravity responses (see Q2-Architecture). While there is isotopic similarity in the basement, the relationship of the Kalkadoon Arc to the NAC remains tentative, and an inferred subduction zone is placed along May Downs Fault (Figure 13).

1800-1640 Ma: Superbasin development

In this *ca.* 210 Ma period, three successive Superbasins developed. From a geodynamic perspective, a key question is the nature of the switching of extensional modes in different orientations leading to successive basin formation.

There is a spread of interpretations in this regard:

- Periodically rejuvenated intra-continental rift (Derrick 1982, O'Dea et al. 1997), punctuated by mild contraction and inversion
- Continental backarc (Giles et al. 2002; Betts et al. 2006) related to retreat of a northward dipping subduction zone during LSB and CSB, with the ISB as a sag phase due to ocean basin opening between Australia and Laurentia. Interspersed contraction is related to accretion events along the southern plate boundary
- Rift to rift-drift and passive margin development (Gibson and Hitchman 2005), *not* punctuated by mild contraction and inversion, but rather by differential uplift and block rotation. Was there an earlier (pre-Isa Superbasin) compressional deformation? Previous workers have suggested mild inversion/compression to shut down the LSB and CSB (e.g. Betts 1999) whereas Gibson and Hitchman's (2006) model proposes extension and tilt block rotation can account for apparent compressional features of other workers
- Ramp and strike slip basins, during ISB, related to far field subduction to the south (Scott et al. 2000)
- Later foreland basin in the upper part of the ISB in the LHP (McConachie et al. 1993).

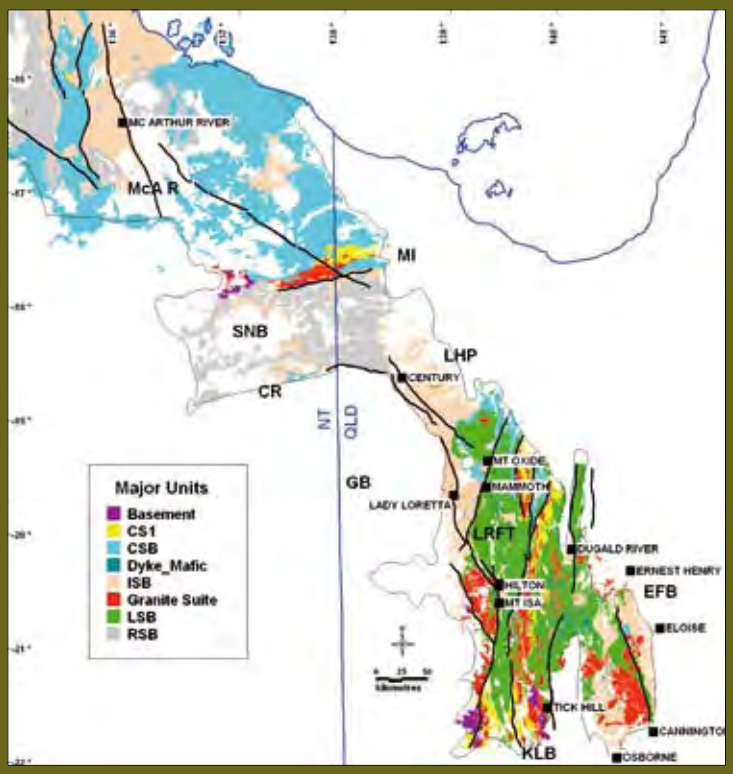

Figure 11: Major units and Superbasins. Key: CS1 = Cover Sequence 1, CSB = Calvert Superbasin; LSB = Leichhardt Superbasin; ISB = Isa Superbasin; RSB = Roper Superbasin; KLB = Kalkadoon Leichhardt Belt, LRTF = Leichhardt River Fault Trough, LHP = Lawn Hill Platform; SNB = South Nicholson Basin; MI = Murphy Inlier; McA R = McArthur River region; CR = Carrara Range; EFB = Eastern Fold Belt.

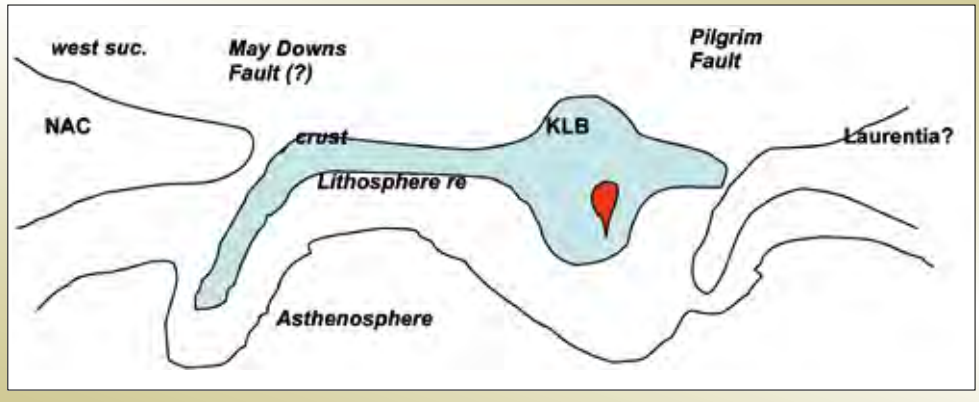

Figure 13: Sketch section of ~1850 Ma configuration.

Figure 12: Time-space plot.

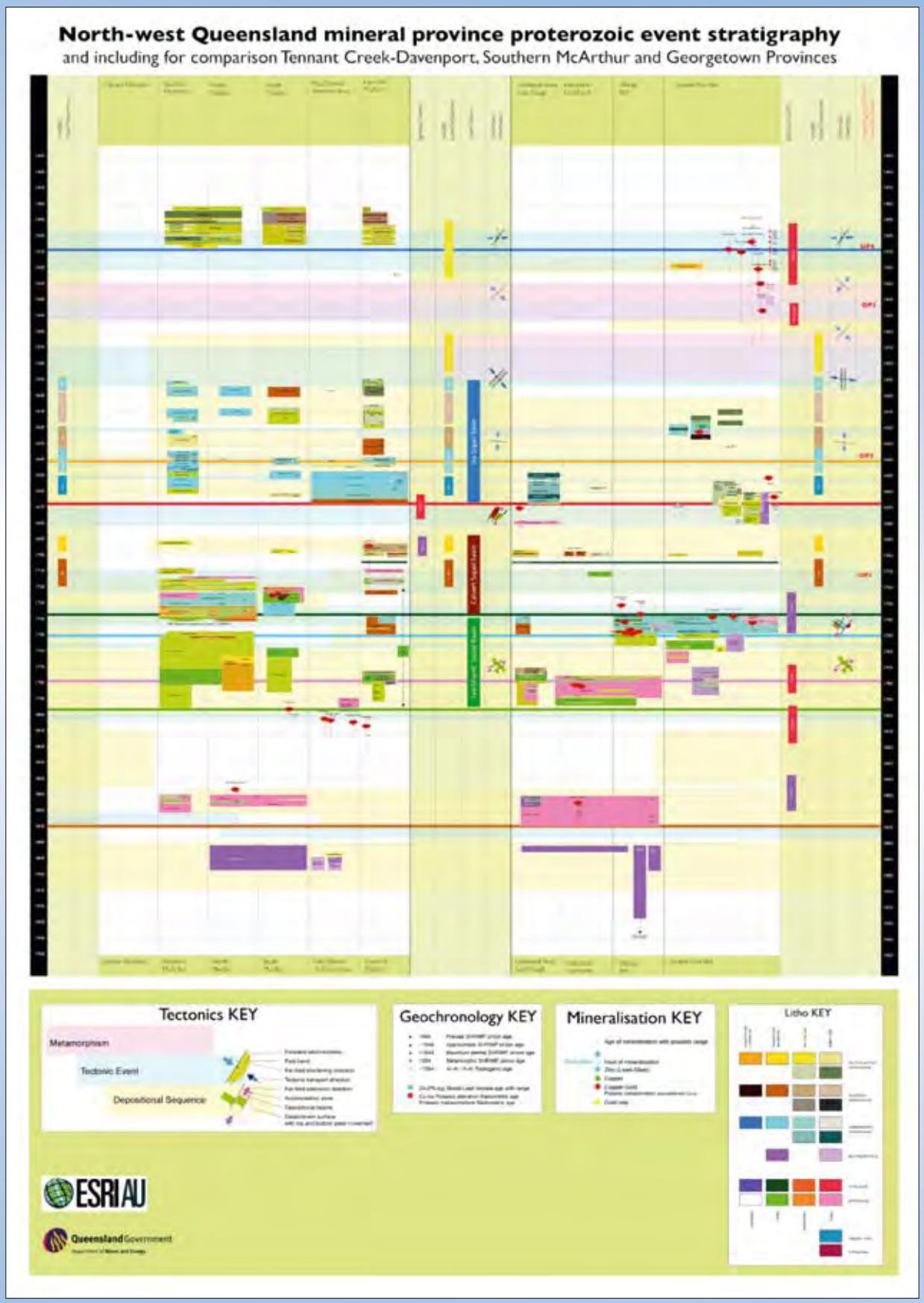

The Superbasins are:

- Leichhardt Superbasin (1800-1740 Ma): an intra-continental rift focused in LRFT with major north-south graben reflecting east-west extension (O'Dea et al. 1997; Betts et al. 2006) or, perhaps more correctly, ENE-WSW extension (NWQMPR 2000, Gibson and Hitchman 2005). O'Dea et al. (1997) suggest the influence of a mantle plume or upwelling asthenosphere to generate the thermal energy responsible for the flood basalts. Superbasin ended with development of mid-crustal (north-south?) oriented extensional detachment and emplacement of Wonga Granite (*ca.* 1745-1725 Ma; Figure 14)
- Calvert Superbasin (1740-1670 Ma): following 20 Ma hiatus, renewed extension on WSW-ENE trending growth faults and north-south trending LSB faults. A thinned continental crust is inferred further east (1712-1654 Ma; Giles et al. 2004; Beardsmore et al. 1998) based a deep marine depositional setting of the Soldiers Cap Group (SCG; but see Foster and Austin 2006). An apparent offset between locus of crustal extension (sedimentation in LRFT) and locus of sub-crustal lithosphere extension (magmatic rocks in LHP) is interpreted to indicate asymmetric extension on eastward facing detachment (Betts et al. 1998). Progression into deeper marine settings northeastwards, with upward fining cycles and thicker shales, suggests the rift may have evolved (drifted) into a passive continental margin setting (Figure 15 Gibson and Hitchman 2005). End of CSB sedimentation was closely followed by intrusion of the Sybella Granite at 1670 Ma (into the LSB), an "A-type" granite from lower crustal melting (Wyborn et al. 1988) in a core complex-model which presumably commenced during sedimentation, with magmatic inflation leading to uplift and cessation of sedimentation (Figure 15; Gibson and Hitchman 2005). There is no record of erosional breaching of the lower plate rocks during the Calvert sedimentary cycle
- Isa Superbasin, lower part (1670-1640 Ma): Sedimentation closely followed Sybella Batholith emplacement and represents a major series of transgressions. This has been related to decay of a thermal anomaly, initiated at 1710 Ma and culminated at 1670 Ma (Gibson and Hitchman 2005). The Isa and Lower McNamara Groups are interpreted as sag phase sedimentation (1670-1640 Ma) with episodic syn-depositional faulting in a fluviatile to shallow marine environment. The locus of post-rift subsidence in the LHP (Krassay et al. 1997) was where the earlier locus of Calvert magmatism and sub-crustal extension was focused. This argues for an asymmetric, east-facing extensional detachment (Betts et al. 1998; Gibson and Hitchman 2005).

1640-1570 Ma Isan Orogeny to post-orogenic history

Although the drivers and geometry of this orogeny are still poorly constrained, continental collision is most likely. Several deformations and thermal events are recognized (Figure 16). Early (D1) effects involved *ca.* 1640 Ma north-south compression which is variably preserved in the inlier (Rubenach, Appendix 1). During this deformation, sedimentation was on-going in the Upper McNamara Group of the LHP and McArthur regions. This may be

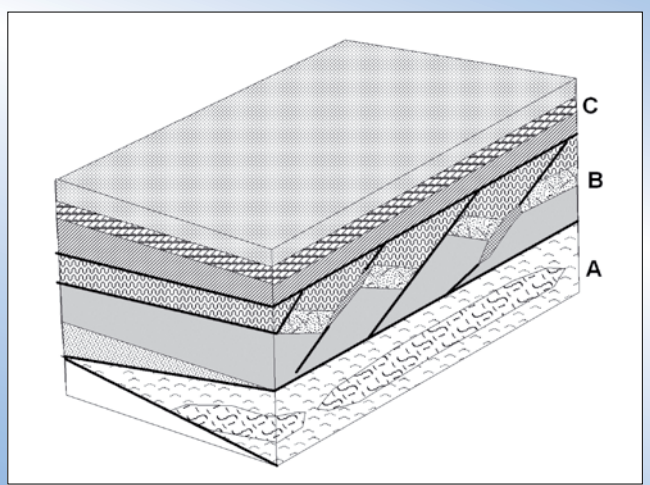

Figure 14: Schematic block diagram representation of Wonga Belt Detachment, A) Wonga Belt mylonites and granite, B) Upper plate Little Beauty Syncline, C) overlying mylonites. Based on Holcolmbe et al. (1991) and redrawn from G. Gibson presentation at 17 project meeting. (Vertical dimension ~ 3km).

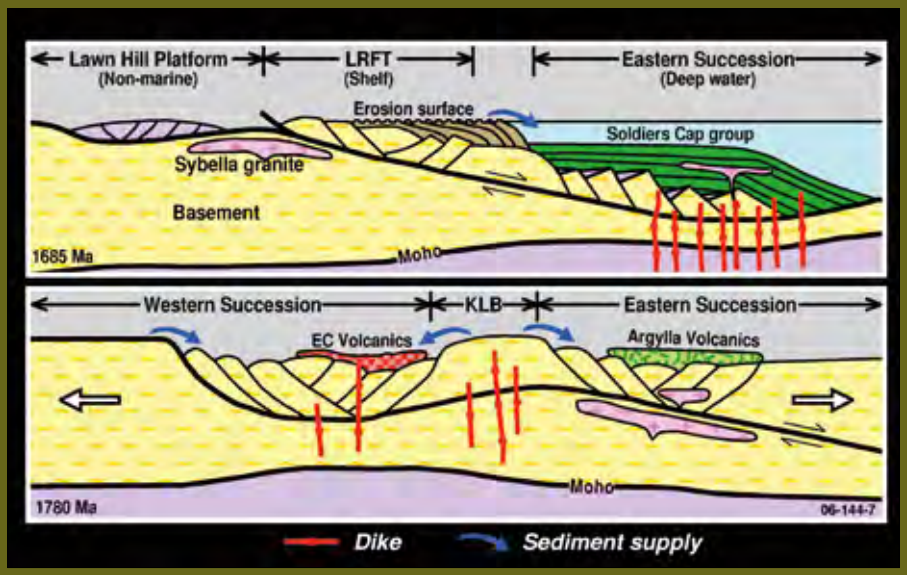

Figure 15: Extensional detachment model for the development of the LSB and CSB (from G. Gibson, presented at I7 Project meeting, 2005).

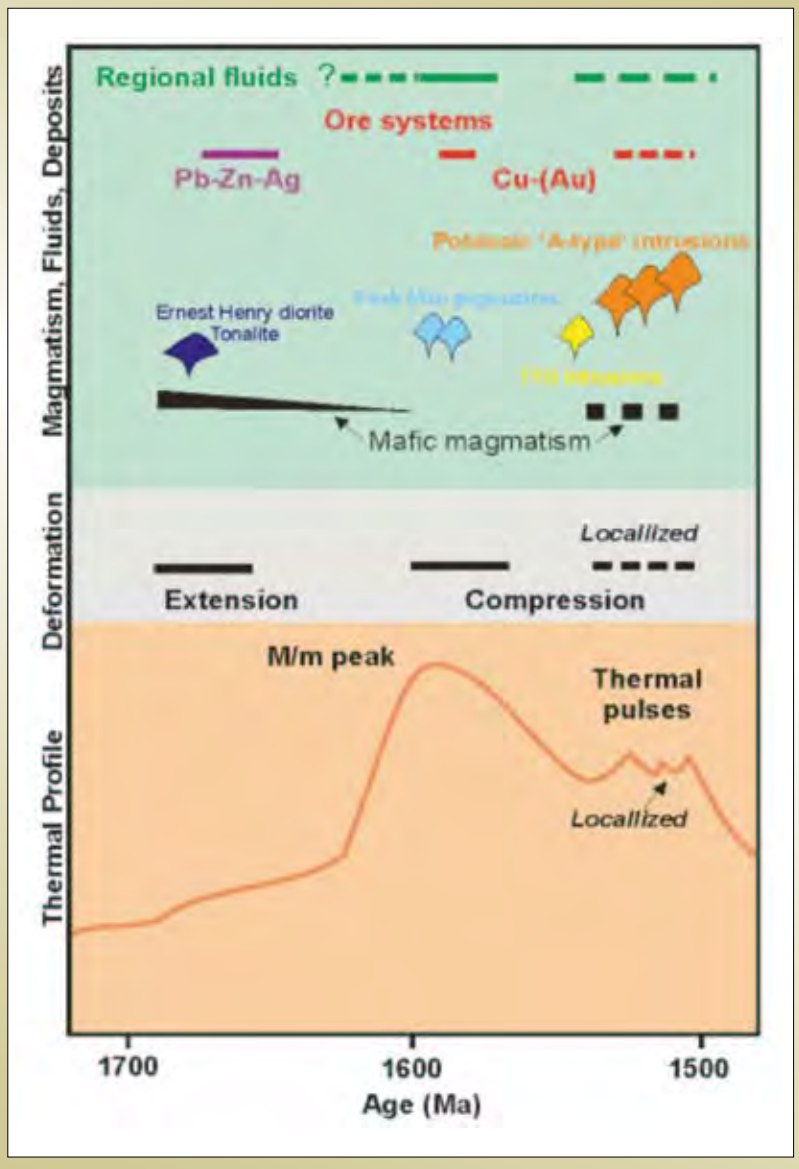

Figure 16: Schematic tectono-thermal evolution.

related to development of a foreland basin (1640-1590 Ma) and a topographic front to the south as the Isan Orogeny propagated (McConachie et al. 1993). The change in sedimentation correlates with a hair-pin bend in the APWP (Southgate et al. 1997; Indrum 2000). Generally, crustal over-thickening leads to uplift and widespread exposure of granulite facies rocks. The absence of granulites and of a significant foreland basin is notable. Granulite facies metamorphics, however, occur in the southern Arunta region (Scrimgeour et al. 2005) at about this time and may be interpreted as an orogenic front.

D2 involved thick-skinned east-west shortening (MacCready et al. 1998) in both the EFB and WFB. Folding in the LHP is much less intense, has a different orientation, and steep strike slip faults may be dominant here (Scott et al. 2000), as well as folding in relation to reactivated normal faults (Betts and Lister 2001). Following the peak deformation and metamorphism at ~1590 Ma, there was no significant uplift and erosion until after 1500 Ma (perhaps 1 kbar of erosion in the EFB). It is suggested that the previously thinned crust was restored to roughly normal thickness, resulting in no significant uplift and erosion.

Late- to post-orogenic magmatism (1550-1490 Ma) is a characteristic feature of the EFB, but is absent from the WFB. These magmas are interpreted as mantle-derived material which ponded at <30 km depths during early stage of partial melting and granite emplacement. Episodic thermal pulses overlapped with east-west compression (Figure 17). Isotopic data suggest a two component magmatic source: Paleoproterozoic (2.2-2.3 Ga?) crustal mantle or similar material recycled in crustal sequences and a juvenile mantle-derived component (ca 1.5-1.55 Ga). A tonalitic crustal source can generate 20-30 % melting but the volume of granite and periodicity suggest input of mafic magmatism and significant heating (>850°C) in the lower crust. A residence time of 1-10 Ma is suggested for ponding of magmas, with magma escape a function of %melt in an oscillating deformation. This may be related to slab roll-back in a back arc environment (Figure 17).

Thermal Modelling

The region is characterised by high heat flow, a high geothermal gradient with evidence from HTLP metamorphism, HHP granites and mafic underplating. Thermal modelling at a lithospheric scale was undertaken to evaluate some of the sensitivities deriving from these components under conditions of extension and compression. Results suggests that the enrichment of heat-producing elements resulted in very thin and hot continental lithosphere, for which an upper crust geothermal gradient of up to 50 °C/km and a total lithosphere thickness of 30 km are plausible. The resulting lack of shear strength in the thermally weakened lower crust and upper mantle favoured the exhumation of granite-cored metamorphic complexes in extension, and suppressed the formation of shallow detachments in contraction. Different burial depths of the basement during rifting produced a thermally-induced lateral strength contrast in the lithosphere which caused a preference for steep shear zones and fabrics during shortening of the rift complex during the Isan Orogeny. It is proposed that the deformation behaviour of hot continental lithosphere favours hydrothermal mineralization through the preferential generation of steep fluid conduits. Increased permeability along steeply dipping faults and shear zones enables fluids to flow at higher rates across gradients of pressure, temperature, and chemical concentration between magmatic, metamorphic and surface reservoirs. Higher flow rates facilitate advection of heat, fluids, and solutes, and therefore increase mineralization rates. This means that economic concentrations of minerals are much more likely to form in hot thin lithosphere, particularly in continental backarcs.

Metamorphic Core Complex model

The exhumation of mid-crustal rocks in the footwall of detachment systems creates basement highs adjacent to supra-detachment basins. The basement highs are predicted to have cooled and strengthened the lithosphere by exhuming the radiogenic enriched parts of the lithosphere to shallower crustal levels. Unconsolidated sediments in the basins had an insulating effect and increased the geothermal gradient. The juxtaposition of weak lithosphere in the basins, and stronger lithosphere in the basement highs made the lithosphere in the basin areas more sensitive to localisation of deformation during further extension and led to steepening of stratigraphy and existing structures during orogenic shortening, somewhat similar to what Weinberg et al. (2003) suggested for granite-greenstone belts in the Yilgarn craton of Western Australia.

Intrinsic vs external drivers for tectonic processes

Weak continental crust caused by burial of high-heat producing elements in the mid-crust has affected the tectonic style during extension and shortening events. An inability of the Isan lithosphere to support large stresses needs to be taken into account when far-field plate boundary processes are considered as driving forces for tectonic processes, as suggested by Betts et al. (2002 and 2006) for the NAC. In their model, an orogen-scale, west-over-east directed thrust is inferred to have cut the lithosphere during the main deformation event. From thermal modelling results, it appears questionable that stress levels could have been high enough to localise a plastic fault zone in weak middle crust, unless the overburden of the heat producing basement rocks had already been denuded at that stage. In addition to the findings of Pysklywec and Beaumont (2004), who suggested that Rayleigh-Taylor type convective instabilities controlled the tectonic evolution of the Mt Isa Province, Elkins-Tanton (2005) has shown that topographic

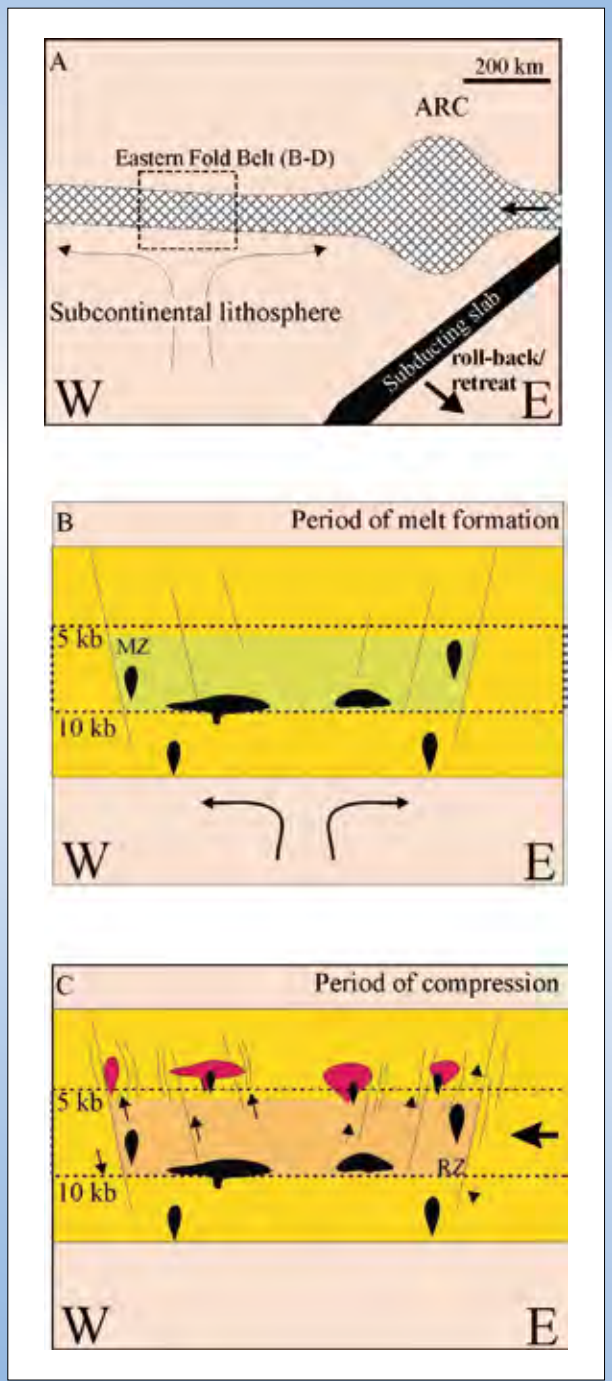

Figure 17: Episodic magmatism in a back arc setting for the Eastern Succession, with oscillating periods of melt formation during extension and periods of melt emplacement during compression (from G. Mark, presented at I7 project meeting, 2006).

uplift and hydrous, alkali-rich melts can form as a direct consequence of removal of the lower lithosphere by convective instabilities. This could very well have been the case at the time of the Williams-Naraku magmatic event, which marked the end of magmatic activity in the entire crustal province, and was followed by denudation and rapid cooling post-1490 Ma. (Spikings et al. 2001; Spikings et al. 2002). The restites of intruded and erupted melts in regions of upwelling (Elkins-Tanton and Hager, 2000), and crustal thickening (Houseman et al. 1981), would have contributed to increased density of the lower lithosphere, which may have been sufficient to drive gravitational instabilities and would have lead to delamination of parts of the lower lithosphere. In the case of the Mt Isa Province, the restites of the highly evolved Fe-rich Eastern Creek Volcanics, as well as those of source regions of the syn-rift granitoids melting events during rifting episodes would have provided a significant volume of high density material in the lower lithosphere across the Inlier.

Thickening of the crust during the Isan orogeny mostly occurred in the eastern part of the province, and may have been the ultimate cause for a delamination event which provided the advection of mafic melts into the mid-crust, causing the Williams-Naraku crustal melting event. This delamination event would also have caused a pronounced surface uplift, as shown by Stern et al. (2006) for the North Island of New Zealand, causing erosional denudation of high heat-producing mid-crustal rocks. The overall effect of denudation would be a lowering of the geothermal gradient, leading to strengthening of the lithosphere by increasing the thickness of the elastic-plastic upper crust. This increased strength of the upper crust would in turn favour structurally controlled, focussed fluid flow in brittle mid-to upper crustal settings, as observed in the late orogenic Fe-sulphide copper deposits at Mt Isa and Mammoth (Bell et al. 1988; Clark et al. 2002).

Thermo-mechanical process model

The substantial enrichment and redistribution of radiogenic elements in the continental lithosphere of the NAC, greatly increased the geothermal gradient during extension and orogenic shortening of the lithosphere. The increased geotherm resulted in a low strength lithosphere, where a relatively thin elastic-plastic upper crust overlay a thick viscous layer of partially molten mid- to lower-crustal material (Figure 18). This stratification exerted a crucial control on the tectonic style of deformation on a lithospheric scale during the multiple rifting events,

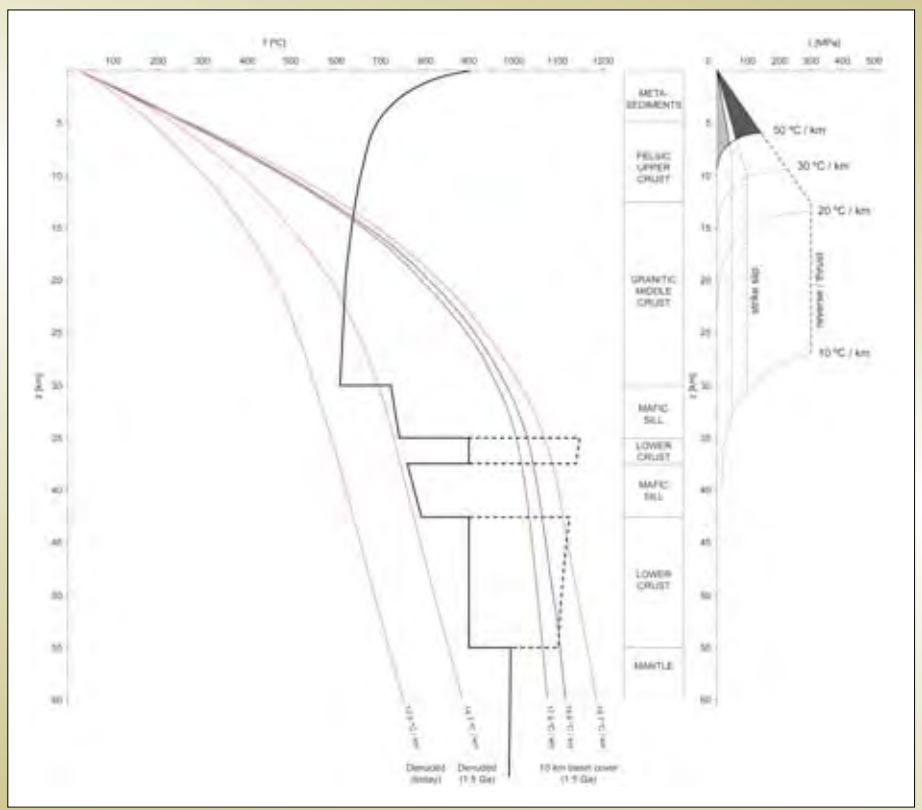

Figure 18: Lithospheric strength profiles for different thermal gradients (Gessner, in preparation).

as well as during contraction in the Isan Orogeny. Since the contribution of radiogenic heat production to the continental geotherm is highly sensitive to burial depth, cratonisation of high-geotherm lithosphere is only possible by denudation of the overburden. This seems to have occurred after the mid-crustal emplacement of the Williams-Naraku intrusive complex at the end of the Isan Orogeny. Some form of up-welling as part of a large-scale Rayleigh-Taylor instability is a plausible scenario to provide the large volume of basic magma required to melt the mid-crust.

For the extensional case, as has been explored in recent modelling (Richardson 2007), a number of consequences can be predicted in a weak lithosphere with a thick viscous layer:

1. Metamorphic core complexes form. The thick viscous layer in the mid-lower crust favours the formation of metamorphic core complexes over a distributed rifting style (Wijns et al. 2003). This leads to tectonic denudation, and exhumation of basement complexes to shallow levels, perhaps even to the earth's surface. These basement complexes may contain pre- to syn-tectonic granitoids

2. Rheological, thermal, and chemical segregation of the crust. Since denudation of mid-to lower crust material is limited to the basement complexes, a laterally inhomogeneous upper crust is generated, where basement highs occur next to supra-detachment basins. Since in the basement highs the heat-producing elements are at a shallow crustal level these segments may cool, and become stronger over time. Basins however, will stay hot and weak. The boundaries between these crustal segments are characterised by a 'telescoped' stratigraphy, and provide short transport distances between chemical reservoirs in the basement to those in basins

3. The lower crust is too soft to fail. This is illustrated by thermal-mechanical models of continental extension which showed that the high geotherm leads to softening of the mid to lower crust, and in the upper mantle when it is wet, i.e. a water-saturated olivine rheology is assumed (Richardson, 2007). This means that stress levels required to localise plastic shear zones in the lower crust are unlikely to be reached (Figure 19a). Even if the lithospheric mantle was dry and strong and shear zones could localise at this level (Figure 19b), fault zones that cut the entire continental lithosphere are unlikely to form. Therefore passive margins and oceanic basins are not likely to forma as long as a weak lower crust can respond to lateral pressure gradients by ductile flow (e.g. Block and Royden, 1990). In this situation, continual stretching of the lithosphere will result in overall distributed exhumation of deep lithosphere levels and decompression melting of the mantle leading to magmatic accretion at the base of the crust. This also means that there is a 'continuous' presence of magma as long as the system stays insulated by basins and radiogenic upper crust

4. Saline basins. The basins formed in hot continental rifts will tend to be shallow and highly saline, providing fluids which are highly capable to leach base metals from magmatic and metamorphic basement source rocks (e.g. Yardley, 2005; Yardley and Baumgartner, 2007).

For the contractional case, the hot and weak lithosphere architecture will lead to a number of effects following from the 'vice-tectonics' model (Cruden et al. 2004; Cagnard et al. 2006a,b):

- Vertical partitioning of deformation. Thickening of the lithosphere will force the thick, predominantly viscous layer in the lower crust to flow laterally, while the elastic-plastic upper crust will be folded into steep upright fold trains (Cagnard et al. 2006 a, b; Cruden et al. 2004)

- Lateral partitioning of deformation. The segmentation into cool and strong basement complexes and weak and hot basins leads to more deformation in the basin regions, and less deformation in the basement complexes, with a strong localisation of deformation predicted across regions of mechanical contrast, as for example the boundaries between basement complexes and basins

- Creation of vertical permeability. Steepening of upper crustal stratigraphy and initially shallow dipping structures (e.g. shallow dipping extensional detachments), will result in a steeply dipping fabric, which will facilitate vertical permeability. The key effect of vertical permeability on mineralization in hydrothermal systems is enhancing fluid flow across steep gradients of pressure and temperature

- Orogen-parallel stretching and formation strike slip systems. Steepening of the structural grain will favour orogen-parallel stretching and strike-slip movements in subsequent increments of the same shortening event, or during a later event with a similar shortening direction. Orogen-parallel stretching may boudinage the mechanically stronger basement complexes, leading to enhanced magma and fluid permeability in boudin necks. For example, the ~1530 Ma lithium-rich pegmatites intruded in a boudin-neck position (Figure 1 in Rubenach (1992)) of the ~1650 Ma Sybella Batholith (Connors and Page, 1995), suggesting increased permeability for melts and fluids during orogen-parallel stretching. In addition, the syn-copper mineralization deformation geometry is related to oblique convergence across the Mt Isa Fault system, which was resolved by strike-slip movements along steep foliations and structures (Bell et al. 1988; Gessner et al. 2006; Swager, 1986). Finally, changes in strike direction along strike-slip systems in general are likely to be prime locations for structurally controlled ore deposits (Cox and Ruming, 2004), since they provide vertical zones with enhanced fracture permeability
- Short-cuts between chemical reservoirs. Strike slip faults will further enhance mineral prospectivity by providing short pathways between deep and shallow fluid reservoirs, and therefore facilitating fluid flow across gradients of chemical composition
- Higher permeability on the mine scale. The overall steep fabric orientation in the upper crust favours the formation of highly permeable fracture networks in steeper orientations than would otherwise be predicted by Andersonian fault theory (Sibson and Cathles, 1990).

Cratonization of the Mt Isa Province was probably achieved sequentially by (i) the local exhumation of high-heat-producing basement in the lower plates of metamorphic core complexes, and (ii) the erosion of upper crustal levels after crustal shortening.

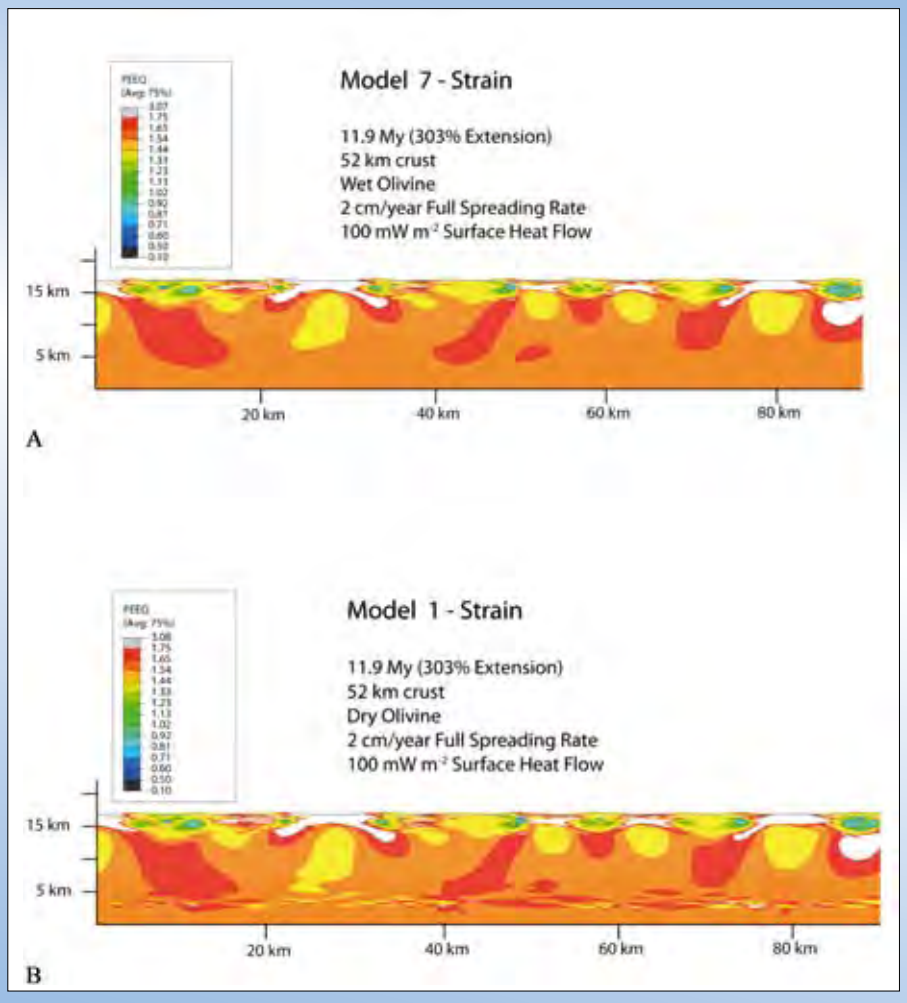

Figure 19: Strain pattern in thermal-mechanical coupled models of extension in high heat flow continental crust with A) wet and B) dry olivine rheology.

Conclusions

The geodynamic setting for metallogenesis in the Mt Isa region has been related to a) the position and geometry of the terrane as an intra-cratonic rift on the fringes of the NAC, where earlier subduction had occurred (KLB arc), and/or b) its location as a distal back arc basin related to subduction elsewhere (to the south and east?), and/or c) in a passive margin. Regardless of which of these settings holds most validity and during what time period, extension and thermal input dominate the early history. A high geothermal gradient suggests a relatively thin brittle crust which nucleates steep faults, over a hot, soft continental lithosphere that undergoes repeated extension and core complex development. Cycles of crustal extension and Superbasin sedimentation are interspersed with thermal pulses and synkinematic felsic magmas and emplacement of mafic rocks. This is overprinted in a collisional-style orogeny, where early north-south shortening overlapped with sedimentation, and culminated in east-west convergence which reactivates the rift-related architecture. It is considered that the orogeny restored the thinned crust to a greater than average thickness for the NAC.

Q2: What is the Architecture?

(Major Contributors: Murphy, Hutton)

Introduction

An assessment of the architecture is built from an understanding of the stratigraphy, structure, magmatic and thermal evolution. There are essentially four Superbasins developed (Figures 11 and 12): LSB, CSB, ISB and Roper (RSB). The geographical distinction of EFB and WFB, separated by the older KLB, has tended to mask some important commonalities in architecture. However, correlations of stratigraphic units, the nature of sedimentary facies belts and linkages in detrital source regions strongly suggest widespread Superbasin development (Betts et al. 2006). This is further emphasised through 3D modelling of the geology (Appendix 1, Murphy et al.). Architecture-related questions of interest are:

- What are commonalities and differences between the WFB and EFB?
- How extensive are the Superbasins in 3D and under cover?
- Which are the controlling faults?
- Do crustal-scale extensional detachments control the Superbasins?
- What was the permeability distribution at the times of mineralisation?

Stratigraphic Architecture

Pre-Barramundi Basement

These comprise mostly gneissic (meta-sedimentary?) rocks and granitoid sweats which have been intruded and metamorphosed (some to migmatites) during the Barramundi Orogeny (1.87-1.85 Ga). Key points are:

- In the LHP and WFB, basement outcrops to the west of Mt Isa, to the northwest in the Carrara Range and in the Murphy Inlier, and is interpreted at relatively shallow depths elsewhere (Figure 11; NWQMPR 2000). In the WFB, the basement/cover contact relationship is mainly interpreted as autochthonous but locally sheared
- The KLB represents a basement-cored ridge on which Cover Sequence 1 developed. Note, the extent of basement in this region is probably more than is represented in the current 1:100 000 scale geological maps. A relative homogeneous isotopic signature is apparent between KLB basement and that to the west of the Mt Isa Fault (Bierlien and Betts 2004; Bierlein et al. 2008), and both have inherited Archaean signatures. The eastern boundary of the KLB is the Pilgrim Fault and related geophysical gradient (Pilgrim Worm; Blenkinsop et al. 2005)
- In the EFB, no rocks older than *ca.* 1760 Ma are recognised; this also applies to the Georgetown Province to the east. The Double Crossing Metamorphics were regarded as possible basement (Blake 1987) but are now interpreted as part of the Argylla Formation (*ca.* 1760 Ma; Foster and Austin 2007). The basement/cover contact relationship in the EFB may be a para-autochthonous (Blenkinsop et al. 2005)
- Mafic rocks in the EFB provide evidence for the nature of the basement, with depleted mantle T_{DM} ages ranging from 2.45-2.57 Ga., which closely resemble the ca 1.89-1.85 Ga felsic basement rocks (T_{DM} 2.45-2.58 Ga; Mark et al. 2005; Blenkinsop et al. 2005). Broad-scale Nd isotope patterns of the 1.74 Ga magmatic rocks suggest the mid- to lower-crustal basement east of the

Pilgrim Fault has younger average crustal residence ages (~2.25 Ga) than that to the west, and implies the Pilgrim Fault is a major basement boundary (Blenkinsop et al. 2005, 2008). Note, however, the complexity in Lu-Hf-O-U-Pb isotopes means that differing Nd model ages from different granite suites does not necessarily mean that a basement terrane boundary has been crossed (Bill Collins *pers. comm.*)

- The broad inlier-scale variation in gravity signature of a high intensity eastern region and a lower intensity western region (see Figure 10 in Murphy et al., Appendix 1) must be explained by sources other than basement. More basement outcrops in the western regions where gravity is relatively low. The eastern highs may be related to a high proportion of mafic rocks in the mid to upper crust, as is also indicated from the AGCRC seismic profile (MacCready et al. 1998). The low intensity region to the west, below the Georgina Basin, may be related to granites in the basement (NWQMPR 2000)
- Faults that penetrate the basement have influenced Superbasin development (Gibson and Hitchman 2005), a corollary being that the major bounding faults within the Superbasins may be re-activated basement faults. Fracturing and propagation of faults from the basement into the cover rocks may be an important mechanism for focussing fluids into or out of the metamorphic rocks. The localisation of upper level deposits and related quartz veins (Polito et al. 2006 a, b, c) in relative proximity to first order (i.e. basement penetrating) faults is well know (Huston et al. 2006)
- An interpreted top of basement shows a relatively continuous, undulating form (Figure 20). A major change in depth to basement occurs across the Pilgrim Fault, the level on the eastern side is inferred from regional geophysics. There is a large change in basement elevation southwards across the Murphy Ridge. In the McArthur River region, this interface is interpreted as deepening westwards beneath the Roper Superbasin.

Cover Sequence 1

- Cover Sequence 1 (~1.86 Ga; Blake and Stewart 1992) volcanics and co-genetic magmatic rocks occur in the KLB, Murphy inlier and southern McArthur regions. There is a subsequent widespread magmatic event, the Toby-Ewan Suite (Figure 11; NWQMPR 2000). The KLB was a particular focus of crustal addition and defines a linear north-south trending magmatic

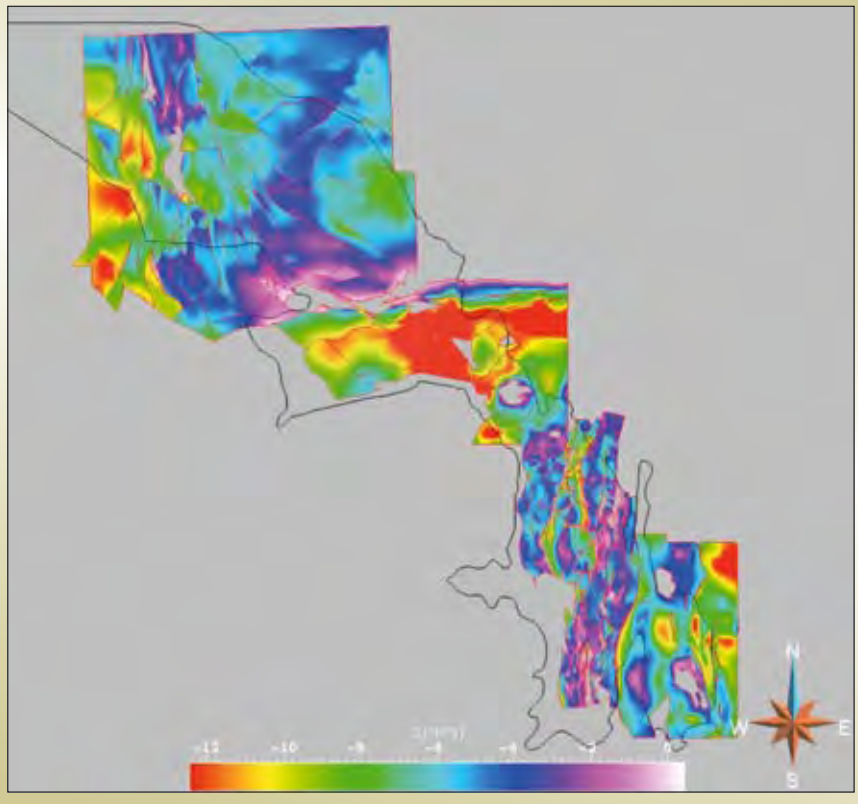

Figure 20: Image of interpreted depth to top to basement based on 3D modeling (Murphy et al., Appendix 1).

belt with a strike length of 300 km (Figure 11) and, including undercover to the south and north, has a combined strike length of >700 km. It is a unique feature of the Proterozoic in northern Australia. Felsic volcanics within this may be potential source rocks for Pb-Zn metals.

1850-1800Ma

This time interval is generally not described in the Mt Isa region and is more related to Tennant Creek and the Davenport Ranges in the Northern Territory to the west. Mafic rocks to the west of the Rufus Fault Zone in the southern Mt Isa region have been equated with the ECV (in the LSB), however, these have trends which suggest correlation with mafic rocks in the Tennant Creek and the Davenport Ranges, rather than mafic volcanics in the LRFT. Furthermore mafic and felsic volcanics in the Saint Ronans Metamorphics have yielded ages of 1829 Ma (Chris Carson GA, personal communication) which are equivalent to the Edmirringee Event in the Tennant Creek and the Davenport Ranges. Other mafic volcanic events in the Northern Territory, such as the Mount Hay event (~1810 Ma) are not found at Mt Isa. It is possible that mafic volcanics SW of Ardmore (Oroopo Metabasalt), which has trends that link to the Tennant Creek and the Davenport Ranges, may belong to the Mount Hay event. This suggests that the Northern Territory geology continues eastwards to as far as the Barramundi Worm (Hobbs et al. 2000; Murphy *in* Gibson and Hitchman 2005).

Leichhardt Superbasin (LSB)

The LSB encompasses "Cover Sequence 2" and is best represented, volumetrically, in the LRFT, where deposition occurred in a north-south trending graben with thick sequences of mafic volcanics (with high magnetic intensity) that give way to much thinner sequences to the west. It comprises three Supersequences:

- The *Guide Supersequence* of basal greywacke, conglomerate and bimodal to felsic volcanics overlain by quartzite-dominant sediments. Mostly exposed in the southern parts of the WFB, these were probably sourced from an emergent KLB to the east. Correlative units occur in the Murphy inlier and the McArthur region
- The *Myally Supersequence* of flood basalts and sediments formed in a continental rift setting (ECV). Temporal equivalents occur to the east and the northwest, in the LHP and the Murphy inlier. Broadly bimodal in character, with more felsic elements in the east, and the Argylla Volcanics as coeval with or slightly older than the ECV. This event is accompanied by intrusive rocks at mid crustal levels. The volcanics are in turn overlain by feldspathic and quartz sandstones where active extension in a marine to lacustrine setting was followed by sag phase red-brown shales and siltstones in a tidal or lagoonal environment
- The *Quilalar Supersequence* marks a return to widespread quartzo-feldspathic sandstone deposition, suggesting renewed extension, and followed by a sag phase of dolomitic sediments and carbonates in both the WFB and EFB
- Oppositely dipping boundaries of the rift are inferred growth faults with a dominantly north-south trend in the LRFT. These faults are partially re-activated and may be occluded by younger sequences, and the LSB extends across the rift shoulders as thinner sequences. The eastern boundary is placed along the Quilalar/ Dajarra Fault, while the western boundary of the LRFT is at least in part defined by the Mt Isa Fault, and structures to the northwest (Twenty Nine Mile Fault)
- The Mt Gordon Arch is interpreted as having influenced LSB sedimentation, with the Myally Supersequence thinning across it (Derrick 1982). Gibson and Hitchman (2005) interpret it as a syn-extensional feature, though accentuated by later deformation. Numerical modelling of extensional deformation (Appendix 1, McLellan, (b)) indicates emergence in the central region of the trough, adding support to the Gibson and Hitchman (2005) interpretation
- The oldest known rocks in the EFB are the Argylla Formation dated at 1760 Ma in the core of the Duck Creek Anticline. These were also deposited in a graben structure and have been equated to the LSB rocks to the west, included with the Myally Supersequence. However, the mafic Marraba Volcanics in this region are younger than the ECV as they overlie felsic volcanics dated at 1760 Ma. Deposition in the Duck Creek graben is interpreted to have occurred during a lapse in sedimentation in the LRFT. The Pilgrim Fault marks the boundary between the LRFT and the Duck Creek graben

- An image of the 3D distribution of the LSB is shown in Figure 21, colour-coded by depth to base and by apparent thickness. This emphasises the LRFT with up to 13 km of LSB, and also shows increased thickness in the southern reaches of the Murphy inlier.

Calvert Superbasin (CSB)

The CSB, part of "Cover Sequence 3", comprises two Supersequences, Big and Prize, separated by an unconformity. It is best represented in the WFB, LHP and Myally Shelf and is extensive in the McArthur River region (Figure 11). Correlation is less well constrained in the EFB, other than with the Llewellyn Creek Formation in the Snake Creek region (Foster and Austin 2007).

- The *Big Supersequence* comprises coarse clastics (Bigie Formation) that infill topography then bi-modal magmatism (Fiery Creek Volcanics) and coeval granite (Weberra Granite, 1710 Ma). These are more localised in development in the WFB and LHP, and not recognized in the EFB
- The *Prize Supersequence* comprises sediments formed in a deltaic to shallow marine transgression with siliciclastics, deepening into shallow marine shelf with shales and quartzite, interpreted as thermal relaxation

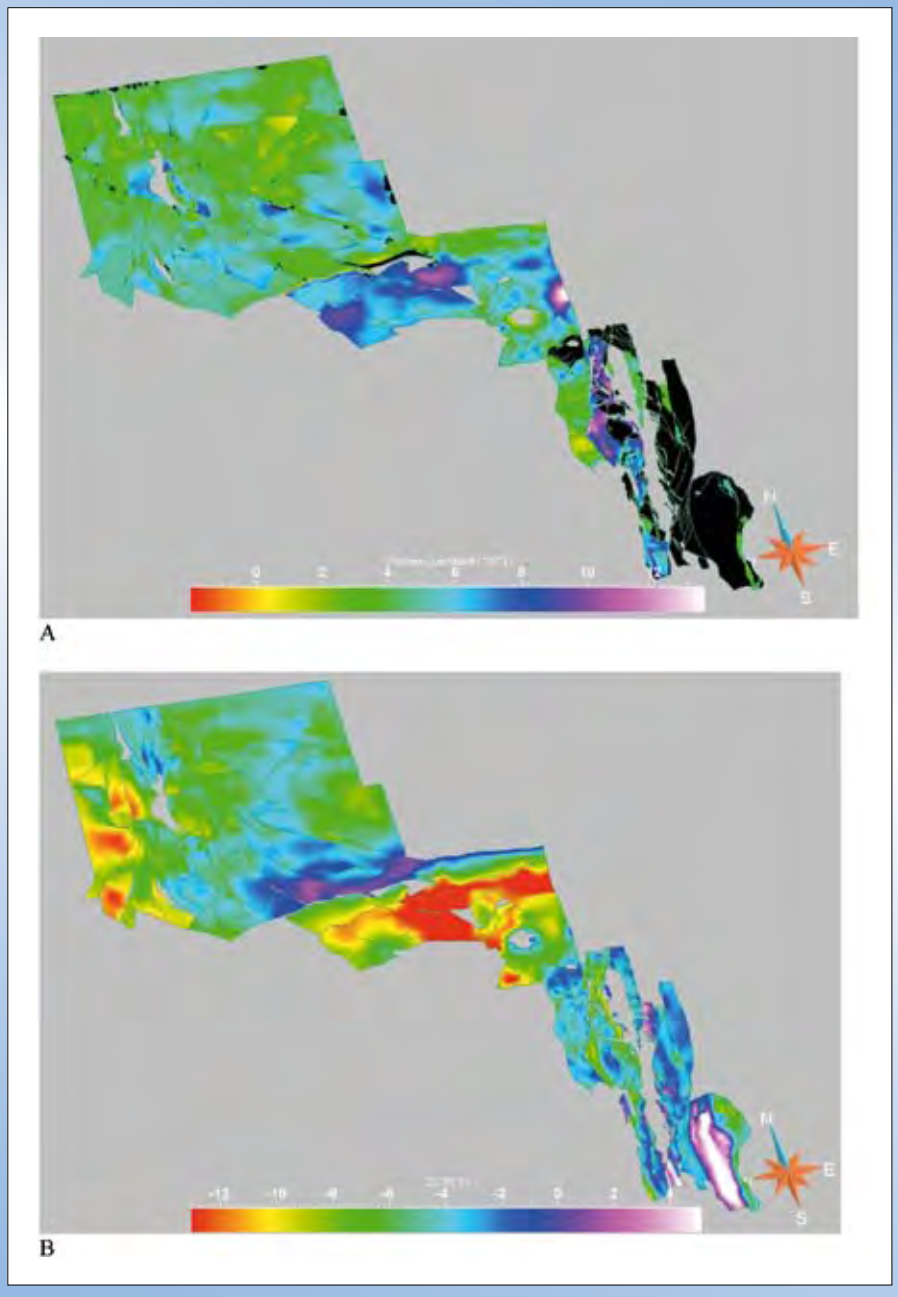

Figure 21: Leichhardt Superbasin imaged by A) apparent thickness and B) depth to base from 3D modeling (Murphy et al., Appendix 1).

and sag sedimentation. Sedimentary linkage across the KLB was established between the WFB and Mary Kathleen domain during this interval (Neumann et al. 2006). The basal Surprise Creek conglomerate sits above a regional unconformity which extends from Ardmore in the south to Fiery Creek in the north, a distance of *ca.* 150 km. The nature of this unconformity, whether related to a contractional or extensional event, is still uncertain. If extensional, the event could have occurred synchronously with the Fiery Creek Volcanics. If compressional, then the event presumably post-dates the Fiery Creek Volcanics. Tilt block rotation during extension in a passive margin setting of may best explain the field relationships (Gibson and Hitchman 2005). Magmatic input occurred late in history (Carters Bore Rhyolite, 1678 Ma)

- Overall NNE-SSW directed extension in LRFT with a northward deepening basin (Gibson and Hitchman 2005). Calvert-aged faults (e.g. Fiery Creek Fault) typically northwest-southeast trending, northwest dipping in LHP (Sweet and Hutton 1982; Betts et al. 1998, 1999, 2004), compared to east-west trending in the LRFT. One scenario is that faults on the LHP were dextrally rotated during the Isan Orogeny into an east-west orientation in the LRFT. A preferred explanation is that the different geometries are inherited from the underlying LSB and basement architecture (Betts et al. 2006; Gibson and Hitchman 2005)

- Cessation of the CSB is followed by emplacement of the Sybella Batholith (1670 Ma). Detrital zircons in the SCG (Llewelyn Creek Formation in Snake Creek region) show input of a 1670 Ma source region, suggesting derivation from unroofed Sybella Granite (Neumann et al. 2006) or equivalent magmatic rocks (Giles and Nutman 2003). These deep marine turbidites contrast with the CSB sediments in the Mark Kathleen Domain and a locus of this change is placed along the Cloncurry Worm, a deep seated geophysical boundary, re-activated locally as the Cloncurry Overthrust (Austin and Blenkinsop, this volume)

- An image of the 3D distribution of the CSB is shown in Figure 22, colour coded by apparent thickness and depth to base. The locus of deposition has shifted from the LRFT, although still with significant thickness, and the LHP has variable thickness, with increases towards the Murphy inlier.

Isa Superbasin (ISB)

The ISB has a widespread distribution in the LHP and the LRFT, with an overall thinning towards the west. Current interpretation separates the Superbasin into two sequences (Figure 12): a 1670-1640 Ma sequence (Mt Isa and Lower McNamara Groups) and a 1640-1590 Ma sequence (Upper McNamara Group). It is characterised by a succession of facies belts of shales, siliciclastics and carbonates with seven Supersequences separated by maximum flooding surfaces (Southgate et al. 1997).

- In the 1670-1640 Ma interval, two Supersequences are recognized: *Gun* and *Loretta*. In the lower parts, quartzites are followed by shales and are in turn overlain by shallow marine stromatolitic carbonates and cherts on the LHP, while a deeper marine environment existed to the east in the LRFT (Southgate et al. 2000b). The Mt Isa Group is dominated by shales and dolomitic siltstone while the Lower McNamara Group mostly contains stromatolitic dolomite. Possible interpretation is a shelf to deeper water progression from west to east, essentially across the margin of the LRFT. These rest on basement to the west of the May Downs Fault. Stratal thickening towards NW- and WNW-trending normal faults indicates architecture inherited from the underlying CSB. Rocks of this age are now recognised in the EFB, including the Milo Beds in the Tommy Creek block with depositional ages of between 1660-1653 Ma, and shale hosts of the Dugald River deposit with a maximum depositional age of *ca.* 1686 Ma; the Pb/Pb age of the deposit is *ca.* 1665 Ma. This shows that the Superbasin was inlier-wide and is now only sporadically preserved in synclinal keels or faulted blocks

- In the 1640-1590 Ma interval, five Supersequences are recognized: *River*, *Term*, *Lawn*, *Wide* and *Doom*. These crop out mainly in the NW of the Inlier and appear to be deposited in a different setting to the Lower McNamara and Mt Isa Groups. Seismic profiling in the area north of Lawn Hill shows an inversion during River Supersequence (1640-1630), with deposition of the Shady Bore Quartzite representing a significant change in environment (Southgate et al. 1997). Units above this show wedge-shaped geometries, thinning across the Murphy Ridge and thickening to *ca.* 8 km in the LHP (Krassay et al. 1997). East of Lawn Hill, in the Kamarga Dome, 1820 Ma granite (basement)

lies within a few metres of the base of the McNamara Group indicating no thick sequences of LSB or CSB developed across the dome. The Kamarga Dome shows evidence of controlling sediment thickness and supply during ISB (Sweet and Hutton 1982) and was probably emergent since or before CSB-times. Rocks of this age are also found in the EFB: in the Tommy Creek Block, in the Marimo Basin, the Quamby Conglomerate in fault-controlled graben adjacent to the Boomarra Horst, and the Young Australia Group (Foster and Austin 2007; formerly in the SCG; see Figure 12)

- An image of the 3D distribution of the base of the ISB is shown in Figure 23, colour coded by apparent thickness and depth to base. The locus of greatest thickness values is to the south of the Murphy inlier, in the Isa Valley and in the EFB.

Roper Superbasin (RSB)

This is represented by the South Nicholson and Roper Groups (Figure 11 and 12) which unconformably overlies the ISB Superbasin and locally rests on basement. Previous

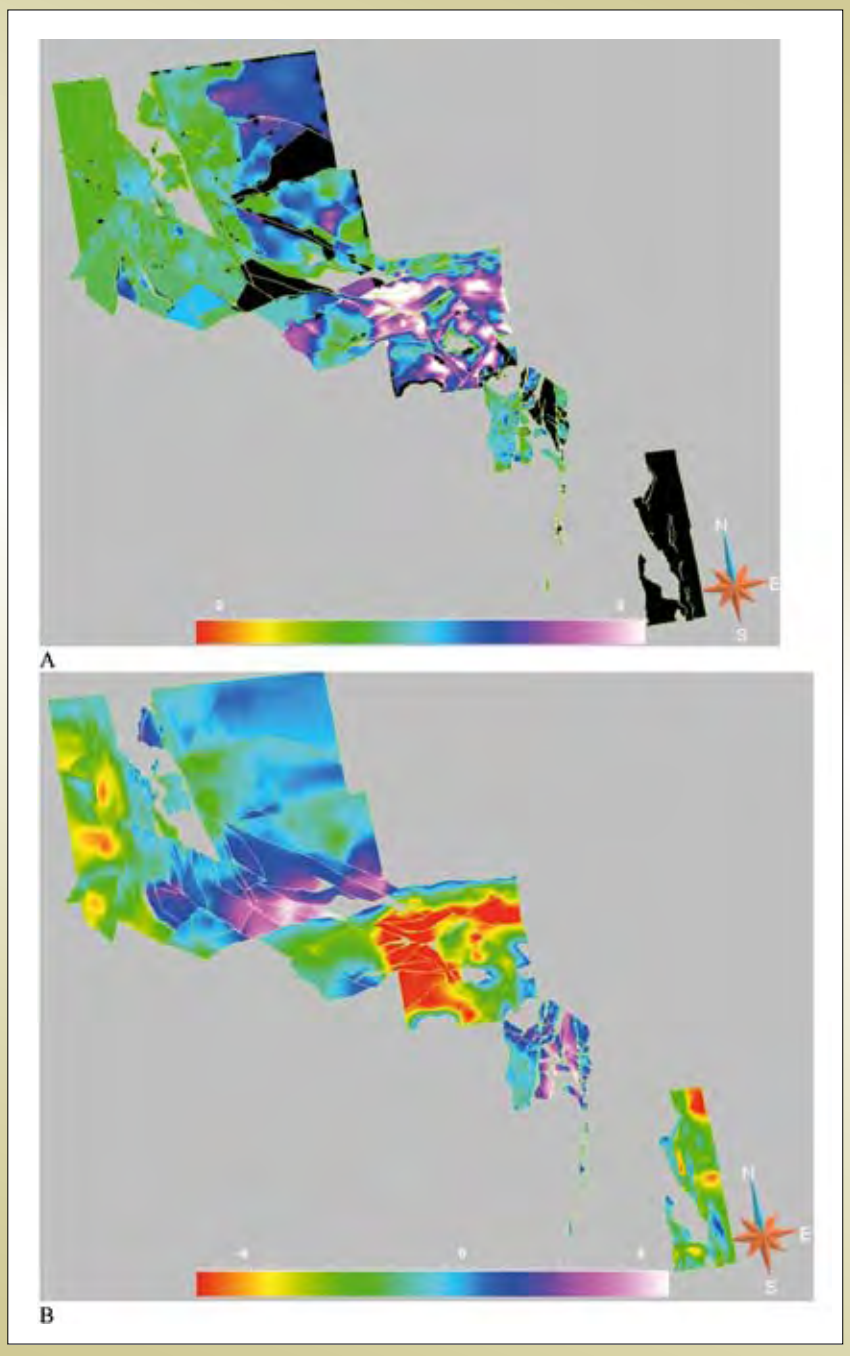

Figure 22: Calvert Superbasin imaged by A) apparent thickness and B) depth to base from 3D modeling (Murphy et al., Appendix 1).

interpretation (NWQMPR 2000) suggested deposition late in the Isan Orogeny, but detrital zircon populations in the Roper Group appear too young for this to be the case (Jackson et al. 1999). These also represent potential aquifer units, with draw down of surficial fluids, and there are ironstones developed. Although mildly deformed along similar trends as the underling ISB, this is not implicated in the mineral system *per se* as it post-dates the Isan Orogeny. The level of incision along the basal unconformity is variable, some hundreds of metres at the most in places, yet along the margins of the Murphy ridge, the RSB rests on basement. The RSB was perhaps extensive, as a blanket across the region, but was stripped away prior to the Cambrian.

Deformation, Metamorphic and Magmatic History

These processes are intrinsically linked in time and space with the development of the Superbasins. The history is dominated by extension, creating the depositional space, with fault control at varying orientations. Superbasins are generally separated by magmatic events, metamorphism, deformation and unconformities/disconformities.

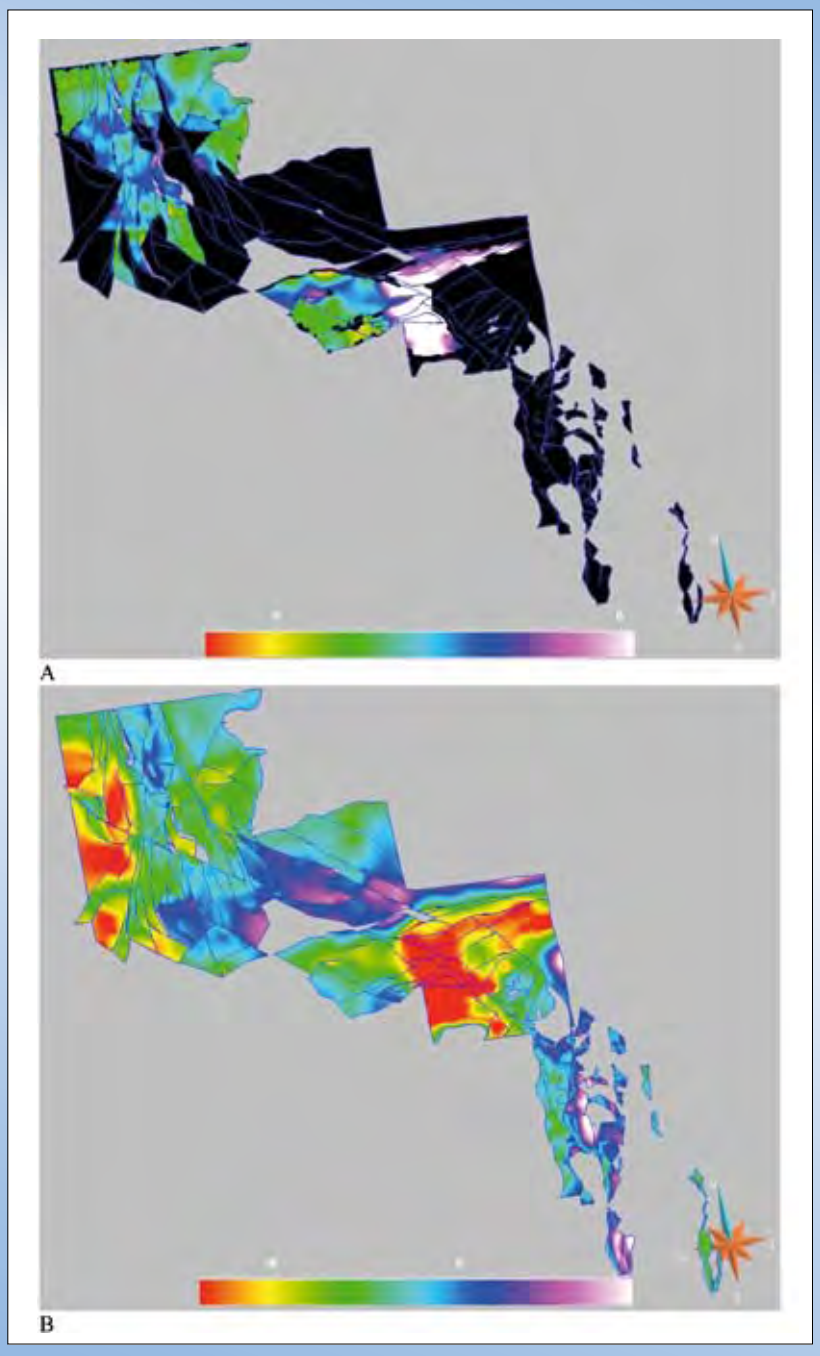

Figure 23: Isa Superbasin imaged by A) apparent thickness and B) depth to base from 3D modeling (Murphy et al., Appendix 1).

Isan Orogeny and late magmatic systems

The *Isan Orogeny* affected the entire region to varying degrees. High strains are especially seen in the EFB and appears to diminish in intensity northwest through the LHP and into the McArthur River region where localised faulting is the main response. The onset of orogeny (D1 deformation) in both WFB and EFB is suggested from Rubenach's results (Appendix 1) which indicates east-west folds, low/med P metamorphism and migmatisation related to a 1640 Ma event. This was a thin-skinned thrusting (or perhaps extensional?) event. It is proposed that north-south structures are related to a foreland thrust belt which initiated at 1640 Ma and continued through to 1590 Ma during deposition of the Upper McNamara Group. This would imply that "D1" folding of the Lawn Hill Formation on the LHP is a reorientation of D2 elsewhere in the inlier to the south and east. Positive inversion in the EFB is interpreted from the association of major structures in cover rocks with deep seated geophysical gradients (Blenkinsop et al. 2005). The inference is that the basement/cover relationship in the EFB may be parautochthonous, and does not demand larger scale lateral translations to develop thin-skinned, nappe-style structures (*cf.* Giles et al. 2006). This will be tested in recently acquired seismic lines.

D2 was the main east-west compression which is characterised by thrust development and peak metamorphism. This is highest grade/most intense in the south east of the inlier and lowest grade/least intense (absent?) from the northwest around Century. It starts at about 1600 Ma in the EFB and lasts for *ca.* 20 Ma. Sedimentation continued at Lawn Hill until *ca.* 1590 Ma, and suggests that the compression was diachronous across the inlier. It may also change in orientation to a more northwest-southeast compression direction around Century, possibly reflecting proximity to a basement high beneath the Georgina Basin; the fact that the Lawn Hill Formation is probably not underlain by LRFT (or other north-south grabens) may play a role. The rotation to more east-west structures on the Murphy Tectonic Ridge probably also reflects basement tectonics and a waning intensity of D2 to the north.

D3 was a more southeast-northwest compression direction and appears to be associated with more brittle than ductile structures. Many workers link Cu mineralisation to this event (Figure 24) citing space creation where the brittle structures interact with earlier ductile structures (D2) and possibly with basin forming structures (i.e. normal faults which define the edge of LSB). The age is less well

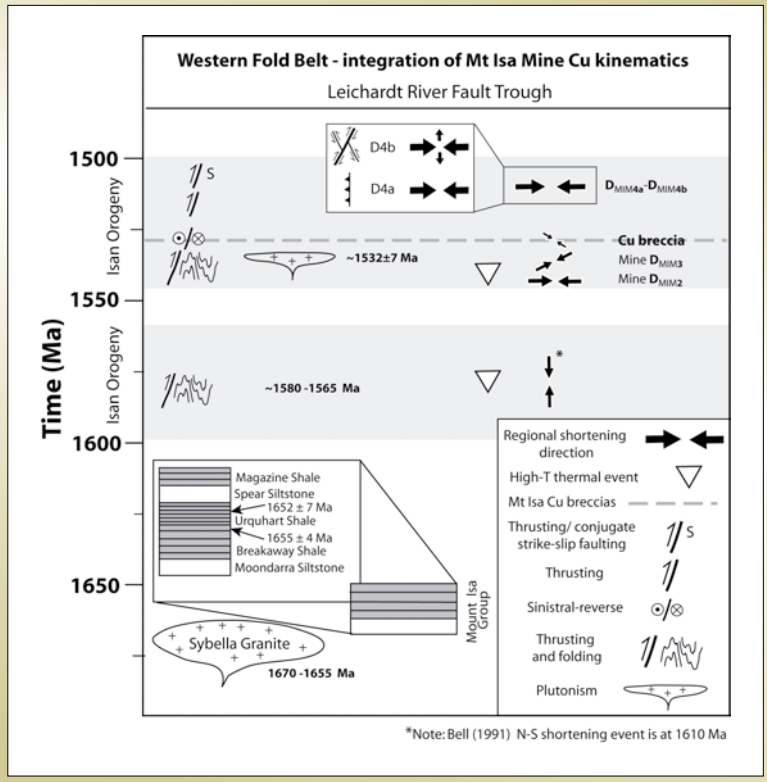

Figure 24: Deformation in the WFB and Cu mineralisation (Appendix 1: Keys et al.).

constrained but probably between 1550-1530Ma. Strike slip faulting and a Christmas-tree pattern of structures developed with dextral NE trending, including the Fountain Range Fault (>30 km lateral offset), and sinistral NW trending.

Late- to post-orogenic magmatism is widespread in the EFB but absent from the WFB (Appendix 1, Murphy et al.). It is characterised by episodic intrusion of a number of Supersuites (Pollard et al. 1998), including TTG magmas (1.55 Ga) and 'A-type' magmatism of the Williams-Naraku Batholith, (1.53-1.49 Ga). There are different temporal and spatial domains, and mingling of mafic and felsic components is a feature (Wyborn et al. 1992; Mark et al. 2006). The timing of emplacement overlaps with east-west compression and extension (implied for generation of "A-type" magmas). The shapes of the granites are much less elongate than earlier suites and relatively flat bases are inferred in the modelling (Appendix 1, Murphy et al.).

Pre-Isan Orogeny events

Pre-Isan Orogeny tectonothermal, magmatic and deformation events are significant in the architecture of the region, and can be recognised through the orogenic overprint. These include:

- The Sybella Event at *ca.* 1670 Ma is represented by metamorphism, deformation and magmatic inflation associated with core complex development of the Sybella Batholith. This immediately preceded and perhaps overlapped with the ISB. The batholith forms a north-south trend along the western flanks of the LRFT and may extend northwards beneath the Mount Gordon Arch (Derrick 1982). This is related to an interpreted east facing detachment. Lower plate and upper plate rocks are identified west of Mt Isa (note: gneissic rocks south of Mt Isa may be lower plate or may be associated with the Barramundi Orogeny)
- The Weberra Event between 1710-1690 Ma is represented by a regional unconformity between the Big and Prize Supersequences of the CSB, is coeval with emplacement of the Weberra Granite and related to the Fiery Creek Volcanics. This may be a compressional (Betts et al. 2006) or, following Gibson et al. (2006), an extensional event (as is adopted here)
- The Wonga Event at *ca.* 1740 Ma is mostly represented east of the KLB in the Wonga Belt where synkinematic emplacement of the Wonga Granite along a mid-crustal extensional detachment is evident (Pearson et al. 1987; Holcombe et al. 1991; Oliver et al. 1991). This is similar to the Sybella event and is thought to represent an elongate core complex ribbon, developed towards the end of the LSB. The orientation of this detachment is poorly constrained within the architecture of the region. The response to this extensional event in the upper plate rocks of the WFB was through development of east-west normal faults (Gibson and Hitchman 2005). Other magmatic input in this interval is represented by the Lunch Creek Gabbro, Burstall Granite and dolerite sills
- The Toby-Ewan event at about 1820-1800 Ma is represented by granites mostly to the west of the KLB and beneath the LSB.

Metamorphic Architecture

There is a complex distribution of metamorphic zones through the region, as seen in the revised metamorphic map (Figure 25). Regionally extensive areas of low grade rocks (sub-greenschist facies) occur in the Isa Valley, LHP, McArthur River and parts of the EFB. Higher grade (greenschist, amphibolite facies) is mostly seen in the EFB and to the west of the Mt Isa Fault. In these regions, there are significant gradients in pressure-temperature conditions which affect all parts of the stratigraphic pile, from basement to the ISB. In general, the highest grades are developed in the south and southeast, where there is a greater degree of inversion of the Superbasins. It is generally thought that the main topography created by the Isan orogeny was probably located to the south, rather than to the east. Studies by Rubenach (Appendix 1) have unravelled complex pressure-temperature-time paths in both the east and west (west of the Mt Isa Fault). It is now believed that a large part of the zonation may be ascribed to thermal input related to magmatic activity (Appendix 1, Rubenach). The dip of the regional metamorphic isograds is not well constrained, but may be influenced by the regional enveloping surfaces to the Superbasins.

Fault Architecture

The fault architecture can be described in terms of first order faults with considerable strike length and effect significant geological contrasts or changes in Superbasin

Figure 25: Metamorphic zonation map of the southern parts of the Mt Isa inlier.

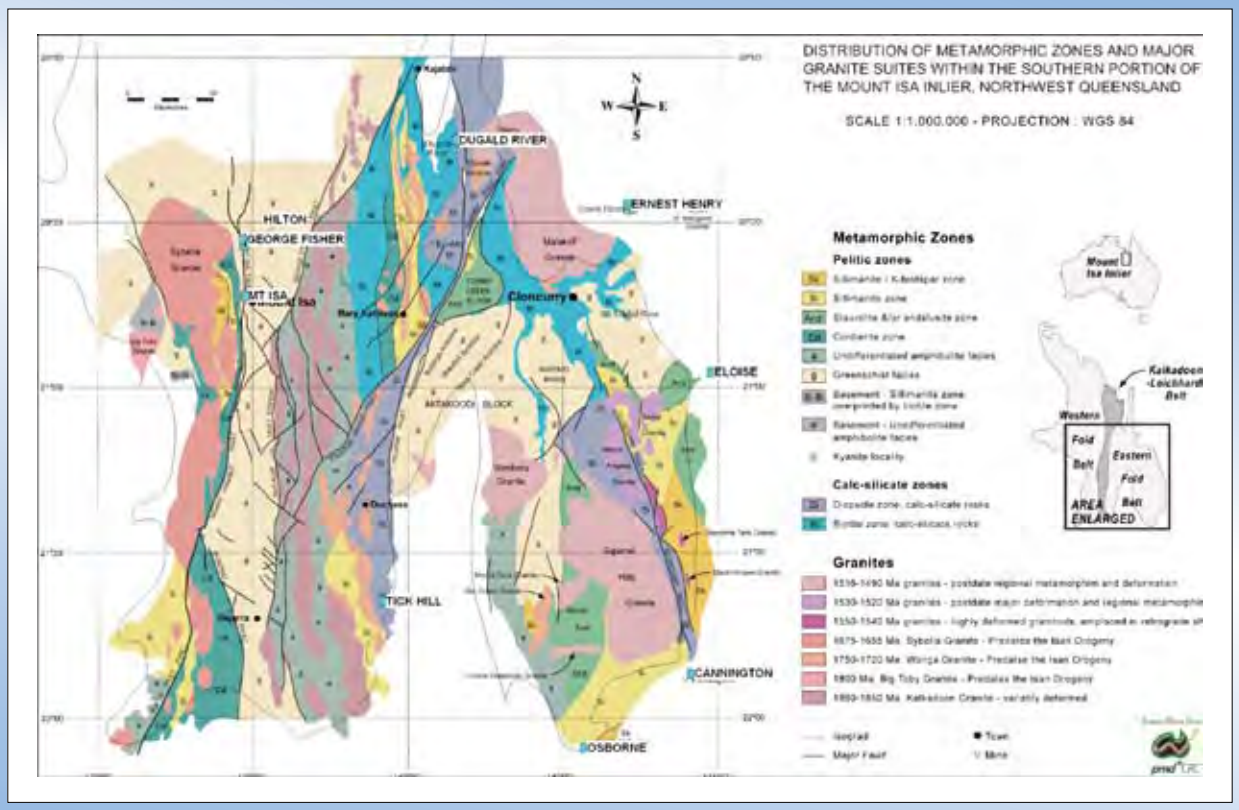

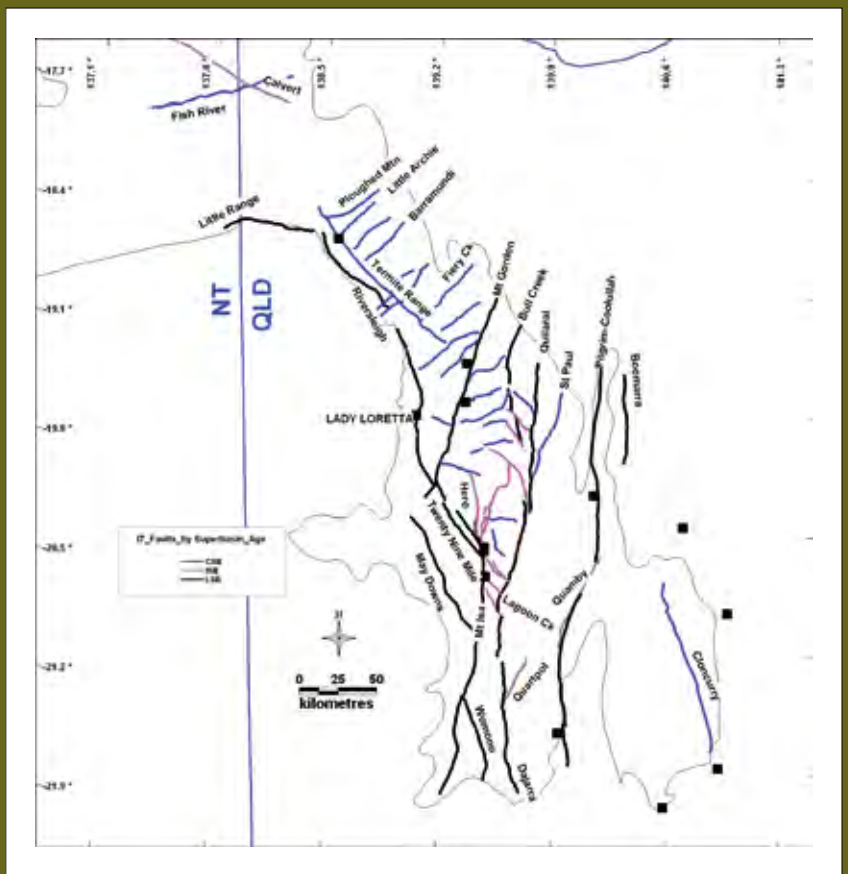

Figure 26: Fault architecture in the Mount Isa Inlier showing faults by inferred age of first Superbasin influence.

distribution, second order faults of generally lesser dimensions and geological impact, etc. (Appendix 1, Murphy et al.). They can also be represented by inferred age of first generation of the fault (Figure 26).

- LSB-related faults are typically first order structures that describe north-south boundaries to the principal domains. There is an arcuate swing in inferred LSB structures to northwest trending to the north of Mt Isa, along the Twenty Nine Mile Fault and this is inferred to link though to the Riversleigh Fault along the southwest edge of the LHP. Mostly this boundary corresponds to a deep seated gravity gradient, the Barrmundi Worm (Hobbs et al. 2000; Murphy *in* Gibson et al. 2005) and is interpreted as a major basement dislocation (Figure 27). Recently acquired seismic data puts this concept to the test
- CSB-related faults are generally "second order" structures with a range of orientations in the LRFT and LHP, separated by the Mt Gordon Fault. There are possible CSB faults in the EFB but these need further work to constrain
- ISB-related faults are in themselves difficult to discriminate from reactivated faults and, again, need further analysis
- The deep seated elements are indicated in Figure 28 and included is a west dipping detachment along which a high velocity, presumed mafic slab occurs (MacCready et al. 1998; Figure 29). This needs further

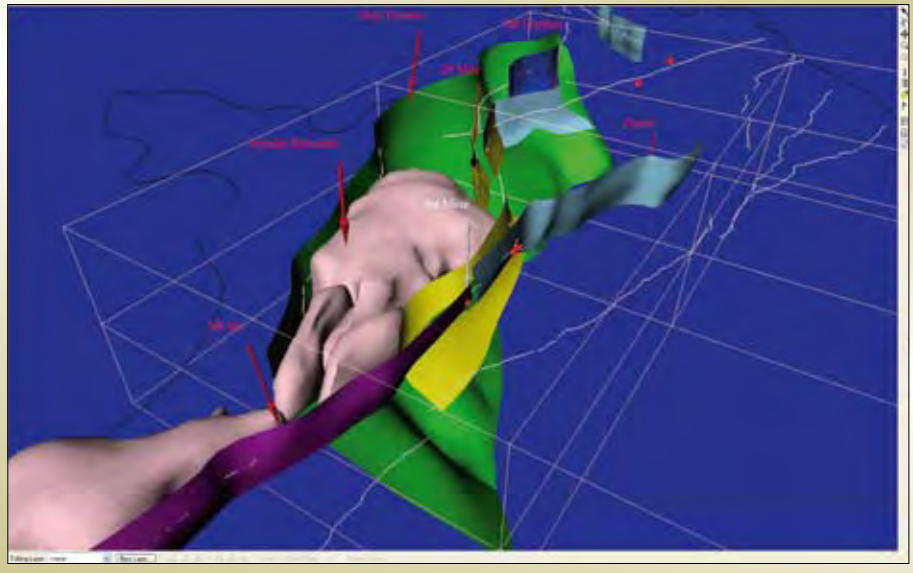

Figure 27: Perspective view of 3D modelled faults and Sybella Batholith (lilac) in the western regions of the Mount Isa Inlier. May Downs Fault (green) interpreted as major east dipping structure linking at depth with the Twenty Nine Mile Fault (yellow) beneath. Mt Isa Fault (purple) in hanging wall of May Downs Fault. Paroo Fault (blue) also shown, branching northwards from Mt Isa/Twenty Nine Mile Fault system. While lines = first order fault traces, black line = Proterozoic outcrop boundary; red dots = major deposits. Grid from +10 to -40 km.

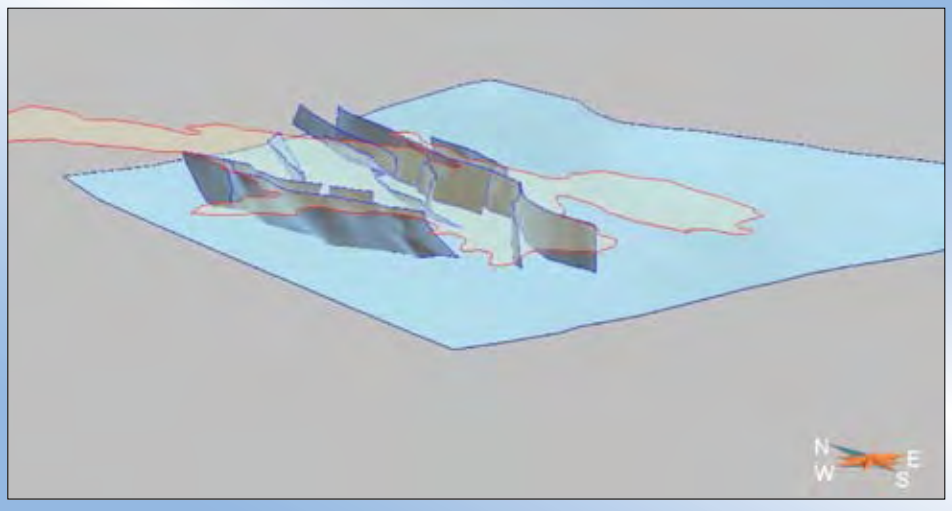

Figure 28: Major, deep seated structures in Mount Isa region in perspective view towards NE showing, from west to east, the May Downs, Mount Isa, Quilalar and Pilgrim Faults. Blue surface beneath these represents interpreted position of west dipping detachment seen in the AGCRC seismic profile (MacCready et al. 1998).

modelling in the light of more recent seismic data. However, the up dip projection of the seismic boundary may correlate with a major gravity gradient which in upward continued data has a westerly dip. This is here termed the Eastern Suture Zone (Figure 30) and is located about 90 km from the eastern end of the seismic line. New seismic data in this region will improve this picture

- The architecture extends under-cover for considerable distances (NWQMPR 2000) and interpreted potential field gradients (Appendix 1, Murphy et al.) help to map out the major fault trends (Figure 30). This gives a fuller appreciation of the north-south trends and how they are manifest as a distinctive feature in the region. It also emphasises the east-west elements and basement trends that dominate in the northern and western regions.

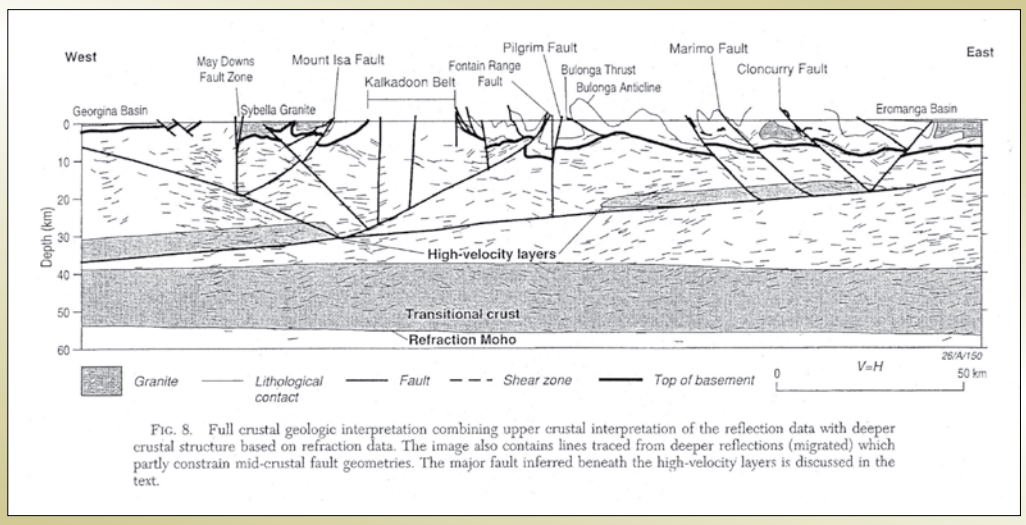

FIG. 8. Full crustal geologic interpretation combining upper crustal interpretation of the reflection data with deeper crustal structure based on refraction data. The image also contains lines traced from deeper reflections (migrated) which partly constrain mid-crustal fault geometries. The major fault inferred beneath the high-velocity layers is discussed in the text.

Figure 29: Interpreted east-west seismic profile across the Mount Isa Inlier (after MacCready et al. 1998).

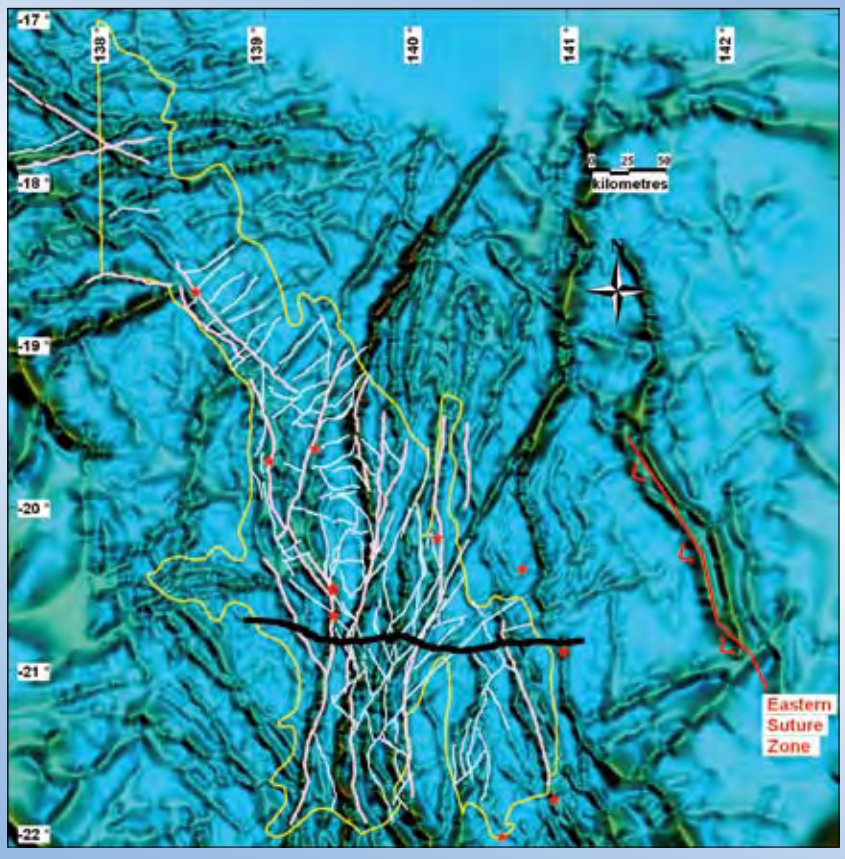

Figure 30: Edge length image from combined gravity and aeromagnetic interpretation (Appendix 1, Murphy et al.). Major deposits (red dots) and outline of inlier (yellow line) and AGCRC Seismic Line 94_01 (black) and west dipping gravity gradient (Eastern Suture Zone).

Permeability Architecture

The most comprehensive analysis to date of permeability distribution is by Polito et al. (2006 a, b and c) undertaken as part of the AMIRA P552 in the Mt Isa, Lawn Hill platform and southern McArthur regions. This evaluates the diagenetic history of various units within the Superbasins and examines their potential as aquifers and source regions for metals. These data help to identify potential fluid source regions, aquifer and seal units. Secondary porosity is a key factor in determining diagenetic aquifers, with the more proximal fluvial clastics (heterolithic units) showing well developed secondary porosity compared to cleaner quartz sands of the distal and near-shore facies.

- In the LSB, these facies are best represented by the Bottletree Formation, lower Mount Guide Quartzite and Lena Quartzite, and represent successions of several kilometres thickness. These display the greatest diagenetic alteration and highest fluid to rock ratios during peak diagenesis (Polito et al. 2006a). These are likely sources of brines, particularly as they are interbedded with or overlain by the ECV which are regarded as a metal source to deposits in the region (Wilson et al. 1985; Wyborn 1987; Heinrich et al. 1995; Matthai et al. 2004). Burial depths for creating and maintaining porosity in these aquifers are estimated at 5 to 10 km (Polito et al. 2006 a and b), assuming a minimum geothermal gradient of 24°C/km (Glikson et al. 2006). Similarly, LSB equivalents in the McArthur River region, the Westmoreland Conglomerate, lower Yiyinti Sandstone and Sly Creek Sandstone, show evidence of secondary porosity generation while the associated Siegal Volcanics are a possible metal source (Cooke et al. 1998). In addition, red beds in the Lochness Formation of the Myally Subgroup are a possible source of oxidised fluids

- In the CSB, diagenetic aquifers in proximal fluvial facies are seen in the Bigie Formation and lower parts of the Surprise Creek Formation, and are generally less than several hundreds of meters thick. Despite the coarse grained and heterogeneous composition of the sediments, these are considered as diagenetic aquitards in the LRFT (Polito et al. 2006a). Peak diagenesis created up to 15% porosity in some units, such as the Surprise Creek, yet early quartz cements appear to be pervasive and to have occluded porosity in these units. Although the thickness of the CSB (up to 4 km) was sufficient to generate secondary porosity, subsequent erosion events (between 1700-1695 Ma and 1688-1668 Ma) are considered to have promoted the quartz overgrowths that arrested aquifer development (Polito et al. 2006a). These uplift events may have prevented deep burial of the CSB, at least in the LRFT. In the LHP, however, there is seismic evidence to suggest the LSB was too deeply buried (20-25 km) to be a metal source for the Century deposit, whereas CSB elements were sufficiently buried for the generation of secondary porosity (Southgate et al. 2006; Polito et al. 2006a). Metals may have been sourced from leaching of the Fiery Creek Volcanics in the LHP, and from the Settlement Creek Volcanics, Gold Creek and Peters Creek Volcanics in the southern McArthur region (Polito et al. 2006b)

- In the ISB, proximal fluvial facies are thin or absent at the base. Poroperm characteristics suggest that although there is variable development of early diagenetic features, most of the sandstone units in the Gun, River, Term and Wide Supersequences display diagenetic aquitard characteristics (Polito et al. 2006a) Peak diagenesis and secondary porosity generation is patchily developed within thin poorly connected sandstone units.

A key consideration is the storage of brines in deep reservoirs for long periods, for over 100 Ma, as breaching through faulting period is a significant risk. McLellan ((a) in Appendix 1) shows that extension tends to focus fluid flow downwards into the basin whereas compression has the opposite effect. That these reservoirs could have been maintained for long periods may be indicative that the *pre*-Isan Orogeny uplift and erosion events were dominated by extension (Gibson and Hitchman 2005) and that the inversion related to the Isan Orogeny *per se* was the main mechanism by which the brines escaped to higher levels into the ISB. Fluid migration may have begun as early as *ca.* 1680 Ma, possibly overlapping with "syngenetic" Pb-Zn mineralisation at McArthur River, and continued through to at least *ca.* 1540 Ma (Polito et al. 2006b).

Distributions of the Superbasins, their contained Supersequences, and related units are in large part controlled by fault architecture, particularly the first order features (Appendix 1, Murphy et al.). In addition, the major deposits are closely related to long strike length features,

suggesting a deep plumbing system (Figure 3). There is evidence for multiple generations of faulting, at different orientations over time, and for significant re-activation. Early north-south trending faults that control sedimentary thickness distributions in the LSB, for example, have been re-used during the Isan orogeny and during younger events (Spikings et al. 2006). Similarly, the east-west faults in the LRFT are regarded as being initiated during the LSB, had a strong influence on the CSB distribution, and were later re-activated during the Isan Orogeny.

The inverted geometry of the LRFT has an overall northerly plunge and is constricted southwards from Mt Isa, with increasingly deeper levels exposed to the south. The central part of the LRFT is dominated by the Mt Gordon Arch, plunging southwards towards Mt Isa and northwards towards the Gunpowder region (Figure 31). As an interpreted original LSB feature, it is likely that it had topographic influences on subsequent events, such as fluid flow during extension of the ISB and during Isan Orogeny.

Conclusions

The architecture of the Mt Isa and McArthur River regions reflects a position within and along the outer margins of the NAC (Myers 1996). An early subduction-related magmatic arc developed in a north-south orientation (KLB), apparently discordant to trends within the pre-Barramundi basement. The top of basement is modelled at relatively shallow through much of the region, with deepest levels in the central parts of the LHP (to -18 km). Basement is not seen east of the Pilgrim Fault, but is inferred to -20 km in parts of the EFB (Blenkinsop et al. 2006). The LSB and CSB are stacked basins along the LRFT and related troughs which, together with

Figure 31: Perspective view of the Mount Gordon Arch, with dark green surface representing base of the Bottletree Formation (dark green is above ground, light green is below ground), and Sybella Batholith (dark red is interpreted above ground shape).

magmatic input and core complex development, were broadly controlled by (roughly) east-west and north-south extension respectively. The LSB was widespread and linkage between the WFB and EFB was established at least by the Myally Supergroup. The CSB was more extensive in the LRFT and LHP and sedimentary linkage across the KLB was established by Prize Supersequence time. Other than the Llewellyn Creek Formation rocks in the Snake Creek region, the CSB appears to be absent from the EFB, although it could be present at depth. The ISB is interpreted as a sag phase basin which was widespread in the WFB and in the EFB. The upper parts of the ISB are preserved in the LHP, interpreted as a foreland basin ahead of the evolving Isan Orogen to the south and east.

The fault architecture is mostly dominated by relatively steep structures in the near surface. Low angle detachments and listric geometries are likely to be developed, especially within basins. Some large scale dipping structures are inferred on the basis of Superbasin character as crustal scale dislocations, such as an east dipping detachment along the western margins of the LRFT (May Downs/Twenty Nine Mile Fault), and the east dipping Cloncurry Fault. The Pilgrim Fault is interpreted as a steep structure, following MacCready et al. (1998) representation. Early formed extensional detachments are inferred but there are few constraints on their extent.

The preservation of diagenetic aquifers within proximal facies of the LSB and CSB are key elements for the generation of metal bearing brines. Their ability to access higher levels of the ISB is mainly through faults acting as permeable pathways. The undercover regions have significant potential in this regard.

Question 3: What are the fluid and chemical sources and reservoirs?

Major Contributors: Cleverley, Kendrick, Walshe, Oliver, Bertelli & Blake

Introduction

The nature and origin of fluids are a key consideration for understanding the Isan mineral system. There is a diversity of fluids in this system which, in their sometimes tortuous path to deposition, can be significantly modified and take on new guises. Thus, tracing them back to their roots is a complex issue. The dominant fluid-types at the district to deposit scales include:

1. Sedimentary Formation Waters. Potential sources include but are not restricted to the Leichhardt, Calvert and Isa Superbasins in the WFB

2. Metamorphic fluid components such as Cl, CO_2 and SO_4 derived from metasediments including the Corella Formation

3. Metamorphic fluids derived from the crystalline pre-Barramundi basement

4. Magmatic fluids (including Cl, CO_2 and SO_4) derived from granitic intrusions such as the Williams-Naraku Batholiths and less abundant mafic phases in the EFB.

In addition, other fluid types that may have been present include meteoric water and H_2-rich fluids derived directly from the mantle. However, these latter fluid components are difficult to constrain and, thus, there is uncertainty regarding their input to the system.

Geological observations are an essential context in which different fluid sources are evaluated. Geochemical data, including stable and radiogenic isotopes (Ar, Ne, S, C, O, D, Os) and fluid inclusion Br/Cl and I/Cl values, provide a useful means of discriminating the different fluid types. The geochemical parameters used in this analysis, and their limitations, are summarised in Table 3. Most of the ore deposits and regional alteration have mixed geochemical signals indicating the involvement of at least two of the fluid end-members. Proportional estimates of fluid end-members in the deposits studied are given in Table 4. The discriminant elements of interest are outlined below, followed by a discussion on contributions from different source regions. This is illustrated by two case studies drawn from the WFB (Isa Copper) and EFB (Ernest Henry and regional hydrothermal breccias), respectively.

Discriminator characteristics and limitations

Noble gas

Noble gas measurements are obtained from fluid inclusions in quartz and carbonate, many of which have a secondary origin but are interpreted to be related to mineralisation (Kendrick et al. 2006a, b, c, 2007a, b). Sedimentary Formation Waters have molar $^{40}Ar/^{36}Ar$ of <2000 and

Table 3: Parameters used to distinguish fluid types. Nb – all ratios are molar. ASW = air-saturated water (includes meteoric and seawater)

	ASW		Formation Waters		Metamorphic Fluids		Magmatic Fluids	
	Met.	Sea-water	Bittern Brine	Halite Dissolution	Meta-sed (Corrella involvement)	Basement-derived	A-type related	Mantle-derived
Noble gases								
$^{40}Ar/^{36}Ar$	300		< 2000		< 2000	> 30,000	> 30,000	40,000
^{36}Ar ppb	1.7-2.7	1.3-2.1	~3-100		~1-20	<3	~3-12	0.1
$^{40}Ar_E$ /Cl			~ 10^{-5}-10^{-6}		~ 10^{-5}-10^{-6}	~ 10^{-3} - 10^{-4}	~ 10^{-3} - 10^{-4}	~ 10^{-3} - 10^{-4}
Halogens and salinity								
Br/Cl ($\times 10^{-3}$)	-	1.5	>1.5	0.1 - 0.3	0.1 - 0.3	0.1 - 30	1-2	1-2
I/Cl ($\times 10^{-6}$)	-	0.8	~10-1000	0.5 - 2	0.5 - 2	0.5 – 500?	10-80	10-80
NaCl Wt%	~0	3.5	~30	30-70	<70	5-20	<70	5-30
Stable isotopes								
$\delta^{34}S_S$ ‰			~ +15 – +30			~ -5–10	~ -15– +10	0
$\delta^{34}S_{SO4}$ ‰			~ +20 – +40				~ 0 – +15	
$\delta^{13}C_{CO3}$								
δD		0						
Radigenic isotopes								
$^{188}Os/^{187}Os$			≥ 1	≥ 1	≥ 1	≥ 1	≥ 1	~ 0.1

^{36}Ar contents greater than or equal to air-saturated water (>2-3 ppb). In contrast basement-derived magmatic, metamorphic or deep-Earth fluids, derived from the mantle, are characterised by $^{40}Ar/^{36}Ar$ values of ~30,000+. The order of magnitude variation in $^{40}Ar/^{36}Ar$ means that minor components can be identified when these different fluid types mix.

The biggest uncertainty regarding the interpretation of Ar data is that sedimentary formation waters and metamorphic fluids derived by devolatilisation of the meta-sedimentary host rocks could have very similar $^{40}Ar/^{36}Ar$ values. Therefore, the interpretation of sedimentary formation water is heavily influenced by stable isotope data that demonstrate external fluid buffering (see below). Similarly, high $^{40}Ar/^{36}Ar$ values of >30,000 do not distinguish basement-derived magmatic or metamorphic fluids, and He or Ne isotope data is required together with the Ar data to distinguish these basement-derived fluids from a possible mantle input.

Finally, the noble gases could become decoupled from major volatile species (H_2O and CO_2) during phase separation. Decoupling could allow the original noble gas signature of a fluid to be overprinted. However, none of the fluid inclusions studied have the fractionated noble gas signatures (Xe/Kr/Ar) that characterise phase separation, and they have a limited range of ^{36}Ar concentrations. These data, and the preservation of a magmatic signature in Ernest Henry, the deposit with the most extensive brecciation, suggest that overprinting during phase separation has not been a major problem.

Halogens and salinity

Halogen values are also measured in fluid inclusions and salinities are determined by microthermometry. Magmatic fluids have a restricted range of Br/Cl and I/Cl similar to values determined for mantle diamond (Table 3). The Br/Cl and I/Cl characteristics of metamorphic fluids are likely to be extremely variable and encompass a range at least as great as Sedimentary Formation Water. Sedimentary Formation Waters are subdivided on the basis of halogen data into bittern brine and halite dissolution waters (Hanor, 1994; Worden, 1996). Figure 32 summaries the Mt Isa data.

Bittern brines are characterised by molar Br/Cl values of greater than the seawater value of 1.5×10^{-3} and elevated I/Cl values of $50\text{-}500\times10^{-3}$. The high Br/Cl values result

Table 4: Estimated significance of different fluid types. Nb – metamorphic fluids at Osborne include those that have interacted with anatectic melts and the use of 'magmatic fluid' is restricted to cases where external volatiles are introduced from the basement (A-type related) or the mantle Mantle involvement has been suggested previously based on the presence of CO_2 fluid inclusions. However, the Corella Fm. is an alternative source of CO_2

	ASW		Sed Form Waters		Metamorphic		Magmatic	
Deposit	Met	SW	Bit	HD	meta-sed	Basement-derived	A-type	Mantle (mafic)
Western Fold Belt								
Mt Isa			X			X		
Eastern Fold Belt								
EH	?		40%		20 %?		40%	10 %?
Osborne	?		X	X	X			
Eloise	?		80-90%		10%	X ?	<10% ?	
Starra	?		80-90%		10%	X ?	« 10% ?	
L. Creek	X		X	X				
Regional alteration (albitisation)								
MKFB	?		80%		10 %?	10%		10%?
Clon.Dist			80%		10 ?	10 ?	10 ?	

from the evaporation of seawater beyond the point of halite saturation, at the paleosurface. The elevated I/Cl values result from fluid interaction with organic-rich sedimentary rocks, in the sub-surface. Halite dissolution waters are characterized by low Br/Cl and I/Cl ratios of ~0.1×10^{-3} and ~10^{-6}, respectively (Holser 1979).

Bittern brines have salinities of ~30 wt % salts, the point of halite saturation in seawater, because they form by the evaporation of seawater. The salinity of metamorphic devolatilisation fluids is related to the volatile (H_2O) and Cl content of the host rock and is probably <20 wt % in most cases (Kendrick et al. 2006). Magmatic fluids can have bulk salinities of between 2 and 84 wt %. Any of these fluids can increase their salinity by the dissolution of halite in the subsurface. Meta-evaporitic scapolite is present throughout the EFB and may have a similar effect on fluid compositions (salinity and Br/Cl-I/Cl) as halite.

Stable isotope constraints

In contrast to the noble gases and halogens, stable isotope measurements are typically made on minerals, and fluid values are calculated based on available temperature and pressure constraints. The O, H and C isotopes are essential for distinguishing open and closed fluid system behaviour. The major limitation of stable isotopes is that they vary by small amounts (parts per thousand) and that magmatic fluids, metamorphic fluids and sedimentary formation waters all have similar δD and $\delta^{18}O$ values.

Sulphur isotopes provide an important constraint on the source of ore constituents. Seawater or sedimentary sulphate is characterised by highly positive values of up to 40 (Table 3). Sulphide can retain a positive value if reduction occurs in a closed system, however, open system behaviour can result in strongly negative $\delta^{34}S$ values

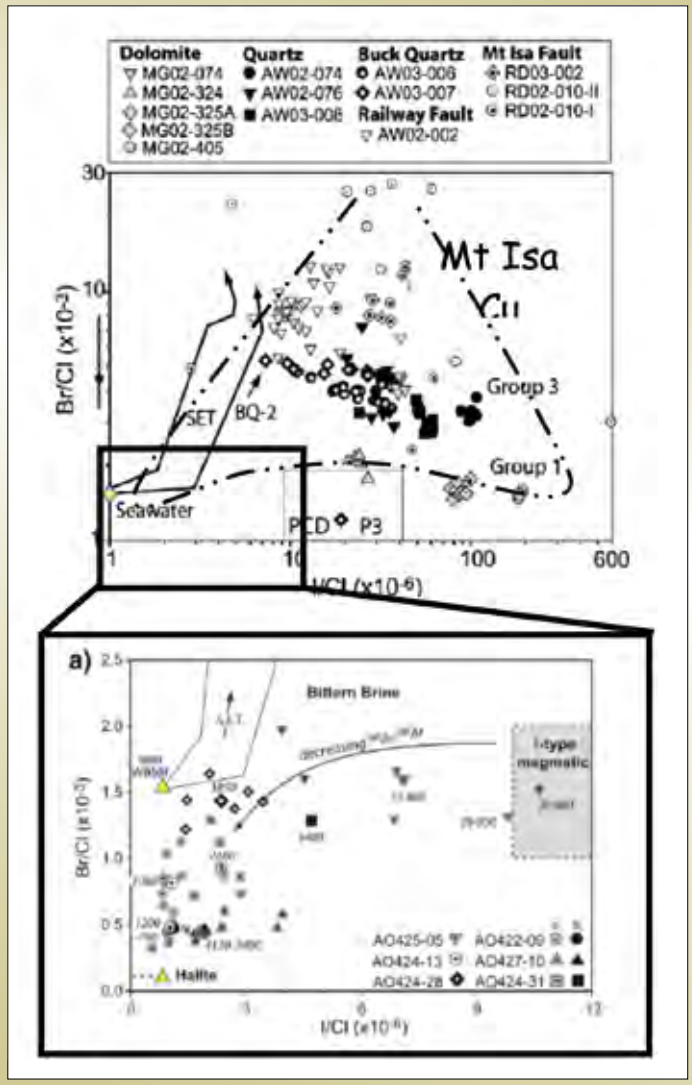

Figure 32: Halogen ratios (Br/Cl and I/Cl) for the Mount Isa Cu and Ernest Henry deposits showing proposed end-members fluids. Data and figure for Mount Isa Cu deposit from Kendrick et al. 2006c and Ernest Henry Fe oxide–Cu–Au deposit from Kendrick et al. 2007a.

(~ -40 to 0). Reduction can occur by a variety of organic or inorganic reactions. The total fractionation is about 75‰ at 25 ˚C but is reduced as temperature increases (~ 21 ‰ at 300 ˚C and ~ 11‰ at 500 ˚C), meaning less variation in high temperature fluid systems. Magmatic or mantle $\delta^{34}S$ values should cluster around 0. Limitations of S isotopes include that it is impossible to distinguish if a value around 0 represents a mantle or magmatic fluid, or reflects leaching of an igneous rock by a fluid of unknown origin. The strong fractionation of S isotopes during redox reactions means that, in many cases, they are not a reliable indicator of source but can be extremely useful for tracing redox reactions.

Radiogenic isotopes

Os isotope measurements have been obtained by TIMS on sulphide minerals. In theory, the Re-Os decay system can be used to date ore minerals and the initial Os isotope composition could trace a mantle input during mineralisation. Unfortunately, this technique is still in its infancy and knowledge of Re and Os mobility from sulphide minerals (analogous to closure temperature) is scarce. Extensive Os isotopic work was conducted within the inlier (under the auspices of the H4 pmdCRC project) with a view to investigating whether specific isotopic features could be used to characterise specific mineralising processes and the time dimension associated with them. Further, it was hoped that terrane scale signatures may be detected which would enable assessment of the relative roles of mantle versus crustally derived fluid inputs into mineralised systems. The outcomes of this research suggest that each style of mineralising system produced significantly different responses to the Os isotopic signature preserved, thereby precluding generation of a holistic investigative tool (Bruce Schaefer, *pers. comm.* 2008). The specific details regarding such behaviour are discussed in the H4 Final Report, and are not investigated here. This is essentially because the minerals were open systems to Os diffusion after mineralisation and they may not reflect the composition of the ore fluids at the time of mineralisation. Other radiogenic isotope systems (e.g. Sm-Nd) have been applied to IOCG deposits, such as Olympic Dam in South Australia, and provide a useful analogue for interpretations based on stable isotope and noble gas data in the Mt Isa Inlier.

Interpreted fluid types

Sedimentary Formation Waters

Possible reservoirs for sedimentary formation waters in the Mt Isa Inlier include the Leichhardt, Calvert and Isa Superbasins. Such fluids could also have been sourced from unknown sedimentary basins above the present erosion level. In addition, in the EFB, depending on the timing of mineralisation and metamorphism, they could have been present as pore-fluids within the host strata (e.g. at Osborne; Fisher and Kendrick, 2008).

The involvement of bittern brines is favoured in the Mt Isa copper mineralising system on the basis of Ar and halogen data, and is supported by sulphur isotope data which implies sedimentary sulphate was an important sulphur source (Figures 33 and 34; Heinrich et al. 1989; Andrew et al. 1989). Sedimentary formation waters are also indicated in the major Pb-Zn mineralizing systems that produced the Century, Hilton and George Fisher deposits and, by analogy, the McArthur River deposit.

In addition, the noble gas and halogen data suggest bittern brine sedimentary formation waters were dominant during late-Isan Orogeny albitisation in the Mary Kathleen Fold Belt (MKFB) and were present throughout the Cloncurry District during the Isan Orogeny. However, strongly correlated Br/Cl and I/Cl values, which converge on values slightly higher than expected for halite (Figure 35), suggest that interaction with evaporites (or meta-evaporitic scapolite) has been a major process in increasing the salinity of sedimentary formation waters above 30 wt % salts, in the EFB. Based on the noble gas and halogen data, many of the ultra-high salinity multi-solid fluid inclusions that have traditionally been related to magmatism are in fact most likely to have a mixed origin dominantly from sedimentary formation water and halite dissolution. It is important to note that these interpretations are compatible with stable isotope data.

Magmatic fluids

There is, as yet, no evidence for the involvement of magmatic fluids in any of the mineral systems of the WFB. The *ca.* 1650 Ma Sybella Batholith predates mineralisation at the Mt Isa Cu deposit by at least 100 Ma. In contrast, there is abundant evidence of magmatic activity throughout the EFB during the latter part of the Isan Orogeny (1550-1500 Ma) when many of the IOCG mineral systems formed.

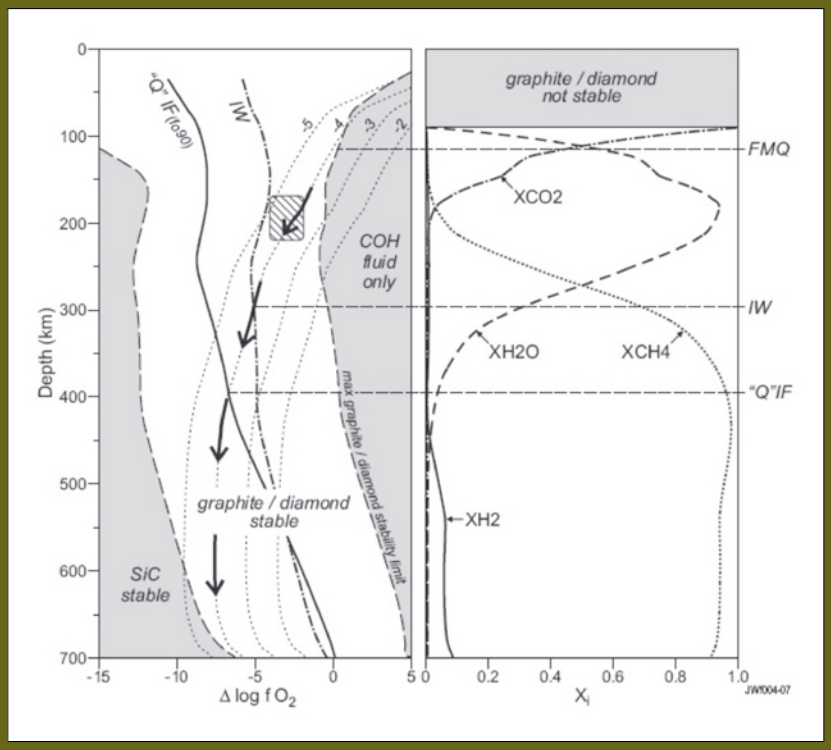

Figure 33: Redox-depth evolution of C-saturated fluids at upper mantle conditions. COH fluids will be dominated by CH4 and H2 at depths greater than ~ 300 km (Right panel). Maximum stability limits for graphite/ diamond and for SiC (Moissanite) with respect FMQ (Fayalite, Magnetite, Qtz) are shown in left panel. Also shown are evolution paths for the mineral redox buffers IW (Iron/Wustite) and "Q"IF ("Quartz"/Iron/Fayalite; XFa = 0.1).

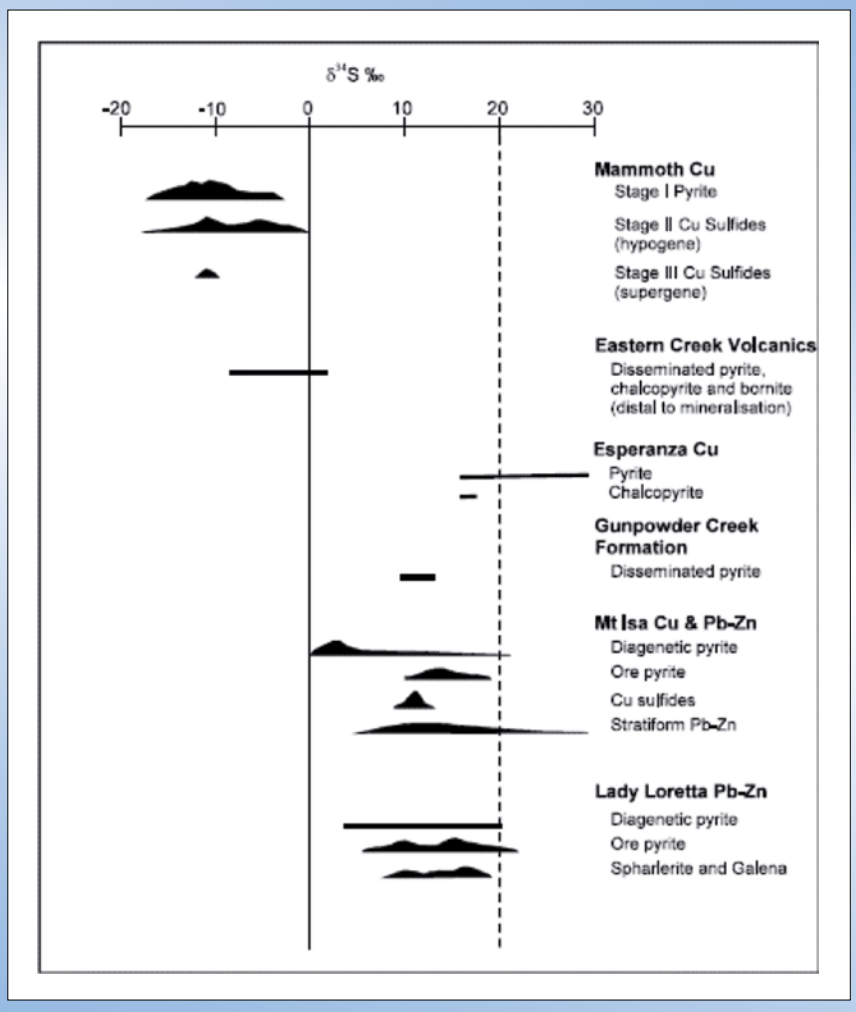

Figure 34: WFB S isotope data (compilation by Clark 2001).

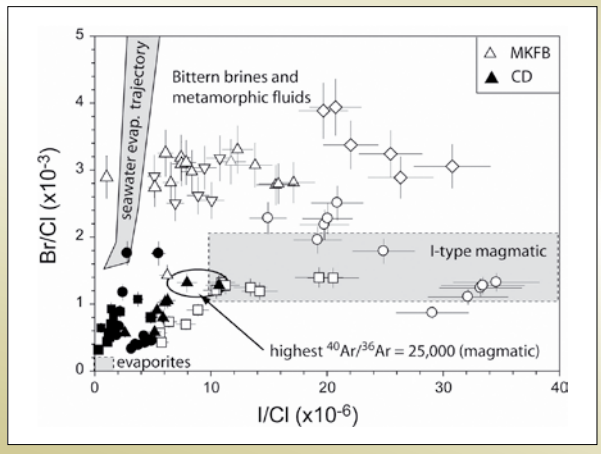

Figure 35: Fractionated halogen signature in the Mary Kathleen Fold Belt and Cloncurry District, favours fluid interaction with halite.

The spatial correlation between ore deposits and mafic intrusions is much stronger than the spatial correlation between ore deposits and granite intrusions (Oliver et al. 2008). However, the Williams-Naraku Batholiths (1550-1500 Ma) are traditionally favoured as an important source of magmatic fluids. Volatiles that may have had a magmatic origin include ultra-high salinity aqueous fluid inclusions and $CO_2 \pm SO_2$. CO_2 has a low solubility in granitic melts, but it could have been introduced by the less abundant mafic phases, or acquired by assimilating meta–carbonate host rocks.

Given the extent of magmatic activity in the EFB (Figure 11), it is difficult to conceive that the granite (and mafic) intrusions did not play some role in the mineralisation-related fluid systems. However, recent noble gas and halogen data suggests this role may have been much smaller than previously thought (Table 4) and good evidence for the involvement of magmatic fluids has only been obtained for Ernest Henry (Table 3). Magmatic volatiles have also been confirmed in isolated unmineralised parts of the Mary Kathleen Fold Belt (CO_2-rich fluids are Knobby Quarry) and the Cloncurry District (close to the Saxby Granite).

Metamorphic fluids

Quartz hosted fluid inclusions in the Mt Isa Cu deposit have high $^{40}Ar/^{36}Ar$ values of ~30,000. These are similar to magmatic fluids, but the fluid inclusions are characterised by salinities of less than 20 wt % and high Br/Cl and I/Cl values that are dissimilar to the mantle. Kendrick et al. (2006) demonstrated the salinity, ^{36}Ar concentration, and $^{40}ArE/Cl$ value of these high $^{40}Ar/^{36}Ar$ fluids are similar to those expected for devolatilisation of the basement rocks. Together with the lack of syn-mineralisation magmatic activity in the WFB, these data suggest the Mt Isa Cu deposit is the best example of a hydrothermal system with a large basement-derived metamorphic fluid component.

Metamorphic fluids may also have been derived from metasedimentary rocks. Although stable istope data do not favour an exclusive fluid origin from metasedimentary rocks in the EFB, the Corella Formation could have been an important source of CO_2, SO_4 and Cl. Recent revisions to the timing of IOCG mineralisation in the EFB suggest that not only Osborne, but also Eloise and Starra, formed close to the metamorphic peak and preceded intrusion of Williams-Naraku Batholith by up to 60 Ma (Oliver et al. 2008). Each of these deposits had a high abundance of CO_2 fluid inclusions which is most likely to be of metamorphic origin.

Other fluids

This concerns fluids that may have passed through the mineral system almost without trace. Some have argued 'hidden' fluids such as mantle-derived methane and other H-rich species could control redox reactions and may be essential for mineralisation in many Proterozoic and Archaean terranes (e.g. Walshe et al. see Y4 – final report). Although the presence of these fluids is considered conjectural by many workers, their existence cannot be readily discounted, and it is now widely recognised that these fluid species are generated by serpentinisation of ultramafic rocks in the mantle. A major obstacle to confirming this hypothesis is that oxidation of methane during mineralisation would produce carbon dioxide and

water, thereby removing evidence for its involvement. At the present time, there is no strong evidence for the presence of these fluids in the Mt Isa Inlier. Os isotopes have a primitive signature suggesting a possible link between mineralisation and the mantle. However, these primitive signatures are associated with anomalously young Re-Os ages that demonstrate open system behaviour after the mineralisation event.

District- and Deposit-scale Case Studies

The WFB and Mt Isa Copper

The Mt Isa Copper Deposit is the largest 'Isa-style' deposit in the WFB (255 Mt @ 3.3 % Cu), similar deposit styles occur at Mammoth and Gun Powder. Most recent workers have accepted an epigenetic origin for the Mt Isa Cu deposit and mineralisation probably occurred toward the end of the Isan Orogeny. The Cu deposit is spatially associated with a giant stratiform Pb-Zn deposit. However, the genetic relationship between the Cu and Pb-Zn has been controversial.

Fluid inclusions in the Mt Isa Copper deposit are dominated by moderately low salinity aqueous inclusions (Figure 36A; Heinrich et al. 1989). CO_2 and halite daughter minerals are relatively rare although, importantly, some dolomite-hosted fluid inclusions contain up to 20 % CO_2. Noble gas data from quartz- and dolomite-hosted fluid inclusions are most easily explained by mixing basinal brines and basement-derived metamorphic fluids. The basinal brines with low $^{40}Ar/^{36}Ar$ and high ^{36}Ar concentration are best preserved in the dolomite-hosted fluid inclusions and in faults outside the mine area (Figure 36B). Quartz-hosted fluid inclusions are dominated by the metamorphic component and are paragenetically most closely associated with Cu mineralisation. Miller et al. (Appendix 1) suggest steeply dipping quartzites beneath the major ore bodies were a major fluid aquifer for the deep metamorphic fluid.

Sources of Sulphur and the sedimentary input

The range in $\delta^{34}S_{sulfide}$ for the major mineral deposits in the WFB is from -18 to 30 ‰ (excluding fine grained pyrite). The Mt Isa Cu orebody (and the discordant

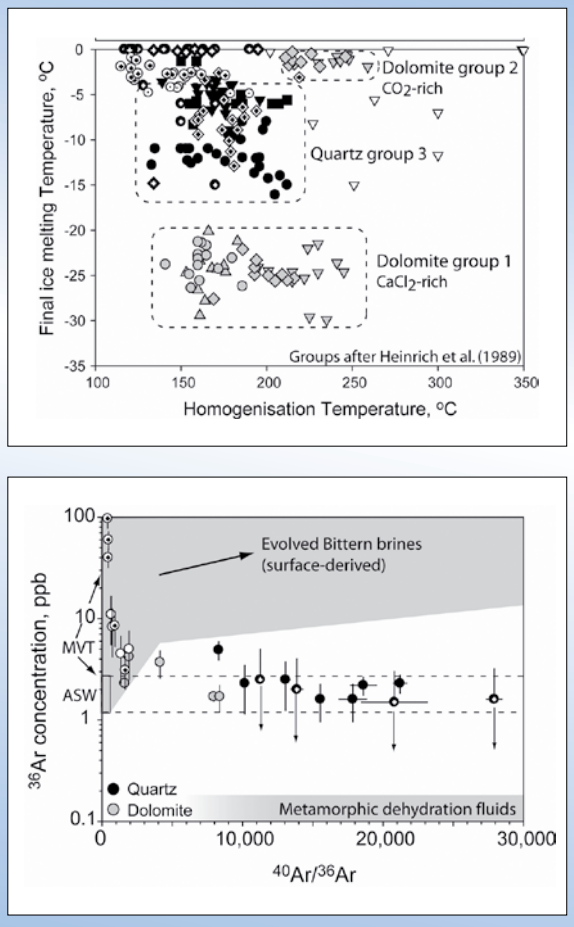

Figure 36:
A) Fluid inclusion data for minerals associated with Cu mineralisation in the Mount Isa deposit., B) $^{40}Ar/^{36}Ar$ versus ^{36}Ar concentration plot. Indicates mixing between deep metamorphic fluid and sedimentary formation water.

sulfides within the Burketown Mineral Field including the Century deposit) account for the most positive values of ~ 15 to 30 ‰ (Andrew et al. 1989; I4 report and references therein; Polito et al. 2006a; Broadbent et al. 1998). The Mammoth Cu deposit accounts for the most negative $\delta^{34}S$ values (Clarke, 2003).

The range of $\delta^{34}S_{sulfide}$ at Mt Isa (~15 to 30 ‰) is consistent with high temperature inorganic reduction of marine sulphate, implying the involvement of either bittern brines or halite dissolution waters, at temperatures of greater than ~ 300 °C. The only other process that could yield this range of values would be low temperature, biogenetically driven, closed-system reduction of seawater sulphate. Resolving these processes is important as it implies resolving when and where the reduction of marine sulphate occurred in the system. Arguably for the Mt Isa Cu deposit, the reduction was *in-situ* Thermochemical Sulphate Reduction (TSR; see later discussion)

The negative range of $\delta^{34}S_{sulfide}$ from the Mammoth Cu deposit could be interpreted as low temperature, biogenetically driven, open-system reduction of seawater sulphate. However, on balance, Clarke (2003) interprets the data in terms of high temperature *in-situ* redox processes with a non-marine source of sulphur of isotopic composition close to zero.

The extent and timing of TSR

The inorganic reduction of sulphate is strongly temperature dependent. Laboratory experiments show that TSR will proceed in hours to days at temperatures above about ~250–300°C but is very sluggish at lower temperatures (100–200°C). The reaction is also faster at more acidic conditions. Despite the problems in the laboratory, it is commonly assumed by workers in the petroleum and minerals industry that TSR operates at lower temperatures (100–200°C) at rates sufficient to promote *in-situ* reduction of sulphate to H_2S. Broadbent et al. (1998), Cooke et al. (1998) and Large et al. (1998) all assume significant rates of TSR at low temperature in the formation of the Pb-Zn deposits.

One possible mineralogical measure of the extent of sulfate – sulphide equilibrium in the system is the presence/absence of coarse-grained or hydrothermal pyrite. The pyrite precipitation reaction at the species level is given by:

$$Fe^{2+} + S_2^{2-} = FeS_2$$

The polysulfide species (S_2^{2-}) is a minor species, intermediate in redox state between sulfate and H_2S and hence its concentration is dependent on the extent of equilibrium between the dominant oxidized and reduced species:

$$1.75H_2S + 0.25SO_4^{2-} = S_2^{2-} + 1.5H^+ + H_2O$$

Assuming a sufficient supply of iron in the fluids, then the pyrite saturation reaction should act as a proxy for the rate of production of the polysufide iron (S_2^{2-}). Pyrite is the only common sulphide with a polysulfide in its crystal structure. Sphalerite, galena, pyrrhotite, chalcopyrite, bornite all have the sulphide ion (S^{2-}) in their structures. Hence, the precipitation of the other common sulfides is not affected directly by the issue of the extent of thermochemical sulphate reduction.

Notably, hydrothermal (coarse) pyrite is paragenetically late in the Century deposit and correlates with distinctly positive $\delta^{34}S_{sulfide}$ values (Broadbent et al. 1998; Polito et al. 2006a). Paragenetically early sulfides have $\delta^{34}S$ between 5 and 10 ‰, while paragenetically late fracture – filling and replacement-styles sulfides, associated with coarse pyrite, have $\delta^{34}S$ up to 20 to 25 ‰ in galena. These data are consistent with a thermally prograding system such that early sphalerite deposition occurs at low temperature (100–200°C) in the absence of significant TSR and hydrothermal pyrite precipitation. The presence of siderite at this stage of the paragenesis implies ample availability of iron in solution. Late replacement-style sulfides with galena, positive $\delta^{34}S$ and coarse pyrite are all consistent with increases in temperature to ~250–300°C and enhanced TSR. The general pattern of increasing $\delta^{34}S$ with time for the discordant veins of the Burketown Mineral Field is also consistent with increasing temperature and extent of TSR with time. This suggests the thermal prograding event is regional rather than local. The George Fisher deposit also shows paragenetic stages from early, layer parallel vein-hosted sphalerite, sphalerite breccias with minor galena and pyrrhotite to vein and breccia-hosted galena with sphalerite, pyrrhotite and euhedral pyrite. Similar paragenetic relationships occur at Hilton and Mt Isa Pb-Zn deposits (Chapman, 2004; Perkins, 1997 and references therein). This evolution from early sphalerite to late galena with euhedral pyrite is also consistent with a thermally prograding event; increasing extent of TSR and saturation of hydrothermal pyrite.

Nature and location of reservoirs of formational brines

At the time of formation of the Mt Isa Cu deposit, possible locations of bittern brine reservoirs were:

LSB or CSB Reservoirs

Possible sites within the LSB and CSB include dolomitic red-beds that may have contained deposits of anhydrite and dirty clastic rocks with potential to develop secondary porosity (Polito et al. 2006b&c, Southgate et al. 2006). Within the LRFT, the Lochness Formation was potentially a source of anhydrite, is dominated by red-brown siltstone and shale and is interpreted to have formed in a periodically emergent tidal or lagoonal environment. This formation is part of the Myally subgroup that thickens to the north both on the eastern and western side of the Mt Gordon arch. If the Lochness Formation or the enclosing feldspathic sands were the reservoirs/aquifers for bittern brines, then fluid migration at the time(s) of formation of the Mt Isa Pb-Zn and Cu deposits was upwards from north to south.

In the Century area on the LHP, the equivalent rocks occur 5- 8 km beneath the deposits, as inferred from recent seismic studies. A north-south elongate dome, approximately 10 km in width, occurs west of the Century deposit and is bounded by the Termite Range Fault and the Riversleigh Lineament. The dome approximates the area of the discordant Pb-Zn-Ag lode-style deposits of the Burketown Mineral Field (Broadbent et al. 1998; Polito et al. 2006a) and represents a potential area of upward fluid flow.

The Mallapunyah Dome at the southern end of the Batten Fault Zone in the McArthur River region is a similar scale feature to that at Century. Within the dome area, dolerite sills of the Settlement Creek and Gold Creek Volcanics (CSB correlates) intrude a sequence of fluvial, lacustrine and shallow marine hematitic sandstones, evaporitic siltstones and carbonates. Base-metals were leached from the dolerites by oxidized, saline brines (Cooke et al. 1998) suggesting the dome was also a region of upwelling of bittern brines from deeper in the section.

ISB Reservoirs

Possible reservoir localities in the ISB are salty fluids from the McNamara Group, in particular the Lady Loretta and Paradise Creek Formations, that occur broadly to the north and west of Mt Isa. An interesting observation is that the geographic distribution of deposits with $\delta^{34}S$ sulfide from ~ 15 to 30 ‰, all occur close to or to the west of the Mount Gordon Fault The list of deposits includes Esperanza, Mount Kelly, Lady Loretta, Mt Isa Cu and Pb-Zn and the deposits of the Burketown Mineral Field, including the Century deposit. This raises the possibility that brine reservoirs were located within the McNamara Group and major structures such as the Mt Gordon Fault partitioned and/or focused fluid flow. Uplift to the north of the region, say in the vicinity of the Murphy Inlier may have driven fluids to the south. This pattern of fluid flow is perhaps counter intuitive given that the high grade metamorphic rocks occur in the south of the Inlier so that fluid flow might be expected to be south to north during the Isan Orogeny.

Perched reservoirs in syn-orogenic clastics rocks

A possible source of bittern brines is perched basins that may have existed at the time of the Isan Orogeny and subsequently been eroded. Such basin could be considered Quamby Conglomerate equivalents. In this scenario major structures such as the Mt Gordon Fault may have focused the downward flow of bittern brines from perched basins in the system.

Links to super-reductants?

Re-Os data obtained for the Mt Isa Cu and Pb-Zn ores, the George Fisher Pb-Zn deposits and the Century deposit all yielded rather similar results with ages of ~ 1350-1450 Ma and initial $^{187}Os/^{188}Os$ intercepts close to the mantle (e.g. 0.16 ± 0.17 for century and 0.2 ± 0.25 for Mt Isa). The age of Cu and Pb-Zn mineralization defined by these studies is significantly younger than the accepted Pb-Pb model ages. The Isa Cu systems typically appeared to have remained open and hence susceptible to Re and Os mobility for protracted periods of time after ore formation (Bruce Schaefer, *pers. comm*. 2008).

The source of the metals in most sediment-hosted Pb-Zn-Ag deposits has usually been attributed to the rocks in the sedimentary basins hosting the deposits. This model is supported by Pb isotope studies that demonstrate Pb has a strong crustal isotopic signature. A primitive Os signal at Century points to a reduced mantle reservoir component (Bruce Schaefer, *pers. comm.* 2008) and the capacity to tap this reservoir may be a key part of the process of forming most of the larger deposits within the Isan mineral system.

Deep-Earth H_2-rich fluids have the capacity to transport acid volatiles as well as drive Na and Mg metasomatism at district scale.

The EFB IOCG deposits (Ernest Henry), Albitisation and Hydrothermal breccia systems (1530 Ma)

IOCG mineralisation and albitisation in the EFB are regarded as different parts of the same fluid system. However, it is now recognised that there were multiple mineralisation and albitisation events spanning a period of >100 Ma and Ernest Henry is regarded as the only IOCG deposit formed predominantly during the same time period as late-Isan magmatism at ~1530 Ma (Oliver et al. 2008). The age of the Ernest Henry IOCG deposit is constrained as 1525 Ma by hydrothermal titanate U-Pb ages and is within error of the 15 km distant Mt Margaret Granite. Ernest Henry has a number of unique characteristics that distinguish it from other IOCG deposits in the district:

- has strong noble gas evidence of a magmatic fluid component (Figure 37).
- has strongly focused K-feldspar alteration and widely developed brecciation. K-feldspar alteration is a natural consequence of cooling fluids equilibrated with a two feldspar granite and characterises magmatic ore deposits world-wide. Other IOCG such as Osborne are characterised by sodic alteration.
- has extensive late-Isan hydrothermal breccia pipes, similar to those proximal to granite intrusions in the Cloncurry District.

The close physical, petrographic and chemical similarity of Ernest Henry and regional hydrothermal breccias makes the regional breccias and alteration economically interesting. Several features support a genetic link between regional albitisation and IOCG mineralisation including: 1) the synchronous timing of some albitisation and mineralisation at 1530 Ma (Oliver et al. 2004); 2) geochemical arguments that link the acquisition of ore constituents to the alteration reactions taking place during albitisation (Oliver et al. 2004); and 3) the similarity of noble gas and halogen data in regional fluid inclusions and the Ernest Henry ore body. These latter data confirm the presence of magmatic volatiles in barren regional alteration.

District-scale Hydrothermal Breccia Systems

Marshall (2003; 2006) described Na-Ca alteration and associated brecciated rocks from the Mary Kathleen Fold Belt and Cloncurry districts. In particular Marshall and Oliver (2006) and Oliver et al. (2006) characterised the

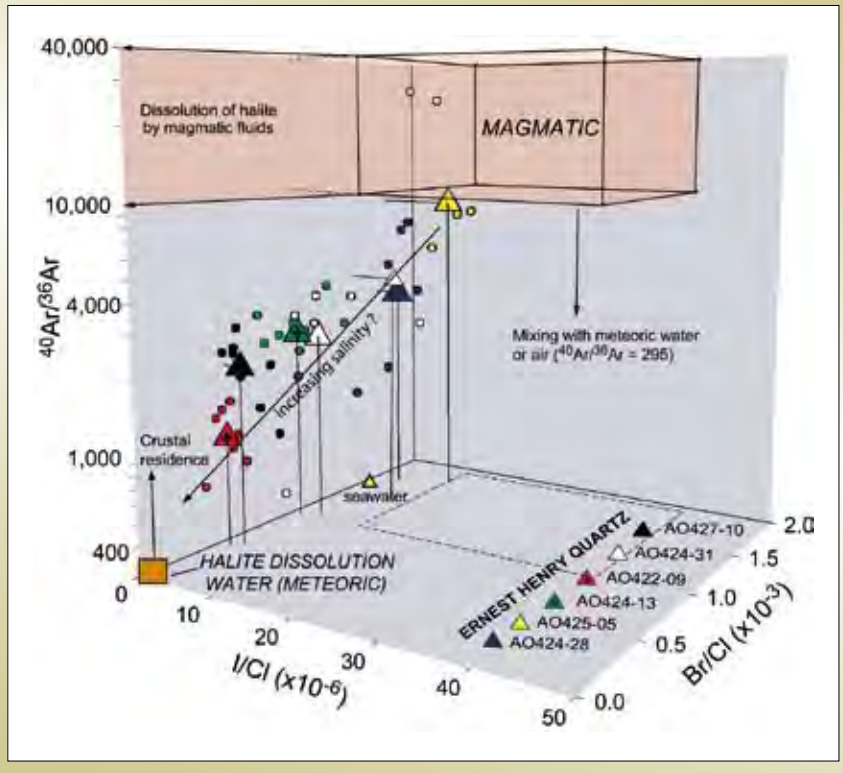

Figure 37: Noble gas and halogen data are most easily explained by mixing a deeply derived fluid of probable magmatic origin and upper-crustal halite dissolution sedimentary formation waters.

breccias into 3 distinct types; peak-metamorphic, Na-Ca, b) retrograde, hematite-k-feldspar, and c) magmatic hydrothermal, while Oliver et al. (2006) suggested that the breccias most associated with Fe-oxide Cu-Au where formed from magmatic CO_2 discharge at high pressures (hydrothermal breccia pipes).

In particular one group of metasomatic rocks, dominated by Na-(Ca) alteration assemblages were found in polymict, milled, matrix supported breccias (Marshall and Oliver 2006). These regional hydrothermal breccias occur as pipe or dyke like structures cross cutting the local stratigraphy and have a close spatial association with the Williams-age felsic intrusives (1580-1515 Ma). A description of the breccia classifications, mechanics of formation and genetic constraints has been attempted by Marshall (2003) and Oliver et al. (2006). The hydrothermal breccias are economically interesting because of the close physical, petrographic and chemical similarity to ore-hosting breccias at the Ernest Henry iron-oxide copper-gold deposit (Mark et al. 2006), as shown in Figure 38. Most of the work discussed in this section is from samples within the Snake Creek area including the Drowning Child, Suicide Ridge and Gilded Rose breccias, and we separate these breccias by their spatial distribution with respect to outcropping granite bodies. For details about the location of these systems and the local geology the reader is referred to Oliver et al. (2006).

Granite Proximal Hydrothermal Breccias

The **Suicide Ridge** breccia pipe (Bertelli 2007) is a well characterised example of a hydrothermal breccia emanating from a brecciated, Na-altered granite carapace (Saxby granite, 1520 Ma). The breccia (Figure 39) includes clast material derived from the local wall rock (Snake Creek pelites), and exotic clasts of Corella marble, mostly intact and relatively unaltered, that maybe derived from as much as 1 km away. The breccia also includes "clasts" of igneous material, including pegmatites, aplites, hydrothermal products and granites that exhibit an intrusive and brecciated contact relationship. This indicates that the process of magmatic crystallisation and fluid exsolution was taking place prior to, and synchronous with the emplacement of the breccia.

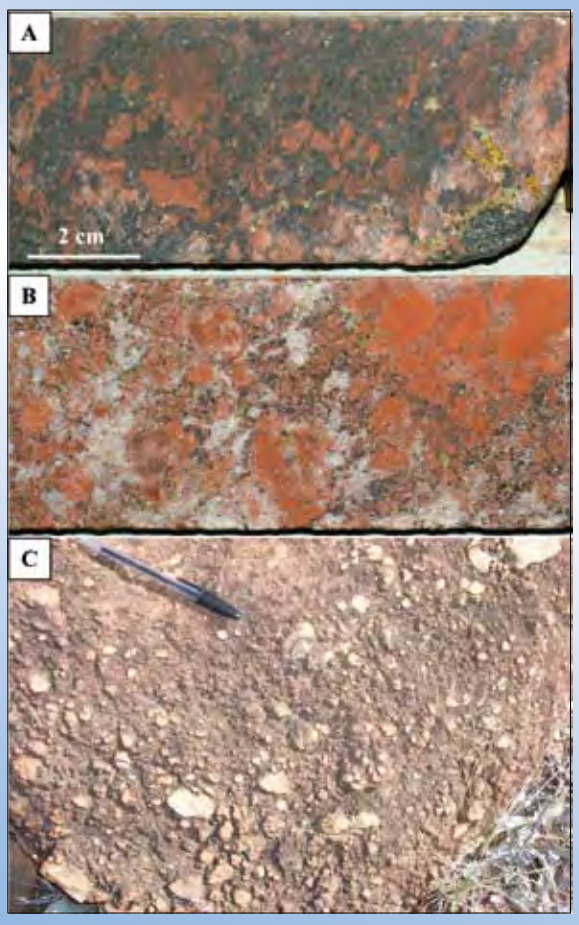

Figure 38: Examples of mineralised (Ernest Henry) and unmineralised hydrothermal breccias in the Cloncurry district. A) High grade (> 1 wt% Cu), magnetite-chalcopyrite matrix supported breccia, B) lower grade (?? % Cu) clast supported carbonate-magnetite-chalcopyrite breccia and, C) regional hydrothermal breccia from the Snake Creek area consisting of albitsied clasts and calcite-albite-magnetite matrix.

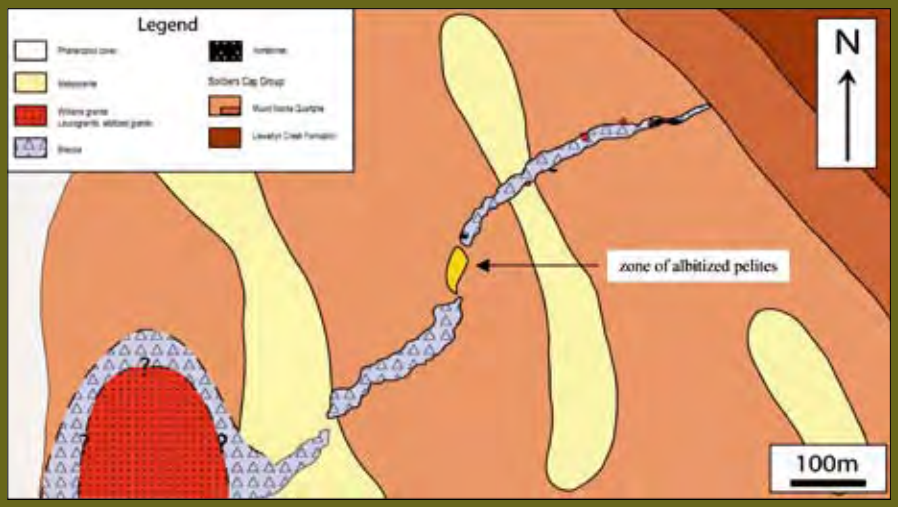

Figure 39: Map of the Suicide Ridge breccia pipe (after Bertelli, 2007) that emanates from a brecciated, albitised granite of the Saxby quite (~1520 Ma), and cuts across SCG pelites.

There is also a broad fractionation of igneous material from proximal to distal portions of the dyke where the included granite and pegmatite clasts actually follow a reverse fractionation with distance (i.e. the most fractionated and hydrothermally alteration granite clasts are found furthest from the mapped granite contact). Assuming that the mapped outcrop is representative of the distribution, then this may indicate that the outer portions of the granite where entrained first and carried furthest during breccia emplacement, while inner portions followed such that the breccia preserves the original zonation within the magmatic-hydrothermal system. This most fractioned part of the sequence shows a zonation from hematite-magnetite-bearing quartz-albite pegmatites, hematite-quartz to hematite with subordinate quartz. This sequence, assuming the magnetite-hematite is a primary product of the melt-hydrothermal system, indicates that the magma was oxidised, at least in the carapace region.

Bertelli (2007) has measured fluid inclusions in samples of entrained magmatic material and the hydrothermal Fe-stones and has shown that there are two dominant fluid inclusion types formed during the genesis of the breccia pipe (type I and III inclusions, Table 5). Broadly

Table 5: Summary of the fluid inclusion types characterised from the Suicide Ridge breccia system. The types can be categorised as A) primary inclusions related to magmatic system (red box), B) inclusions in trails associated with secondary Na-alteration (i.e. bright CL albite, blue box) and C) inclusions that are later paragenetically, but type IV are overprinted by type V (green box). Type Ic and II inclusions are rare and of uncertain provenance

Type		Phases	Origin	Abundance	Size (μm)	Fluid Inclusion	Sal NaCl (wt% NaCl eq)	Th
Type I - Carbonic	Type Ia	CO_2(L)	P	common	<5-15			-17.5 to +0.5
	Type Ib	CO_2(L)	PS	common	<5-15			-1.1 to 30.5
Type II - Mixed Aqueous-Carbonic and Mixed Brine-Carbonic	Type IIa	CO_2 (L)+H_2O (L)	P?	common	< 10		5.9 to 16.8	276.4
	Type IIb	CO_2 (L)+H_2O (L)+H	P?	very rare	< 10		31.2 to 38.7	
Type III - Liquid-rich or halite-bearing	Type IIIa	L+V+H	S	abundant	<5-20		30.3 to 45.4	147.5 to 360
	Type IIIb	L+V	S	common	<5-20		22.4 to 28.1	109.2 to 183.5
Type IV - Liquid-rich or halite bearing	Type IVa	L+V+H	S	common	<5-20		32.1 to 35.1	203.6 to 256.7
	Type IVb	L+V	S	common	<5-20			166.3 to 184.7
Type V -Liquid-rich		L+V	S	common	< 10		8.8 12.8	144 to 245.4

type I (CO_2-H_2O) formed as primary inclusions in the granitic rocks associated with the brecciation, while type III (NaCl-$CaCl_2$-H_2O) formed in trails associated with albitisation post-brecciation, and possibly dominate the hydrothermal Fe-stones.

- **CO_2-H_2O**: the primary inclusions record a wide range of calculated densities that can be seen as scatter in the isochors plotted in Figure 40 (red – primary, blue – later). By assuming a confining pressure for the pre-breccia granite of 300 MPa (Rubenach, 2005), and a crystallisation temperature of ~540°C (albite-quartz geothermometry, see similar rocks in Mark & Foster, 2000), then the type Ia inclusions record pressures of around 420 MPa. This is 120 MPa overpressure relative to the assumed confining pressure. However the paragenetically slightly later type Ib inclusions record an average pressure of between 270 MPa, which is within error of the estimated confining pressure. The common primary inclusions don't contain much Cl, however some rarer mixed carbonic-salt inclusions have been observed. Figure 41a is a summary plot of the calculated mole fractions of NaCl-CO_2-H_2O in stage I carbonic inclusions from Bertelli (2007) data. It is interesting to note the constant ratio of NaCl-H_2O but variable CO_2. This dataset indicates that the chemical coupling is between the salt-water and the CO_2 is added external to this system
- **NaCl-CaCl-H_2O**: the breccia samples, in particular the quartz-albite rich granite samples are cross-cut by trails containing high salinity mixed salt inclusions (type III, Table 5). These trails are observed to be associated with second stage albite alteration of some of the samples, where the second generation albite is luminescent in CL (related to the presence of Fe^{3+}). This generation of inclusions have a range of salinities from 45 to ~22 wt% NaCl eq. (Figure 41b), without an obvious change in the paragenetic stage or relationship. If we assume that these fluids interacted with the breccia pipe at similar metamorphic pressures (300 MPa) just after the emplacement of the breccia, then the calculated trapping temperatures range from ~440°C (45 wt% NaCl) to 300°C (32-22 wt% NaCl), which maybe in line with the background thermal regime of the sequences upon cooling of the granites at ~1520 Ma. It is not obvious what causes the progressive shift to lower salinity in these fluids. If the pressures are correct this may be a function of mixing with a cooler, aqueous-rich fluid. However the temperature-salinity curve is parallel to the halite-liquid curve but shifted to higher pressures. If we assume the temperatures are correct and the trend tracks the halite liquidus (i.e. halite saturation is maintained down temperature) the pressures would need to be ~100-150 MPa. This is significantly less than calculated for the intrusion of the Saxby granite (300 MPa).

CO_2 Driven Brecciation in Granite

One of the paradoxes of these CO_2-rich breccia systems, and their relationship to granitic magmas, is the low solubility of CO_2 in felsic melts. There are two ways that we

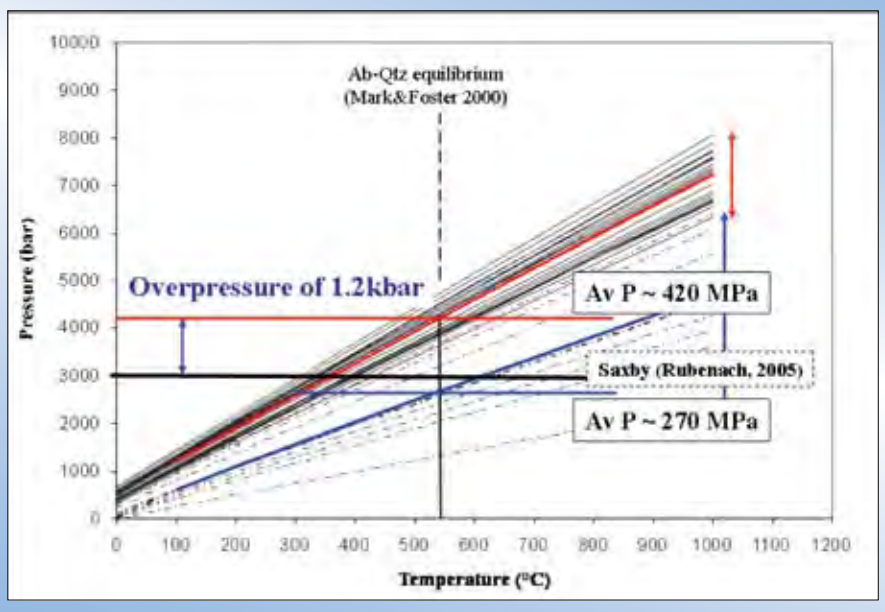

Figure 40: Isochores for the CO_2-H_2O primary inclusions in granitic material of the Suicide Ridge breccia (Bertelli, 2007), showing the large range of densities in type Ia (red) and Ib (blue) inclusions. Using an estimate for the metamorphic pressure (Rubenach, 2005) and Qtz-Ab equilibrium temperature for these granites (540°C) it can be shown that it is possible the type Ia inclusions record overpressures of ~120 MPa prior to brecciation and subsequent relaxation to litholstatic pressures (~300-270 MPa). Higher temperatures of emplacement of the granite would lead to higher pressures of the type Ia inclusions.

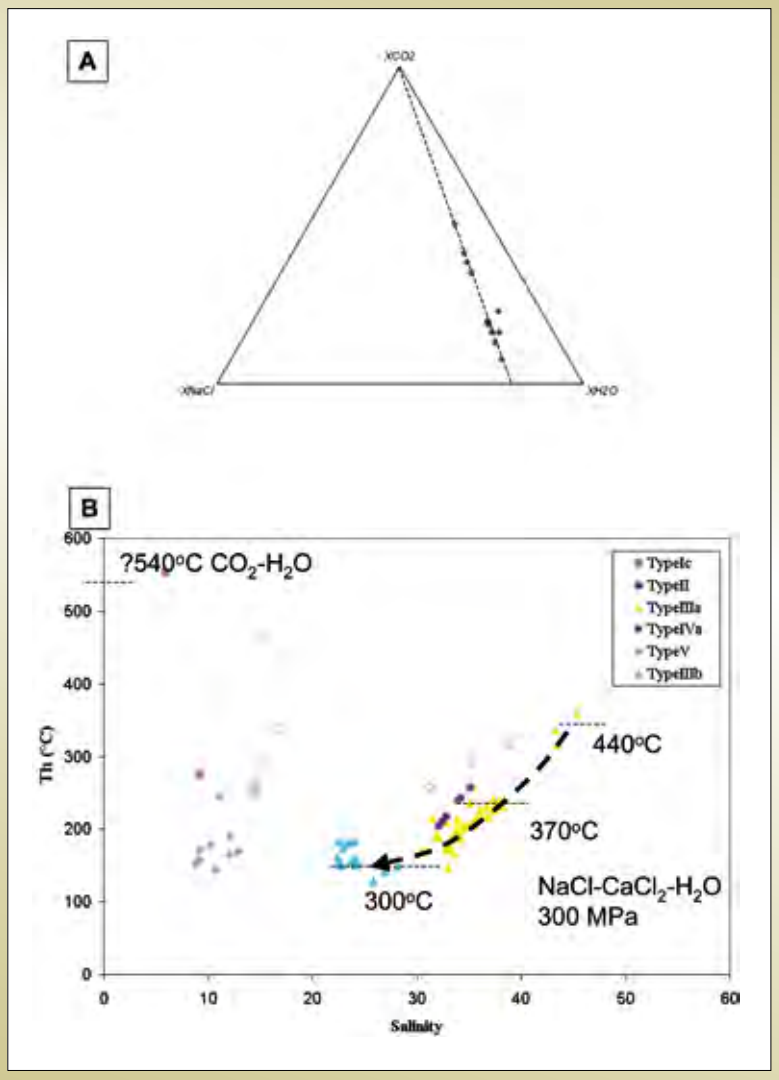

Figure 41: Summary data from Suicide Ridge fluid inclusions (Bertelli, 2007) A) Calculated mole fractions of NaCl-CO_2-H_2O in the stage I carbonic inclusions. B) Summary Th-salinity diagram for the Suicide Ridge fluids form Bertelli (2007). The CO_2-H_2O primary inclusions (XCO2 ~ 0.9) are thought to be trapped at 540°C (ab-qtz equilibrium) at confining pressures of ~300 MPa (Rubenach, 2005). The secondary NaCl-CaCl-H_2O inclusions fall on a variable salinity and Th curve. Assuming the confining pressure of 300 MPa this equates to a trapping temperature range of between 440–300°C as indicated on the diagram (see text for further discussion).

might record high X_{CO_2} fluids from felsic rocks with low solubility for this component:

a) The volatile phase exsolves from the melt in the two phase field for H_2O-CO_2-NaCl fluids. This process could generate (depending on the exact phase relationships) a high X_{CO_2} fluid in equilibrium with a high XNaCl fluid

b) CO_2 could be added as a volatile component directly to the melt at the site of granite emplacement, so that the melt immediately became saturated in a high X_{CO_2} fluid.

Mass balance constraints mean that it is unlikely that melt exsolving fluid in the mixed fluid two phase region can generate large quantities of high X_{CO_2} fluid; this process would generate significantly more high-saline brine than CO_2 fluid. This is not observed, and there is no evidence for brine in equilibrium with the CO_2-H_2O fluid within the granitic fragments at Suicide Ridge. A more likely scenario is that the CO_2 was added to the melt as an external component, and this process drove rapid, catastrophic exsolution of volatiles from the melt. This process has been suggested as the trigger mechanism for some explosive volcanic eruptions (Murphy et al. 1998).

Can volatile transfer into the melt cause the large overpressures that are calculated from the fluid inclusions? To test this idea a simple model was setup to look at the transfer of CO_2 from a mafic rock (with high CO_2 solubility) to the granite. This process has been considered because of the commonly observed mafic magma mingling textiures in the Saxby granites (M. Rubenach, *pers. comm.*), and because the isotopic modelling of these granite systems indicates that a mafic mixed component is quite common in these systems (Mark and Pollard 2006; I2/3 report).

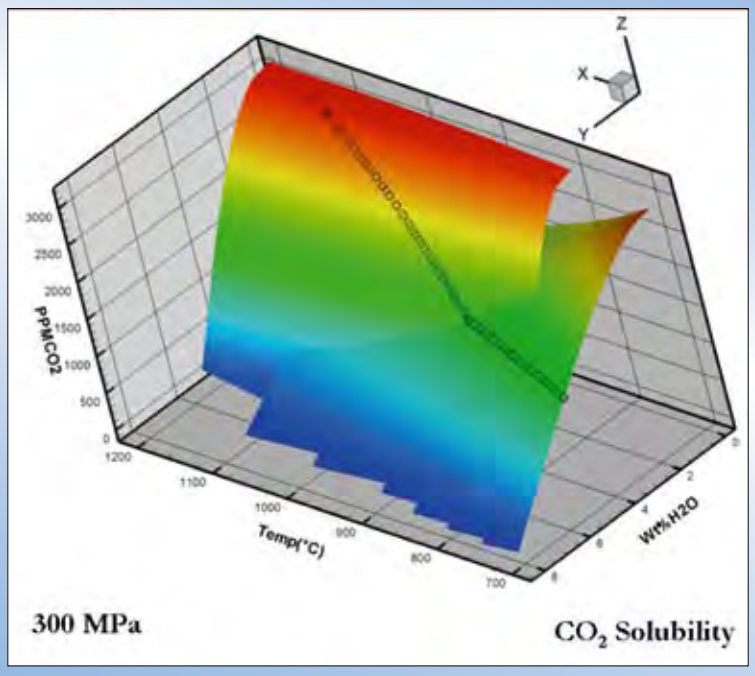

Figure 42: Solubility curves for CO_2 (ppm) in felsic and tholeiitic basalts for variable temperature, melt water contents (wt%) and pressures of 300 MPa. The hypothetical mafic-granite mixing curve is illustrated at dots on the two curves (high T, low H_2O mafic to low T, higher H_2O felsic).

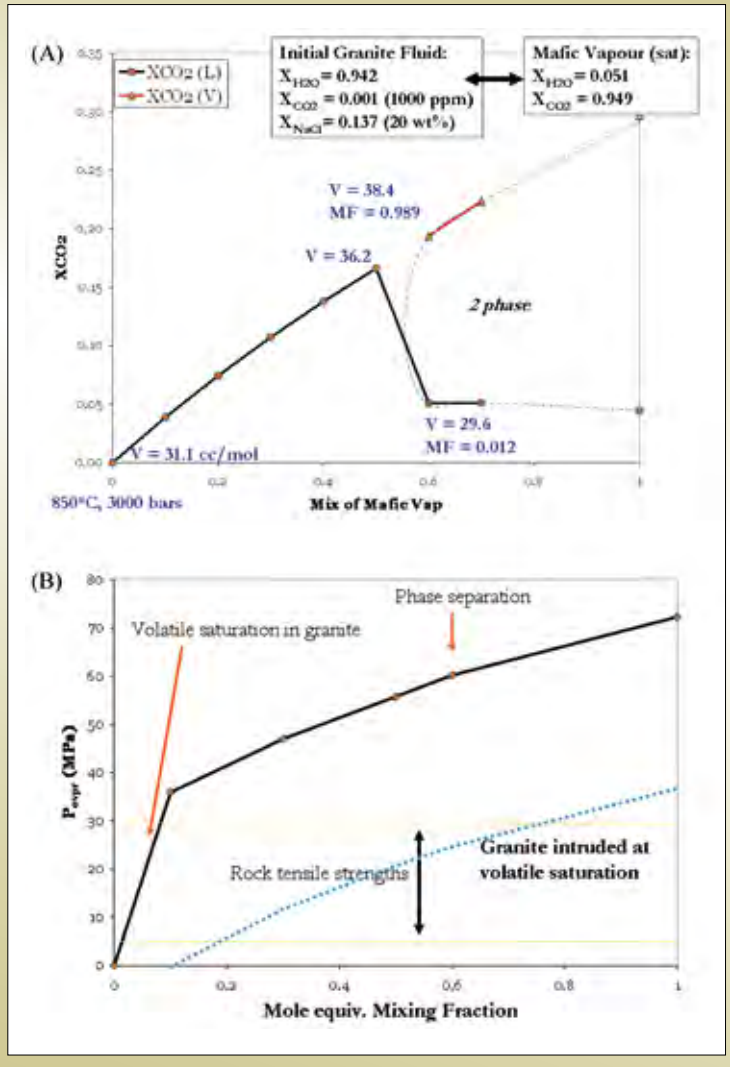

Figure 43: Model for mixing mafic volatile into felsic rocks. A) Calculated molar volume of the resulting fluids at 300 MPa and 850°C. Volatile saturation in the granite occurs very early (???) while the resulting fluid only phase separates after ~60% of mafic volatile has been added to the felsic. B) Calculated overpressures within an incompressible granite for the modelled volatile mixing and volume changes. The overpressure is calculated for initially volatile under saturated granite (black line) and initially volatile saturated granite (blue line). Assuming general rock tensile strengths of ~10-30 MPa, fracturing and failer would occur with between 10 and 80% mafic volatile component (depending on the initial state of the granite).

Figure 42 shows the starting scenario for this model where the CO_2 solubility curves are plotted for felsic and mafic magmas (calculations with VolatileCalc, Newman and Lowenstern 2002) for variable temperature and water contents. The dotted line is the assumed mixing line between CO_2-rich mafic melts and CO_2-poor, water-rich felsic melts. There is a significant drop in the total concentration of CO_2 that is soluble in melt during this process.

From the initial data plotted in Figure 42 and knowledge of typical water contents of melts in the granite-mafic system a model, fluid was constructed for both end-members. The initial fluid compositions are recorded on Figure 43, where the mafic was assumed to be at CO_2 saturation at 300 MPa (i.e. CO_2 degassing during adiabatic ascent from deeper crustal levels). Figure 43a shows the calculated molar volume of resulting volatile in the granite with progressive mixing of mafic volatile component (plotted as molar mixing fraction) and increasing X_{CO_2} of the volatile phase. Volatile saturation in the granite would occur at ~10% mafic component (based on the total water-CO_2 content). The molar volume of the volatile phase increases rapidly to start with (exsolution in the melt) and then continues to rise until intersecting the two phase region (~60% mafic component). At this point, three phases are present; silicate melt, high X_{NaCl} and high X_{CO_2} fluid. The mass fraction of the two fluid components is heavily waited towards the CO_2 fluid (~99% molar), with X_{CO_2} ~ 0.25.

Using the molar volume of the calculated volatile phase generated in the melt we can attempt to calculated the over pressures that this would generate. By assuming that the granite is incompressible we can use Boyles law ($P_0V_0 = P_1V_1$) to calculate the overpressure generated by the change in volatile molar volume, which in this case is just $P_{o/pressure} = P_0 - P_1$ (i.e. the reaction to the force try to get the system to P_1). Figure 43b is a plot of the mafic mixed fraction of the model plotted against calculated overpressure for granite initially under saturated (black line) and initially saturated (blue line). If we assume that rock tensile strengths are ~10-30 MPa and that rock failure will take place when $P_{melt} = P_{confining} + \theta$, where θ is the tensile strength, then catastrophic failure is likely for the melt-rock system in the initially under saturated system. If the process of volatile transfer is quick relative the rate at which failure can take place, then it is possible in this model to generate up to 70 MPa of overpressure. Although there are many assumptions in this approach, and the starting conditions and evolution of the model can change, it does demonstrate the ability to generate overpressures in granite systems that approach those recorded in the Suicide Ridge breccia (120 MPa).

Source of CO_2 in K-granites

The model discussed above assumes CO_2 was derived from the mafic magmas that intrude synchronously with the Williams and Saxby granites. A mantle/magmatic contribution is supported by noble gas and stable isotope data (Oliver et al. 1993; H6 final report). However, in addition, these data provide evidence for crustal CO_2 sources. There are three distinct reservoirs in the Cloncurry block:

a) Corella Formation marbles (~1740 Ma, metamorphism ~1600 Ma)
b) Mantle CO_2 transported via mafic melts or directly to the crust
c) CO_2-bearing lower crust (melt source region).

The arguments made previously about CO_2 solubility in felsic magmas probably preclude significant large scale transport by these systems, indicating a deep-crustal component is not favoured. Geological evidence at Suicide Ridge (textural location of fluid inclusions, halogen data and fluid composition) indicates that the local source of CO_2-rich fluids in the breccia is the magmatic system. However, clasts of the Corella Formation in this breccia indicate a possible upper crustal contribution of carbonate CO_2. Furthermore, contamination of the granites by crustal material seems to be minor at the level of emplacement (Mark and Foster 2000; Mark and Pollard 2006).

Granite Distal Hydrothermal Breccias

Granite distal breccia systems are those described with no obvious mapped relationship to granites, although they may be close vertically to non-outcropping magmatic bodies. This work recognised two key petrographic groups based on the absence or presence of amphibole as an infill phase. The amphibole-absent breccias are dominated by calcite – albite infill with accessory magnetite – rutile – apatite (Figure 44a). The most amphibole-rich breccias contain albitised rounded clasts in a matrix of tremolite – titanomagnetite – titanate (Figure 44b & c). The tremolite can be overgrown and replaced by actinolite with concomitant alteration of alanite/titanite to monazite/

huttonite. Clasts are similar in both breccia types and are a mixture of locally derived wallrock fragments, dominated by calc-silicates and/or pellites, and transported material. Field evidence suggests that some material may have been transported up to 1-2 km (Oliver et al. 2006). Apatite is present in all samples of breccia but is most abundant in the calcite-rich breccia samples. Marshall et al. (2004) suggest a further division to retrograde breccias (hematite-kfeldspar), of which Ernest Henry and Gilded Rose are examples. It is likely that the difference between the breccia-types is a function of the dominant fluid chemistry or the proportion of wallrock interaction (fluid/rock ratio) during brecciation and alteration. The assemblage amphibole – Ti-magnetite – titanite forms at different X_{CO_2} than that of calcite – rutile – magnetite (*cf.* Spear 1995).

One common difficulty is distinguishing between minerals that are clastic components as opposed to hydrothermal precipitates. In most samples apatite can be found within clast material, as clastic components within the matrix and as a precipitate. The morphology, chemical signature and zoning can help to distinguish these different types, however most clast apatite appears to have partially re-equilibrated during brecciation.

Apatite Chemistry and Modelling

Using the halogen (F, Cl) contents of the apatite that is found in many of the metasomatic environments, it is possible to reconstruct the main features of the fluid chemistry. HCh (Shvarov and Bastrakov 1999) has been used to model simple rock-fluid buffered systems to attempt to back calculate the actual halogen contents of the fluids from apatite data.

Figure 45 is a summary plot of all apatite chemical analysis from breccia or related material in the Cloncurry district from this work. Fluorine is plotted against Cl (atomic formula units) and there are five distinctive groupings on the plot. The best example of a magmatic apatite is represented by group 1 from a gabbro within the Drowning Child area. This is the core of a zoned apatite in the gabbro and contains $F \sim H_2O >> Cl$. Group 2 apatites are regional hydrothermal breccia systems, typically containing carbonate, with $F > H_2O >> Cl$, group 3 are apatites with excess F (i.e. more than 2 afu), possibly as a consequence of the substitution of CO_2. This includes all the Ernest Henry apatites from the ore body breccia (black circles). Group 5 represents apatite from the metasomatised margin of the gabbro, where the mineralogy includes scapolite –

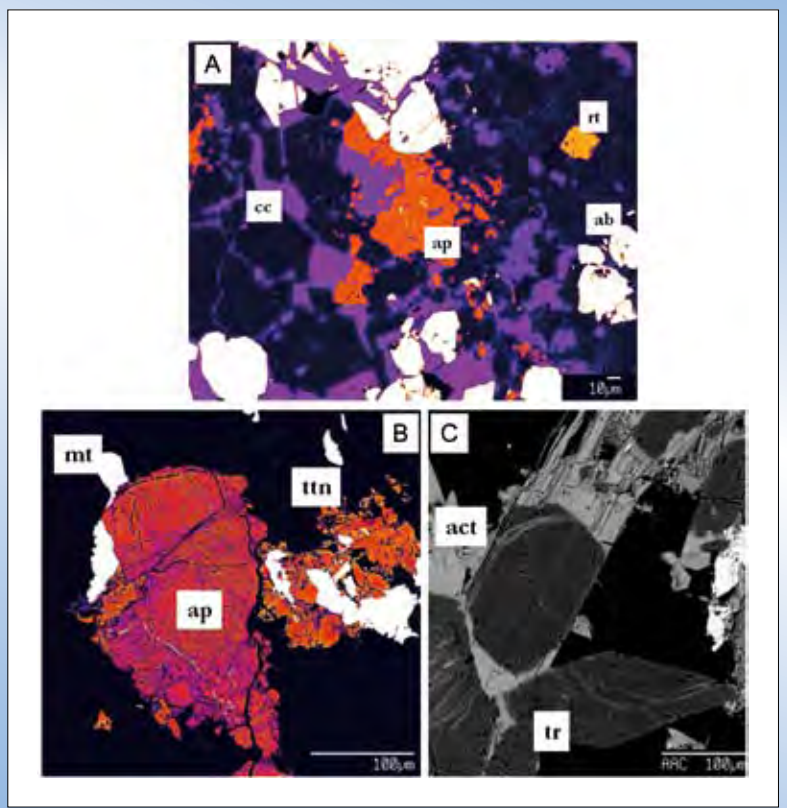

Figure 44: False coloured and grey scale Backscatter Electron Images (BSEI) showing the key petrographic features of the calcite and amphibole hydrothermal breccias. A) Calcite-type breccia with infilling calcite-albite and dominated by magnetite-apatite and rutile. B) Amphibole-type breccia showing apatite clast partially reequilirbriated by the fluids overgrown by magnetite-titanite and, C) Amphibole-type breccia showing tremolite cores and actinolite rims (Northern Snake Creek area).

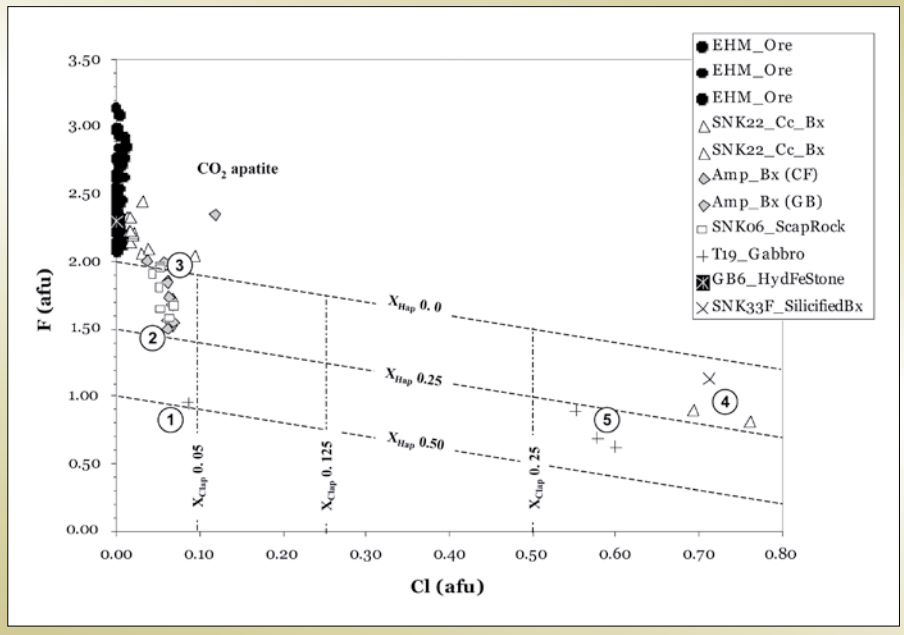

Figure 45: F-Cl (atomic formula units) data for apatites from hydrothermal breccias, Ernest Henry ore breccia, mafic intrusive and Corella marble (see text for sample details). Dashed lines are location of constant mole fractions of apatite-OH (Hap) or apatite-Cl (Clap). Data above the X_{Hap} = 0 line contain non-stoichiometric F that may indicate the presence of CO_2.

k-feldspar as an alteration product. These latter apatites contain F>~Cl>H_2O, while group 4 represent apatite from late-stage hematite-chalcopyrite-chlorite breccia rocks.

Figure 46 shows the distribution of the key apatite trace elements in the samples from this study. As and S are seen to vary from zero to 0.5 and 0.18 afu respectively (relative to 10 Ca apatite). The samples from Ernest Henry (black dots) are typically the most enriched in the trace components relative to the regional samples (for details see *Q5 Deposition* in this volume). Some of the breccia samples also show enrichment, especially in As. Hydrothermal Fe-stone within the Na-Ca altered Gilded Rose breccia contains apatite with enriched S compared to most other samples (square with cross, Figure 44b).

The exchange of halogens can be shown on a diagram comparing X_{Hap} and X_{Fap} (Figure 47). The single trend line with the majority of the data points marks the 1:1 exchange of F:OH in the apatite. Data to the left of this line (the more Cl enriched samples) are a departure from this 1:1 exchange with Cl substituting for the halogen site. Data are not permited to fall to the right of the line by stoichiometric constraints in the apatite formula. The dominant exchange of F – OH may indicate that in the large part these systems (in which apatite is precipitating) are influenced by external supplies of HF rather than HCl.

Calculating the fluid chemistry

The halogen contents of apatite are a function of the mixing properties on the apatite OH site, and the ratios of the activities of the species H_2O-HCl-HF. The mixing models for apatite have been shown to be relatively close to ideal, on-site mixing (Zhu and Sverjensky 1991; Zhu and Sverjensky 1992), and as such using geochemical batch modelling can be used to estimate the fluid chemistry (bulk F vs Cl) from the apatite data.

HCh (Shvarov and Bastrakov 1999) has been used to model the simple albite-anorthite-mica-quartz – HF-NaCl-H_2O system at between 600-450°C and 300 MPa. (For references to thermodynamic data and model setup see Cleverley & Oliver (2005)). Figure 48 shows the results of the model at 600°C (approximating the gabbro apatite) and 450°C (approximating the regional rocks). The graphs depict the contours of X_{Hap} and X_{Clap} in the apatite in equilibrium with a fluid of a particular NaCl-F composition. The extimated fluid compositions in equilibrium with the natural apatite data discussed from Figure 45 are illustrated as numbered circles. As an example, if we assume a temperature of 450°C for the formation of the core apatite in the scapolite-bearing rocks then the fluid composition would be approximately 0.8 mNaCl and 3000 ppm F (Figure 48). This assumes pH buffering by albite-anorthite-muscovite-quartz which is not unreasonable for these rocks.

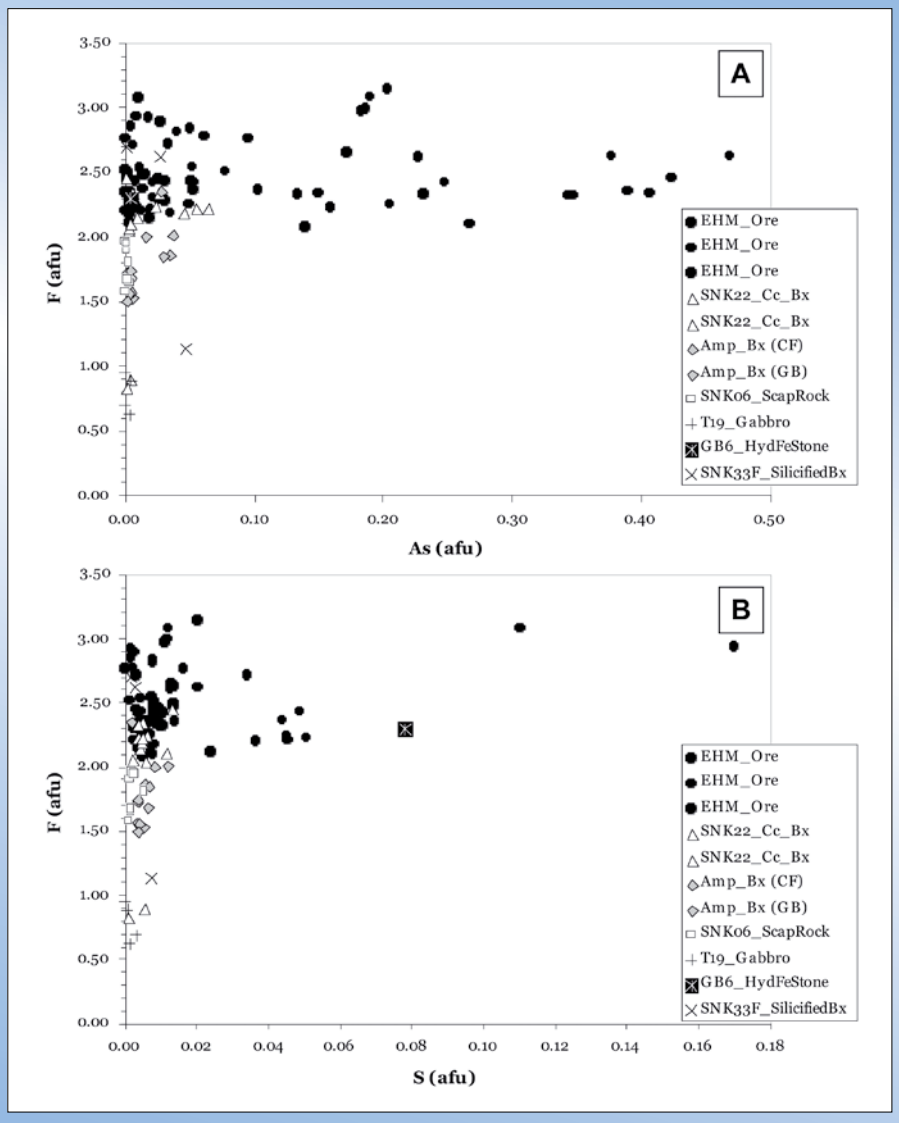

Figure 46: A) F-As (afu) and B) F-S (afu) for the same apatites as Figure 43.

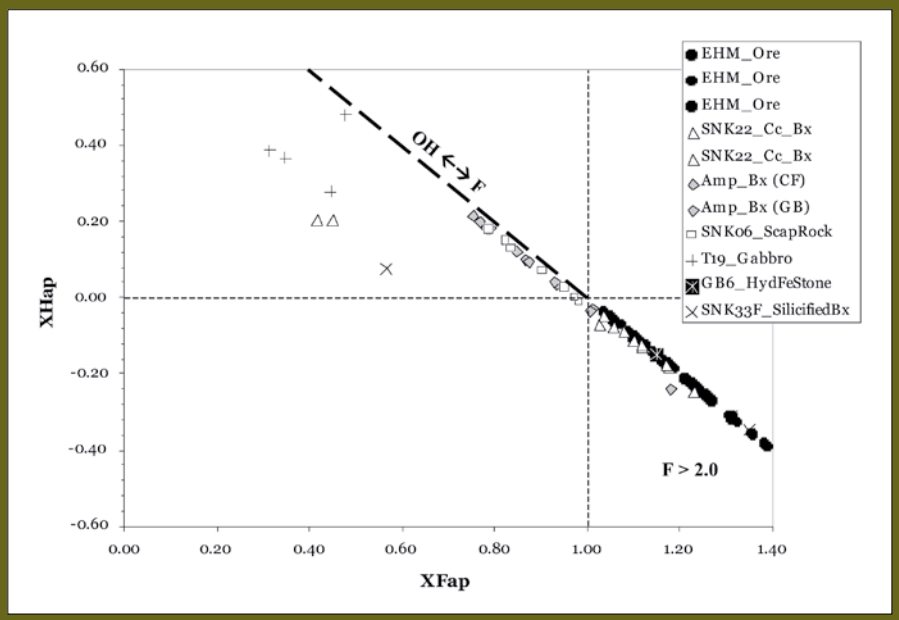

Figure 47: Calculated mole fraction of the theoretical OH and F molecules (X_{Hap} and X_{Fap}). Values in the box on the lower left are indicitive of 'excess' F, probably from CO_2 substitution. Points along the molar OH-F line (thick, dashed) indicate direct replacement of F by OH in without changing the Cl.

It should be noted that these calculations are only valid based on the assumptions of the model system – T, P and aH_2O. We can not currently use this data to reconstruct the aCO_2 which could have a large influence on the overall model results. However, by making the same assumption for all the apatites considered here it is at least possible to compare like-for-like and get important comparative information. For apatite with non-stoichiometric F this technique can not be applied because the mixing relationships in the crystal lattice are far from ideal.

Cl-Fe Metasomatism of Gabbro

Samples of the freshest gabbro, dominated by magmatic textures (plagioclase-hornblende-quartz), contain some restricted hydrothermal phases (Cl-amphibole, sulphides). These samples also have magmatic apatite with rims that form during the hydrothermal stage. The halogen chemistry indicates that the transition from magmatic core to hydrothermal rim is related to a shift from low Cl to high Cl fluids (0.8 to 3.5-5 molal Cl) at almost constant F (1 to 5, Figure 48). The gabbros themselves are more intensely alterted close to the margins, and in places the original mgmatic textures are almost destroyed (see hyperspectral data and images of this same example in *Q4 Pathways* in this volume). Alteration at the margins includes phases such as Cl-K-amphibole, biotite, scapolite consistent with a similar to the Fe-Cl metasomatism at Ernest Henry (dark rock). From the apatite analysis it appears that the post-crystallisation phase of the gabbro showed evidence for the influx of a Cl-rich fluid that likely did not contain much F, preserving the magmatic F signature.

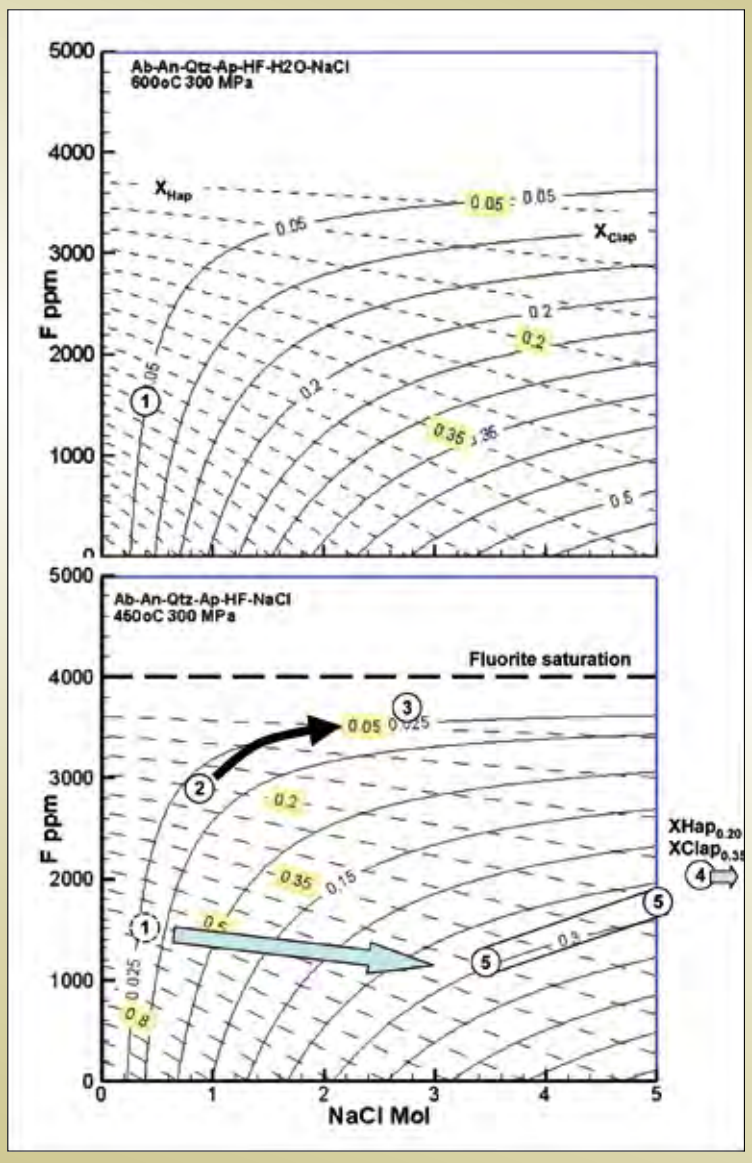

Figure 48: Models for the composition of apatite in equilibrium with albite-anorthite-quartz-H_2O with variable NaCl (molal) and F (mg/kg) at A) 600°C and 300 MPa and, B) 450°C and 300 MPa. Data points are end-member positions calculated from the natural dataset in figure 11 represented by 1) magmatic (mafic), 2) core of scapolite marble, 3) towards F enrichment in scapolitic marble, 4) extreme Cl enriched apatite from breccias and 5) range of compositions of rim of magmatic apatite (external fluids).

Figure 49 shows the isochon (mass balance) plot for fresh gabbro (at Drowning Child Breccia) versus that affected by the intense Cl metasomatism as recorded by the apatite. Interesting to note is the significant Cu striping that occurs during this event. A model where fluids strip the Cu from mafic rocks was first suggested by K. Butera (I2/3 report) and is also suggested by Oliver et al. (in press). Here the evidence would suggest that the influx of locally derived brine causes Fe-Cl metasomatism and strips Cu in the process, lending some weight to this argument, although the ultimate source of the salt-rich fluid is unknown at this stage.

Metasomatism and Metamorphic Fluids

Apatite from scapolite-bearing marble from the Snake Creek area also shows core-rim textures. These are interpretated as the core forming during peak metamorphism while the rim represents the influx of some externally derived fluid with unknown source. The core-rim evolution is marked by the trend from 2 to 3 on Figure 48. This trend shows an increase in both F and Cl at the expense of H_2O and indicates that the incoming fluid was F-Cl-rich (~3 molal Cl, 3500 ppm F) but contained little H_2O. This data indicates that at least these scapolite marbles contained reservoired salty fluids during post metamorphism (1 – 3 molal NaCl ~3-12 wt%). These compositions are within the range calculated for peak metamorphic rock equilibriated fluids (with respect to reaction progress and scapolite composition) from Oliver et al. (1992) and as calculated later in this section (see rock fluids section).

Salt-rich Breccias

The last sample of apatite comes from breccias that appear to form in equilibrium with salt-rich fluids. These samples are also commonly associated with 1) apatite cores within calcite-bearing breccias (probably reflecting clast material from the wallrock) and, 2) k-feldspar, hematite, quartz and chalcopyrite bearing breccias (i.e. Afternoon Low, Roadmaker and Drowning Child Breccias). The apatite in these samples gives calculated values beyond the modelling results but extrapolation on Figure 48 indicates ~ 6-7 molal NaCl (20-25 wt%). The textures in the hematite-quartz breccias are indicative of late fluid processes, and are similar in appearance to many of the hematite-quartz-Cu occurrences around the IOCG district. It is likely that these assemblages formed post-breccia emplacement but there is no evidence to suggest when this happened.

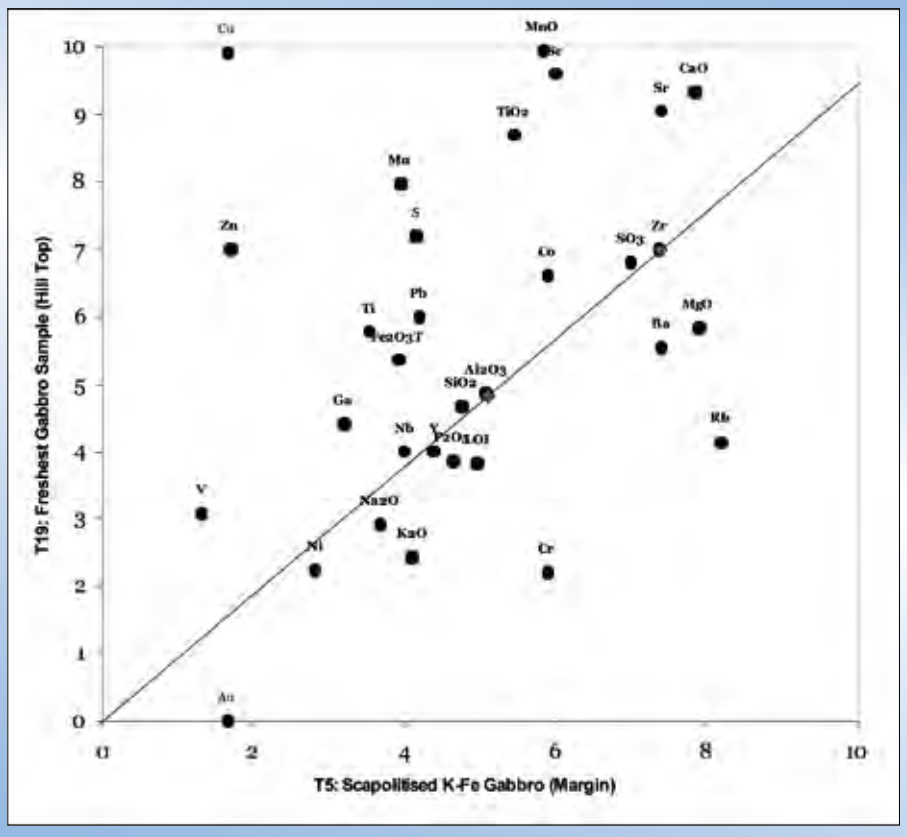

Figure 49: Drowning Child area of the Northern Snake Creek district. Isochon for the "fresh" versus altered gabbro shown by the stars (see text). The magnetite susceptibility also drops towards the margin of the body.

Fluids in equilibrium with scapolite marbles

Scapolitic calc-silicates in the MKFB and EFB are characterised by minimal external fluid infiltration during regional metamorphism (1600-1580 Ma). Using mineral chemical and thermodynamic calculations, Oliver et al. (1992) have calculated the range of rock buffered fluid compositions that can be generated in typical Corella calc-silicates in the MKFB. In particular Oliver et al. (1992) suggest that the rock buffered fluids can change composition on the 1-50m scale (as dictated by compositional layering in the calc-silicates), and that there is evidence for compartmentalisation of fluids during metamorphism (i.e. no significant migration) and external infiltration. The range of reaction progress values calculated during their study also illustrated that fluid was able to migrate through the deforming sequence without impacting on adjacent layers, probably as transient grain boundary and fracture flow.

Using the data from Oliver et al. (1992) derived from the Corella formation in the MKFB the range of possible fluid compositions are calculated, where the max-min is a function of the calculated rock buffered reaction progress (%cpx, Oliver et al. 1992). Here the approximate mole fractions of NaCl-H_2O-CO_2 (being the major components) are; max – 0.25_{NaCl}-0.40_{H_2O}-0.35_{CO_2} and min – 0.05_{NaCl}-0.70_{H_2O}-0.25_{CO_2}. While Oliver et al. (1992) suggested that the range of fluid compositions they calculated never fell within the fluid two-phase field for NaCl-H_2O-CO_2 at the estimated peak metamorphic conditions (~600°C & 350 MPa) there has been recent developments of a high PT equation of state for this system (Duan et al. 1992a; Duan et al. 1992b; Duan et al. 1995; Duan et al. 2000, UCSD Geofluids software). Using the new fluid thermodynamic data for these fluid compositions we find that at peak metamorphic PT the max fluid composition does indeed phase separate (Table 6).

The calculated range of single and two phase fluids are consistent with the range of fluid inclusion types (hypersaline, mixed salt carbonic and CO_2) and densities recorded for regional Na-Ca metasomatism in the district (Fu et al. 2003; Kendrick et al. 2007). The phase separation and consequent volume expansion related to the generation of high mass fractions of vapour (X_{vap} 0.43) in the max %cpx fluid may account for the extensive but localised

Table 6: Calculated equilibrium fluid compositions for the range of rock buffered fluids presented in Oliver et al (1992) for the MKFB. P-T-conditions are calculated for peak metamorphism (1600-1580 Ma). Calculated using the Geofluids Model 1 (UCSD Geofluids)

600oC and 350 Mp			
Type	max %cpx		min %cpx
Phase	L	V	L only
XNaCl	0.44	0.00	0.05
XH2O	0.48	0.29	0.70
XCO2	0.08	0.71	0.25
Flinc Type	MS	CO2	LV
Density	1.40	0.85	0.86
Mass fract	0.56	0.43	1.00

metamorphic-related brecciation within the Corella and Doherty Formations of the MKFB an EFB (Marshall 2003; Oliver et al. 2006).

The Evidence for Different Fluid Types

Unlike the Suicide Ridge example there are no direct fluid inclusion studies on the northern Snake Creek hydrothermal breccias (i.e. Drowning Child Breccia etc). Here we have used the mineral assemblages, textures and in particular apatite chemistry to help to determine the nature of the fluids associated with brecciation and alteration. Details about the breccias and there mechanical genesis can be found in Oliver et al. (2006) and the chemistry/ paragenesis of much of the breccias is well described in Marshall et al. (2006; 2006). The apatite chemistry has been used to help reconstruct the fluid chemical fingerprints, details about apatite chemistry and analysis at Ernest Henry can be found in *Q5 deposition* in this report.

Fluids from the wallrocks

Post-brecciation infiltration of NaCl-$CaCl_2$-H_2O fluids has been documented for the Suicide Ridge breccia system (Type III fluids; Bertelli, 2007 and above). In areas without the fluid inclusion data there is still good evidence for the infiltration and migration of a brine fluid that is, at least partly, derived from the metamorphic pile. Kendrick et al. (2007) also use noble gas and halogen data from

fluid inclusions to discuss the likely source of many of the hydrothermal fluid components as crustal derived.

Within the hydrothermal breccias there is also textural-chemical evidence for the source of fluids. Figure 50 shows cathodeluminescence textures and spectra from albite within hydrothermal breccias. Figure 50a is a marble clast within a calcite-breccia in a false coloured CL image (spectral wavelength range). The clast and the breccia matrix contain albite, however the albite within the clast is strongly luminescent (red colour), unlike the albite in the matrix which is non-lumnecent. This same pattern is seen in a quart-albite rock from the Suicide Ridge breccia (Figure 50b) which contains dark albite cross-cut by luminescent albite fractures. Figure 50c is the spectral response of the albite from Figure 50a (clast versus matrix) showing the strong luminescent response at 700 nm related to the presence of Fe^{3+} (Richter et al. 2002) and some much weaker responses at 460 nm (Ti^{4+}). The CL luminescent albite with Fe^{3+} enrichment (see Bertelli, 2007 qualitative microprobe assessment of this) also commonly weathers to a pink colour and maybe mistaken for k-feldspar under some circumstances.

The bright CL (Fe) albite is found within scapolite marble and in later cross-cutting fractures at Suicide Ridge. The latter is probably associated with the type III (300-400°C, 20-40 wt% NaCl) fluids at Suicide Ridge (Bertelli, 2007 and this document) and probably represent fluids derived from the Corella formation (metamorphic and/or flow of bittern brine). The presence of Fe^{3+} in the albite suggests that these fluids were not only Cl-rich but also potentially highly oxidised.

There is sufficient evidence in the mineral chemistry and fluid inclusion work that fluids are derived from the wall rocks during the emplacement of melts and breccias. These fluids on the whole are saline and have the ability to metasomatise the rocks that they interact with. Fluids interacting with the gabbro, for instance, caused local Fe-Cl metasomatism as shown in the isochon for fresh versus altered gabbro (Figure 49). Calculation of the range of fluids that can be generated in equilibrium with the Corella marble shows that there is a wide range of salt-CO_2-water contents that are possible, and that under peak metamorphic conditions some of these would instantaneously phase separate. This process drives the

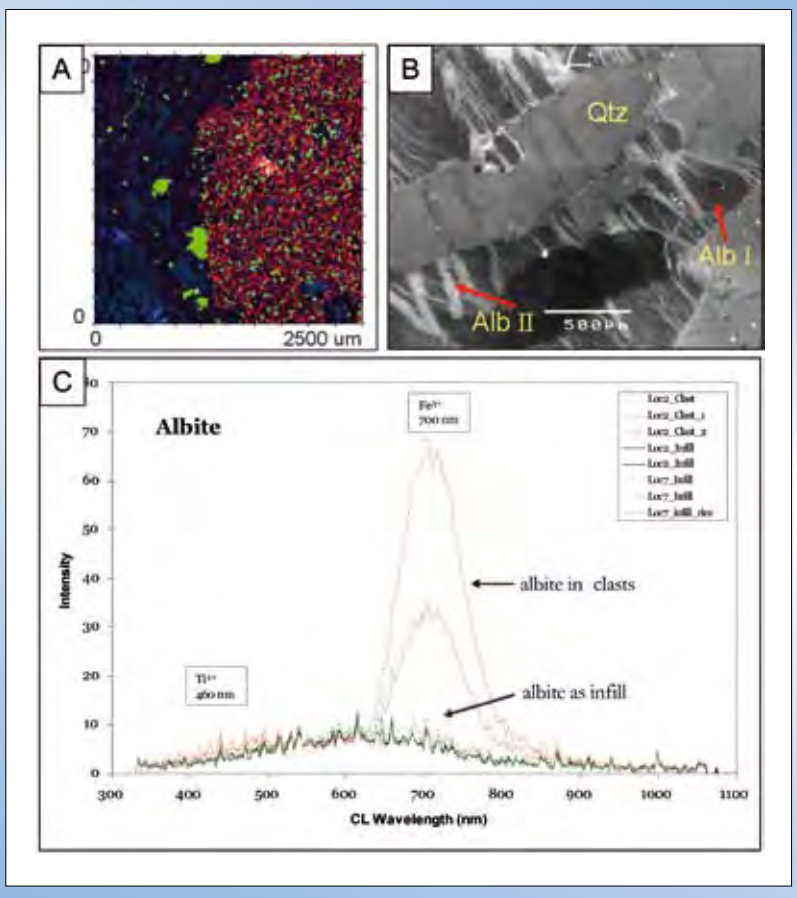

Figure 50: A) False coloured composite CL image (400, 600 and 700 nm), showing the (red) luminescent albite within a clast of Corella marble (bt-kfs-scap-ab), compare to the non-luminescent albite with the breccia infill (dark). B) Stage II albite luminescing in a grey-scale SEM CL image of a pegamtite from Suicide Ridge (Bertelli, 2007). C) CL spectra from albite wihtin calcite breccia for luminescent and non-luminescent albite showing the strong peak feature at ~700 nm. This is thought to equate to Fe^{3+} in the structure.

"tectonic" or "deformation" brecciation that is observed in the Corella units.

Fluids from the Magmas

The Suicide Ridge breccia illustrates the role of magmatic volatiles in the generation of hydrothermal breccias of the type that host the Ernest Henry IOCG system. Mineral chemical and fluid inclusion evidence suggests that these fluids contain CO_2-HF with variable amounts of S, probably as SO_2 (Bertelli, 2007 crush leach experiments). Williams batholith age gabbro contains melt crystallised apatite that indicates the fluid in equilibrium with the melt contained a few 1000 ppm F and ~1 molal NaCl. The primary crystallisation of amphibole in these rocks indicates that initially at least the aH_2O was not low. Previous work has shown that in magmatic=hydrothermal systems with high magmatic CO_2 contents the amphiboles commonly become destabilised and phases such as andradite or pyroxene form instead (Cleverley et al. 2003). The Suicide Ridge magma, which exhibits strong albitisation, does show evidence for pyroxene-bearing assemblages proximal to the intrusion within the breccia. Further away (>500 m) the primary mafic minerals as amphibole and biotite.

Depending on the intrusion that is being studied the magmatic-derived fluid phases have different compositions. Brecciation appears to be driven by exsolution and phase separation of a CO_2-rich volatile, however some intrusive seem to contain magmatic fluid of fairly average composition which is then swamped by externally derived fluid (i.e. salt-rich Corella fluids).

The ultimate source problem

One of the difficulties in determining the source of fluids is to distinguish ultimate source from processes of interactions along the flow path. For instance it was discussed that some of the CO_2 in the volatile phases from magmas may be lower crustal, but if the transport is via melt is this classified as a crustal or magmatic fluid? IOCG systems preserved Os isotopic signatures which were dominated by inherited Os isotopic components. It is important to recognise processes and the modification of source signal in our datasets on fluid sources and reservoirs, and this will be a goal for future research. It has been shown here that the range of fluid types (as prescribed by NaCl-CO_2-HF-SO_2-H_2O) can vary significantly by locality or geological setting and certainly questions such as "which granite produces the fluid required for brecciation?" or "what is the timing of brecciation relative to the ingress of wallrock fluids?" will form the basis of the next tranche of research.

Q4: What are the fluid pathways and drivers?

(Main contributors: Laukamp, McLellan, Austin, Blenkinsop, Cudahy, Cleverley, Duckworth, Ford, Jones, Keys, Miller, Oliver, Rubenach, Thomas)

Introduction

Given the many possible fluid sources and reservoirs, we are at once faced with the question of how such fluids came to be concentrated into ore deposits, through a variety of pathways and fluid flow drivers. Permeability generally decreases as a function of depth in the crust, however, permeable pathways (in addition to diagenetic aquifers) are present in the form of faults, shear-zones or fractured crystalline rocks, and these are key structural components in facilitating fluid migration from deep in the system to shallow ore depositional sites, or from meteoric sources. The driving forces may be topography, stress partitioning and regime, the tectonic evolution and the thermal structure at all scales. Several techniques were utilised in different areas to gain a better insight to the question, through:

- 2D and 3D numerical modelling of fluid flow at the deposit- to regional-scale. These studies concentrated on the LRFT, and are combined with earlier work on the EFB (McLellan & Oliver, in press). In 3D, FLAC is capable of fully coupling mechanics, fluid flow and thermal processes while, in 2D, UDEC enables numerical simulations of the response of a fractured rock mass to stress and strain partitioning during deformation. Methodologies are described in McLellan (Appendix 1, (a) and (b))
- Detection of hydrothermal footprints using remote sensed data from outcrop- to district-scale, around the Mt Isa Pb-Zn-Ag deposit (Appendix 1, Duckworth) and in the Cloncurry and Selwyn regions (Appendix 1, Austin and Laukamp et al.)
- Constraining the tectonothermal and metasomatic history using petrographic studies and age dating on monazites (U-Pb). Results described by Rubenach (Appendix 1) provide a history of the various

deformational and metamorphic events, spanning the Sybella Event and early albitisation (1670 Ma) through to the end of the Isan Orogeny around 1500 Ma, and provide insights to the development and distribution of fluid pathways through time and the possible drivers of the fluid pulses.

Metamorphic and Metasomatic Events

Field, microstructural and monazite age dating demonstrate that the "Isan Orogeny" incorporates multiple events, from at least *ca.* 1630 Ma to 1527 Ma, with the peak around *ca.* 1590 Ma (D2; Figure 51). In the EFB, the Selwyn Zone records major albitisation around *ca.* 1640-1680 Ma and medium-P metamorphism late in D1 to early D2. The D2 history consists of multiple events, which are mainly low-P isobaric. D4 (1527 Ma) was broadly synchronous with many of the granites and dolerites of the Williams Batholith, and with the brecciation, Na-Ca alteration and Ernest Henry mineralization. In the WFB, the metamorphic events include the Sybella Event (*ca.* 1670 Ma) and D3 (*ca.* 1550 Ma). In contrast to the WFB and Selwyn Zone where multiple events are recorded, monazite dating in the Mary Kathleen area (EFB) reveals a sharp metamorphic peak, with little evidence for either the shallowly dipping Wonga Event of Pearson et al. (1992), Holcombe et al. (1991), Oliver et al. (1991) or the alternative D1 shear zone event of Bell et al. (1992). The Wonga Belt may be, instead, a steep D2 high strain zone.

Kyanite-bearing shear zone events give D2 (1590 Ma) ages, suggesting isobaric cooling soon after the metamorphic peak. Heating/cooling spikes of up to 500°C imply igneous intrusions, superimposed on the geotherms already elevated due to the abundance of heat producing elements. It is proposed that most of the metamorphic events in the Inlier are the result of such igneous-induced spikes. During the metamorphic peak it is proposed that pegmatites transferred heat from the lower crust (where gabbros caused extensive partial melting).

Significant epigenetic ore deposits are not necessarily related to specific metasomatic events but occur in areas showing abundant metasomatic assemblages. Many deposits are hosted or spatially related to albitites, Na-Ca alteration, potassic alteration, magnetite and silica-dolomite. Examples are the silica-dolomite host for the Mt Isa Cu ore body or potassic alteration at Ernest Henry. Detailed analysis of the metamorphic assemblages in the Mt Isa Inlier is therefore crucial for successful exploration.

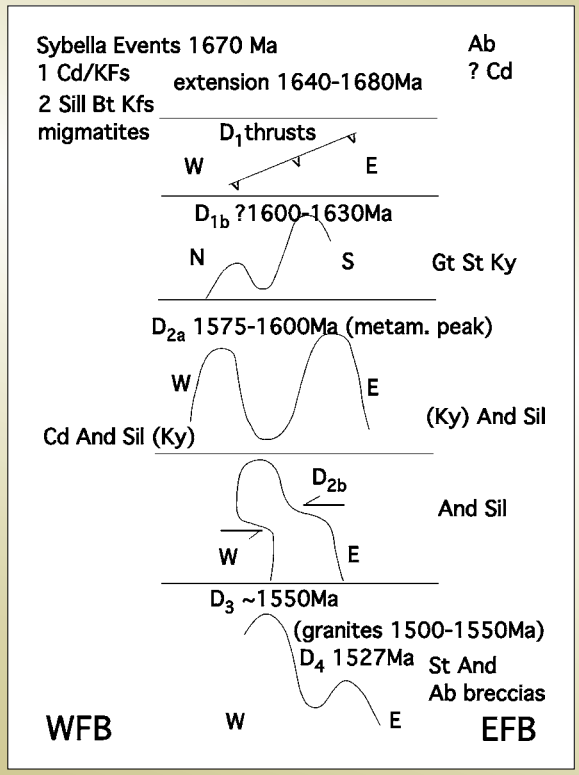

Figure 51: Summary of deformational and metamorphic events across the Mt Isa Inlier.

Fluid migration during basin development

3D modelling of the LRFT during basin development shows that extension drove downward migration of surficial fluids and brine reflux (Appendix 1, McLellan (a)). Downward migration is interpreted as the result of dilation and failure during extensional. At shallow levels, permeable sediments appear to be important, not only for storing fluids, but also for within-basin lateral transport. Shallow level permeable faults are also important pathways, which facilitate downward migration of surficial derived fluids into the system, either as a result of extension or topography (Figure 52).

Topographic or emergent highs formed during extension provide a credible fluid driver in the system (Appendix 1, McLellan (a)). Topographic highs can form on the footwalls of basin bounding faults (see below) but they may also develop in the central parts of the trough as a result of shear strain and shear failure being focussed on the outer basin bounding faults, in conjunction with thermal dependence and isostatic flexure. This flexure and development of a topographic high, together with emergence, may drive downward fluid flow into permeable structures or sediments and may serve as an analogue for the Mt Gordon Arch structure. In extension, basin bounding faults are important fluid conduits at deep crustal levels and provide pathways for deep derived fluids to reach shallower depths in the crust.

Thermal structure is an important driver of fluids within permeable rocks, and convection is often cited as a key driver for migrating fluids from shallow sediments into deeper parts of the system and back to shallow levels again. This process may have been important in Pb-Zn-Ag mineralisation in parts of the Mt Isa Inlier (Oliver et al. 2006), however, it is more likely that convection cells would be more discrete, such as in specific permeable units or structures and may have allowed partial mixing or transfer of fluids at specific locations where cells accessed deeper fluid conduits. Fault intersections, for example, could provide such loci.

Fluid migration during Isan Orogeny

During compressional events, faults and lithological boundaries can act as pathways for focusing fluid flow as well as providing the mechanical-chemical contrasts which are critical factors in the formation of large hydrothermal ore deposits. Tectonic compression generally results in a net upward migration of fluids through permeable pathways, due to an increase in pore pressures, contraction and dilation. Within the LRFT an interesting feature is observed during compression, where the flow is generally focussed into the hanging wall sediments, and less so into the footwall, and these areas may facilitate fluid mixing scenarios (see Figure 53).

FLAC3D modelling of simple strike-slip fault bend/jog systems demonstrates that small changes in the fault geometry can vary the amount of fluid flux substantially (Ford, this volume). Using dilation and integrated fluid flux as proxies for prospectivity, this allows the ranking of

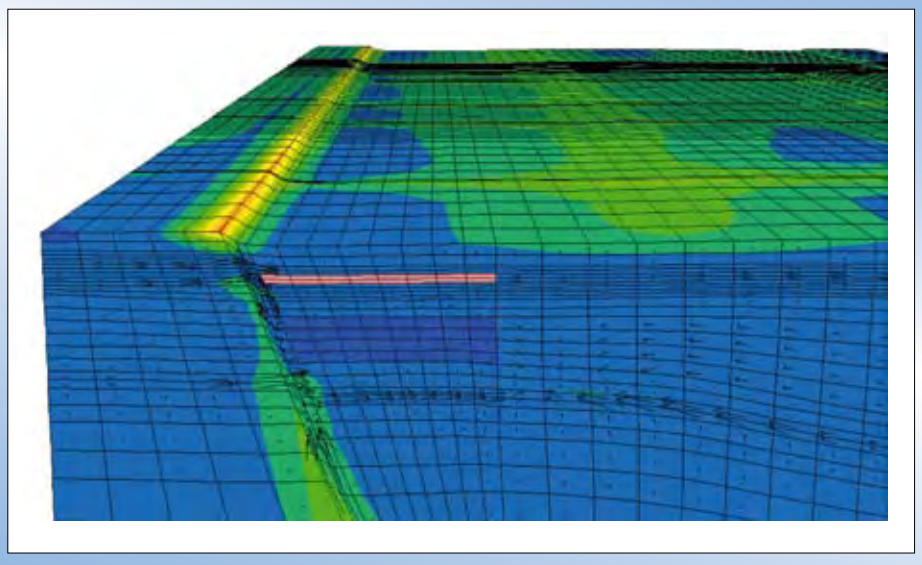

Figure 52: Shallow level faults acting as fluid pathways during extensional tectonic events, allowing surfically derived fluids to migrate to deeper levels in the crust, either as a result or topography or dilation and failure.

different fault geometries to determine which variables or combination of variables generate the most promising results. Results of the scenario setting indicate that the highest dilation and integrated fluid flux values are located near the tops of the models after 10% shortening. As the models were buried at 5 km, these highest values are located at a depth of 5-7 km which is consistent with the depth at which the Mt Isa copper orebody was emplaced. The integrated fluid flux values are maximised (in order of priority) by: a) fault width, b) contrast in lithology, c) fault dip, d) fault bends and e) cross-cutting faults. In the models containing a contrast in lithology across the fault, the faults are acting as seals rather than conduits for fluid flow between low permeability and high permeability rocks. However, only the faults can focus the fluid flow in this model, acting as a channel between the contrasting lithologies (Appendix 1, Ford). Particularly during compressive tectonic events, such as basin inversion (Figure 53), basin bounding faults are important fluid conduits.

The combination of faults and lithological boundaries can also be described as geological complexity. Studies of the geological complexity indicate that there are significantly high correlations between copper endowment and geological complexity in both the Eastern and WFBs, Appendix 1 Ford. The area of highest geological complexity in the Mt Isa Inlier is a north-south trending corridor in the LRFT stretching from south of Mt Isa to north of Gunpowder, which is where the major Cu deposits of the terrane are located.

The focussing of fluid flow at the deposit scale can be determined by highlighting areas that indicate partitioning of low values of minimum principal stress and high positive volumetric strain. Structural configurations relating to Cu deposition during Isa Orogeny D4 deformation in the LRFT and the WFB highlight numerous potential sites for fluid focussing when examined using discrete element modelling (Appendix 1, McLellan et al.). Applied to shortening scenarios, there are strong spatial correlations between sites of low values of minimum principal stress, failure and dilation with known deposits and prospects. A best-fit ESE-WNW orientation of maximum principal stress in the WFB correlates with findings for the EFB (McLellan & Oliver in press). A range of ore deposits were tested by numerical modelling (using UDEC) at the mine scale (Appendix 1, Keys), comprising the Gunpowder deposits (Mammoth and Esperanza), the Mount Kelly deposit and the Mt Isa Copper Mine in the WFB and the Greenmount deposit and the Eloise Mine in the EFB. A maximum principal stress orientation of approximately ESE-WNW was optimal for dilation at all of the deposits, with more complex patterns around the Mt Isa Copper Mine (Appendix 1, Miller). In the latter case the mechanism for breccia development relied on sinistral, reverse movement on dominantly north-south oriented bedding. This again implied that an approximate southeast-northwest component of shortening was required to form the Mt Isa Cu ore breccias. At the Mammoth deposit, drive mapping showed that the ore lodes had formed in response to shear on the Mammoth and Mammoth Extended Faults. Shallow dipping striations on the fault surfaces indicate movement was predominantly dextral strike slip. UDEC modeling of the Gunpowder area shows a good fit with the major deposit sites in this area (Figure 54).

Spectral Analysis

PIMA studies on shale-hosted Pb-Zn-Ag mineralisation

A limited program of spectral and petrological studies of the alteration around the Mt Isa Pb-Zn deposit were undertaken (Appendix 1, Duckworth) to identify the alteration mineralogy in the Urquhart Shale and to

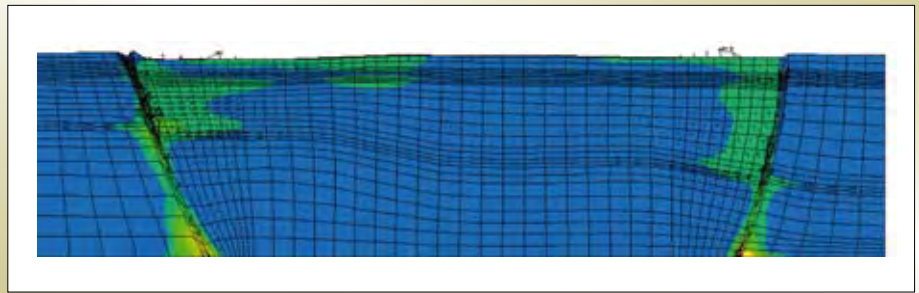

Figure 53: Basin bounding faults at deep crustal levels acting as fluid pathways during compressive tectonic events, allowing deep seated fluids to migrate to shallow levels in the crust. Lighter colours indicate areas of higher cumulative fluid flux, which is greatest in the hangingwall at shallow levels.

characterise possible fluid pathways. The paragenetic sequence recognised is biogenic pyrite, carbonate, sphalerite + pyrrhotite, pyrite, galena, chalcopyrite. Petrographic observations suggest the fluids preferentially followed zones of carbonate cement, leading to a partial replacement of many of the sedimentary layers and early structures. Abundant, dark grey aspectral material is not resolved by PIMA, but using GADDS (general area detection diffraction system), XRD and whole rock XRF suggests that while the proportions of quartz and feldspar mineral groups vary, the essential mineralogy is unchanged. In general, the PIMA spectra suggest that the alteration is strongly Mg-rich with minerals identified as phengite, dolomite, intermediate chlorite, ankerite, talc and calcium and potassium sulphates. The rocks distal to the Pb-Zn mineralisation are more Fe-rich with minerals identified as biotite, siderite and Fe-chlorite. Weathering of the shales overlying mineralised and un-mineralised areas produces kaolinite, dickite and muscovite, with less feldspar breakdown above the un-mineralised areas.

Integrated Remote Sensing analysis

The detection of hydrothermal alteration patterns and potential fluid pathways is assessed using ASTER and HyMap remote sensing facilities, followed by field mapping, using field and lab based analytical systems like PIMA, GADDS and XRD. The development of advanced spectral and hyperspectral remote sensing technologies has proven to be a boon for mapping alteration, particularly for defining phyllic and argillic alteration using ASTER (e.g. ***pmd*CRC*** project I1 Van der Wielen et al. 2005). An objective here is the calibration of this data with new

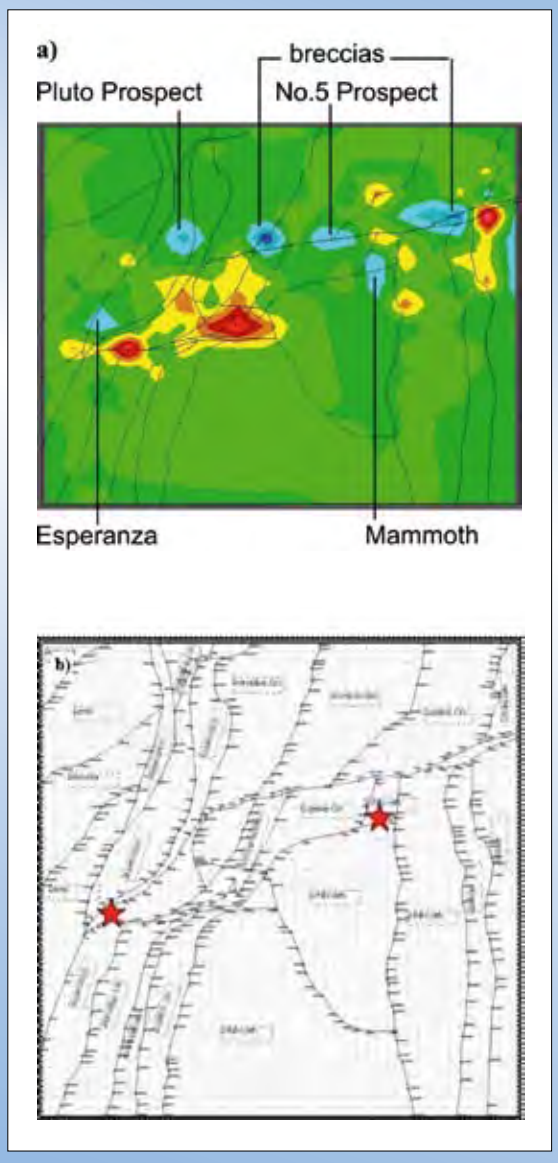

Figure 54: a) Plot of volumetric strain. Cool colours (blue and dark green) represent dilational sites and other colours are contractional (light green to red); b) Plan view of 2.3km x 2.3km area over the mines. Red star on left is Esperanza and on right is Mammoth.

high-resolution HyMap data (Thomas, this volume). The raw HyMap data were used to make approximately 150 *Regions of Interest*, which were used to constrain the ASTER data. The new suite of calibrated and reprocessed data products are being interpreted (Thomas, this volume), with large volumes of mosaiced, masked and calibrated data available as an ftp download from the www.em.csiro.au/NGMM webpage.

Ground-truthing of the newly processed HyMap data in the EFB has involved discriminating four different types of hydrothermal alteration patterns (Laukamp et al., this volume):

1) metasomatic 1 – metasediments (e.g. Snake Creek Anticline)
2) metasomatic 2 – igneous bodies (e.g. Camel Hill gabbros, Gin Creek Granites)
3) fluid channels 1 – faults (e.g. Cloncurry Fault, Mount Dore Fault)
4) fluid channels 2 – breccia pipes (e.g. Suicide Ridge north of the Saxby Granite).

In general widespread metasomatic alteration of metasediments, such as sodic-calcic alteration in the Snake Creek Anticline, was successfully detected with single mineral maps (e.g. white mica abundance). Mineral maps showing content of ferrous iron (associated or not with MgOH) and white mica composition detect alteration of igneous bodies (e.g. alteration rims of Camel Hill gabbro bodies). The recognition of hydrothermal alteration along faults can be limited in some areas because of masking effects. However, detected albitisation of the Gin Creek Granite in the western vicinity of the Cloncurry Fault might indicate fault-related fluid migration. Identification of discrete breccia pipes in the SCG and along the contact zones with the Corella Formation, as possible fluid conduits for IOCG deposits (Oliver et al. 2006) are, thus far, problematic because of the complicated mineral chemistry. However, single breccia pipes north of the Saxby Granite have been identified with a number of mineral maps (e.g. MgOH composition, Figure 55). This on-going research holds much promise in detecting and characterising mineralisation-related footprints.

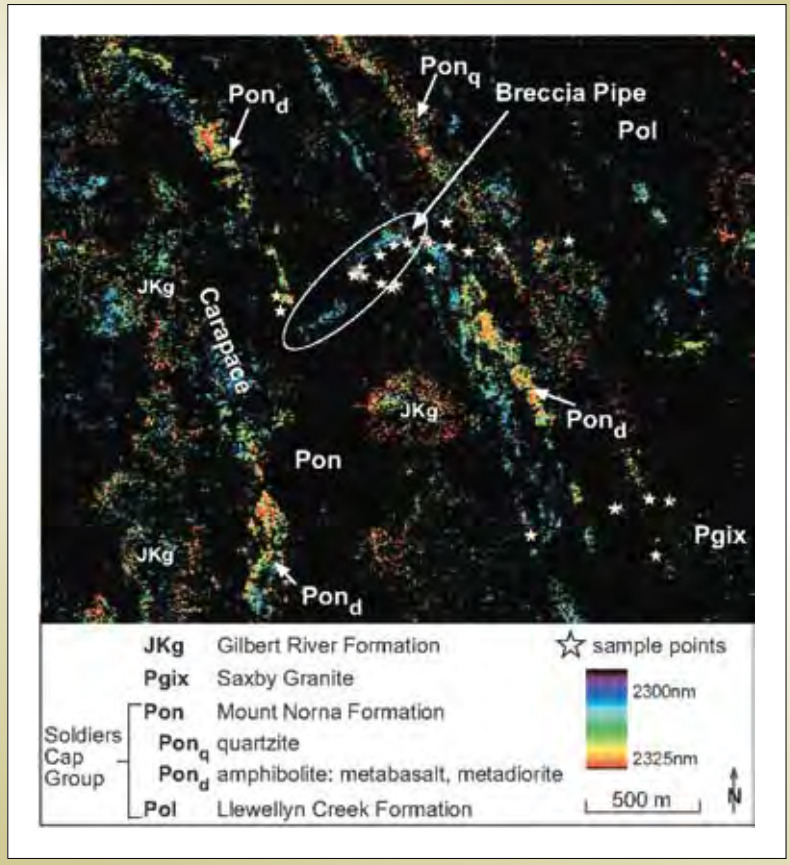

Figure 55: MgOH composition image of area northwest of the Saxby Granite (see Figure 1 for location). Breccia Pipe extending from a carapace on the north-eastern rim of a granite body to the NE (white ellipse). For carbonates: blue colours: magnesite, dolomite; red colours: calcite, siderite. For MgOH-bearing rocks: blue colours: e.g. talc; red colours: amphibole, epidote, chlorite. Black is below threshold.

In the EFB, ASTER data was evaluated for mapping of sodic-calcic alteration along major crustal fault zones (Appendix 1, Austin). Mineral indexes were used to map minerals such as amphiboles and calcite as a means of identifying sodic-calcic alteration. While this appears to be effective, there are ambiguities due to numerous mineral species having similar absorption features. However, through integration ASTER band 8 data with aeromagnetic and K-radiometric data, Austin (Appendix 1) derived a modified mineral index which highlights albite-actinolite-magnetite assemblages. Many of these are spatially coincident with copper mineralisation, e.g. the Selwyn Corridor, Kuridala, Monakoff, and deposits along faults in the Stavely Formation, and under-cover deposits in the EFB (Ernest Henry, Eloise and Osborne) coincide with moderate highs in the index. It is hoped that this mineral index may be used to assist with exploration targeting of IOCG deposits.

Conclusions

The prolonged sedimentary history and tectonothermal evolution of the Mt Isa Inlier was accompanied by a long termed fluid evolution, its accumulation, dispersal and ultimate focussing at the hydrothermal deposit. Basin bounding faults played a major role for the downward migration of surficial fluids. At shallow levels also, permeable sediments and faults allowed downward migration and circulation of these fluids and their access to deeper fluid conduits. These locations may have been important for the development of Pb-Zn-Ag mineralisation in the Mt Isa Inlier.

Tectonic compression during the multiple deformational events of the Isan Orogeny triggered upward migration of fluids. The focussing of fluids along faults may have been maximised by wide fault width, contrast in lithology, shallow fault dip, fault bends and cross-cutting faults. Correlations between copper endowment and geological complexity (combination of faults and lithological boundaries) is significantly high, pointing to the importance of the connection of various fluid pathways. Numerical modelling in the WFB shows that fluid focusing during the development of Cu-mineralisation was related to a maximum principal stress orientation of approximately ESE-WNW, confirming former studies in the EFB.

ASTER data were processed with newly developed techniques and calibrated with the superior HyMap data. The evaluation of such spatial data as a tool for exploration is still ongoing, but already shows some promising results, as does the integration of ASTER band 8 data with magnetic and K-radiometric data for highlighting Cu-related alteration in the EFB.

Question 5: What are the deposition and hydrothermal processes?

(Major Contributors: Cleverley, Walshe, Oliver, Keys, Fisher)

The aim here is to synthesise the knowledge about the processes of deposition and localisation of mineral deposition within the Cu and Cu-Au mineral system, with a focus on observations at Ernest Henry, Osborne, Mt Isa and some other WFB copper deposits. The questions arising from thinking about deposition impact the mineral systems analysis at the smaller scales from mine-, ore body- to thin section-scale. A wealth of information exists for each of the deposit types that occur within the inlier and this document aims to highlight the key questions that need to be synthesised and the information that has been collected during the I7 (and I1/2/3/4) project. Much of the chemical work has been conducted as part of the terrane contribution from the F6 (Fluids) project. It is still useful to consider the broadly distinct deposit genres that exist, with a focus on the former two in this project:

- Breccia hosted, Fe-oxide/silicate Copper-Au-U (EHM, Osborne)
- Vein or breccia hosted quartz-copper-carbonate deposits (Mt Isa etc)
- Sediment hosted Pb-Zn (Century, Mt Isa).

There has also been some limited work on uranium prospects in the Mt Isa valley, but mostly in the context of a broader mineral system. It should also be considered that these deposit styles did not form at the same time in the evolution of the terrane, and that mutually overprinting styles are observed within the same locality.

The question of deposition leads to consideration of:

- Why did the deposition occur there?
- Why did deposition not occur there?

- What controls the geometry and spatial distribution of ore components in the deposit?
- What are the features to look for to help mining and exploration practise?
- What are the key controls on changing solubility of the component of interest to us at this location at the time of interest?
- What was the mechanism by which fluid(s) got into the immediate location?
  a. How did fluid(s) and rock meet at this location, did this influence the deposition mechanism (e.g. condensation).
- What were the mechanisms by which sulphur, metals, carbon and other redoixicants (e.g. O_2, H_2) where transported to the site of deposition?
  a. Building on information from macro-scale chemistry, mineral chemical and textural analysis and fluid inclusion analysis.
- What was the physical mechanism that drove the deposition and dissolution that is recorded in the mineral system?
  a. Both fluid-chemical and mechanical mechanisms need to be built into this answer.
- What is the physio-chemical evidence for the process of deposition?
  a. For example isotopes, geochemical trends etc
  b. Can we map it spatially?

1530 Ma Breccia Hosted IOCG – Ernest Henry

The Ernest Henry Fe-oxide Cu-Au deposit located 30 km northeast of Cloncurry is one of the largest of a group of breccia-hosted Cu-Au deposits in the EFB with a measured resource of 96 Mt @ 0.98% Cu and 0.49 g/t Au (Collier and Bryant 2003). A thorough review and description of the Ernest Henry geology and alteration can be found in Mark et al. (2006). The deposit is hosted within a package of metavolcanic and intercalated metasedimentary rocks, and is bound by broadly northeast trending fault and shear zones. Alteration is dominated by early Na- and Na-Ca which effected much of the sequence and resulted in intense albitisation, thought to be related to the district-scale Na-Ca alteration (de Jong and Williams 1995). This alteration is overprinted by pre-ore K-(Mn-Ba) alteration represented by intense biotite-magnetite, best represented in Fe-rich lithologies, and rarer k-feldspar-garnet alteration. The K-alteration forms a halo around the mine (see Mark et al. 2006). The syn-ore alteration assemblages are represented by K(Ba)-feldspar-quartz-calcite and some minor sericite.

Mineralisation is hosted by breccias of K-feldspar altered meta-andesites from the local host lithology and infill of magnetite-calcite-quartz with chalcopyrite-pyrite and lesser, but locally important, barite. The style of brecciation changes across the deposit from a crackle type to clast supported and matrix supported, with variable degrees of tectonic versus chemical clast corrosion (Laneyrie, 2004, Oliver et al. 2006). The proportion of calcite-quartz-magnetite infill also changes locally (compare Figure 38 a, b and c). It has been suggested that Cu grade is directly related to the clast distribution and/or breccia classification (Collier and Bryant 2003; Laneyrie 2004) indicating a strong chemical-mechanical control on grade distribution (Figure 56).

Ernest Henry IOCG ore samples were studied to understand their pretrographic relationship to the regional breccia samples and to look for chemical and physical similarities that might indicate a genetic link between the regional breccias and the Ernest Henry ore hosts. A small subset of samples has been studied in detail, however a more complete paragenesis of the whole Ernest Henry hydrothermal system can be found in (ref -> Mark, 2000; Mark et al. 2006).

The Ernest Henry breccia samples are very similar to the regional breccias in macro- and micro-scale appearance and mineralogy (see Figure 38). There is an overall change in the nature of the mineralized breccia spatially from crackle -> clast dominant -> milled, clast poor brecciation. The clast-rich samples are dominated by k-feldspar, zoned with Ba, as an alteration of previously albitised clasts as well as an infill component. Other minerals include amphibole – biotite – calcite – magnetite – titanite – apatite – chalcopyrite, in samples with less clasts the mineralogy becomes dominated by magnetite – chalcopyrite – pyrite. Throughout the Ernest Henry breccias there is evidence for distinct quartz-rich zones that contain secondary euhedral quartz (discussed later) with associated fractures containing hematitic alteration of magnetite, FeMgMn-rich mica/clay and chalcopyrite. The exact spatial relationships of these quartz-zones and their orientation within the deposit are unknown at this time.

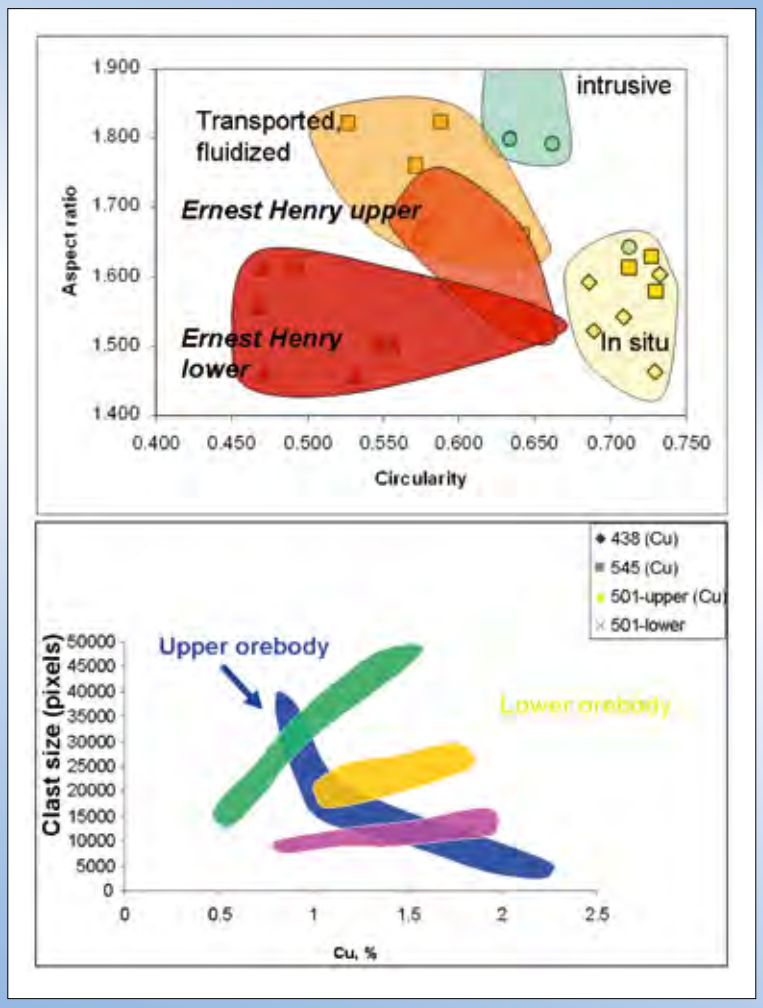

Figure 56: Breccia shape attributes for the EHM breccia pipe showing: A) Aspect ratio vs circularity for EHM data points and how these compare to various breccia classification types (after Laneyrie, 2004), B) Groups of measurements for clast size in the breccia vs grade (Cu%).

There are also discrete zones of carbonate enrichment within the ore-body and surrounding rocks, often seen as carbonate flooding. The most concentrated of these is within a unit called the marble matrix breccia which is carbonate dominated (similar to the Eribus mineralised prospect). Marshall et al. 2006 used stable isotopes to conclude that this unit was dominated by sedimentary carbon, and as such maybe a pre-exisiting unit within the mine. However whole rock geochemical data shows that Ca (and possibly CO_2) have been mass added to many parts of the ore system.

Whole Rock Geochemistry

Whole rock chemistry was analysed as part of honours work at James Cook University (Lannery, 2004) and this provides some basic insights into the nature of ore deposition at Ernest Henry. Principally the ore deposit is dominated by dilution processes, that is, the original rock has dilated and the space has been infilled with precipitated (and transported) material. These processes are common in brecciated systems.

Plotting two immobile elements against each other can help to show whether the hydrothermal rocks have a common precursor, and if dilution played a large part in the generation of the ore system. Figure 57 is a plot of TiO_2 vs Al_2O_3 which are considered to be immobile in this system. Almost all of the data points lie on a straight line that intercepts the origin and this indicates that there is a common Ti/Al which probably relates to a common host rock in the samples that were taken. Also the data points are scattered along the line from a position thought to represent the precursor rock composition towards the origin. This represents a variable proportion of dilution in the system (see the 50% infill position marked). For the samples shown here there is a distinct separation between rocks from the upper ore body (Figure 58) and those of the lower ore body.

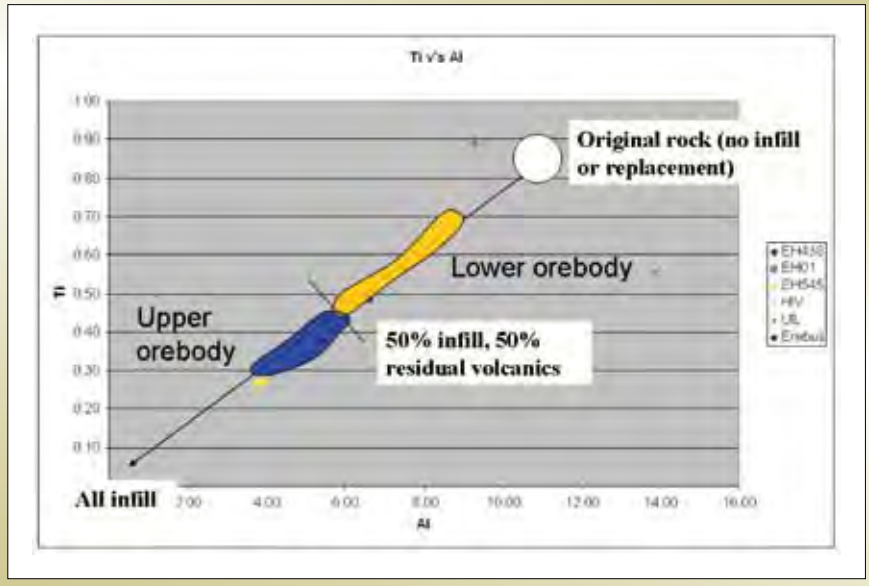

Figure 57: Al vs Ti for whole rock data at EHM (after Laneyrie, 2004; Oliver pers. comm.) showing the consistent host rock trend for all ore samples (i.e. clasts are locally derived) and the change in the proportion of chemical dilution within the upper to lower orebody transition.

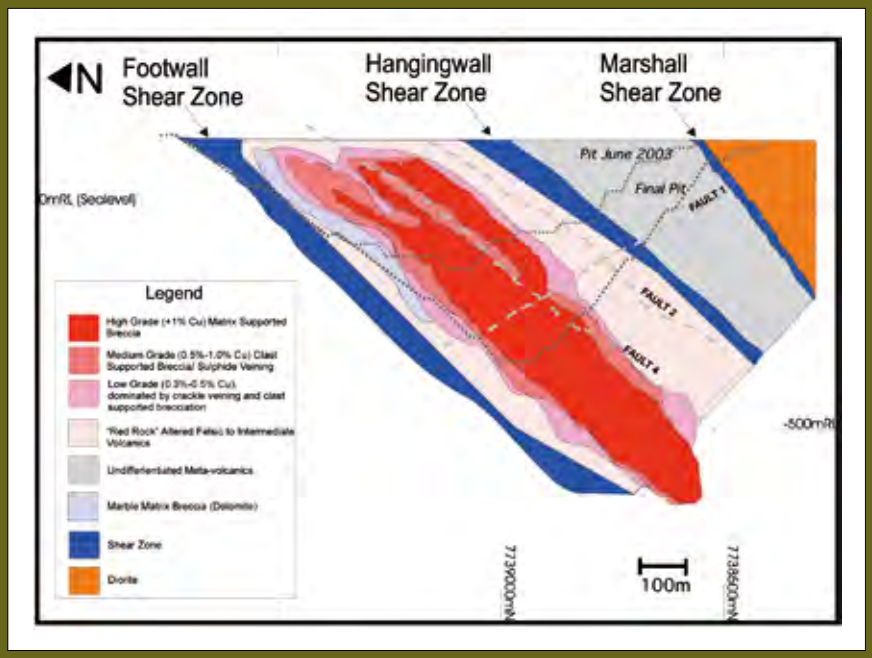

Figure 58: Cross section through the Ernest Henry deposit showing the major geological and ore units (courtesy EHM Ltd).

Because the Al/Ti ratio is constant, the decrease in TiO_2 (or Al_2O_3) can be used to proxy dilution. Figure 59a shows that the K behaves as an immobile element because the data are distributed along a constant K/Ti ratio line. This is in agreement with petrographic observations that K metasomatism slightly predates ore precipitation (Mark et al. 2006). Other components such as Ca and Fe show mobile (Figure 59b) behaviour and when plotted against each other indicate that there is a competition between Ca and Fe as the key diluting component (i.e. negative data trend). This trend fits the observations that calcite and magnetite are not always found together, and areas of the ore body tends to be more calcite or magnetite rich.

Copper is also a diluting component (Figure 60) although there is no consistent trend between Ti and Cu. This pattern is explained by the Cu grade not being directly related to the proportion of dilution and/or infill in this case.

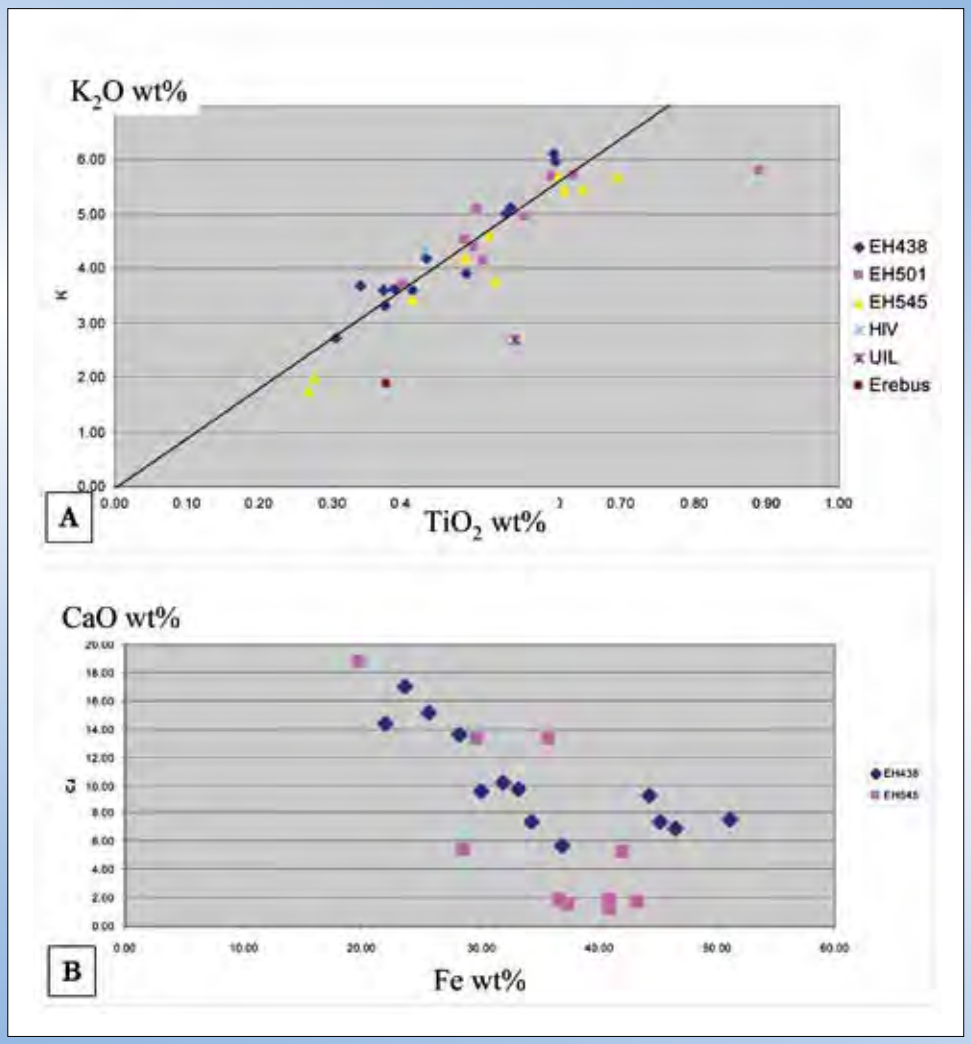

Figure 59: Whole rock geochemistry for EHM rocks A) K2O vs TiO2 (wt%) as an indicator of dilution of the feldspar phase during brecciation. B) CaO vs Fe2O3 (wt%) showing a string inverse relationship indicating that Ca and Fe compete during the infill/precipitation process (both components are correlated with Ti not shown).

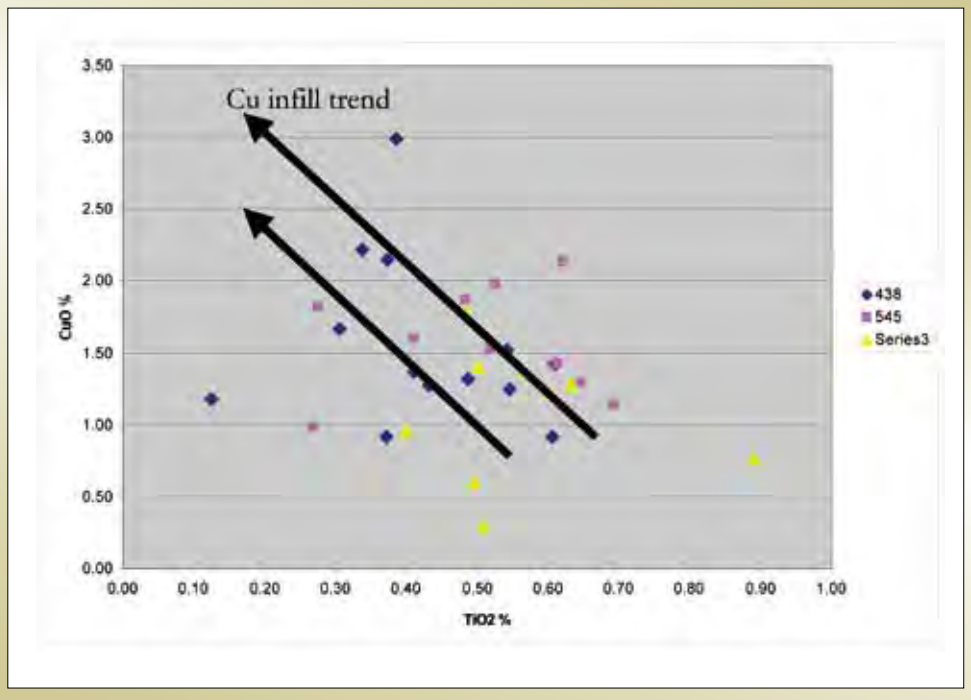

Figure 60: TiO2 vs CuO for EHM rocks showing that while there is a broad negative correlation showing that Cu is added during dilution (brecciation) the complicated relationship indicates that the process of Cu addition into the rocks is not only a function of the brecciation and precipitation process.

3D Spatial Patterns

Using the Leapfrog (www.leapfrog3d.com, version 2 Beta) software the Ernest Henry drilling database has been analysed to look for large scale patterns in the geochemistry that can help to build a chemical architecture for the mineral system. This approach has proved useful at places such as St Ives gold camp (see ***pmd****CRC* projects Y3 and Y4).

Drilling data was acquired from the mine and is dated to August 2006. The data used in the leapfrog models was the resource drilling and a limited section of blast hole data. The drilling data includes geology logging (major and minor), alteration (primary, secondary and trace) and the assay data suite of Cu, Au, As, Co, Ni, Mn, Fe and U. All images are shown in mine grid which matches with AMG.

Grade Shells

Leapfrog has the ability to generate isosurfaces for concentrations of components such as Cu. These are not strictly grade shells as there is no geostatistical constraints performed within the program, however if the geostatistical parameters and domains were utilised then the isosurfaces would be a good approximation. Isosurfaces for Cu have been generated using the reported geostatistical fitting parameters for the upper ore body (orientation of 35° to 155°, 80° plunge and ellipses of 3,2,1) and compared with high resolution isotropic isosurfaces.

Figure 61a is a plot of the leapfrog Cu shell for the available Ernest Henry resource drilling database. The shell is drawn for the 1.25% Cu concentration. Figure 61b is the same view with the 500 ppm As shell added (blue). While

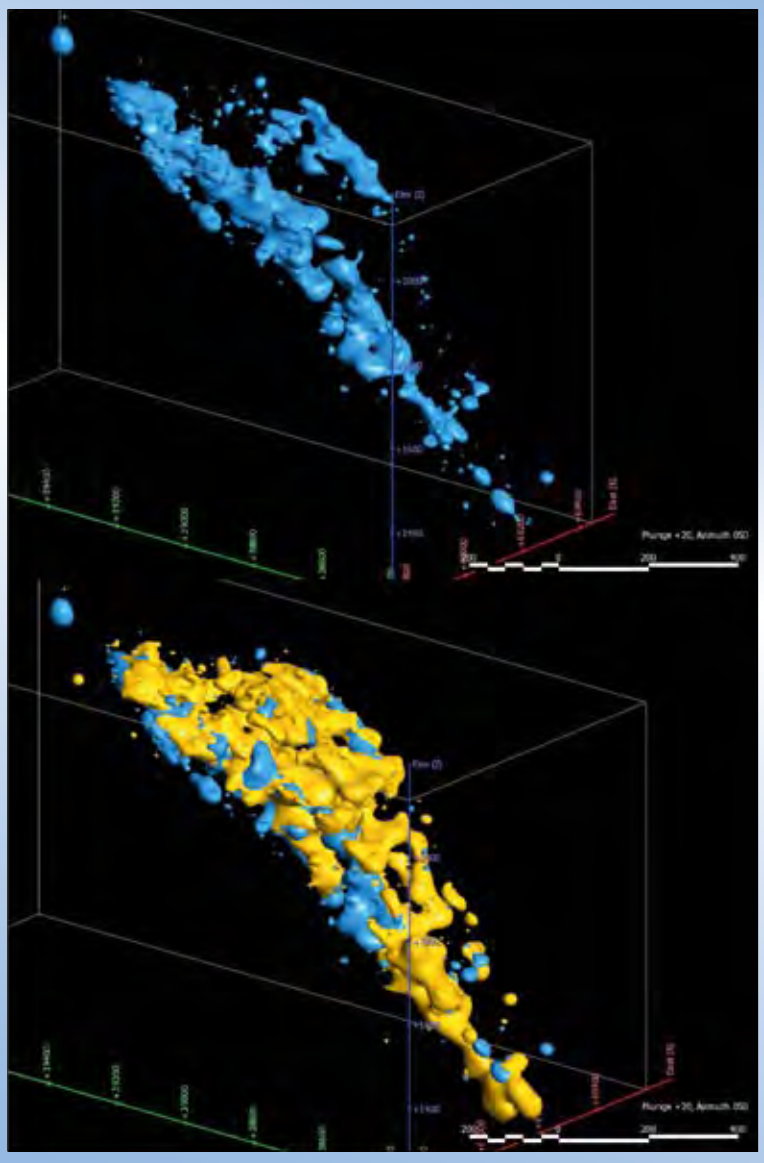

Figure 61: View to NE of the Leapfrog model for EHM showing the A) 500 ppm As isosurface (isotropic, spheroid fit) and, B) combined with the 1.25 wt% Cu isosurface. The As and Cu are broadly similar but not directly co-located indicating that these components where transported in different fluids.

the As is broadly co-located with Cu, in general the As is offset and in places much of the footwall to the ore body is As-rich (associated with the marble matrix breccia). To illustrate this further the blast hole data from several benches where used to plot a high resolution isosurface for Cu and 750 ppm As (Figure 62a). Arsenic is again observed in the footwall of the system, not co-located with Cu. Figure 62b shows a 2D cross section through the blast hole data (looking towards 065°, perpendicular to the plunge of the ore body). The contours of Cu, As and Co can be used to distinguish fine scale chemical architecture: The ore body dipping to the south-east (Cu), As not co-located and in the footwall, and Co appears to map out linking structures that dip both south and steeply north.

Mineral Maps

Using the available assay geochemical datasets for Ernest Henry, the mine staff have developed a methodology for back-calculating the approximate mineral distributions in the deposit (pyrite, magnetite, chalcopyrite). The mineral maps are useful in detecting broad changes in the major assemblages but should be treated with caution as they based on limited available data. If phases exist that include components used in the mineral maps but that are not considered then the calculations will generate spurious results (i.e. the presence of baryte effecting the S budget).

Figure 63 shows the distribution of pyrite (0.28 mol, light blue, relative to the copper 1.25% isosurface (plotted

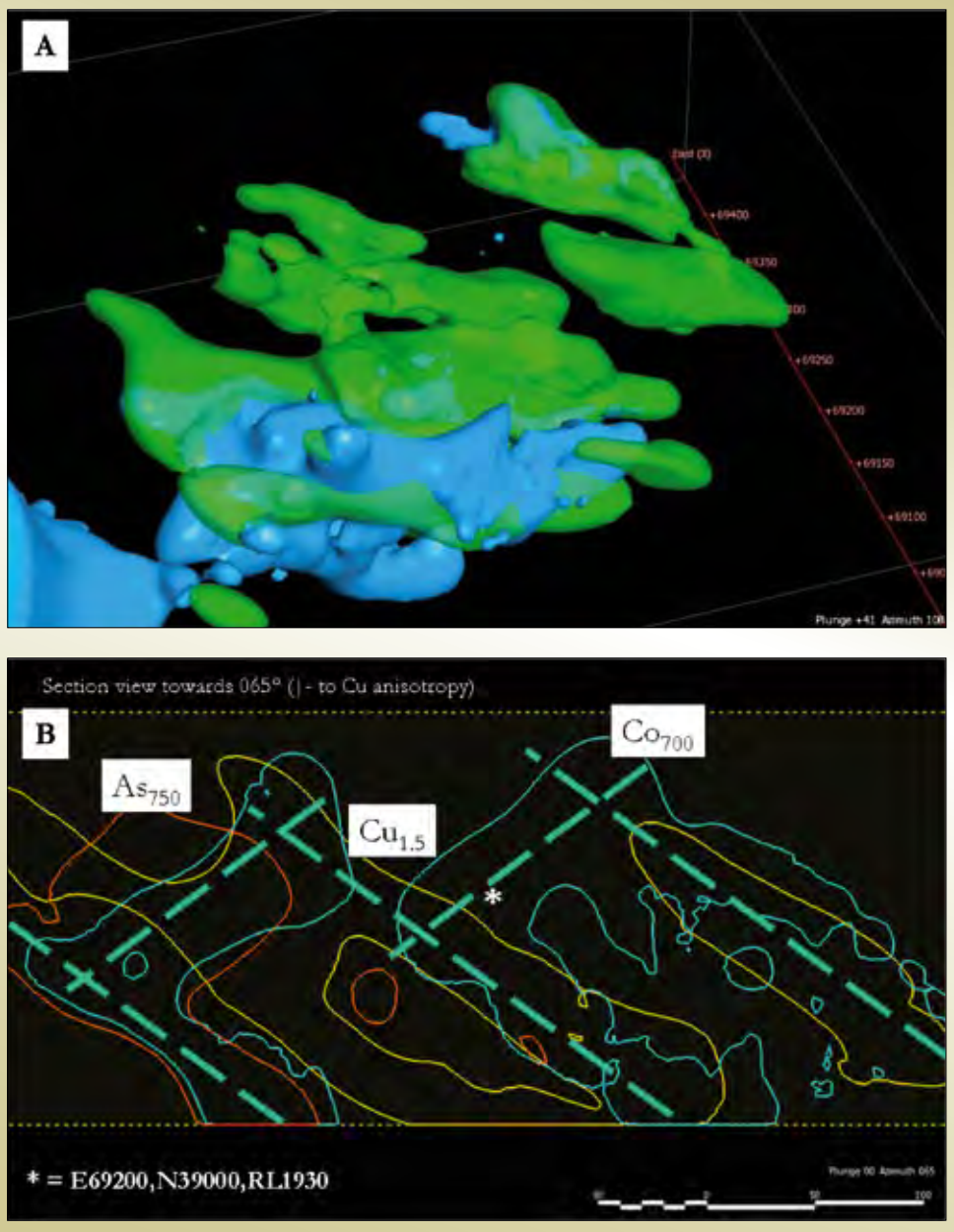

Figure 62: Detailed distribution of As and Cu in blast hole data from 3 benches in the EHM open pit. A) Isosorfaces for 500 ppm As and 1.25 % Cu and, B) cross-section looking NE showing the outlines of various isosurfaces and the possible interpretation of feeder structures or pathways in this data.

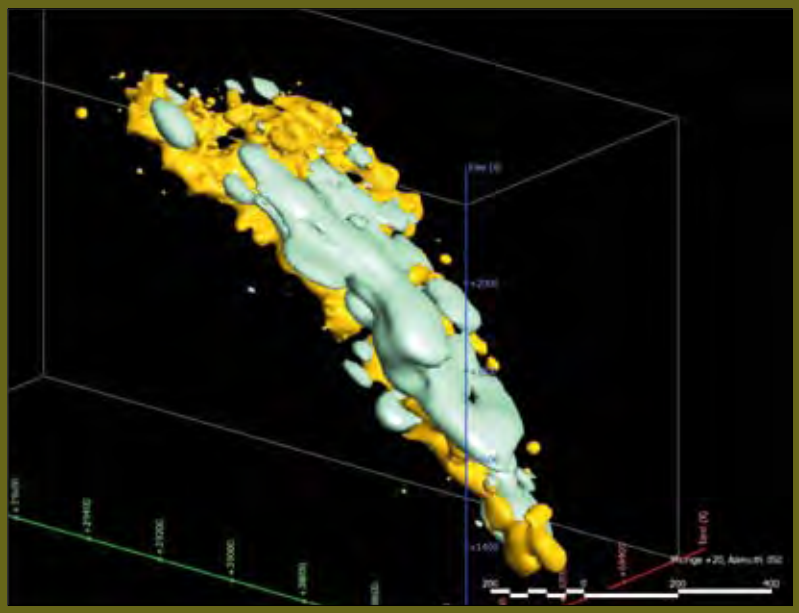

Figure 63: Leapfrog isosurface model for the 0.28 mol calculated pyrite shell (calculated using the EHM approved min-mol procedure).

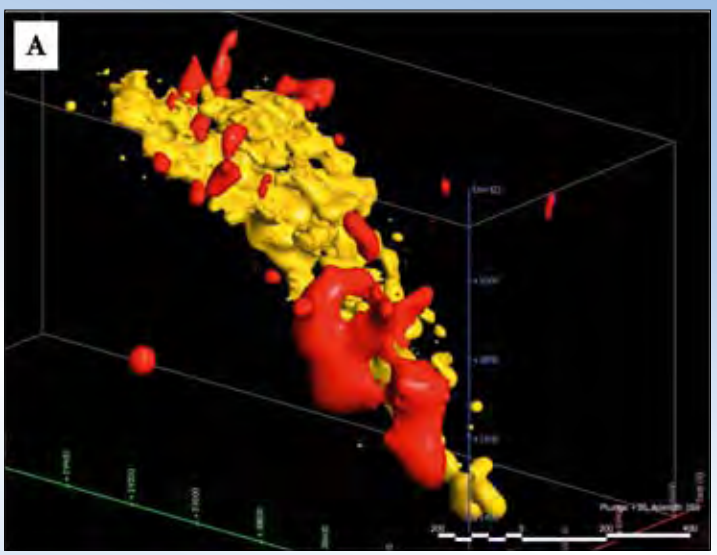

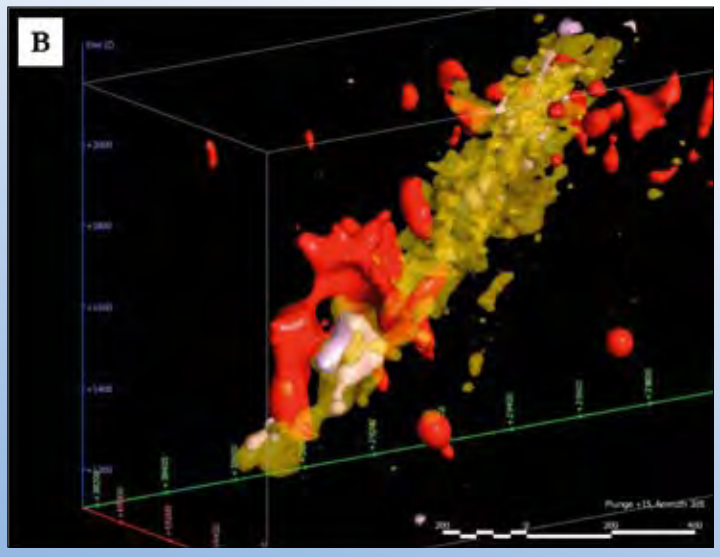

Figure 64: Views of the leapfrog models for Cu (1.25 wt%, orange), Fe (30 wt%, pink) and logged k-feldspar + hematite (red). A) view looking 050° and, B) view looking 305°.

using the mine published variography data). The pyrite shell is offset and sits above and to the west of the main copper concentrations. This does not appear to be related to a lithological change, although this can not be entirely discounted.

Alteration Patterns

Using the logged alteration codes in the drilling database, leapfrog was used to try to look for broad redox patterns. The models show a clustering of logged k-feldspar and hematite that appeared to be spatially constrained, as well as cutting across some of the ore body (Figure 64a). The main focus of this alteration type is of interest because it is coincident with the change in the orientation of the ore body (southeast to south plunge), and the disruption of the upper ore zone. The main kfs-hm alteration zone is also seen to occur as a shell around high grade Fe (>30%) in the bottom section of the ore zone (Figure 64b). This high-grade Fe shell occurs within the ore body which has variable Fe contents throughout the Cu-bearing breccia.

Using the CIMS drillhole photo database, an example of the transition to kfs-hm alteration was logged for EH554 (Figure 65; section 450-471m). The upper unit is logged as biotite alteration and is dominated by dark rocks with light selvages of carbonate; in contrast the logged k-feldspar-hematite marks a transition to brecciated rocks, but again with zones of carbonate-quartz. These transitions are fundamentally redox driven and are critical to map within the ore system.

Regional Potential Field Data

Using the total magnetic intensity (TMI) draped over the topographic surface (Figure 66) for the base of cover (top of

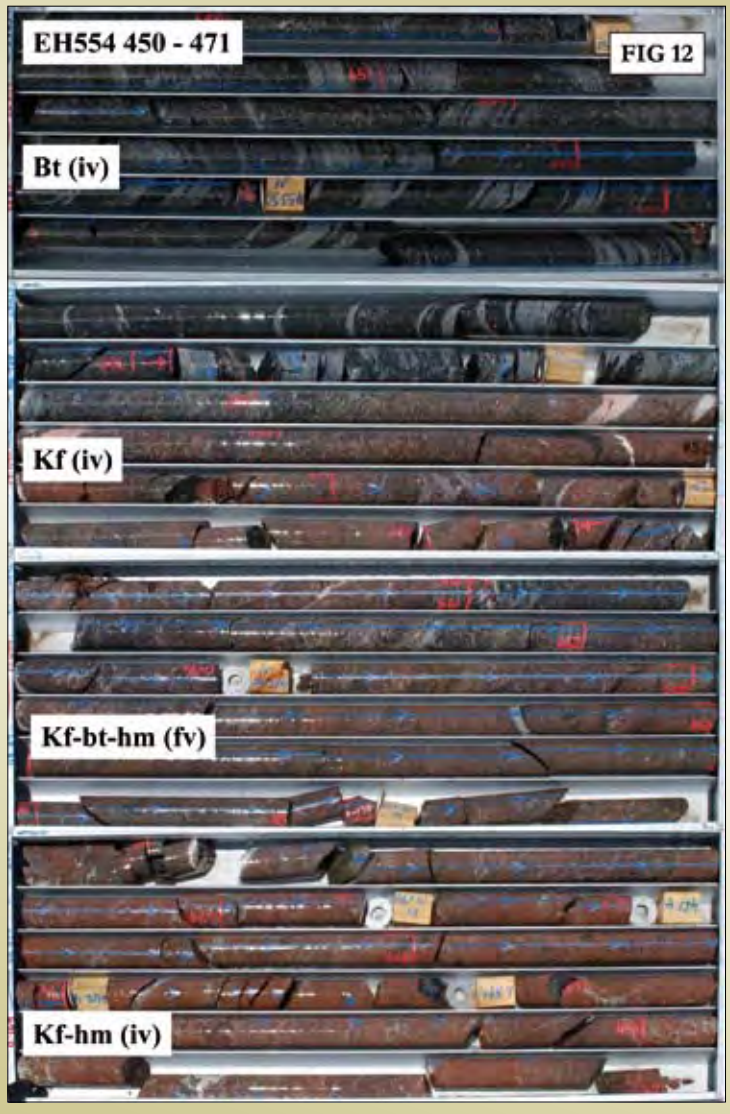

Figure 65: Ernest Henry Mine, Core Photo_EH554) Example of typical transition from bt alteration to kf-hm (EH554).

Proterozoic), it is observed that the areas of magnetic high intensity values, delineating northeast-southwest trending lineaments are also represented by highs in the pre-Mesozoic paleotopography. These magnetic highs are thought to be associated with the footwall and hanging wall shear zones.

Figure 67 shows the regional Bouguer gravity image superimposed on the mine-scale TMI image. Gradient lines in the TMI (i.e. worms), the orientations of kfs-hm alteration and possible new structures, and the sharp edges of the regional gravity all appear to line up in a general northeast-southwest orientation. This matches the trend

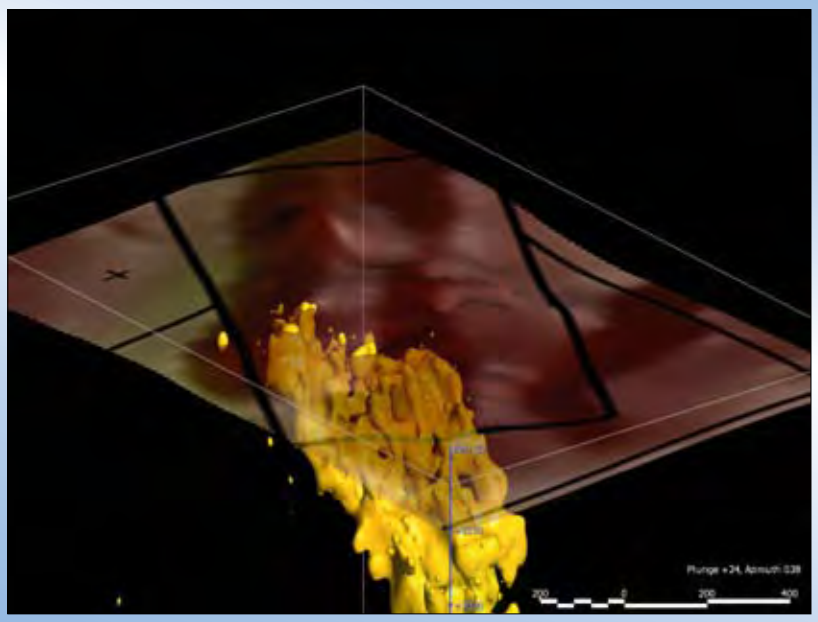

Figure 66: Total Magnetic Intensity image draped over the modelled topography of the base of the Phanerozic cover with the 1.25% Cu isosurface in yellow of the Ernest Henry deposit. All data is vertically exagerated x2. Note the relationship between magnetic high values and topographic relief in the unconformity and the distinct NE trend in magnetic data ridges, similar to that seen in the disrupting fault at depth in the copper grade. View looking down towards 038°.

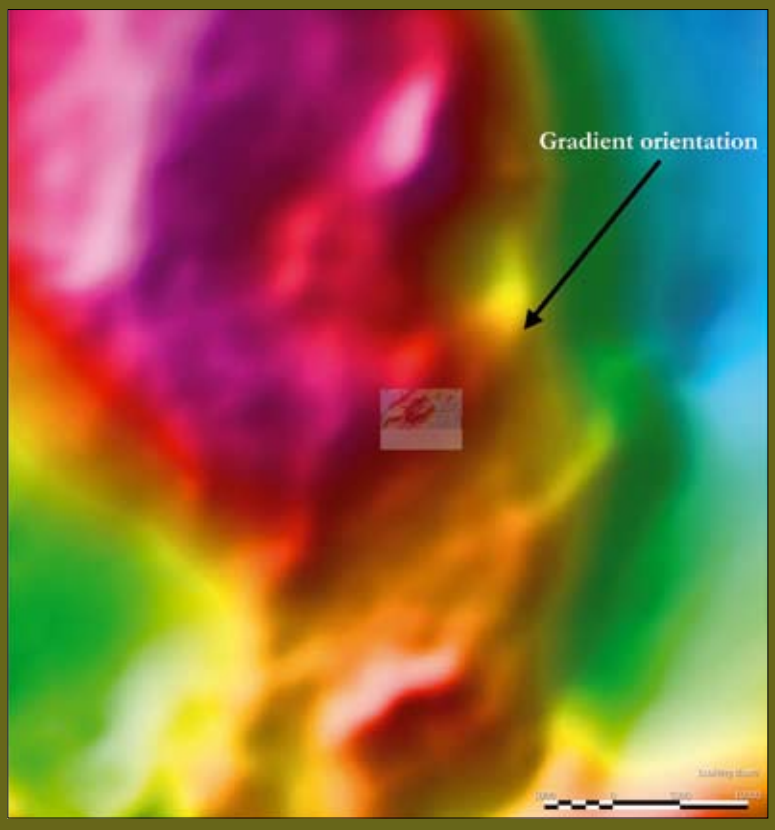

Figure 67: Regional Bouguer gravity with the magnetic image for Ernest Henry (see previous figure) inset. Note that the gravity gradients parallel the magnetic ridges in the image.

defined by Austin and co-workers (project I2/3) as a preferred orientation of deposits in the EFB.

Petrographic Relationships

Figure 68 shows examples of typical breccia-hosted ore from Ernest Henry in backscattered electron image (BSEI). The key minerals are commonly extensively zoned and include complex overgrowth textures. This and the presence of coexisting phases in the rock such as (Ba) K-feldspar, baryte and pyrite indicate that fluid mixing was an important process at EHM. The textures in Figure 68a and b are from the same area with a different backscattered contrast (to highlight different minerals).

Figure 68a shows zoned apatite overgrown by titanate and magnetite-chalcopyrite, while Figure 68b shows the k-feldspar (zoned with Ba), quartz (black) and some calcite as infill phases. This view contains little in the way of true clast material and is fairly high-grade. The precipitation of titanate and k-feldspar, even when they are shown to be immobile is related to the nature of transport scale. Here those components are probably moving at the micron-mm scale within a sample but are conservative at the hand-specimen scale. These images also illustrate the difficulty in distinguishing clast material from hydrothermal precipitate in these breccias.

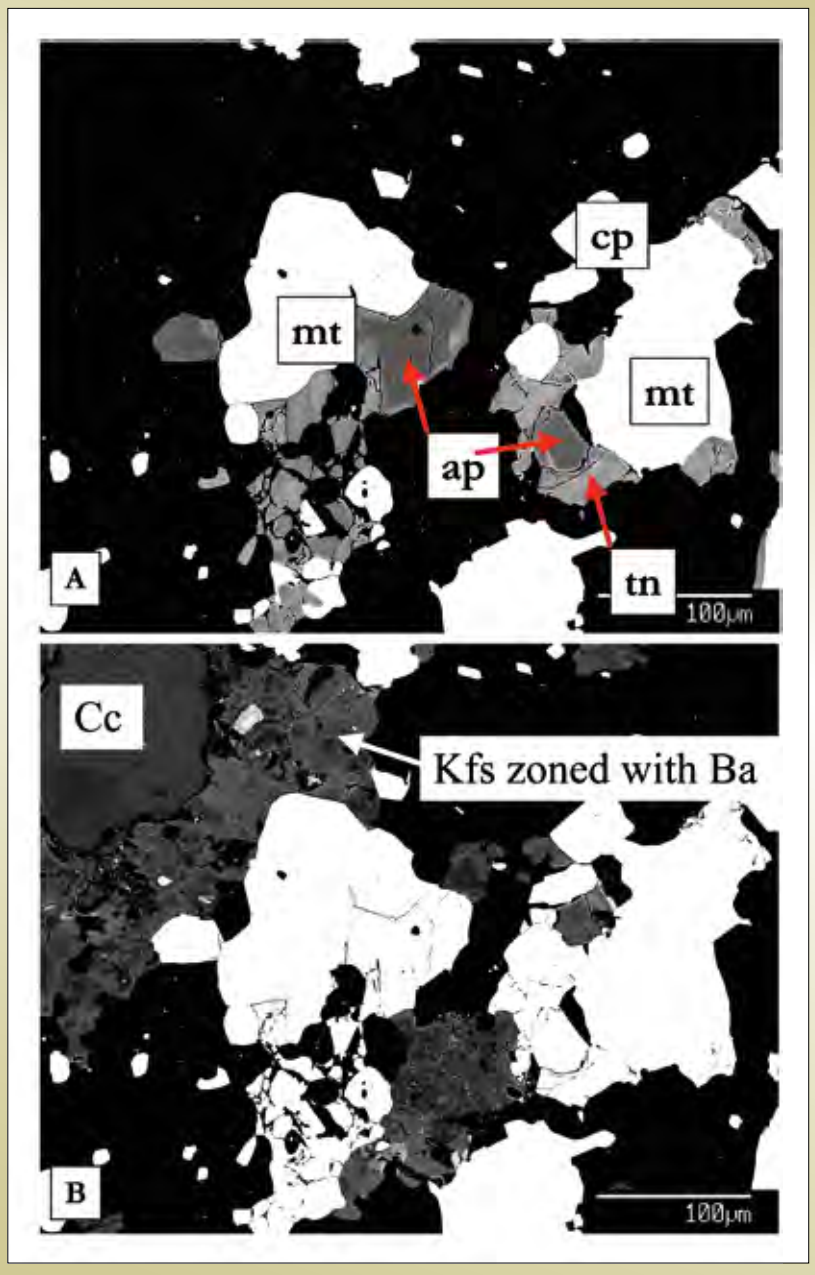

Figure 68: Typical breccia-hosted ore as seen in backscattered electron image showing A) Zoned apatite and titanite overgrowths with chalcopyrite-magnetite and B) zoned k-feldspar and calcite, with quartz (black) as the matrix phase.

Figure 69 is an example of a crackle breccia peripheral to the ore zone (EH440/119) which is logged as kf-mt alteration in felsic volcanic. The crackle texture is obvious in the thin section scan (A). The BSEI of the fracture (B) shows that these are dominated by amphibole and subordinate biotite (all showing strong, but texturally preserving) alteration to chlorite. The k-feldspar is pervasive and likely replaces pre-existing albite/anorthite, but is associated with rounded quartz that appears to be generated in the reaction. The contact between biotite and k-feldspar is rich in titanite, probably from the breakdown of biotite in the fracture during chloritisaton. Figure 69c illustrates the carbonate flooding that is common in some localised areas within the ore body and peripheral crackle breccia. Here the carbonate appears to be associated with an increase of Ba in the k-feldspar (lighter in Figure 69c) as well as possible As-enrichment in apatite (see details below).

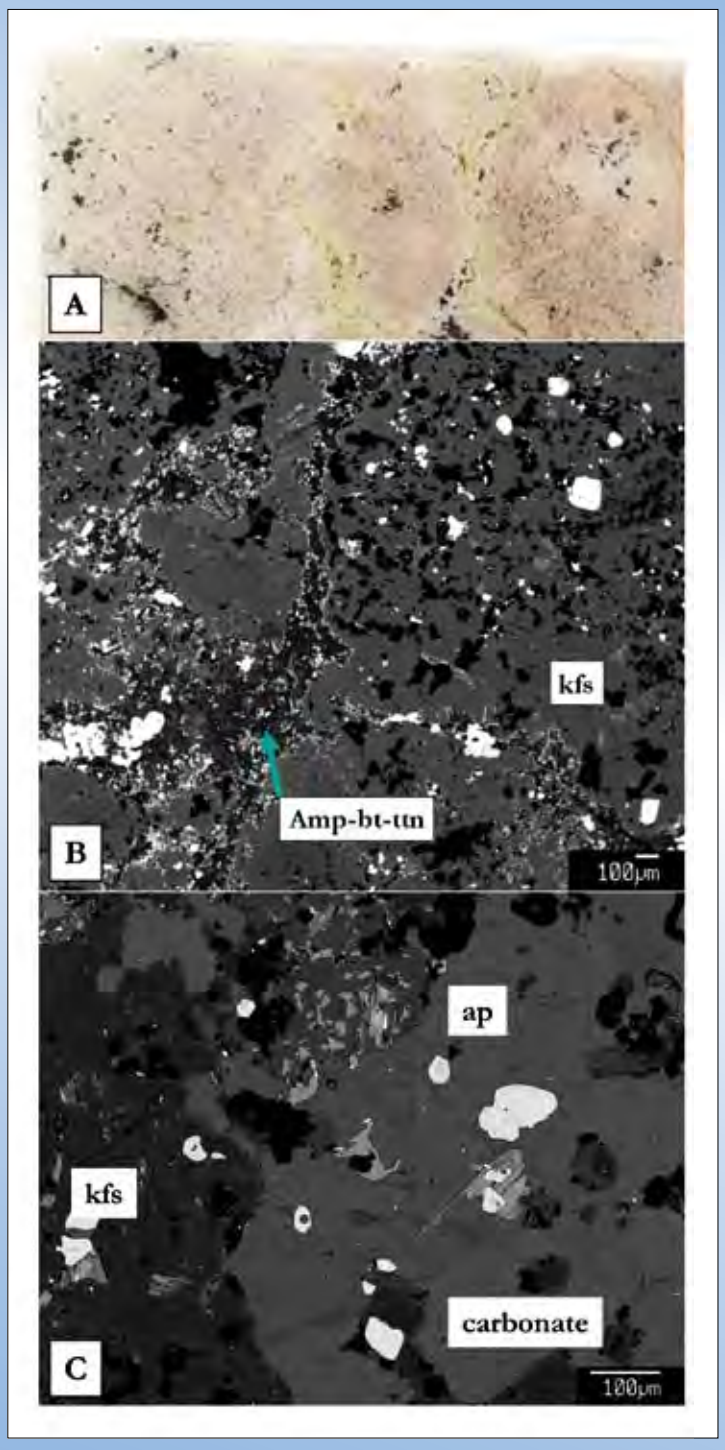

Figure 69: EHM_BSEI_02)
A) Thin section scan showing the textures of a crackle breccia rock, with fractures of amphibole-biotite in a k-feldspar altered rock (pink coloured in this example). Pale patches are carbonate.
B) BSEI of amphibole-biotite ?fracture cutting k-feldspar-quartz (black), and C) carbonate alteration of the k-feldspar with bright zones related to increased Ba content of k-feldspar. Note also zoned apatite (arrowed) within carbonate patch.

Late stage processes

The Ernest Henry deposit contains a protracted and complicated history as recorded by the paragenesis of ore and alteration mineral assemblages (i.e. Mark et al. 2006). Some textures in the deposit appear to be very late, such as the cross-cutting carbonate veins with coarse remobilised chalcopyrite. However some ore breccia samples contain evidence for later, lower temperature processes that may have been important. Some core contains discrete zones of silica enrichment. Backscattered imaging of these zones reveals quartz with disrupted euhedral textures and an acicular mineral (possibly Mg-mica or chloritoid).

The textures (Figure 70) indicate late-stage processes, also associated with Cu deposition, but that post-date the main brecciation event. The quartz can be seen to contain remnent euhedral textures (CL image, B) which may indicate insitu growth, although there has been post-solidification modification. A prismatic, botryoidal mineral phase overgrows the quartz and is often found overgrowing the magnetite. This phase is zoned with Mn, Mg and Fe (see Mn map, C), and maybe a form of chloritoid(?). Magnetite is fractured and altered to a more oxidised (although not true hematite) Fe-oxide, and associated secondary chalcopyrite.

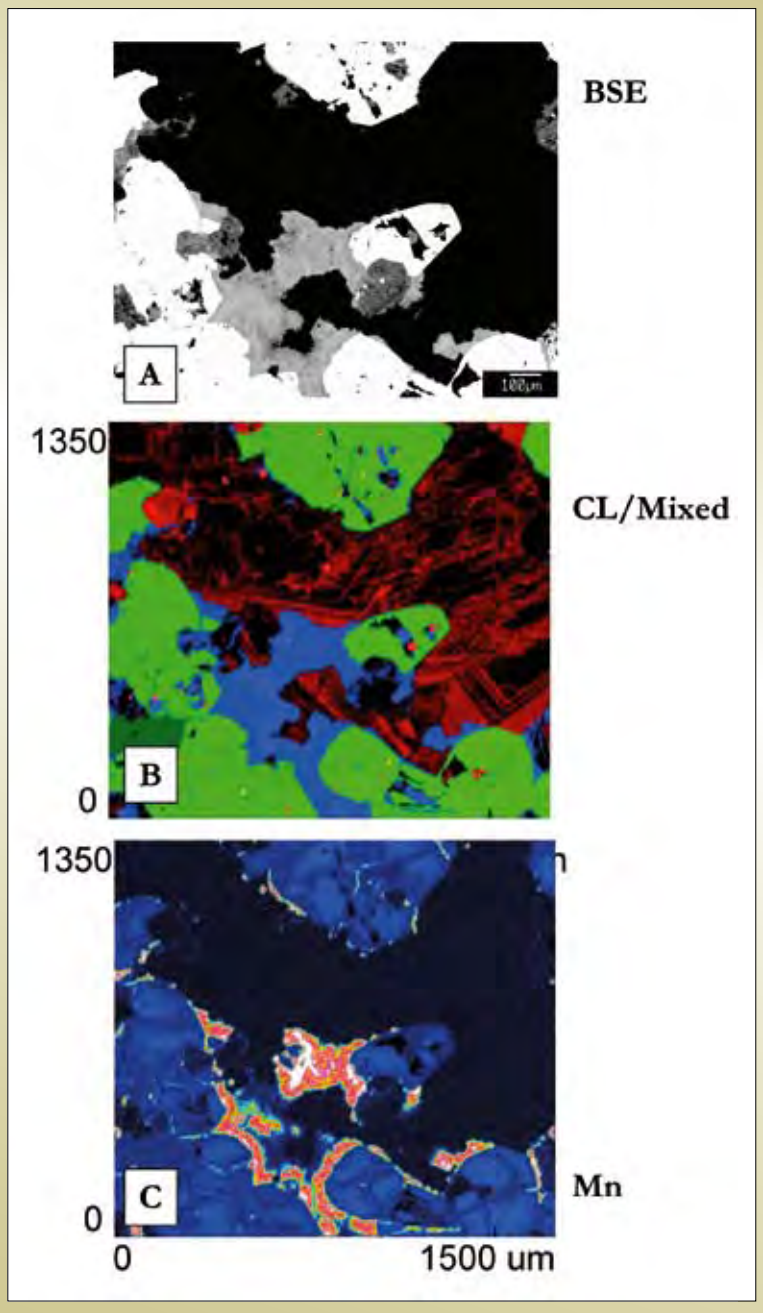

Figure 70: EHM_ images from a thin section of typical quartz-rich part of the ore body in A) backascatter, B) cathodoluminecence and C) Mn element map.

These hematitc-quartz-chalcophyrite assemblages can be seen to occur as discrete zones within the Ernest Henry ore body, and has been observed in regional prospects (i.e. The Roadmaker in the drowning child breccia region) as well as other IOCG classes of deposit. Some of the mineral assemblages and textures appear similar to those observed in Mt Isa copper style ore bodies, and these zones may represent reactivation or secondary processes overprinting an earlier IOCG breccia.

Fluid Processes Recorded by Apatite

The chemistry of apatite [$Ca(PO_4)_3(OH)_2$] is strongly influenced by the chemistry of the volatile components in the hydrothermal fluid. Common elemental substitutions include Ca by REE, Sr, and Na; PO_4 by CO_3, and SO_4; and OH by F and Cl. Determination of the apatite chemistry and its paragentic relationship to other phases in the mineral system can be useful in constraining the chemical evolution of fluids or their chemical characteristics.

The apatite at Ernest Henry is petrographically very different from that in the regional brecciated rocks as it exhibits very strong concentric zonation in backscattered electron images (generally dark cores to light rims). Often the apatites are overgrown by titanite or intergrown with magnetite – chalcopyrite associated with the brightest rim (Figure 68a). The textures indicate that the apatite probably grew in relative open space and at least partly predates or is synchronous with the magnetite – chalcopyrite ore association. The zonation is highly complex with evidence for multiple growth and resorbtion surfaces but the overall trend (dark cores to bright rims) is common in all ore breccia samples. Apatite from regional breccia samples has also been analysed and is plotted here for comparison (see Question 3, this volume).

Halogens (F,Cl)

One of the key chemical substitutions in apatite is between the halogen-water end-members: fluorapatite (FAp), chlorapatite (ClAp) and hydroxyapatite (HAp). All of the apatites in this study except those from the regional gabbro exhibit strong F-enrichment. The complete database of samples is plotted recalculated as atomic formulae units (to 10 Ca) in Figure 71. Under this scheme, the OH-site in the apatite should contain 2 atoms. It can be seen that three distinct groups emerge from the data: a) samples with F > 2 afu, b) samples with Cl 0.06 and F 1.5 to 2 afu and, c) gabbro samples with < 1 afu F and core to rim variation of 0.1 to 0.6 afu Cl (cross symbols on figure). The dashed line for X_{OH} = 0 on Figure 70 demarcates samples with little or no OH (on the line) and samples with excess halogens for the stoichiometric OH-site (above the line). As can be seen from the figure Ernest Henry apatites and those from some of the regional breccia systems have excess F in the apatite structure. Samples in group b (regional breccia and scapolite marble) show a general core to rim progression to more F-rich compositions at constant Cl (indicating loss of OH).

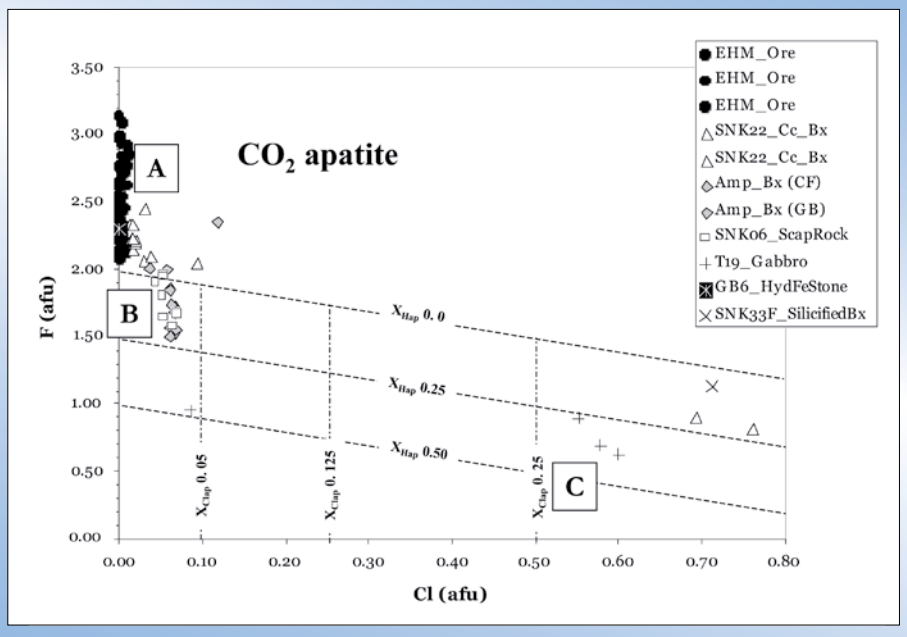

Figure 71: EHM_APATITE_F_Cl (atomic formula units) data for apatites from hydrothermal breccias, Ernest Henry ore breccia, mafic intrusive and Corella marble (see text for sample details). Dashed lines are location of constant mole fractions of apatite-OH (Hap) or apatite-Cl (Clap). Data above the X_{Hap} = 0 line contain non-stoichiometric F that may indicate the presence of CO_2.

Group A apatites (excess F) include the Ernest Henry apatite (all chemical zones), calcite-rich breccia and a breccia-hosted Fe-stone (Gilded Rose locality). These apatites also have the best evidence for direct hydrothermal precipitation. The group B apatites include the amphibole-rich breccia, scapolite marble and clast-rich breccia with minor calcite. Group C represent the evolution from core to rim of the apatite within the Williams Batholith age mafic intrusive (see Question 3, this volume).

Arsenic & Sulphur

None of the strong concentric zonation observed in backscatter images from the Ernest Henry apatite can be attributed to variations in halogens in the OH-site. However there is strong zonation in the S and As cotents of these apatites with variations from S-rich cores (SO_3 0.5 wt%) to As-rich rims (max As_2O_5 5 wt%) and this is illustrated in a detailed traverse from a single EH apatite grain in Figure 72. This zonation from S-rich core to As-rich rims is common to all apatites observed within the ore zone breccia (Figure 72).

Comparison of the regional dataset with those apatites from EH shows that none of the other samples contain the extreme enrichment in As, however the calcite-rich breccia sample (white triangle on Figure 73) do show enrichment relative to other regional samples. The apatite recorded in breccia-hosted ironstone records the most extreme S-enrichment, even in comparison to EH samples. The relative observed increase in S and/or As in other samples is not statistically valid using electron microprobe data.

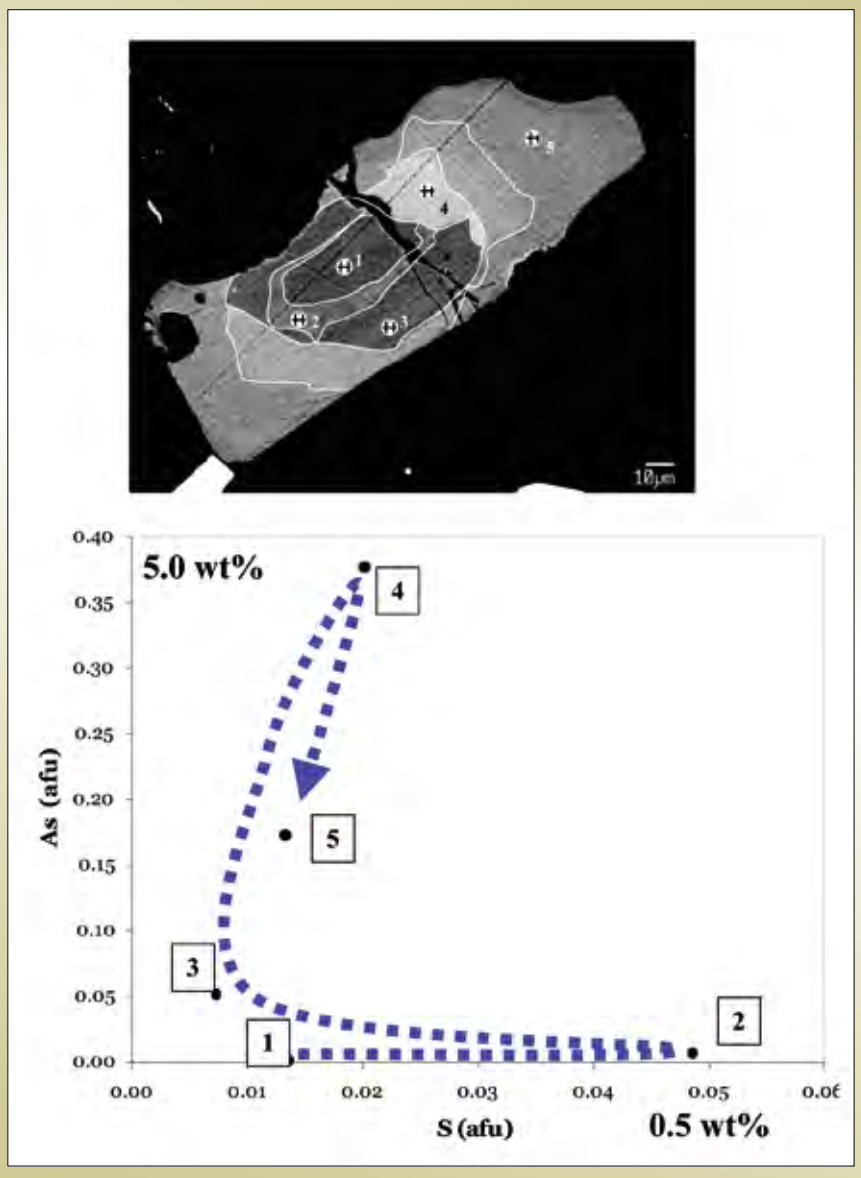

Figure 72: Microprobe chemistry for zoned apatite in typical EHM magnetite-chalcopyrite ore, showing variations in As and S.

Interpretation of Apatite Chemistry

F-apatite is common in all the breccia systems, especially associated with carbonate and CO_2 inclusions. The phase relationships for F vs Cl vs OH apatite are a function of the relative activities of the phases in the fluid (HF-HCl-H_2O), and the controls of temperature, pH etc. The F-apatite at Ernest Henry is not obviously associated with fluorite and for rocks containing Ca-phases (calcite, anorthite etc) the range of conditions that stabilise F-apatite but not fluorite are relatively narrow (Figure 74), after Zhu & Sverjensky, 1992). F-apatite becomes more stable at lower temperatures for a given activity ration between HF-HCl-H_2O, but any reasonable HCl activities at 500°C (EHM conditions) would give some Cl-apatite

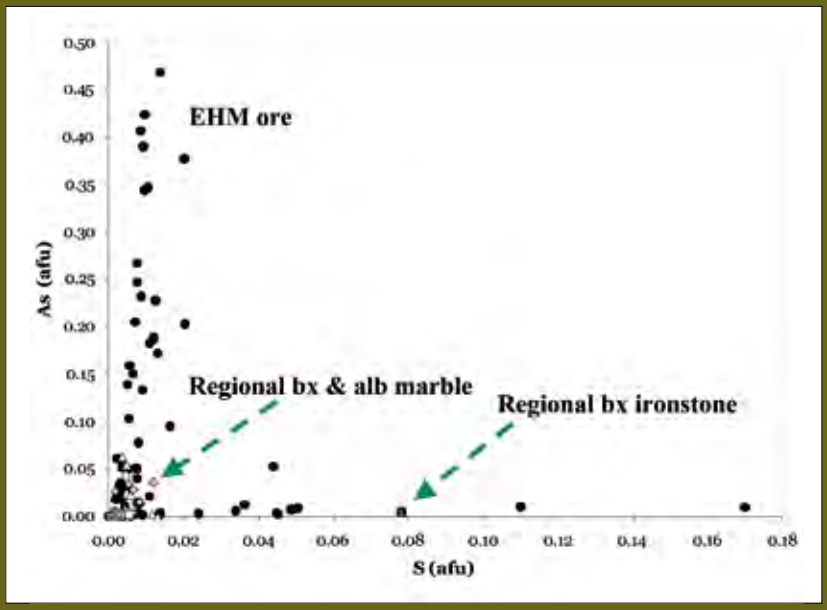

Figure 73: Microprobe chemistry for apatites from EHM and regional hydrothermal breccia systems showing variations in As and S.

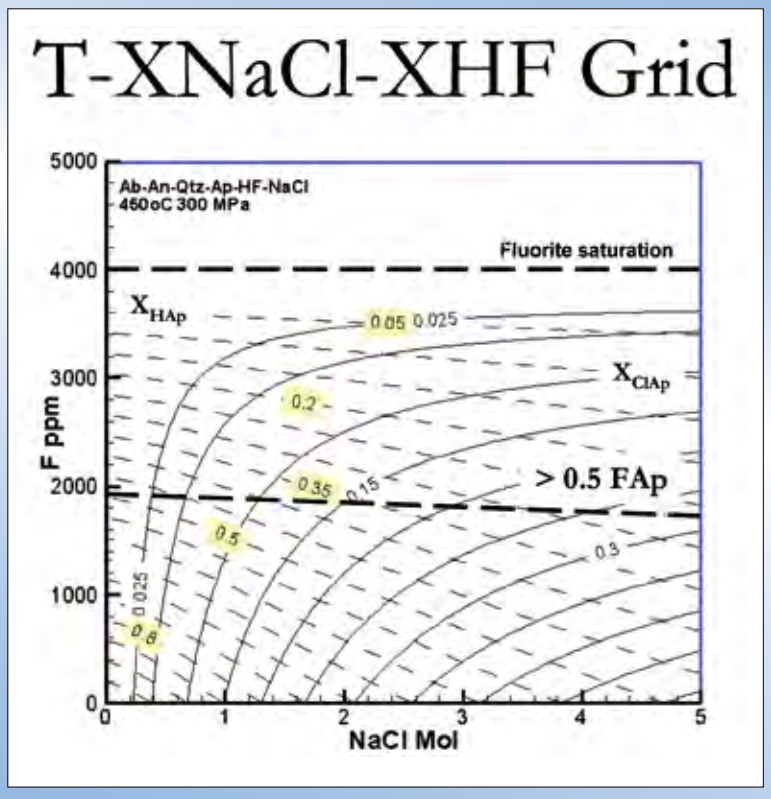

Figure 74: Phase diagram for NaCl-F (modelled using HCh) and anorthite-bearing assemblage showing the region of fluorite saturation (~4000 ppm F) and F-apatite (apatite with > 0.5 FAp). This model is for 300MPa and 450°C but the relationships are similar under different PT conditions.

component. Therefore it is likely that the apatite is precipitated from a fluid that is dominated by F relative to H_2O or Cl.

The Ernest Henry apatite all contains excess F (i.e. > 2 afu), although this maybe in part an artefact of the microprobe analysis (Stormer, 1993), repeat analysis, analysis along the c-axis and standard analysis indicate that there is a real component of excess F in the EHM apatite. Nichino et al. (1981) show from FTIR analysis of apatites similar to this (and teeth) that this is often associated with the substitution of CO_2 for PO_4 ($PO_4^{3-} = CO_3^{2-} + F^-$). Although this has not directly been quantified in this work, qualitative analysis with the light-element detection beam (JCU superprobe) showed a broad C peak in the apatite that was better defined than background.

While there is some published literature on the S contents of apatite in natural magmatic-hydrothermal environments, little exists for As. Streck and Dilles (1998) report that S occurs in apatite as the S^{6+} oxidation state and replaces PO_3 as a coupled substitution with Si^{4+} or Na^+; $SO_4^{2-} + Si^{4+} = PO_4^{3-}$.

Arsenic has been reported in apatite, and the As end-member apatite (Johnbraumite) is found in the Franklin Hills locality. Arsenic is also assumed to substitute for the PO_4-group with a direct non-coupled substitution by the As^{5+} ion (Narasaraju et al. 1985; Perseil et al. 2000).

Assuming that there is no in-situ oxidation of S or As during substitution into apatite these quantities can be used to record the changes in the activites of the oxidised fluid species. More accurately the apatite records the changing sulphate/phosphate and arsenate/phosphate activity ratios. A pH-fO_2 diagram for As-S (Figure 75) shows that the S^{2+}/S^{6+} (pyrite-hematite) and As^{3+}/As^{5+} (hematite) buffers are located at very different redox states. It would be tempting to interpret the change in As/S in apatite as a shift in redox conditions, however it is unlikely that the As-S substitutions occur at fixed charge states, and the actual redox state of the elements in apatite is largely unknown for As (S is better defined). Future work will use the Australian synchrotron to better determine the redox state of the chemical zones in the EHM apatites.

Summary

The apatites record evidence for PO_4-HF-SO_2-CO_2 fluids that are at least in part carrying $As^{(6+)}$ and/or SO_4 and that have little or no Cl or H_2O. The evolution from SO_4 to As could be related to mixing of external fluids at that time or

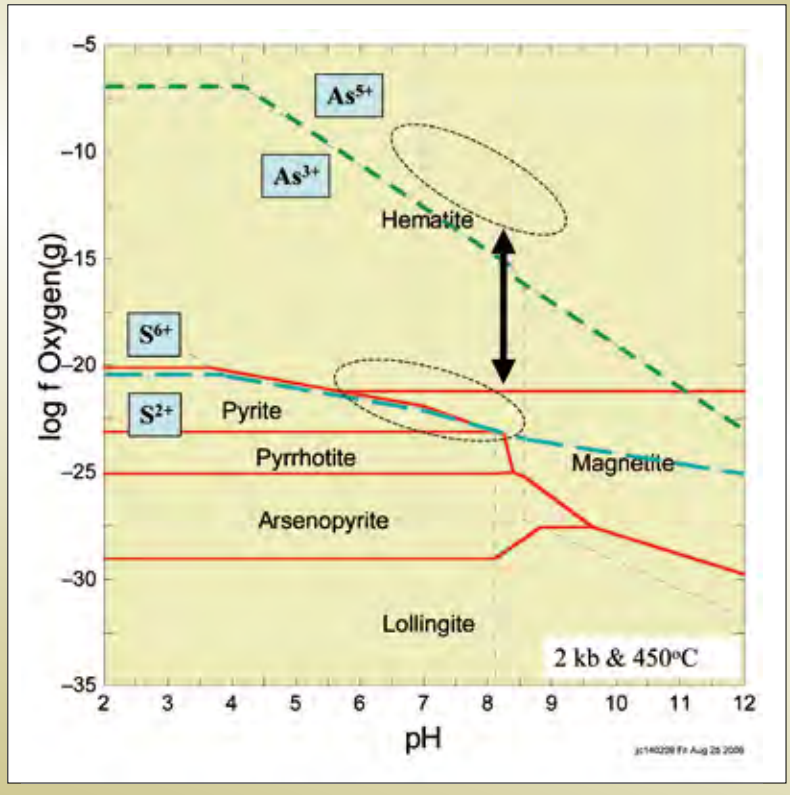

Figure 75: Phase diagram of pH and fO_2 at 2 Kbar and 450°C.

an in-situ change in the redox state of carrier fluid (because of mixing or phase separation). The overgrowth of apatite by titanate (see textural photos) might record the transition from volatile-rich fluids to brine liquids (evidence from the regional breccias suggests that titanate forms instead of apatite in breccias more associated with brines than CO_2). The extreme nature of the chemistry of the Ernest Henry apatites relative to the regional rocks indicates that there are processes that existed within the deposit that certainly did not occur in barren rocks that are structurally similar.

Stable Isotopes

The compilation of Mark et al. 2000 (SPIRT Report to MIM) contains a database of stable isotope values including S, C and O. While the C and O are published elsewhere (Oliver et al. 2004, Marshall et al. 2006), the S isotope data is described here in some detail. The S, C and O isotope data is (where possible) available in 3D within the Leapfrog model.

Sulphur

Figure 76 is a plot showing the $\delta^{34}S$ values for pyrite (A) and baryte, and chalcopyrite (B). For pyrite the bulk of the data lie between 0-5‰, with outlying clusters at around -4‰ and +11‰. This range is similar to that observed for chalcopyrite with the bulk of the data between 0-5‰ and some heavier values at +11‰. Baryte occurs in two values at +11 and +23‰. While the bulk of the analysed samples in pyrite and chalcopyrite are restricted to 0-5‰, the negative and positive samples are still from within the ore body, although their exact textural relationships are unclear.

Figure 76a includes equilibrium lines for $\delta^{34}S$ between a species and pyrite under different conditions in an attempt to explain the distribution of the data. Line A is for SO_4 at +23‰ (hematite-magnetite buffer), line B is for SO_4 at +11‰ (hematite-magnetite buffer) and, line C is for 0‰ H_2S (pyrite-magnetite buffer). Using this simple approach the +23‰ baryte appears to not be associated with any

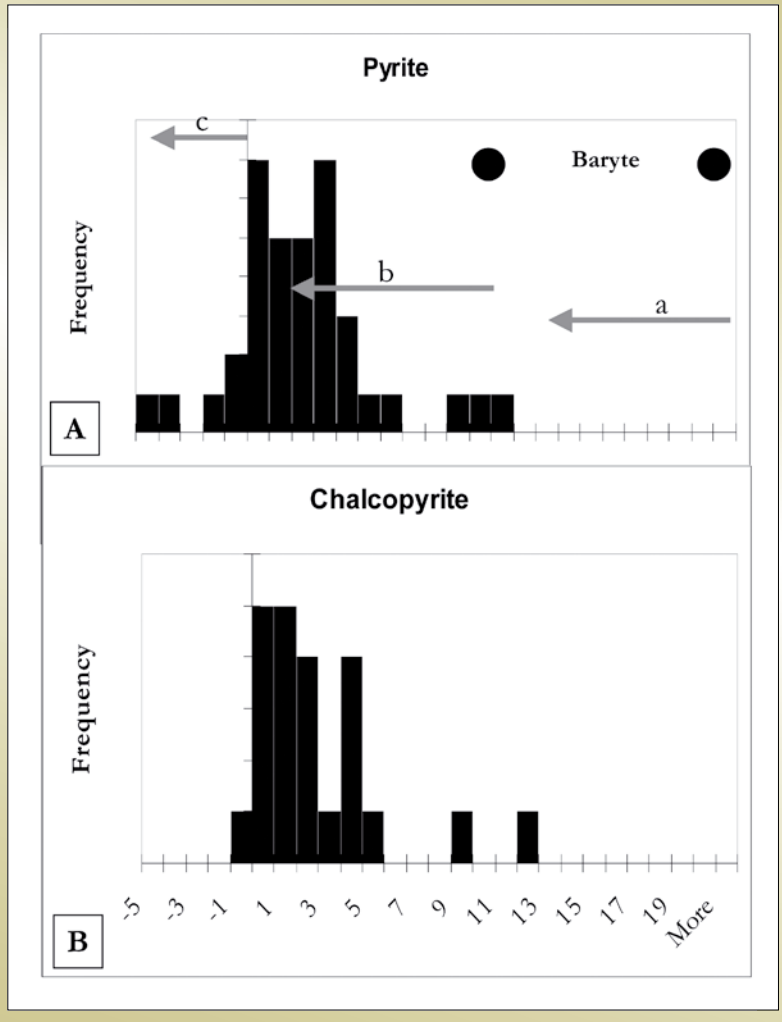

Figure 76: Ernest Henry sulphur data for A) pyrite and B) pyrrhotite. $d^{34}S$ isotopes for pyrite and chalcopyrite from compilations in SPIRT report (Mark et al. 2000) for Ernest Henry ore body. Data also includes Baryte = +11, +23‰ (n=3), and Pyrrhotite = +3, +11‰ (n=2).

equilibrium sulphides, while the +11‰ baryite could potentially be in equilibrium with the bulk of the 0-5‰ pyrite and chalcopyrite. The small propotion of ~3% pyrite could also be a function of equilibrium with a 0‰ H_2S S source. In this simple model the +11‰ pyrite-chalcopyrite would occur where SO_4 was fully reduced, thus no fractionation occurred to the sulphide phase.

Another possible explanation of the heavy pyrite-chalcopyrite is the influx of (late) +23‰ SO_4 (seawater sulphate value) into a rock with average +3‰ S (pyrite-chalcopyrite-magnetite). Reduction of the seawater SO_4 would lead to a range of heavier sulphide values. This scenario has been modelled using Geochemists Workbench (Bethke, 1996) and a simple chemical system (Figure 77). Here the rock is assumed to be magnetite-chalcopyrite-pyrite + H_2S (+3‰) and this rock is titrated with SO_4 at +23‰ (300°C, Psat). The model predicts a range of S isotope values from +3‰ to +14‰ covering the full range of heavy values at Ernest Henry. However the natural data do not show a complete range between +3 and +11‰, and as such is it is more likely that the +23‰ baryte is a late phenomena unrelated to the breccia ore body and the sulphide numbers.

It appears from the S data that two dominant S reservoirs existed at the time of breccia ore generation: a) +11‰ SO_4 and b) ~0‰ H_2S. The bulk of the ore body was dominated by oxidation and incomplete oxidation of the H_2S leading to a bulk range from 0-5‰. Some parts of the ore body experienced extreme and total reduction of a +11‰ SO_4 fluid, giving rise to the +11‰ sulphide values. While 0‰ H_2S is typical a magmatic or magmatic-related source (i.e. S scavenged from volcanic rocks), +11‰ SO_4 is more typical of magmatic SO_2 values at the conditions of the magma chamber (600-800°C). For instance, primary magmatic anhydrites at Mount Pinatabu were recorded with values of +8-+11‰. While we can not rule out the involvement of a S sourced from Proterozoic seawater (+25‰), only further analysis and textural relationships can distinguish between this and a magmatic SO_4 (+11‰) source.

Processes of Ore Deposition at EHM

The Ernest Henry deposit is a hydrothermal breccia hosted Magnetite-chalcopyrite ore system that has been shown to date from 1525Ma but with some evidence of inherited material (~i.e. Re-Os on molybdenite at ~1600Ma, Bruce Schaefer *pers. comm.* 2008). The evidence presented in this (and see Q3) suggest that fluid-mixing is the dominant process operating at the time of deposition and the fluid sources probably include sedimentary derived brines and magmatic fluids. It maybe that 3 fluids are present and that the system is long lived such that the deposit suffers a "Mt Isa Cu-style" overprint (i.e. hematite-quartz). Micro (zoned minerals) to macro (isotopes, leapfrog model) textures show that different fluids were important and

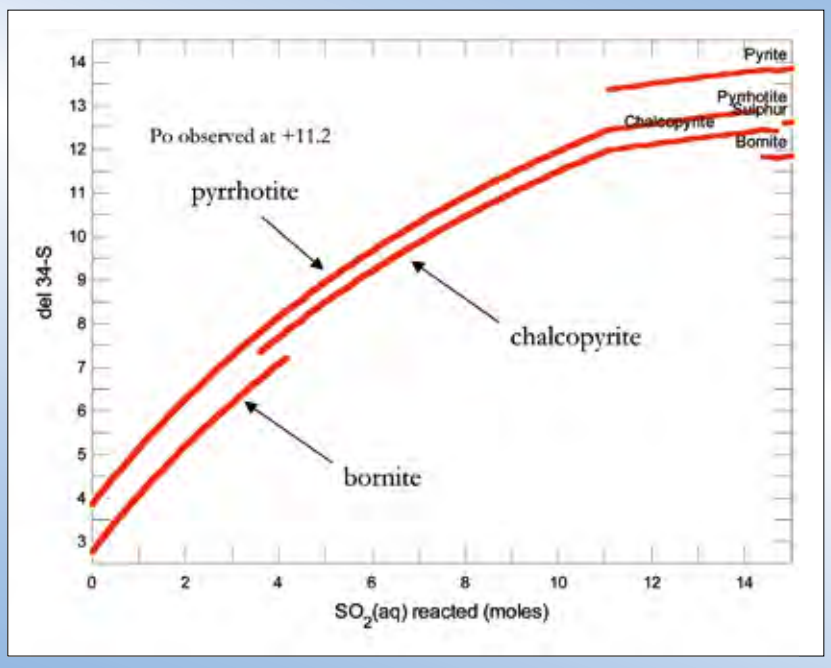

Figure 77: Geochemists Work Bench (GWB) S isotope modeling for simple EHM late ore forming process (T = 300°C), Mt-Py-Cpy rock + H2S (δ34S = 3‰) reacting with SO2 (δ34S = 23‰, Proterozoic seawater value).

the macro-scale distribution of chemical components (chemical architecture) obersverd with the leapfrog model can be used to define a simple mixing architecture showing possible pathways of oxidised and reduced fluids. Figure 78 shows a single possible interpretative scenario for the approximate geometries of fluid pathways that are proposed to have existed in the EHM deposit. Fluid mixing is considered the dominant mechanism of chalcopyrite deposition. Domains of dominantly oxidized fluid flow are inferred from domains of pyrite in excess of chalcopyrite and the broad zones of red K-feldspar ± magnetite ± hematite that mantle the ore zone, particularly in the hanging wall. Domains of dominantly reduced fluid flow are inferred from the As-rich zones in the orebody and the footwall amphibole-biotite alteration. The architecture of the mixing box is defined by NE trending, steeply northwest dipping that appear to have constrained oxidized fluid flow and NNW trending structures defined by the strike of the mineralization. An E-W trending lineament in the regional magnetic image suggests some additional control on the fluid flow; possibly that the flow of reduced fluid is sub-vertical along the intersection of E-W and NNW trending structures. From the character of the regional magnetic image, the district-scale pattern of oxidized fluid flow may have been from south to north. The exact nature of these pathways, and the ability to map this spatially is subject to further research, however, based on this geometry and the orientations in the potential field data it maybe possible to relate the two.

Based on the available evidence it seems likely that a magmatic SO_2-CO_2, and separate $HAsO_4$-rich gaseous fluid and reduced brine (S,Ba,K) fluid are important in the formation of the EHM deposit. However at this stage it is still difficult to decipher the exact mixing geometry or model for the deposit. The similarities to regional breccia systems have been discussed in Chapter Q3, however of all the localities in the EFB that are most similar chemically and mechanically to EHM, the Gilded Rose breccia is high on the list. The distinct absence of direct Cu-S mineralisation is still unclear although better descriptions of the pathways mapped in the potential field data may indicate possible deeper and/or undercover targets for further investigation.

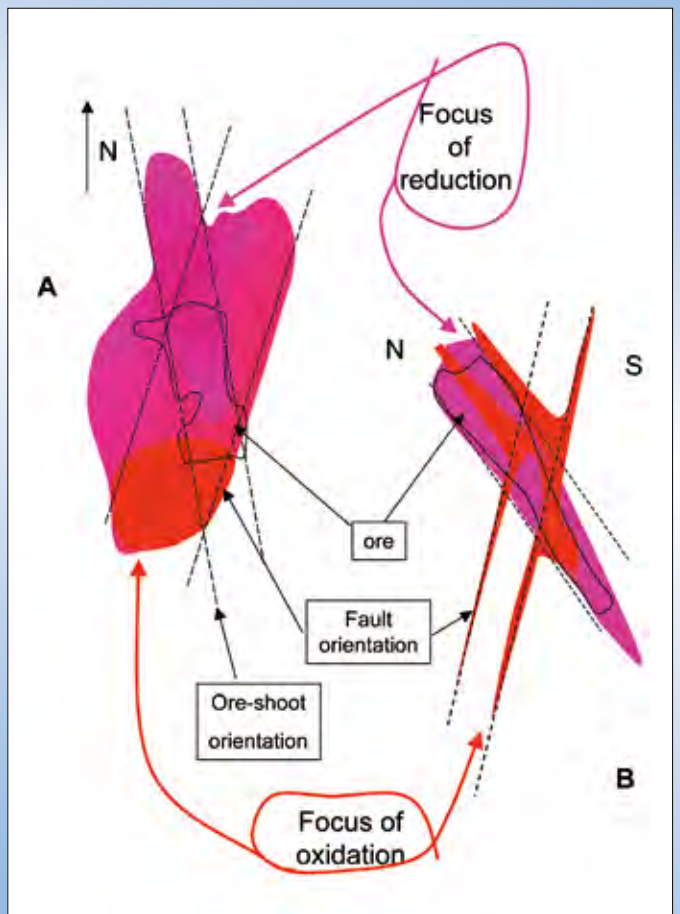

Figure 78: Mixing box model for the Ernest Henry deposit. A Plan view at level of open-cut. B. Long-section view looking east. Mixing of reduced (CH_4 - H_2 –rich; magenta shading) and oxidized (SO_2 bearing; red shading) fluids is inferred from the stable isotope data.

1600/1530Ma Breccia hosted IOCG – Osborne

This section represents a brief synopsis of the key findings from a PhD study by Louise Fisher (JCU). The complete manuscript is available as part of the TWiki/***pmd****CRC* student delivery to sponsors. The findings of the PhD work relative to the Osborne IOCG deposit are reproduced below. Hydrothermal processes at the Osborne IOCG deposit are documented by the fluid inclusion assemblage. The main processes identified are:

- Decompression resulting in the un-mixing of a CO_2-bearing brine and precipitation of massive hydrothermal quartz.
- Cooling and dilution of a high salinity brine over the period of Cu-Au ore deposition.

Movement on deposit-bounding shear zones is suggested to be a probable cause of decompression, and the shear zones are identified as potential pathways for fluid flow. Analysis of the chemistry of the fluid inclusions from quartz from the ore body can be interpreted to show that:

- Halogen data indicates multiple sources of salinity in the ore forming fluids (Figure 79). Br/Cl and I/Cl data suggests that the end member compositions are:
  - A halite dissolution fluid
  - A bittern brine-like fluid.
- The halite dissolution fluid end member has been identified as a fluid component in several Cu-Au deposits in the Cloncurry district including Eloise and Ernest Henry (Kendrick et al. 2006a; Kendrick et al. 2007)
- Noble gas data is compatible with sedimentary formation waters or locally derived metamorphic fluids being significant fluid sources at Osborne
- The noble gas and halogen data is not consistent with an external magmatic fluid component such as that identified at Ernest Henry (Kendrick et al. 2007a). However, fluids derived from local anatectic pegmatites may be involved (considered magmato-metamorphic).

PIXE has been used to investigate the chemistry of the fluid inclusions (Figure 80), and this is an important tool when trying to understand complex mutli-solid fluids such as those observed here.

- The ore fluids have extremely high salinities with Fe and Mn contents equivalent to those measured in fluids of magmatic origin. The high metal and salt content of the fluids is attributed to the high temperatures and pressures the fluids reached
- The ore fluids have low Cu concentrations (<150 ppm) relative to other IOCG deposits in the Cloncurry

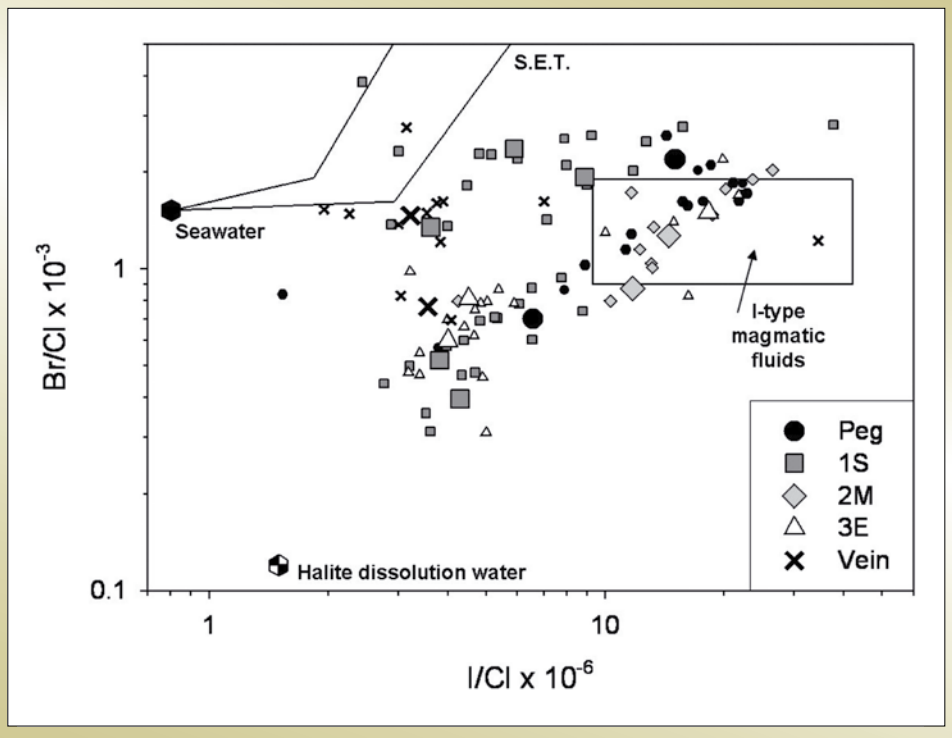

Figure 79: Plot of Br/Cl and I/Cl compositions of halogens in fluid inclusions from quartz in the Ernest Henry deposit.

district. At temperatures of 500-600°C (as measured by microthermometry in MS-type inclusions) these fluids would have been significantly undersaturated with respect to chalcopyrite (Figure 81)

- Fluid mixing is identified as the most likely cause of Cu-Au precipitation with geochemical modelling suggesting that the resultant cooling and redox changes are the main controls on ore deposition (Figure 82).

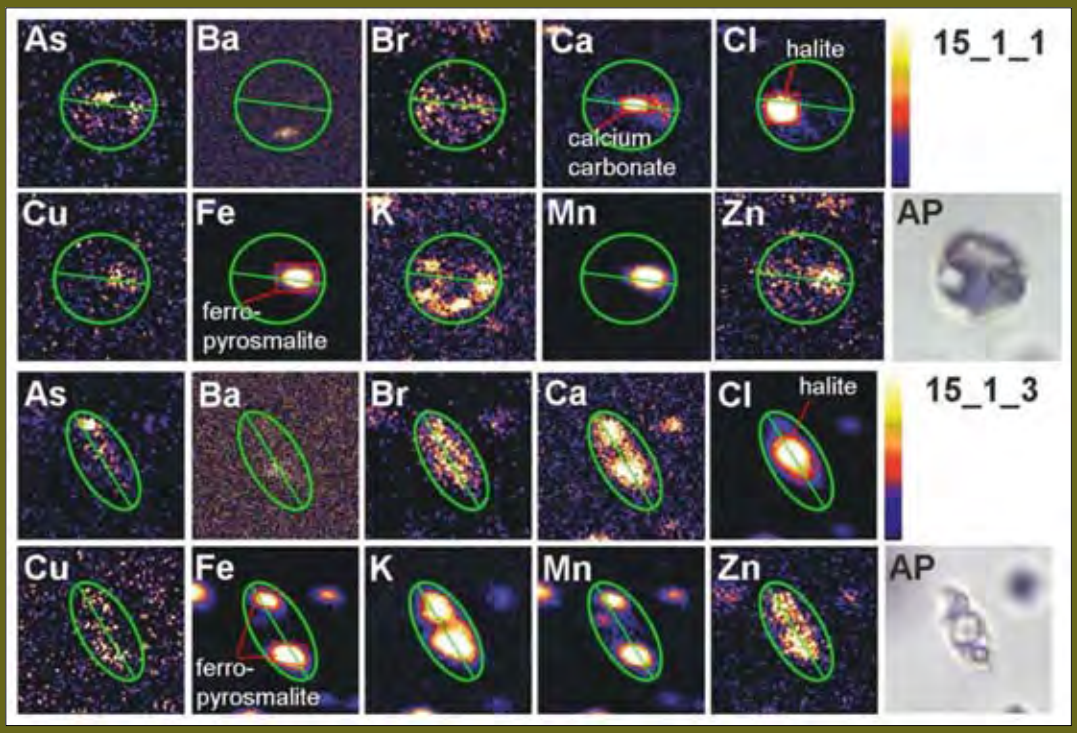

Figure 80: PIXE images of the chemistry of fluid inclusions.

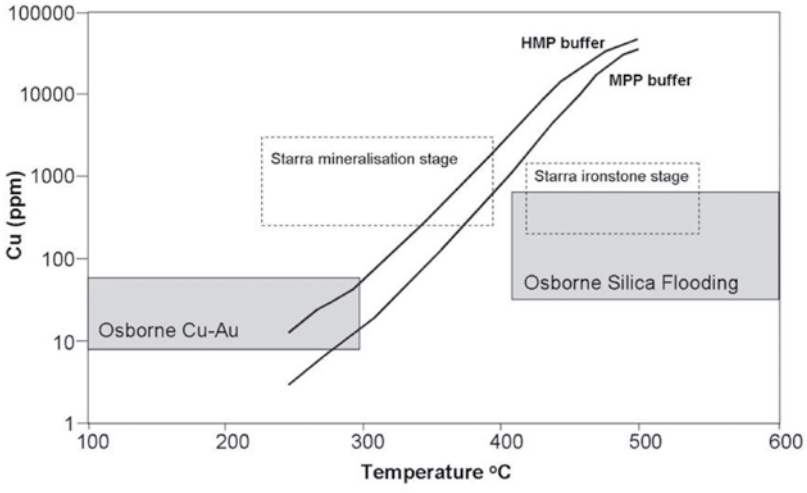

Comparison between calculated chalcopyrite solubility and Cu concentrations measured by PIXE and LA-ICP-MS at the Osborne deposit (modified after Liu and McPhail, 2005). The solid lines denote calculated chalcopyrite solubility in 10 molal chloride solutions (equivalent to 37 wt% NaCl – similar to highest values measured in post deposition LVD inclusions at Osborne) at 1 kbar in equilibrium with hematite-magnetite-pyrite (HMP) and magnetite-pyrite-pyrrhotite (MPP). The grey shaded boxes represent the measured ranges of homogenization temperatures and Cu concentrations measured in pre- and post-ore deposition fluids at the Osborne deposit. Data from the Starra deposit are given for comparison (Williams et al., 2001).

Figure 81: Comparison between calculated chalcopyrite solubility and Cu concentrations measured by PIXIE and LA-ICP-MS at the Osborne deposit (modified after Liu and McPhail 2005). The solid lines denote calculated chalcopyrite solubility in 10 molal chloride solutions (equivalent to 37 wt% NaCl – similar to highest values measured in post-deposition LVD inclusions at Osborne) at 1kbar in equilibrium with hematite-magnetite-pyrtie (HMP) and magnetite-pyrite-pyrrhotite (MPP). The grey shaded boxes represent the measured ranges of homogenisation temperatures and Cu concentrations measured in pre- and post-ore deposition fluids at the Osborne deposit. Data from the Starra deposit are given for comparison (Williams et al. 2001).

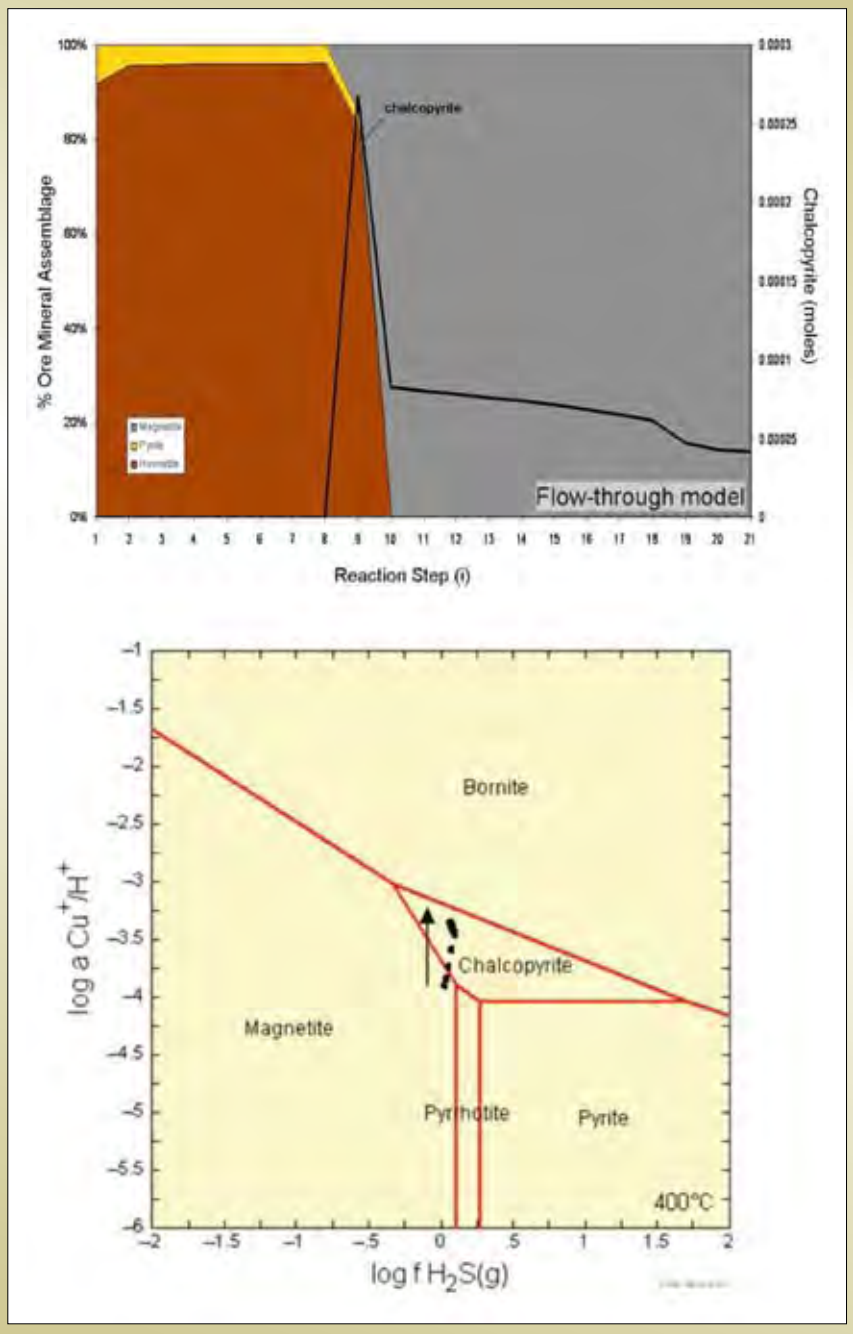

Figure 82: Results of HCh modelling of the ore formation at Osborne (see Fisher, 2007 for details). A) Model results for flow-through HCh model showing chalcopyrite (line) precipitation at the transition from hematite-pyrite to magnetite. B) Phase diagram for Cu+/H+ and log fH2S showing the relationships between the Cu-Fe-S phases and the path for the geochemical model in Figure 82A.

Key ingredients for an IOCG deposit – Osborne

The study of ore forming processes at Osborne has identified key processes and fluid components that are important in ore deposition. However, the Osborne deposit formed over 50 Ma before other known IOCG deposits in the Cloncurry district, making it less likely that it would share common fluid ingredients with the other deposits. Despite this, some common features can be established including the presence of a high salinity fluid that has interacted with evaporite sequences and the importance of fluid mixing as an ore deposition mechanism.

A magmatic fluid is not an essential component and has only been identified at one deposit in the region, Ernest Henry, using noble gas and halogen data (Kendrick et al. 2007a). However, Ernest Henry is the largest IOCG deposit in the Cloncurry district which raises the question of whether the presence of a magmatic fluid component is required to form the largest deposits. Nd, O, H and S isotopic studies of IOCG systems in the Gawler Craton show a similar association. The highest grade and tonnage ore system in the region, Olympic Dam, has a primitive, mantle derived, fluid component while lower

grade prospects do not record this fluid input (Skirrow et al. 2005). However, as the Osborne, Starra and Eloise deposits can not be considered low grade and have all been productive, the data for the Cloncurry district suggests that fluid pathways that promote fluid mixing may be the more important criteria for ore formation.

The findings of this study and of studies of other deposits in the region (see Mark et al. 2004; Kendrick et al. 2006) suggest that IOCG deposits, even within a single district, can have both magmatic and non-magmatic fluid sources or a combination of the two. This is similar to findings in studies of IOCG deposits in South America (Chiaradia et al. 2006) which found that a spectrum of deposits were to be observed; from iron oxide-apatite and IOCG deposits associated with magmatic fluids to IOCG deposits associated with evaporitic fluids. That no single mechanism can be invoked to model the genesis of these deposits will be an important consideration when revising exploration strategies.

Late Orogenic Vein & Breccia – Mt Isa Cu

The Mt Isa Cu orebodies are hosted in the steeply dipping dolomitic siltstones and shales of Urquhart Shale above the upper basement (ECV) as illustrated in Figure 83. The syn-tectonic timing of the copper mineralization and related silica and dolomite alteration was documented by Perkins (1984). The copper, silica and dolomite are broadly zoned with respect to the basement contact, with an inner siliceous zone and an outer dolomitic alteration (Figure 84 and Waring, 1980). The copper mineralization is focused on the siliceous zone. Talc is most abundant on the southern extremities of the known Cu system (Figure 84) but also occurs in the north on the footwall of the 3500 orebody. Carbon is well developed on the basement contact and stilpnomelane ± biotite ± talc ± pyrrhotite assemblages as well as chlorite – pyrrhotite assemblages occur in marginal zones to the copper orebodies (Perkins, 1984; Swager, 1985; Swager et al. 1987; Miller, 2006; Figure 85).

The structural control on the distribution of alteration elements is illustrated for the 3000/3500 orebodies in Figures 86 and 87. Notably the distribution of pyrrhotite with respect to chalcopyrite is controlled by 3500FW fault, with pyrrhotite mostly occurring in the footwall of the fault and chalcopyrite in the hanging wall. The distribution of carbon and talc is also partitioned along the 3500FW fault.

Mixing box model for the 3500 ore body

Salient features of the "chemical" architecture for the 3500 orebody are:

- The orebody is bounded by the basement contact, the 3500 FW fault and west dipping, NNW trending faults in the hanging wall

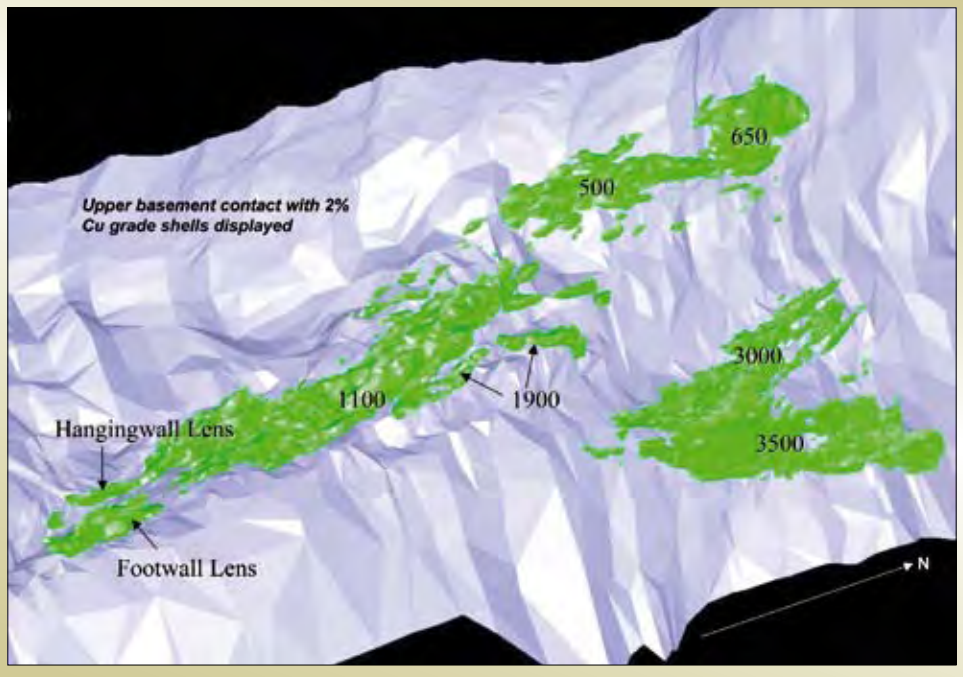

Figure 83: Model of the Mount Isa Cu ore-bodies (2% Cu grade shells shown) above the upper basement (Eastern Creek Volcanics). White - Basement contact (looking down and to the west). Green – ore shells of (from south to north): HW-FW- X41 Orebodies, 1100, 3000, 3500 (Enterprise Orebodies), 500, 650.

- The silica alteration of the core zones to dolomite and coarse hydrothermal pyrite across the hanging wall structures
- Pyrrhotite rather than pyrite is stable in the footwall to the 3500 FW Fault
- Carbonaceous rocks occur on the basement contact
- A zone of quartzite occurs in the basement beneath the ore body.

These observations may be explained in terms of a "mixing box" model (Figure 88) that envisages mixing of an oxidized sulfate-bearing formational water with a reduced deep-seated fluid from the lower crust or mantle. The major pathway for the deep-seated fluid was steeply dipping to sub-vertical and possibly defined by the quartzite in the basement. The hanging wall and footwall structures acted as seals with the major flow of oxidized occurring in a hanging wall compartment with secondary pyrite and

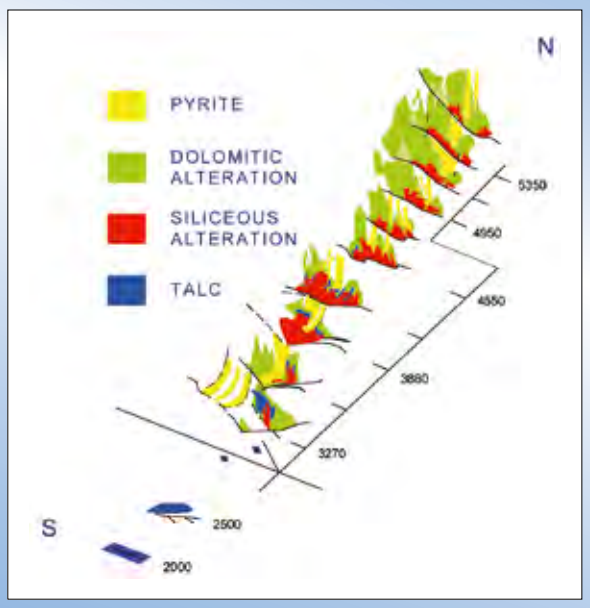

Figure 84: 3D projection of the alteration zoning of the 1100 orebody. Diagram from Waring (1980). The yellow zones represent the pyritic "ribs" of fine-grained pyrite that predate the Cu mineralization.

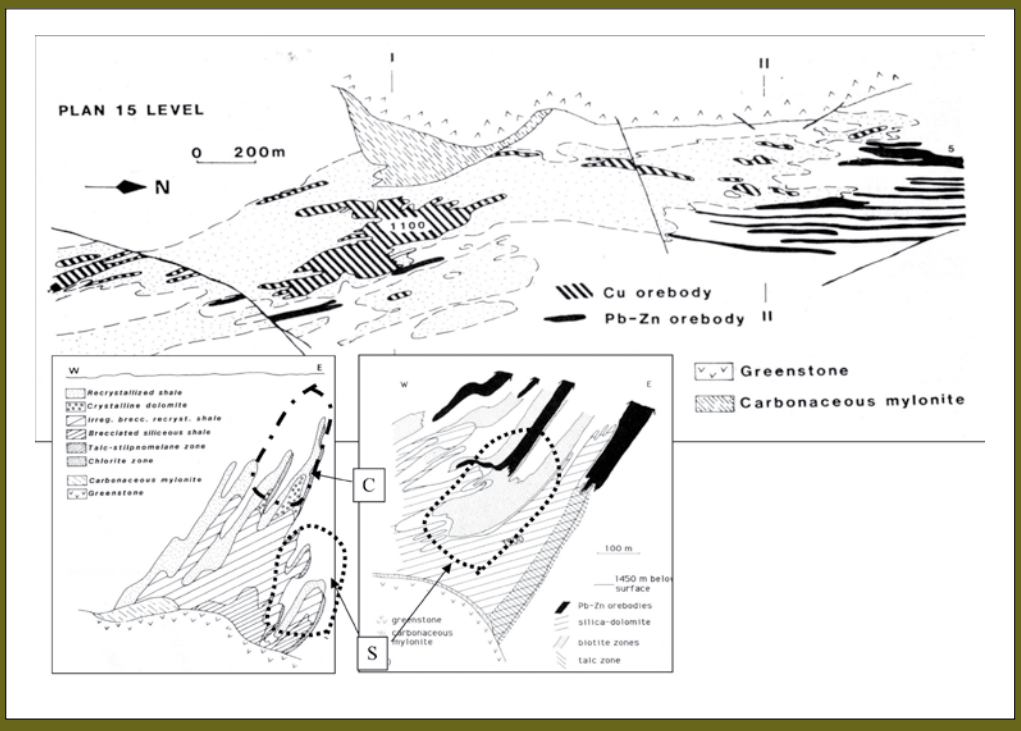

Figure 85: Distribution of silicates and carbon around the Isa Cu ore system. Carbonaceous mylonite is developed on the basement contact. Stilpnomelane ± biotite ± talc – pyrrhotite assemblages (S) and chlorite – pyrrhotite assemblages (C) occur marginal to the copper ore bodies. Figures from Swager (1985) and Swager et al. (1987).

dolomite as stable phases in the pathway of the oxidized fluid. The carbonaceous mylonite is considered to have acted as a seal on the base of the mixing box.

Testing the mixing-box model

A stable isotope study of DDH S678ED4 across the proposed region of the mixing box was undertaken to determine the presence of redox gradients predicted by the model. Changes in the ratio of oxidized and reduced sulphur species in mineralising fluids should be recorded by changes in the value of $\delta^{34}S$ pyrite, chalcopyrite and pyrrhotite and, similarly, changes in the ratio of oxidized and reduced carbon should be recorded in changes in the value of $\delta^{13}C$ of carbonate and graphite. The results and interpretation are given in Figures 89 to 91. The most significant result was the evidence from $\delta^{13}C$ values in carbonate and carbon of partial reduction of carbonate and reduction of carbonate to carbon, in the footwall transition zone of the 3500 ore body. The ^{13}C enrichments in carbonate reflect partial reduction of oxidized carbon

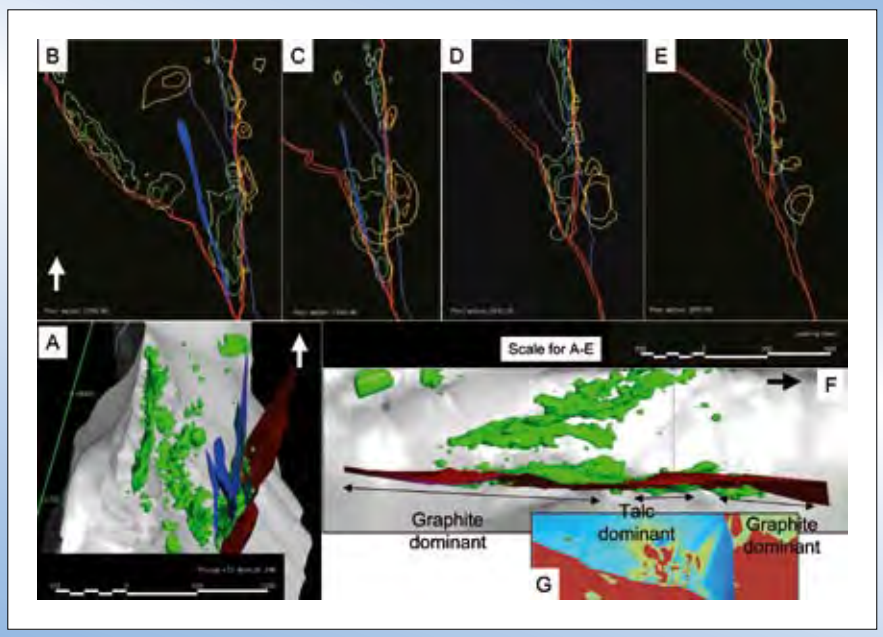

Figure 86: Geological elements and mineral zoning of the 3000, 3500 (Enterprise Mine) orebodies. A Top-down view of 3000 and 3500 ore bodies. Blue – NNW 3500 faults and dark red is the 3500 FW Fault. B, C, D, E: Top-down views of mineral zoning with increasing depth from levels 1990, 1940, 1890 and 1840 respectively. Yellow = pyrrhotite, green = chalcopyrite, red –basement/3500FW and blue – NNW 3500 faults. F Top-down (north – right) illustrating the distribution of graphite and talc on the footwall of the 3500 orebody. G. Inset shows distribution of talc (as observed) on the plane of the 3500 FW Fault 3D model (by Peter Neumayr and Damien Keys).

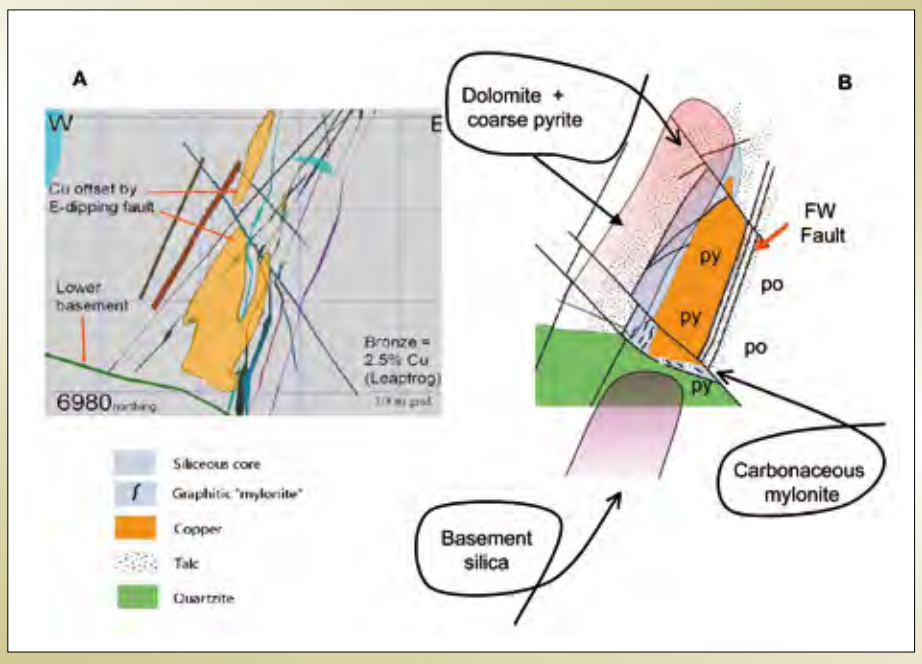

Figure 87: A: Section showing the structural architectural controls on the 3500 orebody (by Xstrata). The orebody is bounded by basement contact, the 3500 FW Fault and W dipping, NNW trending faults in the hanging wall. B: A simplified overlay of the alteration on the architecture for the 3500N ore body. The silica alteration of the core zones to dolomite and coarse hydrothermal pyrite across the hanging wall structures and pyrrhotite rather than pyrite is stable in the footwall to the 3500 FW Fault. There is a zone of quartzite in the basement, directly beneath the orebody (after Miller 2006).

species to methane with the residual oxidized species being enriched in ^{13}C (Figure 91) and implies *in-situ* reduction of carbonate to carbon. Both reactions require a reductant to proceed. The most likely reductant was H_2. Specifically:

- The carbonate sample in the transition zone to the footwall gave a replicated $\delta^{13}C$ value of + 5.6 ‰
- In comparison, $\delta^{13}C$ values of carbonate from the hanging wall range between -3.9 and -5.5 and footwall carbonate samples ranged between -5.7 and -9.9 ‰
- The $\delta^{13}C$ value of the carbon sample in the transition zone to the footwall gave a value of -9.9 ‰
- The $\delta^{13}C$ values of four carbon samples in the ore zone were remarkably consistent around -23.78± 0.2 ‰
- The $\delta^{34}S$ values of pyrite, chalcopyrite and pyrrhotite vary in a coherent way from the hanging wall to the footwall. These patterns suggest isotope equilibrium between the species. In the hanging wall zone $\delta^{34}S$ values of pyrite and chalcopyrite vary between +13.8 and

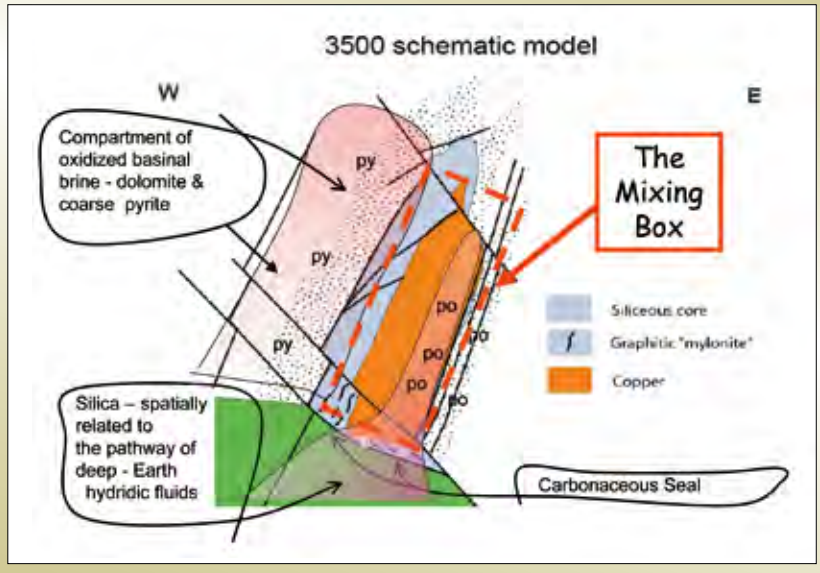

Figure 88: Mixing box model for the formation of the 3500 orebody. The model envisages mixing of an oxidized sulfate-bearing formational water with a reduced deep-seated fluid from the lower crust or mantle.

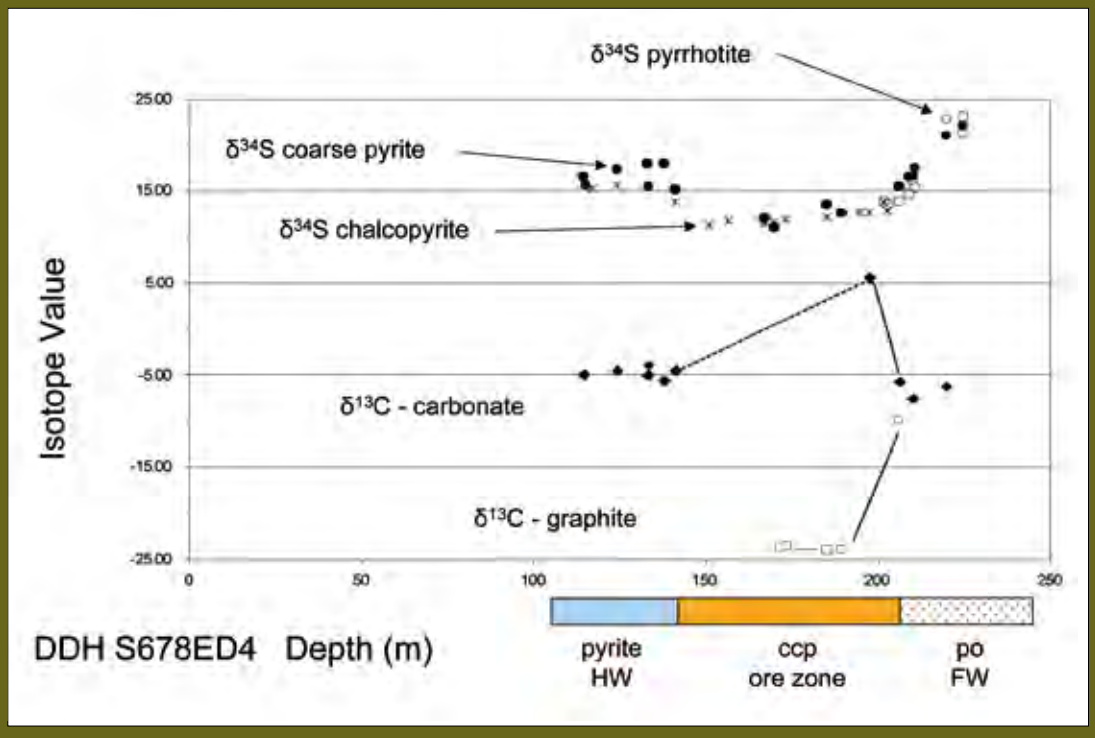

Figure 89: Stable isotope study of DDH S678ED4.

+ 18 ‰ with chalcopyrite tending to be lighter than pyrite. Within the ore zone there is a small but systematic increase in the $\delta^{34}S$ values of pyrite and chalcopyrite from +11.3 to +13.8 ‰ from the hanging wall to the footwall. Below the ore zone $\delta^{34}S$ values of pyrrhotite and pyrite increase into the footwall systematically and significantly from +13.9 to 23 ‰.

The ^{13}C enrichment in carbonate reflects partial reduction of oxidized carbon species to methane:

$CO_2 + 4H_2 = CH_4 + 2H_2O$ (eq. Q5-1)

The residual oxidized species (CO_2, H_2CO_3, $CaCO_3$) become enriched in ^{13}C as ^{12}C partitions preferentially to methane. The ^{13}C enrichment in carbon, such that the $\delta^{13}C$ value of carbon approaches that of the carbonate implies *in-situ* reduction of carbonate to carbon:

$CaCO_3 + 2H_2 + 2H^+ = Ca^{2+} + C + 3H_2O$ (eq. Q5-2)

The textural setting of the carbon in sample 206 (Figure 90) is consistent with this proposed mechanism. In this sample carbon is dispersed with the carbonate and in parts rims carbonate. More commonly carbon occurs as relatively late cross-cutting features (e.g. sample 185.1).

Addition of a strong reductant to the system is required for the above reactions to proceed. The most likely reductant was H_2. The flow path for the hydridic fluid was probably steeply dipping to sub-vertical and entry point was across the Paroo Fault, and focused on the footwall transition zone of the 3500 orebody. The carbonaceous mylonite was probably a product on the carbonate reduction occurring on the basement contact. It may have subsequently acted as a seal on the base of the mixing box.

The consistency of the $\delta^{13}C$ value of carbon in the ore zone suggests the ratio of CH_4 / CO_2 or CH_4 / H_2CO_3 is buffered for fluids in the base of the 3500 ore zone. The most likely buffering reaction is the carbon hydrolysis reaction:

$2C + 3H_2O = CH_4 + H_2CO_3$ (eq. Q5-3)

The carbon $\delta^{13}C$ ~ - 24 ‰ is enriched in ^{13}C by ~ 10 ‰ compared with expected sedimentary C values for the middle Proterozoic. The value of $\delta^{13}C$ carbonate in equilibrium with carbon with $\delta^{13}C$ at *ca.* - 24 ‰ should be ~ -12 to - 16 ‰ for temperatures of 300 to 400 °C. No values as light as this were obtained in this study but $\delta^{13}C$ carbonate values down to -14 ‰ are known from the Cu system (Waring, 1990).

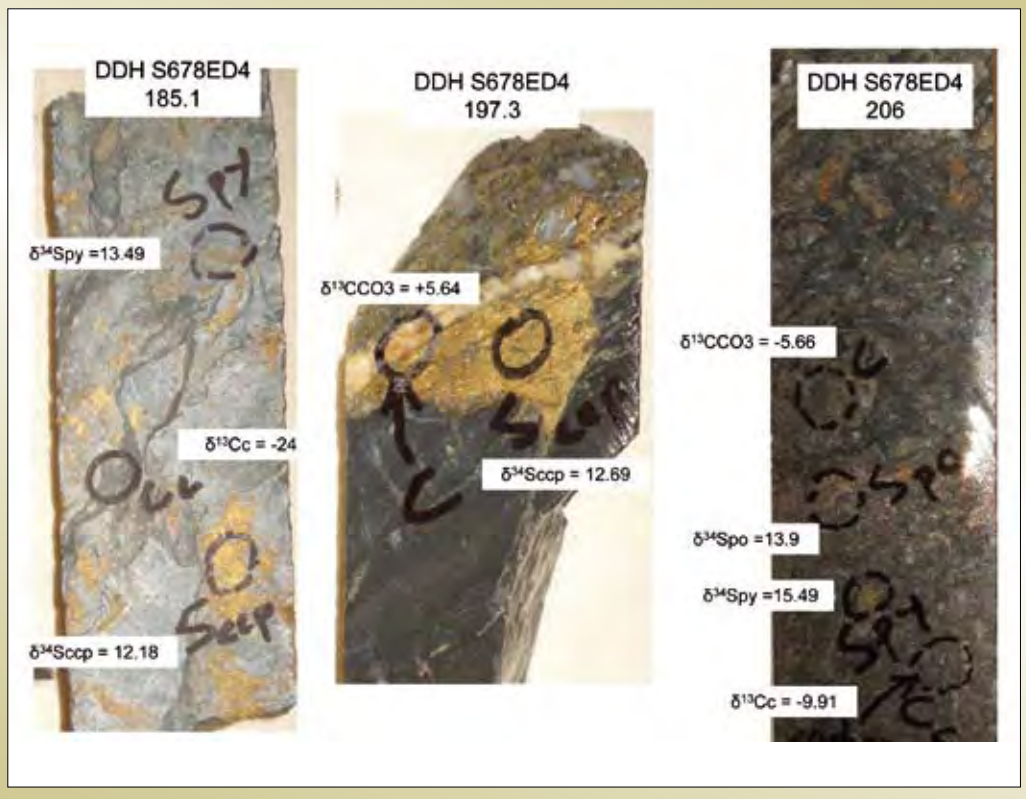

Figure 90: Samples from DDH S678ED4 showing textural context of stable isotope samples for depth intervals 185.1. 197.3 and 206m. Samples 197.3 and 206 show the enrichments for ^{13}C for carbon and carbonate respectively.

The $\delta^{34}S$ values of pyrite, chalcopyrite and pyrrhotite vary in a coherent way from the hanging wall to the footwall of the 3500 ore body.

- In the hanging wall zone, $\delta^{34}S$ values of pyrite and chalcopyrite range between +13.8 and + 18 ‰ with chalcopyrite tending to be lighter than pyrite
- Within the ore zone, there is a small but systematic increase in the $\delta^{34}S$ values of pyrite and chalcopyrite from +11.3 to +13.8 ‰ from hanging wall to footwall
- Below the ore zone, $\delta^{34}S$ values of pyrrhotite and pyrite increase into the footwall systematically and significantly from +13.9 to 23 ‰.

The small but systematic increase in the $\delta^{34}S$ values of pyrite and chalcopyrite from hanging wall to footwall of the 3500 ore body is again suggestive of some buffering mechanism operating to constrain the ratio of reduced/oxidized sulphur species in the fluid. The ratio of reduced/oxidized sulphur species may be related to the pH and the ratio of CH_4 / H_2CO_3 through reactions such as:

$H^+ + HSO_4^- + CH_4 = H_2CO_3 + H_2S + H_2O$ (eq. Q5-4)

for which:

$HSO_4^-/ H_2S = (H_2CO_3 / CH_4)^*(K)^{-1*} (H^+)^{-1}$ (eq. Q5-5)

If CH_4 / H_2CO_3 is buffered by carbon saturation, as suggested above, then the reduced/oxidized sulphur species in solution becomes a function of pH. Hence systematic variations in $\delta^{34}S$ values of pyrite and chalcopyrite across the 3500 ore body could reflect changes in pH in a carbon saturated environment. Decreasing the pH (increasing H^+) would decrease the ration of HSO_4^-/ H_2S in solution. In a mixing environment, this would promote the reduction of sulphate in solution and lead to an increase in $\delta^{34}S$ values for reduced sulphur species. This effect progressively increased into the footwall as evidenced by the increase of $\delta^{34}S$ values of pyrite and pyrrhotite.

The mixing model is consistent with the inferred fluid reservoirs from the argon isotope and halogen constraints (see Question 3). The inference from the halogen data is that the oxidized sulfate-bearing formational water was a bittern brine, and is supported sulphur isotope data that implies sedimentary sulphate was at least one of the sources of sulphur in that system, and by earlier studies (Heinrich et al. 1989; Andrew et al. 1989).

There is still considerable discussion around the question of the origin of the reduced, deep-seated fluid. The major difference in thinking is around the depth of the source/reservoir for this fluid. Was it sourced from the lower curst or from the mantle? If from the mantle, at what depth? Kendrick takes a minimalist view on this issue arguing (see Kendrick et al. 2006c) that the high Ar^{40} / Ar^{36} reflect a metamorphic fluid derived from pre-Barramundi crustal basement. However, Walshe argues a metamorphic fluid is likely to be a CO_2-rich fluid and contain sufficient H_2 to reduce carbonate to carbon.

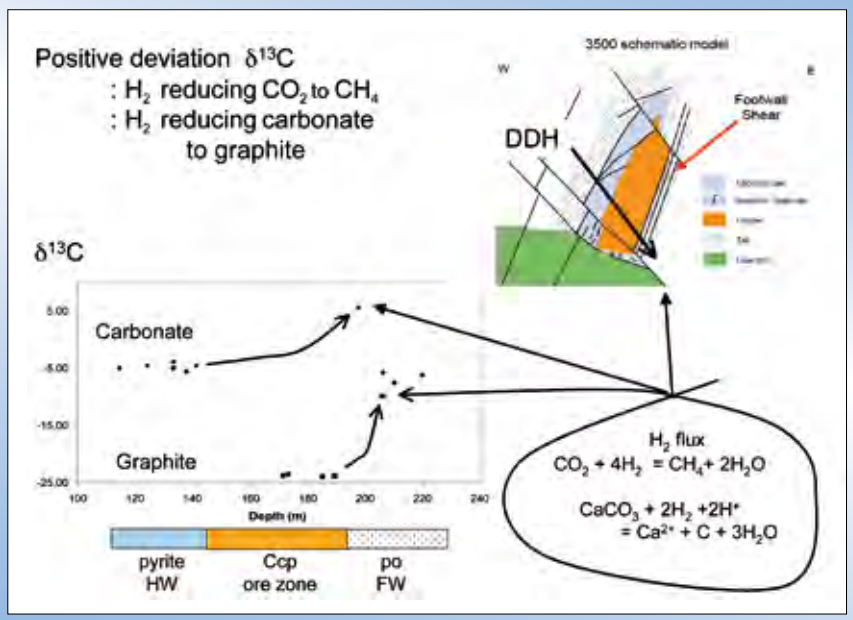

Figure 91: Interpretation of the 13C enrichments in carbonate (sample 197.3) and carbon (sample 206) in the transition zone to the footwall.

Mechanisms of chalcopyrite precipitation

The factors that influence copper solubility are T, P, redox, salinity, pH and sulphur content of the fluid. Depending on conditions, nature of metal and sulfur speciation, copper may be transported in oxidized or reduced fluids or in acid or alkaline conditions, as indicated by the following hydrolysis reactions:

$CuFeS_2 + 3H^+ + 0.5H_2O = Fe^{2+} + Cu^+ + 2H_2S + 0.25O_2$ (eq. Q5-6)

$CuFeS_2 + H^+ + 0.5H_2O + 3.75O_2 = Fe^{2+} + Cu^+ + 2HSO_4^-$ (eq. Q5-7)

$CuFeS_2 + 0.5H_2O + 3HCl = FeCl_2 + CuCl + 2HS^- + 2H^+ + 0.25O_2$ (eq. Q5-8)

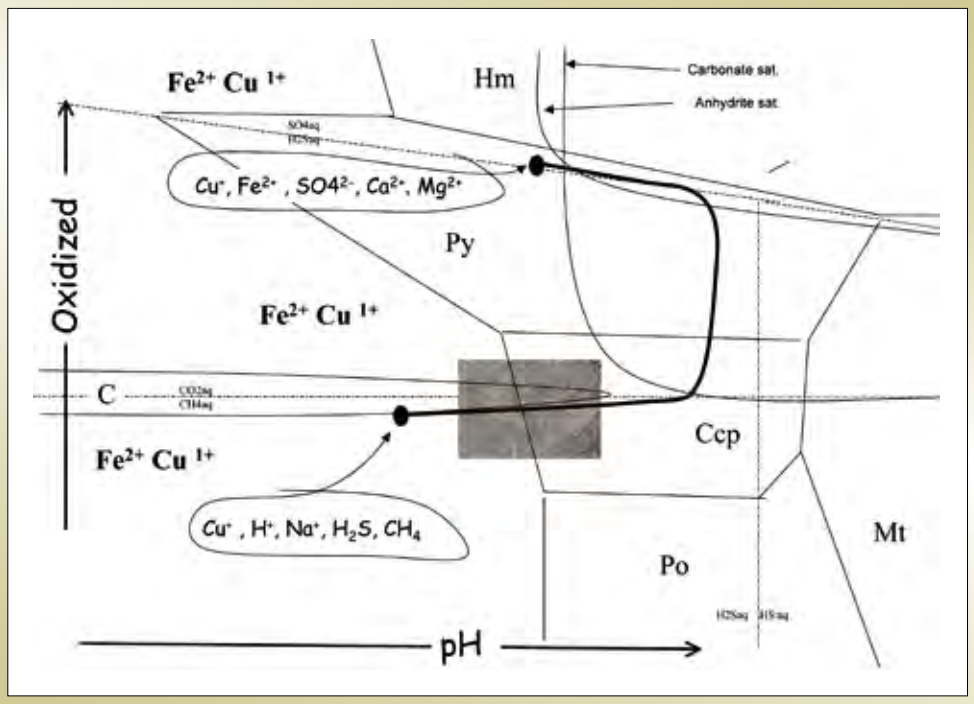

Figure 92: Sketch of log fO2/pH plot redrawn assuming Cu+/H+ - H_2S conditions below the limit of bornite stability and assuming Cu+/H+ as well as H_2S is constant. The mixing trend is based on numerical modelling experiments by Ed Mikucki (CSIRO) for Archean gold systems (MERIWA358 report).

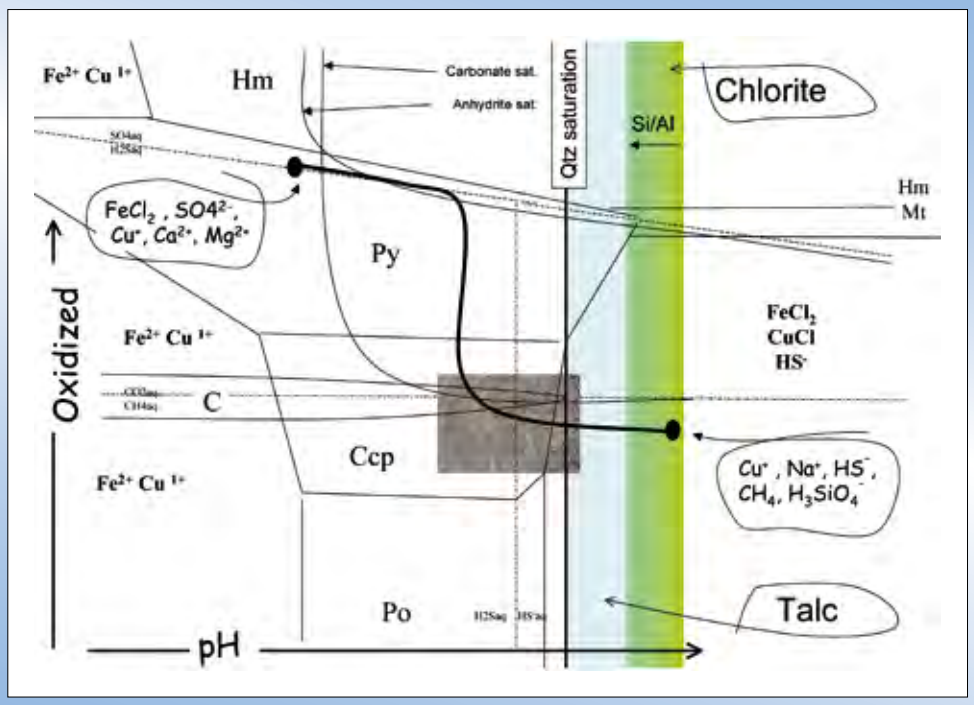

Figure 93: Sketch of log fO_2/pH plot assuming chalcopyrite is soluble at high pH as well as low pH. The stabiliy fields for talc (blue) and chlorite (green) occur at high pH conditions with H3SiO4- the stable aqueous species.

The phase diagram sketched in Figures 92 and 93 show the diversity of possibilities for copper transport. Given the constraints imposed on Figure 92, the mixing trend would avoid the bornite stability field. The mixing trend on Figure 93 is between an oxidized, slightly acidic fluid and a reduced, highly alkaline fluid. As the fluid becomes progressively acid and oxidized then chlorite will become progressively more Si-rich, talc will eventually precipitate and quartz saturated. Sketch assumes Cu+/H+ - H_2S conditions below the limit of bornite stability and Cu+/H+ as well as H_2S are constant.

A feature of the Mt Isa Cu ore bodies is the absence of bornite. Hence, in considering the mechanism(s) of transport and deposition of Cu, an important question is how the system avoided precipitating bornite. The sketch shown in Figure 94 illustrates the limits on the stability of pyrite – chalcopyrite assemblages with respect to bornite as a function of log Cu^+/H^+ and logH_2S. There is a rather limited set of conditions at which pyrite and chalcopyrite will be stable. The boundary of bn with ccp and bn with hm is independent of presence of third phase so that these boundaries are a general uppers limit of Cu+/H+ - H_2S conditions of ccp stability rather than bornite. The hint is that the fluids in the system were buffered in some way to avoid exceeding those limits. The phase diagrams assume Cu+/H+ - H_2S conditions below the limit of for bornite stability and Cu+/H+ as well as H_2S is constant.

Mixing Scenarios

The mixing trends shown in Figures 92 and 93 consider two scenarios:

a)

- an oxidized, sulphate bearing brine that was buffered by dolomite and anhydrite (anhydrite is known from the upper, northern limits of the Cu Mine) and transported Ca^{2+}, Mg^{2+}, Fe^{2+}, Cu^+, HSO_4^-

and

- a reduced, acidic fluid, enriched in CH_4 and H_2 that transported Cu^+, Na^+, Mg^{2+}, H_2S

b)

- an oxidized, sulphate bearing brine

and

- a reduced, alkaline fluid enriched in CH_4 and H_2 that transported Cu^+, Na^+, Mg^{2+}, H_2S

Both mixing paths could produce:

- carbon ± chalcopyrite ± pyrite ± pyrrhotite assemblages
- dolomite ± pyrite assembalges
- a wide range in $\delta^{34}S$ values of pyrite and pyrrhotite reflecting reduction significant reduction of sulphate
- a wide range in $\delta^{13}C$ values of carbon and carbonate as a result of either oxidation of methane or reduction of carbonate/ H_2CO_3.

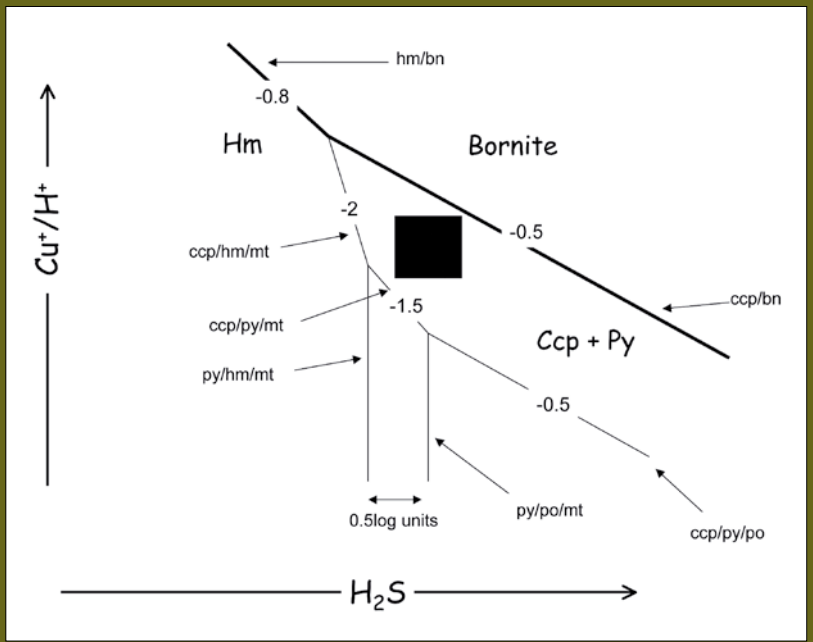

Figure 94: Sketch of log Cu+/H+ vs logH_2S illustrating the limits on the stability of chalcopyrite (ccp) and pyrite (py) assemblage. Note the boundary of bornite (bn) with ccp and bn with hematite (hm) is independent of presence of third phase. Hence these boundaries are a general upper limit of Cu+/H+ - H_2S conditions of chalcopyrite stability with respect to bornite. The slopes of the phase boundaries are indicated on the diagram.

The second scenario allows the possibility of switching from dolomite to quartz saturated conditions with decreasing pH. It also allows a progression with decreasing pH from chloritic assemblages with progressively more Si-rich chlorite to talc. The changes in fluid chemistry from Ca-rich to Na-rich brines (Heinrich et al. 1989; ***pmd*CRC*** I4 report) are taken to reflect the mixing process.

Exploration implications of the mixing model

The available chemical and mineralogical information (mineral zoning, carbon and sulfur isotope data) allow construction of a simplified, mine-scale mixing model (Figures 95 and 96). Data sources are Waring (1990); Andrew et al. (1989), Heinrich et al. (1989), Painter (2001); Painter et al. (1999). The zones of talc alteration are taken

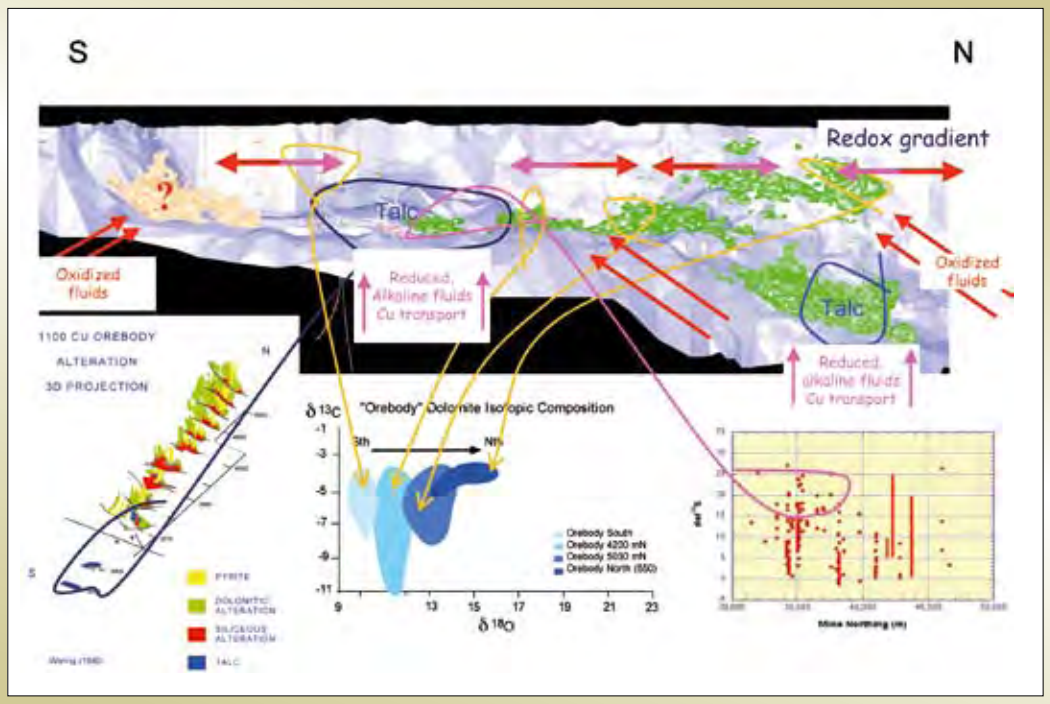

Figure 95: A simplified, mine-scale mixing model constructed from mineral zoning and carbon and sulfur isotope data. The mixing model is overlain on a long-section of the copper ore system.

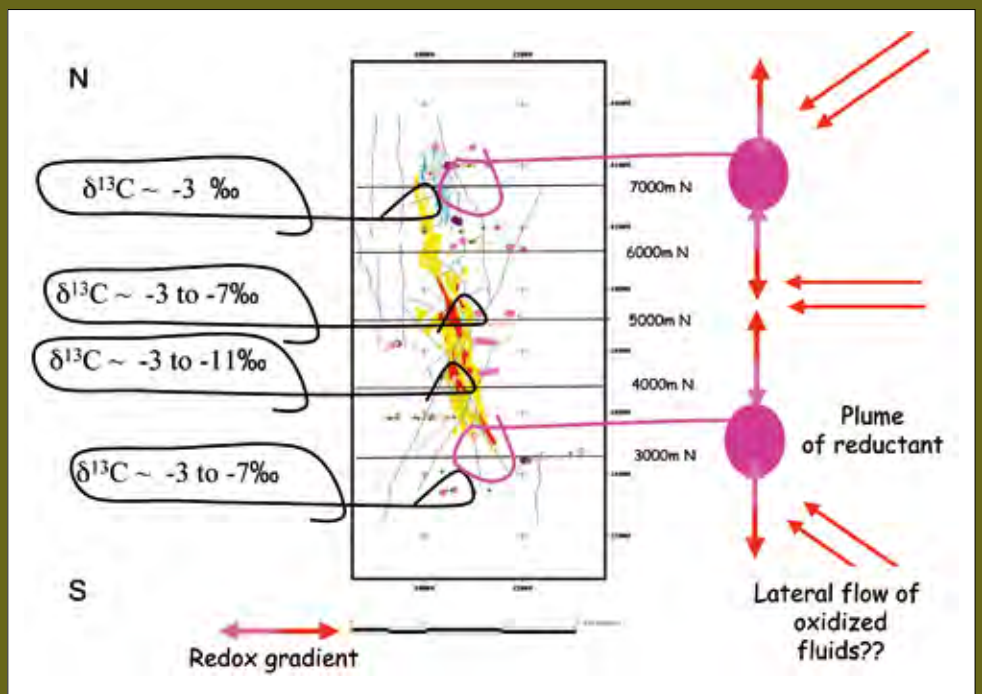

Figure 96: Plan view of mine-scale mixing model overlain on alteration image (suppled by Andy Wilde).

to be the focus of reduced and alkaline fluid flow. The redox gradients are identified by:

- domains of δ34S > ~ 15 ‰ i.e. where there has been significant reduction of sulfate and/or
- domains of δ13C carbonate < ~ -6 to -7 ‰
- i.e where there has been significant reduction of sulphate to H_2S coupled with significant oxidation of CH_4 to H_2CO_3 as per the reaction:

$H^+ + HSO_4^- + CH_4 = H_2CO_3 + H_2S + H_2O$ (eq. Q5-9)

One implication of the model is that there is potential for a repetition of Cu mineralization to the south of current mining. In addition, the distribution of the near-zero S – isotope signal in the fine grained pyrite in the Urquhart Shale to the north of Isa Cu and Pb-Zn systems, together with the primitive Os isotope signal in the shale, suggests a flux of mantle-derived hydridic fluid was centred to the north of the known deposits (Figure 97). The reduced alkaline fluids of the Cu system are postulated to be related to this hydridic fluid flux. Potential exists for mixing architectures to be replicated north of the suggested domain of hydridic fluid flux i.e. there is the possibility of replicating the Cu system in this area.

Based on the evidence for multiple fluid pathways, complex oscillating mineral chemistry, ranges in isotope signals, gradients in redox and coexisting phases it seems likely that fluid mixing played an important role in ore deposition within the Mt Isa copper systems. One critical aspect of all of these systems is the possibility that multiple events occurred together in the same place over a protracted period of time.

Synthesis and predictive mineral discovery

The five questions addressed here, geodynamics, architecture, fluid reservoirs and sources, pathways and deposition, are intrinsically linked in a cascade of scales that underpin an understanding of the Isan mineral system. At the broadest scale, repeated extension and thermal input set up a high geothermal gradient rift architecture of thin crust on a weak lithosphere. Accretion of mantle-derived material, via plumes, is a likely input, leading to core complex development, magmatic inflation and concurrent sedimentary basins. Intracontinental rift, back arc basin and passive margin models have application to the region at different times.

At the terrane scale, it is considered significant in an exploration sense that the depositional cycle of the system only operated during the later stages of the 400 Ma history, that is, during the Isan Superbasin and in the ensuing Isan Orogeny. A pre-requisite is a sedimentary basin

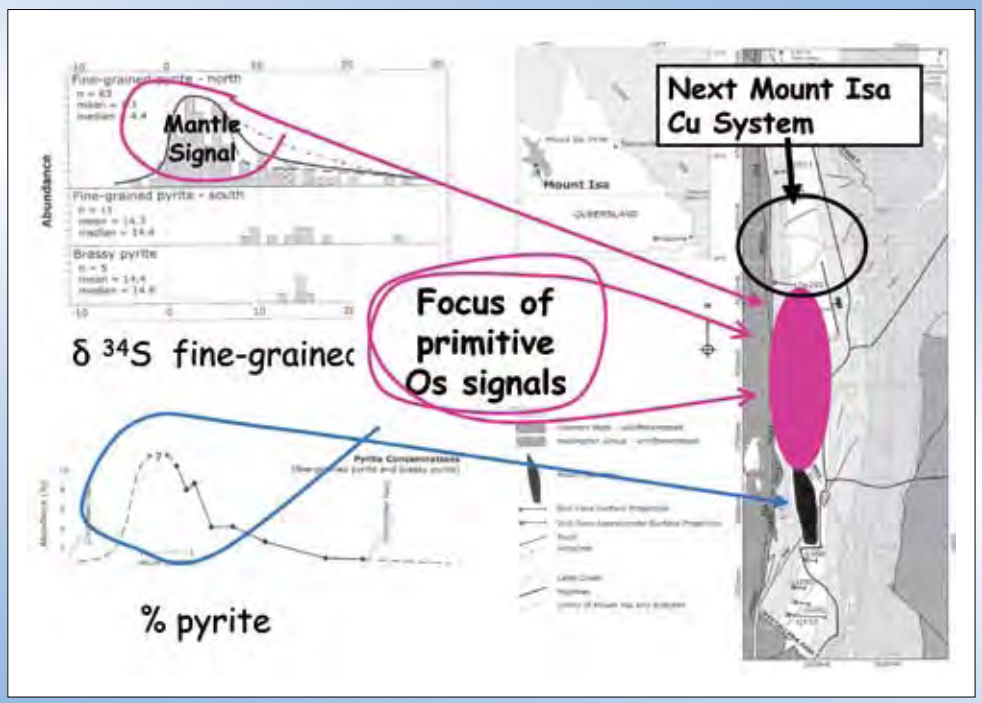

Figure 97: District-scale mixing model and speculation of the location of the next Mount Isa Cu system. Geology map from Painter et al. (1999).

substrate with an inherited fault architecture. This served to partition different fluid source regions, particularly sedimentary formation waters in basal aquifer units. The connectivity between different fluid sources seems to be achieved by faults that tap deeper in the crust and potentially perturb convective flow regimes. Complex fluid flow patterns emerge and compete with convective circulation, in extension and compression. The latter may be a more important driver, though topographic uplift and thermal input, than previously thought for the world class Pb-Zn-Ag massive sulphide mineralisation, particulary in areas of geological complexity. For the syn-tectonic and syn-metamorphic Cu and Cu-Au (IOCG) deposits, stress anomalies associated with particular structural configurations (fault bends, jogs, intersections) are identified as a localisation control. Recognition of ore deposit footprints using high resolution remote sensing techniques is an emerging tool of immense benefit in outcropping regions. In the strike extensive regions under surficial cover, potential field gradient data is critical for defining the 3D architecture as a platform for exploration.

At the ore deposit scale, mixing with other fluids from a range of sources is largely influenced by gradients in temperature, salinity and redox potential. There are recurrent instances from isotopic footprints of fluid mixing as a depositional mechanism. The potential involvement of mantle and perhaps deep Earth fluids emerges from studies of IOCG CuAu to sediment-hosted Cu and to sediment hosted PbZnAg hydrothermal deposit styles.

REFERENCES

Andrew A; Heinrich C; Wilkins R. 1989. Formation of the copper ores at Mount Isa. Exploration and Mining Research News.1. pp.6–7.

Beardsmore T.J., Newberry S.P., & Laing W.P. 1988. The Maronan Supergroup: an inferred early volcanosedimentary rift sequence in the Mt Isa Inlier, and its implications for ensialic rifting in the Middle Proterozoic of Northwest Queensland. *Precambrian Research*. **40/41**. 487–507.

Bertelli M. 2007. Hydrothermal processes in barren and mineralized systems Insights using fluid inclusion microanalysis and geochemical modelling. In: School of Earth and Environmental Sciences Townsville, James Cook University, PhD, 331.

Betts P.G., Lister G.S., O'dea M.G. 1998. Asymmetric Extension of the Middle Proterozoic Lithosphere, Mount Isa Terrane, Queensland, *Australia Tectonophysics*, #296, 293–316.

Betts P.G., Lister G.S. 2001. Comparison of The 'Strike-Slip' versus the 'Episodic Rift-Sag' Models for the origin of the Isa Superbasin. *Australian Journal of Earth Sciences*, # 48, 265–280.

Betts P.G., Giles D., Lister G. S., Frick L. R. 2002. Evolution of the Australian Lithosphere. *Australian Journal Of Earth Sciences*, #49, 661–695 1453.

Betts P.G., Lister G.S. 2004. Aeuromagnetic patterns of half-graben and basin inversion: implications for sediment hosted massive sukphide Pb-Zn-Ag exploration. *Journal of Structural Geology*, **26**, 1137–1156.

Betts P.G. 1999. Palaeoproterozoic Mid-Basin Inversion in the Northern Mt Isa Terrane, Queensland, *Australian Journal Of Earth Sciences.*

Betts P.G., Giles D., July 2000. Evolution of the Australian Continent: a northern, central and eastern Australian perspective, *Geological Society Of Australia Abstracts*, No 59.

Bierlein, F. B., Black, L. P., Hergt, J. and Mark, G. 2008. Evolution of Pre-1.8 Ga basement rocks in the western Mt Isa Inlier, northeastern Australia – Insights from SHRIMP U–Pb dating and in-situ Lu–Hf analysis of zircons, Precambrian Research, **163**, p. 159–173.

Bierlein, F.P. and Betts, P.G. 2004. The Proterozoic Mount Isa Fault Zone, northeastern Australia: is it really a ca. 1.9 Ga terrane-bounding suture? *Earth and Planetary Science Letter*, **225**, 279–294.

Blake D.H. 1987. Geology of the Mount Isa Inlier and environs, Queensland and Northern Territory. *BMR Bulletin* **225**, 83p.

Blake D.H., Stewart A J. 1992. Geology of the Mount Isa-Cloncurry transect. Stewart A J (editor), Blake D H (editor) In: Detailed studies of the Mount Isa Inlier. *AGSO Bulletin*. Report # 243.

Bell T. H. 1991. The role of thrusting in the structural development of the Mount Isa Mine and its relevance to exploration in the surrounding region, *Economic Geology*, **86**, 1602–1625.

Blenkinsop, T. (Editor) (2005): Total System Analysis of the Mt Isa Eastern Succession. – ***pmd**CRC* I2+3 Project Final Report, 2005, 51.

Blenkinsop, T.G., Huddlestone-Holmes, C.R., Foster, D.R.W., Edmiston, M.A., Lepong, P., Mark, G., Austin, J.R., Murphy, F.C., Ford, A., Rubenach, M.J., 2008. The crustal scale architecture of the Eastern Succession, Mount Isa: The influence of inversion, *Precambrian Research*, **163**, p.31–39.

Block, L. and Royden, L., 1990. Core complex geometries and regional scale flow in the lower crust. *Tectonics*, **9**: 557–567.

Broadbent G.C., Myers R.E., Russell E., Wright J.V., 1998. Geology and origin of shale-hosted Zn-Pb-Ag mineralization at the Century Deposit, Northwest Queensland, Australia. Williams Patrick J (prefacer) In: Metallogeny of the McArthur River-Mount Isa-Cloncurry minerals province. *Economic Geology and the Bulletin of the Society of Economic Geologists*. **93**; 8, 1264–1294. 1998.

Butera K., Oliver N.H.S., Rubenach M.J., Collins B., Cleverley, J. 2005. Multiple generations of metal and sulphur contribution from mafic rocks to the IOCG budget of the Mount Isa Eastern Succession. In: Blenkinsop, T.G. (ed) Final Report, Total Systems Analysis of the Mt Isa Eastern Succession, Predictive Mineral Discovery CRC, 325–342.

Cagnard, F., Brun, J.-P. and Gapais, D., 2006. Modes of thickening of analogue weak lithospheres. *Tectonophysics*, **421** (1–2): 145–160.

Cagnard, F., Durrieu, N., Gapais, D., Brun, J.-P. and Ehlers, C., 2006. Crustal thickening and lateral flow during compression of hot lithospheres, with particular reference to Precambrian times. *Terra Nova*, **18**: 72–78.

Chapman L. H. 2004. Geology and mineralization styles of the George Fisher Zn-Pb-Ag deposit, Mount Isa, Australia. *Economic Geology and the Bulletin of the Society of Economic Geologists*. **99**; 2, 233–255.ss.

Chevrot S., van der Hilst R.D. 2000. The Poisson ratio of the Australian crust; geological and geophysical implications. *Earth and Planetary Science Letters*. 183; 1–2, 121–132.

Cleverley JS & Oliver NHS (2005) Comparing closed system, flow-through and fluid infiltration geochemical modelling: examples from K-alteration in the Ernest Henry Fe-oxide-Cu-Au system. *Geofluids*, **5**, 289–307.

Cleverley J.S., Willan R.C.R. & Yardley B.W.D. 2003. Chlorine-water evolution in arc-magmas. In: Magmas, Fluids and Porphyry-Epithermal Deposits Extended Symposium Abstracts eds Baker T, Cleverley JS & Fu B) Townsville, EGRU Contributions, 61, 26–37.

Collier P & Bryant J (2003) Successful mineral resource definition at the Ernest Henry copper-gold mine, NW Queensland. In: Proceedings Fifth International Mining Geology Conference Bendigo, The Australian Institute of Mining and Metallurgy, 73–88.

Cooke D.R., Bull S.W., Donovan S., Rogers J.R., 1998. K-metasomatism and base metal depletion in volcanic rocks from the McArthur Basin, Northern Territory; implications for base metal mineralization. Williams Patrick J (prefacer) In: Metallogeny of the McArthur River-Mount Isa-Cloncurry minerals province. *Economic Geology and the Bulletin of the Society of Economic Geologists*. 93; 8, 1237–1263.

Cruden, A.R., Nasseri, M.B. and Pysklywec, R.N., 2004. Three-dimensional strain partitioning in analogue versus numerical models of convergent orogens. Bolletino di Geofisica teorica et applicata, 45: 70–73.

Cull, J. P. and Denham, D. 1979. Regional variations in Australian heat flow. BMR J. Aust. Geol. Geophys. 4, 1–13.

de Jong G & Williams PJ (1995) Giant metasomatic systems formed during exumation of mid-crustal Proterozoic rocks in the vicinity of teh Cloncurry fault, northwest Queensland. *Australian Journal of Earth Sciences*, 42, 281–290.

Derrick G. M. A Proterozoic rift zone at Mount Isa, Queensland, and implications for mineralisation. *BMR Journal of Australian Geology and Geophysics*. 7; 2, pp.81–92.

Donchak P.J.T., Blake D.H., Noon T.A., & Jaques A.L. 1983. Kuridala region, Queenslandm 1:100 000 Geological Map Commentary. Bureau of Mineral Resources, Canberra.

Drummond, B. J. and Collins, C. D. N. 1986. Seismic evidence for underplating of the lower continental crust of Australia. Earth and Planetary Science Letters 79, 361–372.

Drummond, B.J., Goleby B.R., Goncharov A.G. Wyborn L.A.I, Collins C.D.N., & Maccready T. 1998. Crustal-scale structures in the Proterozoic Mount Isa Inlier of North Australia: their seismic response and influence on mineralisation, *Tectonophysics*, Vol 288, Issue 1–4, 43–56.

Etheridge M.A., Rutland R.W.R., & Wyborn L.A.I., 1987. Orogenesis and tectonic process in the early to middle Proterozoic of northern Australia. Kroener A (editor) In: Proterozoic lithospheric evolution. *Geodynamics Series*. **17**, 131–147.

Duan Z.H., Moller N. & Weare J.H. 1992a. An equation of state for the Ch_4-CO_2-H_2O System .1. Pure Systems from 0-Degrees-C to 1000-Degrees-C and 0 to 8000 Bar. *Geochimica Et Cosmochimica Acta*, **56**, 2605–2617.

Duan Z.H., Moller N. & Weare J.H. 1992b. An equation of state for the Ch_4-CO_2-H_2O System .2. Mixtures from 50-Degrees-C to 1000-Degrees-C and 0 to 1000 Bar. *Geochimica Et Cosmochimica Acta*, **56**, 2619–2631.

Duan Z.H., Moller N. & Weare J.H. 1995. Equation of state for the NaCl-H_2O-CO_2 System – Prediction of phase-equilibria and volumetric properties. *Geochimica Et Cosmochimica Acta*, **59**, 2869–2882.

Duan Z.H., Moller N. & Weare J.H. 2000. Accurate prediction of the thermodynamic properties of fluids in the system H_2O-CO_2-CH_4-N-2 up to 2000 K and 100 kbar from a corresponding states/one fluid equation of state. *Geochimica Et Cosmochimica Acta*, **64**, 1069–1075.

Eriksson K A; Simpson E L; Jackson M J. 1993. Stratigraphical evolution of a Proterozoic syn-rift to post-rift basin; constraints on the nature of lithospheric extension in the Mount Isa Inlier, Australia. Frostick L E (editor), Steel R J (editor) In: Tectonic controls and signatures in sedimentary successions. Special Publication of the International Association of Sedimentologists. **20**; 203–221.

Foster, D. R. W. and Austin, J. A. 2008. The 1800–1610 Ma stratigraphic and magmatic history of the Eastern Succession, Mount Isa Inlier, and correlations with adjacent Paleoproterozoic terranes, *Precambrian Research*, **163**, p.7–30.

Fu B, Williams PJ, Oliver NHS, Dong G, Pollard PJ & Mark G (2003) Fluid mixing versus unmixing as an ore-forming process in the Cloncurry Fe-oxide-Cu-Au District, NW Queensland, Australia: evidence from fluid inclusions. *Journal of Geochemical Exploration*, 78–79, 617–622.

Gibson , G. M. and Hitchman, A. P. 2005. 3D basin architecture and mineral systems in the Mount Isa Western Succession (editors), Project I1 ***pmd**CRC*** Internal Report.

Gibson, G. M., Henson, P., McIntyre A. and Neumann N. 2006. Expanding our knowledge of Mt Isa to a third dimension. *Aus Geo News*. **82**.

Giles D., Nutman A P. SHRIMP U-Pb zircon dating of the host rocks of the Cannington Ag-Pb-Zn deposit, southeastern Mt. Isa Block, Australia. *Australian Journal of Earth Sciences*. **50**; 3, 295–309. 2003.

Giles D. & Betts P.G. 2002. Paleoproterozoic to Mesoproterozoic assembly of Australia; implications for Rodinia reconstructions. Preiss V P (editor) In: Geoscience 2002; expanding horizons; abstracts of the 16th Australian geological convention. *Abstracts – Geological Society of Australia*. **67**; 118p.

Giles D. & Nutman A.P. 2002. SHRIMP U-Pb monzanite dating of 1600–1580 Ma amphibolite facies metamorphism in the southern Mt Isa block, Australia. *Australian Journal of Earth Sciences* **49**, 455–465.

Giles D., Betts P.G., Lister G.S. 2004. 1.8-1.5-Ga links between the North and South Australian cratons and the early-middle Proterozoic configuration of Australia. *Tectonophysics*. **380**; 1–2, 27–41. 2004.

Giles D., Betts P. G., Allieres L., Hulscher B., Hough M., Lister G. S. 2006. Evolution Of The Isan Orogeny At The Southeastern Margin Of The Mt Isa Inlier, *Australian Journal Of Earth Sciences*, **#53**, 91–108.

Glikson, M., Golding., and Southgate P.N. 2006. Thermal Evolution of the ore-hosting Isa superbasin: Central and northern Lawn Hill Platform: *Economic Geology*, **101**, 1211–1229.

Heinrich C.A., Bain J.H.C., Mernagh T.P., Wyborn L.A.I., Andrew A.S., Waring C.L. 1995. Fluid and mass transfer during metabasalt alteration and copper mineralization at Mount Isa, Australia. *Economic Geology and the Bulletin of the Society of Economic Geologists*. **90**; 4, Pages 705–730.

Heinrich C.A., Andrew A.S., Wilkins R.W.T., Patterson D.J. 1989. A fluid inclusion and stable isotope study of synmetamorphic copper ore formation at Mount Isa, Australia. *Economic Geology and the Bulletin of the Society of Economic Geologists*. 84; 3, 529–550.

Holcombe R.J., Pearson P.J., Oliver N.H.S. 1991. Geometry of a middle Proterozoic extensional decollement in northeastern Australia. Perez Estaun A (editor), Coward Michael P (editor) In: Deformation and plate tectonics. *Tectonophysics*. **191**; 3–4, 255–274.

Huang, W. & Rubenach, M.J. 1995. Structural controls on syntectonic metasomatic tremolite and tremolite-plagioclase pods in the Molanite Valley, Mt Isa, Australia. *Journal of Structural Geology*, **17** (1), 83–95:

Hutton L J; Rienks L P; Wyborn D. Granitoids in the Ravenswood Batholith Northeast Queensland. Chappell Bruce W (editor) In: Second Hutton symposium on Granites and related rocks. *Record – Bureau of Mineral Resources, Geology and Geophysics*. Report # 1991/25, 51p.

Huston D.L., Stevens B., Southgate P.N., Muhling P., Wyborn L. 2006. Australian Zn-Pb-Ag ore-forming systems; a review and analysis. *Economic Geology and the Bulletin of the Society of Economic Geologists*. **101**; 6, 1117–1157.

Indrum M., Giddings J.W. & Plum K.A. 1993 Paleamagnetism of the southeastern McArthur Basin: poles overprints and reversals. *Exploration Geophysics*. **24**, 227–230.

Jackson, M.J., Sweet, I.P., Page, R.W. and Bradshaw, B.E. 1999. The South Nicholson and Roper Groups: evidence for the early Mesoproterozoic Roper Superbasin *in* Bradshaw, B.E. and Scott, D.L. (eds.) Integrated basin analysis from the Isa Superbasin using Seismic, Well-log and Geopotential data: an evaluation of the economic potential of the northern Lawn Hill Platform. AGSO Record 1999/19.

Krassay A., Bradshaw B., McConachie B. & Domagala J. 1997. Stratigraphy of the Upper McNamara Group, Lawn Hill region; Lawn Hill Formation. Luodvalkis A (compiler), Barnett K (compiler) In: NABRE workshop; abstracts. Record – Australian Geological Survey Organisation. Report # 1997/12.

Kendrick M.A., Phillips D., Miller J.McL. 2006. Part I, Decrepitation and degassing behaviour of quartz up to 1560 degrees C; analysis of noble gases and halogens in complex fluid inclusion assemblages. *Geochimica et Cosmochimica Acta*. **70**; 10, 2540–2561.

Kendrick M.A., Miller J McL., Phillips D. 2006. Part II, Evaluation of (super 40) Ar/ (super 39) Ar quartz ages; implications for fluid inclusion retentivity and determination of initial (super 40) Ar/ (super 36) Ar values in Proterozoic samples. *Geochimica et Cosmochimica Acta*. **70**; 10, 2562–2576.

Kendrick M.A., Duncan R., Phillips D. 2006. Noble gas and halogen constraints on mineralizing fluids of metamorphic versus surficial origin; Mt Isa, Australia. *Chemical Geology*. **235**; 3–4, 325–351.

Kendrick M.A., Mark G. & Phillips D. 2007. Mid-crustal fluid mixing in a Proterozoic Fe oxide-Cu-Au deposit, Ernest Henry, Australia: Evidence from Ar, Kr, Xe, Cl, Br, and I. *Earth and Planetary Science Letters*, **256**, 328–343.

Laneyrie T. 2004. Correlation of brecciation and grade at Ernest Henry Fe-oxide-Cu-Au deposit. In: School of Earth Sciences Townsville, James Cook University, 107.

Large Ross R; McGoldrick Peter J. 1998. Lithogeochemical halos and geochemical vectors to stratiform sediment hosted Zn-Pb-Ag deposits; 1, Lady Loretta Deposit, Queensland. *Journal of Geochemical Exploration*. **63**; 1, Pages 37–56.

Large, R.R., Bull S.W., McGoldrick P.J. 2000. Lithogeochemical halos and geochemical vectors to stratiform sediment hosted Zn-Pb-Ag deposits; Part 2, HYC Deposit, McArthur River, Northern Territory. *Journal of Geochemical Exploration*. 68; 1–2, 105–126.

Lister G.S., O'Dea M.G., & Somaia I. 1999. A tale of two synclines; rifting, inversion and transpressional popouts at Lake Julius, northwestern Mt. Isa Terrane, Queensland. *Australian Journal of Earth Sciences*. **46**; 2, 233–250.

MacCready, T., Goleby, B. R., Goncharov, A., Dummmond, B. J. & Lister, G. S. 1998. A framework of overprinting orogens based on interpretation of the Mount Isa deep seismic transect. *Economic Geology* **93**, 1422–1434.

Mair, J.L., Ojala, V.J., Salier, B.P., Groves, D.I., Brown, S.M. 2000. Application of stress mapping in cross-section to understanding ore geometry, predicting ore zones and development of drilling strategies – *Australian Journal of Earth Sciences*, **47**, 895–912.

Mark G., Wilde A., Oliver N.H.S., Williams P.J., Ryan C.G. 2005. Modeling outflow from the Ernest Henry Fe oxide Cu-Au deposit; implications for ore genesis and exploration. *Journal of Geochemical Exploration*. **85**; 1, 31–46.

Mark G. & Foster D. 2000. Magmatic-Hydrothermal Albite-Actinolite-Apatite-Rich Rocks From The Cloncurry District, Nw Queensland, Australia. *Lithos*, **51**, 223–245.

Mark G., Oliver N.H.S. & Williams P.J. 2006. Mineralogical And Chemical Evolution Of The Ernest Henry Fe Oxide-Cu-Au Ore System, Cloncurry District, Northwest Queensland, Australia. *Mineralium Deposita*, **40**, 769–801.

Mark G. & Pollard P. 2006. Episodic, potassic, 'A-type' Mesoproterozoic magmatism in the mount isa inlier, NE Australia: A syn-tectonic origin? *Geochimica Et Cosmochimica Acta*, **70**, A393–A393.

Marshall L.J. 2003. Brecciation within the Mary Kathleen Group of the Eastern Succession, Mt Isa Block, Australia: implications for Fe-oxide-Cu-Au mineralization. In: School of Earth Sciences Townsville, James Cook University, PhD, 325.

Marshall L.J. & Oliver N.H.S. 2006. Monitoring Fluid Chemistry In Iron Oxide-Copper-Gold-Related Metasomatic Processes, Eastern Mt Isa Block, Australia. *Geofluids*, **6**, 45–66.

Marshall L.J., Oliver N.H.S. & Davidson G.J. 2006. Carbon And Oxygen Isotope Constraints On Fluid Sources And Fluid-Wallrock Interaction In Regional Alteration And Iron-Oxide-Copper-Gold Mineralisation, Eastern Mt Isa Block, Australia. *Mineralium Deposita*, **41**, 429–452.

Matthai, S. K., Heinrich, C. A., and Driesner, T. 2004. Is the Mount Isa deposit the product of forced brine convection in the footwall of a major reverse fault? *Geology*, **32**, p. 357–360.

McLaren S., Sandiford M. & Hand, M. 1999. High Radiogenic Heat-Producing Granites And Metamorphism: An Example From The Western Mt Isa Inlier, *Australia*. *Geology*, **27**, 189–196.

Mclaren S., Sandiford M. & Powell, R. 2005. Contrasting Styles Of Proterozoic Crustal Evolution: A Hot-Plate Tectonic Model For Australian Terranes. *Geology*, **33**, 673–676.

Miller J M. 2006. Structural controls on Cu distribution at Mt Isa; implications for exploration targeting. Barnicoat A C (editor), Korsch R J (editor) In: Predictive Mineral Discovery Cooperative Research Centre; extended abstracts from the April 2006 conference. *Record – Geoscience Australia*. Report # 2006/07. 68–71.

Muirhead K.J. & Drummond B.J. 1991. The Base Of The Lithosphere Under Australia. Drummond Barry (Ed) In: The Australian Lithosphere. *Special Publication – Geological Society Of Australia*. **17**; 23–40. 1991.

Murphy M.D., Sparks R.S.J., Barclay J. Carroll M.R., Lejeune A.M., Brewer T.S. Macdonald R., Black S. & Young S. 1998. The Role Of Magma Mixing In Triggering The Current Eruption At The Soufriere Hills Volcano, Montserrat, West Indies. *Geophysical Research Letters*, **25**, 3433–3436.

Myers R.E., Ceremuga C., Clark D., McSkimming D., Price S., Tuesley M., Wilkinson D. 1996. Mount Isa lead-zinc mineralisation; what controversy?. Baker Timothy (editor), Rotherham Jackie F (editor), Richmond Julie M (editor), Mark Geordie (editor), Williams Patrick J (editor) In: MIC '96; New developments in metallogenic research; the McArthur-Mount Isa-Cloncurry minerals province; extended abstracts. Contributions of the Economic Geology Research *Unit*. 55; 85–89.

Narasaraju T.S.B., Lahiri P., Yadav P.R., & Rai U.S. 1985. Solubility Equilibria Of Solid-Solutions Of Hydroxyl-Apatite And Chlor-Apatite Of Arsenic. *Polyhedron*, 4, pp.53–58.

Neumann, N., Gibson, G., Southgate, P. and Hutton, L. 2006. Mount Isa Inlier – Western and Eastern Succession Correlations, I7 Project Internal Report.

Newman S. & Lowenstern J.B. 2002. Volatilecalc: A Silicate Melt-H_2O-CO_2 Solution Model Written In Visual Basic For Excel. *Computers & Geosciences*, **28**, 597–604.

Nichino M., Yamashita S., Aoba T., Okazaki M. & Moriwaki Y. 1981. The Laser-Raman Spectroscopic Studies On Human-Enamel And Precipitated Carbonate-Containing Apatites. *Journal Of Dental Research*, **60**, 751–755.

NWQMPR: Queensland Department of Mines and Energy, Taylor Wall & Associates, SRK Consulting Pty Ltd & ESRI Australia 2000. *Northwest Queensland Mineral Province Report. Queensland Department of Mines and Energy, Brisbane*.

Oliver N.H.S., Holcombe R.J., Hill E.J., Pearson P.J. 1991. Tectono-metamorphic evolution of the Mary Kathleen Fold Belt, northwest Queensland; a reflection of mantle plume processes? *Australian Journal of Earth Sciences*. **38**; 4, 425–455.

Oliver N.H.S., Butera K.M., Rubenach M.J., Marshall L.J., Cleverley J.S., Mark G., Tullemans F. & Esser D. 2008. The protracted hydrothermal evolution of the Mount Isa Eastern Succession: a review and tectonic implications. *Precambrian Research*, **163**, p. 108–130.

Oliver N.H.S., Cleverley J.S., Mark G., Pollard P.J, Fu B., Marshall L.J, Rubenach M.J., Williams P.J., & Baker T. 2004, Modeling the role of sodic alteration in the genesis of iron oxide-copper-gold deposits, Eastern Mount Isa Block, Australia. *Economic Geology*, **99**, 1145–1176.

Oliver N.H.S., Rubenach M.J., Fu B., Baker T., Blenkinsop T.G., Cleverley J.S., Marshall L.J. & Ridd P.J., 2006. Granite-related overpressure and volatile release in the mid crust: fluidized breccias from the Cloncurry district, Australia. *Geofluids*, **6**, 346–358.

Oliver N.H.S., Wall V.J & Cartwright I. 1992. Internal control of fluid compositions in amphibolite-facies scapolitic calc-silicates, Mary-Kathleen, Australia. *Contributions to Mineralogy and Petrology*, **111**, 94–112.

Oliver N.H.S., Pearson P.J, Holcombe R.J., Ord A. 1999. Mary Kathleen metamorphic-hydrothermal uranium-rare-earth element deposit; ore genesis and numerical model of coupled deformation and fluid flow. *Australian Journal of Earth Sciences*. 46; 3, 467–484.

O'Reilley S.Y., Griffin W.L., Djomani Y.H. & Morgan p. 2001. Are lithospheres forever? Tracking changes in subcontinental lithospheric mantle through time. GSA Today 11, 4–10.

Pearson D.G. 1999. The age of continental roots. *Lithos* **48**, 171–194.

Pearson P.J., Holcombe R.J., Oliver N.H.S., 1987. The Mary Kathleen Fold Belt, Northwest Queensland; D1, A Product Of Crustal Extension?. Anonymous In: International Conference On Deformation Of Crustal Rocks. *Abstracts – Geological Society Of Australia*. **19**; pp.37–38. 1987.

Pearson, P.J., Holcombe, R.J., Page R.W., 1992. Synkinematic Emplacement Of The Middle Proterozoic Wonga Batholith Into A Mid-Crustal Extensional Shear Zone, Mount Isa Inlier, Queensland, Australia. In: Stewart, A.J. And Blake, D.H., (Eds.), Detailed Studies Of The Mount Isa Inlier. *Australian Geological Survey Organization, Bulletin* **243**, pp.289–328.

Perkins W G. 1997. Mount Isa lead-zinc orebodies; replacement lodes in a zoned syndeformational copper-lead-zinc system? *Ore Geology Reviews*. **12**, 2, 61–111.

Perseil E.A., Blanc P. & Ohnenstetter D. 2000. As-Bearing Fluorapatite In Manganiferous Deposits From St. Marcel Praborna, Val D'aosta, Italy. *Canadian Mineralogist*, **38**, pp.101–117.

Pollard P.J., Mark G., Mitchell L.C. 1998. Geochemistry Of Post-1540 Ma Granites In The Cloncurry District, Northwest Queensland. Williams Patrick J (Prefacer) In: Metallogeny Of The Mcarthur River-Mount Isa-Cloncurry Minerals Province. *Economic Geology And The Bulletin Of The Society Of Economic Geologists*. **93**; 8, pp.1330–1344.

Polito P.A., Kyser T.K., Southgate P.N., and Jackson M.J., 2006a. Sandstone diagenesis in the Mount Isa basin: An isotopic and fluid inclusion perspective in relationship to district-wide Zn, Pb, and Cu mineralization: *Economic Geology*, **101**, 1159–1188.

Polito P.A., Kyser T.K., Jackson M.J., 2006b. The role of sandstone diagenesis and aquifer evolution in the formation of uranium and zinc-lead deposits, southern McArthur basin, Northern Territory, Australia: *Economic Geology*, **101**, 1189–1209.

Polito P.A., Kyser T.K., Golding S.D., & Southgate P.N. 2006c. Zinc deposits and related mineralization of the Burketown mineral field, including the world-class Century deposit, northern Australia. Fluid Inclusion and stable isotope evidence for basin fluid sources: *Economic Geology*, **101**, 1251–1273.

Richardson, S.A., 2007. Extension Of Precambrian Lithosphere: Numerical Modelling, The University of WA, Crawley, 71p.

Rubenach, M.J. 1995. Low-P/High-T Metamorphism In The Mount Isa Inlier, Northeastern Australia: Significance of Porphyroblast Inclusion Trails And P-T-T Paths. In: Thermal & Mechanical Interactions In Deep Seated Rocks A-41 (Ed N/A). Praha University.

Rubenach M.J. 2005. Relative timing of albitization and chlorine enrichment in biotite in Proterozoic schists, Snake Creek Anticline, Mount Isa Inlier, northeastern Australia. Pattison David R M, St Onge Mark R, Begin Normand J In: Truth and beauty in metamorphism; a tribute to Dugald Carmichael. *The Canadian Mineralogist*. **43**, Part 1; 349–366.

Richter D.K., Gotte T. & Habermann D. 2002 Cathodoluminescence Of Authigenic Albite. *Sedimentary Geology*, **150**, pp.367–374.

Scott D.L., Rawlings D.J., Page R.W., Tarlowski C.Z., Idnurm M., Jackson M.J., Southgate P.N. 2000. Basement Framework And Geodynamic Evolution Of The Palaeoproterozoic Superbasins Of North-Central Australia; An Integrated Review Of Geochemical, Geochronological And Geophysical Data. Southgate P N (Prefacer) In: Carpentaria-Mt. Isa Belt; Basement Framework, Chronostratigraphy And Geodynamic Evolution Of Proterozoic Successions. *Australian Journal Of Earth Sciences*. **47**; 3, pp.341–380.

Shvarov Y.V. & Bastrakov E.N. 1999. Hch: A Software Package For Geochemical Equilibrium Modelling. User's Guide. Canberra, Australian Geological Survey Organisation.

Sheldon, H.A., Barnicoat, A., Ord, A. 2005. Faults As Pathways Versus Faults As Seals: Contrasting Behaviour Of High And Low Porosity Rocks. *European Geosciences Union General Assembly. Geophysical Research Abstracts*. Vol. 7.

Sibson, R.H. And Cathles, L.M. 1990. Rupture Nucleation On Unfavorably Oriented Faults-Scales And Effects Of Fluid Flow In The Upper Crust. *Bulletin Of The Seismological Society Of America*, 80(6a): pp.1580–1604.

Simons, F. J., Zielhuis, A. And Van Der Hilst, R. D. 1999. The Deep Structure Of The Australian Continent From Surface Wave Tomography. *Lithos* 48, 17–43.

Southgate P., Domagala J., Jackson J., Krassay A., Mcconachie B., Sami T., Wells A. 1997. Sequence Stratigraphy Correlations Between The Mt Isa And Lower Mcnamara Groups: Implications For Basin Shape And Sediment Architecture. Luodvalkis A (Compiler), Barnett K (Compiler) In: Nabre Workshop; Abstracts. *Record – Australian Geological Survey Organisation*. Report # 1997/12.

Southgate, P.N., Kyser, T.K., Scott, D.L., Large, R.R., Golding, S.D., Polito, P.A. 2006. A Basin System And Fluid-Flow Analysis Of The Zn-Pb-Ag Mount Isa-Type Deposits Of Northern Australia: Identifying Metal Source, Basinal Brine Reservoirs, Times Of Fluid Expulsion, And Organic Matter Reactions. *Economic Geology*, V. 101, 6, pp.1103–1115.

Spear F.S. 1995 Metamorphic Phase Equilibria And Presure-Temperature-Time-Paths 2edn, Mineralogical Society.

Spikings R.A., Foster D.A., Kohn B.P. 2006 Low-Temperature (<1100 C) Thermal History Of The Mt Isa And Murphy Inliers, Northeast Australia: Evidence From Apatite Fission Track Thermochronology, *Australian Journal Of Earth Sciences*, **#53**, pp 151–165.

Stormer J.C. Jr., Pierson M.L., Tacker R.C., 1993. Variation of F and Cl X-ray intensity due to anisotropic diffusion in apatite during electron microprobe analysis. *American Mineralogist*. **78**; 5–6, 641–648.

Streck M.J. & Dilles J.H. 1998. Sulfur Evolution Of Oxidized Arc Magmas As Recorded In Apatite From A Porphyry Copper Batholith. *Geology*, **26**, pp.523–526.

Swager C.P. 1985. Syndeformational carbonate-replacement model for the copper mineralization at Mount Isa, Northwest Queensland; a microstructural study. *Economic Geology and the Bulletin of the Society of Economic Geologists*. **80**; 1, 107–125.

Swager C.P., Perkins W.G., Knights J.G., 1987. Stratabound phyllosilicate zones associated with syntectonic copper orebodies at Mt. Isa, Queensland. *Australian Journal of Earth Sciences*. **34**; 4, 463–476

Sweet I.P. & Hutton L.J. 1982. 1:100 000 Geological Map Commentary – Lawn Hill Region Queensland, Geological Survey Of Queensland.

Van Der Wielen, S.E., Oliver, S., Kalinowski, A.A., Creasy, J. 2005. Remotely Sensed Imaging Of Hydrothermal Footprints In The Western Succession, Mount Isa Inlier. – ***pmd*CRC*** I1 Project Final Report, March 2005, pp.177–185.

Waring C.L. 1990 The Mt. Isa Cu system: alteration, fluid flow, and pre-disposing factors. Anonymous In: Mount Isa Inlier geology conference; abstracts. 69–71.

Waring C.L. 1990 Metamorphism of Mt. Isa Group rocks, and timing relative to Cu mineralisation. Anonymous In: Mount Isa Inlier geology conference; abstracts. 56–57.

Wilde, A. (2006): Finding The Next Century Deposit: Geochemical Studies. – ***pmd*CRC*** G14 Project Final Report, May 2006, pp.67.

Wilson I H. 1978. Volcanism On A Proterozoic Continental Margin In Northwestern Queensland. *Precambrian Research*. 7; 3, pp.205–235.

Wilson I.H. 1978. Mineral Exploration Under Authorities To Prospect In The Camooweal 1:250,000 Sheet Area. *Queensland Government Mining Journal*. **79**; 915, 15–25.

Wilde, A. (2006): Finding The Next Century Deposit: Geochemical Studies. – ***pmd*CRC*** G14 Project Final Report, May 2006, pp.67.

Wyborn L.1988. Petrology, Geochronology And Isotope Geochemistry Of The Post-1820 Ma Granites Of The Mount Isa Inlier: Mechanisms For The Generation Of Proterozoic Anorogenic Granites. *Precambrian Research*. 40–41, 509–541.

Wyborn L.A.I. 1992. The Williams And Naraku Batholiths, Mt Isa Inlier; An Analogue Of The Olympic Dam Granites? *BMR Research Newsletter*. 16; 13–16.

Yardley, B.W.D. 2005. 100th Anniversary Special Paper: Metal Concentrations In Crustal Fluids And Their Relationship To Ore Formation. *Economic Geology*, V. 100, No. 4, pp.613–632.

Yardley, B.W.D. & Baumgartner, L.P. 2007. Fluid Processes In Deep Crustal Fault Zones, In Handy, M. R., Hirth, G., And Hovius, N., Eds., Tectonic Faults: Agents Of Changeon A Dynamic Earth: Cambridge, Ma, Mit Press, pp.295–318.

Zhu C & Sverjensky Da (1991) Partitioning Of F-Cl-Oh Between Minerals And Hydrothermal Fluids. *Geochimica Et Cosmochimica Acta*, **55**, 1837–1858.

Zhu C & Sverjensky Da (1992) F-Cl-Oh Partitioning Between Biotite And Apatite. *Geochimica Et Cosmochimica Acta*, **56**, 3435–3467.

G14 project with Zinifex (Murphy et al. 2007; Zhang et al. 2007).

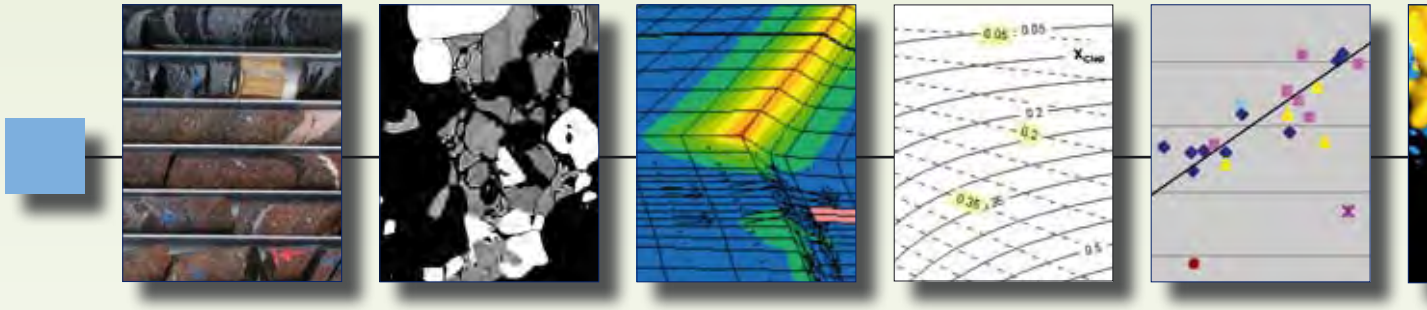
0.05
0.05
x_{CH4}
0.2
0.2
0.35
0.35
0.5

The pre-1.8 Ga Tectono-Magmatic Evolution of the Kalkadoon-Leichhardt Belt - Implications for the Crustal Architecture and Metallogeny of the Mt Isa Inlier

F.P. Bierlein, R. Maas & J. Woodhead

Report for the pmd*CRC I-7 Project

10 December 2007

Abstract

New geochemical, U-Pb zircon and Nd-Hf isotope data for felsic and mafic components of the Kalkadoo-Leichardt Belt (KLB) confirm that the evolution and tectonic make-up of this belt prior to 1.8 Ga was closely aligned with that of the Western Fold Belt. Like pre-1.8 Ga magmatic rocks of the Western Fold Belt, those in the KLB are characterised by late Archaean to Palaeoproterozoic crustal residence ages (T_{DM} *ca.* 2.3 to 2.6 Ga) but the geochemical data suggest stronger within-plate affinities, implying that the KLB intrusions underwent a greater degree of crustal assimilation and/or were emplaced further inboard of the active subduction margin. A new SHRIMP U-Pb zircon age of ca. 1.86 Ga from a felsic intrusion in the northern KLB confirms earlier age constraints for the main phase of the Kalkadoon Granite. Nd isotope patterns for intrusions in the Western Fold Belt and the KLB are distinct from those of *ca.* 1.7 to 1.5 Ga intrusions in the Eastern Fold Belt. This isotopic discrepancy suggests the Eastern Fold Belt underwent a separate evolutionary history and was accreted to the WFB/KLB at some stage prior to, or during, the *ca.* 1.86 Ga Barramundi Orogeny. The occurrence of widespread, isotopically homogeneous *ca.* 1.72 Ga magmatism (Argylla Event) across the entire Mt Isa Inlier implies that amalgamation of the allochthonous Eastern Fold Belt with the North Australian Craton was completed by that time. The significantly elevated metallogenic potential of the Eastern Fold Belt for iron-oxide-copper-gold, relatively low endowment of the Kalkadoon-Leichhardt Belt, and predominance of base metal occurrences in the Western Fold Belt, are all a direct function of the tectonic interplay and lithospheric processes that controlled the evolution of the Mt Isa Inlier prior to *ca.* 1.8 Ga.

Introduction

The Kalkadoon-Leichhardt Belt (KLB) extends for about 250 to 300 km (N-S) by 30 to 50 km (E-W) and consists of predominantly felsic intrusive rocks (i.e., Kalkadoon Granite) and comagmatic volcanics (Leichhardt Volcanics). Emplacement of these igneous suites in generally considered to have occurred at ca. 1.87 – 1.85 Ga (Page, 1983), during the final stages of the Barramundi Orogeny (Page and Williams, 1988; Neumann et al., 2006). The KLB separates the Western Fold Belt (comprising the Lawn Hill Platform and Leichhardt River Fault Trough) from the Eastern Fold Belt (Blake, 1987) via a series of variably well-defined, fault-bounded contacts (Fig. 1).

Extensive studies have been carried out on the structure and sedimentary sequences of the Western and Eastern fold belts, as well as the KLB, and consequently, the post-1.8 Ga evolution of the Inlier and its superbasins have been reasonably well constrained (e.g. Betts et al., 2006, and references therein). However, major uncertainties remain regarding the pre-1.8 Ga crustal architecture and nature of the basement in each of the three belts, and the nature of the tectonic setting that led to and prevailed during the amalgamation of the fold belts. Previous studies have highlighted differences in crustal architecture between the Western and Eastern Fold Belts, and various models to explain these differences have been proposed (Drummond et al., 1998; MacCready et al., 1998; MacCready, 2006). These include the presence of a mafic underplate, or subduction of oceanic crust, beneath the Western Fold Belt, or the presence of thick basaltic horizons within the supracrustal succession in the Eastern Fold Belt, or the emplacement of mafic intrusions along a decollement that once separated the Western from the Eastern Fold Belt. However, limited exposure of pre 1.8 Ga basement rocks, largely confined to the southern portions of the Western Fold Belt and the western KLB, has rendered difficult any interpretation regarding the Palaeoproterozoic tectonic setting and geological evolution of the Mt Isa Inlier.

Such basement rocks include variably deformed and metamorphosed supracrustal successions, and the comagmatic ca. 1.87 – 1.85 Ga intrusive and extrusive rocks of the KLB. Bierlein and Betts (2004) studied a range of pre 1.8 Ga basement rocks from either side of the Mt Isa Fault Zone to investigate the nature of this metallogenically important structure. The main findings of this study were that the Mount Isa Fault is unlikely to represent a suture zone that separates discrete Palaeoproterozoic crustal fragments. Furthermore, the data presented in Bierlein and Betts (2004) indicated that the crustal blocks on both sides of the Mt Isa Fault Zone must have been within close proximity of each other since the Palaeoproterozoic, and that the Western Fold Belt was part of the (ancestral) North Australian Craton well before the ~1.89 – 1.87 Ga Barramundi Orogeny. The study by Bierlein and Betts (2004) was limited to the southern portion of

the Western Fold Belt and the westernmost part of the KLB within relatively close proximity of the Mt Isa Cu-Pb-Zn deposit.

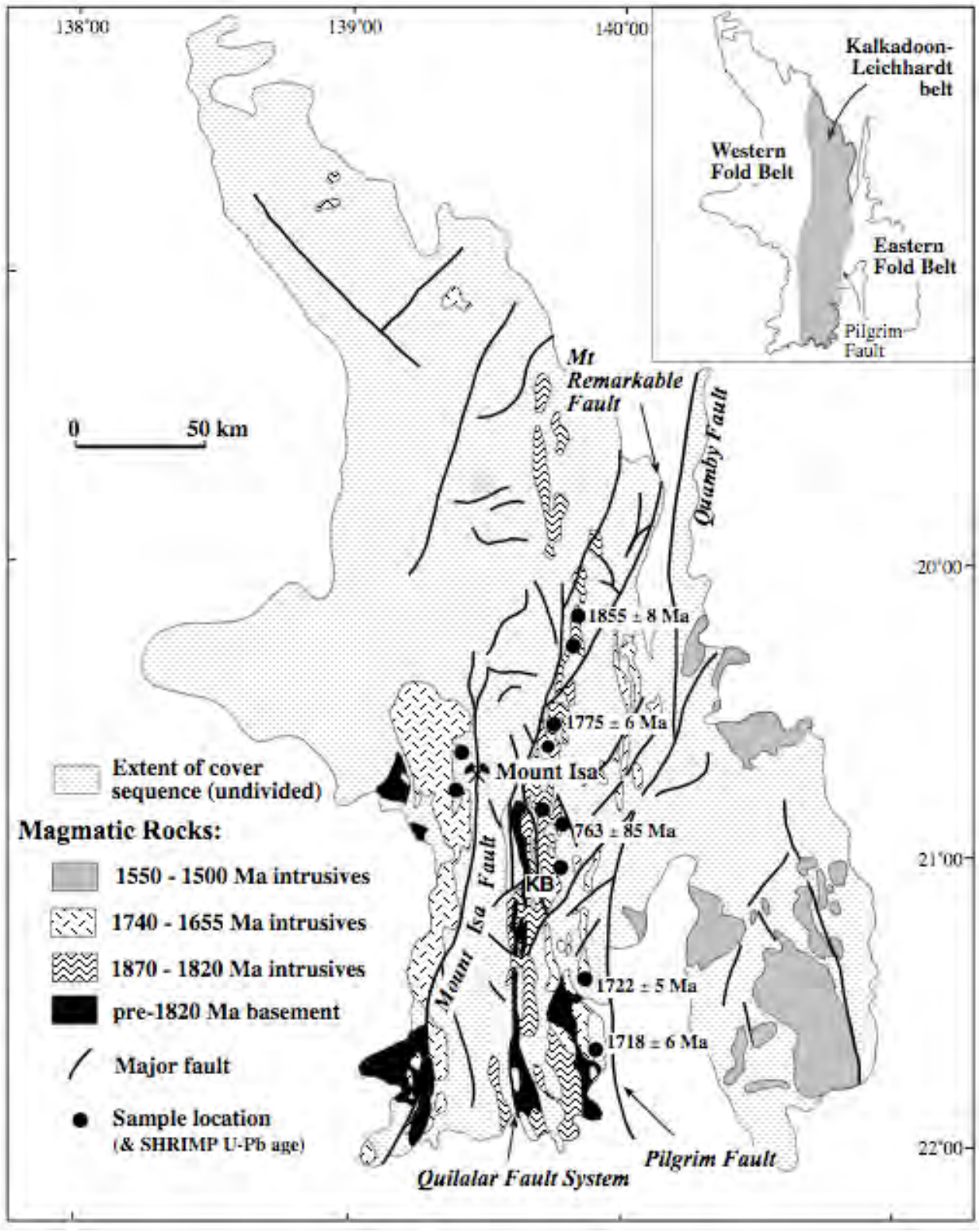

Figure 1: Geological sketch map of the Mt Isa Inlier, showing the extent of the Kalkadoon-Leichhardt Belt (KB), major structural elements, location of samples collected for this study, and new SHRIMP U-Pb ages (modified from Bierlein and Betts, 2004).

In this study, we have investigated a range of mafic – felsic igneous rocks from the northern, central and southern extremities of the KLB to obtain further constraints on magma sources, nature of the

basement these magmas were injected into, and to better determine the role of the KLB in the amalgamation of the Mt Isa Inlier.

Methods

Regional field work and sampling was carried out during two campaigns in 2005 and 2006. During this work, it became clear that existing geological maps of the KLB did not capture the range of texturally and lithologically diverse igneous rock types present, and thus did not accurately convey the apparently complex emplacement history of the Kalkadoon Batholith. Samples collected during 2005/6 include undeformed pegmatite in foliated gneiss and weakly deformed pink feldspar granite, porphyritic hornblende-bearing syno-granite, quartz porphyry, and megacrystic homogeneous to rapakivi-textured diorite-granite phases, all from the Kalkaldoon Batholith, to homogeneous, basaltic-doleritic-gabbroic (in part magnetite-olivine-bearing) enclaves (ranging from several cm to several m in diameter) within the granitic intrusions, and highly deformed, hydrated amphibolite gneiss within homogeneous to moderately deformed Kalkadoon granite (Fig. 2). In some instances, the contact between mafic and felsic-porphyritic phases is rather diffuse and characterized by abundant schlieren, implying comagmatic formation in a fractionating system, hybridization at depth, and more or less coeval emplacement of these compositionally distinct phases.

Thirtyfour petrographically documented samples were prepared for chemical analysis by jaw crushing (2-5 kg) and milling in WC. Abundances of major and trace elements were determined at Geoscience Australia, Canberra (XRF & ICP-MS). Major and minor elements (Si, Ti, Al, Fe, Mn, Mg, Ca, Na, K, P, S) were determined by wavelength-dispersive XRF on fused disks using methods similar to those of Norrish and Hutton (1969). Precision for these elements is better than ±1% of the reported values. Arsenic, Ba, Cr, Cu, Ni, Sc, V, Zn and Zr were determined by pressed pellet on a wavelength-dispersive XRF using methods similar to those described by Norrish and Chappell (1977). Selected trace elements (Cs, Ga, Nb, Pb, Rb, Sb, Sn, Sr, Ta, Th, U, Y) and the Rare Earth elements were analysed by ICP-MS (Perkin Elmer ELAN 6000) using methods similar to those of Eggins et al. (1997), but on solutions obtained by dissolution of fused glass disks (Pyke, 2000). Fe_2O_3/FeO ratios were determined by electrochemical titration using a modified methodology based on Shapiro and Brannock (1962). Whole-rock analytical data of these samples are summarised in Table 1.

SHRIMP U-Pb zircon data were obtained for 5 samples, to expand the existing zircon age data base for pre-1.76 Ga basement lithologies in the Mt Isa Inlier, and compare the Palaeoproterozoic crustal evolution of the KLB with that of the western and eastern fold belts. Samples FBMI-6504 and -6510 are from the northern KLB; FBMI-6518 is from a mafic intrusion

in the central portion of the KLB; FBMI-5601 was collected from the Mt Erle Igneous Complex and FBMI-5605 from the Revenue Granite, which are both located in the southernmost part of the KLB. Zircons from samples FBMI-6504, -6510, -5601, and -5605 were of similar texture, and generally more angular (euhedral) in shape and abundant than zircon grains from Sample FBMI-6518 (Fig. 3). Prismatic, oscillatory zoning is common in cathodoluminescence and transmitted light images. Zircon grains from all five samples were mounted in epoxy SHRIMP zircon grain mounts with chips of the BR266 standard, polished to reveal mid-sections and gold coated for SHRIMP analysis. The five samples were analysed during four analytical sessions on the SHRIMP B ion microprobe at Curtin University in Perth in July and October 2007. The primary standard, BR266 ([U] = 903ppm, 559Ma), was used as the calibration standard. Gold coating was provided by The Centre for Microscopy, Characterisation and Analysis at the University of Western Australia. Standard SHRIMP procedures for zircon analyses were used. The primary ion beam diameter ranged between 20 and 30 micrometers with a beam current ranging from 1.7nA to 5.0 nA throughout the sessions. Six scans of the mass spectrum were recorded for each analysis. Gold coating and any surface contamination around the analysis spot were removed by rastering the primary ion beam for 2 minutes prior to analysis. Mass resolution of the secondary ion beam was 5190 (1% valley definition) during the analysis. SQUID software (Ludwig, 2001) was used to produce calibrated Pb/U and Th/U data, in addition to Pb/Pb isotope ratios. Summarized results are given in Table 2.

Zircon-Hf isotope analyses were done using a Nu Plasma MC-ICPMS coupled to an ArF excimer laser (193 nm) at University of Melbourne (see Woodhead et al., 2004 for details). Static spot sizes used for the analyses varied from 38 to 60 μm depending upon the size of the grains, complexity of the cathodoluminescence images and Hf content of the zircons. A power density on the sample of between 2-4 J/cm^2 was employed, with a repetition rate of 4 Hz. A background measurement of 60 seconds was followed by between 30-60 seconds of data acquisition 'on peak', again, often depending upon the thickness of the zircon. Where possible, Hf analytical spots were co-located with areas from which SHRIMP U-Pb age data had been obtained previously, allowing for the capture and integration of geochronological and isotopic information from the same grain. The $^{176}Hf/^{177}Hf$ ratios listed in Table 3 are corrected for interfering Lu and Yb, mass bias (by internal normalization to constant $^{179}Hf/^{177}Hf = 0.7325$) and are reported relative to $^{176}Hf/^{177}Hf$ =0.281630 for the BR266 zircon standard (Belshaw et al., 1998; Woodhead et al., 2004).

Whole rock Sm-Nd isotope data were obtained for 14 samples, including those for which SHRIMP U-Pb and *in-situ* Hf isotope analyses had been obtained. Following Maas et al. (2005), powders (30-50 mg) were spiked with mixed ^{149}Sm-^{150}Nd tracer solution and dissolved at high pressure. Sm and Nd were extracted using a combination of EICHROM RE and LN resin columns,

FBMI6501; dolerite in Kalkadoon Granite

FBMI6516

FBMI6504; transitional contact between Kalkadoon main phase and quartz porphyry (along pencil)

FBMI5602

FBMI6510

Myabee Granite (gabbroic phase; FBMI5608d)

Figure 2; examples of KLB phases sampled.

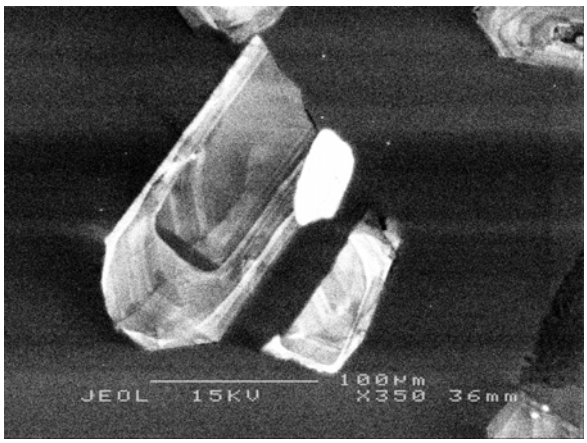

FBMI5604 (CL image)

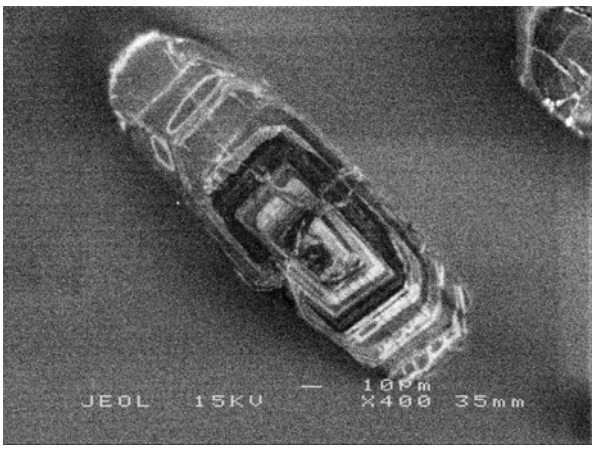

FBMI5610 (CL image)

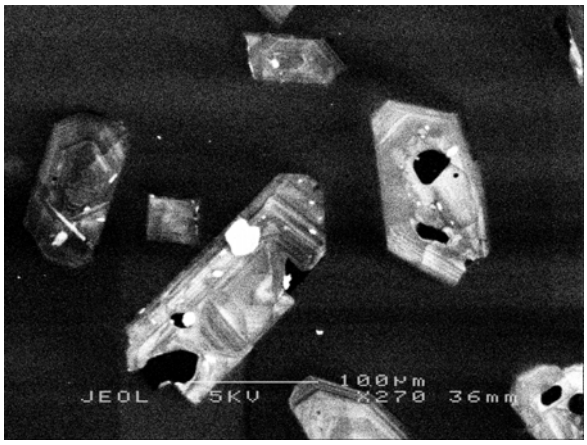

FBMI5604 (CL image)

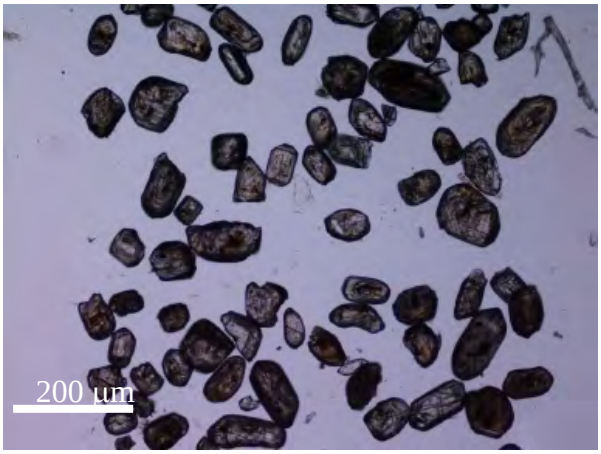

FBMI6505 (transmitted light image)

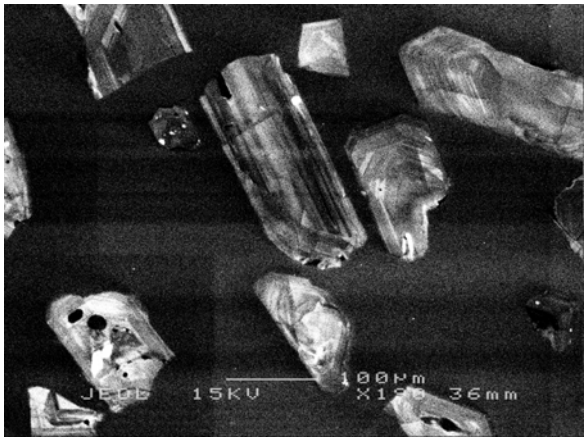

FBMI5604 (CL image)

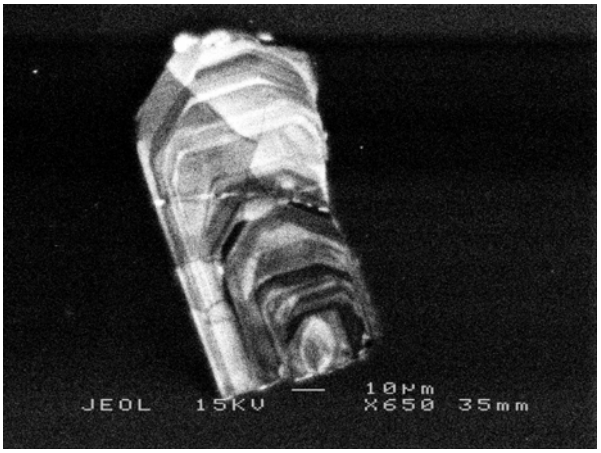

FBMI5618 (CL image)

Figure 3; CL images of zircons from samples FBMI5610, FBMI5604, FBMI5605, and FBMI5618.

with total procedural blanks below 0.1 ng. Isotopic analyses were carried out on the Melbourne University NU Plasma multi-collector ICP-MS. Further details are given in Table 4.

Results

The felsic phases of the Kalkadoon Batholith analysed in this study comprise peraluminous (Fig. 4) and predominantly potassic (Fig. 5) rocks, and plot in the field of sub-alkalic diorites and granites (Fig. 6) on the SiO_2 versus Na_2O+K_2O diagram of Le Maitre et al. (1989). This is supported by immobile trace element systematics (Winchester and Floyd, 1977): all our felsic samples plot entirely within the extrusive equivalents of dioritic-granitic rocks (i.e., rhyodacites/dacites and rhyolites; Figs 7a, b), illustrating the validity of using immobile trace elements. With increasing SiO_2, the felsic samples show a general decrease in TiO_2, P_2O_5, MgO, CaO, Cr, and Ni, with increasing K_2O, Rb, and Ba (Figs 8, 9). This probably reflects early crystallization/removal of apatite, hornblende, biotite, plagioclase and titanite. The intermediate sample is also from a potassic and peraluminous rock (Figs 4, 5), and plots into the syenodiorite field in Figure 6 (andesite field in Figs 7a and b). In the Harker diagrams shown in Figures 8 and 9, the syenodiorite plots away from the tail end of the diorite-granite samples. These samples straddle the fields for ‘within-plate’ or ‘A-type’ granites, and ‘volcanic-arc’ and ‘syn-collisional’ granites in a discrimination diagram (Fig. 10) from Pearce et al. (1994).

The samples of mafic enclaves are mostly from peraluminous, low- to medium-K, sub-alkaline rocks that plot into the field for gabbros (Figs 4, 5, 6), but they also include metaluminous dolerites, and high-K, alkaline rocks of shoshonitic composition. Immobile trace element discrimination plots for volcanic rocks classify the mafic enclaves as having calc-alkaline, andesitic-basaltic to sub-alkaline, basaltic compositions (Figs 7a, b), despite the degree of alteration that has affected most of these enclaves and accounts for their deviation from the field of ‘normal, unaltered basalt’ in a diagram of CaO versus Na_2O (Fig. 11). Ternary discrimination diagrams used to identify main magma types and discriminate tectonic settings are shown in Figure 12 (after Pearce, 1996). On a Nb-Zr-Y diagram (Fig. 12a), the mafic enclaves (and intermediate syenodiorite) delineate a transitional trend that includes MORB, VAB and WPB fields. A somewhat stronger arc-related affinity is evident from the Zr-Th-Nb diagram in Figure 12b, with evidence for the assimilation of continental crust and/or a subduction component also apparent on a Ti-Zr-Y diagram (Fig. 12c).

On a primitive mantle-normalised element diagram (Fig. 13), the felsic samples from the KLB are characterized by a general enrichment in low field-strength (LFSE) and large ion lithophile elements (LILE), and irregular normalized abundances of high field-strength elements

(HFSE) abundances. Notably, the diorites and granites from the KLB display negative Ba, Sr, Nb, TiO_2, and Cr anomalies, while Th, Zr and Y are enriched. Both Rb/Sr and Rb/Ba ratios generally increase with SiO_2 concentrations, indicative of the crystallization of feldspar. Furthermore, the felsic samples from the KLB are all characterised by low Sr/Y ratios and are thus Sr-depleted/Y-undepleted. Such ratios rule out an origin by deep-crustal melting with garnet as a stable residue phase, a signature typically displayed by some (adakite-like) granitoids derived from the deep section of overthickened arc crust (e.g., Tulloch and Kimbrough, 2003). Low Sr concentrations also imply plagioclase was stable during crustal melting, which, in turn, points to melting of the felsic KLB magmas at much shallower depths in the crust.

The intermediate rock sample also displays general enrichement in LILE and LFSE over conservative elements such as Cr and Ni (Fig. 14). However, the primitive mantle-normalised element diagram of the synodioritic enclave from the central portion of the Kalkadoon batholith displays only minor positive and negative anomalies with respect to Ba, Th, Nb, Zr, TiO_2, Y, and Sc.

The mafic samples from the KLB are characterized by scattered primitive mantle normalised element trends (Fig. 15) for Rb, Ba, K_2O, Pb and Cr, but generally consistent positive anomalies of Th and V, while also displaying negative Nb and Sr anomalies. In general, with increasing SiO_2, the concentrations of K_2O, TiO_2, P_2O_5 increase. These rocks are also characterized by relatively 'flat' Zr/Y and TiO_2/Y ratios, typical of basaltic rocks associated with attenuated continental terrane settings (Pearce, 1996). The scattered trends with respect to the more mobile elements such as Rb, Ba, and K_2O in these samples is probably, at least to some extent, due to the effects of alteration, but also indicative of mixing between the mafic enclaves and the dioritic-granitic host material.

Initial SHRIMP U-Th-Pb analyses of zircons from basaltic dyke FBMI-6518 indicated unusually young ages of <1000 Ma, which were thought to stem from contamination. However, re-sampling of residual material and isotopic analyses of a second zircon separate from this sample confirmed the anomalously young age for this sample. The associated ^{204}Pb-corrected ^{206}Pb/^{238}U ages and isotopic ratios are presented in Table 2a. Excluding data omitted as a result of either high common Pb >1% or discordance > 5% for age estimation, the ^{206}Pb/^{238}U age associated with zircon grains in sample FBMI-6518 containing <1% common Pb only is estimated at 795 ± 28 Ma (MSWD = 13, n = 8).

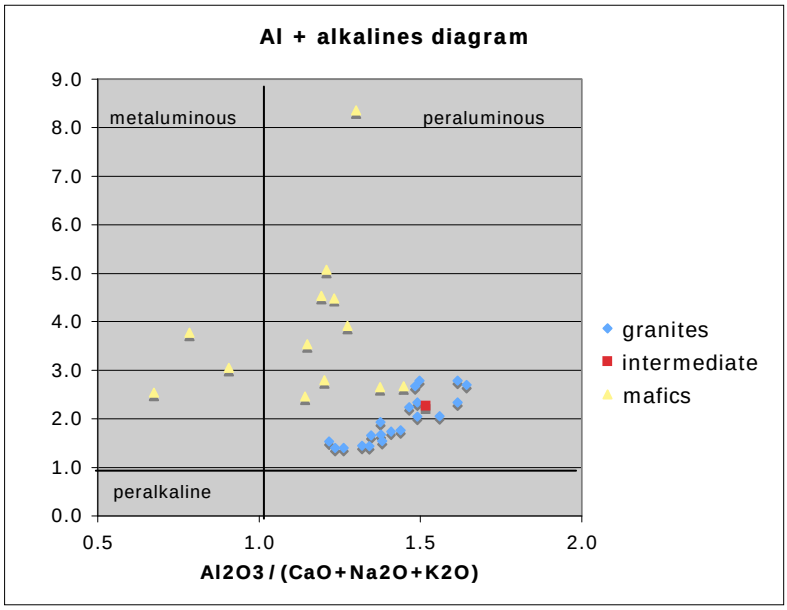

Figure 4.

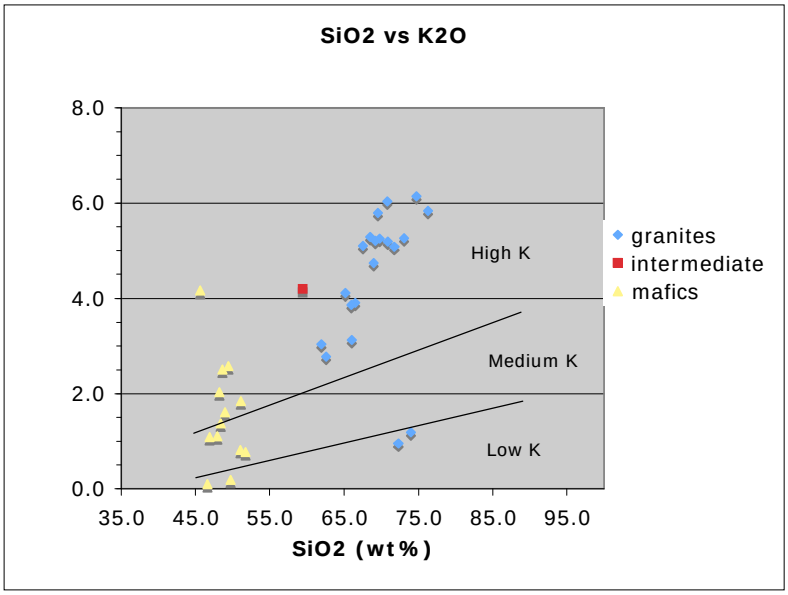

Figure 5.

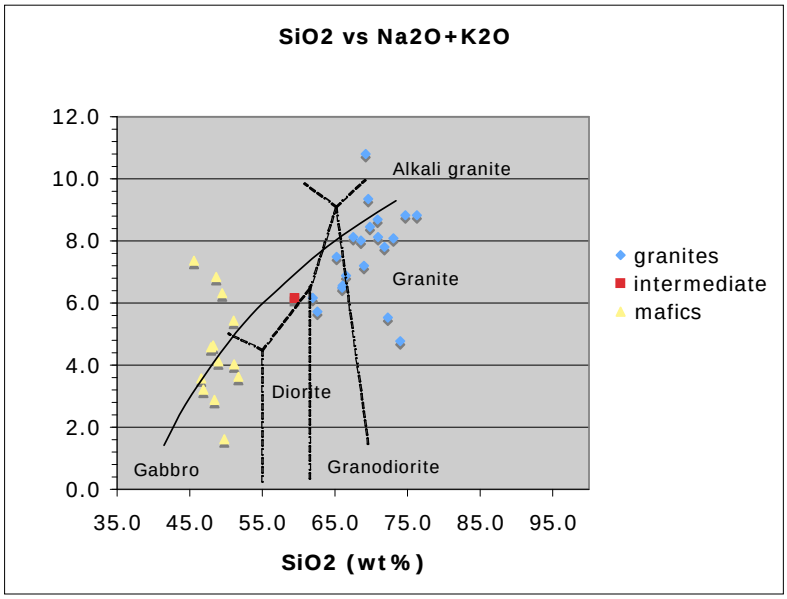

Figure 6.

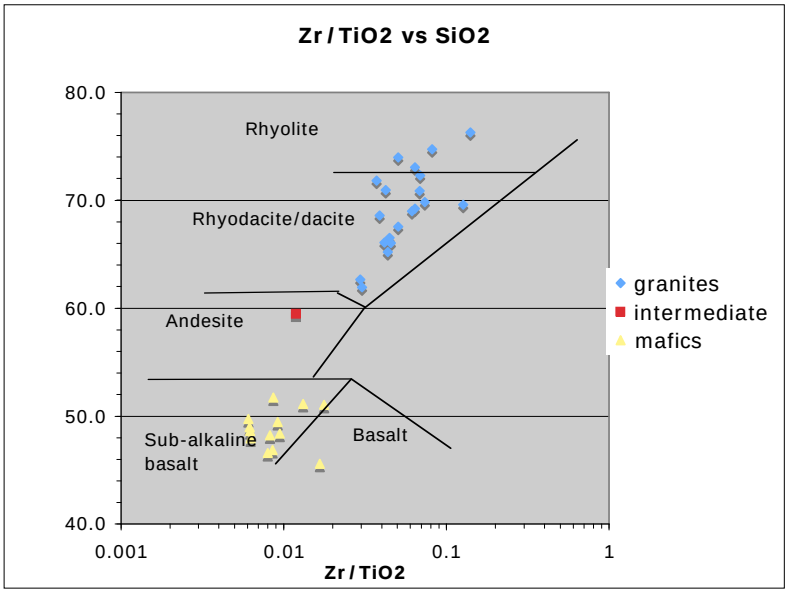

Figure 7a.

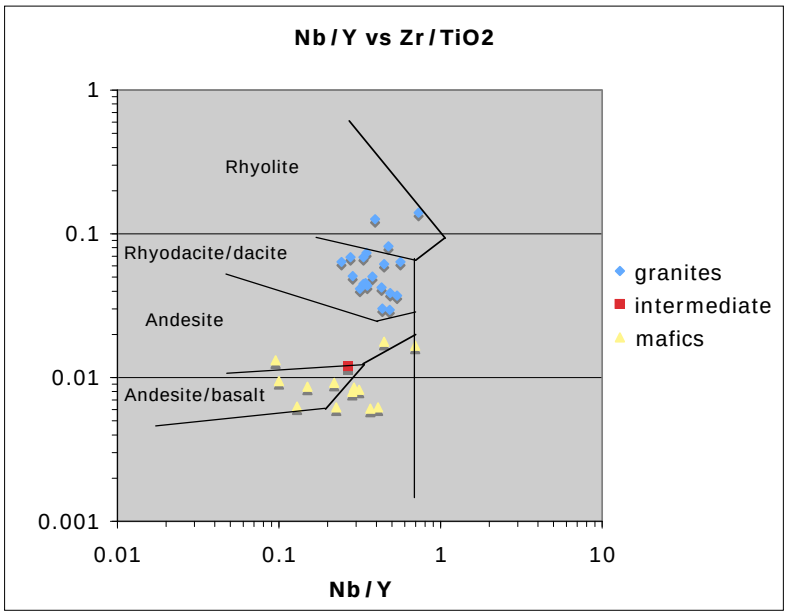

Figure 7b.

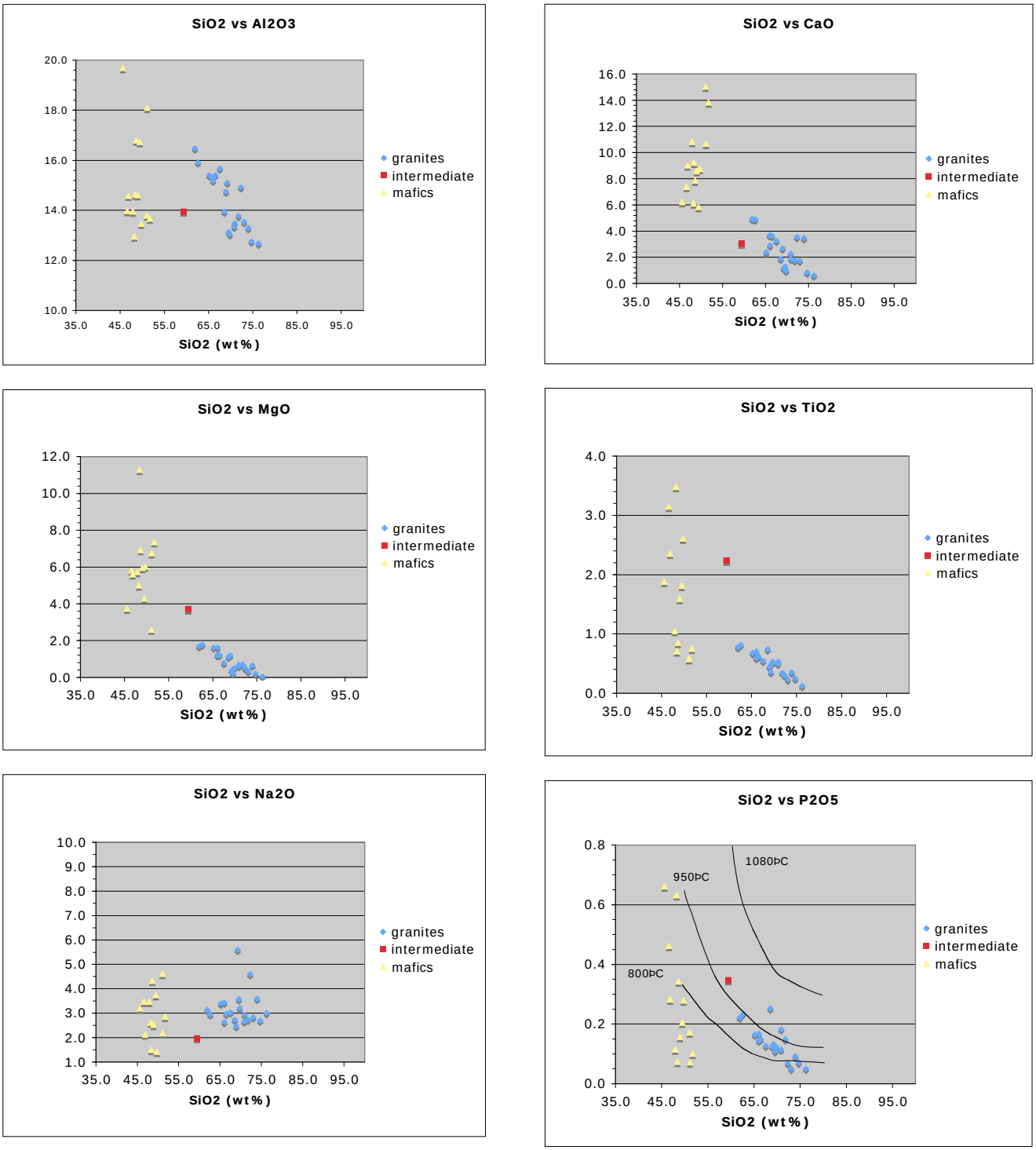

Figure 8; Harker diagrams for major oxides.

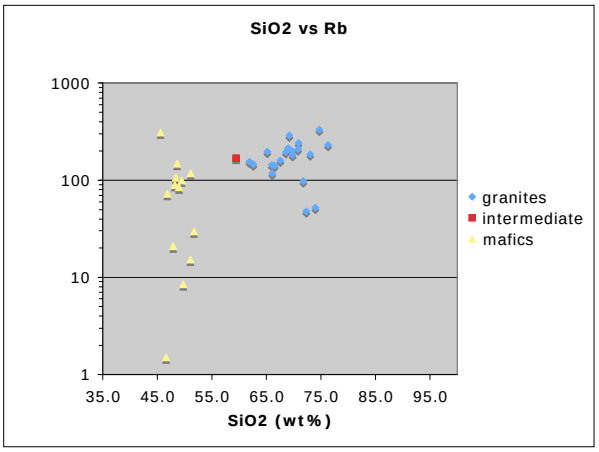

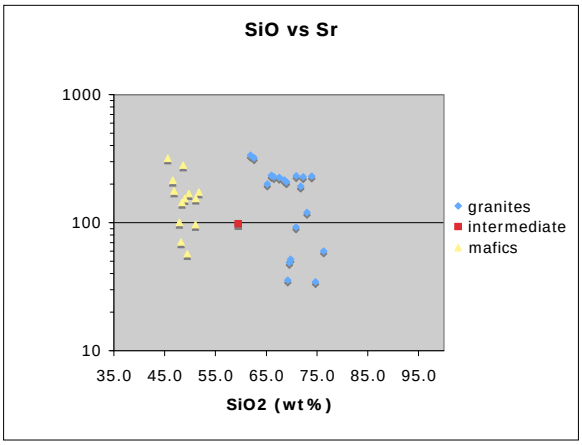

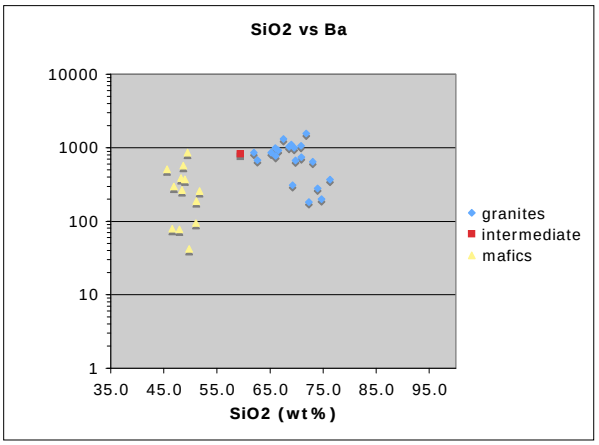

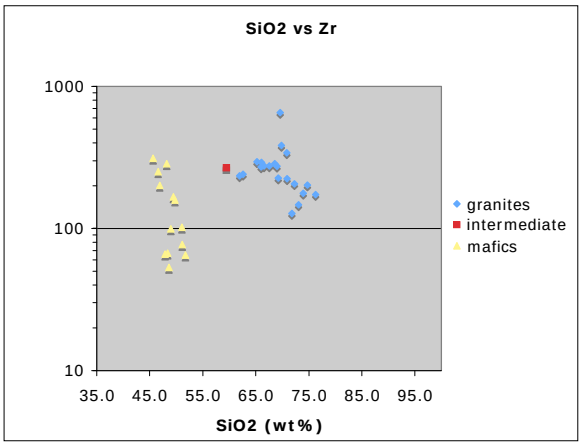

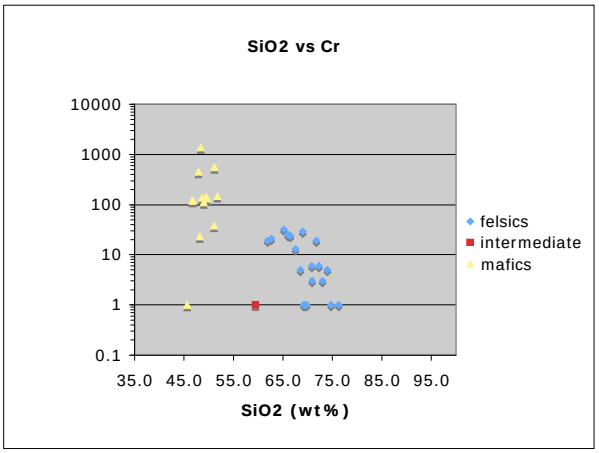

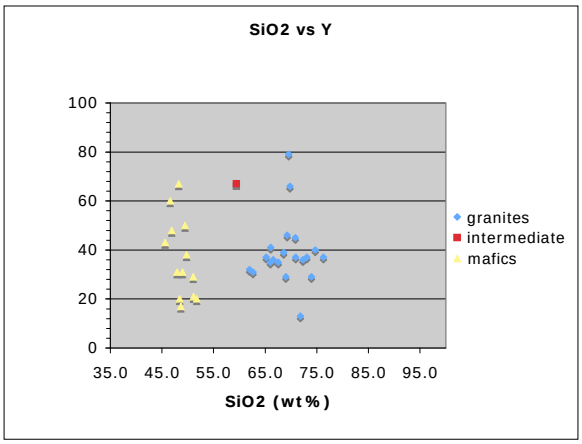

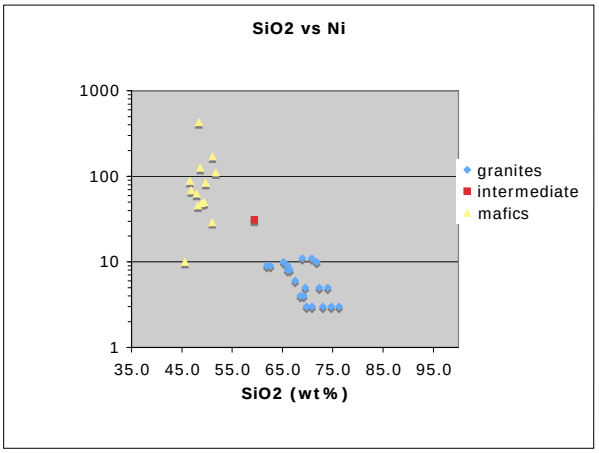

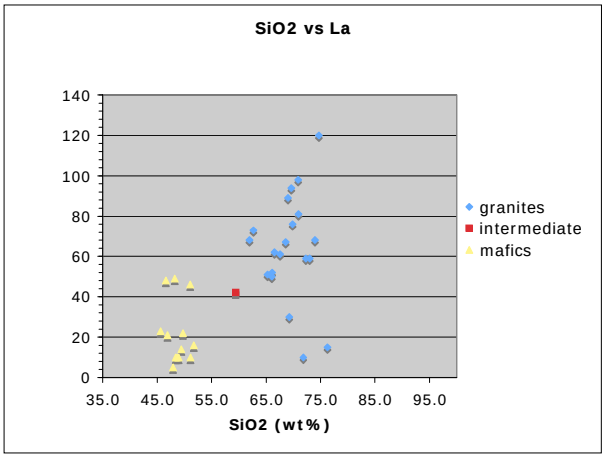

Figure 9; Harker diagrams for trace elements.

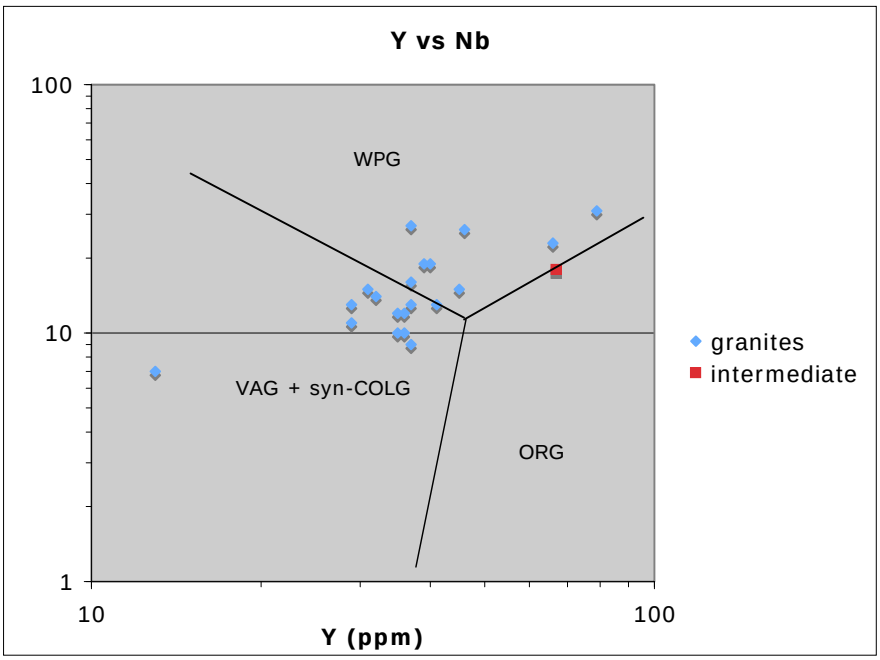

Figure 10

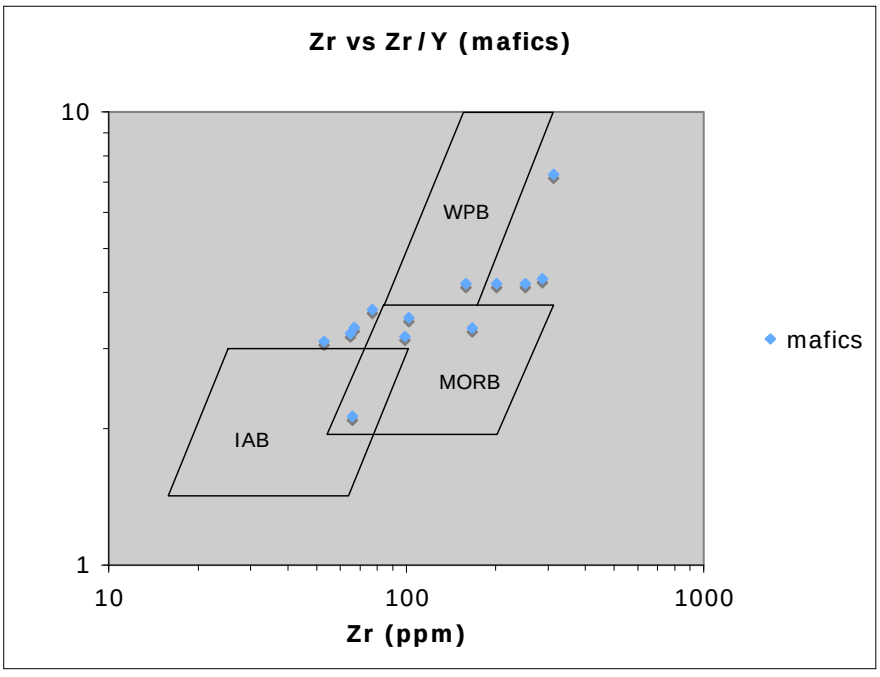

Figure 11

a

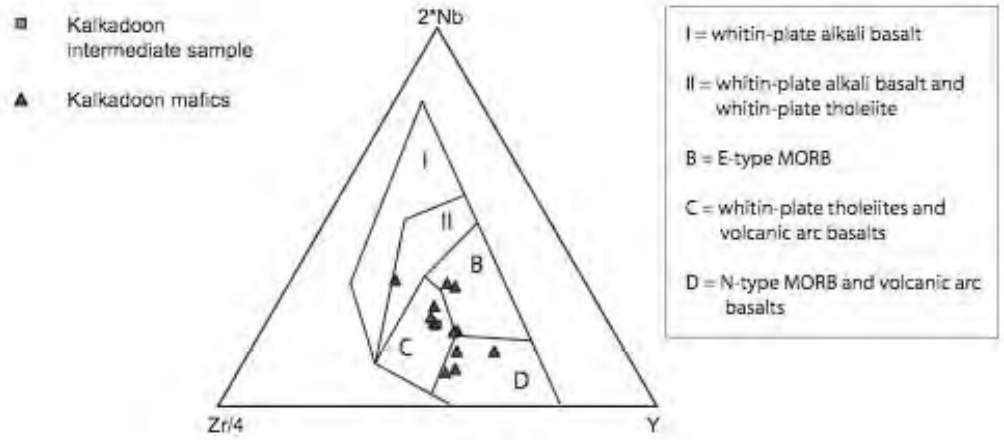

b

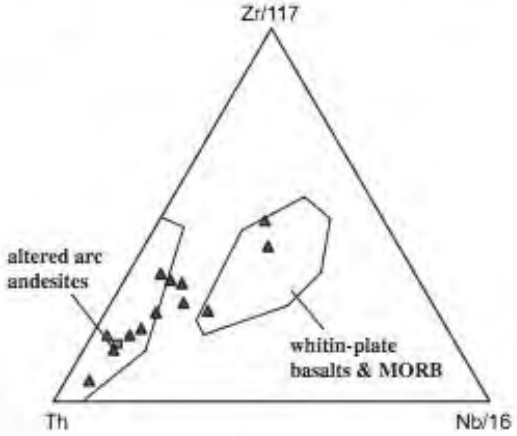

c

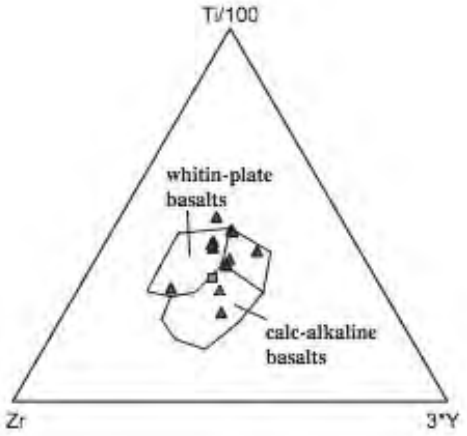

Figure 12

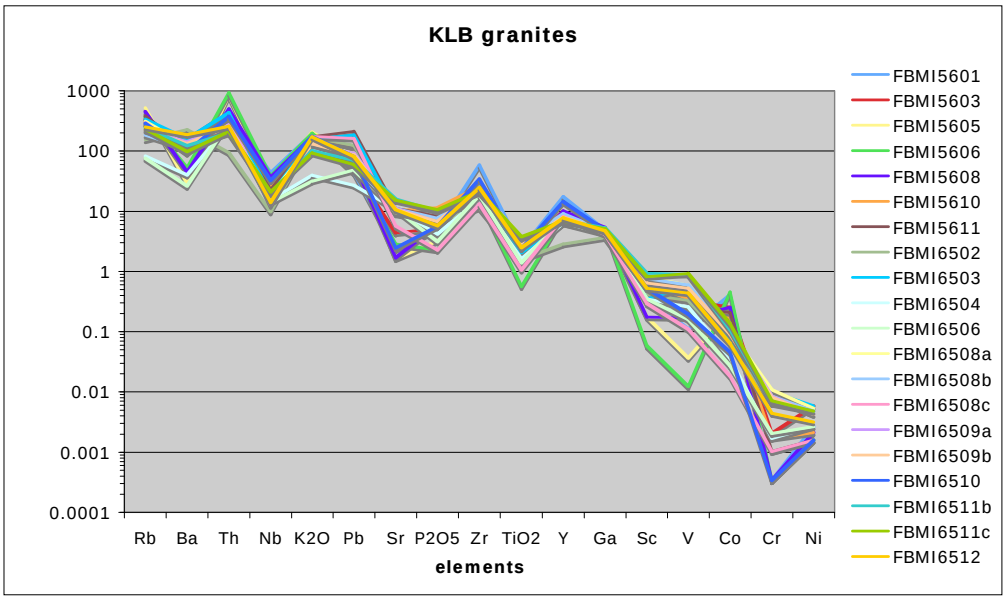

Figure 13

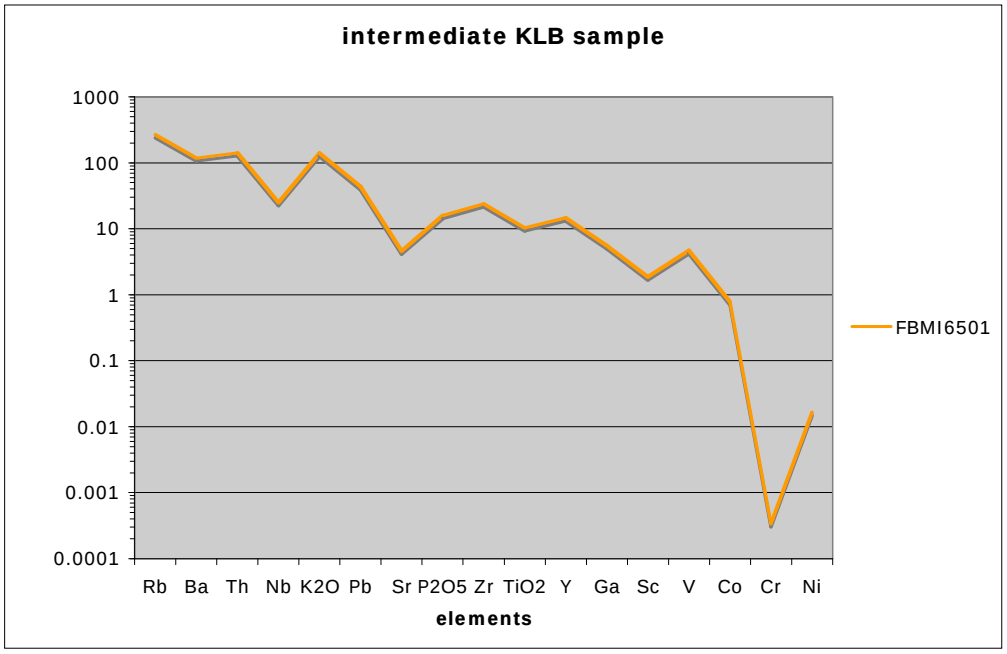

Figure 14

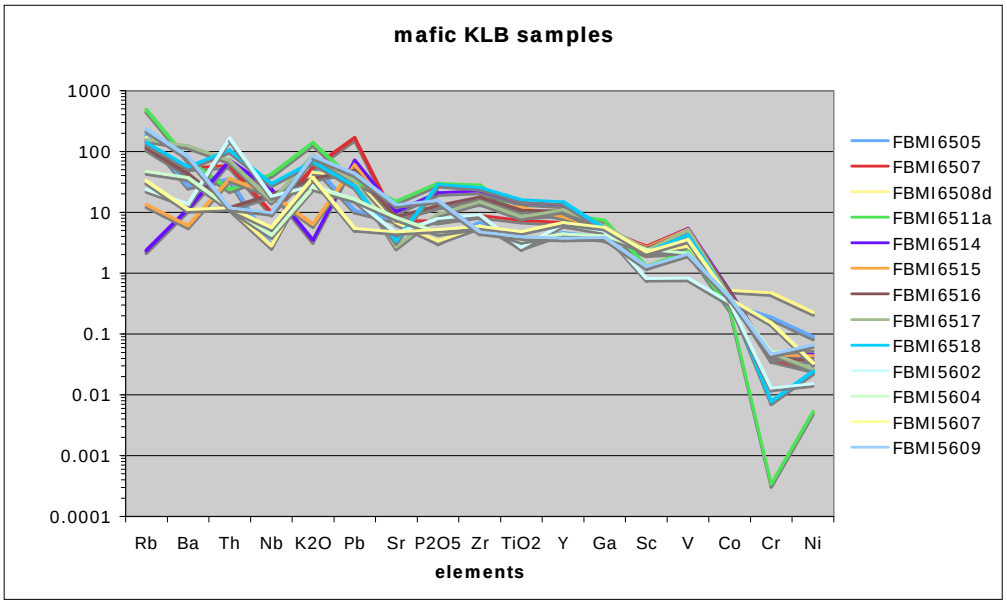

Figure 15

Taking into account discordant data reduces the data set to 5 grains with an estimated age of 785 ± 62 Ma (MSWD =0.3). Re-analysis of several zircons from FBMI-6518 yielded a ^{204}Pb-corrected ^{206}Pb/^{238}U age of 763 ± 85 Ma. Magmatic zircon ages near 750-800 Ma have not previously been reported from the Mt Isa Inlier. Basaltic dikes of this age may be related to magmatic events associated with the break-up of Rodinia; for example, *ca.* 800 Ma mafic rocks are known from large parts of eastern and central Australia (e.g., Condie, 2004; Wingate et al., 2004). The occurrence of extensional tectonics almost 1,000 Ma after the emplacement of its Palaeoproterozoic counterparts might also explain why the mafic dyke is geochemically indistinguishable from the other samples.

U-Th-Pb isotope data for zircons from samples FBMI-6504 and FBMI-6510 (northern portion of the KLB) are listed in Table 2b. The zircons in sample FBMI-6510 are concordant to slightly discordant (Fig.16) and yield an average ^{207}Pb/^{206}Pb age of 1775 ± 6 Ma (MSWD = 1.25, 27 analyses, 2 points with > 1% common Pb omitted), while five analyses from FBMI-6504 (<5% discordant) give an average ^{207}Pb/^{206}Pb age of 1855 ± 8 Ma (MSWD=1.09, Fig.17). Younger ages are indicated for the two measured samples from the southern part of the KLB. Zircons in FBMI-5601 are concordant to ≈20% discordant (Table 2c, Fig.18) and yield an average ^{207}Pb/^{206}Pb age of 1718 ± 6 (MSWD = 2, data >10% discordant excluded). A majority of the analysed zircons in sample FBMI-5605 (Table 2c, Fig. 19) have U>1300ppm and were excluded from consideration because of potential Pb/U calibration problems with high-U zircon. The remaining analyses combine to give a ^{204}Pb-corrected ^{207}Pb/^{206}Pb age of 1722 ± 5 Ma (MSWD =2).

^{176}Hf/^{177}Hf ratios in 21 analysed zircons from sample FBMI-6504 vary from 0.281286 to 0.281661 with typical in-run uncertainties (2se) of <±0.000040 for an individual analysis. Zircons from sample FBMI-6510 show a much smaller range (0.281598 - 0.281773, Table 3; Figure 20). ^{176}Lu/^{177}Hf ratios range from 0.00049 to 0.00209, and 0.00045 to 0.00115, respectively, and are thus considerably lower than in average upper continental crust (0.0078); this is typical of zircon and greatly reduces the size of corrections for ^{176}Hf ingrowth. Multiple Hf isotope analyses of some grains show that Hf isotope zoning is negligible compared to analytical error, consistent with the lack of U-Pb isotopic evidence for distinct zircon cores.

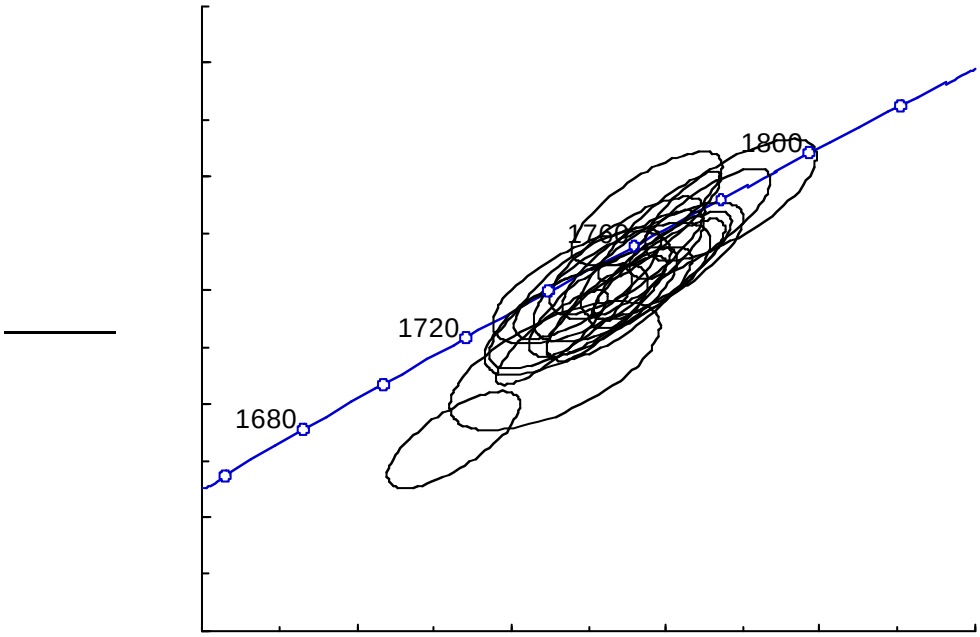

Figure 16: Concordia plot showing SHRIMP U-Pb data for zircons in sample FBMI-6510 from northern KLB. Error ellipses are 1σ. Pooled data for 25 analyses provide an average $^{207}Pb/^{206}Pb$ age of 1775 ± 6 Ma (means square of weighted deviations, MSWD, is 1.25).

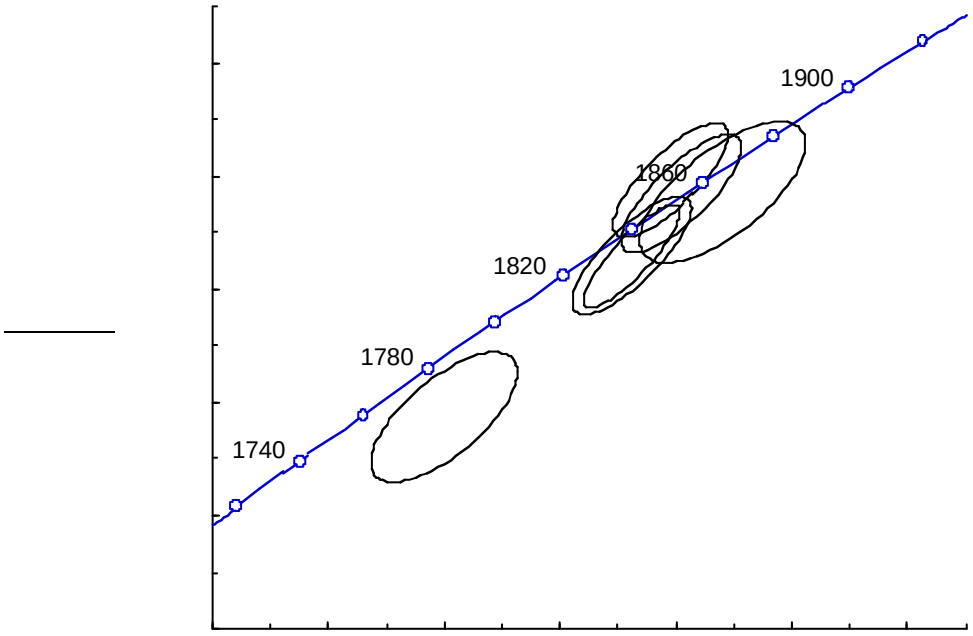

Figure 17: Concordia plot for zircons in sample FBMI-6504 from northern KLB. The average $^{207}Pb/^{206}Pb$ age for 5 concordant to near-concordant analyses is 1855 ± 8 Ma (MSWD 1.09).

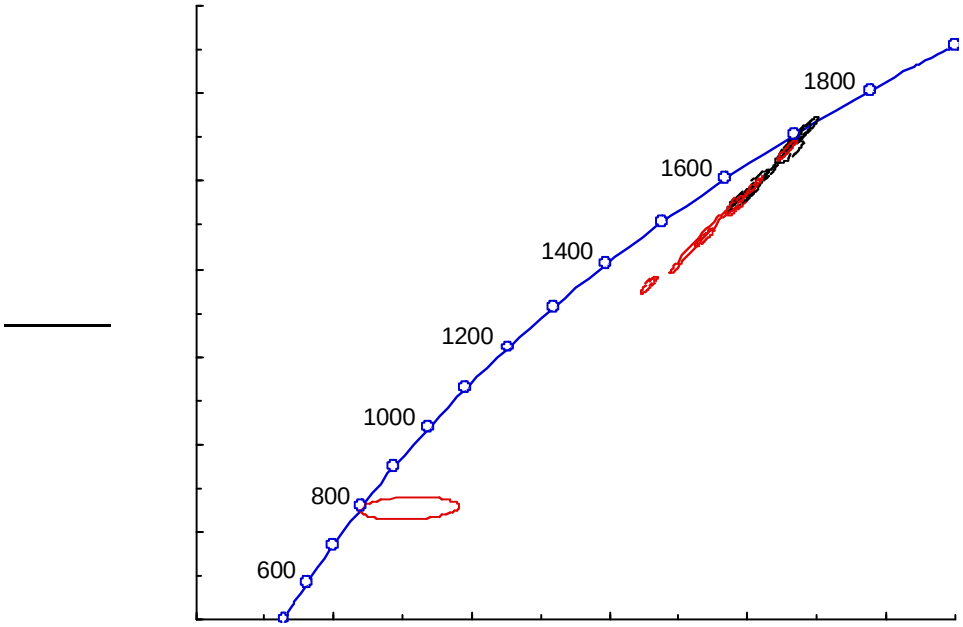

Figure 18: Concordia plot for zircons in sample FBMI-5601 from the southern KLB. Analyses that are <10% discordant (black ellipses) define a $^{207}Pb/^{206}Pb$ age of 1718 ± 6 Ma (MSWD 2). Data >10% discordant (red ellipses) omitted.

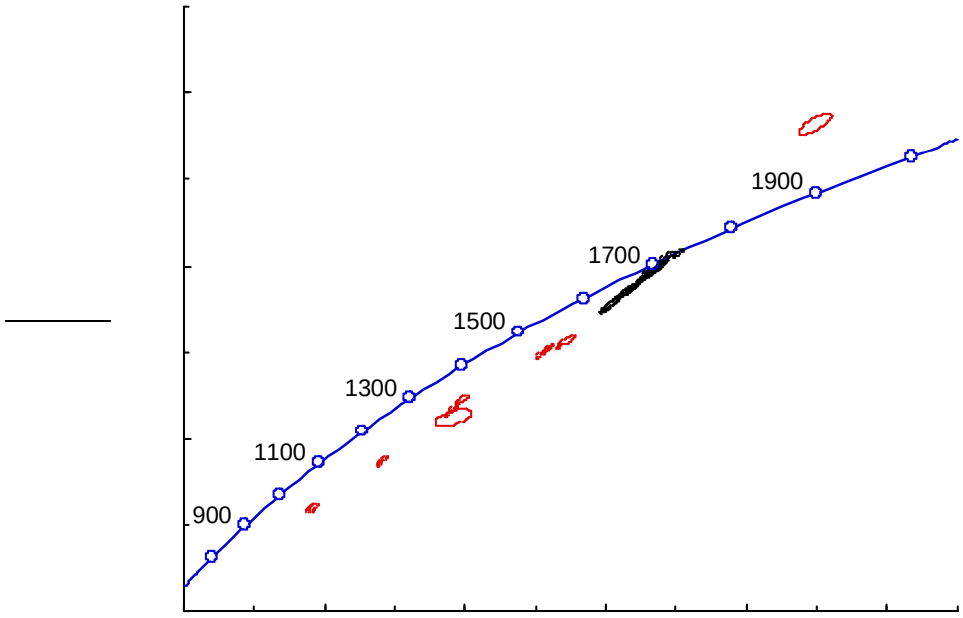

Figure 19: Concordia plot for zircons in sample FBMI-5605 from southern KLB. Most analyses had U.1300 ppm and were ignored (red ellipses, see text). Remaining analyses (black) yield a $^{207}Pb/^{206}Pb$ age of 1722 ± 5 Ma (MSWD 2).

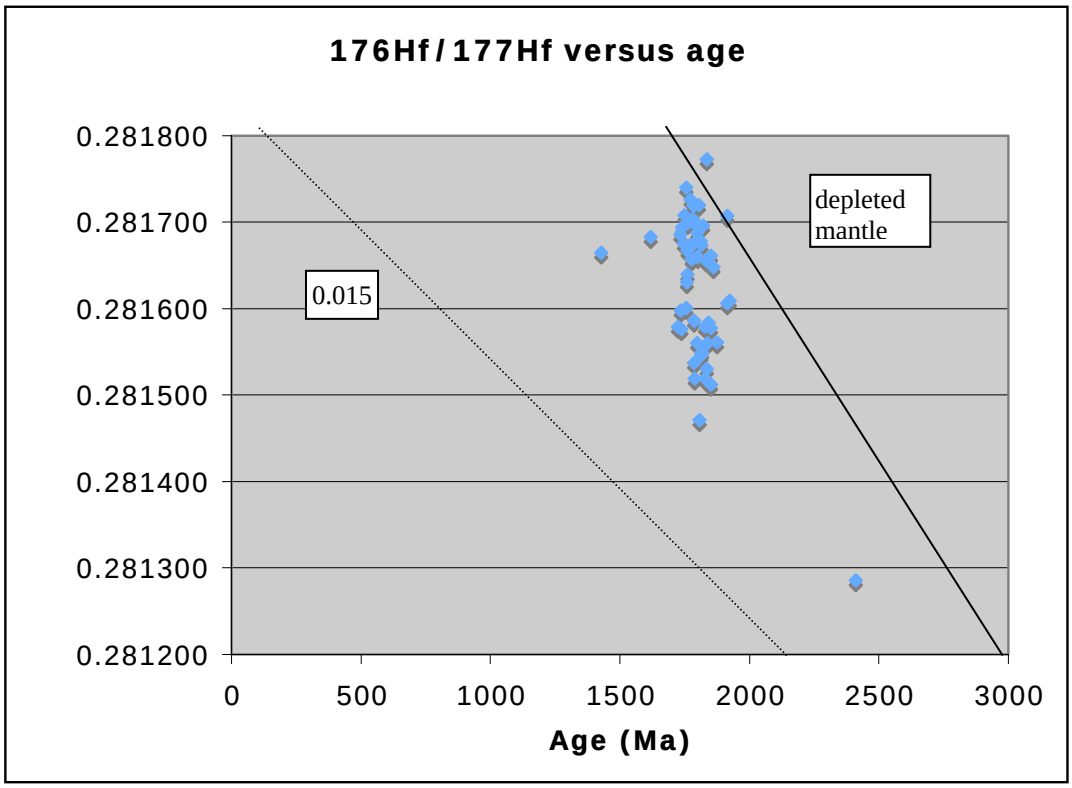

Figure 20: Plot of $^{176}Hf/^{177}Hf$ versus age for zircons in FBMI-6504 and -6510 from the northern KLB. The equivalent range in ε_{Hfi} is ≈ -6 to ≈ +6. Data are compared with model Hf isotope evolutions in depleted mantle (present-day $^{176}Lu/^{177}Hf$ 0.04, $^{176}Hf/^{177}Hf$ 0.283281, from Corfu and Stott, 1993 and Salters and Stracke, 2004, respectively) and in 3.6 Ga crust (using a $^{176}Lu/^{177}Hf$ = 0.015, equivalent to the bulk crustal ratio from Griffin et al., 2006). 3.6 Ga crust was chosen as a limiting end-member based on evidence for zircon inheritanceas old as 3.6 Ga in the Western Fold Belt Ga (Bierlein et al., 2007). The decay constant for ^{176}Lu of 1.865E-11/yr (Scherer et al., 2001).

Initial ε_{Nd} for thirteen samples with ages in the range 1.86-1.72 Ga varies from -4.1 to +2.3 (Table 4). The felsic and dioritic rocks have slightly lower values than the dolerites (-1.3 to -4.1 vs +2.3 to -2.4, see Fig 21). Depleted mantle model ages (T_{DM2}) range from 2.12 to 2.60, suggesting a dominant Paleoproterozoic crustal signature in the source rocks of the 1.86 - 1.72 Ga felsic intrusions from the KLB. The larger ε_{Nd} range in the dolerites and dioritic intrusives presumably reflects mixed of crustal and mantle sources (Fig. 21). Admixture of juvenile components also appears to be important in the mid-Proterozoic TTG and potassic granitoids of the Eastern Fold Belt. The ≈790 Ma mafic dyke in the KLB, with ε_{Ndi} = -7.0, clearly contains a dominantly crustal Nd isotope signature, reflecting extensive modification of the mafic magma through crustal contamination or a magma origin in "enriched" lithospheric mantle.

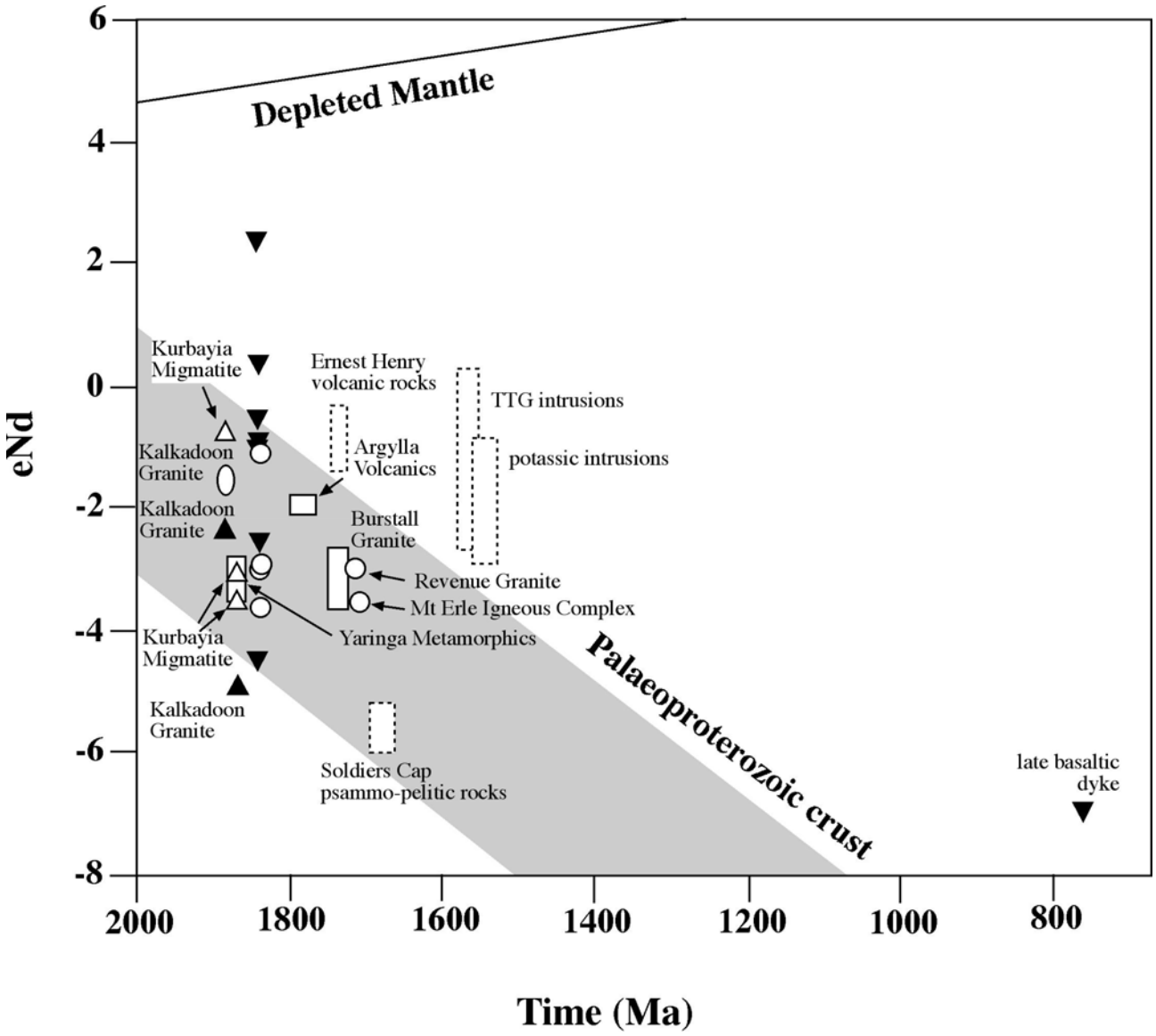

Figure 21: Nd isotope evolution diagram for felsic (open circles) and mafic/intermediate (inverted black triangles) igneous rocks from the Kalkadoon-Leichhardt Belt (this study). Also shown are data for Burstall Granite, Argylla Volcanics (unpubl. data, Geoscience Australia), granite (open ellipsoid) and mafic enclaves (upright black triangles) in Kalkadoon Granite, Kurbayia Migmatites (upright open triangles) and Yaringa Metamorphics from the western Fold Belt (all data from Bierlein and Betts, 2004), and ranges for diverse rock types from the Eastern Fold Belt (i.e., east of the Pilgrim Fault, dashed rectangles; G. Mark, unpubl. data). Evolution trajectories of hypothetical depleted mantle and model Paleoproterozoic continental crust (T_{DM} 2.5-2.0) shown for comparison.

Discussion

The geochemical and isotopic data presented herein, when placed into the context of previous studies and the new Lu-Hf constraints, allow us to make broad inferences regarding the pre-1.8 Ga evolution of the KLB, as well as tectonic and metallogenic comparisons between the KLB and the fold belts on either side.

Petrogenetic constraints from whole-rock geochemistry

The potassic nature of the diorites and granites from the KLB is a common feature of granites throughout the Mt Isa Inlier (e.g., Williams and Naraku batholiths, Pollard et al., 1998; Sybella Granite, Hoadley, 2000), and also typical of batholiths in Proterozoic terranes elsewhere (e.g. Wyborn, 1988; Rämö and Haapala, 1995; Creaser, 1996). The alkali-enriched (but not peralkaline) intrusions typically carry rapakivi-textured K-feldspar phenocrysts, which result from variations in the stability of the crystallizing feldspar during magma mixing and mingling. Most rapakivi granites elsewhere are classified as 'A-type' or 'within-plate' and are thought to be derived from (high-temperature) melting of older (i.e. Proterozoic or Archaean) crust (Wyborn, 1988). As illustrated in Figure 10, about 50% of the KLB diorites and granites plot in the field of within-plate granites. However, the extent of the negative Nb anomaly with respect to Th in all samples is indicative of the involvement of subduction in an arc-like setting, as Nb is preferentially retained in high-pressure stable phases such as amphiboles, titanite and rutile in the subducting plate (e.g., Pearce and Peate, 1995). Conversely, the high K concentrations, low Ti/Y and Sr/Y ratios, and lack of Y depletion in these samples suggest that their source was garnet-absent and contained a significant concentration of K-bearing phases. The lack of a high Ti/Y ratio also suggests that melting occurred at relatively shallow levels, unlike those expected in a typical intra-plate setting. Thus, garnet formation would have been inhibited due to pressures below 8 to 10 kbar (Drummond and Defant, 1990), or garnet could have been melted out due to the relatively high degree of partial melting caused by added water from the subduction process. On the other hand, estimated temperatures of magma generation for the KLB diorites and granites range from approximately 780˚ to 980˚C (c.f. SiO_2 vs P_2O_5 in Fig. 8), suggesting partial melting of amphibole-bearing crust occurred predominantly under fluid-absent conditions. Heating of continental crust to bring on extensive melting in that temperature range would require the injection of mantle-derived melts (Clemens and Vielzeuf, 1987; Hoardley, 2000). This mechanism, in turn, would have promoted magma mixing and mingling of originally heterogeneous melts to produce the fractional crystallization and hybridization processes (enclaves) that are so widespread in the Kalkadoon Batholith (e.g., Christiansen and Keith, 1996). Significant crustal contamination of the parental magmas that gave rise to the KLB diorites and granites is also apparent from the relatively high Th enrichment, with the degree of continental assimilation greater than what has been observed in felsic intrusions from the Western Fold Belt (Bierlein and Betts, 2004). This is in contrast to the findings by McDonald et al. (1997) who argued on the basis of strongly fractionated REE and persistent significant Nb, Ti and P anomalies (in primitive mantle normalized plots) that the Kalkadoon Batholith was characterized by a strong arc-like geochemical affinity.

The mafic enclaves and dolerites from the KLB are compositionally diverse and thus cover a range of model tectonic settings on Pearce-type discrimination plots. This may be accounted for by magma mixing and mingling of heterogeneous melts in a transitional tectonic setting. The least fractionated of the mafic rocks samples have sub-alkaline MORB-like characteristics, while the most fractionated samples displaying within-plate affinities (Fig. 12c; note that fractional crystallization has little effect on the Ti-Zr-Y composition of these basaltic rocks; Dudás, 1992). Hi Fe contents in some of the mafic samples may reflect thinning and melting of the lithosphere in the source region. It has long been recognized that the geochemical characteristics of basalts derived from magmas that form in areas of attenuated continental lithosphere (i.e., 'within-plate') can significantly depart from their typical affinity and resemble volcanic-arc or even MORB basalts (Pearce, 1996, and references therein). Thus, some ambiguity remains regarding the 'true nature' of the geodynamic setting for the formation of the mafic precursor rocks of the enclaves within diorites and granites from the KLB. The pattern in Figure 12c can be best explained by a combination of processes that involved variable degrees of partial melting of a metasomatised mantle wedge in an attenuated continental (possibly back-arc) setting, coupled with crustal subduction and/or assimilation of upper crustal material with volcanic-arc-like characteristics.

Significance of SHRIMP U-Pb and Sm-Nd data

The SHRIMP age of 1855 ± 8 Ma for sample FBMI-6504 is in good agreement with the accepted *ca.* 1.87 – 1.85 Ga age of emplacement of the Kalkadoon Batholith (Page and Williams, 1988; McDonald et al., 1997; Bierlein et al., 2007). In contrast, the younger zircon ages, from *ca.* 1.85 to 1.75 Ga, and the 1775 ± 6 Ma age for sample FBMI-6510 are unexpected and somewhat difficult to reconcile with field and petrographic evidence which would predict a ca. 1.86 Ga age for this pink, plagioclase-bearing porphyritic granite. Inspection of the FMBI-6510 zircons and SHRIMP U-Pb data shows no obvious problems with the zircon age: the grains appear generally homogeneous without evidence for cores and/or metamorphic/hydrothermal overgrowths, common lead is low, the data points are largely concordant, Th/U ratios are within the magmatic range, and the age is based on a well-clustered population of $^{207}Pb/^{206}Pb$ ages, i.e. it is not susceptible to Pb/U calibration problems in the ionprobe. The *ca.* 1.78 Ga age for sample FBMI-6510 is therefore considered a valid estimate for the emplacement of this intrusion. Elsewhere, magmatic ages in the range 1.79-1.73 Ga are known from widespread, bimodal magmatism in the Leichhardt Superbasin (Betts et al., 2006; Neumann et al., 2006), but magmatic activity in the western Fold Belt during this period produced mainly mafic volcanics (e.g., Eastern Creek Volcanics) and was limited to the margins of the superbasin in the north-south orientated Leichardt River Fault Trough (O'Dea et al., 1997). Sample FBMI-6510, collected to the NE of Lake Julius well within the KLB, shows a co-magmatic

relationship with the surrounding dioritic-granitic phase of the Kalkadoon Batholith (Fig 2) and is quite different from the basaltic rocks of the Eastern Creek Volcanics or their equivalents (Wilson et al., 1984). The most plausible explanation therefore is that this intrusion forms part of the *ca.* 1.78 – 1.74 Ga Argylla Suite (e.g., Wilson, 1978), which is characterised by pinkish-grey, porphyritic rhyolite and dacite. Although more widespread in the eastern and western fold belts, Wilson (1978) documented an occurrence of ryholitic volcanics belonging to the Argylla Formation within the outcrop area of the Kalkadoon Granite just south of the Mt Remarkable Fault (Fig. 1). The *ca.* 1.78 Ga Mairindi Creek (approx. 4 km north of Dutchess) and Bowlers Hole A-type granites in the southern part of the KLB were also considered to be part of this suite (Budd et al., 2001). By contrast, the Mt Erle Igneous Complex (sample FBMI5601; *ca.* 1718 Ma) and Revenue Granite (sample FBMI5605; *ca.* 1722 Ma) belong to the *ca.* 1.74 – 1.72 Ga Burstall Suite which intrudes the southern and central portions of the Kalkadoon Batholith (Page and Sun, 1998). Both of these granites show A-type affinities, are spatially associated with minor (Fe-oxide?) Au-Cu mineralisation (Budd et al., 2001) and probably represent the products of relatively fractionated, late-stage melts that developed towards the end of the Burstall magmatic event.

An important observation in the zircon data reported here and by others is the apparent paucity of inherited zircons in granitoids from the northern, central, and southern portions of the KLB. An absence of inherited zircon could be interpreted in terms of relatively young magma sources. This echoes Wyborn and Page (1983) and McCulloch (1987) who argued - on the basis of Nd model ages and zircon U-Pb ages - that crustal material within the Mt Isa Inlier had largely formed by differentiation from the mantle at 2.1 - 1.9 Ga. However, detrital zircon cores as old as ≈ 2.2 Ga from the Yaringa Metamorphics and Leichhardt Metamorphics were considered to provide a maximum age for supracrustal migmatitic protoliths in the Western Fold Belt and the KLB (Page and Williams, 1988). McDonald et al. (1997) reported a number of 2.42 - 2.50 Ga zircon cores from the “Black Angel Gneiss” in the western part of the KLB and argued that the crustal evolution of the Kalkadoon-Leichhardt Belt commenced in the Late Archaean. Nd model ages of 2.42 - 2.58 Ga for the same rocks were thought to be consistent with this model while T_{DM} ages of 2.75 to 2.83 Ga for mafic supracrustal units were considered to indicate the presence of even older Archaean crust (McDonald et al., 1997). U-Pb zircon ages of 2.53 to 2.5 Ga were also reported by Griffin et al. (2006), for recycled zircons in modern stream sediments from a large portion of the Eastern Fold Belt. These data indicate that much of the Mt Isa Inlier are comprised of rocks with similar isotopic characteristics that can be used to suggest that the basement to the inlier is broadly homogeneous and formed at the same time.

More recent work by Bierlein and Betts (2004) on pre-1.8 Ga basement lithologies from both sides of the Mt Isa Fault confirmed the Late Archaean to Early Proterozoic timing of initial

crust formation in the Western Fold Belt and at least the western part of the KLB. In-situ $^{176}Hf/^{177}Hf$ isotope data of zircons published in Bierlein et al. (2007) confirmed that Archaean – Palaeoproterozoic magmatic zircons from both the Western Fold Belt and the western part of the KLB were sourced from the same parental lithospheric isotopic reservoir, which evolved over time from more primitive mantle to more supracrustal compositions, without significant contributions from juvenile sources in the Palaeoproterozoic. The oldest inherited zircons recorded by Bierlein et al. (2007) yield SHRIMP ages of *ca.* 3.6 – 3.3 Ga, representing the earliest geochronological evidence for the existence of an Archaean protolith in the western Mt Isa Inlier. Although not diagnostic of the nature and age of the basement beneath this region, these inherited zircons, together with isotopic data from other studies, are permissive of a tectonic reconstruction involving Archaean crust underlying much of the Proterozoic succession in the Western Fold Belt, and possibly at least the northern and central portions of the KLB. The lack of inherited zircons in samples FBMI-6504 and FBMI-6510 can be accounted for by *in-situ* growth of zircon during upper amphibolite facies metamorphism, or extensive reaction of the magma during ascent and emplacement at ca. 1.86 Ga and 1.78 Ga, respectively.

The close similarity in Hf isotopic compositions of felsic intrusive rocks from the northern segment of the KLB with those from the western portion of the central KLB and Palaeoproterozoic basement rocks from west of the Mt Isa Fault constrains their thermo-tectonic evolution and strongly supports the notion that the composition of these rocks formed as a result of crustal reworking of a common protolith. The general lack of inherited zircons in samples FBMI-6504 and -6510 is consistent with observations reported in previous studies (e.g., Page, 1983; Wyborn, 1988; Bierlein et al., 2007). A sample from a mafic enclave within Kurbayia Migmatites in the central portion of the KLB analysed for inherited zircons by Bierlein et al. (2007) also lacked evidence for inheritance. Due to a general lack of exceedingly low Th/U ratios that characterise many metamorphic zircons (Rubatto, 2002), absence of complex zonation patterns and internal age coherence of zircons analysed in the study by Bierlein et al. (2007), and virtually no evidence for a ~1,100˚ C intrusion in the Kalkadoon Batholith that could account for the near-quantitative melting of inherited zircons in the enclave, these authors concluded that these intrusions derived from a Zr-undersaturated, mafic to intermediate precursor. The same explanation is considered applicable to the northern segment of the KLB, and supported by Hf isotopic compositions of zircons that point to their derivation from a heterogeneous source with contributions from both primitive (mantle) material and older crustal components. Such a scenario can also account for the apparent lack of inherited zircons in *ca.* 1.74 and 1.55 – 15. Ga intrusions east of the Pilgrim Fault (e.g., Page and Sun, 1998; Davis et al., 2001), rather than having to invoke a model that precludes the existence of older (possibly Archaean) components within the basement in the eastern Fold Belt. Similarly, it

can explain why metasedimentary rocks such as the Soldiers Cap Group lack inherited *ca.* 1.89 – 1.84 Ga zircons (e.g., Giles and Nutman, 2002), even if they were derived solely from crystalline units in the KLB.

Tectonic setting of the KLB and metallogenic considerations

The above data indicate that much of the western and central portions of Mt Isa Inlier consist of rocks with similar isotopic characteristics which, in turn, can be used to suggest that the basement to the Western Fold Belt and KLB is broadly homogeneous and formed at the same time. The ca. 2.36 and 2.60 Ga T_{DM} ages of felsic and mafic igneous rocks from across the KLB are very similar to those reported from the Western Fold Belt and western KLB by previous workers (e.g., McDonald et al., 1997; Bierlein and Betts, 2004) and confirm that these portions of the Mt Isa Inlier were underlain by an isotopically indistinguishable lithospheric block, with both felsic and mafic intrusions sampling Palaeoproterozoic to late Archaean basement. In contrast, detailed Sm-Nd isotopic data across the inlier (Page and Sun, 1998; Mark, 2001; G. Mark, unpublished) show that the basement rocks to the east of the Pilgrim Fault probably represent an allochthonous block that was accreted to the inlier between 2.20 Ga and 1.85 Ga. As illustrated in Figure 21, most of the ca. 1.74 – 1.50 Ga magmatic rocks in the Eastern Fold Belt are isotopically distinct and characterised by younger average crustal residence ages (T_{DM} ca. 2.08 – 2.30 Ga). This apparent contrast in Nd T_{DM} of the source material was considered by Page and Sun (1998) to represent either the result of significantly greater mafic underplating of a common protolith, or that the Eastern Fold Belt was an allochthonous block. Given the lack of a more heterogeneous spread of Nd T_{DM} ages - which would be expected if magmatism in the Eastern Fold Belt were the result of mixing between old basement and various proportions of juvenile material following underplating - and the isotopically homogenous profile of Argylla intrusions in both the KLB and the Eastern Fold Belt (Fig. 21), we favour a model involving the accretion of the allochthonous Eastern Fold Belt to the North Australian Craton margin some time prior to *ca.* 1.86 Ga. In light of the geochemical and isotopic data presented herein, the preferred model for the pre-1.8 Ga evolution of the KLB involves its derivation from an older, Palaeoproterozoic to Archaean crust (or magmatic arc) that was rejuvenated by the injection of mantle material and possible contributions from a subducting slab associated with the amalgamation of the North Australian Craton. In terms of their geochemical characteristics, tectonic affinities and Nd T_{DM} profiles, the intrusive rocks of the KLB are closely aligned with the Western Fold Belt, but dominated by a less obvious arc-like signature and a greater extent of crustal assimilation (Figs 21, 22). The distribution of rocks belonging to the Argylla magmatic suite across all three segments of the Mt Isa Inlier, as well as the Palaeoproterozoic to

Archaean isotopic source signature of psammo-pelitic rocks of the Soldiers Cap Formation in the eastern Fold Belt (Fig. 21) confirm that the amalgamation of the western Fold Belt and the KLB with the eastern Fold Belt had been completed well prior to *ca.* 1.78 Ga.

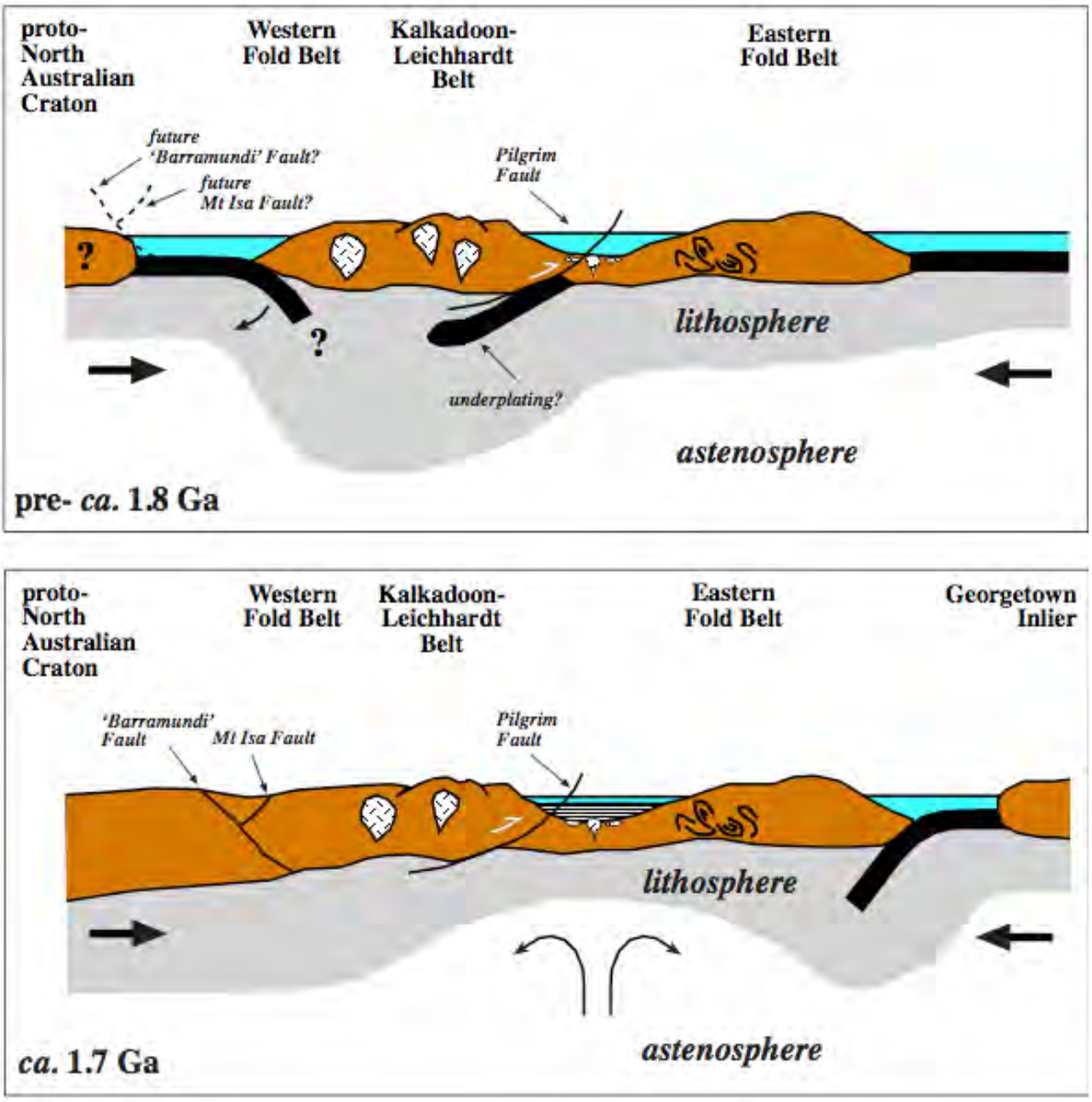

Figure 22: composite tectonic make-up of the Mt Isa Inlier prior to *ca.* 1.8 Ga (top) and *ca.* 1.7 Ga (bottom). The 'Barramundi' Fault represents the future 'back stop' suture on the western side of the evolving Inlier, with the Pilgrim Fault demarcating the collisional suture between the amalgamated western Fold Belt and the KLB, and the eastern Fold Belt. Plume-induced or back-arc extensional thinning of the lithosphere to as little as 10km (B. Collins, pers. comm.. 2007) underneath the Eastern Fold Belt gave rise to IOCG in the eastern Fold Belt.

Their derivation from a thickened (but attenuated following the Barramundi Orogeny), metasomatised continental lithosphere, and fractionation processes involved in the formation of the magmas, are less likely to favour the generation of major IOCG deposits in the KLB, when compared to the tectonic setting of the Eastern Fold Belt in the Mid-Proterozoic. This is because IOCGs are related spatially and temporally with widespread anorogenic, alkaline or A-type granitic igneous events in an intracratonic setting in lithosphere that is several hundred million years older than the metallogenic event (Groves and Bierlein, 2007). These associations strongly suggest that iron-oxide Cu-Au deposits are related to plume-induced partial melting of SCLM previously metasomatised during subduction or other tectonic processes along cratonic margins. The deposits are spatially and temporally related to less fractionated, subalkaline to alkaline granites that were emplaced at relatively high crustal levels, in a tectonic setting dominated by transpression and basin inversion in a long-lived arc-parallel fault system related to subduction (e.g., South American Cordillera; Groves and Bierlein, 2007, and references therein). In view of the post-1.8 Ga deformation history of the KLB, which involved attenuation, and subsequent thickening, underplating and uplift of the central section of the Mt Isa Inlier (e.g., Betts et al., 2006), the crustal levels currently exposed in the KLB would indicate that this long-lived and uplifted basement region of the Inlier is characterised by a relatively poor preservation potential for most deposit types that form in shallow crustal levels in arc and backarc settings.

Conclusions

In spite of a general absence of inherited zircons in two samples from felsic igneous phases of the northern and central portions of the KLB, whole-rock geochemical and Lu-Hf data presented herein confirm findings of previous studies that have proposed formation of the KLB from older, Palaeoproterozoic to Archaean crust with arc affinities, and varying degrees of crustal contamination. These data support a model whereby the pre-1.8 Ga evolution of the KLB was closely aligned with that of the Western Fold Belt in terms of their tectonic setting and lithospheric make-up, but the KLB may represent the remnant of a magmatic arc or transitional continental ribbon inboard of the zone of active subduction during the amalgamation of the North and West Australian cratons. Marked differences in the isotopic and geochemical signature of deeper crustal rocks in the Eastern Fold Belt suggest that this portion of the inlier underwent a distinct thermo-tectonic history in the Palaeoproterozoic and was accreted to the margin of the amalgamating North Australian Craton between *ca.* 2.2 and 1.85 Ga. The apparent differences in lithospheric evolution and tectonic make-up can account for the distinct metallogenic character and mineral potential of the Eastern Fold Belt, when compared with that of the KLB and the Western Fold Belt.

Acknowledgements

Input from Bruce Schaefer and Geordie Mark (Monash University), Nick Oliver (James Cook University), Laurie Hutton (Queensland Department of Mines and Energy), and Barry Murphy (University of Melbourne) have helped clarifying the concepts expressed in this report. R. Korsch and David Champion (Geoscience Australia) are thanked for assistance with XRF analyses; Russell Smits (Monash University) assisted with sample preparation and processing. Cindi Mispagel (University of Western Australia) is acknowledged for performing SHRIMP U-Pb analysis of zircons at the Western Australian SHRIMP facilities operated by a WA university-government consortium with ARC support.

References

Belshaw, N, Freedman, P.A., O'Nions, R.K., Frank, M., Guo, Y., 1998. A new variable dispersion double-focussing plasma mass spectrometer with performance illustrated for Pb isotopes. Int. J. Mass Spect. and Ion Process. 181, 51-58.

Betts, P.G., Giles, D., Mark, G., Lister, G.S., Goleby, B.R., Ailleres, L., 2006. Synthesis of the Proterozoic evolution of the Mt Isa Inlier. Aust. J. Earth Sci. 53, 187-211.

Bierlein, F.P., Betts, P.G., 2004. The Proterozoic Mt Isa Fault Zone, northeastern Australia – is it really a ca. 1.9 Ga terrane-bounding suture? Earth Planet. Sci. Lett. 225, 279-294.

Bierlein, F.P., Black, L.P., Hergt, J., Mark, G., 2007. Evolution of pre-1.8 Ga basement rocks in the western Mt Isa Inlier, northeastern Australia – insights from SHRIMP U-Pb dating and *in-situ* Lu-Hf analysis of zircons. Precambrian Research (in press).

Blake, D.H., 1987. Geology of the Mount Isa Inlier and environs, Queensland and Northern Territory. Bureau of Mineral Resources Australia Bulletin 225, 83 pp.

Budd, A.R., Wyborn, L.A.I., Bastrakova, I.V., 2001. The metallogenic potential of Australian Proterozoic Granites. Geoscience Australia, Record, 2001/1.

Christiansen, E.H., Keith, J.D., 1996. Trace element systematics in silicic magmas: a metallogenic perspective. In: Wyman, D.A. (Ed.), Trace Element Geochemistry of Volcanic Rocks: Applications for Massive Sulphide Exploration. Geol. Assoc. Can. Short Course Notes 12, pp. 115-151.

Clemens, J.D., Vielzeuf, D., 1987. Constraints on melting and magma production in the crust. Earth and Planetary Sciences Letters, 86, 287-306.

Condie, K.C. 2005. Earth as an Evolving Planetary System. Elsevier Academic Press, Amsterdam, 447p.

Corfu, F., Stott, G.M., 1993. Age and petrogenesis of two late Archaean magmatic suites, northwestern Superior Province, Canada; zircon U-Pb and Lu-Hf isotopic relations. J. Petrol. 34, 817-838.

Creaser, R.A., 1996. Petrogenesis of a Mesoproterozoic quartz latite-granitoid suite from the Roxby Downs area, South Australia. Precambrian Research, 79, 371-394.

Davis, B.K., Pollard, P.J., Lally, J.H., McNaughton, N.J., Blake, K., Williams, P.J., 2001. Deformation history of the Naraku Batholith, Mt Isa Inlier, Australia: implication for pluton ages and geometries from structural study of the Dipvale Granodiorite and Levian Granite. Aust. J. Earth Sci. 48, 113-129.

Drummond, B.J., Goleby, B.R., Goncharov, A.G., Wyborn, L.A.I., Collins, C.D.N., MacCready, T., 1998. Crustal-scale structures in the Proterozoic Mount Isa Inlier of North Australia: their seismic response and influence on mineralization. Tectonophysics, 288, 43-56.

Drummond, M.S., Defant, M.J., 1990. A model for trondhjemite-tonalite-dacite genesis and crustal growth via slab melting: Archaean to modern comparisons. Journal of Geophysical Research, 95, 21,503-21,521.

Dudás, F.O., 1992.Petrogenetic evaluation of trace element discrimination diagrams. In: Batholomew, M.J., Hyndman, D.W., Mogk, D.W., Mason, R. (Eds.), Basement Tectonics 8, Kluwer, Dordrecht, pp. 93-127.

Eggins, S.M., Woodhead, J.D., Kinsley, L.P.J., Mortimer, G.E., Sylvester, P., McCulloch, M.T., Hergt, J.M., Handler, M.R., 1997. A simple method for the precise determination of >40 trace elements in geological samples by ICPMS using enriched isotope internal standardization. Chemical Geology, 134, 311-326.

Giles, D., Nutman, A.P., 2002. SHRIMP U-Pb monazite dating of 1600-1580 Ma amphibolite facies metamorphism in the southeastern Mt Isa Block, Australia, Australian Journal of Earth Sciences, 49, 455-465.

Griffin, W.L., Belousova, E.A., Walters, S.G., O'Reilly, S.Y., 2006. Archaean and Proterozoic crustal evolution in the Eastern Succession of the Mt Isa district, Australia: U-Pb and Hf-isotope studies of detrital zircons. Australian Journal of Earth Sciences, 53, 125-149.

Groves, D.I., Bierlein, F.P., 2007. Geodynamic settings of mineral deposit systems. Journal of the Geological Society of London, 164, 19-30.

Hoadley, E., 2000. Evolution of the Sybella Batholith, Mount Isa: magma mingling, mixing and emplacement. PhD Annual Report, James Cook University (unpublished).

Le Maitre, R.W., Bateman, P., Dudek, A., Keller, J., Lemeyre, J., Le Bas, M. J., Sabine, P.A., Schmid, R., Sorensen, H., Streckeisen, A., Wooley, A.R., Zanettin, B., 1989. Classification of igneous rocks and glossary of terms. Blackwell Science Publications, Oxford, United Kingdom, 193pp

Ludwig, K.R., 2001**.** SQUID 1. Berkeley Geochronology Center.

Maas, R., Kamenetsky, M.B., Sobolev, A.V., Kamenetsky, V.S., Sobolev, N.V., 2005. Sr-Nd-Pb isotopic evidence for a mantle origin of alkali chlorides and carbonates in the Udachnaya kimberlite, Siberia. Geology, 35, 549-552.

MacCready, T., 2006. Structural cross-section based on the Mt Isa deep seismic transect. Aust. J. Earth Sci. 53, 5-26.

MacCready, T., Goleby, B.R., Goncharov, A., Drummond, B.J., Lister, G.S., 1998. A framework of overprinting orogens based on interpretation of the Mount Isa deep seismic transect, Economic Geology, 93, 1422-1434.

Mark, G., 2001. Nd isotope and petrogenetic constraints for the origin of the Mount Angelay igneous complex: Implications for granitoid formation in the Cloncurry district, Australia. Precamb. Res. 105, 17-35.

McDonald, G.D., Collerson, K.D., Kinny, P.D., 1997. Late Archean and Early Proterozoic crustal evolution of the Mount Isa block, northwest Queensland, Australia. Geology 25, 1095-1098.

Neumann, N.L., Southgate, P.N., Gibson, G.M., McIntyre, A., 2006. New SHRIMP geochronology for the Western Fold Belt of the Mt Isa Inlier: developing a 1800–1650 Ma event framework. Aust. J. Earth Sci., 53, 1023-1039.

Norrish, K., Chappell, B.W., 1977. X-ray fluorescence spectrometry. In: Zussman, J. (Ed.), Physical Methods in Determinative Mineralogy, 2nd Edition. Academic Press, London, pp. 201-272.

Norrish, K., Hutton, J.T., 1969. An accurate X-ray spectrographic method for the analysis of a wide rage of geological samples. Geochim. Cosmochim. Acta, 33, 431-453.

Page, R.W., 1983. Timing of superposed volcanism in the Proterozoic Mount Isa Inlier, Australia, Precambrian Research, 21, 223-245.

Page, R.W., Williams, I.S., 1988. Age of the Barramundi orogeny in northern Australia by means of ion microprobe and conventional U-Pb zircon studies. Precamb. Res. 40/41, 21-36.

Page, R.W., Sun, S-S., 1998. Geochronology and Sm-Nd provenance studies in the Eastern fold belt, Mount Isa inlier, Aust. J. Earth Sci. 45, 343-362.

Pearce, J.A., 1996. A user's guide to basalt discrimination diagrams. In: Wyman, D.A. (Ed.), Trace Element Geochemistry of Volcanic Rocks: Applications for Massive Sulphide Exploration. Geol. Assoc. Can. Short Course Notes 12, pp. 79-113.

Pearce, J.A., Peate, D.W., 1995. Tectonic implications of the composition of volcanic arc magmas. Annual Review of Earth Planetary Sciences, 23, 251-285.

Pearce, J.A., Ernewein, M., Bloomer, S.H., Parson, L.M., Murton, B.J., Johnson, L.E., 1994. Geochemistry of Lau Basin volcanic rocks. Geological Society of London Special Publications, 81, p. 53-75.

Pyke, J., 2000. Minerals laboratory staff develops new ICP-MS preparation method. AGSO Newsletter, 33, 12-14.

O'Dea, M.G., Lister, G.S., MacCready, T., Betts, P.G., Oliver, N.H.S., Pound, K.S., Huang, W., Valenta, R.K., 1997. Geodynamic evolution of the Proterozoic Mount Isa terrane, in: J.P. Burg, M. Ford (Eds.), Orogeny Through Time. Geological Society of London Special Publication 121, pp. 99-122.

Rämö, O.T., Haapala, I., 1995. One hundred years of rapakivi granite. Mineralogy and Petrology, 52, 129-185.

Rubatto, D., 2002. Zircon trace element geochemistry: partitioning with garnet and the link between U–Pb ages and metamorphism. Chemical Geology, 184, 123-138.

Richard, P., Shimizu, N., Allegre, C.J., 1976. $^{143}Nd/^{144}Nd$, a natural tracer: An application to oceanic basalts, Earth and Planetary Science Letters, 31, 269-278.

Rudnick, R.L., Fountain, D.M., 1995. Nature and composition of the continental-crust—a lower crustal perspective. Rev. Geophys. 33, 267–309.

Salters, V.J.M., Stracke. A., 2004. Composition of the depleted mantle. Geochemistry Geophysics Geosystems, 5, Issue 5, CiteID Q05004.

Scherer, E., Münker, C., Mezger, K., 2001. Calibration of the Lutetium-Hafnium Clock. Science, 293, 683-687.

Shapiro, L., Brannock, W.W., 1962. Rapid analysis of silicate, carbonate and phosphate rocks. United States Geological Survey Bulletin, 1144-A.

Tulloch, A.J., Kimbrough, D.L., 2003. Paired plutonic belts in convergent margins and the development of high Sr/Y magmatism: Peninsular Ranges Batholith of Baja California and Median Batholith of New Zealand. Geol. Soc. Am. Special Paper 374, pp. 275–295.

Vance, D., Thirlwall, M.F., 2002. An assessment of mass discrimination in MC-ICPMS using Nd isotopes, Chemical Geology, 185, 227-240.

Wilson, I.H., Derrick, G.M., Perkin, D.J., 1984. Eastern Creek Volcanics: their geochemistry and possible role in copper mineralization at Mount Isa, Queensland. BMR Journal of Australian Geology & Geophysics, 9, 317-328.

Wilson, I.H., 1978. Volcanism on a Proterozoic continental margin in northwestern Queensland. Precambrian Research, 7, 205-235.

Winchester, J.A., Floyd, P.A., 1977. Geochemical discrimination of different magma series and their differentiation products using immobile elements. Chemical Geology, 20, 325-343.

Wingate, M.T.D., Pirajno, F., Morris, P.A., 2004. The Warakurna large igneous province: a new Mesoproterozoic large igneous province in west–central Australia. Geology, 32, 105–108.

Woodhead, J.D., 2002. A simple method for obtaining highly accurate Pb isotope data by MC-ICP-MS, Journal of Analytical Atomic Spectrometry, 17, 1-6

Woodhead, J., Hergt, J., Shelly, M., Eggins, S., Kemp, R., 2004. Zircon Hf-isotope analysis with an excimer laser, depth profiling, ablation of complex geometries, and concomitant age estimation. Chem. Geol. 209, 121-135.

Wyborn, L.A.I., 1988. Petrology, geochemistry and origin of a major Australian 1880-1840 Ma felsic volcano-plutonic suite: a model for intracontinental felsic magma generation. Precamb. Res. 40/41, 37-60.

Wyborn, L.A.I., Page, R.W., 1983. The Proterozoic Kalkadoon and Ewen Batholiths, Mount Isa Inlier, Queensland: source, chemistry, age, and metamorphism. BMR Journal of Australian Geology & Geophysics, 8, 53-69.

Table 1: whole-rock data for 34 igneous samples from the Kalkadoon-Leichhardt Belt.

Table 2: Summarised SHRIMP U-Pb data for 5 felsic intrusive samples (FBMI-6504, -6510, -6518, 5601, 5605) from the Kalkadoon-Leichhardt Belt.

Table 3: $^{176}Hf/^{177}Hf$ data for zircons from two felsic intrusions (FBMI-6504, and -6510) in the northern Kalkadoon-Leichhardt Belt. where possible, corresponding age information from SHRIMP U-Pb analysis of the same grain is also listed. Suffices '1' and '2' refer to core-rim analyses of the same grain.

Table 4: Summary data for Nd and Sm concentrations and isotopic ratios for 14 felsic and mafic igneous samples from the Kalkadoon-Leichhardt Belt.

TECTONOTHERMAL AND METASOMATIC EVOLUTION OF THE MOUNT ISA INLIER

Mike Rubenach
School of Earth and Environmental Sciences
James Cook University

Table of Contents

SUMMARY – MAIN POINTS

- High grade and lower grade metamorphic belts alternate EW across the inlier. Although their present dips are unknown, is proposed that the isograd surfaces originally had shallow dips**.**
- The Wonga Event (~1740 Ma) and the Sybella Event (~1670 Ma) are significant but localized high-grade shear zone events associated with granite and gabbro/dolerite emplacement that occurred prior to the Isan Orogeny. New age determinations indicate that two tectonothermal episodes occurred during the Sybella Event in the May Downs Gneiss, with earlier cordierite/Kfeldspar assemblages overprinted by migmatitic biotite/sillimanite/Kfeldspar gneisses.
- A new monazite age of 1651 Ma places constraints on the early albitization and cordierite growth in the Selwyn Zone. Whether or not the albitization/cordierite growth is included in the Isan Orogeny is a matter of definition.
- The peak of metamorphism in the Isan Orogeny (D_2 events) occurred ~1580 Ma in both the Mary Kathleen/Duchess Zone and the Mount Isa area, but an extended period, 1580-1595 Ma, is suggested by age dates from the Selwyn Zone.
- A new monazite age determination of 1596± 27 Ma for the Mica Creek Pegmatites is consistent with structural interpretations that they formed during D_2. Thus pegmatites occur in sillimanite zone metamorphics throughout the Inlier.
- Both the Mary Kathleen/Duchess Zone and the Mount Isa area show anticlockwise P-T-t paths close to the Al_2SiO_5 triple point for the metamorphic peak and post-peak events. This is also the case for the Selwyn Zone, but in addition the latter also shows early cordierite metamorphism followed by, in D_1 and early D_2 times, a clockwise medium pressure P-T-t loop. Although the diversity in bulk compositions in the Selwyn Zone makes this clockwise loop more easily recognizable, the lack of similar loops in the other zones is probably real.
- Part of the thermal budget in the Isan Orogeny is probably the result of elevated values of radioactive heat producing elements in the crust. However, abundant mafic intrusions occur throughout the Isan and pre-Isan metamorphic history, and the highly fractionated nature of these intrusions at the current level of erosion implies large bodies of layered gabbros deeper in the crust. It is proposed that repeated intrusions of gabbros occurred under the higher grade areas, resulting in migmatization of middle crustal rocks and upwards transfer of heat via advection due to rise of pegmatites into what are now the sillimanite zones.
- The Mount Isa Inlier is not only highly endowed with mineralization, but is also extraordinary in the abundance and lithological diversity of metasomatic rocks that formed throughout the tectonothermal history. Epigenetic ore deposits are more abundant in areas of significant metasomatism, regardless of whether they formed contemporaneously. Mixing of metal-rich and barren metasomatic fluids was probably crucial in determining whether particular metasomatic lithologies are mineralised.

2. ISOGRAD MAP AND CROSS SECTION
2.1 Isograd map

The isograd map (Fig. 1) was modified from Foster & Rubenach (2006) by James Austin to make it GIS compatible. The following discussion has been adapted from Rubenach (2005). The zones are composite, and are not related to any specific metamorphic event, although they mainly the peak of metamorphism in the Isan Orogeny. Pelitic isograds were given preference, but otherwise calcsilicate zones were used. The biotite zone in calcsilicate rocks extends from greenschist facies to lower amphibolite facies, whereas the diopside isograd corresponds approximately to the sillimanite isograd in the Mount Isa Inlier. Note that regional "rock buffered" calcsilicate zones were plotted, not fluid buffered zones related to granite intrusions and/or hydrothermal activity.

Significant points concerning isograd patterns are as follows:

1.The overall isograd pattern is a series of amphibolite facies tongues that are elongate north-south, and which alternate with greenschist facies belts. As a generalization, in the Selwyn Zone the metamorphic grade decreases northwards, with the largest areas of sillimanite and sillimanite/Kfeldspar rocks in the southeast of the Mount Isa Inlier. In the Eastern Fold Belt the higher-grade rocks are concentrated in two NS zones, one though Duchess and Mary Kathleen and the other from Osborne to the Snake Creek Anticline (Fig. 1).

2. There are no obvious relationships between metamorphic grade and stratigraphy. For example, lower units of cover sequence 2 rocks in the Duck Creek Anticline are greenschist facies, while the cover sequence 3 Soldiers Cap Group is mainly amphibolite facies. More locally, isograds are roughly parallel to the stratigraphy from the Middle Creek Anticline across to the eastern part of the Snake Creek Anticline, but sharply transect the stratigraphy on the northern and western sides of the Snake creek Anticline.

3. Grade changes occur across major faults such as the Cloncurry and Pilgrim Faults. The easterly-dipping Cloncurry Fault is almost certainly an old structure that was probably repeatedly reactivated. In the Snake Creek area, the juxtaposition of sillimanite zone Soldiers Cap Formation against greenschist facies Corella Beds to the west implies reactivation of the Cloncurry Fault as a post-metamorphism reverse and/or strike-slip fault.

4. There is a curious relationship between the presence of large granite bodies and amphibolite facies metamorphism, but with no large bodies of granite (as opposed to smaller-scale magmatic rocks in migmatites and as pegmatites) emplaced during the metamorphic peak, Thus granites are absent from such greenschist facies areas as the Marimo Basin and the Duck Creek Anticline. A zone of granites (e.g. the Wonga Batholith) corresponds to the narrow high grade Wonga Belt extending through the Mary Kathleen-Duchess zone (Fig. 1). These granites intruded ca. 1730-1750 Ma, with accompanying deformation and amphibolite facies metamorphism (Oliver et al., 1991),

but amphibolite facies metamorphism also occurred along the belt in the Isan Orogeny. This could be in part explained by the presence of elevated values of heat-forming elements in the granites, as suggested by McLaren et al. (1999) for the Sybella Granite at Mount Isa, but the peak of metamorphism in the Isan Orogeny occurred ca. 150 Ma after the Wonga Batholith and ca. 100 Ma after the emplacement of the Sybella Granite. There appears to be a broad spatial relationship between amphibolite facies metamorphic rocks and the Williams Batholith in the SE of the Inlier (Fig.2). If the Marramungee granites are included, the plutons were emplaced in the period 1500-1550 Ma, ca. 40-50 Ma after the metamorphic peak but synchronous with weaker ductile deformation events (D_3, D_4). However, there is no correlation between amphibolite facies and the Wimberu and Naraku granites, almost all of which are younger than 1520 Ma.

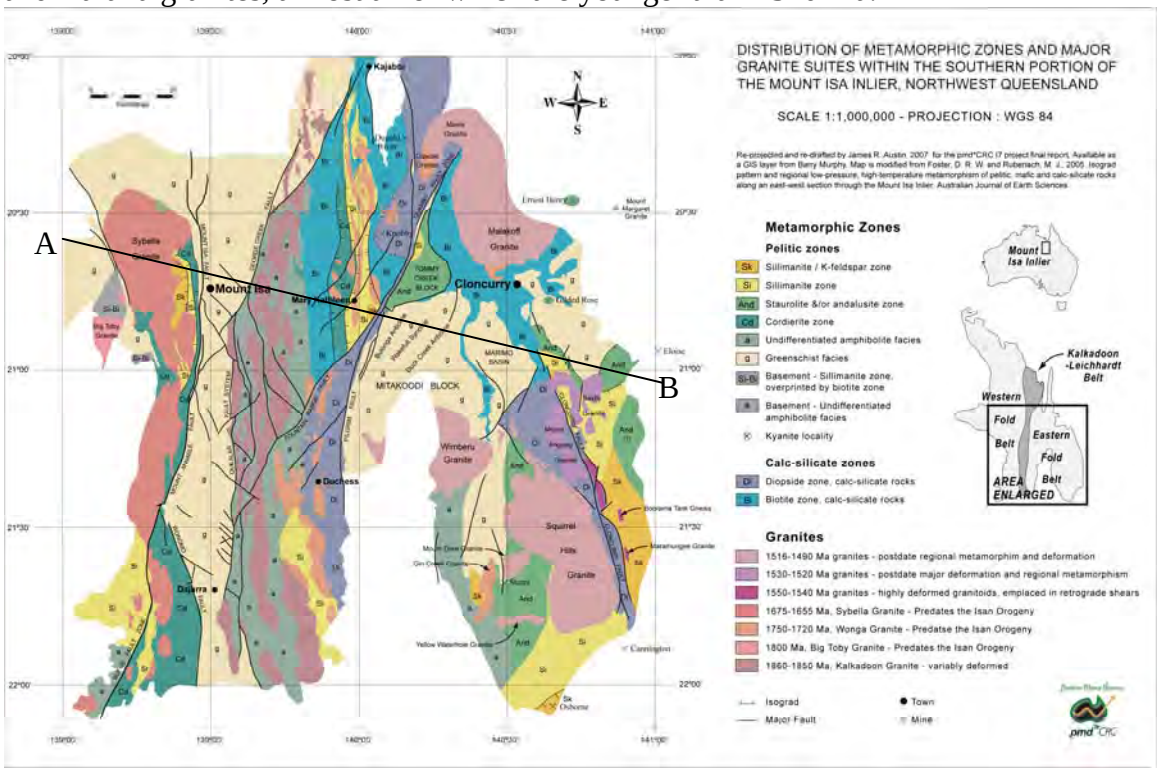

Figure 1. Isograd map of the Mount Isa Inlier, after Foster and Rubenach (2006), made GIS compatible by J. Austin. The section line through Mount Isa (Fig. 2) is shown.

2.2 Metamorphic cross-section

The metamorphic cross-section A-B (Fig. 2) shows Isan Orogeny peak of metamorphism temperatures rather than isograds. Unfortunately the dips of the isograds and isothermal surfaces are unknown, so the dips shown on the section are speculative. It is assumed that the surfaces were dominantly shallow dipping when formed, and were folded in post-D_2 events. The temperatures are based on the following:

1. Greenschist facies, less than 550ºC.
2. Amphibolite facies, greater than 550ºC. In pelitic rocks, the cordierite, andalusite or staurolite incoming isograds correspond to ~550º at 3-4 kbar
3. The sillimanite isograd, using the Pattison (1992) triple point in the Al_2SiO_5 system, is about 580ºC at 4 kbar. This also corresponds approximately to the diopside isograd in regional calcsilicate rocks in the inlier (Foster & Rubenach, 2006).
4. The sillimanite/Kfeldspar isograd is roughly 650ºC at 3kbar and 690ºC at 4 kbar.

For convenience the old terminology of cover sequences 1-3 is used in Figure 2. Cover sequence 1 still correlates with the rocks of the Kalkadoon-Leichardt Block (Leichardt Volcanics, KalkadoonBatholith), cover sequence 2 approximates the Leichardt Superbasin, whereas cover sequence 3 roughly corresponds to the Calvert and Isa superbasins (Southgate et al., 2000).

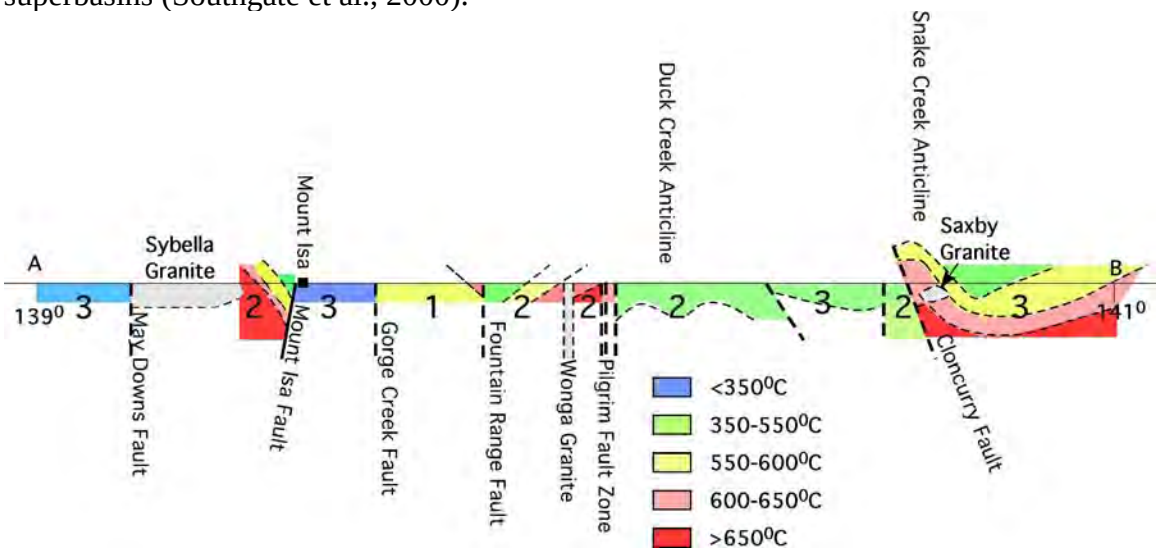

Figure 2. NNW-SSE cross section through the Mount Isa Inlier through Mount Isa. For convenience cover sequences 1-3 are included rather than the more recent superbasins. The dips of the isograd surfaces are unknown, so are schematic. See text for the derivation of the temperatures.

3. DEFORMATION/METAMORPHIC HISTORY

3.1 Deformation events

Models for the tectonothermal evolution of the Eastern Fold Belt are based on the regional mapping and age determinations of geologists from the Bureau of Mineral Resources, now Geoscience Australia (e.g., Blake & Stewart, 1992; Jaques et al, 1982; Ryburn et al, 1988; Page & Sun, 1998; and references therein). Most researchers agree that during the Isan Orogeny, NS to NNW-SSE compression (D_1 events) was followed by EW compression (D_2 and most subsequent events) (e.g., Loosveld 1989; O'Dea et al, 1997; Betts et al, 1997; Adshead-Bell, 2000; Mares, 1998; Lewthwaite, 2001; Rubenach & Lewthwaite, 2002; Sayab, 2006a, b; Rubenach et al., in press). However, significant differences between JCU workers and others concerns their use of FIA's (foliation intersection axes) within porphyroblasts, predicated on the arguments that porphyroblasts commonly do not rotate during ductile deformation (Mares, 1998; Sayab, 2005a). In contrast, researchers from Monash University (e.g., O'Dea et al, 1997, 2006; Betts et al., 2006; Giles et al., 2006a, b) emphasize thin-skinned tectonics and nappe formation during D_2.

D_w . Wonga event, Pearson et al. (1992). Correlated with the "Big" event of Southgate et al. (2000) in the Eastern Fold Belt. Ages in the range 1735-1750 Ma. Affected the Corella Formation and correlatives (Doherty Formation, Corella beds) and the Double Crossing Metamorphics. Greenschist to amphibolite facies, with the number of discrete events unknown.

D_{sg}. After recognition that a localized high-grade shear zone event was synchronous with the emplacement of the Sybella Granite a SHRIMP zircon age of 1673 ± 2.5 Ma was determined for a granite that cross-cut highly deformed main-phase Sybella Granite (Hoadley et al., 2001). The latter was dated at 1671 ± 8Ma (Connors & Page, 1995), so the shear zone developed during the batholith emplacement. Recent mapping and monazite dating (this project, see below) has established two deformation/metamorphic events synchronous with the emplacement of the Sybella Granite, an earlier one producing a shallowly dipping gneissic foliation and cordierite-Kfeldspar assemblages, and a younger steep E-W foliation and migmatitic sillimanite-biotite-Kfeldspar assemblages. Both these events are penecontemporaneous with the main-phase Sybella Granite.

The nomenclature of Rubenach et al. (in press) is followed for the Isa Orogeny events, as outlined below (also see Fig. 3).

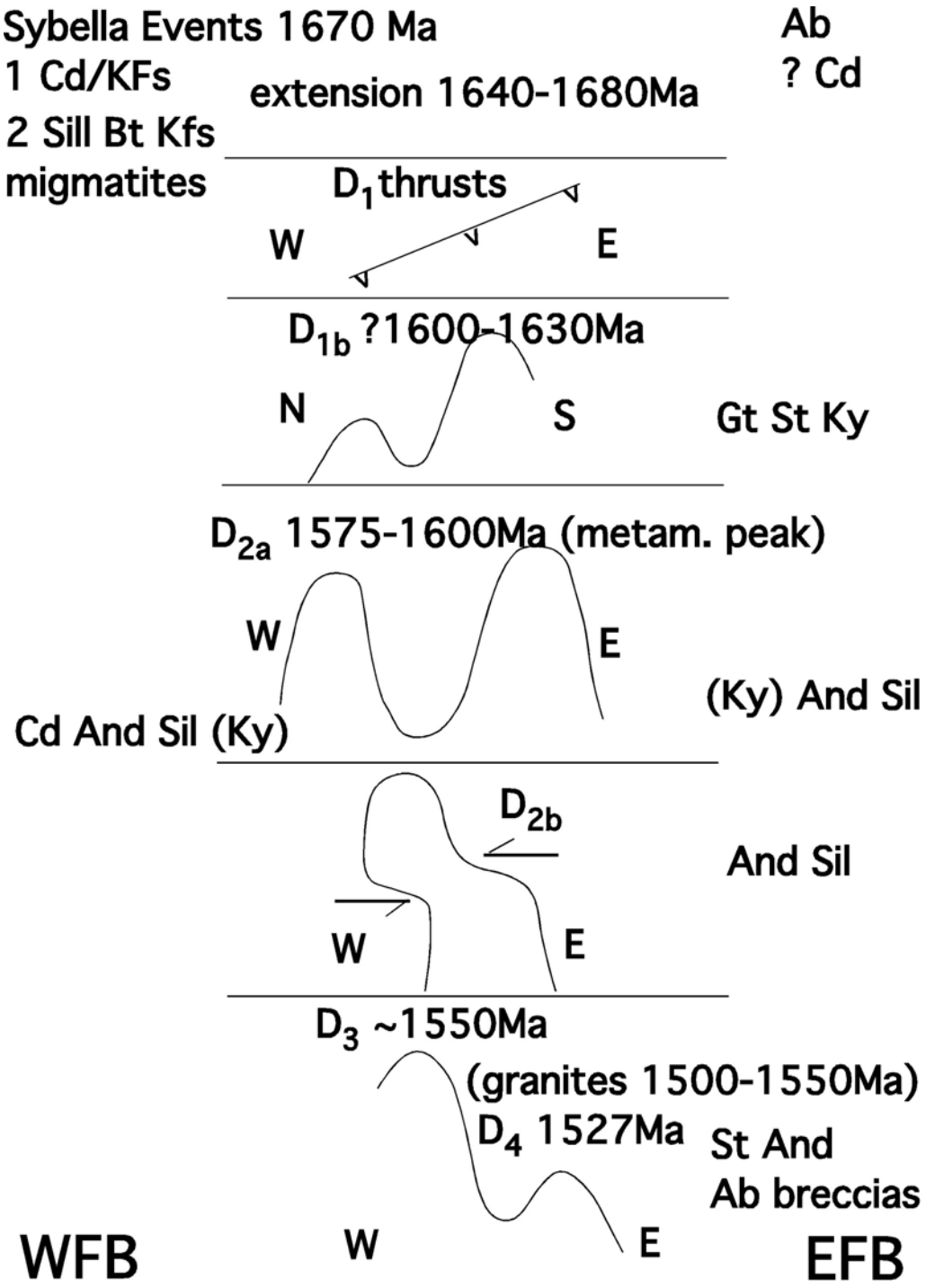

Figure 3. Schematic history of the Mount Isa Inlier during the Isan Orogeny. WFB, Western Fold Belt; EFB, Eastern Fold belt. Deformation events are schematically represented as either plan views or sections. Age dates are based on this report. Mineral abbreviations are after Kretz (1983; also see appendix. The deformation history is based largely on JCU work and other models are discussed in Rubenach et al. (in press; appendix).

D_{bp}. A bedding-parallel foliation is the earliest recognized. At least one event produced a flat foliation sub-parallel with bedding in rocks throughout most of the Eastern Fold belt. I interpret this as being mainly extensional. However, rare recumbent folds with E-W axes overprinted by N-S F_2 folds are also present (e.g. in the Snake Creek Anticline), and these may represent pre-D_2 thrusting. It is therefore possible that the bedding-parallel foliation in some locations could be a combination of extensional and thrusting events.

D_1. E-W folds with steep axial surfaces are best preserved in the area north of the Snake Creek Anticline and in the Corella Formation, but they occur throughout the Inlier. Giles et al (2006a) interpret both the N-S Snake Creek Anticline and the E-W folds as being associated with the one thrusting event, but on metamorphic and structural grounds, particularly the widespread occurrence of the E-W folds, it is proposed that they represent separate events. Further evidence of this event is provided by foliations preserved in porphyroblasts throughout the EFB (e.g. Reinhardt, 1992, in the Rosebud Syncline, Mary Kathleen area; Mares, 1998, in the Fairmile area; Adshead-Bell, 1998, in the Selwyn Ranges area; Sayab, 2005a, 2006, in the Snake Creek and White Blow areas).

D_{2a}. This event produced N-S folds with mainly steep axial planes. The most intense foliation in the region is S_{2a}.

D_{2b}. Small-scale folds formed in this event are relatively uncommon; they have N-S axes, shallow axial planes, and show top-to-the west sense of shear. Crenulations are more common but localized. This event is discussed in Bell and Hickey (1998), Rubenach and Barker, (1998), Mares (1998), Adshead-Bell (1998), Rubenach and Lewthwaite (2002), and Sayab (2005a, 2006), with many of these authors designating it as D_3. The peak of metamorphism in the Isan Orogeny throughout the Inlier occurred around late D_{2a} to D_{2b}.

D_3. This event, recognized by all workers, produced NNW-trending folds, with steep axial surfaces. It produced crenulations and/or resulted in reactivation or re-use of $S_{2a.}$

D_4. This event resulted in NE-trending folds with steep axial surfaces, and crenulations and/or reactivation of S_{2a}. D_4 structures are relatively uncommon in the Inlier, but can be recognized over much of the Snake Creek Anticline where it was probably synchronous with the intrusion of the Saxby Granite and the formation of breccias and late albitization in the Corella Formation. Although a ductile event in the Snake creek Anticline, this event could be a significant brittle event, associated with copper and Cu-Au mineralization, elsewhere in the inlier (pmd*CRC report, D. Keys).

3.2 Metamorphism in the Eastern Fold Belt-previous work

Former work includes regional metamorphic studies (Jaques et al., 1982; Foster & Rubenach, 2006), the Snake Creek Anticline (Rubenach & Lewthwaite, 2002; Rubenach et al., in press, Appendix 1; Giles et al, 2006b) the Eastern Selwyn Ranges (de Jong, 1995), the Fairmile area (Mares, 1998), the Eloise Mine (Baker, 1996) the Selwyn Range area (Adshead-Bell, 2000;), the Gilded Rose area (Lewthwaite, 2001; Sayab, 2005) the Sandy Creek area (Sayab, 2006; Giles et al., 2006a), the Cannington Mine (Kim & Bell, 2005) and the Osborne Mine (Adshead, 1995; French, 1997; Banville, 1998). Other significant studies elsewhere in the Eastern Fold Belt (Wonga Belt, Tommy Creek Block) include those of Oliver et al. (1991), Reinhardt (1987, 1992), Reinhardt & Rubenach (1989), Bell et al. (1992), Hill et al. (1992), Lally (1997) and Sayab (2006). For pelitic rocks between the biotite and sillimanite zones the assemblages are quite similar. A common progression is garnet zone followed by staurolite/andalusite (Eastern Selwyn Ranges, Gilded Rose, Tommy Creek Block, Sandy Creek, White Blow Formation, Selwyn Ranges. Exceptions include much of the Mary Kathleen-Duchess Zone, where the progression is biotite zone, cordierite zone and andalusite zone (Foster & Rubenach, 2006), with areas of unusual high-Mg rocks that metamorphosed to assemblages that include anthophyllite, talc, cordierite and cordierite (Reinhardt, 1987). As is the case at Snake Creek, some outcrops in the Selwyn Ranges, commonly with associated albitization, have cordierite + andalusite assemblages in association with the dominant garnet-staurolite-andalusite assemblages (Adshead-Bell, 2000).

The tectonothermal evolution of the eastern part of the EFB (the Selwyn Zone) is discussed in Rubenach et al (in press; Appendix 1). Based on new data from the Snake Creek Anticline a modified composite P-T-t path has also been constructed (Fig. 4).

The Mary Kathleen Zone of the EFB shows high metamorphic field gradients (as indicted by the closely-spaced isograds) located along a central high-strain belt, the Wonga Belt. Although most authors recognize that at least some of the strain is a D_2 Isan Orogeny overprint, two competing hypotheses have been proposed for pre-D_2 deformation. In one of these the Wonga Belt is interpreted as an original extensional shear zone at ~1740 Ma (the "Wonga Event) (Pearson et al., 1992). In an alternative hypothesis, Bell et al. (1992) interpret the Wonga Belt as forming as a vertical shear zone during Isan Orogeny D_1 thrusting. These hypotheses are discussed below in the light of new age determinations.

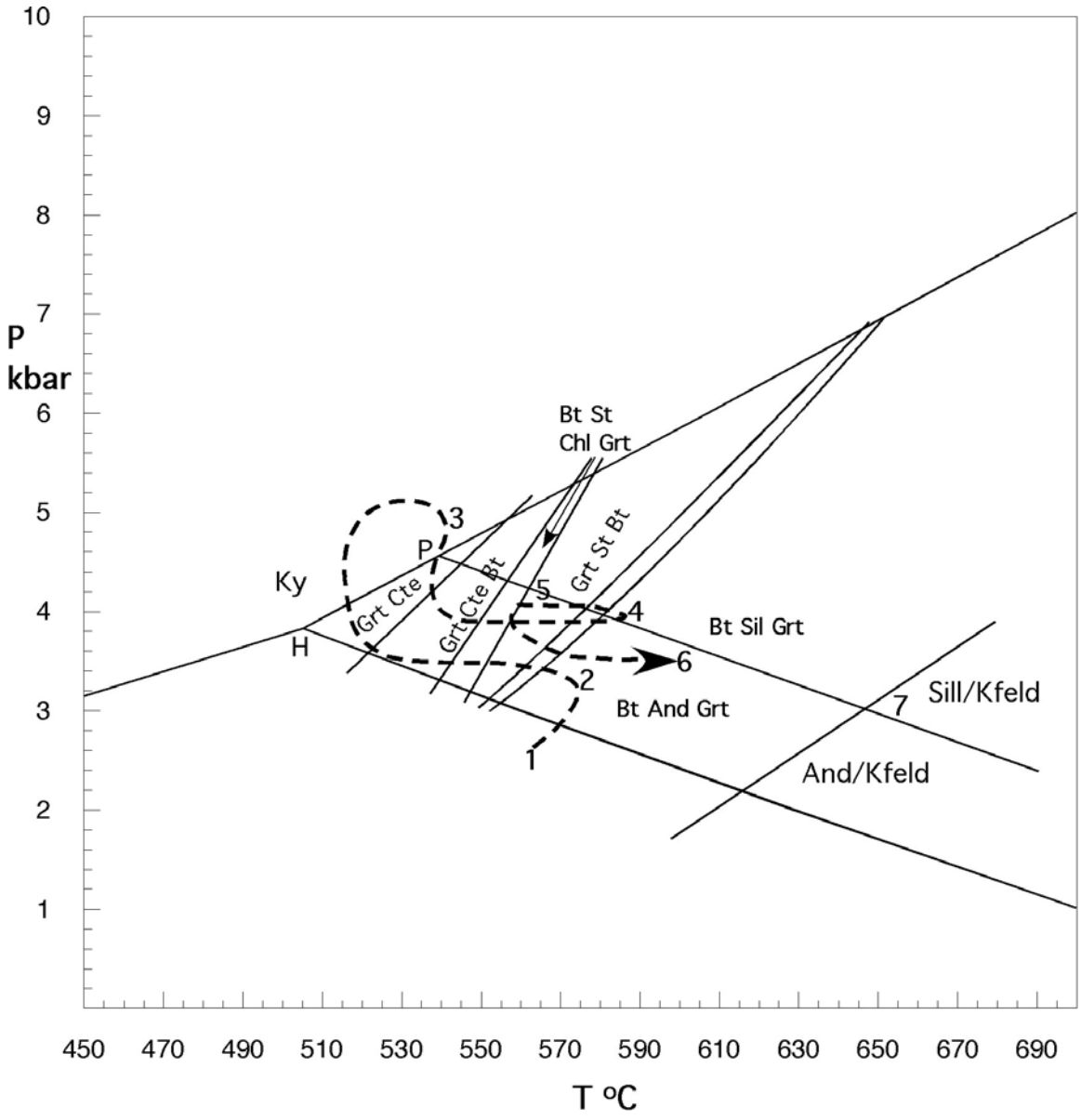

Figure 4. Composite P-T-t path plotted on a psuedosection (THERMOCALC NCMnKFMASH system, Holland & Powell, 1998) for a typical andalusite-garnet-biotite-muscovite schist from the Snake Creek Anticline (on the sillimanite isograd). The path was determined from psuedosections for a variety of compositions, and is modified from Rubenach et al. (in press). 1, albitization (not in this sample); 2, growth of cordierite (not this sample) and andalusite; 3, growth of kyanite (not this sample) and garnet; 4, growth of andalusite and sillimanite, D_2(~1580 Ma); 5, growth of staurolite, probably D_3 (~1550 Ma); 6, late overgrowths of andalusite, D_4(1527 Ma); 7, sillimanite/Kfeldspar schists, aureole of the Saxby Granite only (1527 Ma).

3.3 P-T-t path, Mary Kathleen/Duchess Zone – new data

The work of Reinhardt (1987, 1992) established the broad peak metamorphic conditions and P-T-t path for the Rosebud and Little Beauty Synclines in the Mary Kathleen area. A revised P-T-t path (Fig. 5) is included in this report and is based on Reinhardt's thin sections and chemical data and using the cordierite-aluminosilicate-biotite isopleths of Pattison et al. (2002) and the aluminosilicate triple point of Pattison (1992). The prograde path was determined from reaction relationships between cordierite, andalusite and sillimanite (e.g. Figs. 6, 7), whereas kyanite-bearing assemblages (with or without andalusite and sillimanite) define the "retrograde" path (Figs. 9-11; these figures indicate a complex loop around the aluminosilicate triple, as depicted as 2 in Fig. 5). Note that the temperature peak in the sillimanite zone in the Rosebud Syncline is ~ 600ºC at ~ 4 Kbar; this is consistent with values of ~ 540-580ºC/ 4 Kbar determined using THERMOCALC by Sayab (2006) for a lower grade staurolite-garnet-biotite schist sample WB161 from the White Blow Formation, just SW of the Rosebud Syncline (The White Blow Formation is upper andalusite zone whereas the Rosebud Syncline is sillimanite zone). It is important to note that parts of P-T-t path for the Rosebud Syncline are unknown. For example, a clockwise medium pressure loop such as that which occurs in the Snake Creek Anticline and the Tommy Creek Block would not be recorded in the mineral assemblages in of the Rosebud Syncline, as they are too magnesium-rich to record. However such a loop would quite likely be preserved in some schists from the White Blow Formation, so, as discussed below, there appear to be real differences between the P-T-t path for the Selwyn and Mary Kathleen/Duchess zones. The tectonothermal implications of the P-T-t path in the light of new monazite dating are discussed below.

Figure 6. Sample 454 of Reinhardt (1987), typical andalusite-sillimanite-biotite-muscovite-quartz schist. Two poorly defined inclusion trails are preserved in the andalusite, one subparallel to the external S_2 foliation. Sillimanite, upper left. An inclusion of cordierite (right) in the large andalusite porphyroblast has been replaced by biotite and quartz. Length of photo 4.6 mm, PP light.

Figure 7. Also sample 454. In this photo inclusions of oxides parallel to S_1 are more clearly visible, and the matrix S_2 strongly wraps around the andalusite. Length of photo 4.6 mm, PP light.

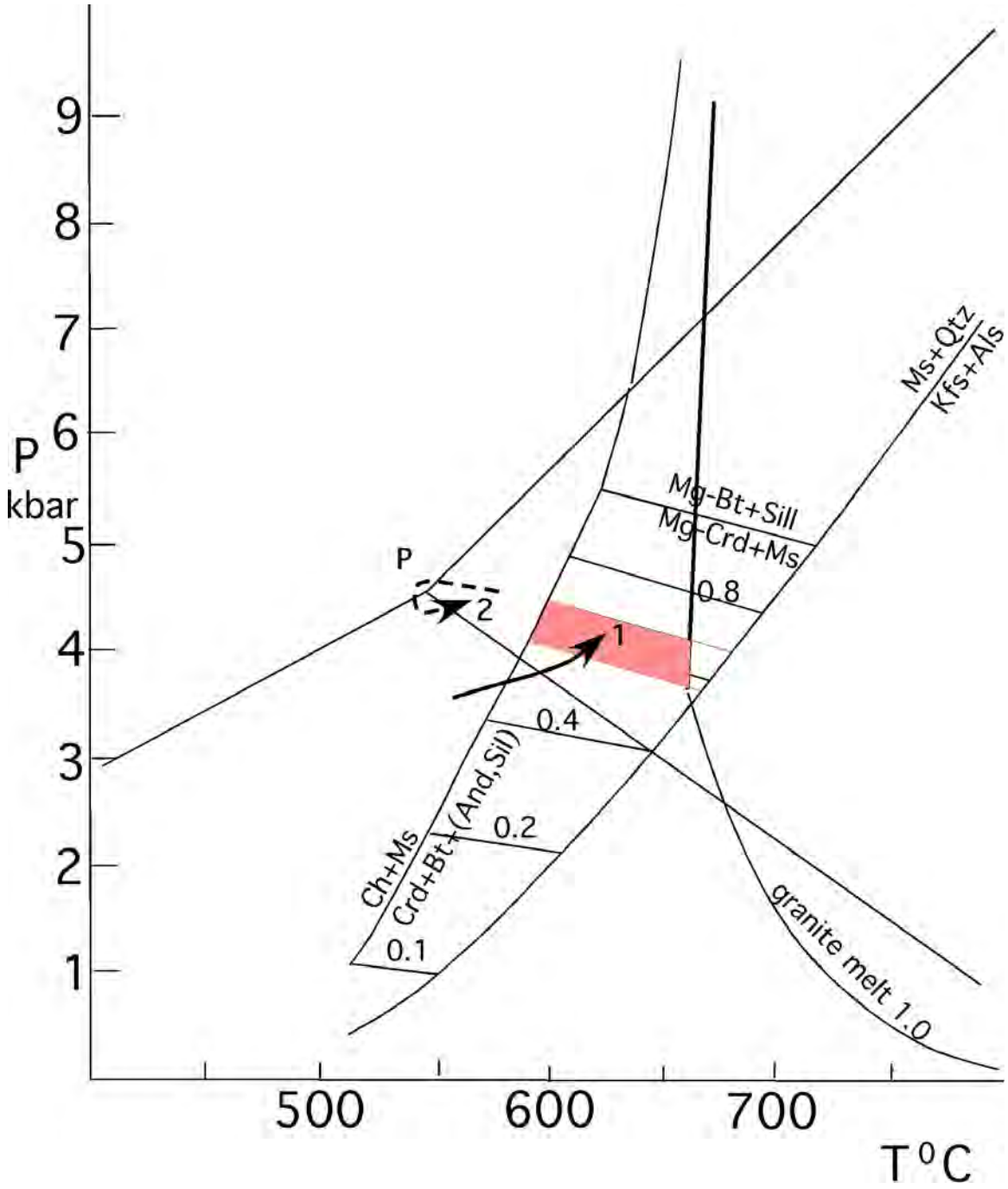

Figure 5. P-T-t path for the Rosebud Syncline and Wonga Waterhole, Mary-Kathleen-Duchess Zone. 1, peak of metamorphism (D_2) for typical (Crd)-And-Sil schists, Rosebud Syncline (~1575 Ma). 2, Wonga Waterhole area, And-Sil-Ky rocks (also ~1575 Ma). The Al_2SiO_5 triple point used is from Pattison et al. (2002), and chemical data from Reinhardt (1987) was used in locating the cordierite-Al_2SiO_5 reaction on the isopleths of Pattison et al. (2002).

Figure 8, sample WWH16. Andalusite has been partly replaced by muscovite, which is intergrown with acicular sillimanite. Sillimanite also occurs as inclusions in andalusite (lower right). Length of photo 4.6 mm, PP light.

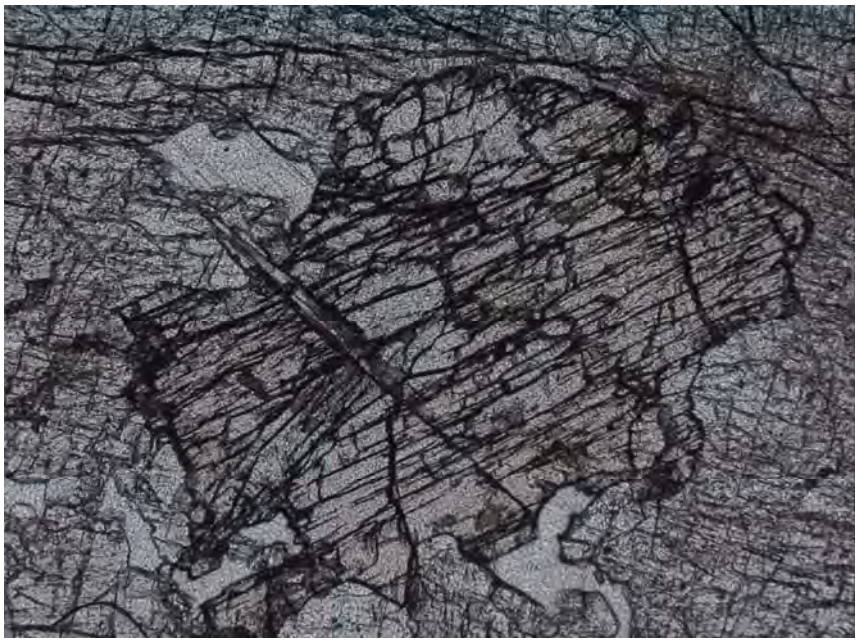

Figure 9, sample WWH16b. Partly replaced kyanite grain (central) included in andalusite and cut by sillimanite. Length of photo 4.6 mm, PP light.

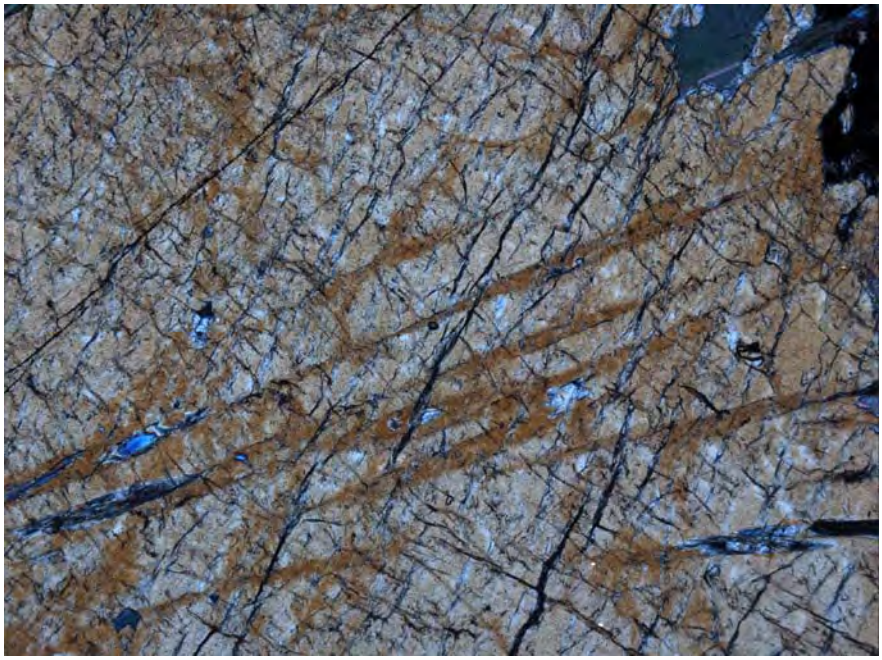

Figure 10, sample WWH6b. The host andalusite shows “ghosts” of largely replaced acicular sillimanite grains, with some relict sillimanite (blue). Length of photo 4.6 mm, XP light.

3.4 Peak metamorphic conditions, Kalkadoon-Leichardt Block

In terms of metamorphic grade, no useful pelitic or calcareous/dolomitic assemblages have been identified in this block. In terms of structure, the dominant N-S foliation and steep mineral elongation are consistent with D_2 timing, suggesting that the mineral assemblages in the rocks probably equilibrated in the metamorphic peak in the Isan Orogeny. Hornblende-plagioclase thermobarometry from mafic rocks from the Kalkadoon-Leichardt Block provided temperatures in the range 510-600ºC, that is greenschist to lower sillimanite grade, at low to medium pressures (Foster & Rubenach, 2006). Thus the peak metamorphic conditions during the Isan Orogeny in the Kalkadoon-Leichardt Block appear to be similar to belts on either side. However, the shape of the pre-D_2 portion of the P-T-t path is unknown.

3.5 Western Fold Belt – metamorphism and P-T-t path

The isograds and zones are shown in Figure 1, and a revised P-T-t path, using the cordierite-aluminosilicate-biotite isopleths of Pattison et al. (2002), shown in Figure 12. Although the isograds essentially relate to D_2, new monazite dating in this project has revealed that the sillimanite/Kfeldspar zone and its relict pods of cordierite/Kfeldspar gneiss are both related to the Sybella event at ~1670 Ma (see Fig. 12 and Section 6).

The Sybella Granite outcrop that was dated (Hoadley et al., 2001) is shown in Figure 13, while Figures 14-17 are typical outcrops of the May Downs Gneiss. Photomicrographs of cordierite gneiss and overprinting sillimanite-biotite-Kfeldspar gneiss, both of Sybella age (see below), are included as Figures 16-17. Interestingly, the overprinting D_2 assemblages in the northern part of the May Downs Gneiss, and extending into the lowermost Eastern Creek Volcanics, are also of sillimanite-biotite-Kfeldspar grade, although these change to the lower temperature sillimanite-muscovite-biotite to the south.

The Eastern Creek Volcanics exhibit cordierite, andalusite/sillimanite, and (locally) sillimanite/Kfeldspar isograds, all related to D_2. D_{2b} is manifested as localized folds (Fig. 19), overturning and shallowly dipping crenulation cleavages (Bell & Hickey, 1998; note that they call it $D_{2.5}$). D_3 overprint, as NNW-oriented folds and crenulation cleavages (Fig. 20), or reactivation of S_2, is also localized. The presence of kyanite in a few retrograde chlorite-rich shear zones cutting cordierite-andalusite rocks suggests an anticlockwise P-T-t path (Rubenach, 1992; Fig. 11). The kyanite is located at the margins of the shear zones, indicating localized lower water activities. The shear zone foliation is locally overprinted by D_3 crenulations, indicating that the shear zones developed pre-D_3; this is consistent with monazite dating, as discussed below. Note that Bell & Hickey (1998) record syn-D_3 growth of cordierite for a sample from the Mica Creek area (i.e. south of the areas where I found kyanite), showing that at least locally in the WFB the metamorphic grade during D_3 was amphibolite facies.

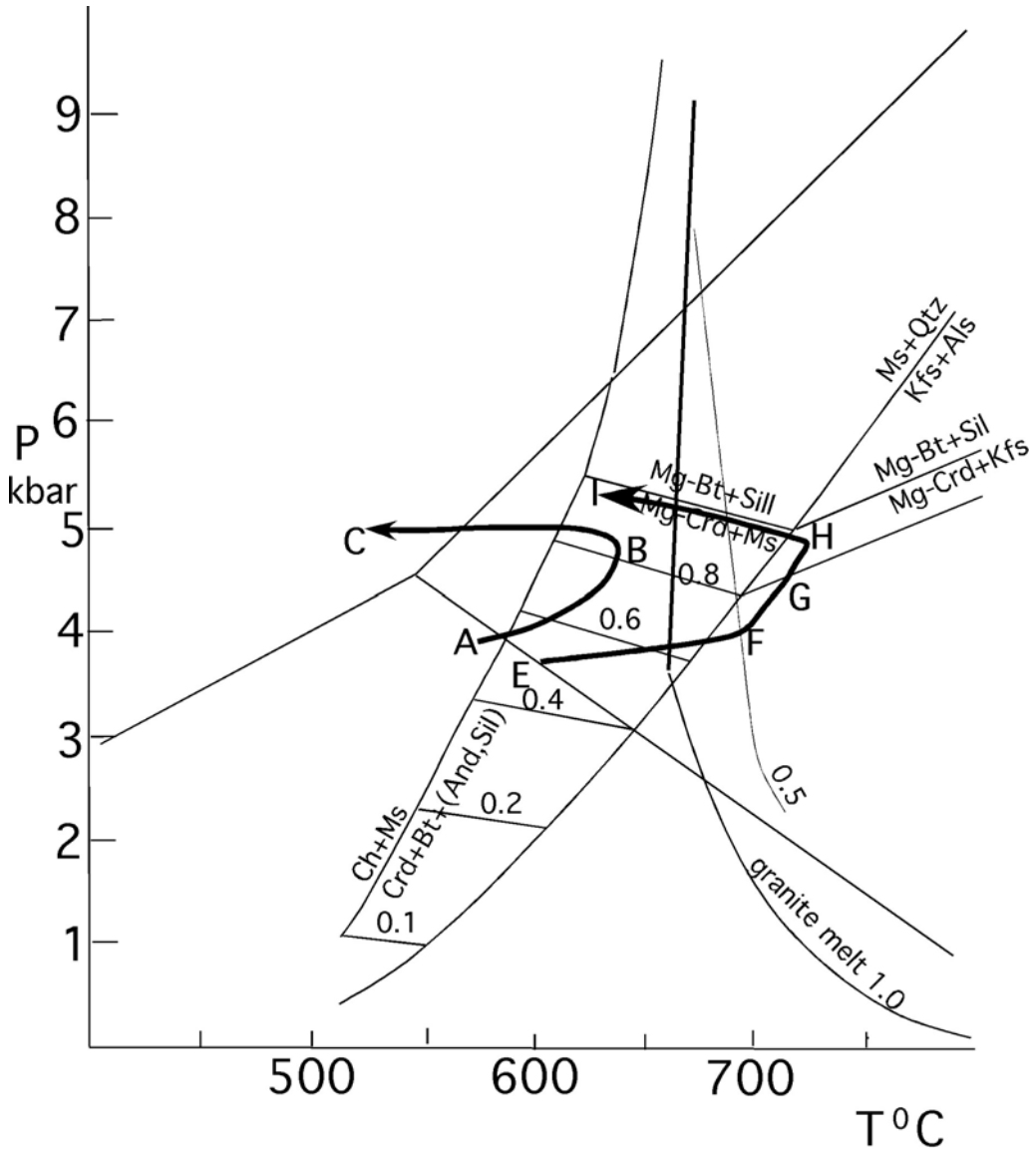

Figure 11. P-T-t path for the May Downs Gneiss (E-I) and cordierite-andalusite-sillimanite schists of the Eastern Creek Volcanics (A-C), west of Mount Isa. A, growth of cordierite, probably early in D_2. B, growth of andalusite and sillimanite late in D_2. C, formation of kyanite in local chlorite-rich shear zones cutting cordierite-andalusite rocks. E-F, formation of cordierite/Kfeldspar gneisses in the May Downs Gneiss during the Sybella Event (~1670 Ma). F-G-H, commencement of partial melting and formation of migmatitic sillimanite-biotite-Kfeldspar gneisses, probably later in the Sybella Event. I, formation of sillimanite/muscovite schists in the southern part of the May Downs Gneiss during D_2. Note that sillimanite-biotite-Kfeldspar gneisses formed in the northern part at the same time.

Figure 12. Field photo of dated Sybella Ganite location, edge of Kitty Plain. The granite is a weakly foliated medium grained granite, with dark inclusions of strongly deformed mingled/mixed igneous rocks of the Sybella Granite. The host granite age (1673 Ma) is within error the same age as the highly deformed Main Phase Sybella Granite, showing that the Sybella deformation event occurred synchronous with the intrusions (Hoadley et al., 2001).

Figure 13. Cordierite/Kfeldspar gneiss, northwestern margin of the May Downs Gneiss. Note the incipient partial melting. Monazite from the sample IN1.1 was dated.

Figure 14. Near the northwestern margin of the May Downs Gneiss. A relict pod of cordierite/Kfeldspar gneiss, with a Sybella event foliation, is included in sillimanite-biotite-Kfeldspar gneiss that shows a strong D_2 deformation.

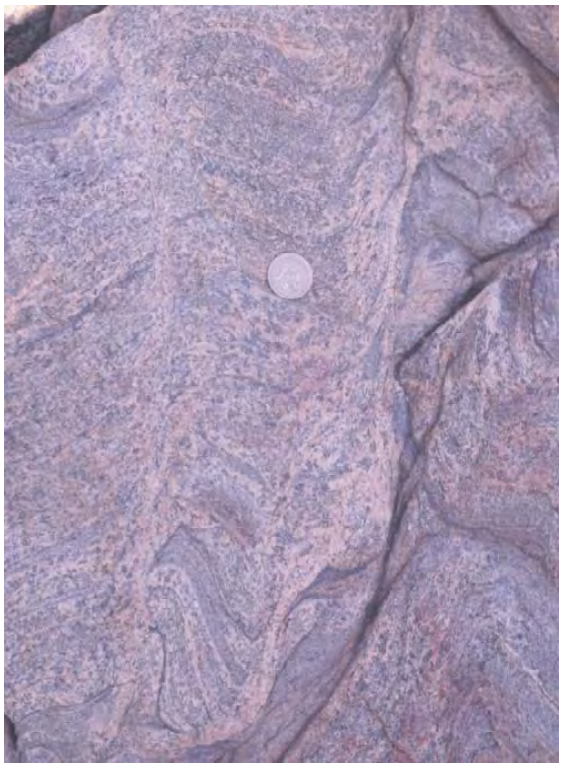

Figure 15. May Downs Gneiss (sillimanite-biotite-Kfeldspar) showing steep EW folds (second Sybella event), migmatization, and ellipsoidal dark cordierite grains now replaced by sillimanite and biotite.

Figure 16. Photo of typical migmatitic sillimanite-biotite-Kfeldspar gneiss, showing a strong EW upright foliation (second Sybella event) and boudinage.

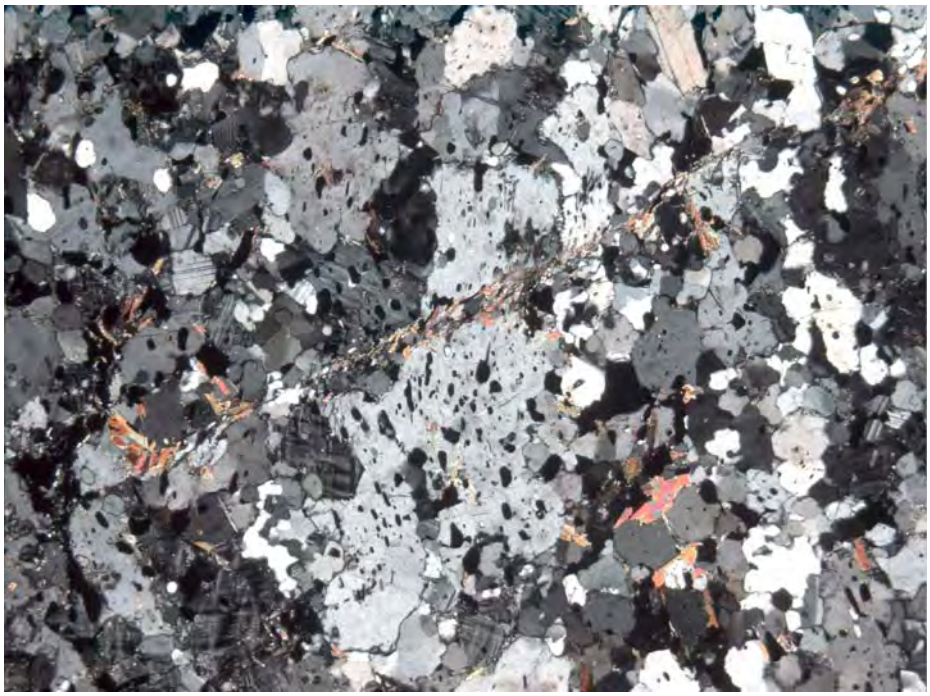

Figure 17. Sample IN1.1, cordierite-Kfeldspar gneiss (May Downs Gneiss, dated sample). A very thin diagonal sillimanite-biotite cross-cuts the rock. Length 4.6 mm, XP light.

Figure 18, sample 504.4 (dated). Typical sillimanite-biotite-Kfeldspar gneiss. Length 4.6 mm, PP light.

Figure 19. Cordierite schist and quartz-tourmaline vein overprinted by S_2 and folded by an F_{2b} fold with a shallow axial plane.

Figure 20. F_3 folds with sub-vertical axial plane crenulation cleavage, schists, Eastern Creek Volcanics west of Mount Isa

West of the Mount Isa Fault in the Molanite Valley, the Myally Group includes calcareous/dolomitic red bed siltstones and shales, including an epidote-calcite-quartz-Kfeldspar-haematite-plagioclase assemblage that suggests temperatures in the range 400-500ºC (Fig. 21). This temperature range is consistent with the abundant pods of metasomatic tremolite, plagioclase-tremolite and talc-chlorite rocks described by Huang & Rubenach (1995). The Myally Group is separated from the Eastern Creek Volcanics by the Tailings Dam or Meernurker Fault, and the temperature difference of at least 50ºC across the fault suggests at least some fault movement after D_2. The Myally Subgroup west of Mount Isa is bounded on the eastern side by the Holly Fault, followed by strongly deformed sedimentary rocks that are probably basal Mount Isa Group (Bell, 1987). The strip of basal Mount Isa Group is greenschist facies, but the peak metamorphic temperature is unknown. It is bounded to the east by the Mount Isa fault, followed by low-strain upper Mount Isa Group sediments showing peak metamorphic temperatures of ~300-350ºC. It is not known if there is a temperature change across the mount Isa Fault.

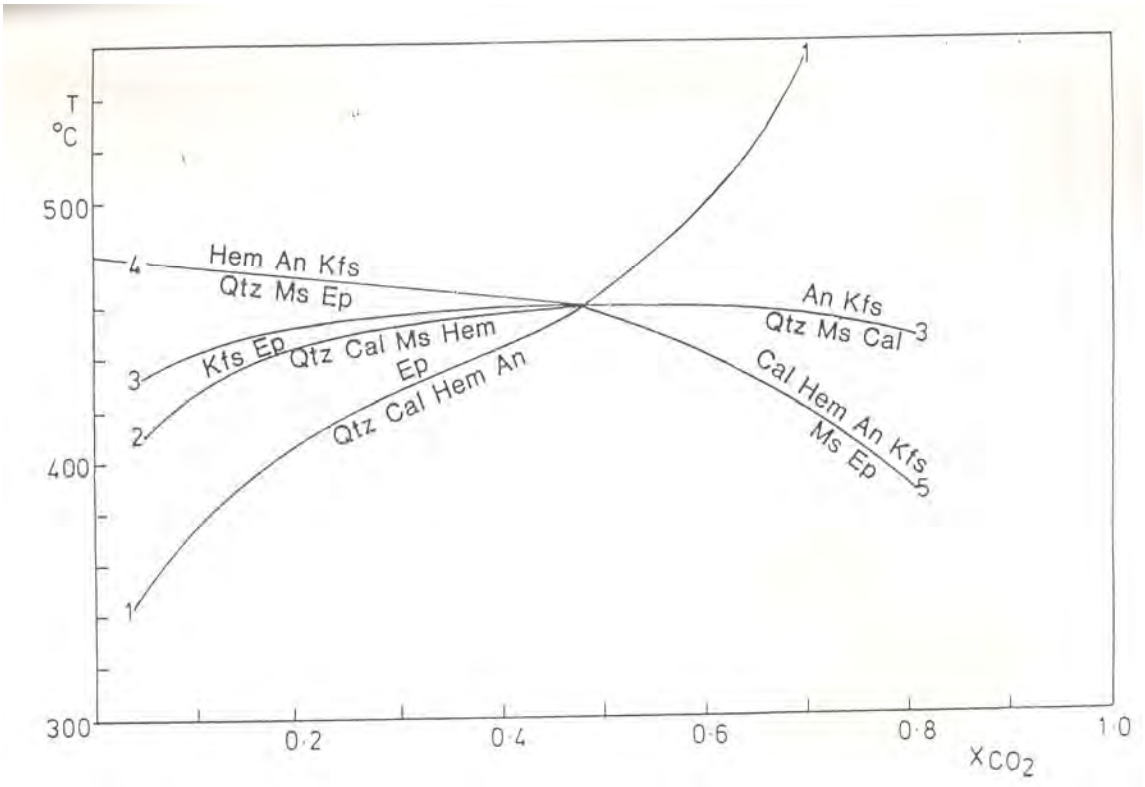

Figure 21. Phase diagram for the system CaO-K_2O-SiO_2-Al_2O_3-Fe_2O_3-H_2O-CO_2 system, calculated using THERMOCALC at 2 Kbar. A fairly common assemblage in the Myally Group in parts of the Molanite Valley would be located at the invariant point in this system, if Na_2O is ignored.

4. AGE DETERMINATIONS OF METAMORPHIC EVENTS

4.1 Previous age determinations

Table 1 summarizes previous work relevant to the metamorphic peak in the Mount Isa Inlier. Ar-Ar dating (that essentially provides cooling ages) has not been included. A 1532 Ma zircon date from the Mica Creek Pegmatites west of Mount Isa, interpreted as corresponding to the metamorphic peak (Connors & Page, 1995) is considered unreliable as the zircons are metamict and older ages have been obtained from monazites in samples of pegmatites (see below).

Sample	Location	Lithology	Method	Age Ma	Reference
92220.8004	35km N of Cannington	Gneiss	U-Pb, zircon	1587±17	Page & Sun (1998)
	Rosebud Syncline	Crd-Ath gneiss	U-Pb, Mnz	1570 1540 rim	Hand & Rubatto (2002)
	"	Crd-And Schist	"	1570 1510 rim	"
	"	Grt schist	Nd-Sm, Grt	1570	"
	Tommy Creek	Grt-St schist	"	1585, 1575	"
CAD159	Cannington	Migmatitic gneiss	U-Pb Mnz	1585±5	Giles & Nutman (2002)
DGC96.3	"	Pegmatite	"	1585±5	"
DGC96.2	Middle Creek Anticline	Meta-psammite	"	1599±10 corrected	"
"	"	"	"	1630±7 uncorrected	"
	Osborne Mine	Albitized calcsilicate	U-Pb titanite	1595±6	Gautier et al. (2001)
	"	Albitite at pegmatite contact	"	"	"
	Hazeldene area	Metasomatic cordierite rock	U-Pb Mnz	1575	Hand & Rubatto (2002)
	Kitty Plain	Sybella Granite	U-Pb, zircon	1673 ± 2.5	Hoadly et al. (2001)

Table 1. Published metamorphic ages. These relate to the peak temperatures during the Isan Orogeny, with the exception on the Sybella Granite date which relates to the Sybella Event.

4.2 New age determinations, Eastern Fold Belt

Previous superprobe dating of monazite from the EFB, discussed in the I3 report (Rubenach, 2005) are further described in Rubenach et al. (in press) (see Appendix 1, this report). The only new age concerns samples AV3, AV5, which are cordierite-andalusite albitites from a single locality in the Snake Creek Anticline. Monazite inclusions in both the early growth cordierite and later growth andalusite were dated in order to place limits on porphyroblast growth, but instead the data indicates a single age of 1651± 8.5 Ma, with monazite grains as inclusions in cordierite and andalusite along with matrix monazite statistically providing the same age. (Fig. 22). This is probably the age of albitization and provides an older limit for cordierite growth in the Snake Creek Anticline.

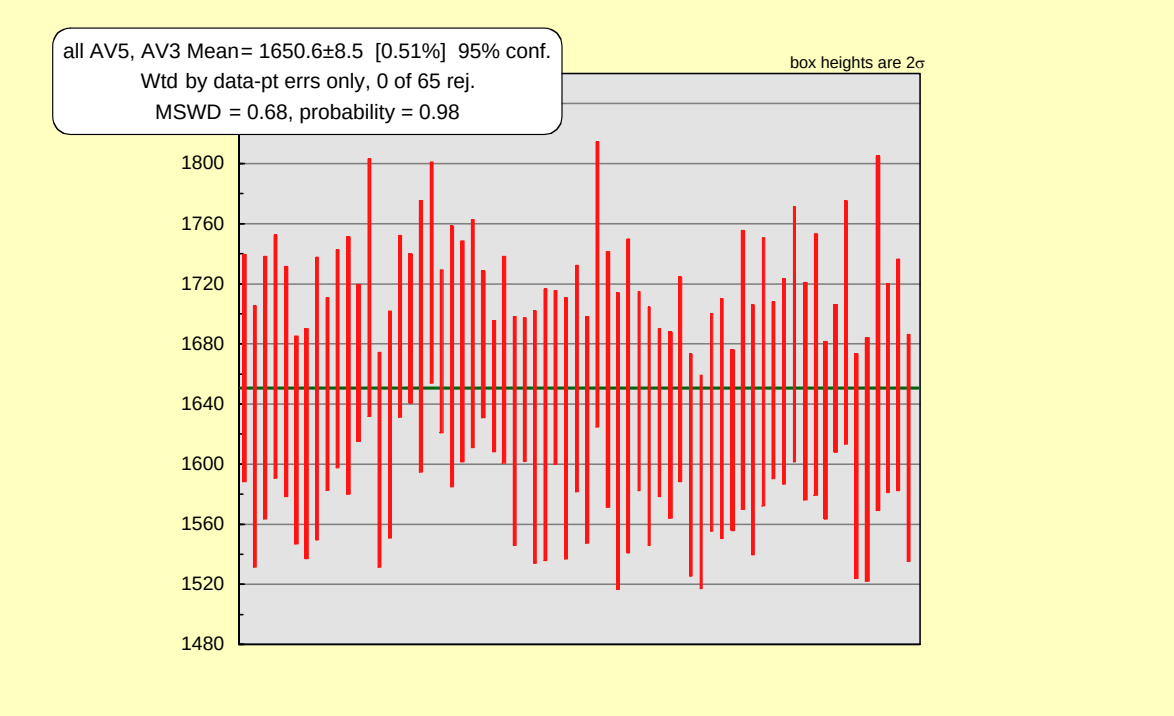

Figure 22. Weighted mean plot for new monazite age determinations, samples AV5, AV3, cordierite-andalusite albitites, single outcrop, Snake Creek Anticline.

Monazite age determinations, Rosebud Syncline and Wonga Waterhole (Little Beauty Syncline)

A monazite dating program of schist samples from the Rosebud Syncline and the Wonga Waterhole (southern end of the Little Beauty Syncline) was undertaken in collaboration with Dr J. Reinhardt, currently at the University of KwazuluNatal, Durban. The Rosebud samples (schists with varying combinations of cordierite, andalusite and sillimanite) were supplied by Reinhardt from his thesis collection (Reinhardt, 1987), whereas the Wonga Waterhole samples ("retrograde" schists with andalusite, sillimanite, kyanite and chlorite) were collected by him subsequently. Given the possibilities of the Bell et al. (1992) and Pearson et al. (1992) models for the origin of the Wonga Belt, older inclusion trails preserved in the porphyroblasts and polymetamorphic prograde path (Figs 4-6), and the "retrograde" nature of the Wonga Waterhole samples, we expected a range

of age dates. However, although a few spot analyses suggest possible older ages and the rim of one monazite suggests a younger age, when processed statistically (Isoplot, Ludwig, 2004) the data point to a dominant single age, probably D_2) of 1581±5 Ma (Figs. 23, 24).

Neither of the two published models for the origin of the Wonga Belt (the extension model at ~1740 Ma of Pearson et al., 1992, or the D_1 tear zone of Bell et al., 1992) are supported in the age data. Either recrystallization during D_2 obliterated most of the older monazite, or alternatively neither model is correct and the Wonga Belt simply a high-strain zone in D_2. The latter hypothesis is preferred, implying that the Wonga deformation of Pearson et al. (1992) was a more localized event.

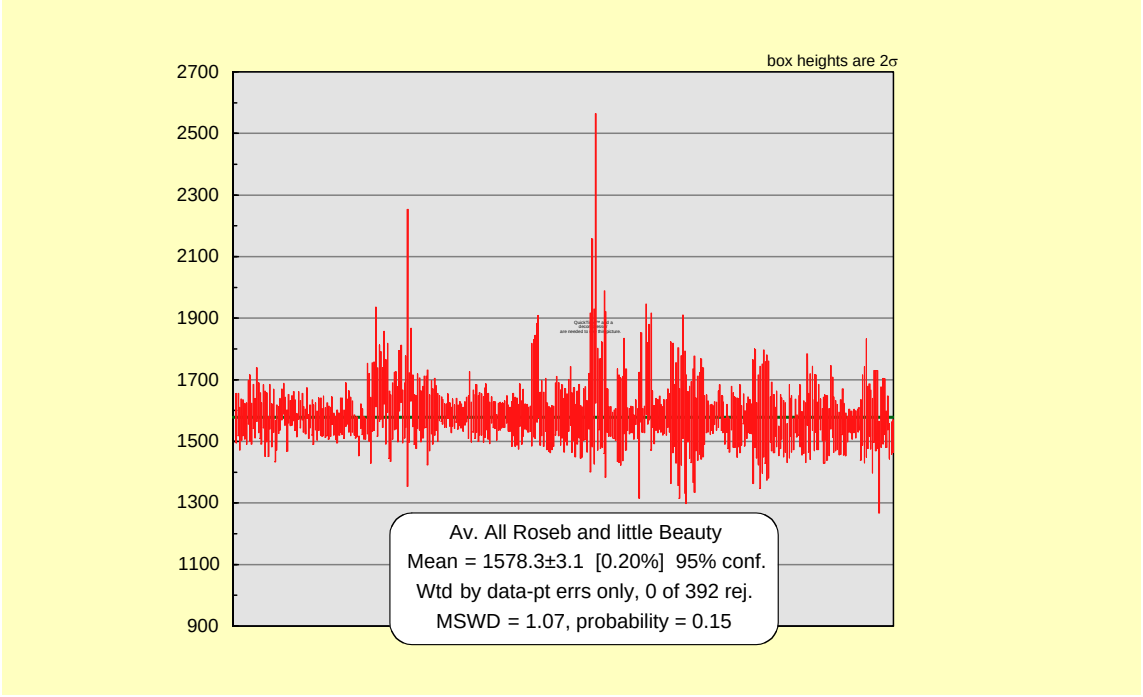

Figure 23. Weighted mean plot for all Rosebud Syncline and Wonga Waterhole monazite dates (n=392).

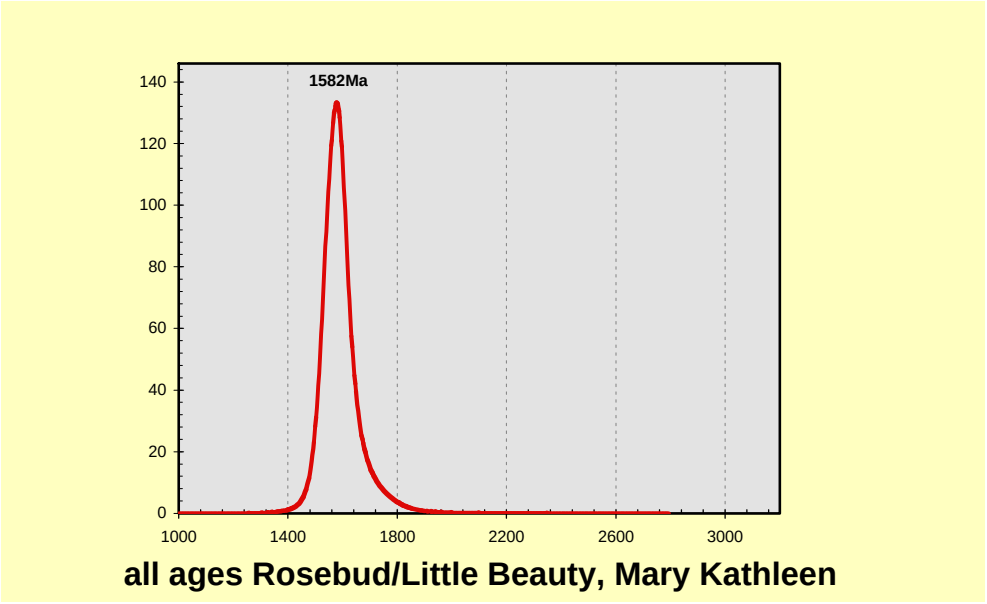

Figure 24. Probability plot for all Rosebud Syncline and Wonga Waterhole analyses. Note the single peak at D_2.

The data from the Wonga Waterhole "retrograde" samples is just as intriguing. Viewed separately, monazite dates from two samples, WWH3b and 10d, gave 1585±5.5 Ma and 1588± 13 Ma respectively, each age being within error of the Rosebud and the combined data (Fig. 23). It could be argued that the Wonga Waterhole monazite ages are simply inherited from D_2, however they are quite unique monazite grains, being relatively coarse, euhedral or subhedral and showing broadly concentric zoning (in comparison to Rosebud monazites that are quite small, generally anhedral, contain more common inclusions, and show no zoning or poorly defined zoning; Figs. 27, 28). On this basis the monazite grains in the Wonga Waterhole samples are interpreted as growing during the retrograde event, which must have occurred very soon after D_2 as the ages are within error of each other. Dating of a very narrow but distinct rim on part of the 3b monazite gave a younger age of 1570±30 Ma, but this too is within error of the metamorphic peak (Fig. 29). The tectonothermal implications of these dates are discussed below.

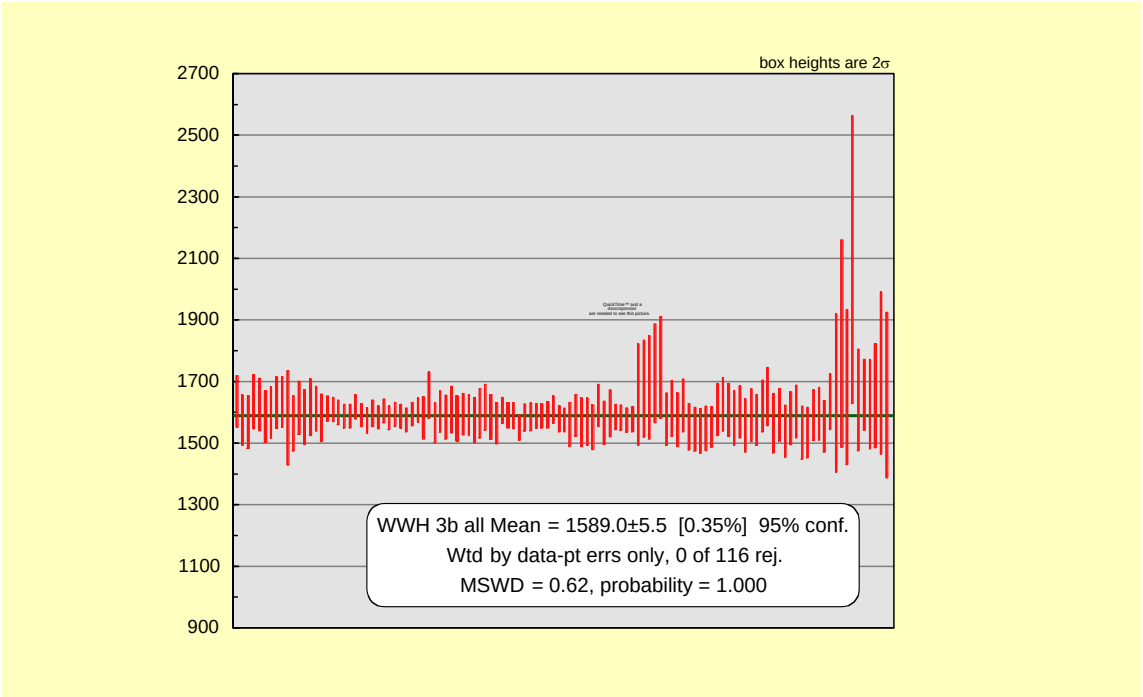

Figure 25. Weighted mean plot of monazite ages for sample WWH 3b. Most of the analyses are from a single large monazite (Fig. 26).

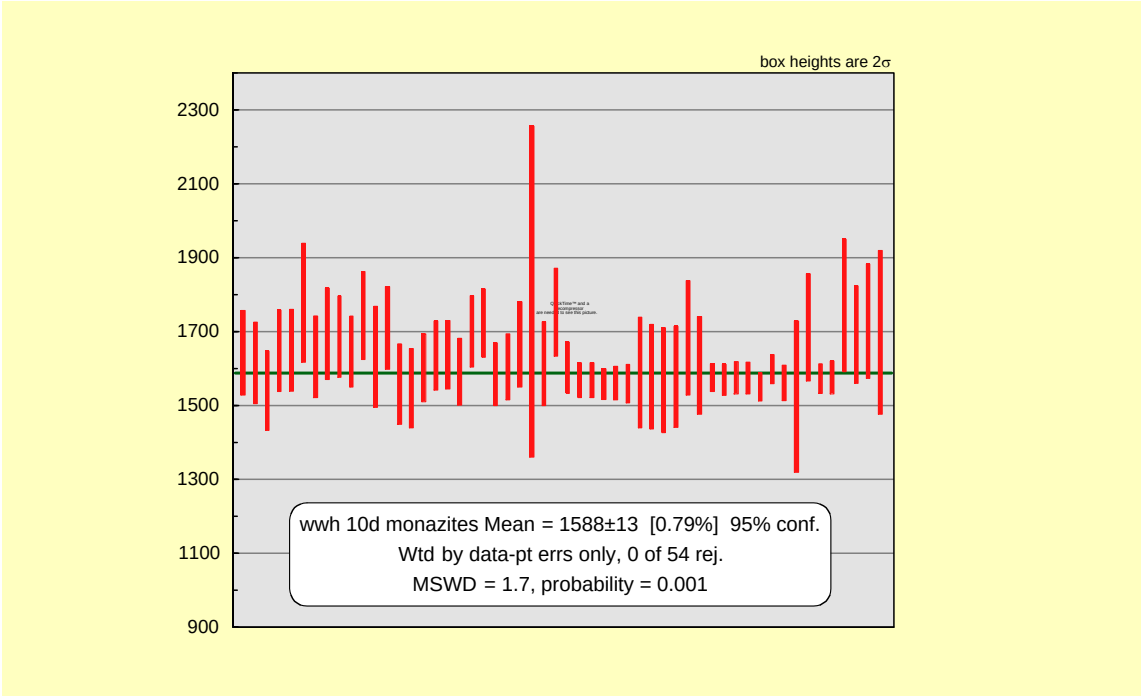

Figure 26. Weighted Mean plot, monazite ages for sample WWH10d (Fig. 28).

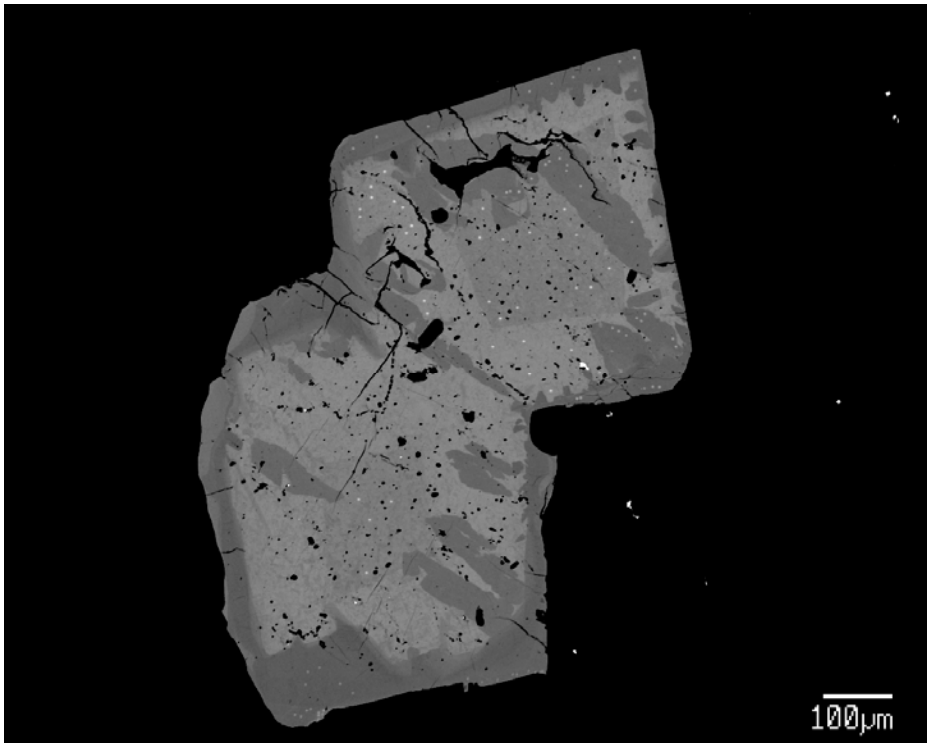

Figure 27. Electron microprobe backscatter image of a large monazite, sample WWH3b (Wonga Waterhole). Note the zoning, for a large part resulting from Th variations, and that all zones provided the same age (1585 ma), except the very narrow rim lower right. From its relatively large size and subhedral nature the monazite is interpreted as growing during the “retrograde” event at rather than being relict from the metamorphic peak. Most analysis positions show up as bright spots.

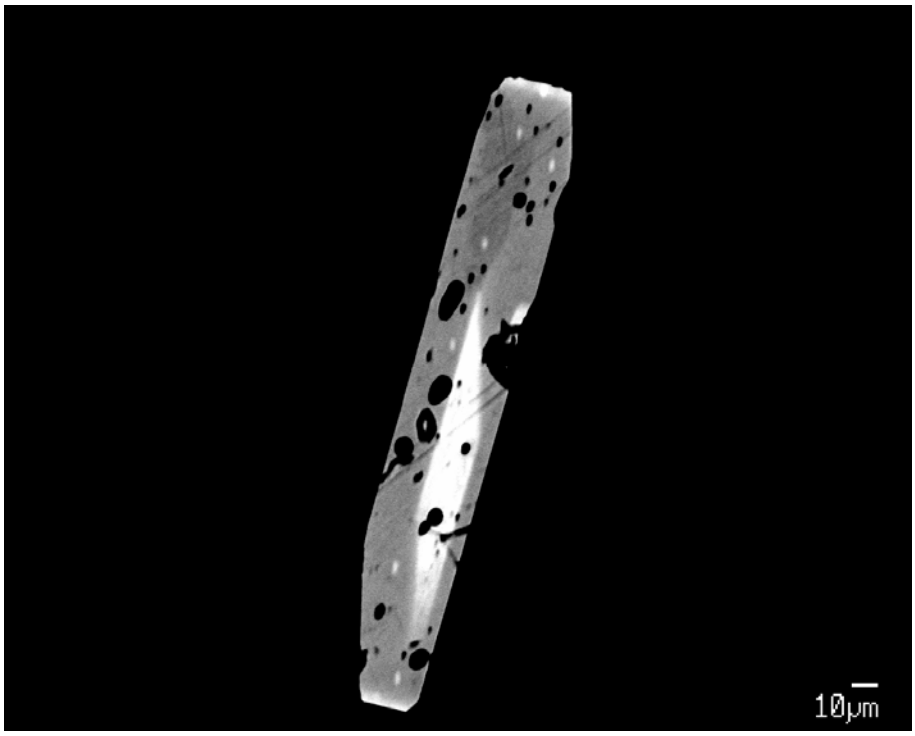

Figure 28. Backscatter image of a zoned monazite, sample WWH10d. From its euhedral nature and elongate prismatic shape the monazite is interpreted as growing in the "retrograde" event, rather than being relict from the metamorphic peak.

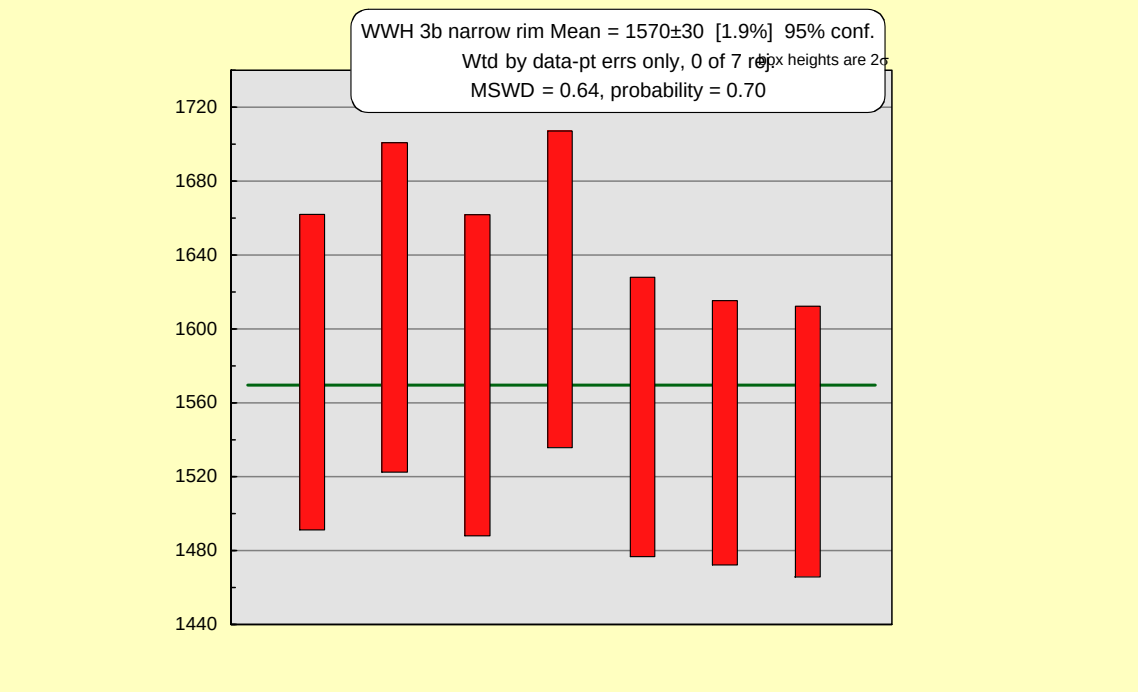

Figure 29. Weighted mean plot for narrow rim, monazite, sample WWH3b.

4.3 Monazite age determinations, Western Fold Belt

Mica Creek Pegmatites and the age of D_2

It was argued in Rubenach (1992) that the Mica Creek Pegmatites intruded during D_2 They appear only weakly deformed, but they typically contain tourmaline, and metasomatic tourmaline in some schists in contact with the pegmatites are aligned in L_2 (plunge ~80ºS). Connors & Page (1995) obtained a 1532 Ma U-Pb zircon date for a pegmatite and argued that this was the age of D_2. However, this age is suspect as they reported that the zircons were metamict. Hand & Rubatto (2002) report a 1575 Ma U-Pb monazite age for a schist west of Mount Isa, and this older date is supported by the data from schists in this report. In addition, a superprobe monazite date of 1596±27 Ma was obtained from a Mica Creek Pegmatite (Fig. 30), and this is within error of the age of D_2.

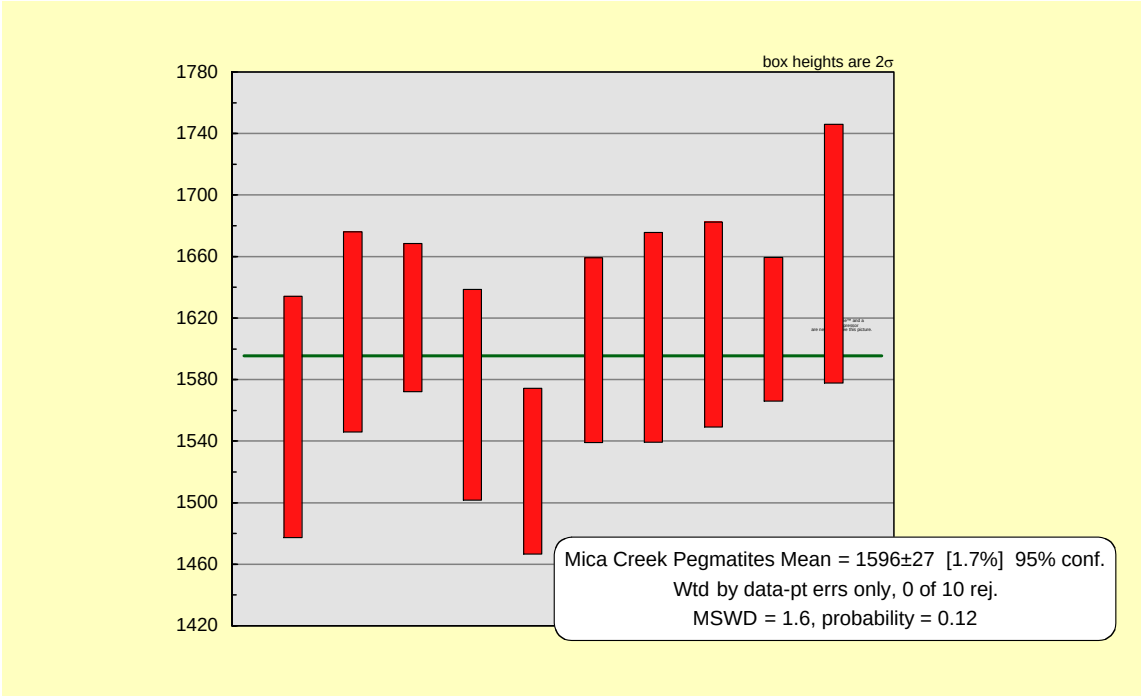

Figure 30. Weighted mean plot, small monazite from Mica Creek Pegmatite.

Age determinations, May Downs Gneiss and Eastern Creek Volcanics

Monazite age dates were determined for 4 samples of May Downs Gneiss, and 8 samples of Eastern creek Volcanics, the latter including schists, metasomatic cordierite rocks and a tourmalinized schist. The results are tabulated in the appendices.

Figure 31 is a probability plot of all these data. It shows a main peak at 1607 Ma, and subsidiary peaks at 1529, 1560, 1585 and 1642 Ma. This plot is consistent with microstructural data that indicate polymetamorphism. Although these peaks and plateaux are probably mixed they are consistent with the data for events in the EFB (Rubenach et al., in press; see appendix); thus 1529 Ma corresponds with the D_4 event, 1560 Ma with the D_3 event, and 1585/1607 with the D_2 event. The 1642 Ma peak is probably a mixed Sybella/D_2 age. However, it is probably more useful to examine the May Downs Gneiss and the Eastern Creek Volcanics separately.

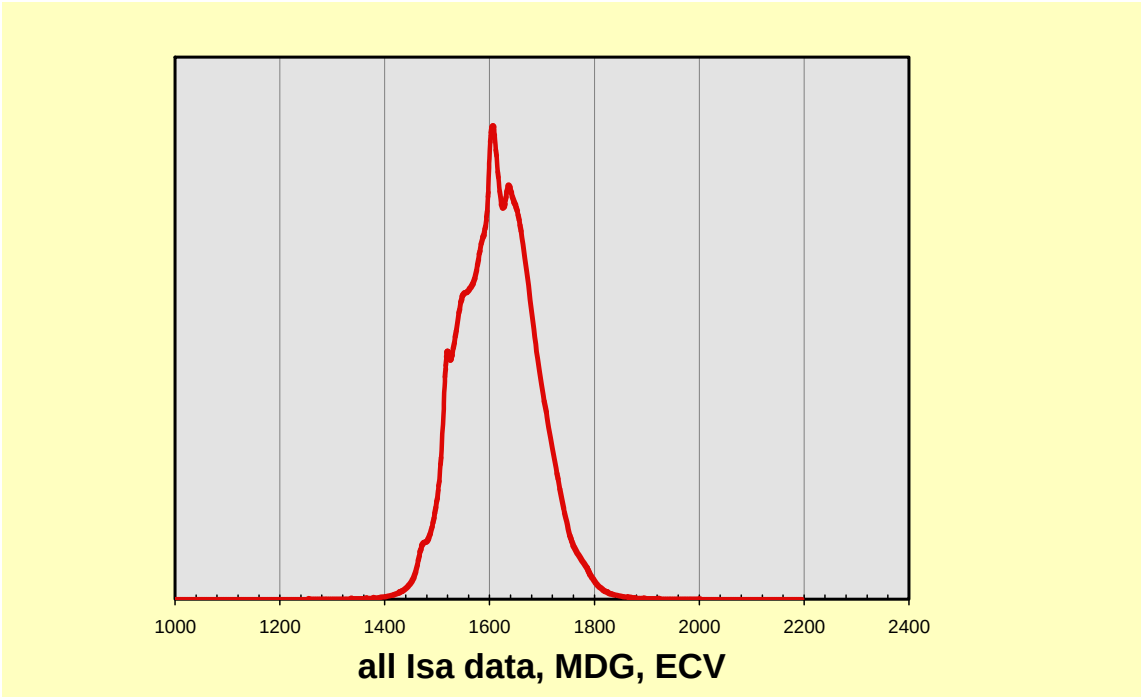

Figure 31. Probability plot of monazite ages, May Downs Gneiss and Eastern Creek Volcanics.

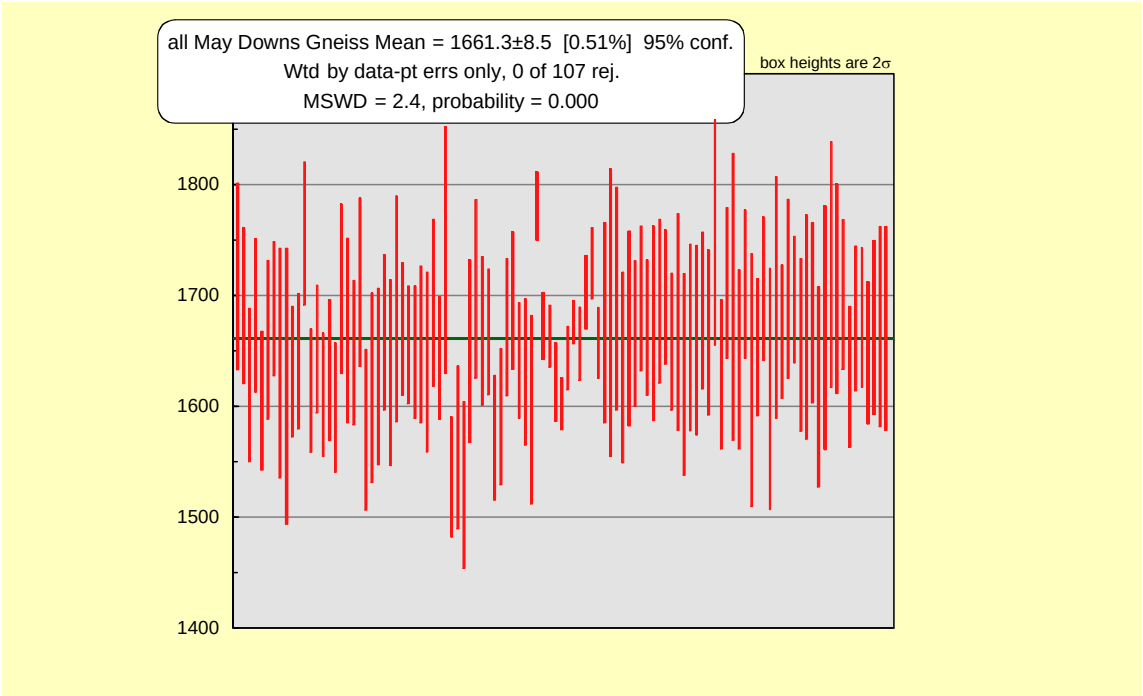

Figure 32. Weighted mean plot for monazite age dates for all gneisses (Crd-Kfeld and Sil-Bt-Kfeld) from the May Downs Gneiss.

The May Downs data (Fig. 32) provide a mean age of 1661±9 Ma, but this is a combination of a number of ages. As discussed above, the rocks were initially metamorphosed as cordierite/Kfeldspar gneisses in a Sybella event, followed by

sillimanite/biotite/Kfeldspar migmatitic gneisses in both a subsequent Sybella event and Isan Orogeny D_2 event. Thus monazite inclusions in cordierite in samples IN1.1 and 504.4 provide ages of ~1672 Ma (i.e. Sybella), whereas individual monazite grains in the matrix of IN3 and 504.4 gave ages of ~1580 Ma (D_2). Other monazites provided mixed ages. A large number of analyses (72), mostly on matrix monazites, were performed for sample 504.4, and the weighted average is 1662±10 Ma, similar to the combined gneisses. This sample is a sillimanite/biotite/Kfeldspar gneiss with some relict cordierite grains, with most of the monazite grains situated at silicate grain boundaries, making them unlikely to be relicts from the previous metamorphism and thus confirming the two Sybella events.

The samples from the Eastern Creek Volcanics provided a weighted mean of 1578±8 Ma (Fig. 33). Individual monazite ages of ~1570 and ~1550 Ma are also preserved, consistent with the polymetamorphic nature of the schists and suggesting some ages are probably mixed. Regardless, the mean age is within error of the above Mica creek Pegmatite age, the Hand and Rubatto (2002) U-Pb monazite age from an ECV sample, U-Pb ages of tourmaline in uranium prospects (Duncan et al, 2006) and the ages of D_2 determined for both the Mary Kathleen-Duchess and Selwyn zones of the Eastern Fold Belt.

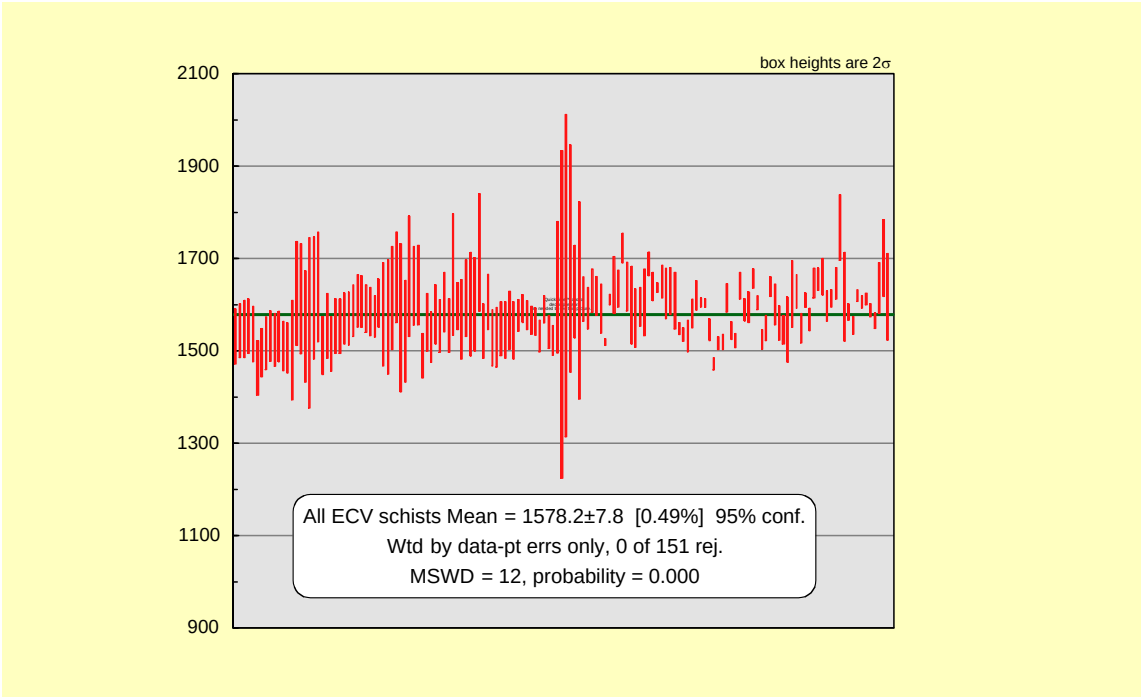

Figure 33. Weighted mean plot for monazite age dates, schists from the Eastern Creek Volcanics

5. METASOMATIC HISTORY OF THE MOUNT ISA INLIER
5.1 Eastern Fold Belt – Selwyn Zone

The metasomatic history of the Selwyn Zone has been dealt with in the I3 report, and in Rubenach (2005) and Rubenach et al. (in press), and only a brief summary and a few upgrades are given in this report. Aside from the mineralization the main metasomatic rocks are as follows:

1. Albitites and associated biotite-rich schists. These are restricted to the Soldiers Cap group and are structurally controlled by proximity to amphibolite bodies (former gabbro and dolerite sills) and small faults and shear zones. They show their best development in the Snake Creek anticline and the Osborne Mine. Monazite dating indicates that they formed in the period 1640-1680 Ma (Rubenach et al., in press), and recent dating from a key locality, reported in Section this report, suggests a probable abitization age of 1651± 8.5 Ma. It is suggested that fluids sourced from the Corella Formation were focussed along extensional faults, shear zones and the contacts of mafic sills during the latter stages of basin development, as shown in Figure 34. The up-temperature fluid migration resulted in large-scale resetting of oxygen isotopes in the Snake Creek Anticline (Rubenach and Oliver, I3 report). The formation of albitites ("adinoles") by fluid focussing along dolerite contacts is described from an area in Ireland by Angus and Kanaris-Sotiriou (1995). Minor Kfeldspar alteration in the Snake Creek Anticline is possibly related to the fluids moving down-temperature following albitization.
2. Breccias and associated Na-Ca alteration. These are abundant in the Corella Formation in the Selwyn Zone, but breccias with calsilicate clasts (and some igneous clasts) in pipes and selvages around small igneous bodies, together with late-stage albite veins, occur in some areas of the Soldiers Cap Group, especially near the Cloncurry Fault. They are described in Mark et al. (1999) and Marshall (2003). In the Snake Creek area the breccias are clearly synchronous with the Saxby Granites, dated at 1527 Ma (Rubenach et al., in press). The relationships between the breccias and some Cu-Au deposits (especially Ernest Henry) are documented in Mark et al. (1999; 2004; 2006a, b) and Oliver et al. (2004).

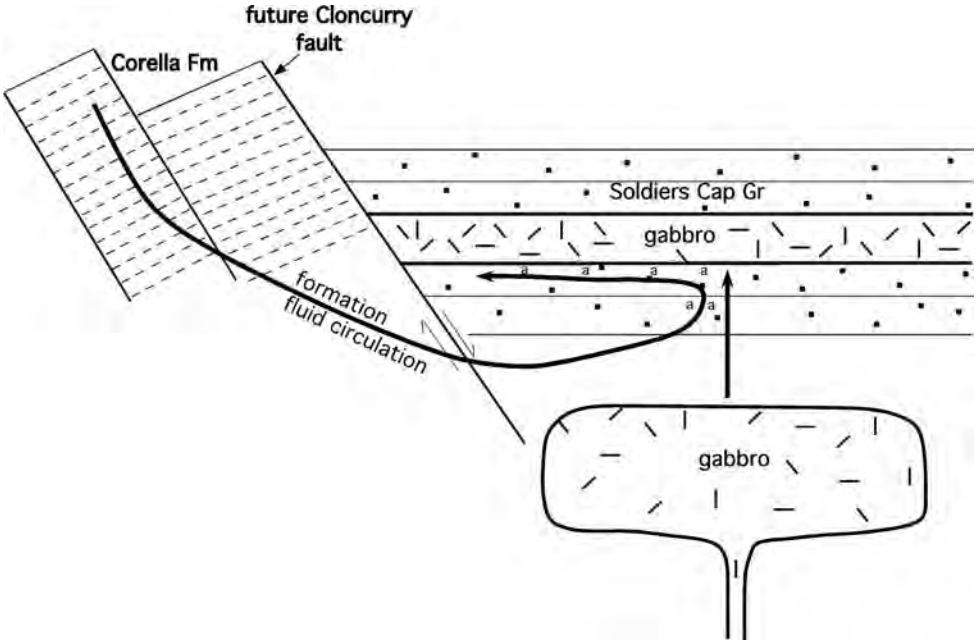

Figure 34. Schematic model for the formation of 1640-1680 Ma albitites (a), Soldiers Cap Group

5.2 Metasomatic rocks of the Mary Kathleen/Duchess Zone, EFB

Metasomatic rocks in the Mary Kathleen/Duchess Zone are described in Oliver (1995), Oliver et al. (1993; 1995; in press), and Marshall (2003). They include skarns (e.g., Mary Kathleen), calcite pipes, scapolite alteration, albitization, pyroxene-garnet-Kfeldspar rocks, "red-rock" (haematite-stained albite, epidote, amphibole, pyroxene alteration) and breccias. Some of this alteration (e.g. skarns) is associated with granites and is of Wonga age (~1740 Ma), other examples could be syn-D_2, but most (e.g. the calcite pipes, albitization, scapolite alteration, red rock alteration) is late in the history (e.g., U-Pb titanite ages of 1555-1520 for albitization associated with the calcite pipe at the Knobby quarry, Oliver et al., 2004). The abundance of the late alteration is interesting because of the lack in this zone of granites and associated mafic rocks of a similar age bracket, in contrast with the Maramugee, Williams and Naraku granites/batholiths of the Selwyn Zone.

5.3 Metasomatic Rocks of the Mount Isa area, Western Fold Belt

The sequences west of the Mount Isa Fault exhibit extensive metasomatism and a large diversity in metasomatic types (Fig. 39). The most abundant are as follow:

1. Pods of tremolite (± calcite, talc, epidote) and tremolite-plagioclase are abundant in a strip of Myally Group greenschist facies rocks just west of Mount Isa (Figs. 35-39). These formed were argued to have formed during D_2 (Huang and Rubenach, 1995). Attempts to find suitable titanite grains for age dating were unsuccessful. Interestingly many of these rocks imply similar alteration (dolomite/silica) to the host metasomatic rocks of the Mount Isa copper deposit, but the latter formed in D_3 or later. However an S_3 crenulation cleavage superimposed on a strong S_2 in talc schist (Fig. 38) indicates that the Molanite Valley pods did form in D_2 (and not S_2 reactivated in D_3). This implies similar

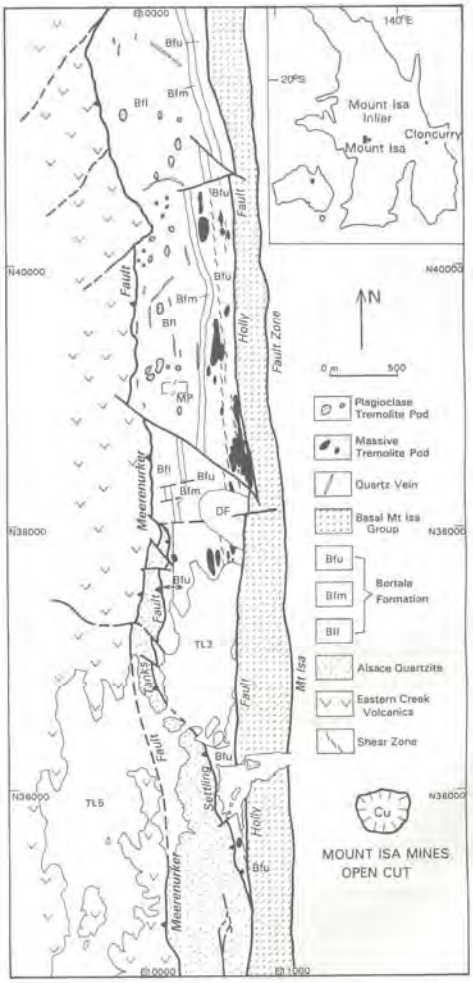

Fig. 1. Simplified geological map of the Molanite Valley. Note that the tremolite pods occur in a strip of the Bortala Formation which forms the hinge region of a large F_2 anticline which has been truncated by faults. Bfu—upper Bortala Formation; Bfm—middle Bortala Formation; Bfl—lower Bortala Formation; DF—mine dump; TL—Tailings Dam; MP—Molanite Plant. Geographic co-ordinates are based on Mt. Isa Mines grid. Inset map shows location of studied area.

Figure 35. Map of metasomatic pods in the Molanite Valley.

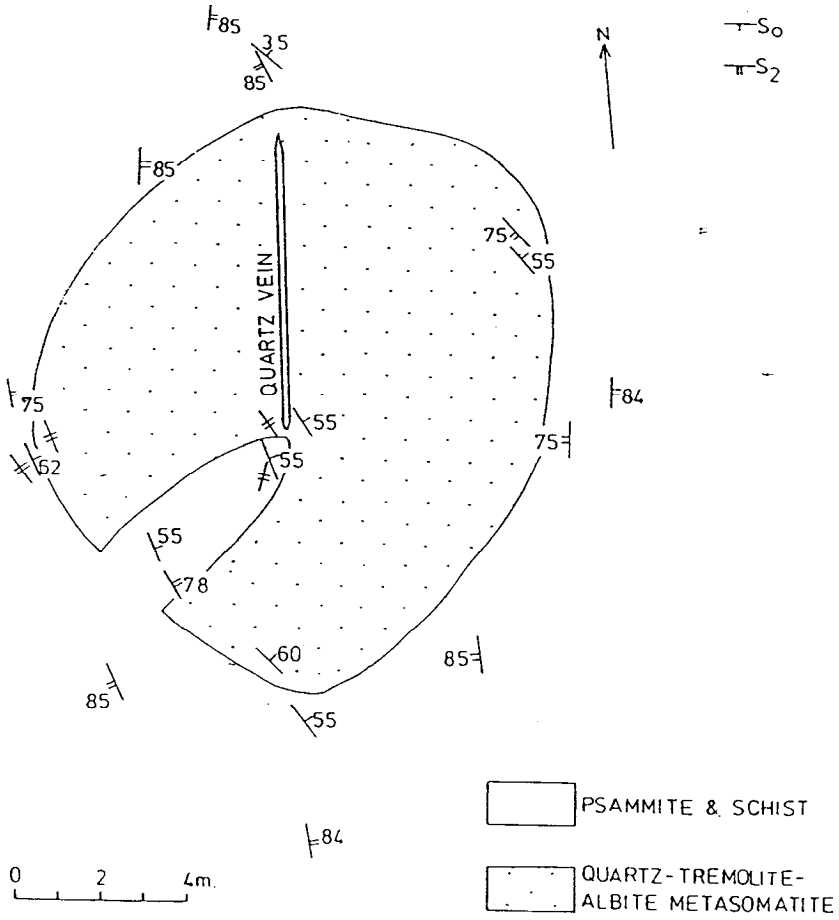

Figure 36. Map of a tremolite/plagioclase pod. This is centred around a vertical quartz lens. Tremolite clusters are aligned in S_2, with the pod cutting across S_2 and S_2 also deflecting around and through the pod. The contact between the metasomatic pod and the enclosing muscovite-biotite-quartz-chlorite schist and psammite is very sharp.

Figure 37, tremolite-talc pod. Above the hammer is talc-chlorite-calcite marble and schist. Below is mainly massive tremolite, with a layer of quartzite. Relict bedding is preserved in the tremolite. This is part of a large pod enclosed in muscovite schist and psammite. In places the metasomatic rocks have replaced marble, whereas elsewhere they have replaced psammite and calcareous psammite. Layers such as the commonly occurring 100% tremolite rocks are clearly metasomatic rather than calcareous/dolomitic rocks that lost only CO_2.

Figure 38. Talc-chlorite-calcite schist showing an S_3 crenulation cleavage.

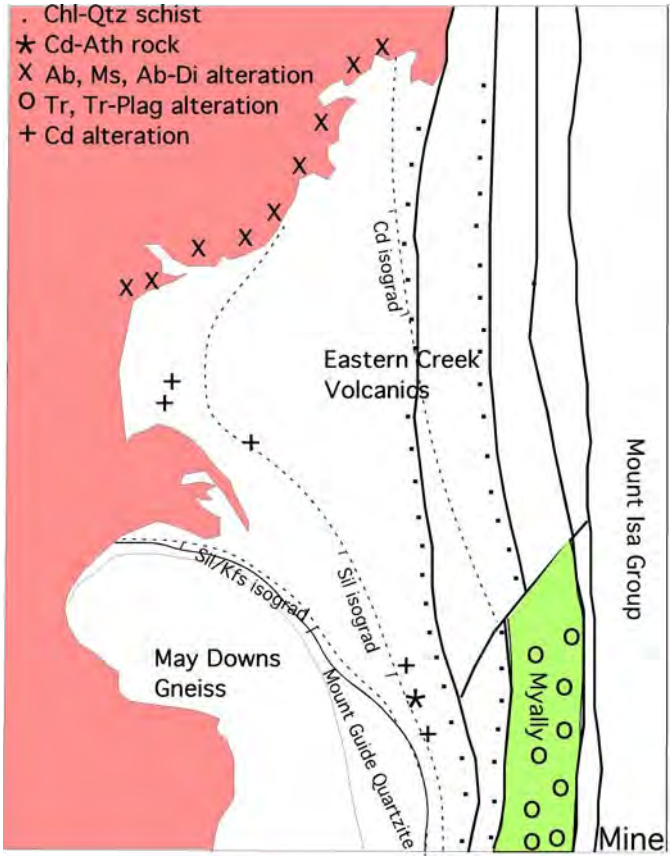

Figure 39. Schematic representation of metasomatic rocks NW of Mount Isa. The tremolite and tremolite-plagioclase rocks are restricted to the Myally Subgroup. The chlorite-quartz schist (together with the higher grade equivalent cordierite-anthophyllite rocks, and, not shown, epidozites, occur preferentially along faults and localized shear zones. Cordierite metasomatic rocks that have replaced pelitic schists occur close to or within the sillimanite zone and are associated with boudinaged mafic rocks. Albitized granite, and granite replaced by muscovite, occur close to the contact with the Sybella Granite (pink) at the edge of the Kitty Plain; plagioclase-clinopyroxene alteration has replaced some mafic rocks at the edge of Kitty Plain.

2. Altered mafic rocks, Eastern Creek Volcanics. These include the quite abundant chlorite-quartz-rutile schists (± talc, cummingtonite, anthophyllite – Figs. 40, 41) and the less common epidozites (epidote, quartz, titanite – Fig. 42). These are located preferentially along major fault zones and localized small shear zones, as well as lenses with no obvious fault associations. Cordierite-anthophyllite rocks (Fig. 43), sillimanite zone equivalents of chlorite-quartz schists, occur as isolated pods. The rocks typically show a strong S_2, in places an S_2 crenulation cleavage, so clearly formed early in the history (in contrast to those described from east of the Mount Isa Fault by Heinrich et al., 1995, which they believe to have formed late, probably syn-D_3, and are implicated in providing Cu to the fluids that formed the Mount Isa Cu orebodies). The alteration styles are very similar (but higher grade of metamorphism) to those described from Mid-Ocean Ridges where they formed by circulation of seawater through the volcanic pile (e.g., Motl, 1983). The Mount Isa examples, of course, did not form at a mid-ocean ridge, but almost certainly formed early in the history (e.g., during deposition or syn-Sybella) by saline fluid circulation. This would imply that major faults, such as the Mount Gordon and Tailings Dam/Meernurker faults, had protracted histories of

Figure 40. Chlorite-quartz schists along the Mount Gordon Fault, west of Mount Isa. A small relict mafic pod, now an amphibolite, occurs in the central upper part.

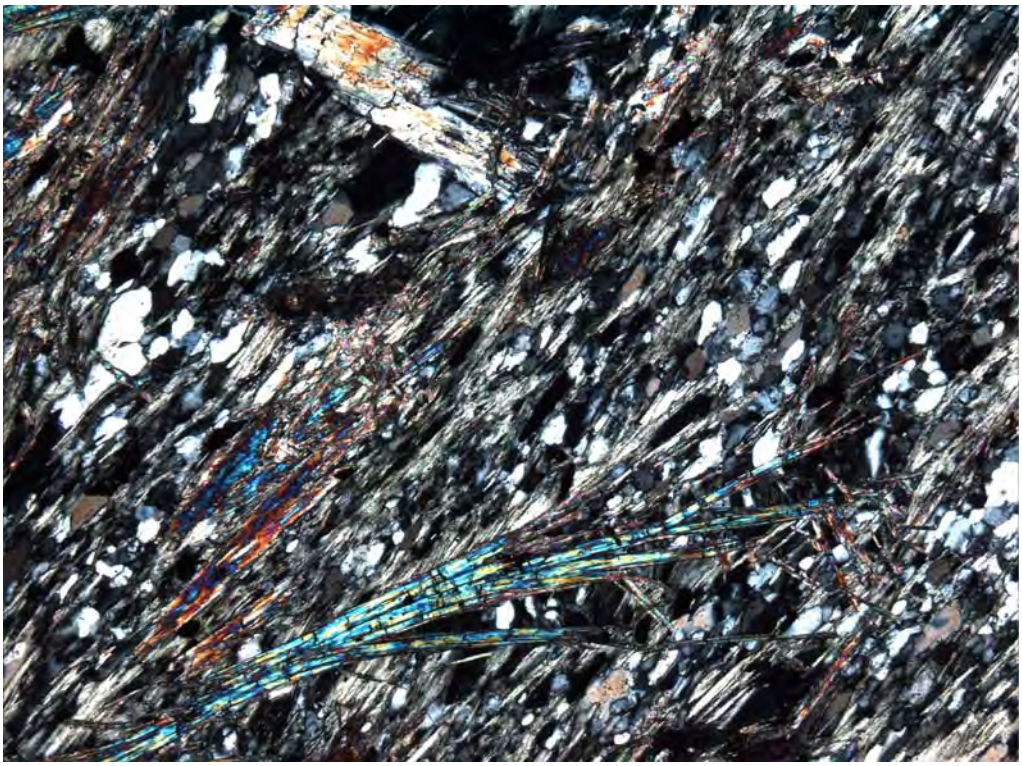

Figure 41. Chlorite-quartz schist showing a strong S_2, and late syn-D_2 acicular cummingtonite porphyroblasts. Crossed polars, length 5.6 mm. Such porphyroblasts indicate that the schists did not form as post-D_2 retrograde shear zones.

Figure 42. Epidozite, comprised mainly of quartz and epidote. The epidote clusters are amygdales now elongate in L_2, the flat surface being parallel to S_2.

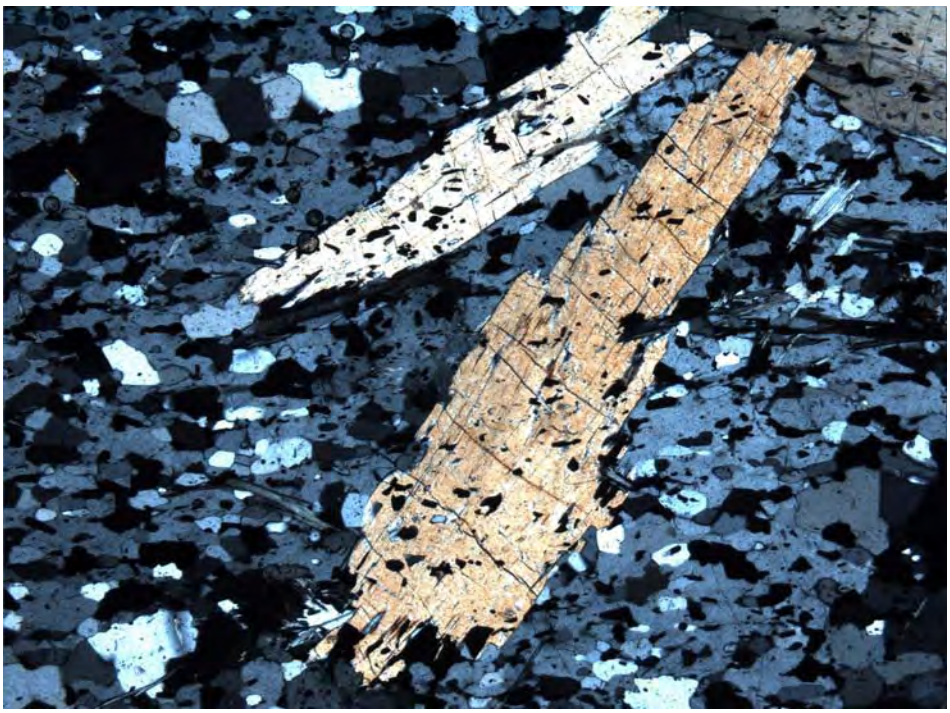

Figure 43. Cordierite-anthophyllite rock, showing a strong S_2 foliation (sub-vertical in the field, sub-horizontal on the photo). Crossed polars, length 5.6 mm. The porphyroblasts clearly overgrew S_2 and the rock formed by metamorphism of chlorite-quartz schists.

3. Cordierite metasomatic rocks. These are the most unusual in the area, as they consist of cordierite, quartz (± andalusite, sillimanite, plagioclase, phlogopite) that have replaced typical muscovite-quartz-biotite-cordierite schists adjacent to pods of amphibolite (mainly metadolerite) that have been boudinaged during D_2 (Fig. 44). They typically show two growth stages of cordierite; one, schist cordierite, that grew early in D_2, and a second metasomatic cordierite that has replaced the muscovite matrix later in D_2 (Fig. 45). The metasomatism thus probably occurred late in D_2. Monazite grains in schists and both stages of cordierite in the metasomatic rocks gave ages that are all in error of D_2. The metasomatic fluids subtracted K and added Mg to form the cordierite rocks, and as they occur at a metamorphic grade where chlorite-quartz rocks are metamorphosed to cordierite-anthophyllite rocks (also late D_2) it is suggested the fluids were derived from the latter (chlorite loses ~20% water on dehydrating to form Crd/Anth, and such fluids would be saturated in Mg and undersaturated in K). Previous unpublished work by Rubenach determined that the cordierite-anthophyllite rocks, of mafic derivation, are geochemically quite distinct from cordierite metasomatic rocks of pelitic derivation in terms of immobile elements such as Ti, Zr, Y, and Nb.

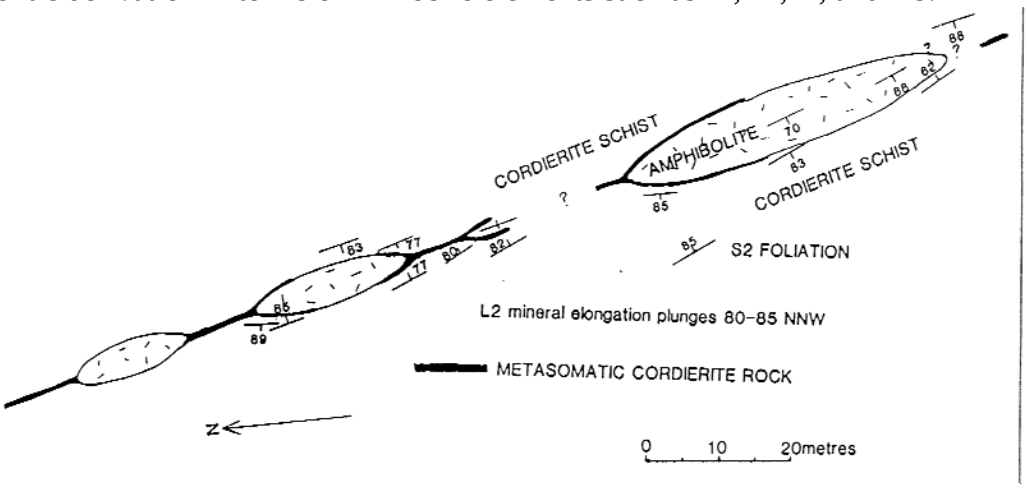

Figure 44. Map of some boudinaged amphibolite pods with associated cordierite metasomatic rocks that have replaced cordierite schists. It is proposed that strain contrasts between the schists and boudinaged amphibolites helped localize the metasomatic fluids.

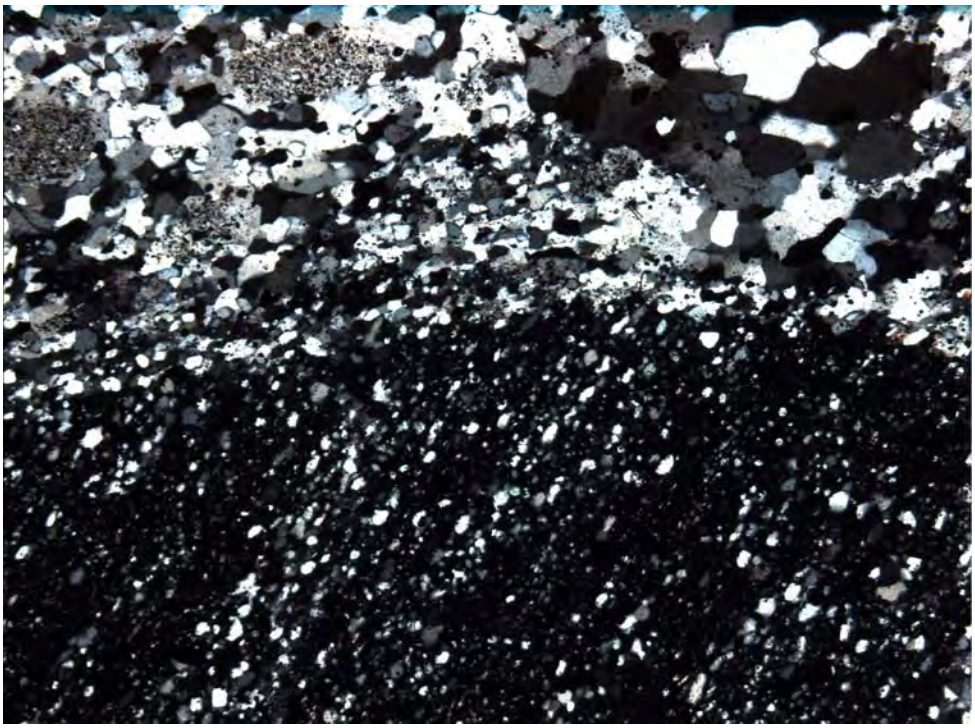

Figure 45. Cordierite metasomatic rock. The cordierite porphyroblast in extinction shows an older foliation but probably grew during D_2 in the precursor pelitic schist. The upper part of the matrix consists of a second (metasomatic) generation of cordierite and coarser quartz that have replaced the muscovite-rich matrix. Crossed polars, length of photo 5.6 mm.

4. Metasomatic rocks along the Sybella Granite contact, edge of Kitty Plain (Fig. 39). At or near the contact the Sybella Granite shows lenses (up to 100 m long) of alteration, either albitization (replacement of pink Kfeldspar by white albite – Fig. 46), alteration of granite to muscovite schist (± quartz, andalusite, corundum), or rarely a muscovite core surrounded by an albite halo. It is not certain whether the foliation shown by these rocks, especially the schists, is S_2, and older foliation or (more likely) both. In the same area, mafic rocks, including syn-Sybella dolerites and country rock amphibolite of uncertain derivation, show alteration to plagioclase-rich rocks and plagioclase-clinopyroxene rocks. The latter are either striped with a strong foliation that is probably syn-Sybella (Fig. 47), or occur as pods in plagioclase-titanite rocks ((Fig.48). It is concluded that the metasomatic rocks along the contact at the edge of Kitty Plain probably formed syn-Sybella. Although breccias do not occur here, the alteration types have many similarities to the metasomatic rocks that have affected the Corella Formation and the granites and dolerites of the Williams Batholith in the Selwyn Zone, and, on analogy with the latter, it is suggested that the fluids were saline and derived from adjacent sedimentary basins, the igneous rocks acting as heat engines. Ductility contrasts between the igneous rocks and the Eastern Creek Volcanics may have helped in focusing the fluids along contacts during the Syn-Sybella deformation event.

Figure 47. This is an outcrop of a metasomatized mafic rock at the situated at the contact of the Sybella Granite. It shows a strong foliation defined by plagioclase-rich and clinopyroxene-plagioclase bands. The foliation is EW and is more likely to be syn-Sybella than S_2.

Figure 48. The light-coloured rock consists mainly of plagioclase and titanite, with the dark rounded “inclusions” consisting of clinopyroxene, plagioclase and titanite. The outcrop is part of a NE-oientated vein within dolerite that shows mingling/mixing relationships within the Sybella Granite near the edge of Kitty Plain. From the abundance of titanite it is likely that both of the lithologies replaced dolerite. The timing is uncertain, but, as with the Figure 47 locality, more likely to be syn-Sybella.

5. Veins and alteration patches are associated with uranium prospects, such as Eldorado and Easter Egg, in the eastern Creek Volcanics west of Mount Isa (Duncan et al., 2006, and references therein). These were not studied in any detail by myself, but veins containing epidote, clinopyroxene and epidote, along with allanite-clinopyroxene alteration of a foliated amphibolite (Fig. 49) were noted. The alteration and veining appears late to post-D_2. U-Pb dating of tourmaline by Duncan et al. (2006) yielded an age of 1577±48 Ma, but a better D_2 age of 1573±12 Ma was obtained by these authors from tourmaline from the Andersons uranium prospect NE of Mount Isa.

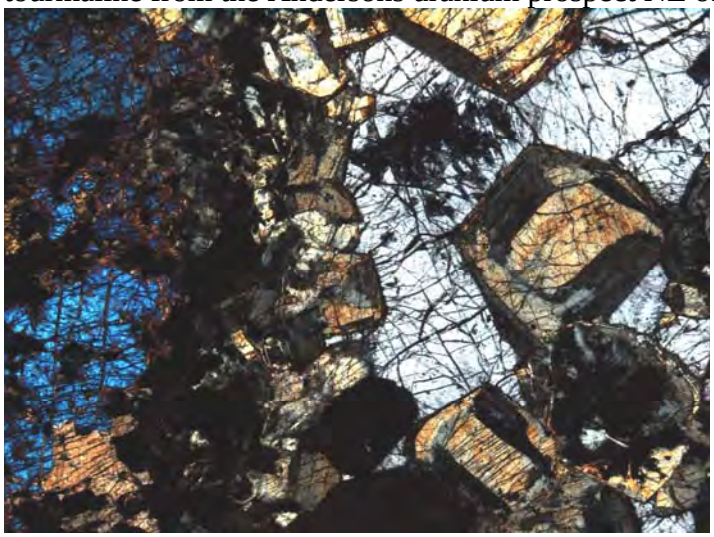

Figure 49. Euhedral zoned grains of allanite (brown) enclosed in clinopyroxene (blue, blue-grey), Eldorado prospect. Crossed polars, length 4.6 mm.

6. DISCUSSION AND CONCLUSIONS

6.1 Pre-Isan events

The events occurring prior to the Isa Orogeny are as follows:

1. The Wonga Event occurred at the close of deposition in the Leichardt Superbasin at ~1740 Ma during the emplacement of the Wonga Batholith in the Mary Kathleen/Duchess Zone and the Gin creek Granite in the Double Crossing Metamorphics in the Selwyn Zone (Pearson et al., 1992; Holcombe et al., 1991; Page & Sun, 1998). There is currently some doubt as to whether this event was a widespread extension shear zone as proposed by Holcombe et al. (1991), or whether it was associated with local granite emplacement. Wonga ages did not show up in the monazite dating in this report, although it is possible that Wonga Event-related monazites were largely obliterated in D_2.
2. The Sybella Event was a localized ductile shear zone at ~ 1670 Ma and was associated with the emplacement of the Sybella Batholith in the WFB, some granites and dolerites pre-dating the shear zone (or were synchronous with it) while others intruded after deformation largely ceased (Hoadley et al., 2001; Gibson et al., in press). The May Downs Gneiss was initially metamorphosed to cordierite-Kfeldspar rocks with a shallowly dipping foliation, and these were largely overprinted by sillimanite-biotite-Kfeldspar migmatitic gneisses (at 4-5 kbar), still within the Sybella Event (monazite dating, this report). Although the Sybella Event is restricted to part of the WFB, intrusions of diorite at the Ernest Henry Mine Mark et al., 2006b) and gabbro/dolerite/trondhjemite sills in the Snake Creek area (1686 Ma, Rubenach et al. in press) shows that igneous activity was not restricted to the Sybella Granite during the early stages of development of the Isan Superbasin.
3. Early albitization in the Soldiers Cap Group, Selwyn Zone, has been dated at 1640-1680 Ma (Rubenach et al, in press), with recent monazite dating of two samples yielding better statistics of 1651± 8.5 Ma (see section 4.2). Cordierite and andalusite in these rocks have overgrown weak foliations, but their timing, and the age of these foliations is uncertain, but must be between 1651 Ma and the subsequent D_1 event. Whether or no the early albitization and cordierite growth should be included in the Isan Orogeny is largely a matter of definition.

6.2 Isan Orogeny across the Inlier

Structural, microstructural and age determinations indicate that the peak of metamorphism in the Isan Orogeny occurred in the D_2 event(s) across the inlier. Monazite ages of 1580-1595 Ma for the Selwyn Zone, ~1580 Ma for the Mary Kathleen area, and ~1580 Ma for the Mount Isa area are consistent with most published metamorphic peak U-Pb dates for monazite and zircon. It is possible from these data that D_2 (metamorphic peak) commenced earlier and was longer-lived in the Selwyn Zone.

The D_{1b} event (north-south shortening, steep EW structures) has associated porphyroblastic growth in the Selwyn Zone and the White Blow Formation, Mary Kathleen-Duchess Zone (Sayab, 2005a), but elsewhere this is uncertain. Likewise, a poorly defined age of 1610-1630 Ma was obtained for the Selwyn Zone, but elsewhere it is undefined in terms of age. It is quite likely that, except for a few localities in the EFB, that the grade during D_1 was greenschist facies or lower, so, in the absence of significant synchronous hydrothermal activity monazite growth was very limited.

D_3 structures (NNW, steep) occur across the inlier, but are not common in the Mary Kathleen-Duchess zone. Porphyroblast growth occurred across the inlier, but the age is poorly defined at ~1550Ma. Ductile D_4 structures, common in the Selwyn Zone, are rare elsewhere: the likely explanation is the emplacement of the Williams and Naraku batholiths, ~1500-1530 Ma.

6.3 Causes of metamorphic events in the Mount Isa Inlier

Excluding events in the basement (pre 1870 Ma) metamorphism in the Mount Isa Inlier is known to have extended from 1500 Ma to 1740 Ma. Most of this metamorphism is low-pressure/high temperature (~3-4 Kbar), requiring significant mid-crustal thermal anomalies. Models explaining the tectonothermal evolution of the Mount Isa Inlier need to explain its polymetamorphic character (events extending over 100 Ma for the Isa Orogeny alone), the synchronous nature of the metamorphic peak across the inlier in the Isan Orogeny, and the alternating high and low grade belts. The following possibilities for the anomalous thermal conditions have been proposed for various areas:

1. Mantle delamination (with or without igneous intrusions). This was proposed by Loosveld & Etheridge (1990) to explain the low-P/high-T metamorphism during crustal shortening in the EFB. Its main limitation (besides requiring instantaneous mantle delamination and replacement by hotter mantle) is that it can explain a single event but not the multiple events, extending for over 100 Ma, during the Isan Orogeny.

2. Large-scale extension, with or without igneous intrusions. Giles et al. (2006) proposed extension during basin formation to explain the low-P/high-T metamorphism in the Snake Creek Anticline. This may work for the metamorphism producing early cordierite, but Rubenach et al. (in press) argue that the peak of metamorphism occurred during both the formation of a sub-vertical foliation (S_{2a}) and the immediately following sub-horizontal shearing event (D_{2b}). Extension during granite emplacement has been proposed by Holcombe et al. (1991) for the Wonga Event and Gibson et al. (in press) for the Sybella Event.

3. Self-heating resulting from relatively high values of radiogenic heat-producing elements within a crustal sequence, commonly coupled with thermal blanketing due to overlying shale-rich sedimentary basins. This is proposed by Sandiford et al. (1995) and by McLaren et al (1999) for the metamorphic zones around the Sybella Batholith with high radiogenic heat-producing granites locally important, and for the Mount Isa Inlier as a whole by Gessner (pmd*CRC reports). As mentioned by Reinhardt (1992), Rubenach (1992) and Foster & Rubenach (2006), high radiogenic heat-producing elements probably form an important component of the overall thermal budget, but it is proposed that they are not the sole explanation for the high-T/low-P metamorphism in the inlier. Specifically, age dating shows that the peak of metamorphism (~ 1580-1595 Ma) was broadly contemporaneous across the inlier, whereas the Kalkadoon Granites are over 250 Ma older, the Wonga Batholith is 150 Ma older, the Sybella Batholith over 90 Ma older, and, with the exception of the small Gin Creek Granite, pre-D_2 granites are

4. Intrusion of large igneous bodies synchronous with deformation. This model clearly explains the metamorphism during the Wonga and Sybella events, and almost certainly is a significant factor during the D_4 event associated with granites of the Williams Batholith in the Selwyn Zone. Mafic volcanics and intrusives are quite abundant in space and time, but with the exception of a minor dyke swarm in the Snake Creek Anticline, large mafic bodies synchronous with the metamorphic peak in the Isan Orogeny are unknown (this, however, could be a dating problem as very few amphibolite bodies have been directly dated). However, all the known mafic rocks are highly fractionated quartz tholeiites, implying high degrees of partial melting of the upper mantle lithosphere and, because of their high-Fe contents, considerable fractionation, indicating the presence of large layered gabbro bodies deeper in the crust. The existence of such gabbros is consistent with geophysics data (Blenkinsop et al., in press). What is certain is that migmatites and pegmatites are abundant in the sillimanite/Kfeldspar and lower sillimanite zones throughout the inlier, and that direct dating has demonstrated that they formed during the Isan Orogeny metamorphic peak in the Sewyn Zone (Giles & Nutman, 2002) and the Mount Isa area (Mica Creek pegmatites, section 4.3 this report).

6.4 Tectonothermal Model for the Mount Isa Inlier

Regarding events prior to the Isan Orogeny, it is proposed that granites and associated mafic rocks intruded during extensional shear zone events for both the Sybella and Wonga events. It is suggested that fluid circulation and metamorphism associated with mafic intrusions during extension during basin development (1640-1680 Ma) resulted in the albitization and metamorphism to form cordierite (± andalusite) in some albitites in the Soldiers Cap Group, Selwyn Zone.

Regarding the Isan Orogeny, it is suggested that the multiple deformation events (D_1 to D_4) occurred in crust showing relatively elevated geotherms resulting from the combined effects of high radiogenic heat-producing elements and mafic intrusions in the lower crust. Crustal thickening, probably more pronounced in the Selwyn Zone producing metamorphism at 5-6 Kbar, occurred in the D_{1a} thrust event and the D_{1b} NS shortening event. By the time of the metamorphic peak (late D_{2a} to D_{2b}) the pressure was ~ 4-4.5 Kbar, so that (in particular in the case of the Selwyn Zone) a drop in pressure of ~ 1 Kbar had taken place (Fig. 4). Similarly, a drop in pressure to ~ 3 Kbar had taken place in the Selwyn Zone by 1527 Ma, the intrusion age of a Saxby Granite and the D_4 event. However, a detailed P-T-t path is available only for the Selwyn Zone. Nevertheless, there are sufficient data from the Mary Kathleen/Duchess Zone and the area west of Mount Isa

to suggest that both the metamorphic peaks and the retrograde shear zones with kyanite formed at ~ 4.5-5Kbar (Figs. 5, 11).

The age data for the Rosebud Syncline and Wonga Waterhole areas are quite significant as they indicate that the metamorphic peak and the retrograde shear zones are within error of each other. If the metamorphism were entirely the result of elevated high heat producing elements such a relatively sudden cooling (without a pressure drop) would not be expected (Fig. 5; section 4.3). Instead the data are consistent with a relatively sudden heat pulse followed by rapid cooling, as would occur if the extra heat was supplied by igneous rocks. That intrusion of igneous rocks did occur around the metamorphic peak is confirmed by field relationships regarding mafic dykes in the Snake Creek Anticline (Rubenach et al, in press), the ages of pegmatites at Cannington (Giles & Nutman, 2002) and Osborne (Gauthier et al., 2001), and the ages of pegmatites west of Mount Isa (this report). The abundance of such pegmatites in the sillimanite zones and sillimanite/Kfeldspar zones throughout the inlier certainly indicates that the middle crust melted during D_2, but does not demonstrate either the ultimate sources of heat for crustal melting were deeper gabbros, or elevated values of heat producing elements in the crustal section, or a combination both these processes.

The preferred model for this study combines of elevated values of heat producing elements and mafic rocks from the mantle. Arguments that the latter are implicated are as follows:

1. Mafic intrusions occurred at intervals covering most of the prolonged history of metamorphic events in the Inlier, including the Wonga Event, the Sybella Event, the albitization/cordierite growth in the Selwyn Zone, the metamorphic peak in the Snake Creek Anticline, the Maramungie Granites (? ~ D_3), and the Williams and Naruku Batholiths (~ D_4).

2. The mafic rocks are, at the current level of exposure, all high-Fe quartz tholeiites, implying considerable fractionation in deeper crustal magma chambers. The presence of numerous large magma bodies in the lower crust, emplaced episodically during a period of over 200 Ma, would have resulted in considerable heat transfer by both conduction and by advection resulting from the rise of crustal melts initiated by the gabbros. No such large bodies are currently exposed, but a thrust slice of metamorphosed peridotite at the Osborne Mine (Adshead, 1995) was derived from a large layered intrusion, and a small layered peridotite/gabbro body occurring under Mesozoic cover at the Titree Ni-Cu deposit is associated with the Naraku Batholith.

An interesting feature of metamorphism in the Mount Isa Inlier is that repeated high grade events occurred in the same locations. Thus peak Isan Orogeny metamorphism broadly coincided with both the Wonga Event and the Sybella Event in their respective areas, and in the Snake Creek Anticline amphibolite facies metamorphism broadly coincided for the cordierite growth and D_1, D_2, D_3, and D_4 events, extending over 100 Ma. Mafic intrusions are associated with number of these metamorphic events, so why not all of them?

The high grade metamorphism in the Selwyn and Mary Kathleen/Duchess Zones and west of Mount Isa broadly correspond to geophysical worms, that is the Cloncurry, Wonga and Barramundi worms respectively. It is suggested that each of these deep-seated structures was the locus of episodic gabbro emplacement. The proposed model for metamorphism in the Mount Isa Inlier is summarized in Figure 50. Note that during the peak of metamorphism that the thermal anomaly, a combination of elevated values of radiogenic heat producing elements and gabbro intrusions, was sufficient to cause partial melting to occur within mid-crustal metasediments. Pegmatites (water-rich melts) so derived intruded upwards, solidifying at a depth corresponding to the solidus for water-saturated melts (i.e., ~ 4Kbar). Heat was therefore transferred upwards via magmatic advection, with the upper limit of pegmatites corresponding to the sillimanite isograd and lower grade metamorphic zones forming above. This model is similar to that proposed by Miyazaki (2004) for a metamorphic belt in Japan. The three high grade areas (Fig. 50) schematically correspond, from NNW to SSE, the Mount Isa area, the Mary Kathleen/Duchess Zone and the Selwyn Zone high grade areas respectively. Note in this model that pegmatites (which are S-type granites) did not intrude into the intervening greenschist facies belts (cf. Figs. 1, 2) as, in contrast to the upper crustal metasedimentary rocks, the lower crustal rocks either did not melt or such melts were unable to rise. However melts derived from the lower crust did subsequently intrude into the middle crust as the Williams and Naraku batholiths in the period 1500-1530 Ma (a period that included the amphibolite facies regional/thermal metamorphism in D_4 at 1527 Ma). Note that the granites of the Williams and Naraku batholiths are A-type, derived from meta-igneous sources (pmd*CRC reports of Mark).

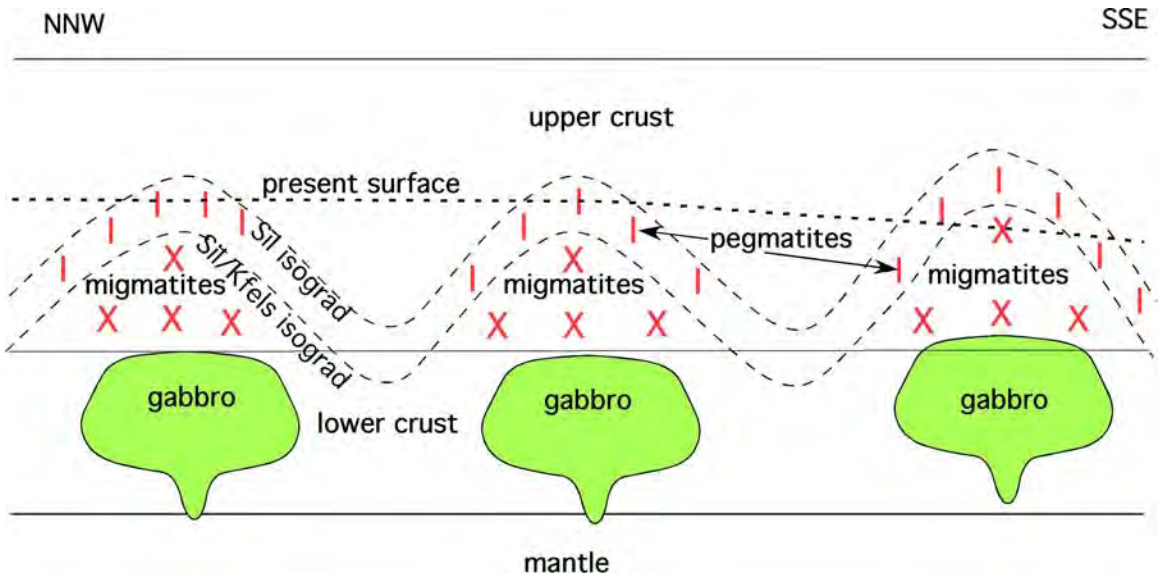

Figure 50. Schematic tectonothermal model for the Mount Isa Inlier, based approximately on the metamorphic section of Figure 2. Although the model has been drawn for the metamorphic peak, metamorphism occurred in multiple events (see text) and multiple episodes of gabbro emplacement are proposed. The pegmatites were derived from partial melting of metasedimentary rocks in the sillimanite/Kfelspar zones.

6.5 Implications for ore deposits

This report is mainly considering the Architecture of the Inlier, providing a tectonothermal evolution as a framework for other studies directly concerned with the ore deposits and ore-forming fluids. However a few general conclusions can be drawn.

1. There are no obvious relationships between metamorphic grade and mineralization. As the dips of the isograd surfaces are unknown, it is not known whether there are any relationships between mineralization and sharp metamorphic gradients.

2. Concerning metamorphic events, significant mineralization occurred in events other than the peak of metamorphism (D_2, Isan Orogeny). This is more likely to be a question of structural geology (e.g., focussing of fluids into particular brittle structures) than one of metamorphic grade

3. Metasomatic rocks in are quite abundant in the Mount Isa Inlier, both in space and in time, and a wide variety of metasomatic lithologies are represented. In terms of abundance and diversity the inlier is the most extraordinary metamorphic belt known. Most of the pre-Isan and Isan Orogeny tectonothermal events have contemporaneous metasomatic assemblages. Mineralization, while not necessarily being related to specific metasomatic events, is clearly more abundant in areas where metasomatic assemblages are relatively abundant, the Selwyn Zone and Mount Isa areas being the best examples. Some deposits have wall-rock or host metasomatic assemblages, such as albitites, Na-Ca alteration, potassic alteration, magnetite and silica-dolomite. To what extent relatively unmineralized metasomatic areas represent pathways for mineralising and exiting fluids is considered in other reports. Also considered elsewhere is the importance of mixing of diverse fluids in structural or chemical traps. An example briefly discussed above concerns the silica-dolomite host for the Mount Isa Cu orebody, as the Myally Group immediately west of the Mine contains abundant metasomatic pods with tremolite and talc that are slightly higher grade silica-dolomite, but which are unmineralized and older (i.e. syn-D_2) than the Mount Isa copper (syn-D_3 or syn-D_4). It is suggested that similar metasomatic fluids were involved in each of these at different times, but there was no mixing with other fluids (presumably Cu-bearing) in the case of the Myally Group example. An additional possibility is that the presence of graphite and pyrite were critical in the Mount Isa deposit, the Myally Group rocks being oxidized.

References

Adshead, N.D., 1995. Geology, alteration and geochemistry of the Osborne Cu-Au deposit, Cloncurry district, NW Queensland. Unpublished PhD thesis, James Cook University.

Adshead-Bell, N.S., 1998. Evolution of the Starra and Selwyn high-strain zones, Eastern Fold Belt, Mount Isa Inlier: implications for Au-Cu mineralization. Econ. Geol. 93, 1450-1462.

Angus, N.S., Kanaris-Sotiriou, R., 1995. Adinoles revisited: hydrothermal Na (Ca)-metasomatism of pelite screens adjacent to tholeiitic dykes in the Dublin terrane, Ireland. Mineral. Mag. 59, 367-382.

Banvill, G., 1998. Textural and geochemical investigation of magnetite species at the Osborne Cu-Au deposit, Cloncurry District, Mount Isa Inlier, NW Queensland. Unpubl. BSc Hons thesis, JCU.

Bell, T.H., 1991. The role of thrusting in the structural development of Mount Isa mine and its relevance to exploration in the surrounding region. Econ. Geol. 86, 1602-1625.

Bell, T.H., Hickey, K.A., 1998. Multiple deformations with successive subvertical and subhorizontal axial planes in the Mount Isa region: their impact on geometric development and significance for mineralization and exploration. Econ. Geol. 93, 1369-1389.

Betts, P.G., Giles, D., Mark, G., Lister, G.S., Goleby, B.R., Ailleres, L., 2006. Synthesis of the Proterozoic evolution of the Mt Isa Inlier. Aust. J. Earth Sci. 53, 187-211.

Betts, P.G., Lister, G.S., O'Dea, M.G., 1998. Asymmetric extension of the Middle Proterozoic lithosphere, Mount Isa terrane, Queensland, Australia. Tectonophysics, 296, 293-316.

Blake, D.H., Stewart, A.J., 1992. Stratigraphic and tectonic framework, Mount Isa Inlier. In: Stewart, A J., Blake, D.H., eds. Detailed studies of the Mount Isa Inlier. Australian Geological Survey Organization Bulletin, 243, pp. 1-12.

Blenkinsop, T.G, Huddlestone-Holmes, C.R., Foster, D.R.W., Edmiston, M.A., Lepong, P., Mark, G., Austin, J.R., Murphy, F.C., Ford, A., Rubenach, M.J. The crustal scale architecture of the Eastern Succession, Mount Isa: the influence of inversion. Precambrian Res. (in press).

Connors, K.A., Page, R.W., 1995. Relationships between magmatism, metamorphism and deformation in the western Mount Isa Inlier, Australia. Precambrian Res. 71, 131-153.

Duncan, R.J., Wilde, A.R., Bassano, K., Maas, R., 2006. Geochronological constraints on tourmaline formation in the Western Fold Belt, Mount Isa Inlier, Australia. Precambrian Res. 146, 120-137.

Foster, D.R.W, Rubenach, M.J., 2006. Isograd pattern and regional low-pressure, high-temperature metamorphism of pelitic, mafic and calc-silicate rocks along an east-west section through the Mt Isa Inlier. Aust. J. Earth Sci. 53, 167-186.

French, T., 1997. Genesis of albitites and anthophyllite-bearing lithologies of the Osborne Cu-Au deposit, Cloncurry District, Mount Isa Inlier, Queensland. Unpubl. BSc Hons thesis, JCU.

Gauthier, L., Hall, G., Stein, H., Schaltegger, U., 2001. The Osborne deposit, Cloncurry district: a 1595 Ma Cu-Au skarn deposit. In Williams, P.J. (ed.) 2001: a hydrothermal odyssey, new developments in metalliferous hydrothermal systems research, extended conference abstracts. EGRU contribution 59, 58-59.

Gibson, G.M. Rubenach, M., Neumann, Hutton, L.J, in press. Syn- and post-extensional tectonic activity in the Palaeoproterozoic sequences of Broken Hill and Mount Isa and its bearing on reconstructions of Rodinia. Precambrian Res.

Giles, D., Aillères L., Jeffries D, Betts, P., Lister, G., 2006a. Crustal architecture of basin inversion during the Proterozoic Isan Orogeny, eastern Mount Isa Inlier, Australia. Precambrian Res. 148, 67-84.

Giles, D., Betts P. G., Aillères L., Hulscher B., Hough M., Lister G. S., 2006b. Evolution of the Isan Orogeny at the southeastern margin of the Mount Isa Inlier, Aust. J. Earth Sci. 53, 91-108.

Giles, D., Nutman, A.P., 2002. SHRIMP U-Pb monazite dating of 1600-1580 Ma amphibolite facies metamorphism in the southeastern Mt Isa Block, Australia. Aust. J. Earth Sci. 49, 455-565.

Hand, M., Rubatto, D., 2002. The scale of the thermal problem in the Mount Isa Inlier. Geological Society of Australia Abstracts 67, 173.

Heinrich, C.A., Bain, J.H.C., Mernagh, T.P., Wyborn, L.A.I., Andrew, A.S., and Waring, C.L., 1995. Fluid and mass transfer during metabasalt alteration and copper mineralization at Mount Isa, Australia. Economic Geology 90, 705-730.

Huang, W., Rubenach, M.J., 1995. Structural controls on syntectonic metasomatic tremolite and tremolite-plagioclase pods in the Molanite Valley, Mt Isa, Australia. J. Struct. Geol. 17, 83-94.

Hill, E.J., Loosveld, R.J.H., Page, R.W., 1992. Structure and geochronology of the Tommy Creek Block, Mount Isa Inlier. In: Stewart, A.J., Blake, D.H., (eds.), Detailed studies of the Mount Isa Inlier. Australian Geological Survey Organization, Bulletin 243, 329-348.

Hoadley, E., Rubenach, M.J., Coleburn, D., Sisois, I., Fanning, M., 2001. Significance of an amphibolite facies shear zone event synchronous with the emplacement of the Sybella Batholith, Mount Isa. Geological Society of Australia Abstracts 64, 83.

Holcombe, R.J., Pearson, P.J., Oliver, N.H.S., 1991. Geometry of a middle Proterozoic extensional detachment surface. Tectonophysics, 191, 255-274.

Holland, T.J.B, Powell, R., 1998. An internally consistent thermodynamic data set of petrological interest. J. Metam. Geology 16, 309-343.

Jaques, A.L., Blake, D.H., Donchak, P.J.T., 1982. Regional metamorphism in the Selwyn Range, northwest Queensland. Journal of Australian Geology and Geophysics, 7, 181-196.

Kretz, R., 1983. Symbols for rock-forming minerals. Am. Mineral. 68, 277-279.

Lally, J., 1997. Structural history of the central eastern fold belt, Mt Isa Inlier. Unpubl. PhD thesis, JCU.

Lewthwaite, K.J., 2000. The structural and metamorphic development of the Soldiers Cap Group SE of Cloncurry: implications for the orogenic development of the Eastern

Fold Belt of the Mount Isa Inlier, Australia. Unpublished PhD thesis, James Cook University, Townsville.

Loosveld, R.J.H., 1989. The synchronism of crustal thickening and high T/low P metamorphism in the Mount Isa Inlier, NW Queensland, Australia. Part 1: an example, the central Soldiers Cap Group. Tectonophysics, 158, 173-190.

Loosveld, R.J.H., Etheridge, M.A., 1990. A model for low-pressure facies metamorphism during crustal thickening. J. Metamorph. Geol. 8, 257-267.

Ludwig, K.R., 2004. Isoplot/Ex version 3.0 a geochronological toolkit for Microsoft Excel. Berkeley, California Geochronology Centre, Special Publication Vol. 4.

Mares, V.M., 1998. The Structural development of the Soldiers Cap Group within a portion of the Eastern Fold Belt of the Mount Isa Inlier: a succession of horizontal and vertical deformation events and large-scale shearing. Aust. J. Earth Sci. 45, 373-387.

Mark, G., Darvall, M., Tolman, J., Foster, D.R.W., Williams, P.J., Pollard, P.J., 1999. Magmas and regional Na-Ca alteration, Cloncurry district, Australia. In Stanley, C.J. et al., eds, Mineral deposits: Processes to processing. Rotterdam, Balkema, 385-388

Mark, G., Foster, D.R.W., Pollard, P.J., Williams, P.J., Tolman, J., Darvall, M., Blake, K.L., 2004. Stable isotope evidence for magmatic fluid input during large-scale Na-Ca alteration in the Cloncurry Fe oxide Cu-Au district, NW Queensland, Australia. Terra Nova 16, 54-61.

Mark, G., Oliver, N.H.S., Carew, M.J., 2006a. Insights into the genesis and diversity of epigenetic Cu-Au mineralisation in the Cloncurry district, Mt Isa Inlier, northwest Queensland. Aust. J. Earth Sci. 53, 109-124.

Mark, G., Oliver, N.H.S., Williams, P.J., 2006b. Mineralogical and chemical evolution of the Ernest Henry Fe oxide-Cu-Au ore system, Cloncurry district, northwest Queensland, Australia. Miner. Deposita 40, 769-801.

Marshall, L.J., 2003. Brecciation within the Mary Kathleen Group of the Eastern Succession, Mount Isa Block, Australia: implications of district-scale structural and metasomatic processes for the Fe-oxide-Cu-Au mineralisation. Unpubl. PhD thesis, JCU.

McLaren, S., Sandiford, M., Hand, M., 1999. High radiogenic heat-producing granites and metamorphism - An example from the western Mount Isa Inlier, Australia: Geology, 27, 679-682.

Miyazaki, K., 2004. Low-P-high-T metamorphism and the role of heat transport by melt migration in the Higo Metamorphic Complex, Kyushu, Japan. J. Metamorph. Geol. 22, 793-809.

Motl, M.J., 1983. Metabasalts, axial hot springs and the structure of hydrothermal systems at mid-ocean ridges. Geological Society of America Bull. 80, 157-182.

O'Dea, M.G., Betts, P.G., MacCready, T., Aillères, L., 2006. Sequential development of a mid-crustal fold-thrust complex: evidence from the Mitakoodi Culmination in the eastern Mt Isa Inlier, Australia. Aust. J. Earth Sci. 53, 69-90.

O'Dea, M.G., Lister, G.S., MacCready, T., Betts, P.G., Oliver, N.H.S., Pound, K.S., Huang, W., Valenta, R. K., 1997. Geodynamic evolution of the Proterozoic Mount Isa terrain. In: Burg, J.P. and Ford, M., (eds.), Orogeny through time. Geological Society of London, Special Publication 121, pp. 99-122.

Oliver, N.H.S., 1995. Hydrothermal history of the Mary Kathleen Fold Belt, Mount Isa Block, Queensland. Aust. J. Earth Sci. 42, 267-279.

Oliver, N.H.S., Cleverley, J.S., Mark, G., Pollard, P.J., Bin Fu; Marshall, L.J., Rubenach, M.J., Williams, P.J., Baker T., 2004. Modelling the role of sodic alteration in the genesis of iron oxide-copper-gold deposits, eastern Mount Isa Block, Australia. Econ. Geol. 99, 1145-1176.

Oliver, N.H.S., Holcombe, R.J., Hill, E.J., Pearson, P.J., 1991. Tectono-metamorphic evolution of the Mary Kathleen Fold Belt, northwest Queensland: a reflection of mantle plume processes? Aust. J. Earth Sci. 38, 425-456.

Page, R.W., Sun, S-s., 1998. Aspects of geochronology and crustal evolution in the Eastern Fold Belt, Mount Isa Inlier. Aust. J. Earth Sci. 45, 343-361.

Pattison, D.R.M., 1992. Stability of andalusite and sillimanite and the Al_2SiO_5 triple point: Constraints from the Ballachulish aureole, Scotland. J. Geol. 100, 423-446.

Pattison, D.R.M., Spear, F.S., DeBuhr, C.L., Cheney, J.T., C.V. Guidotti, 2002. Thermodynamic modelling of the reaction Muscovite + cordierite→ Al_2SiO_5 + biotite + quartz +H_2O: constraints from natural assemblages and implications for the metapelitic perogenetic grid. J. Metamorph. Geol. 20, 99-118.

Pearson, P.J., Holcombe, R.J., Page R.W., 1992. Synkinematic emplacement of the Middle Proterozoic Wonga Batholith into a mid-crustal extensional shear zone, Mount Isa Inlier, Queensland, Australia. In: Stewart, A.J. and Blake, D.H., (eds.), Detailed studies of the Mount Isa Inlier. Australian Geological Survey Organization, Bulletin 243, 289-328.

Reinhardt, J., 1987. metamorphic and structural evolution of the Proterozoic Corella formation in the Rosebud syncline, NW Queensland. Unpubl. PhD thesis, JCU.

Reinhardt, J., 1992a. The Corella Formation of the Rosebud Syncline (central Mount Isa Inlier): deposition, deformation and metamorphism. In: Stewart, A.J. and Blake, D.H., eds., Detailed studies of the Mount Isa Inlier. Australian Geological Survey Organization, Bulletin 243, 229-226.

Reinhardt, J., 1992b. Low-pressure, high-temperature metamorphism in a compressional tectonic setting: Mary Kathleen Fold Belt, northeastern Australia. Geol. Mag. 129, 41-57.

Rubenach, M.J., 1992. Proterozoic low-pressure/high-temperature metamorphism and an anticlockwise P-T-t path for the Hazeldene area, Mount Isa Inlier, Queensland, Australia. J. Metamorph. Geol. 10, 333-346.

Rubenach, M.J., 2005. Relative timing of albitization and chlorine enrichment in biotite in Proterozoic schists, Snake Creek Anticline, Mount Isa Inlier, northeastern Australia. Can. Mineral. 43, 349-366.

Rubenach, M.J., Lewthwaite, K.J., 2002. Metasomatic albitites and related biotite-rich schists from a low-pressure polymetamorphic terrane, Snake Creek Anticline, Mount Isa Inlier, north-eastern Australia: microstructures and P-T-d paths. J. Metamorph. Geol. 20, 191-202.

Ryburn, R., Wilson, I.H., Grimes, K.G., Hill, R.M., 1988. Cloncurry, Queensland, 1:100 000 geological map commentary. Bureau of Mineral Resources, Canberra.

Sayab, M. 2005a. Microstructural evidence for N-S shortening in the Mount Isa Inlier, NW Queensland, Australia; the preservation of early W-E-trending foliations in

porphyroblasts revealed by independent 3D measurement techniques J. Struct. Geol. 27, 1445-1468

Sayab, M., 2005b. N-S shortening during orogenesis in the Mt Isa Inlier: the preservation of W-E structures and their tectonic and metamorphic significance. Unpublished PhD thesis, James Cook University.

Sayab, M. 2006. Decompression through clockwise P-T path; implications for early N-S shortening orogenesis in the Mesoproterozoic Mount Isa Inlier (NE Australia). J. Metamorph. Geol. 24, 89-105

Southgate, P.N., Bradshaw, B.E., Domagala, J., Jackson, M.J., Idnurm, M., Krassay, A.A., Page, R.W., Sami, T.T., Scott, D.L., Lindsay, J.F., McConachie, B.A., Tarlowski, C., 2000. Chronostratigraphic basin framework for Palaeoproterozoic rocks (1730-1575) in northern Australia and implications for base-metal mineralisation. Aust. J. Earth Sci. 47, 461-483.

Spikings, R.A., Foster, D.A., Kohn, B.P., Lister, G.S., 2001. Post-orogenic (<1500 Ma) thermal history of the Proterozoic Eastern Fold Belt, Mount Isa Inlier, Australia. Precambrian Res. 109, 103-144.

3D modelling of Superbasins and fault architectures in the Mt Isa and southern McArthur regions of Northern Australia and relationship to metal distributions.

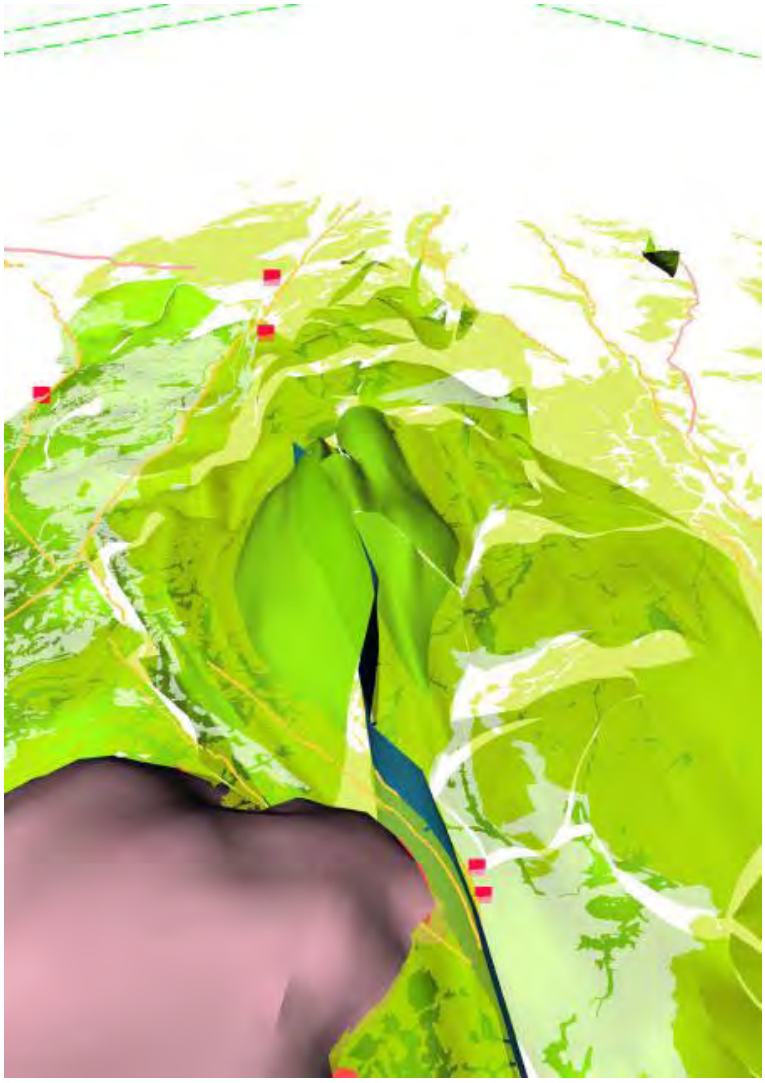

Project I7
Final Report
(December 2007)

Barry Murphy[1], Laurent Ailleres[2], Ben Jupp[2] and Indrajit Roy[3]

1 – University of Melbourne
2 – Monash University
3 – Geoscience Australia
bmurphy@unimelb.edu.au

List of Figures

List of Tables

List of Appendices

1 Summary

The 3D geology of the Mt Isa and McArthur regions has been modelled using 1:250,000 and 1:100,000 scale maps, integrated analysis of geophysical data (gravity and aeromagnetics), with limited seismic constraints, and serial geological cross sections. This builds on existing 3D models of the region, both in the Eastern and Western Fold Belts, and on the Lawn Hill Platform, and the current model extends NW into the southern McArthur Basin. Together, this covers a region of ~200,000 km^2 to a depth of ~20 km and, by necessity, is a simplification of complex geological relationships and, by design, a non-unique solution. Newly acquired seismic data will doubtless lead to revision of this 3D architecture. Notwithstanding this, the Superbasin distributions and the bases of other internal regional scale lithostratigraphic units and major fault structures are rendered in the model.

There is a widespread distribution of the component lithostratigraphic units which are interpreted to be autochthonous or parautochthonous with respect to the pre-Barramundi basement. This relationship is reasonably well constrained in the Western Succession/Fold Belt, less so in the strongly inverted Eastern Succession/Fold Belt. The lithostratigraphic architecture can be modelled as a broadly sheet-like and pseudo-layer cake geometry within a relatively flat/gently inclined enveloping surface. Dome and basin features characterise the WFB and LHP, in most part related to granite emplacement. In the LRFT, the Mt Gordon Arch is modelled as an early emergent feature, but may be underlain by a northern extension of the Sybella Batholith. Further east, the KLB was a positive topographic feature at least during early LSB sedimentation. Correlations between the Western and Eastern Successions are apparent later in the rift history of the LSB and especially during the CSB. Variations in sediment thickness distributions are generally related to basin margin and intra-basin growth faults and the effects of magmatic inflation/doming, such as in relation to the Kamarga and Fiery Creek Domes on the LHP, and the Murphy Tectonic Ridge. The ISB is mainly preserved in the McArthur region, LHP and WFB, and in the EFB. The modelling also serves to emphasise the magmatic belts that make of the essential framework of the Isa inlier: Kalkadoon, Toby-Ewan, Wonga, Weberra, Sybella, and the later Williams Suite.

Fault architecture is a critical component of the model. While most faults show Isan orogeny effects, there are distinct trends which are related to earlier Superbasin development and perhaps to original boundaries in the pre-Barramundi crust which have been reactivated over the 400 Ma of history. Typically the longer strike length faults with a greater perceived depth extent are those that are captured in the modelling. The first and second order faults are a focus of the modelling as these represent significant penetrative boundaries, and are typically associated with gradients (“worms”) in the potential field. The worm data help to provide some constrain dip directions and depth extents of some of the major boundaries, and are used to extend the 3D modelling under cover and to depth.. The majority of faults represented in the model have steep dips, except where seismic data shows otherwise and where geological interpretation demands it. This is imposed from the relative lack of depth control and physical property contrasts or constraints. The Mitakoodi Culmination is the only large scale, nappe-like feature represented in the Eastern Succession modelling. The penetrative first order faults that are steep in the near

surface are interpreted to flatten at depth, and only the most fundamental of these are drawn below 30 km. A dominant feature is a west dipping detachment beneath the Isa region, associated with a high velocity slab in the mid-crust.

An analysis of the metal distributions in relation to the interpreted fault architecture emphasises the importance of fault control on the hydrothermal mineral system, for a range of commodity groups. Large and giant deposits are more proximal to first order fault structures, as determined from empirical observation of map data and from quantitative assessment of geospatial distributions. That more metal is associated with penetrative features speaks to a process model where faults act as pathways for mineralising fluids and can access deeper level and shallow level fluid reservoirs. The strike length of faults and related potential field gradient may be a proxy for depth extent, and can provide a tool for narrowing the exploration search area, especially in under cover regions.

2 Introduction

An objective of the pmd*CRC is to build 3- and 4-D models of mineral systems. This tests our ability to visualise the complexity of such systems and informs conceptual and numerical models of mineralisation at a range of length and time scales. In the Mt Isa and McArthur River regions (Figure 1), a number of 3D models have been constructed through a series of projects focussing in different areas of the Eastern Succession (I2 project; Blenkinsop *et al.* 2005), in the Western Succession (I1 project; Gibson *et al.* 2005), in the Isa Valley (I4 project; ?Jones 2004) and the Lawn Hill Platform (G14 project; Murphy *et al.* 2007). A coherent inlier-wide 3D model has been developed here, combining information from previous models and integrating these in a more holistic way. In particular, we seek to map the distributions of the Superbasins and major fault bounding surfaces. This involves regional scale interpretation of digital geology and potential field data cognisant of, and building from, existing 2D compilations (NWQMPR 2000). The 3D model covers about ~200,000 km^2 of the studied area (~1 million km^2) to a depth of 10 to 20 km, of which the outcrop area is ~150,000 km^2. We have available higher resolution gravity and aeromagnetic data sets than were used in the NWQMRP (2000), and have applied new processing routines, so that the current interpretation differs in detail (particularly under cover). A work flow is outlined in Figure 2. The distribution of metals in the hydrothermal mineral system is assessed, here through statistical treatment of the 2D data, with the ultimate aim to translate this to an exploration strategy for a range of commodity groups.

A significant body of research over several decades provides the framework for the current modelling. The basic template is contained the digital 1:100 000 and 1:250 000 scale map series. This is supplemented with information from numerous published articles and research initiatives, such as the NABRE and AMIRA P552 projects and by the AGCRC (e.g. Giles *et al.* 2006a and b). These have provided significant insights to the geological evolution of Superbasins, as encapsulated in the revised time/space correlation chart (Table 1), and is summarised below. The potential field data is critical for constraining the 3rd dimension and for mapping the architecture in under cover regions. The E-W seismic transect through the central parts of the Mt Isa inlier provides key constraints on the deep structure (Drummond *et al.* xxxx; MacCready 2006), while that through the McArthur River region has revealed hitherto unrealised relationships (Korsch *et al*. 2004). More recently, a major phase of seismic acquisition has been completed over several areas, but incorporation of these data will have to await a further round of interpretation and model development. It is recognised that this 3D model is but one of several possible solutions, and is a simplified representation of complex geology. Also, it was not in the scope of the project to verify the interpreted relationships through field work, but to utilise, integrate and interpret existing data. Forward modelling of selected cross section interpretations has helped constrain the 3D model. Notwithstanding this, however, the model provides a basis to evaluate the distributions of the various entities in a way that has not been previously possible.

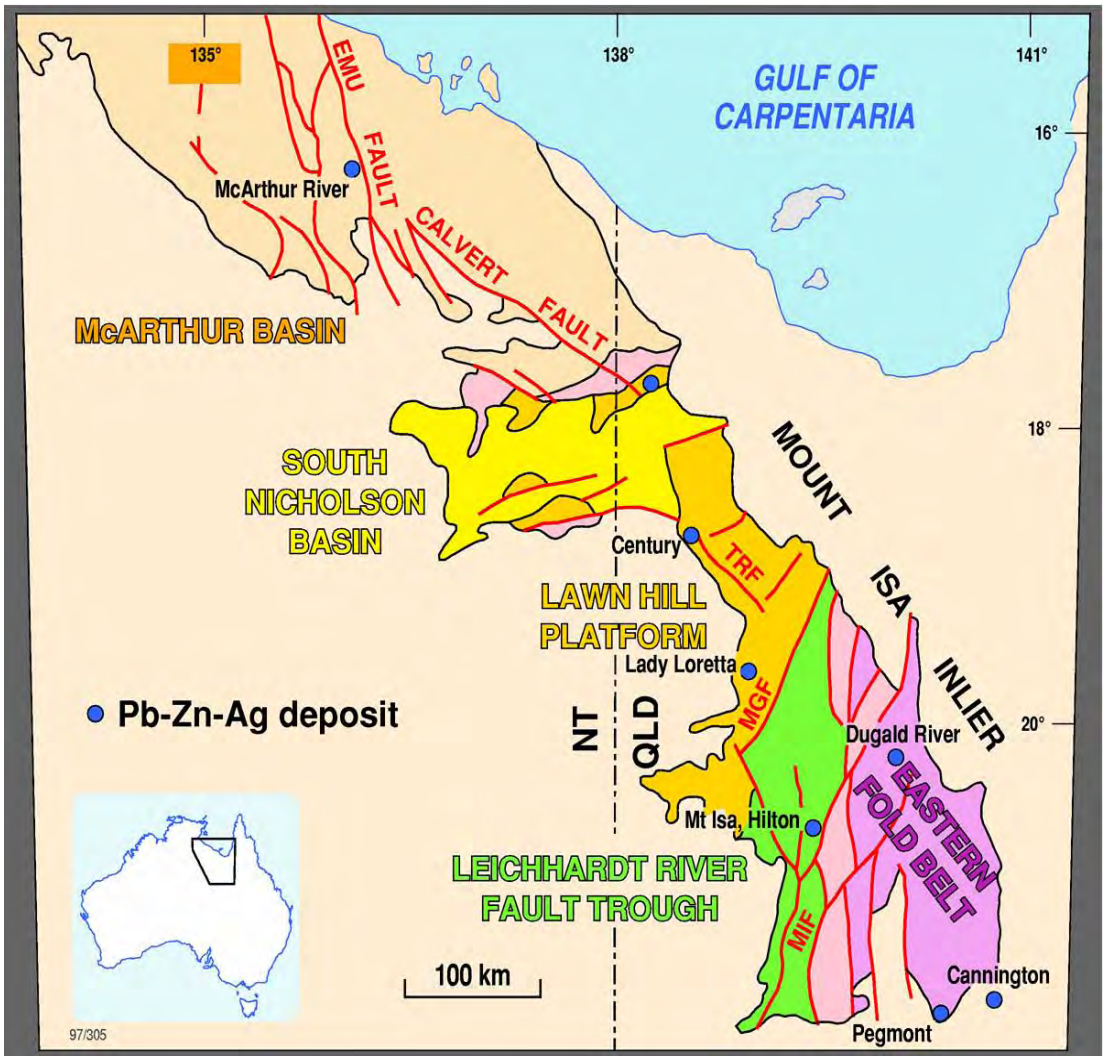

Figure 1: Regional map of Mt Isa and McArthur regions

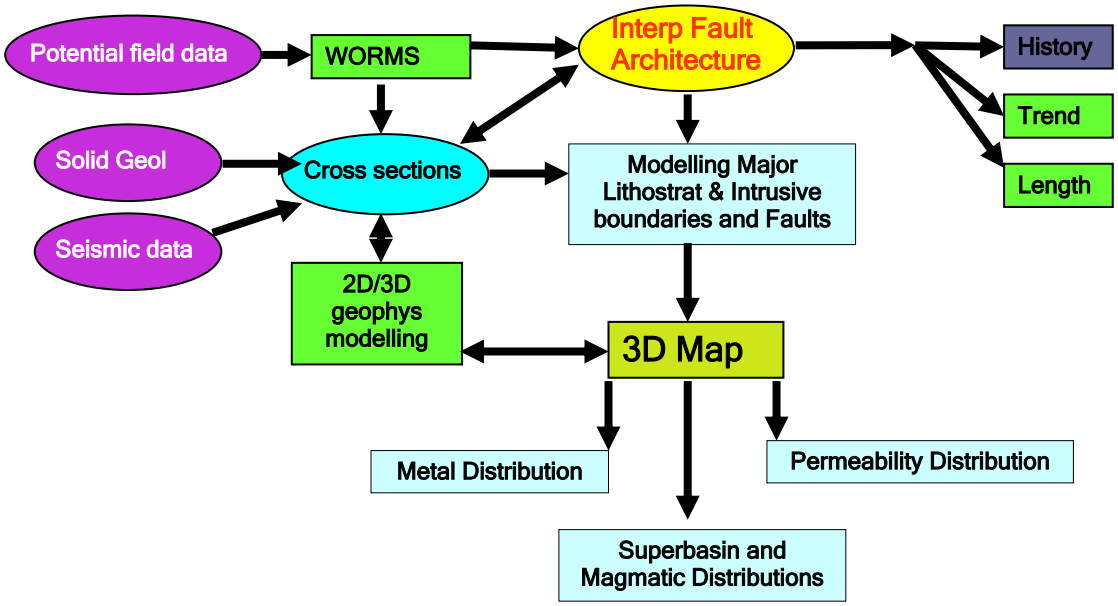

Figure 2: 3D Modelling workflow

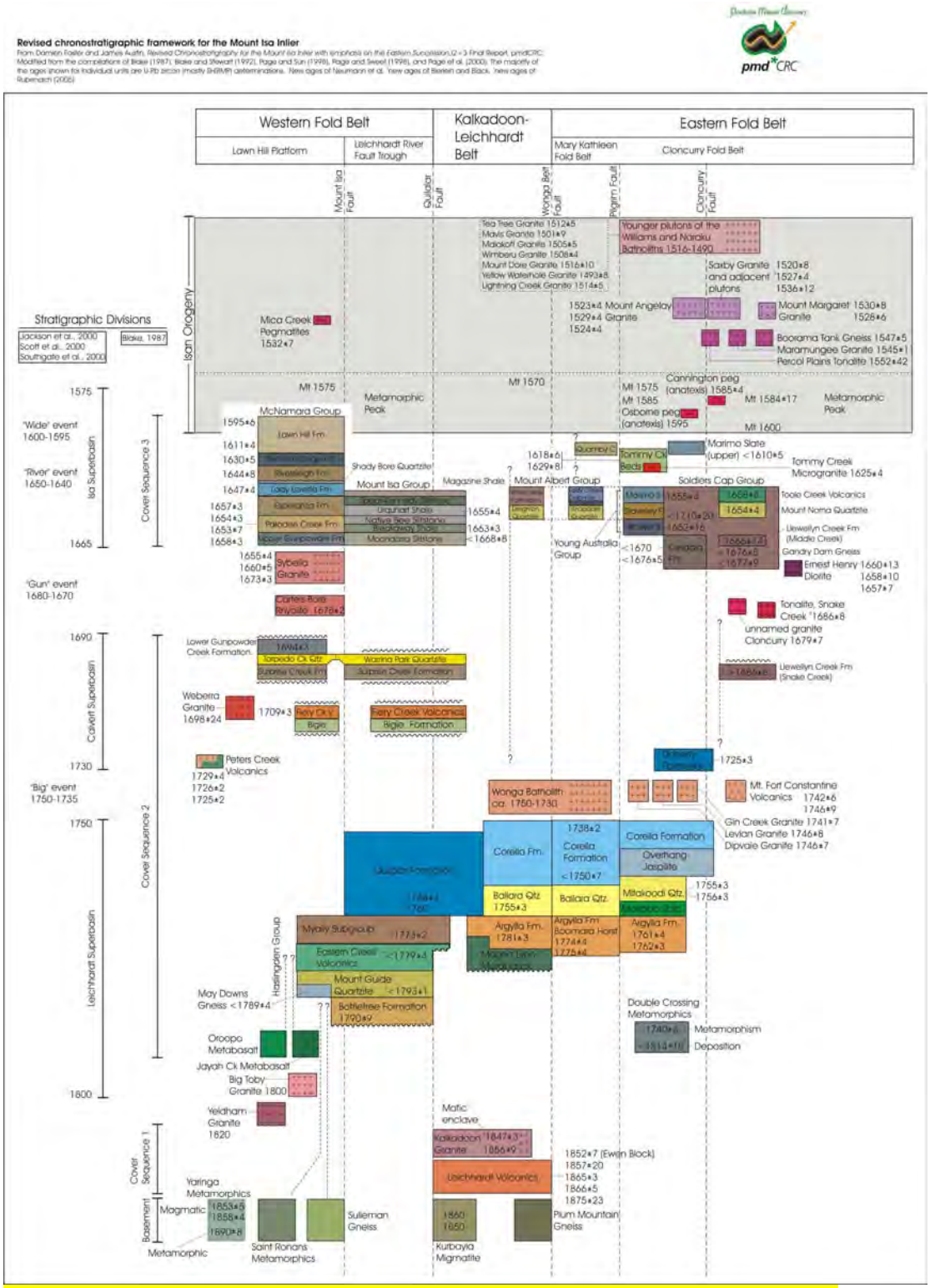

Table 1: Time-space chart – to be updated and include McArthur River region

3 Superbasin Lithostratigraphic Elements

Subdivisions into domains are well established, with the 1:500 000 scale map of the Mt Isa inlier being most effective (Figure 3; Blake 1987). This geology essentially continues into the McArthur River region (Figure 1). The domains are typically bounded by major faults, with characteristic N-S trends in the Mt Isa region. As

currently understood, the history is described in terms of four Superbasins that overlying a basement terrain and its immediate cover rocks (Cover Sequence 1). These Superbasins can be superposed on top of each other, and subsequent inversion has removed large tracts of once extensive depositional systems. We draw from compilations by previous workers (Betts *et al.* 2006; Gibson *et al.* 2005; NWQMPR 2000) and stratal thickness estimates from a variety of sources (e.g. Blake and Stewart 1992; Stewart and Blake 1997; Southgate *et al.* 2000). Using the revised correlation chart, a standard legend was defined and applied throughout the region. From this, the bases of eight major lithostratigraphic boundaries were selected for modelling (Table 1). These were traced from the mapped geology and interpolated under cover and at depth (in serial cross sections; Figure 2). Several granite suites are also represented in the model. The stratigraphic and structural elements are described first below.

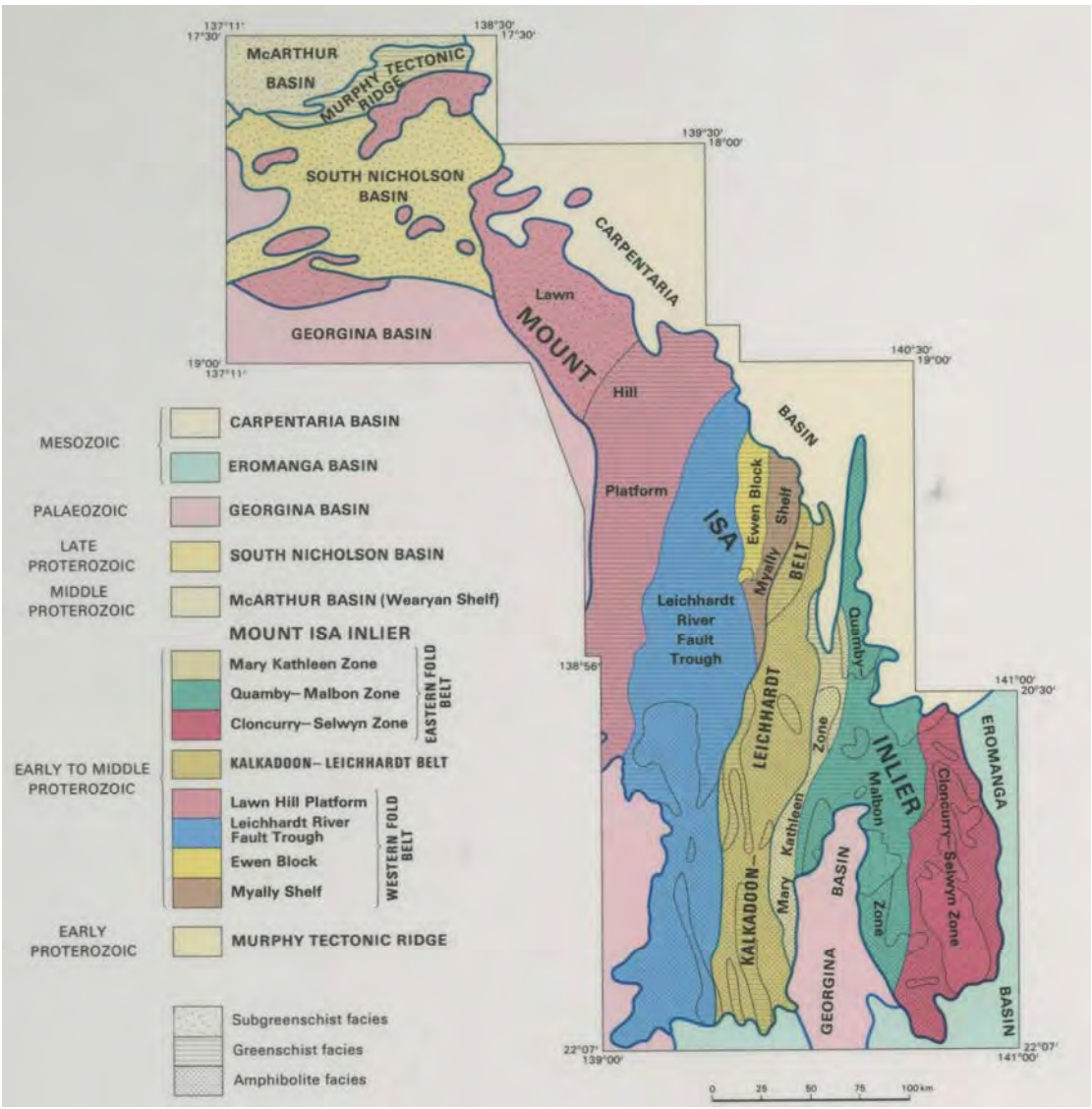

Figure 3: Major domains of the Mt Isa inlier (Blake 1987).

3.1 Pre-Barramundi Basement

Metasediments and igneous rocks at varying metamorphic grade affected by the Barramundi Orogeny (1.87 Ga) are seen in (Figure 4):

- the Murphy inlier and the Cararra Range of the South Nicholson Basin, both comprising the Murphy Metamorphics,
- the WFB, the Yaringa and St Ronans Metamorphics occur to the west of the Mt Isa Fault, and the Sulieman Gneiss to the east of the Mt Isa Fault.
- the KLB, basement is represented by the Plum Mountain Gneiss and Kurbayia Migmatite.
- the EFB, the Double Crossing Metamorphics south of Selwyn were interpreted as possible basement (Blake 1987), while Foster and Austin (2006) regards these as younger (Argylla/LSB). Evidence for basement is seen, however, from isotopic signatures within granites in the EFB.

3.2 Cover Sequence 1

Unconformably overlying basement or interleaved with it, this has a widespread distribution (Figure 4), comprising:

- Leichhardt Volcanics (>1 km thick; ~1.86 Ga) above basement in the KLB.
- Candover Metamorphics (>1 km thick) in the Ewen Block (Figure 2).
- Cliffdale and Scrutton Volcanics (~1.85 Ga) in the Murphy inlier and Mc Arthur regions respectively.
- Co-genetic magmatic rocks are the Kalkadoon Granite within the Leichhardt Volcanics and the Nicolson Granite Complex within the Cliffdale Volcanics.
- Post-dating the volcanics, a widespread magmatic event, the Toby-Ewan suite (NWQMPR 2000), is seen in the LHP (Yeldham Granite) and the WFB (Big and Little Toby, Monaghans and Ewan Granites).

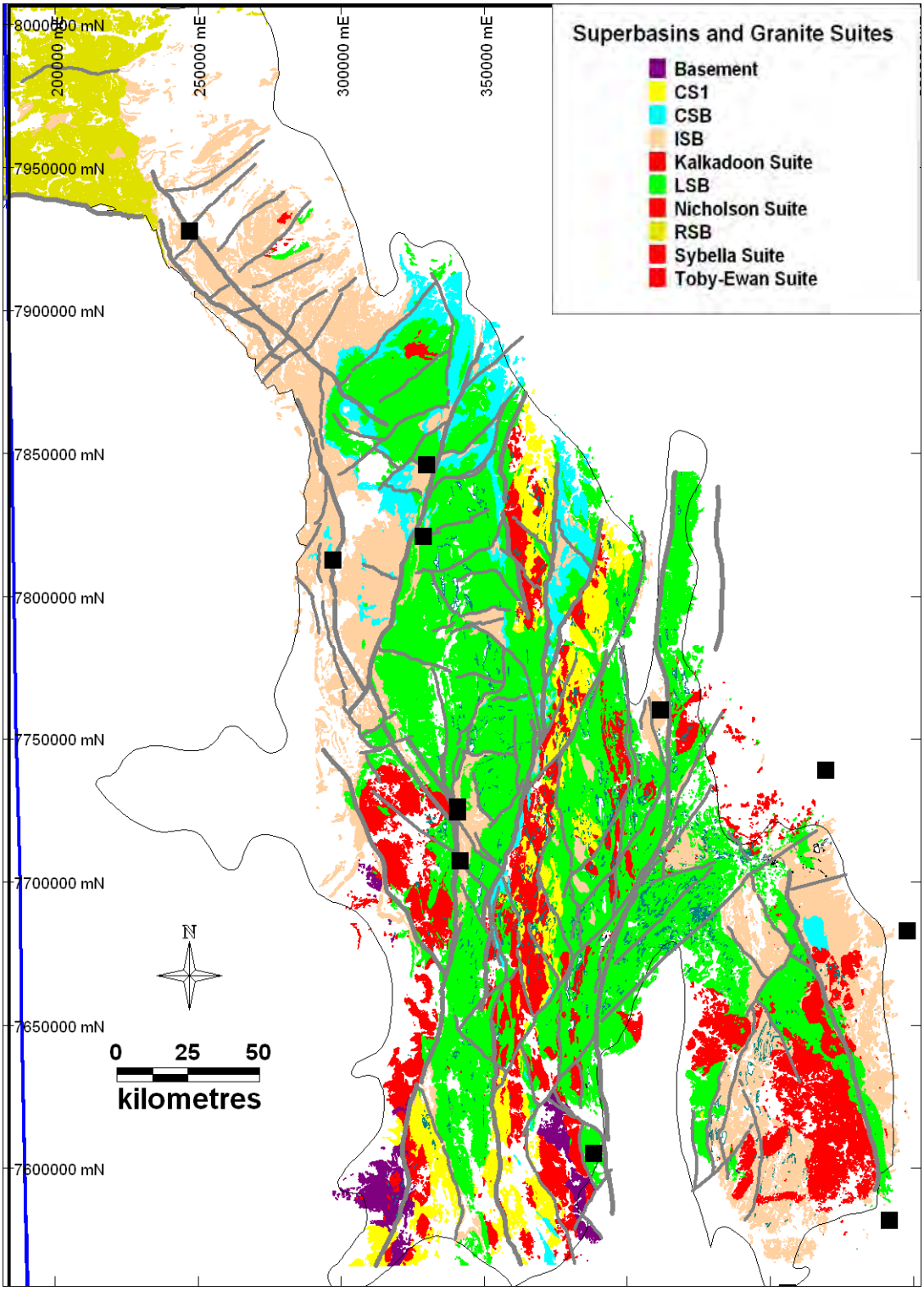

Figure 4: Standard Legend map of Superbasin and Granite Suites in a) Mt Isa region (b) McA region

3.3 Leichhardt Superbasin (LSB)

This encompasses “Cover Sequence 2” and is best represented, volumetrically, in the LRFT, a continental rift setting. There is uncertainty in the ages and correlations of some units between the WBF and EFB, however, and the interpretation by Hutton (in

Gibson *et al.* 2006, Chapter 2) is followed here. The Superbasin is subdivided into three Supersequences (Figure 5): Guide, Myally and Quilalar.

Guide Supersequence

This comprises the Bottletree Formation (~1.79 Ga) of greywacke, conglomerate and bimodal to felsic volcanics, up to 3 km thick in the LRFT. This is overlain by the Mt Guide Quartzite (greywacke, conglomerate and quartzite), estimated up to at 6km thick. This was deposited in a N-S trending rift (LRFT) and probably sourced from an emergent KLB to the east. Correlative units are the Wire Creek Sandstone and Westmoreland Conglomerate (in the Murphy inlier) and Yiyintyi Sandstone (in the Mc Arthur region), with an aggregate thickness of >5.5 km

Myally Supersequence

Flood basalts and intercalated sediments of the Eastern Creek Volcanics (ECV, ~1.77 Ga; ~7 km thick) in the LRFT, and temporally equivalent rocks east of the KLB are the Magna Lynn Basalt and felsic Argylla Formation (>2 km thick). The Marraba Volcanics (~3 km thick) in the EFB are possible EVC correlatives but age constraints are poor. The Kamarga Volcanics (in the LHP), the Buddawadda Basalt and Siegal Volcanics (in the Murphy inlier) are also correlated with the ECV. There is a broadly bimodal character of the volcanics, although spatially distinct regions are evident, with the felsic portions mainly in the Argylla Formation (and Bottletree Formation). Uncertainties in lateral correlations remain and variations in source regions and diachronous development are suggested. For example, the Argylla Formation in the Duck Creek Anticline of the EFB maybe 20 Ma younger than Argylla Formation in the Wonga Belt to the west.

The volcanics are overlain by sediments (Myally Subgroup, ~ 4 km thick; ~1.76 Ga) where active extension on E-W faults in the lower parts (Alsace and Whitworth Quartzites) in a marine to lacustrine environment was followed by red-brown shales and siltstones (Lochness Formation) in a sag phase of an emergent tidal or lagoonal environment. The Myally Subgroup forms a southward thinning wedge that onlaps underlying strata. In the McArthur region, the Sly Creek Sandstone, Rosie Creek Sandstone (with halite casts) and McDermott Formation were deposited in a fluvial to shallow marine environment, with a variable thickness of up to 1500 m.

Quilalar Supersequence

The Quilalar Formation (~1.5 km thick; ~1750 Ma) marks a return to quartzo-feldspathic sandstone deposition, suggesting renewed extension, followed by fine grained dolomitic sediments interpreted as a sag phase. Correlative units in the EFB are the Ballara (1.25 km thick) and Mitakoodi Quartzites (3 km thick) which are overlain by carbonates of the Corella Formation (>1 km thick). In the McArthur region, no time equivalent rocks are recorded.

There is a strong N-S basement fault control on basin architecture in the LRFT, with an eastward deepening half graben (Gibson *et al.* 2005). No single fault, however, currently marks the eastern margin with the LSB. It is represented in part by the Quilalar and Lake Julius Faults, while elsewhere the fault may be blind (i.e. buried), such as in the Bull Creek region (Gibson *et al.* 2005). In the region south of

the Fountain Range Fault, the domain-bounding structure is the Dajarra Fault (Figure 5), modelled here as a west dipping growth fault. Similarly, a position for the western border fault of the LSB, or "breakaway" structure (Gibson *et al.* 2005), is not well constrained. The Mt Gordon Fault separates the LRFT from the LHP and, together with the Twenty Nine Mile Fault to the south, may define a limit to thick volcanics (Figure 5). A major deformation zone in the SW part of the LHP, termed the Russell Creek Fault (Gibson *et al.* 2005) may correspond to the western limit of LSB. The extension northwards is here interpreted as the Riversleigh Lineament (Figure 5), a blind or weakly re-activated structure. The southern extension of the LRFT narrows considerably, with the NW trending Wonomo Fault representing a westerly outcrop limit.

The Mt Gordon Arch (Figure 5; Derrick 1982) is interpreted by Gibson *et al.* (2005) as a topographic uplift former during extension along oppositely dipping trough-bounding faults to the east and west. This culmination has been amplified during the Isan orogeny. There is, however, a prominent gravity low beneath the Arch. This may represent a buried extension of the Sybella granite. There is also a spatial association with U-Cu deposits in this region (Wilde 200x).

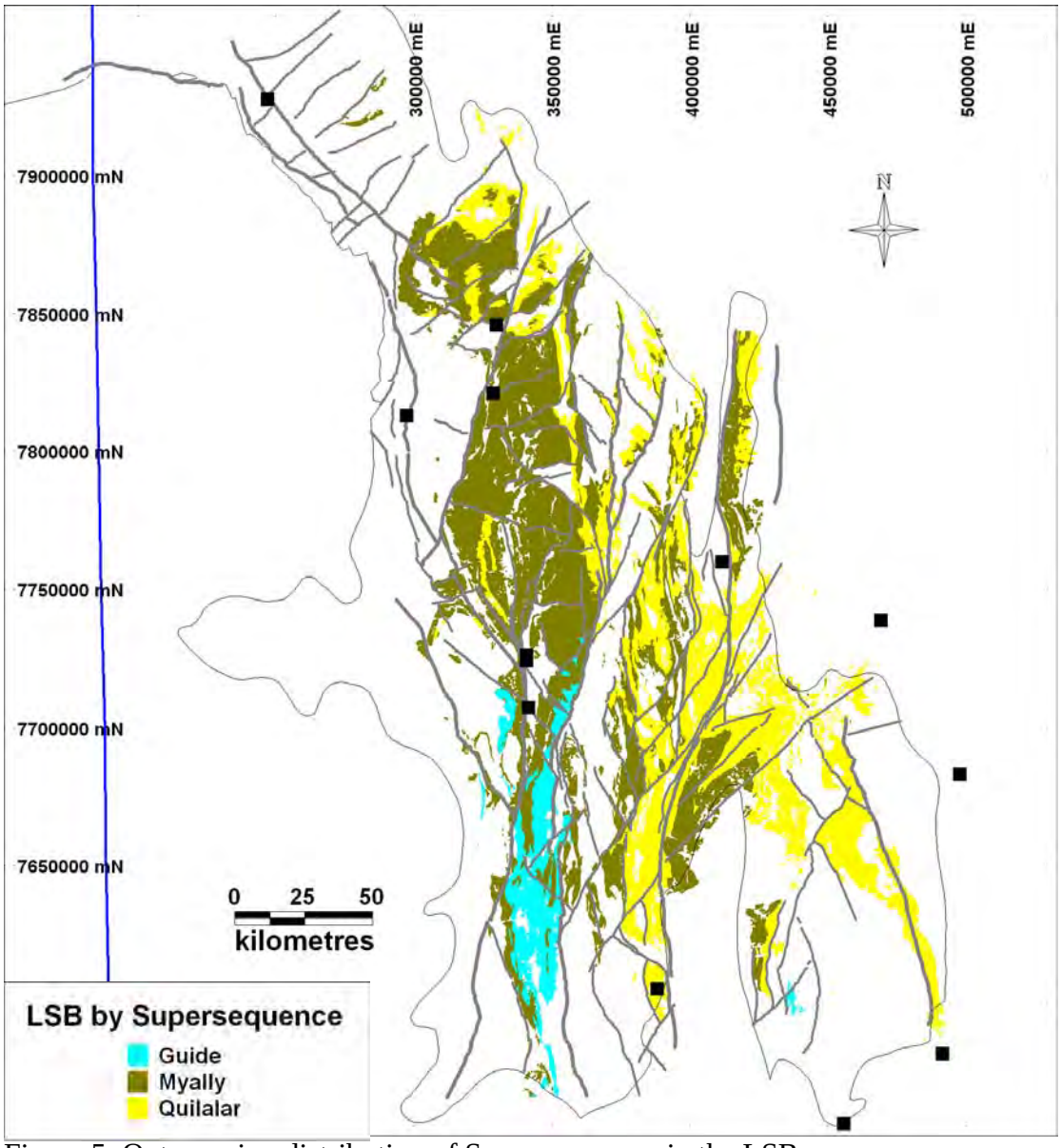

Figure 5: Outcropping distribution of Supersequences in the LSB

3.4. Calvert Superbasin (CSB)

Formerly part of "Cover Sequence 3", this comprises two Supersequences, Big and Prize. It is best preserved (Figure 6) in the WFB and LHP and identified with less certainty in the EFB, in the Soldiers Cap Group (Giles et al. 2004).

Big Supersequence

The Bigie Formation of lithic and feldspathic sandstone and conglomerate shows thickness variations (up to 600 m thick) in relation to an underlying topography. The bimodal character of the overlying Fiery Creek Volcanics attests to renewed extension. Laccolithic domes (e.g. Weberra Granite, ~1.71 Ga) in the southern LHP may have formed topographic highs that separated sub-basins of clastic syn-rift sediments. There is little or no CSB preserved across the Kamarga Dome (Sweet and Hutton 1982), either through non-deposition or pre-ISB erosion (note: this interpretation is contingent on the Torpedo Quartzite Formation representing the base of the Isa Group at this

location). Similar topographic effects on CSB sedimentation are seen around the margins of the Fiery Creek Dome (Betts *et al.* 1999). The basal part of the Deighton Quartzite and interbedded basalts in the Mary Kathleen Belt, east of the KLB, are correlated with the Big Supersequence (Neumann *et al*. 2006).

Correlative units in the McArthur region and Murphy inlier are fine to medium grained sandstones and dolomitic mudstones in a marginal marine setting (Wununmantyala Sandstone, Aquarium Formation; ~700 m aggregate thickness) overlain by subaerial bimodal volcanics (Settlement Creek Volcanics; up to 200 m), interbedded dolostones and carbonaceous shales (Wollogorang Formation; up to 270 m), followed by subaerial basaltic volcanics (Gold Creek Volcanics), felsic rocks (Hobblechain Rhyolite and Packsaddle Microgranite ~1725 Ma); and uppermost fluvial sediments and volcaniclastics and rhyolite (Echo Sandstone, Tanumbirini Rhyolite (1713 Ma) and Nyanantu Formation).

Prize Supersequence

A regional unconformity marks the base of the Surprise Creek Formation (up to 2.5 km thick; ~1.69 Ga) in the LHP and WFB. It is thin to absent in places and the base erodes deeper levels westwards. Tilt block rotation (during Big Supersequence extension) followed by thermal relaxation and sag sedimentation (Prize Supersequence) may best explain the field relationships (Gibson *et al.* 2005), rather than requiring deformation preceding deposition to explain the unconformity. In the EFB, the Deighton Quartzite units 1 (upper parts), 2, 3 and 4 are included with the Prize Supersequence (Neumann *et al*. 2006). Correlative units in the McArthur region and Murphy inlier are the lower Masterton Sandstone and lower Fish Creek Formation (thickness?).

The prominent series of E-W faults though the central parts of the LRFT are ascribed to the extension during CSB times (Gibson *et al.* 2005), particularly the Investigator and Mammoth Faults. Thicker sedimentary units to the north in the LRFT suggest the CSB deepened in that direction (Gibson *et al.* 2005). In addition, the pre-existing N-S trending boundaries to the LRFT are interpreted as having influenced CSB sedimentation. Possible Calvert-aged faults on the LHP are NE trending, the Fiery Creek Fault being best know (Betts *et al.* 1999). In addition, the NW trending faults on the LHP may also have been active during CSB times (Sweet and Hutton 1982). CSB-aged faults within the EFB are not well constrained, although E-W trends are evident in places (Tommy Creek Block) which suggest geometries similar to those seen in the WFB.

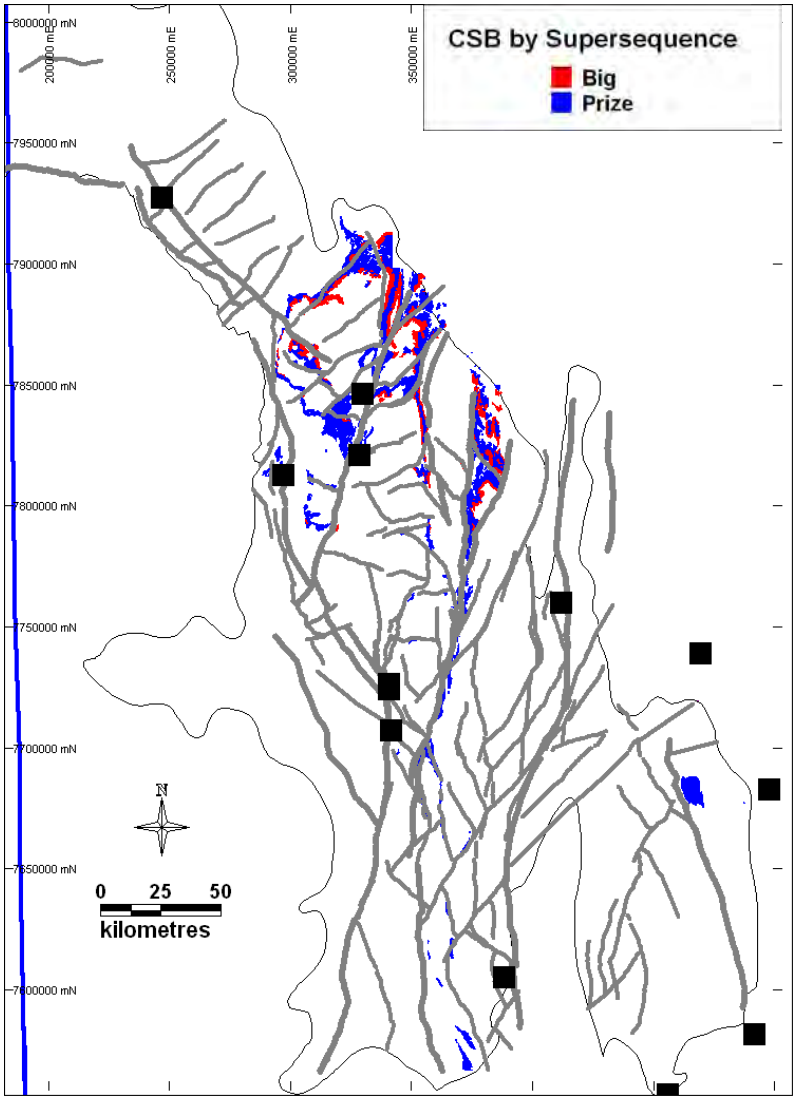

Figure 6: Outcropping distribution of Supersequences in the CSB

3.5 Isa Superbasin (ISB)

The ISB has a widespread distribution but is variably preserved due to inversion during the ~1.58 - 1.5 Ga Isan Orogeny. It comprises the Lower McNamara Group and the Mt Isa Group (in the LRFT) and the Upper McNamara Group (in the LHP). These are distinguished here as Lower_ISB and Upper ISB respectively (Figure 7). An overall thinning towards the west is seen. The Torpedo Creek Quartzite forms the base of the Lower McNamara Group, but is discontinuous in some areas, where the Lower Gunpowder Creek Formation shales rest on Surprise Creek Formation. The inclusion of the Lower Gunpowder Creek Formation with the CSB (Southgate *et al* 200b) may be an incorrect assignment (Hutton, in Gibson *et al.* 2005). Above the Gunpowder Creek Formation, the Paradise Creek Formation, Esperanza Formation and Lady Loretta Formation are dominated by shallow marine stromatolitic carbonates and chert. The Mt Isa Group was deposited in a deeper marine environment than the Lower McNamara Group equivalents (Southgate *et al* 200b). Correlative units in the EFB are the Marimo-Answer Slates, Tommy Creek Beds and Dugald River Shale-Croocerina Formation-Lady Clayre Dolomite:

In contrast to the layer-cake stratigraphy of the lower units, the Upper McNamara Group forms a SE thickening wedge southwards from the Murphy inlier (Scott *et al*. 1998; Krassay *et al*. 2000). Up to 8 km thickness of Upper McNamara Group is preserved in the LHP (Krassay *et al.* 1997), and volcanic input to the sediment pile is significant in places. Correlative unit in the EFB is the Young Australia Group (Foster and Austin, 2007)

Seven Supersequences separated by maximum flooding surfaces are identified in the WFB and LHP (Southgate *et al.* 1997, 2000 a and b), with the lower three representing the Lr_ISB grouping in Figure 7:

Gun Supersequence

~ 3000 m?? thick. Laminated fine grained sandstones and siltstones, deposited (~1670 Ma) in deep marine to subtidal, lagoonal and peritidal settings. Seismic data show on-laps of the Murphy ridge. In the Mary Kathleen region, fluvial conglomerates at the base of the Deighton Quartzite 5 are correlated with the Gun Supersequence.

Loretta Supersequence

???m thick. Laminated fine grained sandstones and siltstones, dolograinstones and laminated carbonates, deposited in subtidal and peritidal to deep marine settings.

River Supersequence

15-230m thick. Conglomerates and fine grained arenaites deposited in fluvial and shallow to deep marine settings as mid to outer shelf turbidites. Thicken southwards from the Murphy ridge.

Term Supersequence

<10-70m thick. Basal conglomerates and sandstones with overlying interbedded mudstones and sandstones deposited in submarine fans as mid to outer shelf turbidites.

Lawn Supersequence

10-900m thick. Mudstones to sandstones with provenance from volcanogenic and quartzose sources deposited in deep marine, outer to inner shelf conditions.

Wide Supersequence

50-1200m thick. Medium to coarse grained sandstones as turbidites in outer shelf to proximal submarine fans. The lowermost Widdallion Sandstone is unconformable and represents a significant change to thickening and coarsening upwards sandstones, compared to the fining upwards cycles in underlying units (Krassay et al. 2000). This on-laps the Murphy palaoehigh.

Doom Supersequence

600-1050m thick. Medium to coarse grained sandstones and shales formed in basin floor fan deposits and mid shelf turbidites.

Near Century, the TRF exerted a control on sedimentation (Broadbent *et al.* 1998) and records evidence of switching in depocentres on either side of the fault over time; the River Supersequence is thicker in the SE of the TRF, while later Supersequences are thicker on the NE side of the TRF (Krassay *et al.* 2000 a and b). Faulting during the Wide Supersequence occurred on both WNW and NE trends.

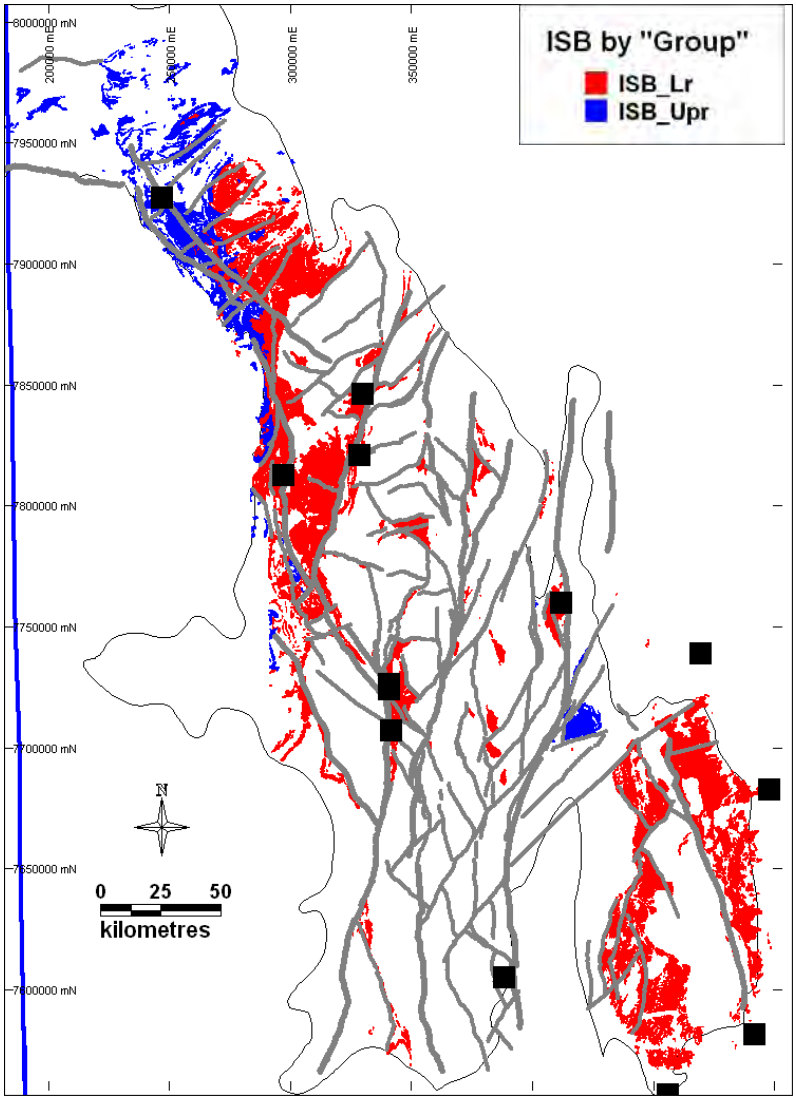

Figure 7: Isa Superbasin by major grouping of ISB_Lr equivalent to the Lower McNamara Group and the Mount Isa Group and ISB_Upr representing the Upper McNamara Group.

3.6. Roper Superbasin (RSB)

This late stage Superbasin is preserved in the northern parts of the LHP as the South Nicholson Group and in the McArthur region as the Roper Group. It unconformably overlies the ISB, yet in the LHP it displays fault trends and dome/basin style folds that appear to be inherited or mimic that of the underlying geology. The basal Constance Sandstone erodes several hundreds of metres of section near the NT border, whereas in other areas there is apparent conformity which suggested to McConachie and Dunster (1998) a foreland basin setting in relation to the Isan orogeny; the style of folding and faulting is consistent with both N-S and E-W compression. However, the South Nicholson Group is now regarded as post-Isan orogeny in age, with an estimated break in sedimentation of 80-90 Ma between the ISB and the RSB (Jackson *et al* 1999; Abbott and Sweet 2000), based on correlation with Roper Group sandstones in the McArthur River region which contain young detrital zircons.

4 Superbasin Fault Architecture

Networks of faults make up the skeleton of the model, and are the containers for the litho-surfaces. These comprise a hierarchy of size and importance, with the first order faults commonly defining domain boundaries, followed by a relatively complex system of second and third order faults with varying orientations and timing of generation (Figure 8). While most faults show Isan orogeny effects, there are distinct patterns and orientations which are related to earlier Superbasin development (see above) and perhaps to original boundaries in the pre-Barramundi crust which have been reactivated over the 400 Ma of history (NWQMPR 2000). The Isan Orogeny involved early ~N-S compression (D1 ~ 1640 Ma). This led to re-activation of the CSB E-W growth faults as thrusts, and presumably strike slip transpression along the LRFT bounding faults. Later E-W shortening (D2, ~ 1580 Ma) created a fold/thrust belt geometry in the east, and more uptight fold and steep fault structures in the west (MacCready 2006). The N-S faults responded through high angle reverse displacement, and a conjugate NE dextral and NW sinistral set of faults developed later in the history. In addition, post-Isan Orogeny denudation and faulting have played a part in the configuration of the geology (Spikings *et al.* 2006).

Typically the longer strike length faults with a greater perceived depth extent are those that are captured in the modelling. A first response is to evaluate fault length attributes from the 1:100 000 and 1:250 000 map data. The available digital fault data sets are highly segmented in their native form and, to provide a more meaningful picture of the fault population, the line elements were concatenated, i.e. contiguous lines were joined together. There is subjectivity with interpreting linkages between structures, and reference is made to continuity in strike direction, to solid geology constraints and to potential field response. Naturally, some faults die or are displaced and linkages are lost, or perhaps never existed. The principal of Ockham's Razor ("entities should not be multiplied unnecessarily") is employed in the interpretation routine so as to maintain line continuity. Figure 9 shows the fault population as an image of strike length (derived from digital processing of the fault lines). Most of the "named" faults (Figure 8) are those captured as surfaces in the 3D model.

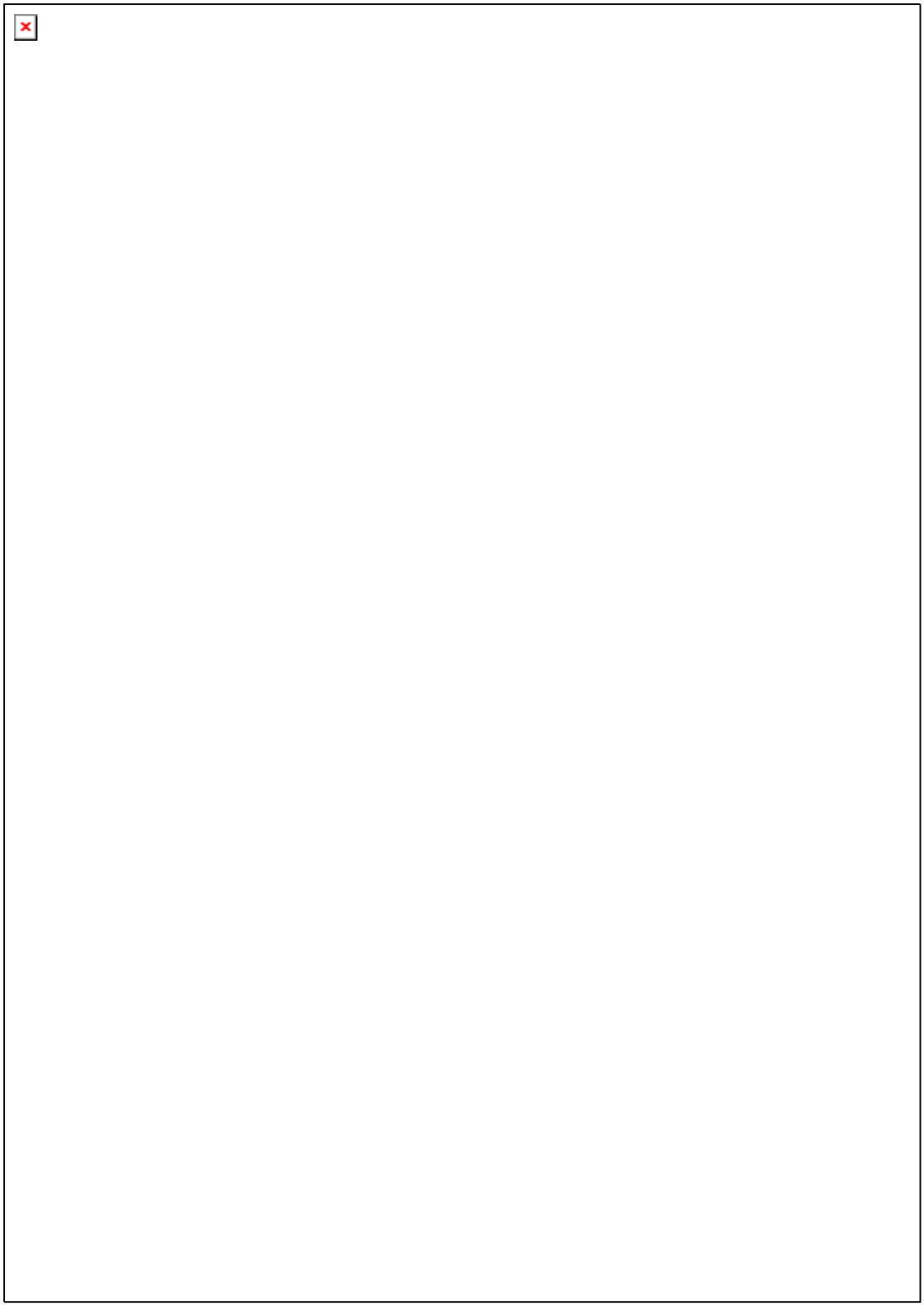

a)

b) McA fault map (Ben?)

Figure 8: Map of fault networks and named faults, a) Mt Isa and b) McArthur regions Major folds: Ploughed Mtn and Mt Caroline, Mitokoodi Culmination, Mt Gordon Arch…

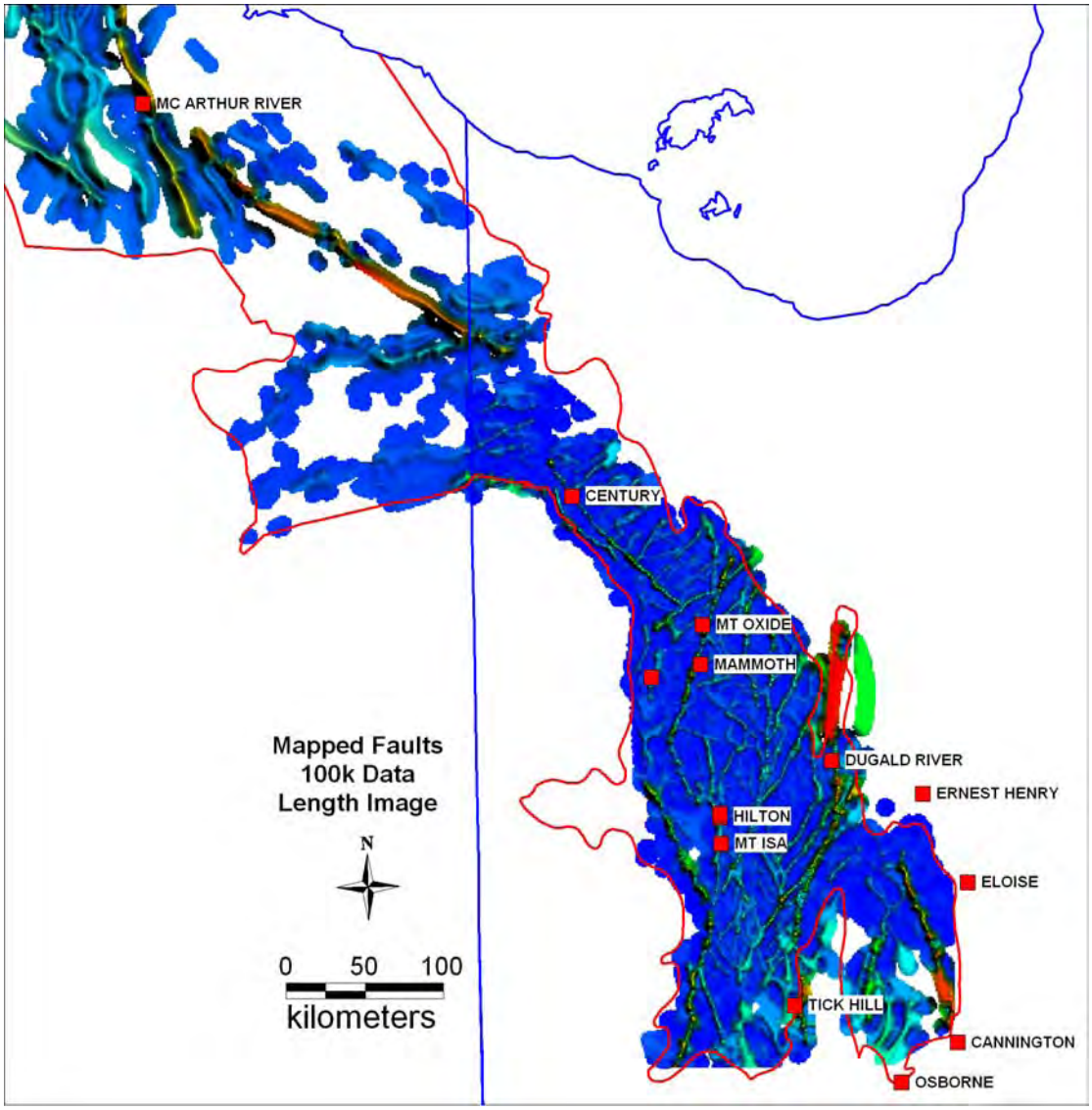

Figure 9: Image of Fault length based on 1:100 000 and 1:250 000 geology maps.

In the Mt Isa region, first order faults are:
May Downs Fault: This is the westernmost structure modelled
Twenty Nine Mile Fault
Mt Isa Fault
Mount Gordon Fault
Quilalar Fault
Dajarra Fault
Pilgrim Fault
Cloncurry Fault

On the LHP, the main structural elements are through-going faults and doubly plunging, dome and basin fold trends that are commonly spatially related to the fault structures. The largest of these, the Ploughed Mountain and Mount Caroline anticlines (Figure 8a) have been interpreted as "buttress folds" developed over basement-penetrating, rift-related faults that were re-activated during the Isan orogeny (Betts *et al*. 2004). The major mapped faults have discrete trends:

- ENE to E trending: Fish River Fault dips steeply south, along the southern margin of the Murphy ridge. The Elizabeth Creek Fault was highlighted in other

studies as a south dipping thrust (Scott *et al* 1998; Krassay *et al*. 2000b). However, here the fault is modelled as a north dipping structure. The Little Range Fault which partly defines the northern outcrop edge of the Georgina Basin is interpreted as a north dipping fault across which the basement and cover configuration may change (Scott *et al*. 1998).

- NE trending: Ploughed Mountain, Little Archie Creek, Archie Creek, Barramundi, Wangunda, Fiery Creek and Weberra Faults The interpreted dip direction of these faults is to the NW (Betts *et al* 2004; cf. Scott *et al*. 1998).
- NW trending: Termite Range, Riversleigh Lineament and Calvert Faults. The Riversleigh Lineament is a less prominent or continuous fault in the outcropping Proterozoic and is mainly interpreted from geophysical evidence (see below). This deep seated fault also controls the erosional edge of the Georgina Basin, suggesting intermittent re-activation since the Cambrian, with similar features to the Little Range Fault.

In the McArthur River region (Figure 8b), the fault architecture is defined by N-S and NW trend. The primary faults are:
Emu, Tawallah, Hot Springs, Mallapunyah, Calvert…

5 Granite Supersuite Distribution

There are a number of important granite suites represented in the 3D model. (Figure 10): Kalkadoon, Toby-Ewan, Wonga, Weberra, Sybella, Williams-Naraku.

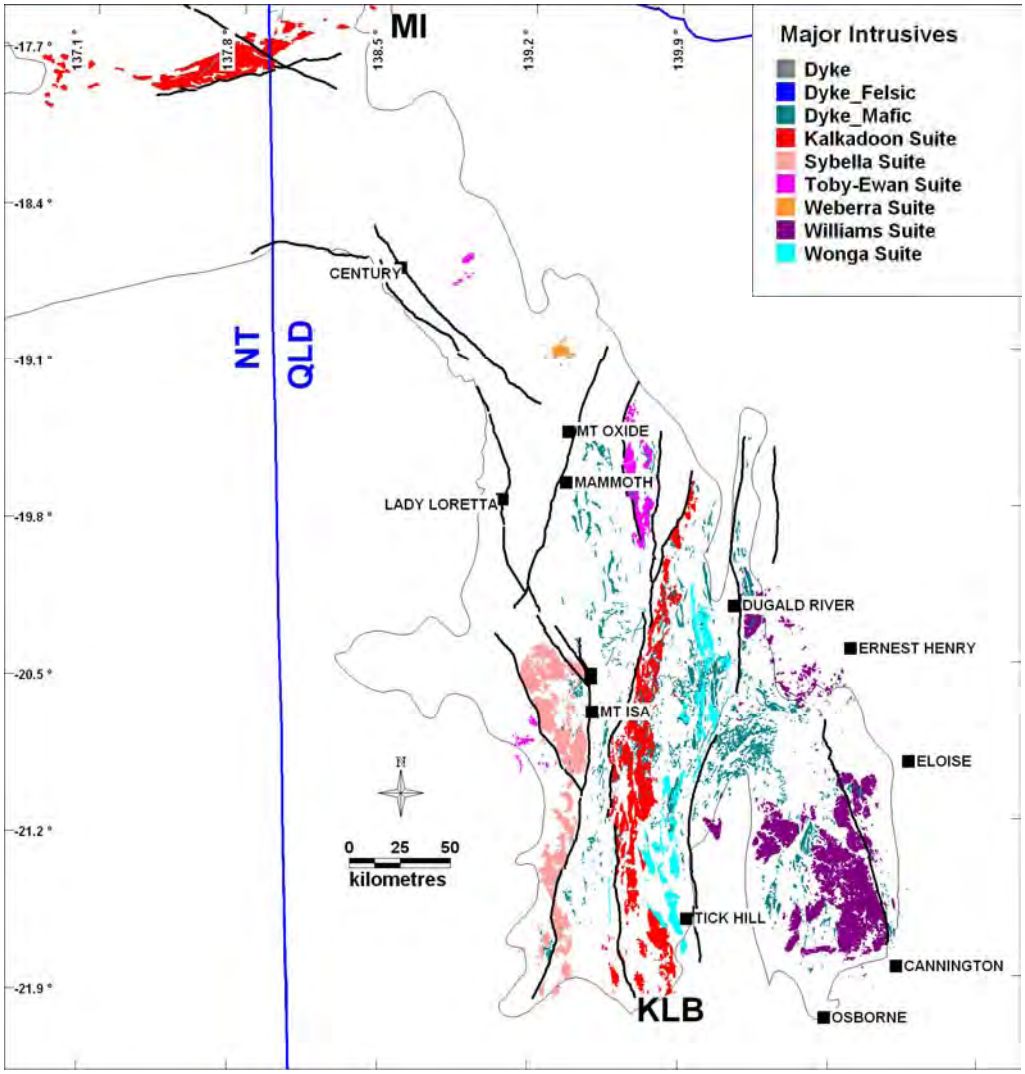

Figure 10: Distribution of granite suites and related intrusives.

6 Potential Field Gradients

A key input to the 3D modelling involves interpretation of gravity and aeromagnetic data sets. The gradient field, in particular, provides information on the shapes and extents of interpreted boundaries in the 3D model. Traditional 2D interpretation of such data requires us to trace a boundary (or gradient) line between contrasting bodies to represent a geological contact (e.g. fault, intrusive, stratigraphic contact). One person's line can differ from that of another's, which impacts on reliability. To reduce ambiguity, the analysis used here employs a technique called multiscale wavelet edges ("worms") to trace the positions of gradients in the potential field. As an automated technique, it makes for a more robust interpretation (Hornby *et al.* 1999; Archibald *et al.* 1999). It is applied to gravity and aeromagnetic data over multiple (above-ground) heights of upward continuation (u.c.) and the gradients that are detected range from high frequency-short wavelength signals ("fine scale" at low u.c. levels) to low frequency-long wavelength signals ("coarse scale" at high u.c. levels).

The "worm" points (x, y, z, w) when viewed at appropriate scales (i.e. over multiple height levels) appear to coalesce as clouds that are termed "worm sheets" (Figure 11). The shape of a worm sheet can inform us about the source boundary, its

dip and relative depth (Holden *et al.* 2000). Importantly, the height extent of a worm sheet may relate to the source depth, with a rule of thumb being that the u.c. height (z) is approximately twice the source depth (i.e. a worm gradient at 10 km height may relate to a geological edge at 5 km depth). Hence, long wavelength-low frequency worms may indicate deep crustal boundaries. Gravity data are generally more reliable than aeromagnetics in this regard. A caveat is that such interpretations carry considerable uncertainty when made in isolation, and need to be evaluated on a case-by-case basis, using other independent data where available (e.g. geological maps, seismic data). In addition, the worm points have an amplitude value (w) that is a measure of the relative contrast across the boundary, i.e. a high amplitude value indicates juxtaposition of strongly contrasting bodies. Along strike amplitude variations in a worm sheet may be a sensitive indicator of alteration processes, such as magnetite creation or destruction.

The worming process offers significant advantages over conventional methods in that it captures virtually all of the visually observed gradients across multiple scales. In doing so, however, it generates enormous data sets that can be cumbersome to manage and manipulate, whether on 3D or 2D platforms. A systematic analysis of such data becomes a signal processing issue and proprietary software, Geoscope, was developed through the pmd*CRC to enable more efficient post-processing of the data (Murphy and Russell-Head 2006; see TWiki New Tools web page). Outputs include bitmaps of worm data coloured by height (z) and amplitude (w), and vector lines with parameters of length, height, trend and straightness. These provide a basis for quantitative interpretation of what is a mixed population of gradients from a variety of geological sources. At one end of the spectrum are long, straight and high level-long wavelength gradients that typically relate to penetrative faults and/or boundaries of major stratigraphical or intrusive units and, at the other end of the spectrum, are short, highly curved (or enclosed) gradients, such as due to shallow, depth limited intrusives. Importantly, visual inspection of worm data (in combination with conventional images) often reveals linear breaks and offsets of gradient traces and these may be interpreted as cross-faults which have no density contrast across them. The interpretation seeks to capture such “breakline” elements and incorporate them with the digital processing.

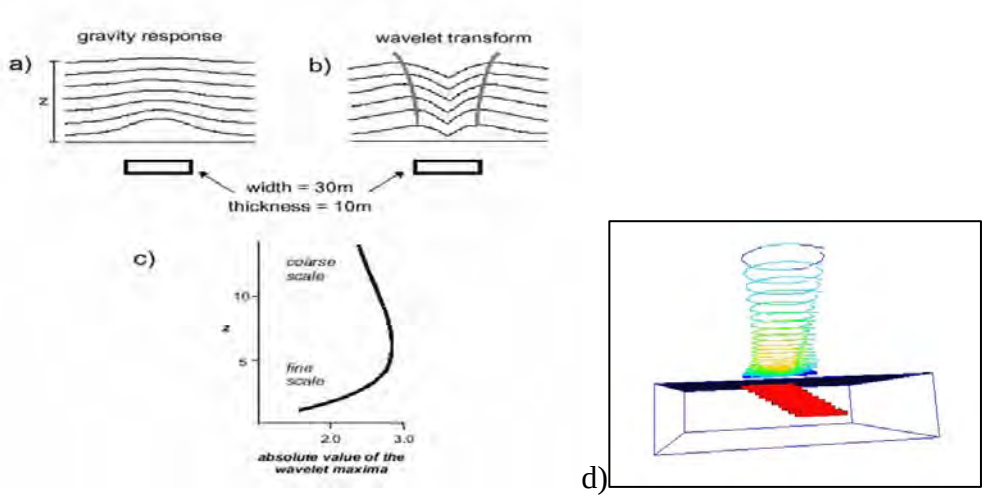

Figure 11: Multiscale wavelets: a) vertical profile of a buried body and its gravity response decaying across upward continued levels (Z), b) wavelet transform to determine worm points of maximum gradient at each height

level, joined across levels as a worm sheet, c) plot of amplitude (W) against height (Z), from fine to coarse scale, reaching maxima at height level related to depth of body, d) perspective view of synthetic model of dipping cylinder (red) with above ground, upward continued levels defining a worm sheet (coloured by amplitude); shape of worm sheet mirrors dip of cylinder in lower u.c. levels. (Hornby *et al.* 1999; Archibald *et al.* 1999)

6.1 Regional Gravity

New gravity data collected on ~3km station spacing as part of the Smart State Initiative (Queensland Government, 2007) has lead to a much clearer resolution of the density distributions (Figure 12). The broad scale pattern shows generally high Bouguer regions to the east are …..

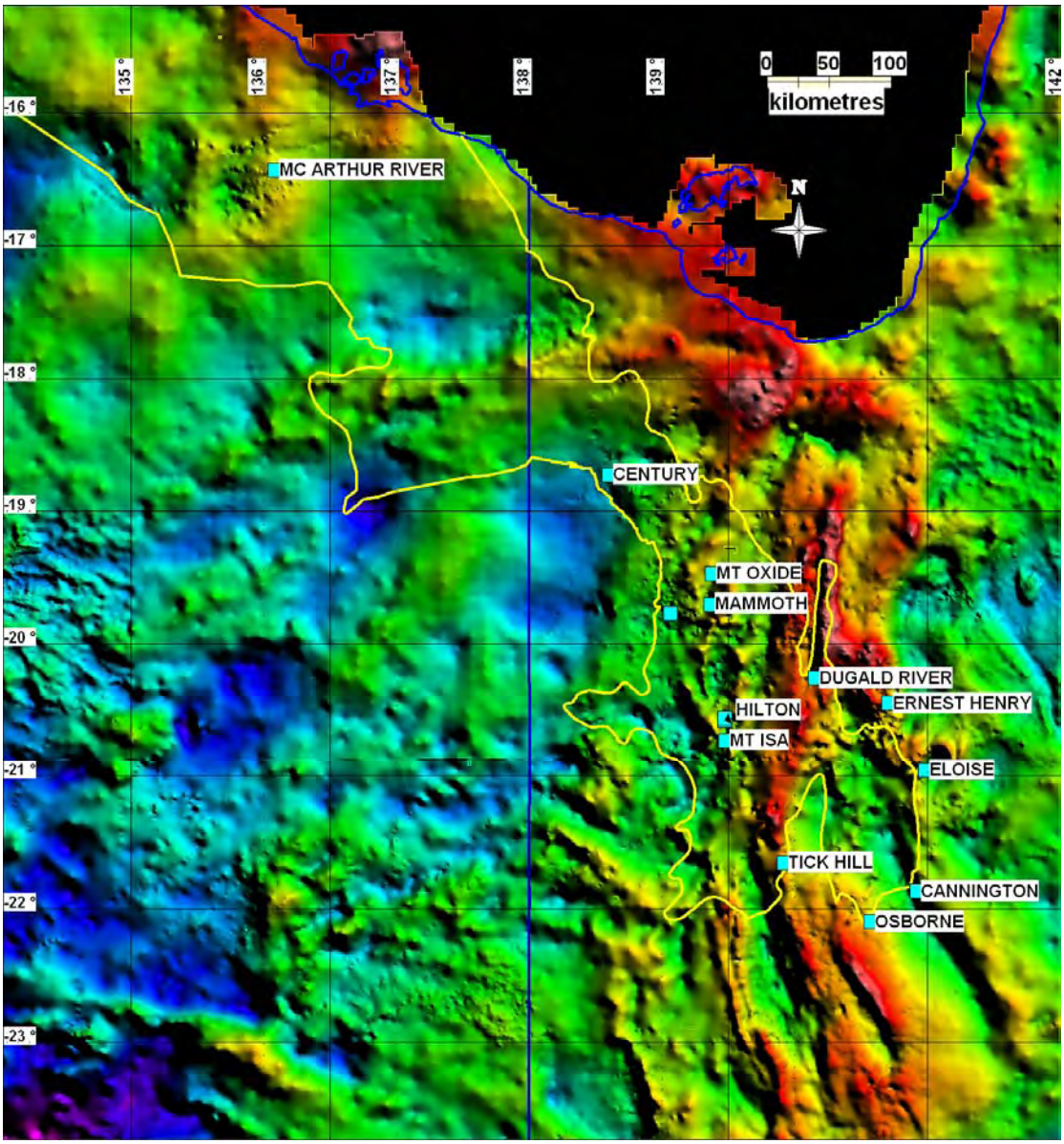

Figure 12: Regional scale Bouguer image of density distributions.

To assess this further, the gravity data was upward continued (by Geoscience Australia algorithms) from 500 m to 104 km height (Figure 13). The resultant

gradient image displays higher level gradients as warmer colours. Although a range of geological sources is represented, several of the major gradients appear to correlate with the trends and positions of mapped faults. As a way to isolate the significant gradients, Figure 14 shows the 5 km level worms as a downward migrated image where the brighter colours represent gradients that persist to higher levels and, by inference, are the more fundamental crustal features.

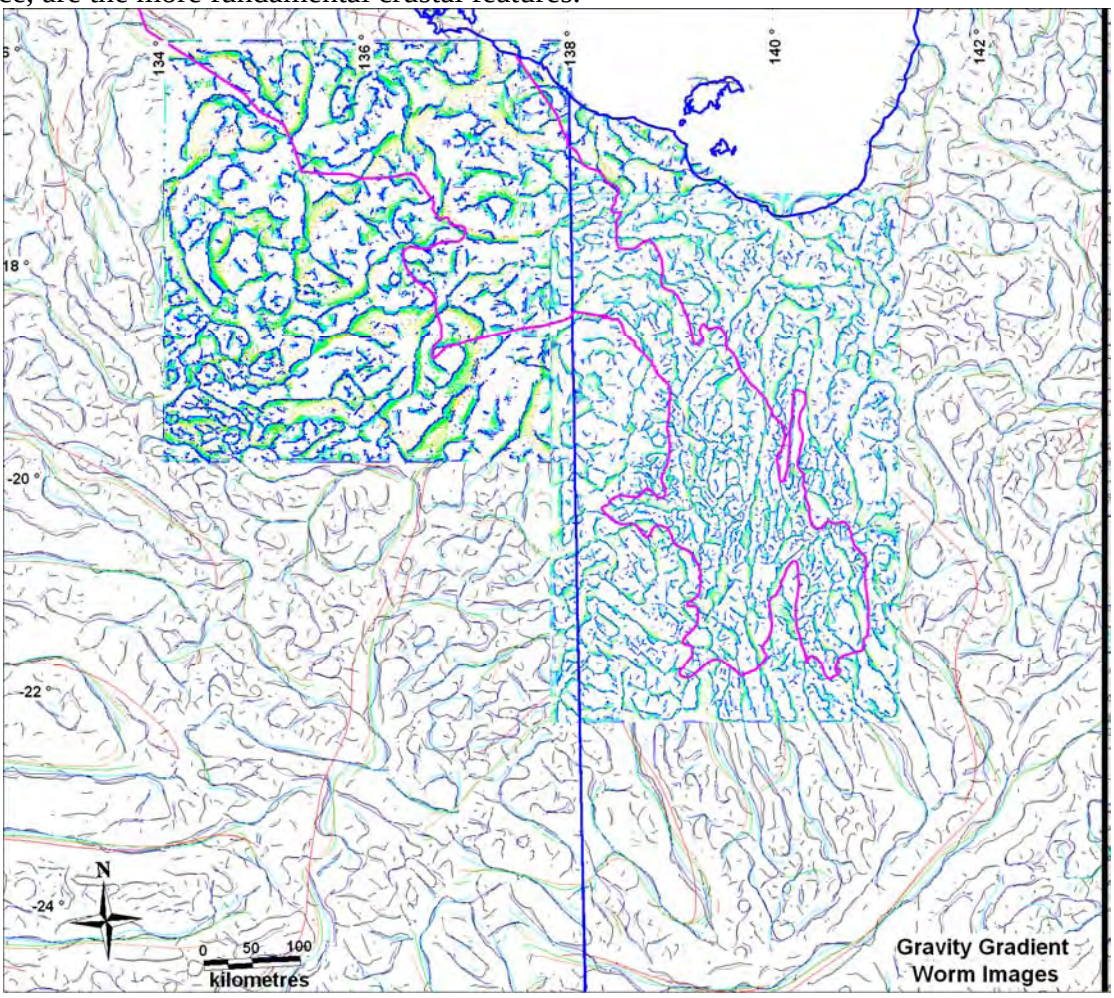

Figure 13: Regional gravity worm image showing regions where processing was undertaken (blue/green areas) surrounded by coarser scale data coverage from Geoscience Australia (courtesy P. Milligan).

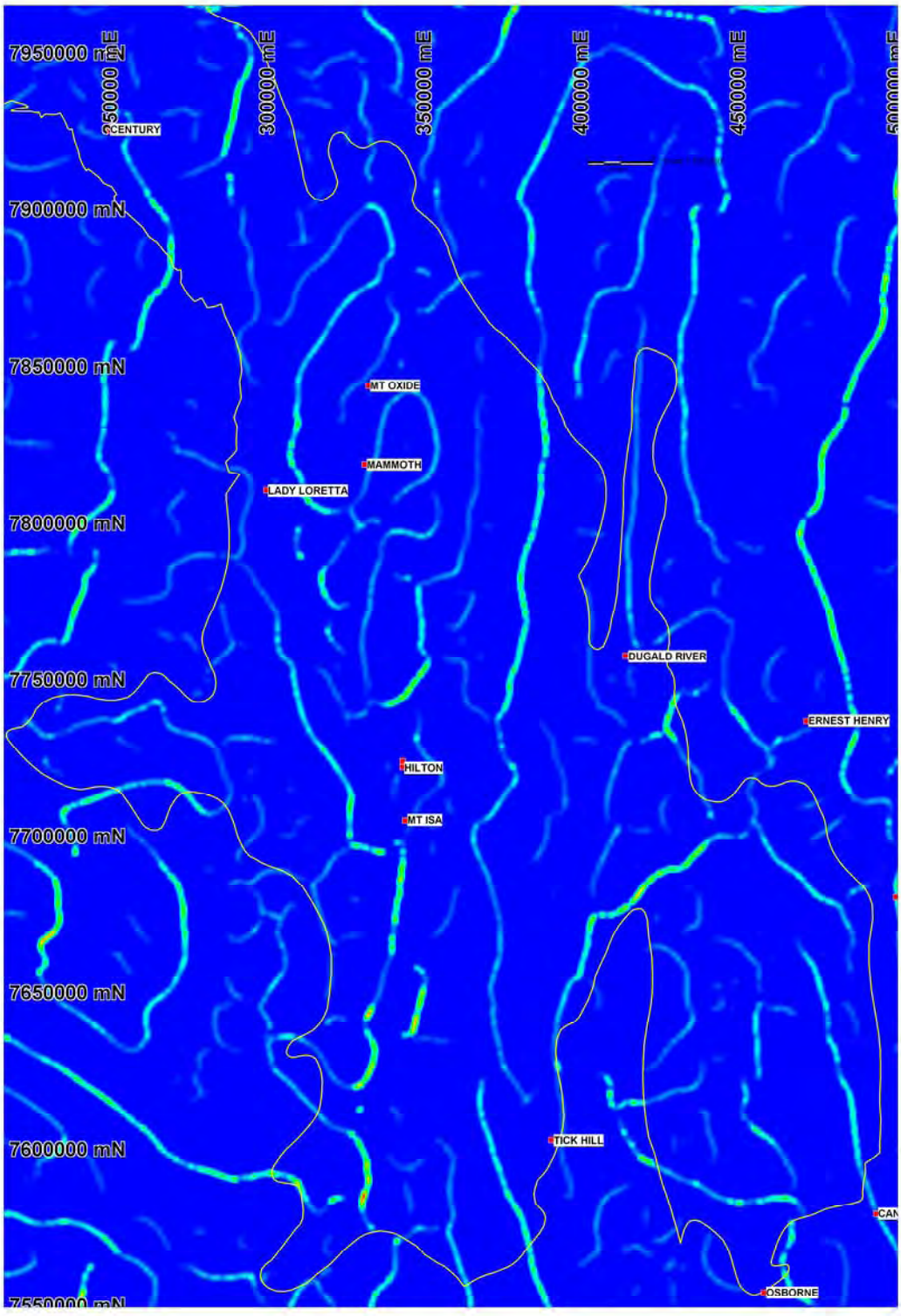
7950000 mN
7900000 mN
7850000 mN
7800000 mN
7750000 mN
7700000 mN
7650000 mN
7600000 mN
7550000 mN
300000 mE
350000 mE
400000 mE
450000 mE
CENTURY
MT OXIDE
MAMMOTH
LADY LORETTA
DUGALD RIVER
ERNEST HENRY
HILTON
MT ISA
TICK HILL
OSBORNE

a)

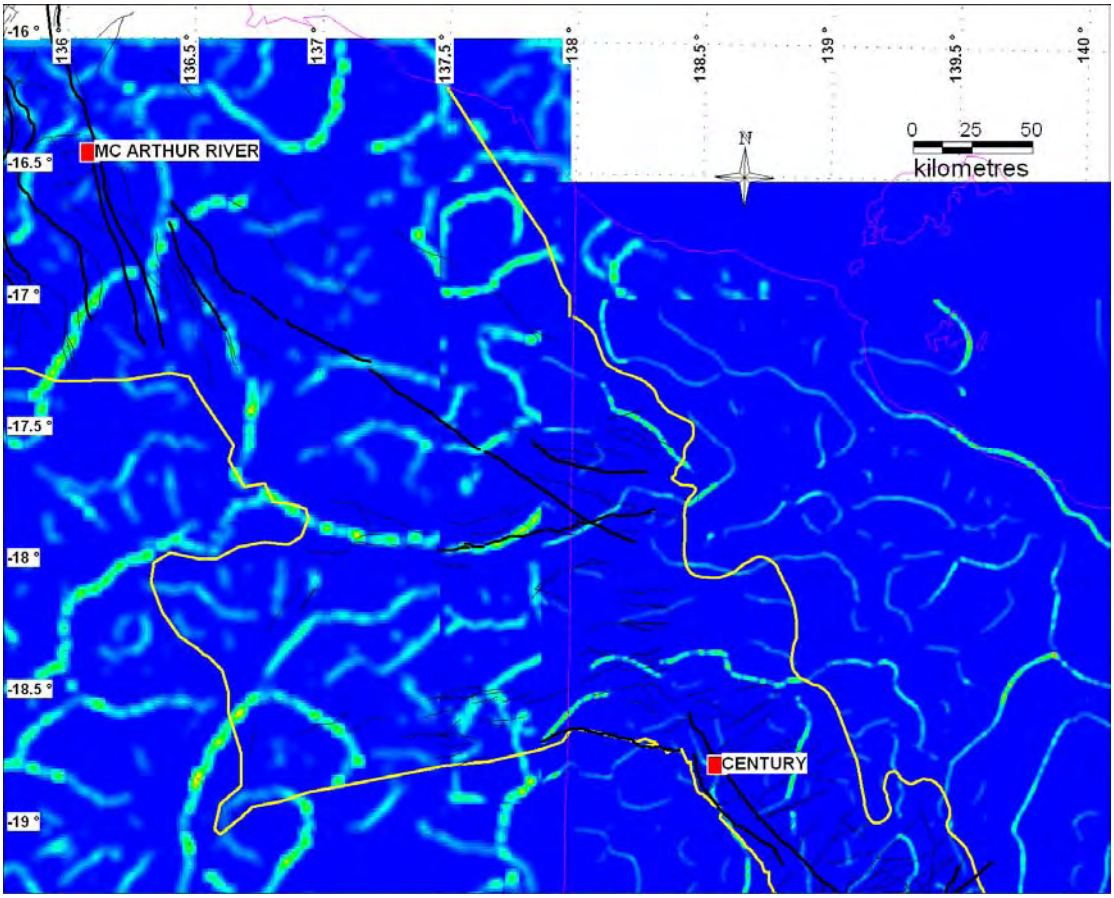

b)

Figure 14: Downward migrated gravity worms at 5km upward continuation. Intensity or brightness of edge reflects degree of connectedness or continuity at higher levels. a) Mt Isa and b) McArthur regions.

6.2 Regional Aeromagnetics

A number of regional aeromagnetic surveys of different vintages and resolution cover the region. Of particular importance is the 400 m line spaced survey flown by MIM over the bulk of the inlier, now on open file. More recently, as part of the Smart State Initiative (Queensland Government, 2007), a surveys have been flown in the west and south of the inlier. These are new surveys are incorporated in the Total Magnetic Intensity image (Figure 15) (but have not been interpreted or processed further).

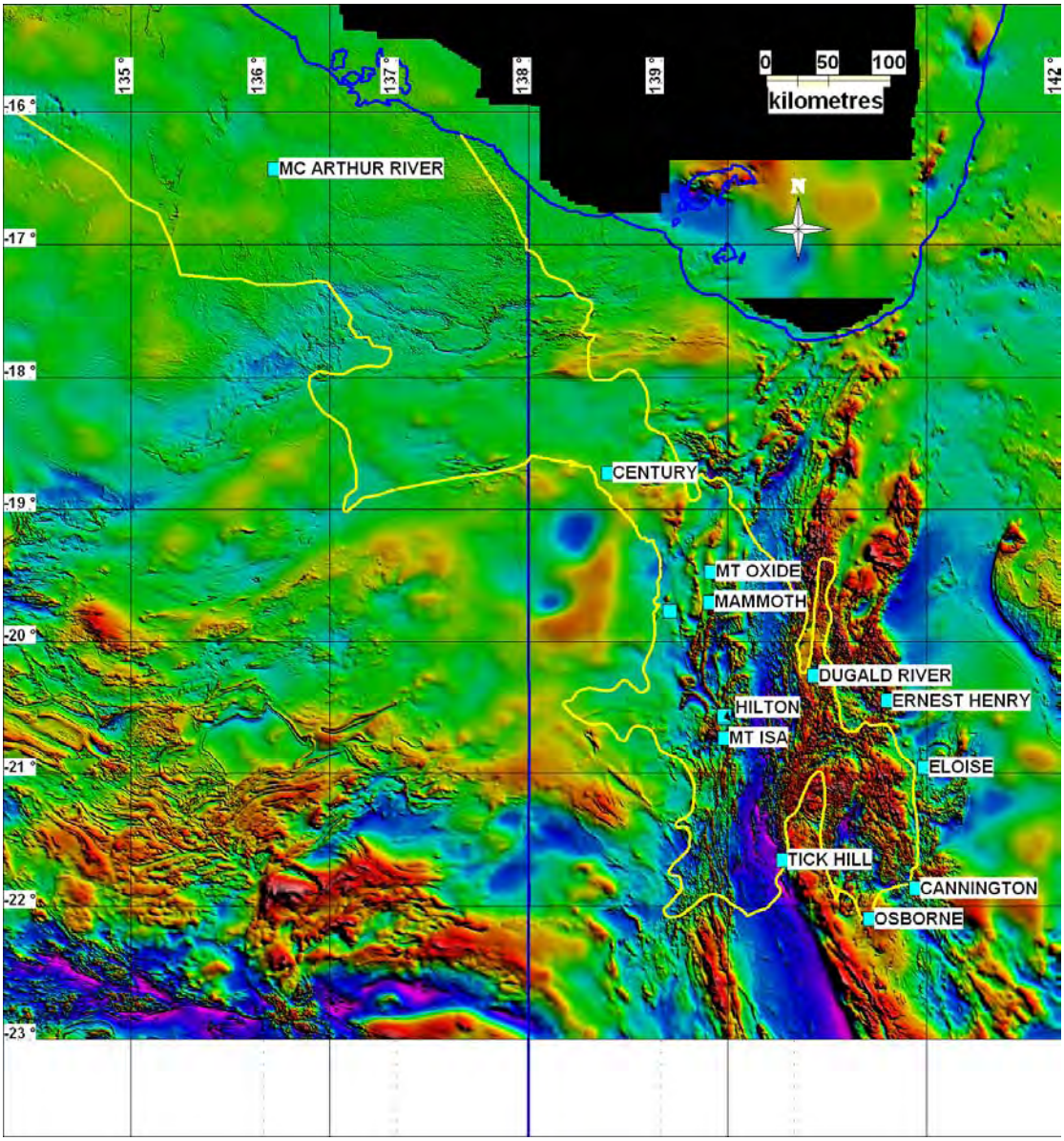

Figure 15: Regional scale total magnetic intensity image.

A series of worming routines were applied to the data (Figure 16). The MIM data was processed by Fractal Graphics algorithms, from which 32 levels of upward continuation from 200 m to 30 km height were derived (House 2002; Murphy 2002). Two types of processed worms were used: Max (maximum gradient) and EFVD (effective first vertical derivative); the latter provides a more complete representation of near surface gradients. A second set of worms was generated for the region to the north of the MIM survey, in the Mornington area (from 8000000N) using Geoscience Australia's algorithm, over 33 levels of upward continuation from 300 m to 45 km height. A third set of worms were generated for the McArthur River region, from 1200m to 80 km height. In addition, an Australian-wide grid of worms generated by Geoscience Australia (P. Milligan, pers. comm.) were made available for the interpretation (Figure 16). As with the gravity data, a way to isolate the significant gradients is shown in Figure 17 as the 5 km level downward migrated worms with the brighter colours depicting gradients that persist to higher levels and, by inference, are the more fundamental crustal features.

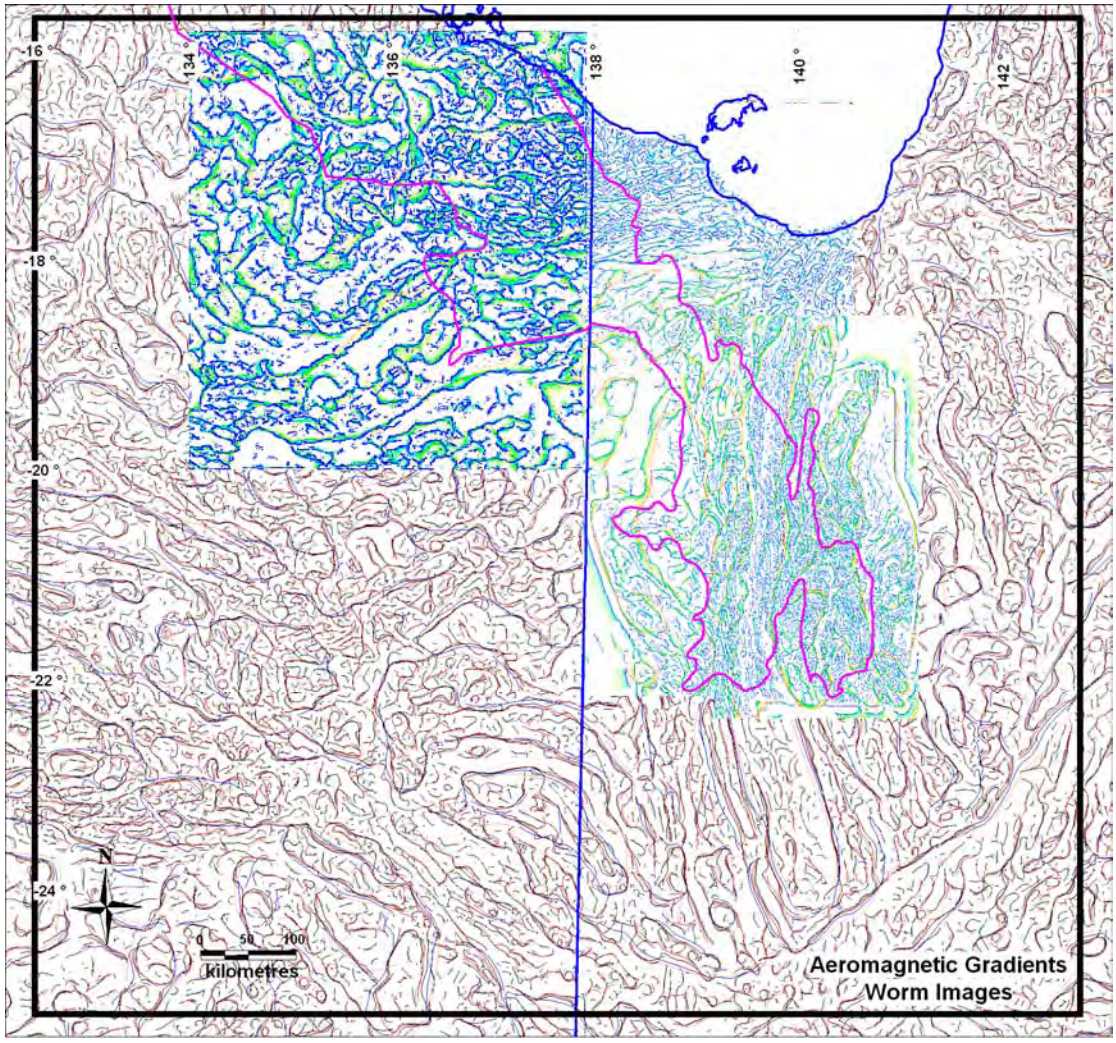

Figure 16: Regional magnetic worm image showing regions where processing was undertaken (blue/green areas) surrounded by coarser scale data coverage from Geoscience Australia (courtesy P. Milligan).

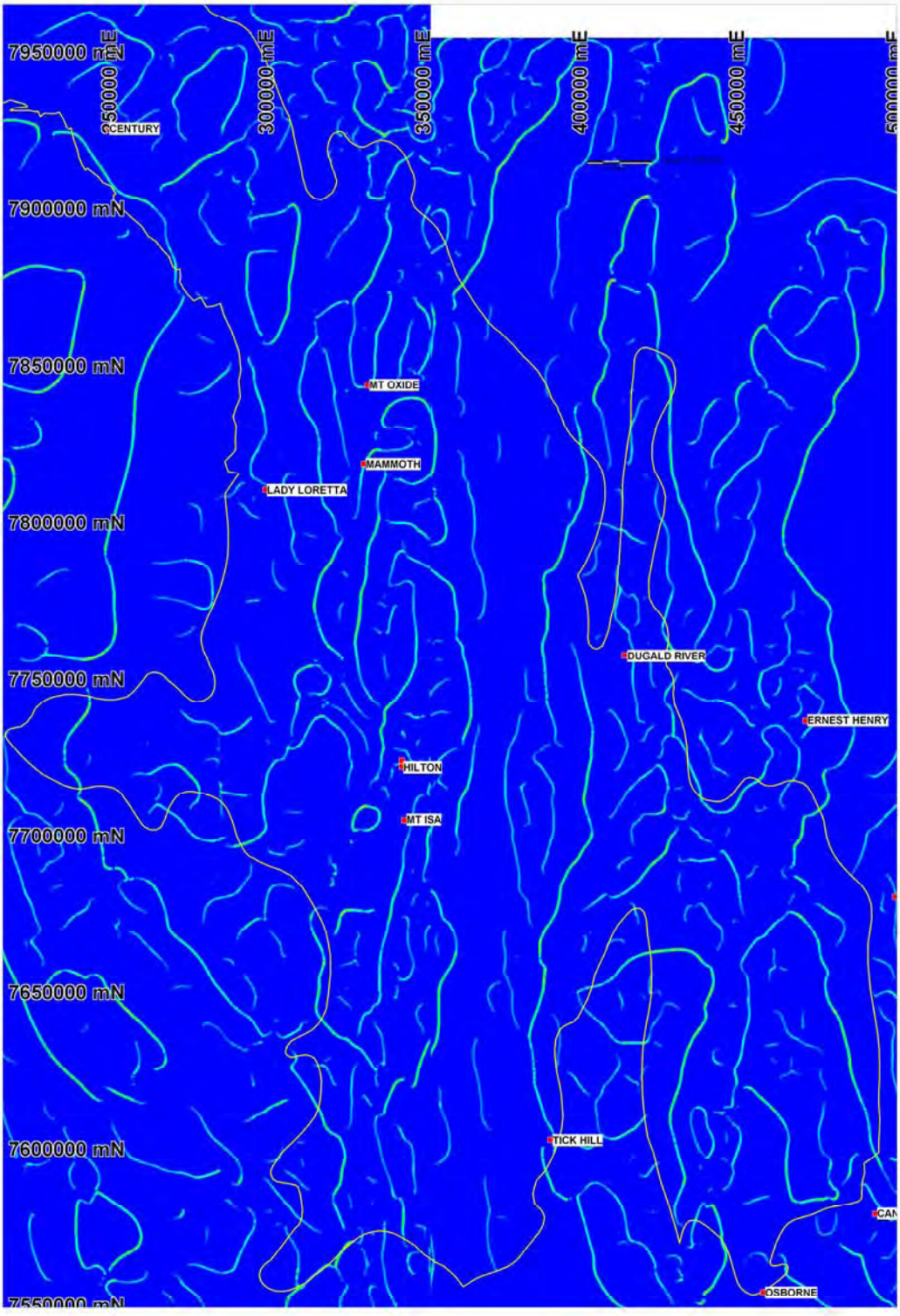
7950000 mN
7900000 mN
7850000 mN
7800000 mN
7750000 mN
7700000 mN
7650000 mN
7600000 mN
7550000 mN
300000 mE
350000 mE
400000 mE
450000 mE
CENTURY
MT OXIDE
MAMMOTH
LADY LORETTA
DUGALD RIVER
ERNEST HENRY
HILTON
MT ISA
TICK HILL
OSBORNE

a)

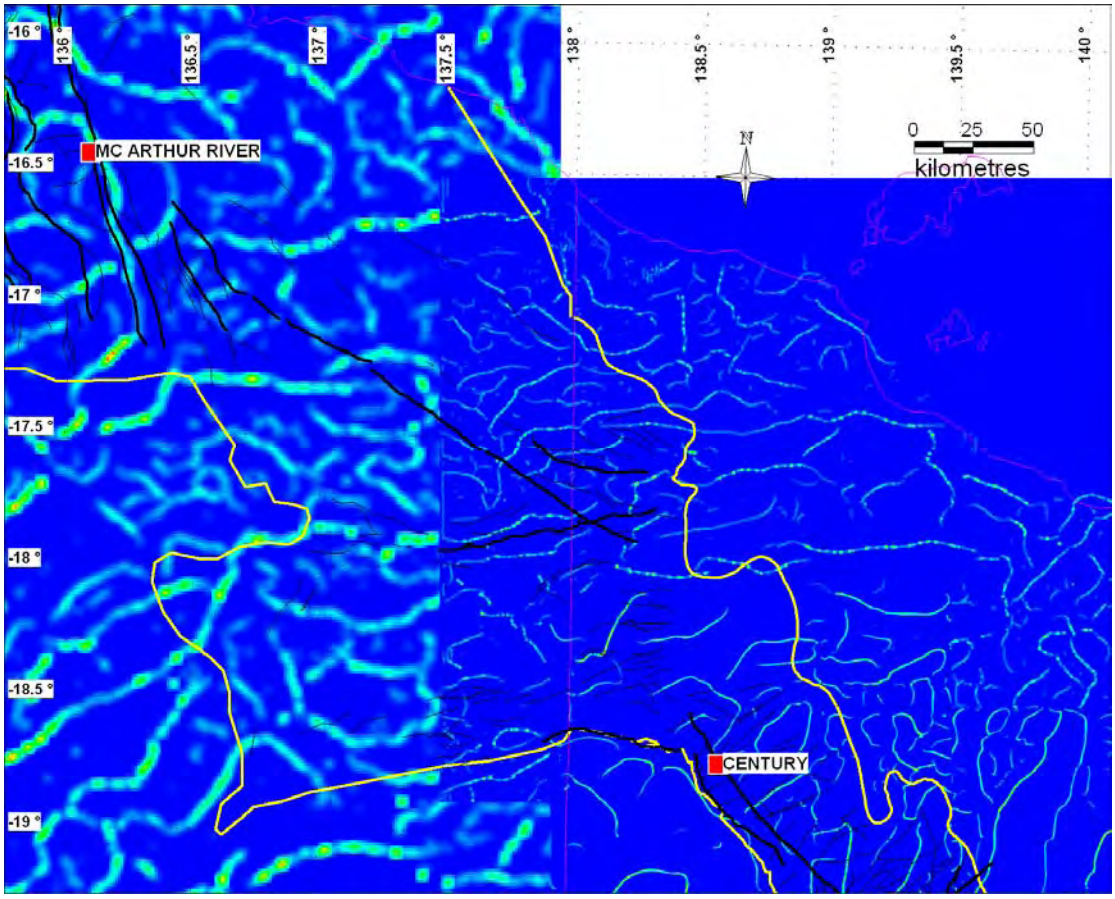

b)

Figure 17: Downward migrated magnetic worms at 5km upward continuation. Intensity or brightness of edge reflects degree of connectedness or continuity at higher levels. a) Mt Isa and b) McArthur regions.

6.3 Potential Field Gradient Interpretation

A categorisation of line elements is made based on whether the gradient encloses a coherent body (e.g. an intrusive) or if the gradient is "open" or linear in character. The latter features most often relate to faults, intrusive and stratigraphical contacts. The majority of linear gradients appear fault-related, consistent with the large population of mapped faults (Figure 8). These line elements are shown in Figures 18 and 19 for gravity and aeromagnetics respectively. Superposition of the different orientations of fault elements has not been resolved in detail. Strike directions of the interpreted fault lines are colour coded in Figures 18a and 19a, with certain trends more prevalent within some areas. Notwithstanding inherent differences in the gravity and aeromagnetics, strike length is a common attribute to both data sets. These are shown as colour coded maps in Figures 18b and 19b. Length values were extracted from the lines as a point file, gridded and imaged. These are displayed for the gravity and aeromagnetics (Figure 20a and b). There is a broad coherence in the distribution of the gravity and aeromagnetic gradients. At a regional scale, similar linear trends are seen but each data set shows a slightly different emphasis on the patterns developed. For example, beneath the Georgina Basin, the gravity gradients emphasise a series of NE trending gradients whereas the magnetic gradients a NW trend is more pronounced.

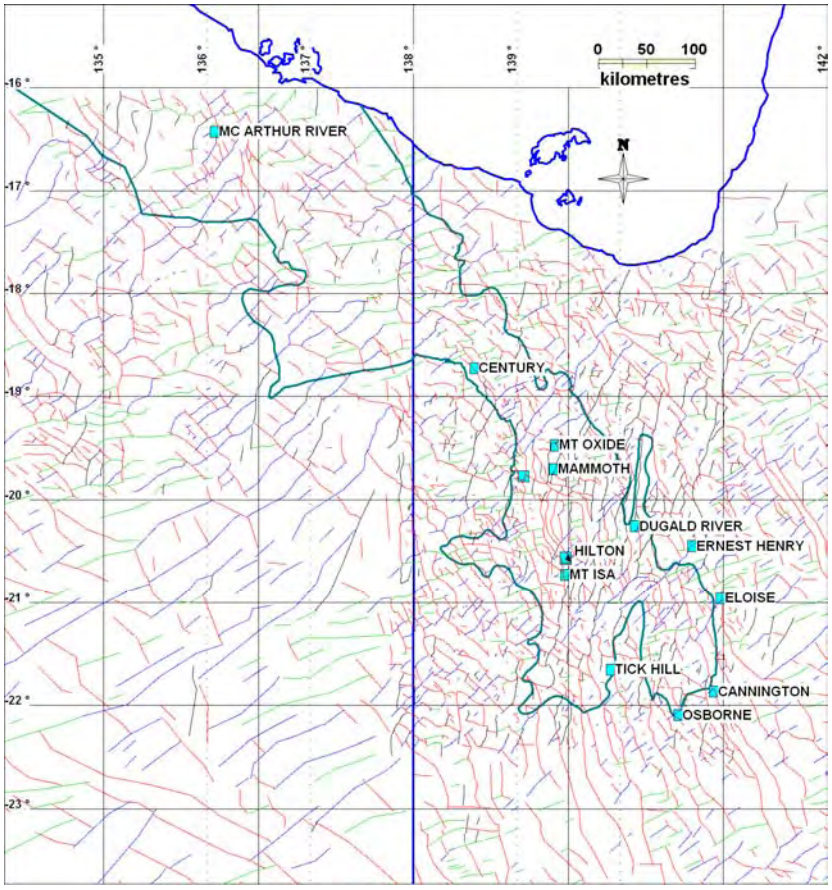
0 50 100
kilometres
N
MC ARTHUR RIVER
CENTURY
MT OXIDE
MAMMOTH
DUGALD RIVER
ERNEST HENRY
HILTON
MT ISA
ELOISE
TICK HILL
CANNINGTON
OSBORNE
135°
136°
137°
138°
139°
142°
16°
17°
18°
19°
20°
21°
22°
23°

a)

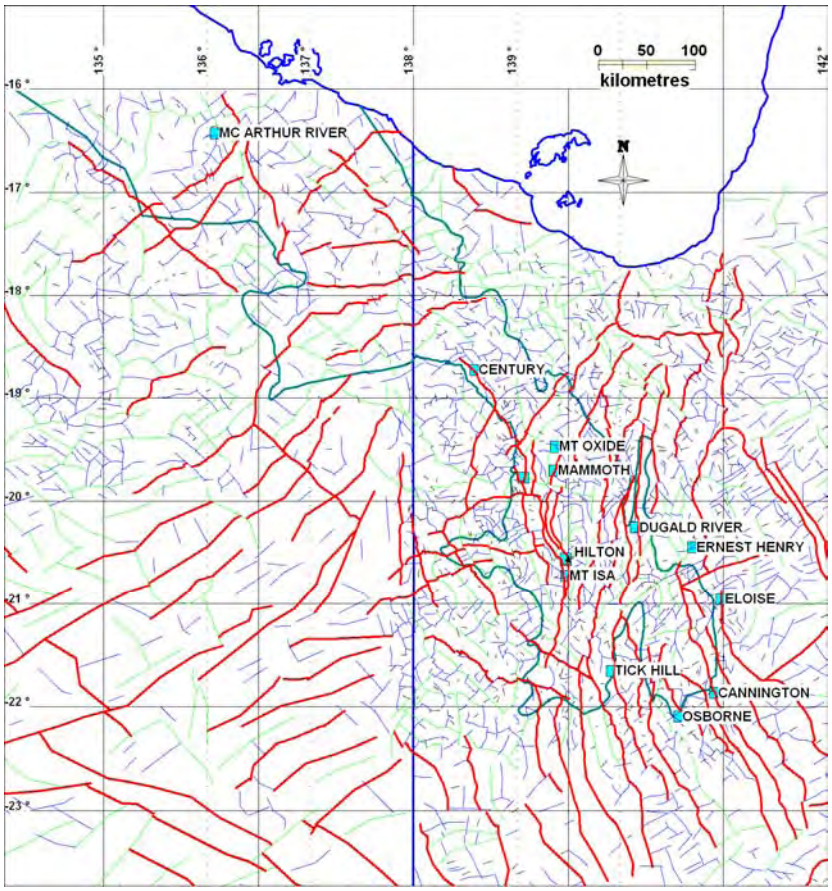
0 50 100
kilometres
N
MC ARTHUR RIVER
CENTURY
MT OXIDE
MAMMOTH
DUGALD RIVER
ERNEST HENRY
HILTON
MT ISA
ELOISE
TICK HILL
CANNINGTON
OSBORNE
135°
136°
137°
138°
139°
142°
16°
17°
18°
19°
20°
21°
22°
23°

b)

Figure 18: Interpreted gravity lines, a) trend, b) length

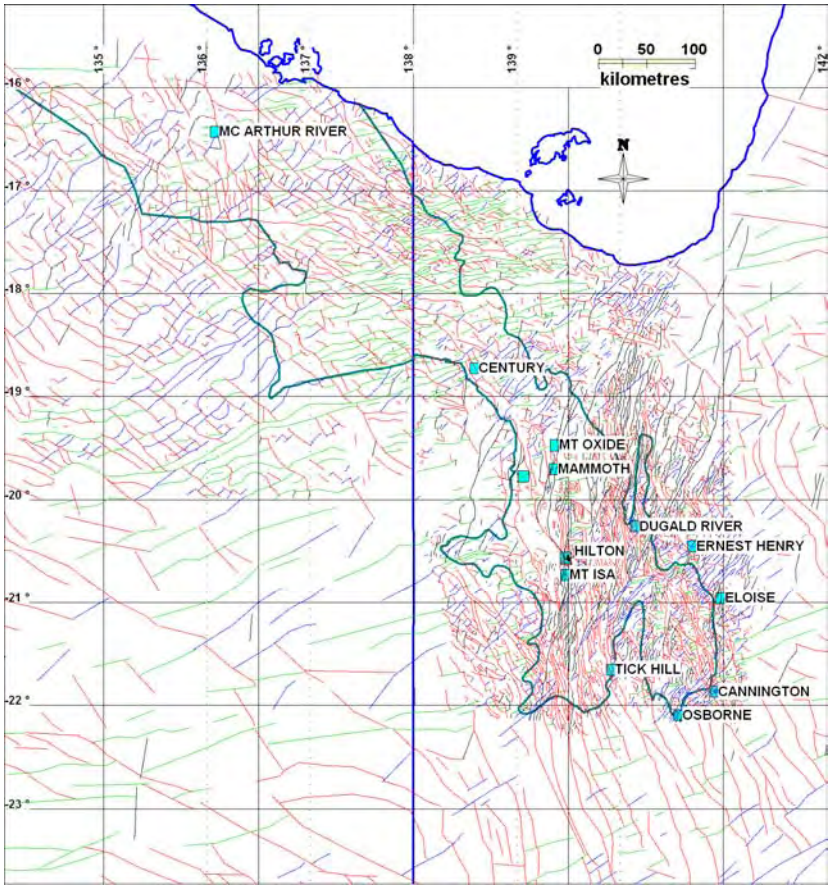

a)

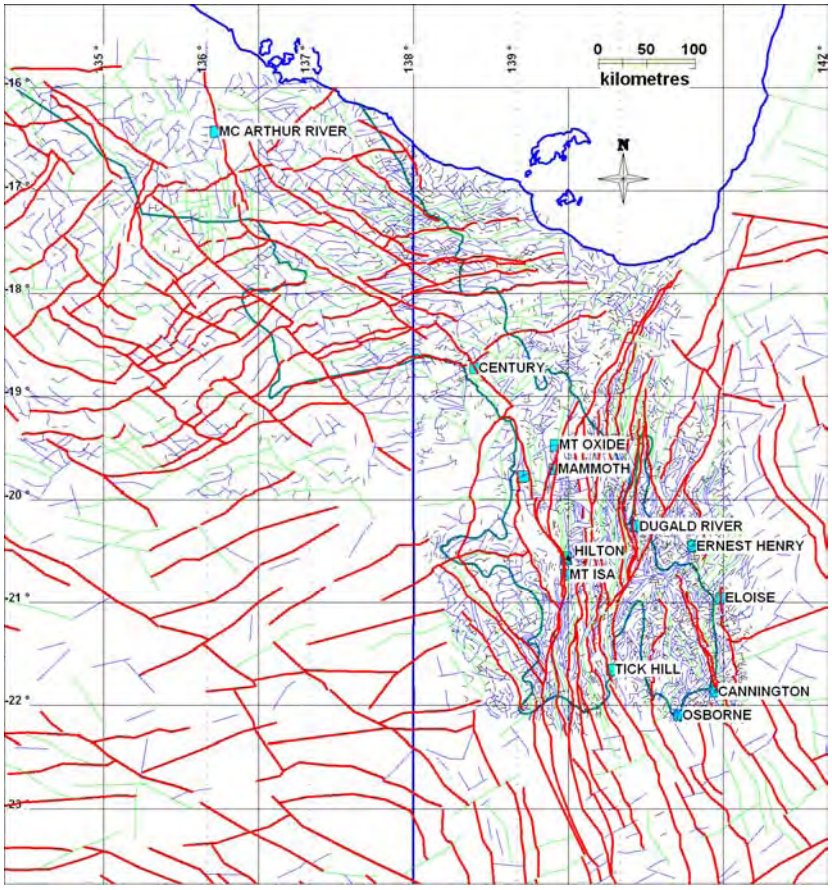

b)

Figure 19: Interpreted aeromagnetic lines, a) trend, b) length

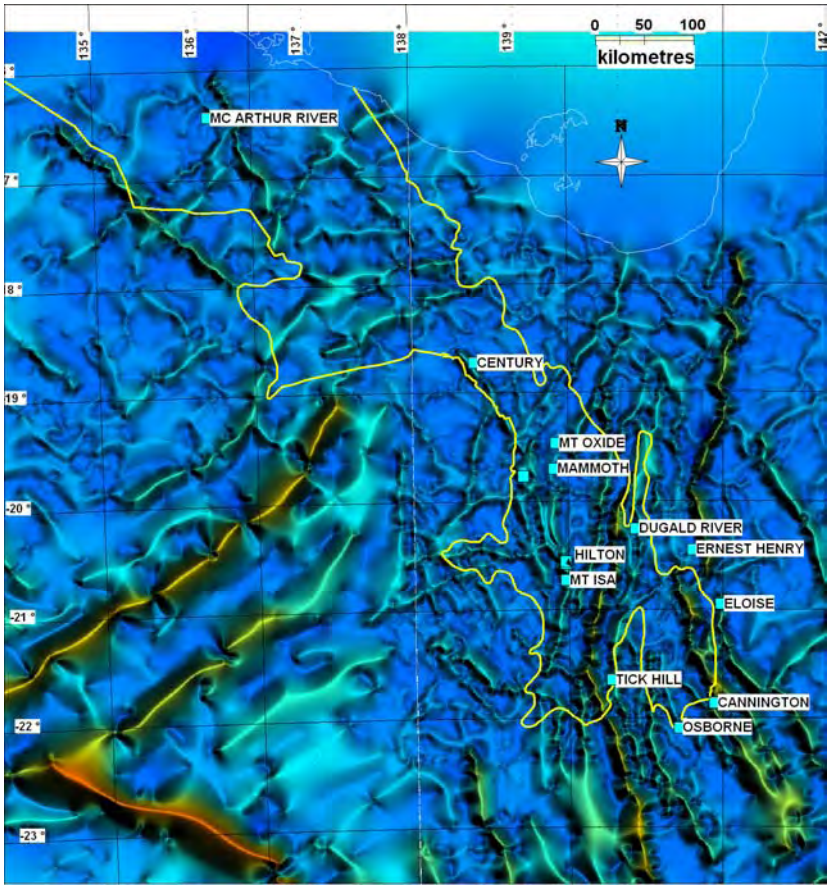

a)

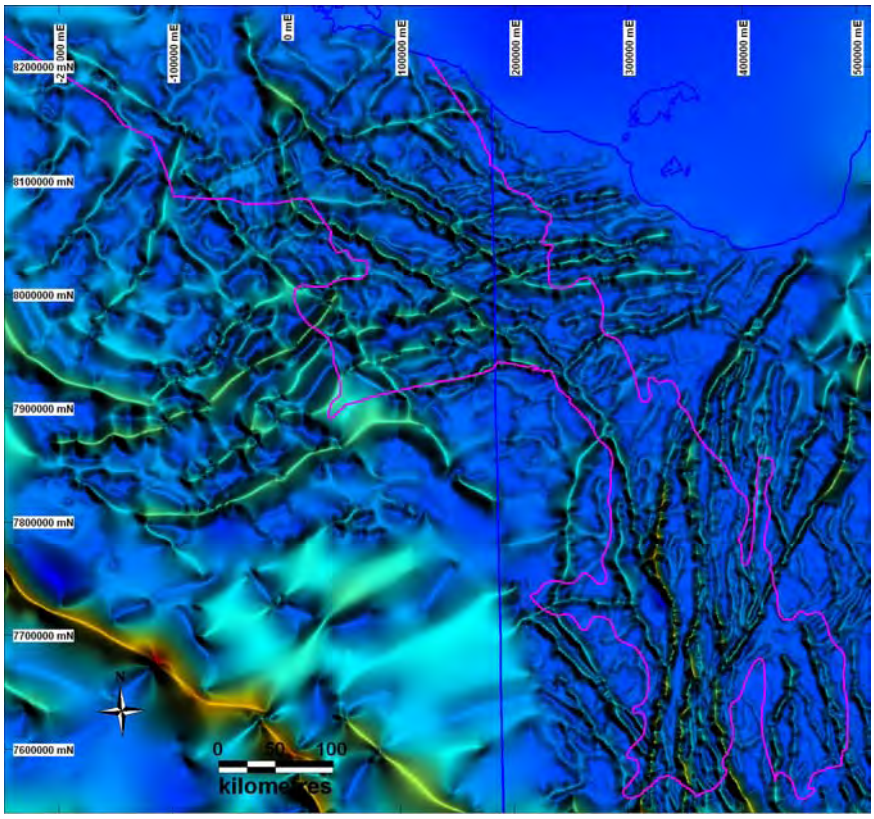

b)

Figure 20: Line length images of a) gravity and b) aeromagnetic gradients

7 3D Geological Modelling

7.1 Cross Sections and Forward Modelling

The methodology follows that used in other regions where the pmd*CRC have successfully built regional scale 3D models (Figure 2; Tasmania – T3 project, Murphy *et al.* 2002; and W Victoria – T1 project, Murphy *et al.* 2006). The positions of major faults in the near surface are reasonable well constrained, from mapped geology (Figure 8) and interpreted geophysics (Figures 18 and 19). Serial geological cross sections provide a framework from which to build the 3D model (Figure 21). These were based on map and profile templates showing the upward continued worm data and mapped geology (e.g. Figure 22). In all, eighty three cross sections for a cumulative length of 12,500 kms were made (Figure 21; Appendix 1). These have slightly different specification in different areas:

- In the Mt Isa region, east-west sections at 10 km spacing and some north-south sections were made. Initial sections were to 5km depth.
- In the EFB a series of east-west sections, constructed under the I2 project, were modelled. They link with the east-west sections (above) and are drawn to 20 km depth. A block model of first order features has also been developed (Lepong, on-going Ph. D. research project).
- In the LHP, sections and modelling were completed under a separate project (G14; Murphy *et al.* 2007), aspects of which are incorporated here. These east-west and north-south sections were drawn on a wider spacing, and the 3D model in this region was constructed using Geomodeller software (compared to elsewhere where Gocad was used).
- In the McArthur River region, with sparser data coverage, 20 km spaced east-west and north-south sections were constructed to 20 km depth.

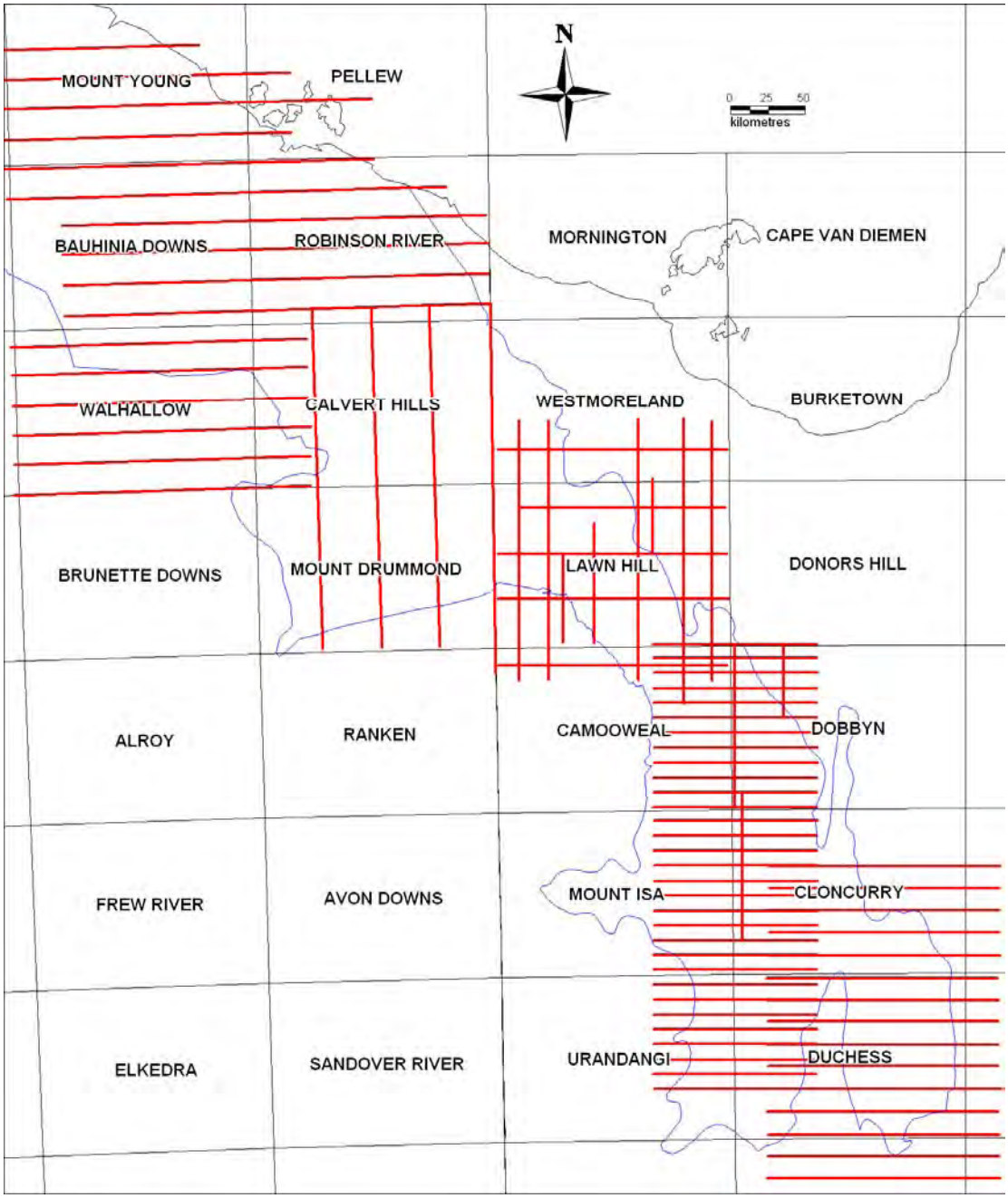

Figure 21: Locations of geological cross sections (red) for input to 3D modelling. Proterozoic outcrop boundary, coastline and 1:250 000 sheet boundaries are also shown.

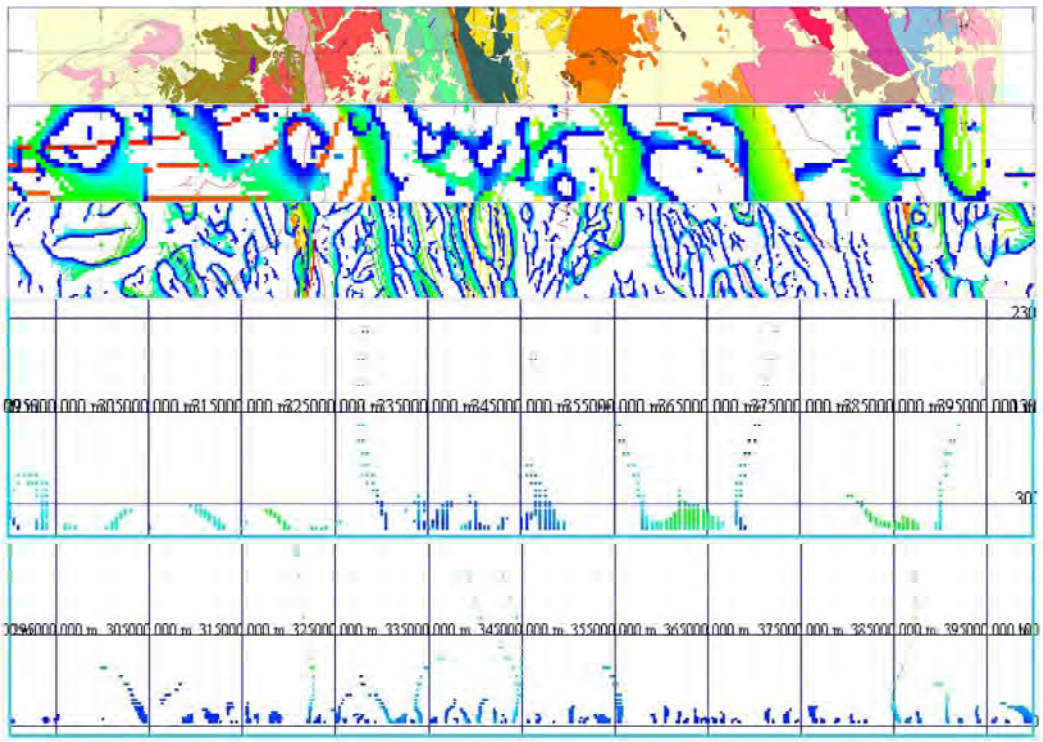

Figure 22: Template for cross section interpretation (Line 7600000N) showing (from top) three strip maps of geology, gravity worms and aeromagnetic worms, and two profiles of upward continued worm features from gravity and aeromagnetics, respectively.

Forward modelling of three east-west trending cross sections in the Mt Isa region was undertaken to examine the sensitivities of different fault dips and thicknesses of units. Profiles at northing 7600000, 7640000 and 7770000 with profile length of 100 km starting from easting 300000 and ending to easting 400000 (Figure 23). This used the same physical property data as in the I1 project (Gibson *et al.* 2005). In each profile, there is a remarkable agreement between the observed data and the computed response, which is necessary (although not sufficient) to validate the proposed structural settings of the area. In general, the level of the basement has the greatest influence in the profiles.

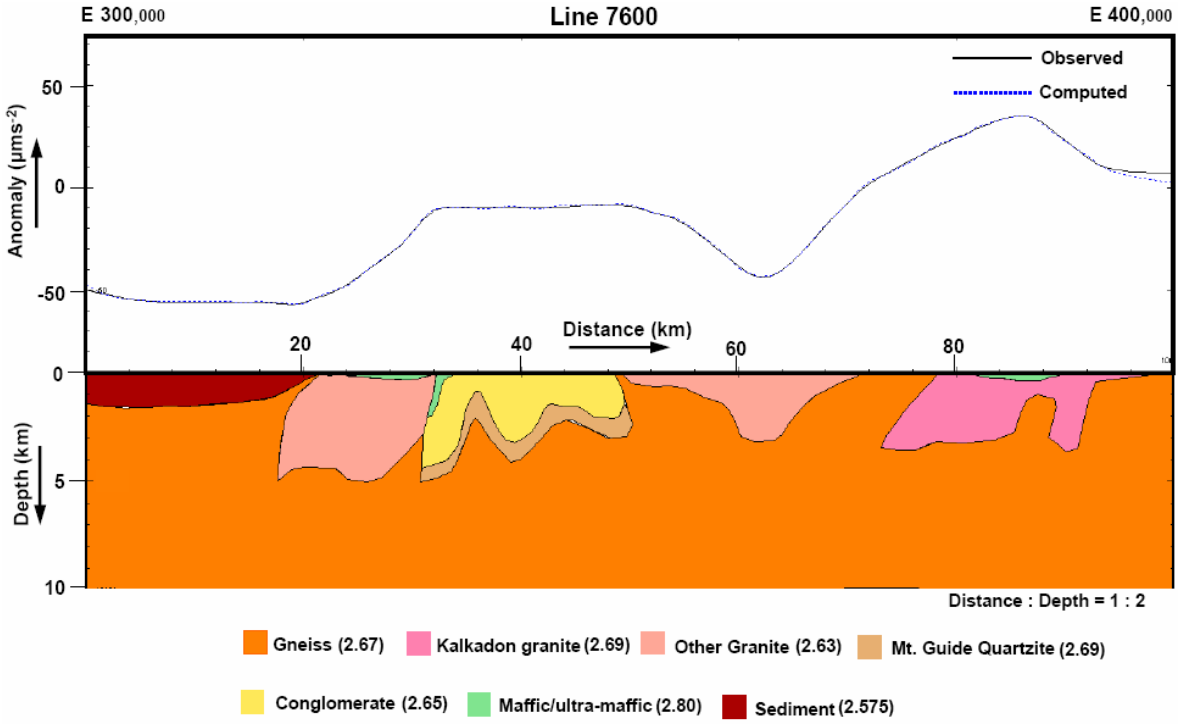
E 300,000
Line 7600
E 400,000
Observed
Computed
Anomaly (μms-2)
50
0
-50
Distance (km)
20
40
60
80
0
Depth (km)
5
10
Distance : Depth = 1 : 2
Gneiss (2.67)
Kalkadon granite (2.69)
Other Granite (2.63)
Mt. Guide Quartzite (2.69)
Conglomerate (2.65)
Maffic/ultra-maffic (2.80)
Sediment (2.575)

a

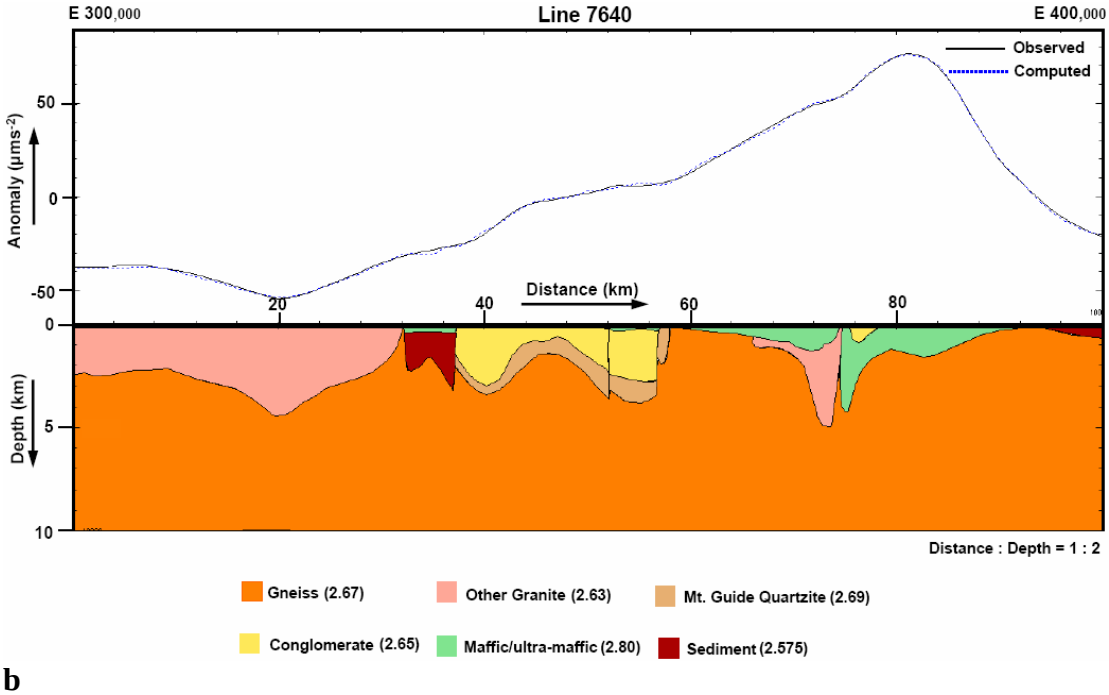
E 300,000
Line 7640
E 400,000
Observed
Computed
Anomaly (μms-2)
50
0
-50
Distance (km)
20
40
60
80
0
Depth (km)
5
10
Distance : Depth = 1 : 2
Gneiss (2.67)
Other Granite (2.63)
Mt. Guide Quartzite (2.69)
Conglomerate (2.65)
Maffic/ultra-maffic (2.80)
Sediment (2.575)

b

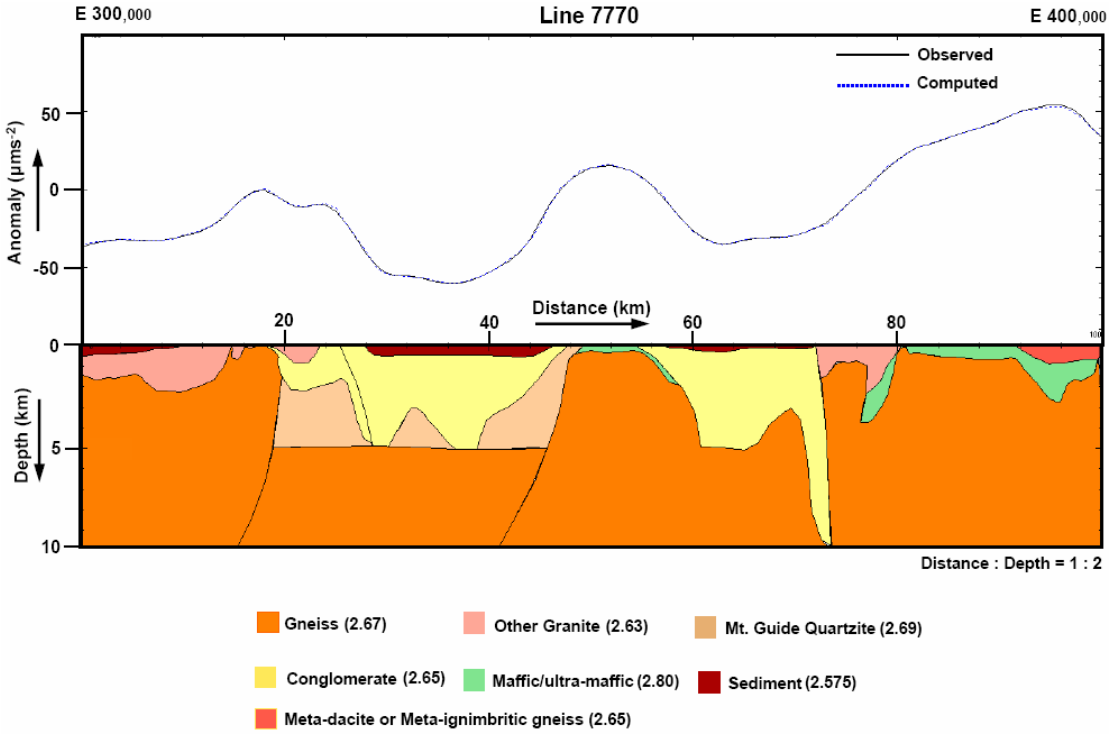

c

Figure 23: 2.5D gravity forward modelling of the profiles a) 7600000N, b) 7640000N and c) 7770000N. Vertical exaggeration x2.

7.2 Critical Geometries

To visualise the 3D architecture a series of 3D PDF's were made and are embedded here (but need help doing so).
(these are available on TWIKI I7 _3D Models)

The modelled fault geometries through much of the Mt Isa and Mc Arthur River regions is interpreted as steeply dipping in the top 5 km. Listric and low angle structures are more common in the EFB, in the northern parts of the LHP and in the central parts of the McArthur region. The first order fault structures are described below. The regional scale pattern of faults interpreted from gravity and aeromagnetic gradients help to pick out the major trends and corridors, with Figure 24 showing a combined edge length image of the data. Relationships of the 3D modelled faults to the edge length data is shown in Figure 25, showing a correlation of depth penetrative with strike extensive features. Enveloping surfaces are a key part of the geometry at this scale. Our analysis shows that even in the more complexly deformed and metamorphosed parts of the terrain, in the EFB, the broad scale relationships can be interpreted within a relatively shallowly inclined sheet dip cut by steeply inclined faults.

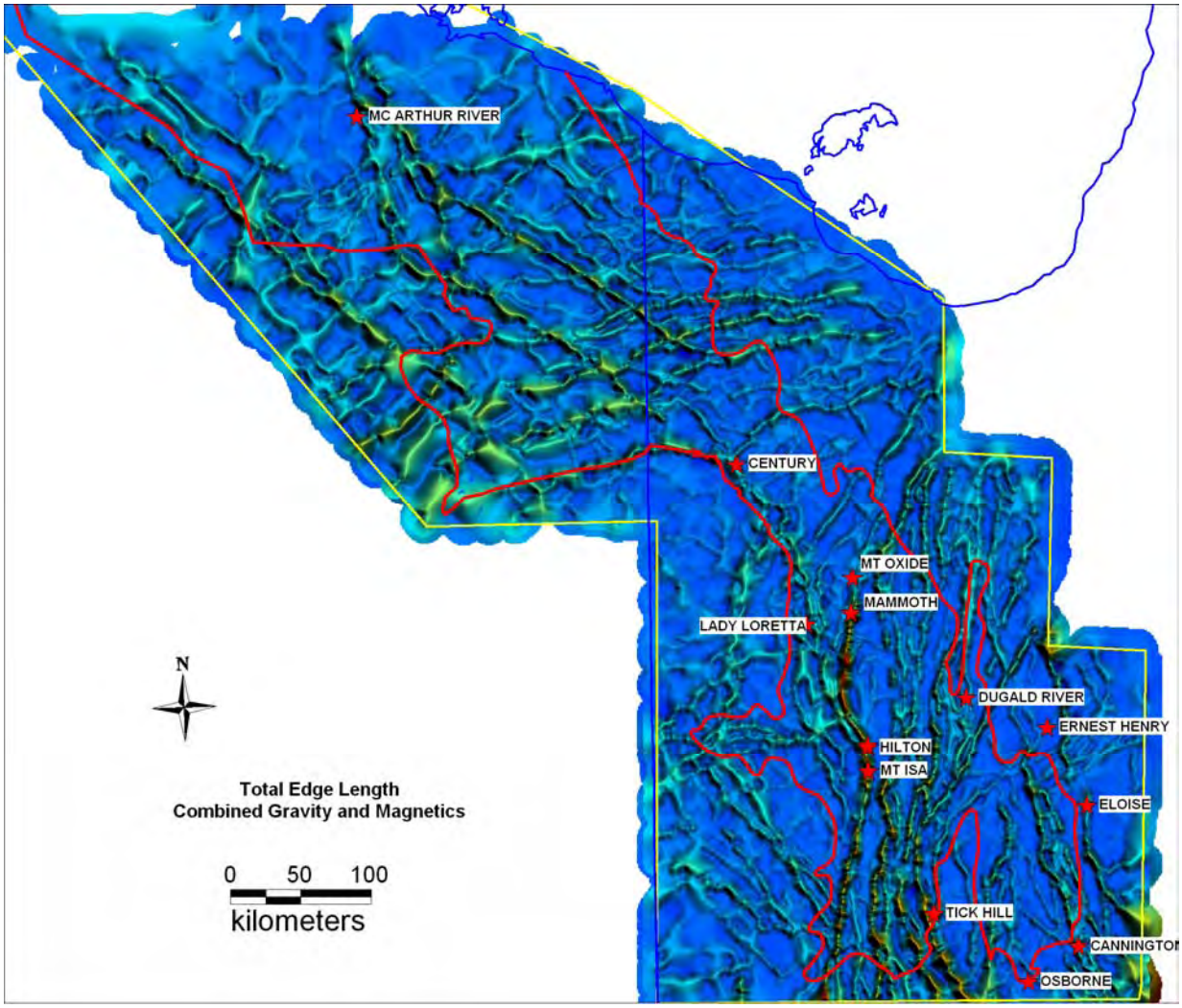

Figure 24: Edge length image from combined gravity and aeromagnetic interpretations.

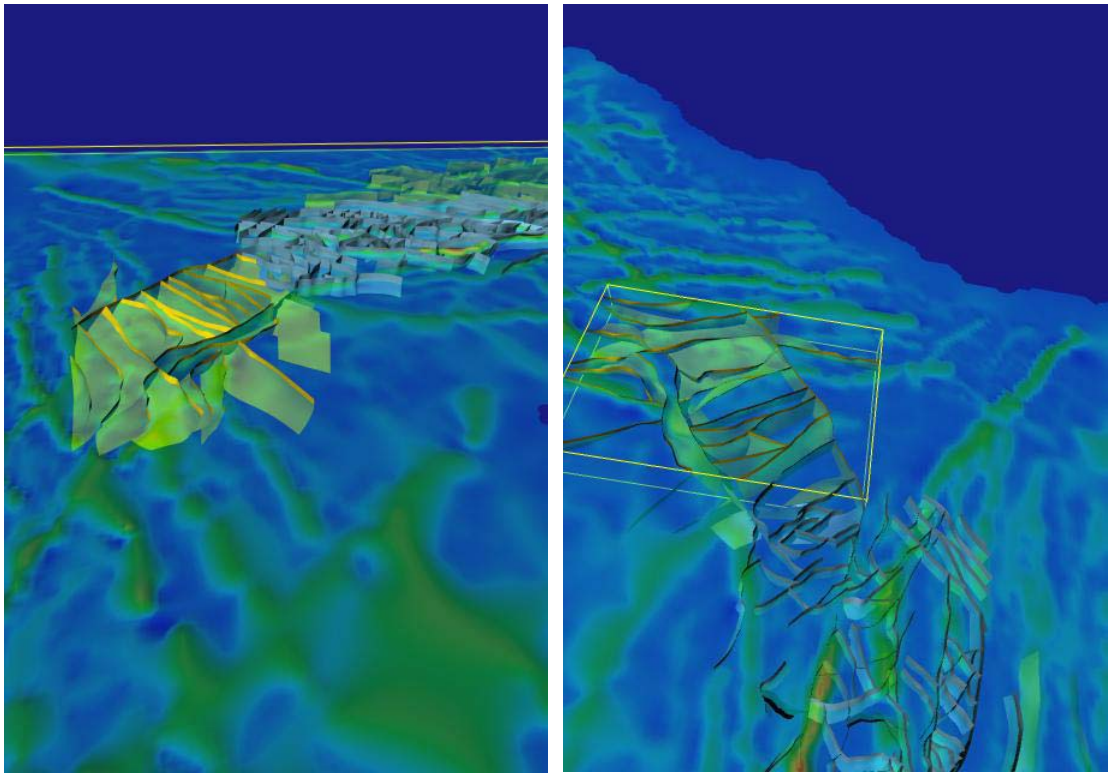

Figure 25: Perspective views of edge length image (combined gravity and aeromagnetics) and 3D fault surfaces, a) from NW across LHP and SNB, and b) from SW across northern Mt Isa and southern LHP.

The basement topology has a major bearing on the distribution of Superbasins. This is because the basement/cover interface is interpreted as essentially autochthonous or parautochthonous (Blenkinsop *et al.* 2005). Representations of the top of basement are shown for the Lawn Hill region (Figure 26) and the EFB (Figure 27). Breaks in the surface are interpreted as basement-penetrating faults, the major ones being the Pilgrim and Cloncurry Faults.

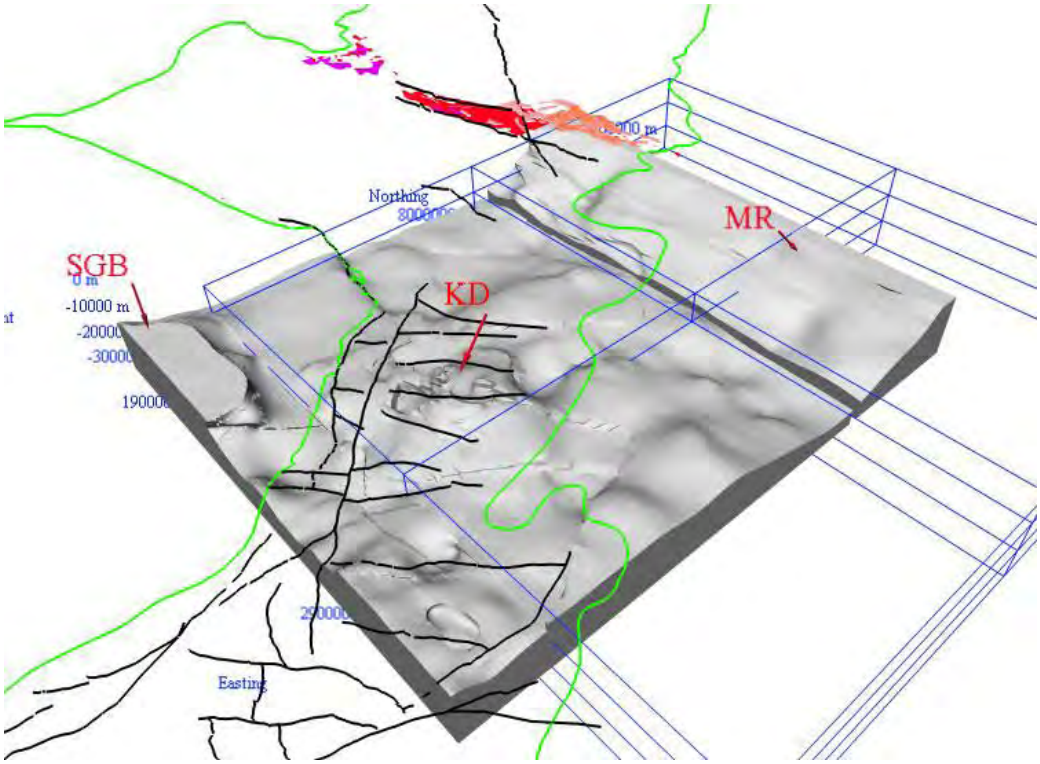

Figure 26: 3D model of basement topology in Lawn Hill and parts of Camooweal and Westmoreland 1:250,000 sheets. KD = Kamarga Dome, MR = Murphy Ridge, SGB = Sub-Georgina Basin. First order surface fault traces (black), Proterozoic outcrop boundary (green), basement outcrop (magenta), Cover Sequence 1 (pink) and Kalkadoon Suite (red). Perspective view towards NW. Grid at 10km depth intervals. (Model under construction).

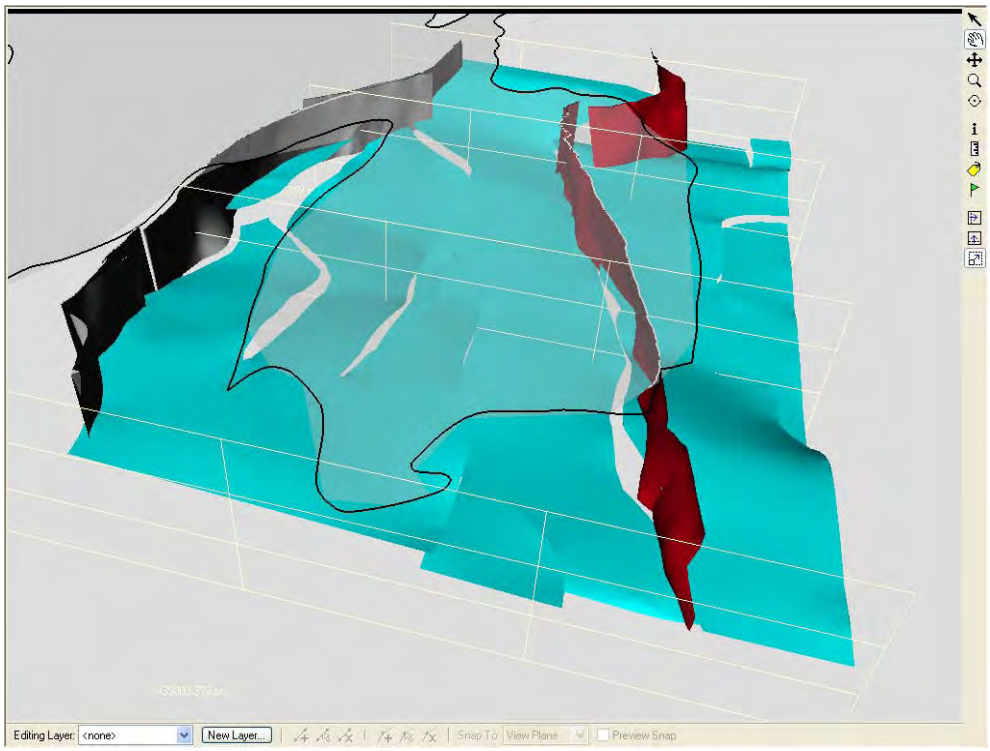

Figure 27: Modelled top of basement surface (blue) beneath the EFB and showing major fault surfaces (Pilgrim = grey, Cloncurry = red). Shaded region inside black line is Proterozoic outcrop boundary. Grid depth to-30 km. (Model under construction)

A dominating geometry of the LRFT is the Mt Gordon Arch (Figure 28; Derrick 1982) which appears to have originated during LSB sedimentation (Gibson *et al.* 2005) and was maintained as a topographic feature during CSB sedimentation. The eastern boundary, along the Quilalar Fault and the ECV extending across a proposed rift shoulder is represented.

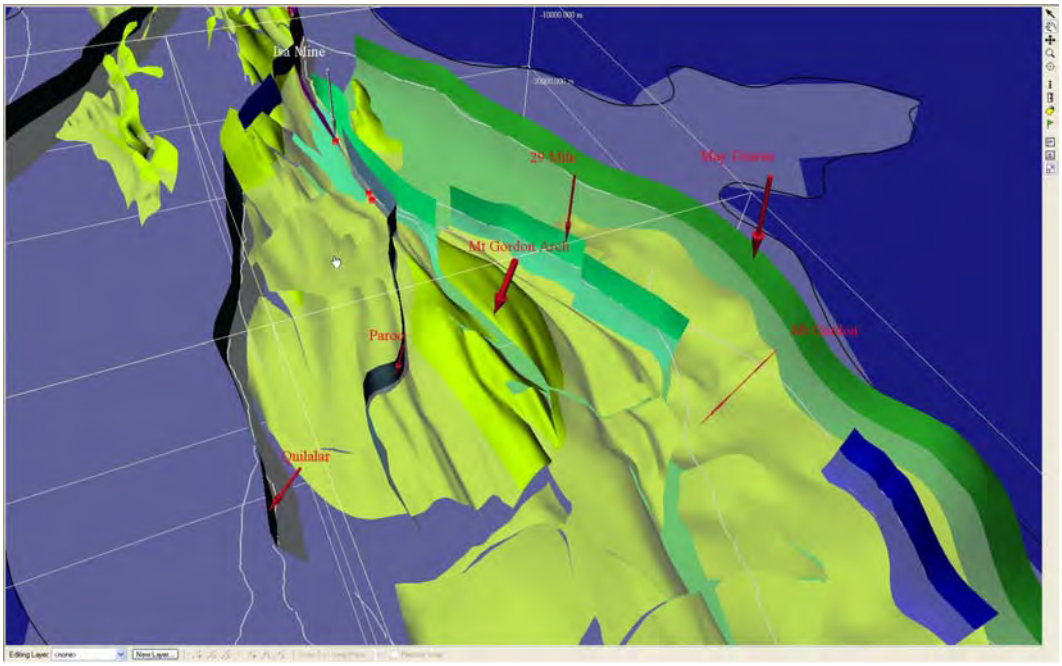

Figure 28: Perspective view from NE of LRFT with base of ECV in green (darker below surface, lighter above surface), highlighting the Mt Gordon Arch, and boundaries to the east (Qulalar Fault) and west (May Downs Fault). Grid depth to -40 km. (Model under construction)

There is a significant below surface extend of the CSB, as (incompletely) indicated in Figure 29. Gibson *et al* .(2005) show a northward deepening of the basin.

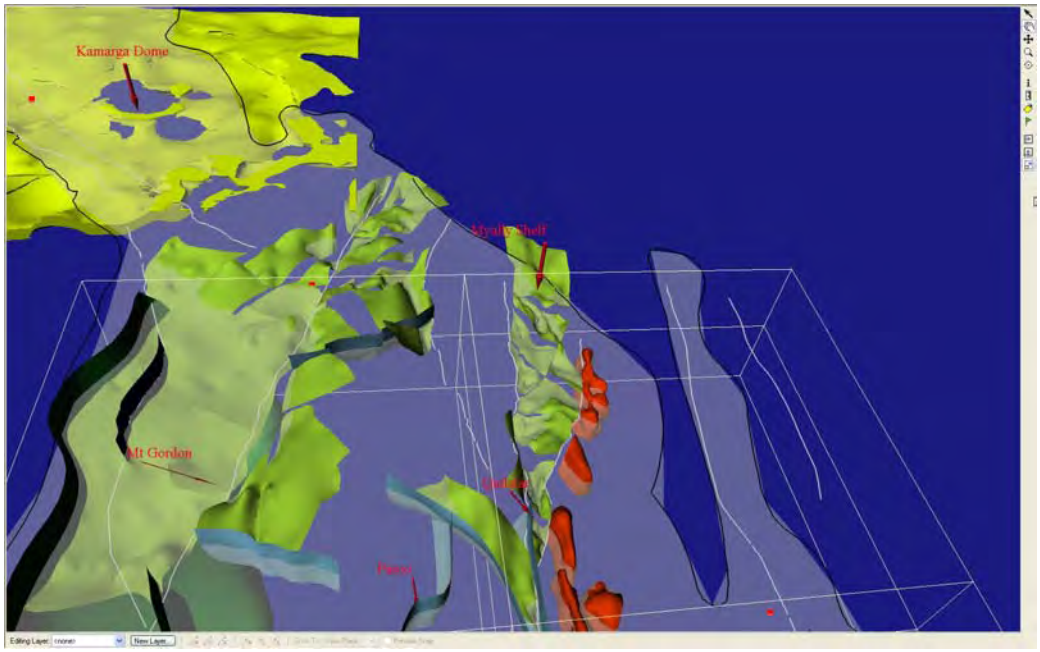

Figure 29: Perspective view from south of base of Calvert Superbasin (green, more intense where surface is above ground within inlier and where below ground outside inlier, under cover) and includes Kalkadoon Batholith (red). Quilalar Fault marks the western boundary to CSB outcrop in Myally Shelf. Grid depth to -40 km. (Model under construction).

The Sybella Batholith is an elongate north-south and is interpreted as a relatively flat bottomed body (Figure 30). It is located along or between interpreted major extensional detachments (May Downs and Twenty Nine Mile Faults) in a core complex scenario (Gibson *et al.* 2005).

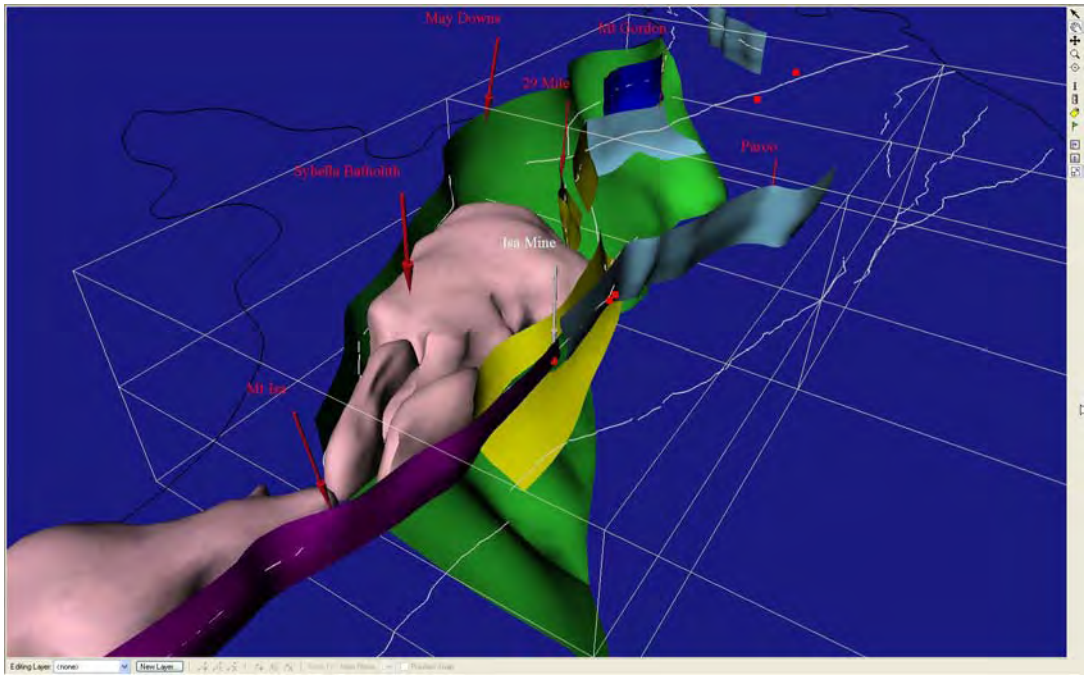

Figure 30: Perspective view of 3D modelled faults and Sybella Batholith (lilac) in the western regions of the Mount Isa Inlier. May Downs Fault (green) interpreted as major east dipping structure linking at depth with the Twenty Nine Mile Fault

(yellow) beneath. Mt Isa Fault (purple) in hanging wall of May Downs Fault. Paroo Fault (blue) also shown, branching northwards from Mt Isa/Twenty Nine Mile Fault system. While lines = first order fault traces, black line = Proterozoic outcrop boundary; red dots = major deposits. Grid from +10 to -40 km. (Model under construction).

The Riversleigh and Termite Range Faults define an important corridor on the LHP where seismic and magnetotelluric data have helped to constrain the depth extent of the faults (Figure 31). Preliminary interpretation of the Lawn Hill seismic (Lines M1 and M2) shows a major NE dipping structure correlated with the Riversleigh Lineament. It is interpreted that the Riversleigh Lineament is a major crustal-scale NE dipping fault with growth history during CSB and ISB times. This is an inferred boundary to a basement block to the SW, and concealed by the Cambrian Georgina Basin. Basement crops out to the NW in the Carrara Range (Murphy Metamorphics), and to the SW of Mt Isa (Yaringa Metamorphics).

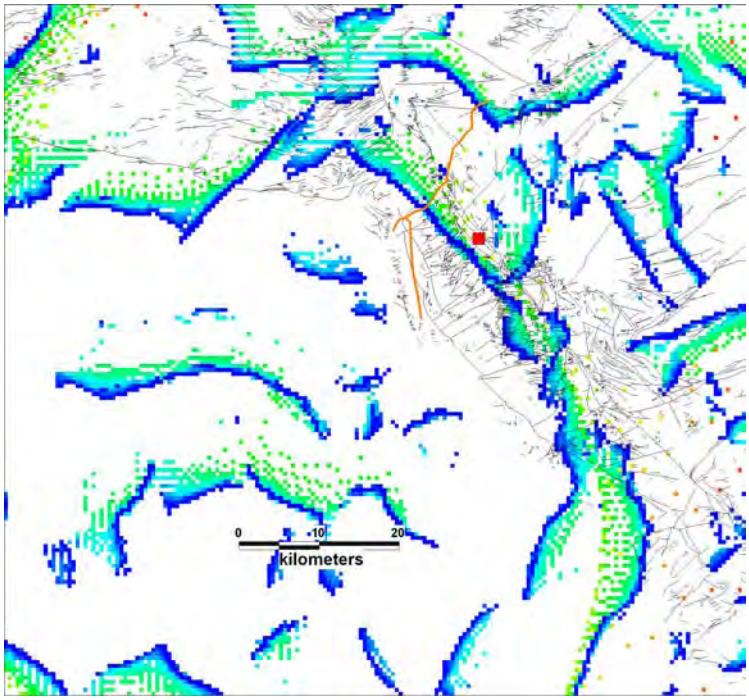

a)

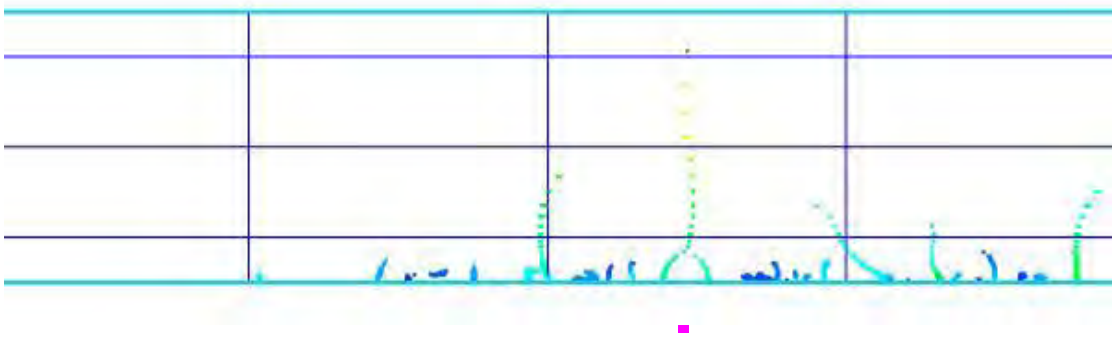

b)

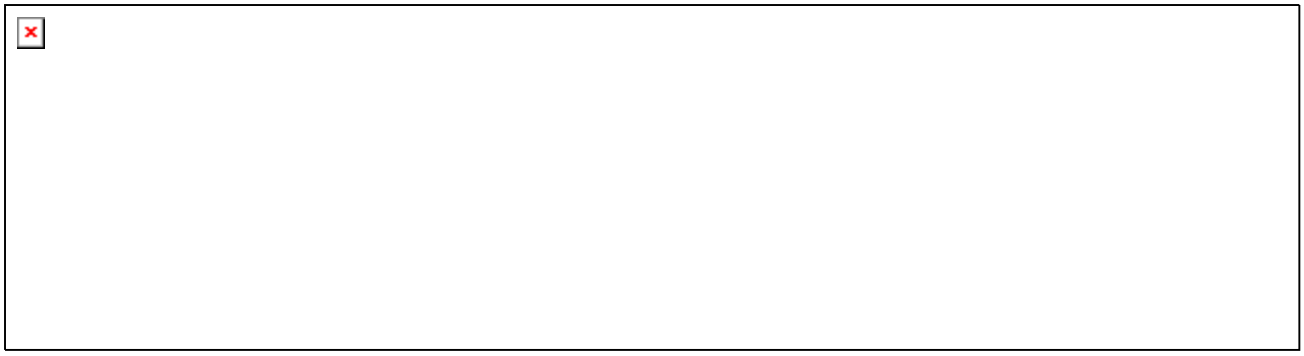

SW NE

c)

Figure 31: Termite Range/Riversleigh Fault Corridor and the Century deposit, a) map of gravity gradients, b) profile of gravity gradients as upward continued levels, c) seismic lime M1, 6sec migrated data.

The Mt Isa Fault is imaged (poorly) in seismic data as a steep west dipping structure (MacCready *et al*.1998; Figure 32). The Hero Fault represents an extension of the Mt Isa Fault northwards into the Bonus Basin and Mt Gordon Arch regions. The Mt Isa Fault *per se* is here regarded as a relatively late fault developed (as a backthrust) through re-activation of deep seated LSB structural elements. In our modelling, a major east dipping detachment is interpreted close to this position, or further to the west as the Twenty Nine Mile Fault (?), a major NE dipping gravity worm. Seismic data in the Mt Isa area (MacCready *et al*.1998) is permissive of an east dipping feature. This western side of the LRFT corresponds to the "Barramundi Worm" seen in gravity data (Hobbs *et al*. 2002; Murphy in Gibson *et al.* 2005). It is parallel to the Rufus and Mt Annable Faults in the south, but swings to a NW trend into the LHP where it is equated with the Riversleigh Lineament.

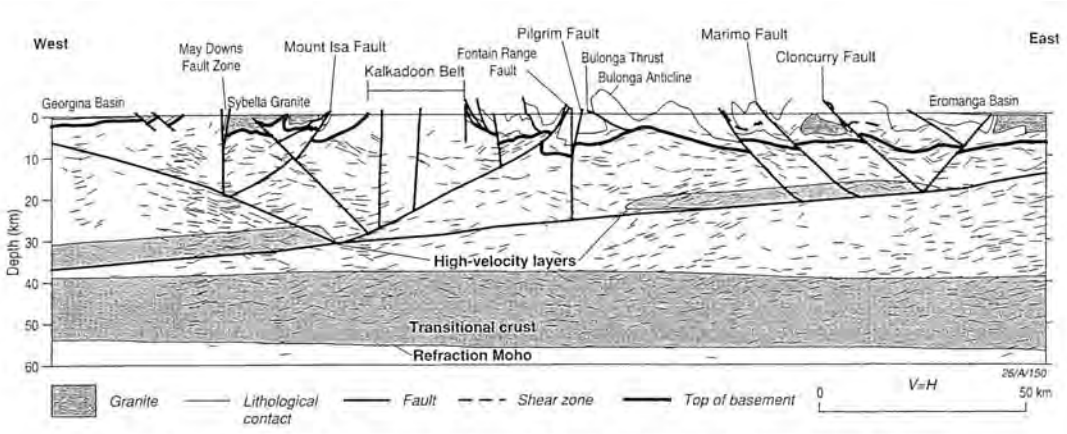

FIG. 8. Full crustal geologic interpretation combining upper crustal interpretation of the reflection data with deeper crustal structure based on refraction data. The image also contains lines traced from deeper reflections (migrated) which partly constrain mid-crustal fault geometries. The major fault inferred beneath the high-velocity layers is discussed in the text.

Figure 32: Interpreted east-west seismic profile arcoss the Mount Isa Inlier, AGCRC Line 94_01 (after McCready *et al* 1998).

- Mt Gordon Fault – most expressed as an Isan Orogeny D4 fault, but earlier history??
- Quilalar Fault - an east dipping gravity worm
- Dajarra Fault – west dipping gravity worm

- Pilgrim Fault….- east dipping gravity worm
- Coolullah Fault – west dipping gravity worm
- Cloncurry Fault - east dipping gravity worm
- Boomarra Fault - east dipping gravity worm
- KL Worm - Corella Boundary Zone/Mary K/Wongas
- Cloncurry Flexure
- Eastern Suture Zone
- Calvert Fault
- Emu Fault
- Mallapunya Fault
- Hot Springs Fault

The distribution of the ISB is a critical factor, particularly with respect to targeting Pb-Zn-Ag systems (see Part II of the Final Report). An example of the EFB model (Figure 33) is shown to illustrate the different components now recognised, the Young Australia Group and the Soldiers Cap Group.

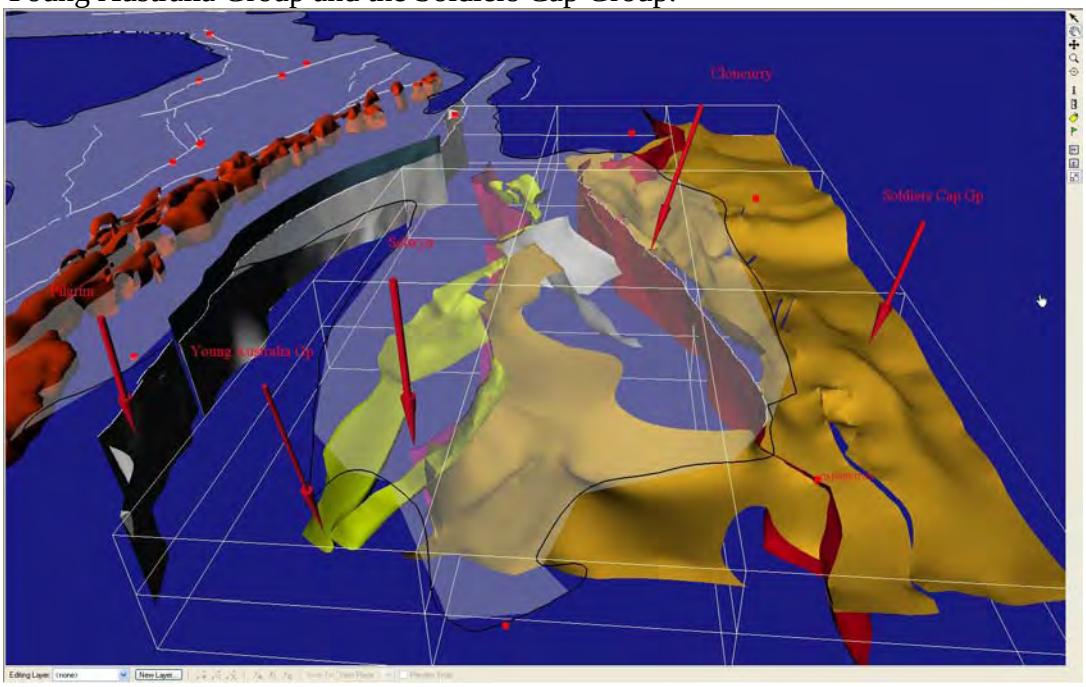

Figure 33: Perspective view of EFB from south showing Soldiers Cap Group (brown) and Young Australia Group (green) and major faults labelled – Cloncurry Fault (red), Selwyn Shear (purple) and Pilgrim Fault (grey). Proterozoic inlier in grey shading, Kalkadoon Batholith (red). (Model under construction)

Distribution of EFB granitoids (Figure 34)

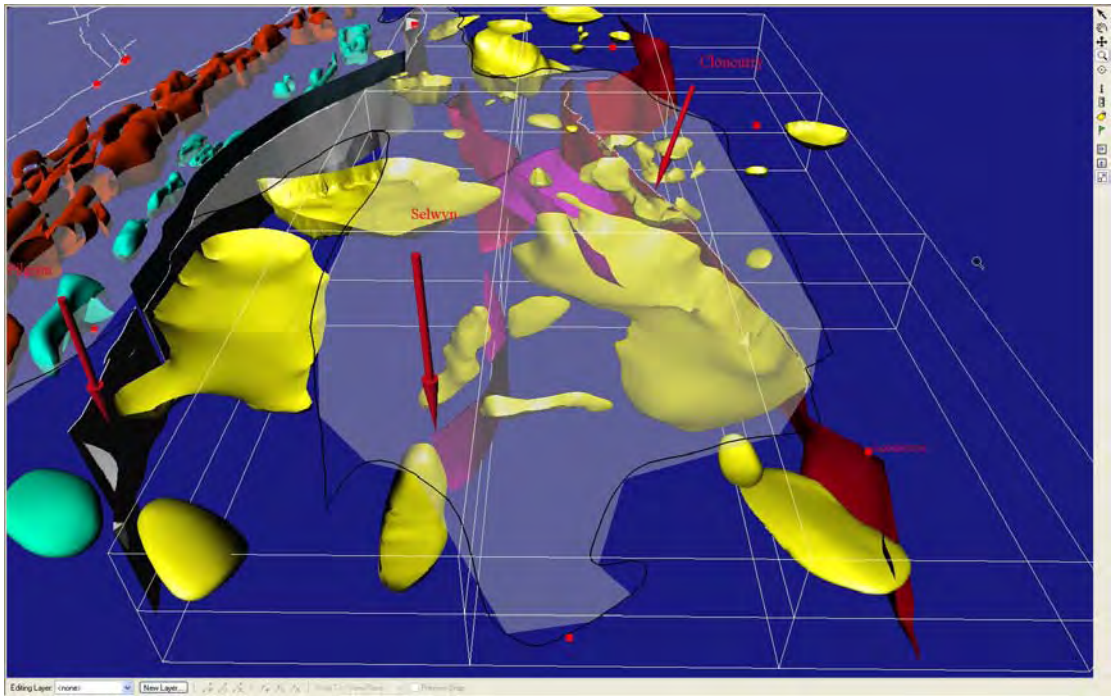

Figure 34: Perspective view from south of granite suites in the EFB Williams Suite = yellow, Wonga Suite = blue, Kalkadoon Suite = red, and major faults (Cloncurry, Selwyn, Pilgrim). Grid to -20 km. (Model under construction)

(THIS IS INCOMPLETE)

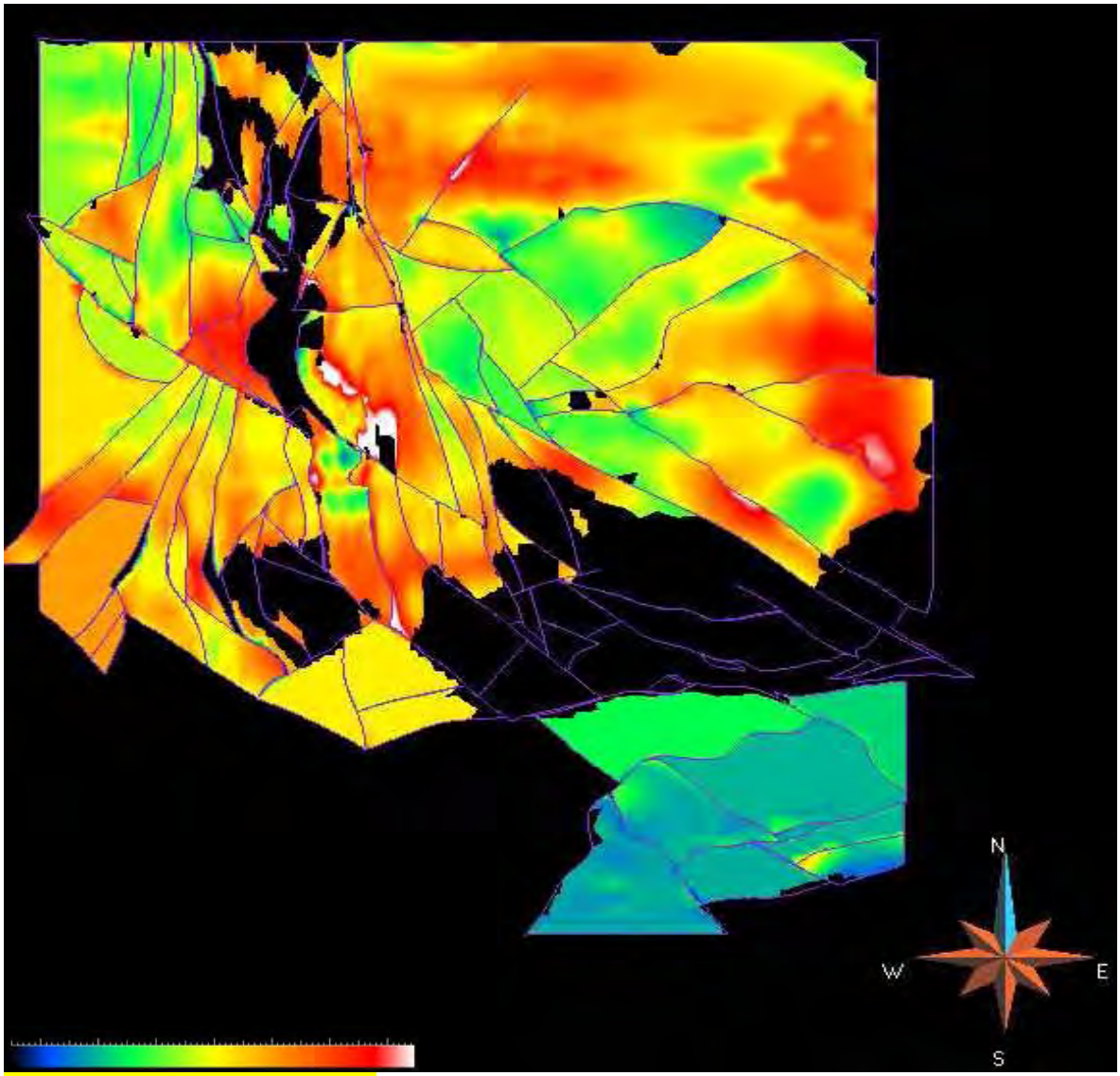

Figure 35: Mc Arthur region - LSB: apparent thickness distribution

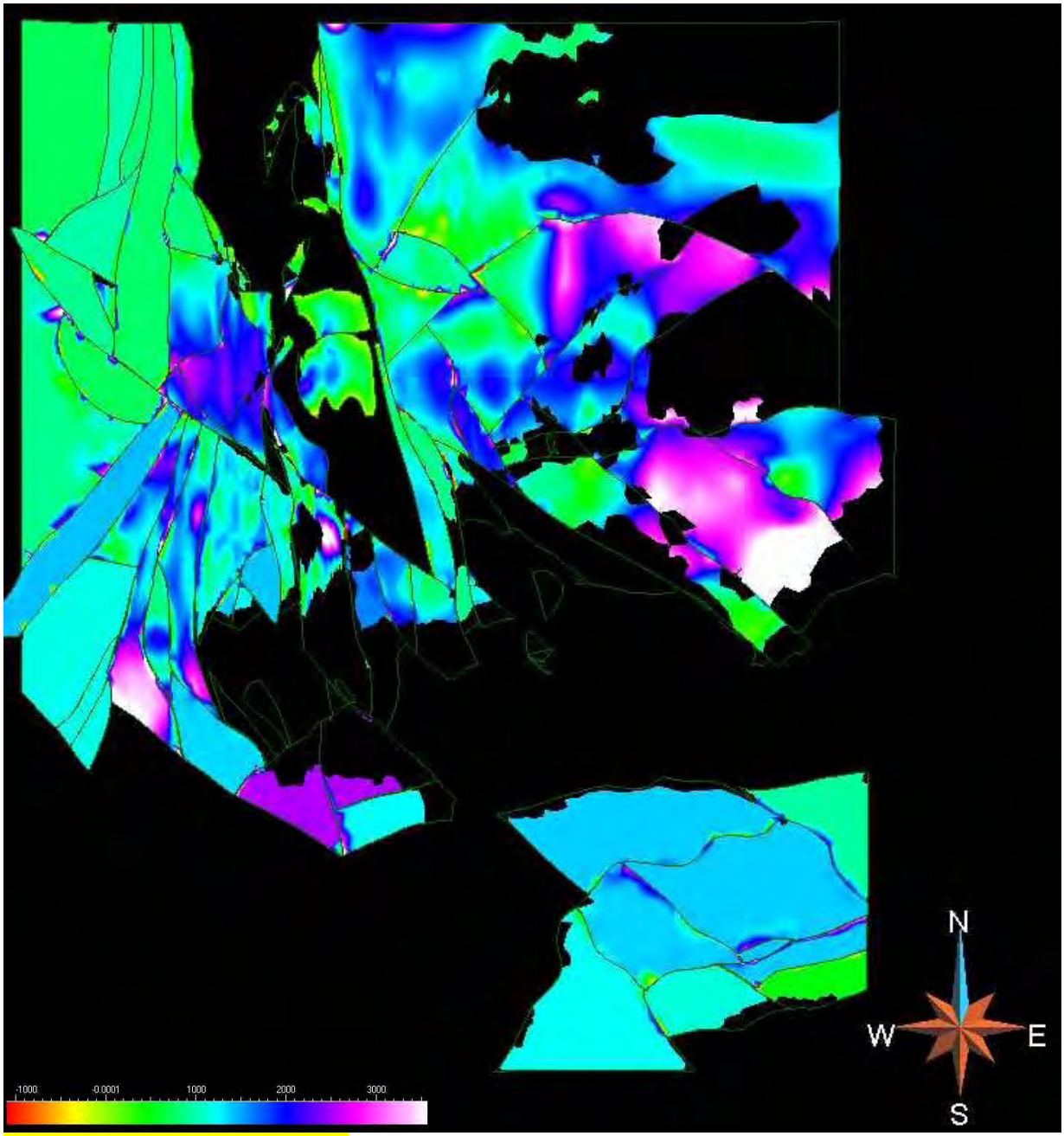

Figure 36: Mc Arthur region – CSB: apparent thickness distribution

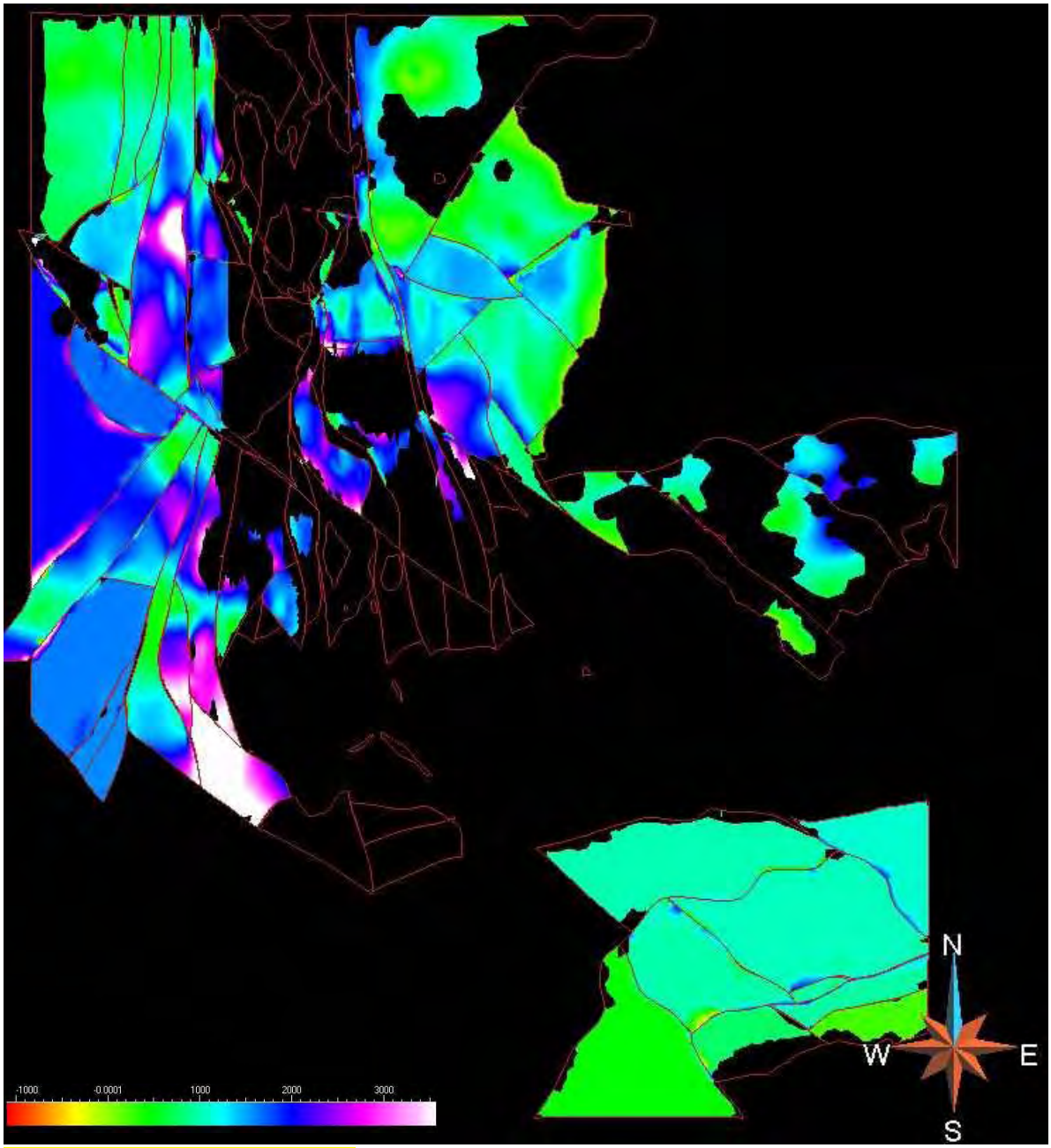

Figure 37: Mc Arthur region – ISB: apparent thickness distribution

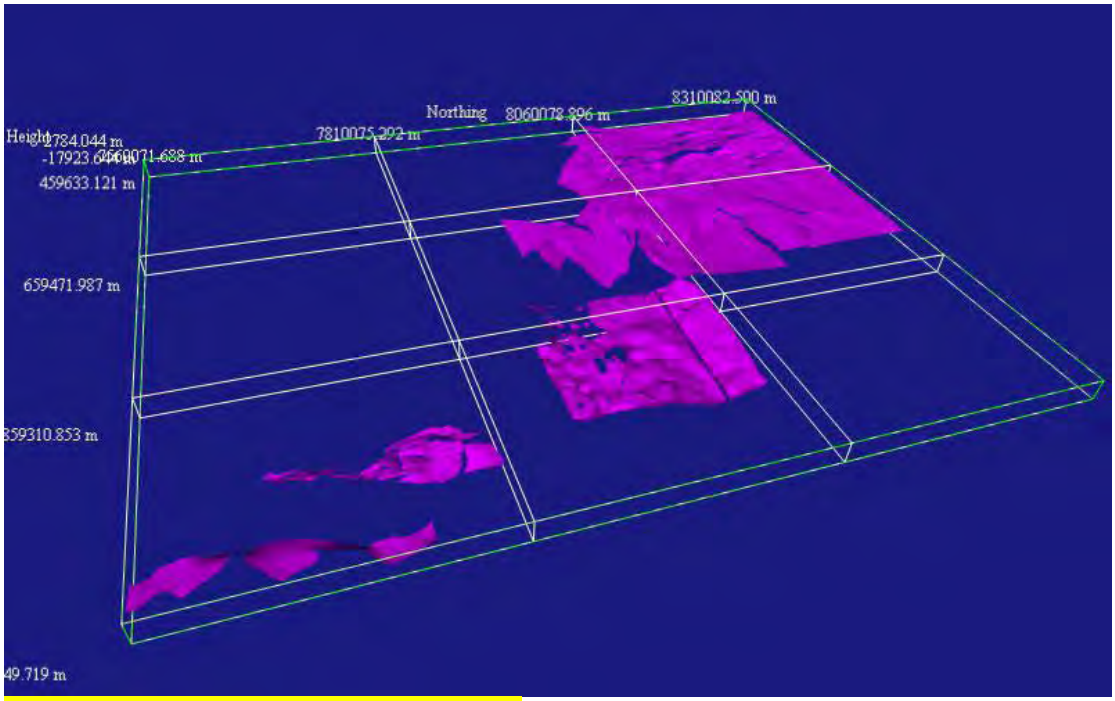

Figure 38: BASE LSB– to be completed

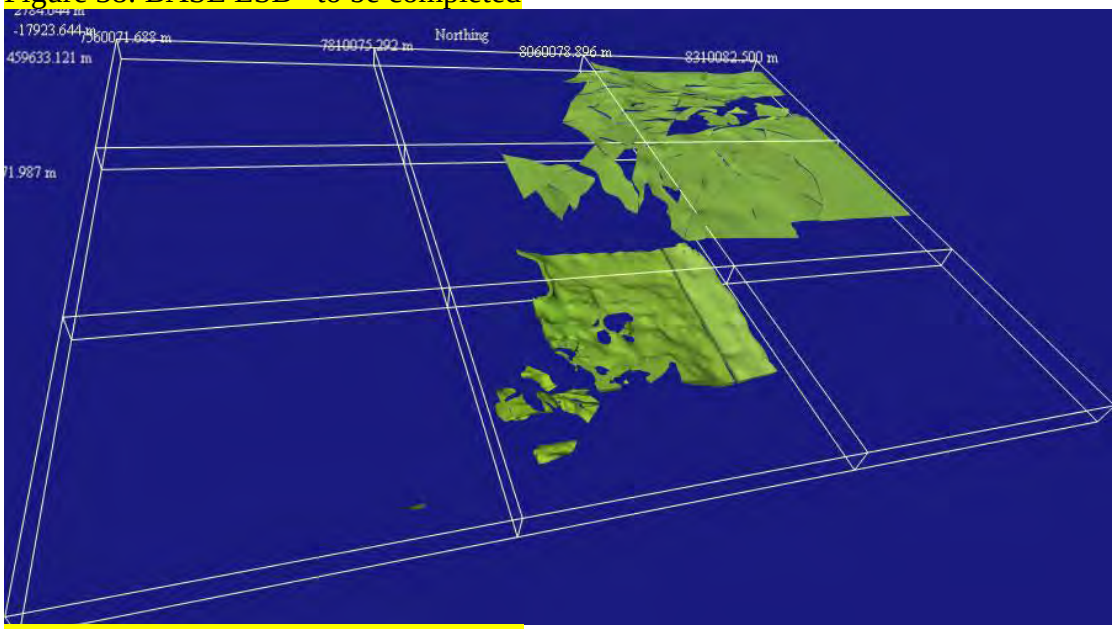

Figure 39: BASE CSB– to be completed

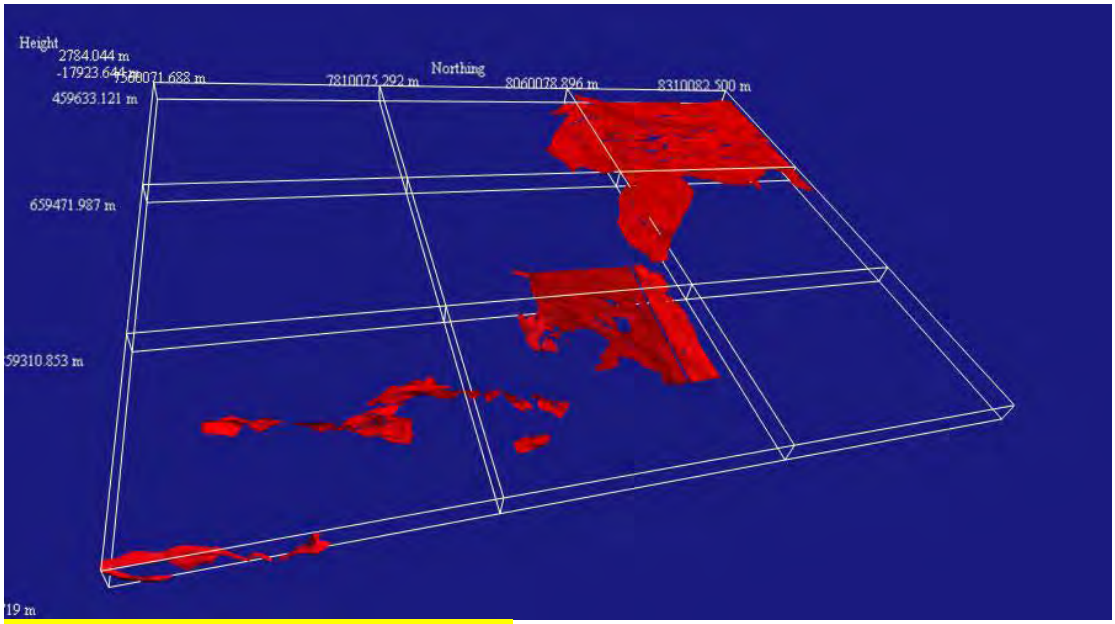

Figure 40: BASE ISB– to be completed

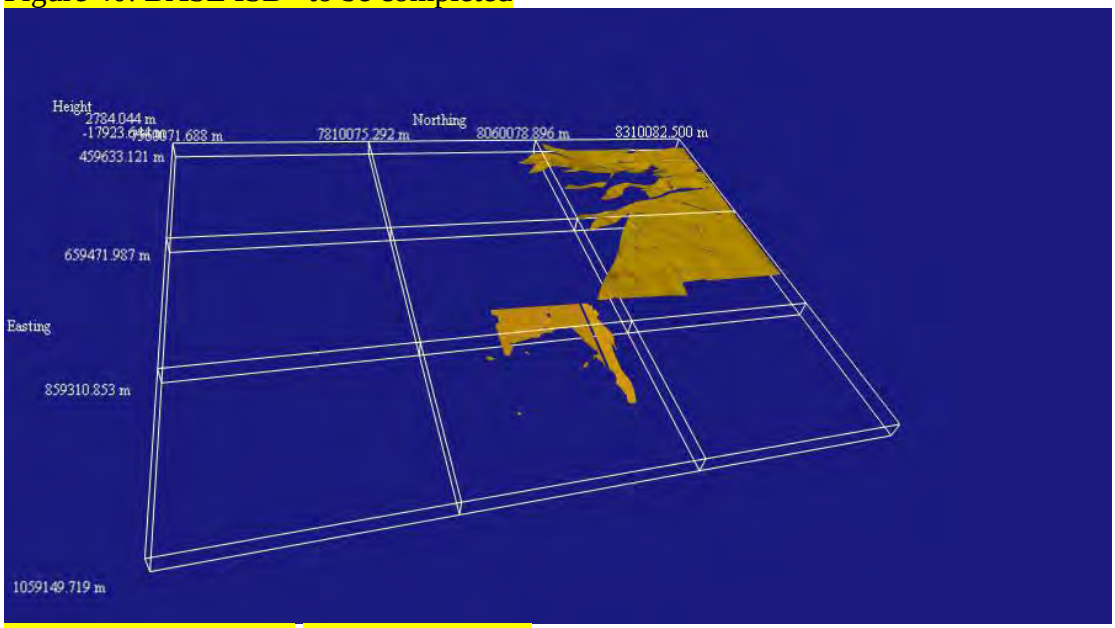

Figure 41: BASE RSB – to be completed

8 Fault and Metal Distributions

The known distribution of metals should provide pointers to future discoveries of similar deposit styles with the region. The approach here focuses on structurally controlled hydrothermal deposits which encompasses a range of deposit types, from sediment-hosted Zn-Pb (SHMS), Cu (Isa-, Mammoth-style) and Cu-Au-Fe massive sulphides (Ernest Henry, IOCG). Rather than "pigeon-holing" deposit types, a broad perspective is taken here of the mineral system and uses metal associations or "commodity groups". This allows for statistical analysis of the entire mineral deposit data set, as to apply a generic classification (to otherwise unclassified occurrences) is too ambiguous. A spatial analysis is applied to the entire deposit data set in relation to proximity to interpreted fault structures. Such empirical information can inform a process model for the hydrothermal systems. A genetic association of major deposits with major faults is well know (e.g. Huston et al. 2006). Examples include the world

class Mt Isa and Hilton-George Fisher deposits along the Mt Isa Fault, Century on the Termite Range Fault, Mammoth on the Mt Gordon Fault, Cannington on the Cloncurry Fault and McArthur River on the Emu Fault. This association is emphasised in an image of interpreted fault length (Figure 9). To quantify this observation, a series of spatial and statistical queries were performed on the data sets to examine the sensitivity of metal content per unit area with proximity to interpreted faults, and the influence of strike length on such distributions. This follows a similar methodology used in the Eastern Goldfields of WA (Bierlein *et al.* 2006) and in the Tasmanides (Murphy 2007). Existing deposit coverage in Queensland and the Northern Territory were combined into a single table ("I7_Ranked Deposits") and, while maintaining the fidelity of the data sources, two high level fields added, termed Commodity Group and Deposit Rank, and are the basis for the analysis here. Appendix 2 shows maps of the major commodity groups, their relative size ranking and lists the highly ranked members.

8. 1 Commodity Groups

There are numerous possible groupings of commodities in the existing data sets. Nine categories of metallic Commodity Groups are defined and their distribution is shown in Figure 42. Note that each Commodity Group spans a range of possible Deposit Models, potential host rocks and deposit ages.

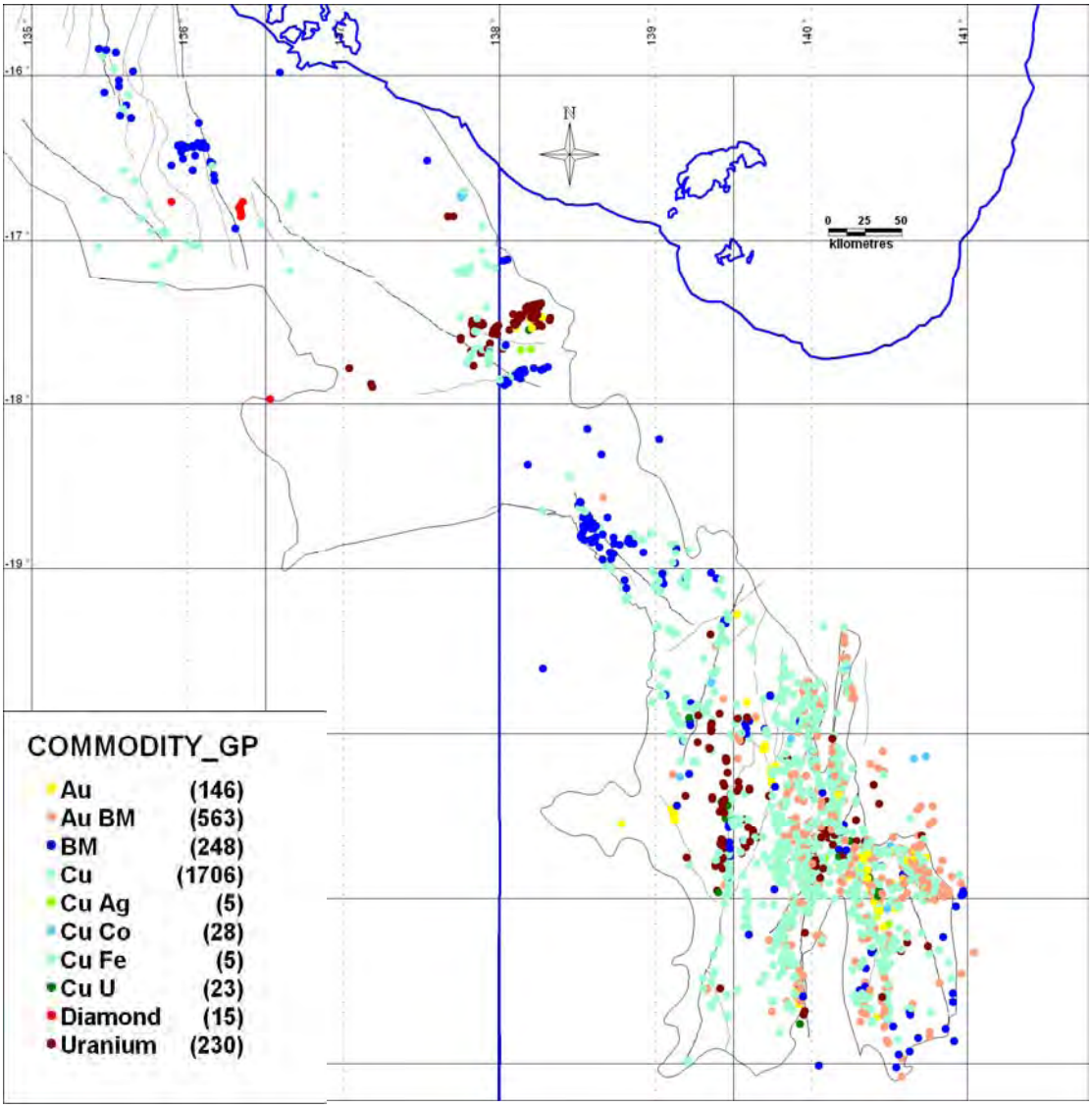

Figure 42: Deposit distributions according to major commodity groups.

8.2 Deposit Size Ranking

Deposit size is recorded as a text field in the individual state data sets. A relative numeric ranking was applied to the data according to Table 2 on a semi-logarithmic scale. Large deposits were, as far as practicable, validated against published sources. Figure 43 shows a map of the I7 deposits (all commodity groups) coded according to deposit ranking.

Size	Qld_ID	NT_ID
1	very small	occurrence only
10	small	small
100	medium	medium
1000	large	large
10000	giant	giant

Table 2: Deposit Rank classification

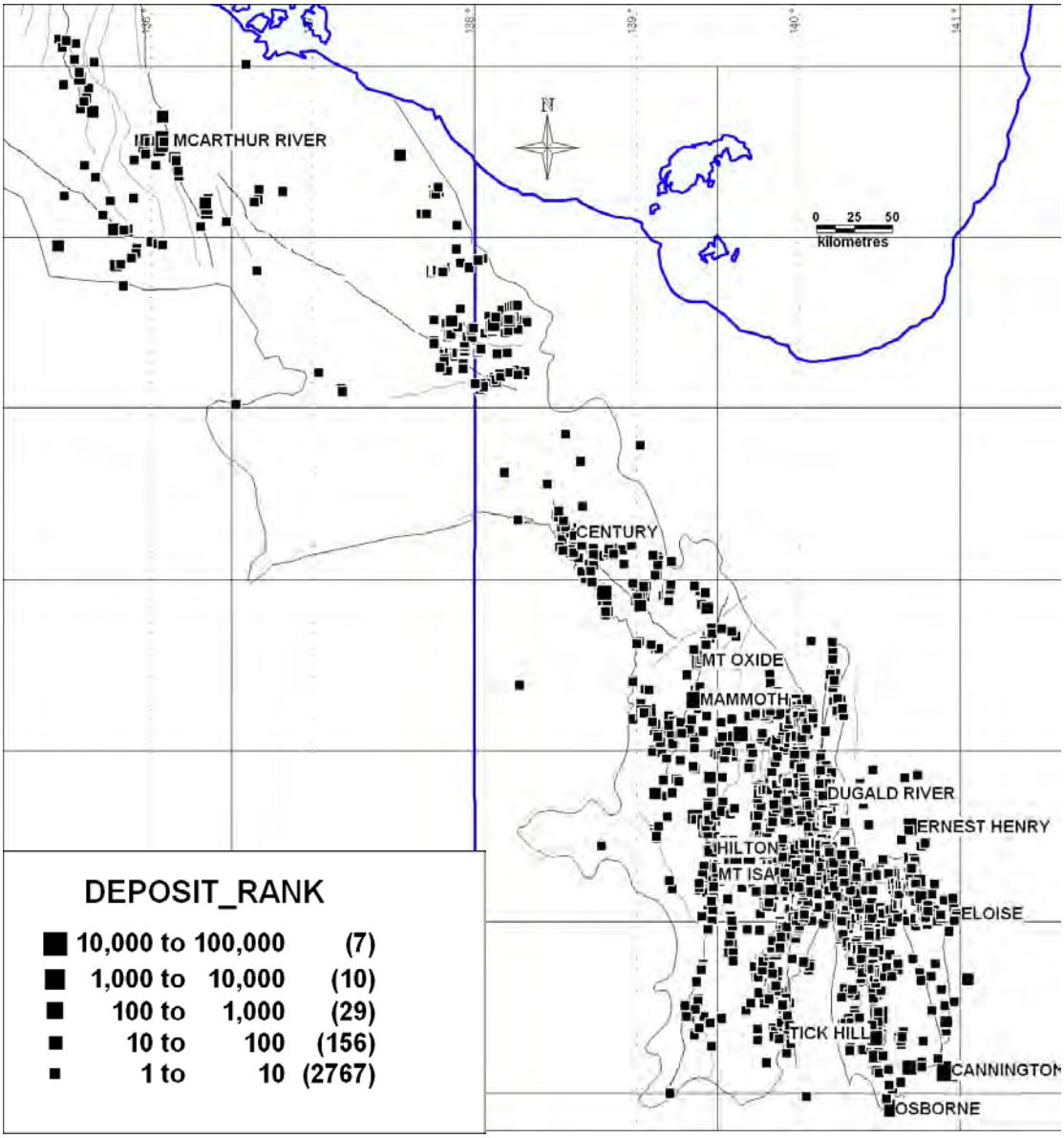

Figure 43: Deposits ranked by size.

8.3 Metal Deposits and Potential Field Gradients

The objective is to integrate the distribution of deposits with the fault architecture derived from potential field interpretation. Appendix 3 shows a series of maps of the major deposits in relation to these data sets, and serves to illustrate specific examples. As in many hydrothermal systems, deposits can be spatially related to faults and zones of cleavage development, and may appear more closely related to smaller scale faults that are peripheral to, but not necessarily directly linked to, the major faults. The inference for the mineralisation process model is that large scale faults provide pathways for deeper sourced mineralising fluids that subsequently migrate along and away from the major conduits to form deposits peripheral to the major fault (e.g. Cox and Ruming 2004). This can be tested using strike length as a proxy for depth extensive faults that can tap mineralising fluids. The distributions of the major commodity groups have been examined in relation to the gravity and aeromagnetic vector lines (Figures 13 and 14). A measure of metal endowment, here termed "Metal Rank", is calculated. This is based on the cumulative deposit size per unit

area (km^2), an approach that involves creating incremental buffer regions that enclose the interpreted fault lines. Two types of query were made. In the simplest case, the buffer is a set distance from the line and this distance is increased so as to enclose the entire region of analysis (see Figure 44a). As buffer width is independent of line length, each fault has a similar aerial influence. The incremental change in cumulative deposit size per buffer area is then factored to derive a Metal Rank value.

In the second buffer method, buffers of variable width are created as a function of the length of the line (Figure 44b). Longer features have a greater aerial significance in this analysis. This seems a reasonable approach, geologically, as large dimension faults typically have wider damage zones than small displacement structures. Note, different sized star symbols in Figure 44 represent deposits that can be associated with different fault buffers depending on which type of buffer is applied (fixed or variable). An example from the LHP is shown below (Figure 45). Results from applying this analysis to the Isa-McArthur data sets are documented in Appendix 4. Key points from this are outlined below, for both gravity and aeromagnetics, and across the range of commodity groups.

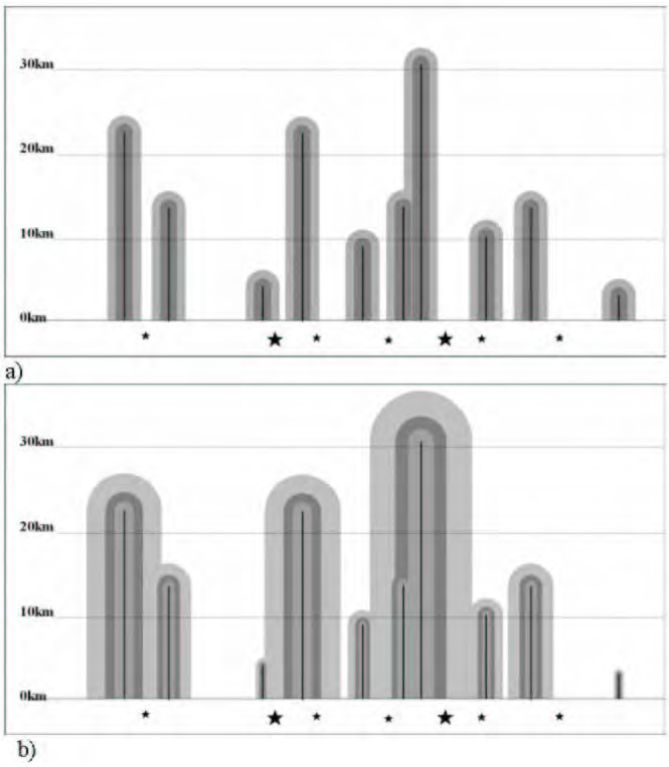

Figure 44: Schematic representation of fault lines (black) of different lengths (up to 30km on y axis) with buffer regions (in grey shades) for (a) fixed width (1km, 2km etc) and (b) length-weighted variable width (grey). Fault lines are identical in each plot. Stars symbols on x axis represent deposits of varying size, identically placed in each plot (from Bierlein *et al*. 2006)

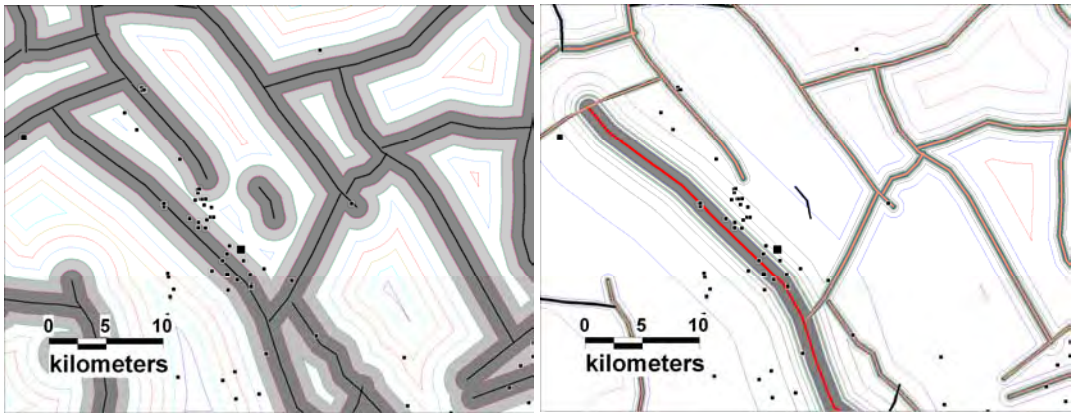

a) b)

Figure 45: Example of buffers and deposits (dots) for a) fixed and b) variable width buffers in relation to gravity gradient lines. In a) faults are black lines, in b) faults are coloured by strike length.

Figure 46 shows plots of Metal Rank against distance (km) for both the fixed and variable width buffer analysis of the gravity gradients. Each commodity group has a coloured line and one line to represent the combined groups. The BM group makes up most of the Metal Rank in the data set, these being the "giants" of the region. However, this masks the details of the other commodity groups so, for completeness, the distribution of each group is detailed in Appendix 4. In relation to the fixed width buffers, there is a systematic increase in Metal Rank from low endowment at distances of over 5 km from gravity gradients to greater endowment in buffer regions closer to gravity gradients (Figure 46a). The fall off on the distribution close to the origin is interpreted as a function of the sampling routine. We can infer from this that, in general, proximity to gravity gradients has a significant influence on metal distributions. For the strike length weighted buffers (Figure 46b), note that the size of the buffer is a function of the length of the associated line, so the buffer distance is a range, rather than a unique value, and the maximum value (based on the longest line) is plotted on the x axis. A similar pattern, though with significantly higher Metal Rank values, is seen. This suggests the variable width buffers are more efficient in capturing the distribution of metals. An important and critical difference in the two buffer routines is highlighted in the buffer size distribution (Figure 46c). For example, taking a 7 km maximum width in each of the buffer routines results in capturing almost all metals in the region (compare Figures 46a and b). However, the associated search areas (Figure 46c) differ by an order of magnitude (variable = 82,000 km^2 vs fixed = 312,000 km^2). Although a somewhat crude area selection tool, it is evident from this that using the strike length of gravity gradients as a filter in regional scale ground selection significantly reduces the search area (and cost), and increases the chance of discovery.

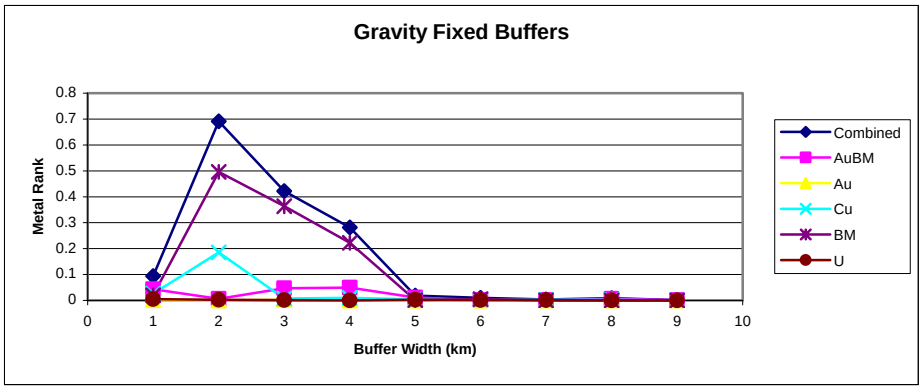

a)

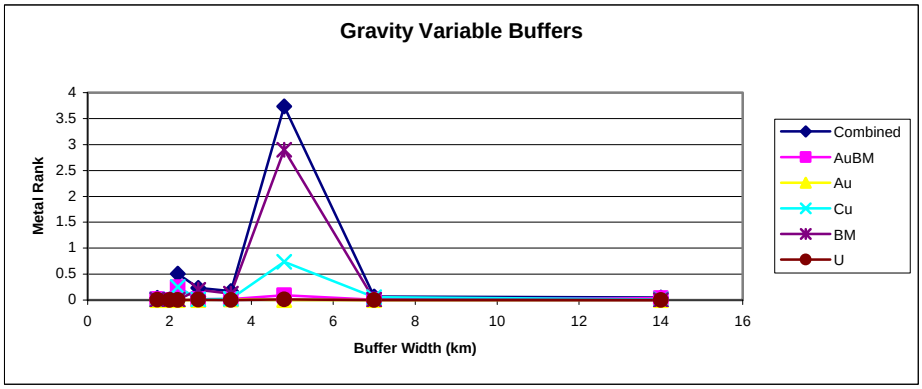

b)

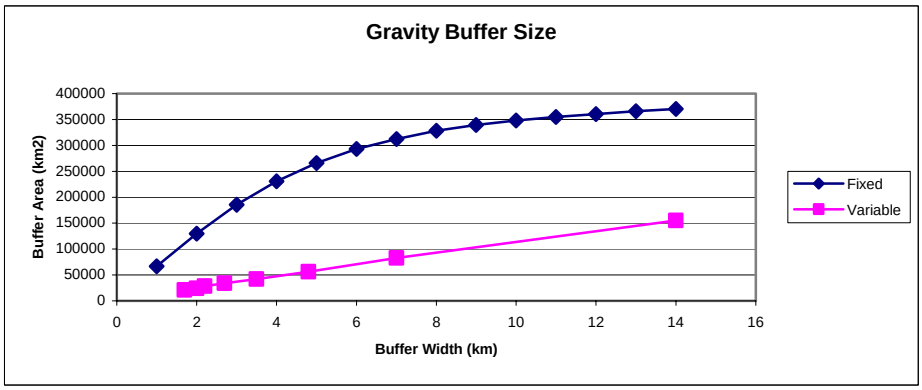

c)

Figure 46: Plots of metal rank per unit area with increasing distance from gravity gradients using a) fixed width and b) variable buffers, and c) buffer width vs buffer area for the fixed and variable results.

The magnetic data show broadly similar results (Figure 47a and b), with a general increase in Metal Rank with proximity to gradients, and dominated by the base metal category. Copper distribution is strongly linked to faults, and especially with the larger strike length features. As an area selection criterion, the variable buffers involve smaller areas in which to capture a similar metal rank for a comparable fixed width buffer (Figure 47c), however, the distinction between the two methods is less emphasised than in the gravity. For example, a 2 km fixed width buffer (Figure 46a) captures most of the metals for an area of 200,000 km^2 while, in the variable width buffers, a 10 km maximum buffer width captures most of the metals (Figure 47b) rank for a similar area (Figure 47c). This may indicate that metals are more proximal to magnetic gradients, and are less strongly influenced by individual strike lengths.

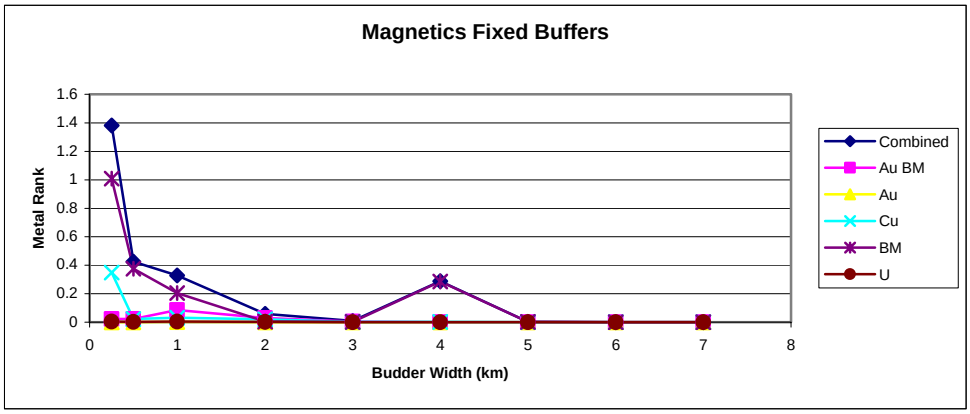

a)

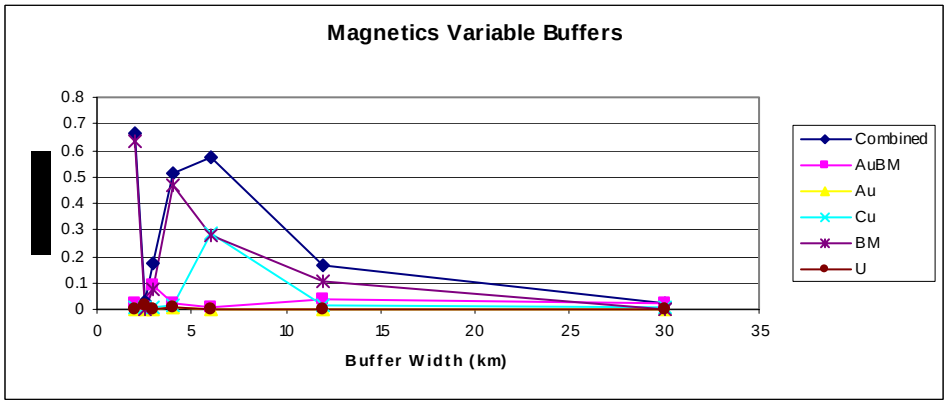

b)

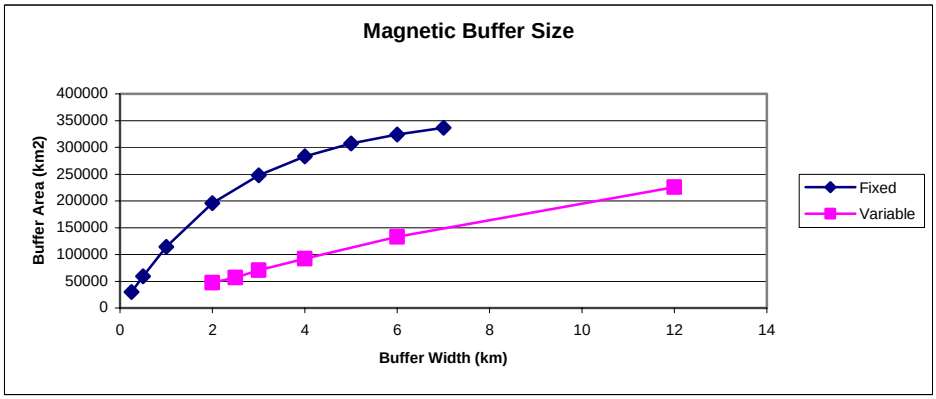

c)

Figure 47: Plots of metal rank per unit area with increasing distance from magnetic gradients using a) fixed width and b) variable buffers, and c) buffer width vs buffer area for the fixed and variable results.

The results, however, are inherently different because of the nature of the source data. The distributions of faults vary significantly in sample density, from mapped (Figure 8), gravity- (Figures 18) and magnetic-related (Figure 19) features. There is a higher density of shorter strike length magnetic gradients compared to the gravity, and a greater proportion of short mapped faults (at 1:100 000 scale). This is examined in Figure 48 as a plot of strike length distributions for the different data sources. This reveals some key features related to the scale of sampling. While the gravity and magnetic data follow similar distributions, the mapped faults depart significantly from this pattern. The fault curve has a "tail" towards the origin, reflecting a larger number of relatively short faults. Such small scale features are under-sampled in the magnetic and gravity data, hence the rapid drop off in their distributions. At the other end of the size spectrum, the mapped faults appear to

under-sample the longer strike length features, as seen in the potential field data. A likely limitation here is the scale of the outcropping geology compared to the entire region. (Check against other fault pop plots in literature – Walsh et al ?.) Another possible reason for the departure of the potential field populations from the mapped geology is these may be a mixed population that include non-fault or mis-identified features, inherent in the ambiguity of potential field interpretation.

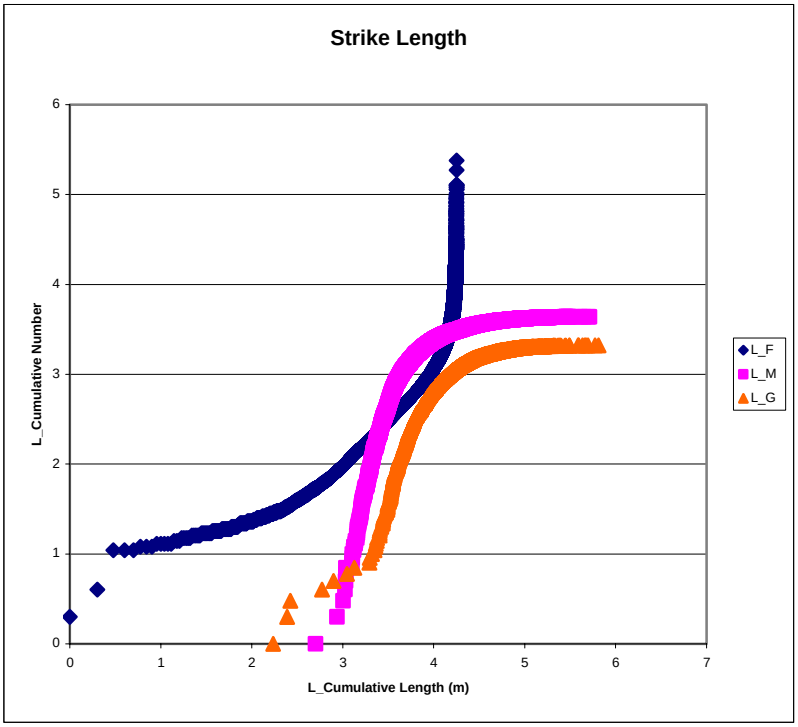

Figure 48: Log-log plot of length vs cumulative number for mapped faults ((L_F), gravity (L_G) and magnetic (L_M) fault-related features.

9 Conclusions

Through an interpretation of existing geological and geophysical data sets, and building from related pmd*CRC projects, a 3D map has been developed of the major lithostratigraphic elements that comprise the 4 Superbasins and their substrates in the Mt Isa and southern McArthur River regions. The regional scale of this undertaking provides a unique depiction of the architecture to ~20 km depth over a ~200,000 km^2 area. It seeks to determine the fundamental crustal scale features that controlled the development of the superposed rift basins at various times in the evolution.

Basement is inferred at relatively shallow levels throughout much of the region. The topology of the basement has influenced the nature of structures and stratigraphy in overlying sequences. For example, the Barramundi Worm appears to mark the edge of a relatively upstanding basement block (beneath the Georgina basin) in the west during LSB and CSB sedimentation, and is onlapped by ISB to the west of Mt Isa. Even the outcrop pattern of the Cambrian Georgina Basin is in some way controlled by shallow level basement in this region. However, the situation is complicated as the inferred fault boundaries between basement blocks can be buried beneath the later Superbasins as, for example, the western boundary of the KLB. Similarly, the Murphy Tectonic Ridge exerted a strong influence on the sedimentary

record along its southern flanks, especially during the ISB, where varying uplift and subsidence events suggest E-W fault control in this region. The major faults in the northern parts of the LHP parallel the Murphy Ridge and are interpreted as dominantly north dipping, such as the Elizabeth Creek, Mt Oscar and Ploughed Mountain Faults.

The widespread distribution of the Superbasin elements has been modelled as a pseudo-layer cake geometry contained in a shallow enveloping surface and cut by relatively steeply inclined faults. Thickness variations from a variety of sources have been incorporated in the serial section interpretations. Although this simple geometry is locally invalid, the scale of the analysis challenges the ability to show small scale variations and such information is lacking in under cover regions. The complex structure of the Eastern Succession is also contained by a shallow dipping enveloping surface with a major control being deep seated faults and shears controlling the outcrop pattern, rather than requiring large (10's km) horizontal nappe translations.

Fault control was exerted at an early stage, related to the development of the KLB ridge and magmatic arc, the western and eastern boundaries of which are associated with strong gravity gradients. This ridge was maintained as a topographic feature during rift sedimentation in the LSB until being blanketed by younger Superbasins. The LRFT faults were re-activated at various times in the 400 Ma history, during CSB and ISB sedimentation. Extension, magmatic inflation, doming and footwall uptilts created local topographic features that influenced sediment thickness and facies development. Asymmetries in the locus of magmatic and sediment basin infill, between the LHP and LRFT, during LSB, CSB and ISB events attest to the existence of a crustal scale boundary in the Western Fold Belt, termed the Barramundi Worm. This is interpreted as a major east dipping detachment, immediately to the west of the younger (later) Mt Isa Fault, and is expressed in the LHP as the Riversleigh Lineament (immediately SW of the Termite Range Fault). Other fundamental faults represented in the model are:

- The Quilalar Fault is modelled as the eastern boundary between the KLB and the LRFT, and is interpreted as a west dipping growth fault during the LSB.
- The KL worm (Blenkinsop *et al*. 2005) marks the eastern side of the KLB, and is interpreted as an east dipping feature.
- The Pilgrim Fault …
- The Cloncurry Fault is interpreted as a major basin bounding, east dipping structure that influenced the accumulation of the turbiditic Soldiers Cap Group, and was subsequently inverted during the Isan Orogeny.
- The "EROMANGA"
-

An analysis of where metals are currently distributed with respect to faults in the region reinforces well known empirical observations, that large dimension faults are often proximal to the world class deposits. A quantitative assessment of fault strike length data, for mapped and interpreted potential field data, shows a strong control on deposit location. Although a somewhat crude area selection tool, it is evident from this that using the strike length, as a filter in regional scale ground selection significantly reduces the search area (and cost), and increases the chance of discovery.

10 Acknowledgements

Thanks to S. Harrison (Geomix) for input to geological cross sections in McArthur region, L. Hutton (GSQ) and B. Perkins (GSQ) for input to geological cross sections in Mt Isa region, T. Denaro (GSQ) for access to mineral deposit data sets and P. Milligan (Geoscience Australia) for supplying an Australia-wide worm data set.

11 References

Abbott, S. T. and Sweet, I. P. 2000. Tectonic control on third-order sequences in a siliciclastics ramp-style basin: an example from the Roper Superbasin (Mesoproterozoic), northern Australia. Australian Journal of Earth Sciences, 47, 637-657.

Archibald, N. J., Gow, P. and Boschetti, F. 1999. Multiscale edge analysis of potential field data. Exploration Geophysics, 30, 38-44.

Betts *et al.* 1999

Betts *et al* 2004

Bierlein, F. P., Murphy, F. C., Weinberg R. F. and Lees, T. 2006. Distribution of Orogenic Gold Deposits in Relation to Fault Zones and Gravity Gradients: Targeting Tools Applied to the Eastern Goldfields, Yilgarn Craton, Western Australia. Mineralium Deposita, 41, 107-126.

Broadbent *et al.* 1998

Cox, S. F. and Ruming, K. 2004. The St Ives mesothermal gold system, Western Australia – a case of golden aftershocks? Journal of Structural Geology 26, 1109-1125.

Drummond *et al.* xxxx

Gibson *et al.* 2005

Giles, D., Ailleres, L., Jeffries, D., Betts, P. and Lister, G. 2006a. Crustal architecture of basin inversion during the Proterozoic Isan Orogeny, Eastern Mt Isa inlier, Australia. Precambrian Research, 184, 67-84.

Giles, D, Betts, P. G., Ailleres, L., Hulschier, B., Hough, M. and Lister, G. S. 2006b. Evolution of the Isan Orogeny at the southeastern margin of the Mt Isa inlier. Australian Journal of Earth Sciences, 53, 91-108.

Holden, D. J., Archibald, N. J., Boschetti, F. and Jessell, M. W. 2000. Inferring geological structures using multiscale edge analysis and forward models. Exploration Geophysics, 31, 617-621.

Huston, D. L., Stevens, B., Southgate, P. N., Muhling, P. and Wyborn, L. 2006. Australian Zn-Pb-Ag ore-forming systems: a review and analysis. Economic Geology
101, 1117-1152.

House, 2002

Hornby, P., Boschetti, F. and Horowitz, F. 1999. Analysis of potential field data in the wavelet domain. Geophys. J. Internat. 137, 175-196.

Jackson, M. J., Sweet, I. P., Page, R. W. and Bradshaw, B. E. 1999. The South Nicholson and Roper Groups: evidence for the early Mesoproterozoic Roper Superbasin. In: Bradshaw, B. E. and Scott, D. L. (eds). Integrated Basin Analysis of the Isa Superbasin using Seismic, Well Log and Geopotential data: an evaluation of the economic potential of the Northern Lawn Hill Platform (unpaginated). Australian Geological Survey Organisation Record 1999/19.

Korsch, R. K., Rawlings, D. J., Goleby, B. R., Gibson, G. M. and Johnstone, D. W. 2004. Deep seismic profiling in the southern McArthur basin: Implications for mineralisation. (abs). Centre for Global Metallogeny, University of Western Australia Publication 33, 289-291.

Krassay, A. A., Bradshaw, B. E., Domagala, J., and Jaclson, M. J. 2000a. Siliciclastic shoreline to growth-faulted, turbiditic sub-basins: the Proterozoic River Supersequence of the upper McNamara Group on the Lawn Hill Platform, northern Australia. Australian Journal of Earth Sciences, 47, 533-562.

Krassay, A. A., Domagala, J., Bradshaw, B. E. and Southgate, P. N. 2000b. Lowstand ramps, fans and deep-water Palaeoproterozoic and Mesoproterozoic facies of the Lawn Hill Platform: the Term, Lawn, Wide and Doom Supersequences of the Isa Superbasin, northern Australia. Australian Journal of Earth Sciences, 47, 563-597.

MacCready, T. 2006. Structural cross-section based on the Mt Isa Deep Seismic Transect. Australian Journal of Earth Sciences, 53, 5-26.

McConachie, B. A. and Dunster, J. N. 1998. Regional stratigraphic correlations and stratiform sediment-hosted base-metal mineralisation in the northern Mt Isa Basin. Australian Journal of Earth Sciences, 45, 83-88.

Murphy, F. C. 2002. Structural framework and target generation in the Proterozoic Mt Isa region, Queensland, through analysis of potential field multiscale wavelets ("worms"). pmd*CRC report to MIM, available on Twiki web site).

Murphy, F. C. 2007. Structural architecture, potential field gradients and meta distributions in the Tasmanides of Victoria and New South Wales. Pmd*CRC Final Report, Project T5.

Murphy *et al.* 2002 T3 Tasmania

Murphy, F. C. and Russell-Head, D., 2006. Characterisation of Potential Field Gradients using post-processed Multiscale wavelet edges. Abstract in Australian Earth Science Convention, Melbourne, p149.

Murphy *et al.* 2006 Victoria

Murphy *et al.* 2007 G14 report

Scott *et al*. 1998

Discrete element modelling applied to mineral prospectivity analysis in the Western Succession of the Mount Isa Inlier

John G. McLellan

Predictive Mineral Discovery Co-operative Research Centre, Economic Geology Research Unit, James Cook University, Townsville, Queensland, 4811

* Corresponding author. Tel: +61-7-6774; fax: +61-7-4725-1501. E-mail address: John.McLellan@jcu.edu.au

Abstract

Numerical modelling using a discrete element technique is employed here to examine the response of a fracture system in the Western Succession of the Mount Isa Inlier to an applied stress regime. Models were tested in two different areas at similar regional scales, to include both the southern and northern regions of the Leichhardt River Fault Trough. Numerous parameters were tested, in particular the orientation of an applied stress regime (σ_1) to examine model response and correlate favourable anomalous areas of stress and strain partitioning with known Cu deposits and prospects. Modelled areas of combined low minimum principal stress (σ_3), low fluid pressure required for failure (P_fF), high volumetric increase or dilation (ψ), and shear and tensile failure show the best correlation with deposits, but these areas do not clearly correspond to specific fault orientations or configurations. Rather, the models produce complex zoning of stress anomalies in response to the partitioning of stress across complex fault blocks, and the interaction between more competent igneous bodies, less competent meta-sedimentary rocks, and the fault and rock boundary complexities. A far field ESE stress orientation provides the best visual results and correlation with known mineralisation in the region, and therefore inferred as the most likely orientation of σ_1 during genesis of many of the deposits. This corresponds well with recent work carried out in the Eastern Succession of the Mount Isa Inlier, and suggests an inlier-wide stress regime may have been responsible for both Cu and Cu-Au mineralisation in the region.

Keywords: Numerical modelling, discrete elements, stress, fluid flow, Cu-Au prospectivity, Mount Isa

1. Introduction

The Proterozoic Mount Isa Inlier (Fig. 1) hosts a variety of economic deposits, some world class, such as Mount Isa Cu, Mount Isa Pb-Zn-Ag, Cannington Ag-Pb-Zn, Century Zn-Pb and Ernest Henry Cu-Au. The Western Succession is particularly well endowed in Pb-Zn-Ag, Cu, and U deposits and prospects, however, there has been no clear relationship highlighted between the Cu mineralisation in the east and west of the inlier. There has been a plethora of previous studies carried out on the genetic, structural and fluid inclusion analysis of the Fe-oxide Cu-Au deposits of the Eastern Succession (e.g. Laing, 1993; 1998; Oliver, 1995; Davidson & Davis, 2001; Pollard, 2006; Pollard *et* al., 1998; Williams, 1998; Mark *et al*., 2001, 2006; Wang & Williams, 2001; Oliver *et al*., 2004; Kendrick *et al*, 2007; Marshall & Oliver, in press). However, historically there has been less emphasis placed on similar studies relating to Cu mineralisation in the Western Succession, with the main emphasis being placed on the Mount Isa Cu deposit (e.g. Matthäi, et al. 2004; Kendrick *et al*., 2006; and others). Structural analysis by several previous authors (e.g. Scott and Taylor 1982; Bell et al. 1988; Nijman et al. 1992; Laing 1998) of the Western Succession has revealed major N-S to NE-SW striking structures that were most likely formed or reactivated during a major compressive phase (D_2) of the Isan Orogeny ca. 1595 Ma. These N-S trending structures include the Mount Gordon Fault Zone, the Western Border Fault and the Mount Isa Fault, all of which are steeply dipping (Van Dijk 1991; Drummond et al. 1998) and in conjunction with smaller scale structures, have a spatial relationship to Cu mineralisation in the area.

There is an obvious structural control on Cu mineralisation, and less so a geochemical, fluid/rock interaction or lithological control, as many of the deposits are hosted in brecciated sediments of varying compositions (Scott and Taylor 1982; Blake et al. 1990; Van Dijk 1991) with a close spatial association to steeply dipping faults. There is a general consensus that the Cu mineralisation in the western Mount Isa inlier appears to have been late in the Isan Orogeny, and most likely during reactivation of the major faults during a D_4 deformation event ca. 1530 Ma (Rubenach *et al*., in press). Therefore, the fault architecture and to some extent the lithological contrasts, may have been the most important factors in localising fluids responsible for much of the Cu mineralisation in the Western Succession.

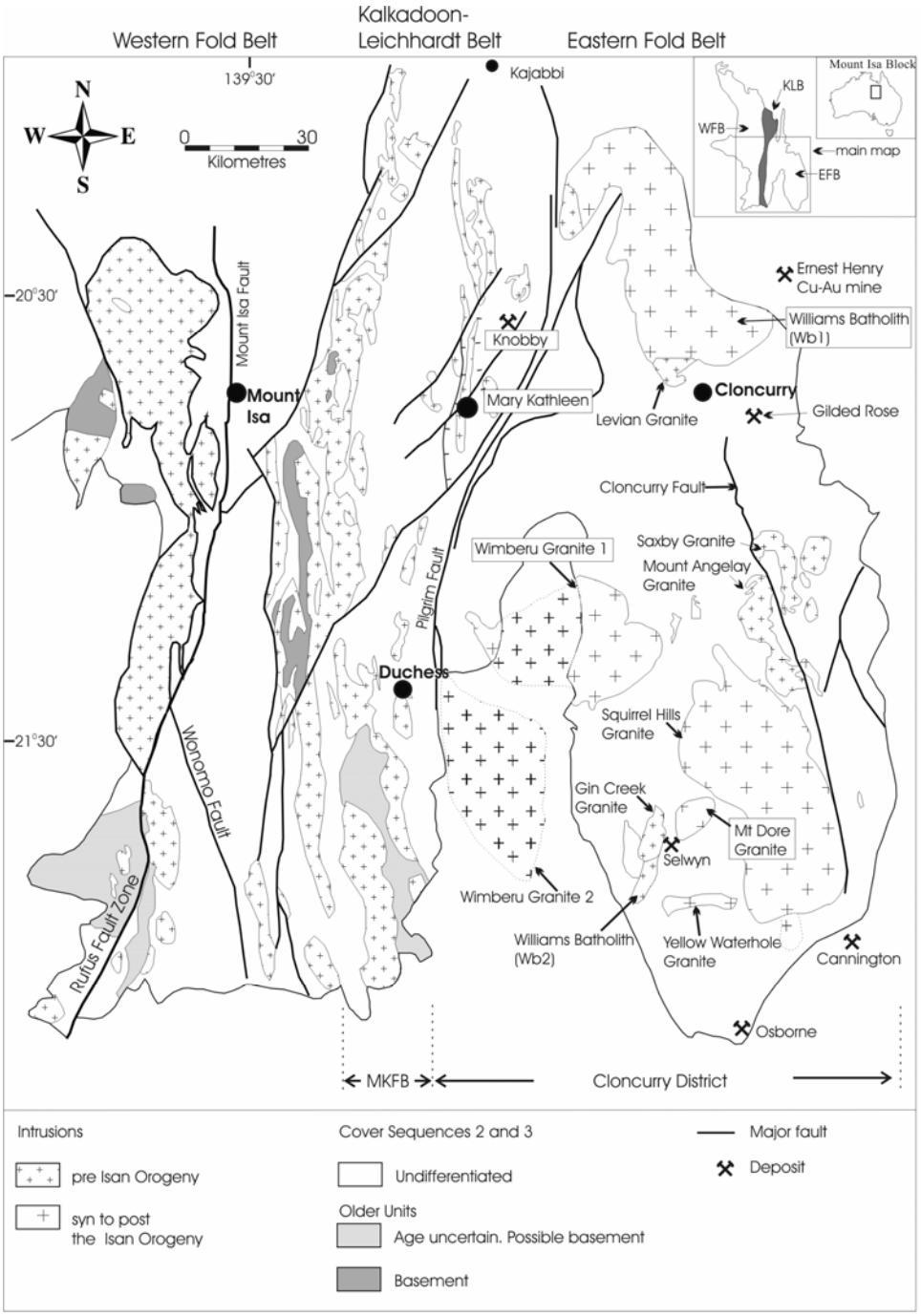

Fig. 1. Location (inset) and general geology of the Western, Kalkadoon-Leichhardt and Eastern Fold Belts showing the further division of the Eastern Fold Belt into the Mary Kathleen Fold Belt (MKFB) and Cloncurry District after McLellan & Oliver (2008). The spatial distribution of Cover Sequences 1-3 and intrusive features pre- and syn- to post-Isan Orogeny are shown, as well as some of the major mineral deposits in the Eastern Succession (redrawn from Foster, 2003, adapted from original geology by Blake, 1987 and interpreted geology from NWQMPR, 2000).

Coupled numerical models have been proven to be extremely useful in understanding the key processes involved in different mineralising systems (e.g. Ord & Oliver, 1997; Oliver *et al*., 2001; McLellan *et al*., 2004; Schaubs *et al*., 2006), however, there has been little published work on the Western Succession deposits (e.g. Matthäi, et al. 2004). The numerical modelling in this study focuses attention on the structural scenarios pertinent to the latter part of the Isan Orogeny in which fluid flow and mineralisation were hosted mostly in D_3 or later structures (e.g. Laing, 1998). The structural architecture and deformational history is reasonably well known, providing a good basis for application of discrete element techniques incorporating the interaction of fault movement (slip) and stress partitioning, as used in this study.

The ability to numerically simulate and 'map' the effects of deformation can provide important data in understanding the spatial and temporal consequences of such processes. This technique has been used in determining the magnitude and distribution of stress in many mineralised faulted terranes and at many different scales (e.g. Oliver *et al*., 1990, 2001; Holyland *et al*., 1993; Holyland & Ojala, 1997; Jiang *et al*, 1997; Mair *et al*., 2000; McLellan *et al*., 2007; McLellan & Oliver, in press). Recent work by McLellan & Oliver (in press) has indicated that fault architecture, competency contrasts and a broad scale stress regime of WNW-ESE are the main larger-scale structural components responsible for Cu-Au localisation in the Eastern Succession of the Mount Isa Inlier during a D_4 ca. 1530 Ma deformation event. The main aims of this study is to apply the discrete element modelling technique in the Western Succession of the Mount Isa Inlier in two different areas to identify key architectural, structural and stress controls on the localisation of Cu, and to compare this to recent work by McLellan & Oliver (in press) in the Eastern Succession, in an attempt to gain a holistic view of broad scale Cu mineralisation in the Mount Isa Inlier. The two areas under consideration will be a) a model that encompasses most of the southern extent of the Western Succession (Fig. 2) and b) a model that encompasses the northern area of the Western Succession, or Leichhardt River Fault Trough (NLRFT) (Fig. 2), much of which is under sedimentary cover, with the main objective here to apply this technique to areas undercover to better enhance our predictive capacity.

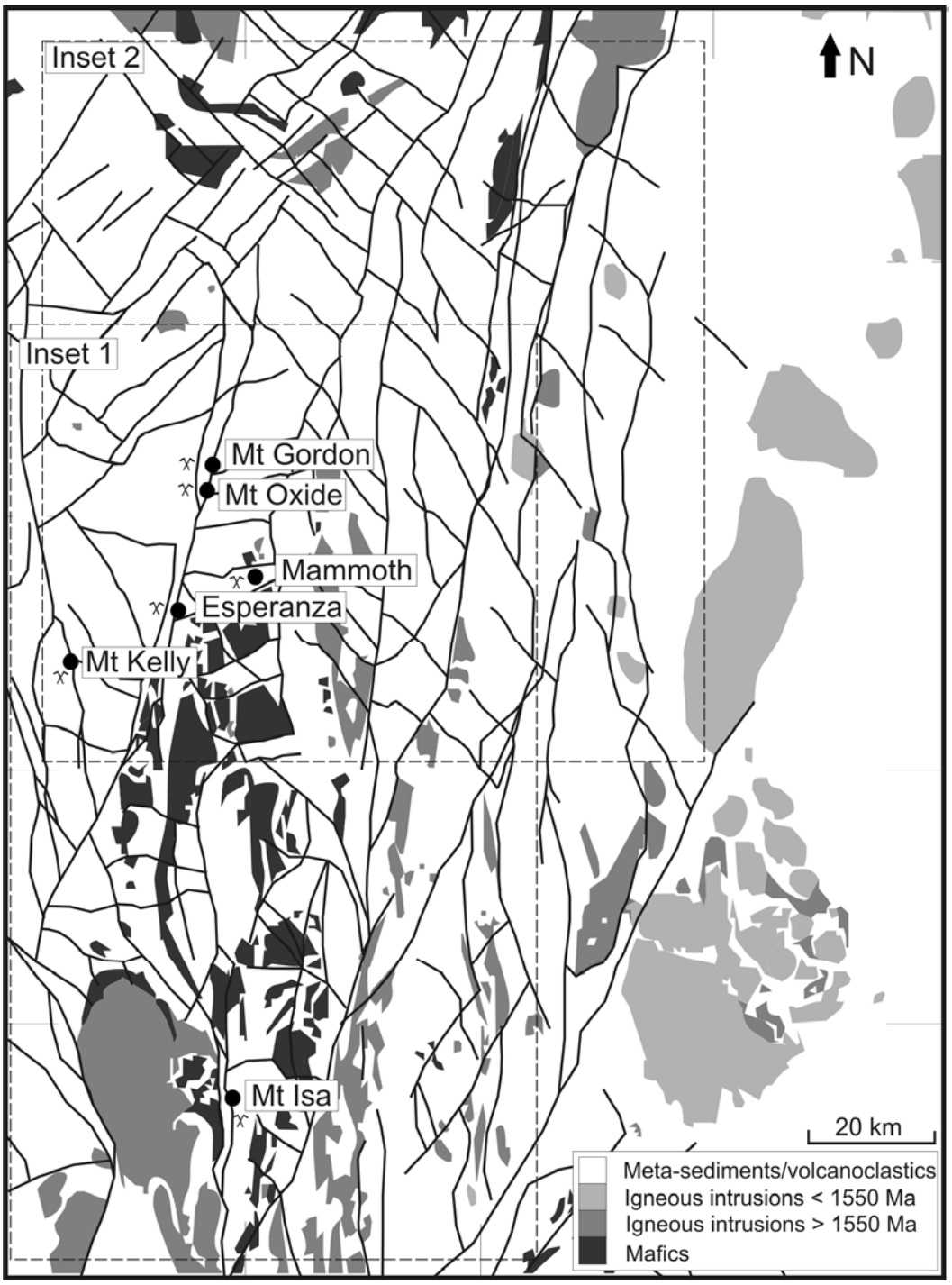

Fig.2. Simplified geological map of the Mt Isa Western Succession, indicating the main structural trends, basic lithologies and several of the main Cu deposits. Inset indicates study areas for numerical models (Inset 1: Southern part of the western Mt Isa Inlier, and Inset 2: Northern Leichhardt River Fault Trough).

2. Geology of the Mount Isa Inlier

The Mount Isa Inlier of Northwest Queensland (Fig. 1) comprises three major tectonic units; from west to east, the Western Fold Belt (Western Succession), the Kalkadoon-Leichhardt Belt and the Eastern Fold Belt (Eastern Succession), which are predominantly north-south trending sedimentological and structural domains (Blake & Stewart, 1992; O'Dea *et al.* 1997). The area is characterised by lower to middle Proterozoic meta-sedimentary rocks, rhyolitic and basaltic meta-volcanic rocks, gabbro, dolerite and widespread I-type granitoids. The major stratigraphic cycles and basin- forming events of the region have been described by many previous authors (e.g. Blake & Stewart, 1992; Page & Sun, 1998; Southgate *et al*., 2000) as have the main structural events (e.g. Page & Bell, 1986; Etheridge *et al*. 1987; Holcombe *et al.* 1991). Following many episodes of intracratonic rifting and basin formation, the main period of protracted deformation that is closely associated with the majority of mineralisation in the region took place during the Isan Orogeny (ca. 1600-1500 Ma; Blake & Stewart, 1992).

2.1 Western Succession

The Western Succession is host to three main superbasins that have been described in detail by several authors in terms of stratigraphic successions (e.g. Jackson *et* al., 2000; Scott *et* al., 2000; Southgate *et al*., 2000), which are namely the Leichhardt (ca. 1800 to 1740 Ma), Calvert (1730 to 1670 Ma) and Isa (ca. 1665 to 1575 Ma) Superbasins. The Leichhardt Superbasin is essentially comprised of a thick package of proximal conglomeratic sediments, both felsic and mafic volcanics, and well sorted marine and sandstone dominated sediments. The Calvert Superbasin is comprised of fluvial to marine conglomeratic sediments, felsic and mafic volcanics, carbonates and sandstone dominated sediments and which sits unconformably over the Leichhardt Superbasin. The youngest of the three superbasins is the Isa Superbasin which is comprised of conglomeratic sediments, arenites, mudstones and carbonaceous siltstones and shales. The Isa Superbasin is host to the majority of the mineralisation in the region. Although Cu mineralisation is hosted in the Isa Superbasin, there is a distinct variation in host rocks throughout the region. The Mount Isa Cu deposit is hosted within the Urquhart Shale, the Mammoth deposit is hosted within the Myally subgroup and conversely the nearby Esperanza deposit is hosted within the Esperanza Formation (see Keys *et al*., 2008 this volume), which again provides evidence

for a strong argument for a structural control rather than geochemical control with respect to the depositional site.

2.2 Deformation and metamorphism

A complex and protracted deformational and metamorphic history is evident within the Mount Isa inlier, related to cycles of extension and shortening between 1900 and 1500 Ma. Following the 'Wonga' extensional event ca. 1750 – 1730 Ma (Holcombe et al., 1991; Oliver et al., 1991), there are four main deformational events during the Isan Orogeny (D_1, D_2, D_3 and D_4), as initially proposed by Bell (1983) and others, in the western Mount Isa inlier. Several authors have attempted to correlate the deformational events across both the Eastern and Western Successions (Page & Bell, 1986; Etheridge *et al*. 1987; Holcombe *et al.* 1991; O'Dea *et al.* 1997; Adshead-Bell, 1998; Bell & Hickey, 1998; Laing, 1998; Mares, 1998). The main deformational event (D_2) during the Isan Orogeny and the peak of metamorphism has been suggested to have taken place ca. 1580 -1595 Ma (Rubenach *et al.*, in press; Rubenach, 2008 this volume), which appears to have been an inlier wide event, with both the Eastern and Western fold belts undergoing similar events at a similar times (Rubenach, 2008 this volume). Slightly later in the deformational history, the ENE D_3 event ca. 1550 Ma (Bell, 1983; Rubenach *et al*., in press), which is less evident in the Western Succession, has been responsible for the reactivation of many major D_2 structures as has the more prominent ESE D_4 event. This later structural event resulted in dominant strike-slip reactivation of major faults, particularly steeply dipping faults in the region, and sinistral strike-slip displacement on north-south striking faults is evident. Recent work by Miller (2007 this volume) at the Mount Isa Cu deposit has also indicated that the orientation of the stress regime responsible for Cu mineralisation was most likely in the NW quadrant. Detailed seismic profiles in the region provide good evidence that the majority of the faults in the Western Succession are steeply dipping (Drummond *et al.*, 1998; MaCready, 1998), which suggests that during the D_4 event strike-slip deformation was prominent, with a lesser influence of dip-slip movement, and resulted in brecciation in many cases.

2.3 Fluid flow and metallogenesis

Mineralising fluids in the Mount Isa Inlier have been accredited to several different sources, and there is quite possibly a distinction between deposits based on fluid inclusion

and isotope analysis work that has been carried out in the region (e.g. Kendrick, *et al*., 2007; Fisher & Kendrick, in press). The Fe-oxide Cu-Au deposits in the Eastern Succession appear to have two or more distinct fluid sources responsible for the majority of the mineralisation (Kendrick, *et al*., 2007; Fisher & Kendrick, in press), namely an evolved meteoric fluid, bittern brines and in some cases granitic intrusion related fluids. In terms of Cu bearing fluids the Western Succession has had less interest; however, Kendrick, *et al*. (2006) has shown that the Cu fluids at Mount Isa most likely have a mixed origin. One thing is clear however, regardless of the potential for many fluids involved in the system the depositional sites are closely related to steeply dipping faults and structures and late movement on these structures. Fluid flow has potentially been focussed up and along steeply dipping structures and has accessed areas more suitable for metal deposition as a result of variable stress partitioning during deformation.

3. Numerical modelling and conceptual models

The two main modelling techniques employed to simulate the response of rocks to deformation and contemporaneous fluid flow can be broadly categorised as continuous and discontinuous modelling. Continuous modelling treats rock masses as continuous elasto-plastic media and focuses on pervasive fluid flow (e.g. Ord & Oliver, 1997), whereas discontinuum modelling treats rock masses as elastic-plastic discrete blocks, and focuses on the deformation along faults and boundaries between such blocks. Areas of low minimum principal stress (σ_3) and low mean stress (σ_m) may indicate dilation and potential sites of fluid focusing, and are of great interest in mineralised hydrothermal systems. The ability to predict areas that are more susceptible to failure, and hence focus fluids, can be advantageous in defining sites of increased prospectivity within any region. The localisation of most deposits in the Western Succession, on or very close to faults, suggests the importance of faults in the mineralisation process. The discrete element modelling method, a powerful tool to simulate fault-slip and stress-strain partitioning along faults, is therefore a suitable approach in exploring this structural control in the mineralisation process. The discontinuous approach to modelling the interfaces or contacts between discrete bodies must take into account two types of mechanical behaviour; a) behaviour of the discontinuities (faults and rock contacts); and b) behaviour of the solid material involved. Blocks of material within these models may be assigned rigidity or mechanical properties, and the contacts between blocks may also be given mechanical properties.

3.1 UDEC (Universal Distinct Element Code) overview

UDEC, the software used in this study, is a 2- dimensional numerical program based on the distinct element method for discontinuum modelling (ITASCA, 2000). The code enables a numerical simulation of the response of a jointed or fractured rock mass, subjected to either static or dynamic loading. The models are represented by blocks and the discontinuities (faults and rock contacts) represented as discrete boundaries between the blocks. The discrete blocks are subdivided into a finite difference mesh and each zone or element within the mesh behaves according to a prescribed linear or non-linear stress/strain law. UDEC uses a time-marching scheme to solve equations of motion (Zhang and Sanderson, 2002), and the relative motion of the discontinuities is governed by a linear or non-linear force displacement relationship for movement according to Newtons laws of motion, in both the normal and shear directions. The stress-displacement relationship, which is assumed to be linear, is governed by the stiffness properties applied to the fractures. The fractures and discrete blocks have a limiting tensile strength, and when exceeded, tensile failure occurs. Similarly, in shear the response is controlled by the shear stiffness, and shear stress is limited by a combination of cohesive and frictional strength of the fracture. Dilation of fractures may occur at the onset of slip, and this dilation is governed by a specified dilation angle. UDEC has been proven as a useful numerical tool in simulating geological processes (e.g. Oliver *et al*., 1990, 2001; Holyland & Ojala, 1997; Mair *et al*., 2000), and in particular for fault arrays and fluid flow (e.g. Oliver, 1995; Jiang *et al*., 1997; Zhang and Sanderson, 2002).

3.2 Boundary conditions and conceptual models

The geometry of the models (Figs. 3 and 4) was constructed by digital tracing of fractures from both the 1:100 000 maps of the area and the NWQMPR (2000) to construct the central region model (Model 1) encompassing the main Cu deposits in the south e.g. Mt Isa, Hilton, and a northern region model covering the NLRFT (Model 2) encompassing the main Cu deposits in the north e.g. Gunpowder and Mount Kelly areas. Other input that was incorporated was fault interpretations from both density and magnetic worming data, which allowed a structural interpretation in areas with little to no available data, particularly undercover. Certain limitations of the UDEC program mean that no fractures can be inserted that are not directly or indirectly connected to the model edges, hence all fractures

are joined. A rounding parameter is assigned to each block, which applies to the contact mechanics, to prevent unrealistic locking of the corners during the modelling process. The constitutive model behaviours are elastic-plastic Mohr-Coulomb for the deformable blocks, and Coulomb slip failure for the fault and granite contacts, which provide good representation of upper-crustal rock behaviour (e.g. Oliver *et al*., 1990; Jiang *et al*., 1997; Holyland & Ojala, 1997).

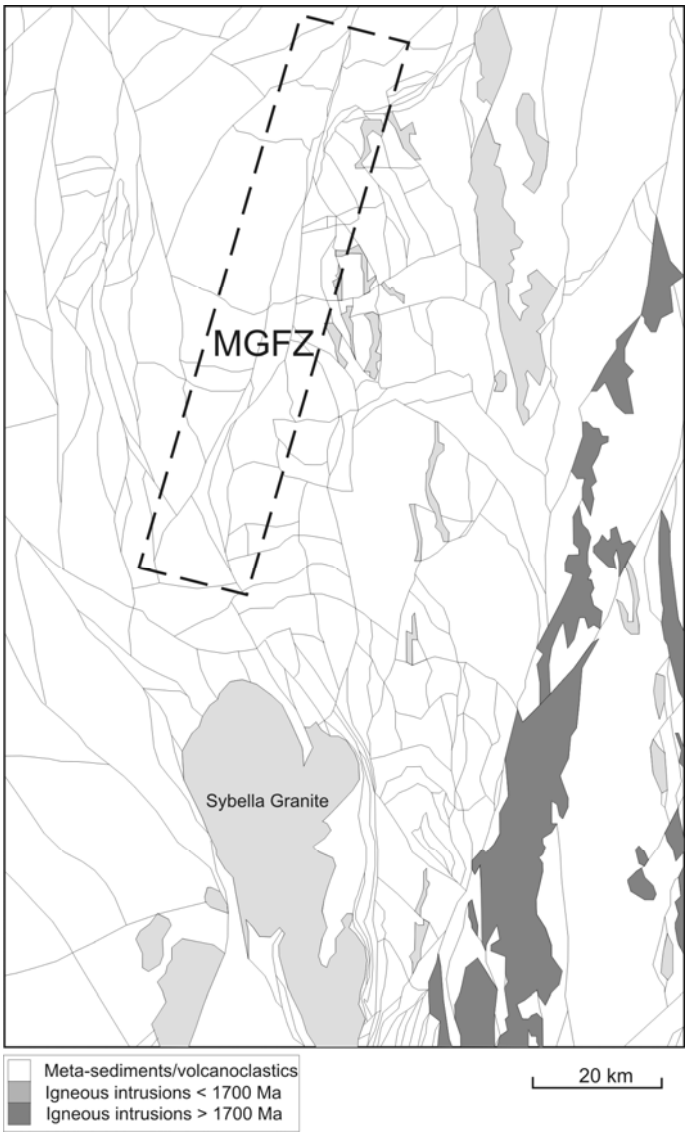

Fig. 3. Conceptual Model 1 (120 x 184 km) representing complex geological features and structures found in the western succession. Also highlighted are the Sybella Granite and the Mount Gordon Fault Zone region (MGFZ). Boundary conditions applied to this model are appropriate to an E-W compression (σ_1 = 90°) and a rotation to ESE-WNW (σ_1 to 112.5°) and SE-NW (135°) respectively.

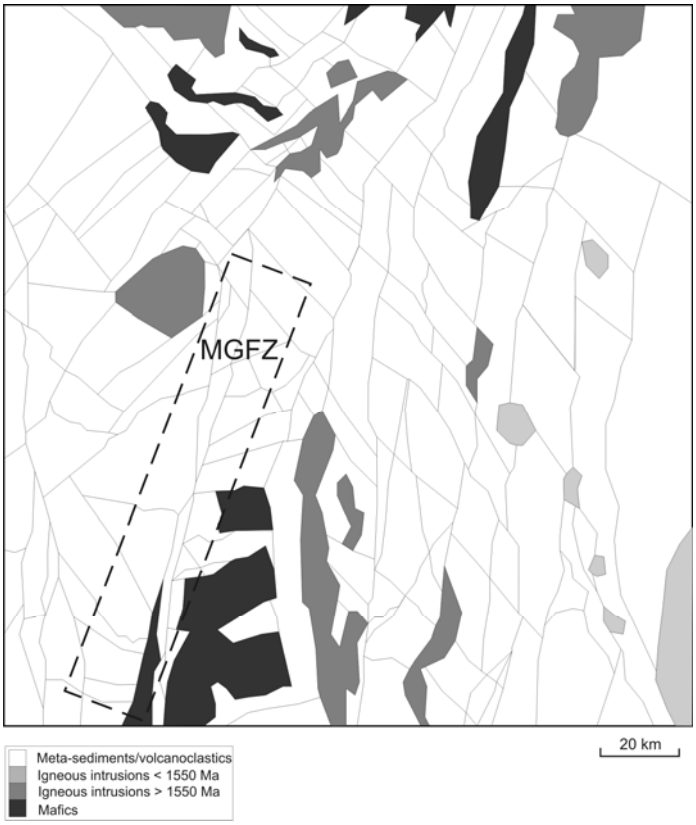

Fig.4. Conceptual Model 2 (166 x 158 km) representing complex geological features and structures found in the northern Leichhardt River Fault Trough. Also highlighted is the Mount Gordon Fault Zone region (MGFZ). Boundary conditions applied to this model are appropriate to an E-W compression (σ_1 = 90°) and a rotation to ESE-WNW (σ_1 to 112.5°) and SE-NW (135°) respectively.

The maximum principal stress (σ_1) was initially modelled as 090° (E-W; Model 1a see Fig. 4), following the general understanding of the main shortening phase of the Isan Orogeny (Page & Bell, 1986). However, many north trending faults show apparent sinistral displacements, suggesting they were optimally orientated for shear (Sibson, 1985, 1998). Two alternate orientations of σ_1 = 112.5° (ESE-WNW; Model 1b) and 135° (SE-NW; Model 1c), representing the general stress field of the D_4 deformational event were chosen, such that σ_1 for the far-field stresses orients between 22.5° to 45° to the majority of these faults, and provides a likely optimum angle for shear failure (Sibson, 1985, 1998). The stress conditions for the models are set at a ratio of $\sigma_1 / \sigma_2 = 1.2$ and $\sigma_3 / \sigma_2 = 0.8$, resulting in a phi ($\phi$) value of 0.5 (where $\phi = \sigma_2 - \sigma_3 / \sigma_1 - \sigma_3$). These are similar ratios to those used by Mair et al. (2000), Zhang & Sanderson (2002) and McLellan & Oliver (in press).

Although UDEC is 2-dimesional plane-strain, three stress values (σ_1, σ_2 and σ_3) are required to define a state of stress, with σ_2 representing the vertical in-plane stress component acting on a two-dimensional map-view plane (i.e. the depth in the crust). The imposed stresses ($\sigma 1$ = 210 MPa, σ_2 = 175 MPa, σ_3 = 140 MPa) are within reasonable ranges of CO_2 fluid- inclusion entrapment pressures estimated for the Isa inlier late during the Isan Orogeny, which approximate 175 to 200 MPa (e.g. Adshead, 1995; Rotherham et al., 1998; Mark et al., 2001, 2006). The chosen depth and stress applied to the models (σ_2 – 175 MPa at 7 km) correspond well to the independent data on the depths (6 to 8 km) of ore formation for many deposits found in the Mount Isa Inlier (e.g. Heinrich et al., 1989; Rotherham et al., 1998; Perring et al., 2000; Matthai et al., 2004; Kendrick *et al*, 2006). Varied additional pore fluid pressures were tested from supra-hydrostatic values (87.5 MPa at 7km depth) to sub-lithostatic values (122.5 MPa at 7km depth), and these were applied to the fractured rock mass. Model parameters are summarised in Table 1.

Table. 1. Physical properties of rocks, contacts, faults and model variations.

Property	**Mafics & Granitic Intrusions**	**Metasedimentary rocks**	**Lithological contacts**	**Faults**
Density (kg/m^3)	2650	2850	-	-
Bulk modulus (Pa)	49e9	25e9	-	-
Shear modulus (Pa)	27e9	25e9	-	-
Cohesion (Pa)	20e6	10e6	10e2	4e2
Tensile strength (Pa)	10e6	5e6	3e6	2e6
Friction angle (°)	37	31	35	30
Dilation angle (°)	5	4	5	5
Normal stiffness (Pa/m)	-	-	5e9	5e6
Shear stiffness (Pa/m)	-	-	1e5	1e3
Permeability factor (Pa/s)	-	-	238	300
Aperture at zero normal stress (m)	-	-	0.03	0.05
Residual hydraulic aperture (m)	-	-	0.01	0.03

MODEL	**σ_1 orientation**	**pp variations**
1a	90°	Hydro to litho
1b	112.5°	“
1c	135°	“
2a	90°	“
2b	112.5°	“
2c	135°	“

Models were run to equilibrium by examining the relationship between unbalanced forces and displacements. For a static analysis, a model is in exact equilibrium if the unbalanced force or net nodal force vector at each block centroid or grid point is zero. The maximum nodal force vector is also referred to as the "unbalanced" or "out-of-balance" force (ITASCA, 2000). The unbalanced force will never exactly reach zero for a numerical analysis, and the model is considered to be in equilibrium when the maximum unbalanced force is small compared to the representative forces in the problem. History points were placed to monitor changes in physical parameters at particular locations in the model throughout the procedure. Physical properties chosen for both the rock and joint materials (Table 1) are similar to those of previous authors (e.g. Oliver *et al*., 1990; Holyland & Ojala, 1997; Jiang *et al*, 1997; Zhang & Sanderson, 2002) and represent metasedimentary rocks, granitoids and mafic bodies, lithological contacts and faults. Granitoid intrusions and mafic bodies were chosen to be the most competent rock type, and the lithological contacts were assigned a higher stiffness than the faults (see Table 1).

4. Modelling results

Although many aspects of the models were investigated (e.g. displacement vectors, shear displacement, shear stress, dilation, differential stress and principal strain), this contribution focuses on the criteria required for failure, plasticity or failure state, minimum principal stress (σ_3) and or dilation (ψ), and differential stress ($\Delta\sigma$) values, as these values are the most sensitive and are considered most important for the localisation of shear and tensile failure, and hence mineral deposition (e.g. Etheridge *et al*., 1984, Sibson, 1994). Failure in shear and tension may occur when effective stress conditions are such that the initial *in-situ* stress conditions are driven to the failure envelope by the fluid pressure (P_f). The amount of P_f required for this to occur for a given stress state can be termed 'fluid pressure required for failure' and is referred to as P_fF. All models were run as close to an equilibrium state as possible prior to interrogation of numerous physical parameters, and in cases where the equilibrium state was not fully reached the model was examined at the closest possible point to equilibrium during the model run. Models were compared on the basis of their orientation of σ_1 and the specific fluid pressures that were applied to these models, resulting in three variants of each model with E-W, ESE-WNW and SE-NW σ_1 orientations.

4.1 Southern region (Models 1a, b, c)

At a regional scale in the models with lowest applied pore pressures (87.5 MPa), σ_3 displays a stress distribution pattern in Model 1a, which indicated lowest values around the northern and eastern sides of the Sybella Granite (Fig. 5a) and a partitioning trend which runs parallel to the Mount Gordon Fault Zone (MGFZ). When the stress field is rotated to ESE-WNW in Model 1b, a very similar partitioned pattern emerges (Fig. 5b), however additional areas of low values of σ_3 are also evident on the western side of the Sybella Granite and at several fault intersections. In Model 1c, a SE-NW stress orientation appears to result in less variability in its distribution of lowest σ_3 values, with the major areas of low values large and focussed around the centre of the model and the Sybella Granite (Fig. 5c). Model 1a displays a lower overall range of σ_3 values compared to Models 1b and 1c, but areas indicating the lowest values are generally 20 MPa less in the latter two models. Some of the locations highlighted with lowest values, particularly in Model 1a and Model 1b, correspond to the approximate locations of some of the larger Cu occurrences in the region, e.g. Mount Isa and Hilton.

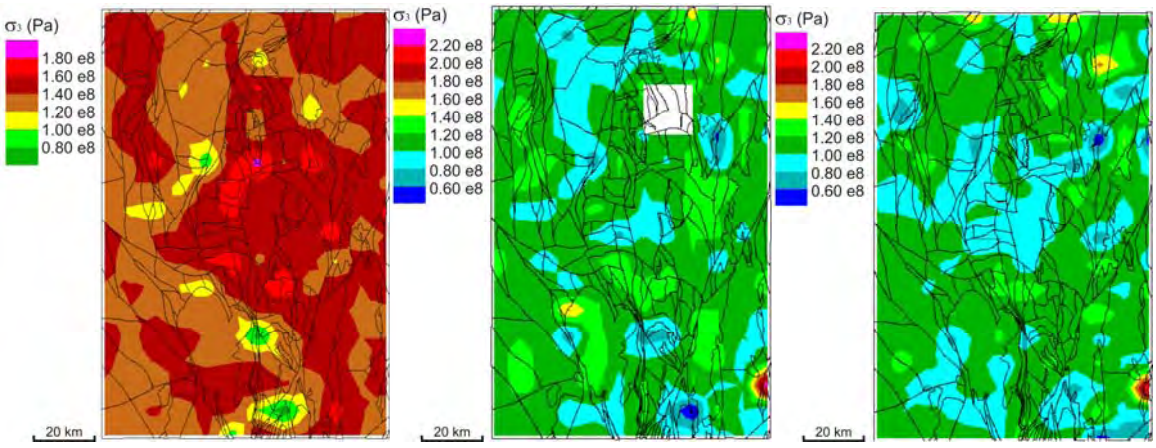

Fig. 5. Plots of minimum principal stress (Pa): a) Model 1a (E-W) indicating lowest values around the northern and eastern margins of the Sybella Granite and close to the MGFZ; b) Model 1b (ESE-WNW) indicating lowest values around the Sybella Granite and close to the MGFZ, with additional low values noted at several fault intersections, and c) Model 1c (SE-NW) indicating lowest values mainly on the west margins of the Sybella Granite and along the MGFZ, with a large broad scale distribution of low values noted in the centre of the model.

The distribution of positive volumetric strain increments, or dilation, closely corresponds to the distribution of lower values of σ_3. This strain partitioning is evident in Model 1a where the distribution of highest positive volume increases (Fig. 6a) displays a similar distribution to the previously highlighted distribution of σ_3 (c.f. Fig. 5a), and again we see areas of dilation on the eastern side of the Sybella Granite and the MGFZ. With a rotation of the stress field to an ESE-WNW orientation, Model 1b again displays a similar distribution to its σ_3 values with both east and west sides of the Sybella Granite, the MGFZ and several fault intersections displaying relatively low values (Fig. 6.b). When the stress field is rotated further towards SE-NW, Model 1c again shows a similarity in its distribution of dilation with its previous distribution of σ_3 (Fig. 6c). The overall values of dilation are similar in Model 1a and Model 1c; however Model 1b has a notable increase in values of dilation in comparison two the other two models. The main interesting feature of this model is the broad dilation zone over the Mount Isa and Hilton location, which is not so evident in Model 1c.

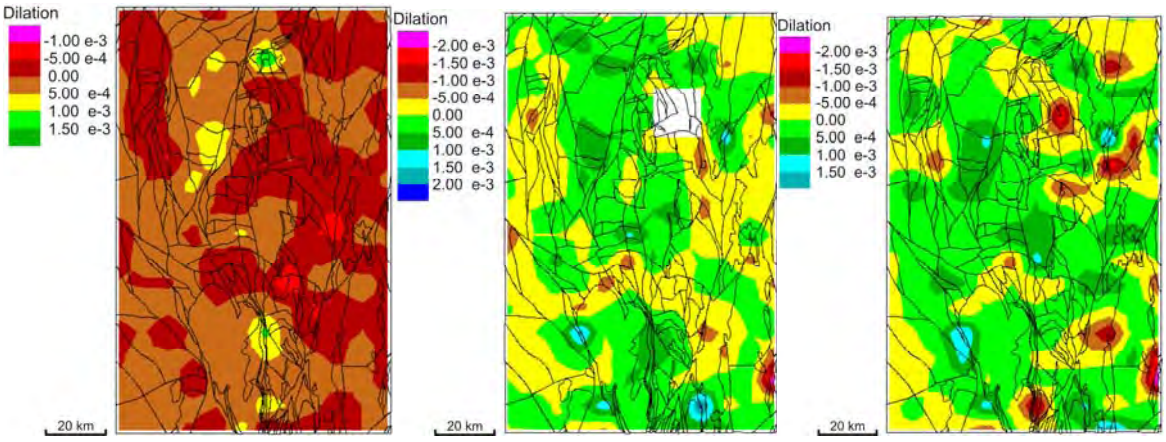

Fig. 6. Plots of volumetric strain increment, with negative values indicating contraction and positive values indicating dilation: a) Model 1a (E-W) indicating highest values around the eastern margins of the Sybella Granite and parts of the MGFZ; b) Model 1b (ESE-WNW) indicating highest values around the Sybella Granite (particularly around the Mt Isa location) and close to the MGFZ, with additional high values noted at several fault intersections and around competent bodies, and c) Model 1c (SE-NW) indicating highest values mainly on the west margins of the Sybella Granite and along the MGFZ, with additional high values noted at several fault intersections.

The distribution of high $\Delta\sigma$ values broadly coincides with the previous distribution of low σ_3 values (although there are limited exceptions noted around fault intersections), particularly in Models 1a and 1b (Fig. 7a, b), and this is much less evident in the Model 1c (Fig. 7c). This close association between the low values of σ_3 and higher values of $\Delta\sigma$ may potentially highlight areas that are most likely to fail in shear. Conversely, the areas that indicate a low value of $\Delta\sigma$ that coincided with low values of σ_3, may highlight areas that would be more likely to fail in tension. Such areas in these models include the Mount Isa, Mammoth and Investigator fault systems (see Figs 5, 6, and 7).

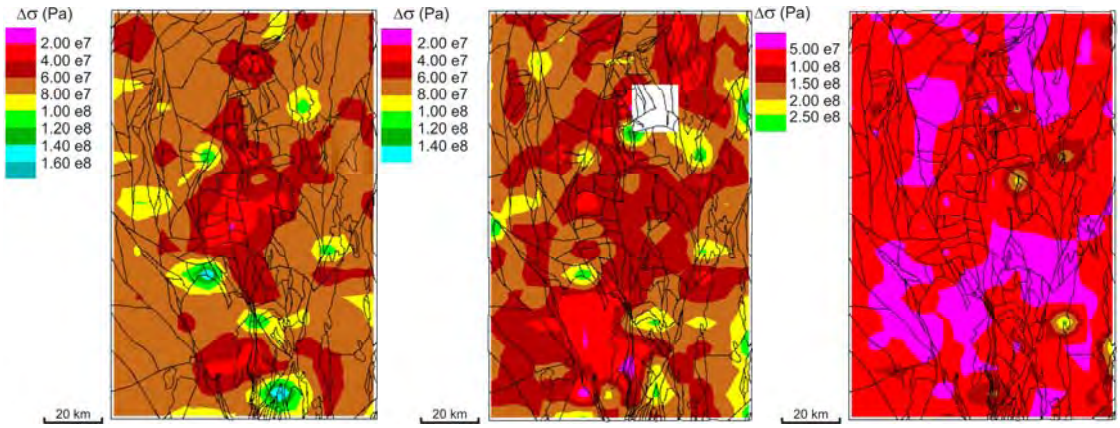

Fig. 7. Plots of differential stress (Pa): a) Model 1a (E-W) indicating highest values around the northern and eastern margins of the Sybella Granite and close to the MGFZ and lowest values near the Mt Isa location; b) Model 1b (ESE-WNW) indicating highest values around the Sybella Granite and close to the MGFZ, with additional low values noted at the Mt Isa location, and c) Model 1c (SE-NW) indicating highest values at a few isolated fault intersections.

Given at particular fluid pressure is established within these models (varied) we can examine what fluid pressure is required to initiate failure in either shear or tension (P_fF). On this regional scale Model 1a highlights that areas requiring least P_fF are preferentially located around competent bodies (e.g. Sybella Granite), at fault bends or intersections, and most notably between N to NE trending structures and their intersections with E to SE trending structures (Fig. 8a). Models 1b and 1c give a similar distribution as Model 1a but they highlight more areas more likely to fail with lower values of P_fF, particularly in the north and northeast regions of the model (Fig. 8b, c).

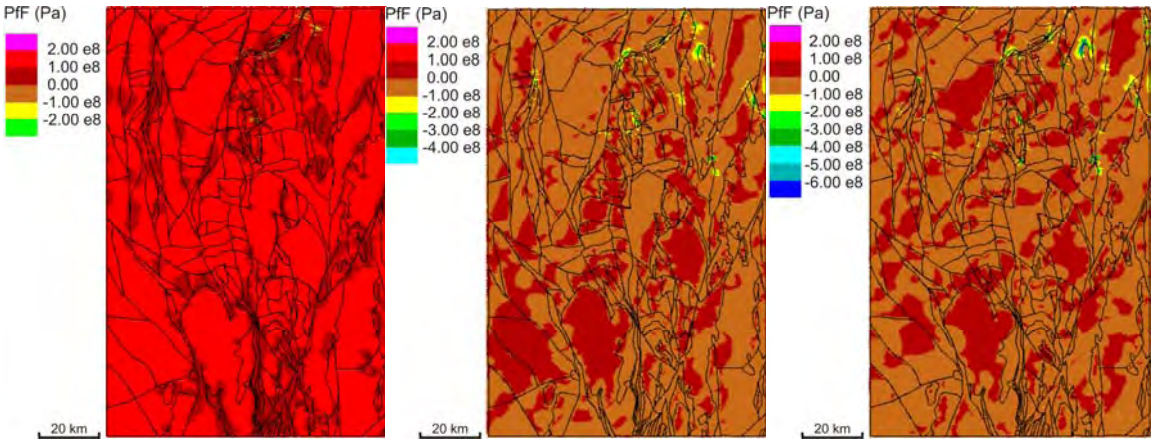

Fig. 8. Plots of fluid pressure required for failure (Pa): a) Model 1a (E-W) indicating lowest values around fault bends and the intersections of N to NE and S to SE trending structures; b) Model 1b (ESE-WNW) indicating a similar but more widespread distribution, but lower values than Model 1a, and c) Model 1c (SE-NW) indicating similar values and distribution of values as Model 1b.

When a subset of the regional model is examined (e.g. the Mount Isa area) we can see in Model 1a that most of the background P_fF values are around 100 to 150 MPa, with areas around N to NE trending faults and Sybella contacts around 50 to 100 MPa (Fig. 9a). Similar distributions of low P_fF values are shown in Models 1b and 1c (Fig. 9b, c); however Model 1b values are up to 20 to 40 MPa less in some instances, which reflects the higher likelihood for failure given a fluid pressure increase. This is most apparent in on the east side of the Sybella Granite around the Mount Isa area (see Fig. 9b).

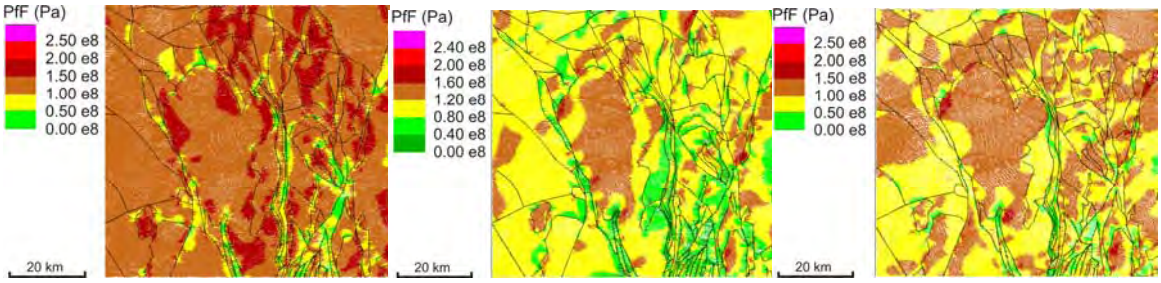

Fig. 9. Plots of fluid pressure required for failure (Pa) for the Mt Isa region and around the Sybella Granite: a) Model 1a (E-W) indicating lowest values around the margins of the Sybella Granite, and around fault bends and the intersections of N to NE and S to SE trending structures; b) Model 1b (ESE-WNW) indicating a similar but more widespread

distribution, but indicating overall lower values than Model 1a and 1c, and c) Model 1c (SE-NW) indicating similar values and distribution of values as Model 1a.

Failure plots indicate more intense failure in and around the Sybella granite and in the north-eastern region of the regional model (Fig. 10a), and a rotation of the stress field results in more intense failure in the same areas and also an overall a more widespread distribution of failure within Model 1b and 1c (Fig. 10b, c). The increase of fluid pressure in these models had no major effect on the distribution of all the major parameters investigated, but mostly resulted in models that displayed more intense failure plots (Fig. 11a, b, c). Model 1b resulted in the highest number of failure locations, several of which are located at or in close proximity to major economic deposits.

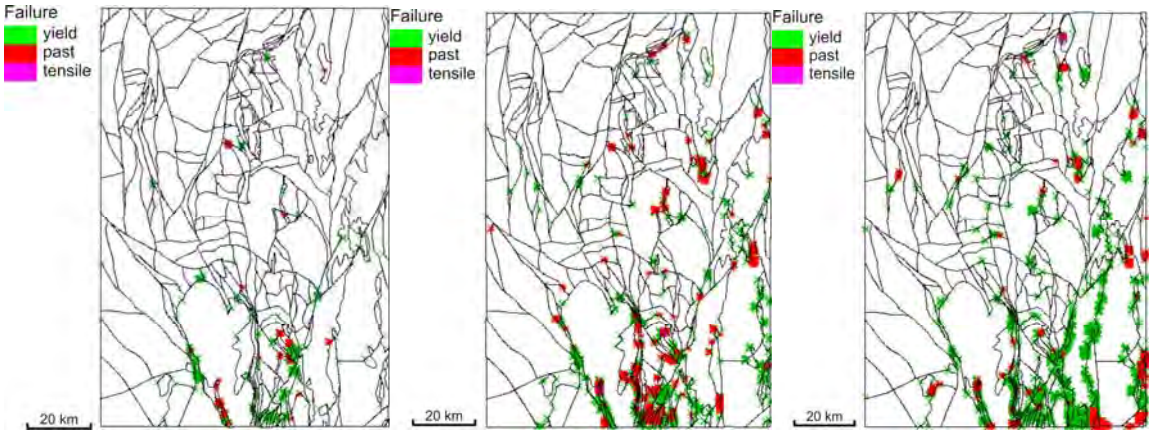

Fig. 10. Plots of failure (presently at yield, at yield in the past and failed in tension): a) Model 1a (E-W) indicating most areas at yield around the margins of the Sybella Granite; b) Model 1b (ESE-WNW) indicating a similar but more widespread distribution, with many other areas at yield being associated with fault intersections and bends, and c) Model 1c (SE-NW) indicating a similar distribution of failure as Model 1b.

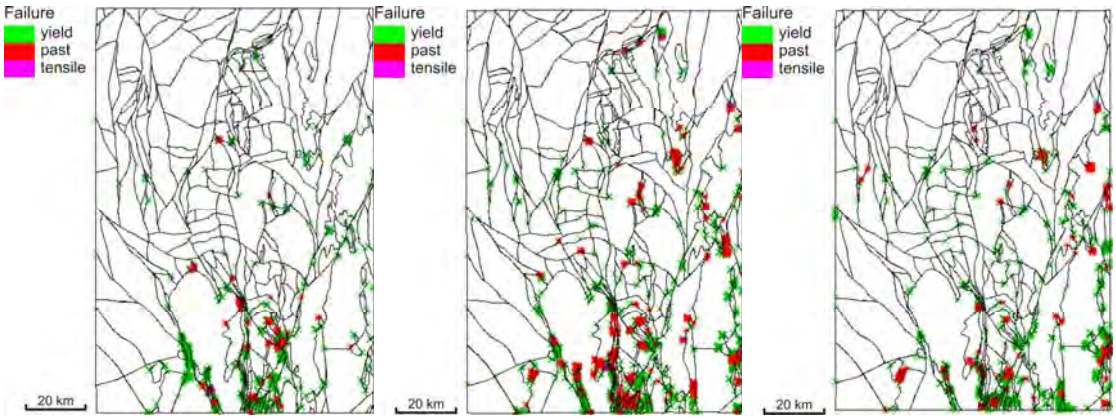

Fig. 11. Plots of failure (presently at yield, at yield in the past and failed in tension) with an increase in fluid pressure. Models 1a, 1b and 1c display a very similar distribution to previous models of failure (c.f. Fig. 10); however there are more areas of failure as a result of the fluid pressure increase.

4.2 NLRFT (Models 2a, b, c)

In the northern region of the Leichhardt River Fault Trough, the distribution of σ_3 in Model 2a displays lowest values associated with fault intersections, bends and on the edges of competent intrusive bodies (Fig. 12a). A somewhat similar distribution of σ_3 is seen when the stress field is rotated by 22.5° (ESE-WNW) with Model 2b displaying lowest values around intrusive bodies and fault intersections, with a notable absence of lower values in the centre of the region (Fig. 12b). Rotation of the stress field to and ESE-WNW direction has also resulted in lower overall values of σ_3 by around 40 MPa in some cases. A further rotation of the stress field to SE-NW in Model 2c again results in a similar distribution to the previous two models, however the range of values are more similar to Model 2a than Model 2b (Fig. 12c).

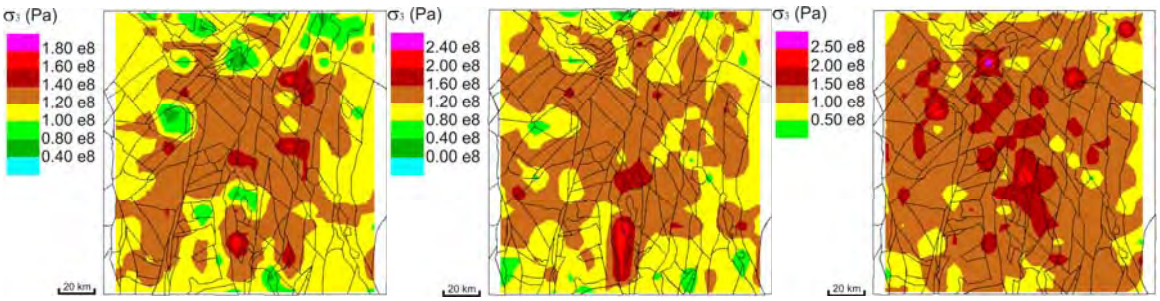

Fig. 12. Plots of minimum principal stress (Pa): a) Model 2a (E-W) indicating lowest values around competent intrusive bodies and at fault intersections and fault bends; b) Model 2b (ESE-WNW) overall a similar distribution as Model 2a, but a notable lack of low values within the centre region of the model and overall a broader range of values and lowest values are around 40 MPa less than Model 2a, and c) Model 2c (SE-NW) indicating a similar broad scale distribution as the previous Models 2a and 2c but higher values than Model 2b.

Model 2a displays isolated regions of positive volume change or dilation (Fig. 13a), however a large area of the model is under contraction. The most notable regions of dilation are seen at fault intersections and around competent bodies such as the Weberra Granite and the Wonga Suite Granite. The rotation of σ_1 to an ESE-WNW orientation in Model 2b results in a focussing of dilation at fault intersections, lithological contacts and close to fault bends (Fig. 13b). There is significantly more dilation in this model than in the previous model, and most of the highest values correspond to the approximate locations of some of the larger Cu occurrences in the region, e.g. Mount Kelly, Esperanza, Mammoth, Big One and Crusader (Fig. 13b). Model 2c shows a similar range of dilation values as Model 2b, and the overall pattern of distribution is somewhat similar (Fig. 13c), however, Model 2b appears to have a higher incidence of isolated areas indicating higher values of dilation (cf. Fig 13b and Fig 13c) particularly in the faults and lithological contacts around the Weberra and Ewen Granite.

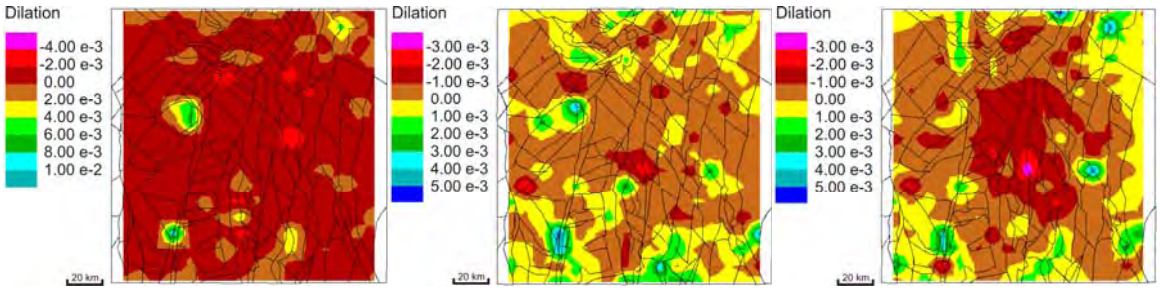

Fig. 13. Plots of volumetric strain increment, with negative values indicating contraction and positive values indicating dilation: a) Model 2a (E-W) indicating dilatant areas at a few fault intersections, however the majority of the model is in contraction; b) Model 2b (ESE-WNW) indicating a more widespread distribution of dilatancy particularly in close proximity to competent bodies and fault intersections, and c) Model 2c (SE-NW) indicating a similar, but not as widespread, distribution to Model 2b.

The distribution of high $\Delta\sigma$ values in Model 2a (Fig. 14a) broadly coincides with the previous distribution of low σ_3 values, but again as seen in previous models in the southern region, there are exceptions. This relationship between high values of $\Delta\sigma$ and low values of σ_3 is not so clearly evident in Model 2b (Fig. 14b) or Model 2c (Fig. 14c), where the partitioning of stress is obviously affected by the change in orientation of σ_1. In the latter two Models we can see there is a relationship between low values of σ_3 and low values of $\Delta\sigma$ (cf. Fig. 12b, 14b). This close association between the low values of σ_3 and higher values of $\Delta\sigma$ may potentially highlight areas that are most likely to fail in shear, and conversely, the areas that indicate a low value of $\Delta\sigma$ that coincided with low values of σ_3, may highlight areas that would be more likely to fail in tension. Such areas in these models include the Esperanza and Mammoth regions (see Figs 12, 13, and 14).

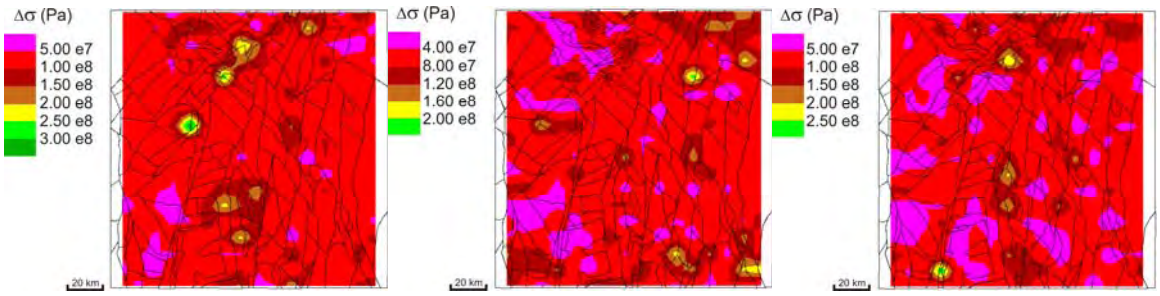

Fig. 14. Plots of differential stress (Pa): a) Model 2a (E-W) indicating highest values at isolated fault intersections and around some competent bodies and lowest values are evident in close proximity to the MGFZ; b) Model 2b (ESE-WNW) indicating highest values at isolated fault intersections and competent bodies and lowest values in close proximity to the MGFZ, values in this model are overall lower than the other two models, and c) Model 2c (SE-NW) indicating highest values at a few isolated fault intersections and competent bodies, but with a more widespread distribution of lower values than the previous Models 2a and 2b.

A failure plot of Model 2a indicates more intense failure in and around the more competent bodies and less so on the faults or within the fault blocks (Fig. 15a). Rotation of the applied stress field in Model 2b and Model 2c results in a more widespread failure pattern which is not solely concentrated around competent bodies but also on fault intersections, bends and within fault blocks (Fig. 15b, c). Less failure is apparent on NW trending structures, which is most likely due to the orientation of these structures to the applied stress. There is no major difference noted between Model 2b and Model 2c in failure distribution, however, Model 2b is noted to have a higher incidence of failure overall.

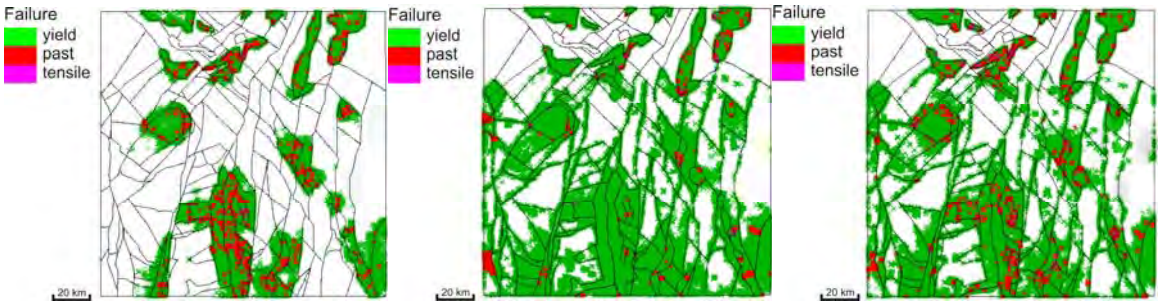

Fig. 15. Plots of failure (presently at yield, at yield in the past and failed in tension): a) Model 2a (E-W) indicating most areas at yield around the margins of competent bodies; b)

Model 2b (ESE-WNW) indicating a more widespread distribution of failure, with many areas at yield being associated with fault intersections and bends, and c) Model 2c (SE-NW) indicating a similar distribution of failure as Model 2b.

4.3 Results summary

As a generalisation, speculation on areas most likely to promote fluid migration and fluid flow are areas that have a combination of the favourable mechanical ingredients which in turn may be responsible for Cu mineralisation. Such areas would have a combination of low values of σ_3, high values of positive volumetric strain (dilation), low values of P_fF, and shear failure in combination with higher values of $\Delta\sigma$ or tensile failure in combination with lower values of $\Delta\sigma$. Some of the notable areas that fall into some or all of the above categories are the Mount Isa, Hilton, Native Bee and Mt Kelly locations (Fig. 16a), with many other identifiable areas particularly around the Sybella Granite and to the east and southeast of that area. In the NLRFT there is an obvious relationship with fault architecture, competent bodies and areas containing low values of σ_3, high values of positive volumetric strain (dilation), low values of P_fF, and shear failure in combination with higher values of $\Delta\sigma$ or tensile failure in combination with lower values of $\Delta\sigma$. Several areas containing some or all of these ingredients include Mt Kelly, Esperanza, Mammoth, Mt Oxide and Mt Gordon (Fig. 16b), with many other identifiable areas particularly around the Kamarga Volcanics and the Burstall Suite Granites. These results have a good correlation with known Cu deposits and prospects within the region and they have also identified areas with the essential mechanical and structural ingredients that have an excellent potential for hosting Cu mineralisation.

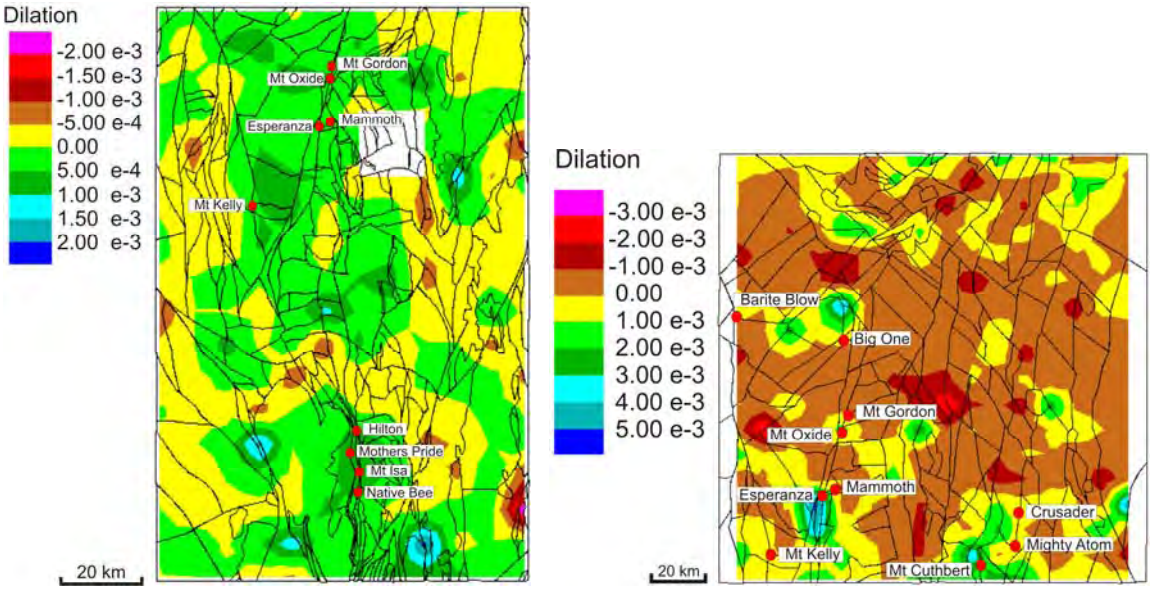

Fig. 16. Plots of volumetric strain increment and locations of the main Cu occurrences in the region for a) Model 1b (ESE-WNW), indicating positive values and dilation which appear to have a strong correlation with areas of Cu mineralisation: b) Model 2b (ESE-WNW) again indicating positive values and dilation which appear to have a strong correlation with areas of Cu mineralisation, particularly in close proximity to the MGFZ. There are also many prospective areas under cover to the N-NW of the region.

5. Discussion and conclusions

Most of the breccia-hosted Cu mineralisation in the Western Succession of the Mount Isa Inlier is closely related to the fault architecture, and has a wide variety of lithological host rocks. One of the key outcomes of this study is the demonstrated effects of complex fault architecture and competency contrasts in partitioning both stress and strain during deformation. One of the main results is the effect on stress and strain partitioning when the far field stress regime is rotated from an initial east-west orientation, resulting in isolated areas that display several of the essential mechanical ingredients for a Cu mineralised system in the Western Succession. Competency contrasts between the granitic intrusions and meta-sedimentary rocks in association with a fault or fault network, result in significant partitioning of stress around these structures. This is clearly evident around some of the major intrusives in the area, in particular the Sybella Granite in the southern region, and

smaller igneous rocks in the NLRFT such as the Weberra Granite, the Ewen Granite and the Cromwell basalt.

Faults have proven very important in localising the stress, strain and failure patterns observed, and it is evident that in a general sense, NW orientated faults appear to have the least favourable ingredients (low σ_3, dilation and failure) that we would expect to produce fluid focussing and mineralisation. This result may be somewhat counter intuitive; given the far field stress orientation is in the same general direction and one would expect faults at low angles to σ_1 to result in shear failure. This result however, highlights a complex interplay between the fault blocks and competent bodies and not all faults of any particular orientation show the same distribution of values, level of partitioning or overall prospectivity as a result of failure. This is due to the more complex interactions of block geometry or fault blocks and variations in block displacement relative to the applied far-field stress (σ_1), which assist in partitioning stress as these blocks move and deform. We can see that certain isolated areas have lower values of P_fF, and σ_3 and this may correspond with either low values of $\Delta\sigma$ (which may indicate a higher potential for tensile failure) or high values of $\Delta\sigma$ (which may indicate a higher potential for shear failure). These parameters indicate a higher potential for failure at specific locations within the model, and hence represent an overall increase in prospectivity for Cu mineralisation based on a structural controls and mechanical criteria approach. The main areas of interest in terms of prospectivity have been clearly identified in the previous section. The interesting thing to note is that many of these potential target areas are under variable amounts of younger sedimentary cover, and may have so far been overlooked as prospective exploration areas.

This work provides a good comparison between the Eastern and Western Successions of the Mount Isa Inlier, in terms of stress partitioning and Cu prospectivity. The work of McLellan and Oliver (in press) highlighted many areas in the Eastern Succession that have a higher potential (based on structural controls and stress partitioning) for Cu-Au mineralisation. Their main findings were that the most likely far field stress orientation responsible for localising fluids and Cu mineralisation was 112.5° (ESE). In comparison the most likely stress orientation responsible for Cu mineralisation in the Western Succession has been of a very similar orientation given that the ESE orientated models

(Model 1b and Model 2b) produced the most favourable results when comparing with known mineralisation. Miller (2007) and Keys *et al*. (2008) also attribute a far field stress of similar orientation to be responsible for mineralisation at the Mount Isa Cu deposit and the Mammoth Cu deposit respectively. This study therefore provides strong evidence that there may have been an 'inlier wide' far field stress regime responsible for both Cu and Cu-Au mineralisation in the Mount Isa Inlier during a late stage in the Isan Orogeny (c. <1550 Ma). Both at the regional and local scale this process is an effective exploration tool, which can highlight areas that have undergone stress partitioning and strain localisation, and highlight areas that show an increased potential for mineralisation as measured by stress and failure distributions. Incorporating a more detailed geometry including lithological contacts and small-scale structures to further examine the role of smaller scale structures in stress and strain partitioning would allow a more precise targeting strategy at tenement-to-mine-scale based on the structural approach. However, these two-dimensional models provide a good basis for further modelling studies, and highlight the basic conditions required for structurally controlled Cu mineralisation in the Western Succession of the Mount Isa Inlier.

7. Acknowledgements

I would like to acknowledge Barry Murphy from the University of Melbourne for many useful discussions and providing gravity and magnetic worm data for inputs to this study. This research has been funded by the Cooperative Research Centre for predictive mineral discovery (pmd*CRC), and this paper is published with the permission of the CEO, pmd*CRC.

8. References

Adshead, N.D., 1995. Geology, alteration and geochemistry of the Osborne Cu-Au deposit, Cloncurry district, NW Queensland. Unpublished Ph.D. thesis, James Cook University, Townsville, Queensland, Australia. 382 p.

Adshead-Bell, N.S., 1998. Evolution of the Starra and Selwyn high-strain zones, Eastern Fold Belt, Mount Isa Inlier: Implications for Au-Cu mineralisation. Economic Geology, 93, 1450-1462.

Bell, T.H., 1983. Thrusting and duplex formation at Mount Isa, Queensland, Australia. Nature, 304, 493-497.

Bell, TH. & Hickey, K.A., 1998. Multiple deformations with successive subvertical and subhorizontal axial planes in the Mount Isa Region: Their impact on geometric development and significance for mineralisation and exploration. Economic Geology, 93, 1269-1289.

Bell, T.H., Perkins, W.G., Swager, C.P., 1988. Structural controls on the development and localization of syntectonic copper mineralisation at Mount Isa, Queensland. Economic Geology, 83, 69-85.

Blake, D.H., Etheridge, M.A., Page, R.W., Stewart, A.J., Williams, P.R., Wyborn, L.A.I., 1990. Mount Isa Inlier – Regional Geology and Mineralization. Australasian Institute of Mining & Metallurgy, 14, 915-925.

Blake, D.H., Stewart, A.J., 1992. Stratigraphic and tectonic framework, Mount Isa Inlier. In: Stewart, A.J. & Blake, D.H. (Eds.) Detailed studies of the Mount Isa Inlier. Australian Geological Survey Organisation Bulletin, 243, 1-11.

Davidson, G.J., Davis, B.K., 2001. Structural and geochemical constraints on the emplacement of the oxide Cu-Au Monakoff deposit. In: Williams, P.J. (Ed.) A Hydrothermal Odyssey, Townsville,17-19th May 2001, Economic Geology Research Unit Contribution 59, 4445.

Drummond, B.J., Goleby, B.R., Goncharov, A.G., Wyborn, L.A.I., Collins, C.D.N., MaCready, T., 1998. Crustal-scale structures in the Proterozoic Mount Isa Inlier of north

Australia: their seismic response and influence on mineralisation. Tectonophysics, 288, 43-56.

Etheridge, M.A., Wall, V.J., Cox, S.F., 1984. High fluid pressure during regional metamorphism and deformation: implications for mass transport and deformation mechanisms. Journal of Geophysical Research, 89, 4344-4358.

Etheridge, M.A., Rutland, R.W.D., Wyborn, L.A.I., 1987. Orogenesis and tectonic process in the early to middle Proterozoic of Northern Australia. American Geophysical Union, Geodynamic Series 17, 131-147.

Fisher, L.A. and Kendrick, M.A., (in press). Metamorphic fluid origins in the Osborne Fe oxide-Cu-Au deposit, Australia: Evidence from noble gases and halogens. Mineralium Deposita.

Heinrich, C.A., Andrew, A.S., Wilkins, R.W.T., Patterson, D.J., 1989. A fluid inclusion and stable isotope study of synmetamorphic Copper Ore Formation at Mount Isa, Australia. Economic Geology 84, 529–550.

Holcombe, R.J., Pearson, P.J., Oliver, N.H.S., 1991. Structure of the Mary Kathleen Fold Belt. In: Sinclair, A.J., Blake, D.H. (Eds.), Detailed studies of the Mt Isa Inlier, Australian Geological Survey Organisation Bulletin, 243, 257-287.

Holyland, P.W., Ridley, J.R., Vearncombe, J.R., 1993. Stress mapping technology (SMT). In: Parnell, J., Ruffel, A.H., Moles, N.R. (Eds), Geofluids ’93: Contributions to an International Conference on Fluid Evolution, Migration and Interaction in Rocks, Geological Society of London, 272-275.

Holyland, P.W., Ojala, V.J., 1997. Computer-aided structural targeting in mineral exploration: two- and three-dimensional stress mapping. Australian Journal of Earth Sciences, 44, 421-432.

ITASCA, 2000. UDEC, Universal Distinct Element Code Command Reference, Itasca Consulting Group Inc. Minnesota, USA.

Jackson, M.J., Scott, D.L., Rawlings, D.J., 2000. Stratigraphic framework for the Leichhardt and Calvert superbasins: review and correlations of the pre-1700 Ma successions between Mt Isa and McArthur River. Australian Journal of Earth Sciences 47, 381–404.

Jiang, Z., Oliver, N.H.S., Barr, T., Power, W.L., Ord, A., 1997. Numerical modelling of fault-controlled fluid flow in the genesis of tin deposits of the Malage ore field, Gejiu Mining District, China. Economic Geology, 92, 228-247.

Kendrick, M.A., Duncan, R., Phillips, D., 2006. Noble gas and halogen constraints on mineralizing fluids of metamorphic versus surficial origin: Mt Isa, Australia. Chemical Geology, 235, 325–351.

Kendrick, M.A., Mark, G., Phillips, D., 2007. Mid-crustal fluid mixing in a Proterozoic Fe oxide–Cu–Au deposit, Ernest Henry, Australia: Evidence from Ar, Kr, Xe, Cl, Br, and I. Earth and Planetary Science Letters 256 (2007) 328–343

Keys, D., Miller, J. McL., McLellan, J.G., 2008 (this volume) Structural controls on depositional sites for Cu deposits in the Western Fold Belt, Mount Isa: integration of field observations and UDEC modelling. I7 pmd*CRC Final Report.

Laing, W.P., 1993. Structural/metasomatic controls on ore deposits in the east Mount Isa Block: the key to tonnes and grade. Australian Institute of Geoscientists, Bulletin, 13, 17-24.

Laing, W.P., 1998. Structural-metasomatic environment of the East Mount Isa Block base metal-gold province. Australian Journal of Earth Sciences, 45, 413-428.

MaCready, T., Goleby, B.R., Goncharov, A., Drummond, B.J. & Lister, G.S., 1998. A framework of overprinting orogens based on interpretation of the Mount Isa deep seismic transect. Economic Geology, 93, 1422-1434.

Mair, J.L., Ojala, V.J., Salier, B.P., Groves, D.I., Brown, S.M., 2000. Application of stress mapping in cross-section to understanding ore geometry, predicting ore zones and development of drilling strategies. Australian Journal of Earth Sciences, 47, 895-912.

Mares, V.M., 1998. The structural development of the Soldiers Cap Group within a portion of the Eastern Fold Belt of the Mt Isa Inlier: a succession of horizontal and vertical deformation events and large-scale shearing. Australian Journal of Earth Sciences, 45, 3, 373-387.

Mark, G., Williams, P.J., Ryan, C., Mernagh, T., 2001. Fluid chemistry and ore-forming processes at the Ernest Henry Fe oxide-copper-gold deposit, NW Queensland. In: Williams, P.J. (Ed) A Hydrothermal Odyssey, Extended Conference Abstracts, Economic Geology Research Unit Contribution 59, 124-125.

Mark, G., Oliver, N.H.S., Williams, P.J., 2006. Mineralogical and chemical evolution of the Ernest Henry Fe oxide-Cu-Au ore system, Cloncurry district, northwest Queensland, Australia. Mineralium Deposita, 40, 769-801.

Marshall, L.J., Oliver, N.H.S., (in press) Constraints on hydrothermal fluid pathways within Mary Kathleen Group stratigraphy of the Cloncurry iron-oxide- copper-gold district, Australia. Pre Cambrian Research.

Matthäi, S.K., Heinrich, C.A., Driesner, T.,2004. Is the Mount Isa copper deposit the product of forced brine convection in the footwall of a major reverse fault? Geology, 32, 4, 357–360.

McLellan, J.G., Oliver, N.H.S., (in press) Discrete element modelling applied to mineral prospectivity analysis in the eastern Mount Isa Inlier. Pre Cambrian Research.

McLellan, J.G., Oliver, N.H.S. & Schaubs, P.M., 2004. Fluid flow in extensional environments; Numerical modelling with an application to Hamersley iron ores. Journal of Structural Geology, 26, 6-7, 1157-1171.

McLellan, J.G., Blenkinsop, T., Nugus, M., Erickson, M., 2007. Numerical simulation of deformation and controls on mineralisation at the Sunrise Dam Gold Mine, Western Australia, SGA Dublin 2007 Digging Deeper Extended Abstract Volume, 2, 1455-1458

Miller, J. McL., 2007 (this volume) Structural Controls on the Mount Isa Copper Deposit, Qld. I7 pmd*CRC Final Report.

Nijman, W., Mijnlieff, H.F., and Schalkwijk, G., 1992. The Hero Fan delta (Lower Mount Isa Group) and its structural control: deformation in the Hero/Western Fault Zone and Paroo Range compared, Proterozoic, Mount Isa Inlier, Queensland, Australia, In: Stewart, A.J., and Blake, D.H., (Eds.), AGSO Bulletin 243: Detailed Studies of the Mount Isa Inlier: Canberra, Australian Geological Survey Organisation, p. 75-111.

NWQMPR, 2000. Northwest Queensland Mineral Province Report, Department of Mines and Energy, Queensland Government, Australia. Version 1.1.

O'Dea, M.G., Lister, G.S., Betts, P.G., Pound, K.S., 1997. A shortened intraplate rift system in the Proterozoic Mt Isa terrain, NW Queensland, Australia. Tectonics 16, 425-441.

Oliver, N.H.S., 1995. Hydrothermal history of the Mary Kathleen Fold Belt, Mount Isa Block, Queensland. Australian Journal of Earth Sciences, 42, 267-279.

Oliver, N.H.S., Valenta, R.K., Wall, V.J., 1990. The effect of heterogeneous stress and strain on metamorphic fluid flow, Mary Kathleen, Australia, and a model for large-scale fluid circulation. Journal of Metamorphic Geology 8, 311-331.

Oliver, N.H.S., Ord, A., Valenta, R.K., Upton, P., 2001. Deformation, fluid flow, and ore genesis in heterogeneous rocks, with examples and numerical models from the Mount Isa District, Australia. Reviews in Economic Geology, 14, 51-74.

Oliver, N.H.S., Holcombe, R.J., Hill, E.J., and Pearson, P.J. 1991. Tectono-metamorphic evolution of the Mary Kathleen Fold Belt, northwest Queensland: a reflection of mantle plume processes? Australian Journal of Earth Sciences, 38, 425-455.

Oliver, N. H. S., Cleverley, J.S., Mark G., Pollard, P. J., Fu, Bin., Marshall, L. K., Rubenach, M. J., P. J., Williams, Baker, T., 2004. Modelling the role of sodic alteration in the genesis of iron oxide-copper-gold deposits, Eastern Mount Isa Block, Australia. Economic Geology, 99, 1145-1176.

Ord, A., Oliver, N.H.S., 1997. Mechanical Controls on Fluid Flow during Regional Metamorphism: Some Numerical Models. Journal Metamorphic Geology, 15, 345-359.

Page, R.W., Bell, T.H., 1986. Isotopic and structural responses of granite to successive deformation and metamorphism. Journal of Geology, 94, 365-379.

Page, R.W., Sun, S.S., 1998. Aspects of geochronology and crustal evolution in the Eastern Fold Belt, Mt Isa Inlier. Australian Journal of Earth Sciences, 45, 343-363.

Perring, C.S., Pollard, P.J., Dong, G., Nunn, A.J., Blake, K.L., 2000. The Lightning Creek Sill Complex, Cloncurry District, Northwest Queensland: A source of fluids for Fe-oxide Cu-Au mineralisation and sodic-calcic alteration. Economic Geology, 95, 1067-1089.

Pollard, P.J., 2006. An intrusion-related origin for Cu–Au mineralization in iron oxide–copper–gold (IOCG) provinces. Mineralium Deposita, 41, 179–187.

Pollard, P.J., Mark, G., Mitchell, L., 1998. Geochemistry of post-1540 Ma granites in the Cloncurry District. Economic Geology, 93, 1330-1344.

Rotherham, J.F., Blake, K.L., Cartwright, I., Williams, P.J., 1998. Stable isotope evidence for the origin of the Mesoproterozoic Starra Au-Cu deposit, Cloncurry district, Northwest Queensland. Economic Geology, 93, 1435-1449.

Rubenach, M.J., 2008 (this volume) Tectonothermal and metasomatic evolution of the Mount Isa Inlier. I7 pmd*CRC Final Report.

Rubenach, M.J., Foster, D.R.W., Evins, P. M., Blake, K.L., Fanning, C. M., (in press) Age constraints on the tectonothermal evolution of the Selwyn Zone, Eastern Fold Belt, Mount Isa Inlier. Pre Cambrian Research.

Schaubs, P.M., Rawling, T.J., Dugdale, L.J., Wilson, C.J.L., 2006. Factors controlling the location of gold mineralisation around basalt domes in the Stawell corridor: insights from coupled 3D deformation – fluid-flow numerical models. Australian Journal of Earth Sciences, 53, 841–862.

Scott, K.M., and Taylor, G.F., 1982, Eastern Creek Volcanics as the source of copper at the Mammoth mine, Northwest Queensland: BMR Journal of Australian Geology and Geophysics, 7, 93-98.

Scott, D.L., Rawlings, D.J., Page, R.W., Tarlowski, C.Z., Idnurm, M., Jackson, M.J., Southgate, P.N., 2000. Basement framework and geodynamic evolution of the Palaeoproterozoic superbasins of north central Australia: an integrated review of geochemical, geochronological and geophysical data. Australian Journal of Earth Sciences 47, 341-380.

Sibson, R.H., 1985. Short notes. A note on fault reactivation. Journal of Structural Geology, 7, 6, 751-754.

Sibson, R.H., 1994. Crustal stress, faulting and fluid flow. In: Parnell,J. (Ed) Geofluids: Origin, migration and evolution of fluids in sedimentary basins: Geological Society of London, Special Publication, 78, 69-84.

Sibson, R.H., 1998. Brittle failure mode plots for compressional and extensional tectonic regimes. Journal of Structural Geology, 20, 655-660.

Southgate, P.N., Bradshaw, B.E., Domagala, J., Jackson, M.J., Idnurm, M., Krassay, A.A. Page, R.W., Sami, T.T., Scott, D.L., Lindsay, J.F. McConachie, B.A., Tarlowski, C., 2000. Chronostratigraphic basin framework for Palaeoproterozoic rocks (1730–1575 Ma) in northern Australia and implications for base-metal mineralisation. Australian Journal of Earth Sciences, 47, 461–483.

Van Dijk, P.M., 1991, Regional Syndeformational Copper Mineralization in the Western Mount Isa Block, Australia, Economic Geology, 86, 278-301.

Wang, S., Williams, P.J., 2001. Geochemistry and origin of Proterozoic skarns at the Mount Elliott Cu-Au (-Co-Ni) deposit, Cloncurry district, NW Queensland, Australia. Mineralium Deposita, 36, 109-124.

Williams, P.J., 1998. Metalliferous economic geology of the Mount Isa Eastern Succession, Queensland. Australian Journal of Earth Sciences, 45, 329-341.

Zhang, X., Sanderson, D.J., 2002. Numerical modelling and analysis of fluid flow and deformation of fractured rock masses. Pergamon, Elsevier, Oxford. 288 p.

Numerical Modelling of the Leichhardt River Fault Trough; insights into basin development, fluid flow and associated mineralising systems

John G. McLellan

Predictive Mineral Discovery Co-operative Research Centre, Economic Geology Research Unit, James Cook University, Townsville, Queensland, 4811.

* Corresponding author. Tel: +61-7-6774; fax: +61-7-4725-1501. E-mail address: John.McLellan@jcu.edu.au

Abstract

The Leichhardt River Fault Trough (LFRT) in the western Mount Isa Inlier, northwest Queensland, provides a good example of a relatively well preserved rifted basinal architecture, which allows a framework for rigorous testing of numerical scenarios in such a setting. The Pb-Zn-Ag and Cu mineral endowment of the Mount Isa Inlier is world-class, and this provides a strong foundation for current and future exploration in the region. The LRFT has undergone a protracted deformational history and here the deformation, fluid flow and mineralisation processes are addressed by several simulations in the numerical code FLAC3D. During extensional rifting deformation is partitioned, with major structures accommodating the majority of the strain, resulting in high shear strain, dilation and fluid flow in basin bounding structures, particularly on the western basin margin. Extension and topography play an important role in facilitating downward migration of fluids deeper into the system, and basin inversion facilitates mixing of fluids before migration to depositional sites in the hangingwall sediments of the Isa Superbasin. The hangingwall sediments and intersections of N-S trending basin bounding structures and E-W trending structures are key areas for focussing shear strain, dilation, high fluid flux and potential mineralisation in the Leichhardt River Fault Trough, western Mount Isa Inlier.

Keywords: Numerical modelling, FLAC, fluid flow, Pb-Zn, Cu, mineralisation, Mount Isa Inlier

1. Introduction

The Mount Isa Inlier (Fig. 1) is host to many economic deposits, some world class, such as Mount Isa Cu, Mount Isa Pb-Zn-Ag, Century Zn-Pb-Ag, Cannington Ag-Pb-Zn, and Ernest Henry Cu-Au. The sediment hosted Pb-Zn-Ag deposits of this region have a varied genetic interpretation, from synsedimentary-(exhalative) to early diagenetic, and also syntectonic in origin (e.g. Perkins, 1997; Broadbent *et al*. 1998; Large *et al*. 1998; Cooke *et al*. 2003; Chapman, 2004; Davis, 2004). This varied interpretations of deposit genesis leads us to ask questions about exploration, and how do we predict new mineral discoveries if these types of deposits are interpreted to form in many different ways? The process driven approach is a robust technique in understanding and evaluating why deposits may have formed under certain circumstances. The Predictive Mineral Discovery Cooperative Research Centre (pmd*CRC) has tackled this problem by using a process understanding framework based around five key questions; 1) what is the geodynamic setting and pressure-temperature history of the system? 2) what is the architecture of the system? 3) what are the fluids, their source and/or reservoirs? 4) what are the fluid flow drivers and pathways? 5) what are the metal transport and depositional processes? In understanding the processes involved we should therefore enrich our knowledge of the system and subsequently enhance our predictive capacity. The economic mineralisation in the Mount Isa Inlier is largely a result of the storage and transport of hydrothermal fluids during the tectonothermal evolution of the terrane. Many fluid sources have been discussed (e.g. Heinrich *et* al., 1995; Polito *et al*, 2006a; 2006b; Kendrick, 2006; 2007) but it is the timing and transport of these fluids that is ultimately important if we want to engage our knowledge in a predictive capacity. Understanding the main processes involved in fluid transport towards depositional sites and what drives these processes is a key aspect in understanding the mineralising system.

This project investigates the coupled interaction of deformation, fluid flow and heat transport during basin development and basin inversion, and concentrates on the main processes involved during these events e.g. rifting, sedimentation, burial, compaction, diagenesis, and basin inversion. The Leichhardt River Fault Trough (LRFT) (Fig. 2) covers an area of approximately 4000 km^2, and is host to many economic deposits. It is

an important prospective region in the Mount Isa Inlier and much of the original basinal architecture is largely still preserved. This provides a strong framework for developing a conceptual model, to test and understand the processes involved in mineralisation of the area.

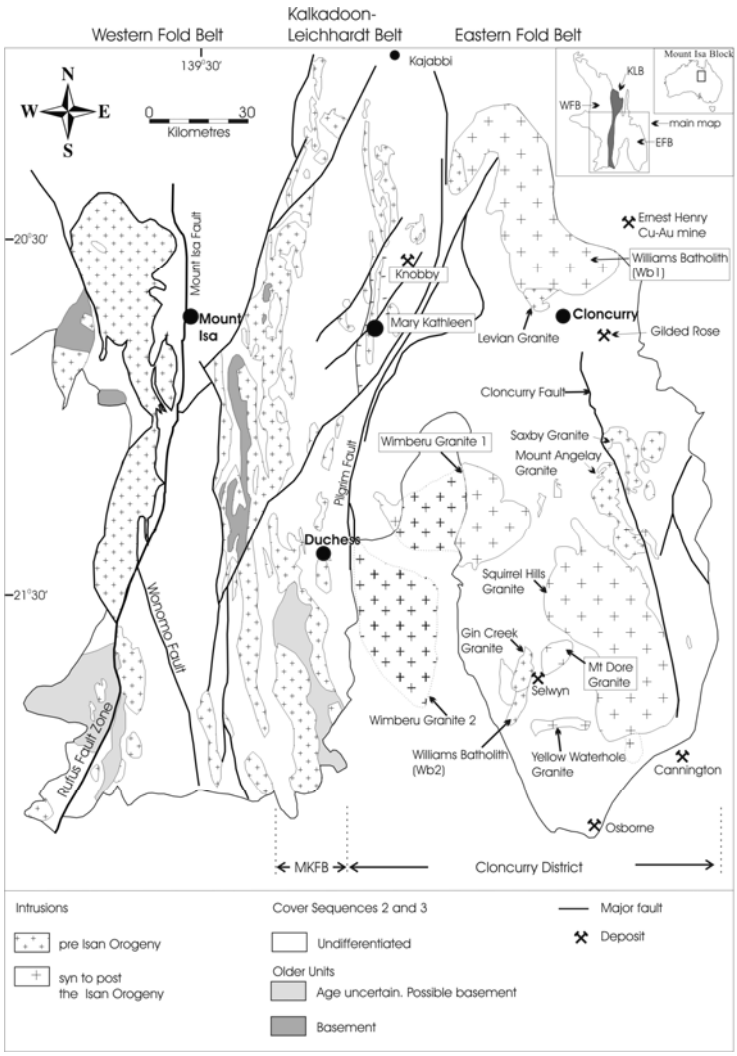

Fig. 1. Location (inset) and general geology of the Western, Kalkadoon-Leichhardt and Eastern Fold Belts showing the further division of the Eastern Fold Belt into the Mary Kathleen Fold Belt (MKFB) and Cloncurry District after McLellan & Oliver (2008). The spatial distribution of Cover Sequences 1-3 and intrusive features pre- and syn- to post-Isan Orogeny are shown, as well as some of the major mineral deposits in the Eastern Succession (redrawn from Foster, 2003, adapted from original geology by Blake, 1987 and interpreted geology from NWQMPR, 2000).

Fig.2. Simplified geological map of the Mt Isa Western Succession, indicating the main structural trends, basic lithologies and several of the main deposits. Dashed black line indicates the approximate outline of the Leichhardt River Fault Trough area.

The main aims of this study are to investigate and identify key areas, in a conceptual sense, that may provide information in the architectural development of the system, the potential fluid reservoirs and the fluid flow drivers and pathways. The answers to these questions may then indicate key areas, again in a conceptual sense, that have an increased prospectivity value in terms of economic mineralisation in the region. Although this study will be focussed on Pb-Zn-Ag mineralising systems, it could apply to many other mineralising systems that have similar generic architecture and conditions.

2. Geology of the Mount Isa Inlier

The Mount Isa Inlier of Northwest Queensland (Fig. 1) comprises three major tectonic units; from west to east, the Western Fold Belt (Western Succession), the Kalkadoon-Leichhardt Belt and the Eastern Fold Belt (Eastern Succession), which are predominantly north-south trending sedimentological and structural domains (Blake & Stewart, 1992; O'Dea & Lister, 1997; O'Dea *et al.* 1997). The area is characterised by lower to middle Proterozoic meta-sedimentary rocks, rhyolitic and basaltic meta-volcanic rocks, gabbro, dolerite and widespread I-type granitoids. The major stratigraphic cycles and basin-forming events of the region have been described by many previous authors (e.g. Blake & Stewart, 1992; Page & Sun, 1998; Southgate *et al*., 2000) as have the main structural events (e.g. Page & Bell, 1986; Etheridge *et al*. 1987; Holcombe *et al.* 1991). Following many episodes of intracratonic rifting and basin formation, the main period of protracted deformation that is closely associated with the majority of mineralisation in the region took place during the Isan Orogeny (ca. 1600-1500 Ma; Blake & Stewart, 1992).

2.1 Western Succession and basin formation

Historically the Mount Isa Inlier has been subdivided into three main cover sequences that unconformably sit on ca. 1800 Ma or older crystalline basement, which is best exposed in the Kalkadoon- Leichhardt Block (Blake, 1987). Relatively recent chrono-stratigraphic work by several authors suggest a new basin subdivision nomenclature (e.g. Domagala et al., 2000; Idnurm, 2000; Jackson, et al., 2000; Krassay et al., 2000a; 2000b; Page, et al., 2000; Southgate, et al., 2000a; 2000b). Regionally correlatable superbasins or stratigraphic successions are now recognized, namely the Leichhardt (ca. 1800 to ca. 1740 Ma), the Calvert (ca. 1730 to ca. 1670 Ma), and the Isa (ca. 1670 to 1575 Ma) Superbasins, all of which are still variably preserved to some extent in the Leichhardt River Fault Trough of the Mount Isa Inlier.

2.2 Leichhardt Superbasin

The Leichhardt Superbasin (ca. 1800 to 1740 Ma) is essentially comprised of a thick package of proximal conglomeratic sediments, both felsic and mafic volcanics, and well sorted marine and sandstone dominated sediments (Jackson, et al., 2000; Polito *et al*.,

2006a; 2006b) and formed during an early rifting event. This E-W to ENE-WSW rifting event was most likely influenced by older basement structures, where basement may have somewhat controlled the orientation of younger growth faults and sedimentation patterns as a result of the regional stress field (Gibson, 2005). In the centre region of the LRFT the Mount Gordon Arch (Fig. 3) has been interpreted as an original basin feature and the result of the early rifting event (Derrick, 1982), however, it has also been interpreted as a large scale regional fold formed during the Isan Orogeny D_2 deformational event (Bell, 1983). There is strong evidence for sedimentation control exhibited by the Mount Gordon Arch and Derrick (1982) believed that it has acted as an emergent topographic high. This interpretation of the Mount Gordon Arch as an original feature requires that the main structural features or LRFT bounding structures be normal faults e.g. the Twenty-nine Mile and Lake Julius Fault systems, and Gibson (2005) has demonstrated that these two systems are co-incident with marked changes in stratal thickness and changes in basin geometry.

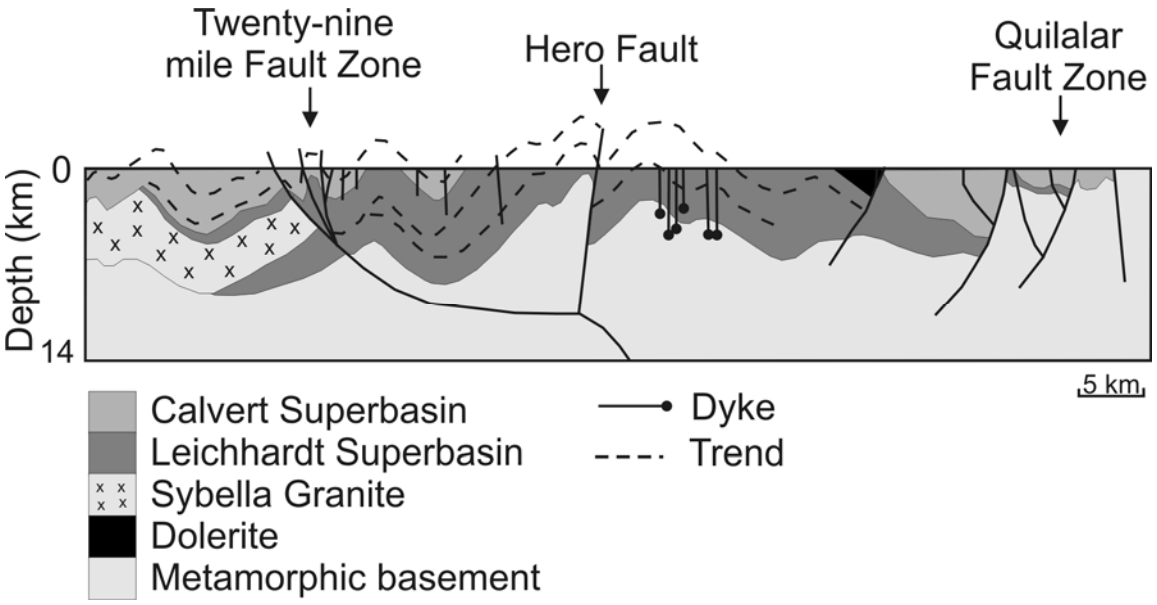

Figure 3. East-west structural cross section through the Mount Gordon Arch indictaing the eastern and western margins of the Leichhardt River Fault Trough. Modified from Gibson et al. (2005).

2.3 Calvert Superbasin

The Calvert Superbasin is comprised of fluvial to marine conglomeratic sediments, both felsic and mafic volcanics, carbonates and sandstone dominated sediments (Jackson, et al., 2000; Polito *et al*., 2006a) and formed during an N-S to NNE-SSW rifting event (ca. 1730 to 1670 Ma; Gibson, 2005). This package was deposited on an erosion surface that is related to the Wonga extensional event (ca. 1755 to 1730 Ma; Jackson *et al*., 2000; Southgate *et al*., 2000a). There is good evidence that several of the prominent E-W striking structures in the LRFT (e.g. Investigator fault, Crystal Creek fault) represent growth faults as they highlight changes in sedimentary thickness (Derrick, 1982; O'Dea *et al*., 1997; Betts *et al.*, 1998), however, there is still some controversy over the exact timing of these structures and whether reactivation played a role, and again there is also potential for deeper structures to have played a key role in the positioning of these shallower fault structures.

2.4 Isa Superbasin

The Isa Superbasin (ca. 1665 to 1575 Ma) is comprised of conglomeratic sediments, arenites, mudstones and carbonaceous siltstones and shales, the latter being a common host rock for Pb-Zn-Ag mineralisation in the region. In the LRFT the Mount Isa Group evidence of sedimentation and transgression has been dated at ca. 1674 to 1688 Ma (Southgate *et* al., 2000a; Neuman *et al*., 2005). The Isa Superbasin sits unconformably above the Calvert Superbasin, with a time delay of approximately 20 Ma, and this basin forming event coincides with the cessation of the proposed extensional unroofing of the Sybella Batholith as a result of NNE-SSW extension (Gibson, 2005). Basin closure is thought to have occurred at the onset of the Isan Orogeny, as much of the deformation and metamorphism in the Mount Isa Inlier post-dates the cessation of sediment deposition (Blake, 1987). In terms of basin architecture and the tectonic evolution of the Isa Superbasin there are two main geodynamic models that have been discussed in the literature a) strike-slip (e.g. Southgate *et al*., 2000b) and b) rift-sag (O'Dea *et al*., 1997), with earlier work within the pmd*CRC by Gibson (2005) demonstrating that the rift-sag model may be more appropriate to the LRFT and southern Lawn Hill Platform.

2.5 Regional deformation, metamorphism and metallogenesis

A complex and protracted deformational and metamorphic history is evident within the Mount Isa inlier, related to cycles of extension and shortening between 1900 and 1500 Ma. Following the 'Wonga' extensional event (ca. 1750 to 1730 Ma), there are three main deformational events during the Isan Orogeny (D_1, D_2 and D_3) as initially proposed by Bell (1983) in the western Mount Isa inlier, and a succinct description of the metamorphic history of the inlier has been presented by Rubenach (2007). The tectonothermal evolution of the Isa Inlier has been mostly driven by mafic underplating, migmatisation, felsic intrusives and a general abundance of high heat forming elements in the Proterozoic crust (see Rubenach, 2007; Rubenach this volume), Timing of the main events have always remained controversial and as new age dating techniques are employed the consensus is that the peak of metamorphism and the main structural east – west compressional event (D_2) across the whole Mount Isa Inlier is 1580 to 1595 Ma (Rubenach, 2007; Rubenach this volume). The Pb-Zn-Ag mineralising events are varied in age across the inlier with a broad scale younging of deposits in a general north-west trend e.g. from Cannington pre 1677± 9 Ma (Page and Sun, 1998) to Century 1575± 5 Ma (Carr, 1996). As eluded to earlier, interpretation of the genesis of these deposits e.g. Mount Isa, Hilton, George Fisher, Cannington, Century, McArthur River, vary from mineralisation taking place at or just below the seawater-sediment interface (Eldridge *et* al, 1993; Large, *et al* 1998), or up to 2 km depth (Broadbent, *et al* 1998). So in relation to the main deformational events there appears to be a vast timing overlap particularly with regards to the main east-west D_2 deformation in these Pb-Zn-Ag deposits. On the other hand, there is confidence that the majority of the Cu and Cu-Au mineralisation across the inlier has taken place during the D_3 deformational event (ca. 1550 to 1530 Ma) where a strong structural control is evident (see McLellan, Miller, Keys this volume). In summary the main tectonic events in the overall history of the LRFT based the work of Gibson (2005) and others are shown in Table 1.

Table.1. Summary of the main tectonic events

Event	Tectonics	Age
Basin Formation		
Leichhardt	ENE-WSW Rifting	1800 - 1740 Ma
Calvert	N-S Rift-drift	1730 - 1670 Ma
Isa	Sag	1660 - 1595 Ma
Basin Inversion		
D_1	N-S thrusting	1640 Ma
D_2	E-W Compression	1595 Ma
D_3	ESE-WNW Compression	1550 Ma
D_4	ENE-WSW Compression	1530 Ma

3. Numerical Modelling and Conceptual Models

Numerical modelling techniques have been proven as a very useful tool in simulating coupled deformation, thermal and fluid flow processes (e.g. McLellan *et al.*, 2004; Oliver *et al.*, 2006), and they are becoming more widely used in specifically targeting mineralisation (e.g. Schaubs *et al.*, 2006; McLellan *et al.*, 2007). However, the most useful outcome from a modelling study is the process understanding or the knowledge gained in the relevant mineral system during the multiple scenario testing that is a generic part of the modelling process. The main aims were to test the processes involved during basin rifting and basin inversion, and examine the likely areas for fluid focusing as a result of the mechanical and architectural development of the region. In this we hope to understand the main processes involved during the tectonic history of the LRFT and highlight areas that would be most likely to promote focusing of fluid flow.

3.1 FLAC 3D and theoretical relationships

The software package FLAC3D is best suited for modelling coupled deformation and fluid flow in porous media. The classical Mohr–Coulomb material with non-associated plasticity is most suited to represent the rheology of the mid to upper crust (Vermeer and de Borst, 1984; Hobbs et al., 1990; Ord and Oliver, 1997). A Mohr–Coulomb material will deform elastically up to a yield point and then deform in a non-recoverable plastic manner (Ord and Oliver, 1997). The main advantage of using FLAC3D is the non-associated plasticity flow rule incorporated in the Mohr-Coulomb constitutive model, which allows us to accurately simulate deformation induced dilatancy, which in turn

focuses fluids, and hence, highlights areas of interest in any mineralising system. FLAC treats rock masses as a continua represented by average values of mechanical and fluid properties. Fluid flow obeys Darcys Law and is considered to be compressible.

$$V_i = k_{ij} \frac{\gamma_f}{\eta_f} \left(\frac{\partial H}{\partial X_j} \right) \tag{1}$$

where V_i is the Darcy fluid flow velocity (m s^{-1}), k_{ij} is the permeability tensor (m^2), γ_f is the specific weight (kg m^{-2} s^{-2}), η_f is the viscosity (kg m^{-1} s^{-1}) of the fluid, H is the hydraulic head ($P/\rho g + z$) (m) and X_j is the position of a material point. Darcy's Law shows that differences in hydraulic head are required for flow to occur, and a static homogenous rock package with topographic relief displays classical Darcian flow as a result of these head gradients. Darcy fluid flow vectors are by definition orthogonal to contours of hydraulic head in an isotropic medium with a constant density. However, most of the hydrodynamic action in the models is a consequence of the change of volume affecting the hydraulic head, induced as a consequence of the deformation of dilatant rock materials. During plastic deformation a Mohr–Coulomb material will shear, and this can be associated with dilation or a volume change. The microstructural processes involved have been highlighted by Vermeer and de Borst (1984), Ord and Oliver (1997), and more recently by Gow et al. (2002). During deformation rocks can compact and dilate, therefore dilation can be represented by both positive and negative values of strain:

$$\sin\psi = \frac{\varepsilon_v^p}{\gamma_s^p} \tag{2}$$

where ψ is the dilation angle, ε_v^p the rate of plastic volumetric strain, and γ_s^p is the rate of plastic shear strain. Local positive dilation is crucial in deforming porous media as it typically influences fluid flow direction more abruptly than the gentle gradients associated with topography or broadly distributed strains. For a more comprehensive explanation see Vermeer and de Borst (1984). The emphasis of previous work (e.g. Ge and Garven, 1992) has been focused on the elastic part of stress–strain behaviour (the poro-elastic effect) and has concentrated on the generation of regions of high pore pressures due to elastic decrease in total volume by an imposed stress. This typically results in fluid being 'squeezed' out of the stressed regions. In contrast, in poro-plastic

models high strain typically causes positive dilation of rocks and pore pressure decrease, and hence fluid is drawn in. Changes in volume due to plastic deformation are governed by the dilation angle of the rocks (ψ), and these changes in volume result in changes in pore pressure (Ord, 1991; Ord and Oliver, 1997). This effect on pore pressure is linked to changes in hydraulic head, which drives fluid flow, in accordance with Darcys Law. Therefore, volume change is related to changes in effective stress, which can lead to further plastic deformation, which feeds back to more volume change. Therefore this feedback between deformation and fluid flow continues in a coupled manner.

3.2 GOCAD

GOCAD v.2.08 (Earth Decision Sciences) is a 3D geologically optimised CAD package designed to model naturally occurring objects, in contrast to other traditional CAD packages that are based on mathematical formulations and polynomial algorithms to model manufactured objects. Mallet (2002) presents a comprehensive review of GOCAD and the mathematical descriptions and algorithms used in the discrete smooth interpolation algorithm (DSI) that represents the core of this application. In this study the general workflow was to create a representative solid state 3D model in GOCAD from a geological interpretation and basinal analysis of the region. Surfaces were created (Fig. 4) and volumes were then produced to represent the main lithological components of the interpreted geology (Fig. 5). Following volume creation a structured stratigraphic grid (SGRID) was produced which incorporated all the specific features of the model in hexahedral cells. The SGRID was then transferred into an XMML for Finite Element Mesh format (through pmd*CRC developed algorithms) which enabled the resultant mesh file to be imported into the numerical software FLAC3D (Fast Lagrangian Analysis of Continua, Cundall and Board, 1988). Once the numerical mesh was available in FLAC3D, data files could then be written for the many numerical simulations to proceed.

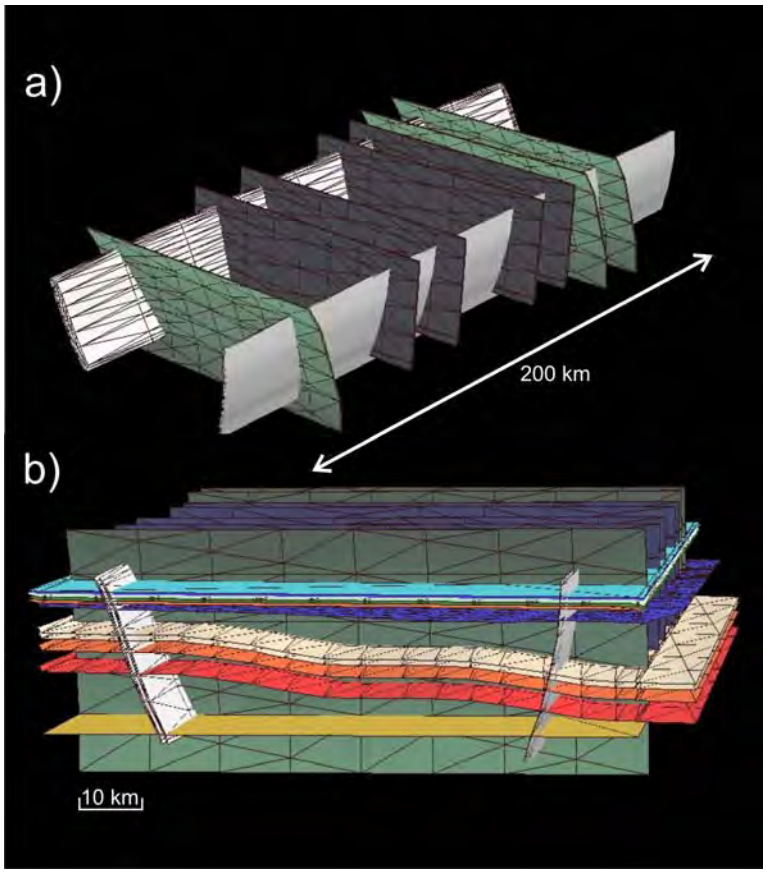

Figure 4. GOCAD surfaces a) N-S trending basin bounding faults and E-W trending rift faults looking from the SE, and b) all the major surfaces looking from the south.

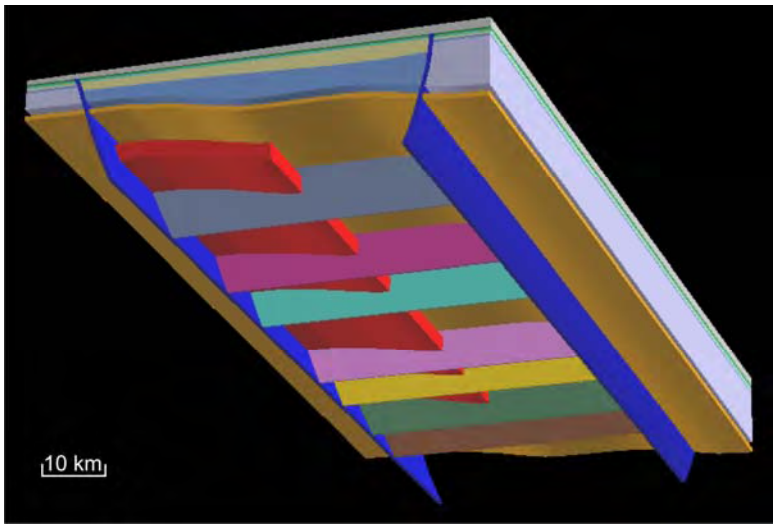

Figure 5. Solid geology model created in GOCAD looking from below and from the SE. Blue indicates the basin bounding faults, and red solid indicates the Sybella Batholith.

3.3 Conceptual models

The conceptual models tested in this study were based on the basin evolution and subsequent tectonic history of the LRFT in the Mount Isa Inlier. The preservation of some of the original features of the basin was helpful in determining a simple architecture for the geometric considerations, and thickness data was also invaluable in determining the extent and nature of the stratigraphic units. The conceptual model (Fig. 5) was developed to represent simplified basin geometry, and the main architecture consisted of basin bounding faults, normal faults, detachment zones and the main stratigraphic units, which was then converted into a numerical mesh (Fig. 6). Thickness data (Table. 2) was averaged and based on previous work carried out by Gibson (2005), with a general east thickening and north thickening sedimentary wedge applied. A simplification of the main stratigraphic units was applied, which involved the many units in the Leichhardt and Calvert Superbasins being assigned into a classification of aquifer or aquitard status based on the proposed permeability evolution of the basin (Polito *et al*, 2006a). The permeability evolution involved during burial and diagenesis of the stratigraphy was a distinct cementation of the upper units in both the Leichhardt and Calvert Superbasins during deposition. The lower units in the basins e.g. the Mount Guide and Lena Quartzite in the Leichhardt Superbasin display high fluid-rock ratios and diagenetic alteration and have been interpreted to be the metal-bearing aquifers and the most likely metal source for many of the Pb-Zn-Ag deposits in the area. The upper units however, have cemented very early and have acted as aquitards (Polito *et al.* 2006a). In the Calvert Superbasin the Bigie and Surprise Creek Formation have been interpreted as aquifers in the system, with the remaining units above sealing or cementing early in the basin history and therefore acting as aquitards. The conceptual model therefore has a distinction within these basins that include the work of Polito *et al*. (2006a) and divides the both the Leichhardt and Calvert Superbasins into aquifer and aquitard units.

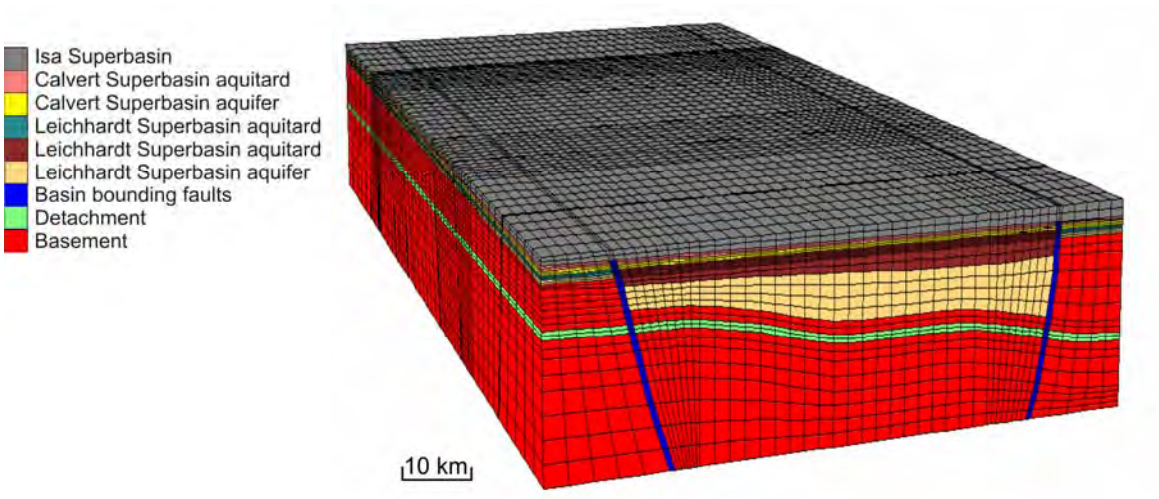

Figure 6. Numerical mesh for FLAC3D, looking from the SW.

Table. 2. Stratigraphic thickness estimate data of the LRFT for the conceptual model.

Superbasin	Units	South	Centre	North	Max Avg. Thickness
Isa	Magazine shale				***1 - 2 km***
	Spear/Kenedy siltstone				
	Urquart shale	400	400		
	Native Bee siltstone		500 - 1000		
	Moondara/Gunpowder	500			
Calvert	Torpedo Creek	100	300	500	***2 - 5 km***
	Surprise Creek (aquifer)	100	300	500	
	Bigie Formation (aquifer)	100	300	500	
Leichhardt	Quillalar Formation	1000	1500	2000	***10 - 15 km***
	Myally Subgroup	1200	2000	4000	
	Eastern Creek Volcanics	1000	3000	5000	
	Mt Guide Quartzite (aquifer)	2000	3000	4000	
	Bottletree Formation (aquifer)	2000	3000	4000	

Values are given in metres (except where stated) and are estimated in some instances and given an average value for the conceptual model. Data sourced from Gibson (2005), Jackson et al. (2000) North Aust. Basin Resource Evaluation (NABRE), amongst others. Blank fields indicate poor or no available data.

The conceptual models were constructed to represent the basin at the approximate times of mineral deposition, whether mineralisation is the result of a synsedimentary/exhalative (modelled by a period of extension) or a syntectonic genetic model (modelled by a period of compression). Boundary conditions applied to the models were representative of the appropriate stress regimes (as seen in Table. 1), with extension representing a possible Isa 'sag' phase (**Model 1**), and compression representing a basin inversion 'D_2' phase (**Model 2**). Transpression was also applied to evaluate the potential for different fluid

pathways and strain localisation during a switch in stress regime (local or regional) and which could quite possibly also be considered as a simple scenario for later stage Cu mineralisation during the Isan D_3 deformational event (**Model 3**). Physical properties and model parameters were based on several previous authors (e.g. Ord & Oliver, 1997; McLellan *et al*., 2004; Oliver *et al*., 2006; Schaubs *et al*., 2006) and are listed in Table. 3.

Table. 3. Physical properties and model input paramaters

MODEL INPUTS	Density (kg m-3)	Bulk Modulus (Pa)	Shear Modulus (Pa)	Cohesion (Pa)	Friction angle °	Dilation angle °	Permeability (m2)
Basement	2650	4.95×10^{10}	2.97×10^{10}	5.00×10^{7}	30	3	1.00×10^{-16}
Detachment	2500	2.30×10^{8}	2.00×10^{8}	3.00×10^{5}	30	3	8.00×10^{-14}
Sybella Granite	2650	3.33×10^{9}	2.00×10^{9}	1.00×10^{7}	30	4	1.00×10^{-16}
Leichhardt Aquifer	2400	3.20×10^{10}	1.92×10^{10}	$4..00 \times 10^{6}$	30	4	1.00×10^{-13}
Leichhardt Aquitard	2400	3.20×10^{10}	2.20×10^{10}	$8..00 \times 10^{6}$	30	4	1.00×10^{-15}
Calvert Aquifer	2400	3.20×10^{10}	1.92×10^{10}	$4..00 \times 10^{6}$	30	4	1.00×10^{-13}
Calvert Aquitard	2400	3.20×10^{10}	2.20×10^{10}	$8..00 \times 10^{6}$	30	4	1.00×10^{-15}
Mt Isa Group	2400	3.20×10^{10}	2.20×10^{10}	$8..00 \times 10^{6}$	30	4	1.00×10^{-15}
Basin Bounding Faults	2400	2.30×10^{8}	2.00×10^{8}	3.00×10^{5}	30	4	1.00×10^{-13}
Rift Faults	2400	2.30×10^{8}	2.00×10^{8}	3.00×10^{5}	30	4	1.00×10^{-13}

Note: Basin bounding faults relate to the N-S trending structures, rift faults relate to the E-W trending structures.

4. Numerical Modelling Results

The three models tested included a Mohr-Coulomb constitutive model and initial pore pressure gradients approximately at 0.5 x lithostatic conditions, which seemed appropriate in relation to the history of basin subsidence and consequent deformation. The models were subjected to lateral strain, in some instances to a maximum of 20% bulk shortening, with the sides of the model being fixed to remain planar and the top of the model free to deform in any manner, which would either allow sag or topography to form during deformation.

4.1 Model 1: extension and sag phase rifting

During the initial stages extensional deformation shear strain is focussed within the basin bounding faults and to a lesser extent, the detachment zone (Fig. 7a). The western fault accommodates more of the shear strain during extensional deformation than the eastern fault (Fig. 7b), and maximum values of shear strain rates (Fig. 7c) can be seen in shallow levels of the basin (1-3 km) and also at depth near the detachment fault and basin

a)
bounding fault intersection (8-10 km) with both upward and downward fluid migration also evident.

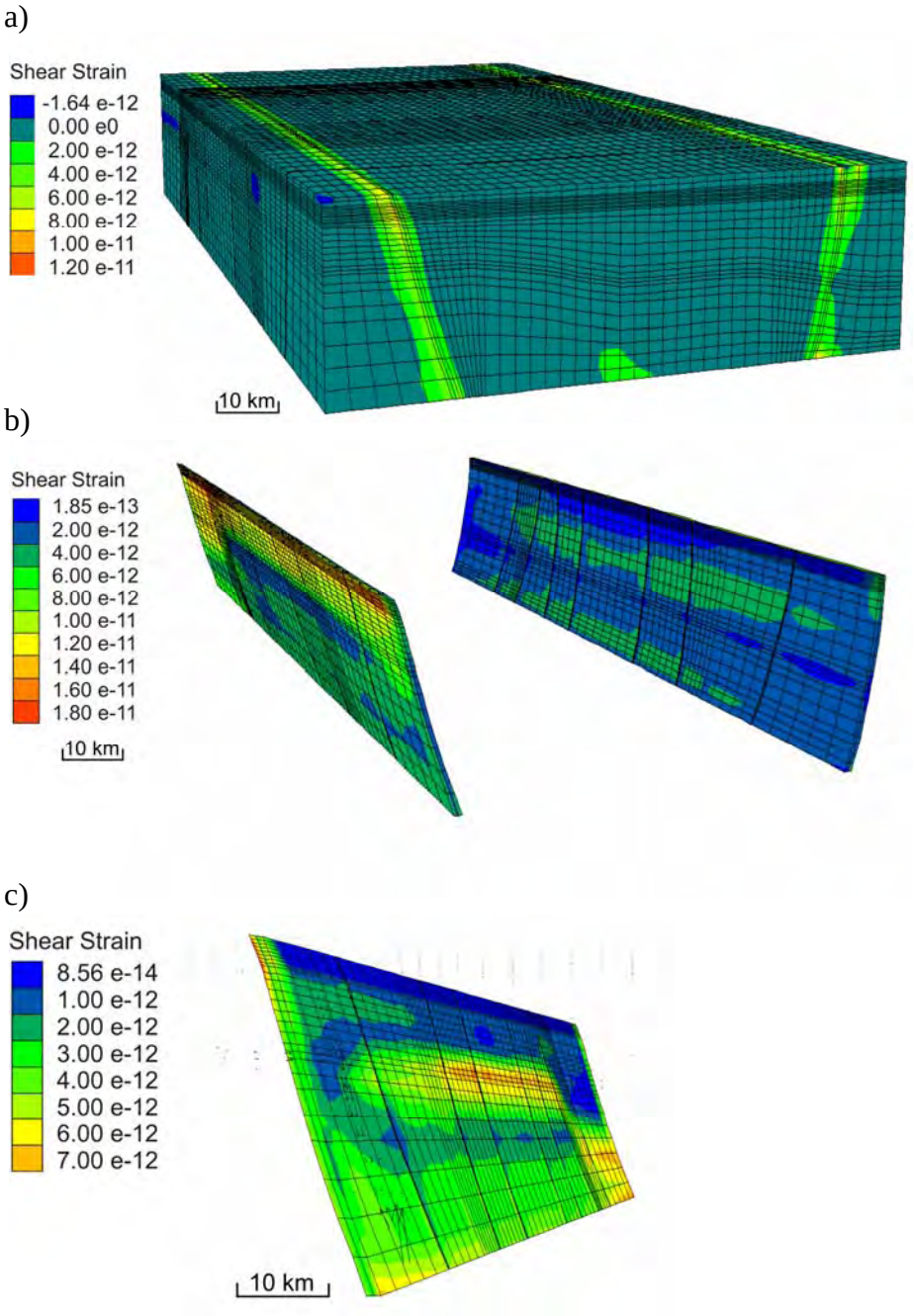

Fig. 7. Numerical output at 1% bulk extension a) contours of shear strain rates b) contours of shear strain rates on basin bounding faults, and c) contours of shear strain rates and fluid flow vectors on the western basin bounding fault.

As extension progresses the focussing of shear strain within fault zones becomes more evident, particularly in the western side of the basin (Fig.8a). A volumetric increase is also noted within areas undergoing higher levels of strain e.g. basin bounding faults, and this is also seen within the detachment zone and at shallow levels within the basinal sediments (Fig. 8b).

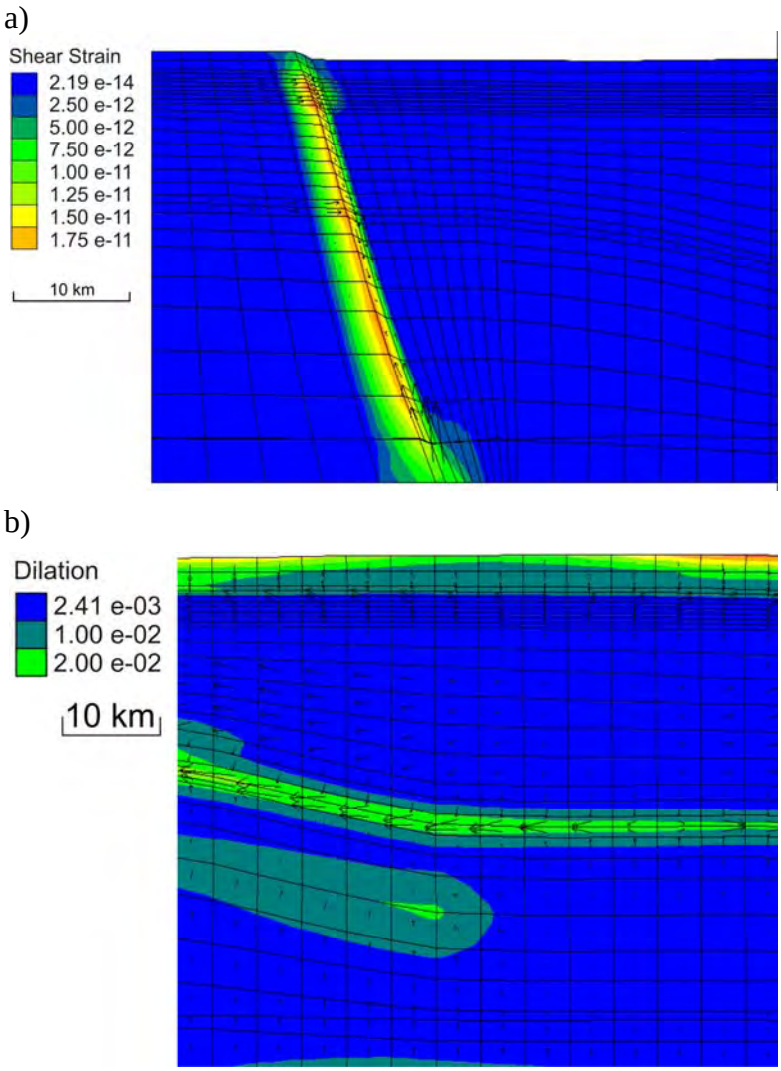

Fig. 8. Numerical output at 3% bulk extension a) contours of shear strain rates on the western basin bounding fault, b) contours of dilation and fluid flow vectors in the model centre and detachment zone indicating topographic driven fluid flow

At increased strains topography starts to form on the top surface of the model, which has an effect in driving flow from the footwwall into the faults and hangingwall aquifers (Fig. 9a). In the centre of the model, where topographic relief acts as an analogue for the Mount Gordon Arch, fluids are driven down into the Calvert and Leichhardt aquifer units (Fig 9a) and high values of cumulative fluid flux can be seen in the Calvert and Leichhardt aquifer units as well as the detachment zone (Fig. 9b). Volumetric increase or dilation is greatest around the western basin boundary and in the top 2 km of the model (Fig. 9c), and similar results are found through continual extensional deformation with both upward and downward migrating fluids (Fig. 10).

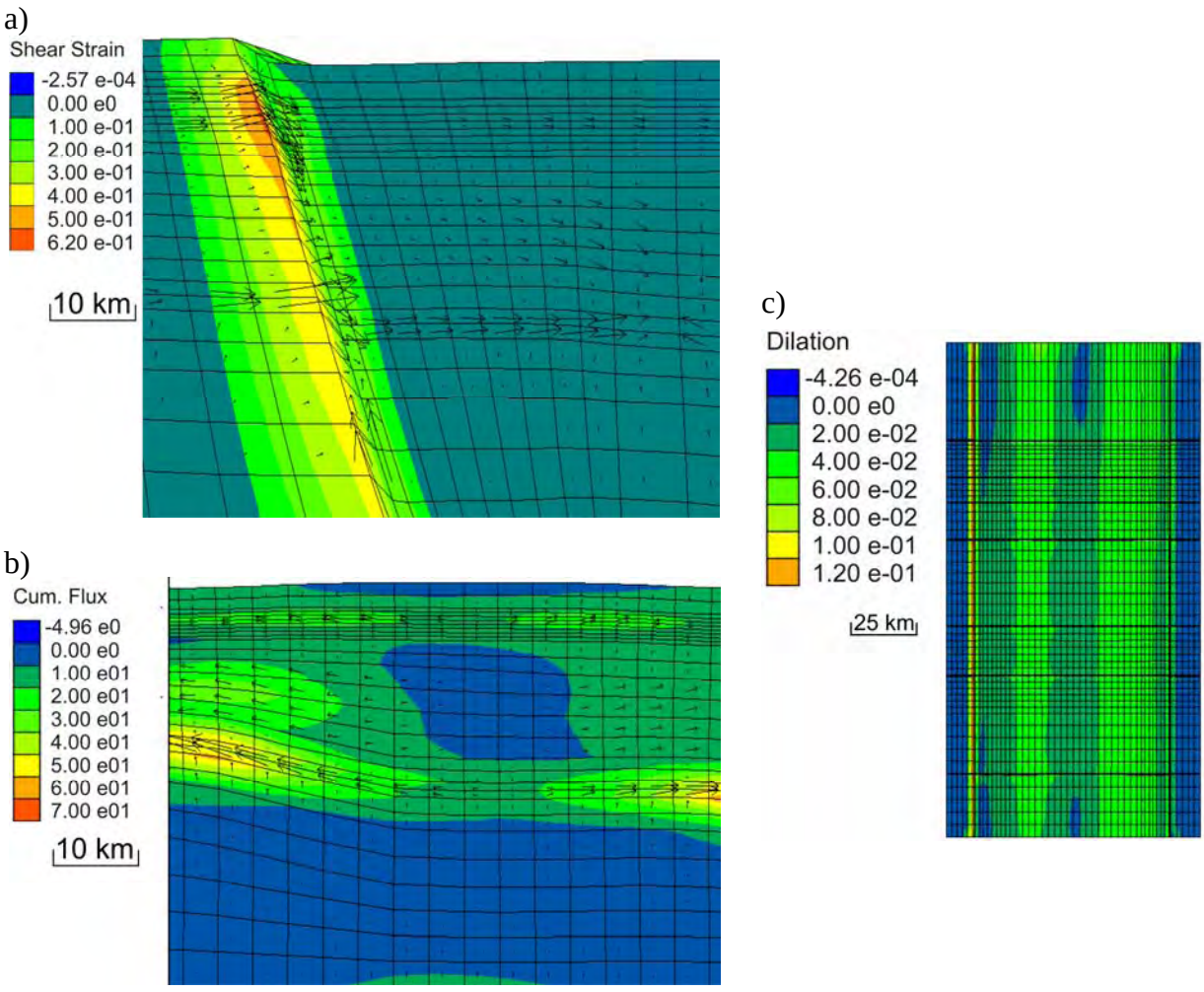

Fig. 9. Numerical output of a) shear strain increment on the western basin bounding fault, b) cumulative fluid flux values and fluid flow vectors indicating high levels of flow in the aquifer units and detachment zone, and c) plan view of dilation at 1.7km depth, within the Isa Superbasin.

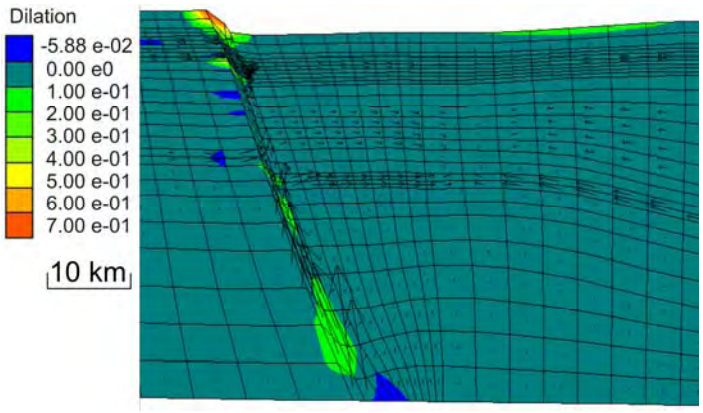

Fig. 10. Numerical output of dilation and fluid flow vectors in the western basin bounding fault, indicating fluid mixing.

4.2 Model 2: basin inversion

At early stages of basin inversion high strain zones are focused in and around the basin bounding faults and detachment zone (Fig. 11a), with little to no dilation noted within the model (Fig. 11b). As deformation progresses these conditions remain stable until 5% bulk deformation where areas of dilatancy are evident within the Isa Superbasin sediments, particularly around the basin bounding faults (Fig. 12a), and the highest values of cumulative fluid fluxes can be seen within the basin bounding faults at depth (Fig. 12b).

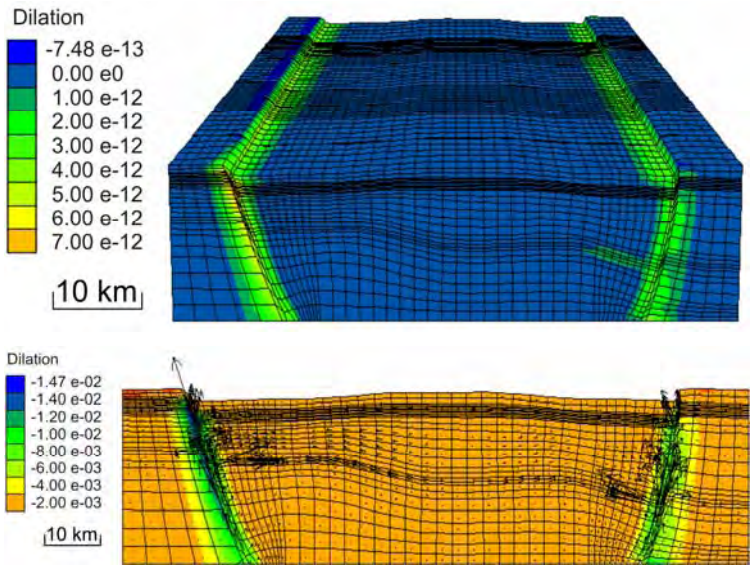

Fig. 11. Numerical output of a) shear strain rate during early stages of compression, b) dilation and fluid flow vectors at early stages of compression indicating upward migration of fluids and contraction.

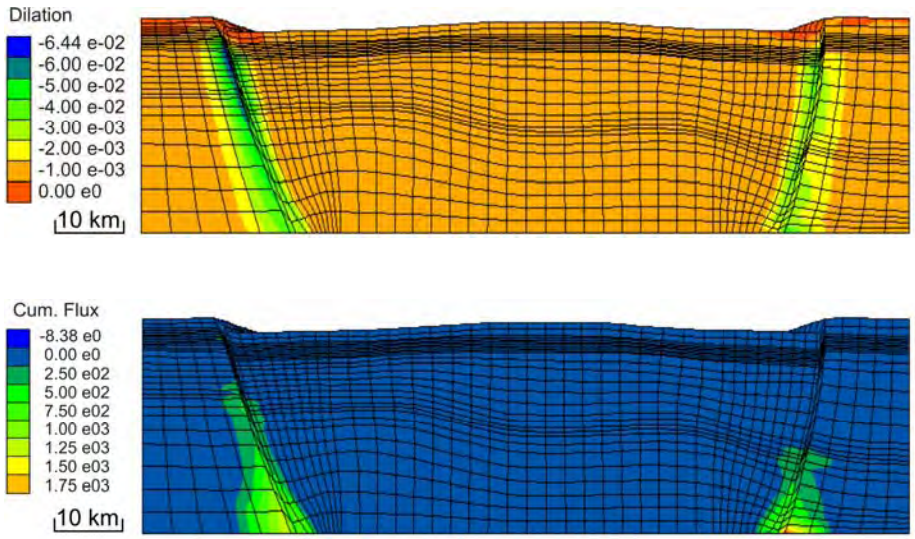

Fig. 12. Numerical output of a) dilation at around 5% bulk deformation, b) cumulative fluid flux values indicating highest values proximal to the basin bounding faults.

Both east and west sides of the Leichhardt River Fault Trough display similar patterns of deformation, dilation and fluid migration, however the west bounding fault appears to be more active and results in higher overall values of cumulative fluid flux, shear strain and volumetric increase or dilation. The western basin bounding fault and associated hangingwall area of the Isa Superbasin display the highest values of dilation, and fluid flow vectors are focused towards these areas (Fig. 13a). Values of cumulative fluid fluxes are also high in corresponding areas of the Isa Superbasin (Fig. 13b), which is in the top 2-3 km of the model. An important aspect when interrogating the distribution of cumulative fluid flux values is the presence of high values at the intersections of the N-S trending basin bounding faults and the E-W trending rift faults (Fig. 13c), where fluid flow vectors and dilation is also focused.

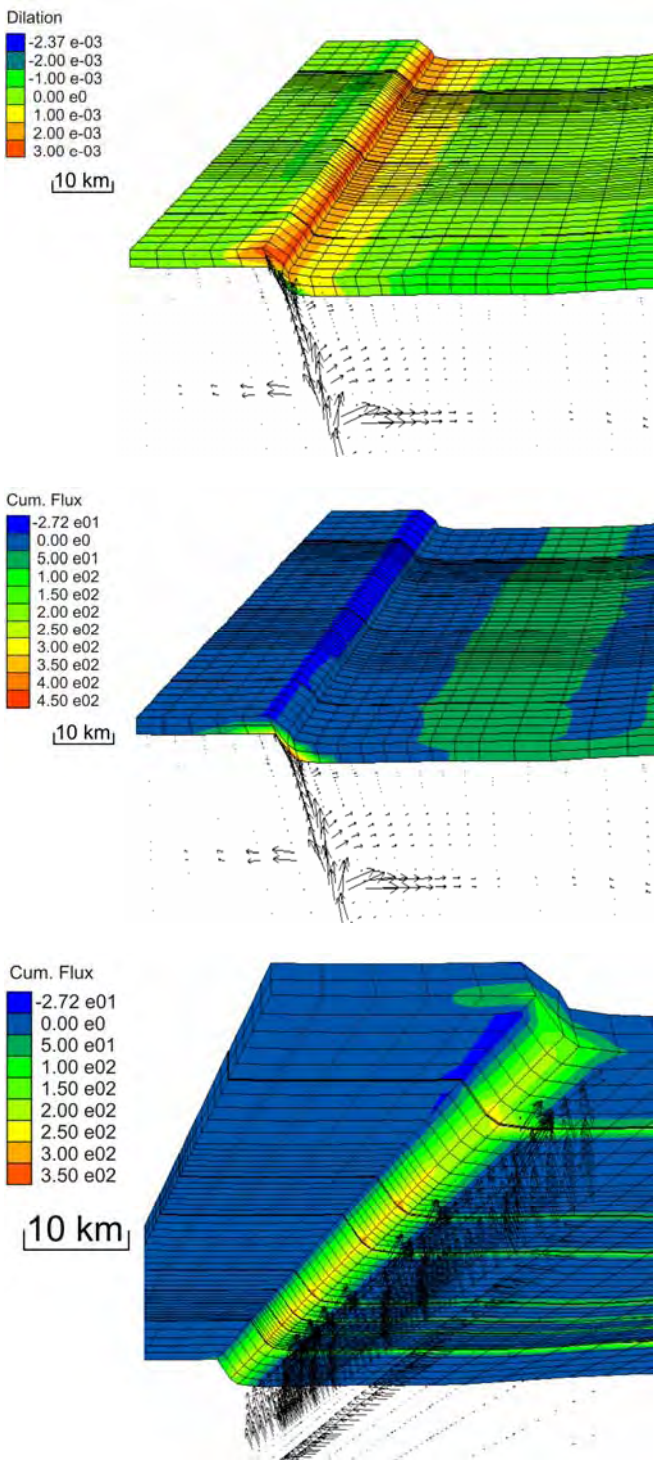

Fig. 13. Numerical output of a) dilation and fluid flow vectors at around 14% bulk deformation indicating highest values proximal to the basin bounding fault, b) fluid flow vectors and cumulative fluid flux values indicating highest values proximal to the basin bounding faults, and c) fluid flow vectors and cumulative fluid flux values indicating highest values around fault intersections and fluid focussing.

4.3 *Model 3*: transpression

At early stages of transpression dilation is evident in the Isa and Calvert Superbasins, particularly in the hangingwall of the main basin bounding faults (Fig, 14a). The western fault appears to localise dilation more than its eastern counterpart, which is also true for cumulative fluid flux values (Fig. 14b).

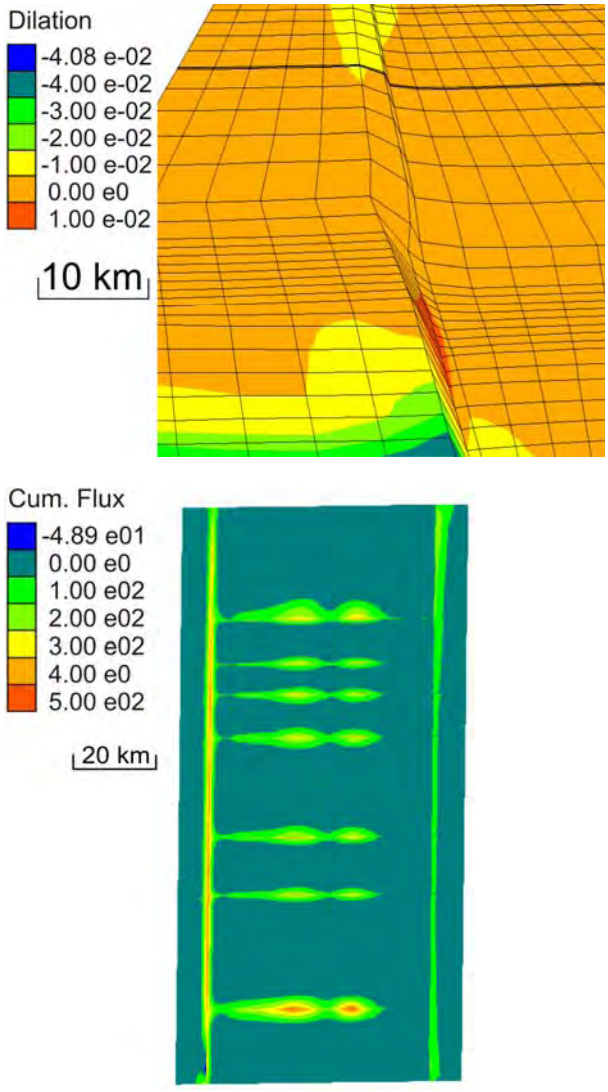

Fig. 14. Numerical output of a) dilation during early stages of transpression indicating highest values proximal to the basin bounding fault, b) plan view of cumulative fluid flux values indicating highest values proximal to the western basin bounding fault and centre of the model above the Mt Gordon Arch region as a result of topographic flow

As deformation progresses shear strain localises in basin bounding faults but also forms prominent NE trending structures (Fig. 15a) which is a common fault orientation in the Mount Isa Inlier. Highest rates of volume increase as a result of deformation are intimately associated with the areas of high shear strain (Fig 15b), which again is prominent on the western fault margin.

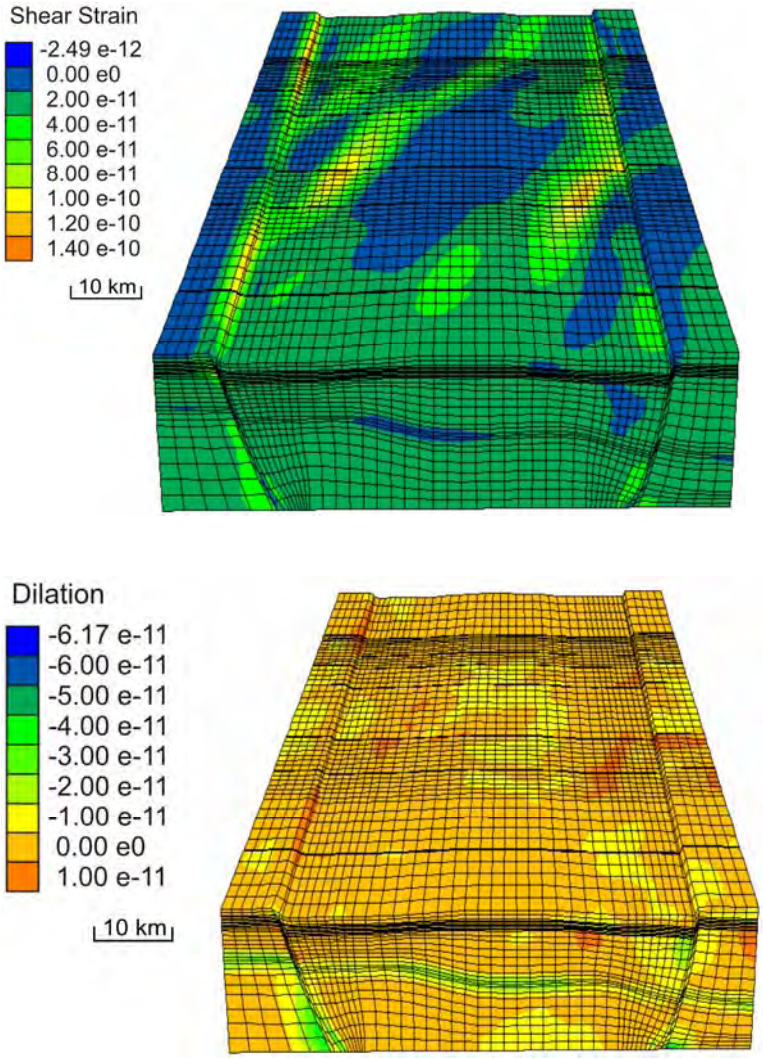

Fig. 15. Numerical output of a) contours of shear strain rate at 3% bulk deformation indicating the formation of NE structural trends and high values associated with basin bounding faults, b) volumetric increase in the same regions as highest shear strain values

Positive volume increases remain distributed on the western basin margin (Fig. 16a) and these are generally focussed at fault intersections (Fig. 16b).

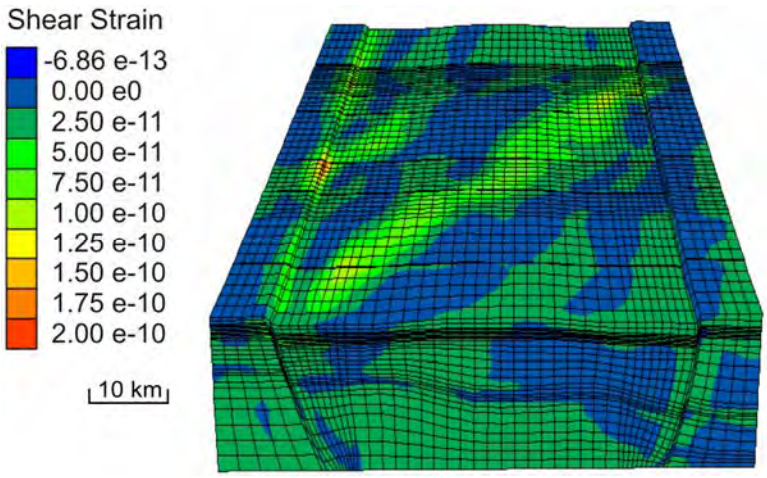

Figure 16a

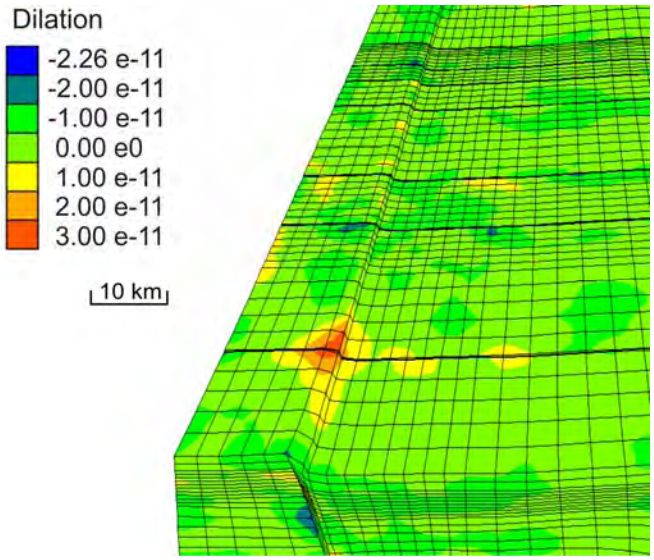

Fig. 16. Numerical output of a) contours of shear strain rate at 7% bulk deformation indicating the continuation of NE structural trends and high values associated with basin bounding faults, b) volumetric increase in the same regions as highest shear strain values, and notably around fault intersections.

The areas of high shear strain rates and high rates of positive volumetric increase also have a large influence in focussing fluids along the basin margin and near fault intersections (Fig. 17).

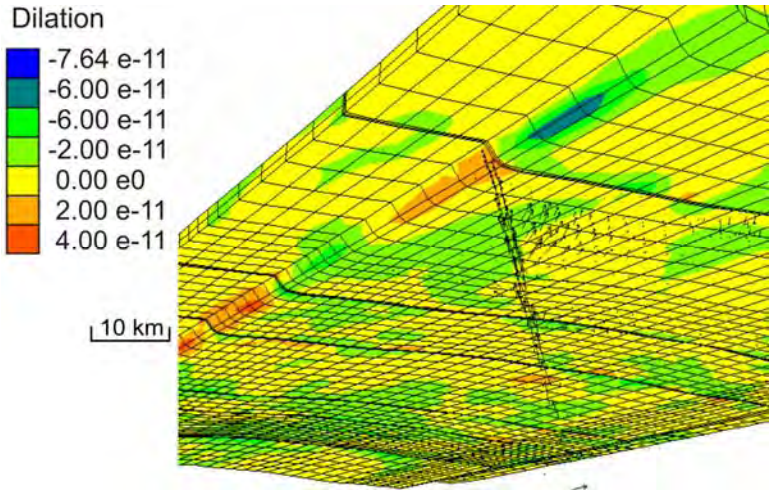

Fig. 17. Numerical output of contours of volumetric increase in the same regions as highest shear strain values, viewed from below, with upward migrating fluid flow vectors focussing towards structural intersections.

5. Discussion

Rifting, basinal development and basin inversion have been explored in these models, and its influence in creating suitable conditions for mineralisation of Pb-Zn-Ag or Cu in the Mount Isa Inlier. This study was not meant to discuss the intricate details of controversy over differing ore genetic models and whether mineralisation is syngenetic or syntectonic, but rather highlights the processes involved during basin development and the potential for moving fluids through the system which may have the capacity to result in various deposit styles.

During extension the partitioning of deformation and localisation of shear strain is mostly accommodated by the basin bounding fault structures and shallow sediments close to the basin margins. Deeper in the system shear strain is also partitioned into basement detachment structures, which may have an influence on controlling the overall basin response to the deformation. As extensional rifting progresses we see this deformational

response focus more on the western basin margin than the eastern basin margin, which has consequences on the amount and distribution of dilation and deformation induced fluid flow around the basin margins. Extensional deformation and topography are key aspects of driving fluids deep into the system (McLellan *et al*. 2004). During rifting and basin formation topography is naturally formed as a result of deformation and this aids in driving surficial fluids and shallow basinal fluids deeper into the system. The 'brine reflux' process (Warren, 2006) is thought to have been very important in driving fluids into the main aquifer units of both the Leichhardt and Calvert Superbasins. These aquifer units lie adjacent to and within the Eastern Creek Volcanics, which have been suggested as a prominent metal source, and fluid inclusion evidence within the aquifer system indicates an evolved meteoric fluid with a variable marine contribution (Polito *et al*. 2006a). During extension there is a strong potential for fluid mixing within the system. Extensional tectonics creates dilational zones and rheological failure which when combined with topography provides a competent driver for strong downward migrating fluids enabling meteoric waters and/or shallow basinal brines to enter fault zones or shear zones culminating in fluid mixing in aquifer units with deep seated basement derived fluids. This process can also be enhanced by convective flow which again aids in driving fluids downwards into the system and promoting fluid mixing in certain circumstances and then returning them to sites of deposition (Oliver *et al*. 2006). This scenario would be most suitable for the majority of SEDEX style deposits in the Mount Isa Inlier.

As the basin structure develops, the evolving topography plays an important role in rate and direction of fluid flow. Topographic relief on the outer basin margins, or distal from this point, can effectively drive fluids downwards and into the system, particularly into hangingwall permeable units, but this is also enhanced by topographic relief in the centre of the basin that may form as a result of thermal structure or isostatic processes e.g. Mount Gordon Arch (Derrick, 1982), which results in a fan-shaped flow regime similar to that described by Toth (1962; 1963) and McLellan *et al*. (2004). This topographic and deformation driven flow allows high volumes of fluids into the Calvert and Leichhardt aquifer units, which could potentially be stored for long periods of time if the system remains sealed.

Basin inversion during the early stages of the Isan Orogeny (ca. 1595 Ma) provides an important mechanism for facilitating upward migration of deep seated fluids towards areas of deformation induced dilatancy and potential sites of mineralisation. The partitioning of strain during basin inversion is accommodated by weaker fault structures such as the basin bounding faults and particularly around the intersections of these N-S trending faults and E-W trending structures, which provide a good location for high strain, maximum positive volume change and fluid focussing. The western basin margin of the Leichhardt River Fault Trough again indicates higher maximum values of shear strain, volume change and fluid flow, which is most likely due to the geometric influence of the thickening of the basin to the east and the underlying detachment zone. There remains controversy over the influence of basement derived fluids versus basinal derived fluids in the genesis of Pb-Zn ores worldwide based on variable isotopic evidence (e.g. Everett *et al*. 2003; Tornos and Chiardia, 2004; Hitzman, 1995; Polito *et al*., 2006a). However, one simple factor remains, deep seated fluids (whether basement derived or deep basinal fluids) are required to reach relatively shallow levels of the basin and depositional sites. A mixing of the deep seated fluids and stored fluids from within shallow aquifer units would provide the most suitable scenario for a syntectonic style of mineralisation for Pb-Zn-Ag deposits in the Mount Isa Inlier, provided these fluids migrate efficiently towards sites of deformation and dilation in the overlying Isa Superbasin. In the Leichhardt River Fault Trough, these sites are most likely proximal to N-S trending basin bounding faults and E-W trending structures, particularly in the hangingwall Mount Isa Group sediments.

A switch in stress regime during the latter stages of the Isan Orogeny (ca. 1550 – 1530Ma) culminates in highest dilational areas being located in the hangingwall sediments of the main basin bounding structures, which is more evident in the western margin than the east. The main basin bounding faults and E-W trending structures indicate higher fluid fluxes, with the western margin accommodating higher levels of shear strain. The deformation partitioning has a strong influence on dilation and volume change, with areas of high shear strain corresponding to areas of higher rates of positive volume increase, which results in the focussing of fluids to these locations. An interesting

feature of the ‘stress rotation’ is the formation of N-E trending structures during deformation, which correspond well to the many N-E trending structures in the Leichhardt River Fault Trough which may have formed around this time. These model conditions simulate a transpression or strike-slip regime at the most likely time of Cu mineralisation (see McLellan, this volume), and indicate areas most likely to focus deep seated fluids. Here, the application of simple conceptual models and numerical simulations allow us to better understand the processes behind the mineralisation of the Leichhardt River Fault Trough, western Mount Isa Inlier.

6. Conclusions

Basin bounding structures and the basement detachment zone have an influential role in deformation partitioning within the Leichhardt River Fault Trough. The western basin margin indicates a higher likelihood of localising shear strain, dilation and fluid flow. The generation of topography in the area has complimented extensional deformation in aiding downward migration of fluids deep into the system, and potentially into aquifer units for long term storage and fluid evolution. Inversion of the basin plays a critical role in facilitating upward migration of fluids to sites of dilation and deposition, particularly in the hangingwall sediments of the western margin. The hangingwall sediments and N-S and E-W fault intersections are key areas for localisation of shear strain, volume increase, high fluid flux, fluid focussing and potential mineralisation. The application of simple FLAC3D numerical models are critical in furthering our understanding of the larger scale mineralising systems, and the relationship between basin evolution, deformation and fluid flow.

7. Acknowledgements

I would like to acknowledge George Gibson, Barry Murphy, Peter Sotuhgate and Andy Barnicoat for many useful discussions. I would also like to acknowledge the other pmd*CRC researchers involved in the I7 Mount Isa project. This research has been funded by the Cooperative Research Centre for predictive mineral discovery (pmd*CRC), and this paper is published with the permission of the CEO, pmd*CRC.

8. References

Bell, T.H., 1983. Thrusting and Duplex Formation at Mount Isa, Queensland, Australia. Nature, 304, 493-497

Betts, P. G., Lister, G. S., O'Dea, M. G., 1998. Asymmetric extension of the Middle Proterozoic lithosphere, Mount Isa Inlier, Queensland, Australia. Tectonophysics, 296, 293–316

Blake, D.H., 1987. Geology of the Mt. Isa Inlier and environs. Queensland and Northern Territory. Bureau of Mineral Resources Bulletin, 225.

Blake, D.H., Stewart, A.J., 1992. Stratigraphic and Tectonic Framework, Mount Isa Inlier. In: Stewart, A.J. & Blake, D.H. (Eds.) Detailed Studies of the Mount Isa Inlier. AGSO Bulletin, 243, 1-11

Broadbent G. C., Myers R. E., Wright J. V. 1998. Geology and origin of shale-hosted Zn–Pb–Ag mineralisation at the Century Deposit, northwest Queensland, Australia. Economic Geology, 93, 1264–1294

Carr G.R., Sun S., Page R.W. & Hinman M. 1996. Recent developments in the use of lead isotope model ages in Proterozoic terrains. In: Baker T., Rotherham J.F., Richmond J.M., Mark G. & Williams P.J. eds. MIC '96: New Developments in Metallogenic Research, The McArthur-Mt Isa-Cloncurry Minerals Province, Extended Abstracts, pp. 33-35. James Cook University, Economic Geology Research Unit Contribution 55.

Chapman, L.H., 2004. Geology and Mineralization Styles of the George Fisher Zn-Pb-Ag Deposit, Mount Isa, Australia. Economic Geology, 99, 233-255

Cooke, D.R., Bull, S., Large, R.R., 2003. Processes of ore formation in the stratiform sediment-hosted Zn–Pb deposits of Northern Australia: testing the Century model. Journal of Geochemical Exploration, 78-79, 519-524

Cundall, P. Board, M., 1988. A microcomputer program for modelling large-strain plasticity problems. In: Swoboda, C. (Ed.), Numerical Methods in Geomechanics. Proceedings of the 16th International Conference on Numerical Methods in Geomechanics, 2101-2108

Davis, T.P., 2004. Mine-Scale Structural Controls on the Mount Isa Zn-Pb-Cu Ore Bodies. Economic Geology, 99, 543-559

Derrick G.M. 1982. A Proterozoic rift zone at Mount Isa, Queensland, and implications for
mineralisation. BMR Journal of Australian Geology & Geophysics, 7, 81-92.

Domagala J., Southgate P.N., McConachie B.A. & Pidgeon B.A. 2000. Evolution of the Palaeoproterozoic Prize, Gun and lower Loretta Supersequences of the Surprise Creek Formation and Mt Isa Group. Australian Journal of Earth Sciences 47, 485-508.

Eldridge C. S., Williams N., Walshe J. L. 1993. Sulphur isotopic variability in sediment-hosted massive sulphide deposits as determined using the ion microprobe SHRIMP II. A study of the HYC deposit at McArthur River, Northern Territory, Australia. Economic Geology, 88 1–26.

Etheridge, M.A., Rutland, R.W.D., Wyborn, L.A.I., 1987. Orogenesis and Tectonic Process in the Early to Middle Proterozoic of Northern Australia. American Geophysical Union, Geodynamic Series 17, 131-147

Everett, C. E., Rye, D. M., Ellam, R. M., 2003. Source or sink? An assessment of the role of the Old Red Sandstone in the genesis of the Irish Zn-Pb deposits: Economic Geology, 98, 31-50.

Ge, S., Garven, G., 1992. Hydromechanical modelling of tectonically driven groundwater flow with application to the Arkoma foreland basin. Journal of Geophysical Research, 97, 9119-9144

Gibson, G. 2005. Chronostratigraphy and geodynamic evolution of the Western Succession. In: G.M. Gibson & A.P. Hitchman (Eds) 3D Basin architecture and mineral systems in the Mount Isa Western Succession. Predictive Mineral Discovery Cooperative Research Centre, I1 Final Report, pp. 257.

Gow, P.A., Upton, P., Zhao, C., Hill, K.C., 2002. Copper-gold mineralisation in New Guinea: numerical modelling of collision, fluid flow and intrusion-related hydrothermal systems. Australian Journal of Earth Sciences 49, 753-771

Heinrich, C.A., Bain, J.H.C., Mernagh, T.P., Wyborn, L.A.I., Andrew, A.S., Waring, C.L., 1995, Fluid and mass transfer during metabasalt alteration and copper mineralization at Mount Isa, Australia: Economic Geology, v. 90, p. 705–730.

Hitzman, M.W., 1995, Mineralization in the Irish Zn-Pb-(Ba-Ag) orefield: Society of Economic Geologists Guidebook Series, v. 21, p. 25–61

Hobbs, B.E., Muhlhaus, H.B., Ord, A., 1990. Instability, softening and localization of deformation. In: Knipe, R.J., Rutter, E.H. (Eds.), Deformation Mechanisms, Rheology and Tectonics. Geological Society Special Publication, 143-165

Holcombe, R.J., Pearson, P.J. & Oliver, N.H.S., 1991. Geometry of a Middle Proterozoic Extensional Decollement in North-Eastern Australia. Tectonophysics, 191, 255-274

Idnurm, M., 2000. Towards a high resolution Late Palaeoproterozoic-earliest Mesoproterozoic apparent polar wander path for northern Australia. Australian Journal of Earth Sciences, 47, 405-429.

Jackson, M.J., Scott, D.L., Rawlings, D.J., 2000. Stratigraphic framework for the Leichhardt and Calvert Superbasins: review and correlations of the pre-1700 Ma successions between Mt Isa and McArthur River. Australian Journal of Earth Sciences 47, 381–404

Krassay, A.A., Bradshaw, B.E., Domagala, J., Jackson, M.J., 2000a. SIliclastic shoreline to growth-faulted, turbiditic sub-basins: the Proterozoic River Supersequence of the upper McNamara Group on the Lawn Hill Platform, northern Australia. Australian Journal of Earth Sciences, 47, 533-562.

Krassay, A.A., Domagala, J., Bradshaw, B.E., Southgate, P.N., 2000b. Lowstand ramps, fans and deep-water Paleoproterozoic and Mesoproterozoic facies of the Lawn Hill Platform: the Term, Lawn, Wide and Doom Supersequences of the Isa Superbasin, northern Australia. Australian Journal of Earth Sciences, 47, 563-597.

Kendrick, M.A., Duncan, R., Phillips, D. 2006. Noble gas and halogen constraints on mineralizing fluids of metamorphic versus surficial origin: Mt Isa, Australia. Chemical Geology, 235, 325 - 351

Kendrick, M.A., Mark, G., Phillips, D. 2007. Mid-crustal fluid mixing in a Proterozoic Fe oxide–Cu–Au deposit, Ernest Henry, Australia: Evidence from Ar, Kr, Xe, Cl, Br, and I. Earth and Planetary Science Letters, 256, 328 – 343

Large R., Bull S., Cooke D., McGoldrick P. 1998. A genetic model for the HYC deposit, Australia: based on regional sedimentology, geochemistry and sulfide sediment relationships. Economic Geology, 93, 1345–1368.

Mallet, J.L., 2002. Geomodeling. Oxford University Press, New York, pp. 599

McLellan, J.G., Oliver, N.H.S., Schaubs, P.M., 2004. Fluid Flow in Extensional Environments; Numerical Modelling with an Application to Hamersley Iron Ores. Journal of Structural Geology, 26,6-7, 1157-1171.

McLellan, J.G., Oliver, N.H.S. 2007 (in press). Discrete element modelling applied to mineral prospectivity analysis in the eastern Mount Isa Inlier, Precambrian Res. (2007), doi:10.1016/j.precamres.2007.08.018

Neuman, N.L., Southgate, P.N., McIntyre, A., 2005. Chronostratigraphy. In: G.M. Gibson & A.P. Hitchman (Eds), 3D Basin architecture and mineral systems in the Mount Isa Western Succession. Predictive Mineral Discovery Cooperative Research Centre, I1 Final Report, pp. 257.

O'Dea, M.G., Lister, G.S., 1997. The Evolution of the Mount Isa Orogen – from Start to Finish. Geodynamics & Ore Deposits Conference Proceedings, 19-21 Feb 1997

O'Dea, M.G., Lister, G.S., Betts, P.G., Pound, K.S., 1997. A shortened intraplate rift system in the Proterozoic Mt Isa terrain, NW Queensland, Australia. Tectonics 16, 425-441

Oliver, N.H.S., McLellan, J.G., Hobbs, B.E., Cleverley, J.S., Ord, A., Feltrin, L. (2006) Numerical models of deformation, heat transfer and fluid flow across basement-cover interfaces during basin-related mineralization, with application to the Mt Isa Pb-Zn district. Economic Geology 100th Anniversary Volume, 101, 1, 1-31

Ord, A., 1991a. Deformation of Rock: A Pressure-Sensitive, Dilatant Material. Pure and Applied Geophysics 137, 4, 337-366

Ord, A., Oliver, N.H.S., 1997. Mechanical Controls on Fluid Flow during Regional Metamorphism: Some Numerical Models. Journal Metamorphic Geology, 15, 345-359

Page, R.W., Bell, T.H., 1986. Isotopic and structural responses of granite to successive deformation and metamorphism. Journal of Geology, 94, 365-379

Page, R.W., Sun, S.S., 1998. Aspects of geochronology and crustal evolution in the Eastern Fold Belt, Mt Isa Inlier. Australian Journal of Earth Sciences, 45, 343-363

Page R. W., Jackson, M. J., Krassay, A. A., 2000. Constraining sequence stratigraphy in north Australian basins: SHRIMP U–Pb zircon geochronology between Mt Isa and McArthur River. Australian Journal of Earth Sciences, 47, 431–459

Perkins, W.G., 1997, Mount Isa lead-Zinc orebodies: replacement lodes in a zoned syn-deformational copper-lead-zinc system. Ore Geology Reviews, 12, 61-110

P. A. Polito, T. K. Kyser, P.N. Southgate, M. J. Jackson. 2006a. Sandstone Diagenesis in the Mount Isa Basin: An Isotopic and Fluid Inclusion Perspective in Relationship to District-Wide Zn, Pb, and Cu Mineralization. Economic Geology, 101, 6, 1159 - 1188

P. A. Polito, T. K. Kyser, M. J. Jackson. 2006b. The Role of Sandstone Diagenesis and Aquifer Evolution in the Formation of Uranium and Zinc-Lead Deposits, Southern McArthur Basin, Northern Territory, Australia, Economic Geology, 101, 6, 1189 - 1209

Rubenach, M.J., Foster, D.R.W., Evins, P.M., Blake, K.L., Fanning, C.M. 2007 (in press). Age constraints on the tectonothermal evolution of the Selwyn Zone, Eastern Fold Belt, Mount Isa Inlier, Precambrian Research, 2007.

Rubenach, M.J., 2007 (this volume). Tectonothermal and metasomatic history of the Mt Isa Inlier.

Schaubs, P.M., Rawling, T.J., Dugdale, L.J., Wilson, J.L. 2006. Factors controlling the location of gold mineralisationaround basalt domes in the Stawell corridor: insights from coupled 3Ddeformation – fluid-flow numerical models. Australian Journal of Earth Sciences, 53, 841 – 862.

Southgate P.N., Bradshaw B.E., Domagala J., Jackson M.J., Idnurm M., Krassay A.A., Page R.W., Sami T.T., Scott D.L., Lindsay J.F., McConachie B.A. & Tarlowski C.Z. (2000a). Chronostratigraphic basin framework for Palaeoproterozoic rocks (1730-1575 Ma) in northern Australia and implications for base-metal mineralisation. Australian Journal of Earth Sciences, 47, 461-483.

Southgate P.N., Scott D.L., Sami T.T., Domagala J., Jackson M.J., James N.P., Kyser T.K. (2000b). Basin shape and sediment architecture in the Gun Supersequence: a strike slip model for Pb-Zn-Ag ore genesis at Mt Isa. Australian Journal of Earth Sciences, 47, 509-532

Tornos, F., and Chiaradia, M., 2004, Plumbotectonic evolution of the Ossa Morena zone, Iberian peninsula: Tracing the influence of mantle-crust interaction in ore-forming processes: Economic Geology, 99, 965–985.

Tóth, J., 1962. A Theory of Groundwater Motion in Small Drainage basins in Central Alberta, Canada. Journal of Geophysical Research, 67, 11, 4375-4387.

Tóth, J., 1963. A Theoretical Analysis of Groundwater Flow in Small Drainage Basins. Journal of Geophysical Research, 68, 16, 4795-4812

Vermeer, P.A., de Borst, R., 1984. Non-associated plasticity for soils, concrete and rock. Heron. 29, 1-62

Warren, J.K., 2006. Evaporites: Sediments, resources and hydrocarbons. Springer, New York, p. 1035.

predictive mineral discovery
COOPERATIVE RESEARCH CENTRE

pmd*CRC

Project Report

Structural controls on the Mount Isa Copper deposit, Qld

Project I7
December 2007

John McL. Miller

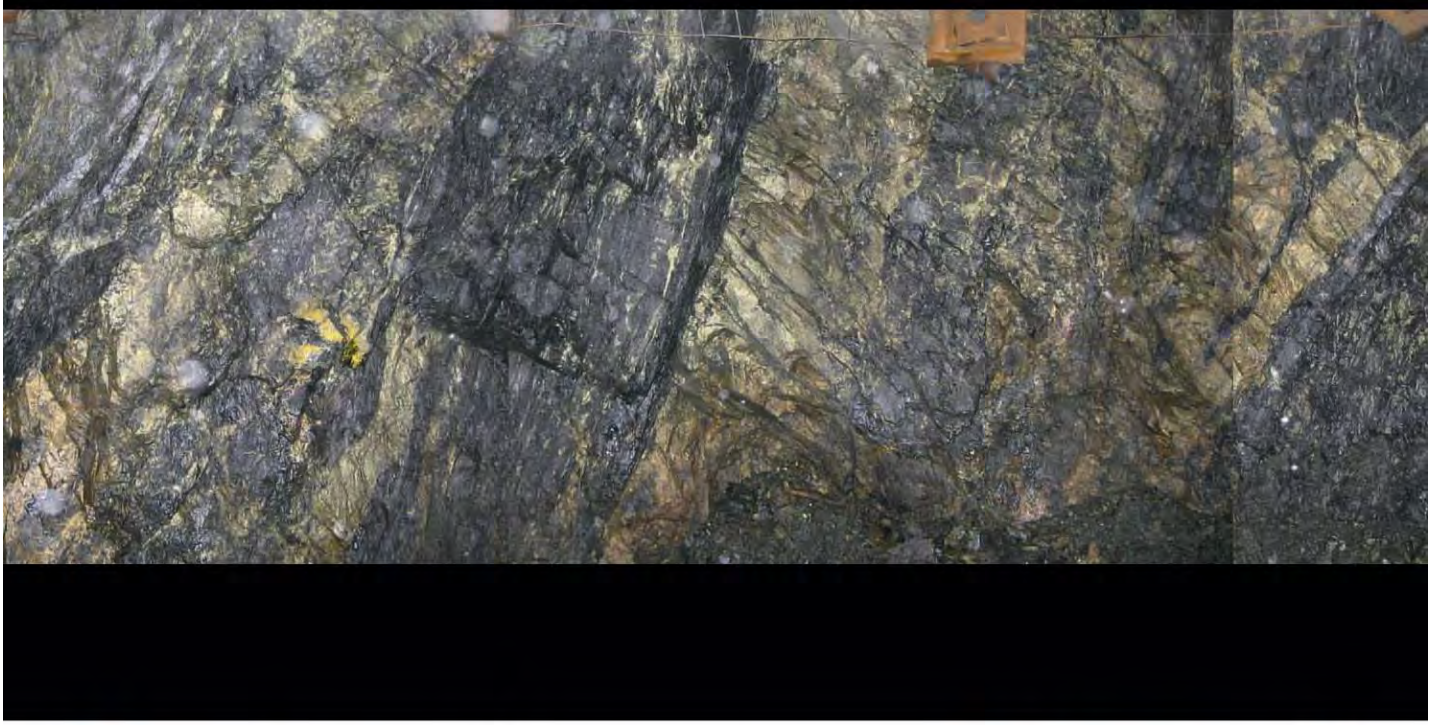

CSIRO
AMIRA INTERNATIONAL
Australian Government
Geoscience Australia
MONASH University
THE UNIVERSITY OF MELBOURNE
JCU JAMES COOK UNIVERSITY
THE UNIVERSITY OF WESTERN AUSTRALIA

Table of Contents

1. Introduction

As part of the I7 project within the *Predictive Mineral Discovery* Cooperative Research Centre (*pmd**CRC) a detailed underground mapping project was commenced at the Mount Isa Mine, with the majority of work focussing on the Enterprise Cu Mine. The Enterprise Mine contains the 3000 and 3500 ore bodies and is located at depth on the northern end of the Mt Isa Zn-Pb-Ag-Cu deposit (Fig.1), which is located in NW Queensland within the Mt Isa Inlier. The Mt Isa Cu ore bodies are spatially distinct to the Zn-Pb-Ag ore bodies (Fig. 2) and occur as large breccias hosted within a silica-dolomite alteration envelope within a westerly dipping shale sequence that is part of the Mt Isa Group (Perkins, 1984)(Fig. 3). These altered and brecciated shale units are juxtaposed against an underlying basement unit (the Eastern Creek Volcanics that also contains inter bedded quartzites) via a complex contact. This contact is commonly termed the Paroo Fault or basement contact fault (Perkins, 1984; Bell et al., 1988)(Fig. 2, 3). Flat dipping zones of this basement contact have previously been defined as zones of structural weakness at a high angle to the extension direction during Cu mineralisation, resulting in fluid focussing and brecciation (Bell et al., 1988).

The silica-dolomite alteration consists of four main types that reflect dolomitisation ("recrystallised shale" and "irregularly brecciated dolomitic shale") and silicification ("fractured siliceous shale" and "siliceous shale") of the host rocks combined with the extent of brecciation (Perkins, 1984). The siliceous alteration defines the core of the envelope (the siliceous inner core) and is associated with the majority of copper mineralisation (Perkins, 1984), however mineralisation also occurs within the dolomitic breccias outside of the siliceous breccia (Fig. 3).

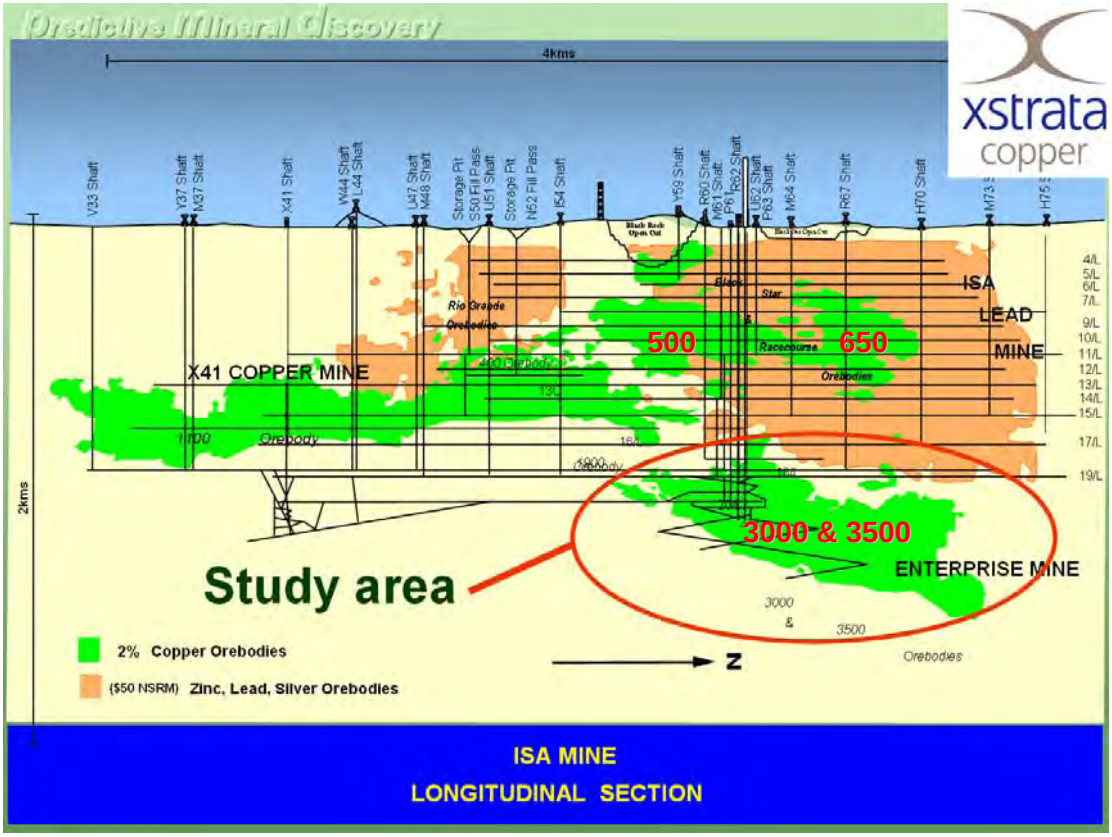

Fig. 1. Location of the Enterprise Mine within the Mt Isa Mine (Longitudinal section from Xstrata Cu). Key ore bodies discussed in this report are labelled.

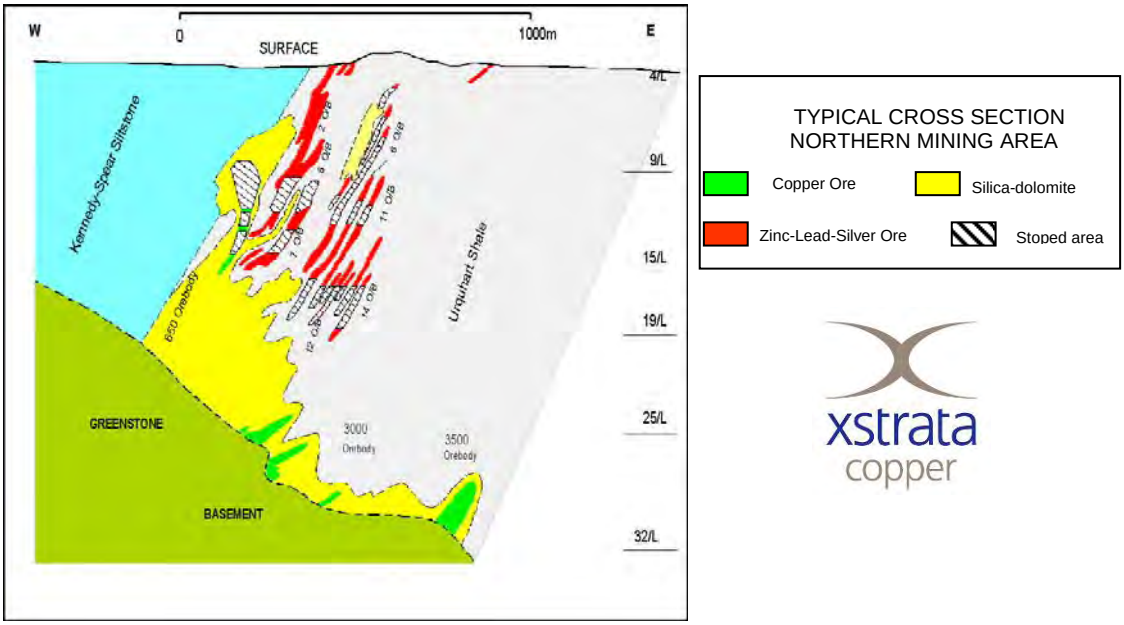

Fig. 2. Typical cross section highlighting basement, Cu and Zn-Pb-Ag ore bodies and key rock and alteration types (from Xstrata Copper).

The Mt Isa Copper deposit sits in the footwall of the Mt Isa Fault (Fig. 3), which is a regionally significant structure. Previous structural studies have shown that the basement contact fault beneath the mineralized Urquhart Shale (the Paroo Fault; Fig. 3) is transected by the mine S_3 cleavage and folded by D_3 folds (Fig. 9 of Bell et al., 1988). In places a wide graphitic "mylonite" zone has developed along the Paroo Fault (labelled graphitic shale in Fig. 3) which contains the S_2 and S_3 cleavages (Fig. 3). These relationships where used by Bell et al., (1988) to argue that the Paroo Fault is a D_1 thrust folded by later D_2 and D_3 regional folding events. Late-stage E-directed movement along the Buck Quartz Fault underlying the Mt Isa Cu ore body produced fault-drag of the S_3 cleavage (Fig. 3), and this event was termed D_4 by Bell et al., (1988), but was not described in detail. The sections of Perkins (1984) and Bell et al., (1988) also clearly show the NE-trending S48 dextral-reverse fault off-setting and truncating the Buck Quartz Fault (Fig. 3). The deformation events at Mt Isa Copper all occurred during the Isan orogeny, and recent regional summaries have argued for an initial phase of N-S shortening followed by later phases of orogenesis that were dominated by E-W shortening with late dextral wrenching (e.g., Fig. 6 of Betts et al., 2006).

In this report the observed fabrics (e.g., the S_3 cleavages) have been labelled with the same deformation numbers as described in Perkins (1984) and Bell et al., (1988). However, other deformation schemes exist for the Mt Isa system (e.g., Connors and Lister, 1995).

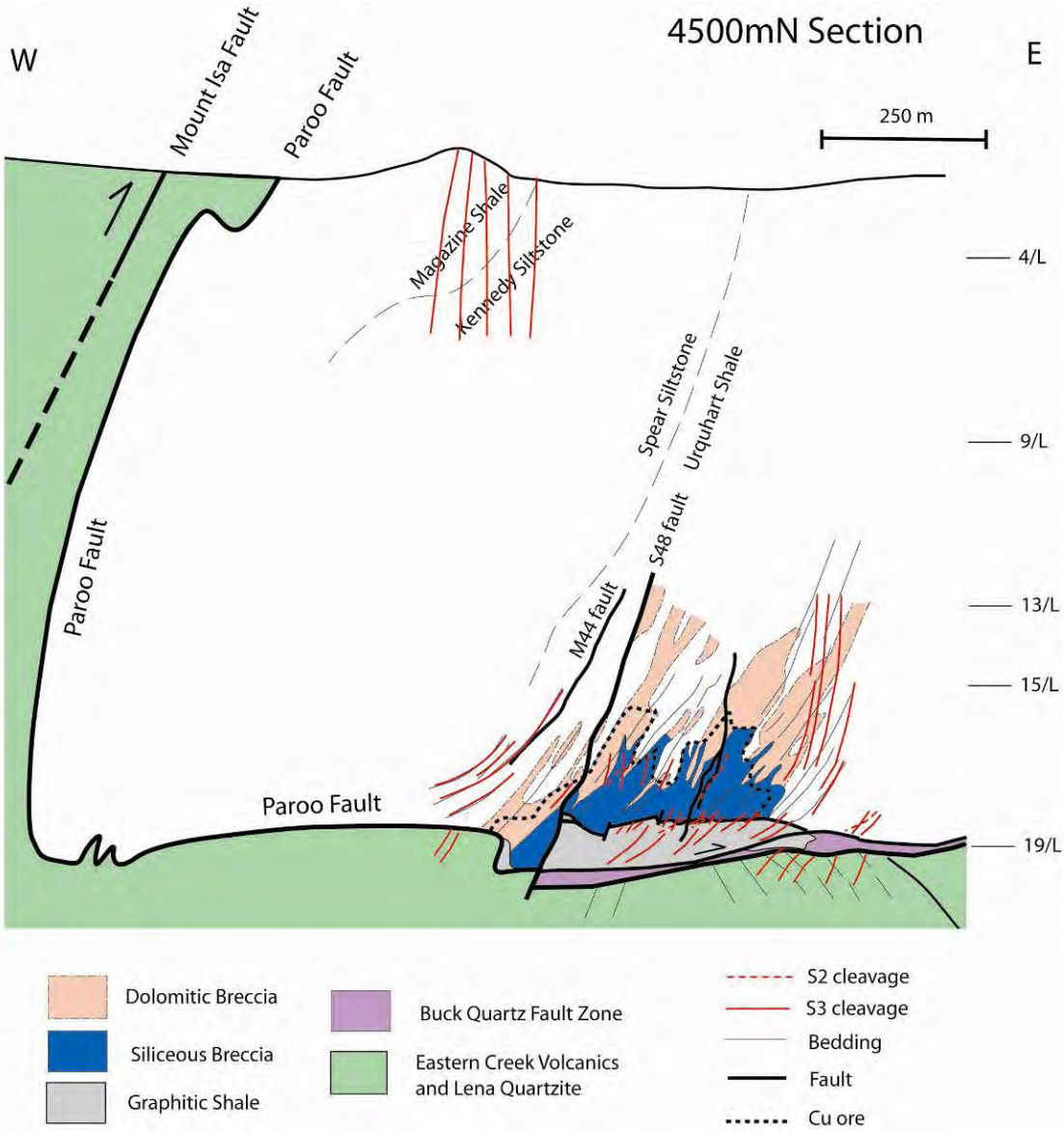

Fig. 3. Typical cross section at 4500 mN through the 1100 ore body in the X41 mine area (see Fig. 1 for locations). Modified from Bell et al., (1988). Note that some of the mineralization lies outside of the siliceous breccia.

The timing of the Cu mineralization has been described as occurring at the end-stage of D_3, and the S_3 cleavages and D_3 folds have a strong control on the development of the breccias (Perkins, 1984, Swager et al., 1987; Bell et al., 1988). There is also remobilization of the earlier formed Pb lodes into D_3 fold hinges (McClay, 1979). Petrographic evidence has been a key element utilised to argue that the introduction of the Cu occurred at a late stage of the D_3 deformation event, with syn-D_3 dolomite, quartz and phyllosilicate growth (Perkins, 1984; Swager, 1985; Swager et al., 1987). The following points are a summary of some of the key textural relationships relevant to the timing of chalcopyrite introduction with respect to the silica-dolomite alteration and deformation;

- The silica breccias have shale clasts that contain the S_3 cleavage, but this is not observed in the silica-chalcopyrite matrix Perkins (194; page 632) indicating a post S_3 age for the silica breccias
- Early dolomite porphyroblasts truncate and over grow S_2 cleavages, but are truncated and dissolved by some of the S_3 cleavages (page 626, Perkins, 1984). In other cases the dolomite porphyroblasts overgrow and truncate the S_3 cleavages, these relationships are consistent with syn-D_3 timing for dolomite growth.

- Perkins (1984; page 630-631) highlighted quartz fibres axial planar to D_3 fold hinges, indicating growth of quartz syn–D_3. However, multiple phases of quartz veins occur within the deposit (Perkins, 1984).
- Swager et al., (1987) identified syn-D_3 growth of sheet phyllosilicates
- Swager (1985) summarised 4 main chalcopyrite associations (Fig. 11 of Swager, 1985), and highlighted fibrous growth of dolomite and quartz with chalcopyrite and also post-chalcopyrite quartz fibres (Fig. 9D and 11D of Swager 1985). All strain increments recorded by the mineral fibres where related to the D_3 event, however the actual extension direction recorded by the fibres (in 3-D) was not documented.
- Perkins (194; page 630) highlight that chalcopyrite is associated with strain free quartz that over grows an earlier fibrous-style of quartz. Perkins (1984) also emphasised that the normal association is strain free quartz with chalcopyrite in the highly silicified breccias. ***This textural phase of "strain free" quartz has also been identified, and placed into a kinematic context, in this study***.
- Perkins (194; page 630) argued that chalcopyrite precipitation occurred very late in D_3 because it forms replacive growths across all generations of veins and microfractures.
- Cobaltite over grows an earlier phase of pyrite with later chalcopyrite precipitated interstitially with some chalcopyrite replacing the cobaltite (and pyrite if the over growth is breached)(Perkin, 1984, page 631). This relationship between chalcopyrite and cobaltite and pyrite has textural continuity in the bedding and S_3 cleavage directions (see Fig. 42 of Perkins, 1984) indicating the chalcopyrite was post the S_3 cleavage.
- In places dolomite over prints quartz, with evidence for quartz and dolomite dissolution during chalcopyrite formation with an inference that chalcopyrite post dates both dolomite and quartz (Wilde et al., 2006).
- No evidence for remobilisation of chalcopyrite was identified by Perkins (1984) i.e. once precipitated the chalcopyrite is not redissolved and reprecipitated

1.1. Mapping methodology

The Isa mine is a large system that is logistically difficult to access and identifying key areas to map was a major problem encountered during the study. The Isa Cu mine has an extensive set of wire frames of major structures and rock types that have been mapped in drill core and via systematic underground drive mapping. The aim of the mapping done by Miller was to delineate the structural kinematics for different aspects of the system (and to describe fault geometries and controls on basement topography) and not to duplicate the existing work. These new kinematic data have been integrated with the existing geological wire frames and sections were drawn in many areas of the Enterprise Mine. The underground mapping areas for defining the kinematics behind the formation of the copper breccias were targeted by using a 3-D model (Fig. 4) compiled in Fracsis (from Fractal Technologies) with mine data (development, grade shells) and Leapfrog (from Zaparo Ltd) modelling of Cu, Co, rock and alteration types (See Miller, 2005 for an outline of the approach). Miller underwent a full mine induction to have the capability to work independently within the underground mine. This report covers the results from the 8 weeks spent on site. **A folder with pdf's of the underground mapping is included with the DVD at the back of this report (this also includes a digital copy of the interim report and this final report).**

1.2. Project and report aims

Key aims of the project were to define:
1) The basement geometries, the controls on how basement topography developed and basement links to ore body development,
2) The kinematics behind the formation of the copper breccias and ore shoot controls,
3) Post ore faulting (and talc).

The aim of this report is to summarize the current understanding of the key structural kinematics and over printing relationships within the Enterprise Mine obtained from the

mapping program (note that the majority of structures within the underground mine have been wire framed). Not all of the Leapfrog modelling is covered by this report, nor is the assessment of talc distribution (and the underground observations). Key Leapfrog models that are not discussed included models of the silica alteration, cobalt grade distributions and talc. The talc models include stoichiometric talc (%), geology logged talc (visual estimates), and talc habit (bedding, fault or joint hosted).

The new results in this report have implications for *pmd**CRC regional programs done within the I7 project. The combination of these projects will provide more predictive models for targeting Cu deposits within the Mount Isa terrane.

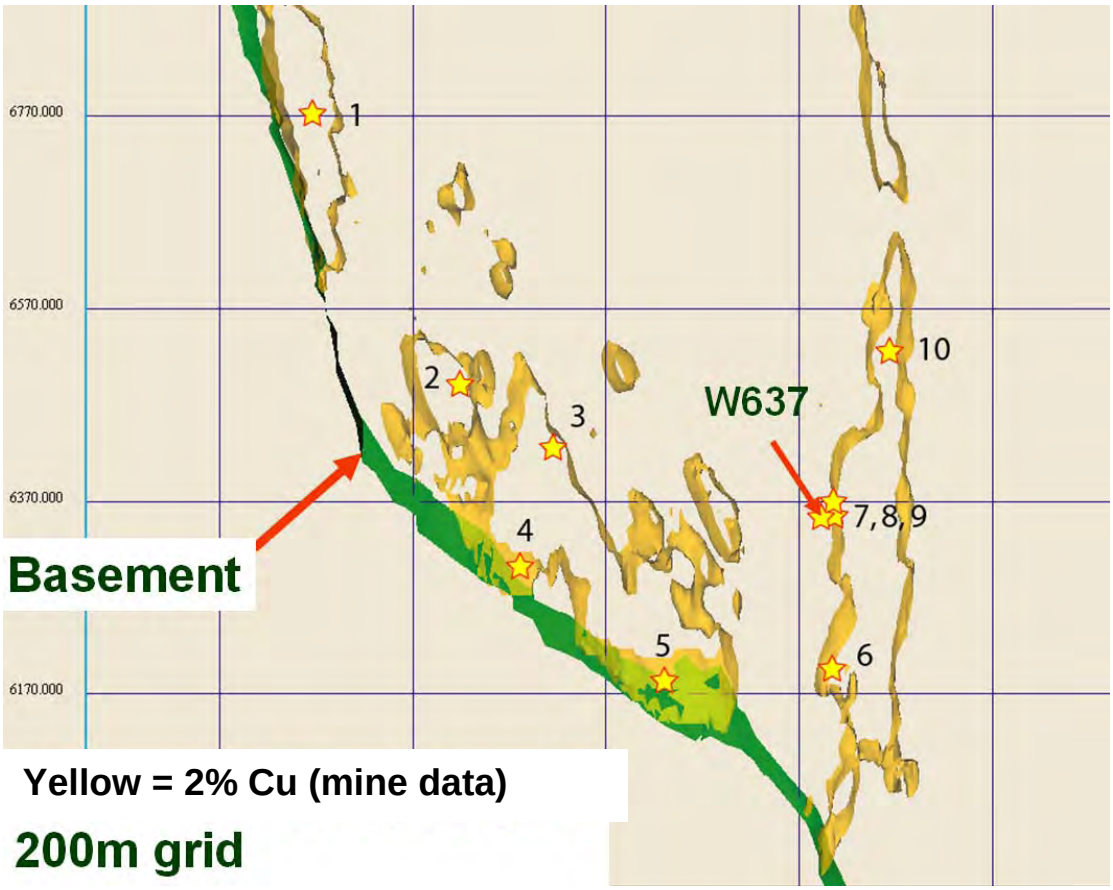

Fig. 4. Horizontal section through the 3-D model through the Enterprise Mine (viewed in Fracsis) highlighting approximate locations of different field area localities where kinematic analysis of the Cu breccias was undertaken (see Table 1). Exact locations are listed in table 1 below. Viewed in Fracsis, 2100RL, 20 metre slice, mine northings shown.

Locality number	Area description	Ore body	Level	Northing	Easting
1	K672	3000	26B	6750N	1500E
2		3000	26B	6530N	1630E
3	M65SEDR (access to N640/L645)	3000	27L	6640N	1670E
4	N640 DPT2	3000	27C	6430N	1700E
5	R631 DDR (R631)	3000	27C	6300N	1835E
6	6240 XC U627	3500S	27C	6240N	2035E
7	W637 DDR	3500S	23A	6360N	2140E
8	W637 CO	3500S	23A	6375N	2130E
9	W637 CO	3500S	24A	6375N	2130E
10	6385XC W637	3500S	25A	6480N	1980E

Table 1. Northings and Eastings of key data locations in Fig. 4.

2. Basement geometry

2.1. Constraints from Leapfrog models

Leapfrog models were generated of the lower basement contact i.e. the contact of the volcanic and quartzite units with the overlying shale and graphite-altered shale (= mine units defined as slaty shale or carbonaceous mylonite). This contact is also a proxy for the base of the Paroo Fault/Fault Zone. Additional Leapfrog models focussed on separating out the two main basement units (the Lena Quartzite versus the Eastern Creek Volcanics). The models generated were isotropic, the advantage of isotropic models is that linear trends within a model are more commonly real. In many cases wireframes built using a sectional approach have linear trends parallel to the section lines due to slight mismatches between sections. This can mask trends that are at a low angle to the orientation of the section lines. The Leapfrog models used a 70 metre search radius from existing drill holes, and the cylinders in the models represent single drill holes that were not close enough to an adjacent drill hole to create a continuous wire frame. This feature of the Leapfrog models is a quick way to assess the amount of drilling constraining a given wire frame (Fig. 5). In areas of extensive drilling there is a good correlation between the mine wire frame and the Leapfrog model (Fig. 5, 6). The basement linear trends observed within the Leapfrog models also exist within basement models produced by Xstrata geology staff. For example, note the two basement over hangs and also the NNW-trending F_3 fold marked on Fig. 5 (labelled F and O respectively).

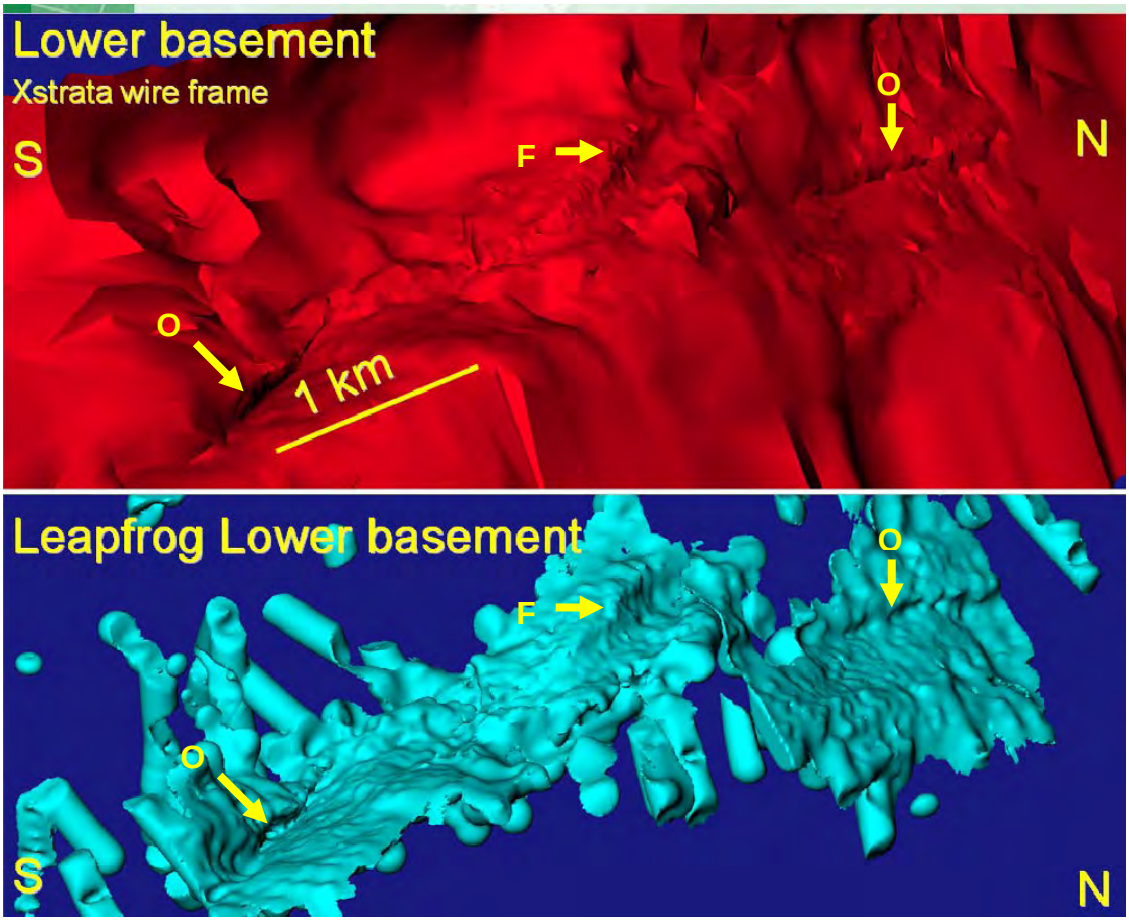

Fig. 5. Comparison of the existing mine wire frame of the lower basement contact (red wire frame at top) and the Leapfrog model. Note that the Leapfrog model used a 70 metre search radius from existing drill holes and the cylinders represent single drill holes. Note that in areas of extensive drilling a good correlation between the mine wire frame and the Leapfrog model. Note the two basement over hangs (marked O) and also the NNW-trending F_3 fold (marked F) in both models.

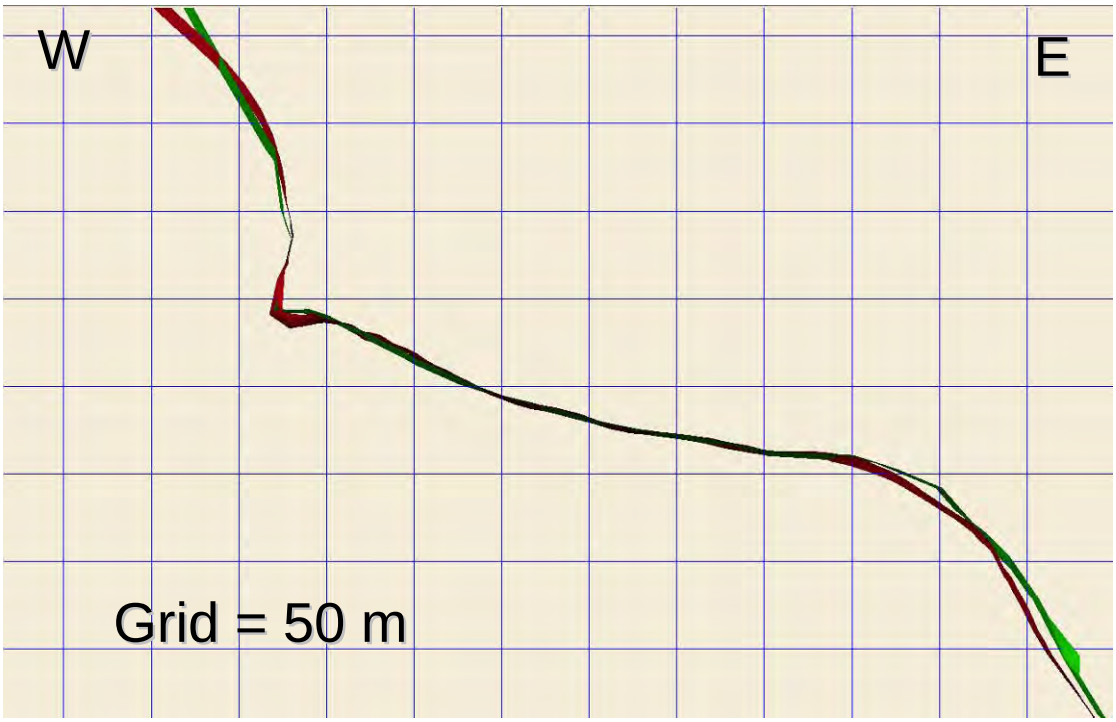

Fig. 6. Section highlighting comparison between Leapfrog model of the lower basement contact (red wire frame) and existing mine wire frame (green). Section 6540, 10m slice.

The Leapfrog models, and the existing Xstrata mine wire frames, highlight a set of N- and NNW-trending (to NW-) basement lineaments that in many areas correlate with the trend of Cu mineralisation at an individual ore body scale (e.g., the Enterprise ore body; Fig. 7) and also at a mine scale (Fig. 8a, 8b). The NNW-trending basement lineaments have previously been mapped as F_3 fold traces (see annotations on Fig. 8b). One notable aspect of the models is that even though there are strong N-S trends in the basement geometry in many areas, the copper does not always solely follow this. For example in the Enterprise Mine area the Cu mineralisation steps across from one N-S trending structure to the next (i.e. from western side of the 3000 ore body across to the 3500 ore body that also lies on a N-S trending basement lineament; Fig. 7). These step-overs occur in areas of relatively consistent N-S striking W-dipping Urquhart Shale. In other areas there are strong N-trending Cu lodes that do not correlate with a basement lineament in the models that combine the Lena Quartzite and the Eastern Creek Volcanics (see green arrow in Fig. 7).

Leapfrog modelling of the individual basement units (specifically the quartzite and volcanic units) was also undertaken (Fig. 8, 9, 10, 11). This was complicated by; 1) the inter-layered nature of the units in many areas, and 2) the Eastern Creek Volcanics in some areas are highly silicified with the appearance of a quartzite.

One significant outcome of the Leapfrog modelling was the identification that some of the within basement variations of the quartzite and volcanic distributions correlate with ore body geometries in the over-lying shale. Another outcome of the modelling was that the Lena quartzite sits in the flatter dipping area of the lower basement contact (= basement ramp). Significantly, some of the within basement variations are not associated with observable lineaments in the Lower Basement Contact. This is significant because it indicates a basement control on the distribution of the ore bodies that has not previously been constrained. A new map of basement lineaments has been produced that includes not only the F_3 fold trends, but also the within basement trends - these trends have a strong correlation with Cu trends (Fig. 9a, 9b). This new basement lineament map is integrated with the syn-Cu kinematics later in the report. Strong zones of S_3 cleavage associated with F_3 folds within the Eastern Creek Volcanic have previously been inferred to be a major fluid conduit associated with Cu mineralisation (Bell et al., 1988).

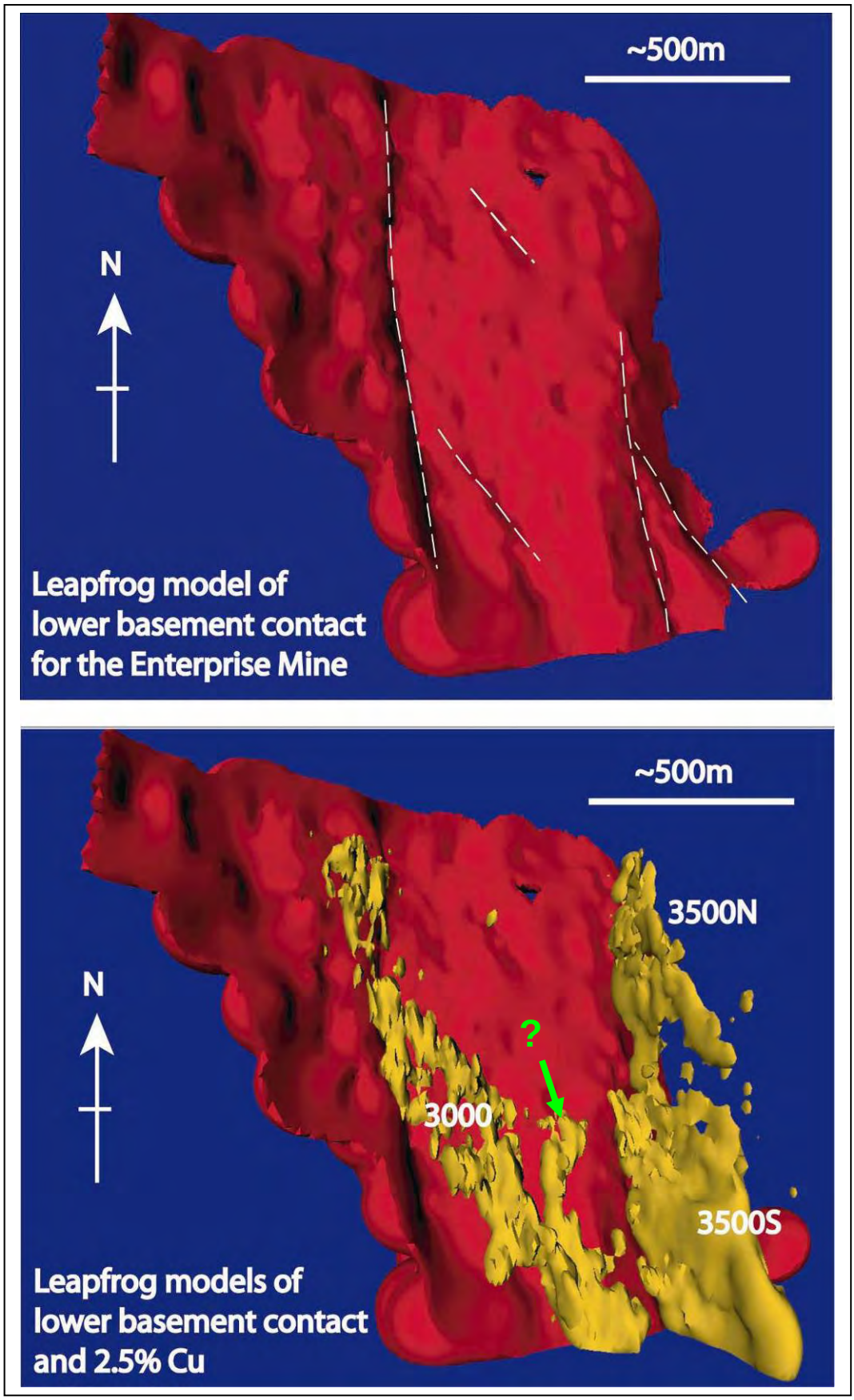

Fig. 7. Leapfrog models of the Lower Basement Contact and 2.5% Cu for the 3000, 3500S and 3500N ore bodies. The edges of the model reflects the edge of drill hole data used to produce Leapfrog model. The green arrow with question mark highlights an area with a strong N-S lode with no basement trend.

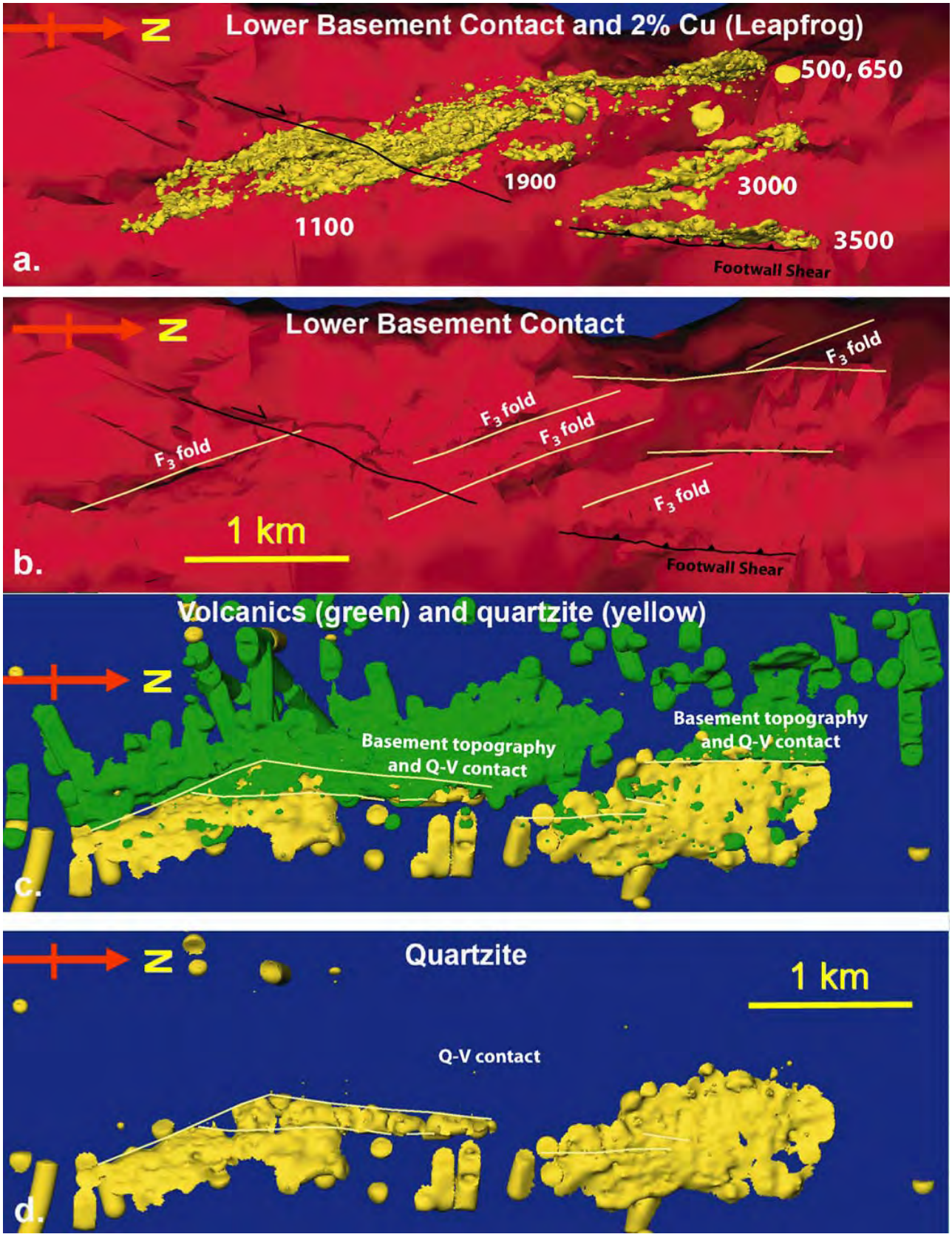

Fig. 8. (a) Xstrata wire frame of the Lower Basement Contact with a 2% Leapfrog Cu model. Viewed looking down. (b) Xstrata wire frame of the Lower Basement Contact with observed basement lineaments annotated as yellow lines. Basement lineaments that are F_3 fold traces and also the W-dipping Footwall shear beneath the 3500 ore body are also marked. Viewed looking down. (c) Leapfrog model of quartzite and volcanics - within basement trends highlighted with yellow lines. Viewed looking down. (d) Leapfrog model of quartzite - within basement trends highlighted with yellow lines. Viewed looking down

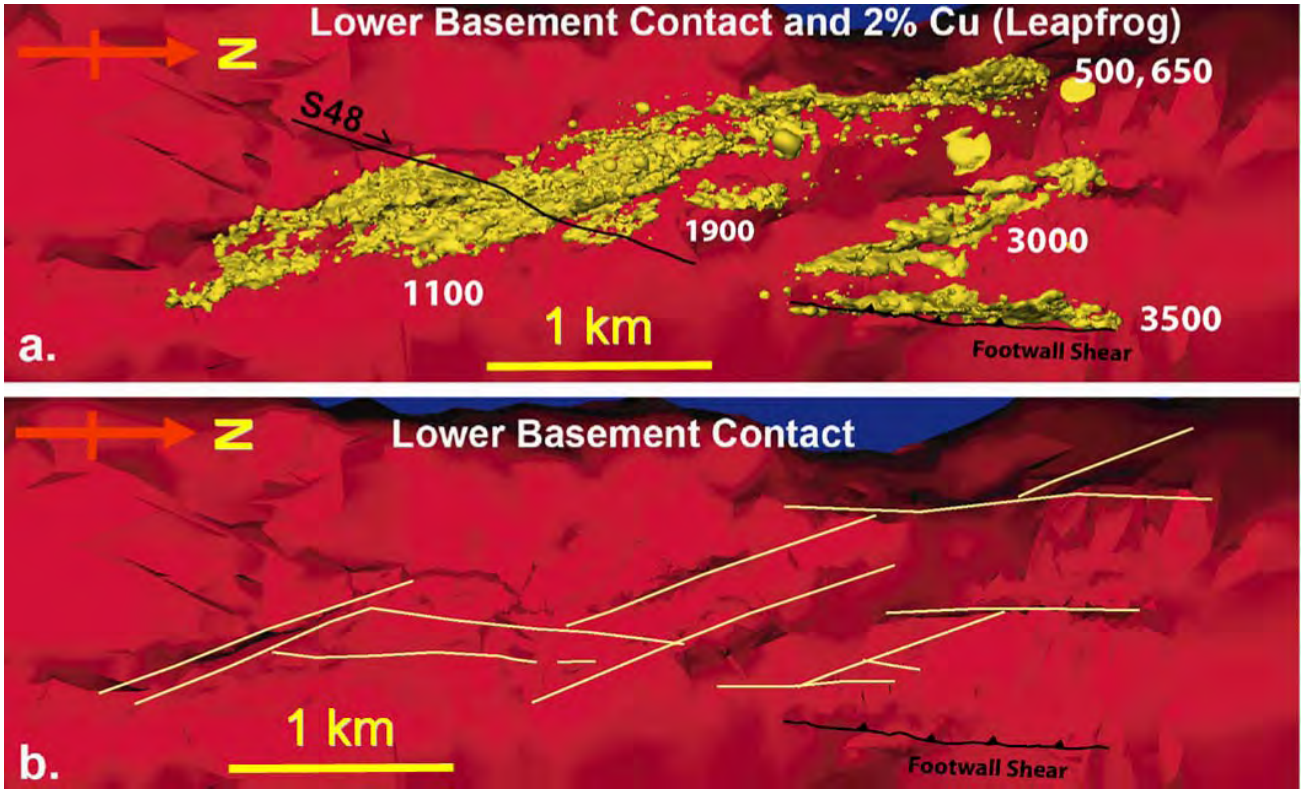

Fig. 9. (a) Xstrata wire frame of the Lower Basement Contact with a 2% Leapfrog Cu model. Viewed looking down. (b) Xstrata wire frame of the Lower Basement Contact with observed basement lineaments annotated as yellow lines. Basement lineaments that are F_3 fold traces, the W-dipping Footwall shear beneath the 3500 ore body and "within basement trends" defined by quartzite and volcanic distributions are both marked. Viewed looking down.

The Leapfrog modelling identified a strong "dog-leg" in the basement quartzite in the 1100 ore body that correlated with a strike-change in the 1100 Cu ore body from NNW-trending to N-trending (Fig. 8a, 8c, 8d). Some of the N-S trending basement topography (marked on Fig. 8c) also correlates with quartzite-volcanic contacts i.e. basement slip may have occurred on these contacts producing some basement overhangs.

The modelling also highlighted areas where lenses of volcanics occurred within the Lena Quartzite. When the quartzite model is viewed alone these appear as troughs within this unit (Fig. 10c). One example of this style of basement is associated with the N-trending Cu lodes within the 3000 ore body highlighted in Fig. 7 that *do not correlate with a basement lineament in the models that combine the Lena Quartzite and the Eastern Creek Volcanics* (see green arrow in Fig. 7 and Fig. 10b, 10c). *These lodes are above a within basement trend clearly visible in the quartzite basement model* (Fig. 8d, 9, 11d) with the infilling volcanic rocks shown in Fig. 11c.

The modelling also suggests that in some areas there appears to be an inverse correlation between massive volcanic rocks (i.e. with no major bodies of inter-layered quartzites) and Cu mineralisation. Zones of massive volcanic rocks correlated with "holes" or low grade zones in the Cu ore bodies (Fig. 11). This is most pronounced for the 3500 ore body which sits in the hangingwall of the footwall shear (shear and lode is marked on 8a, 8b) with a major "dead zone" or "hole" in the ore body associated with a major body of Eastern Creek Volcanics (Fig. 11a, 11b). An exception to this relationship are the Cu lodes that lie above major F_3 folds in the basement. One of these is highlighted in Fig. 5 (labelled F), these are associated with major overlying Cu mineralisation (compare F_3 folds marked on Fig. 8a with Cu on Fig. 8b) but many are not associated with basement quartzite (compare Fig. 8b with Fig 8c, 8d). These lodes above are inferred to be linked to fluid flow along a strongly developed basement S_3 cleavage linked to D_3 folding (Bell et al., 1988).

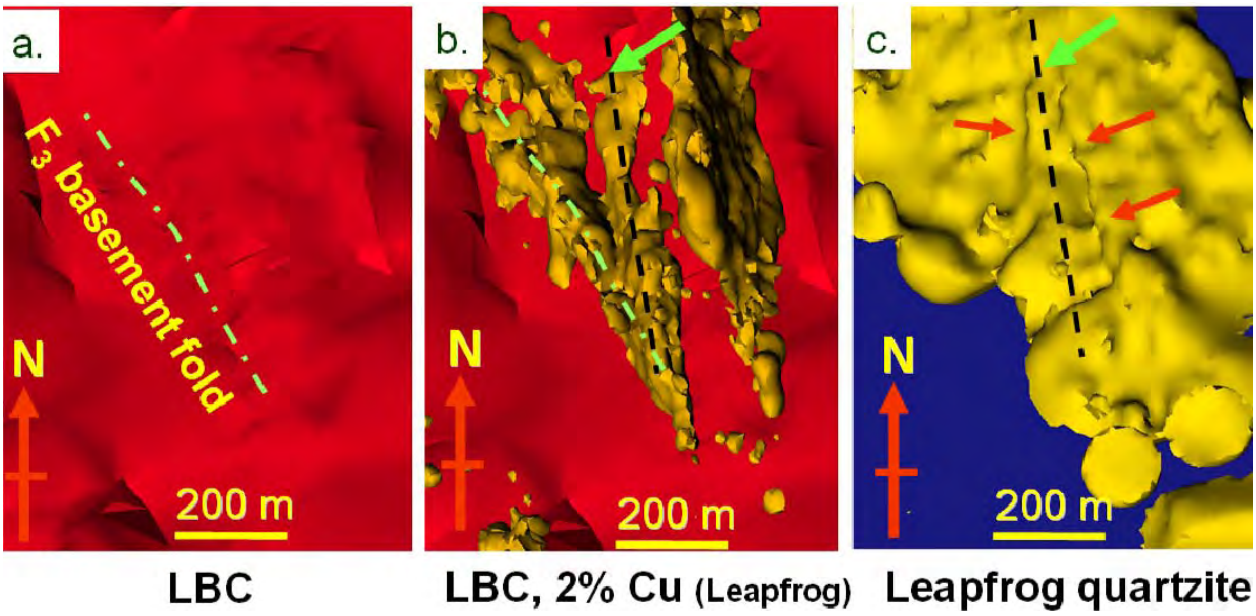

Fig. 10. Basement controls on lodes within the Enterprise Ore Body – refer to Fig. 7 for location. (a) NNW-trending F_3 fold defined by the lower basement contact (Paroo Fault). (b) Green arrow highlighting one of the N-S trending Cu lodes that does not follow the F_3 trend within basement. (c) Leapfrog model of quartzite showing strong correlation with a N-S trending within basement variation highlighted by orange arrows. This trough is in filled by Eastern Creek Volcanics (see Fig. 11c) and the within basement variation is not apparent in the lower basement wireframe (see Fig. 10a).

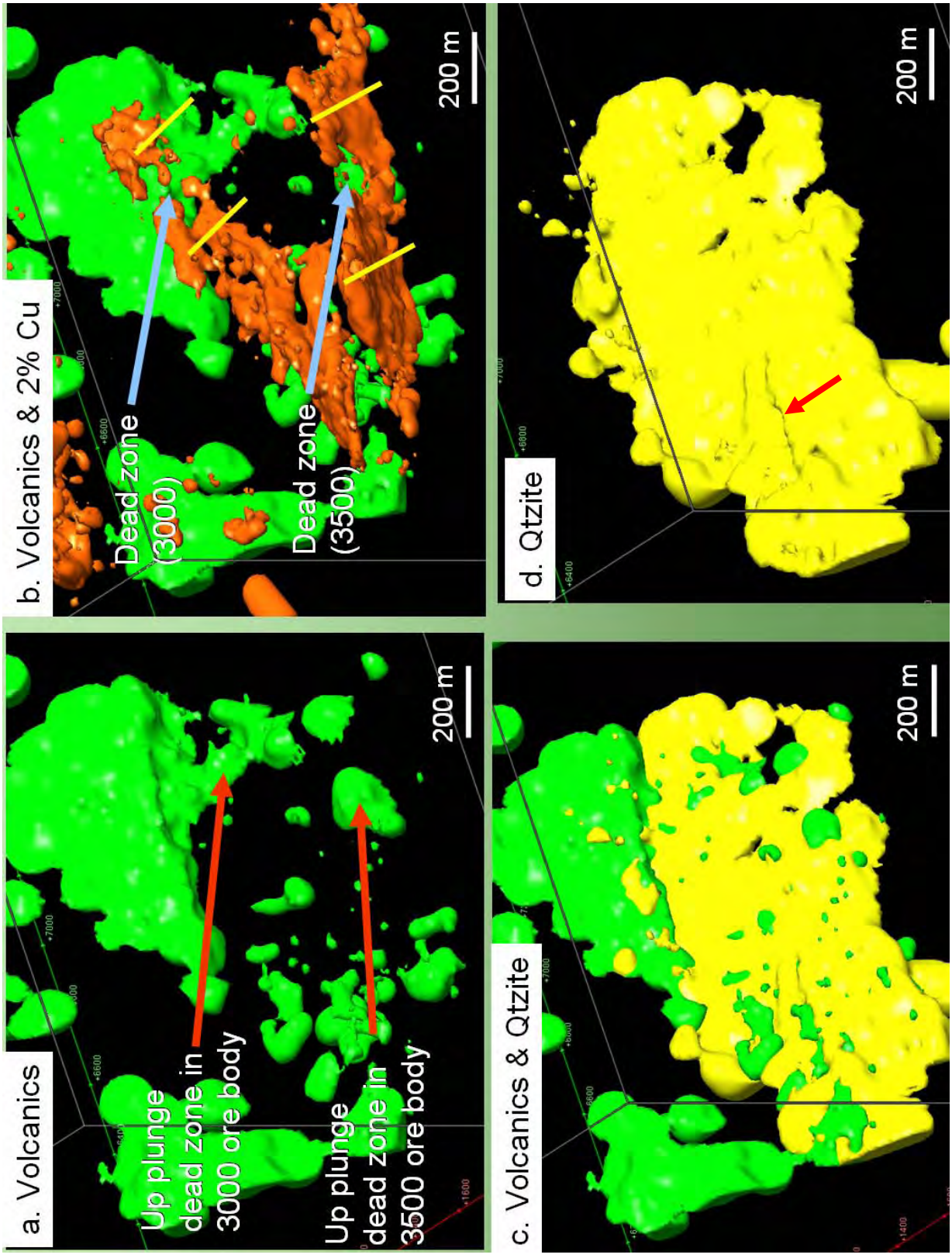

Fig. 11. Isotropic Leapfrog models constraining the distribution of units defining the lower basement. Viewed looking NW – note that the volcanic rocks and quartzites are inter-layered in many areas. (a) Leapfrog model of volcanic rocks – coherent zones of volcanic rocks correspond to dead zones of low Cu grades in the over-lying shale units. (b) Volcanic rocks and 2.5% Cu (Leapfrog model). Yellow lines highlight F_3 fold plunge direction, which is a control on ore shoot plunge (e.g., Perkins, 1984). (c) Volcanic rocks and quartzites – note the quartzites sit in the flatter dipping area of the lower basement. (d) Leapfrog model of quartzites. Red arrow highlights basement trend defined by a depression within the quartzites (this is filled by volcanics –see (c)). This basement trend is parallel to a copper lode within the 3000 ore body and is not obvious in the lower basement contact wire frame that includes both units.

2.2 Correlation of 3-D modelling trends with field observations

Some of the key field observations from the quartzite and volcanic basement units are summarised in Figures 12, 13 and 14. The NW- and N-trending are the dominant features of the basement. Both NW- and N-trending stratigraphic contacts between the Lena Quartzite and Eastern Creek Volcanics were observed (Fig. 12, 13, 14). These relationships are consistent with the observed trends in the Leapfrog models (Fig. 8, 10, 11), and the basement "dog-leg" defined by the Lena Quartzite beneath the 1100 ore body (Fig. 8c, 8d) is inferred to be a real geological feature. The dominant S_3 cleavage trends NW and dips to the SW, however N-S trending, W-dipping cleavages were also observed (Fig. 13) and were mapped as S_3 cleavages, however some of these may have been S_2. In the areas mapped the bedding within the Lena Quartzite trended N-S and dipped between 40° and 60° to the west.

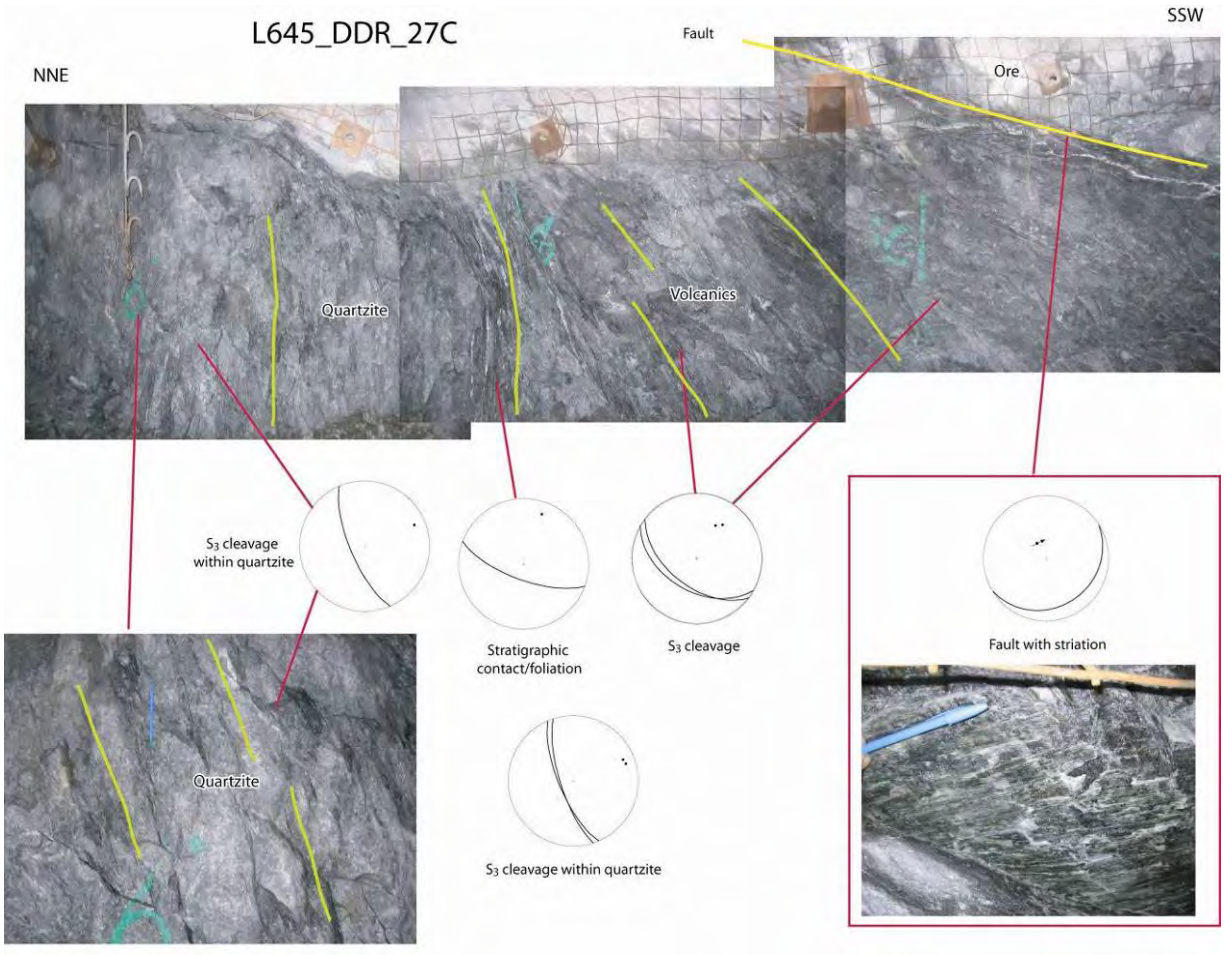

Fig. 12. Basement relationships beneath the 3000 ore body. Both the stratigraphic contacts and S_3 cleavages in this are trend NW. This is consistent with the NW-trending basement lineaments marked by dashed white lines in Fig. 7. Note that the actual contact with the overlying ore body is a late low angle fault with top-to-the-ENE transport. Location is the L645_DDR_27C level.

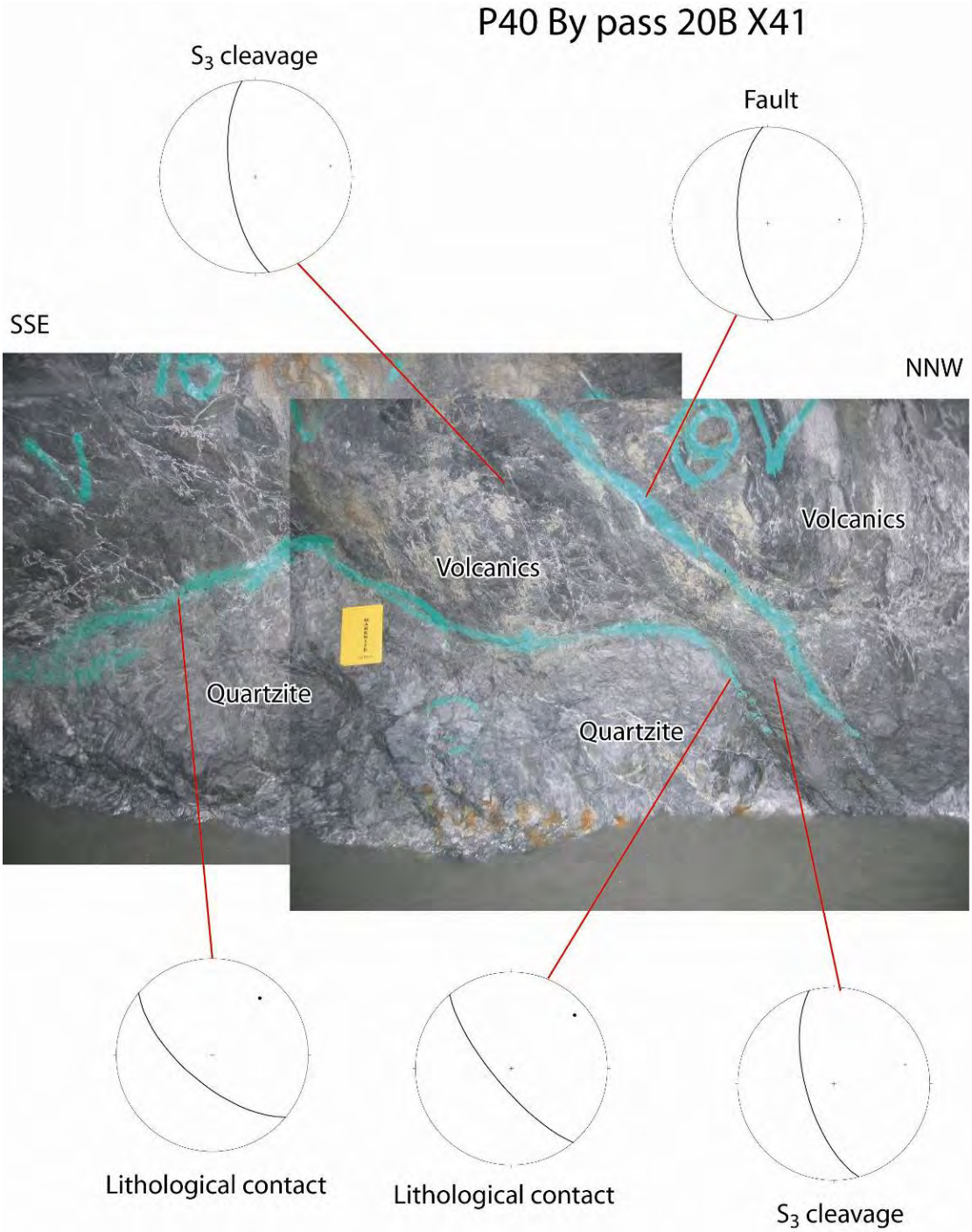

Fig. 13. Basement relationships beneath the 1100 ore body in the X41 mine area. Here the stratigraphic contacts trends NW but the S_3 cleavages trends more N-S. Location is the P40 By pass 20B Level, X41 ore body.

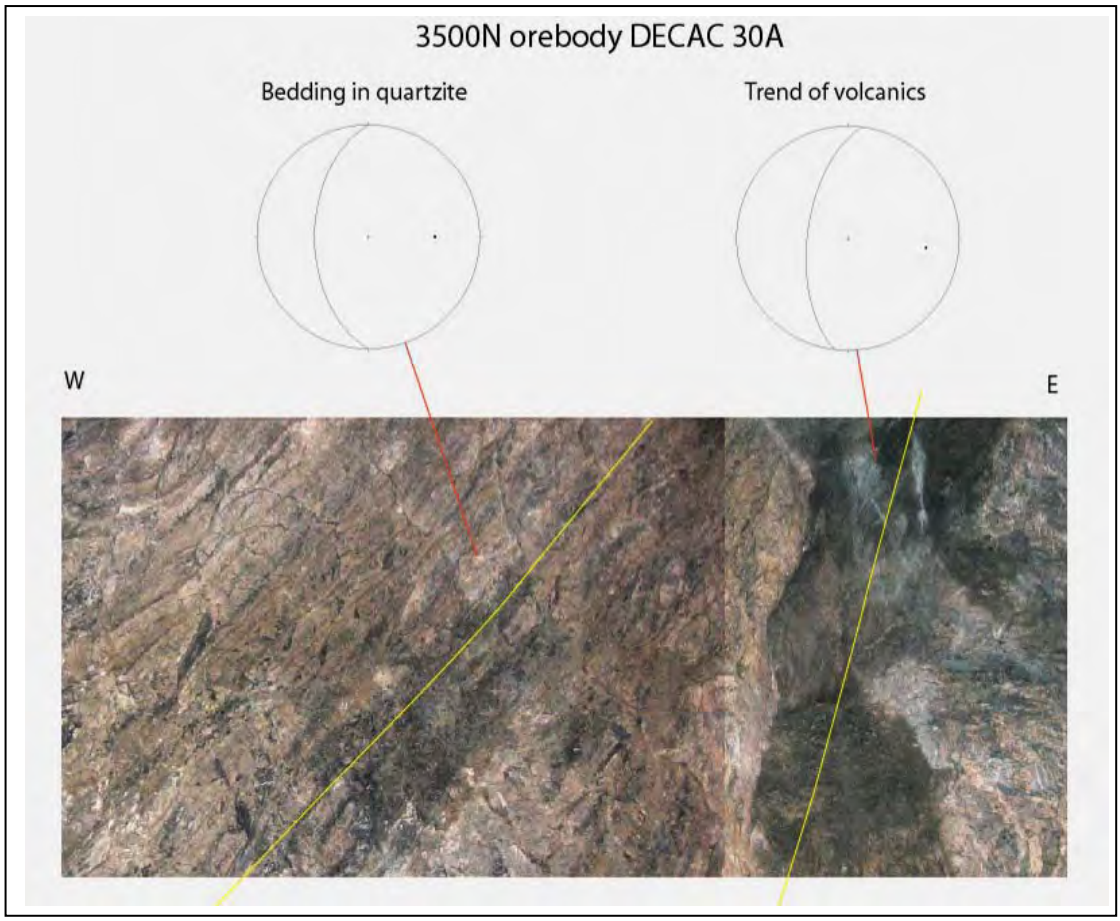

Fig. 14. Basement relationships beneath the 3500 ore body in the Enterprise Mine. Here the stratigraphic contact between the Lena Quartzite and a small lens of Eastern Creek Volcanics trends N-S which is consistent with the Leapfrog trend shown in Fig. 10. The bedding in the quartzite dips to the west – this west dip for this unit was consistent throughout most of the mine. DECAC drive 30A Level, Enterprise Mine.

Three key types of basement geometries occur and can be observed in the Leapfrog models, and the existing mine wire frames. These geometries are found in the both the Enterprise and X41 areas of the mine, and examples have been labelled geometries 1, 2, and 3 on Fig. 15, which is a section through the Enterprise Mine. The shape of these basement geometries are as follows; 1) steep W-dipping basement contact that "overhangs" the shale and commonly the Cu mineralization, 2) a lower angle contacts that can dip shallowly to the E or W and (this occurs beneath the 3000 ore body in the Enterprise Mine and beneath the 1100 ore body in the X41 mine), 3) a steeper E-dipping contact – this type of contact only occurs beneath the 3500 ore body and does not occur beneath the X41 ore body. Finding areas of the mine that provided exposures of these three key basement geometries were targeted during the underground mapping program, with a focus on the Enterprise Mine with an analogy made to the rest of the mine.

In this section lower basement refers to the Eastern Creek Volcanics and the Lena Quartzite, upper basement where mentioned refers to graphite altered shale (commonly termed upper basement, slaty shale or carbonaceous mylonite). On Fig. 3 this upper basement contact defines the top of the graphitic shale with the grey fill colour.

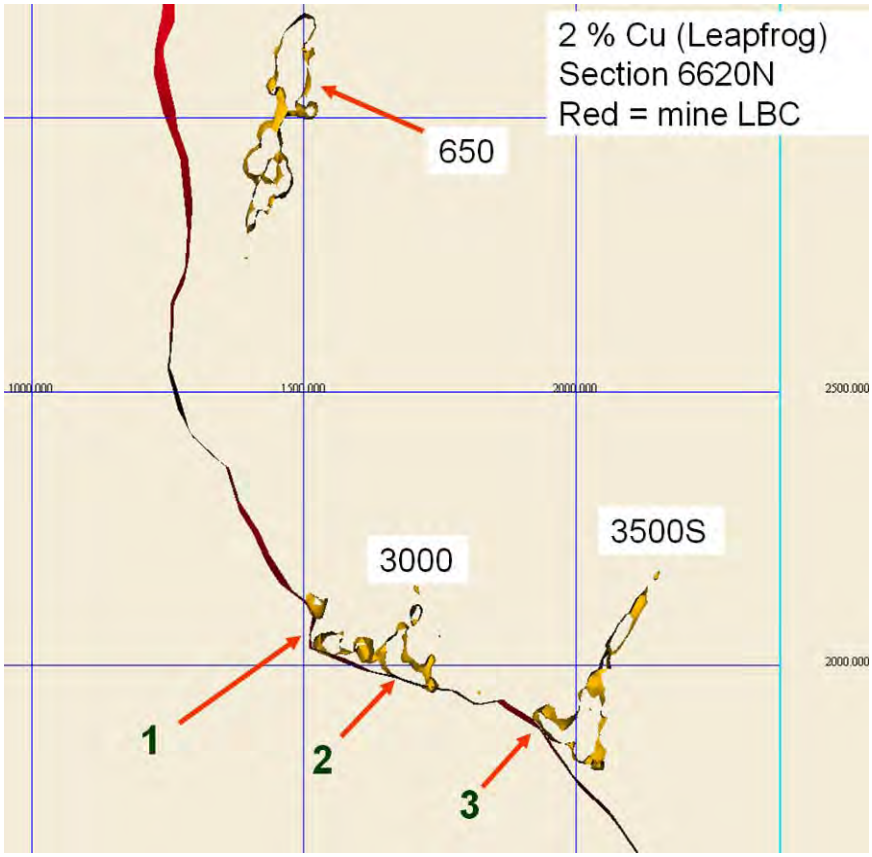

Fig. 15. Section viewed in Fracsis highlighting key basement geometries within the Enterprise Mine. Section 6620N, 500m grid, 40m slice through model, viewed looking north.

Prior to describing the observations at key basement localities, there are several key observations that were consistent throughout the Enterprise Mine – and were also noted within the areas of the southern X41 ore body visited and in most cases agree with existing descriptions by Perkins (1984) and Bell et al., (1988).

- There is a consistent steep W-dipping foliation (mapped as S_3) in both the volcanic rocks and the overlying shale. This foliation actually transects the basement contact (Fig. 16a, 16c), which is folded (as argued by Bell et al., 1988 – see Fig. 9 of that paper). The overturned basement contact have cleavage relationships consistent with being the over turned limb of inclined folds (Fig. 16c).
- Bedding in the basement quartzite has a consistent W-dipping attitude (Fig. 14, 17) with dip-slip striations preserved along bedding surfaces (top-to-the-E transport direction; Fig. 17).
- The S_3 foliation is strongly developed where the shale has a strong graphitic over print directly adjacent to the underlying basement
- The slaty shale (unit X) is a graphitic over print of the Urquhart Shale – it is not a basement unit (commonly termed the Upper Basement). In places this is conformable to and over lying brecciated shale units (that still contain remnant bedding) hosting Cu mineralisation (Fig. 18). In other areas it occurs as narrow "upper basement" spikes associated with ductile D_3 deformation features (Fig. 16b). It has been wire framed as the upper basement contact and, irrespective of the interpretation, the distribution of this graphitic-altered shale controls the basal shape of many ore bodies.
- The S_3 foliation when it is associated with graphite is commonly dragged/reoriented into flatter lying orientation by later faulting. This has been previously documented (see Fig. 3) and was attributed to a D_4 event post Cu. There is no flat-lying or E-dipping mylonite along the basement contact.
- Whilst many of the controls on basement topography noted in this study are similar to previous work (Perkins, 1984; Bell et al., 1988) one major difference to the X41 region is the major control the E-dipping faults have on the basement geometry beneath the 3500 ore body.

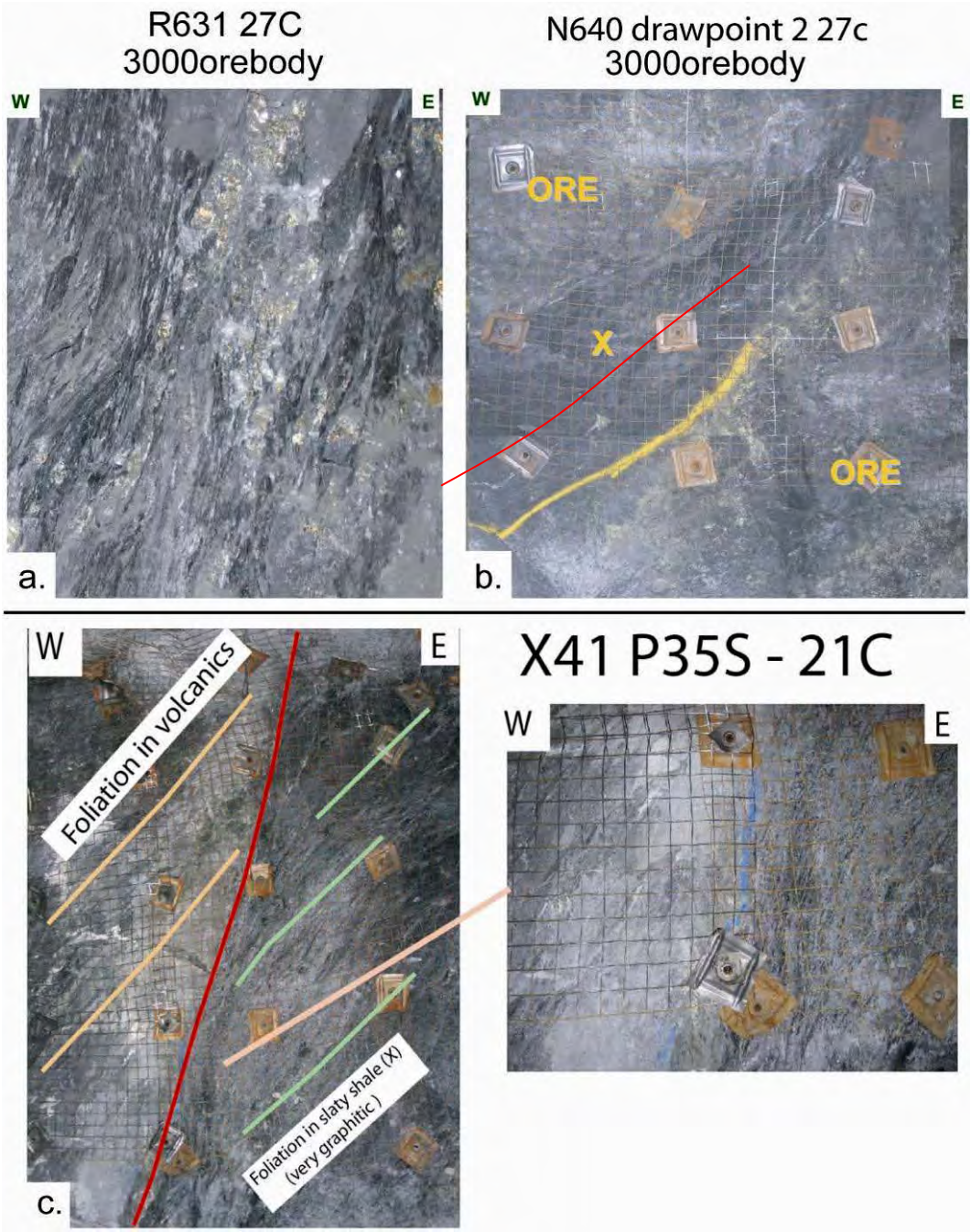

Fig. 16. (a) Strong W-dipping S_3 cleavage within basement volcanic unit. (b) Graphite-altered shale occurring as a thin wedge projecting up into copper breccias, red line highlights the S_3 cleavage. (c) Example of S_3 cleavage transecting the lower basement contact – this example is from X41 and is an over turned basement contact.

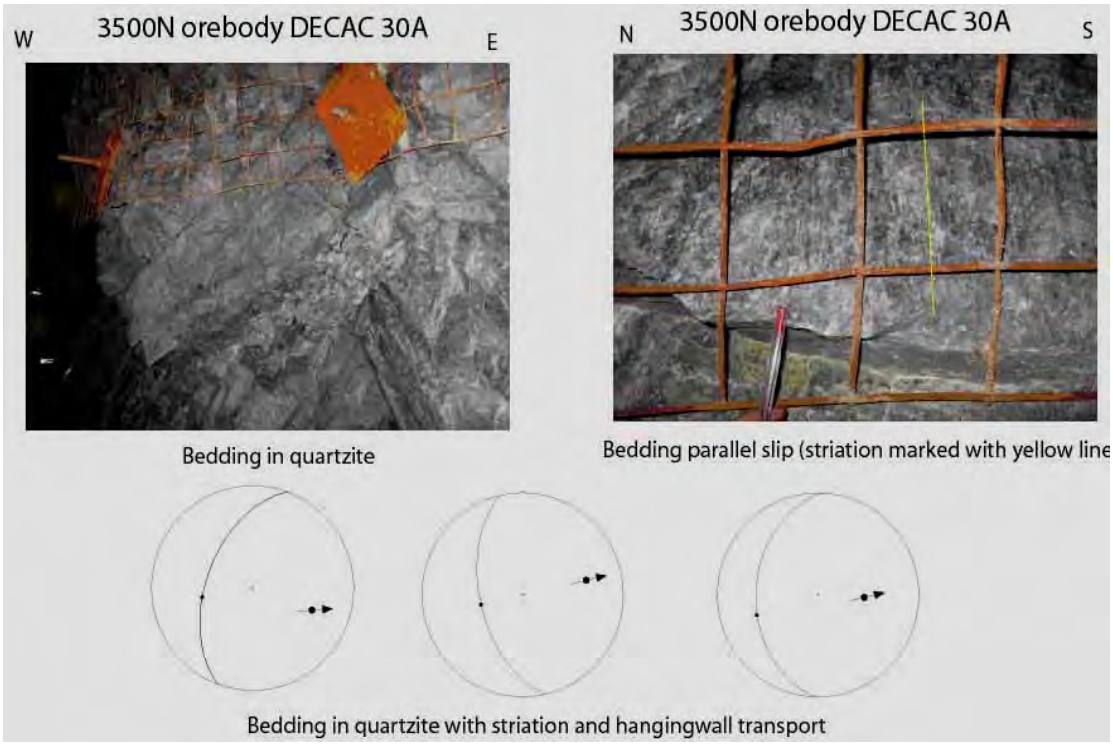

Fig. 17. Photographs of the quartzite basement units. There is strong evidence for bedding-parallel slip related to E-directed transport (note striations and stereonets), these kinematics match some of the post copper faults sets – see section 4.1. Note that in some areas the quartzite is massive and not bedded.

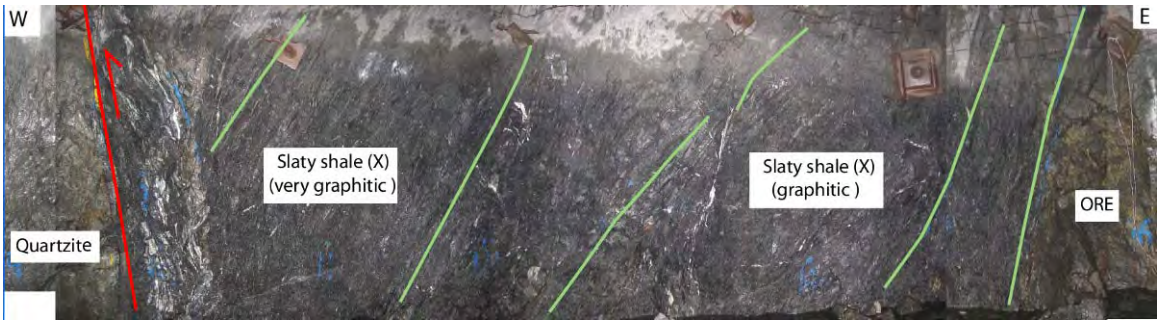

Fig. 18. E-dipping quartzite basement contact, with contact parallel veining. The Slaty Shale (graphitic with an S_3 cleavage and labeled as unit X) is W-dipping and over lies the copper mineralization (labeled as ore). U639 draw point 30E.

2.2.1. Basement geometry 1 – Basement overhang

The steep over hanging basement contacts in the 3000 ore body (Fig. 15) are parallel to very strongly developed S_3 cleavages (green lines in Fig. 19). The field evidence suggests this over hang is related to ductile deformation linked to D_3. This ductile fabric is over printed by later E-dipping thrust faults (Fig. 19) that locally produce complicated field relaitonships. Note that in plan view this overhang is a highly linear contact along the western side of the 3000 ore body (Fig. 7) and also corresponds to a change in basement rocks types (Fig. 11).

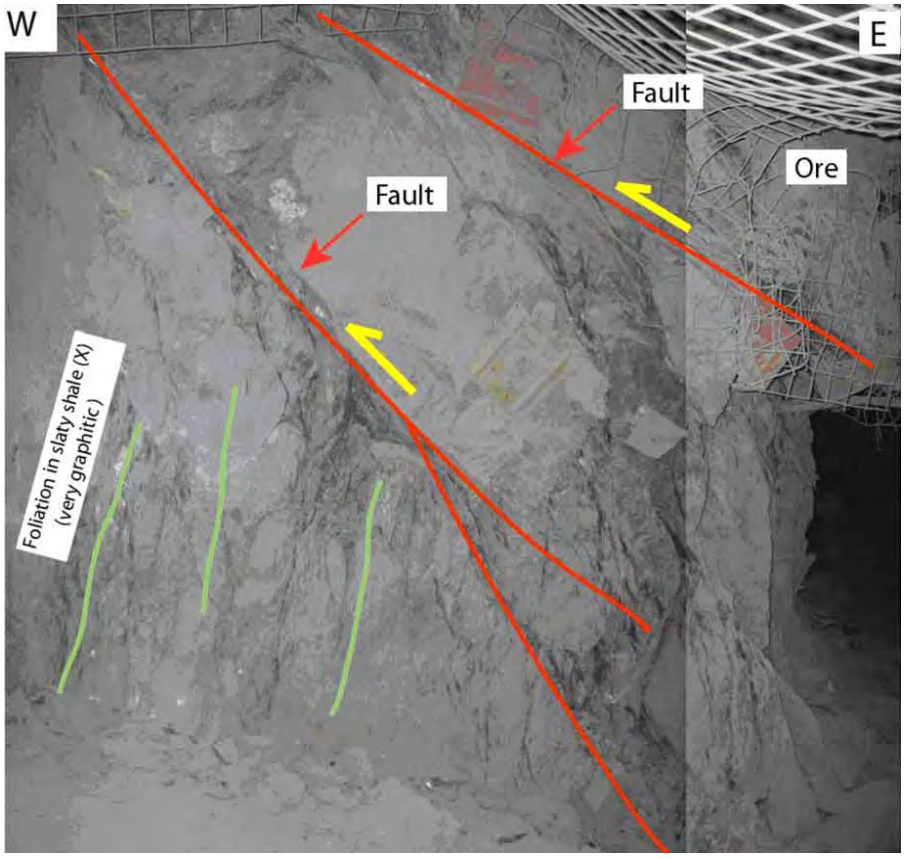

Fig. 19. Field location of geological relationships adjacent to an over hanging basement contact (basement geometry 1 in Fig. 15). Green lines highlight ductile S_3 foliation, red lines highlight late E-dipping faults. K672 DDR, 26b level

2.2.2. Basement Geometry 2 – shallowly dipping contacts.

The basement geometry that defines the shallow-dipping contact beneath the 3000 ore body is quite variable. In many areas the lower basement contact with overlying graphite altered shale is a shallow west-dipping fault (Fig. 20). Fault drag of the steep W-dipping S_3 cleavage in the basement and over-lying graphite-altered shale indicates it is a thrust. This fault geometry beneath the 3000 ore body is similar to the low angle Buck Quartz Fault beneath the 1100 ore body to the south (Fig. 3). The Buck Quartz Fault also has a top-to-the-E transport marked by extension veins (Fig. 21) and also by S_3 cleavages around the Buck Quartz Fault being affected by fault drag (Fig. 3).

A graphite-altered shale unit in many mine areas lies between the underlying lower basement and shale that hosts the Cu breccia ore bodies (commonly termed upper basement or unit X in the core logging codes). The contact between the graphite altered shale and the overlying Cu breccia is either; 1) a low angle fault (Fig. 22) – in some areas chalcopyrite veins occur within these low angle faults or, 2) it is an irregular contact with slivers of graphite altered shale projecting up into the Cu breccias (Fig. 16b). These slivers of graphite altered shale have a strongly developed S_3 cleavage.

Within the 3000 ore body there are also extensive steeper W-dipping N-trending faults in the shale that have been wire framed by Xstrata mine geologists (Fig. 23), but the relationships between the flatter fault along the basement and the steeper dipping faults was not constrained in the mapping program. The NNW-trending lower basement lineament beneath the 3000 ore body that correlates with the trend of the Cu breccias (labelled an F_3 fold in Fig. 8a) is not related to any late faulting that affects the shales – the observed faults are N- to NE-trending (Fig. 23).

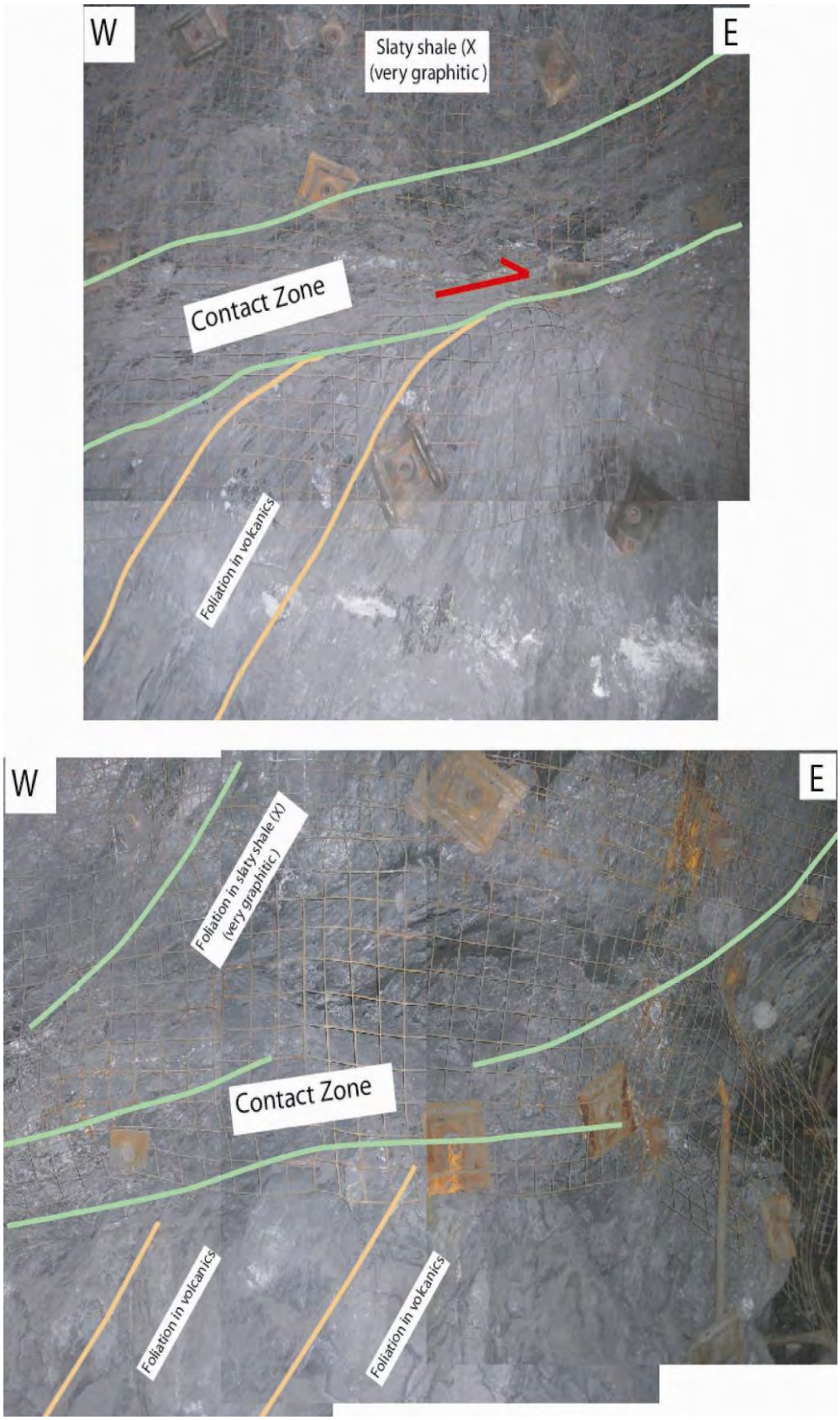

Fig. 20. Examples of basement contacts beneath 3000 ore body (R631 27C). Note steep W-dipping foliation is reoriented by shearing along this contact.

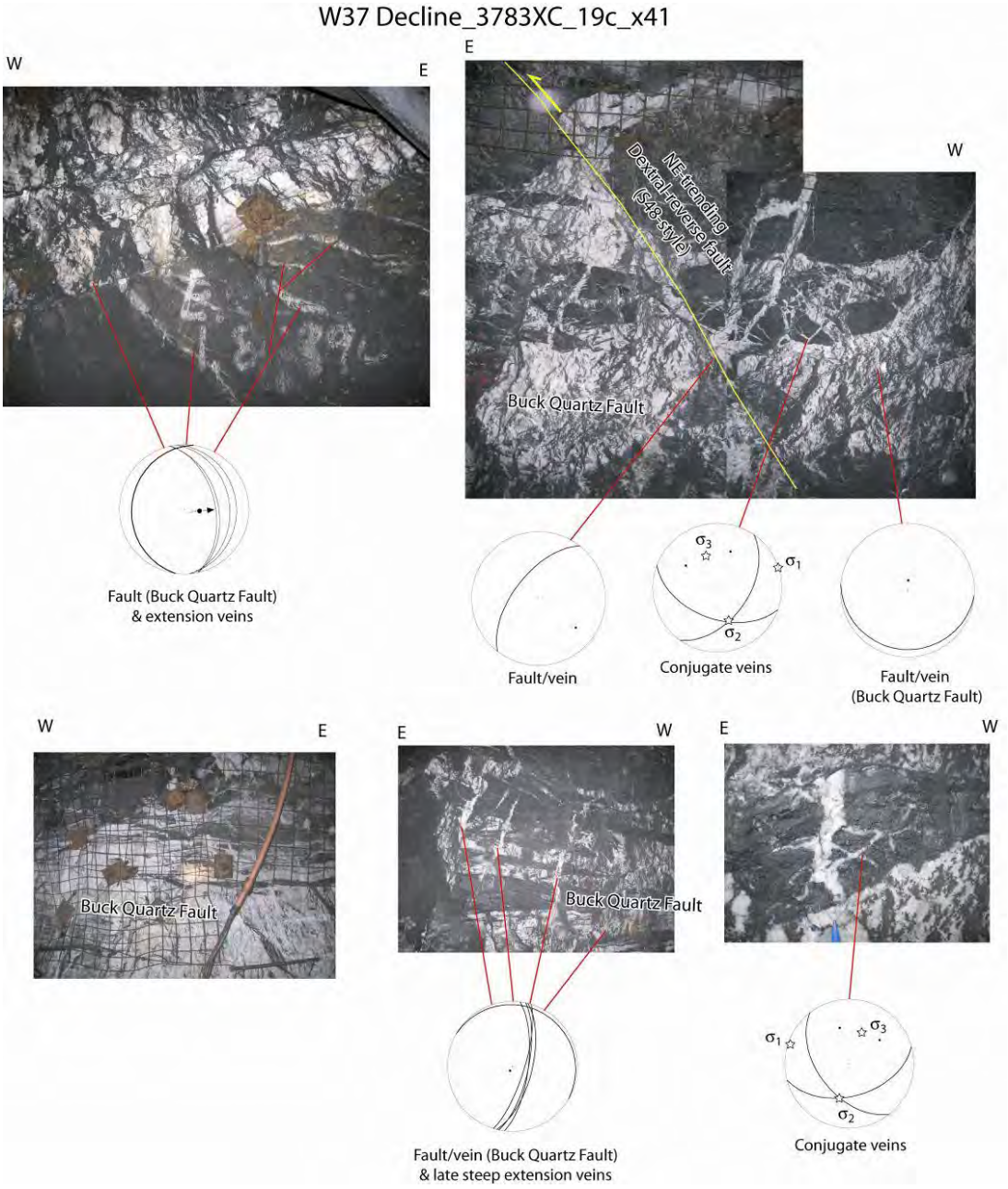

Fig. 21. The Buck Quartz Fault. This structure defines the base of the base of the Urquhart shale in many areas of the X41 mine and is marked by extensive quartz veining. Inspite of the name, some of the vein arrays are laminated, indicating multiple phases of movement and fluid over pressure (bottom right hand of figure). Extension veins arrays (top left of figure), and fault drag of the S_3 cleavages (see Fig. 3), indicate top-to-the-E transport – this phase of transport has been termed D_{4a} by this study). The fault is over printed by later NE-trending dextral reverse faults (top right of figure) – the S48 fault is the major main related feature associated with this (Fig. 3, Fig. 8) and this phase of movement has been termed D_{4b} by this study. There is also evidence for later stages of extensional reactivation of the fault (bottom right figure).

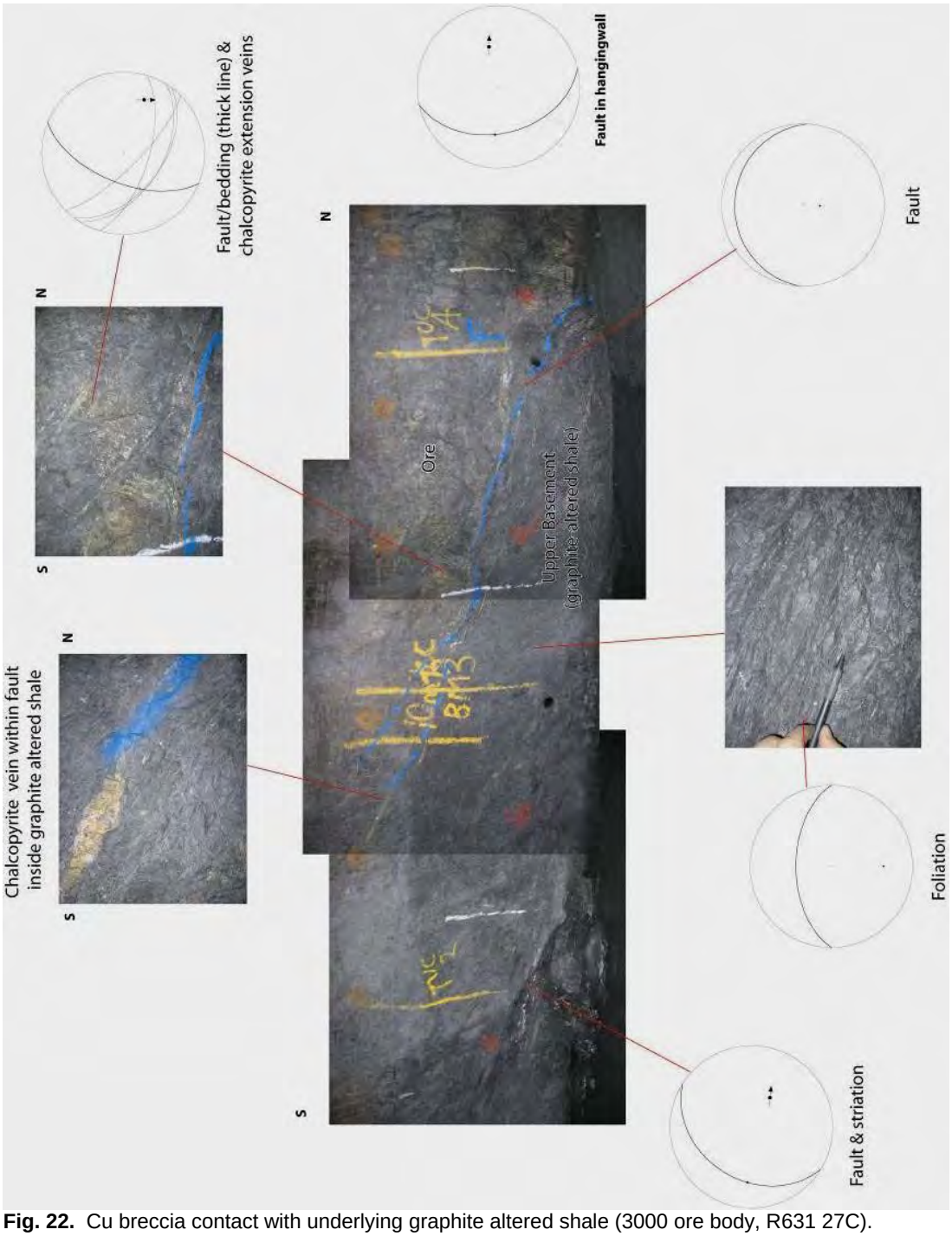

Fig. 22. Cu breccia contact with underlying graphite altered shale (3000 ore body, R631 27C).

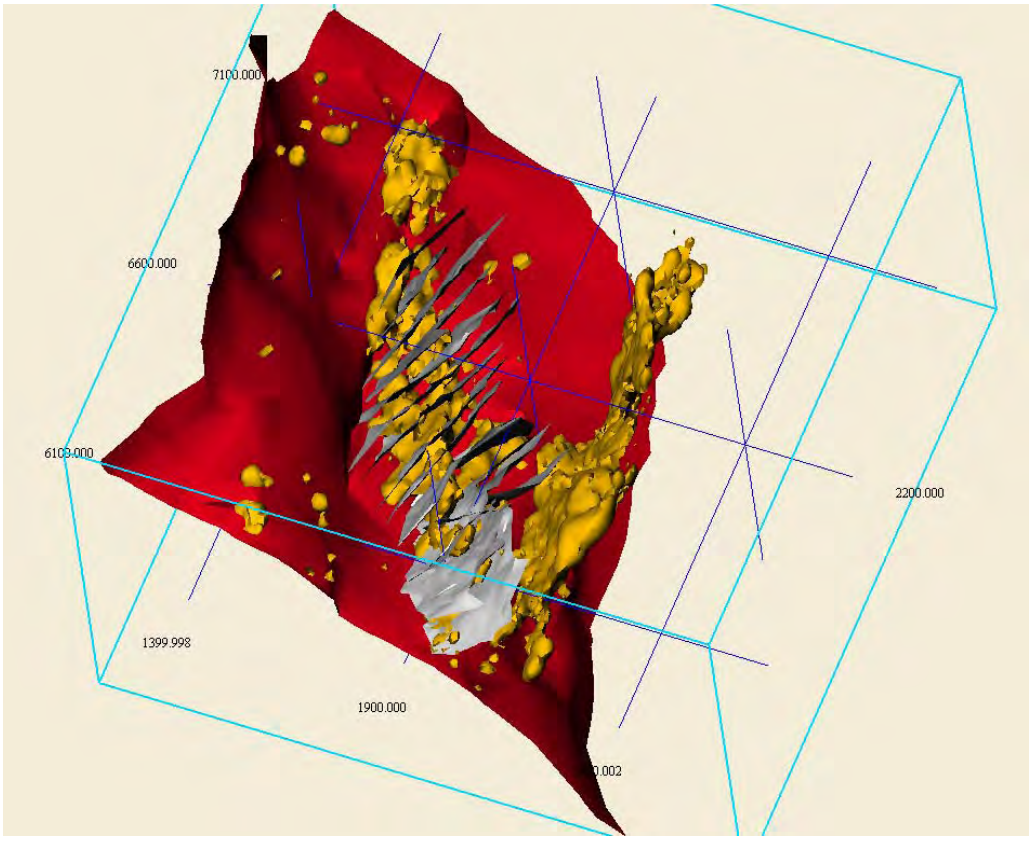

Fig. 23. Grey surfaces are N-trending W-dipping faults (mine wire frames) **for the 3000 ore body only, 3500 ore body wire frames are not included**. Note that the faults are oblique to NW-trending Cu ore within the 3000 ore body. Viewed looking to NW. Red is the mine lower basement contact. Orange surfaces are 2.5% Leapfrog Cu contours, viewed in Fracsis.

2.2.3. Basement Geometry 3 – steeper E-dipping contact beneath the 3500 ore body

In all of the mapped areas beneath the 3500 ore body the contact between the lower basement and overlying units was an E- or NE-dipping fault (Fig. 18, 24). The kinematics of these will be covered in a later section and there is evidence these faults truncate and offset the Cu ore bodies. They also have sudden dip changes from 40 degrees to the east to 80 degrees to the east (Fig. 25). In some areas large laminated quartz veins have developed along this contact with evidence for additional phases of movement represented by fault breccia over prints (Fig. 24). In all areas the S_3 cleavage in the lower basement, and the over lying shales, dipped steeply to the west – this foliation is truncated by the E-dipping faults (Fig. 18, 24). The slaty shale/graphite-altered shale in some places occupies a hangingwall to the Cu breccias (Fig. 18). Whilst extensive N-trending W-dipping faults exist within the 3500 ore body, these do not have an observable control on the lower basement contact with the over lying shales and they will be discussed in a later section. Existing wireframes of these W-dipping faults are truncated at the lower basement contact (Fig. 25).

The N-S basement trends in the 3500 areas (highlighted in Fig. 7) could be controlled by the steep W-dipping faults or by ductile deformation associated with the development of the S_3 cleavage. Unlike the basement trends within the 3000 ore body, some of the some basement trends to the NNW are related to late E-dipping faults that offset the Cu breccias. Therefore caution needs to be used in the interpretation of these particular basement lineaments with respect to the formation of the Cu deposits, as some post date mineralisation.

2.3. Summary of basement topography

Figure 26 summarises the key basement relationships for the Enterprise Mine documented in this study, with the relationships also applicable to other mine areas. Throughout the areas mapped there is a steep W-dipping S_3 cleavage with the development of a graphitic over print within this fabric adjacent to the basement contact in many areas (green unit in Fig. 26). This graphitic unit is strongly over printed by later faulting causing reorientation to a flatter attitude in many areas. However, in areas where no major fault over print occurred, the distribution of this graphitic unit is irregular (e.g., "spike-like" graphite-altered bodies of shale – Fig. 16b) and, in some areas, it is in a hangingwall position to the Cu breccias (Fig. 18). Some of the basement topography, such as the basement overhang (basement geometry 1), appears to be related to the D_3 event. Fig. 27 highlights the inferred pre-Cu basement geometry, with the overhangs linked to D_3 folds. Previous studies have linked the remobilisation of the Pb into F_3 fold hinges at this point (McClay, 1978), and this also is highlighted in Fig. 27. The presence of graphite alteration is inferred to reflect a reduced fluid presence syn-D_3, although the alteration may have occurred preferentially along S_3 cleavage surfaces. There is a large volume of this graphitic unit beneath the much larger X41 ore body to the south (Fig. 3)(carbonaceous mylonite in Fig. 7B of Bell et al., 1988). This graphite–altered unit may have been directly associated with the ore-forming fluids or acted as a reduced package of rocks that facilitated precipitation of Cu from ore-bearing fluids (e.g., Wilde et al., 2006).

The majority of quartzite occurs in flatter dipping lower basement zones (Fig. 8, 28). This may reflect early dip refraction of the lower basement fault (Paroo Fault) through rheologically different units during D_1 or D_2 thrusting – this geometry is substantially modified by the D_3 deformation event. Significantly, the flatter dipping zones of lower basement have previously been linked to focussing of Cu-bearing fluids (Bell et al., 1988). The Leapfrog models (Fig. 8) indicate that the presence of quartzite units, even if just interbedded with the volcanic rocks, appears to have a correlation with Cu mineralisation. These quartzite units may be linked to silicification of the overlying shale producing a unit rheologically favourable for breccia development (Fig. 28). Alternatively the quartzite may have been a fluid conduit for Cu-bearing fluids sourced from deeper units.

The significance of the link between N- and NW-trending basement lineaments to the overlying Cu breccia bodies will be discussed at the end of the next section which establishes the kinematics syn-Cu mineralisation.

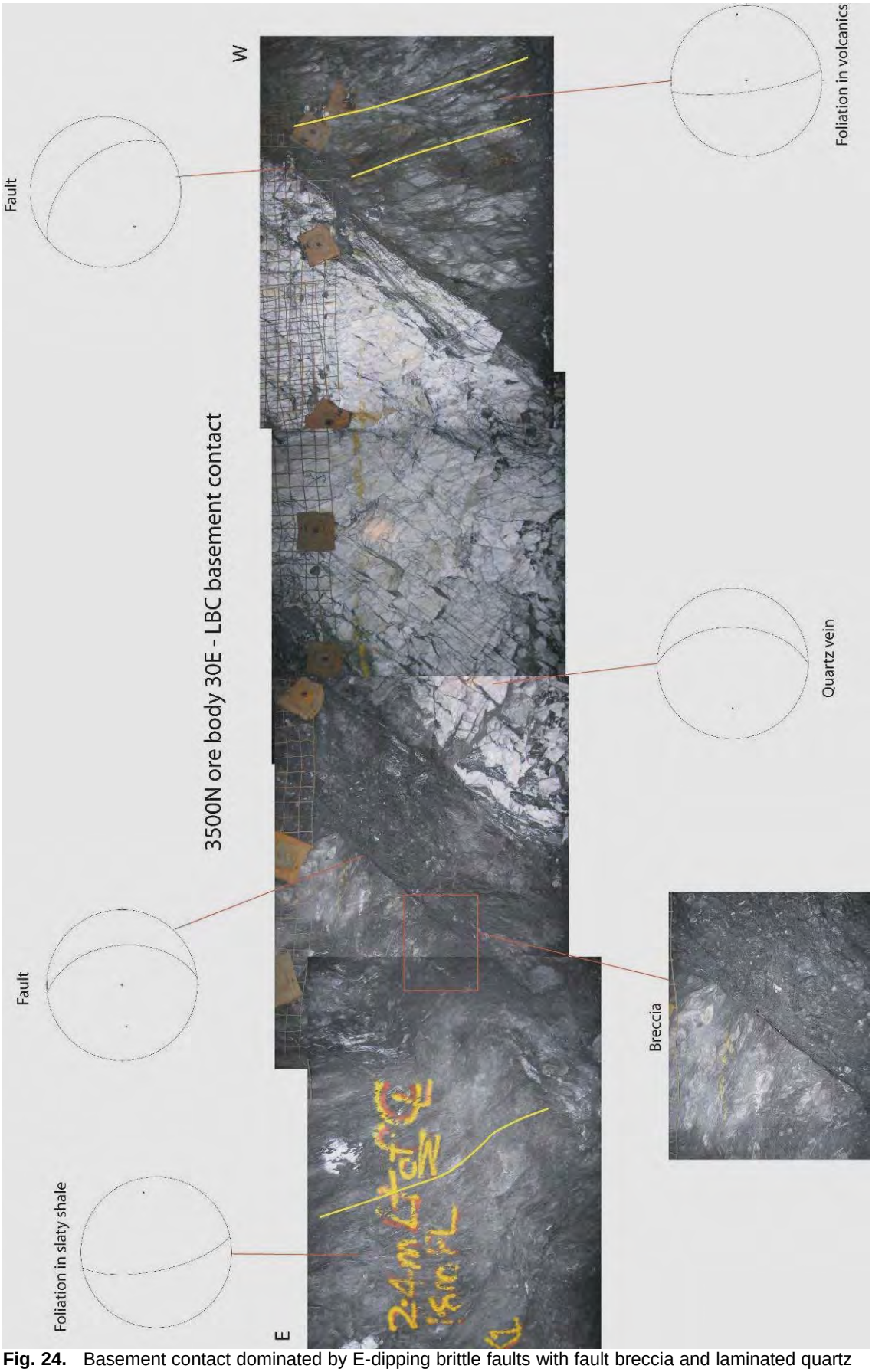

Fig. 24. Basement contact dominated by E-dipping brittle faults with fault breccia and laminated quartz veins (U66 DEC 30E level, 3500N).

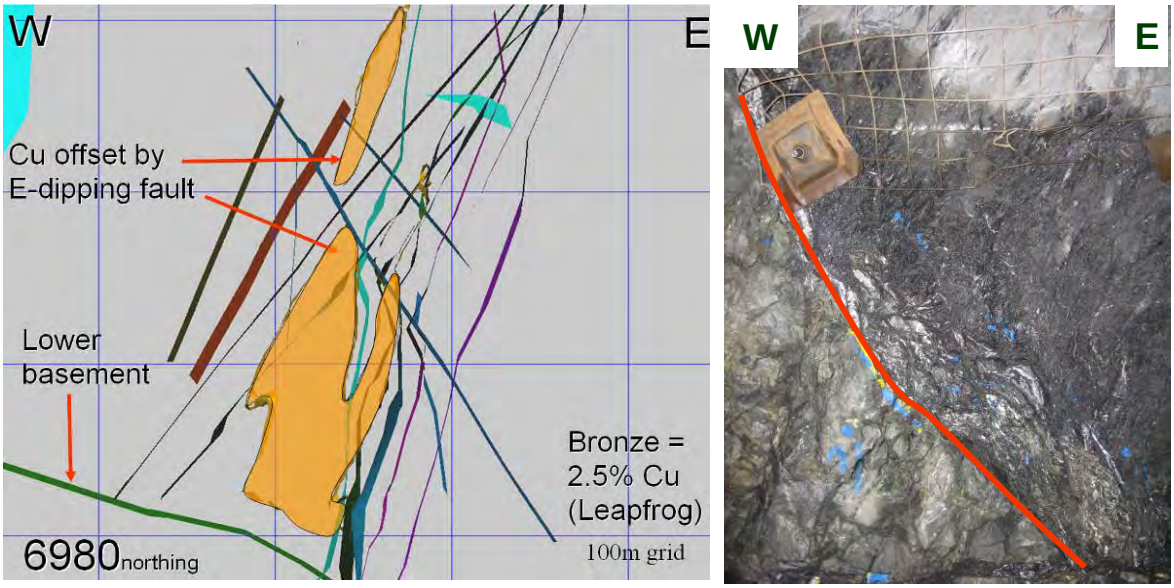

Fig. 25. Section of W and E-dipping faults (produced by Xstrata mine geologists, viewed in Fracsis). Note Cu offset across E-dipping faults. Photograph (right) of sudden dip change on an E-dipping fault juxtaposing lower basement quartzite with over lying slaty shale (U639 draw point 30E).

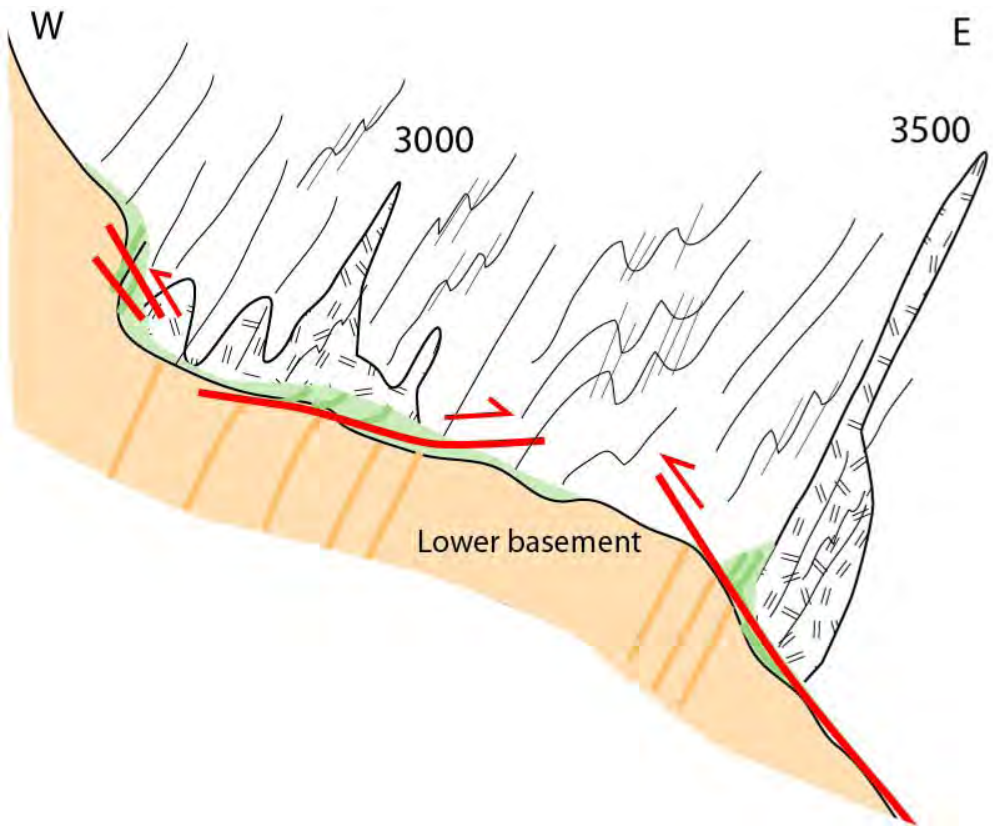

Fig. 26. Observed geometries of graphite-altered shale (green coloured units), S_3 foliation within the lower basement and shale (darker orange and green lines respectively) and later faults (red) along the basement contacts – **note that extensive steeper W- and E-dipping faults exist in the over-lying shales (see Fig. 23, 25), but are not shown on this figure.**

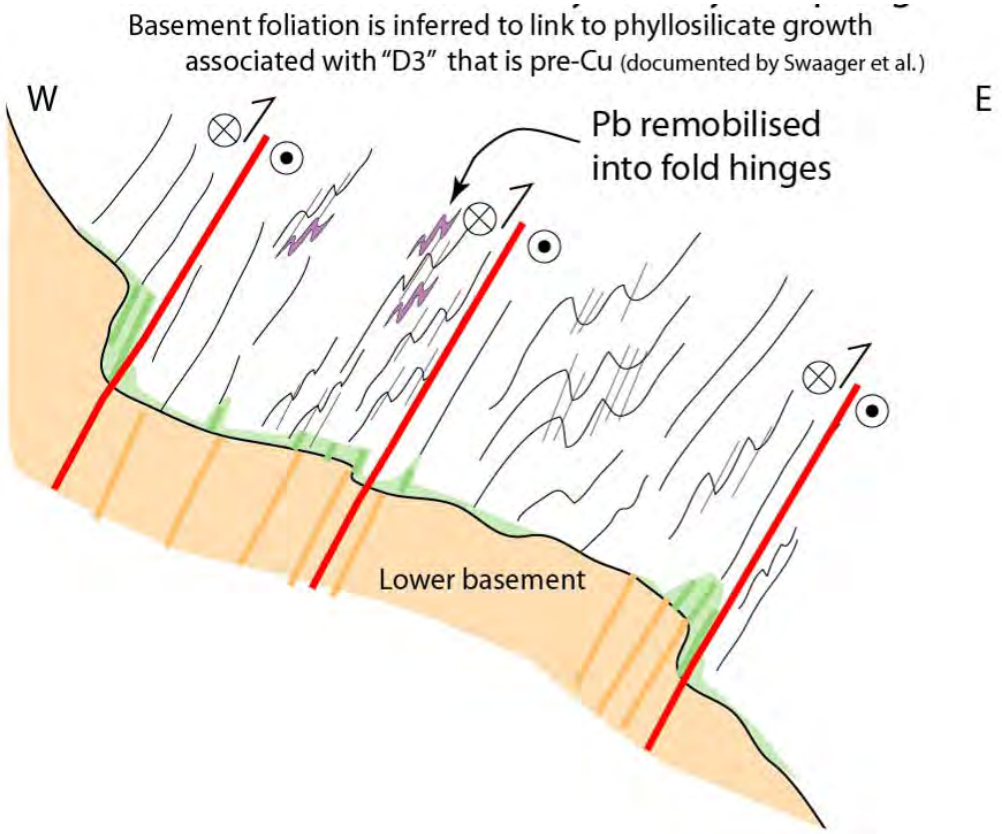

Fig. 27. Inferred geometry of Enterprise basement pre-Cu. The irregular development of the graphitic overprint within the shale (green colour) may reflect the present of a reduced fluid along this basement contact at this time. Purple highlights the syn-D_3 remobilisation of Pb lodes into F_3 fold hinges.

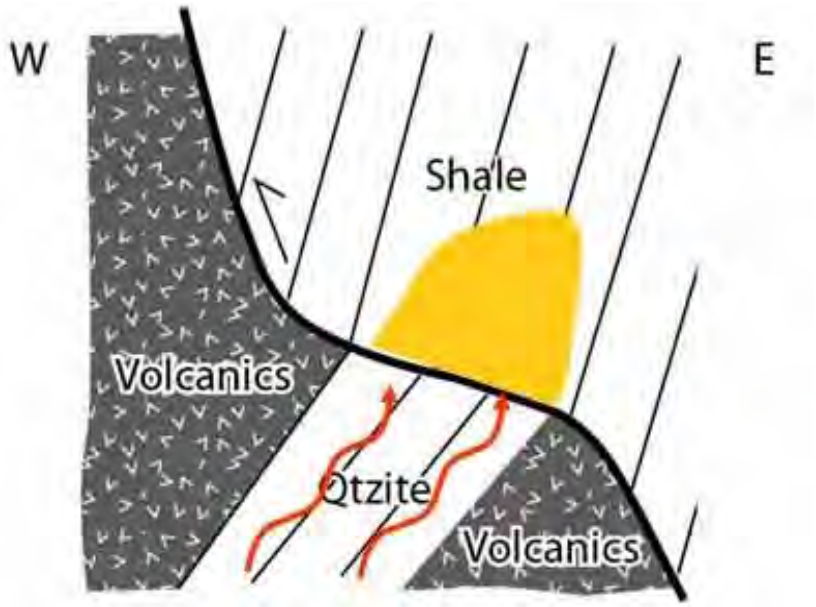

Fig. 28. Model where the silicification of over lying shale is linked to an underlying silica source (quartzites). It is inferred that this creates a unit within the shale that was rheologically favourable for developing Cu breccias. **It should be noted that some mineralisation does occur outside the inner siliceous core of the silica-dolomite alteration halo (Fig. 3).**

3. Kinematic analysis of the Cu breccias

The term copper breccias, instead of syn-Cu deformation, has been used because many of the later faulting events that over print the copper breccia bodies are also associated with chalcopyrite (but no major brecciation). As noted by previous workers (e.g., Perkins, 1984; Bell et al., 1988), the underground study also observed that the key control on the development of the Cu breccias was bedding-parallel slip (and fluid flow) along planes dipping on average 60 degrees to the west (Fig. 29), with some slip along D_3 ductile shears. Previous studies have also highlighted that the F_3 folds control the ore shoot geometries, and that the Cu post dates the development of the S_3 cleavages (Perkins, 1984; Bell et al., 1988) – this study also observed similar features consistent with this interpretation.

Within the majority of the ore bodies mapped remnant bedding could still be identified across the entire zone of high Cu (Fig. 29), even though at the metre-scale bedding can be totally disrupted. The copper breccias have mesoscopic quartz, with chalcopyrite being the dominant infill (with some pyrite). There is no mesoscopic evidence for multiple phases of brecciation (e.g., Fig. 30) and the copper breccias appear to reflect a single discrete event. One outcome of the mapping was that apart from chalcopyrite developing along bedding surfaces, the Cu mineralisation was associated with the development of extension vein arrays (Fig. 30, 31, 32, 33) that in many areas prograded into matrix-supported breccias (the matrix being chalcopyrite and pyrite; Fig. 31, 32).

3.1 Syn Cu breccia slip vector orientation

This study focussed on the systematic mapping of the observed chalcopyrite extension veins within the copper ore bodies along key Cu and basement trends in both plan & vertical directions (Fig. 4, 34). This was done to constrain the extension direction along the bedding planes (= slip vector orientation), the focus was on areas were complete brecciation of the host shale had not occurred. Whilst some variation existed, the dominant intersection between the extension veins and bedding (=slip surface) was remarkably consistent across all of the data localities with the intersection direction pitching steeply to the south on the W-dipping bedding surfaces (Fig. 35). This similarity existed in different structural locations with respect to basement, trend of the Cu ore body and also was independent of fold plunge (which varies between the 3000 to 3500 ore bodies). The dominant angle between the bedding and extension veins in the data set from the Enterprise Mine indicates a component of non coaxial deformation, with the hangingwall transport direction being top-to-SE transport indicative of sinistral-reverse movement (e.g., Fig. 32). The mapping did also identify a component of coaxial deformation with conjugate veins developed in some localities (Fig. 37). Apart from vein/bedding relations, there is also evidence for a component of reverse movement associated with the development of the Cu breccias that, when combined with the extension vein data, indicates the system underwent sinistral-reverse slip. Evidence for this is marked by the presence of dilational jogs indicative of reverse movement associated with copper mineralisation (Fig. 38), and also the location of Cu breccia on lower angle dipping bedding in preference to steeper dips (Fig. 39). The data are inconsistent with a kinematic model utilizing dextral-reverse movement associated with the development of the Cu breccias (for a dextral reverse system the fault/vein intersection direction should plunge to the N not the observed S plunge).

Hangingwall paleotransports (see Miller and Wilson 2004) were calculated for all of the data by taking the average intersection direction between the extension veins and bedding for each data locality and assuming the deformation had a component of reverse movement. This is a similar approach to that highlighted by Davis and Reynolds (1996, p. 299). The results from this analysis are compiled on Fig. 35 and Fig. 36. These arrows represent the transport direction of the rocks in the hangingwall of the fault calculated at the faults pole. This allows the orientation and transport direction of a fault/slip surface to be plotted at one point (the circle at the centre of each arrow is the faults pole). This allows rapid comparison of different structural data sets which will be done later in the report. If faults have the same orientation but different slip directions then there must have been either a change in the shape, or orientation of, the palaeostress tensor. The analysis highlighted a small number of

data points that gave top-to-the-E hangingwall transport. These represent deformation that over prints the earlier Cu breccias and they are discussed in section 4.

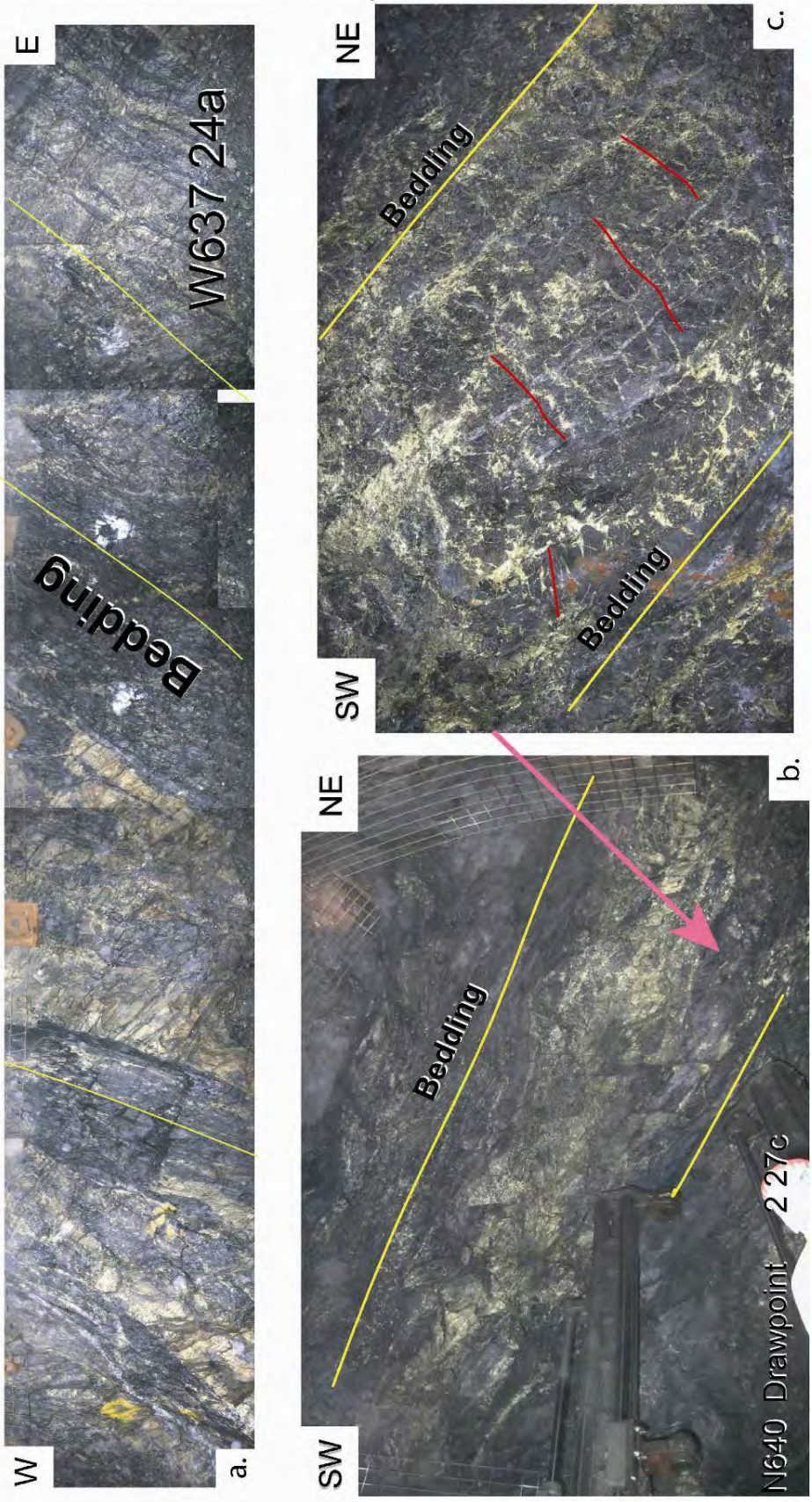

Fig. 29. Bedding slip control on Cu breccias (a) Strongly developed mineralisation parallel to bedding (W647, 24A, 3500S ore body). (b) Cu mineralisation parallel to bedding. N640 DPT2 27c, 3000 ore body. (c) Detail of extension veins from 21b associated with mineralisation (red lines).

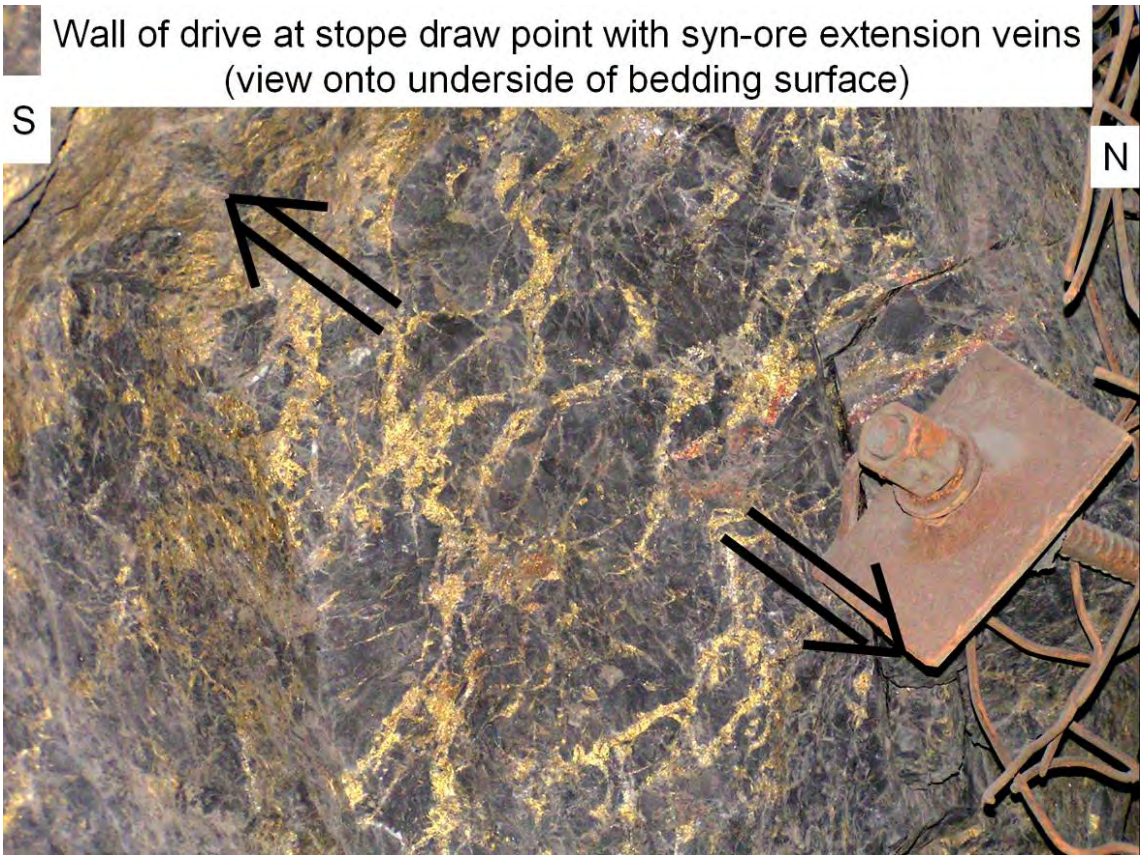

Fig. 30. Syn-Cu extension veins intersecting a bedding surface (infill is dominantly chalcopyrite). Arrows highlight extension direction. There is no evidence for multiple phases of brecciation.

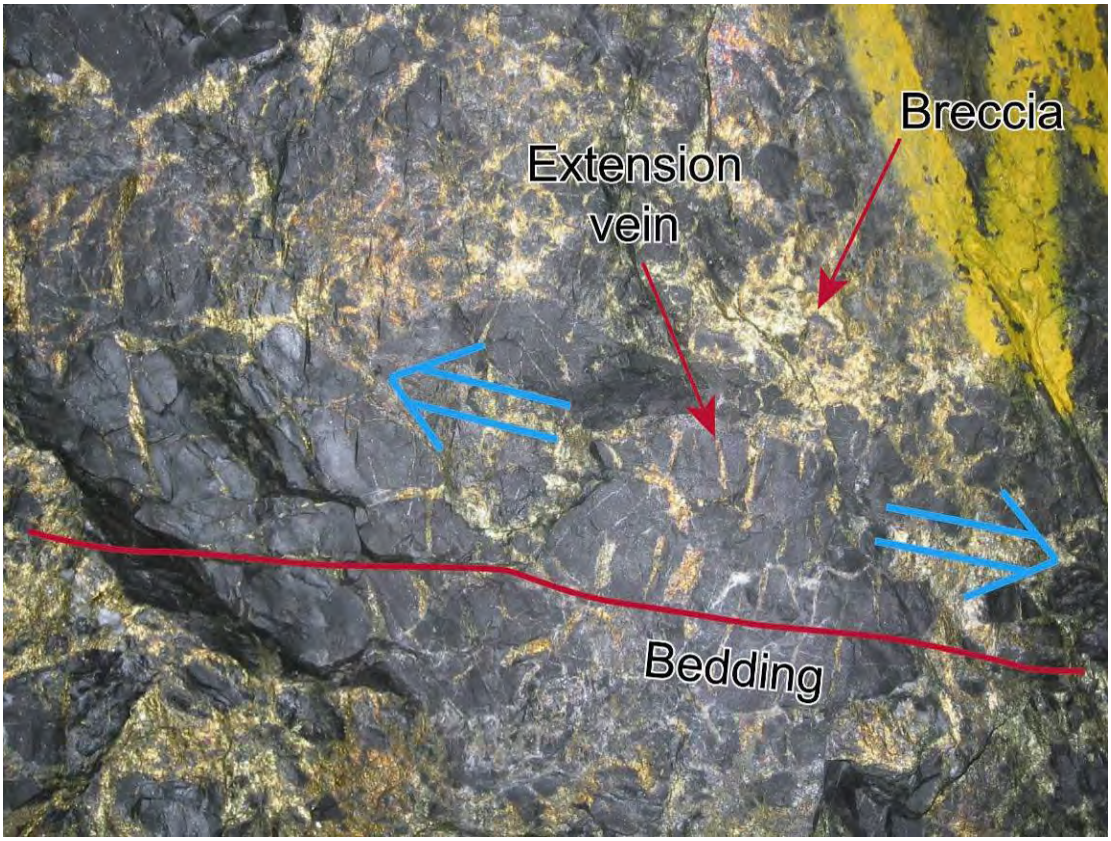

Fig. 31. Syn-Cu breccia veins that grade into a small package of breccia. M65 SEDR, 26b, 3000 ore body.

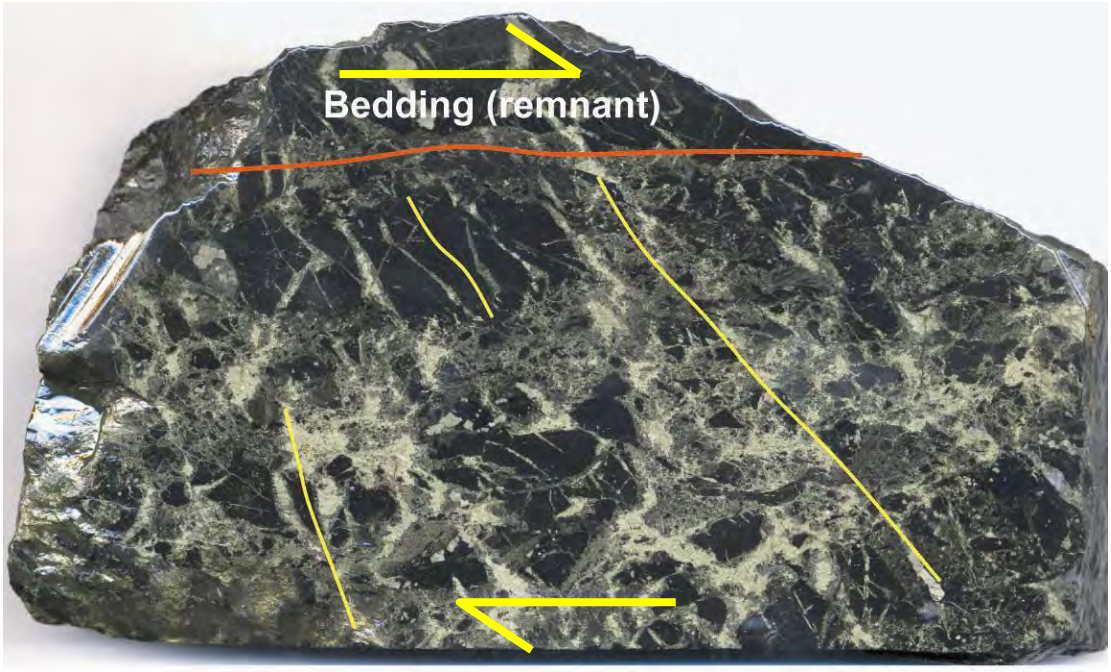

Fig. 32. Syn-Cu extension veins (yellow line) with remnant bedding (red line). The angular relationship between the two indicates a component of non coaxial deformation highlighted by yellow arrows. N640 DPT2 27c, 3000 ore body. Extension vein and bedding data from this locality are given in Fig. 35). Note the veins grade into a breccia on right hand side of sample.

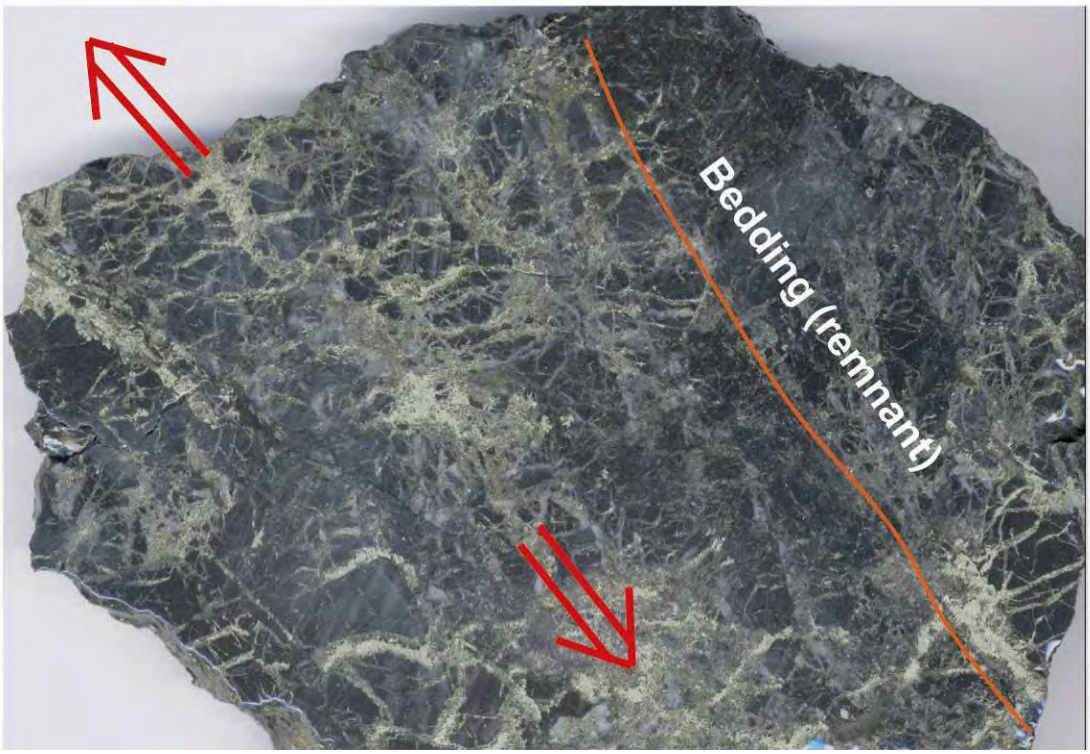

Fig. 33. Syn-Cu extension veins with remnant bedding (sample from 1900 ore body, X515, 18c). Extension vein and bedding data from this locality are given in Fig. 35).

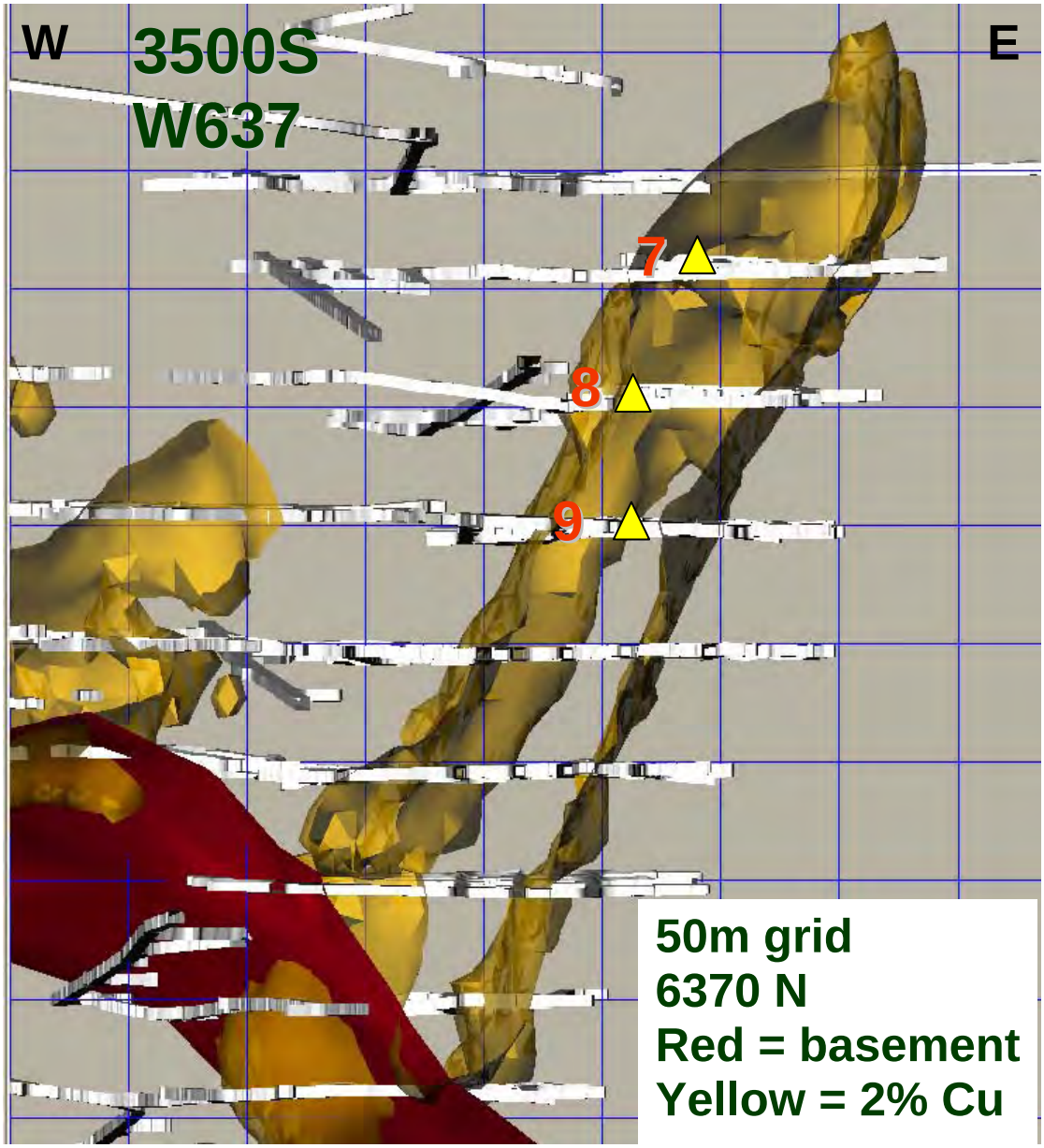

Fig. 34. Figure highlighting vertical extent of data localities for bedding/extension vein analysis (points 7, 8 and 9 lie at a similar northing and easting in Fig. 4). Viewed in Fracsis.

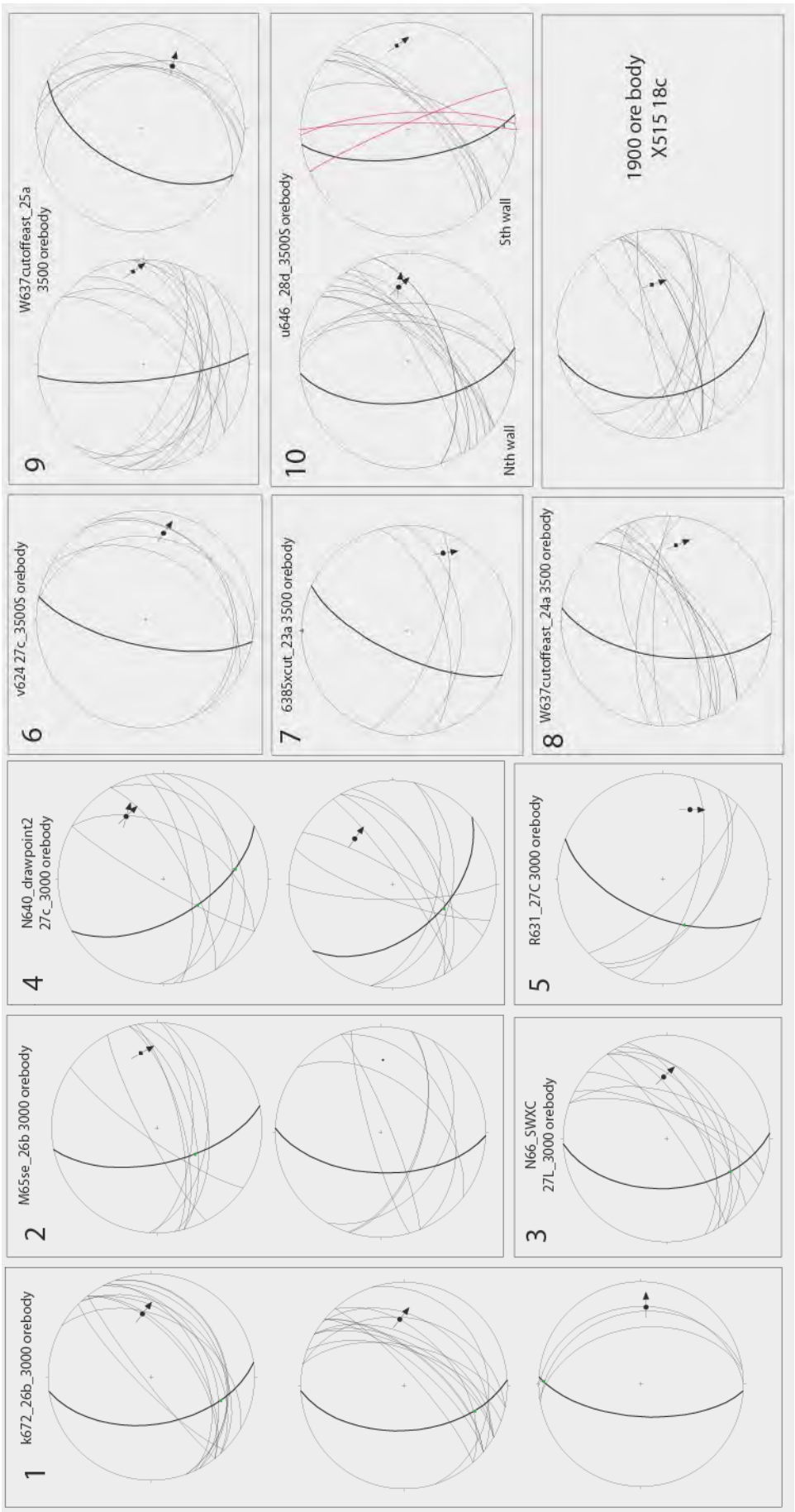

Fig. 35. Bedding and extension vein data. Field localities are marked on Fig. 4, 34 and listed in Table 1.

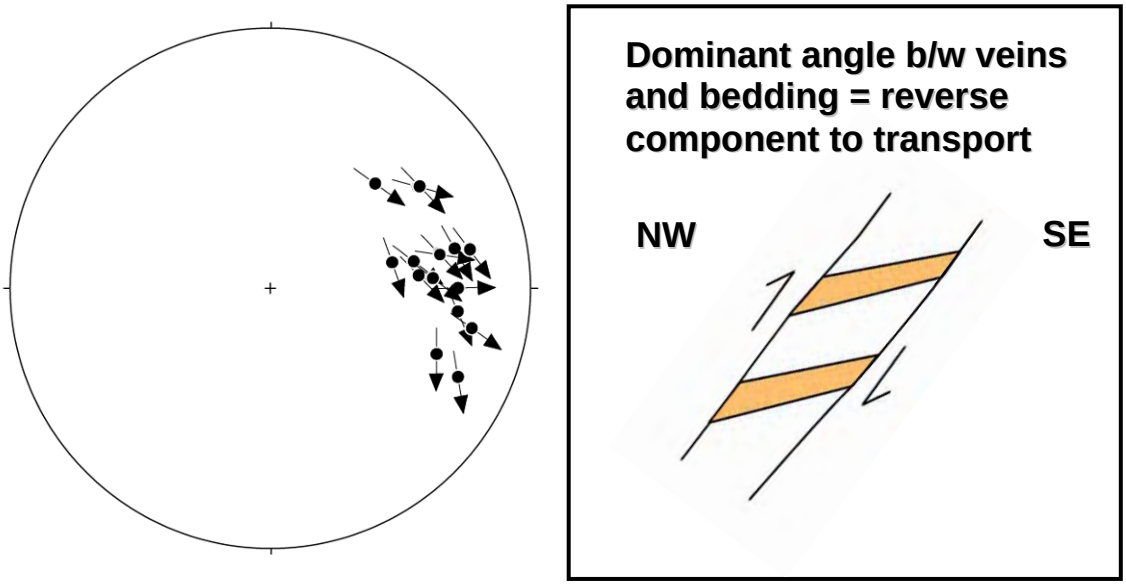

Fig. 36. Stereonet plotting bedding/extension vein data from copper breccia bodies as projected hangingwall palaeotransports. Hangingwall paleotransports (see Miller and Wilson 2004) were calculated for all of the data by taking the average intersection direction between the extension veins and bedding for each data locality and assuming the deformation had a component of reverse movement. These arrows represent the transport direction of the rocks in the hangingwall of the fault calculated at the faults pole. Inset highlights dominant bedding extension vein geometry (see Fig. 32, 35).

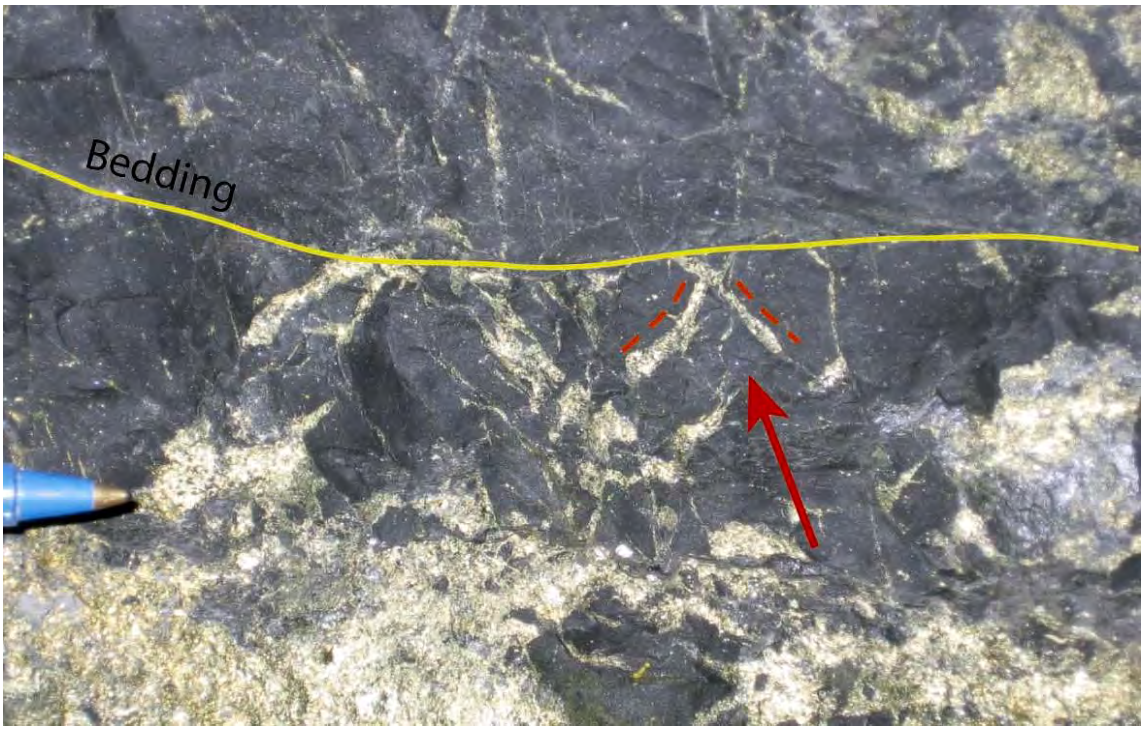

Fig. 37. Note conjugate veins highlighted by red arrow. Bedding is marked with a yellow line. M65 SEDR, 26b, 3000 ore body.

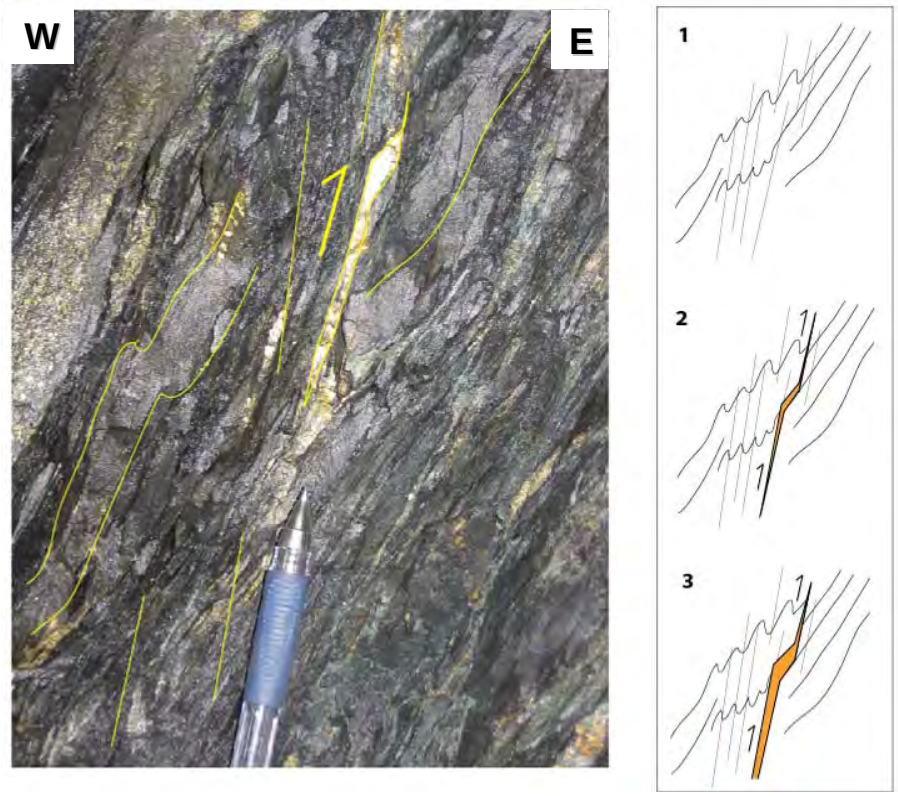

Fig. 38. Jog-related chalcopyrite (slip along an S_3 cleavage plane). v624 6240 XC 27C, 3500S ore body

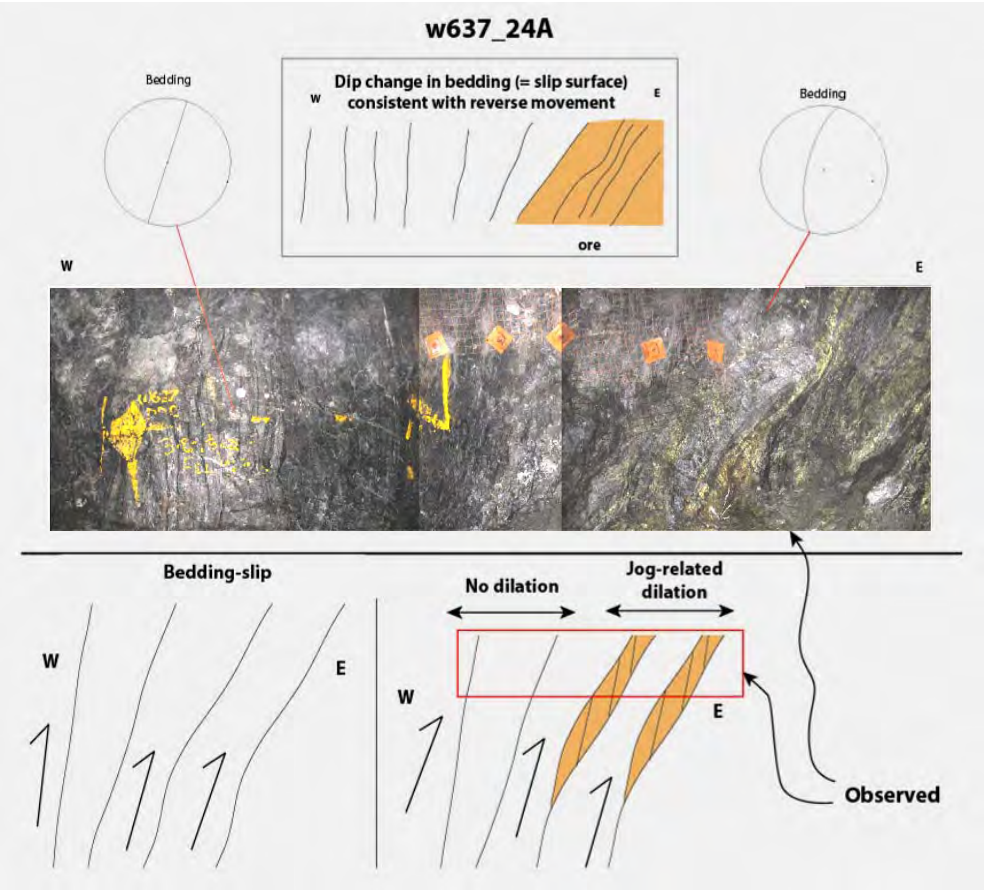

Fig. 39. Copper breccia distribution consistent with reverse movement. Mineralisation is not located on steeper dipping beds, which is consistent with a reverse component of movement associated with Cu mineralisation.

3.2 Microstructure of syn-Cu extension veins

Microstructural analysis was undertaken to assess the nature of the veins arrays used in the kinematic analysis in the previous section. These veins have a consistent extension direction across the entire ore body and the field relationships indicate they formed synchronously with the development of the copper breccias. Fig. 40 is a series of photo micrographs of the vein arrays shown in Fig 32, which is a sample that has vein hosted mineralisation that grades into more massive chalcopyrite breccia. The photomicrographs highlight transitions from vein associated mineralization to breccia-hosted (Fig. 40a, 40b). The quartz within the veins commonly has fibres indicating they are extension veins (Fig. 40c, 40d, 40e and 40f) with median sutures still preserved. Furthermore, in areas of irregular wall rock contact, the fibres indicate a component of extensional shear marked by oblique fibres (Fig. 40b). This indicates the veins are not forming via open space growth. The chalcopyrite has a variable habit and in places is parallel to the quartz fibres but is also disseminated in the wall rock. The quartz in most of the samples is free of later defects and similar to the strain free quartz described by Perkins (1984). Some of the quartz veins are also associated with mica (Fig. 40f).

The quartz fibres highlighted in Fig. 40 are identical to the quartz fibres documented in by Swager (1985) (see Figures 9C, 9D and 11D of that paper). These fibres where related to the D_3 event by Swager (1985), however, he did not constrain the 3-D orientation of the extension direction marked by the quartz fibres. The oriented samples and vein analysis analysed in this study indicate the veins, and associated quartz fibres, represent sinistral-reverse movement (Fig. 35) which is not consistent with the D_3 event. Note that during copper mineralisation slip occurred along bedding and the S_3 cleavage (Fig. 38) and a 2-D thin section cut across the S_3 cleavage would show quartz fibre growth parallel to S_3.

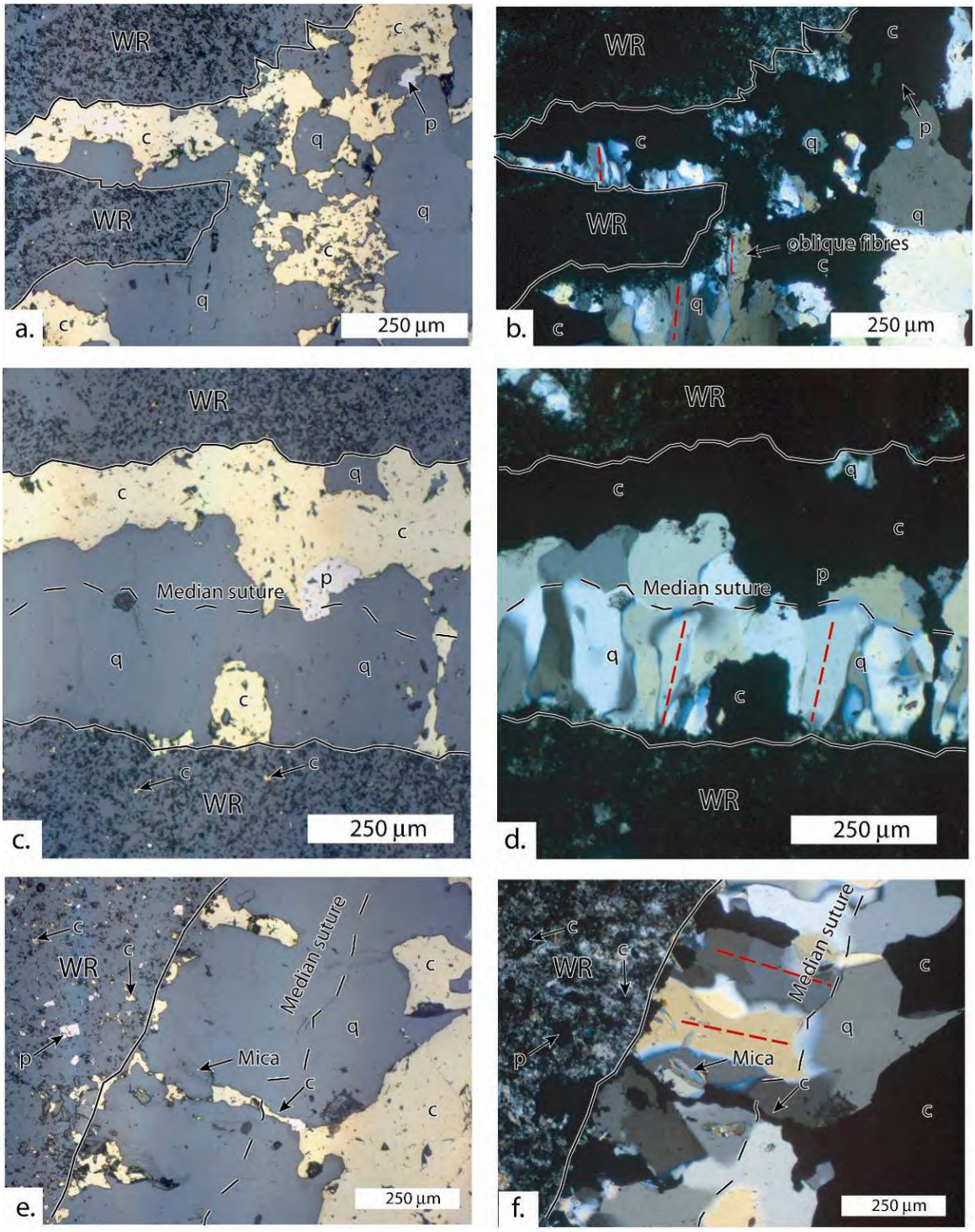

Fig. 40. Photo micrographs of minerlaised extension veins. See text for discussion.

3.3 Foliation/cleavage control to breccia development

Previous studies have highlighted that the F_3 folds control the development of Cu ore bodies, and that the Cu post-dates the development of the S_3 cleavages (Perkins, 1984; Bell et al., 1988), with the plunge of F_3 folds being a control on ore shoot orientation (Fig. 41). Furthermore, ore bodies such as the 650 (Fig. 41), have developed within the axial plane of F_3 folds (=S_3) and also transect the dominant W-dipping bedding surface (see Fig. 7D of Bell et al., 1988). The S_3 cleavage has previously been linked to providing additional permeability for Cu-bearing fluids (see Fig. 17 of Bell et al., 1988). This study has observed field relationships that are consistent with these earlier interpretations.

Apart from providing a mechanism for increasing the pre-existing permeability of the rock mass, the S_3 cleavage also provides a pre-existing anisotropy that facilitates brittle failure and the development of breccias. In areas where the S_3 cleavage is strongly developed, the Cu breccia develops by fragmenting the rock by failure along bedding planes, the development of the extension veins orthogonal to the slip direction (marked as the dominant vein orientation in Fig. 42) and also by failure of the pre-existing S_3 cleavages (note schematic sketch in Fig. 42). The combination of these three fracture directions resulted in the rapid fragmentation of the rock. The result of all the above, is that there is a link between the F_3 fold plunge (i.e. the L_{03} intersection lineation) and ore shoot plunge (Fig. 41).

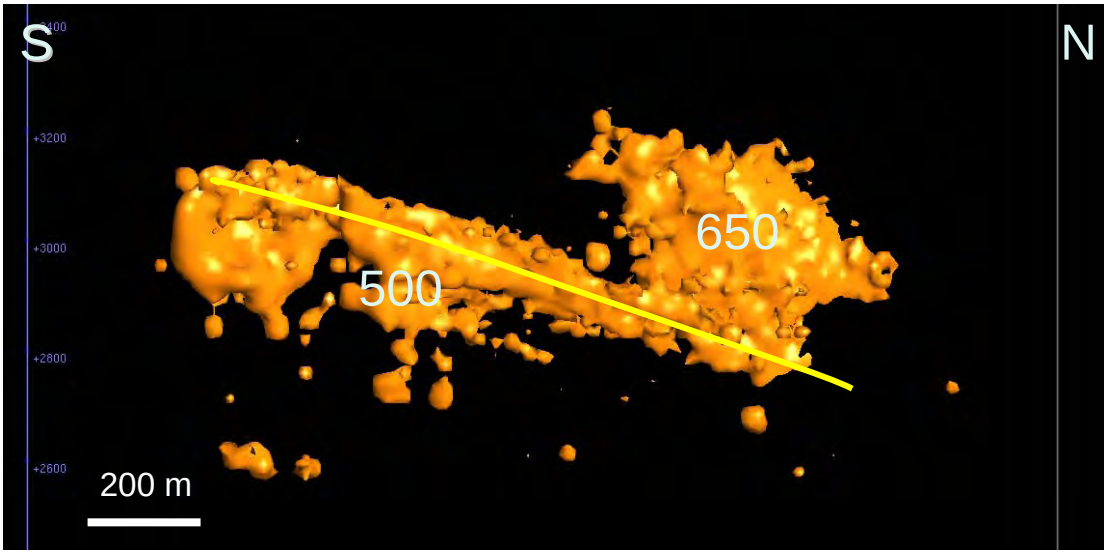

Fig. 41. Leapfrog model (2% Cu) for shallow level ore bodies (these are located in Fig. 1 and the 650 ore body is also shown in Fig. 4). The ore shoot orientation of the 500 ore body (yellow line) is parallel to the F_3 fold plunge.

The underground mapping identified that there are major fold plunge variations within the Enterprise mine. Compared to the rest of the Isa Cu mine the fold plunges are much steeper within the 3500 ore body. This ore body also has much steeper plunging high grade ore shoots (3500S and 3500N), which is inferred to be directly linked to the steeper fold plunge in this particular mine area (Fig. 43). Significantly, the consistent extension direction and inferred bedding parallel slip direction from extension vein arrays (Fig. 35) is the same in areas of steep fold plunges and shallow fold plunges. This indicates the folds pre-date the Cu mineralisation.

The 3500 ore body lies in the direct hangingwall of a major ductile structure termed the footwall shear, which defines a sharp footwall cut off to the 3500 ore bodies and the siliceous inner core (Fig. 44). Cu mineralisation to the east of the footwall shear is hosted by dolomite altered shale (X block) and compared to the 3500 ore body the folds within the direct footwall of this shear have shallower plunges to the north.

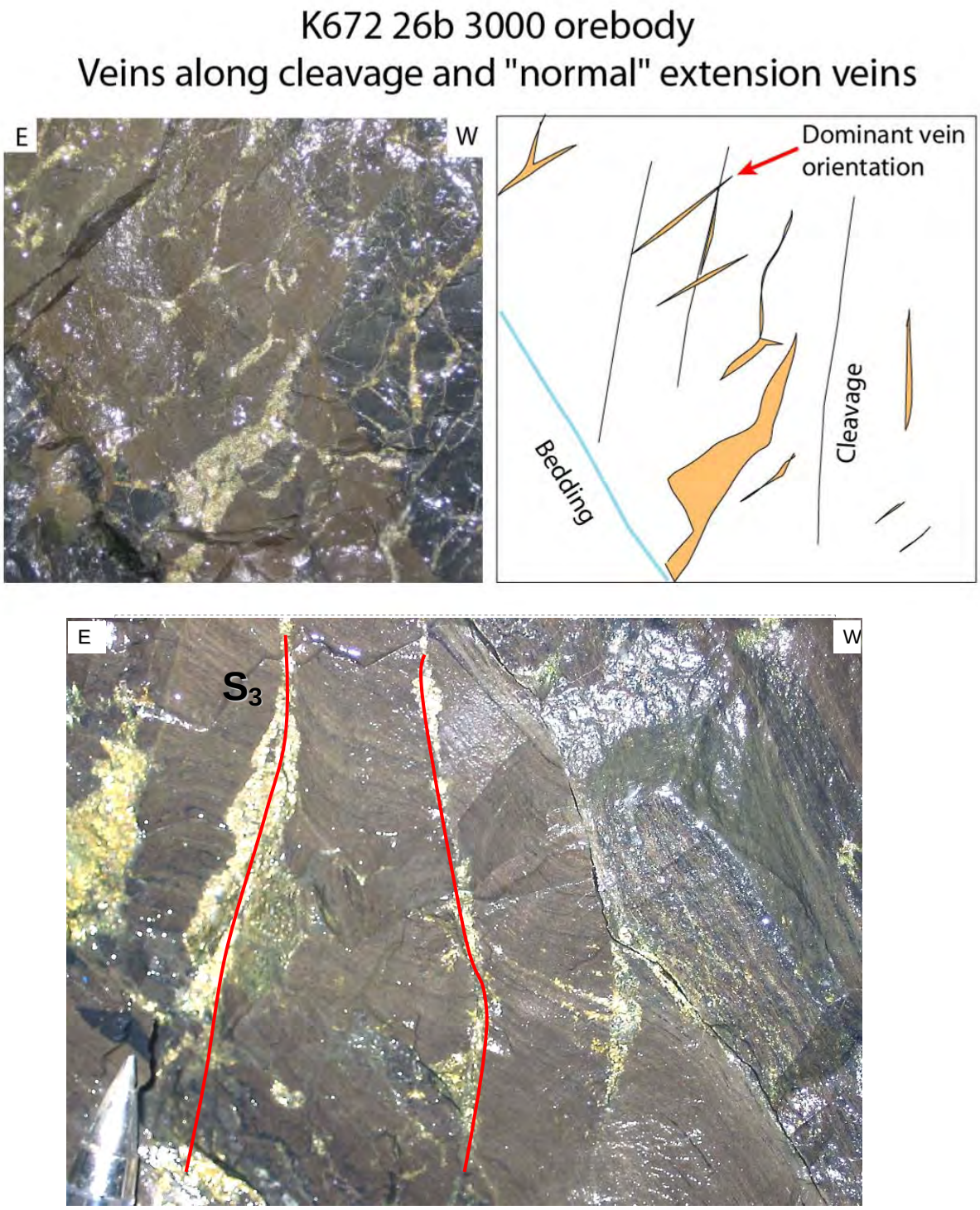

Fig. 42. Chalcopyrite following the S_3 cleavage and bedding. Sketch highlights chalcopyrite veins developing along S_3 cleavage planes and as veins orthogonal to the maximum extension direction and is labelled as the dominant vein orientation (observed in the mine). See text for discussion.

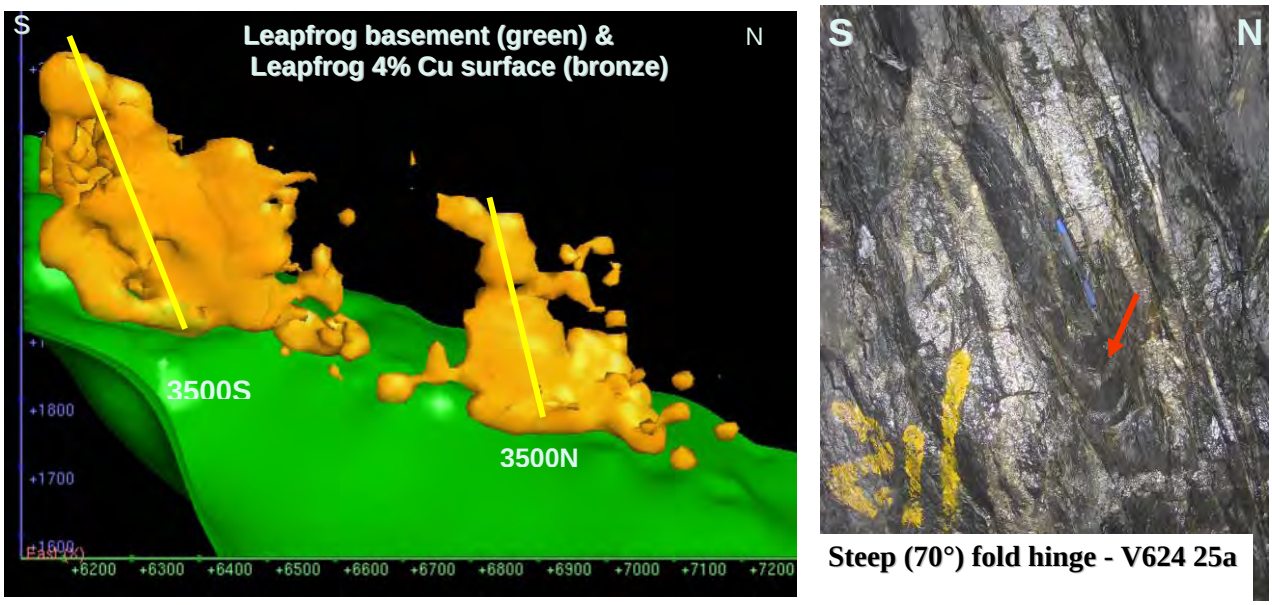

Fig. 43. Leapfrog model of 4% Cu and lower basement (green) highlighting steep ore shoot plunge for 3500S and 3500N ore bodies. These steeply plunging 3500 ore bodies are inferred to be due to much steeper plunging F_3 folds (see photo at right) in this area of the mine compared to other areas.

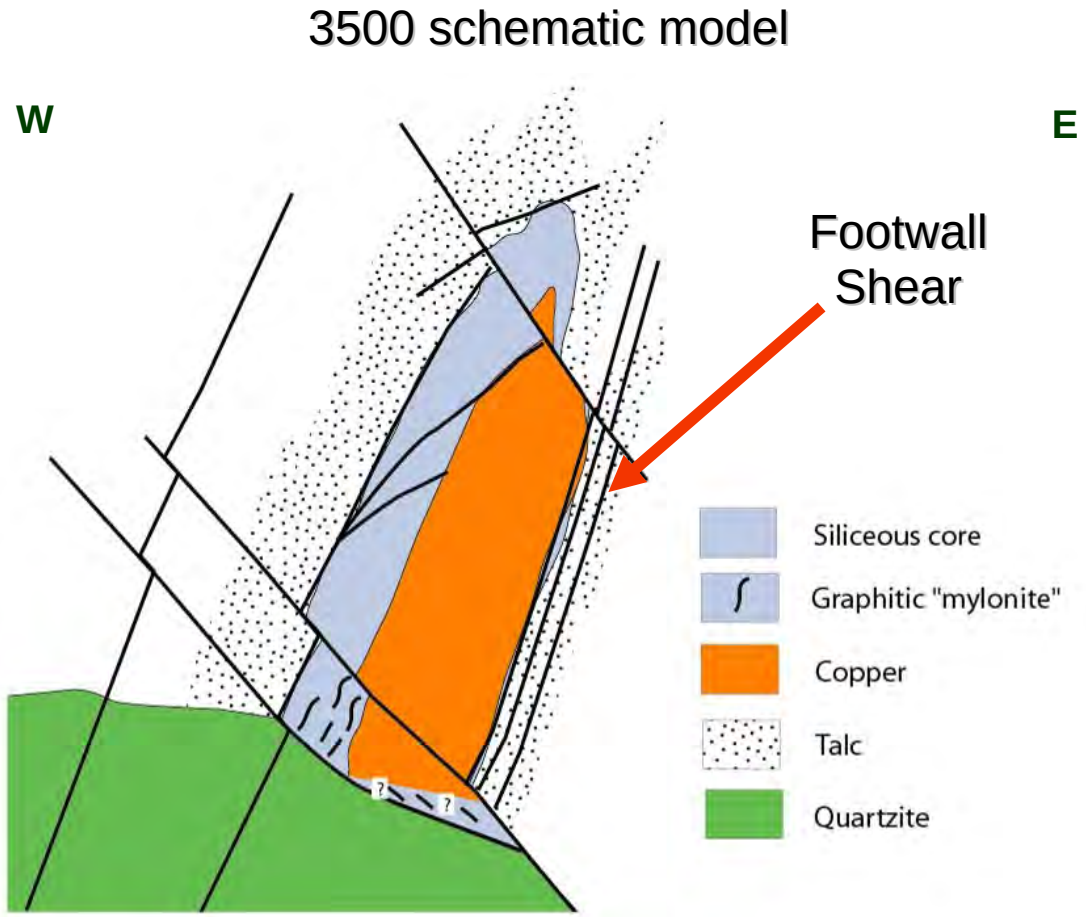

Fig. 44. Schematic model of the 3500N ore body – across the footwall shear the silica alteration (siliceous inner core) ceases abruptly as does the copper within the 3500 ore bodies. Some copper mineralisation does exist to the east of the footwall shear and this is hosted by dolomite altered shale. The folds within the direct hangingwall of the footwall shear have steep plunges, while those in the footwall within dolomite altered shale do not. The footwall shear is associated with high talc.

3.4 Comment on dolomite-hosted Cu ore bodies

Some mapping was also undertaken in the dolomite hosted alteration within X block to the east of the footwall shear. One feature noted that was in this area the S_3 cleavage was more readily identified within the dolomite altered rocks, with a strong mica fabric developed in many localities. This contrasted with areas of strong silicification where the S_3 cleavage is more difficult to recognise – whether this reflects destruction of an initial S_3 cleavage during silicification or reflects weak development of this cleavage in rocks that had already been silicified has not been constrained. Previous work has highlighted that the S_3 cleavage is more strongly developed outside the silica-dolomite alteration and that the phyllosilicate growth predated the dolomitisation (Swager et al., 1987).

The significance of the well developed S_3 is that within the dolomite hosted Cu mineralisation (within X block), there is a much stronger cleavage-related control on the distribution of the Cu mineralisation. In places mineralisation is associated with chalcopyrite-dolomite veins axial planar to folds (Fig. 45), with the majority of chalcopyrite veins representing failure along pre-existing S_3 cleavages (Fig. 46, 47). The analysis of these dolomite hosted ore bodies is complicated by cleavage refraction (Fig. 46). These observations have relevance for potential ore bodies at the periphery of the silica-dolomite alteration zone i.e. the ore bodies perched off the basement may be linked to strongly developed zones of S_3 cleavage.

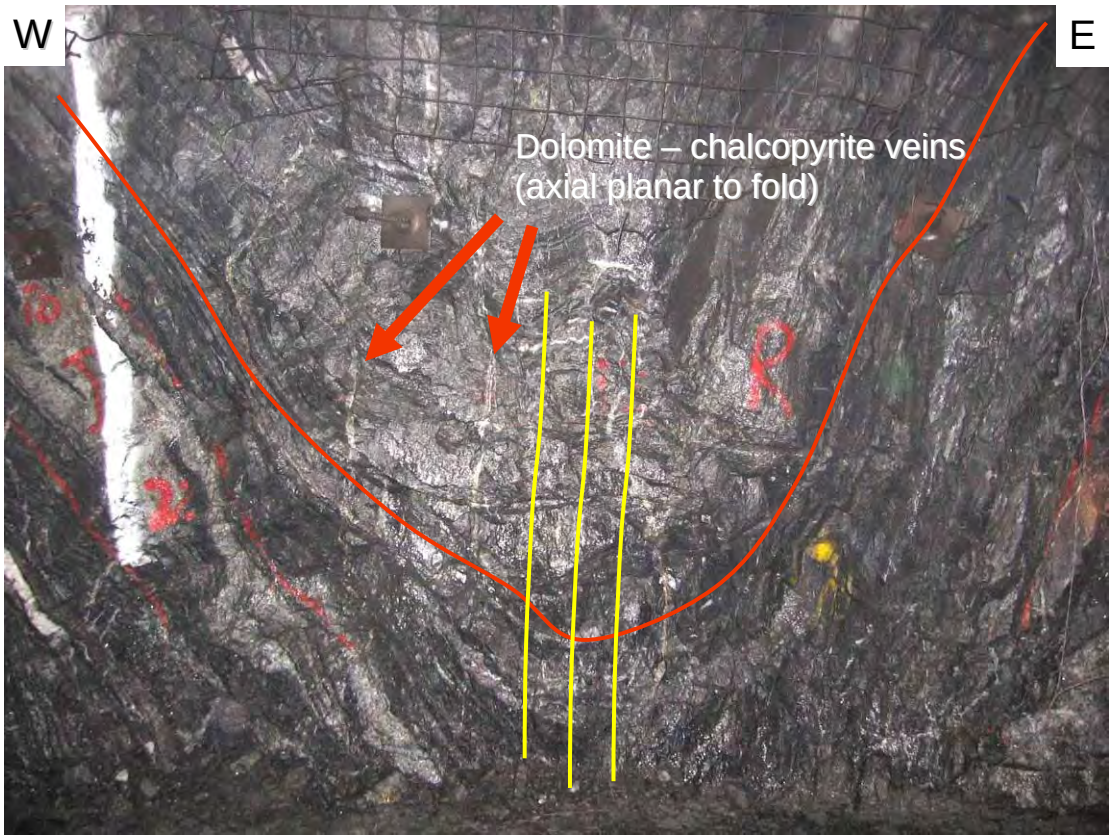

Fig. 45. F_3 fold hinge defined by dolomite altered shale. Mineralisation occurs within axial planar dolomite-chalcopyrite veins. X block ore body, 5877XC, level 23a.

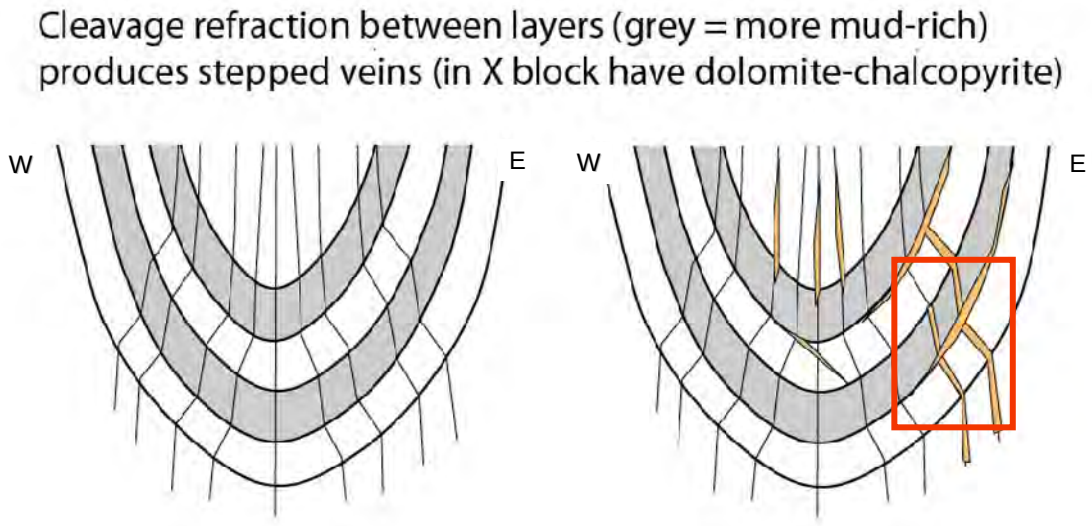

Fig. 46. Sketch highlighting cleavage refraction associated with X block ore bodies within dolomite altered shale. Red box highlights geological relationship for Fig. 47. This relationship was also highlighted by previous workers (see Fig. 4A of Bell et al., 1988).

Fig. 47. Photograph of S_3 cleavage refraction within dolomite altered shale (note large dolomite crystals). Red lines highlight trend of S_3 cleavage. The chalcopyrite mineralisation follows this trend. X block ore body, X589 DPT2, level 24a.

3.5 Kinematic model for the development of the Cu ore bodies

The key element of the kinematic model is the newly identified sinistral-reverse slip direction associated with mineralisation (Fig. 35, 36). This sinistral-reverse slip vector direction was observed independent of fold plunge or location with respect to basement. **To produce the observed slip vector orientation, the stress field associated with the copper breccias would have had σ_1 lying somewhere to the NW (±30°), σ_1 was not oriented E-W. This is significant because the observed D_3 folds, and S_2 and S_3 cleavages either reflect E-W shortening or NE-SW shortening. The field relations indicate the Cu mineralisation is related to a stress field distinct from that associated with D_3. There must have been some type stress switch in the system linked to the development of the breccias, and presumably the influx of Cu-bearing fluids. This may have been a short lived transient field and the deformation appears to have been low strain, with a limited amount of net slip along bedding surfaces.**

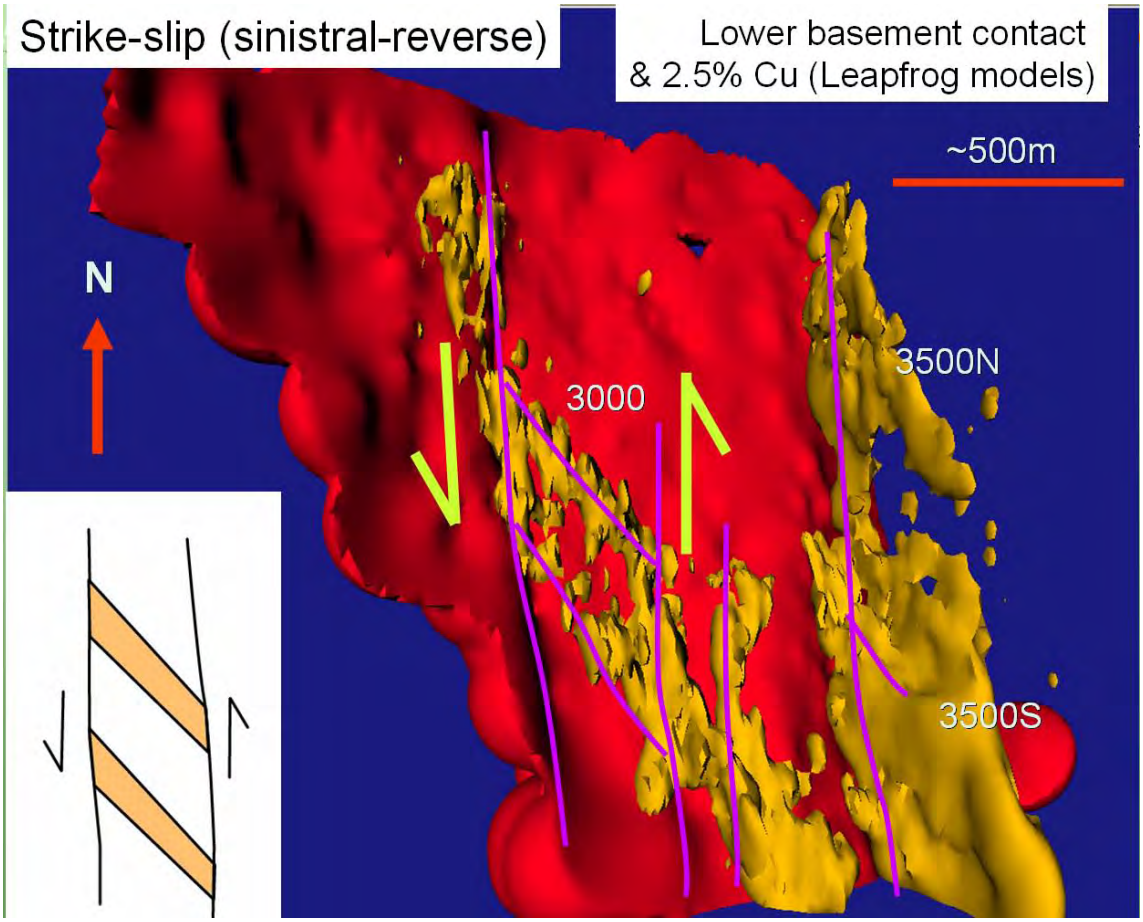

Fig. 48. Leapfrog model of lower basement contact and Cu for the Enterprise Mine area (3000, 3500S and 3500N ore bodies). Kinematic interpretation utilizes slip data in Fig. 35, bedding strikes N-S and dips on average at 60° to the W.

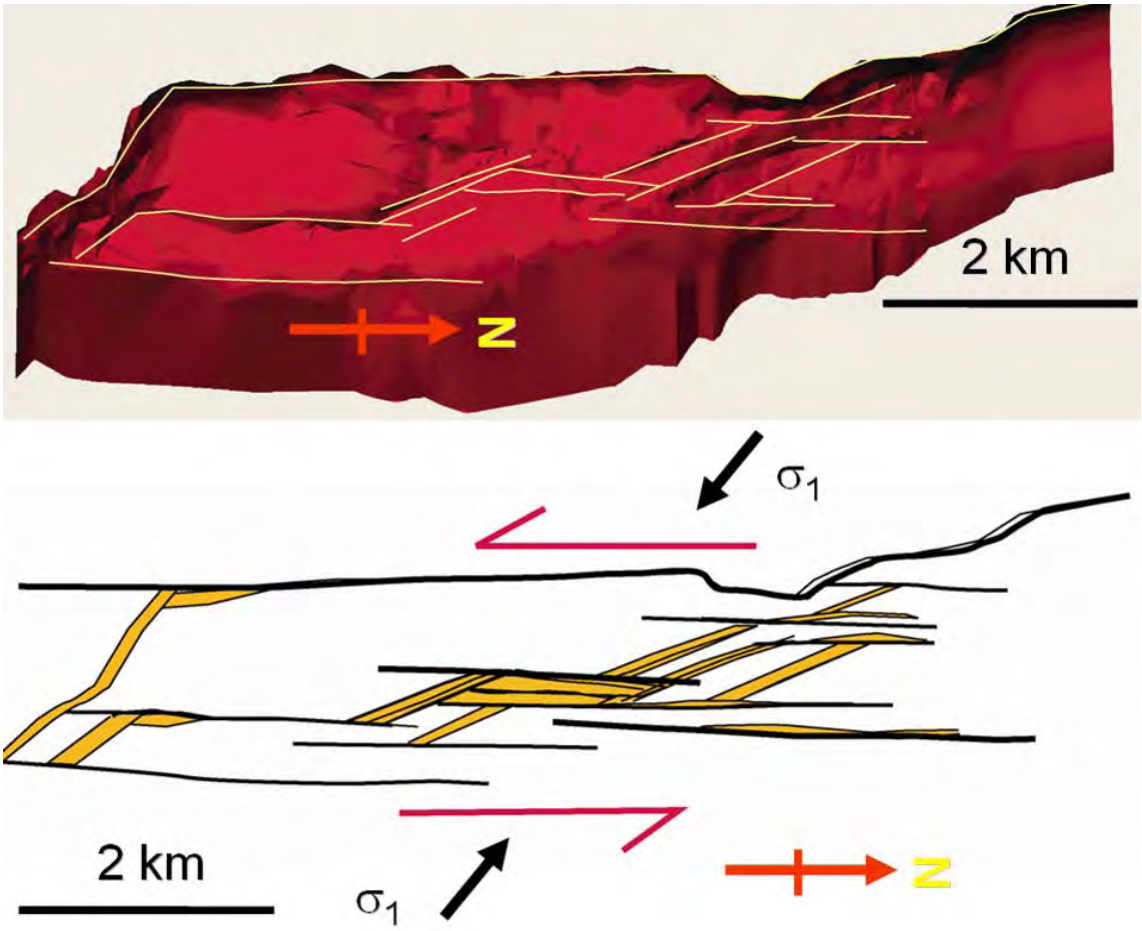

Fig. 49. Basement lineaments (identified in Fig. 9), which area combination of F_3 folds and within basement stratigraphic variations, that were dilated in a sinistral-slip regime. This geometry is inferred to be the permeability pathways in the basment that fluids linked to mineralisation where channelled along during the Cu event. Figure covers the Enterprise Mine, X41 ore body and region to the south of the X41 mine (termed the Crystallina block).

One key complicating factor in developing a simple structural model is the variability of the underlying basement. The Leapfrog modelling highlighted that the distribution of the volcanic rocks and quartzites appears to have a control on the development of Cu mineralisation (Fig. 8). With the basement controls discussed in section 2.1 also taken into consideration, the inferred model is that the lodes within the Enterprise Mine represent a sinistral-slip system (Fig. 48, 49, 50). This appears to be linked to a discrete phase of brecciation (there is no evidence for multiple phases of brecciation) and was probably low strain. The master faults that control the system trend N-S (i.e. parallel to bedding and the 3500 ore body) and are inferred to have projected through into the basement (Fig. 50). These represent reactivated existing D_3 structures (the D_3 architecture is a key control) such as the footwall shear (Fig. 50) and predominantly reflect bedding-parallel slip. In some areas there is a clear asymmetry to the silica-dolomite alteration envelopes and Cu around these structures (Fig. 44). It is inferred that strike changes on these N-S trending faults dilatant during sinistral slip could be a key control on ore shoot development. Not all N-S trending Cu lodes are associated with master faults (such as the Footwall Shear) - some occur above N-S trending quartzite-volcanic contacts in the basement that are inferred to have acted as preferential fluid pathways ways in the basement. Fluid associated with mineralisation are inferred to have flowed up these basement contacts into the over lying shales that may not have an associated structure i.e. these are analogous to blind thrusts in compressional systems. Late-stage slip occurred along bedding surfaces within the basement quartzites (Fig. 17), and these may also have acted as preferential fluid pathways during Cu mineralisation (as inferred in Fig. 28).

The NW-trending zones of mineralisation (e.g., within the 3000 ore body) are inferred to be tensile links (see inset of Fig. 48). These links represent NW- to NNW-trending basement lineaments that were dilated ("jacked open") during sinistral-slip, allowing the focussed flow of Cu-bearing fluids (Fig. 49). The NNW- to NW- basement trends that dilated are in some areas strong S_3 cleavage zones that are parallel to large F_3 folds zones (e.g., Fig. 12), in other areas these NW-trends are defined by stratigraphic contacts (Fig. 13). In some areas the NW trends are combined S_3 cleavage trends and basement contacts. In summary, the 3000 basement trend (Fig. 7, 48) appears to be a D_3 cleavage/fold trend that dilated, allowing fluids to flow up from the basement into the over lying shales. The X41 mine area (1100 ore body) has a range of F_3 folds and within basement trends that control the distribution of mineralisation. The schematic diagram in Fig. 28 highlights the importance of the quartzite basement unit, however, the Leapfrog modelling (Fig. 8) has highlighted that some of the Cu lodes lie above Eastern Creek Volcanics with no adjacent quartzite. These lodes above are inferred to be linked to fluid flow along a strongly developed basement S_3 cleavage linked to D_3 folding (as argued by Bell et al., 1988) – one of these major F_3 folds is highlighted in Fig. 5 and therefore presence of a basement quartzite is not a prerequisite for developing economic Cu lodes.

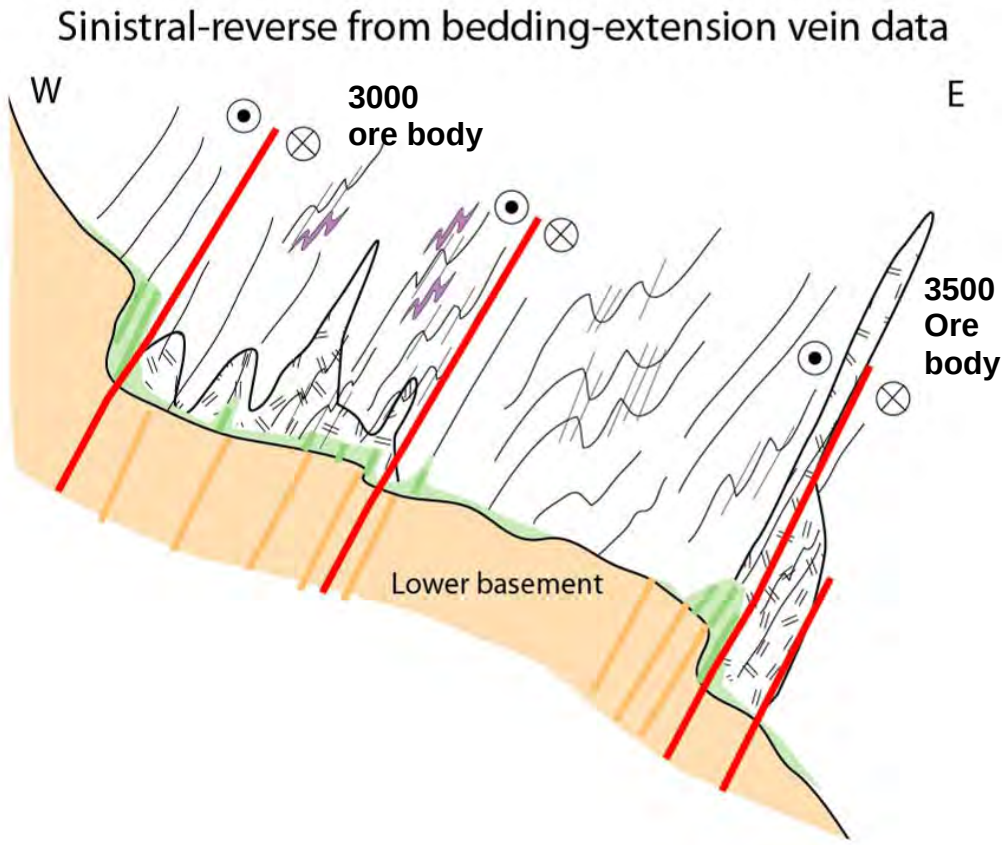

Fig. 50. Red lines indicate steep W-dipping faults that were inferred to be active synchronous with Cu mineralisation (one of which would have included the footwall shear associated with the 3500 ore body). These faults are dominantly slip focussed on bedding planes, but also along earlier D_3 ductile shears (e.g., the footwall shear beneath the 3500 ore body).

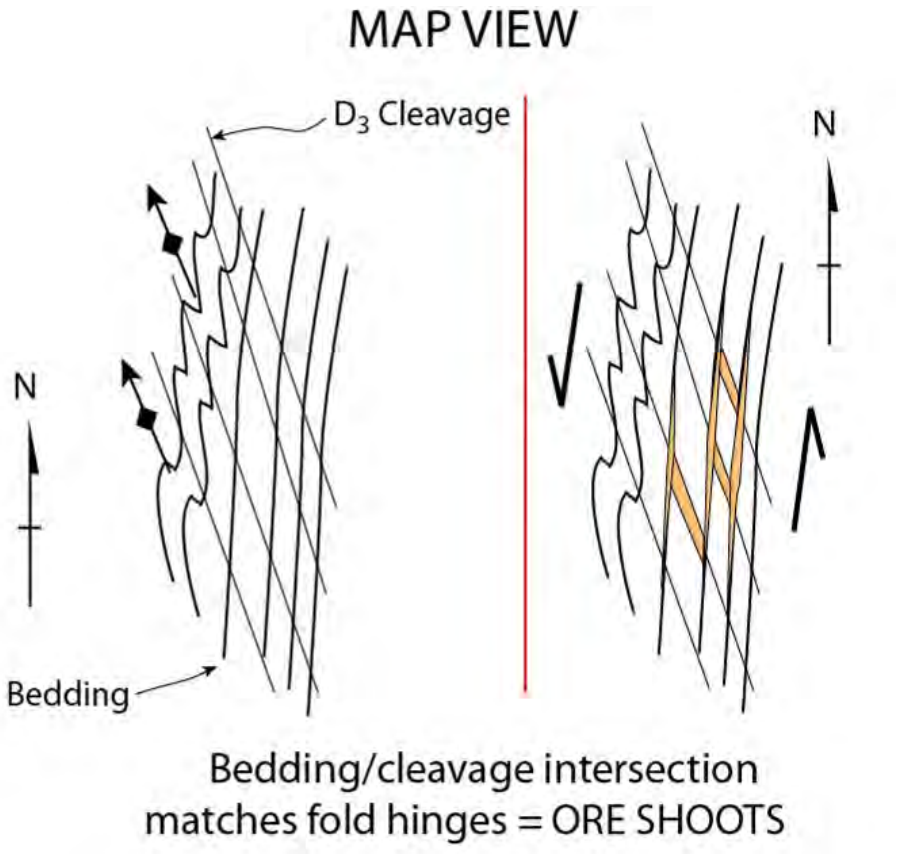

Fig. 51. Model of S_3 cleavage dilation during sinistral-slip.

With the newly constrained kinematics associated with mineralisation (Fig. 36), a new model for many S_3-related Cu breccias involves the NNW-trending D_3 cleavages within the shales dilating during sinistral slip along N-S trending faults focussing Cu-bearing fluids (Fig. 51). Such a model could also explain 650 ore body that lies off the basement (see Fig. 1, 8) and is distinct to the adjacent 500 ore body. In long section the 650 ore body represents a large planar body (Fig. 52b) and it follows the axial plane of a series of F_3 folds (Bell et al., 1988). The 500 ore body has an ore shoot geometry that follows the trend of existing F_3 fold hinges (Fig. 52a), and strikes N-S (Fig. 52b). In plan view the 650 ore body is NNW-striking (Fig. 52b), which reflects its association with the NNW-trending axial planar S_3 cleavages. **This S_3 cleavage trend would have been ideally oriented to develop into a dilational jog during a sinistral-slip regime (Fig. 52c) with the result being the production of a large planar zone of Cu mineralisation (such geometries are typical of gold lodes associated with dilatant jogs). This mechanism is similar to the model for the basement dilation linked to the development of the overlying ore bodies (Fig. 48, 49). However, the difference is that the basement features have acted as a focus and pathway for fluids to move into the overlying shales. In contrast, the 650 ore body is a dilational jog that sits off the basement, and this dilational zone focussed the fluids to form an economic zone of mineralisation within the shale units off the basement contact.**

This model is consistent with field relationships at a mesocsopic scale where the Cu mineralisation within the shale is in part linked to S_3 cleavages that provide additional permeability (Bell et al., 1988), with the bedding cleavage intersections (L_{03} intersection lineation = F_3 fold plunge) being a key control on ore shoot plunge. There are major plunge variations of this lineation between different areas producing variable ore shoot plunges.

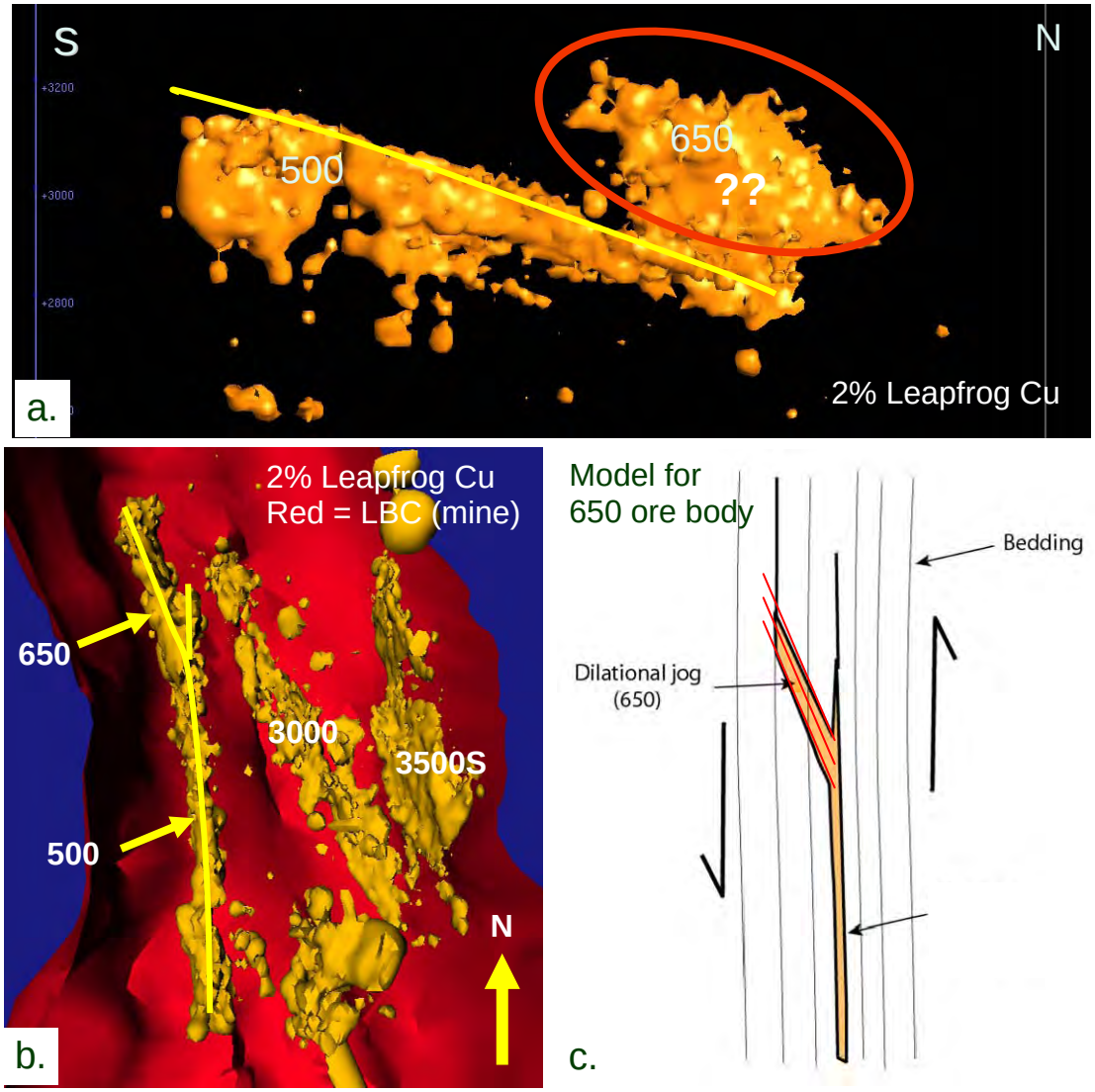

Fig. 52. (a) Leapfrog model (looking W) highlighting steep planar geometry of 650 ore body. (b) Leapfrog model highlighting strike-trends of different Cu ore bodies. (c) Model for 650 ore body forming as a dilatant jog via failure of a pre-existing S_3 cleavage (cleavage depicted as red lines).

4. Kinematics of main post Cu breccia (D_4) faults

4.1. 1st set of post Cu breccia faults – D_{4a} faults

A major set of W-dipping faults over print the copper breccias and there are extensive wire frames of these structures within the current mine data base (note the number of steep W-dipping faults wire framed in the 3000 ore body in Fig. 23). This generation of structures have previously been assigned a D_4 deformation age (e.g., Bell et al., 1988), although many of the structures observed to offset the Cu breccias are reactivated D_3 faults. These W-dipping faults were identified in almost all of the areas of the mine that were mapped (see section lines in the digital appendix), and have a large dip variation (steep to low-angle). The Buck Quartz Fault (Fig. 3, 21) is a major example of this generation of structures and has an initial top-to-the-E transport indicated by extension vein arrays (Fig. 21), but this fault has also been overprinted by later NE-trending dextral reverse faults (e.g. the S48 fault in Fig. 3, 8) and by NW-trending, NE-dipping, sinistral-reverse faults (note wire frame in Fig. 25). The W-dipping thrusts are parallel to the regional Mt Isa Fault Zone (Fig. 3) and have been termed D_{4a} faults, while the later faults have been termed D_{4b}. In reality there appears to be a transition from thrusting to strike-slip faulting associated with continuous E-W shortening, and there is not a clear distinction between the fault types in many areas.

The D_{4a} faults are associated with quartz, pyrite, talc and chalcopyrite (Fig. 53, 54, 55) and also galena in areas near Pb-bearing shales. These faults commonly slip along bedding, with lower angle diverging splays that are associated with large quartz veins (Fig. 53, 54). In contrast to the slip-direction observed within the copper breccias (Fig. 56a), these faults have a consistent hangingwall paleotransport of top-to-the-E or –W (Fig. 56b), and the N-trending structures are predominately dip-slip reverse faults. Whilst these later faults also slip along bedding surfaces, they have a completely different extension direction parallel to bedding compared to the Cu breccias (Fig. 56). Mapping within the Cu ore bodies delineated some areas with E-directed paleotransport associated with chalcopyrite extension veins (note field locality 1 in Fig. 35 and also Fig. 57) indicating that there is some Cu enrichment associated with these faults. There is also a talc association in dolomite altered shale units with clear top-to-the-E transport along the Footwall Shear recorded by talc pressure shadows on pyrite (Fig. 58).

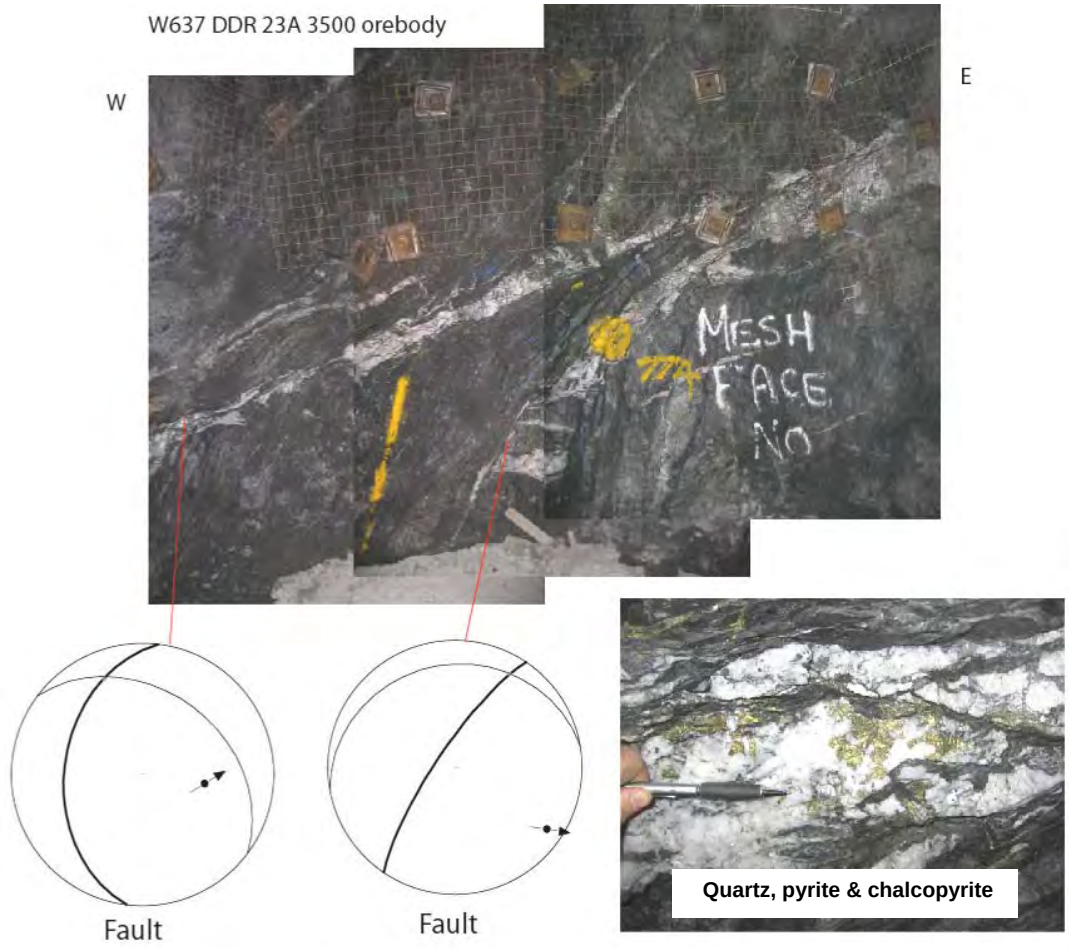

Fig. 53. Post Cu breccia faults and detail of associated mineralogy. Note faults cross cut and also slip parallel to bedding. W637 DDR 23a, 3500S ore body.

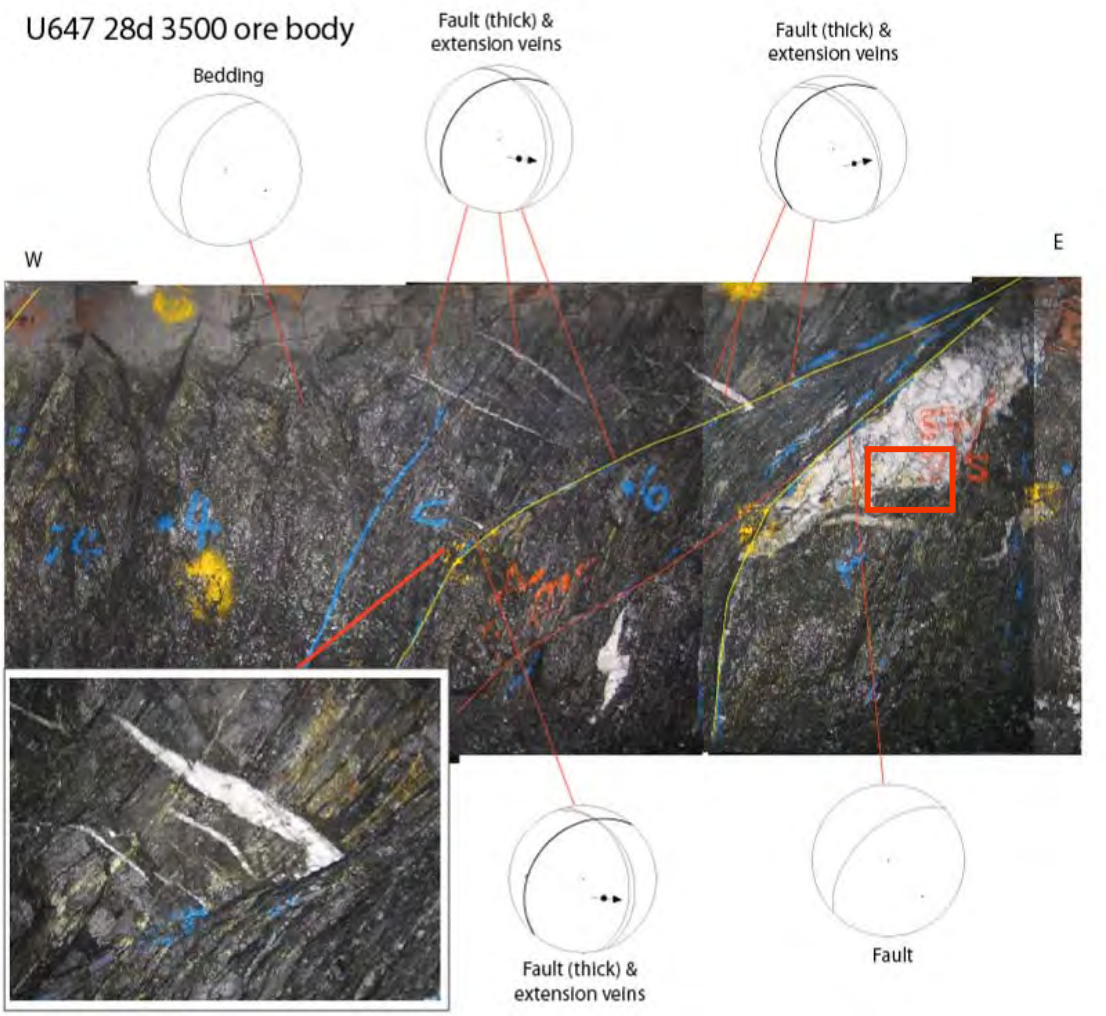

Fig. 54. Post Cu breccia faults and detail of associated extension veins used to constrain slip direction of structures. Note faults cross cut and also slip parallel to bedding, with a large quartz vein present at the point where one of the faults diverges from being parallel to bedding. U647 28d, 3500S ore body. Red box highlights the location of Fig. 55.

Fig. 55. Close up of chalcopyrite and pyrite within massive quartz vein. Photo is located on Fig. 44.

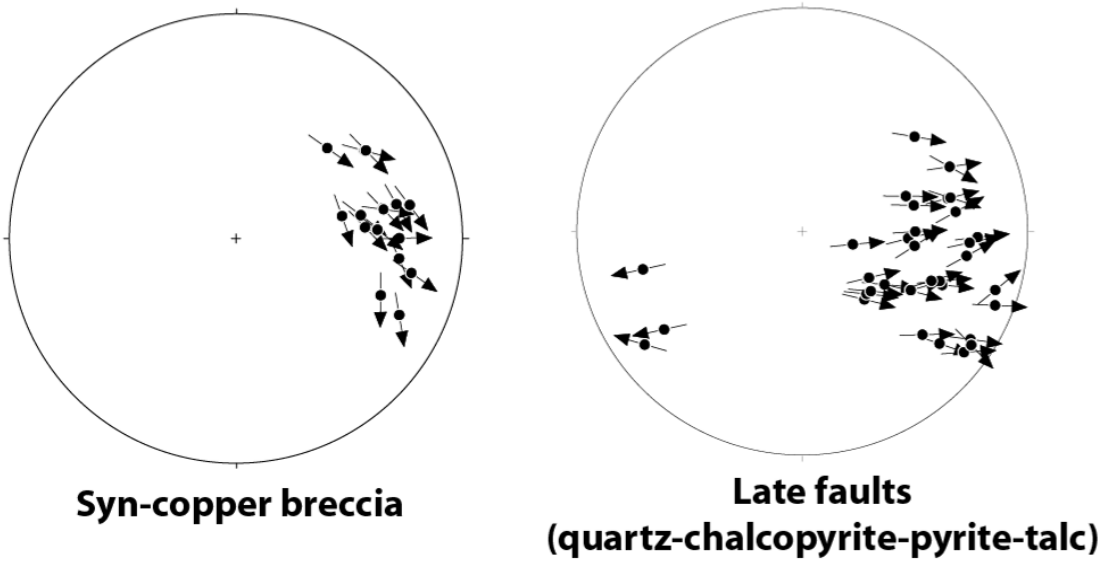

Fig. 56. Hangingwall transport directions (see Miller and Wilson, 2004) plotted at the pole to the slip surface (commonly bedding). (a) Cu breccia (hangingwall top-to-SE). (b) Later D4a and D4b faults (hangingwall top-to-E and -W). Note different transport directions.

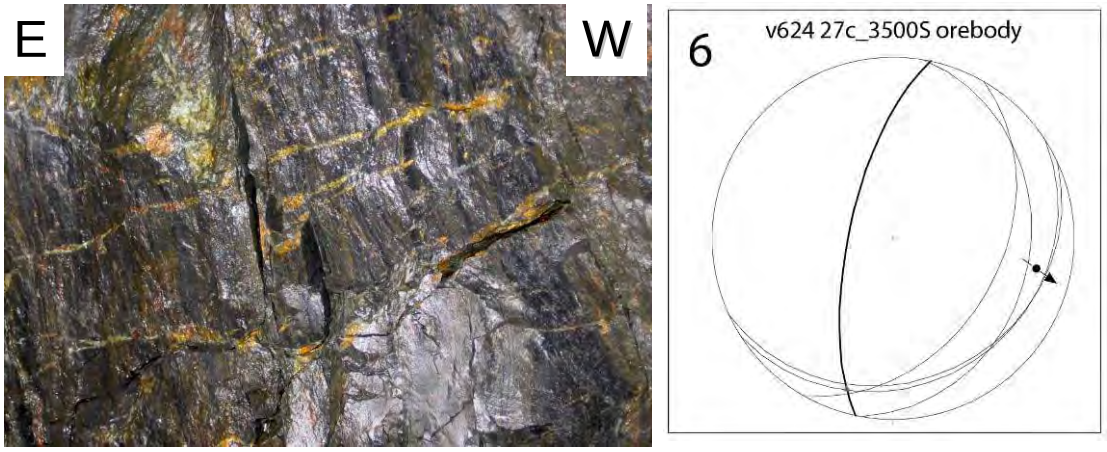

Fig. 57. Photograph (field of view 30 cm) and stereonet plot of chalcopyrite veins that are linked to a more E-directed transport direction. v624 6240XC 27C level, 3500S ore body.

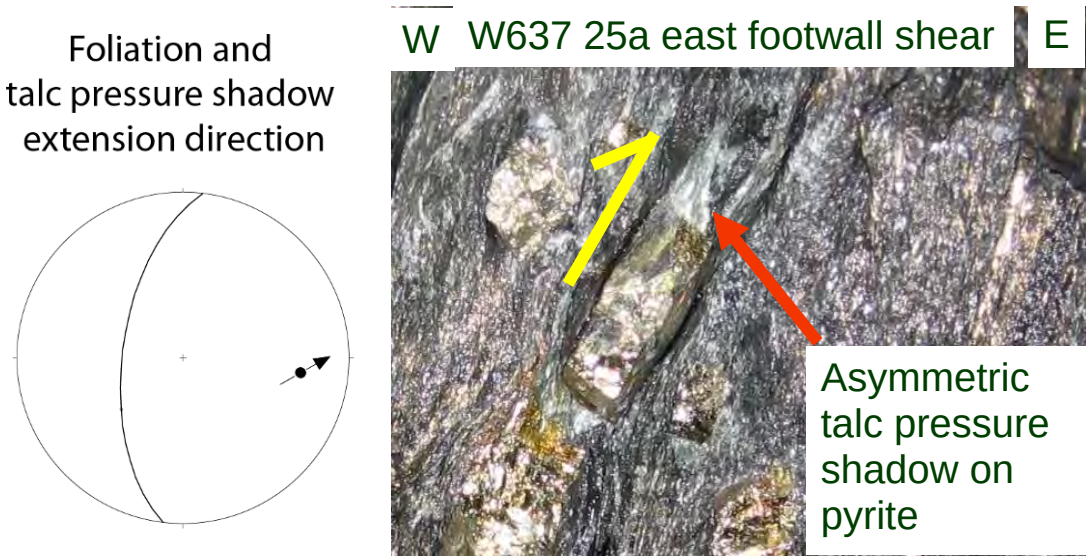

Fig. 58. Photograph (field of view 10 cm) and stereonet analysis of talc pressure shadows linked to E-directed transport. W637 25a, 3500S ore body, field location is within dolomite altered shale E of the Footwall Shear.

4.2. 2nd set of post Cu breccia faults – D_{4b} faults

The W-dipping D_{4a} thrust faults are over printed by later faults with a strike-slip component of movement. In the Enterprise Mine a major set of NE- and E-dipping faults over print the copper breccias, and the W-dipping D_{4a} faults, producing wedge-shaped fault geometries in many areas at meso- and macro-scale (Fig. 24, 25, 59). These faults are dominantly observed in the 3500 ore body region, but were also mapped in areas of steeply over hanging basement in the 3000 ore body (see Fig. 19). The O52 fault in the X41 mine area to the south is inferred to be the same generation (see Fig. 3 of Perkins, 1984). These NE- and E-dipping faults are associated with extensive quartz veining in some areas (note laminated vein in Fig. 24), and they also control the geometry of the lower basement contact beneath the 3500 ore bodies (see section 2.2.3). The faults have complex geometries (inverted flower structures) with big dip changes ranging from 80° to 40° (unlike the W-dipping set this is not caused by slip along bedding). These faults are sinistral-reverse (Fig. 59, 60, 61) and within the existing mine wire frames are interpreted to displace and segment some of the copper breccias in the 3500N ore body (Fig. 44). These offsets may also occur at the base of the 3500 ore bodies, with implications for the potential for offset high grade footwall wedges down-dip.

Late stage faults trending more to the NE are dextral-reverse faults, in the X41 mine area to the south these correlate with the NE-trending S48 associated with clear reverse and dextral offsets in section and plan view (Fig. 3, 8) and T45 faults. The S48 fault offsets the Buck Quartz Fault which is extensively over printed by NE-trending structures (note reverse "S48-style" fault off set in Fig. 21 and also NE-trending vein in Fig. 62). The dextral-reverse faults have a consistent top-the-E transport (e.g., Fig. 63).

The field observations suggest a transition from D_{4a} thrusting to conjugate faulting during D_{4b} (Fig. 64), and all the faults (D_{4a} or D_{4b}) have either top-to-the-E or –W transport consistent with E-W shortening. The similar hangingwall transports imply a relatively low stress shape ratio (ϕ) for D_{4b}. Note that N-S striking faults will still have a top-to-the-E transport direction in D_{4b} (Fig. 64).

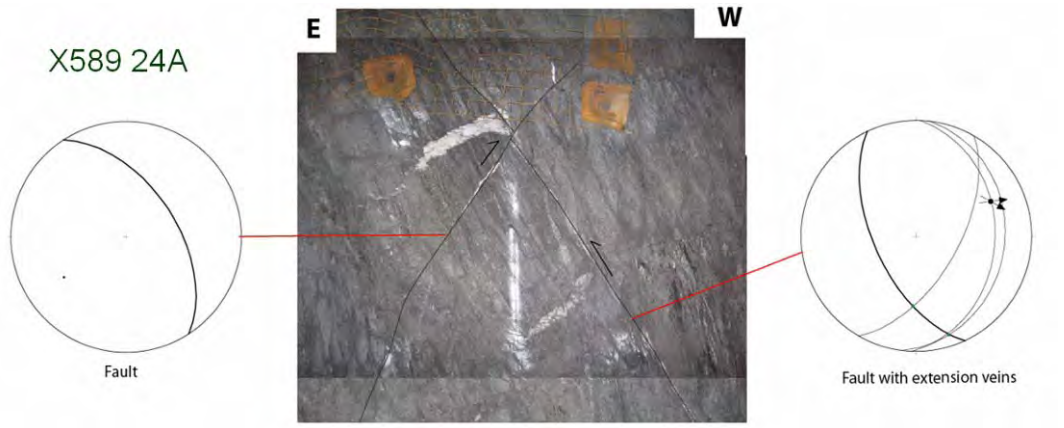

Fig. 59. E-dipping faults over printing earlier W-dipping faults – in this case quartz veins parallel to the W-dipping footwall shear are offset. This produces wedge-like fault geometries at all scales (see Fig. 17). Field locations labelled on figure (top locality is 24A X589 DPT 1).

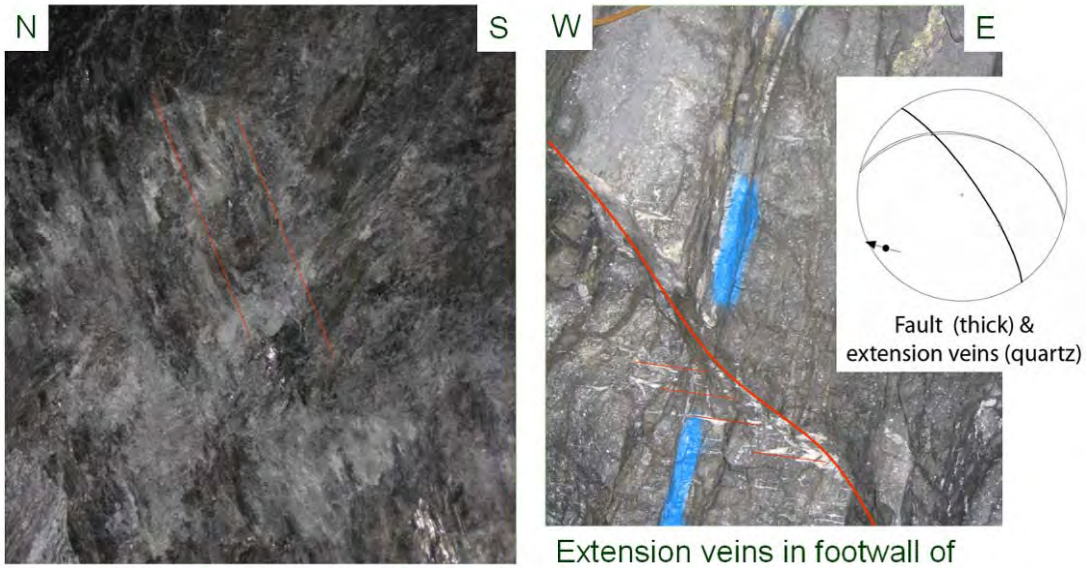

Fig. 60. Photographs of striation and extension vein data that constrains the slip direction of the E- and NE-dipping faults. Field locations labelled on figure.

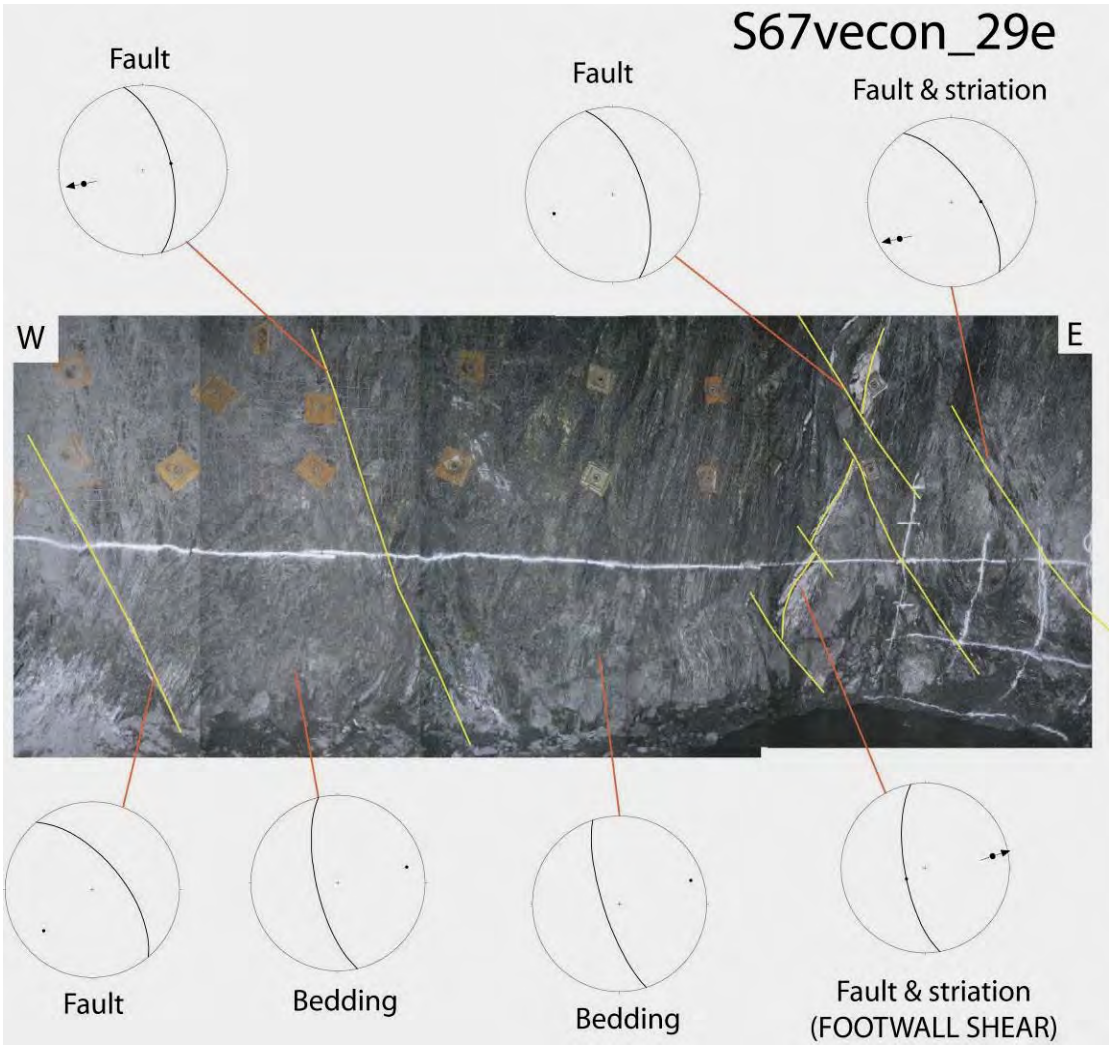

Fig. 61. D_{4a} W-dipping shears over printed by N to NW-trending faults – note that the more NW-trending faults are sinistral reverse.

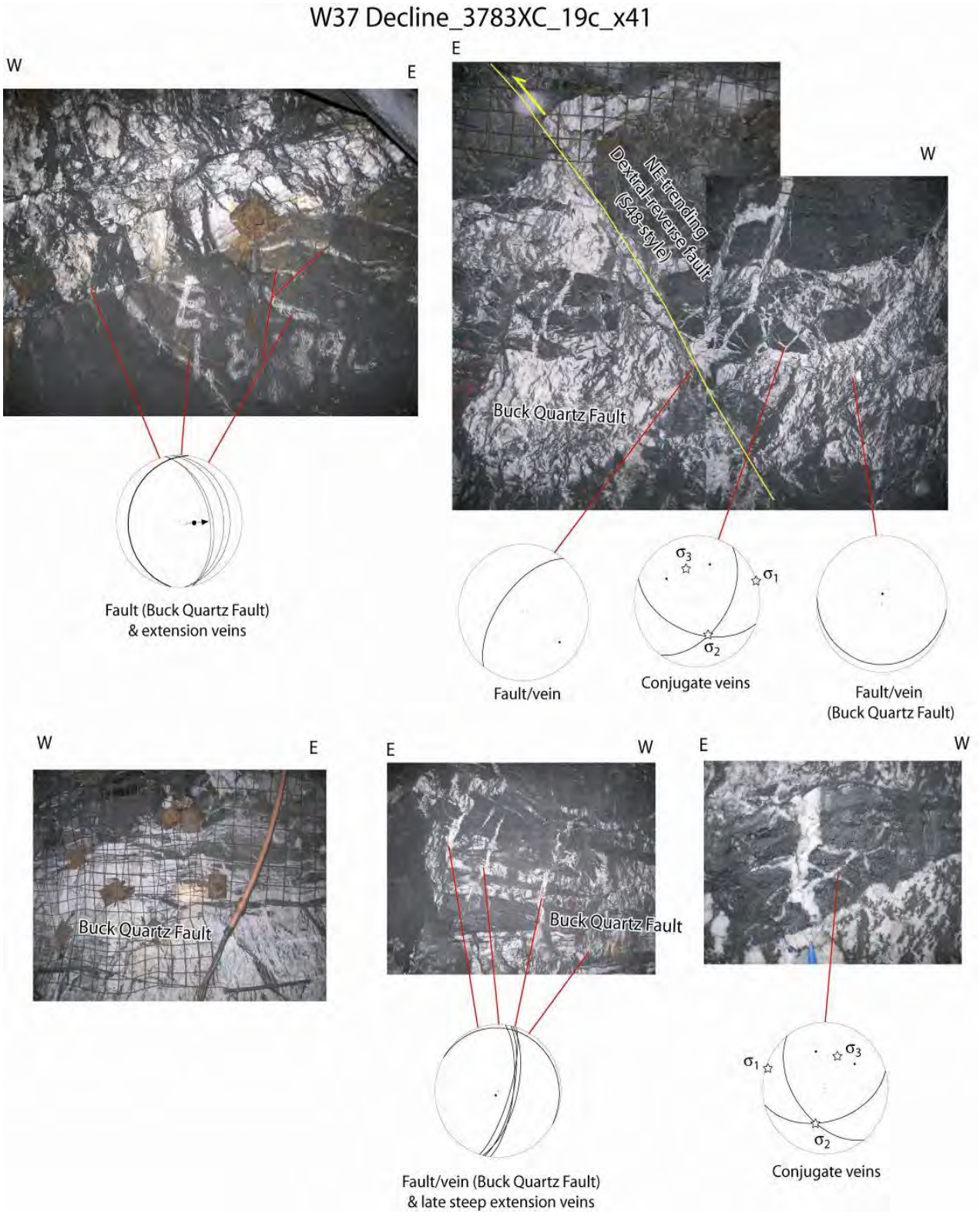

Fig. 62. "S48 style" structure over printing the Buck Quartz Fault. Note NE-trending fault vein at bottom right of figure.

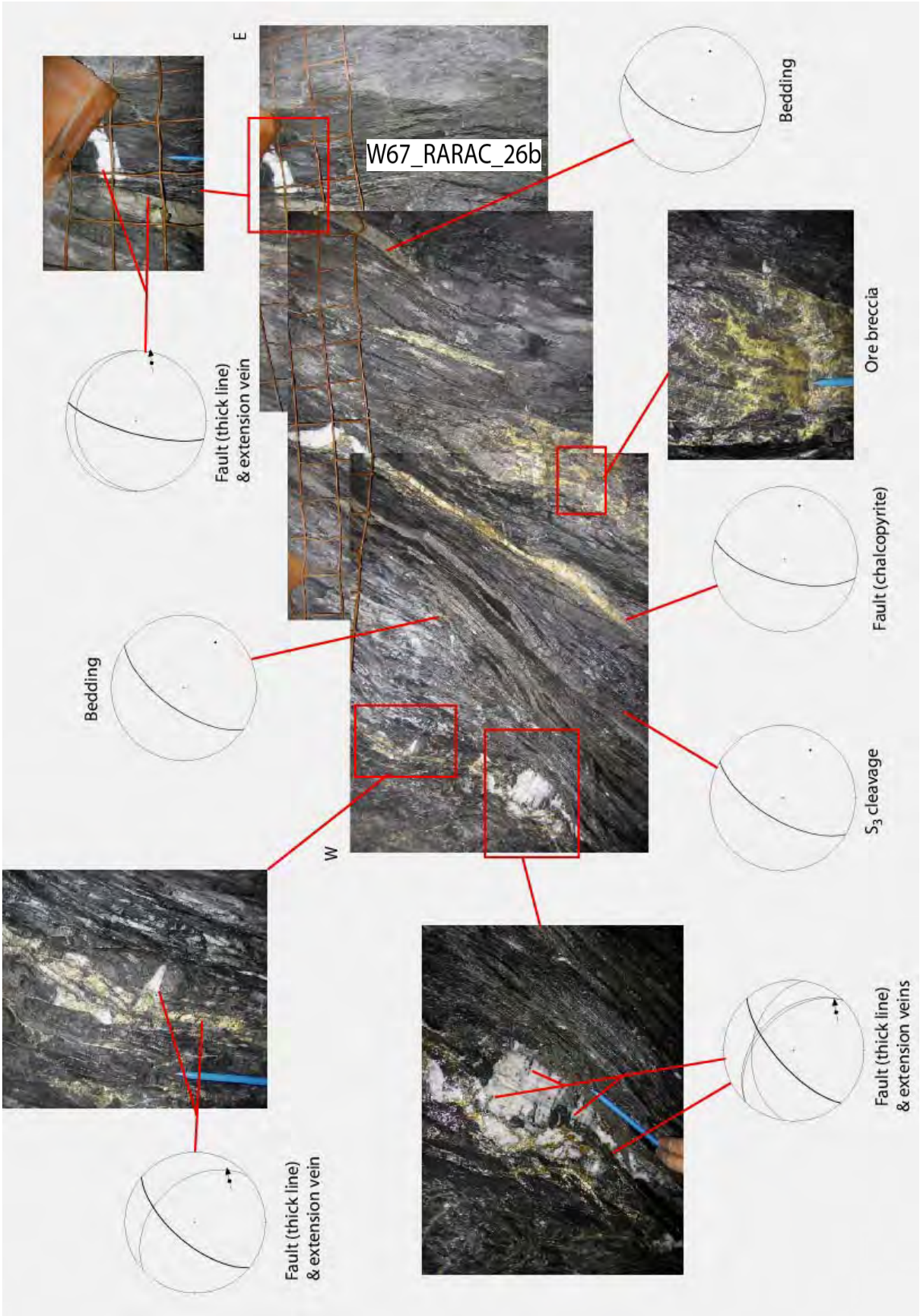

Fig. 63. Examples of NE-trending D_{4b} dextral reverse faults

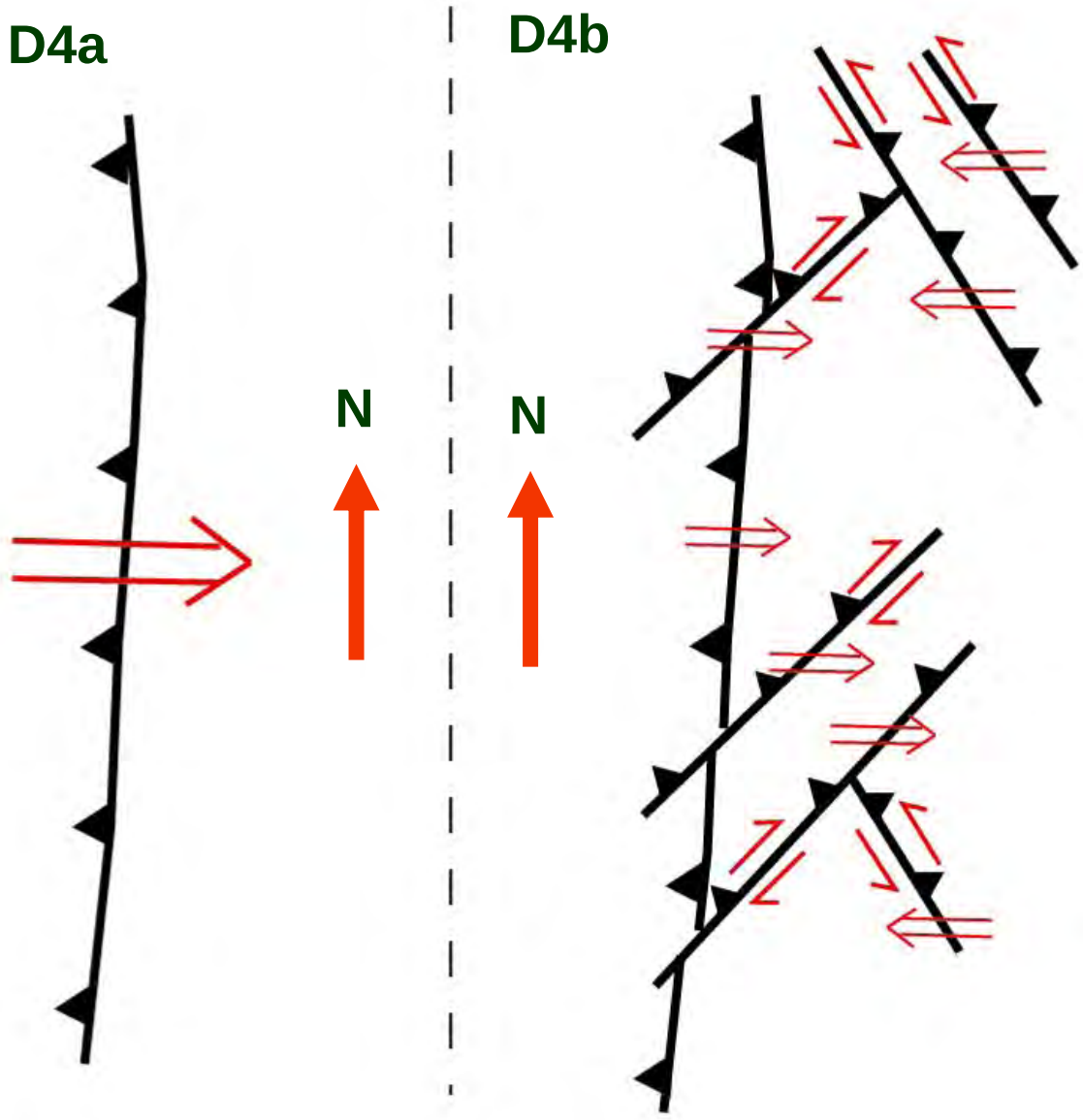

Fig. 64. Transition from D_{4a} to D_{4b}. Note that N-S striking fault will still have a top-to-the-E transport direction during D_{4b} and that all the faults have top-to-the-E or –W transport consistent with E-W shortening. The similar hangingwall transports imply a relatively low stress shape ratio for D_{4b}.

5. Regional implications

5.1 Revisions to existing structural models

Key points and implications for regional targeting

- The mapping program has confirmed the observations made by previous workers (Perkins, 1984; Bell et al., 1988), but has identified the syn-Cu kinematics by doing detailed structural analysis of the Cu breccias. These were previously defined as forming at a late-stage in D_3, but are now defined as a distinct event.
- In the integration of the Mt Isa Copper field relationships into previous work (Betts et al., 2006) the D_3 event is inferred to be linked to NE-SW shortening (instead of E-W) due to the oblique trend of the fold axial surfaces and S_3 cleavages associated with this event (Fig. 65).
- The main Cu breccias are linked to sinistral-reverse movement and post date regional D_3 deformation, and formed in a stress field distinct to D_3. NO REGIONAL EVENT OF THIS NATURE HAS BEEN RECORDED (e.g. Betts et al., 2006). As a result there has been a modification to the regional deformation history (Fig. 65).
- The Cu breccias within the ore bodies do not show evidence for multiple phases of brecciation and appear to be a single discrete event that was probably low strain.
- The Cu event may not be a major regional “orogenic” event (i.e. not the main folding or faulting observed). Fluid over pressure could have caused breccia development in a weak far field stress and one may not see associated deformation any distance from the Cu ore body.
- The master faults associated with Cu mineralisation are inferred to be N-S trending (and localised into bedding-parallel slip within the shale). Strike changes dilatant in a sinistral regime along these Master Faults could be targeted.
- Some ore bodies (e.g., the majority of the 3000 ore body) are inferred to be linked to the dilation of NNW-trending basement lineaments that are inferred to be F_3 axial traces or stratigraphic contacts between the Lena Quartzite and Eastern Creek Volcanics (or both).
- Some ore bodies are linked to dilation of strong NNW-trending cleavages within the shale – these can occur off the basement (perched ore bodies).
- Cu in the dolomite hosted ore bodies was more strongly linked to the S_3 cleavage - this is a key criteria to target grade outside the siliceous inner core of the main Isa Cu ore body.
- Leapfrog modelling suggests that in some areas there is an inverse correlation between massive volcanic rocks (i.e. with no major bodies of inter-layered quartzites) and Cu mineralisation. Zones of massive volcanic rocks correlated with “holes” or low grade zones in the Cu ore bodies - the exception to this are areas with strong S_3 cleavages associated with D_3 folding in the volcanic units.
- The first set of post Cu breccia structures are W- dipping reverse faults termed D_{4a} faults (these have quartz and chalcopyrite) with consistent top-to-the-E hangingwall transport. These have been previously assigned a D_4 age and are inferred to be the same age as major movement on the Mt Isa Fault and are linked to E-W shortening.
- The mapping has raised the question “how many segments of the currently defined Mt Isa fault zone are just a post Cu W-dipping D_{4a} fault?” Exploration needs to target areas that existed syn-Cu – Fig. 66 highlights the implications of this interpretation.
- The second set of post Cu breccia structures (D_{4b}, Fig. 65) are NE- and ENE-dipping sinistral-reverse faults, and NW- to NNW- trending dextral-reverse faults, that offset some of the Cu ore bodies. These still formed via E-W shortening and represent a change from W-dipping thrusts to conjugate faulting during D_4.
- Some regional NE-trending and NW-trending faults may be D_{4b} faults (e.g., the Railway Fault).
- Offset ore lenses across the E-dipping faults (originally defining the base of the 3500 ore body) are a new near mine target.

- The most obvious features are post Cu breccia faults – this will need to be integrated into the interpretation of regional faults - for example some of the NNW basement trends are related to ore, but others are late faults and there is quartz and Cu within all late structures.

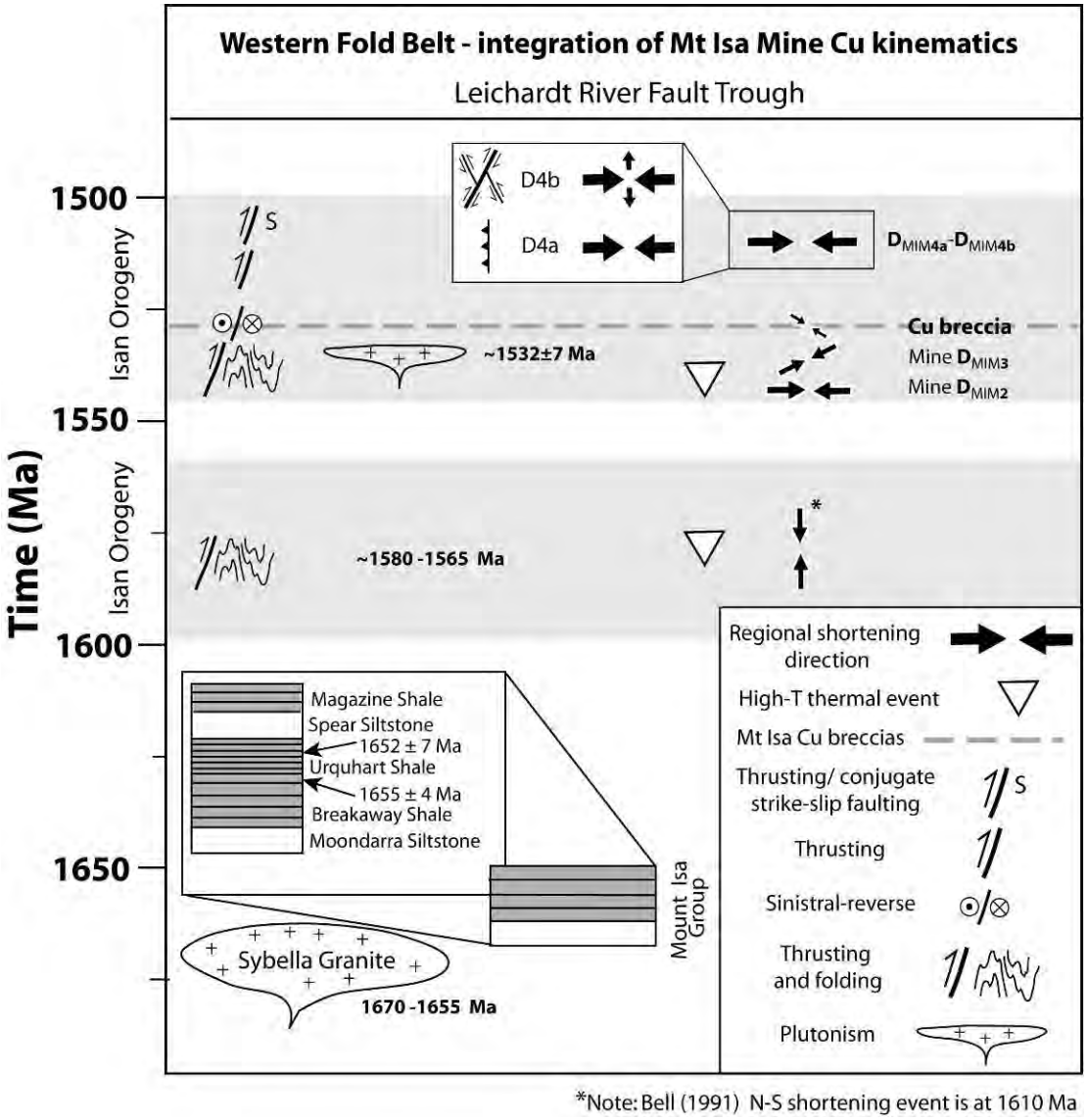

Fig. 65. Integration of the kinematic history at Mt Isa Cu with inferred history of the Leichardt River Fault Trough. ***Note that the Isa Cu mine events have a MIM subscript (=Mount Isa Mine)*** and that the field evidence suggest the ductile S_3 cleavages formed via NE-SW shortening (instead of E-W shortening). The S_2 cleavage at the mine is also inferred to be related to E-W shortening. Modified from Betts et al., (2006).

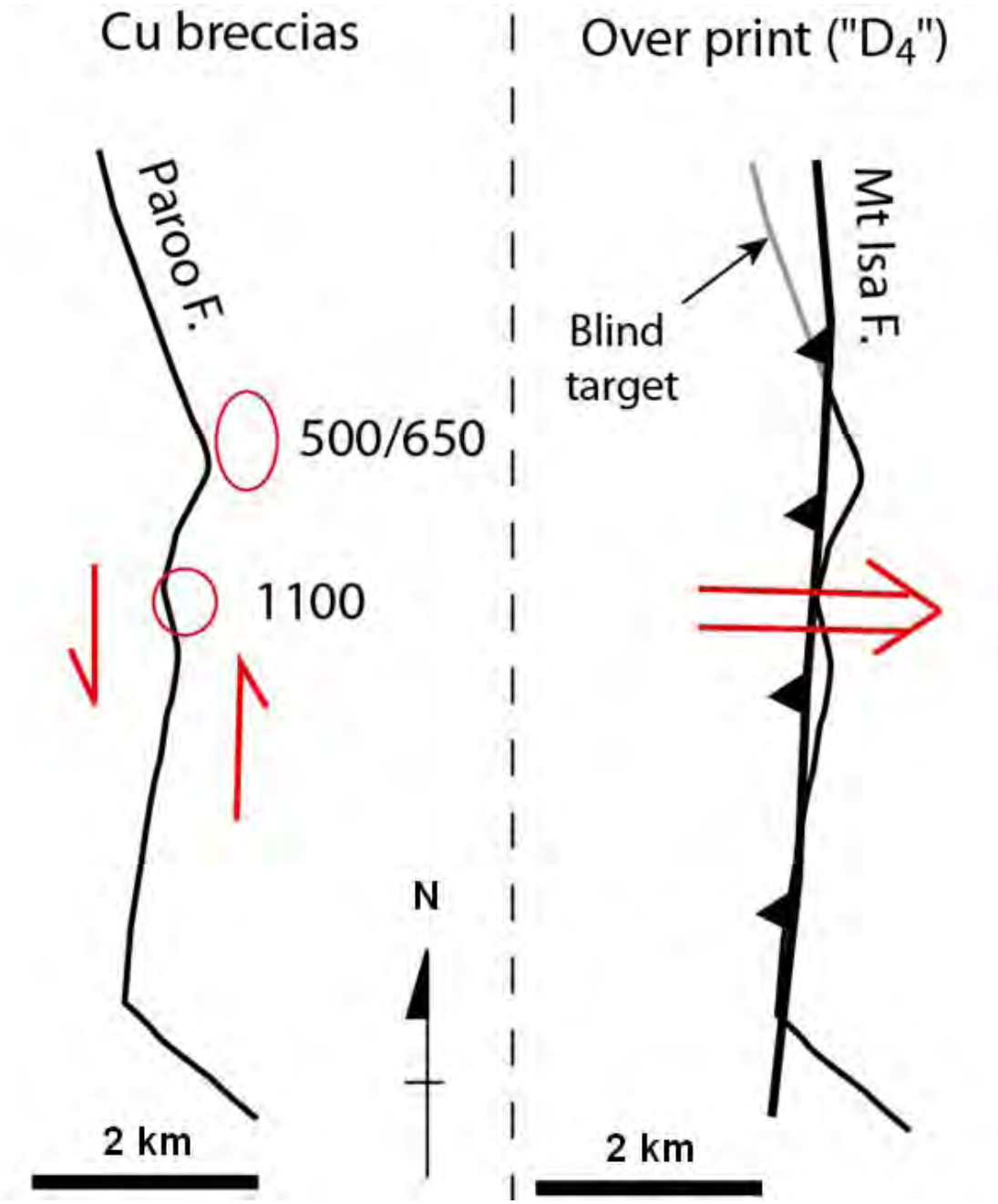

Fig. 66. Interpretation that much of the current trend of the Mt Isa Fault (shown in section in Fig. 3) is a late-stage D_{4a} thrust that over prints the earlier architecture associated with Cu. 1100 and 500/650 ore bodies are marked.

5.2 Implications for fluid mixing models

The chemical processes behind the formation of the Mt Isa Cu ore body has received considerable attention with the Eastern Creek Volcanics previously been favoured as a source of copper and potentially a fluid source rock (Hannan et al., 1993; Heinrich et al., 1995). Halogen ratios on ore stage fluid inclusions have been used to argue that the mineralising fluids where related to a bittern brine (Heinrich et al., 1993), which is compatible with S-isotope data indicating possible involvement of seawater sulphate (Hannan et al., 1993). Reaction path modelling, combined with petrographic and geochemical analysis, has also been used to argue the deposit formed when an oxidised brine, sourced from above, interacted with the carbonaceous Urquhart Shale with resultant reduction and mineralisation

(Wilde et al., 2006). However, recent *combined* noble gas and halogen work (Kendrick et al., 2006) suggests that the fluid inclusions associated with the main stage dolomite alteration better preserve fluids with a bittern brine signal and a metamorphic fluid origin is better preserved in both ore-stage quartz (e.g., the "strain free quartz " style of quartz highlighted in Fig. 40) and also in post copper quartz veins such as the Buck Quartz fault (Fig. 3, 21) which is a D_{4a} fault over printed by later D_{4b} deformation associated with NW- and NE-trending conjugate faults. Kendrick et al., (2006) argue the deposit formed via fluid mixing between a bittern brine sedimentary formation water and a deeply sourced metamorphic fluid – the Barramundi basement was the preferred source (Fig. 67). Kendrick et al., (2006) proposed that the mixing may have occurred via displacement of an existing pore fluid consisting of a bittern brine or via active convection (shown in Fig. 67). They argued that a fluid displacement model "could probably only have occurred once". Figure 67 also highlights the inferred fluid flow through the Lena Quartzite and Eastern Creek Volcanic units.

Perkins (1984) demonstrated that the dolomite porphyroblasts, and some of the quartz, was clearly linked to the mine D_3 event (see over view of key petrographic relationships in section 1) which suggests a bittern brine was the dominant fluid during D_3 due to the main stage dolomite alteration better preserves fluids with a bittern brine signal (Kendrick et al., 2006). The NNW- to NW-trending S_3 cleavages suggest D_3 was linked to NE-SW shortening (Fig. 65). However, the end of D_3 is marked by a stress switch linked to sinistral-slip reactivation, and major copper lode development (Fig. 65).

A transient stress switch from D_3 NE-SW shortening, to the syn-copper sinistral-slip system (Fig. 65), would have suddenly allowed the system the capability to suddenly tap a deep fluid reservoir. Strike-slip systems are very efficient at transporting fluids vertically, potentially from a deep metamorphic fluid reservoir (but also from a shallower crustal level reservoir above). The Mount Isa Copper system only preserves evidence for one major breccia event (not multiple phases of brecciation) which suggests the key fluid mixing Kendrick et al., (2006) linked to the formation of the ore body only occurred as a transient "once off" event. Kendrick et al., (2006) suggested it may have been via passive displacement or by an active convection system (Fig. 67) and either model is compatible with the structural observations. The D_{4a} faults (e.g., the Buck Quartz Fault) also contain the deep metamorphic fluid signal, which suggest that during D_{4a} deformation the system was still actively tapping this deep fluid reservoir. The D_{4a} phase of deformation is still associated with chalcopyrite and quartz, but not major Cu breccia development. Interestingly, the Mt Isa Fault also contains fluid inclusions of composition that cannot be correlated with any currently documented fluid types in the Mt isa Copper Ore body (Kendrick et al., 2006).

Kendrick et al., (2006) highlighted that the NNW-trending Railway Fault, here interpreted as a D_{4b} fault, contained a bittern brine with an exclusively sedimentary formation water origin, but that it was distinct to the bittern brine preserved in the syn-D_3 dolomite alteration preserved at Mt Isa copper. This fluid inclusion population in the Railway Fault was similar to a second group of fluid inclusions preserved within the Buck Quartz Fault (which is strongly over printed by D_{4b} faults and veins). These are inferred to be fluids linked to the D_{4b} phase of deformation. The change to conjugate strike-slip faulting during D_{4b} may have provided a shallower level surface fluid the necessary fracture network to migrate into the system via passive or convection driven flow.

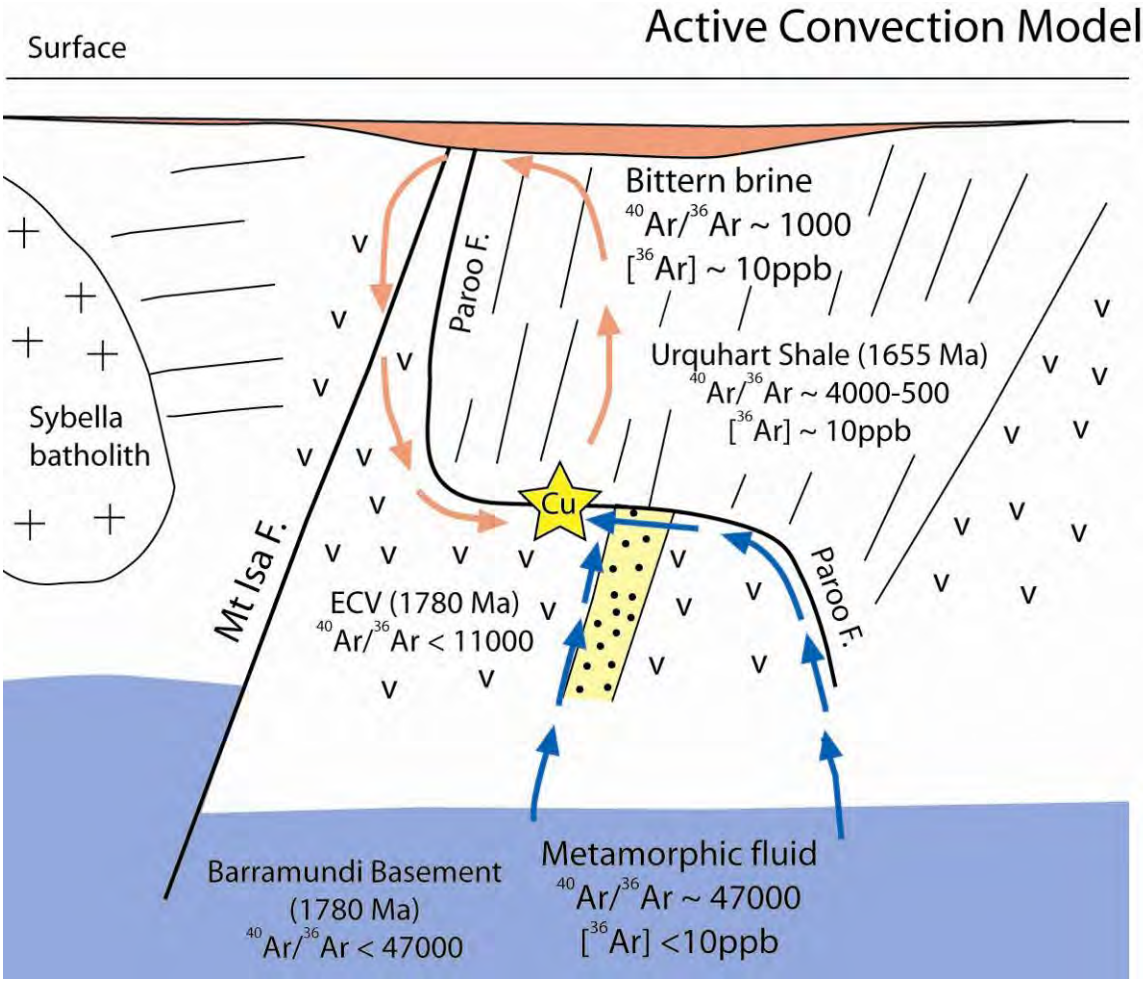

Fig. 67. Model for the evolution of the Mt Isa Copper deposit – modified from Kendrick et al., (2006). The mineralizing event is triggered by a stress switch from D3 NE-SW shortening to sinistral-slip movement syn-copper.

6. Acknowledgements

The project was made possible by major support from Xstrata Staff in particular Ian Holland (Geology Superintendent Isa Cu), Trevor Shaw, Nathan Bullock, Eamonn Dare, and Justin Watson. This work was done as part of the I7 project in the *pmd**CRC. Discussions with Andy Wilde, Mark Kendrick, Alice Clark, Daryl Clark, John McClellan, Cees Swager, Tim Bell, Nick Oliver and Damien Keays are also acknowledged.

7. References

Bell, T.H., 1983. Thrusting and duplex formation at Mount Isa. Nature, 304, 493-497.

Bell, T.H., 1991. The role of thrusting in the structural development of the Mount Isa Mine and its relevance to exploration in the surrounding region. Economic Geology, 86, 1602-1625.

Bell, T.H., Perkins, W.G., and Swager, C.P., 1988. Structural controls on development and localization of syntectonic copper mineralization at Mount Isa, Queensland. ECONOMIC GEOLOGY, v. 83, p. 69–85.

Betts, P.G., Giles, D., Mark, G., Lister, G.S., Goleby, B.R., Aillères, L., 2006. Synthesis of the Proterozoic evolution of the Mt Isa Inlier. Australian Journal of Earth Sciences, 53, 187 – 211.

Connors K. A. & Lister G. S., 1995. Polyphase deformation in the western Mount Isa Inlier, Australia: episodic or continuous deformation? Journal of Structural Geology 17, 305–328.

Davis, G.H., Reynolds, S.J., 1996. Structural Geology of Rocks and Regions, second edition, John Wiley and Sons, U.S.A., pp. 776.

Hannan, K.W., Golding, S.D., Herbert, H.K., Krouse, H.R., 1993. Contrasting alteration assemblages in metabasites from Mount Isa, Queensland: implications for copper ore genesis. Economic Geology 88, 1135–1175.

Heinrich, C.A., Andrew, A.S., Wilkins, R.W.T., Patterson, D.J., 1989. A fluid inclusion and stable isotope study of synmetamorphic Copper Ore Formation at Mount Isa, Australia. Economic Geology 84, 529–550.

Heinrich, C.A., Bain, J.H.C., Fardy, J.J., Waring, C.L., 1993. Br/Cl geochemistry of hydrothermal brines associated with Proterozoic metasediment-hosted copper mineralization at Mount Isa, northern Australia. Geochimica et Cosmochimica Acta 57, 2991–3000.

Heinrich, C.A., Bain, J.H.C., Mernagh, T.P., Wyborn, L.A.I., Andrew, A.S., Waring, C.L., 1995. Fluid and mass transfer during metabasalt alteration and copper mineralization at Mount Isa, Australia. Economic Geology 90, 705–730.

Kendrick, M.A., Duncan, R., Phillips, D., 2006. Noble gas and halogen constraints on mineralizing fluids of metamorphic versus surficial origin: Mt Isa, Australia. Chemical Geology, 235, 325-351.

McClay, K.R., 1979. Folding in the silver-lead-zinc orebodies, Mount Isa, Australia: Transactions of the Institute of Mining and Metallurgy, v. 88, p. B4–B14.

Miller, J.McL., and Wilson, C.J.L., 2004. Application of structural analysis to faults associated with a heterogeneous stress history: the reconstruction of a dismembered gold deposit, Stawell, western Lachlan Fold Belt, Southeastern Australia. Journal of Structural Geology, 26, 1231-1256.

Miller J. McL. 2005. The structural evolution of the Wallaby Gold Deposit, Laverton, W.A., Y4 ***pmd*****CRC* project report, July 2004.

Perkins, W.G., 1984. Mount Isa silica-dolomite and copper orebodies: The result of a syntectonic hydrothermal alteration system. ECONOMIC GEOLOGY, 79, 601–637.

Swager, C.P., 1985. Syndeformational carbonate replacement model for the copper mineralization at Mount Isa, Queensland: A microstructural study: ECONOMIC GEOLOGY, 80, 107–125.

Swager, C.P., Perkins, W.G., Knights, J.G., 1987. Stratabound phyllosilicate zones associated with syntectonic copper ore bodies at Mt Isa, Queensland. Australian Journal of Earth Sciences, 34, 463-476.

Wilde, A.R., Jones, P.A., Gessner, K., Ailleres, L., Gregory, M.J., Duncan, R.J., 2006. Geochemical Process Model for the Mount Isa Copper Orebodies. Economic Geology, 101, 1547–1567.

8. Appendix: Modelling of alteration

As part of the study geology logged pyrrhotite, the siliceous inner core (rock type codes modelled have been shown), Cu, Pb, Zn and Co where modelled in Leapfrog. The results of some of this modelling is shown as long sections in the following figures. The Xstrata wire frame of the lower basement contact (Paroo Fault) and also the dolomite halo are also shown. One key outcome was that the ore body is associated with a pyrrhotite halo which has preciously been used as a way of vectoring in to targets (an example is shown in the last screen capture). Graphite is associated with D_3 cleavages within the mine and it suggests a reduced fluid may have been associated with the D_3 event associated with the development of the dolomite alteration. Whilst the pyrrhotite is spatially associated with the Pb lodes it has a much stronger correlation with Cu, dolomite and the siliceous inner core.

2% Cu (Leapfrog, isotropic) & LBC (mine wire frame)

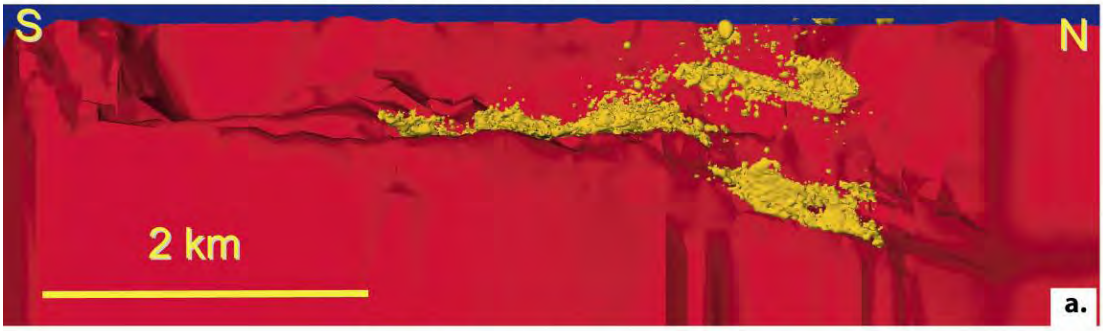

0.5% Cu (Leapfrog , isotropic)

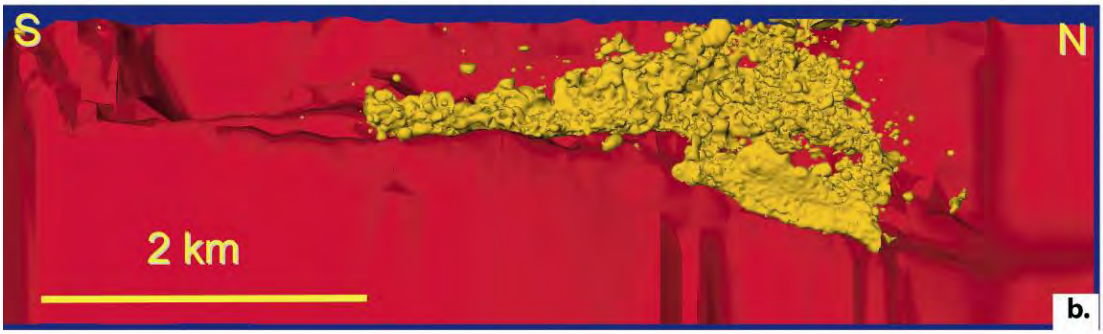

Siliceous Inner Core (Leapfrog, rock types R and C, modeled with anisotropy // to bedding)

Silica-dolomite halo (mine wire frame)
Siliceous Inner Core (Leapfrog, rock types R and C, modeled with anisotropy // to bedding)

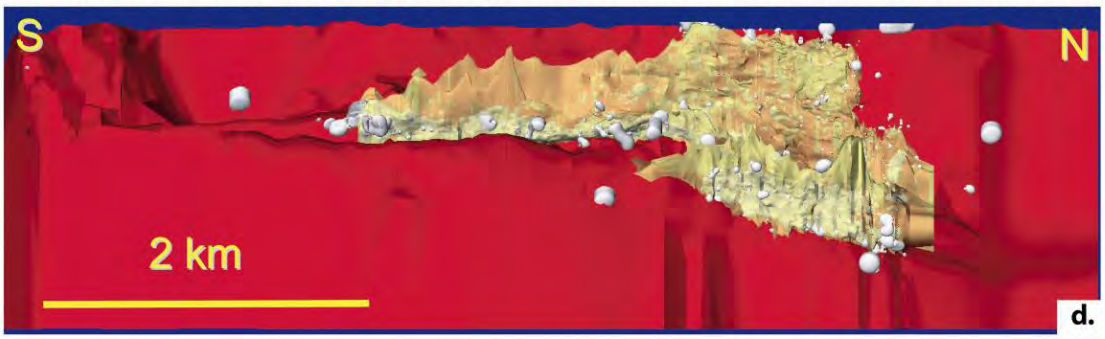

2% pyrrhotite (Leapfrog; geology logged%)

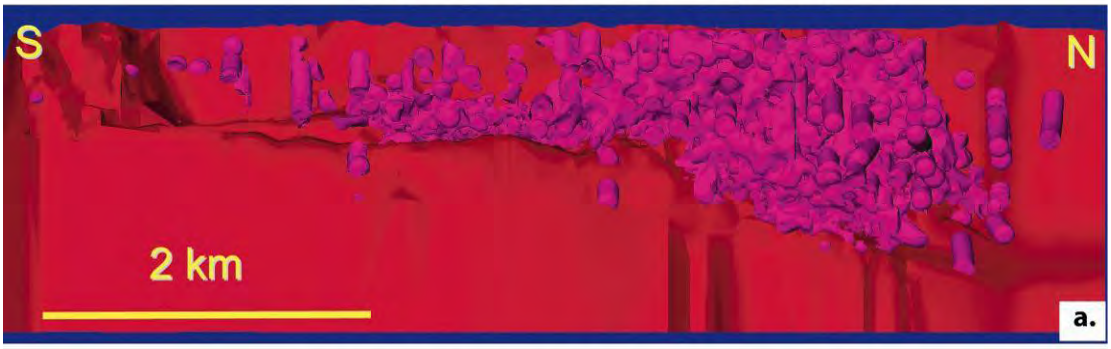

4% pyrrhotite (Leapfrog; geology logged%)

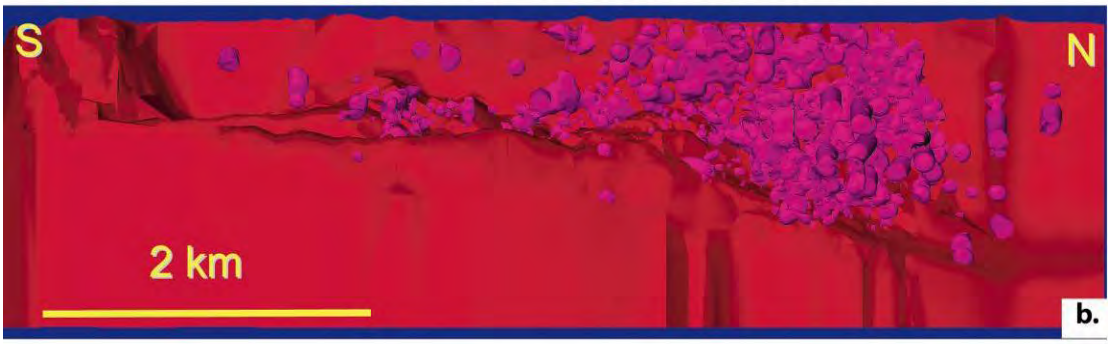

8% Pb (Leapfrog, modeled with anisotropy // to bedding)

2% Po (anisotropic) and Silica model

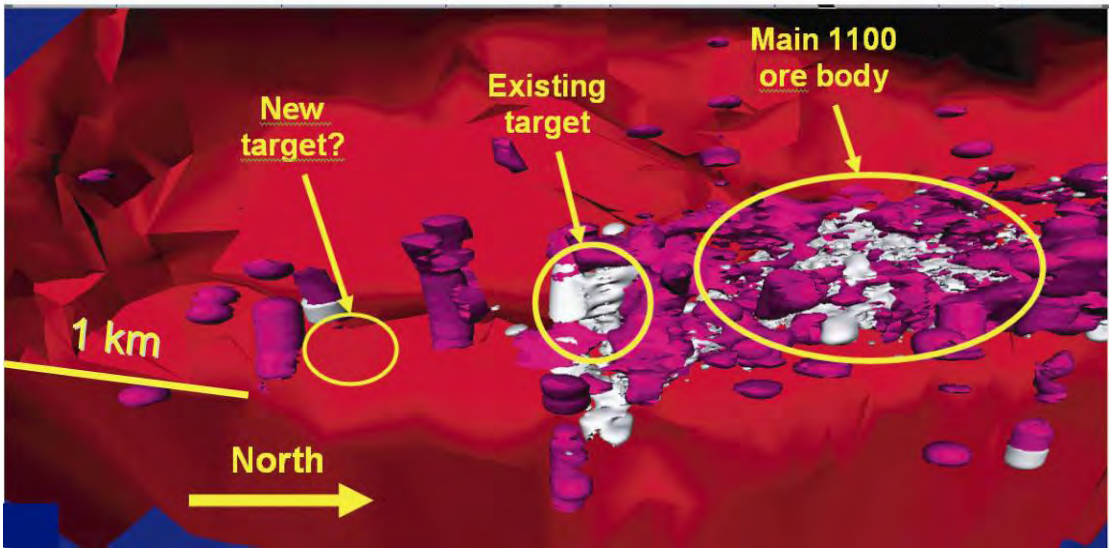

Structural controls on depositional sites for Cu deposits in the Western Fold Belt, Mount Isa: integration of field observations and UDEC modelling

[1]Damien Keys, [2]John Miller and [1]John McLellan

[1]Economic Geology Research Unit, James Cook Univerisity, Townsville, Qld

[2]Centre for Exploration Targeting, University of Western Australia, W.A.

Introduction

The Western Succession of the Proterozoic Mt Isa Block is endowed with a large number of small to medium sized copper deposits with at least one world-class orebody at Mt Isa (Fig. 1). These copper deposits are structurally controlled and developed by the focusing of hydrothermal fluids through structural features such as faults, fault irregularities, shear zones or breccias (Perkins, 1984; Bell et al., 1988; van Dijk, 1994; Laing, 2004; Davis, 2004; McLellan and Oliver, 2008).

The abundant mineralisation and copper deposits occur in a range of different lithological hosts. The Mt Isa, Mt Kelly, Esperanza (at the Mt Gordon Mines), Mt Oxide and Lady Annie deposits are hosted within shales and siltstones, whereas the Mammoth deposit (also of Mt Gordon Mines) is hosted within quartzite. Irrespective of the strong field evidence that the deposits are structurally controlled, and formed at a late-stage in the Isan Orogeny, the location of the deposits within host rocks of markedly different ages is itself a strong argument against a syn-genetic Cu model. However, there is little consensus amongst previous authors on the deposit-scale structural controls at a number of the Western Succession copper deposits, however, the majority of previous authors agree that mineralisation occurred during a late stage of the Isan Orogeny (Mt Isa: Bell et al., 1988; Davis, 2004; Mt Gordon: Askew, 1992; Connors; 1994 Mt Kelly: Da Costa; 2006).

This report provides a synopsis of mine scale structural studies from the Mt Isa and Mt Gordon Copper Mines, and also discusses and compares the results of camp scale and regional scale discrete element modeling with respect to the mine scale structural studies and previous

modelling studies in the Eastern Succession by McLellan & Oliver (2008), which highlights excellent agreement between the results of discrete element models and field studies. This has major implications for targeting structurally controlled Cu-deposits in the Isa Inlier and within any other structurally controlled Cu or Cu-Au terrane.

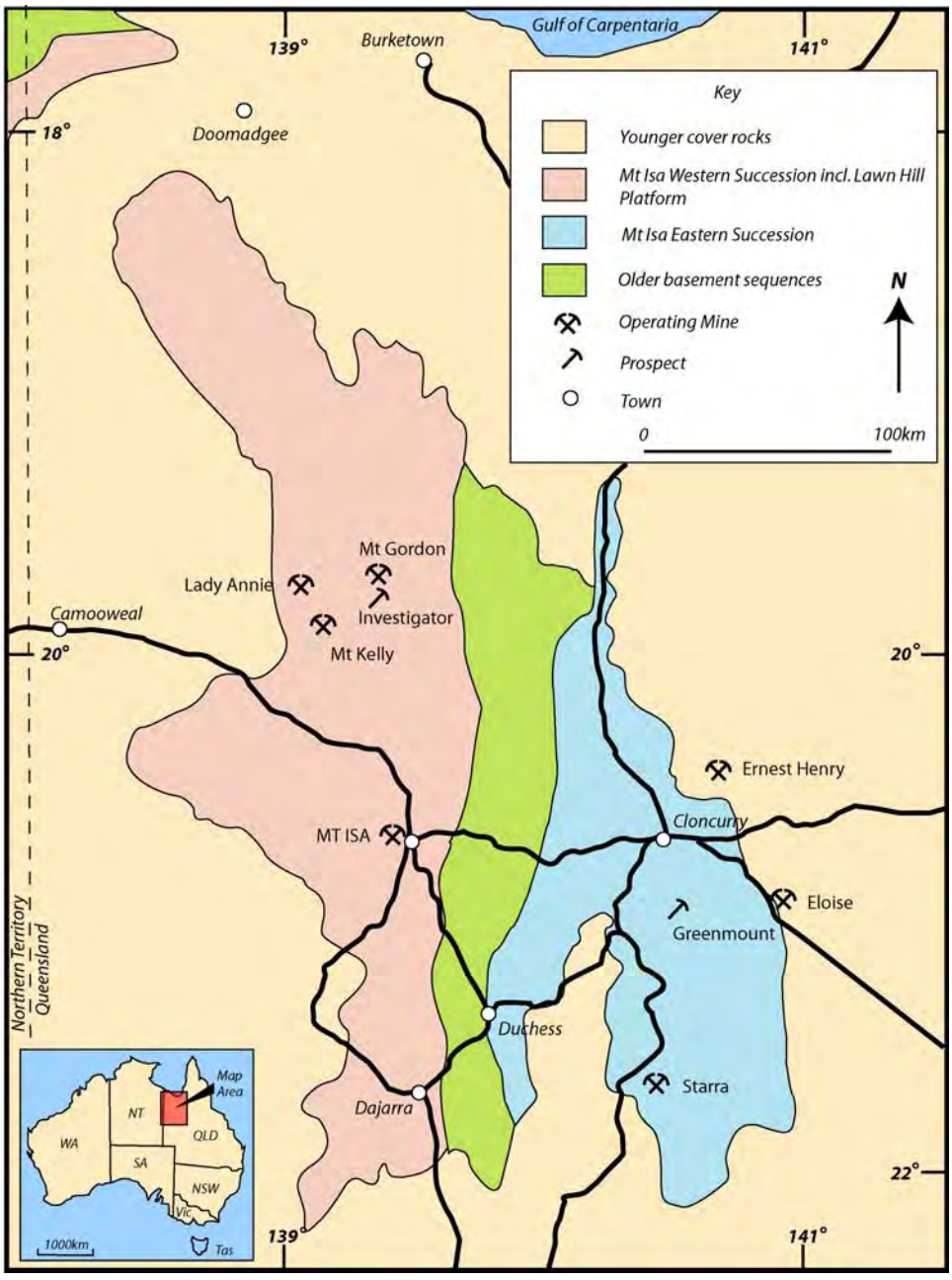

Figure 1. Location of operating Cu mines and prospects in the Mt Isa inlier**.**

Mt Isa Copper - John Miller

The Mount Isa copper mine is located in NW Queensland within the Mt Isa Inlier (Figure 1). Two main ore bodies are currently being mines – the Enterprise and X41 ore bodies (Figure 2). The Mt Isa Cu ore bodies are spatially distinct to the Zn-Pb-Ag ore bodies (Figure 2) and occur as large breccias hosted within a silica-dolomite alteration envelope within a westerly dipping shale sequence that is part of the Mt Isa Group (Perkins, 1984). These altered and brecciated shale units are juxtaposed against an underlying basement unit (the Eastern Creek Volcanics that also contains inter bedded quartzites) via a complex contact. This is commonly termed the Paroo Fault or basement contact fault (Perkins, 1984; Bell et al., 1988). Flat dipping zones of this basement contact have previously been defined as zones of structural weakness at a high angle to the extension direction during Cu mineralisation, resulting in fluid focussing and brecciation (Bell et al., 1988).

The silica-dolomite alteration consists of four main types that reflect dolomitisation ("recrystallised shale" and "irregularly brecciated dolomitic shale") and silicification ("fractured siliceous shale" and "siliceous shale") of the host rocks combined with the extent of brecciation (Perkins, 1984). The siliceous alteration defines the core of the envelope (the siliceous inner core) and is associated with the majority of copper mineralisation (Perkins, 1984).

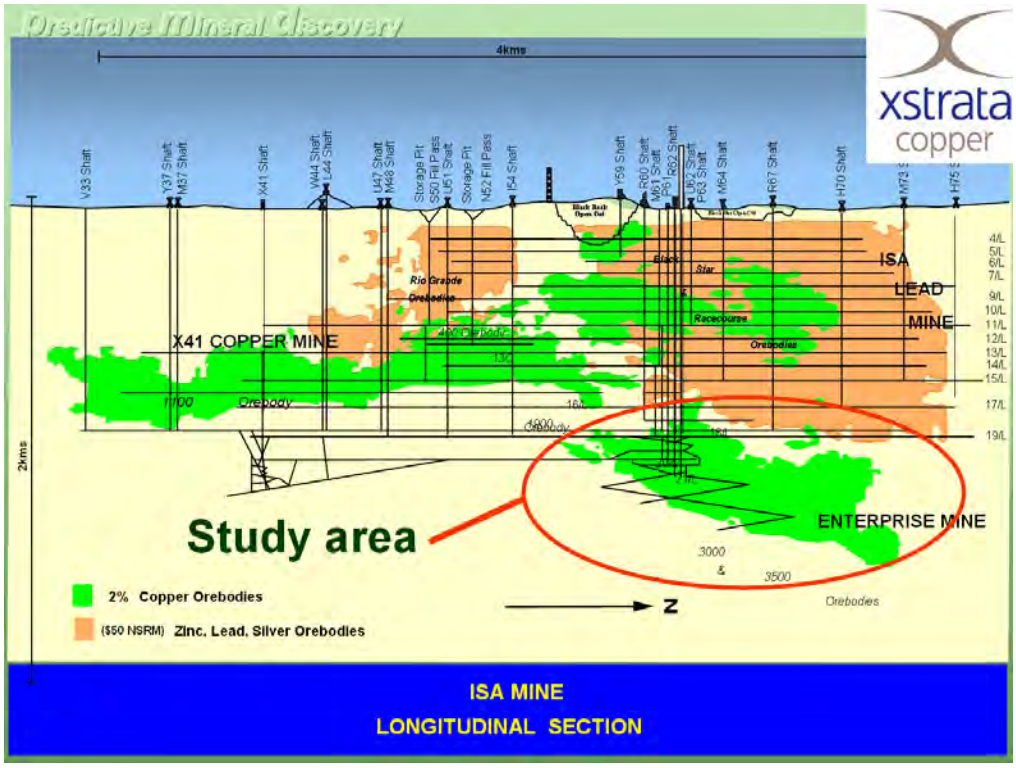

Figure 2. Location of the Enterprise Mine within the Mt Isa Mine (Longitudinal section from Xstrata Cu). Key ore bodies discussed in this report are labeled.

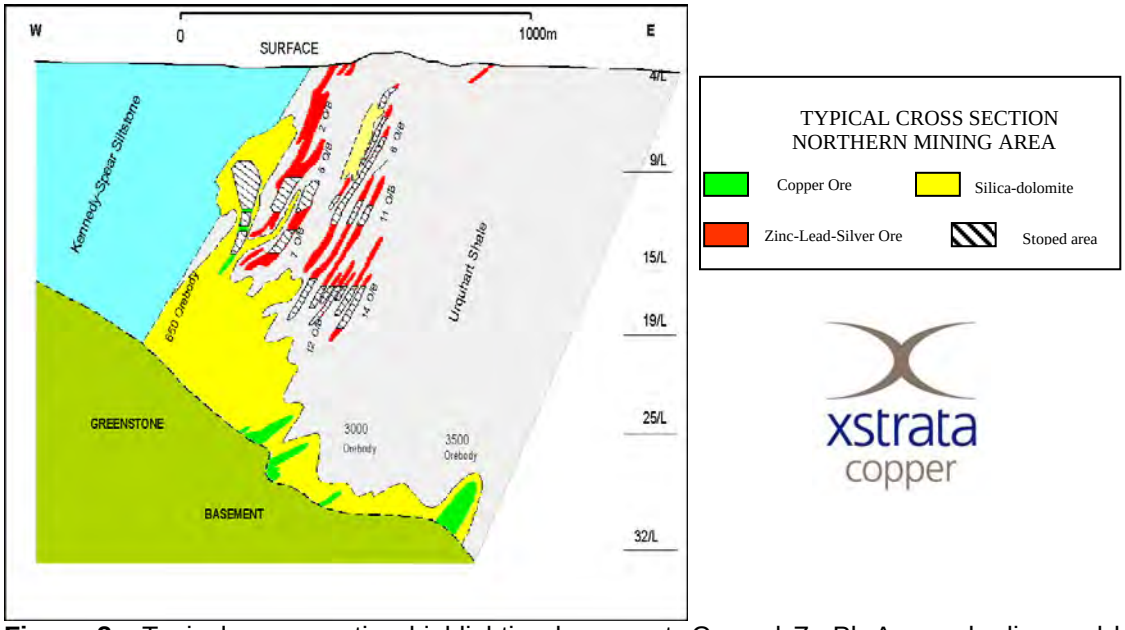

Figure 3. Typical cross section highlighting basement, Cu and Zn-Pb-Ag ore bodies and key rock and alteration types (from Xstrata Copper).

Previous structural studies have argued that the basement contact fault is a D_1 thrust folded by later D_2 and D_3 regional folding events (e.g., Bell et al., 1988). This all occurred during the Isan orogeny, with an initial phase of N-S shortening (Bell, 1983) followed by later phases (D_2 and D_3) of orogenesis that were dominated by E-W shortening to NE-SW, with late dextral wrenching (see Fig. 6 of Betts et al., 2006 for a summary).

The timing of the Cu mineralization has been described as occurring at the end-stage of D_3 - the S_3 cleavages and D_3 folds have a strong control on the development of the breccias (Perkins, 1984, Swager et al., 1987; Bell et al., 1988). Focused mapping of extension veins (both syn- and post-Cu), cleavage and bedding orientations in the Enterprise Mine (3000 and 3500 orebodies) has been undertaken. The Enterprise Mine is located at depth on the northern end of the Mt Isa Zn-Pb-Ag-Cu deposit (Figure 2). This was integrated with 3D models of the Eastern Creek Volcanic basement to determine key structural controls on copper mineralisation

Basement controls

The copper lodes have developed within silicified shale above a basement composed of volcanics and quartzite (Perkins, 1984). This basement/shale contact has been folded with development of a strong cleavage (inferred regional D_3). The observed basement relationships are identical to those reported by Perkins (1984) and Bell et al., (1988) with the basement contact being either a folded D_1 or D_2 fault. The Leapfrog modelling suggests a correlation between the distributions of the volcanics/quartzite contacts and copper mineralisation, with the presence of quartzite units being a key factor. These quartzite units may be linked to silicification of the overlying shale producing a unit rheologically favourable for breccia development. N- and NW-trending basement lineaments are linked to the overlying Cu breccia bodies and these are F3 fold axial surfaces associated with regional D_3 deformation. Extensive graphite is associated with D_3 cleavages within the shale at the contact with the underlying basement, which implies reducing conditions syn-D_3. These graphitic zones are sites of strong fault development and reactivation post the formation of the copper breccias.

Kinematic analysis of the copper breccias

Bedding parallel slip along planes dipping (on average 60 degrees to the west) is the key control on the development of the copper breccias. The presence of the S_3 cleavages provide additional permeability with the $L_{03intersection}$ lineation (= F_3 fold plunge) being a key control on ore shoot plunge. There are major plunge variations of this lineation between different areas producing variable ore shoot plunges and the brecciation appears to post date the S_3 cleavages (also noted by Perkins, 1984). There is no mesoscopic evidence for multiple phases of brecciation - the copper breccias appear to reflect a single discrete event.

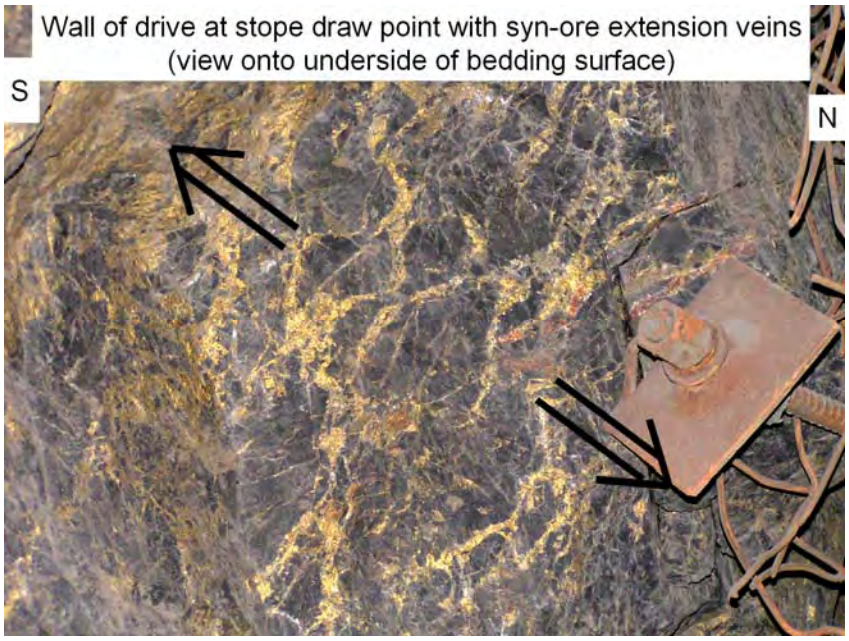

Figure 4. Syn-Cu extension veins intersecting a bedding surface (infill is dominantly chalcopyrite). Arrows highlight extension direction.

Systematic mapping of extension veins (Figure 4) within the copper ore bodies along key Cu and basement trends in both plan & vertical directions constrained the extension direction along the bedding planes (= slip vector orientation). This was remarkably consistent irrespective of fold plunge or location with respect to basement. The majority of vein and fault data indicates top-to-SE hangingwall transport (i.e., sinistral-reverse movement; Figure 5a). The dominant angle between the extension veins and bedding indicates it is not dextral-normal (& can't be dextral-reverse). Apart from vein/bedding relations there is also evidence (dilational jogs etc.) for

a component of reverse movement via reactivation of S_3 cleavages (Figure 6). At a larger scale, the Cu lodes developed along jogs dilatant in a sinistral slip regime, some of these dilatant zones are S_3 cleavages or NW-trending basement lineaments that have dilated during sinistral slip (Figure 6). Three dimensional modelling of the copper distribution at 2.5% showed geometries consistent with a sinistral component of movement at mineralisation (Figure 7). To produce the observed slip vector orientation, the stress field associated with the copper breccias would have had σ_1 lying somewhere to the NW (or SE), σ_1 was not oriented E-W during the major copper breccia event.

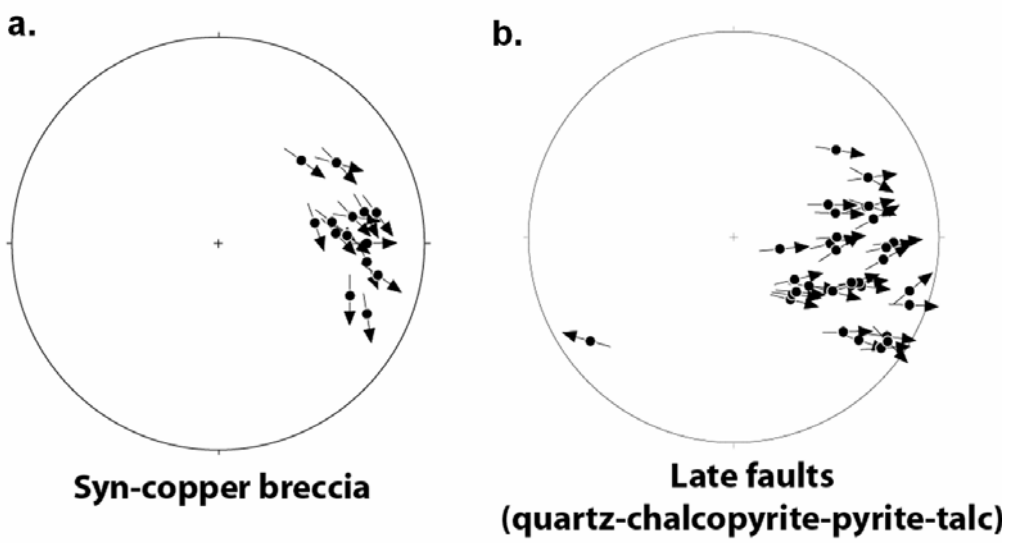

Figure 5. Hangingwall transport directions (see Miller and Wilson, 2004) plotted at the pole to the slip surface (commonly bedding). **(a)** Copper breccia (hangingwall top-to-SE). **(b)** Later W and NW-dipping faults (hangingwal top-to-E). *Note different transport directions.*

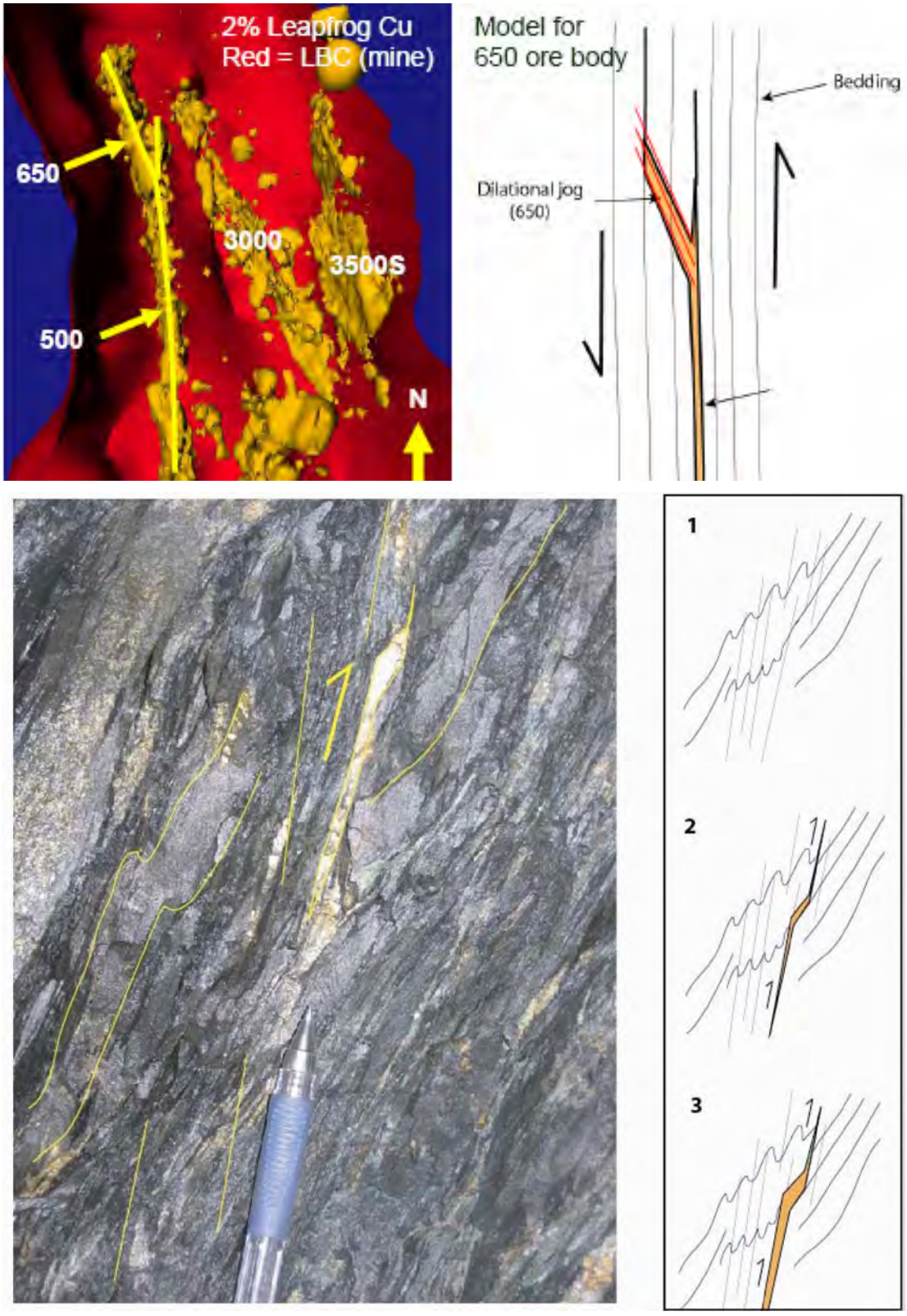

Figure 6. S_3 cleavage control on ore body dilation during sinistral-reverse movement.

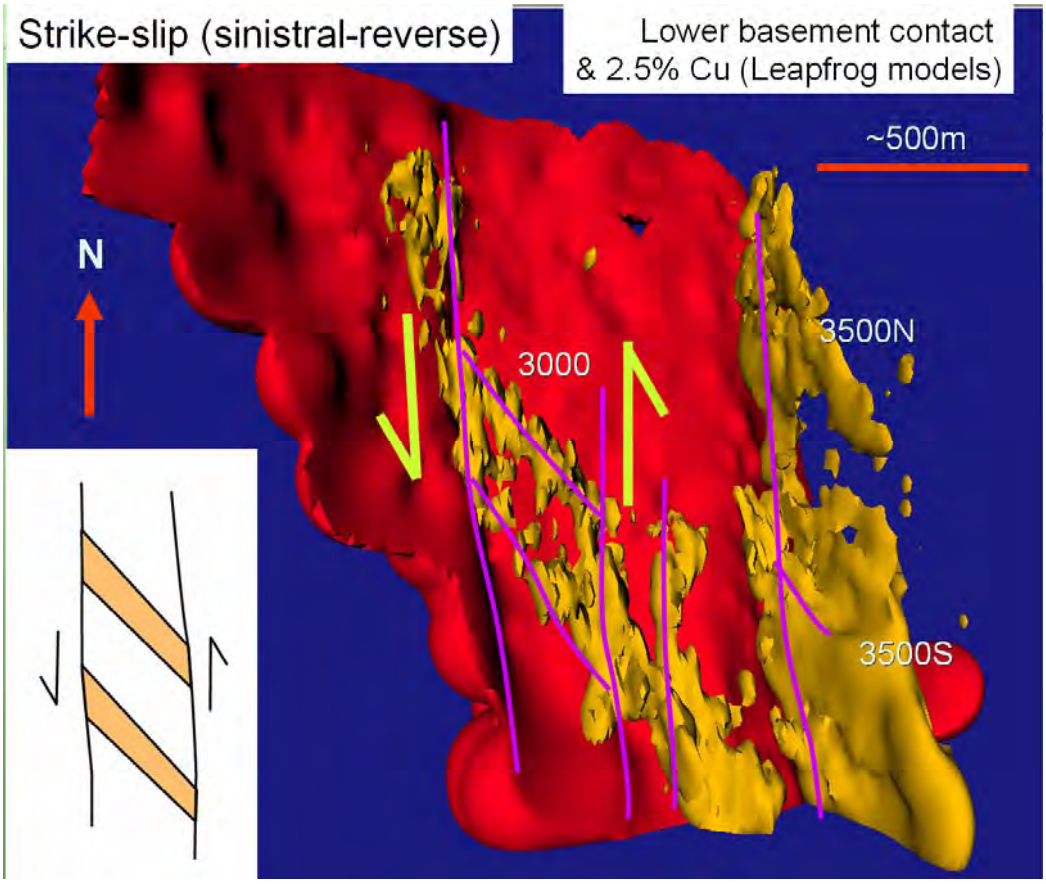

Figure 7. Leapfrog model of lower basement contact and Cu for the Enterprise Mine area (3000, 3500S and 3500N ore bodies). Kinematic interpretation utilizes slip data in Fig. 2a, bedding strikes N-S and dips on average at 60° to the W.

Main post Cu breccia faults

A major set of W-dipping over print the copper breccias. These have an E-directed hangingwall transport with reverse movement and have been termed D4a faults – the Buck Quartz Fault that underlies the X41 ore body is one of these structures (Figure 8). The faults are associated with quartz, pyrite, talc and chalcopyrite (= some enrichment, and there could bee lodes associated with these in some areas) with remobilised galena near Pb lodes.

The second set of post copper faults are a combination of NE-trending faults with dextral-reverse movement (Figure 8 and also the S48 fault highlighted by Bell et al., 1988) and NW-trending sinistral-reverse faults. These faults have a conjugate geometry consistent with E-W shortening (Figure 9) and have been termed D_{4b} faults. The $_{D4b}$ faults displace some of the copper breccias, commonly slip along bedding with lower angle diverging splays and have a completely different extension direction parallel to bedding compared to the Cu breccias (Figure 5).

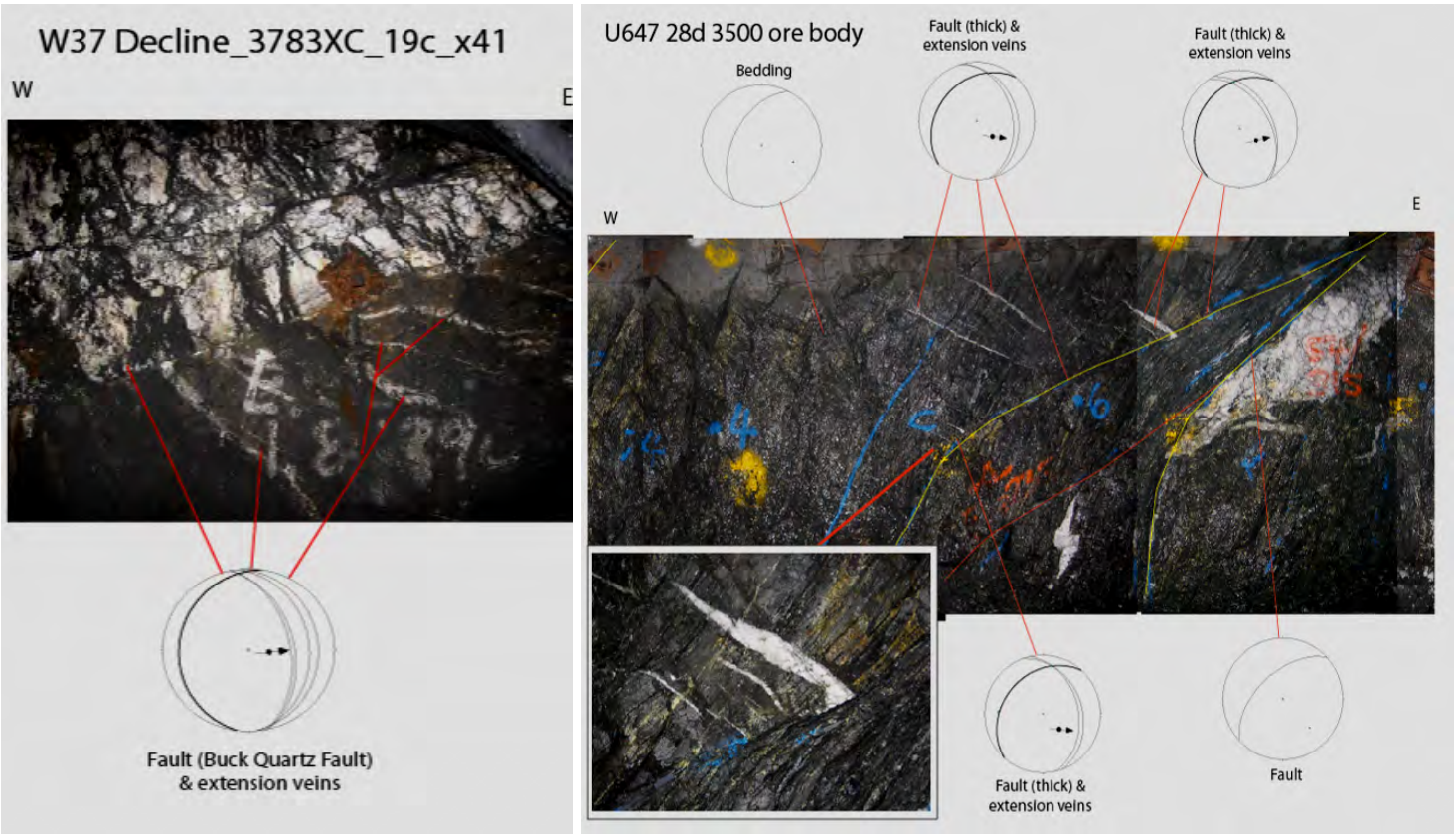

Figure 8. (Left-hand side) Buck Quartz Fault (D_{4a}) structure with top-to-the-east transport. (Right-hand side). D_{4b} dextral-reverse fault from the Enterprise Mine

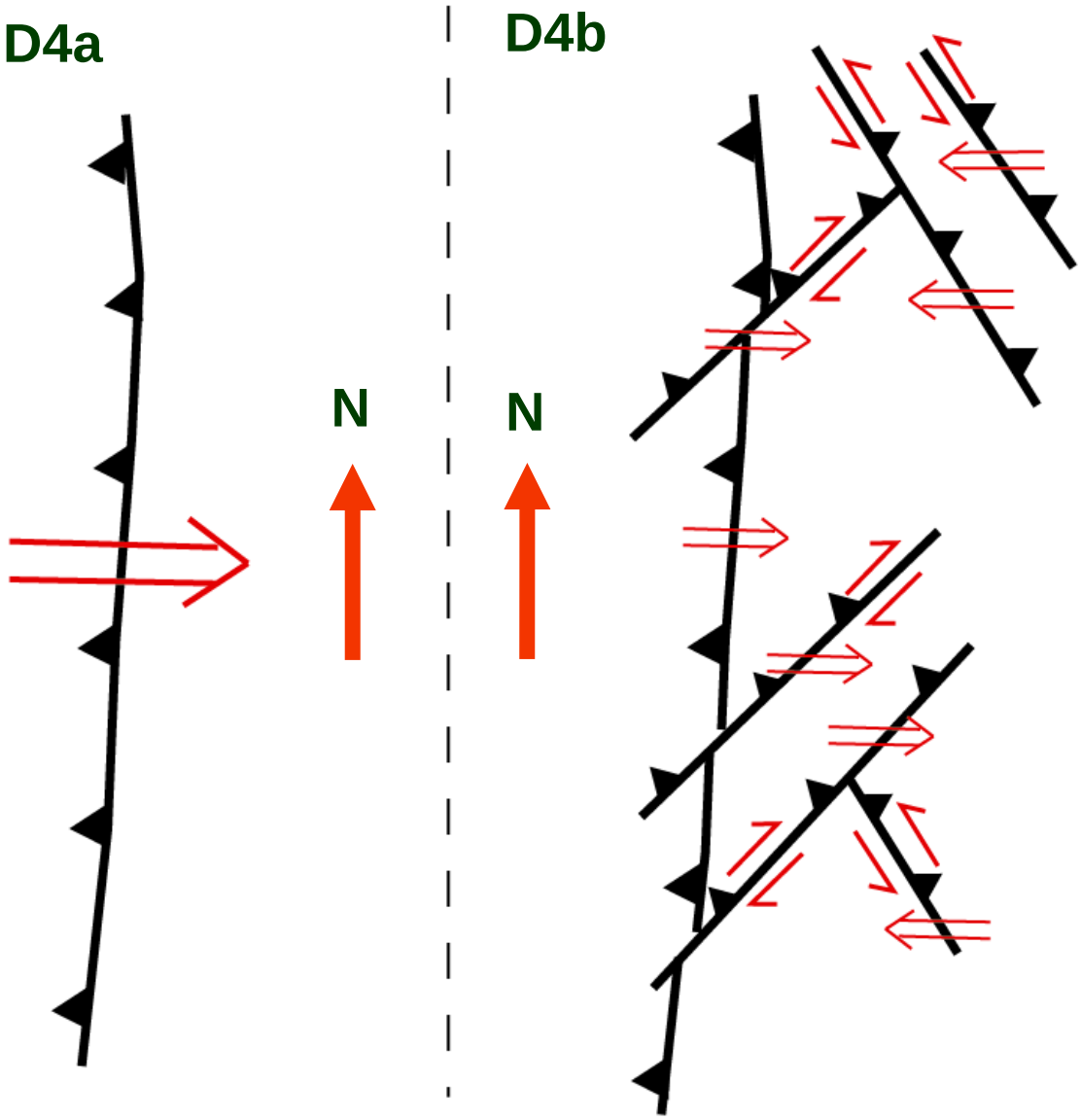

Figure 9. Schematic evolution of D_{4a} and D_{4b} faults within the Isa copper mine.

Key points and implications for the Mount Isa copper project

The structural study at Mount Isa has been integrated with a previous regional synopsis undertaken by Betts et al. (2006). The major change to previous work is the link between sinistral strike-slip movement and copper (Figure 10).

- The main Cu breccias are linked to sinistral-reverse movement and post date regional D_3 deformation – NO REGIONAL EVENT OF THIS NATURE HAS PREVIOUSLY BEEN RECORDED (e.g. Betts et al., 2006)
- Cu may not be a major regional "orogenic" event (i.e. not main folding or faulting observed) – fluid over pressure could cause breccia development and one may not see associated deformation any distance from the Cu ore body
- Strike changes (dilatant in sinistral regime i.e. left stepping arrays) & pre-existing cleavages are important
- Post Cu breccia structures have different slip-vector/extension direction to the Cu breccias.
- The most obvious features are the post Cu breccia faults- these also have an association with chalcopyrite

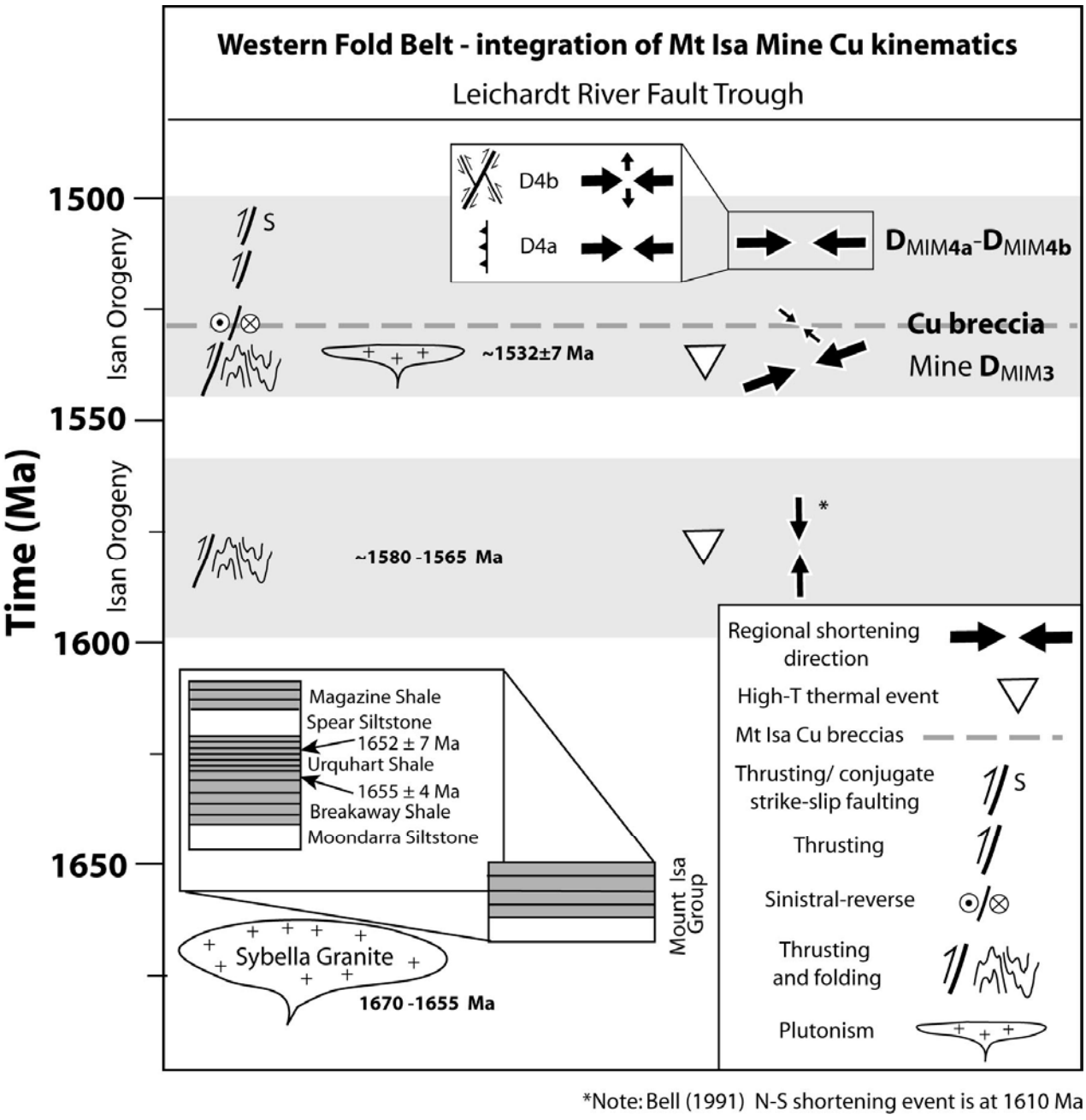

Figure 10. Summary diagram integrating regional kinematics with existing deformation history (modified from Betts et al., 2006). Note that the MIM (Mount Isa Mine) subscript is used to highlight the deformation numbers are for the Mount Isa Copper deposit chronology – different numbers have been used in regional studies.

Mt Gordon – Damien Keys

Late deformational, dextral strike-slip movement on the Mammoth and Mammoth Extended Faults, as indicated by low angle striations (Figure 12a) appears to be related to the copper mineralising event at Mammoth.

Reinterpretation of level plan mapping shows two orientations of intense mineralised brecciation, with the most intense breccias typically oriented either E-W or NW-SE. The E-W trending breccias are always located in close proximity to the 070º oriented faults (Mammoth Fault parallels), and the NW-SE breccias are generally bound by faulting of a similar orientation (130º Fault set), and it would appear these faults were most likely active at the time of mineralisation. To confirm this, a multiple inverse method of stress inversion (Yamaji, 2000) for determining fault striation heterogeneity was used, which yielded a σ_1 orientation of 8 º towards 116 º. Validation of this stress inversion using the Slick software (Ramsey and Lisle, 2000) provided a maximum principal stress orientation of 12º towards 118º. The stress inversion completed on faulting, active at the time of mineralisation in the Mammoth Mine, shows a sub-horizontal orientation for both σ_1 and σ_3. This is in contradiciton with the model of ERA Maptec (1994) who proposed a moderately north plunging σ_3 orientation. The stress inversion and fault plane solution also ruled out the proposed σ_1 orientations of ENE-WSW (Askew, 1992) and NE-SW (Connors, 1997).

Table 1. A summary of stress inversion outputs from each of the inversion methods used

Stress Inversion Technique	***Papers***	***σ_1 plunge***	***σ_1 azimuth***	***σ_2 plunge***	***σ_2 azimuth***	***σ_3 plunge***	***σ_3 azimuth***	***Phi***
Multiple Inverse Method	*Yamaji, 2000*	*8*	*116*			*24*	*014*	*0.4*
P and T Dihedra	*Anglier, 1984*	*0*	*126*	*90*	*-*	*0*	*036*	*-*
Slick	*Ramsay and Lisle, …*	*12*	*118*	*71*	*244*	*15*	*025*	*0.3*

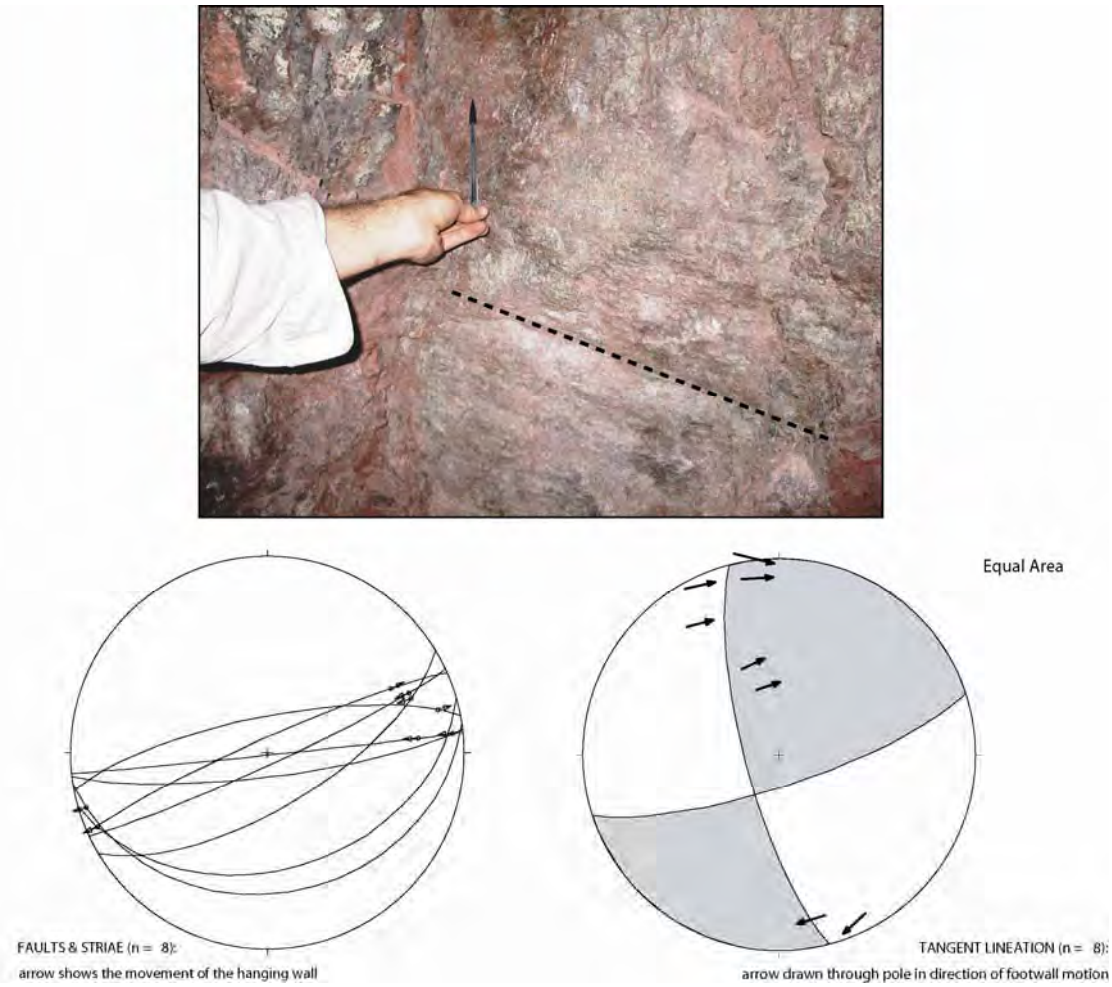

Figure 11. (a) Looking north onto the FW of a Mammoth Fault parallel in the 4745 W1ext. The striations (parallel to the dashed line) step ~15° up to the west giving a dextral reverse sense of movement. The fault contains an earthy hematite fill and in this location is within the 2 Lens orebody. **(b)** Stereographic projection of fault and striation data for Mammoth Fault and associated smaller parallel faults (data collected by Keys, this study, and collated with data from Clarke, 2004). The great circles reflect the orientation of the fault plane and the arrows indicate the direction of hangingwall transport. **(c)** Fault plane solution plot for the data presented in (b). The darker shaded areas reflect areas in tension with the white representing areas in pressure. Hence the triangle reflects an approximate position of σ_3 based on this data and the circle being the approximate position of σ_1. The dark arrows indicate the footwall transport direction. Equal area stereonet projection used, north is up on all stereonets.

Discrete element modelling using UDEC (Itasca Cons.Ltd.) of the Mt Gordon Copper Mines was also undertaken in an attempt to further reconcile the differences between the

mapping of this and previous studies. The conceptual numerical model (Fig. 12) was subjected to a range of maximum principal stress orientations, including the ESE-WNW orientation derived from the stress inversion including the calculated stress ratios (phi value). The best fit model however was the model that employed the stress inversion derived principal stress tensors and ratios. The model utilizing the stress inversion parameters showed an excellent fit between zones of low σ_3, σ_m and P_{fF} with the known deposits and breccias. Inferred failure modes were consistent with mapped breccia characteristics.

Modelling also tested the effects of fault architecture versus variable lithologies. The modelling results suggest that the brecciation observed in the Esperanza/Mammoth system is dominantly a result of the existing fault architecture, with less influence of lithology types or variations in rheological properties. Changes in lithology may influence the amount of dilation, but ultimately the sites for brecciation are determined by the interplay of the fault architecture. This has implications for the exploration for the Mt Gordon lease and for the exploration of other similarly oriented fault arrays along the Mount Gordon Fault Zone, such as the Investigator Fault Sytem.

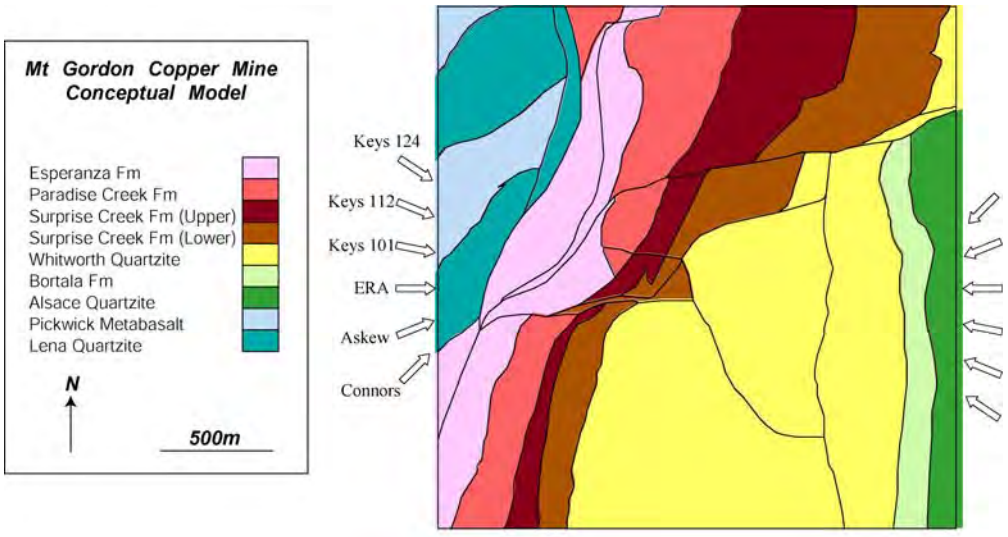

Figure 12. Conceptual model geometry and modelled scenarios. The arrows reflect the σ_1 orientations proposed by previous authors with the Keys 101º, 112º and 124º.

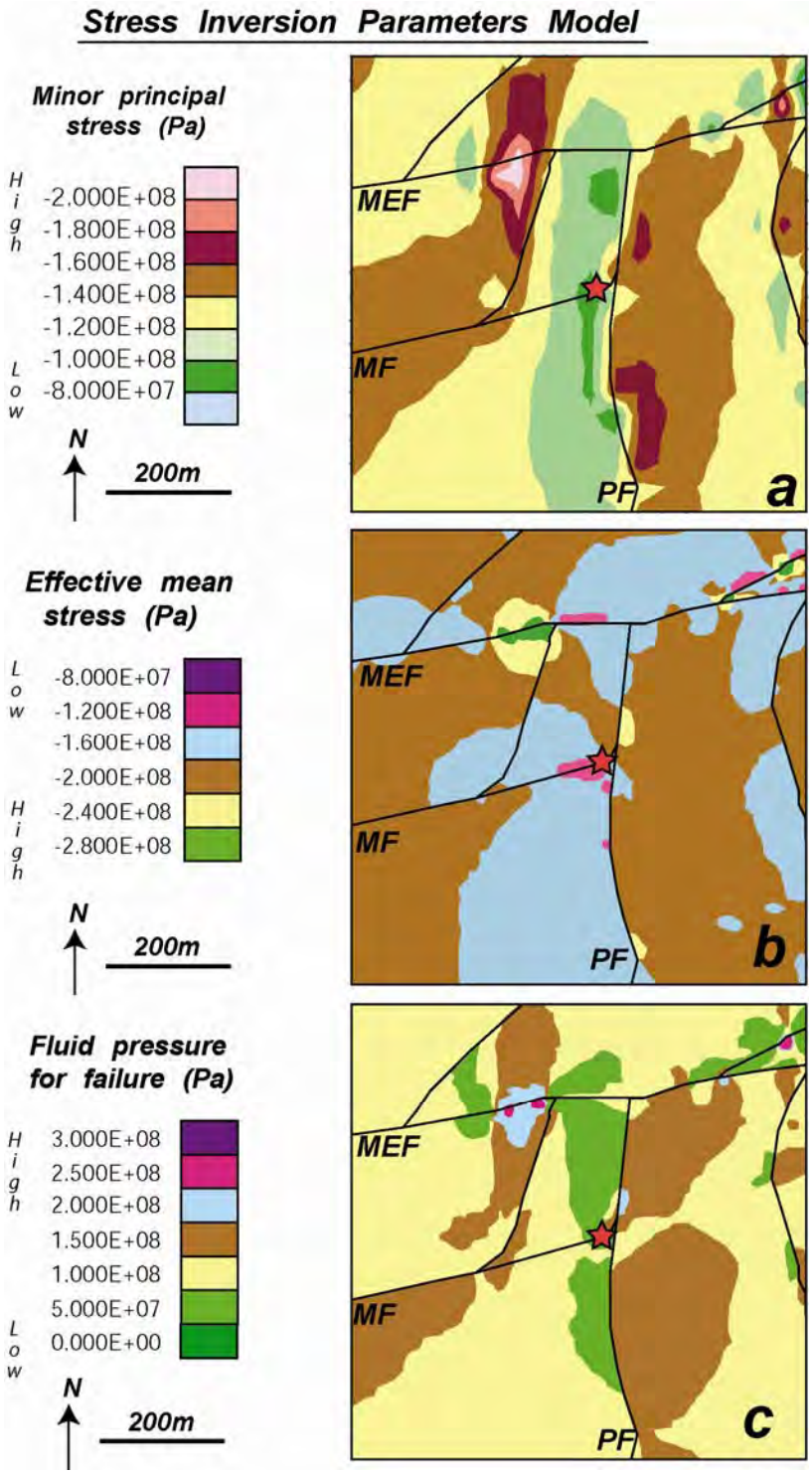

Figure 13.

(a) A corridor of low σ_3 values runs along the western margin of the Portal Fault (Mammoth Mine location red star). The high values to the east of the Portal Fault (PF) are consistent with observations of unbrecciated Whitworth Quartzites in this location.

(b) Low values of effective mean stress are seen in the Mammoth Mine location. High mean stress values are seen to the east of the Portal Fault.

(c) Low Pf_F values are seen in the Mammoth Mine location in both models. Higher values of Pf_F are seen on the east of the Portal Fault

Mt Kelly – Damien Keys

Limited outcrop exists over the Mt Kelly breccias, hence there is little knowledge of the key structural controls on copper mineralisation. This gap in understanding and the success of the numerical modelling at the Mt Gordon and the Mt Isa Copper Mines, provide the framework for study at Mt Kelly. A more comprehensive knowledge of deposit scale structural controls on mineralisation was determined, primarily through the use of numerical modelling, which highlights this study as a very good example for the use of numerical modelling techniques in understanding structural controls on mineralisation.

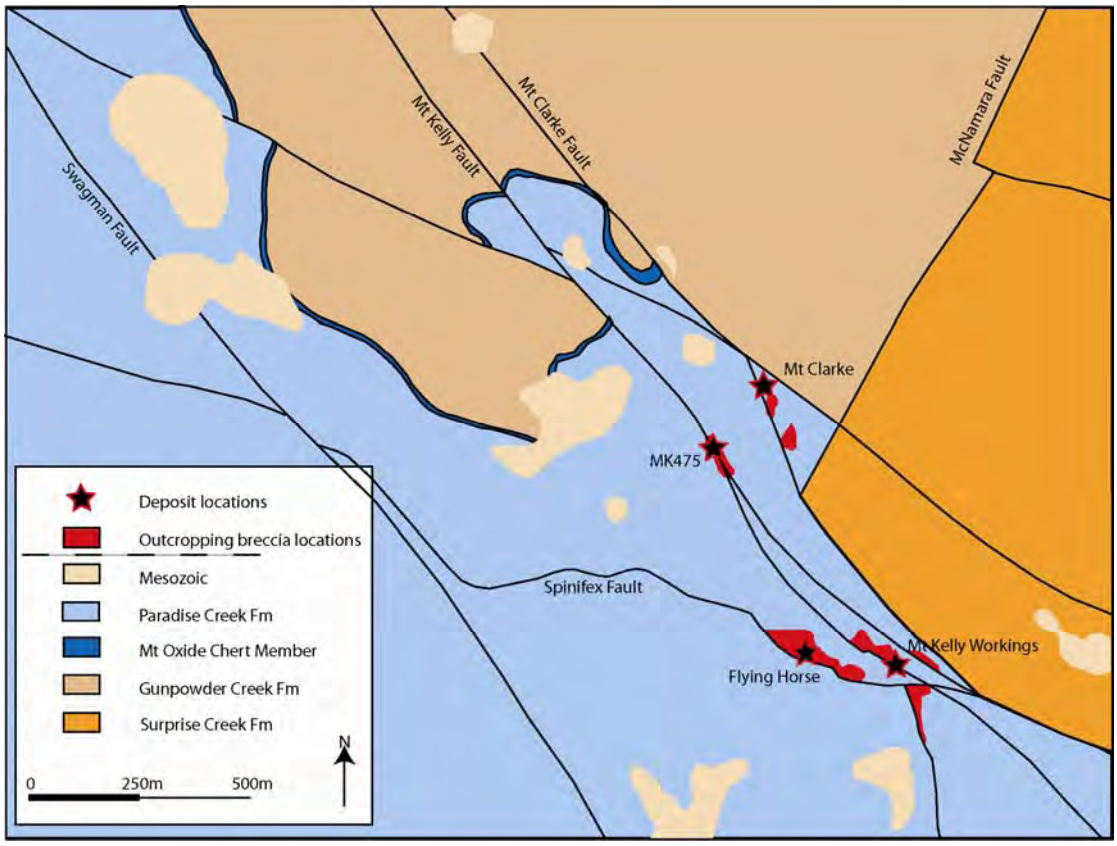

Figure 14. Map of deposit locations associated with Mt Kelly and Mt Clarke

The intersection of the Mt Kelly Fault and the shallowly north dipping Spinifex Fault at depth, is often used to explain a high-grade copper and gold intersection found in the MK475 locality. Four diamond holes were examined for breccia style, breccia relationships to mineralisation, alteration intensity and alteration relationships to mineralisation, with theMK475A

drill hole containing the most mineralisation. The intensity of brecciation was directly proportional to the distance from the Mt Kelly Fault, i.e. the closer the sampled interval to the Mt Kelly Fault, the more intense the brecciation. The style of brecciation also changed depending on the proximity to the Mt Kelly Fault (Figure 15). Breccias containing breccia clasts themselves were found in the inferred Mt Kelly Fault position downhole, which would imply two episodes of brecciation within the Mt Kelly Fault, with the latter event most likely related to copper mineralisation. If the copper is associated with the second breccia phase, then this is consistent with the assumption that the Mt Kelly Fault was present and active pre-mineralisation.

Field mapping completed in this study failed to locate a shallow dipping Spinifex Fault. Conjecture over the existence of this fault has dominated the literature on the Mt Kelly deposit (e.g. Stephens, 2000; Maiden *et al*, 2001; Da Costa, 2006). The numerical models were therefore run with and without the Spinifex Fault present, to test the effect of the faults existence.

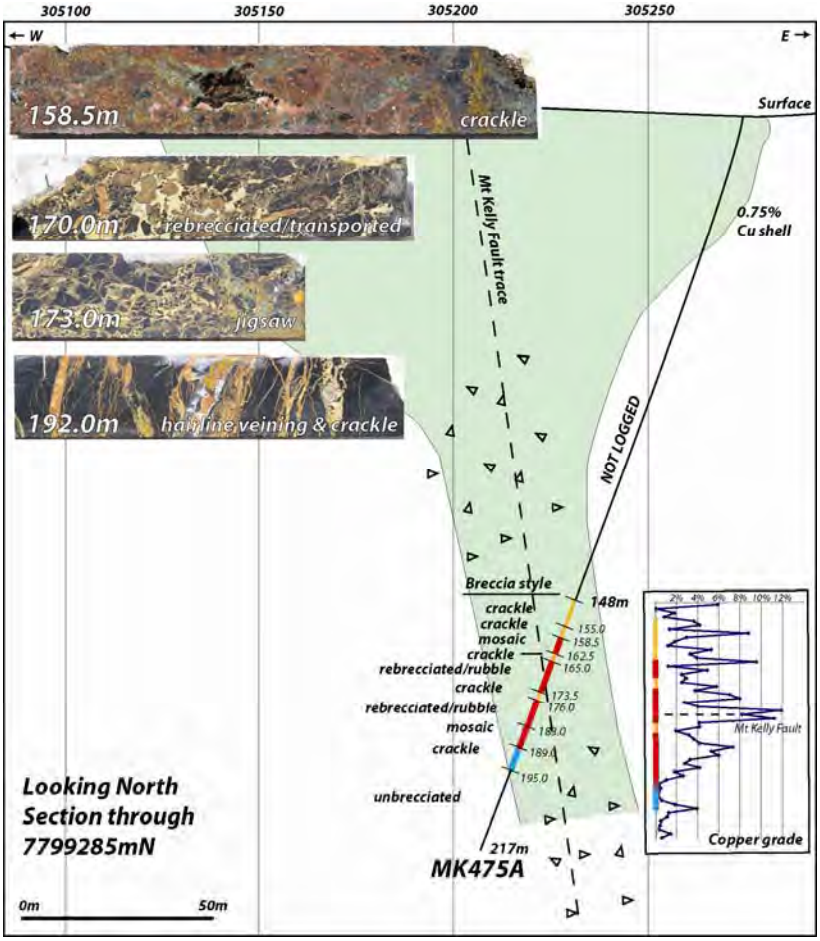

Figure 15 Section through 7799285mN, looking north, at the MK475 deposit at Mt Kelly. The section shows breccia styles and their relationships to grade distributions.

For both of the model runs (with and without the Spinifex Fault), the σ_1 orientation providing the best correlation with known deposits was 112°-292°. When σ_1 was oriented ESE-WNW values of minor principal stress, fluid pressure required for failure and mean stress were seen to be relatively low in the specific deposit locations (Fig. 16).

The Mt Kelly models run without the Spinifex Fault showed significantly lower values of fluid pressures required for failure than the model run with the Spinifex Fault included (see Fig. 16). Although this study cannot conclusively deny or confirm the existence of the Spinifex Fault, it shows that it is not a necessity for the brecciation all of the Mt Kelly Copper Mine deposits.

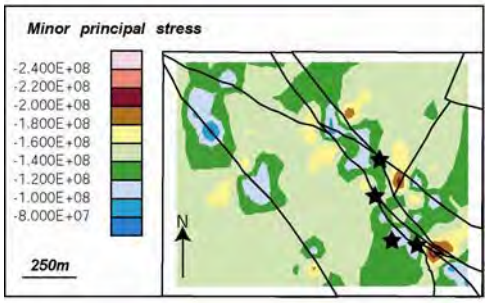

Figure 16 ***(a)*** *Showing contours of minor principal stress. The No Spinifex Model shows a broad area of low σ_3 along the Mt Clarke Fault. Values of σ_3 are slightly lower in the No Spinifex Fault in the known deposit locations.*

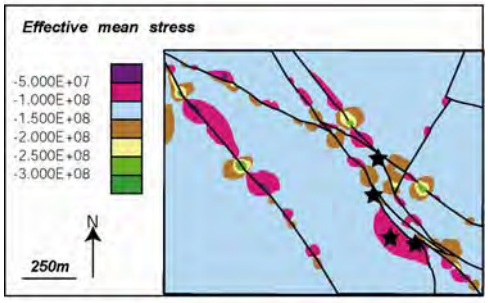

(b) *Showing contours of mean stress. The No Spinifex Fault model shows a large zone of low mean stress extending from the Mt Kelly Workings west to the Flying Horse deposit.*

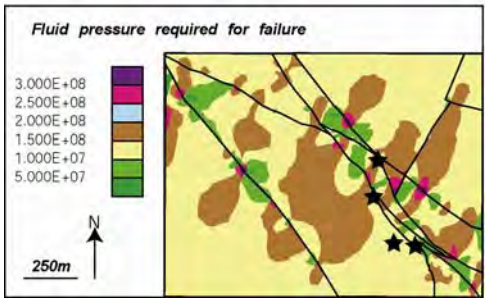

(c) *Showing contours of fluid pressure required for failure. The No Spinifex Fault model shows a NNW orientation to zones of high and low fluid pressures for failure. Both models show low P_{fF} values in the known deposit locations and high P_{fF} values along the SCQ/Paradise Creek Formation contact.*

5.0 **Regional Models** - John McLellan

Numerical modelling is employed here to examine the response of a fracture system in the Western Succession of the Mount Isa Inlier to an applied stress regime. Models were tested in two different areas at similar regional scales, to include both the southern and northern regions of the Leichhardt River Fault Trough (LRFT). Numerous parameters were tested, in particular the orientation of an applied stress regime (σ_1) to examine model response and correlate favourable anomalous areas of stress and strain partitioning with known Cu deposits and prospects. Modelled areas of combined low minimum principal stress (σ_3), low fluid pressure required for failure (P_fF), high volumetric increase or dilation (ψ), and shear and tensile failure show the best correlation with deposits, but these areas do not clearly correspond to specific fault orientations or configurations. Rather, the models produce complex zoning of stress anomalies in response to the partitioning of stress across complex fault blocks, and the interaction between more competent igneous bodies, less competent meta-sedimentary rocks, and the fault and rock boundary complexities.

A far field ESE stress orientation provides the best visual results and correlation with known mineralisation in the region, and therefore inferred as the most likely orientation of σ_1 during genesis of many of the deposits.

One of the key outcomes of this study is the demonstrated effects of complex fault architecture and competency contrasts in partitioning both stress and strain during deformation. One of the main results is the effect on stress and strain partitioning when the far field stress regime is rotated from an initial east-west orientation, resulting in isolated areas that display several of the essential mechanical ingredients for a Cu mineralised system in the Western Succession. Competency contrasts between the igneous rocks and meta-sedimentary rocks in association with a fault or fault network, result in significant partitioning of stress around these structures. This is clearly evident around some of the major intrusives in the area, in particular the Sybella Granite in the southern region, and smaller igneous rocks in the NLRFT such as the Weberra Granite, the Ewen Granite and the Cromwell metabasalt.

Faults have proven very important in localising the stress, strain and failure patterns observed, and it is evident that in a general sense, NW orientated faults appear to have the least favourable ingredients (low σ_3, dilation and failure) that we would expect to produce fluid focusing and mineralisation. This result may be somewhat counter intuitive; given the far field stress orientation is in the same general direction and one would expect faults at low angles to σ_1 to result in shear failure. This result however, highlights a complex interplay between the fault blocks and competent bodies and not all faults of any particular orientation show the same distribution of values, level of partitioning or overall prospectivity as a result of failure. This is due to the more complex interactions of block geometry or fault blocks and variations in block displacement relative to the applied far-field stress (σ_1), which assist in partitioning stress as these blocks move and deform. We can see that certain isolated areas have lower values of P_fF, and σ_3 and this may correspond with either low values of $\Delta\sigma$ (which may indicate a higher potential for tensile failure) or high values of $\Delta\sigma$ (which may indicate a higher potential for shear failure). These parameters indicate a higher potential for failure at specific locations within the model, and hence represent an overall increase in prospectivity for Cu mineralisation based on a structural controls and mechanical criteria approach. The main areas of interest in terms of prospectivity have been clearly identified in the Mt Isa regional (Fig. john1) and Northern Leichhardt River Fault Trough area (Fig. john2) models The interesting thing to note is that many of these potential target areas are under variable amounts of younger sedimentary cover, and may have so far been overlooked as prospective exploration areas.

This work provides a good comparison between the Eastern and Western Successions of the Mount Isa Inlier, in terms of stress partitioning and Cu prospectivity. The work of McLellan and Oliver (2007) highlighted many areas in the Eastern Succession that have a higher potential (based on structural controls and stress partitioning) for Cu-Au mineralisation. Their main findings were that the most likely far field stress orientation responsible for localising fluids and Cu mineralisation was 112.5° (ESE). In comparison the most likely stress orientation responsible for Cu mineralisation in the Western Succession has been of a very similar orientation given that the

ESE orientated models (Model 1b and Model 2b) produced the most favourable results when comparing with known mineralisation.

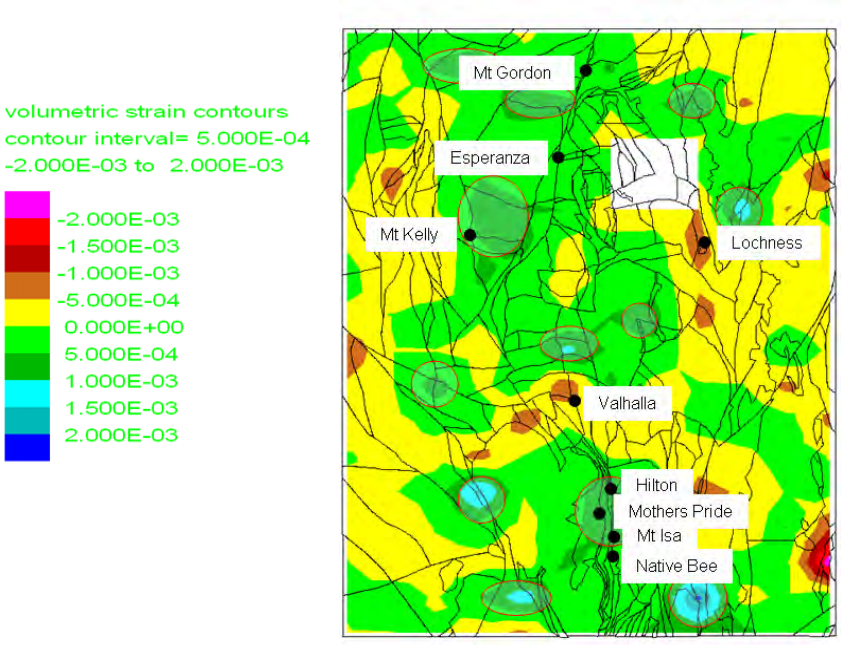

Figure 15 UDEC output plot of dilational areas indicated in green and blue, and major deposits and prospects in the area. Circled regions indicate areas that can be considered prospective for Cu mineralisation based on a mechanical model.

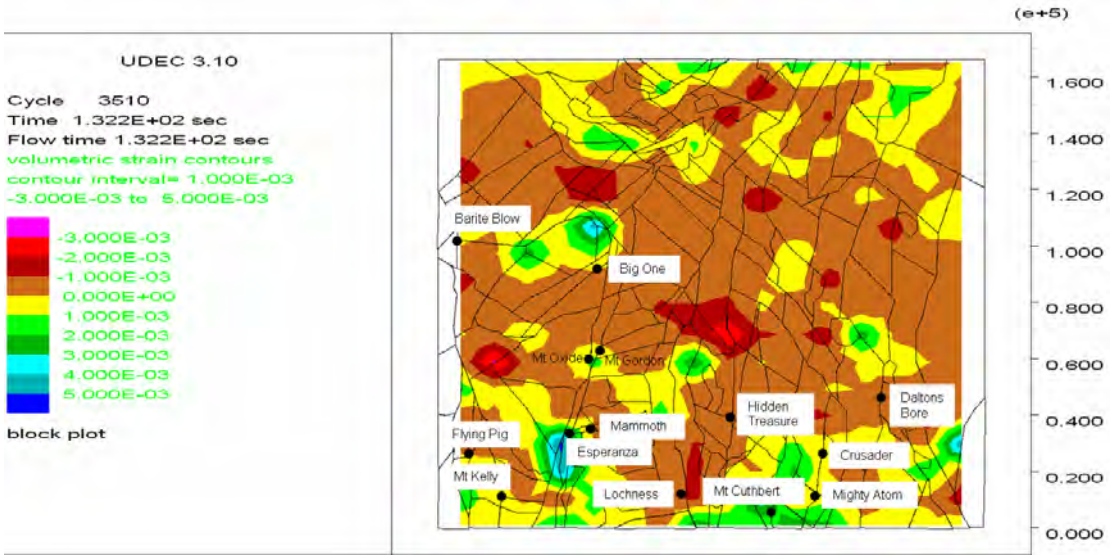

Figure 16 UDEC output plot of dilational areas indicated in yellow, green and blue, and major deposits and prospects in the area.

Discussion and Summary

The results from these studies strongly infer a far field stress orientation of ESE-WNW to be responsible for formation of the breccias hosting copper mineralisation at the Mount Isa, Mt Gordon and Mt Kelly mines and also on the regional scale. These studies therefore provide strong evidence that there may have been a consistent far field stress regime responsible for copper mineralisation in the Western Succession of the Mount Isa Inlier during a late stage in the Isan Orogeny (c. ~1530 - 1510 Ma).

Other studies (McLellan & Oliver, 2008; Rubenach *et al.,* 2007) have determined a similar σ_1 orientation to be responsible for ore-hosting and non ore-hosting brecciation in the Mt Isa Eastern Succession, late in the Isan Orogeny. Deposit to camp scale UDEC modelling by Keys (2008 this volume) has determined an ESE-WNW orientation as being responsible for the brecciation of the Greenmount Copper Deposit approximately 40km south of Cloncurry. The same study has shown that a far field σ_1 orientation of SE-NW refracts around the pre-existing diorites (1660Ma) at the Ernest Henry Cu-Au Mine (50km N of Cloncurry) to produce a local σ_1 orientation of NNE-SSW at the mine scale at mineralisation. This orientation of mine-scale σ_1 for Ernest Henry complies with the structural analyses of Coward (2000) and Laing (2004).

Rubenach *et al.* (2007) document an ESE-WNW shortening event in the Snake Creek Anticline area, expressed as NNE crenulations in several localities near the intruding Saxby Granite (1527 Ma). It is suggested that the granite intruded during D_4 and that deformation had ceased prior to final solidification (Rubenach *et al.*, 2007). Microstructural analysis confirms that porphyroblast growth continued at least as far as the D_4 event, in the Snake Creek Anticline area (Rubenach *et al*., 2007).

This 1527 Ma Saxby Granite age also represents the D_4 (M_6 – low pressure metamorphism) event, and is consistent with the timing of extensive brecciation and late albitization of calc-silicate rocks of the Corella Formation in the Selwyn Zone (Rubenach *et al.*, 2007). Austin and Blenkinsop (*in press*) confirm a brecciation event associated with ESE-WNW shortening along specific parts of the Cloncurry Fault Zone. They document the transition from a ENE-WSW shortening producing NNW or SSE plunging folds at D_3, to a brittle strike-slip event

coincident with massive Na-Ca brecciation at D_4. The inferred sense of movement on the NNW striking Cloncurry Fault is sinistral at D_4, inferring that the σ_1 orientation was ESE-WNW. Intrusive magmatism and IOCG, Cu and Au mineralisation are spatially and temporally related to the D_3-D_5 history of the Cloncurry Fault Zone (Austin and Blenkinsop, *in press*).

Regional scale UDEC modelling of the Mt Isa Eastern Succession (McLellan & Oliver, 2008; McLellan, 2004) produced similar results to previous studies suggesting a regional σ_1 orientation of ESE-WNW. Two primary conceptual models were tested, based on distinct temporal periods. The first was based on a 1540-1530 Ma time frame, being post metamorphic peak and containing the older plutons of the Eastern Succession but being pre-emplacement of the Williams and Naraku Batholiths. The second model tested a 1530-1480 Ma time frame, where additional younger fault architectures and the Williams and Naraku Batholiths were added to the first model. Mclellan & Oliver, 2008 and McLellan (2004) found that modelled areas of low minor principal stress and low mean stress spatially correlated best with the known deposits when σ_1 was oriented ESE-WNW (112.5º-292.5º) in the younger model based on a 1530-1480 Ma time frame.

Evidence from Mt Gordon, Mt Isa, Snake Creek (Rubenach *et al*., 2007) and the Cloncurry Fault Zone (Austin and Blenkinsop, in press) suggests the D_4 event marks the transition to a dominantly brittle strike-slip system. The D_4 ESE-WNW shortening event is quite discrete across the Inlier and is most likely a low strain,

Kendrick *et al* (2006) document fluid mixing of metamorphically derived fluids (from the Barramundi basement) and bittern brines for the formation of the Mt Isa copper orebodies. This implies the introduction of the metamorphic fluids from depth. The strike-slip nature of the D_4 copper event may allow the tapping of deep fluids and the brittle nature of the D_4 deformation may provide the locus for fluid mixing (see also McLellan this volume).

The mapping of the Mt Isa Copper Mines also noted post mineralisation deformational features. The rotation of the stress field back to an east-west orientation (D_{4a} and D_{4b} for the mine scale history in Figure 10, but termed regional D_5) initiates dextral movement on NE striking faults. The NE striking fault S48 Fault in the Mount Isa mine clearly post-dates mineralisation as

the fault dextrally offsets the 1100 orebody by ~200m (Perkins, 1984; Bell et al., 1988). Very minor amounts of copper are associated with the “last gasp” east-west shortening event. This later D_5 deformation was not obvious at the Mt Gordon Mines however the event may possibly be seen regionally with the dextral offset of the NE striking Fountain Range Fault.

Both at the regional and local scale the UDEC numerical modelling process provides a very effective exploration tool, which can highlight areas that have undergone stress partitioning and strain localisation, and highlight areas that show an increased potential for mineralisation as measured by stress and failure distributions. Incorporating a more detailed geometry including lithological contacts and small-scale structures to further examine the role of smaller scale structures in stress and strain partitioning would allow a more precise targeting strategy at tenement-to-mine-scale based on the structural approach. However, the two-dimensional regional scale models provide a good basis for further modelling studies, and highlight the basic conditions required for structurally controlled Cu mineralisation in the Western Succession of the Mount Isa Inlier. Importantly the mapping of the Mt Isa, Mt Gordon and Mt Kelly copper deposits has shown that the brecciation associated with the mineralisation has only undergone one significant brecciation event.

Although there are inherent issues with UDEC only considering two dimensions, the study also highlights that UDEC modeling can be a useful tool in testing select structural scenarios in many instances in the Mt Isa Inlier. This form of numerical modelling may also be a useful tool for testing structural hypotheses in other Cu belts that indicate a strong structural component e.g. Gawler, Porphry Cu systems NSW, Carajas, Brazil. This modelling is particularly effective in areas where mineralisation is inferred to be associated with strike-slip deformation on steeply dipping structures.

Further details of the I7 structural studies discussed can be found attached

Mt Isa; Miller (2006) and also this report

Mt Gordon, Mt Kelly, Investigator Fault, Ernest Henry, Greenmount and Starra; Keys (2008) PhD

Discussion on the geodynamic constraints of an "inlier-wide copper event"; Keys (2008) PhD thesis

Regional UDEC modelling – Eastern Succession; McLellan and Oliver (2008)

- Western Succession; McLellan

Acknowledgements

The Mount Isa Copper mapping project was made possible by major support from Xstrata Staff in particular Ian Holland (Geology Superintendent Isa Cu), Trevor Shaw, Nathan Bullock, Eamonn Dare, and Justin Watson. This work was done as part of the I7 project in the pmd*CRC.

References

Anonymous (ERA Maptec) 1994, A Regional Structural Overview of the Mammoth Copper Deposit Gunpowder, Queensland: Confidential Company Report., ERA-MAPTEC Australia, p. 37.

Askew, R. L., 1992, Structural Setting of E. P. 8297 M, Gunpowder, Qld., & Implications for Further Work: Melbourne, Victorian Institute of Earth and Planetary Sciences, Monash University, p. 30.

Bell, T.H., 1983. Thrusting and duplex formation at Mount Isa. Nature, 304, 493-497.

Bell, T.H., 1991. The role of thrusting in the structural development of the Mount Isa Mine and its relevance to exploration in the surrounding region. Economic Geology, 86, 1602-1625.

Bell, T.H., Perkins, W.G., and Swager, C.P., 1988. Structural controls on development and localization of syntectonic copper mineralization at Mount Isa, Queensland. ECONOMIC GEOLOGY, v. 83, p. 69–85.

Betts, P.G., Giles, D., Mark, G., Lister, G.S., Goleby, B.R., Aillères, L., 2006. Synthesis of the Proterozoic evolution of the Mt Isa Inlier. Australian Journal of Earth Sciences, 53, 187 – 211.

Connors, K., 1997, Regional Fault History of the Waggaboonya Area: Confiedential Company Report., Etheridge Henley Williams, p. 34.

Connors, K. A. & Lister G. S., 1995. Polyphase deformation in the western Mount Isa Inlier, Australia: episodic or continuous deformation? Journal of Structural Geology 17, 305–328.

Da Costa, R., 2005, Structural controls on Mt Kelly Copper Deposits, Northwest Queensland, Unpublished Hons thesis, University of New South Wales.

T. P. Davis, 2004, Mine-Scale Structural Controls on the Mount Isa Zn-Pb-Ag and Cu Orebodies Economic Geology; 99(3): 543 - 559.

Kendrick, M.A., Duncan, R., Phillips, D., 2006. Noble gas and halogen constraints on mineralizing fluids of metamorphic versus surficial origin: Mt Isa, Australia. Chemical Geology, 235, 325-351.

Maiden, K., Hewitt, D., & Stephens, M., 2000, Mt Kelly: A Mount Isa type deposit in the Western Mt Isa block, Queensland. Unpublished paper.

McClay, K.R., 1979. Folding in the silver-lead-zinc orebodies, Mount Isa, Australia: Transactions of the Institute of Mining and Metallurgy, v. 88, p. B4–B14.

McLellan, J.G., Oliver, N.H.S., 2008. Discrete element modelling applied to mineral prospectivity analysis in the eastern Mount Isa Inlier, Precambrian Res., v.163, 174-188.

McLellan, J.G., 2004. Numerical Modelling of Deformation and Fluid Flow in Hydrothermal Sytems. Unpublished PhD thesis, James Cook University.

Miller, J.McL., and Wilson, C.J.L., 2004. Application of structural analysis to faults associated with a heterogeneous stress history: the reconstruction of a dismembered gold deposit, Stawell, western Lachlan Fold Belt, Southeastern Australia. Journal of Structural Geology, 26, 1231-1256.

Miller J. McL. 2005. The structural evolution of the Wallaby Gold Deposit, Laverton, W.A., Y4 pmd*CRC project report, July 2004.

Perkins, W.G., 1984. Mount Isa silica-dolomite and copper orebodies: The result of a syntectonic hydro

Ramsay, J. and Lisle, R.J., 2000. The techniques of modern structural geology, vol. 3: applications of continuum mechanics in structural geology. Academic Press, New York.Rubenach et al

Stephens, M., 2001, A review of the potential of the Mount Kelly area north of Mt Isa, Queensland, Unpublished company report, Reefway Pty. Ltd.

Swager, C.P., Perkins, W.G., Knights, J.G., 1987. Stratabound phyllosilicate zones associated with syntectonic copper ore bodies at Mt Isa, Queensland. Australian Journal of Earth Sciences, 34, 463-476.

Yamaji, A., 2000. The multiple inverse method: a new technique to separate stresses from heterogeneous fault-slip data. Journal of Structural Geology, 22, 441-452.

Spectral and petrological study of the alteration around the Pb-Zn deposits, Mt. Isa

Rowena Duckworth, JCU

Executive Summary

The following are the main points derived from this study:

- Mineralisation paragenesis: calcite-(fine grained pyrite+dolomite+galena)-(sphalerite-pyrrhotite)-chalcopyrite-pyrite
- Sulphides appear to replace calcite cement in Urquhart shale
- Galena is intimately associated with secondary dolomite
- Sphalerite-pyrrhotite cross cuts the main foliation (post deformation)
- Alteration pre and post the Pb-Zn mineralisation was magnesium rich
- Phlogopite micas are pre-foliation (aligned)
- Mg-chlorite cross cuts the main foliation (cross cut)
- Mg-Chlorite cross cuts galena and sphalerite
- No framboidal textures have been observed in fine grained pyrite (using SEM)

Introduction

Aims

- To ascertain the usefulness of the PIMA in identifying the alteration minerals that are characteristic of the Pb-Zn mineralisation in the Mt. Isa area.
- To establish whether illite crystallinity is a viable tool in the Mt. Isa area.
- To identify possible fluid pathways in the Urquhart shale.

Methods

Four Xstrata drillholes were sampled for this study. In total, 224 samples were taken with samples taken at ca. metre intervals or from each lithologic/alteration type. The four holes are:

1. H754NWD1 (aka 920401) that intersects the #5 Pb-Zn orebody in the Urquhart Shale, Spear-Kennedy Siltstone, Paroo Fault anhydrite body and Eastern Creek Volcanics.
2. F968V1 (aka 750738) which intersects the Urquhart Shale and Spear-Kennedy Siltstone to the north of the mine and is weakly mineralised. This was logged extensively by Martin Neudert.
3. DF915ED1 (201120). This hole intersects Moondarra Siltstone, Warrina Park Quartzite and Surprise Creek formation through a remote area approx 15kms north of the Mt. Isa mine (Transmitter hole).
4. Additionally, T706ED1 through the oxidised and altered Urquhart Shale in the Black Star Pit was sampled fresh from the drill rig.

Samples were taken back to JCU and analysed using the PIMA and exactly the same spot was analysed on selected samples using the GADDS. To check the data of the PIMA and GADDS, selected samples were analysed using traditional powder XRD and whole rock XRF. Thin sections were made from selected samples and observed/analysed using petrological microscope and Electron Microprobe techniques.

PIMA/GADDS/XRD

The main problem with the PIMA in the Mt. Isa area is the abundance of dark grey rocks. Many of these dark samples are aspectral and using the GADDS on these samples shows that the mineralogies are not any different, just the proportion of the mineral groups. The GADDS and XRD identified quartz and feldspar in most of the samples; these are not spectrally identifiable with the PIMA.

PIMA and GADDS analyses were done on clean, dry rock faces, whereas for XRD approx. 0.5g of finely crushed rock powder was mixed with water and smeared on to a glass slides and inserted into a plastic cavity mount suitable for insertion into the Siemens D5000 X-ray diffractometer.

Analytical limits:

- Area size of ca.150 mm is analysed using PIMA; limited range of minerals it can pick up (SWIR 1300-2500nm wavelengths). The PIMA can identify minerals such as chlorite, mica, sulphates and carbonate but not mineral groups without OH molecules such as feldspar and quartz.

- Area approximately 0.5 mm analysed by GADDS; results depend on crystal orientation and particular spot analysed. Will only detect minerals if abundance greater than ca.3.5%.

- With XRD there is a limit of detection of 1-2% for most minerals, and overlap of diffracted reflections can occur rendering some ambiguity into the interpretations.

Petrology/Microprobe

A petrological and microprobe study was undertaken using selected samples to identify the alteration mineralogies, and also to characterise possible fluid pathways through the rocks. In order to confirm, and investigate further, the alteration chemistry identified by the PIM and XRD, analysis of mica chemistry was undertaken on the JEOL Superprobe JXA-8200 housed in the Advanced Analytical Centre (AAC) at JCU.

Results

PIMA/XRD

On return to JCU, all the samples were all run through the PIMA (Portable Infrared Mineral Analyser) and the spectral data were imported into The Spectral Geologist software package. However many dark samples are aspectral (and much of the Urquhart Shale is dark grey!); there are also some spurious identifications teflon, wood) by the inbuilt spectral identification software (The Spectral Assistant), but the main minerals that are identified are kaolinite, muscovite, chlorite, siderite, dolomite and calcite (see assemblage histograms for each core below).

Approximately 40 samples were then run through the GADDS in the Advanced Analytical Centre at JCU. Samples were chosen to verify the applicability of the technique and to either confirm PIMA results or to ascertain the bulk mineralogy if the PIMA result was aspectral. Resultant X-ray Diffraction peaks are manually identified (no automatic mineral identification is possible) and therefore some knowledge of what minerals may be in the rock or a background qualitative whole-rock chemistry is recommended. Quartz is the most common mineral (a mineral not able to be “seen” by the PIMA), accompanied commonly by muscovite, dolomite and feldspar. The table below simply shows the results of each technique on the same bit of core.

Table 1. Comparison table of PIMA vs. GADDS results on the same spot on the same sample.

PIMA (automatic ID)	GADDS (manual ID)
Aspectral	qtz, dolomite,muscovite, illite, feldspar, pyrite
Aspectral	dolomite, pyrite
Dolomite	dolomite
Dolomite	dolomite, feldspar
Aspectral	dolomite, qtz, chlorite
IntChlorite	qtz, chlorite
Aspectral	qtz, dolomite, feldspar
Aspectral	qtz, dolomite, feldspar
Aspectral	qtz, dolomite, feldspar (+py, ccp)
Ankerite	qtz, calcite
Aspectral	qtz, dolomite
Aspectral	qtz, dolomite
Diaspore	qtz, dolomite
Aspectral	qtz,dolomite
Aspectral	qtz, dolomite
NULL	qtz, dolomite, illite
Dolomite	feldspar, dolomite
Aspectral	qtz, dolomite, feldspar, muscovite
Phengite	qtz, dolomite, feldspar, phengite, alunite
Aspectral	qtz, dolomite, feldspar, muscovite, illite, alunite
Kaolinite	qtz, muscovite, dolomite, kaolinite
Kaolinite	qtz, kaolinite, alunite, siderite
Muscovite	qtz,, muscovite
Muscovite	qtz,, muscovite
Muscovite	qtz, muscovite
Muscovite	qtz, muscovite
Muscovite	qtz
Muscovite	qtz, muscovite
Aspectral	qtz, dolomite, feldspar, muscovite
Aspectral	qtz, dolomite, feldspar, muscovite
Aspectral	qtz, dolomite, feldspar, muscovite
Aspectral	qtz, dolomite, feldspar, muscovite
Aspectral	qtz, dolomite, feldspar, muscovite
Aspectral	qtz, dolomite, feldspar, muscovite
Talc	qtz, dolomite, albite

Illite crystallinity (IC)

The PIMA results showed no illite in any of the samples but possible illite was identified using GADDS. These spurious samples, along with several others, were then run through traditional powder whole rock XRD and professionally interpreted by Dr Sharon Ness at the AAC, JCU. These results agree with PIMA results, the white mica is muscovite not illite. Therefore, no XRD illite crystallinity studies are possible around the Mt. Isa Pb-Zn deposits as the metamorphic grade at Mt. Isa is just too high to utilise IC as a geothermometer.

Alteration chemistry

Using The Spectral Geologist (TGS) software it is possible to identify the main minerals down core and plot overall assemblage diagrams. These overall assemblages are illustrated in Figures 1 and 2.

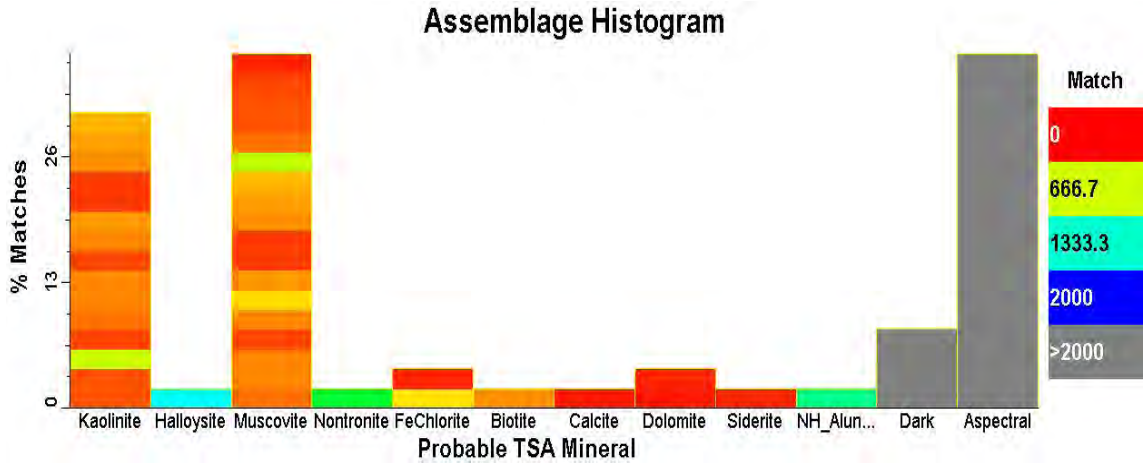

Fig. 1 PIMA assemblage histogram for Black Star core through Urquhart Shale which is higly oxidised at the top (hence high proportion of kaolinite and muscovite) and grey at the bottom of the core giving an aspectral signature.

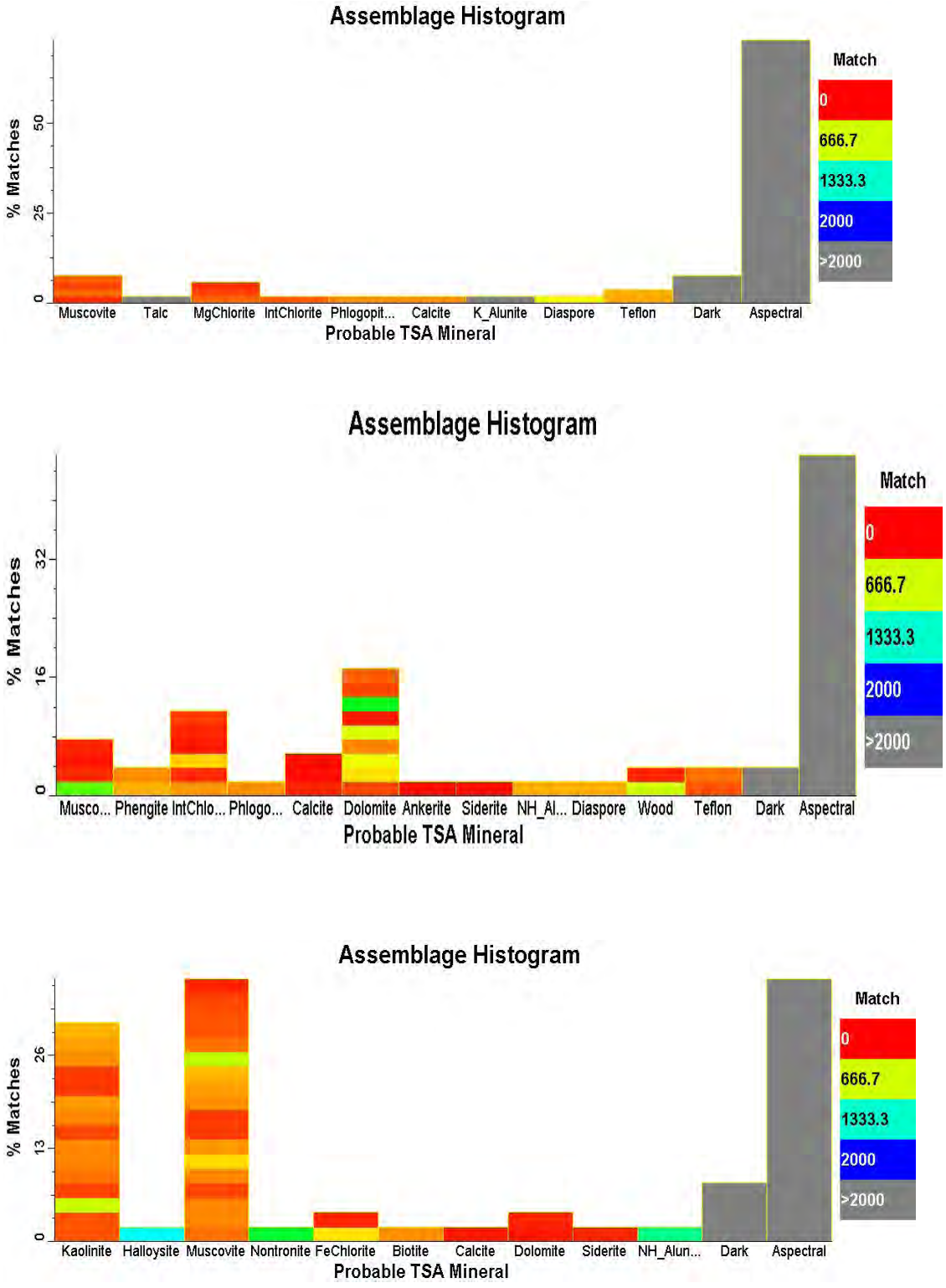

Figure 2. PIMA mineral assemblages of cores F9687 (top) and H754 (middle) through the mineralised sequence and core DF915 (bottom), drilled ca. 15km away from the mineralisation and through a lower stratigraphic sequence.

Two cores in this study recovered oxidised surface rocks (Black Star and DF915): but only one of these cores was mineralised (Black Star). A comparison of the oxidation mineralogy of these two cores was undertaken in order to determine there was a surface expression of mineralogy which reflects the underlying mineralisation (see Table 2).

CORE	STRATIGRAPHIC UNIT & OVERALL MINERALOGY (PIMA and XRD)
D5915	**Moondara siltstone**
	Feldspar (orthoclase), siderite,
	quartz, kaolinite
Black Star T706ED1	**Urquhart Shale**
	Kaolinite, quartz, hematite
	+/- hydrated lead sulphate/
	phosphate phases

Table 2. Mineralogy of cores DF915 and T706ED1 in the upper oxidized sequence

Table 2 demonstrates that the weathered rocks over the unmineralised sequence contain feldspar and siderite, whereas the mineralised weathered sequence does not. However, it must be noted that this study compares weathered Moondara Siltsone to weathered Urquhart Shale, therefore the mineralogical differences may not be due to weathering/oxidation of altered vs. unaltered rock but to differences in primary mineralogy.

Petrology

Preliminary petrological examination suggests that the sulphide paragenesis is:
pyrite, calcite, (galena, dolomite), sphalerite+pyrhotite, chalcopyrite, pyrite.

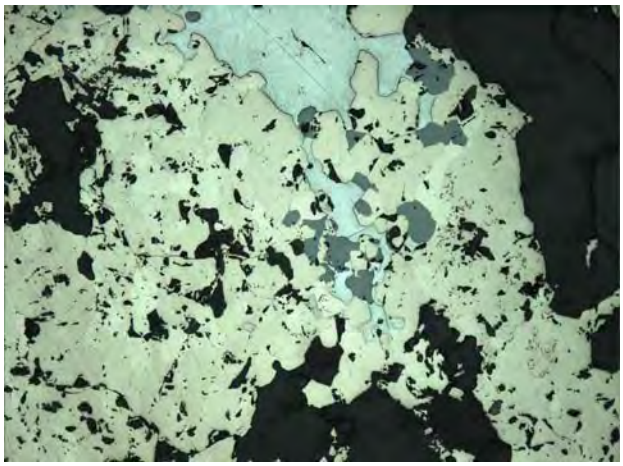

Figure 3: Reflected light photomicrograph showing relationship between yellow chalcopyrite, bluish white galena (careous boundaries) and pinky pyrrhotite. Dark grey minerals are carbonate. FOV=2.3mm

Petrologically, it appears as though the fluids preferentially followed zones of carbonate cement in the Urquhart shales and this fluid flow allowed partial to complete replacement of many of the sedimentary layers and structures. Some dissolution features were also seen in the calcite on the microprobe (Figure 3)

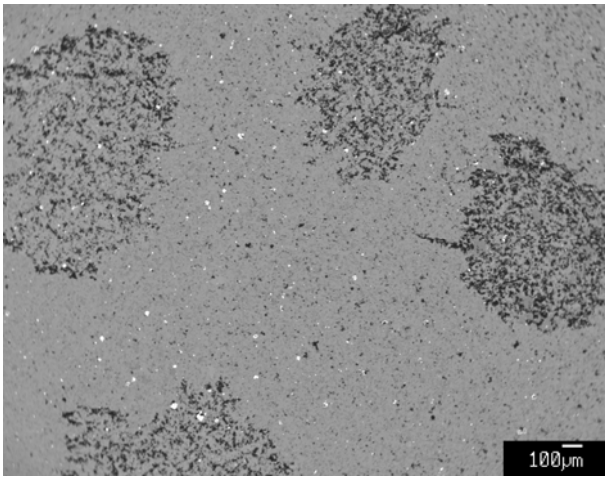

Figure 4. BSE image showing dissolution capillary features in calcite cement, Urquhart shale

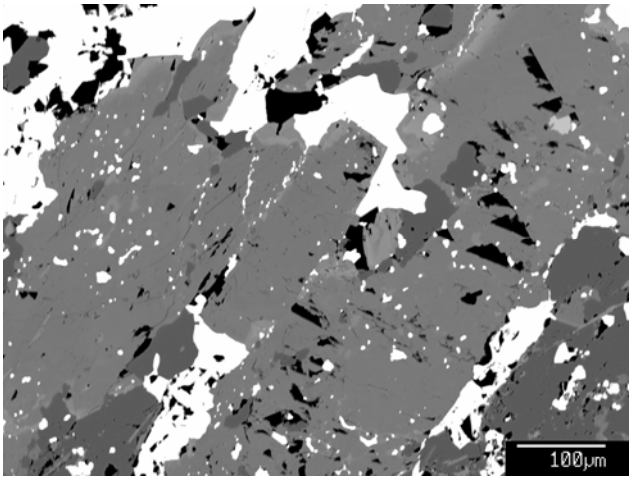

Figure 5: BSE EPMA image showing relationship between bright galena and mid grey laths of dolomite which have triangular etch pits (replacement of galena?) and numerous galena inclusions. Galena infills around dolomite.

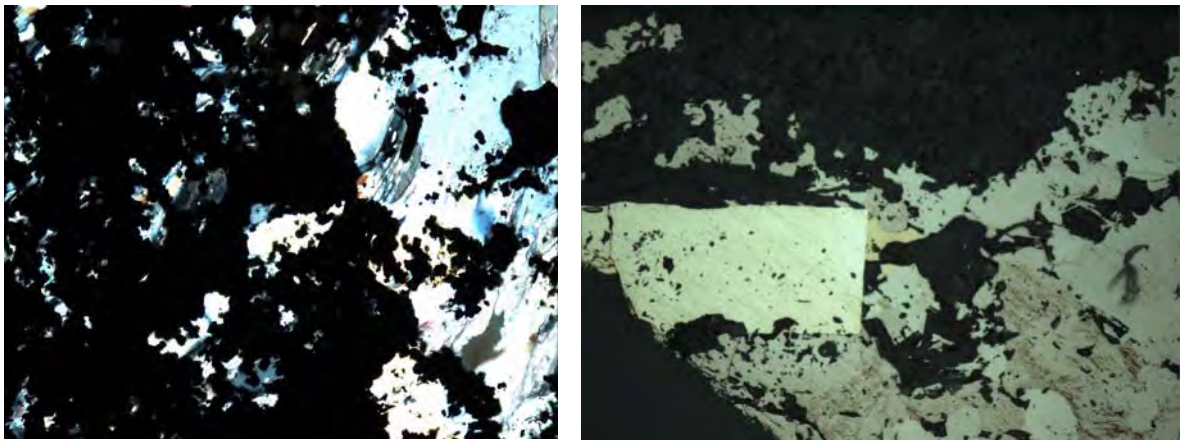

Figure 6: Left: Transmitted light (crossed polars) photomicrograph showing pervasive replacement of carbonate by opaque sphalerite. (FOV= 2.3mm). Right: Reflected light

photomicrograph showing late subhedral pyrite overprinting earlier pinky pyrrhotite and yellow chalcopyrite. (FOV 4.6mm)

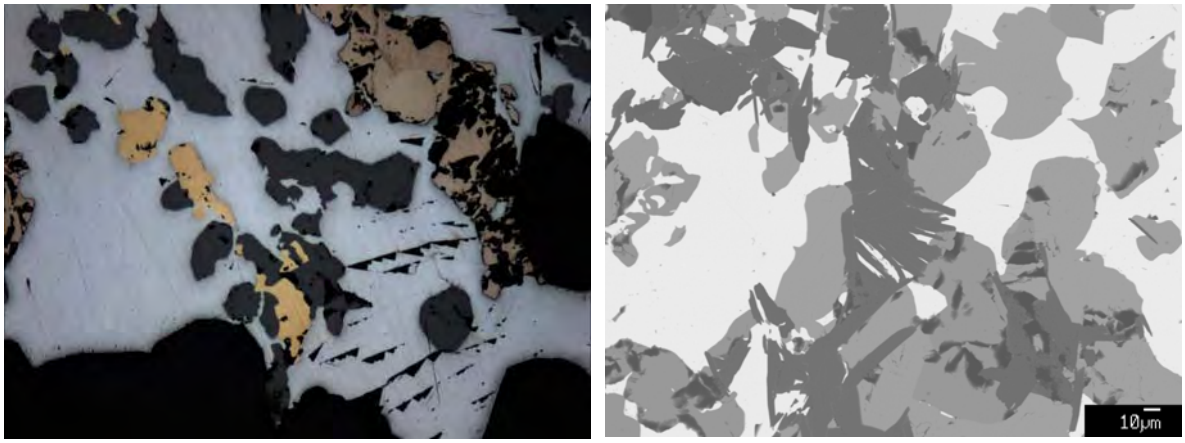

Figure 7: Left: Reflected light photomicrograph showing chalcopyrite (yellow) overprinting earlier galena (white) and carbonate (dark grey)(FOV 4.6mm). Right: BSE EMPA image showing fringe of dark grey chlorite crystals in centre overprinting white galena and mid grey sphalerite

There are two generations of pyrite: a fine grained pyrite and a later coarser grained metamorphic porphyroblastic pyrite. Detailed SEM (Scanning Electron Microprobe) analysis of rock chips from the Urquhart shale has demonstrated that the fine grained pyrite is NOT framboidal, but is related to the porosity of the sediments. However, it is not clear whether the pyrite is primary and it's removal creates a secondary porosity or if the pyrite is later and is infilling a primary porosity.

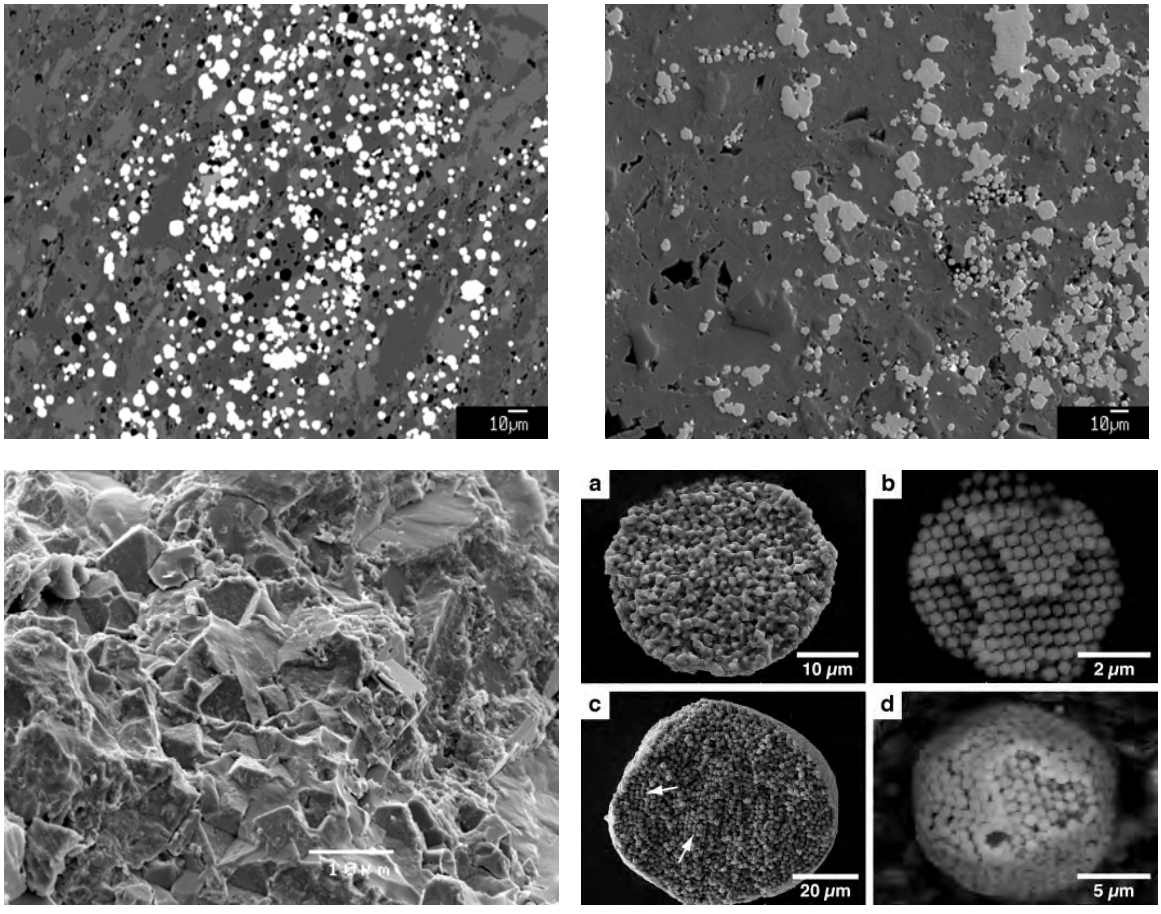

Figure 8: Top two images taken in BS and SE show fine grained pyrite and black holes in the shale.. Bottom left image is detailed SEM image showing random fabric of this fine grained pyrite and show fine grained pyrite from Urquhart Shale. Bottom right photo (from Ohfuji & Rickard 2005) shows typical texture of framboidal pyrite NOT seen in samples in this study.

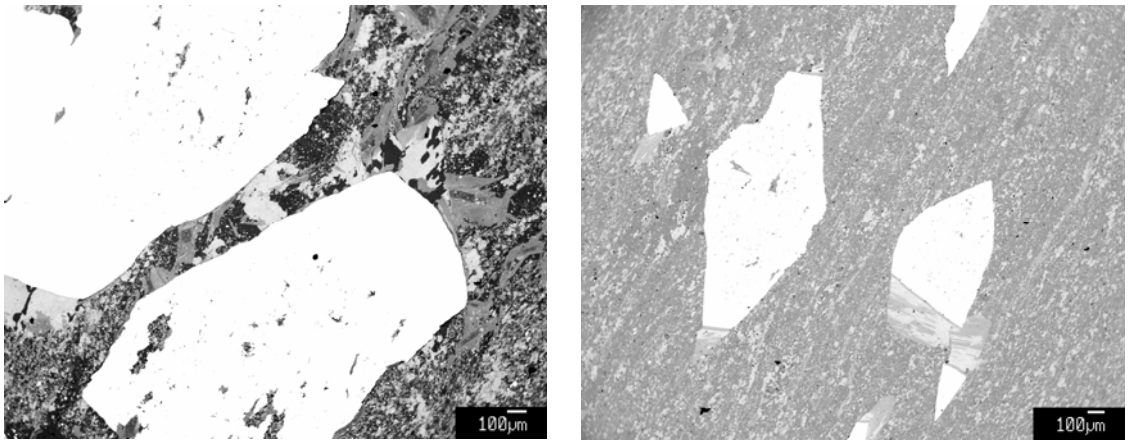

Figure 9: BSE images showing late metamorphic pyrite (white) replacing and overprinting earlier fabric. The development of pressure shadows is illustrated in the right hand image.

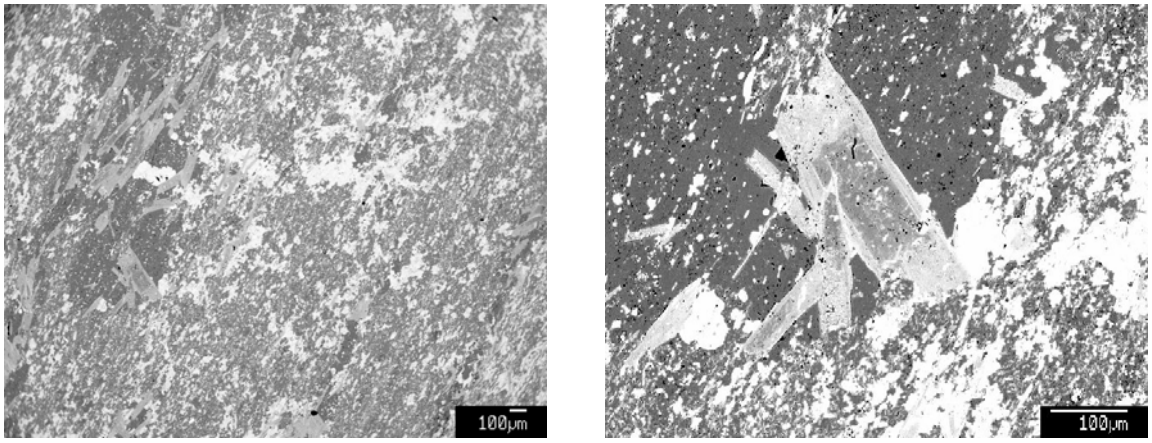

Figure 10: EMPA BSE images showing chlorite cross cutting main foliation and right, chemical zonations in chlorite due to Fe-Mg changes (brighter zones are more Fe enriched)

Microprobe WDS analyses of the micas which define the main foliation in the Urquhart Shale and the chlorites, which are later and cross cut the foliation, show that both alteration minerals are magnesium rich and there is no sodium alteration associated with the Pb-Zn mineralisation (Appendix 1).

Anhydrite Unit

Core H754 intercepted a body of anhydrite-barite-dolomite associated with the Paroo Fault (Fig. 11). The chalcopyrite in this interval appears to be paragenetically later than the sulphates and carbonates (Fig.12, but this rock unit requires further study.

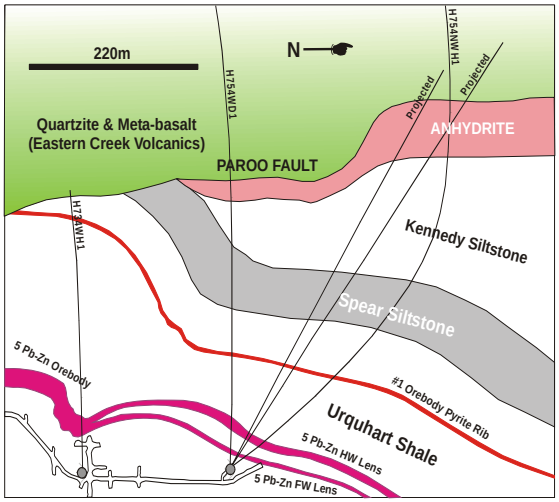

Figure 11. Plan of Drill hole H754 which intercepts the anhydrite body.

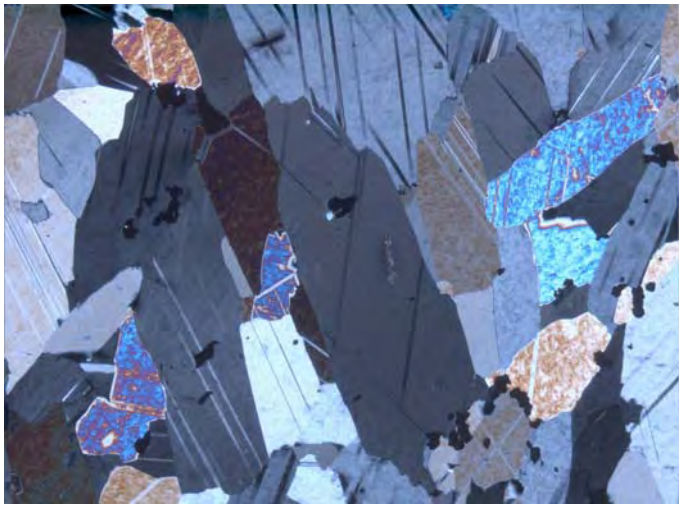

Figure 12. Transmitted light (crossed polars) view of anhydrite-barite-dolomite unit with late chalcopyrite (black). FOV=2.3mm

Alteration of the Spear Kennedy Siltstone

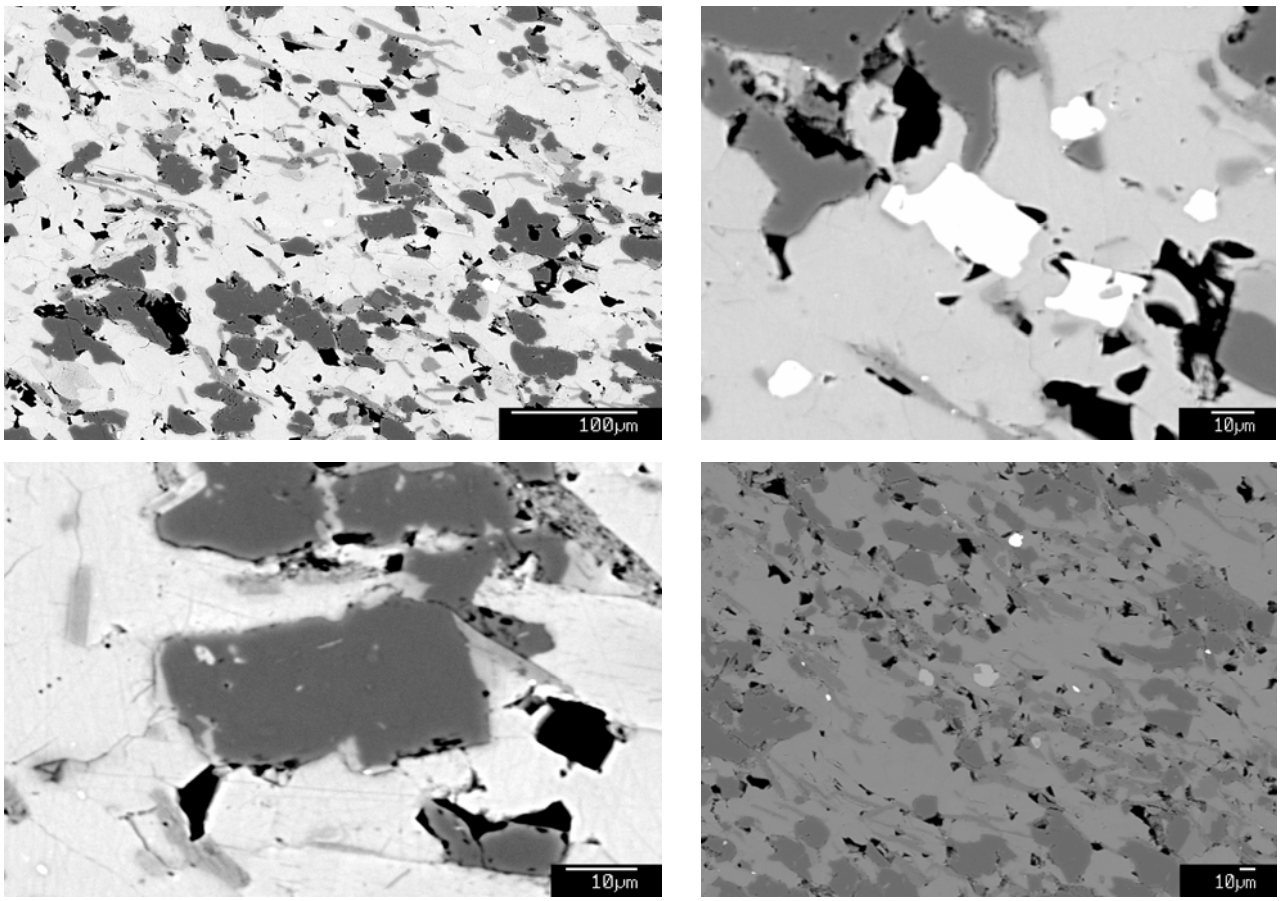

Figure 13. Alteration of the Spear Kennedy Siltstone.

Microprobe analysis of the Spear-Kennedy Siltstone in cores F968 and H754 has shown that although there is a small amount of albite (dark grey top left BSE image) most of this dark grey is actually quartz, with abundant calcite, Mg-Fe chlorite (pale grey), phlogopite (mid-grey), bright white apatite (top right image) and lenses of streaked out pyrrhotite (Figure 12 below).

Figure 12. Core trays of Spear Kennedy siltstone illustrating streaked out lenses of pyrrhotite

DISCUSSION

1. The PIMA spectra suggest that the alteration is strongly Mg-rich with minerals identified as phengite, dolomite, intermediate chlorite, ankerite, talc and calcium and potassium sulphates. The rocks away from the Pb-Zn mineralisation are more Fe-rich with minerals identified such as biotite, siderite and Fe chlorite. Weathering of the shales overlying mineralised and unmineralised areas produces kaolinite, dickite and muscovite, with less feldspar breakdown above the unmineralised areas. The magnesium alteration is confirmed by WDS analysis on the electron microprobe and the magnesium rich minerals are paragenetically constrained as both pre and post the Pb-Zn mineralisation suggesting repeated and/or long lived hydrothermal events

2. PIMA identifies the main OH bearing mineral groups very quickly and conveniently and requires no sample preparation apart from a dry piece of rock or powder. However, it is cumbersome in the field, requires batteries or electricity and a laptop to download the spectra to. Sampling and analysing later is easier, but not always that convenient. Hylogger in tandem with TSG Core is an excellent technique for the spectral analysis of drill core with good resolution and is recommended as a routine core logging tool.

3. GADDS a useful tool for bulk mineralogy of a particular spot, but requires previous knowledge to interpret the spectra. Also, as a point of information, JCU has now sold the GADDS. XRD is reliable and informative but requires sample preparations and bulk chemistry of the sample to interpret the spectra.

4. Petrological study is always good and can paragenetically constrain the alteration events. Coupled with microprobe imaging and analysis this is the best method for determining alteration and fluid pathways, but needs polished thin section to be prepared. It is not an immediate exploration tool but gives the best results.

Appendix 1 WDS Microprobe results on micas and chlorites.

No.	Al2O3	FeO	Cl	Na2O	CaO	SiO2	MnO	MgO	K2O	TiO2	Total	Comment
21	19.0700	14.5500	0.0054	0.0000	0.0458	29.6600	0.0000	24.5200	0.0197	0.0000	87.8709	XX-drk photo1
22	20.2100	15.7800	0.0089	0.0000	0.0278	28.8200	0.0139	23.2000	0.0320	0.0216	88.1142	XX-mid photo1
24	15.0700	18.7200	0.0096	0.0050	0.1094	31.4500	0.0434	23.0300	0.0391	0.0000	88.4766	XX-light2 photo1
25	21.5300	9.5400	0.0072	0.0648	0.0326	29.5900	0.0175	27.0600	0.0651	0.0292	87.9365	xx.centre micphot2 dark
26	19.9000	9.9900	0.0074	0.0903	0.0506	30.6600	0.0228	27.2500	0.1482	0.0000	88.1194	xx.centre micphot2 dark2
27	19.5800	15.0200	0.0057	0.0582	0.0764	29.8200	0.0122	23.8900	0.0447	0.0144	88.5217	xx.edgemicphot2 light2
28	20.3500	16.0600	0.0224	0.1012	0.0482	29.4800	0.0208	22.8100	0.1133	0.0036	89.0095	xx.endmicphot2 light2.1
29	20.3500	15.2400	0.0224	0.0798	0.1046	29.8400	0.0539	23.4500	0.1323	0.0359	89.3090	xx.endmicphot2 light3
30	21.1600	9.6500	0.0087	0.0276	0.0528	30.0700	0.0000	27.0100	0.0159	0.0546	88.0497	xx.darkxtal2
31	20.1600	10.6000	0.0088	0.0202	0.0358	30.2200	0.0280	27.0800	0.0295	0.0872	88.2696	xx.darkxtal3
32	18.8800	16.8800	0.0094	0.0388	0.0391	29.3300	0.0312	22.5100	0.0616	0.0608	87.8410	xx.xtal3 light
33	20.2700	15.5300	0.0044	0.0056	0.0208	29.0700	0.0452	23.1000	0.0940	0.0252	88.1653	xx.xtal3-4 light
34	21.0100	9.8500	0.0000	0.0061	0.0000	29.6300	0.0211	27.0700	0.0223	0.0073	87.6169	xx.xtal4 dark
35	20.6500	9.7000	0.0081	0.0148	0.0116	29.9900	0.0368	27.3600	0.0017	0.0219	87.7950	xx.xtal4 dark2
36	13.2500	10.9500	0.0214	0.0716	0.1328	41.7100	0.0122	18.6000	9.5300	0.4547	94.7327	xxphoto3?mica
37	14.5100	11.3400	0.0227	0.0506	0.0630	41.2800	0.0245	17.7300	9.3700	0.6552	95.0461	xxrim mica
38	15.2500	11.3100	0.0129	0.0481	0.0789	42.0300	0.0193	17.3200	9.7600	0.6995	96.5288	xxcore mica
40	16.5500	14.2600	0.0150	0.0000	0.1090	39.2100	0.0541	19.3800	0.0062	0.0000	89.5844	photo 5 mica ?
41	19.5900	16.1100	0.0107	0.0166	0.0379	29.0900	0.0660	22.5800	0.0072	0.0036	87.5121	photo7 chlorite?1277
42	29.8300	3.1400	0.0108	0.1498	0.0106	47.2900	0.0000	2.8500	10.7000	0.2794	94.2607	photo9 silicates
43	0.8111	0.7209	0.0104	0.0164	0.0123	97.7500	0.0000	0.9669	0.0050	0.0413	100.3342	photo9 slightly darker matrix crap
44	19.8000	18.9400	0.0039	0.0279	0.0065	27.8500	0.0380	20.0100	0.0496	0.0214	86.7474	h754rd7 mica?
45	30.9300	1.5700	0.0062	0.0838	0.0221	52.4900	0.0000	1.6013	7.8500	0.3824	94.9359	df915rd7mica
46	31.4500	2.2100	0.0479	0.3998	0.0000	46.8900	0.0325	0.6124	4.2200	0.4099	86.2725	df915rd7 mica2
47	35.3400	1.9300	0.0000	0.2549	0.0016	50.2700	0.0273	0.7229	6.6200	0.0108	95.1776	df915rd7 mica2
48	34.7900	2.8500	0.0000	0.4421	0.0187	49.8600	0.0000	0.7210	5.9400	0.6180	95.2399	df9157mica3 photo13

49	35.5300	2.1300	0.0000	1.2330	0.0147	49.8300	0.0000	0.5316	5.9400	0.1404	95.3498	df9157mica4 photo13
50	31.9200	3.6000	0.0000	0.2262	0.0297	50.5500	0.0120	1.9100	5.9200	0.3596	94.5275	df9155.3 mica1
51	29.8300	1.8200	0.0053	0.0669	0.0171	53.2700	0.0292	2.5200	5.1700	0.2998	93.0283	df9155.3 mica2
52	36.3800	1.3100	0.0024	0.9470	0.0004	50.5600	0.0086	0.7170	6.3900	0.1445	96.4600	df9155.3 mica3
53	34.3200	0.8631	0.0007	0.2079	0.0000	50.9800	0.0034	2.0000	5.8700	0.8858	95.1310	df9155.3 mica4
54	36.1100	1.6300	0.0036	0.5461	0.0245	50.1600	0.0205	0.4231	7.0300	0.1662	96.1141	df9155.3 mica5
55	17.0200	3.8100	0.0000	0.3388	0.0172	18.8400	0.0373	0.6077	7.6600	0.2112	48.5423	df9155.3 mica1
56	33.4000	3.3000	0.0000	0.3374	0.0347	47.3100	0.0034	0.7144	7.9300	0.3460	93.3760	df9155.3 mic2
57	33.8100	2.8400	0.0003	0.8028	0.0302	47.5500	0.0000	0.6677	7.5500	0.3748	93.6259	df9155.3 mic3
59	13.6500	10.2500	0.0010	0.0416	0.2289	40.8300	0.0271	19.5000	9.6500	0.6832	94.8619	f968rd79mica/clorite2
60	13.5900	9.0900	0.0000	0.0301	1.8900	39.5500	0.0493	18.9000	8.1400	0.6100	91.8495	f968rd79mica/chlorite3
61	19.7300	13.1700	0.0000	0.0069	0.2021	29.4100	0.0862	24.5500	0.0878	0.0174	87.2605	f968rd79mica/chlorite??4
62	33.0600	1.9100	0.0000	0.1843	0.1003	48.6900	0.0154	1.5765	7.5600	0.6436	93.7402	f968rd79mica/chlorite5
63	35.0600	1.1403	0.0011	0.2424	0.0578	49.0800	0.0068	0.7246	7.7200	0.4128	94.4459	f968rd79mica/chlorite6
64	15.4200	0.0536	0.0013	0.1112	6.1800	56.8200	0.0638	0.0491	12.8900	0.0000	91.5891	f96875 mica1
65	17.2500	0.0386	0.0026	0.0968	0.0000	68.4400	0.0172	0.0051	13.9300	0.0695	99.8499	f96875 mica2
66	17.4600	0.0542	0.0048	0.0935	0.0000	68.3400	0.0035	0.0000	14.2800	0.0220	100.2579	f96875 feldspar
67	33.3400	1.2900	0.0000	0.1886	0.1540	48.4300	0.0344	2.1500	8.0900	0.1851	93.8622	f96848mica1
68	30.8600	0.8196	0.0000	0.0618	0.1870	53.0000	0.0275	3.5000	6.3400	0.2978	95.0938	f968rd48mica2
69	32.7800	1.7600	0.0000	0.1958	0.2710	50.4000	0.0618	1.1352	8.3000	0.0000	94.9039	f968rd48mica3
70	29.5900	1.0123	0.0000	0.1100	0.1825	51.2700	0.0121	3.3100	7.4500	0.3744	93.3113	f968rd48mica4
71	17.8000	0.0821	0.0000	0.1573	0.1614	66.1200	0.0500	0.0000	14.2800	0.0000	98.6509	f968rd48sil1

Minimum	0.0196	0.0349	0.0000	0.0000	0.0000	0.0592	0.0000	0.0000	0.0017	0.0000	14.1253
Maximum	36.3800	18.9400	0.0479	1.2330	54.9700	97.7500	0.1918	32.2900	14.2800	0.8858	100.3343
Average	22.1288	6.2294	0.0055	0.1632	1.1479	40.5855	0.0325	11.9310	4.6095	0.1813	87.0145
Sigma	9.0758	6.0813	0.0085	0.2422	7.2397	15.4589	0.0388	12.0619	4.5266	0.2341	15.4142

Combining fractal analysis of mineral deposit clustering with weights of evidence to evaluate patterns of mineralization: Application to copper deposits of the Mount Isa Inlier

A. Ford and T. G. Blenkinsop

Economic Geology Research Unit

Predictive Mineral Discovery CRC

James Cook University

Townsville QLD 4811

Australia

Abstract

Mineral occurrences are typically clustered, and the degree of clustering can be sensitively measured by fractal methods. Clustering may vary significantly within a study area, with obvious exploration implications, and can be measured by a shifting box counting method. Spatial associations between mineral occurrences and geological features such as rock types or structures are most important for exploration, and can also be interpreted in genetic terms. Such spatial associations are quantified in the weights of evidence method by the contrast value, which compares observed spatial distributions to those produced by chance: increasing contrasts indicate increasingly strong spatial associations. A new method is proposed to evaluate mineral occurrence distribution by

combining the power of the fractal description of clustering with weights of evidence approach. Four possible outcomes are: high correlation in clustering/high contrast, high correlation/low contrast, low correlation/high contrast, and low correlation/low contrast. Each of these outcomes has specific exploration implications. This approach is applied to the Proterozoic Mt Isa Inlier in northern Australia, which hosts large numbers of copper deposits, including the world class Mt Isa Cu deposit. Spatial variation in fractal dimension suggests different geological controls on copper occurrence clustering in the east and west of the Mt Isa Inlier . In the Eastern Succession, the clustering of copper occurrences has a high correlation with the clustering of mafic intrusives. In the Western Succession, the clustering of fault bends and fault intersections is highly correlated with the clustering of copper occurrences. Weights of evidence analysis indicates that copper occurrences are localized by fault bends in the Eastern Succession and by fault intersections in the Western Succession. Combining the correlations from the fractal analysis with the contrast values from the weights of evidence analysis shows that fault bends, fault intersections and most mafic rocks have high correlation and high contrast values in both the Eastern and Western Successions, with mafic intrusives in the Eastern Succession falling only just outside this category with a slightly lower contrast value. The correlation between the degree of clustering of a geological feature and the copper occurrences forms a linear relationship with the contrast value, suggesting that the geological features controlling the clustering of the copper occurrences are the same features which control their localization.

Keywords: copper, exploration, fractal dimension, Mount Isa inlier, clustering, weights of evidence

1. Introduction

Perhaps the most obvious feature of any map of mineral deposits is that they exhibit some degree of clustering. Following Mandelbrot's (1983) suggestion that minerals in the Earth's crust have a fractal distribution, Carlson (1991) showed that the clustering of mineral deposits can be sensitively measured by fractal methods, and also proposed genetic interpretations for the fractal dimensions obtained from these analyses. Evidence for a fractal distribution of mineral deposits has been adduced for gold and precious metals (Carlson, 1991; Agterberg et al., 1996; Blenkinsop and Sanderson, 1999; Kreuzer et al., 2006) and preliminary results suggest that base metal distributions may also be fractal (Blenkinsop and Oliver, 2003; Butera, 2004).

Fractal analyses of clustering of mineral deposits has generally attributed a single, global fractal dimension to the data sets studied. This approach can not give a spatial context to the clustering of mineral occurrences within the study area. Blenkinsop and Sanderson (1999) examined fractal dimensions for various subsets of data from gold deposits of the Zimbabwe craton, and suggested that spatial variation in fractal dimension might have exploration implications. This approach is developed further here.

By contrast to fractal analysis of clustering of mineral deposits, the weights of evidence approach emphasises spatial context by focusing on factors that localize mineral deposits, and this method has been widely applied to exploration (eg. Bonham-Carter et al., 1989; Agterberg and Bonham-Carter, 1990; Agterberg et al., 1993; Bonham-Carter, 1994; Carranza et al., 1999; Raines, 1999; Harris et al., 2000; Boleneus et al., 2002; Billa et al., 2004). Although alternative methods such as neural networks and fuzzy logic have been introduced (eg. Cheng and Agterberg, 1999; Singer and Kouda, 1999; Brown et al., 2000; Knox-Robinson, 2000; Brown et al., 2003), and the relative merits of these different methods have been discussed (eg. Agterberg and Bonham-Carter, 2005), the weights of evidence method remains popular, especially among practitioners who favor a data-driven approach to prospectivity.

The primary aim of this paper is to propose a new method of analyzing mineral deposit distributions that combines the power of the fractal geometry to describe the clustering of mineral deposits, with the weights of evidence approach that describes their spatial associations. The method is applied to copper mineralization in the Mt Isa Inlier; ancillary aims of the study are to establish that copper deposit distribution can be described by fractals, and to examine the spatial variation in degree of clustering of copper occurrences. Preliminary results suggest some features that affect the clustering and distribution of the copper occurrences. This approach answers a critical question for understanding the genesis of mineral deposits, and for exploration: are the features that control the degree of clustering of minerals the same features that localize them?

The Mount Isa Inlier in northwest Queensland, Australia is an ideal location for this exercise. Containing a wide range of base and precious metal deposits coupled with a long exploration history, the region provides data which are ideal for analyzing the spatial distribution of mineral occurrences. Copper is particularly suitable because of the large number of mineral occurrences.

2. Geology and Mineralization in the Mt Isa Inlier

The Mt Isa Inlier of northern Australia is a world-renowned Proterozoic base metal province with an area in excess of 50 000 km², containing a variety of base and precious metal deposit types including Cu, Au, Cu-Au (including Iron Oxide Copper Gold (IOCG)), U-REE and Pb-Zn-Ag. Some exceptional examples of these deposits listed in the Northwest Queensland Mineral Province Report (NQMPR) include the Mount Isa copper deposit with resources before mining of 225 Mt ore at a grade of 3.3% Cu, the Ernest Henry Cu-Au deposit at 127 Mt with 1.1%Cu and 0.55g/t Au, the Mary Kathleen U-REE deposit containing 9.5 Mt of ore at 0.131% U_3O_8 and the Cannington Pb-Zn-Ag deposit containing 43.8 Mt of ore at 11.6% Pb, 4.4% Zn and 538g/t Ag (Queensland Department of Mines and Energy et al., 2000). This study focuses on the spatial distribution of copper deposits (excluding those also containing gold and IOCG deposits).

The Mt Isa Inlier is divided into three tectonic units (Fig. 1): the Kalkadoon-Leichhardt Belt lying between the Western Fold Belt and the Eastern Fold Belt (Blake et al., 1990).

Because some differences have been suggested between the characteristics of mineral deposits in the East and West of the Inlier, mineral occurrences are sub-divided into two groups in this study those hosted by the Eastern Succession, including the Eastern Fold Belt, and those hosted by the Western Succession, including the Kalkadoon-Leichhardt Belt and the Western Fold Belt. Though the split between the Eastern and Western Successions is essentially lithostratigraphic (Blake and Stewart, 1992), the boundary is positioned at the western margin of the Eastern Fold Belt, which has been interpreted as a possible terrain boundary (McDonald et al., 1997).

The Mt Isa Inlier experienced two major orogenic events, the Barramundi Orogeny *c.* 1870 Ma, and the Isan Orogeny *c.* 1600-1500 Ma (eg. O'Dea et al., 1997). Relicts of the Barramundi Orogeny outcrop in the older basement sequences of the Kalkadoon-Leichhardt Belt. Deposition of sedimentary cover sequences 1, 2, and 3 postdate the older event and predate the younger Isan Orogeny (Blake et al., 1990). The D_2 E-W shortening event (*c.* 1590 Ma) was responsible for formation or reactivation of the dominant N-S trending structures in the Inlier (Bell et al., 1988; Laing, 1998). Kilometre-scale upright folds with generally northerly trending axial surfaces are prominent throughout the inlier. Major deformation zones and geophysical lineaments also occur in this orientation, and in NE and NW trends. Several of these may have originated as basin-bounding faults during deposition of the cover sequences, and they may have been reactivated as reverse faults during the Isan Orogeny (Queensland Department of Mines and Energy et al., 2000). The fault architecture of the Eastern Succession is dominated by N to NW trending faults, which are generally straighter than

those in the Western Succession. Faults in the Western Succession are less dense and are predominantly larger N to NE striking structures.

The three major cover sequences show significant variations in the stratigraphy of the host rocks to the copper deposits. In the Western Succession, the Lawn Hill platform, which hosts the Lady Annie Cu deposit, consists predominantly of the sideritic and locally carbonaceous shales, mudstones and sandstones of the McNamara Group in cover sequence 3 (Feltrin et al., 2003). In the Leichardt River fault trough (Fig. 1) the stratigraphy of the Western Succession is more complex. The Urquhart Shale (carbonaceous, pyritic, dolomitic siltstone) of cover sequence 3 is host to the Mount Isa Cu deposit, and lies immediately above the Eastern Creek Volcanics (metabasalts) of cover sequence 2 (Wyborn, 1987; Williams, 1998). However, the Mammoth Cu deposit is hosted by the Myally Subgroup (quartzite, sandstone, and siltstone) of cover sequence 2 (Scott and Taylor, 1982). Felsic volcanics of cover sequence 1 and the intrusion of the Kalkadoon and Ewen Batholiths dominate the stratigraphy in the Kalkadoon-Leichhardt Belt, and are poorly mineralized (Blake and Stewart, 1992). The Corella Formation in the western part of the Eastern Succession hosts the Trekelano deposit (Williams, 1998). The Williams-Naraku batholiths, the Corella and Doherty Formations (calcsilicate rocks) and the Soldiers Cap Group (siliciclastic metasediments and metabasalts) are the predominant units in the Eastern part of the Eastern Fold Belt. The latter is host to many small Cu deposits such as Young Australia (Blake et al., 1990). Thus copper deposits are hosted within both cover sequence 2 and 3 rocks.

Both stratigraphy and structure have been suggested as controls on copper mineralization in the Mount Isa Inlier (eg. Bell et al., 1988; Laing, 1998; Williams, 1998). Copper mineralization styles vary significantly between the Western and Eastern Succession. In the Western Succession copper deposits lie in brecciated sediments adjacent to faults. Mineralization is localized on the N and NNE trending structures such as the Mount Isa and the Mount Gordon fault zones, which both contain appreciable amounts of copper in addition to the major Mt Isa deposit (Scott and Taylor, 1982; Nijman et al., 1992). In the Eastern Succession vein and breccia style copper deposits occur in shear zones and faults (Laing, 1998; Marshall, 2003). Many copper deposits *sensu lato* in the Eastern Succession are related to faults, with the larger deposits such as Eloise, Osborne and Kuridala (predominantly Cu±Au) hosted by N to NW trending regional structures such as the Mt Dore fault zone (Blake et al., 1990; Laing, 1998).

Copper mineralization may have occurred late in the Isan orogeny with timing suggested as syn-D_3 in both the Eastern and Western Successions (Williams, 1998; Queensland Department of Mines and Energy et al., 2000). Structures produced or reactivated in the Isan orogeny thus have potential to be mineralized by epigenetic processes. There is also potential for orebodies to be remobilized due to later fault reactivation throughout the Mount Isa inlier. Reactivation is known to have occurred as recently as the Cambrian and Ordovician (Feltrin et al., 2003; Mark et al., 2004).

In the Western Succession, the source of the copper for the world class Mount Isa copper deposit and the significant Mammoth and Esperanza deposits in the Gunpowder area has

been largely attributed to the Eastern Creek Volcanics (Scott and Taylor, 1982; Wyborn, 1987; Connors, 1992; Matthäi et al., 2004). Though the source of the copper for base metal deposits in the Eastern Succession is a contentious issue, recent work on IOCG deposits suggests that the mafic rocks of the Soldiers Cap Group rather than the Williams and Naraku batholiths (cf. Oliver et al., 2004; Mark et al., 2006) may be implicated (Butera and Blenkinsop, 2004). This may also be true for the copper-only deposits studied here.

It has been suggested that regionally extensive brines in the Mount Isa Inlier leached sulfur and possibly copper from mafic dykes just prior to ore deposition in close proximity to major extensional basement structures or D3 faults (Butera, 2004). Mafic rocks can also potentially provide a rheological contrast necessary for entrapment of mineralizing fluids. Fault bends (eg. Allibone et al., 2002a; Allibone et al., 2002b) and fault intersections (eg. Craw, 2000; Twomey and McGibbon, 2001; Allibone et al., 2002a; Allibone et al., 2002b; Nie et al., 2002) may focus fluids in order to form the ore deposits. Mafic rocks and NW, N and NNE trending faults or shear zones and their bends and intersections are therefore potentially critical factors in Cu mineralization in the Inlier (cf. Phillips et al., 1996; Twomey and McGibbon, 2001; Butera, 2004; Mustard et al., 2004).

3. Data and Methods

3.1 Copper occurrences and geological data

The spatial distribution of 1869 copper occurrences is examined on the basis of the Queensland Mineral Resources Database (MINOCC, 2002). The database categorizes the occurrences by various features including: commodity, mineralogy, host rock, age, size, tonnage and grade. All entries containing copper as the main commodity were extracted from the database for use in this study, excluding those which also contained gold. This discrimination was made because the deposits containing gold have potentially different controls. Comprehensive details of the occurrences throughout the Mt Isa Inlier are contained in the database, which was one reason for choosing this study area. Locations of the copper occurrences used in the analysis are shown in Fig. 2.

The NQMPR (Queensland Department of Mines and Energy et al., 2000) contains a Proterozoic fault database divided into fault segments. These segments were initially combined to provide a comprehensive fault database suitable for analysis. Fault bends and fault intersections were investigated as potential controls on copper mineralization. All fault intersections and fault bends (bends were defined as changes in strike between 5º and 45º) were extracted to point data using the MapInfo – Spatial Data Modeller software. Fault bends were located as the mid-point along a given bend within the database in both clockwise and anti-clockwise directions. Equally spaced nodes were extracted from the outlines of the mafic rocks in the study area using Encom's Discover software. The spatial distribution of the mafic rocks, as given by the NQMPR, was also investigated as a potential control on copper occurrences. Metamorphic grade was also

considered for analysis, however maps of the metamorphic grade that covered the whole study area were not available in sufficient detail for analysis.

3.2 Fractal analysis of mineral occurrence and geological clustering

Using the box counting procedure presented by Mandelbrot (1985), the number of boxes *N* with side length *r* required to cover all the mineral occurrences in the study area is counted as a function of *r*, and the fractal dimension, *d*, is given by the relationship:

$$N(r) \propto r^{-d}$$

Values of *N(r)* and *r* were plotted on a log-log graph and linear regression was performed on the straightest part of the line of best fit, with the regression limits chosen by examining the graph. In all cases the largest box size was ignored because its side length *r* was fixed with respect to the size of the study area. This is referred to as the global box counting method as it calculates a fractal dimension for the overall study area. It does not describe how the clustering may vary within the study area itself.

To analyse spatial variation of clustering, fractal dimensions were calculated for occurrences within boxes of side length 126.65 km, one quarter of the size of the largest box size used in the global box counting method outlined above. This box size was chosen in order to contain enough occurrences to calculate a reliable value for *d*. The box was shifted in steps of 50 km across the study area, and fractal dimensions were

calculated for each box containing 10 or more occurrences. This number was determined by examining the log-log plots of $N(r)$ vs. r for several locations with a small number of occurrences: for regions containing less than 10 occurrences the line of best fit for the graph was too erratic for the linear regression to be performed accurately. Looking at a sample of the remaining graphs allowed regression limits to be chosen at 7.5 km and 75 km, automatically excluding the largest box size. By choosing these regression limits, the issue of roll-off (Blenkinsop and Sanderson, 1999) was avoided. Two sample graphs from the shifting box counting of the copper occurrences are shown in Fig. 3.

A contour map was generated to visualize the variation in the fractal dimension across the study area. Values for the contouring were located at the centre of each of the shifting boxes. Null fractal dimension values arising from insufficient data points in the shifting box were excluded from the contour map and further analysis of the clustering.

3.3 Weights of Evidence Approach

The spatial association between features on two or more binary maps is quantified by the contrast value in weights of evidence analysis (Bonham-Carter, 1994). This value compares the spatial association of two features (in this study, copper occurrences and geological features such as fault intersections) with that expected from random distribution of the features, which would give a contrast value of 0. Any contrast values above 0.5 are considered to be indicative of a significant spatial association between the two features (Wang et al., 2002).

Weights of evidence analysis was performed on the data using the MapInfo – Spatial Data Modeller software to determine the spatial correlation between the copper occurrences and the geological features analysed through the shifting box counting method. Buffers around the features were varied from 0 to 3 km to determine the buffer distance for the most appropriate contrast value, as judged by the maximum value, ignoring outliers. Confidence values were also calculated for each of the contrast values. The confidence was calculated as the contrast value divided by its standard deviation (Bonham-Carter, 1994).

3.4 A new method for evaluating mineral distributions: Combining fractal analysis of clustering with weights of evidence

Degrees of clustering were determined for geological features by their fractal dimension in each of the shifting boxes, and compared to the clustering of mineral occurrences in the same boxes by a correlation coefficient. The spatial association of the same geological features with mineral occurrences was measured by their contrast. Fractal analysis for clustering was combined with the weights of evidence approach by plotting the correlations in clustering against the contrast value. Four possible outcomes are shown in Fig. 4. In the top right of the diagram, high correlations are combined with high contrast values: since the geological feature coincides everywhere with the occurrences, they have the same variation in clustering. The top left part of the diagram shows geological features that have similar degrees of clustering as the mineral occurrences, but are not spatially associated with them. The lower right part of the diagram show a

geological feature that is spatially associated with occurrences, but has a different degree of clustering, typically when the numbers of occurrences and geological features are dissimilar. The lower left part of the diagram shows a geological feature that has different degrees of clustering and a lack of spatial association with the occurrences. The plot of Fig. 4 is a therefore a way of evaluating controls on clustering and location of mineral occurrences.

4. Results: Copper deposits of the Mount Isa Inlier

4.1 Fractal analysis of clustering

Results obtained for the global fractal dimension box counting method for all copper occurrences in the study area reveal a fractal distribution (Fig. 5) with a fractal dimension of 1.36 with a correlation coefficient between log $N(r)$ and log r of 1.000 and standard error of regression of 0.02 (Table 1). Global box counting in the Eastern Succession gave a fractal dimension of 1.39 and in the Western Succession a value of 1.29 was obtained (Table 1). The use of small box sizes in the regression may lead to inaccuracy in the calculation of the due to roll-off effects (Blenkinsop and Sanderson, 1999); hence these were excluded.

Fractal dimensions calculated for the copper occurrences in the 127 km squares within the Mt Isa Inlier range from 0.59 to 1.79 indicating that there is a significant variation in the clustering of the occurrences within the study area, as shown in Fig. 6. The copper

occurrences in the centre of the study area (corresponding to the Kalkadoon-Leichhardt Belt and western margin of the Eastern Fold belt) are less clustered, as reflected by the highest fractal dimensions in the region. The fractal dimensions in the eastern part of the Mt Isa Inlier are higher than those in the west. This indicates that the copper occurrences are generally more clustered in the Western Succession.

Correlations between the clustering of the copper occurrences and the clustering of the fault bends and the fault intersections, and between clustering of copper deposits and mafic rocks within the Eastern and Western Successions are shown in Table 2. Spatial variation in the clustering of the copper occurrences has the highest correlation with the clustering of fault bends in the whole inlier. In the Eastern Succession, the highest correlation exists between the clustering of the copper occurrences and mafic intrusives, while in the Western Succession the highest correlation is with the fault intersections. It should be noted that the correlations with aspects of fault geometry in the Western Succession (0.823 for fault bends and 0.862 for fault intersections) are appreciably higher than the bends and intersections in the Eastern Succession (0.696 and 0.658 respectively).

4.2 Weights of Evidence

Results from the weights of evidence analysis are shown in Table 2. The strongest spatial relationships, as indicated by the highest contrast values, were between fault bends and intersections and copper occurrences for both the Eastern and Western Successions. Fault bends in the Eastern Succession have the highest contrast value (0.798) with the copper occurrences, while in the Western Succession, the fault intersections have the

highest value (2.330). With one exception, all contrast values are above 0.5 and are therefore significant (Wang et al., 2002).

4.3 Combining Fractal Analysis and Weights of Evidence

Fig. 7 shows the correlations obtained from the fractal analysis between the clustering of copper occurrences and the clustering of geological features listed in Table 2 plotted on a log-normal graph against the contrast values generated from the weights of evidence analysis. The graph shows a linear trend between the results from the fractal analysis and the results from the weights of evidence analysis. A value of 0.683 (significant at 95% confidence) was obtained for Spearman's rank correlation between correlation of clustering and spatial association, indicating that the log-normal relationship between fractal analysis and weights of evidence analysis is significant.

5. Discussion

5.1 Fractal distribution of copper occurrences and their spatial variation

The global fractal dimensions shown in Table 1 clearly indicate that copper deposit distributions can be described using fractals. Thus it is not only hydrothermal and precious metal deposit distributions that can be described by fractals. The corresponding correlation for the fractal dimension for the entire Mt Isa inlier study area (1.000) is the highest found in the literature for the fractal distribution of mineral deposits (cf. Blenkinsop and Sanderson, 1999). Figure 6 displays significant variation in the fractal

dimension for the copper occurrences from the global value across the Mt Isa inlier study area. This variation permits analysis of what geological features may potentially affect the level of clustering of copper occurrences in a given area.

5.2 Factors affecting clustering and localization of copper occurrences

The variation of fractal dimension indicated in Fig. 6 shows that the occurrences in the Eastern Succession are less clustered than those in the Western Succession. This could be due to the more extensive exploration in the Eastern Succession (cf. Blenkinsop and Sanderson, 1999). This possibility was evaluated from the location of exploration drillhole data within the NQMPR (Queensland Department of Mines and Energy et al., 2000). Over 70% of the drillhole data is from the Eastern Succession. Regions with comparatively low fractal dimensions may not have been fully explored as indicated by the roll-off shown on log-log graphs (see Fig. 3) produced from the box counting (Blenkinsop and Sanderson, 1999). Another factor that might in principle cause differences in the clustering between the Eastern and Western Successions is the style of mineralization. Brecciated sediment-hosted copper deposits are primarily located in the Western Succession whereas the shear and fault controlled vein copper deposits are predominantly found in the Eastern Succession (Blake et al., 1990). It is not clear why or how this would effect the degree of clustering, especially if both styles are epigenetic in origin.

The correlations between the clustering of copper occurrences and geological features listed in Table 2 indicate that the fault geometry may have a greater control on the

clustering of the copper occurrences in the Western Succession, whereas the mafic intrusives (with a correlation of 0.885) have a greater control in the Eastern Succession (cf. Butera and Blenkinsop, 2004).

The weights of evidence analysis indicates that there are strong spatial relationships between the copper occurrences, fault geometry, and mafic rocks (Table 2). The strongest spatial relationship exists between the occurrences and fault geometry in the Western Succession, with contrast values of 2.33 and 1.47 for the fault intersections and bends respectively. In the Eastern Succession, strong spatial relationships also exist between the copper occurrences and the fault geometry; however the contrast values obtained have less variation than those in the west.

Fig. 7 indicates a positive correlation between the logarithms of contrast values from the weights of evidence, and the correlations obtained from the fractal analysis. Since the contrast is a logarithmic function, it is appropriate to plot these values on a logarithmic scale. The positive relationship between the fractal analysis and weights of evidence could be interpreted to indicate that the features controlling the clustering of the copper occurrences in the Mt Isa Inlier may also be the features controlling the localization of the occurrences. Almost all of the data in this study (Fig. 7) plots in the top right of the graph in Fig. 4, and forms a linear trend, although the mafic intrusives in the Eastern Succession do not fall on the general trend. Features with a high correlation in the degree of clustering have high contrast values and features with a lower correlation have a lower

contrast value, within the general constraint that all features have relatively high values of both correlation and contrast.

Fault bends and intersections have a major influence on the spatial association and clustering of the copper occurrences in the Mount Isa Inlier. Though the results indicate that the relationship between the faults and mineralization is stronger in the Western Succession, their control on the occurrences in the Eastern Succession is also significant.

5.3 Integrating fractal analysis and mineral prospectivity

The relationship between the fractal analysis and weights of evidence (Fig. 7) is an interesting result and raises some intriguing questions about the processes influencing both the spatial association and clustering of the occurrences.

While some of the features used in the fractal analysis and the weights of evidence show significant fractal dimension correlations and contrast values (e.g. fault bends and fault intersections in the Eastern Succession), the values are not high enough to say that any of these factors individually play an exclusive part in the clustering and localization of the copper occurrences. However, when combined with other features in this study or those not yet investigated, the results may contribute to the understanding of the spatial distribution of the occurrences.

The significant relationship between the fractal analysis and weights of evidence has potential exploration implications. Four possible implications from combining fractals and weights of evidence as outlined in Fig. 4 can be considered for exploration:

- For features with high fractal dimension correlation and high contrast, (in the top right of Fig. 4): Explore in areas proximal to the feature, and in areas with high clustering of the feature. Examples include fault bends and fault intersections in the Western Succession.
- For features with high fractal dimension correlation and low contrast (top left of Fig. 4): Explore in areas with high clustering of mineral occurrences that are not necessarily in close proximity to the feature, such as mafic intrusives in the Eastern Succession.
- For features with low fractal dimension correlation and high contrast (bottom right of Fig. 4): Explore in areas proximal to the feature.
- For features with low fractal dimension correlation and low contrast (bottom left of Fig. 4): Feature should not be used for exploration targeting.

Future research could focus on subdividing mineral occurrences by their style of mineralization. Consideration of the different styles of mineralization may provide further insights into what is controlling the clustering and localization of the occurrences. However these data are currently only available for the largest deposits. The conclusion that the features controlling the clustering of the occurrences are the same features controlling the localization requires additional testing for different commodities and

geological features in other study areas. Another future avenue for research is discrimination of clustering and spatial associations based on deposit size.

5.4 Limitations of the Analysis

As this study deals with spatial data analysis, the quality of the input data is critical to generating and interpreting the results accurately. Potential limitations include variations in the quality and homogeneity of mapping and the effect of cover.

The quality of mapping should not be a problem since only mafic intrusive and extrusive rocks have been used in the analysis, and there is no reason to doubt that the mapping identifies such distinctive rocks correctly. The issue of the homogeneity of the mapping was addressed by using geological data from the NQMPR (Queensland Department of Mines and Energy et al., 2000). With the data being mapped at the same scale and coming from the same source, it is the most homogeneous available for analysis.

Palaeozoic (and later) cover rocks overlying the outcropping Proterozoic inlier could potentially have some bearing on the results. Any such effects of cover can not be easily quantified. This study is a comparative analysis between the copper occurrences and geological features, and there is no clear evidence to suggest that cover affects one more than the other. Confidence in the value of the fractal dimension would be diminished by increasing levels of cover, but it is not clear whether the fractal dimension value would increase or decrease as a result. Although weights of evidence is sensitive to cover due to "padding" that contains neither mineral deposits or the feature being examined (Bonham-

Carter, 1994), the faults have been interpreted undercover and the contrast values for the mafic rocks were not calculated in covered areas.

6. Conclusions

Combining fractal analysis with weights of evidence has important outcomes for exploration. For mineral occurrences and a geological feature with a high correlation of degree of clustering and a high contrast value (as determined from the weights of evidence), exploration should focus on areas proximal to the feature, and on areas where the feature is clustered, which will also have clusters of mineral occurrences. Where the geological feature has a low correlation of degree of clustering and a high contrast value, exploration should occur in areas proximal to the feature. A high correlation in the degree of clustering and low contrast value suggests exploration may be advantageous in areas with a high degree of clustering of the copper occurrences, not necessarily proximal to the feature analysed.

This approach of combining fractal analysis and weights of evidence can be applied to the copper occurrences in the Mt Isa inlier. Evidence suggests a strong spatial relationship between the copper mineralization and faults in both the Eastern and Western Successions. There is a strong spatial association of mafic intrusives with copper occurrences in the Eastern Succession. This may indicate genetic links between mineralization, mafic rocks and faults. The links can be explained if metals were supplied

from mafic rocks (either at crystallization, or during subsequent metamorphism), combined with mineral transport and deposition in a hydrothermal plumbing system created by faults that promoted mineralization at fault bends and intersections.

Acknowledgments

This paper is published with the permission of the Chief Executive Officer, predictive mineral discovery Cooperative Research Centre. This study is part of the PhD research of AF at James Cook University which is supported by a pmd*CRC scholarship. Nick Oliver is thanked for providing constructive comments which helped improve the manuscript.

References

Agterberg, F.P. and Bonham-Carter, G.F., 1990. Deriving weights of evidence from geoscience contour maps for the prediction of discrete events, Proceedings 22nd APCOM Symposium. Technical University of Berlin, Berlin, Germany, pp. 381-395.

Agterberg, F.P. and Bonham-Carter, G.F., 2005. Measuring the Performance of Mineral-Potential Maps. Natural Resources Research, 14(1): 1-17.

Agterberg, F.P., Bonham-Carter, G.F., Cheng, Q. and Wright, D.F., 1993. Weights of evidence modeling and weighted logistic regression for mineral potential mapping. In: J. Davis and U.C. Herzfeld (Editors), Computers in Geology - 25 Years of Progress. Oxford Univ. Press, New York, pp. 13-32.

Agterberg, F.P., Cheng, Q. and Wright, D.F., 1996. Fractal Modelling of Mineral Deposits. In: J. Elbrond and X. Tang (Editors), Proceedings of the International Symposium on the Application of Computers and Operations Research in the Minerals Industries, Montreal, Canada, pp. 43-53.

Allibone, A. et al., 2002a. Timing and Structural Controls on Gold Mineralization at the Bosogo Gold Mine, Ghana, West Africa. Economic Geology, 97: 949-969.

Allibone, A.H. et al., 2002b. Structural Controls on Gold Mineralization at the Ashanti Deposit, Obuasi, Ghana. In: R.J. Goldfarb and R.L. Nielsen (Editors), Integrated Methods for Discovery: Global Exploration in the Twenty-First Century. Society of Economic Geologists, pp. 65-93.

Bell, T.H., Perkins, W.G. and Swager, C.P., 1988. Structural Controls on Development and Localization of Syntectonic Copper Mineralization at Mount Isa, Queensland. Economic Geology, 83: 69-85.

Billa, M. et al., 2004. Predicting gold-rich epithermal and porphyry systems in the central Andes with a continental-scale metallogenic GIS. Ore Geology Reviews, 25(1-2): 39-67.

Blake, D.H. et al., 1990. Mount Isa Inlier - regional geology and mineralization. In: F.E. Hughes (Editor), Geology of the Mineral Deposits of Australia and Papua New Guinea. Australian Institute of Mining and Metallurgy, Melbourne, pp. 915-925.

Blake, D.H. and Stewart, A.J., 1992. Stratigraphic and tectonic framework, Mount Isa Inlier. In: A.J. Stewart and D.H. Blake (Editors), AGSO Bulletin 243: Detailed Studies of the Mount Isa Inlier, Canberra, pp. 1-11.

Blenkinsop, T. and Oliver, N., 2003. Discrimination of Base/Precious Metal Mineralising Systems by Fractal Analysis, Mt Isa, Australia, Geophysical Research Abstracts. European Geophysical Society.

Blenkinsop, T.G. and Sanderson, D.J., 1999. Are gold deposits in the crust fractals? A study of gold mines in the Zimbabwean craton. In: K.J.W. McCaffrey, L. Lonergan and J.J. Wilkinson (Editors), Fractures, Fluid Flow and Mineralization. Geological Society, London, pp. 141-151.

Boleneus, D.E. et al., 2002. Assessment Method for Epithermal Gold Deposits in Northeast Washington State using Weights-of-Evidence GIS Modeling: U.S. Geological Survey Open File Report OF01-501.

Bonham-Carter, G., 1994. Geographic information systems for geoscientists: modelling with GIS. Pergamon Press, Oxford.

Bonham-Carter, G.F., Agterberg, F.P. and Cheng, Q., 1989. Weights of evidence modelling: a new approach to mapping mineral potential. In: F.P. Agterberg and G.F. Bonham-Carter (Editors), Statistical Applications in the Earth Sciences. Geological Survey of Canada Paper 89-9, pp. 171-183.

Brown, W., Groves, D. and Gedeon, T., 2003. Use of fuzzy membership input layers to combine subjective geological knowledge and empirical data in a neural network method for mineral-potential mapping. Natural Resources Research, 12(3): 183-200.

Brown, W.M., Gedeon, T.D., Groves, D. and Barnes, R.G., 2000. Artificial neural networks: a new method for mineral prospectivity mapping. Australian Journal of Earth Sciences, 47: 757-770.

Butera, K.M., 2004. The role of mafic rocks in the genesis of IOCG and Base Metal deposits, Mount Isa Eastern Succession, NW Queensland, Australia. In: A.C. Barnicoat and R.J. Korsch (Editors), Predictive Mineral Discovery Cooperative Research Centre - Extended Abstracts from the June 2004 Conference. Geoscience Australia, pp. 21-22.

Butera, K.M. and Blenkinsop, T.G., 2004. Fractal analysis of the spatial distributions of mafic rocks and mineralisation in the Eastern Succession, Mount Isa Inlier, Australia: a possible genetic link, 4th International Conference "Fractals and Dynamic Systems in Geoscience", TU München, pp. 16-19.

Carlson, C.A., 1991. Spatial distribution of ore deposits. Geology, 19: 111-114.

Carranza, E.J.M., Hale, M. and Mangaoang, J.C., 1999. Application of mineral exploration models and GIS to generate mineral potential maps as input for optimum land-use planning in the Philippines. Natural Resources Research, 8(2): 165-173.

Cheng, Q. and Agterberg, F.P., 1999. Fuzzy weights of evidence method and its application in mineral potential mapping Natural Resources Research (International Association for Mathematical Geology) 8(1): 27-35.

Connors, K., 1992. Structural Controls on Mineralization in the Gunpowder area, Etheridge & Henley - Geoscience Consultants.

Craw, D., 2000. Fluid flow at fault intersections in an active oblique collision zone, Southern Alps, New Zealand. Journal of Geochemical Exploration, 69-70: 523-526.

Feltrin, L., Oliver, N.H.S., Kelso, I.J. and King, S., 2003. Basement metal scavenging during basin evolution: Cambrian and Proterozoic interaction at the Century Zn-Pb-Ag Deposit, Northern Australia. Journal of Geochemical Exploration, 78-79: 159-162.

Harris, J.R., Wilkinson, L. and Grunsky, E.C., 2000. Effective use and interpretation of lithogeochemical data in regional mineral exploration programs; application of geographic information systems (GIS) technology. Exploration geochemistry; selected papers from "Exploration '97", 16(3-4): 107-143.

Knox-Robinson, C.M., 2000. Vectorial fuzzy-logic: a novel technique for enhanced mineral prospectivity mapping, with reference to the orogenic gold mineralisation potential of the Kalgoorlie Terrane, Western Australia. Australian Journal of Earth Sciences, 47: 929-941.

Kreuzer, O.P., Blenkinsop, T.G., Morrison, R.J. and Peters, S.G., 2006. Ore controls in the Charters Towers goldfield, NE Australia: constraints from geological, geophysical and numerical analyses, and implications for exploring a 'mature' terrain. Ore Geology Reviews, submitted.

Laing, W.P., 1998. Structural-metasomatic environment of the East Mt Isa Block base-metal-gold province. Australian Journal of Earth Sciences, 45: 413-428.

Mandelbrot, B.B., 1983. The fractal geometry of nature. W. H. Freeman and Company, New York.

Mandelbrot, B.B., 1985. Self-affine fractals and fractal dimension. Physica Scripta, 32: 257-260.

Mark, G., Oliver, N.H.S. and Carew, M.J., 2006. Insights into the genesis and diversity of epigenetic Cu-Au mineralisation in the Cloncurry district, Mt Isa Inlier, northwest Queensland. Australian Journal of Earth Sciences, 53: 109-124.

Mark, G., Williams, P.J. and Boyce, A.J., 2004. Low-latitude meteoric fluid flow along the Cloncurry Fault, Cloncurry District, NW Queensland, Australia: geodynamic and metallogenic implications. Chemical Geology, 207: 117-132.

Marshall, L.J., 2003. Brecciation within the Mary Kathleen group of the Eastern succession, Mt Isa block, Australia : implications of district-scale structural and metasomatic processes for Fe-oxide-Cu-Au mineralisation. PhD Thesis, James Cook University, Townsville.

Matthäi, S.K., Heinrich, C.A. and Driesner, T., 2004. Is the Mount Isa copper deposit the product of forced brine convection in the footwall of a major reverse fault? Geology, 32(4): 357-360.

McDonald, G.D., Collerson, K.D. and Kinny, P.D., 1997. Late Archean and Early Proterozoic crustal evolution of the Mount Isa block, northwest Queensland, Australia. Geology, 25(12): 1095-1098.

Mustard, R., Blenkinsop, T., McKeagney, C., Huddleston-Holmes, C. and Partington, G., 2004. New perspectives on IOCG deposits, Mt Isa Eastern Succession, northwest Queensland, SEG 2004 Predictive Mineral Discovery Under Cover: Extended Abstracts. Centre for Global Metallogeny, University of Western Australia, pp. 281-284.

Nie, F.-J., Jiang, S.-H., Su, X.-X. and Wang, X.-L., 2002. Geological features and origin of gold deposits occuring in the Baotao-Bayan Obo district, south-central Inner Mongolia, People's Republic of China. Ore Geology Reviews, 20(3-4): 139-169.

Nijman, W., Mijnlieff, H.F. and Schalkwijk, G., 1992. The Hero Fan delta (Lower Mount Isa Group) and its structural control: deformation in the Hero/Western Fault Zone and Paroo Range compared, Proterozoic, Mount Isa Inlier, Queensland, Australia. In: A.J. Stewart and D.H. Blake (Editors), AGSO Bulletin 243: Detailed Studies of the Mount Isa Inlier, Canberra, pp. 75-111.

O'Dea, M.G. et al., 1997. Geodynamic evolution of the Proterozoic Mount Isa terrain. In: J.P. Burg and M. Ford (Editors), Orogeny Through Time. Geological Society, London, pp. 99-122.

Oliver, N.H.S. et al., 2004. Geochemistry and geochemical modeling of fluid-rock interaction in the eastern Mt Isa Block, Australia: the role of sodic alteration in the genesis of iron oxide-copper-gold deposits. Economic Geology, 99: 1145-1176.

Phillips, G.N., Groves, D.I. and Kerrich, R., 1996. Factors in the formation of the giant Kalgoorlie gold deposit. Ore Geology Reviews, 10: 295-317.

Queensland Department of Mines and Energy, Taylor Wall and Associates, SRK Pry Ltd and ESRI Australia, 2000. North-West Queensland Mineral Province Report (NQMPR), Queensland Department of Mines and Energy.

Queensland Department of Natural Resources and Mines, December 2002. Queensland Mineral Resource Database MINOCC 2002 - Microsoft Access Database.

Raines, G.L., 1999. Evaluation of weights of evidence to predict epithermal-gold deposits in the Great Basin of the Western United States. Natural Resources Research, 8(4): 257-276.

Scott, K.M. and Taylor, G.F., 1982. Eastern Creek Volcanics as the source of copper at the Mammoth mine, Northwest Queensland. BMR Journal of Australian Geology & Geophysics, 7: 93-98.

Singer, D.A. and Kouda, R., 1999. Comparison of the weights of evidence method and probabilistic neural networks. Natural Resources Research, 8(4): 287-298.

Twomey, T. and McGibbon, S., 2001. The Geological Setting and Estimation of Gold Grade of the High-grade Zone, Red Lake Mine, Goldcorp Inc. Exploration and Mining Geology, 10(1-2): 19-34.

Wang, H., Cai, G. and Cheng, Q., 2002. Data integration using weights of evidence model: applications in mapping mineral resource potentials, Proceedings of Int. Society of Photogrammetry and Remote Sensing, Ottawa.

Williams, P.J., 1998. An Introduction to the Metallogeny of the McArthur River-Mount Isa-Cloncurry Minerals Province. Economic Geology, 93(8): 1120-1131.

Wyborn, L.A.I., 1987. The petrology and geochemistry of alteration assemblages in the Eastern Creek Volcanics, as a guide to copper and uranium mobility associated with regional metamorphism and deformation, Mount Isa, Queensland. In: T.C. Pharaoh, R.D. Beckinsale and D. Rickard (Editors), Geochemistry and Mineralization of Proterozoic Volcanic Suites. Geological Society, London, pp. 425-434.

Table 1: Global fractal dimensions (*d*) for Copper occurrences in the study areas examined with number of occurrences (*N*), correlation coefficient (*R*) and standard error of regression (*E*). The regression limits were chosen from the straightest part of the log *r* vs. log *N(r)* graph.

Study Area	*N*	*d*	*R*	*E*	Regression Limits
Mt Isa Inlier	1869	1.36	1.000	0.02	15.83km – 253.30km
Eastern Succession	1412	1.39	0.999	0.04	7.92km – 63.33km
Western Succession	457	1.29	0.999	0.04	15.83km – 126.65km

Table 2: Results of correlation between clustering of copper occurrences and clustering of geological features using fractal analysis, and contrast values obtained from weights of evidence analysis with corresponding confidence values (* indicates significant at 95% confidence)

Location	**Cu occurrences correlated with**	**Correlation**	**Contrast**	**Confidence**
Mt Isa Inlier	Fault Bends	0.762*		
	Fault Intersections	0.391*		
Eastern Succession	Fault Bends	0.696*	0.798	2.249
	Fault Intersections	0.658*	0.617	3.332
	Mafic Intrusives	0.885*	0.536	3.723
	Mafic Intrusives+Extrusives	0.600	0.567	4.261
Western Succession	Fault Bends	0.823*	1.469	2.921
	Fault Intersections	0.862*	2.330	4.006
	Mafic Intrusives	0.670	0.623	1.208
	Mafic Intrusives+Extrusives	0.620*	0.460	1.883
	Mafic Extrusives	0.604*	0.643	1.989

Figure 1: Location of the study area

Figure 2: Copper occurrences in the Mt Isa Inlier (MINOCC, December 2002)

Figure 3: Sample graphs from shifting box counting with side length r and number of boxes N(r).

Figure 4: Schematic illustration of four possible natural outcomes from combining fractal and weights of evidence analyses. Each panel illustrates the pattern of a geological feature (open circle, such as fault bends) and mineral occurrences (closed circles) that characterizes the relevant part of the graph of correlation between degree of clustering and spatial association. Most data in this study plots in top right of this diagram i.e. the features have both similar degrees of clustering and high spatial association with copper occurrences.

Figure 5: Graph of r vs. N(r) for Cu occurrences in the Mt Isa Inlier

Figure 6: Variation of Fractal Dimension for Cu Occurrences in the Mt Isa Inlier with shifting box size 126.65km.

Figure 7: Log-normal graph of Fractal Dimension Correlation vs. Contrast. There is a rank correlation of 0.683 between contrast values and fractal dimension correlations. The

data indicates that fault intersections and fault bends in the Western Succession are useful features to use for exploration in that study area.

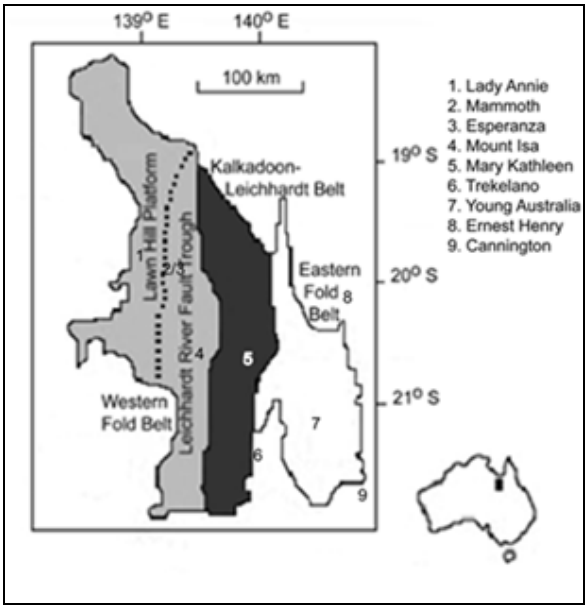
139° E
140° E
100 km
1. Lady Annie
2. Mammoth
3. Esperanza
4. Mount Isa
5. Mary Kathleen
6. Trekelano
7. Young Australia
8. Ernest Henry
9. Cannington
19° S
20° S
21° S
Kalkadoon-
Leichhardt Belt
Eastern
Fold
Belt
Lawn Hill Platform
Leichhardt River Fault Trough
Western
Fold Belt

fig 1

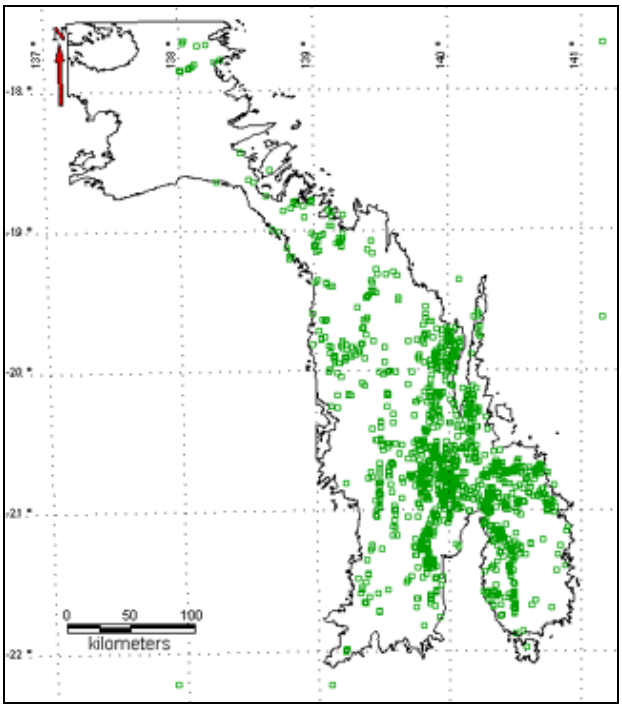
N
0
50
100
kilometers

fig 2

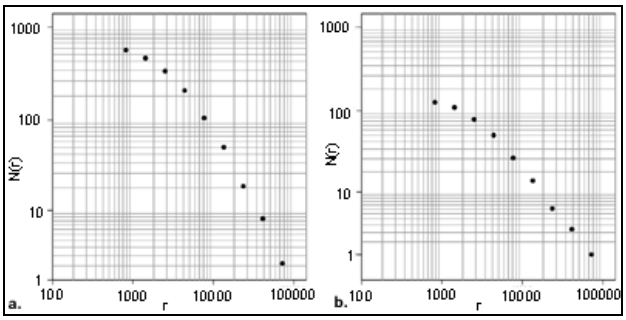
1000
100
10
1
N(r)
100
1000
r
10000
100000
a.
b.

fig 3

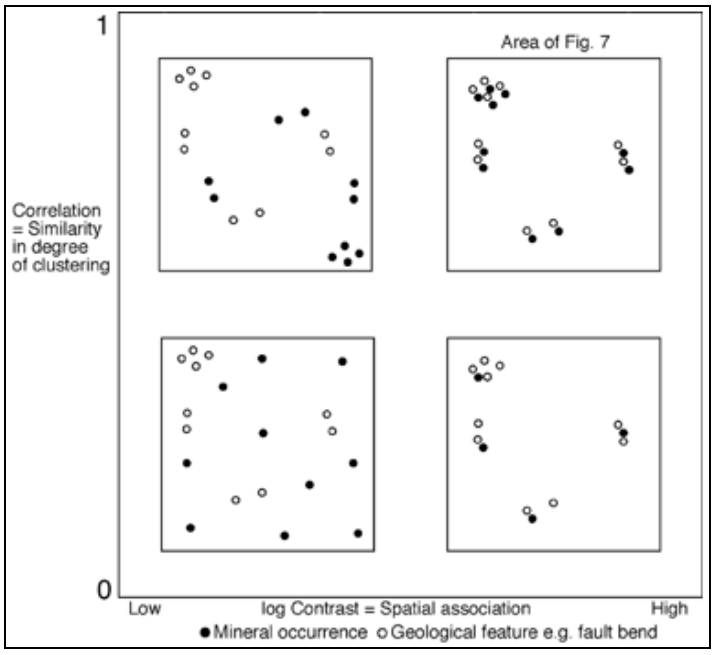
1
0
Area of Fig. 7
Correlation
= Similarity
in degree
of clustering
Low
log Contrast = Spatial association
High
● Mineral occurrence o Geological feature e.g. fault bend

fig 4

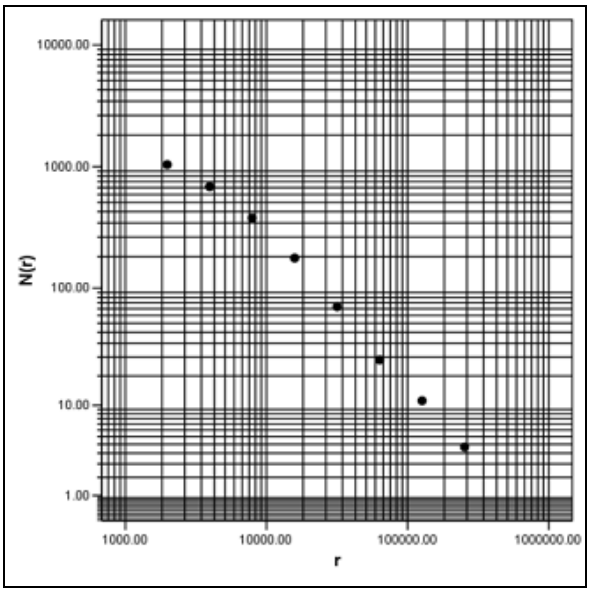
10000.00
1000.00
100.00
10.00
1.00
N(r)
1000.00
10000.00
100000.00
1000000.00
r

fig 5

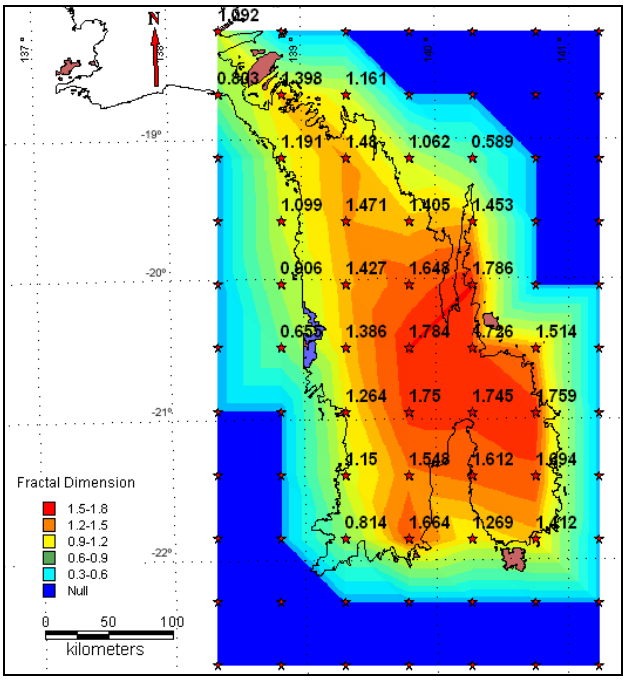
N
137°
138°
139°
140°
141°
-19°
-20°
-21°
-22°
1.092
0.803
1.398
1.161
1.191
1.48
1.062
0.589
1.099
1.471
1.405
1.453
0.806
1.427
1.648
1.786
0.655
1.386
1.784
1.726
1.514
1.264
1.75
1.745
1.759
1.15
1.548
1.612
1.894
0.814
1.664
1.269
1.412
Fractal Dimension
1.5-1.8
1.2-1.5
0.9-1.2
0.6-0.9
0.3-0.6
Null
0
50
100
kilometers

fig 6

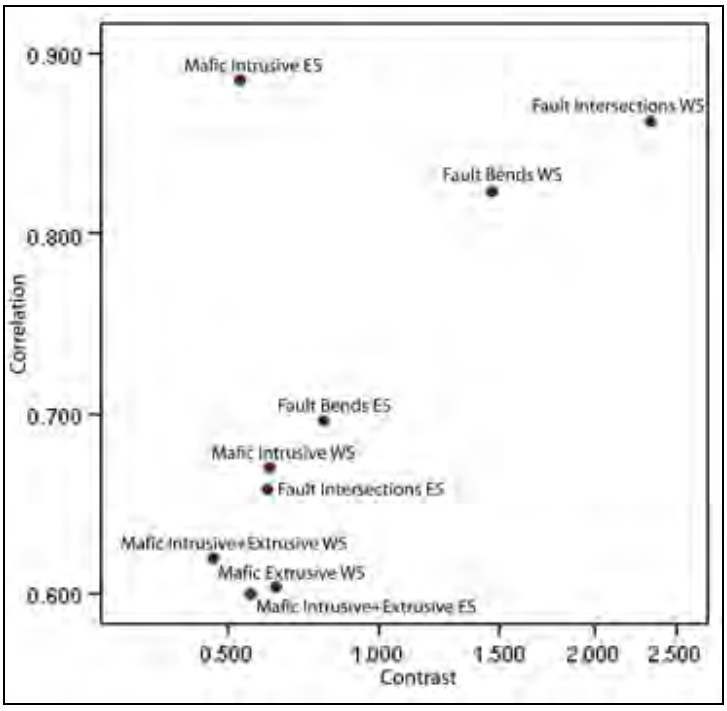
0.900
0.800
0.700
0.600
Correlation
Mafic Intrusive ES
Fault Intersections WS
Fault Bends WS
Fault Bends ES
Mafic Intrusive WS
Fault Intersections ES
Mafic Intrusive+Extrusive WS
Mafic Extrusive WS
Mafic Intrusive+Extrusive ES
0.500
1.000
1.500
2.000
2.500
Contrast

fig 7

Application of Fractal and Multifractal Analysis to Mineralized Systems with Special Reference to the Mount Isa Inlier

Thesis submitted by

Arianne FORD

BSc (Hons), James Cook University

In October, 2007

For the degree of Doctor of Philosophy

In the School of Earth and Environmental Sciences

James Cook University

STATEMENT OF ACCESS

I, the undersigned, author of this work, understand that James Cook University will make this thesis available for use within the University Library and, via the Australian Digital Theses network, for use elsewhere.

I understand that, as an unpublished work, a thesis has significant protection under the Copyright Act and I wish this work to be embargoed until October 2008.

_____ _____

Signature Date

STATEMENT OF SOURCES

DECLARATION

I declare that this thesis is my own work and has not been submitted in any form for another degree or diploma at any university or other institution of tertiary education. Information derived from the published or unpublished work of others has been acknowledged in the text and a list of references is given.

_____ _____

Signature Date

STATEMENT OF CONTRIBUTIONS

Financial contributions towards this PhD have included:

- Project funding from the predictive mineral discovery CRC (*pmd**CRC)
- A School of Earth Sciences PhD Scholarship
- A *pmd**CRC top-up scholarship
- A James Cook University Graduate Research School research grant
- The James Cook University High Performance Computing section is acknowledged for providing in-kind support for time on the supercomputer and for the provision of the necessary programming software.

Contributions to the manuscripts within this thesis have come from:

- Section A – Dr Thomas Blenkinsop is thanked for editorial support as co-author of this paper. Prof. Nick Oliver is thanked for constructive comments which helped improve the manuscript before submission. Dr Oliver Kreuzer and an anonymous *Ore Geology Reviews* reviewer are thanked for their contributions as reviewers of the manuscript.
- Section B – Dr Thomas Blenkinsop is thanked for editorial support as co-author of this paper. Dr Paul Hodkiewicz and Dr Greg Partington are thanked for their contributions in reviewing the manuscript for the *Australian Journal of Earth Sciences*.
- Section C – Dr Thomas Blenkinsop is thanked for editorial support as co-author of this manuscript. Dr Pat Williams is thanked for advice on preparing the manuscript for submission to *Mineralium Deposita*.
- Section D – Dr Thomas Blenkinsop, Dr John McLellan, and Dr Heather Sheldon are thanked for editorial support and advice on numerical modelling. The Computational Geoscience group at CSIRO in Perth are thanked for the provision of training in FLAC^{3D} and for providing licenses to run the numerical models.

Normal supervisory contributions throughout the term of this PhD project by Dr Thomas Blenkinsop are also acknowledged.

"IF WE KNEW WHAT WE WERE DOING, IT WOULD NOT BE CALLED RESEARCH, WOULD IT?" - EINSTEIN

ACKNOWLEDGEMENTS

This PhD project was undertaken at James Cook University with the support of the predictive mineral discovery CRC (*pmd**CRC). I wish to thank my supervisor Tom Blenkinsop for giving me the opportunity to undertake this project and for constant support and advice throughout the course of my PhD. Nick Oliver, Damien Foster, John McLellan, Damien Keys, Alison Ord, Heather Sheldon, Roger Mustard, Kris Butera and Martin Higham are thanked for useful discussions and support during the project.

The Computational Geoscience group at CSIRO in Perth are thanked for their support in helping me to understand GoCad templates and FLAC^{3D} as well as providing the facilities to run my numerical models. High Performance Computing at James Cook University, particularly Wayne Mallet, are also thanked for providing access to the supercomputer facilities, software licenses, and technical support necessary for the data analysis in the project.

I am grateful to my fellow EGRU partners in crime (or is that bbq organization?) for being nice when I was clueless about something geological. It probably happened more than I remember. Thanks also go to Louise, Rowena, Julie, and Haidi for keeping me grounded from time to time. For dealing with my regular "I hate computers" moments (tantrums?), thanks also has to go out to the guys on the JCU IRC channels.

Without my friends and family constantly reminding me that I wasn't allowed to be a uni student forever, I probably would have spent 95% of my time procrastinating rather than the 90% I did anyway. So cheers! In particular, I would like to thank my office mate Louise, for putting up with me over the last year while we were both trying to finish up. Housemate extraordinaire Prue is also thanked for dealing with the late night entrances and exits and reminding me that Tuesday night trivia is a must attend event. I must also thank Jim and Damo for dragging everyone away from their computers occasionally for drinks at The Club. And for constant moral support, even after leaving JCU for the "real world", thanks go out to Diane and Coops.

ABSTRACT

Fractal and multifractal analysis of different facets of mineralized systems has largely been focused on a limited number of study areas and commodities. Previous studies have suggested that controls on mineralization can be inferred from fractal analysis of mineral deposit distributions. Many of these potential controls have however been suggested on a qualitative rather than a quantitative basis. Whereas fractal analysis of mineral deposit distributions simply considers the location of the deposits, multifractal analysis can examine variation in a value assigned to each deposit location such as deposit size. Yet no comprehensive study of the multifractal properties of production data has been presented.

Coupled deformation and fluid flow modelling has been used to verify sites of importance for mineralization in both two- and three-dimensional modelling space. Numerical modelling in three-dimensions of strike-slip faulting has yet to fully examine the effect of variation in fault geometry. Quantitative analysis of model outputs can provide criteria for ranking of different fault geometry parameters in terms of their relative prospectivity.

The Proterozoic Mount Isa Inlier is a rich base metal province in northwest Queensland, Australia. A well studied terrain, with comprehensive literature, geological, and mineral deposit databases available, the Mount Isa Inlier is an ideal study area for investigating and verifying new techniques for brownfields exploration targeting. A quantitative examination of the controls on base metal deposition in the Mount Isa Inlier has substantial implications for future exploration in the region, with the techniques being readily applicable to other study areas and commodities.

A new method is presented which evaluates mineral occurrence distributions by combining fractal analysis of clustering with Weights of Evidence (WofE). Variation in clustering of copper occurrences from the Mount Isa Inlier has a strong positive correlation with variation in clustering of fault bends (R=0.823), fault intersections (R=0.862), and mafic intrusions (R=0.885). WofE analysis as quantified by contrast values indicates that the copper occurrences have a strong spatial association with fault

intersections, and fault bends. Correlation of the variation of clustering of copper occurrences and geological features shows a linear relationship with the contrast values indicating that the geological features controlling the clustering of the copper occurrences may be the same features controlling their localization.

A fractal dimension can be used to quantify geological complexity, defined as the combination of faults and lithological boundaries. Two-dimensional analysis of geological complexity in the Mount Isa Inlier suggests that there exists a strong spatial relationship between geological complexity and copper endowment (R=0.914). A weak inverse relationship is shown to exist between complexity gradients and copper endowment. The results indicate that geological complexity could be used as an exploration targeting tool for copper in the Mount Isa Inlier.

The de Wijs model was developed to describe the distribution of element enrichment and depletion in the crust. An expansion of the de Wijs model is presented to investigate the distribution of ore tonnage as well as grade. The expanded model produces a log-normal relationship between ore tonnage and grade. Multifractal analysis suggests that ore tonnage values from the expanded model are not multifractal. Analysis of production data from the Zimbabwe craton displays a log-normal relationship between ore tonnage and grade and indicates that ore tonnage is not multifractal, as suggested by the expanded de Wijs model.

Variation of fault system geometry parameters during coupled deformation and fluid flow modelling of strike-slip faulting reveals that having a low dipping fault, a contrast in lithology and a wide fault width generates the highest dilation and integrated fluid flux values which can be considered proxies for prospectivity. The fault geometries observed in the modelling to be the most prospective could be incorporated into exploration targeting strategies.

Contents of PhD Thesis

List of Figures

SECTION A

SECTION B

SECTION C

SECTION D

List of Tables

INTRODUCTION

Fractal geometry was first used to describe various natural phenomena by Mandelbrot (1983). Fractal analysis can be used to investigate self-similarity within a system, which can be measured by a fractal dimension. Understanding the fractal dimension of an object or system provides insight into how the fractal it is measuring occupies the space in which it resides (Barnsley, 1988).

Originally used to describe "formless" shapes such as clouds and coastlines, the theory of fractals was further expanded to examine more disconnected phenomena such as the clustering of galaxies using spatial Lévy dusts (Mandelbrot, 1983). One characteristic of fractal dusts is the degree of clustering of points, which can be measured by a fractal dimension. A fractal dust with a fractal dimension of 2 describes a random spatial distribution and a fractal dimension of 0 describes a fractal dust with only one point (Mandelbrot, 1983).

Application of fractal analysis to mineral deposits was first used to describe the spatial distribution of mineral deposits (Carlson, 1991). Further research using fractal analysis to describe mineral deposit distributions was carried out (Blenkinsop, 1994, 1995; Agterberg et al., 1996; Blenkinsop and Sanderson, 1999).

The use of fractal analysis to describe mineral deposit distributions beyond these studies has been largely unexplored, with the results of previous research showing that possible geological controls and exploration potential can be inferred (Carlson, 1991; Blenkinsop, 1994; Weinberg et al., 2004; Hodkiewicz et al., 2005). The economic impact of fractal analysis for exploration has been reviewed by Blenkinsop (1995), which lead to conclusions about how exploration companies could further develop

exploration strategies. Many of these studies have examined what can be termed the "global" fractal dimension of the deposits, which is the single fractal dimension assigned to an entire population of deposits (Carlson, 1991; Blenkinsop, 1994; Agterberg et al., 1996; Blenkinsop and Sanderson, 1999; Blenkinsop and Oliver, 2003; Butera and Blenkinsop, 2004). Very few studies have examined how the fractal dimension may vary over a given study area (eg. Weinberg et al., 2004; Hodkiewicz et al., 2005).

With established studies of fractal analysis in economic geology, the application of existing and new methods of fractal analysis to different mineral systems and commodities is becoming more prevalent. While previous studies have suggested potential controls on clustering of mineral deposits (eg. Carlson, 1991; Blenkinsop, 1994; Blenkinsop and Sanderson, 1999), these controls were proposed on a qualitative basis. By examining variation of clustering over a given study area, it is possible to analyze potential controls quantitatively (eg. Weinberg et al., 2004; Hodkiewicz et al., 2005). However these studies investigated a very limited number of potential controls. Hodkiewicz et al. (2005) present a study which evaluates geological complexity and complexity gradients as potential controls on gold endowment, and suggest that complexity gradients have a greater control on mineralization than geological complexity itself. The qualitative basis for this conclusion is is sparse. The first two chapters of this thesis address these two issues. Chapter 1 explores the variation in clustering of mineral deposits over a study area and examines a series of potential geological controls on the clustering. These results are compared with weights of evidence analysis (Bonham-Carter et al., 1989; Groves et al., 2000; Mustard et al., 2004) to determine whether the geological factors controlling the clustering of the

deposits are the same factors controlling their localization. Chapter 2 investigates geological complexity and complexity gradients as controls on copper mineralization using a more rigorous method of analysis than has been used in previous studies, and suggests potential exploration targeting consequences.

One common criticism of fractal analysis of mineral deposit distributions is that the analysis does not take into consideration the variation of values assigned to the deposit such as the size and grade. Multifractals can be used to investigate the self-similarity of properties which show a spatial variation in value, and as such have been used as a complementary tool for examination of the distribution of mineral deposits (eg. Cheng et al., 1994; Agterberg et al., 1996; Sanderson and Zhang, 1999; Agterberg, 2001). Previous studies have shown that element concentrations can be modelled using multifractals (Agterberg et al., 1996; Cheng, 1999a; Agterberg, 2001; Xie and Bao, 2004). Production data has been examined using multifractal analysis for ore grade data on a mine scale (Roberts, 2005), and Cheng (1999b) has shown that categorized data for deposit size may fit a discrete multifractal model. However there has been no comprehensive multifractal study which investigates the both non-categorized ore tonnage and grade distributions on a regional scale. Various studies have shown that a theoretical model for describing the distribution of elements within the crust developed by de Wijs (1951), can be described using a multifractal model (eg. Xie and Bao, 2004; Agterberg, 2005). Yet no model exists to accurately describe the distribution of ore tonnage. Chapter 3 presents an expanded version of the de Wijs model for describing the distribution of ore tonnage and examines the multifractal characteristics of this model, and also compares the ore tonnage-grade relationship to that derived in previous studies. These theoretical models for describing ore tonnage and grade are then

compared to actual production data to determine whether the models can predict the characteristic multifractal and ore-tonnage grade relationships seen for the production data.

Numerical modelling of coupled deformation and fluid flow has been used to verify sites of importance for mineralization in both two-dimensional (eg. Matthäi et al., 2004; McLellan et al., 2004) and three-dimensional modelling space (eg. Gow et al., 2002; Sorjonen-Ward et al., 2002). Previous numerical modelling studies of strike-slip faulting have examined the variation of input geometry in two dimensions (Chester and Fletcher, 1997), or have investigated the effect of varying modelling parameters on three-dimensional fault geometries (Brankman and Aydin, 2004). However there has been no comprehensive study to examine the effect of varying fault geometry parameters of three-dimensional strike-slip fault models. Chapter 4 examines a series of fault geometries to determine how variation of a set of parameters effects specified outputs which can be used as proxies for the prospectivity of the models.

Though preliminary research shows that it may be possible (Sanderson and Zhang, 1999), it is not well established that the results of numerical modelling can be investigated using multifractal analysis, and as such, various outputs from the numerical models in this study were examined to determine if they could be described using multifractals. Discrete multifractal analysis of the dilation and integrated fluid flux outputs from several FLAC^{3D} © (Itasca Consulting Group, 2002) models indicates that these data can not be described by a discrete multifractal model as no distinct break between populations was observed. It is suggested that this is due to the lack of critical state phenomena which would produce a fractal scaling of features. As FLAC^{3D} is a

continuum code rather than a discrete element code such as UDEC © (Itasca Consulting Group, 2000), it may not be possible to define a critical state for the models, so these models cannot be described by multifractal models. Discussion of this point was originally intended for inclusion in Chapter 4, but the multifractal analysis was excluded from the chapter due to the negative results obtained. Future research could potentially examine outputs from a three dimensional discrete element code such as 3DEC © (Itasca Consulting Group, 1998), in which critical point phenomena might observed.

The overall aim of this study was to investigate the application of fractal and multifractal analysis to different facets of mineralized systems. This was achieved through four independent studies, each of which has direct implications for empirical exploration targeting in brownfields terrains or resource evaluation within the study area examined. The techniques used within each study are generic, so that it is possible to apply the methodology to other commodities and/or mineralized terrains.

These techniques are applied to mineral deposit data with a primary focus on copper deposits in the Mount Isa Inlier, Northwest Queensland, Australia. The Proterozoic Mount Isa Inlier is an ideal study area for investigating potential techniques for exploration targeting. With a rich exploration history, and comprehensive, up-to-date geological and mineral deposit databases available for analysis (Queensland Department of Mines and Energy et al., 2000; Queensland Department of Natural Resources and Mines, 2005), it is possible to test new techniques which are developed.

REVIEW OF FRACTAL AND MULTIFRACTAL TECHNIQUES

As this thesis is presented as a series of manuscripts for publication, it was not possible to include a detailed review of the techniques for fractal and multifractal analysis used for this project. A brief review of the techniques is presented below which details the algorithms used for analyzing the data. The relevance, application and modification of these algorithms is discussed within each manuscript presented in the thesis.

Fractal Analysis

The idea of fractal dimension was rigorously developed by Mandelbrot (1983). Unlike standard Euclidean geometry where all dimensions have integer values and which is used commonly in everyday life, fractal geometry allows for non-integer dimensions to describe the "fractional dimensions". The fractal dimension, *D*, is defined by Mandelbrot as

$$D = -\frac{\log N}{\log \mathrm{r(N)}}$$

where *N* is the number of self-similar shapes that cover an object and *r(N)* is the effective length of each of the self-similar shapes being used.

Knowledge of the fractal dimension of an object provides some insight into how the fractal that it describes occupies the space in which it resides (Barnsley, 1988). Given this information about several objects or datasets, it is possible to compare the results to see how they correlate.

The most common method for evaluating the fractal dimension for a given dataset is known as the box counting method. The aim of this method is to calculate the minimum number of boxes with a specified side length required to cover all points in

the dataset. Results can then be plotted to obtain the fractal dimension for the given dataset using the relationship

$$N(r) \propto r^{-D}$$

where *N(r)* is the minimum number of boxes with side length *r* needed to cover all the data.

Though brute force methods for finding the minimum number of boxes required to cover the data require more computing power, they provide a simple and effective way of generating results. One method is described by Carlson (1991) for calculating the fractal dimension for a set of hydrothermal precious metal deposits. For a given set of deposit locations, the algorithm can be specifed:

- Divide the study area into a grid of many square cells with every cell having the same dimension
- Count the number of cells containing at least one deposit
- Replace the current grid with a scaled version
- Repeat the second and third steps for a range of scaled grid sizes

The size of each of the cells used in this algorithm needs an upper and lower bound. An upper bound may be considered to be the size of a geological province and the lower bound the size of a single ore deposit. By repeating the scaling step for cell sizes from the upper bound to the lower bound, a good approximation of the fractal dimension for the dataset can be made. Given the size of the cell *r* (the side length of the square) at each step, the number of cells *N* that contain at least one ore deposit for that cell size is counted, and from a log-log plot of *N(r)* vs. *r*, the fractal dimension can be evaluated as the absolute value of the slope for the line-of-best-fit over the straightest part of the plot.

More computationally efficient box counting algorithms have also been developed (Liebovitch and Toth, 1989; Block et al., 1990). In a similar method to box counting, the fractal dimension of a dataset can be evaluated using a number-in-circle method (Carlson, 1991; Blenkinsop, 1994). Both the box counting and the number-in-circle methods have their respective advantages. However it has been shown that the box counting method generates results with higher correlation coefficients and lower regression errors than the number-in-circle method when deriving the value of D from the log-log graphs (Blenkinsop, 1994).

Multifractal Analysis

As previously described, fractal analysis is able to describe the spatial distribution of a given set of data points by assigning a fractal dimension. However many geological phenomena are characterized by a variation in a particular value at each data point. Multifractal analysis is able to investigate these datasets of points which have a value assigned to each point. An example of a multifractal is a topographic map where each contour line connecting similar altitudes defined a different fractal with a different fractal dimension (Gagnon et al., 2003).

Two different types of multifractals have been previously discussed; the continuous multifractal, and the discrete multifractal (Cheng, 1997). The method of moments technique for analyzing a continuous multifractal, and the concentration-area technique for analyzing a discrete multifractal, are discussed below for a two-dimensional dataset.

The method of moments technique for determining whether a two-dimensional dataset can be described by a continuous multifractal model takes a grid of equal sized boxes

(side length ε) which are placed over the study area. The number of boxes $N(\varepsilon)$ required to cover all the data points is recorded. If a box contains a single data point, the value of the data at that point is applied to the whole box. If a box contains more than one data point, the mean value of all the data points in the box is applied to that box. The measure for the i^{th} box, $\mu_i(\varepsilon)$, is set to the data value multiplied by the area of the box ε^2. Evertsz and Mandelbrot (1992) present the partition function $\chi_q(\varepsilon)$ for each box size and a range of real numbers q:

$$\chi_q(\varepsilon) = \sum_{i=1}^{N(\varepsilon)} \mu_i^q(\varepsilon)$$

The mass exponent function $\tau(q)$ can be estimated from a plot of q vs ε (Agterberg et al., 1996) by the relationship

$$\chi_q(\varepsilon) \approx \varepsilon^{\tau(q)}$$

$\tau(q)$ is plotted against q and three arbitrary values of q at x, y, and z are chosen for substitution into

$$\tau(\text{total}) = \tau(z) + \tau(x) - 2\tau(y)$$

If the solution to equation 3 is less than zero, the measures are considered multifractal (Cheng, 1999c). The function α can then be obtained by differentiating the mass exponent function with respect to q (Agterberg et al., 1996):

$$\alpha = \frac{\partial\{\tau(q)\}}{\partial q}$$

The multifractal spectrum $f(\alpha)$ is specified by the equation (Agterberg et al., 1996):

$$f(\alpha) = q\alpha - \tau(q)$$

If the plot $f(\alpha)$ vs. α is parabolic and satisfies the conditions outlined by Evertsz and Mandelbrot (1992), the distribution is a continuous multifractal.

Using the concentration-area technique, it is possible to determine whether the data can also be described by what has been termed a discrete multifractal (Cheng, 1999b). This technique places a grid of square boxes (with side length ε) over the study area. The value assigned to each box is determined in the same way as previously described for the continuous multifractal analysis. The area $A(\rho)$ is the number of boxes with box values greater than ρ, multiplied by the area of the box (ε^2). A log-log graph of $A(\rho)$ vs. ρ is then plotted. Threshold values for differentiating between different populations are seen where the slope of the graph changes. The fractal dimension for each population can then be evaluated using the least squares method with a fractal dimension α_1 below the threshold and α_2 above the threshold (Cheng et al., 1994).

STRUCTURE OF THE THESIS

This thesis is presented as four manuscripts which are either published/in press, submitted, or in preparation for peer review publication in international journals. Each manuscript is intended to be independent of the others and as such may be read in any order. The four chapters are summarized below.

Chapter 1 presents a new method for investigating the spatial distribution of mineral deposits. The aim of this study was to give a spatial context to the fractal distribution of mineral deposits using spatial variation of clustering and weights of evidence. This analysis results in the prediction of different outcomes for brownfields exploration. This new technique is applied to copper occurrences in the Mount Isa Inlier, and discusses whether the geological factors which control the clustering of the deposits are the same factors which control their localization. This manuscript has been published in *Ore Geology Reviews* (Ford and Blenkinsop, 2007a).

Chapter 2 aims to evaluate geological complexity and complexity gradients as controls on mineralization. An improved method for evaluating the geological complexity and complexity gradients is presented and applied to data from the Mount Isa Inlier. Results suggest that geological complexity could be considered a new control on copper mineralization within the study area and may be used as a new exploration targeting tool. This manuscript has been accepted for publication in a special issue on Conceptual Exploration Targeting in *Australian Journal of Earth Sciences*, and is currently in press (Ford and Blenkinsop, 2007b).

Chapter 3 examines improvements in quantitative models for predicting grade and tonnage distributions of mineralizing systems. An expansion of the de Wijs model (de Wijs, 1951) is presented to investigate the distribution of ore tonnage as well as grade. The tonnage-grade relationship and multifractal characteristics from the theoretical models are compared to those obtained from vein-hosted gold deposits in the Archaean Zimbabwe craton. This manuscript has been submitted to *Mineralium Deposita*.

Chapter 4 investigates coupled deformation and fluid-flow around simple strike-slip fault geometries using FLAC^{3D} © (Itasca Consulting Group, 2002), with applications to mineral prospectivity. Fault bend, and fault jog geometries, as well as contrasts in lithology, are examined to determine how variation of different fault system parameters affect the models. Outputs from the models are analyzed to evaluate which geometries are the most prospective. This manuscript is currently in preparation for submission to *Geofluids*.

The conclusions chapter discusses how fractal and multifractal techniques can be used to improve exploration targeting and resource evaluation. A summary of the conclusions from each of the four manuscripts contained within this thesis including avenues for further expanding on the research conducted within this project are presented.

SECTION A

Combining fractal analysis of mineral deposit clustering with weights of evidence to evaluate patterns of mineralization: Application to copper deposits of the Mount Isa Inlier, NW Queensland, Australia

ABSTRACT

The clustering of mineral occurrences and their spatial associations with particular geological features are critical aspects of mineral distributions for exploration and understanding ore genesis. Variations in the degree of clustering of mineral occurrences or geological features can be measured by fractal dimensions, obtained from a shifting-box counting method. Spatial associations between mineral occurrences and geological features can be quantified by the weights of evidence (WofE) method using the contrast value, which increases with the strength of the spatial relationship. A new method is proposed to evaluate mineral occurrence distributions by combining the power of fractal analysis of clustering with the WofE approach. The method compares the correlation between the variation in degree of clustering of mineral occurrences and a geological feature in a study area, with the contrast value of the same feature. The possible outcomes can be simplified into four scenarios, depending on whether the correlation in variation of clustering, and the contrast, are high or low, respectively. Each outcome has specific exploration implications. If either a high correlation in variation of clustering or a high contrast value is obtained, the geological feature can be used for exploration targeting.

The integrated fractal and WofE approach is applied to copper occurrences in the Proterozoic Mount Isa Inlier, NW Queensland, Australia, which hosts large numbers of copper deposits (1,869 occurrences), including the world class Mount Isa copper deposit. Variation in clustering of copper occurrences has a positive correlation with variation in clustering of fault bends (R=0.823), fault intersections (R=0.862), and mafic rocks (R=0.885). WofE results indicate that the copper occurrences are spatially associated with fault intersections and bends, and with mafic rocks. Analyses were carried out separately for the two major lithostratigraphic sequences in the Inlier, the

Eastern and Western Successions. The Western Succession copper occurrences are apparently more clustered than those of the Eastern Succession, which may reflect a lower degree of exploration and/or geological factors. The association of copper occurrences with mafic rocks compared with fault bends and intersections is greater in the Eastern Succession, which may reflect genetic factors. Correlations in the variation of clustering of mineral occurrences and geological features have a linear relationship with the contrast values, and the spatial association between all geological features and copper occurrences constitute high correlation/high contrast cases. The linear relationship suggests that the geological features that control the clustering of the copper occurrences could be the same features that control their localization.

INTRODUCTION

Perhaps the most obvious feature of any map of mineral deposits is that they exhibit some degree of clustering. Following Mandelbrot's (1983) suggestion that mineral deposits in the Earth's crust have a fractal distribution, Carlson (1991) showed that the clustering of mineral deposits can be sensitively measured by fractal methods, and also proposed genetic interpretations for the fractal dimensions obtained from these analyses. Evidence for a fractal distribution of mineral deposits has been adduced for gold and precious metals (Carlson, 1991; Agterberg et al., 1996; Blenkinsop and Sanderson, 1999; Kreuzer et al., 2007) and preliminary results suggest that base metal distributions may also be fractal (Blenkinsop and Oliver, 2003; Butera, 2004).

Fractal analyses of clustering of mineral deposits have generally attributed a single, global fractal dimension to the data sets studied. This approach cannot give a spatial context to the clustering of mineral occurrences within the study area, and does not

indicate variations in clustering. Blenkinsop and Sanderson (1999) examined fractal dimensions for various subsets of data from gold deposits of the Zimbabwe Craton, and suggested that spatial variation in fractal dimension might have exploration implications. This approach is developed further here.

By contrast with fractal analysis of clustering of mineral deposits, the weights of evidence (WofE) approach emphasizes spatial context by focusing on geological features that may have localized mineral deposition, and this method has been widely applied to exploration (e.g., Bonham-Carter et al., 1989; Agterberg and Bonham-Carter, 1990; Agterberg et al., 1993; Bonham-Carter, 1994; Carranza et al., 1999; Raines, 1999; Harris et al., 2000; Boleneus et al., 2002; Billa et al., 2004). Although alternative methods such as neural networks and fuzzy logic have been introduced (e.g., Cheng and Agterberg, 1999; Singer and Kouda, 1999; Brown et al., 2000, 2003; Knox-Robinson, 2000), and the relative merits of these different methods have been discussed (e.g., Agterberg and Bonham-Carter, 2005), the weights of evidence method remains popular, especially among practitioners who favor an empirical, data-driven approach to prospectivity. Other reasons for the popularity of the WofE approach to prospectivity include that the method is statistical, it is easily understood by non-specialists, it outputs probabilities explicitly, and there are GUI software packages available to perform the calculations.

Determination of how clustered mineral occurrences are, and their spatial association with particular geological features, are critical for exploration and ore genesis. These characteristics of mineral occurrences can be interpreted in terms of potential controls on the distribution of the occurrences, and can be used to rank these controls.

The primary aim of this study is to present and test a new method of analyzing mineral deposit distributions that combines the power of the fractal geometry to describe the clustering of mineral deposits, with the weights of evidence approach that describes their spatial associations. The method is applied to copper mineralization in the Mt Isa Inlier, NW Queensland, Australia. Ancillary aims of the study are to establish whether copper deposit distribution can be described by fractals, and to examine the spatial variation in degree of clustering of the copper occurrences. The approach of this study addresses a critical question for understanding the genesis of mineral deposits, and for exploration: are the features that controlled the degree of clustering of the copper occurrences the same features that localized them?

The Mount Isa Inlier is selected for this study as it contains a wide range of base and precious metal deposits coupled with a long exploration history, and because the geological and mineral data are appropriate for analyzing the spatial distribution of mineral occurrences. Copper is particularly suitable because of the large number of mineral occurrences.

GEOLOGY AND MINERAL DEPOSITS OF THE MOUNT ISA INLIER

The Mount Isa Inlier, in NW Queensland, Australia, is a significant Proterozoic base metal province covering an area in excess of 50,000 km², containing a variety of mineral deposit types, such as copper, copper-gold, gold, uranium and stratiform lead-zinc-silver. Significant mineral deposits include the Mount Isa copper deposit with resources prior to mining of 225 Mt ore at a grade of 3.3% Cu, the Ernest Henry Cu-Au deposit with 127 Mt at 1.1% Cu and 0.55g/t Au, the Mary Kathleen U-REE deposit

containing 9.5 Mt of ore at 0.131% U_3O_8 and the Cannington Pb-Zn-Ag deposit containing 43.8 Mt of ore at 11.6% Pb, 4.4% Zn and 538g/t Ag (Queensland Department of Mines and Energy et al., 2000). This study focuses on the spatial distribution of copper-only deposits (excluding copper-gold and iron-oxide-copper-gold deposits). Exclusion of copper-gold and iron-oxide-copper-gold (IOCG) deposits is due to the potentially different controls on mineralization, with one example being the Osborne IOCG deposit which is considerably older than the copper-only deposits within the Mount Isa Inlier (Williams, 1998).

The Mount Isa Inlier is divided into three tectonic units (Fig. 1). From west to east these are the Western Fold Belt, the Kalkadoon-Leichhardt Belt, and the Eastern Fold Belt (Blake et al., 1990). Because some differences have been suggested between the characteristics of mineral deposits in the East and West of the Inlier, mineral occurrences are sub-divided into two groups in this study: those within the Eastern Succession, including the Eastern Fold Belt, which are mainly shear and fault controlled vein copper deposits; and those within the Western Succession, including the Kalkadoon-Leichhardt Belt and the Western Fold Belt, which are mainly brecciated, sediment-hosted copper deposits (Blake et al., 1990). The terms Eastern Succession and Western Succession are not synonymous with the Eastern Fold Belt and Western Fold Belt, respectively. The split between the Eastern and Western Successions is essentially lithostratigraphic (Blake and Stewart, 1992), and the boundary was positioned at the western margin of the Eastern Fold Belt. Additional support for this position is the interpretation of this margin as a possible terrain boundary (McDonald et al., 1997).

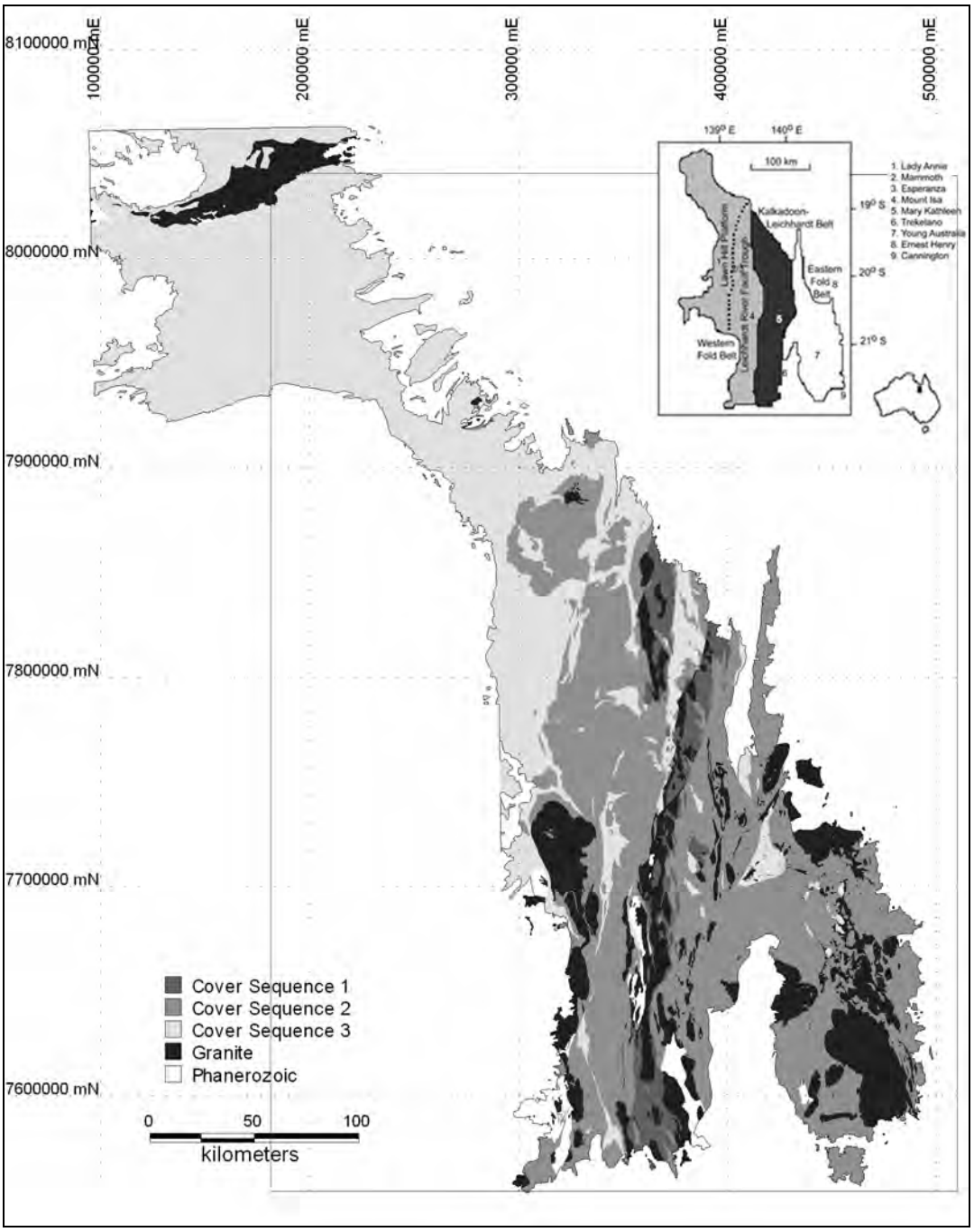

Figure 1: Simplified geological map of the Mount Isa Inlier with box showing outline of entire study area (Queensland Department of Mines and Energy et al., 2000). Inset shows the location of the tectonic belts and major deposits.

Rocks in the Mt Isa Inlier recorded two major orogenic events: the Barramundi Orogeny (ca. 1870 Ma), and the Isan Orogeny (ca. 1600 to 1500 Ma); (O'Dea et al., 1997) (Fig. 2). Relicts of the Barramundi Orogeny outcrop in the older basement sequences of the Kalkadoon-Leichhardt Belt. Deposition of sedimentary cover sequences 1, 2, and 3 postdated the Barramundi Orogeny and predated the Isan Orogeny (Blake et al., 1990). Cover sequence 1 is generally thought to have been deposited in the interval 1870 to 1850 Ma, cover sequence 2 from 1790 to 1720 Ma and cover sequence 3 from 1680 to 1600 Ma (Blake and Stewart, 1992; Williams, 1998). The D_2 EW-shortening event (ca. 1590 Ma; Fig. 2) was responsible for formation or reactivation of the dominant NS-striking structures in the Mount Isa Inlier (Bell et al., 1988; Laing, 1998). Upright, D_2 kilometre-scale folds with generally northerly-striking axial surfaces are prominent throughout the inlier. Major deformation zones and geophysical lineaments occur in this orientation, and also strike NE and NW. Several of these may have formed as basin-bounding faults during deposition of the cover sequences, and they may have been reactivated as reverse faults during the Isan Orogeny (Queensland Department of Mines and Energy et al., 2000). Folds and crenulations of D_2 fabrics, and foliations in and around plutons intruded at ca. 1550 to 1500 Ma indicate that broadly E-W shortening continued for a substantial period after D_2: these deformations are collectively referred to as D_3 (cf. Rubenach, 2005; Fig. 2). Faults in the Eastern Succession commonly strike N to NW and are generally straighter than those in the Western Succession. Faults in the Western Succession are less dense and are generally longer N to NE striking structures.

The distribution of the cover sequences, and their propensity to host copper deposits, varies throughout the inlier. The copper deposits are hosted within both cover sequence 2 and 3 rocks. In the Western Succession, the Lawn Hill platform (Fig. 1), which hosts

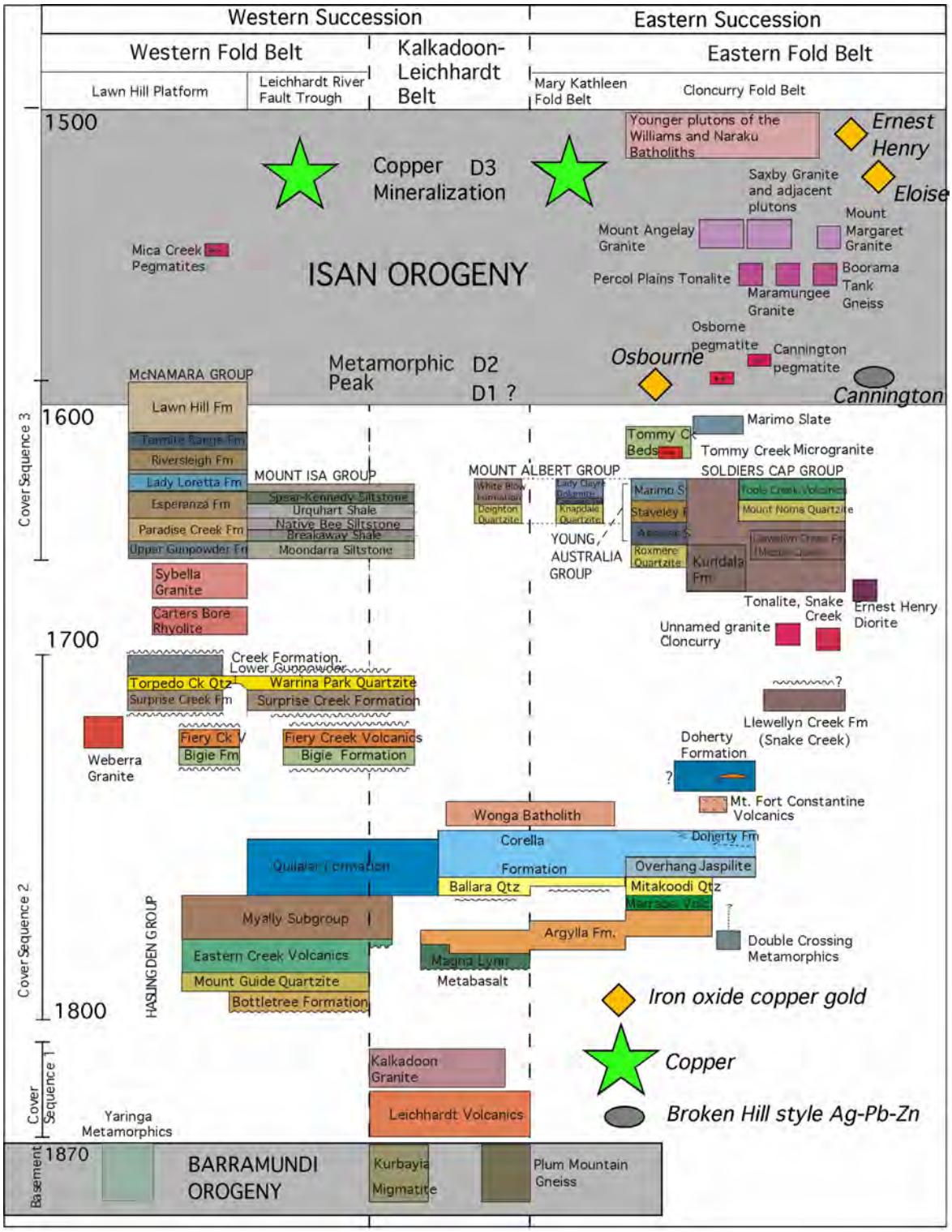

Figure 2: Chronostratigraphic framework of the Mount Isa Inlier (modified after Figure 3 of Foster and Austin, 2005), showing cover sequence deposition, major mineralization (Baker and Laing, 1998; Chapman and Williams, 1998; Williams, 1998; Baker et al., 2001), and orogenic events.

the Lady Annie copper deposit (Fig. 1), consists predominantly of sideritic and locally carbonaceous shales, mudstones and sandstones of the McNamara Group in cover sequence 3 (Feltrin et al., 2003). In the Leichhardt River fault trough (Fig. 1), the stratigraphy of the Western Succession is more complex. The Urquhart Shale (carbonaceous, pyritic, dolomitic siltstone) of cover sequence 3 is host to the Mount Isa Cu deposit, and lies above the Eastern Creek Volcanics (metabasalts) of cover sequence 2 (Wyborn, 1987; Williams, 1998). However, the Mammoth copper deposit is hosted by the Myally Subgroup (quartzite, sandstone, and siltstone) of cover sequence 2 (Scott and Taylor, 1982). Felsic volcanic rocks of cover sequence 1 and the Kalkadoon and Ewen batholiths dominate the stratigraphy in the Kalkadoon-Leichhardt Belt, and do not contain any economic copper deposits (Blake and Stewart, 1992). The calcsilicate Corella Formation in the western part of the Eastern Succession hosts the Trekelano deposit (Williams, 1998). The Williams-Naraku batholiths, the Corella and Doherty Formations (calcsilicate rocks) and the Soldiers Cap Group (siliciclastic metasediments and metabasalts) are the dominant units in the eastern part of the Eastern Fold Belt. The latter is host to many small Cu deposits such as Young Australia (Blake et al., 1990).

Both stratigraphy and structure have been suggested as controls on copper mineralization in the Mount Isa Inlier (e.g., Bell et al., 1988; Laing, 1998; Williams, 1998). Copper mineralization styles vary between the Western and Eastern Succession. In the Western Succession copper deposits are hosted by brecciated sediments adjacent to faults. Mineralization is localized on N- and NNE-striking structures such as the Mount Isa and the Mount Gordon fault zones, which contain appreciable amounts of copper (Scott and Taylor, 1982; Nijman et al., 1992). In the Eastern Succession, vein and breccia style copper deposits occur in shear zones and faults (Laing, 1998;

Marshall, 2003). Many copper deposits in the Eastern Succession are spatially associated with faults, with the larger deposits such as Eloise, Osborne and Kuridala copper-gold deposits being hosted by N- to NW-striking regional structures such as the Mt Dore fault zone (Blake et al., 1990; Laing, 1998).

Copper mineralization may have occurred late in the Isan Orogeny with timing suggested as syn-D_3 in both the Eastern and Western Successions (Williams, 1998; Queensland Department of Mines and Energy et al., 2000). Structures produced or reactivated during the Isan Orogeny thus have potential to host epigenetic mineral deposits. There is also potential for metals to have been remobilized due to later fault reactivation throughout the Mount Isa Inlier. Fault reactivation is known to have occurred as late as the Cambrian and Ordovician (Feltrin et al., 2003; Mark et al., 2004).

In the Western Succession, the source of the copper for the world class Mount Isa copper deposit and the significant Mammoth and Esperanza deposits in the Gunpowder area has been attributed to the Eastern Creek Volcanics (Scott and Taylor, 1982; Wyborn, 1987; Matthäi et al., 2004). Though the source of the copper for base metal deposits in the Eastern Succession is a contentious issue, recent work on IOCG deposits suggests that the mafic rocks of the Soldiers Cap Group rather than the Williams and Naraku batholiths (cf. Oliver et al., 2004; Mark et al., 2006) may be implicated (Butera and Blenkinsop, 2004).

Butera (2004) suggested that regionally extensive brines in the Mount Isa Inlier leached sulfur and possibly copper from mafic dykes prior to ore deposition and close to major extensional basement structures and D_3 faults. Mafic rocks can also potentially provide

the rheological contrast necessary for entrapment of mineralizing fluids. Fault bends (e.g., Cox, 1999; Allibone et al., 2002a, b) and fault intersections (e.g., Craw, 2000; Twomey and McGibbon, 2001; Allibone et al., 2002a, b; Nie et al., 2002; Cox, 2005) could have focused fluids and localized ore deposition. Mafic rocks and NW-, N- and NNE-striking faults or shear zones and their bends and intersections may therefore have been critical factors in localizing copper mineralization in the Mount Isa Inlier (cf. Phillips et al., 1996; Twomey and McGibbon, 2001; Butera, 2004; Mustard et al., 2004).

DATA AND METHODS

Copper occurrences and geological data

The spatial distribution of 1,869 copper occurrences was examined on the basis of the Queensland Mineral Resources Database, MINOCC, (Queensland Department of Natural Resources and Mines, 2002). The database categorizes mineral occurrences using attributes that include commodity, mineralogy, host rock type, age, tonnage, and grade. All entries containing copper as the main commodity were extracted from the database for use in this study, excluding those which also contained gold. This selection was made because the deposits containing gold potentially have different controls. The existence of the wealth of data in the Queensland Mineral Resources database makes the Inlier particularly suitable for this study. Locations of the copper occurrences used in the analysis are shown in Fig. 3.

Fault bends, fault intersections and mafic rocks were investigated as potential controls on copper mineralization as they had already been shown to be important factors for copper mineralization (Blenkinsop, 2005). The Northwest Queensland Mineral Province

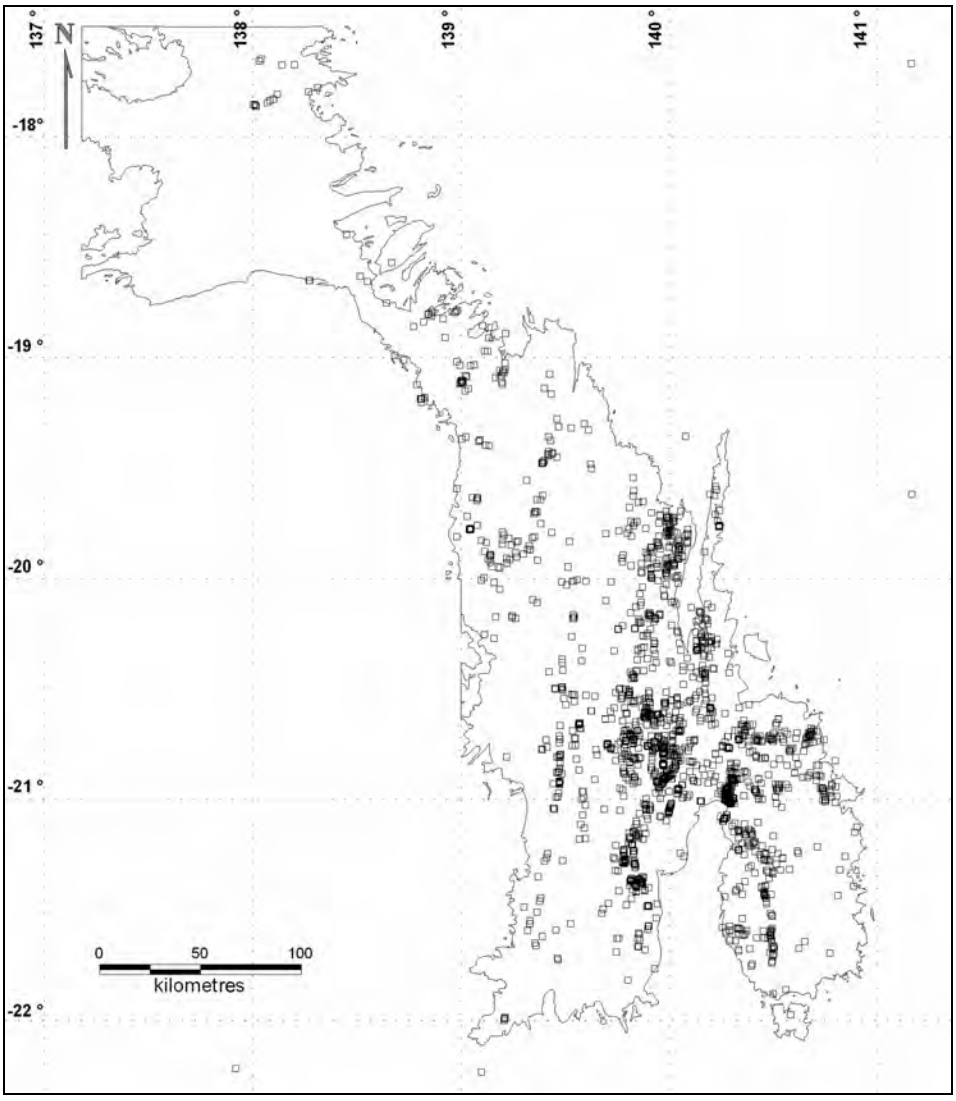

Figure 3: Copper occurrences (n = 1,869) in the Mount Isa Inlier, after MINOCC database, December 2002 (Queensland Department of Natural Resources and Mines, 2002).

Report (NQMPR) (Queensland Department of Mines and Energy et al., 2000) contains a database of faults divided into segments. These segments were combined to provide a comprehensive database of continuous, individual faults suitable for analysis. All fault intersections and fault bends (bends were defined as changes in strike between 5º and 45º) were extracted to point data using the MapInfo – Spatial Data Modeller © package from Avantra Geosystems. Fault bends were located as the mid-point along a given bend within the database in both clockwise and anti-clockwise directions. Equally spaced nodes were extracted from the outlines of the mafic rocks in the study area using Encom's Discover © software in order to perform the fractal analysis on point data of this geological feature for fair comparison with the results of fractal analysis of the point data for the fault intersections, fault bends, and mineral occurrences.

Fractal analysis of mineral occurrence and geological clustering

The log-log approach was used to find the box counting fractal dimension (Mandelbrot, (1985). The number of square boxes N with side length r required to cover all the mineral occurrences in the study area is counted as a function of r, and the fractal dimension, d, is given by the relationship:

$$N(r) = k(1/r)^d$$

A graph of $log(N(r))$ versus $log(r)$ was plotted and a linear regression was performed on the straightest part of the line of best fit, with the regression limits chosen to fit the straightest part of this line. If the deposits have a fractal distribution, the plot produces a straight line with a slope d. In all cases, the largest box size was ignored because its side length r was determined by the size of the study area. This is referred to as the global box counting method as it calculates a fractal dimension for the entire study area (e.g., Carlson, 1991). A random distribution of occurrences would produce a d value of 2 and,

as the deposits become more clustered, the value of *d* approaches zero. However, this method does not describe how clustering may vary within the study area.

A study area of 506.6 km x 334.6 km was used to analyze the spatial variation of clustering across the Mount Isa Inlier (cf. Hodkiewicz et al., 2005). Fractal dimensions were calculated for copper occurrences within boxes with a side length of 126.65 km (¼ of the size of the largest box size used in the global box counting method). This box size was chosen in order to contain a large enough sample of copper occurrences to calculate a reliable value for *d*. The box was shifted in steps of 50 km across the study area so that there is some overlap between the shifting boxes, and fractal dimensions were calculated for each box containing 10 or more copper occurrences. This number was determined by examining the log-log plots of *N(r)* versus *r* for several locations with a small number of occurrences. For areas containing less than 10 occurrences, the results were too erratic for the linear regression to be performed accurately. Examining a sample of the remaining graphs allowed regression limits to be chosen between 7.5 km and 75 km, automatically excluding the largest box size. By choosing these regression limits, the issue of roll-off (Blenkinsop and Sanderson, 1999) was avoided. The roll-off effect occurs on the log-log plot of *N(r)* versus *r*, where for small box sizes the data deviate from the straight line as indicated in Fig. 4. Two sample graphs obtained from the shifting box counting method applied to the spatial analysis of copper occurrences are shown in Fig. 4.

A contour map was generated to visualize the variation in the fractal dimension across the study area (Fig. 5). Values for the contouring were located at the centre of each of the shifting boxes. Null fractal dimension values arising from insufficient copper

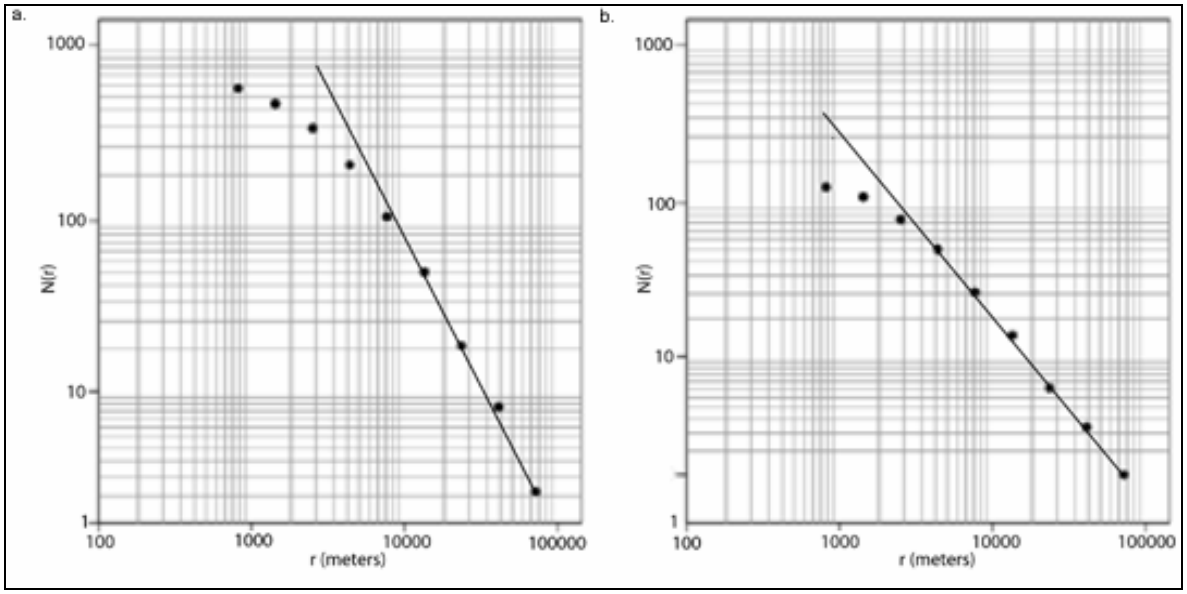

Figure 4: Examples of graphs of number of boxes N(r) against box side length (m) on logarithmic scales using the shifting box method to count copper occurrences. The roll-off effect occurs where plot deviates from the plotted straight line for small box sizes.

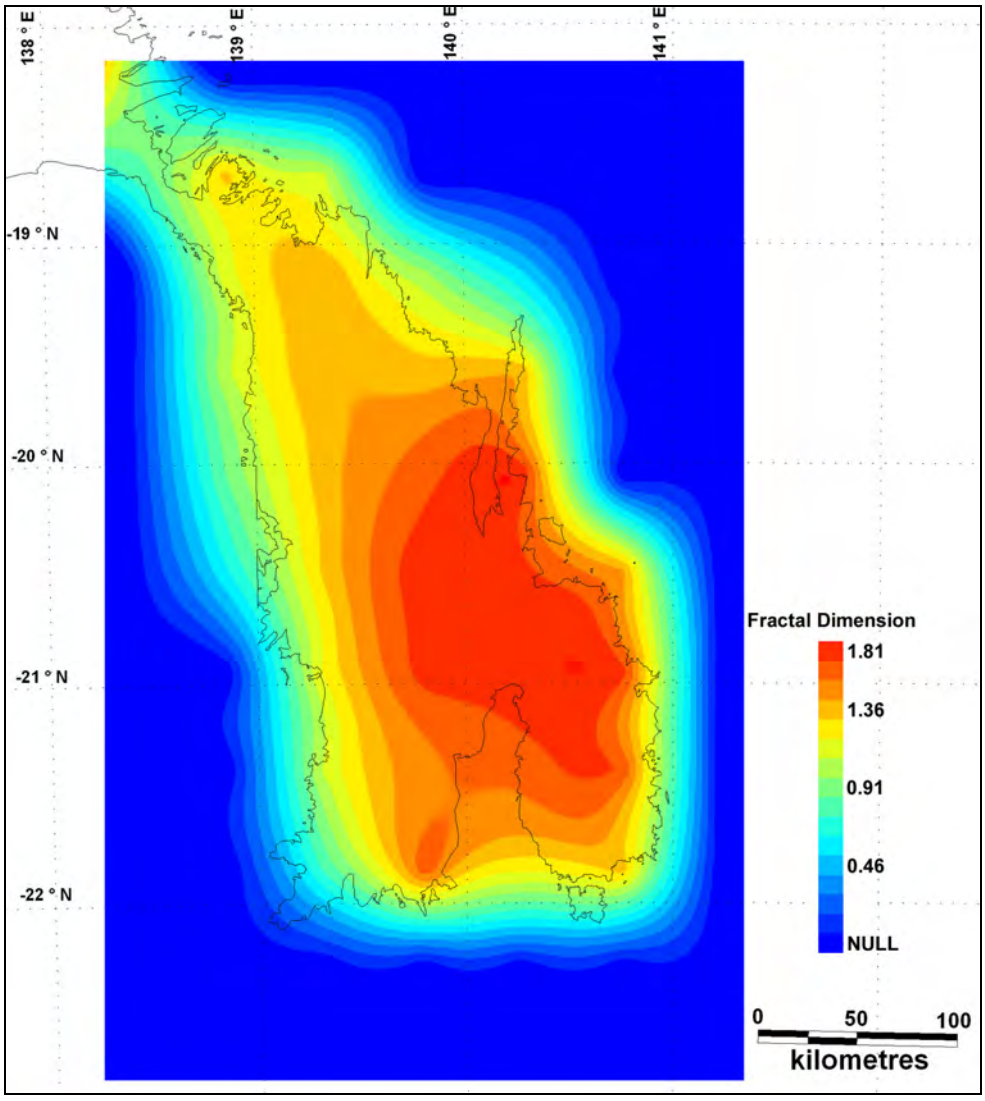

Figure 5: Contour plot of the fractal dimension that measures clustering of copper occurrences determined using the shifting box counting method with a box size of 126.65 km in the Mount Isa Inlier. Apparent variation in contouring outside the area of outcrop is due to the contouring method used, nearest neighbor contouring, which has the least sensitivity to copper occurrences outside the colored area.

occurrences in the shifting box were excluded from the contour map and further analysis of the clustering.

Weights of evidence (WofE) approach

The degree of spatial association between features on two or more binary maps can be quantified by the contrast value in WofE analysis (Bonham-Carter, 1994). The contrast value (C_w) can be found from the relation

$$C_w = ln\ O(B|A) - ln\ O(B|\bar{A})$$

where $O(B|A)$ are the odds of B occurring given the presence of A, and $O(B|\bar{A})$ are the odds of B occurring given the absence of A. This value compares the spatial association of two particular features (e.g., copper occurrences and fault intersections) with that expected from a random distribution of these features, which would give a contrast value of zero. Contrast values above 0.5 are considered to be indicative of a significant spatial association between two features (Wang et al., 2002).

Weights of evidence analysis was performed on the data using the MapInfo – Spatial Data Modeller © software package (Avantra Geosystems) to determine the spatial correlation between copper occurrences and the same geological features examined in the fractal analysis. Buffers around the features were varied from 0 to 3 km to determine the buffer distance that gave the optimum contrast value, as judged by the maximum value. A confidence value was also calculated for each contrast value, calculated as the contrast value divided by its standard deviation (Bonham-Carter, 1994).

A new method for evaluating the spatial distribution of mineral deposits: integrated fractal and WofE analysis

Degrees of clustering were determined for selected geological features by their fractal dimension in each of the shifting boxes, and then compared to the clustering of mineral occurrences in the same boxes by Pearson's correlation coefficient. The spatial association of these geological features with the copper occurrences was measured by their contrast. Fractal analysis of clustering was combined with the weights of evidence approach by plotting the correlation coefficient for the variation of clustering against the contrast value for each geological feature. Four schematic maps representing the range of possible outcomes are superimposed onto the graph for such a plot in Figure 6. In the top right of the diagram, high correlation coefficients are combined with high contrast values: since the geological feature coincides everywhere with the occurrences, they have the same variation in clustering. The top left part of the diagram shows geological features that have similar degrees of clustering as the mineral occurrences, but are not spatially associated with them. The lower right part of the diagram shows a geological feature that is spatially associated with occurrences, but has a different degree of clustering, typically where the numbers of occurrences and geological features are dissimilar. The lower left part of the diagram shows a geological feature that has different degrees of clustering and a lack of spatial association with the occurrences. The plot in Fig. 6 is a therefore a way of evaluating controls on clustering and the spatial association of mineral occurrences with geological features.

Limitations of the analysis

As this study deals with spatial data analysis, the quality of the input data is critical to generating and interpreting the results accurately. Potential limitations include

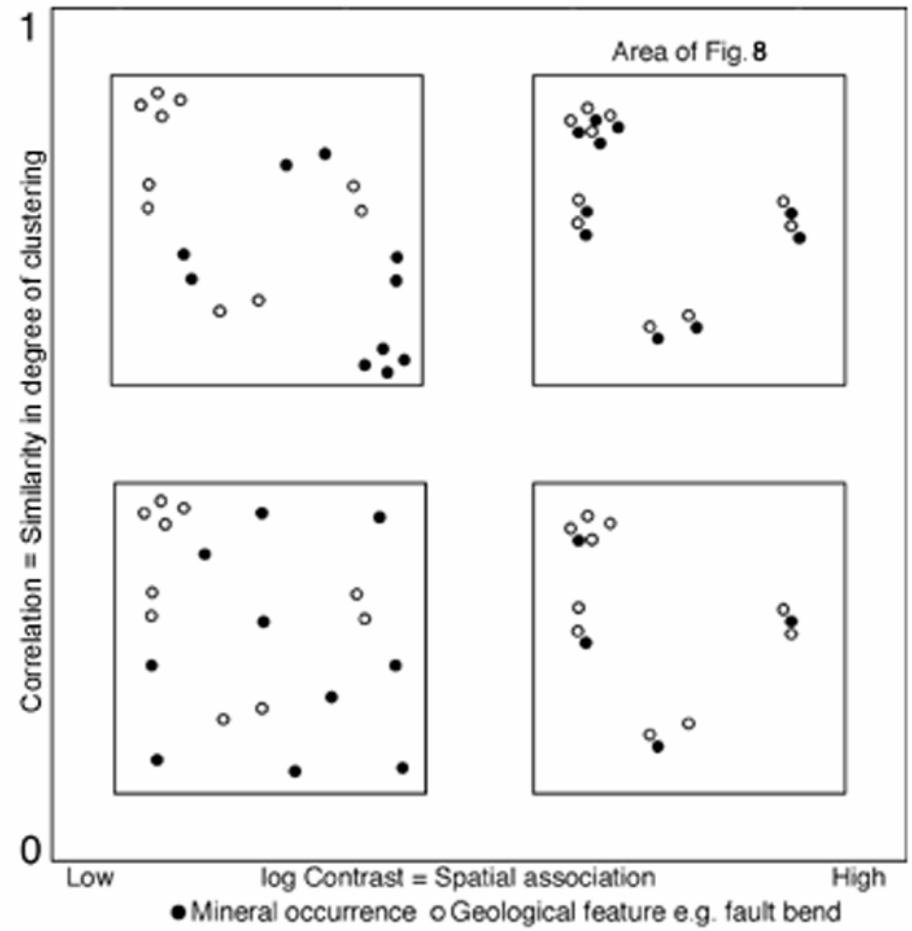

Figure 6: Schematic illustration of four possible natural outcomes from combining fractal and weights of evidence analyses. The y-axis shows the correlation between the variation in degree of clustering of a geological feature (e.g., fault bends) with mineral occurrences, and the x-axis shows the log of the contrast which is a measure of the spatial association of the feature with mineral occurrences. Each panel illustrates a map pattern that characterizes the relevant part of the graph. Open circles are geological features, closed circles are mineral occurrences. Most data in this study plots in top right of the diagram i.e., the features have both similar degrees of clustering and high spatial association with copper occurrences and this panel is schematic of the data seen in Figure 8.

variations in the quality and homogeneity of mapping, the degree of outcrop, and that the study was only done in 2D (Bardossy and Fodor, 2001).

The quality of mapping should not be a problem since only mafic intrusive and extrusive rocks have been used in the analysis, and there is no reason to doubt that the mapping identified such distinctive rocks correctly. The issue of the homogeneity of the mapping was addressed by using only geological data from the Northwest Queensland Mineral Province Report (Queensland Department of Mines and Energy et al., 2000). With a uniform scale and source of mapping, any obvious potential heterogeneities were avoided.

The Palaeozoic and younger rocks that overly the Proterozoic inlier in places could, potentially, have some bearing on the results. Any such effects of cover can not be easily quantified. This study compares copper occurrences with geological features, and there is no clear evidence to suggest that cover affects the distribution of the copper occurrences more than the geological features or vice versa. Confidence in the value of the fractal dimension would be diminished by increasing levels of cover, but it is not clear whether the value of the fractal dimension would change as a result. Although the weights of evidence method is sensitive to cover due to areas that contain neither mineral deposits nor the feature being examined (Bonham-Carter, 1994), this does not represent a problem in this study because the faults have been interpreted under cover, and the contrast values for the mafic rocks were not calculated in covered areas.

RESULTS: COPPER OCCURRENCES OF THE MOUNT ISA INLIER

Fractal analysis of clustering

The global fractal dimension box counting method for all copper occurrences in the study area (Fig. 7) yields a fractal dimension of 1.36, a correlation coefficient between log $N(r)$ and log r of 1.000 and standard error of regression of 0.02 (Table 1). Box counting gave fractal dimensions of 1.39 and 1.29 in the Eastern and Western Successions respectively (Table 1), a difference that is outside the errors of regression, and that apparently indicates more clustering in the Western Succession. Small box sizes were excluded from the regression as they can lead to inaccuracy in the calculation due to roll-off effects with the regression limits listed in Table 1 (Blenkinsop and Sanderson, 1999).

Fractal dimensions calculated for the copper occurrences by the shifting box counting method in the ~127 km squares within the Mt Isa Inlier range from 0.59 to 1.79, indicating that there is a significant variation in the clustering of the occurrences within the study area (Fig. 5).

Correlations between the variations in clustering of the copper occurrences and the variations in clustering of the fault bends and intersections, and between variations in clustering of copper deposits and mafic rocks within the Eastern and Western Successions are listed in Table 2. Spatial variation in the clustering of the copper

Table 1: Global fractal dimensions (d) for copper occurrences in the study areas examined showing number of occurrences (N), correlation coefficient (R) and standard error of regression (E).

Study Area	*N*	*d*	*R*	*E*	Regression Limits
Mt Isa Inlier	1869	1.36	1.000	0.02	15.83km – 253.30km
Eastern Succession	1412	1.39	0.999	0.04	7.92km – 63.33km
Western Succession	457	1.29	0.999	0.04	15.83km – 126.65km

Note: The regression limits were chosen from the straightest part of the log r versus log $N(r)$ graph.

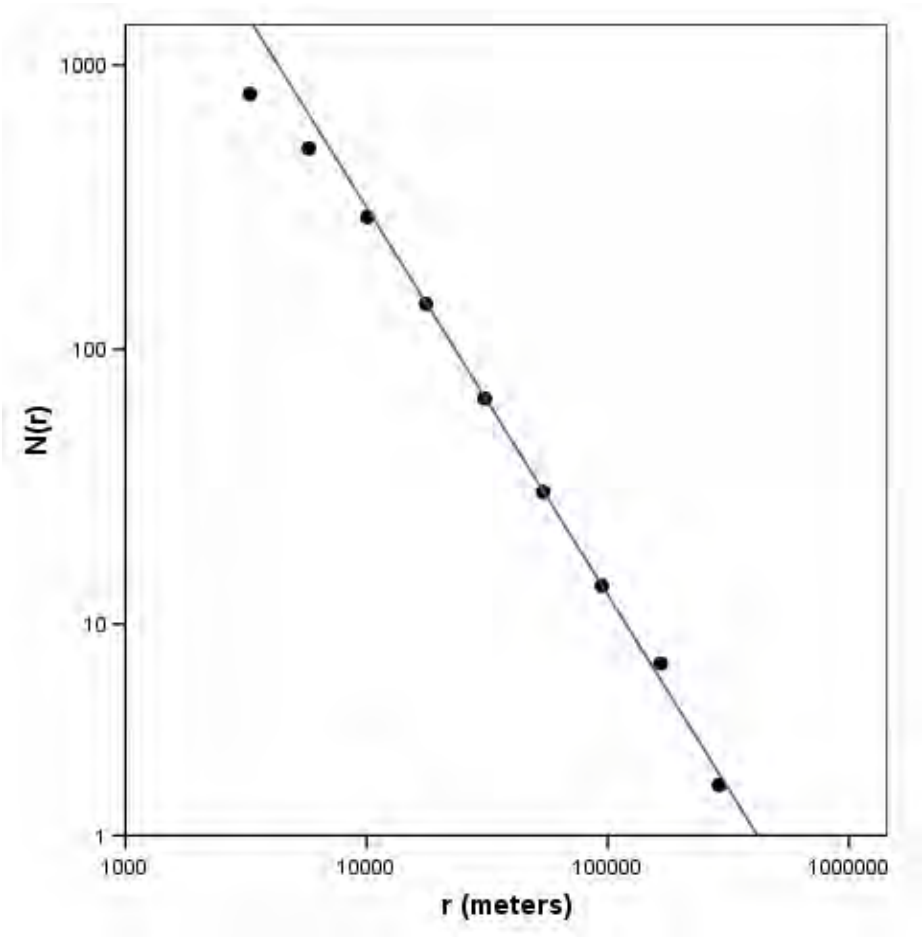

Figure 7: Graph of number of boxes N(r) against box side length (in meters) on logarithmic scales for Cu occurrences in the Mt Isa Inlier. Line of best fit is illustrated.

Table 2: Results of correlation between clustering of copper occurrences and clustering of geological features using fractal analysis, and contrast values obtained from weights of evidence analysis with corresponding confidence values.

Location	Cu occurrences correlated with	Correlation	Contrast	Confidence
Eastern Succession	Fault Bends	0.696*	0.798	2.249
	Fault Intersections	0.658*	0.617	3.332
	Mafic Intrusions	0.885*	0.536	3.723
	Mafic Intrusions+Extrusions	0.600	0.567	4.261
Western Succession	Fault Bends	0.823*	1.469	2.921
	Fault Intersections	0.862*	2.330	4.006
	Mafic Intrusions	0.670	0.623	1.208
	Mafic Intrusions+Extrusions	0.620*	0.460	1.883
	Mafic Extrusions	0.604*	0.643	1.989

Note: * indicates significance at the 95% confidence level.

occurrences has a higher correlation with the variation in clustering of fault bends for the whole Inlier than any of the other geological features analysed. Mafic extrusions in the Eastern Succession were not analysed as there were not enough mafic extrusions present within the study area to perform the analysis. In the Eastern Succession, the highest correlation exists between the variation in clustering of the copper occurrences and mafic intrusions, while in the Western Succession the highest correlation is with the fault intersections. The correlations with fault geometry in the Western Succession (0.823 for fault bends and 0.862 for fault intersections) are appreciably higher than with fault bends and intersections in the Eastern Succession (0.696 and 0.658, respectively).

Weights of evidence

Results from the weights of evidence analysis are listed in Table 2. The strongest spatial relationships, as indicated by the highest contrast values, are between fault bends and intersections and copper occurrences for both the Eastern and Western Successions. Fault bends in the Eastern Succession have the highest contrast value (0.798) with the copper occurrences, whereas in the Western Succession, the fault intersections have the highest contrast value (2.330). With one exception, all contrast values are greater than 0.5 and are therefore statistically significant (Wang et al., 2002).

Integrated fractal and weights of evidence analysis

Figure 8 illustrates the correlation coefficients obtained from the fractal analysis between the variation in clustering of copper occurrences and geological features listed in Table 2 plotted on a log-normal graph against the contrast values obtained from the weights of evidence analysis. Figures 6 and 8 are plotted on the same axes with Figure 8 representing the top right hand corner of Figure 6. Figure 8 shows a linear trend between the results from the fractal analysis and the results from the weights of evidence analysis. A value of 0.683 (significant at the 95% confidence level) was obtained for Spearman's rank correlation coefficient between the correlation of variation in clustering and the log of the spatial association (i.e., contrast), indicating that the log-normal relationship between fractal analysis and weights of evidence analysis is significant. A rank correlation of 0.953 was obtained when only the data plotting in the top right of Figure 6 was examined.

DISCUSSION

Fractal distribution of copper occurrences and their spatial variation

The global fractal dimensions in Table 1 indicate that fractal analysis is a viable tool for the spatial analysis of copper occurrences in the Mt Isa Inlier. The correlation coefficient from the box counting regression for D for the entire Mount Isa Inlier (R=1.000) appears to be the highest reported for fractal distributions of mineral deposits (Carlson, 1991; Blenkinsop, 1994; Blenkinsop and Sanderson, 1999; Blenkinsop and Oliver, 2003). Figure 5 displays significant variation in the fractal dimension for the copper occurrences from the global value across the Mount Isa Inlier. This variation permits analysis of geological features that may have controlled the level of clustering of copper occurrences in the study area.

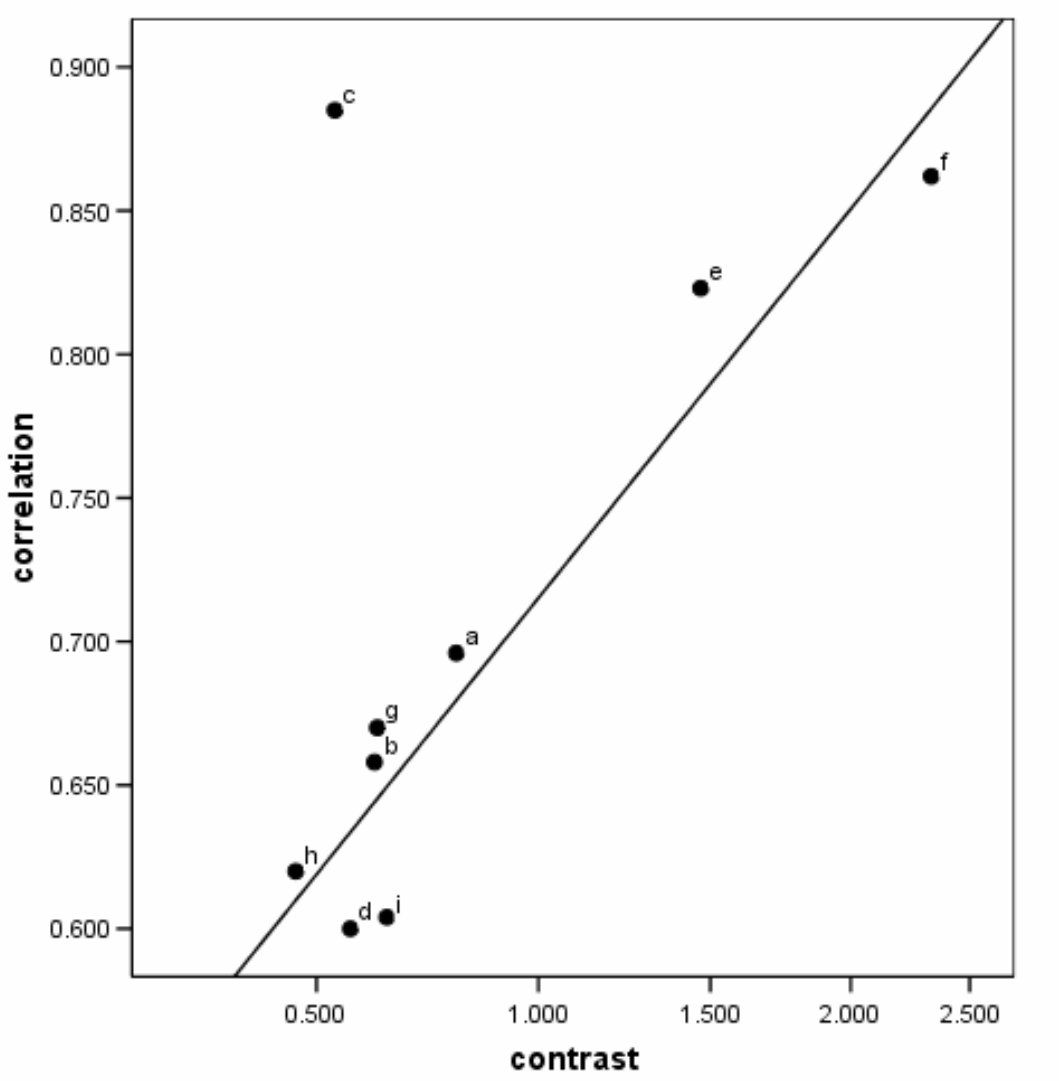

Figure 8: Graph of the correlation in variation of clustering between geological features and copper occurrences versus logarithm of contrast for (a) fault bends in the Eastern Succession, (b) fault intersections in the Eastern Succession, (c) mafic intrusions in the Eastern Succession, (d) mafic intrusions and extrusions in the Eastern Succession, (e) fault bends in the Western Succession, (f) fault intersections in the Western Succession, (g) mafic intrusions in the Western Succession, (h) mafic intrusions and extrusions in the Western Succession, and (i) mafic extrusions in the Western Succession. A trendline is displayed for data points plotting in the top right of Figure 6 (i.e., excluding mafic intrusion in the Eastern Succession), which reveals a rank correlation of 0.953. The data indicate that fault intersections and fault bends in the Western Succession are useful features to use for exploration in that area.

Factors affecting clustering and localization of copper occurrences

Figure 5 illustrates that the copper occurrences in the Eastern Succession are less clustered than those in the Western Succession. This discrepancy could be linked to greater exploration activity in, and greater wealth of information about, the Eastern Succession (cf. Blenkinsop and Sanderson, 1999). This possibility was evaluated from the location of exploration drillhole data within the Northwest Queensland Mineral Province Report (Queensland Department of Mines and Energy et al., 2000). Over 70% of the drillhole data is from the Eastern Succession, with almost 90% being from bedrock drilling. Regions with comparatively low fractal dimensions may not have been fully explored as indicated by the roll-off effect (illustrated in Figure 4) which may occur due to undiscovered mineral occurrences (Blenkinsop and Sanderson, 1999). Another factor that could cause differences in the clustering between the Eastern and Western Successions is the style of mineralization. Sedimentary breccia-hosted copper deposits are mainly located in the Western Succession, whereas the shear- and fault-hosted vein copper deposits are mainly located in the Eastern Succession (Blake et al., 1990).

The correlations between the clustering of copper occurrences and geological features listed in Table 2 indicate that fault bends and intersections have a greater spatial association with the clustering of the copper occurrences in the Western Succession, whereas mafic intrusions (R=0.885) have a greater association, and possibly a greater control on clustering, in the Eastern Succession (cf. Butera and Blenkinsop, 2004).

The weights of evidence analysis indicates that there are strong spatial relationships between the copper occurrences, fault bends and intersections, and mafic rocks (Table

2). The strongest spatial relationships exist between copper occurrences and fault bends (contrast value 2.33), and copper occurrences and fault intersections (contrast value 1.47), in the Western Succession. Strong spatial relationships also exist between the copper occurrences and the fault geometry in the Eastern Succession (0.696 and 0.658 for fault bends and intersections respectively).

Figure 8 shows a positive correlation between the logarithms of contrast values obtained from the weights of evidence analysis, and the clustering correlations obtained from the fractal analysis. The positive relationship between the fractal analysis and weights of evidence can be interpreted to indicate that the features that controlled the clustering of the copper occurrences in the Mt Isa Inlier also controlled the localization of the copper occurrences. Almost all of the data in this study (Fig. 8) plots in the top right of the graph in Figure 6, and forms a linear trend, although the mafic intrusives in the Eastern Succession do not fall on the general trend.

Fault bends and intersections may thus have a major influence on both the spatial association and the clustering of the copper occurrences in the Mount Isa Inlier. Though the results indicate that the spatial relationship between the faults and the copper occurrences is stronger in the Western Succession than the Eastern Succession, their control on the copper occurrences in the Eastern Succession is also significant. The differences between the Eastern and Western Successions appear to be real and suggest that differences exist in the role of the faults in the hydrothermal mineralizing process (Ford and Blenkinsop, 2007b).

Integrating fractal analysis and mineral prospectivity

The results of this study raise questions about the processes that controlled both the spatial association and clustering of the copper occurrences. While some of the features used in the fractal and the weights of evidence analyses show high fractal dimension correlations and contrast values (e.g., fault bends and fault intersections in the Eastern Succession), the values are not high enough to imply that any of these factors individually played an exclusive part in the clustering and localization of the copper occurrences.

The significant relationship between the results of the fractal and weights of evidence analyses has potential exploration relevance. Four possible implications from combining fractals and weights of evidence as outlined in Figure 6 can be considered for exploration.

- For geological features with high fractal dimension correlation and high contrast, (in the top right of Fig. 6): explore in areas proximal to the feature, and in areas with high clustering of the feature. Examples include fault bends and fault intersections in the Western Succession.
- For features with high fractal dimension correlation and low contrast (top left of Fig. 6): explore in areas with high clustering of mineral occurrences that are not necessarily in close proximity to the features, such as mafic intrusives in the Eastern Succession.
- For features with low fractal dimension correlation and high contrast (bottom right of Fig. 6): explore in areas proximal to the features.
- For features with low fractal dimension correlation and low contrast (bottom left of Fig. 6): the features should not be used for exploration targeting.

These outcomes are possibly most relevant to guiding brownfields mineral exploration at the regional scale, and they may be used to re-evaluate areas of previous exploration (Hronsky, 2004).

Future research should focus on subdividing mineral occurrences by style of mineralization. Consideration of the different styles of mineralization may provide further insights into what factors controlled the clustering and localization of the mineral occurrences. However, styles of mineralization are known only for the largest deposits. The conclusion that the features that controlled the clustering of the occurrences are the same that controlled the localization requires additional testing for different commodities and geological features in other study areas.

CONCLUSIONS

Clustering of mineral deposits and their spatial association with selected geological features are basic attributes of mineral deposit distribution that have implications for exploration and understanding ore genesis. This study suggests a method for evaluating the degree of clustering and spatial association simultaneously. In this method, the correlation between spatial variations in degree of clustering of mineral occurrences and geological features is compared with the spatial association of the occurrences with the same geological features, as measured by contrast values.

This integrated fractal analysis and weights of evidence method was tested on the copper occurrences in the Mt Isa Inlier. These copper occurrences have a better-defined fractal distribution than any previously analyzed mineral occurrence populations. However, there are important spatial variations in the degrees of clustering. Significant

spatial associations occur between the copper occurrences, fault bends and intersections, and mafic rocks, in both the major lithostratigraphic divisions of the Inlier, the Eastern and Western Successions. Variations in the degree of clustering of these geological features correlate with variations in the clustering of the copper occurrences.

The higher degree of clustering (lower fractal dimension) observed in the Western Succession may be due to either or both relative lack of exploration and geological factors. Slight differences in the spatial relationships between the Eastern and Western Successions, which are also seen in the respective styles of mineralization, suggest differences in mechanisms of copper mineralization.

SECTION B

Evaluating geological complexity and complexity gradients as controls on copper mineralization, Mount Isa Inlier

ABSTRACT

Faults and lithological boundaries are pathways for focusing the large volumes of fluid required to form hydrothermal orebodies. The distribution of faults and lithological boundaries as a function of scale can be measured by the geological complexity, quantified by a fractal dimension obtained by box counting, that increases with complexity. Copper mineralization in the Mount Isa Inlier has well documented structural and stratigraphic controls, and may therefore have a strong relationship with geological complexity. In this study, a two-dimensional approach is implemented for analyzing the relationship between complexity, complexity gradients and copper mineralization. There is a strong positive relationship between complexity and copper distribution and endowment in both the major lithostratigraphic subdivisions of the inlier, the Eastern and Western Successions. This relationship may suggest that abundant fluid pathways and physico-chemical contrasts are critical factors in copper mineralization. A weak inverse relationship exists between complexity gradients and copper endowment. At small scales, there is a departure from the fractal relationship between the number of boxes containing faults or lithological boundaries and box size, called roll-off. Roll-off is shown to be a function of the detail of mapping. This allows variation in mapping detail to be accounted for in measurements of geological complexity by due consideration of the scale at which roll-off occurs. The results imply that complexity could be used as an exploration tool.

INTRODUCTION

Faults and lithological boundaries are important factors in the genesis of hydrothermal ore deposits, as they can permit significant fluid flow, and create contrasts in physico-chemical conditions by juxtaposing different rock types. For example, these factors are

critical for the genesis of the Yilgarn gold deposits (Groves et al., 2000; Cox and Ruming, 2004). The concept of "geological complexity" (abbreviated hereafter to complexity) has been developed to describe the distribution of faults and lithological boundaries as a function of scale (Hodkiewicz, 2003), which can be quantified using the box counting technique (Weinberg et al., 2004). The variation of complexity over a region can be measured by a shifting box counting method in a similar way to the analysis of spatial variation in mineral occurrence clustering (Ford and Blenkinsop, 2007a). Hodkiewicz et al. (2005) concluded that there was no direct correlation between absolute complexity and gold endowment; rather the gradients in complexity were important for orogenic gold deposits in the Eastern Goldfields Province of the Yilgarn Craton.

The Mount Isa Inlier provides an ideal study area for investigating relationships between complexity, complexity gradients, and mineralization, with an abundance of up to date mineral occurrence data (Queensland Department of Natural Resources and Mines, 2005) and geological data (Queensland Department of Mines and Energy et al., 2000) available for analysis. Lithological and fault controls on copper mineralization have been suggested for both the world class Mount Isa copper deposit (Matthäi et al., 2004), and for other deposits in the inlier such as the Mammoth Cu and Century Pb-Zn-Ag deposits (Scott and Taylor, 1982; Blake et al., 1990; Williams, 1998). Numerical modelling by Oliver et al. (2001) shows that 1) the faults and lithological boundaries in the inlier acted as pathways for fluid flow and 2) that there is a close spatial association between these pathways and copper mineralization.

This study investigates spatial variations in geological complexity and complexity gradients within the Mount Isa Inlier. Both absolute values of the geological complexity and complexity gradients can be regarded as potential controls on copper mineralization.

GEOLOGY AND COPPER MINERALIZATION IN THE MOUNT ISA INLIER

Mid-Proterozoic metasedimentary and metavolcanic rocks of the Mount Isa Inlier are divided into the Eastern and Western Successions based on lithostratigraphic differences (Blake and Stewart, 1992; McDonald et al., 1997). Tectonic divisions of the Inlier from east to west include the Eastern Fold belt, the Kalkadoon-Leichhardt Belt, and the Western Fold Belt (comprising the Leichhardt River Fault Trough and the Lawn Hill Platform). For the purposes of this study the Western Succession incorporates the Western Fold Belt and the Kalkadoon-Leichhardt Belt, and the Eastern Succession incorporates the Eastern Fold Belt.

The Proterozoic stratigraphy of the Mount Isa Inlier (Fig. 1) is usually described in terms of sedimentary cover sequences 1, 2, and 3 (Blake et al., 1990). Cover sequence 1 is generally thought to be deposited at 1870-1850 Ma, cover sequence 2 at 1790-1720 Ma and cover sequence 3 at 1680-1600 Ma (Blake and Stewart, 1992; Williams, 1998). The Lawn Hill platform in the Western Succession consists mostly of cover sequence 3 rocks of the McNamara Group, which are predominantly sideritic and locally carbonaceous shales, mudstones and sandstones (Feltrin et al., 2003). Cover sequence 2 rocks, comprising the Eastern Creek Volcanics (metabasalts) and the Myally Subgroup (quartzite, sandstone, and siltstone), are the predominant rocks in the Leichhardt River Fault Trough (Scott and Taylor, 1982; Wyborn, 1987). The Kalkadoon-Leichhardt Belt is dominated by cover sequence 1 rocks and the intrusive rocks of the Kalkadoon and

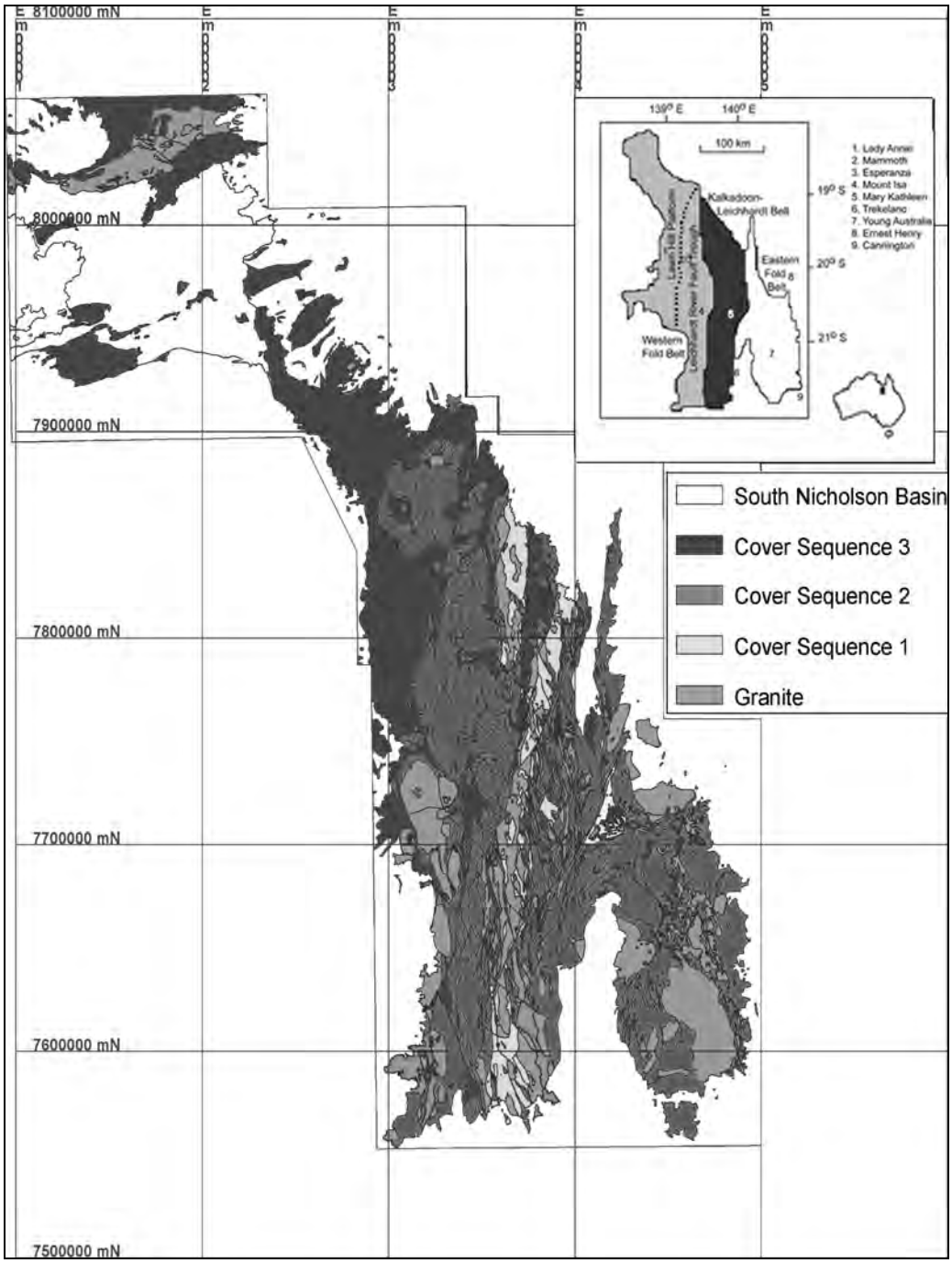

Figure 1: Simplified geology map of the Mount Isa Inlier (Queensland Department of Mines and Energy et al., 2000). Inset shows the location of the tectonic belts and major deposits.

Ewen Batholiths, with the former dated as coeval with cover sequence 1 and the latter dated at c. 1840 Ma (Blake and Stewart, 1992). The calcsilicate Corella and Doherty Formations (cover sequence 2), the siliciclastic metasedimentary and metabasaltic Soldiers Cap Group (cover sequence 3), and the Williams and Naraku granitic Batholiths (1540-1500 Ma) are the predominant units in the Eastern Fold Belt (Blake and Stewart, 1992; Laing, 1998; Williams, 1998).

Three major orogenies occurred in the Mount Isa Inlier. The Barramundi Orogeny at c. 1870 Ma and its remnants outcrop in the older basement sequences of the Kalkadoon-Leichhardt Belt. This was followed by a second orogeny at around 1750-1730 Ma (Holcombe et al., 1991; Pearson et al., 1992), before the major Isan orogeny from ca. 1600 – 1500 Ma, which has been subdivided into a number of deformation events (eg. Bell, 1983; Blake, 1987; O'Dea et al., 1997; Rubenach and Barker, 1998; Giles et al., 2002; Betts et al., 2006). Using a simplified three-event deformation chronology for the Isan orogeny, D_1 produced early layer-parallel fabrics, but its age and kinematics are unclear on a regional scale. D_2 was the major deformation event, involving E-W shortening, and coinciding with peak metamorphism between 1600 and 1570 Ma. E-W shortening continued in D_3 to at least 1530 Ma. D_3 is thought be associated with much of the copper mineralization in the Mount Isa Inlier (Bell and Hickey, 1998; Laing, 1998).

Metamorphic grade generally decreases from upper amphibolite facies in the eastern Mount Isa Inlier to greenschist facies in the west (Foster and Rubenach, 2006). The peak of metamorphism has been suggested to be between 1550-1530 Ma based on U-Pb SHRIMP ages in the Mount Isa area (Connors and Page, 1995), but monazite age dating

in the Eastern Fold Belt suggests a peak metamorphic event between 1600 Ma and 1570 Ma (Foster and Rubenach, 2006).

Copper deposits in the Mount Isa Inlier study area have two primary styles of mineralization: brecciated sediment hosted deposits, and shear and fault controlled vein deposits (Blake et al., 1990). The brecciated sediment hosted copper deposits are most prevalent in the Western Succession, and include the Mount Isa copper deposit (255Mt @ 3.3% Cu). Matthäi et al. (2004) suggest that the Mount Isa Cu deposit formed by mixing of fluid from overlying metasedimentary rocks (Mount Isa Group) with a fluid from underlying metabasalts (Eastern Creek Volcanics) entering a brecciated contact zone. Copper mineralization at Mount Isa lies proximal to the Mount Isa fault zone, which is a potential fluid pathway from the Eastern Creek Volcanics. Matthäi et al. (2004) propose that this sequence is the source of the copper. Wyborn (1987) and Williams (1998) suggest that the copper mineralization and the breccias at Mount Isa were emplaced during the D_3 deformation event of the Isan Orogeny.

The Eastern Creek Volcanics have also been suggested as the source of the copper for the Mammoth-Esperanza deposits near Gunpowder (Scott and Taylor, 1982). Fluids transported along the Portal Fault and Mammoth-Mammoth Extended Fault system in the Mt Gordon fault zone initially leached copper from the Eastern Creek Volcanics, leading to the formation of the Mammoth deposit in the siliclastic Myally Subgroup (Scott and Taylor, 1982; Van Dijk, 1991). Mineralization at Esperanza occurs in the dolomitic Esperanza Formation in the footwall of the Esperanza Fault and proximal to the Mammoth-Mammoth Extended Fault system (Van Dijk, 1991). A D_3 timing is proposed for both deposits (Van Dijk, 1991).

The Mount Kelly copper deposit (Van Dijk, 1991) is hosted near a contact between the siliclastic Gunpowder Creek and mainly dolomitic Paradise Creek Formations. Mineralization is localized by the intersection of a D_3 fold zone with a D_1 thrust fault. The timing of the alteration and mineralization is considered to be similar to that at the Mount Isa deposit. The Lady Annie copper deposit is hosted entirely by the Paradise Creek Formation (equivalent to the Urquhart Shale at Mount Isa) and has formed during D_3 (Van Dijk, 1991). The source of the copper in these deposits is unknown.

Smaller copper deposits in the Western Succession occur in a variety of lithological units, with many located proximal to D_3 structures and some near older D_1 structures (Van Dijk, 1991). High grade, low tonnage shear and fault controlled vein copper deposits are more numerous in the Eastern Succession, with many containing a considerable quantity of gold (Blake et al., 1990). The Great Australia copper deposit (Cannell and Davidson, 1998) is hosted in the greenschist grade Toole Creek Volcanics (part of the Soldiers Cap Group) near a faulted contact with the Corella Formation. Mineralization occurs at the intersection of a N-S striking fault with a NE-SW striking extension of the Cloncurry Fault.

In summary, copper mineralization in the Mount Isa Inlier is hosted in a variety of cover sequence rocks and has a variety of styles. The deposits show strong structural and lithological controls (Blake et al., 1990; Williams, 1998; Oliver et al., 2001) and are associated with faults and lithological boundaries, which acted as pathways for focused fluid flow. Timing of mineralization is generally consistent with D_3 in the Isan orogeny.

Deposits containing gold have been excluded in this study because Cu-Au deposits have potentially different mineralization controls.

MEASURING COMPLEXITY

Complexity values across the Eastern and Western Successions of the Mount Isa Inlier were determined using data from the Northwest Queensland Mineral Province Report or NQMPR (Queensland Department of Mines and Energy et al., 2000). Equally spaced nodes along rock contacts or faults with a maximum spacing of 250m were extracted from the rock type and Proterozoic fault databases to represent these features in the fractal analysis. The 250m spacing was used as it is less than the minimum box size used in the box counting.

Fractal dimensions were measured in the Eastern and Western Succession study areas by shifting a box in 10 km increments over each study area, and calculating complexity in each box. The dimensions of the boxes were ¼ the size of each study area (126.65 km x 35.2 km in the Eastern Succession and 126.65 km x 48.5 km in the Western Succession). Box counting within each shifting box was carried out from a maximum box size of 126.65 km to a minimum box size of 494.7m. The regression to calculate the fractal dimension was calculated over a 75 km-7.5 km range of box sizes. Errors for the fractal dimension are given as standard errors of regression. Figure 2 shows the variation in complexity across the Western Succession.

This shifting box method was also used to determine the spatial variation in fractal dimension of 1687 copper deposits (1299 in the Eastern Succession and 388 in the Western Succession), extracted from the Queensland mineral occurrence database

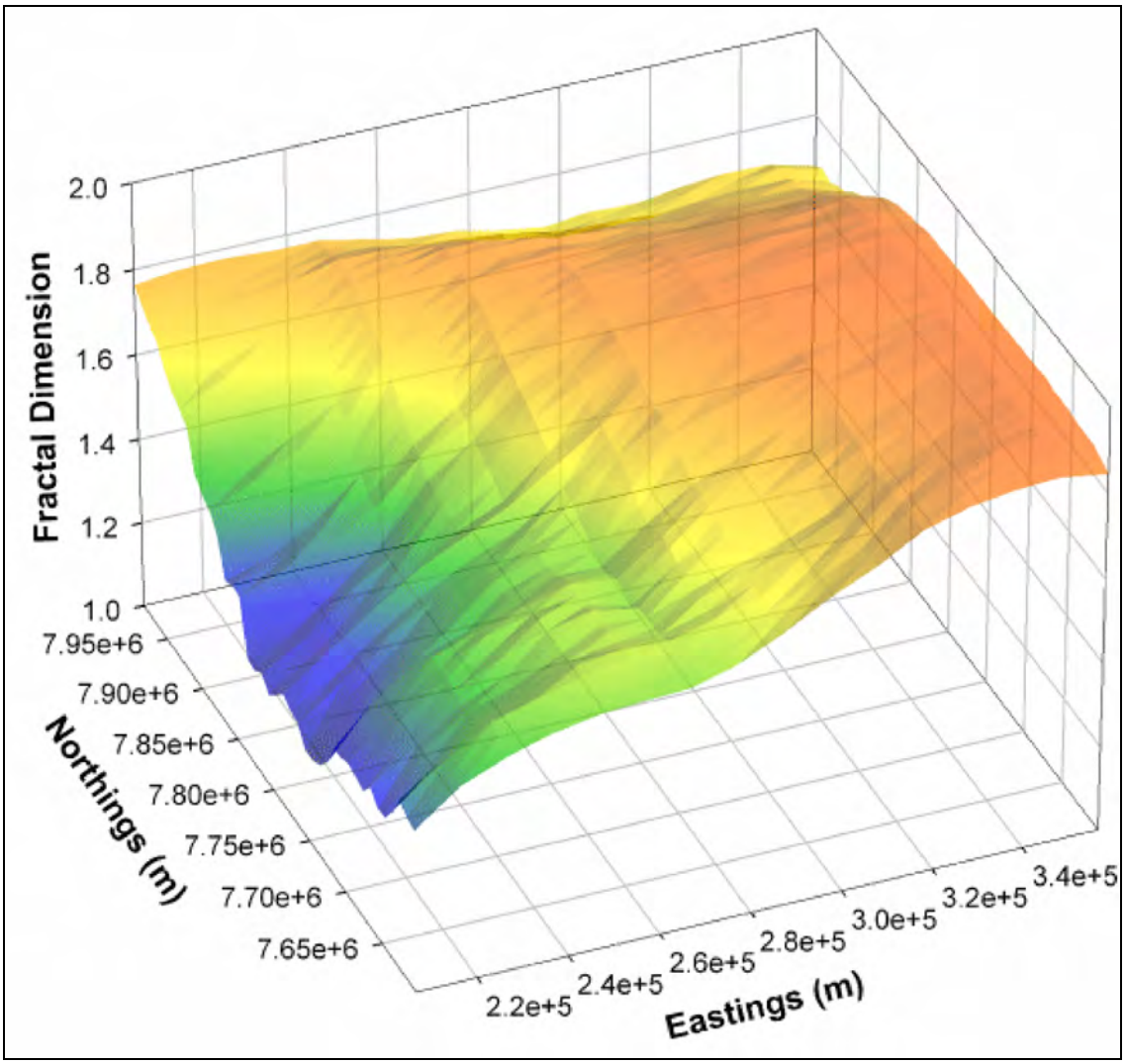

Figure 2: Variation in raw complexity across the Western Succession. Low values in SW correspond to areas outside the Proterozoic inlier.

(Queensland Department of Natural Resources and Mines, 2005). The same box sizes and counting method were used as above and the regression was preformed over a 65 km-1.5 km range of box sizes. Using the same database, the tonnage of each deposit was extracted and the total tonnage for each of the regional areas from the shifting box counting method was calculated. The same method was used to extract data on the metal content for each copper deposit.

Spline functions were generated to fit the 3-dimensional surface of geological complexity for each study area. Splines are piecewise polynomials of n^{th} order used for interpolation of one dimensional or multi-dimensional data (Bonham-Carter, 1994). The polynomial functions provide a good approximation of the actual data for analysis. As the order of the function increases (i.e. increasing the number of terms in the function), more accurate approximations to the actual data can be achieved. For each study area examined the coordinates (x, y) at the centre of the shifting box and their corresponding geological complexity value z were used to generate a spline function of the form:

$$z(x, y) = a + bx + cy + dx^2 + ey^2 + fx^3 + gy^3 + \ldots$$

Functions of the 4^{th} (up to $x^4 + y^4$), 5^{th} (up to $x^5 + y^5$) and 6^{th} orders (up to $x^6 + y^6$) were generated to fit the data. Each function was then differentiated in order to calculate the gradient at a given point on the surface. A grid with 1 km^2 cell sizes was placed over each study area and the value of the gradient calculated for the coordinates at the intersections of the grid lines. This gave an average measure of the gradient in a particular region of each study area (Fig. 3). In order to compare the complexity

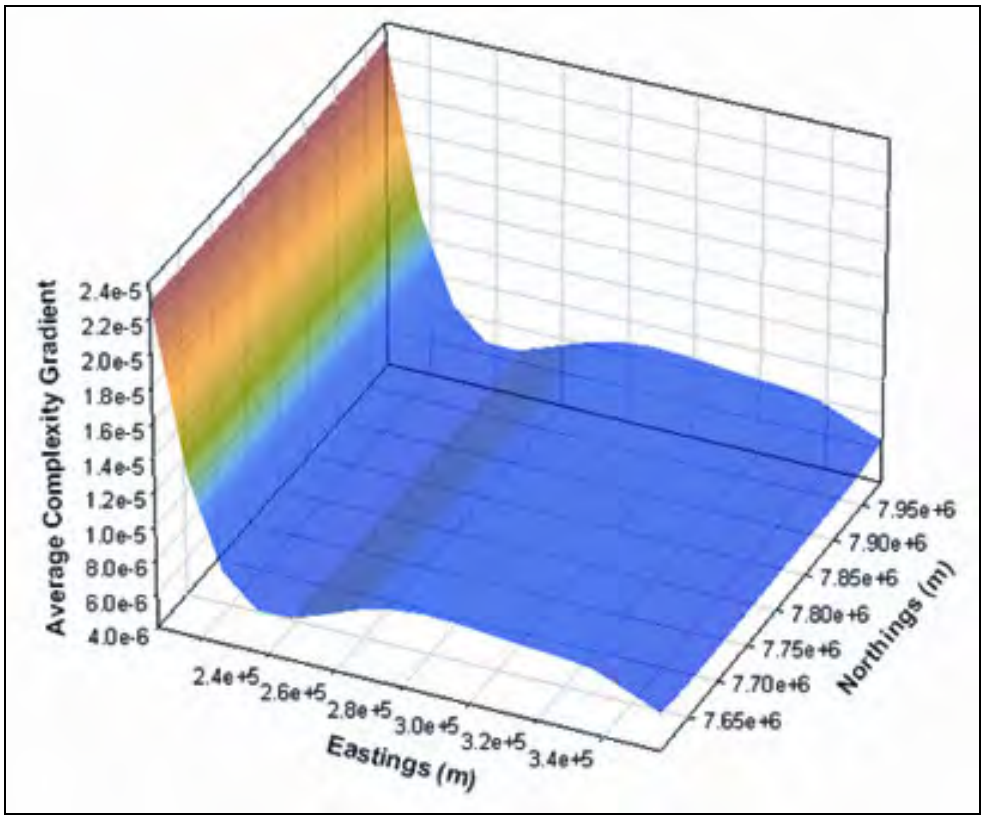

Figure 3: Variation in average complexity gradients across the Western Succession.

gradients and the complexity in a similar way, the average complexity values from the spline functions were calculated in the same fashion as the gradients.

Pearson's moment correlations and Spearman's rank correlations between various map parameters were calculated to test the strength of their spatial associations. Because the nature of the relationships between the complexity, complexity gradients and copper mineralization were not known a priori, correlations between parameters (excluding the regressions for the fractal dimensions from box counting) discussed in this text are Spearman's rank correlations (Conover, 1999).

RESULTS

The faults and lithological boundaries within the Eastern Succession were found to be more complex than in the Western Succession, with fractal dimensions of 1.572 ± 0.053 compared to 1.404 ± 0.050 respectively.

Results of correlations between raw complexity values and mineral deposit data are shown in Table 1. Though the relationships in the Eastern and Western Successions vary, all correlations using raw complexity values were found to be statistically significant at the 95% confidence interval. The results for the Eastern Succession show a correlation of 0.817 between the complexity and the clustering of the copper deposits. Results show a correlation of 0.914 between complexity and the tonnage. Substitution of the metal content for the tonnage makes no appreciable difference to the correlation. The Western Succession indicates slightly different relationships between the complexity and the copper mineralization. A correlation of 0.693 was found between the clustering of the copper deposits and the complexity. The relationship between the

Table 1: Correlations (using Spearman's rho) between complexity and copper deposit characteristics in the Mount Isa Inlier (* indicates significance at 95% confidence). FD = Fractal Dimension

Study area	Correlate with	Spearman's Rho
Eastern Succession	No. of deposits	0.903 *
	FD(deposits)	0.817 *
	Tonnage	0.914 *
	Metal	0.913 *
Western Succession	No. of deposits	0.923 *
	FD(deposits)	0.693 *
	Tonnage	0.914 *
	Metal	0.914 *

complexity and the tonnage was found to be the same as that obtained in the Eastern Succession, 0.914.

Correlations between the average complexity and complexity gradients and copper occurrence data are shown in Table 2. Correlations for the 6^{th} order spline functions are considered the most accurate due to their goodness of fit to the data (0.854 in the Eastern Succession and 0.841 in the Western Succession) and these values are discussed further. Results for the correlations with the average geological complexity indicate that there are high, positive correlations between the average geological complexity values and the copper occurrence data (Fig. 4a and b), including numbers of occurrences, clustering, tonnage, and metal content. Conversely, there are inverse relationships between the complexity gradients and the copper occurrence data (Figures 4c and d). All these correlations with one exception (complexity gradient with deposit clustering in the Eastern Succession) are significant at the 95% level.

North-South and East-West linear profiles were examined to determine whether using a linear complexity method for comparison with the tonnage of the deposits produced differing results to the two-dimensional method used. Figure 5 shows that profiles can produce some negative correlations between the average complexity and copper

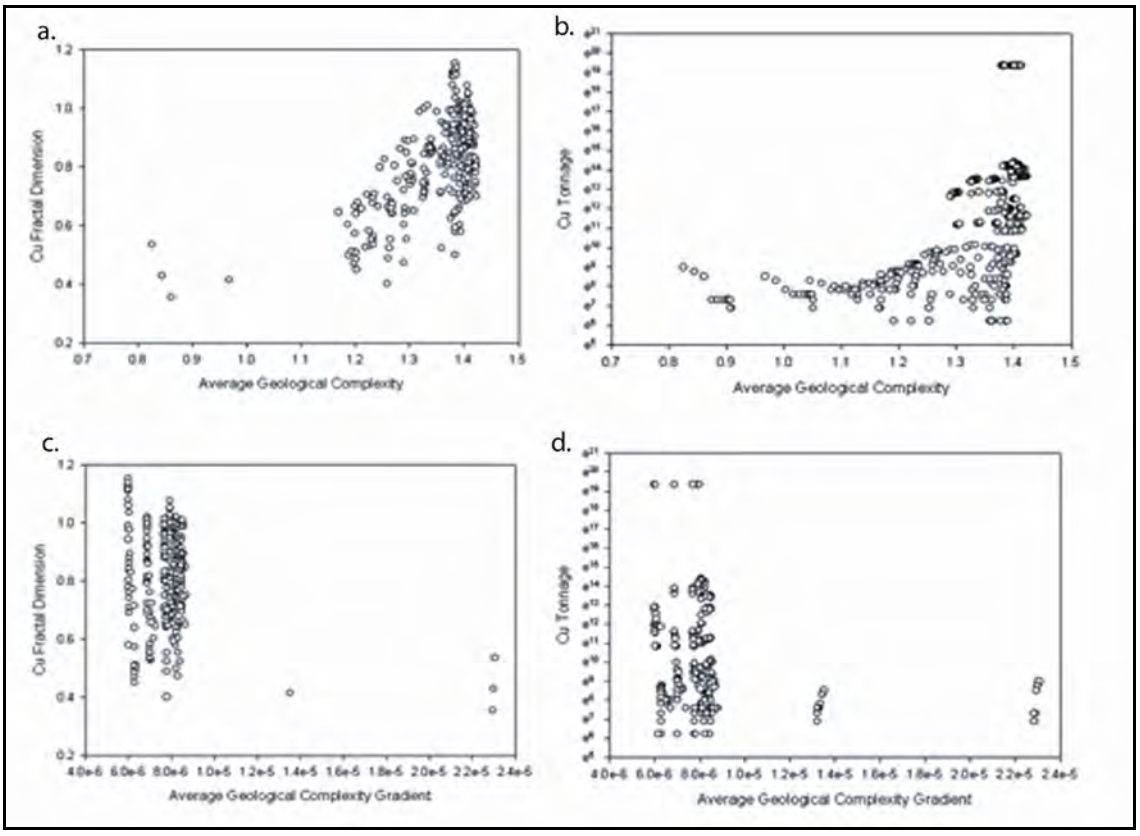

Figure 4: Graphs showing relationships in the Western Succession between (a) average complexity and the fractal dimension of copper occurrences, (b) average complexity and the tonnage of copper occurrences, (c) average complexity gradient and the fractal dimension of copper occurrences, and (d) average complexity gradient and the tonnage of copper occurrences.

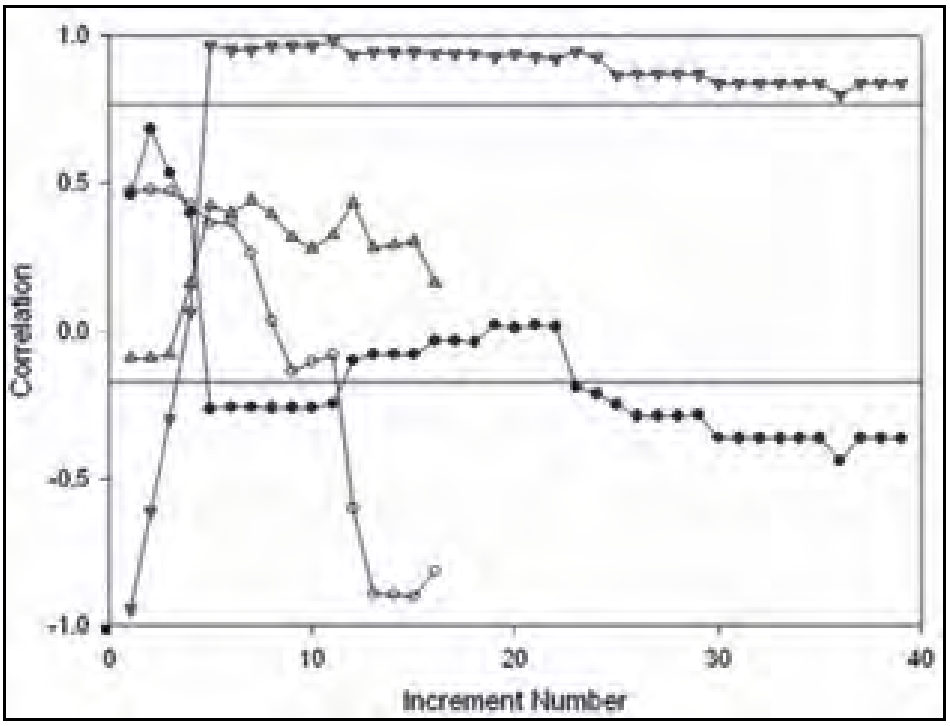

Figure 5: Correlation between average complexity and copper tonnage for incremental N-S profiles (▲) and E-W profiles (▼) across the Western Succession and correlation between complexity gradients and copper tonnage for N-S profiles (○) and E-W profiles (●). The upper horizontal line represents the two-dimensional correlation between the average complexity and tonnage (0.768) and the lower horizontal line is the corresponding correlation between the complexity gradients and tonnage (-0.172).

Table 2: Correlations (using Spearman's rho) of average complexity and complexity gradients with copper occurrence data: number of deposits (N), fractal dimension (FD), tonnage (T), and metal content (M). Fit indicates the goodness of fit of the function to the actual data for functions of the 4th, 5th and 6th order.

Order		Eastern Succession		Western Succession	
	Correlate With	Complexity	Complexity Gradient	Complexity	Complexity Gradient
4		Fit = 0.850		Fit = 0.826	
	N	0.900*	-0.108*	0.354*	-0.252*
	FD	0.813*	0.045	0.423*	0.136*
	T	0.880*	-0.122*	0.373*	-0.256*
	M	0.882*	-0.120*	0.373*	-0.256*
5		Fit = 0.854		Fit = 0.833	
	N	0.941*	-0.248*	0.727*	-0.454*
	FD	0.777*	-0.098	0.519*	-0.242*
	T	0.914*	-0.241*	0.763*	-0.467*
	M	0.915*	-0.241*	0.763*	-0.468*
6		Fit = 0.854		Fit = 0.841	
	N	0.936*	-0.276*	0.736*	-0.147*
	FD	0.790*	-0.078	0.479*	-0.270*
	T	0.912*	-0.276*	0.768*	-0.172*
	M	0.913*	-0.277*	0.768*	-0.172*

Note: * indicates significance at 95% confidence

tonnage when the two-dimensional correlation is positive, and a positive correlation between the complexity gradients and tonnage when its corresponding two-dimensional correlation is negative. These are the opposite relationships to the general, two dimensional cases.

DISCUSSION

Results shown in Table 1 indicate that a significant relationship exists between the raw complexity values and the copper mineralization in both the Eastern and Western Succession study areas. High correlations indicate that the complexity could have a high level of control over the clustering and endowment of copper.

Vein-hosted mineral deposits, such as those found predominantly within the Eastern Succession, form as a result of fluid flow and with the faults and lithological boundaries acting as fluid flow conduits, the relationship between the number and clustering of the

deposits and the complexity of the geology is expected (Sanderson and Zhang, 1999). Though the results in Western Succession differ slightly to those in the Eastern Succession, with rank correlations varying between approximately 0.7 and 0.9, it can be inferred that the complexity is a potential control on copper mineralization in each study area.

The relationship between copper endowment and complexity in the Western Succession is strong. The high tonnage copper deposits also have a high correlation with geological complexity in each study area. The area in the Western Succession with the highest complexity is centered on the Mammoth and Esperanza copper deposits, with the area of next highest complexity focussed on the Mount Isa copper deposit. These deposits lie along a N-S trending corridor of higher complexity that stretches from south of Mount Isa to north of Gunpowder (Fig. 6). Complexity could therefore be used as a tool to explore for large tonnage copper deposits within the Mount Isa Inlier. The spatial analysis suggests that exploration should target areas of higher complexity and comparatively low fractal dimensions for the distribution of the copper deposits. The exploration target area could be further reduced by decreasing the size of the shifting box.

The results in Table 2 indicate that there is a relationship between the complexity gradient and the copper endowment in both the Eastern and Western Successions, as Hodkiewicz et al. (2005) proposed for gold deposits in the Yilgarn craton. However, the results of the present study indicate the nature of the relationship for copper in the Mount Isa Inlier is opposite to that which has been shown for gold in the Yilgarn craton. Instead of the endowment increasing with the complexity gradients, this study shows an

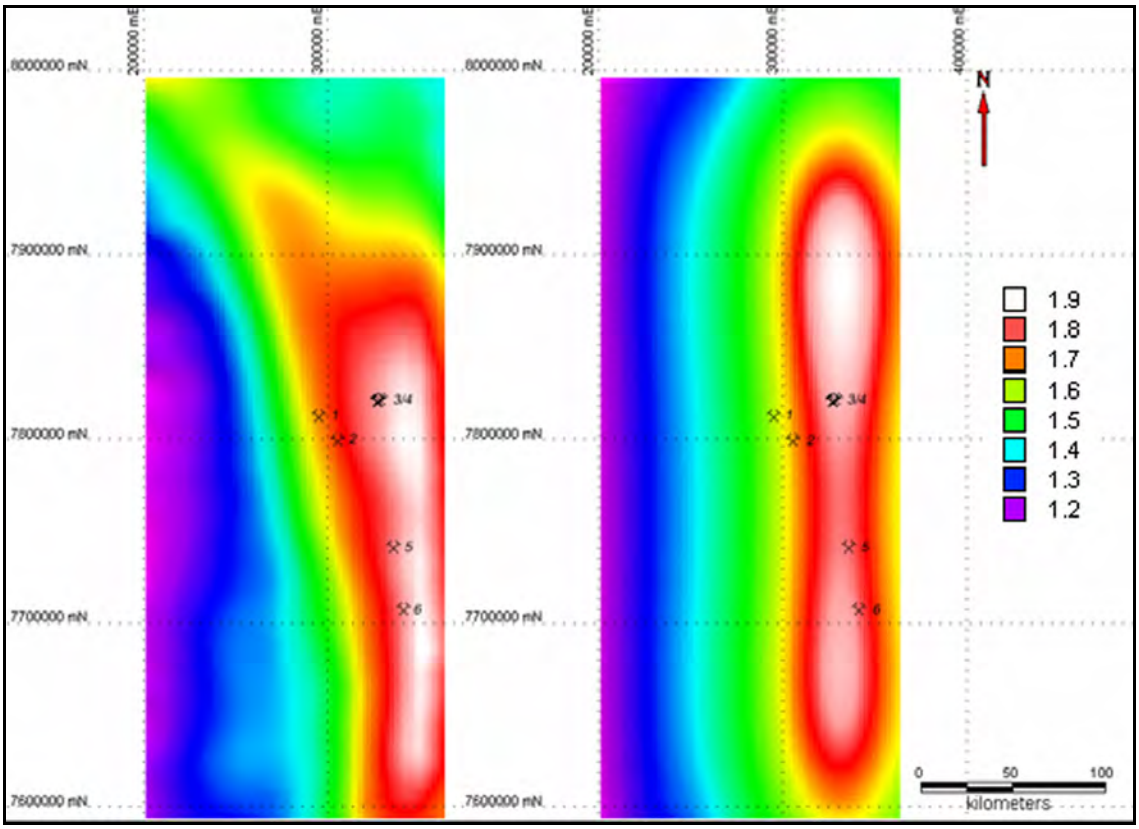

Figure 6: Contour maps of raw complexity (left) and average complexity values (right) in the Western Succession. Major copper deposits (1 – Lady Annie, 2 – Mt Kelly, 3/4 – Mammoth & Esperanza, 5 – Hero, 6 – Mt Isa) are shown to sit proximal to regions of higher complexity.

inverse relationship between the complexity gradients and endowment. Although the relationship in the Western Succession is weaker than that in the Eastern Succession, the correlations in each study area indicate that the relationships between the complexity gradients and copper mineralization are still significant. The results indicate that the complexity may have a greater influence on copper mineralization than the complexity gradients.

The differing conclusions reached on the role of complexity gradients by Hodkiewicz et al. (2005) and those of this study may be due to the differences in the commodities and areas studied (geological factors), and/or to the approaches taken (methodological factors). Hodkiewicz et al. (2005) suggest that complexity gradients are significant for gold mineralization because they mark locations where transitions from the presence of dangling elements of a permeability network (high complexity) to low complexity backbone structure (their Fig.7) focused fluid flow. In the Mount Isa Inlier copper deposits, the high complexity itself is associated with copper mineralization. There are several possible geological reasons for the difference in the role of complexity vs complexity gradients between the two systems. Firstly, the possibility of post-mineralization changes in the distribution of complexity may obscure the true relationship between complexity, complexity gradients, and mineralization. This is unlikely at Mount Isa since copper mineralization generally occurred with the last significant tectonic event. Secondly, there may be differences between the two systems in the relative importance of faulting compared to physico-chemical changes at lithological contrasts in localizing mineralization. Lithological contrasts contribute substantially to the complexity at Mount Isa – hence analysis of the complexity or complexity gradients exclusively in terms of a permeability network may be less applicable because lithological contrasts are important apart from their possible role as fluid pathways.

Thirdly, there are many possible differences in the basic controls of mineralization between the two systems. The copper deposits in the Mount Isa Inlier are hosted in predominantly sedimentary sequences compared to the mesothermal Archaean gold deposits hosted in greenstone belts in the Yilgarn craton. Thus, the temperature, pressure, fluid composition, etc. were all potentially different during mineralization between the two study areas, which could have influenced the relationships between mineralization and complexity or complexity gradients.

The most obvious difference between the methods of the two studies is that this study approached the problem using a two-dimensional method for examining the variation in complexity and the corresponding gradients for comparison with the deposit characteristics, while the previous research by Hodkiewicz et al. (2005) looked in detail at comparisons with complexity and gradients over linear sections of the Bardoc Tectonic Zone and the Boulder-Lefroy Shear Zone. It is possible that complexity gradients are more important in the linear analysis because the permeability network model applies better to an analysis of a single, linear structure than it does to a two dimensional area. Independently of this possibility, however, this study has shown that there are significant local differences in the correlation results when linear profiles are used to calculate geological complexity correlations compared to the two dimensional method used in this study (Fig. 5). Therefore using a single linear profile may reverse the overall nature of the relationship between the geological complexity/complexity gradients and the tonnage locally, and affect the strength of that relationship.

Because the different methodologies in the two studies may have contributed to the different conclusions, it is not possible to resolve the suggestions above. A high priority in future studies should be to compare different mineralising systems with similar methodologies.

The complex distribution of the lithology across the Mount Isa Inlier can be attributed to the complex nature of the deformation history in the terrain. Multiple terrain scale deformation events coupled with local events and intrusions have created regions of high complexity. Complexity may be a response to increased energy in the system. Ord et al. (2007), suggest that kinetic energy and second order work during deformation can cause instability in a system, which can generate fractures on a micro-structural scale under continuous loading. During deformation, 2^{nd} order work is the product of the stress rate tensor and the plastic strain rate tensor with instability occurring when this product is less than or equal to 0. As the instability increases more fractures are generated, thus creating more pathways for fluid flow, which is critical in the formation of hydrothermal mineral deposits. This theory can potentially be expanded to regional scale structures such that areas with a higher dissipation of energy/work into the system will produce larger and denser fault networks, thus creating a region of higher geological complexity.

Blenkinsop and Sanderson (1999) proposed that the roll-off effect observed when using box counting to calculate the fractal dimension of the distribution of Archaean gold deposits, can be due to undiscovered deposits existing in the study area. We propose that a similar situation applies to the box counting method used to calculate the fractal dimension of geological complexity in both this study and the previous work by

Hodkiewicz et al. (2005). Evidence of a roll off effect is apparent for small box sizes (consistently starting at about 1000 m) used in calculating the geological complexity. Box sizes of greater than 1500 m were used in the fractal dimension calculations in order to avoid the effect of roll-off. It is proposed that the roll off effect for the geological complexity is due to the fact that the detail of mapping of the faults and lithologies is inevitably limited at the smallest scale. Similar to the explanation of Blenkinsop and Sanderson (1999), there may be "undiscovered", i.e. unmapped, faults and lithological boundaries within the study area. These structures and rock type boundaries could be "undiscovered" due to being under cover, as well as due to limitations on the detail on mapping at the smallest scale. In order to demonstrate this effect, an 8 km x 8 km region of the study area was selected from NQMPR that had six different rock types (Fig. 7a). Boundaries between the rock types were removed progressively (Fig. 7b), from five down to one rock type, and box counting was carried out at each stage. Figure 8 shows that the onset of the roll-off effect occurs at larger box sizes as fewer boundaries are mapped, and that the fractal dimension decreases due to the slope of the log-log graph not being as steep as the number of "undiscovered" boundaries increases.

The identification and attribution of the roll-off effect given above has a significant positive advantage for studies of complexity. Even with a simplified GIS database, it is possible that some areas will have a higher degree of map detail than others, which is a likely artefact of the amount of exploration and mining that has occurred in certain areas, as well as degree of exposure. Any such inconsistencies in the detail of mapping have been accounted for in this study by measuring the complexity from the linear part of the

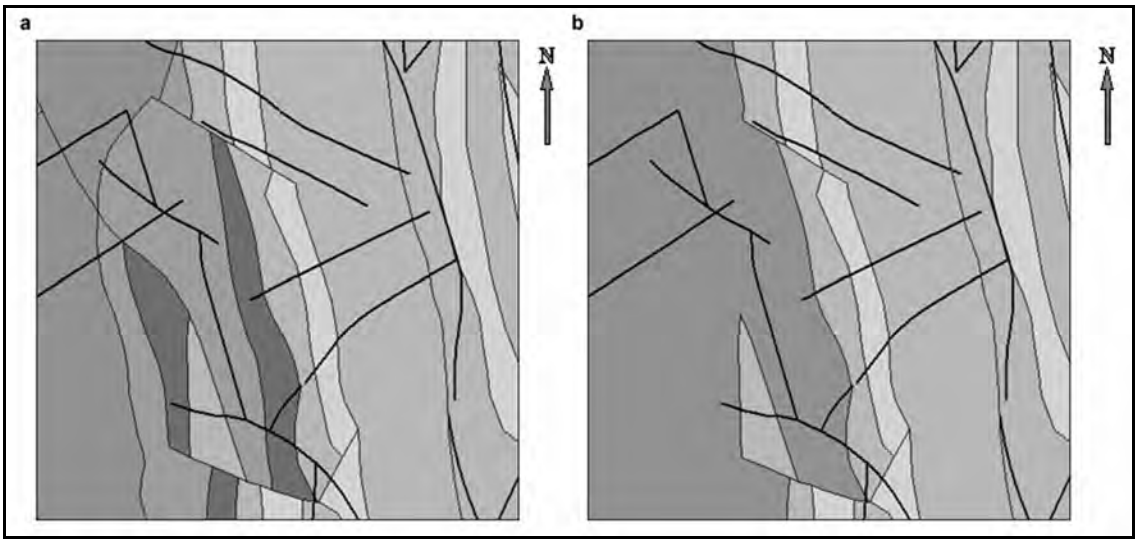

Figure 7: Faults and lithologic boundaries in an 8 km x 8 km study area in the Mount Isa Inlier centred on the point 376076.01 mE; 7723146.35 mN (MGA94 zone 54). Map (a) displays all mapped faults and lithologic boundaries from the NQMPR (Queensland Department of Mines and Energy et al., 2000) and (b) shows same area with 3 rock types combined.

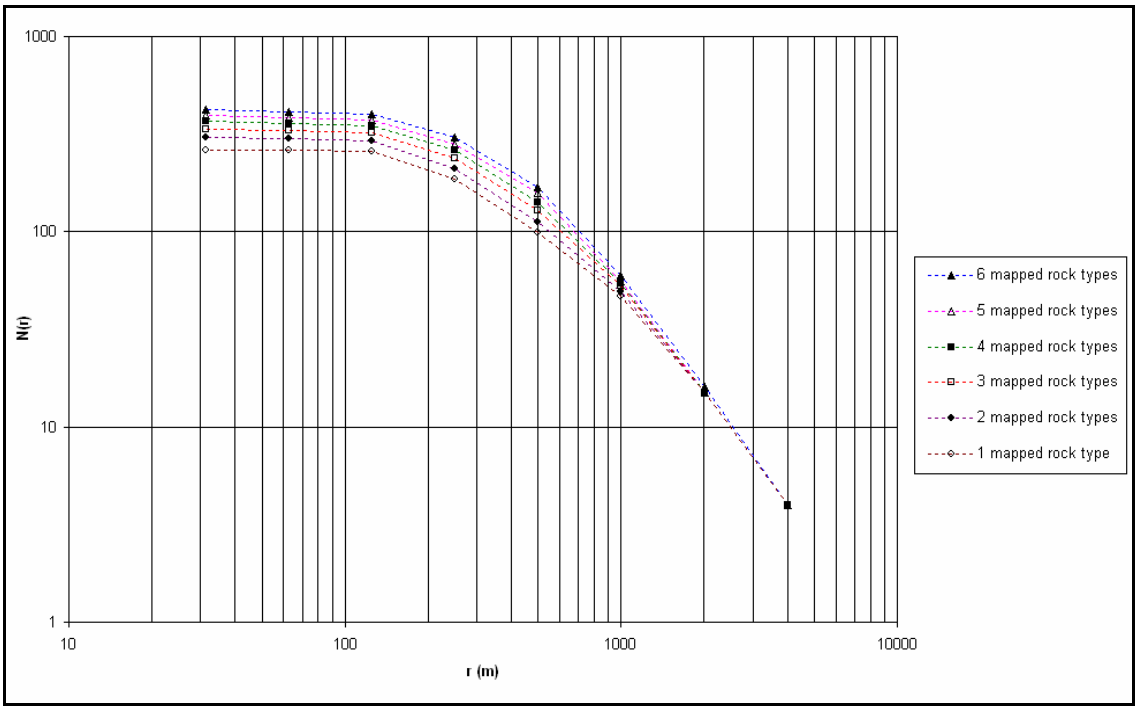

Figure 8: Log-log plot of box size r vs. number of boxes N(r) showing how roll-off varies as the number of undiscovered boundaries increases. Data taken from study area shown in Figure 7.

relationship between number of boxes containing boundaries and box size, so that the fractal dimension is not affected by variations in the detail of mapping or exposure.

CONCLUSIONS

This study highlights the importance of complexity for copper mineralization in the Mount Isa Inlier. Regions with higher complexity, as measured by a fractal dimension, have the potential to transport large volumes of fluid and to provide physico-chemical contrasts, which are both critical in the formation of large hydrothermal ore deposits. There are strong positive correlations between complexity and both clustering and tonnage of copper deposits. The highest fractal dimensions were calculated around the Mammoth, Esperanza and Mount Isa copper deposits. The correlation between the complexity gradients and copper mineralization is significant but negative, and this relationship is much weaker than with the absolute complexity. Complexity and complexity gradients need to be analysed in two dimensions to reveal their full properties and to give an accurate representation of the relationship with mineralization. Based on the results obtained in this study, complexity can be used as an exploration targeting tool for large copper deposits in under-explored areas of the Mount Isa Inlier. Variations in mapping detail can be allowed for by measuring only the linear part of the relationship given by box counting.

SECTION C

An expanded de Wijs model for multifractal analysis of mineral production data

ABSTRACT

Hydrothermal ore deposits form by enriching elements and minerals from background values to very high concentrations in small volumes of the crust. The de Wijs model provides a simple and widely used mathematical description of this process; however, it does not account for the increase in density which generally attends the formation of high specific gravity minerals in many mineral deposits. We present an expanded version of the de Wijs model to investigate the distribution of ore tonnage as well as grade. The expanded model generates a log-normal relationship between ore tonnage and grade. Continuous multifractal analysis of results from the new model using the method of moments technique predicts that ore grades are multifractal (as in the original de Wijs model) but that ore tonnage values are not multifractal. Production data from vein-hosted gold deposits in the Archaean Zimbabwe craton display the log-normal relationship between ore tonnage and grade, the multifractal nature of ore grade, and the non-multifractal nature of ore tonnage as shown in the expanded de Wijs model.

INTRODUCTION

The spatial distribution and several other aspects of mineral deposits are fractal (Turcotte, 1986; Carlson, 1991; Cheng et al., 1994; Sanderson et al., 1994; Agterberg et al., 1996; Johnston and McCaffrey, 1996). Studies analyzing fractal aspects of mineral deposits typically deal with only one or two variables, such as vein thicknesses, or the x and y coordinates of mineral deposits. However, many aspects of mineral deposit research require a more complex approach that can accommodate additional variables. For example, the size of mineral deposits and their grade need to be evaluated as well as their spatial distribution. Multifractals can be used to study the spatial distribution of quantitative measures. Previous research has shown that multifractals can be used to

describe ore grade distributions, to separate geochemical anomalies, and to describe the concentration of elements in the crust as revealed by geochemical surveys (Agterberg et al., 1996; Roberts, 2005).

Ore production data has also been examined using multifractal analysis on a mine scale (Roberts, 2005), and Cheng (1999b) showed that categorized data for deposit size might fit a discrete multifractal model. Turcotte (1989) showed several examples of a fractal relationship between ore grade and tonnage, and proved that such a fractal relationship is predicted by a modified de Wijs model. The de Wijs model redistributes elements such that as one area is enriched, another area is depleted (de Wijs, 1951, 1953). This concept captures the fundamentals of many ore genetic models, namely the progressive enrichment of elements in parts of the crust and their corresponding depletion elsewhere. However, it does not explicitly deal with changes in density accompanying mineralization, and does not describe ore tonnage distributions.

This main aim of this study is to propose a theoretical model for describing the distribution of ore tonnage as well as grade through an expansion of the de Wijs model for element concentration. The distribution of ore tonnage is investigated by allowing for an increase in density at the site of ore deposition. The properties of this model are explored and compared with production data analyzed using the same techniques. A theoretical model that could predict ore tonnage as well as grade distributions would be very significant in assessing mineral resources and exploration, and to ore genesis studies.

CONSTRUCTION OF AN EXPANDED DE WIJS MODEL

The expansion of the de Wijs model proposed here allows for an increase in tonnage within each cell due to the generally higher density of ore minerals compared to rock forming minerals. Figure 1 illustrates the proposed model for distribution of ore tonnage in two dimensions. Using the original definitions specified by de Wijs (1951), a "density" term was added to the ore tonnage. The initial concentration c_0 of an element ($0 \leq c_0 \leq 1$), and initial ore tonnage M_0 can be defined. An enrichment factor ϕ (for $0 \leq \phi \leq 1$), represents the amount of enrichment or depletion of an element at a given iteration of the model. The de Wijs model is effectively a multiplicative cascade (iterative model) in which the ore tonnage at the n^{th} iteration (M_n) of the expanded model, can be derived as follows. The concentration of an element within the model at stage n (c_n) is generalized to give the relationship:

$$c_n = c_0 (1+\phi)^{n-r} (1-\phi)^r$$

which can be re-arranged to show,

$$n = \frac{\ln\left(\frac{c_n}{c_0}\right) - r\ln\left(\frac{1-\phi}{1+\phi}\right)}{\ln(1+\phi)}$$

The ore tonnage within a cell (M_n) can be calculated by multiplying the tonnage of the enriched cell as specified in the original de Wijs model (a fraction of the initial crustal mass) by the concentration of the cell to give the metal content, and adding to this the original tonnage, thus providing the ore tonnage of the cell with a "density" factor, which is the last term on the right hand side:

$$M_n = \frac{M_0}{4^n} + \frac{M_0}{4^n} c_n$$

$$\frac{M_n}{M_0} = \frac{1+c_n}{4^n}$$

$M_0 + M_0 c_0$

$\frac{M_0}{4} + \frac{M_0}{4} c_0 (1+\phi)^2$	$\frac{M_0}{4} + \frac{M_0}{4} c_0 (1+\phi)(1-\phi)$
$\frac{M_0}{4} + \frac{M_0}{4} c_0 (1+\phi)(1-\phi)$	$\frac{M_0}{4} + \frac{M_0}{4} c_0 (1-\phi)^2$

$\frac{M_0}{16} + \frac{M_0}{16} c_0 (1+\phi)^4$	$\frac{M_0}{16} + \frac{M_0}{16} c_0 (1+\phi)^3 (1-\phi)$	$\frac{M_0}{16} + \frac{M_0}{16} c_0 (1+\phi)^3 (1-\phi)$	$\frac{M_0}{16} + \frac{M_0}{16} c_0 (1+\phi)^2 (1-\phi)^2$
$\frac{M_0}{16} + \frac{M_0}{16} c_0 (1+\phi)^3 (1-\phi)$	$\frac{M_0}{16} + \frac{M_0}{16} c_0 (1+\phi)^2 (1-\phi)^2$	$\frac{M_0}{16} + \frac{M_0}{16} c_0 (1+\phi)^2 (1-\phi)^2$	$\frac{M_0}{16} + \frac{M_0}{16} c_0 (1+\phi)(1-\phi)^3$
$\frac{M_0}{16} + \frac{M_0}{16} c_0 (1+\phi)^3 (1-\phi)$	$\frac{M_0}{16} + \frac{M_0}{16} c_0 (1+\phi)^2 (1-\phi)^2$	$\frac{M_0}{16} + \frac{M_0}{16} c_0 (1+\phi)^2 (1-\phi)^2$	$\frac{M_0}{16} + \frac{M_0}{16} c_0 (1+\phi)(1-\phi)^3$
$\frac{M_0}{16} + \frac{M_0}{16} c_0 (1+\phi)^2 (1-\phi)^2$	$\frac{M_0}{16} + \frac{M_0}{16} c_0 (1+\phi)(1-\phi)^3$	$\frac{M_0}{16} + \frac{M_0}{16} c_0 (1+\phi)(1-\phi)^3$	$\frac{M_0}{16} + \frac{M_0}{16} c_0 (1-\phi)^4$

Figure 1: Proposed two-dimensional model for distribution of ore tonnage based on expanded version of the de Wijs distribution model (de Wijs, 1951, 1953). Parameters as described in the text.

Thus,

$$\ln\left(\frac{M_n}{M_0}\right) = \ln(1+c_n) - \frac{\ln\left(\frac{c_n}{c_0}\right) - r\ln\left(\frac{1-\phi}{1+\phi}\right)}{\ln(1+\phi)}\ln 4$$

which gives

$$\frac{M_n}{M_0} = (1+c_n)4^{\frac{\ln\left(\frac{c_0}{c_n}\right)\left(\frac{1-\phi}{1+\phi}\right)^r}{\ln(1+\phi)}}$$

This relationship between ore tonnage and grade differs by a factor of $1+c_n$ from the original de Wijs model. Turcotte (1989) has shown that the original de Wijs model predicts a lognormal relationship between the cumulative ore tonnage and grade as $n\rightarrow\infty$. However, it is contentious whether the relationship between actual cumulative ore tonnage and grade is power-law (fractal) or lognormal (Turcotte, 1989). In order to examine the new relationship between ore tonnage and grade derived above, the ore tonnages for the cells at a particular iteration of the expanded de Wijs model were calculated using the two-dimensional model. Figure 2 illustrates that the expanded de Wijs model predicts a lognormal relationship between cumulative ore tonnage and grade. This relationship is also a property of one-dimensional versions of the original de Wijs model (Turcotte, 1986, 1989).

Using a similar methodology to that outlined by Xie and Bao (2004), a 128x128 grid was generated after seven iterations of the expanded de Wijs model with an initial concentration of $c_0=2\text{x}10^{-7}$ (cf. Phillips et al., 1987), and an enrichment factor of $\phi=0.4$. Ore tonnage distributions were generated with an initial ore tonnage $M_0=4.42368\text{x}10^{10}$ T (assuming each cell is 1km x 1km, and has a mean crustal density of $2.7\text{x}10^3$ kg/m³). Partition functions $\chi_q(\varepsilon)$ and the resultant $f(\alpha)$-curves were generated for a range of q

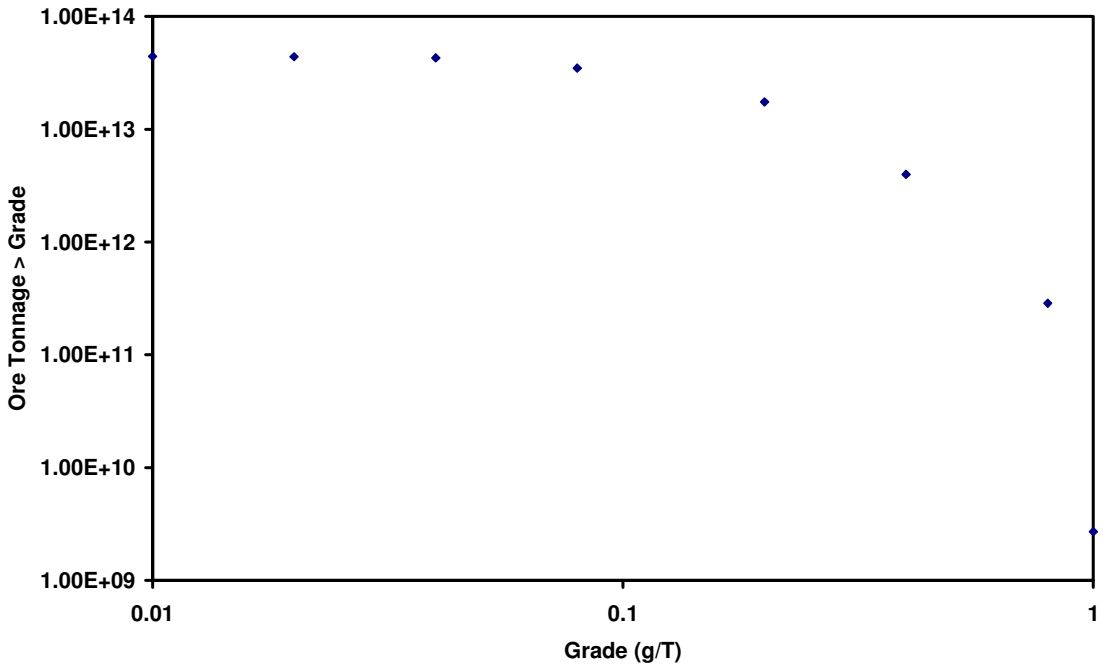

Figure 2: Log-log plot of ore tonnage with a grade greater than a specified value vs. ore grade for the expanded de Wijs ore tonnage model (de Wijs, 1951, 1953).

from -10 to 10 in steps of 1 using the method of moments technique outlined below for continuous multifractal analysis.

DETERMINING MULTIFRACTALITY

In a multifractal, spatial variations in the value of a property are assessed by a multifractal measure. If the measure shows self-similarity, it can be described as a multifractal (Evertsz and Mandelbrot, 1992). To determine whether a multifractal is continuous in two dimensions, a grid of equal size boxes is placed over the study area with the box size ε, and the number of boxes $N(\varepsilon)$ noted. If a box contains a single data point, the value of the property at that point is applied to the whole box. If a box contains more than one data point, the values assigned to each data point in that box are averaged. The multifractal measure $\mu_i(\varepsilon)$ is calculated by multiplying the value assigned to the box by the area of the box. The partition function $\chi_q(\varepsilon)$ for each box size and a range of real numbers q is calculated, allowing the mass exponent function $\tau(q)$ to be estimated and the function α evaluated (in this study) from the derivative of a 4^{th} order polynomial in order to determine the multifractal spectrum $f(\alpha)$. The method of moments technique for evaluating these parameters is detailed in several studies (eg. Evertsz and Mandelbrot, 1992; Agterberg et al., 1996; Roberts, 2005).

VEIN-HOSTED GOLD PRODUCTION DATA

A study area in the Zimbabwe craton was chosen for analysis, where gold mineralization is hosted primarily in Archaean greenstone sequences and is generally considered to have formed in the late Archaean (Blenkinsop, 1994). Gold production is recorded in the database of the Gold Deposits of Zimbabwe (Bartholomew, 1990), which lists location, cumulative gold production reported to the Ministry of Mines to

the end of 1984, and average recovery grade based on production to 1977 (to 1964 for mines with less than 300 kg production), for all deposits that produced more than 100 kg Au, for which it is considered complete in that all known production records are captured in the database (Bartholomew, 1990; Blenkinsop and Sanderson, 1999). Brief geological descriptions of the mines are also given, which were used to filter the data to include only vein-hosted gold deposits. Since not all deposits with a listed ore tonnage (460 deposits) had a listed grade (462 deposits) and vice versa, slightly different subsets of data were used for grade and tonnage analysis. The maximum and minimum grades were 197.8 g/T and 1.2 g/T, and the corresponding figures for tonnage were 3420495600 T and 208800 T. Limiting the study to a single deposit type optimizes the data set for comparison with the model, which only considers a single mechanism for deposit formation, at least in the simple formulation used here.

Each data subset was then studied using continuous multifractal analysis as outlined above. The latitude and longitudes were converted to Eastings and Northings (UTM (WGS 84), Zone 35) for the analysis. Table 1 gives the coordinates and grade and ore tonnage values for 10 sample locations extracted from the dataset used in the analysis.

Table 1: Coordinates (in Eastings and Northings: UTM (WGS 84), Zone 35), and corresponding grade and ore tonnage values for 10 sample locations of vein-hosted gold deposits in the Zimbabwe craton (Bartholomew, 1990).

Eastings (m)	Northings (m)	Grade (g/T)	Ore Tonnage
491706	13446998	3.8	1444000
467888	13546137	12.5	7225000
467180	13545132	18.4	6329600
466822	13540406	5.3	969900
463027	13546618	8.5	4335000
462489	13356169	11.2	2408000
423938	13508356	7.8	62368800
423464	13549545	22.6	8904400
414178	13454106	8.6	5977000
407608	13464777	10.5	19960500

RESULTS

The plots of $\chi_q(\varepsilon)$ vs. ε derived using the expanded de Wijs model for ore tonnage can be seen in Figure 3(a) which shows that the plots are straight as required for multifractals by Evertsz and Mandelbrot (1992). Figure 3(b) illustrates the corresponding plot of $f(\alpha)$ vs. α as derived from the method of moments continuous multifractal technique, which shows that $f(\alpha)=\alpha=2$ for all values of q. This result violates the condition which states that the $f(\alpha)$-curve must be parabolic (Evertsz and Mandelbrot, 1992) for a multifractal.

Figure 4 illustrates the relationship between ore tonnage with a grade greater than a specified value and the ore grade for the Zimbabwe craton production data. The plot illustrates that the data is closer to a lognormal relationship between the ore tonnage and grade than a fractal relationship. Continuous multifractal analysis of the tonnage and grade datasets for the Zimbabwe craton suggests that only the grade dataset could be described using a continuous multifractal model. The plots of $\chi_q(\varepsilon)$ vs. ε as seen in Figure 5a and 5b can reasonably be described as linear. However, only the resultant $f(\alpha)$ vs. α curve for the grade data (Fig. 5a) was then found to fit a parabolic shape and thus to be multifractal.

DISCUSSION

A major advantage of the model and methods of analysis used here is that they use only relative distributions of tonnages or grades. Therefore production data can be compared with the model outputs, even though the production data will lack undiscovered deposits, so long as relative distributions of ore tonnage and grade in the production data are comparable to the natural mineralized system. Although there is no direct way

a.

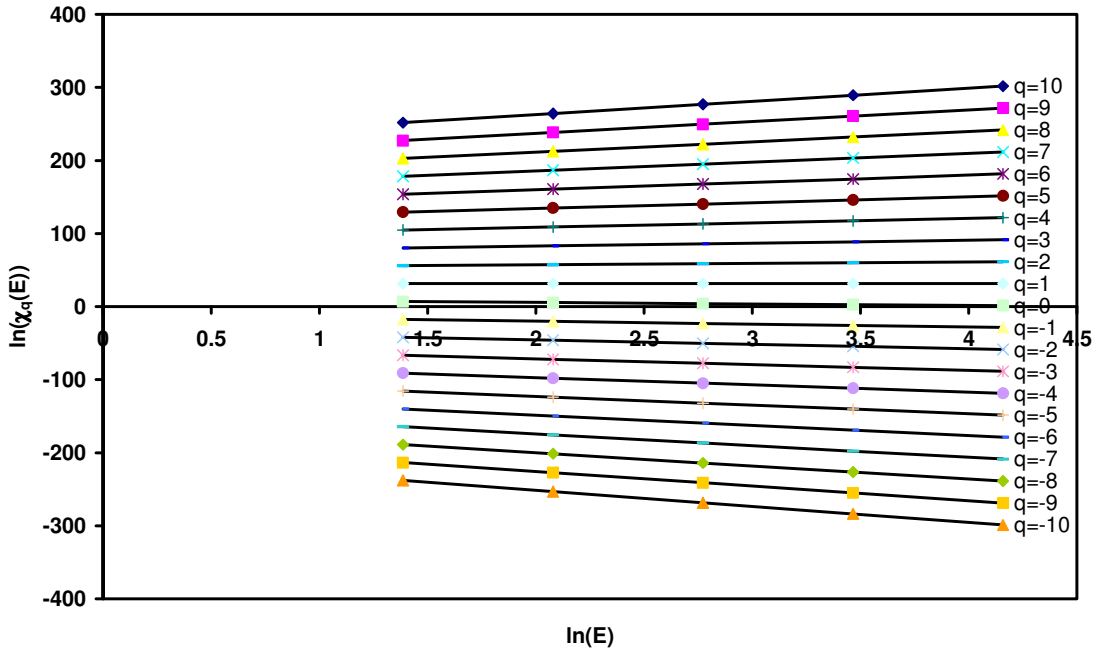

b.

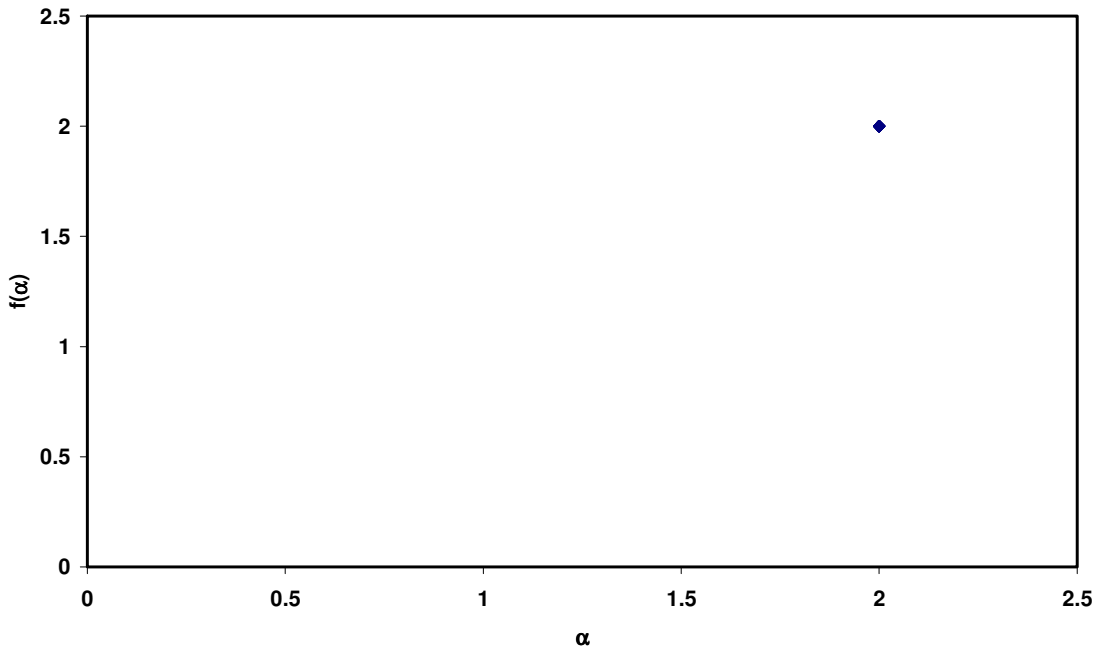

Figure 3: Relationship between (a) natural log of $\chi_q(\varepsilon)$ and natural log of ε, and (b) $f(\alpha)$ and α, of the expanded de Wijs model for ore tonnage (de Wijs, 1951).

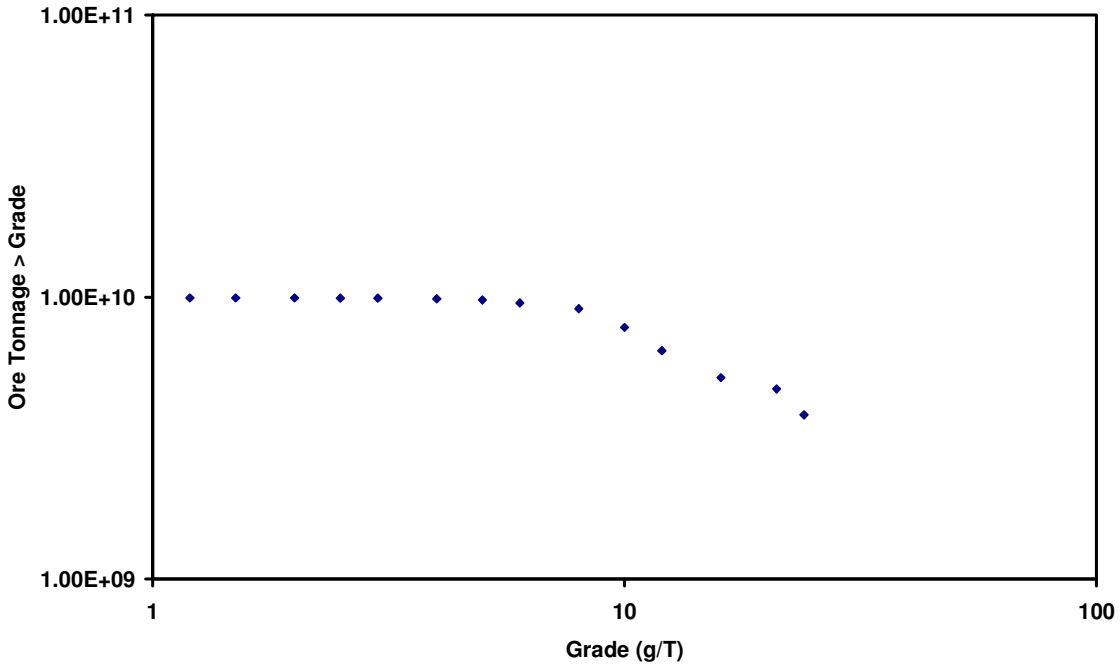

Figure 4: Log-log plot of ore tonnage with a grade greater than a specified value vs. ore grade for vein-hosted gold data in the Zimbabwe craton.

a.

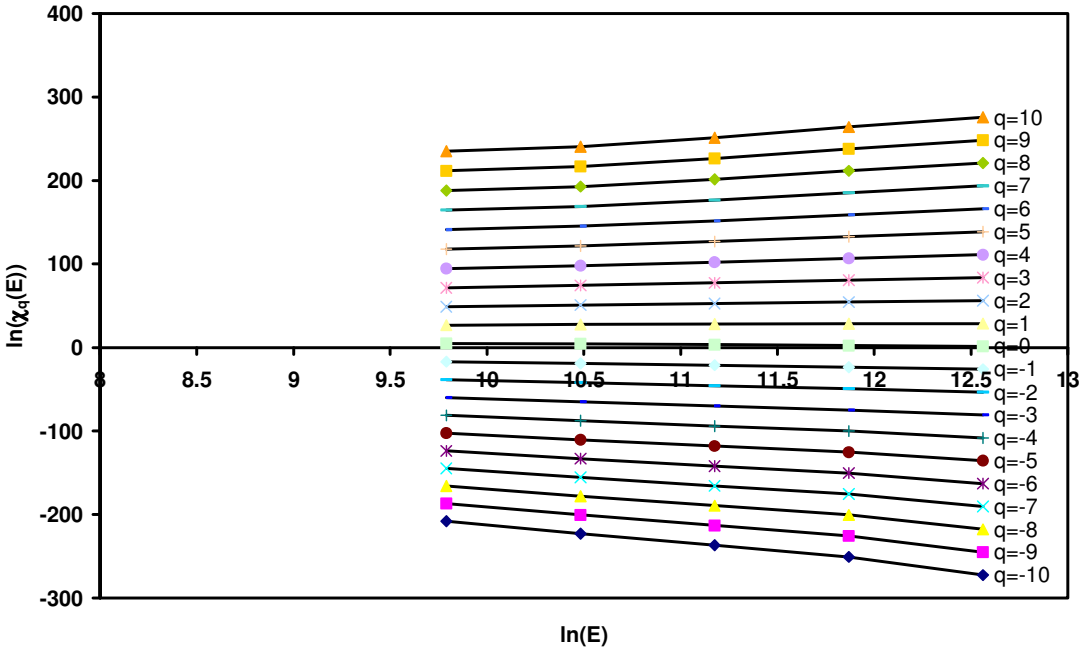
400
300
200
100
0
-100
-200
-300
8
8.5
9
9.5
10
10.5
11
11.5
12
12.5
13
ln(χq(E))
ln(E)
q=10
q=9
q=8
q=7
q=6
q=5
q=4
q=3
q=2
q=1
q=0
q=-1
q=-2
q=-3
q=-4
q=-5
q=-6
q=-7
q=-8
q=-9
q=-10

b.

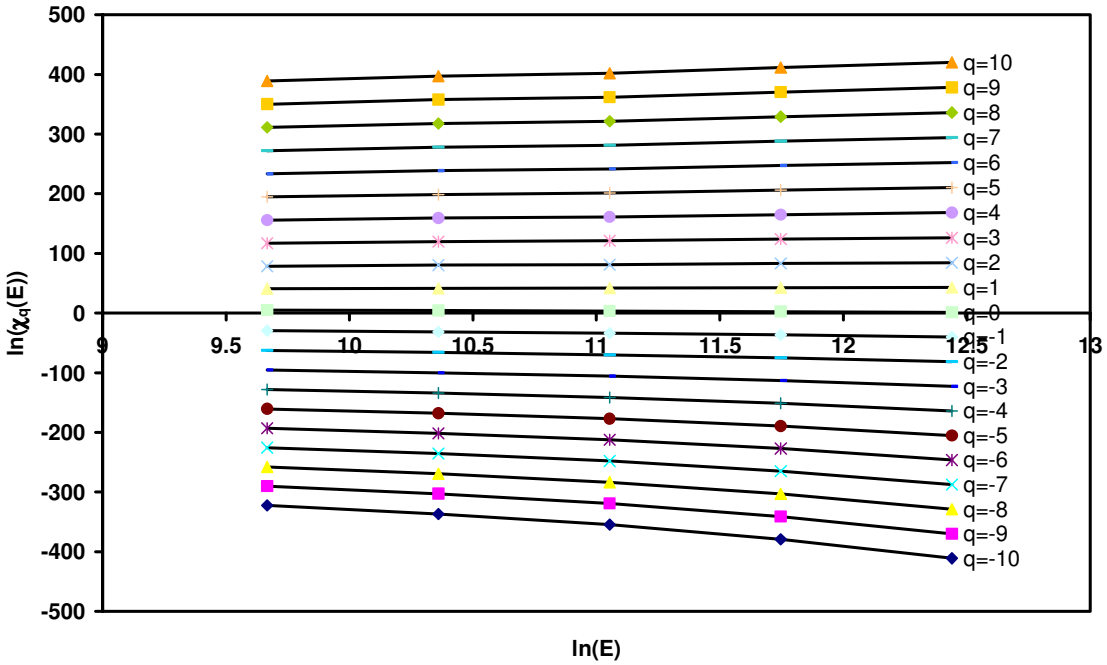
500
400
300
200
100
0
-100
-200
-300
-400
-500
9
9.5
10
10.5
11
11.5
12
12.5
13
ln(χq(E))
ln(E)
q=10
q=9
q=8
q=7
q=6
q=5
q=4
q=3
q=2
q=1
q=0
q=-1
q=-2
q=-3
q=-4
q=-5
q=-6
q=-7
q=-8
q=-9
q=-10

c.

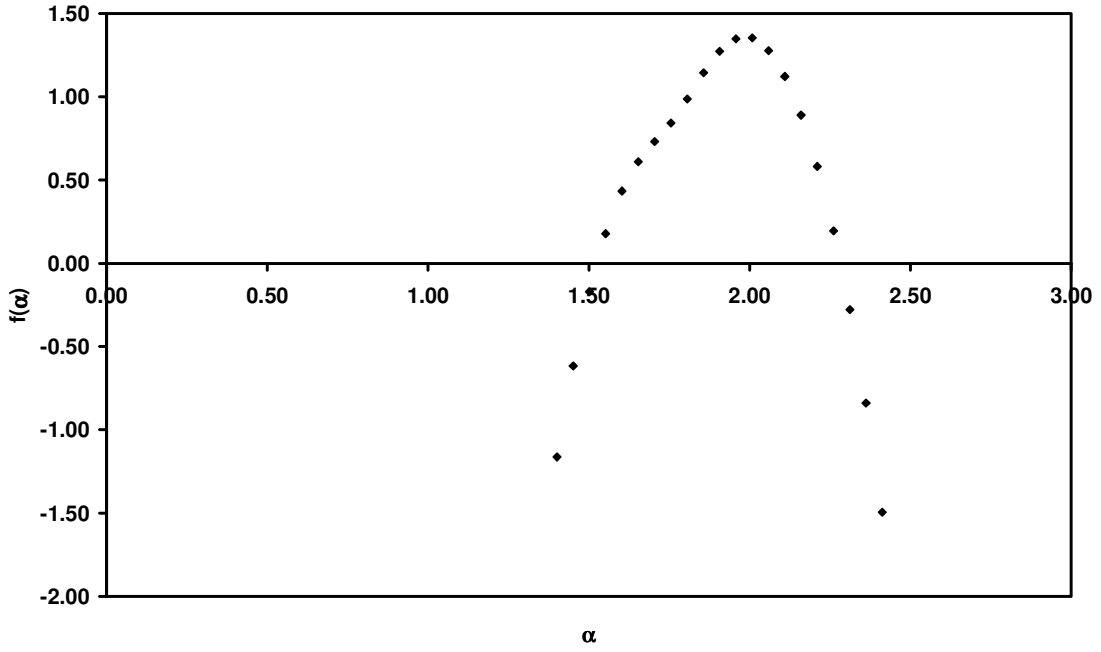

d.

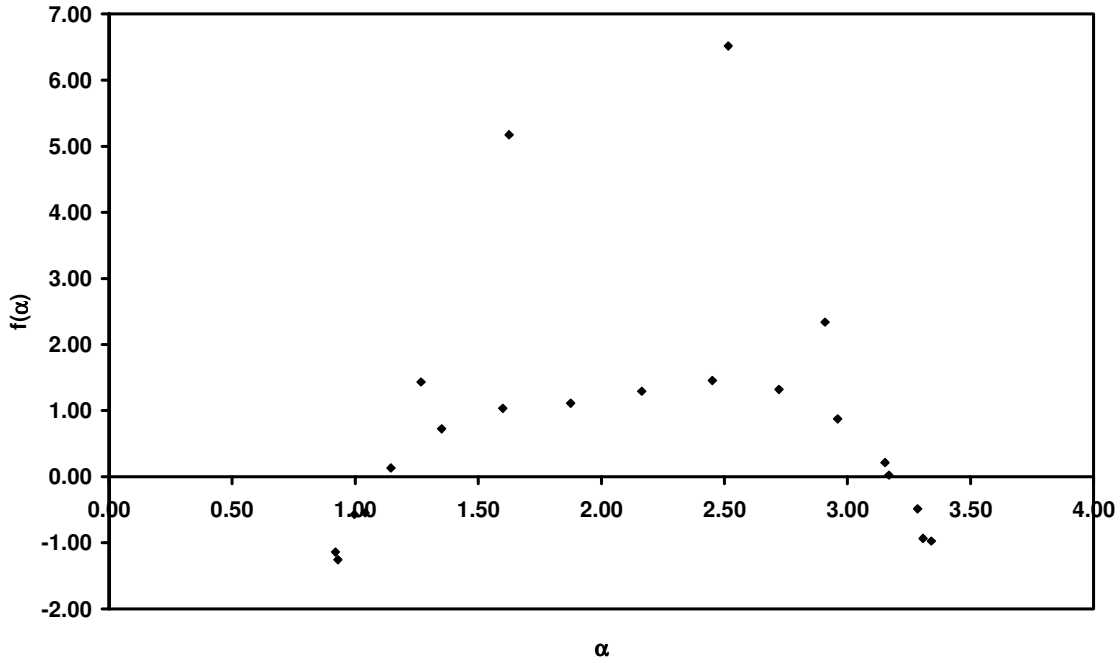

Figure 5: Multifractal relationships for Zimbabwe craton vein-hosted gold production data between (a) natural log of partition function $\chi_q(\varepsilon)$ and natural log of box size ε for grade data, (b) natural log of partition function $\chi_q(\varepsilon)$ and natural log of box size ε for tonnage data, (c) $f(\alpha)$ and α for grade data, and (d) $f(\alpha)$ and α for tonnage data.

to test this, the similarity between the multifractal nature of the database and geochemical survey results discussed below suggests that it is true for grades at least.

Multifractal analysis has established that the relationship between ore tonnage and grade can be described by either lognormal or power-law distributions depending on some unspecified threshold in the size of the deposits being investigated (Agterberg, 1995). Analysis of the expanded de Wijs element distribution model described above indicates that the predicted relationship between cumulative ore tonnage and ore grade is closer to lognormal than power law (Fig. 2), as in the original de Wijs model with a constant ore tonnage (Turcotte, 1989). The Zimbabwe craton production data appears to have a lognormal relationship between ore tonnage and grade, but in view of the uncertainty in the nature of this relationship suggested by the Agterberg (1995) study, better comparisons between models and production data may be made by investigating the multifractal properties of tonnage and grade.

Previous studies have shown that the element concentration distributions predicted from the de Wijs model can be described by continuous multifractals (Xie and Bao, 2004; Agterberg, 2005). The expansion of the de Wijs model may suggest a more realistic way to describe the distribution of enrichment and depletion of elements within the model, and the empirical derivation of the ore tonnages and subsequent analysis using the method of moments technique indicates that the ore tonnage is not multifractal. Figure 3b shows that $f(\alpha)=\alpha=2$ which suggests that the expanded de Wijs model generates mono-fractal rather than multifractal ore tonnages (Håkansson and Russberg, 1990).

Turcotte formulated models for examining the distribution of ore grade and tonnage for both one dimensional (Turcotte, 1989) and three dimensional (Turcotte, 1986) scenarios based on modifications of the de Wijs concentration model (de Wijs, 1951). These studies assumed a constant density for ore tonnage. The Turcotte model does not predict multifractal grade distributions (Agterberg, 2005).

Figure 5a and 5b show that the plots of $\chi_q(\varepsilon)$ vs. ε for production data from the Zimbabwe craton can be considered linear as necessary for continuous multifractal analysis using the method of moments technique. However, analysis of the multifractal spectrum $f(\alpha)$ for the production data suggests that only the grade dataset can be described using a multifractal model (Fig. 5a and c), with the tonnage dataset failing the criteria outlined for the $f(\alpha)$-curve by Evertsz and Mandelbrot (1992). It has been suggested that estimates of $f(\alpha)$ can be unreliable about the point q=1 (Cheng, 1999d), but the curve for the Zimbabwe craton tonnage data (Fig. 5d) deviates from the parabola for a much wider range of values for q.

Several studies of element concentrations from geochemical surveys (Agterberg et al., 1996; Cheng, 1999a; Xie and Bao, 2004) illustrate multifractal plots for $\chi_q(\varepsilon)$ vs. ε and $f(\alpha)$ vs. α for which are even closer to the de Wijs model predictions than the plots for grade data in this study. The closer fits are an expected consequence of the difference between data from geochemical surveys and ore grade data. Geochemical datasets containing stream sediment or rock chip data are sampled at essentially random locations, thus containing a fuller spectrum of data, from low concentrations bordering on the detection limit to the high end, compared to grade data that will emphasize the higher concentrations. Still, Figure 5 shows that ore grade can also be described by a

multifractal model. Given that element concentrations from geochemical datasets have been shown to have multifractal distributions, it is expected that ore grade data should have multifractal properties, as the fractal nature of the data implies scale invariance, with the ore grade data simply occurring at one extreme of the scale.

The results obtained in this study are not conclusive evidence that production data or natural distributions of ore conform to any particular model distribution. However, analysis of the expanded de Wijs model and mineral production data using the same methods does reveal that similar distributions can be observed for a theoretical model (the expanded de Wijs model) and vein-hosted gold production data from the Zimbabwe craton. Neither the de Wijs model, nor the expanded version, predict the multifractal characteristics of tonnage and grade data in addition to the commonly accepted fractal tonnage-grade relationship for production data (de Wijs, 1951; Turcotte, 1989). This study expands the data sets that have been analysed by fractal and multifractal methods, hopefully leading to the selection or development of appropriate theoretical models in the future, and providing useful empirical ways of analyzing production data at present.

CONCLUSIONS

A new model for mineralization is presented that predicts the distribution of ore tonnage in addition to grades, based on expanding the de Wijs model for element redistribution by assigning a density term. This model produces a lognormal relationship between cumulative ore tonnage and grade, and predicts that grade (concentration) is multifractal. These characteristics are observed for gold production data from the Zimbabwe craton when analyzed using the same methodology, establishing that a multifractal relationship can hold for ore grade data in addition to element concentration data. The expanded de

Wijs model predicts that ore tonnage is not multifractal, a result also obtained for ore tonnage data in the Zimbabwe craton. The multifractal properties of grade and ore tonnage may be more reliable ways to compare models with production data than ore tonnage-grade relationships.

SECTION D

Factors affecting fluid flow in strike-slip fault systems: coupled deformation and fluid flow modelling with an application to the western Mount Isa Inlier, Australia

ABSTRACT

Deformation and focussed fluid flow within a mineralized system are critical in the genesis of hydrothermal ore deposits. Dilation and integrated fluid flux due to coupled deformation and fluid flow of simple strike-slip fault geometries were examined using finite difference analysis in three-dimensions. A series of generic fault bend and fault jog geometries consistent with those seen in the western Mount Isa Inlier were modelled, in order to understand how fault geometry parameters influence the dilation and integrated fluid flux. Fault dip, fault width, bend/jog angle and length were varied, and a cross-cutting fault and contrasting rock types were included. The results demonstrate that low fault dips, the presence of contrasts in rock type, and wide faults produce highest dilation and integrated fluid flux values. Increasing fault bend lengths and angles increases dilation and integrated fluid flux, but increasing fault jog length or angle has the opposite effect. There is minimal difference between the outputs from the releasing and restraining fault bend and jog geometries. Model characteristics producing greater fluid flows can be used in a predictive capacity in order to focus exploration on regions with more favourable fault geometries.

INTRODUCTION

Deformation and fluid flow are critical factors for hydrothermal mineralization (Ord, 1990; Laing, 1998; Cox, 1999; Garven et al., 2001; Oliver et al., 2001; Tripp and Vearncombe, 2004; Cox, 2005; Bonson et al., 2007). Coupling of these factors in numerical models can lead to new insights into different mineralizing systems, with implications for ore genesis and potential identification of exploration targets (Oliver et al., 2001; Gow et al., 2002; Zhang et al., 2003; McLellan et al., 2004; Rawling et al., 2006; Schaubs et al., 2006). Faults (and especially fault bends, jogs, and intersections),

and contacts between different lithostratigraphic units can create an environment conducive to increased fluid flow in the system (Craw, 2000; Allibone et al., 2002b; Cox, 2005; Hodkiewicz et al., 2005; Ford and Blenkinsop, 2007b).

Both strike-slip and dip-slip faulting are commonly investigated in two-dimensional modelling (Zhang and Sanderson, 1996; Chester and Fletcher, 1997; Sanderson and Zhang, 1999; Chester and Chester, 2000; Oliver et al., 2001; Zhang et al., 2003; McLellan et al., 2004), with three-dimensional modelling experiments generally focusing on dip-slip faulting (Egan et al., 1999; Gow et al., 2002; Sorjonen-Ward et al., 2002; Rawling et al., 2006). However, two dimensional models of strike-slip faulting do not necessarily provide a good representation of fluid flow during deformation. Brankman and Aydin (2004) took steps to address this issue by modelling a constant overstep fault jog geometry in strike-slip deformation using a boundary element code to examine the effect of variation of the stress regime and to reinterpret the deformation history in three-dimensions. No published example has been found of a numerical modelling study of three dimensional strike-slip fault systems examining the effect of variable fault geometry.

Varying fault geometries in coupled deformation and fluid flow models has the potential to produce vastly different outputs. Previous studies of coupled deformation and fluid flow models for investigating mineralizing systems present qualitative approaches for analyzing the results obtained from numerical modelling (Oliver et al., 2001; Gow et al., 2002; Nemčok et al., 2002; Cox and Ruming, 2004; Matthäi et al., 2004; McLellan et al., 2004). Relatively few studies have presented a quantitative analysis of the model outputs (Sanderson and Zhang, 1999; Harris et al., 2003;

Sanderson and Zhang, 2004). While qualitative analysis is important to appraise the significant controlling variables from a large number of model outputs, outputs may also need to be measured quantitatively to understand the relative importance of different factors on model results in detail.

The aims of this paper are to systematically investigate and quantify the effect of different fault bend and jog geometries and rock types on the results of three-dimensional coupled deformation and fluid flow models of strike-slip fault systems. These results may assist with mineral exploration.

The Western Succession of the Mount Isa Inlier hosts some of the largest copper deposits within the region, such as Mount Isa, Mammoth, and Esperanza, which are associated with regional steeply dipping N-S striking structures (Van Dijk, 1991; Drummond et al., 1998). Model geometries and subsequent results examined in this study are characteristic of Mount Isa Inlier geology at the time of copper mineralization, and are also a generic exploration of fluid flow in strike-slip fault systems.

REGIONAL GEOLOGY

The western Mount Isa Inlier can be separated from the remainder of the outcropping Proterozoic province based on the stratigraphy and seismic refraction data, which shows that a terrain boundary may exist near the Pilgrim Fault (Blake and Stewart, 1992; McDonald et al., 1997). To the west of this line, the stratigraphy is referred to as the Western Succession. The Western Succession is dominated by N-S to NE striking structures (Scott and Taylor, 1982; Bell et al., 1988; Nijman et al., 1992; Queensland Department of Mines and Energy et al., 2000). These structures were formed or

reactivated during the major D_2 E-W shortening event (c. 1590 Ma) (Bell et al., 1988; Laing, 1998). Further, possibly strike-slip, reactivation of these faults occurred during D_3 (c. 1550 Ma), also an approximately E-W shortening event, and perhaps as late as the Cambrian and Ordovician (Feltrin et al., 2003; Mark et al., 2004). Seismic profiles indicate that the majority of faults in the region are steeply dipping (Drummond et al., 1998; MacCready, 2006).

Major fault zones in the Western Succession include the Western Border, Mount Isa, and Mount Gordon fault zones, which are steeply dipping N-S to NNE striking structures (Van Dijk, 1991; Drummond et al., 1998). Splays off each of these major structures have variable strikes. Previous studies have suggested a spatial relationship between major copper orebodies and fault bends and fault intersections within the Mount Isa Inlier (Oliver et al., 2001; Ford and Blenkinsop, 2007a). Figure 1 illustrates a number of copper deposits in the Gunpowder region of the Western Succession proximal to fault bends, fault jogs, and fault intersections.

Copper deposits in the Western Succession are predominantly hosted by brecciated sediments adjacent to faults (Scott and Taylor, 1982; Blake et al., 1990; Van Dijk, 1991). The lithostratigraphic units that host these deposits vary distinctly over the region, and the deposits are commonly proximal to major faults. For example, the Lady Annie Cu deposit in the Lawn Hill Platform is hosted by the McNamara Group, which is dominated by sideritic and locally carbonaceous shales, mudstones, and sandstones, and is proximal to the Western Border fault zone (Van Dijk, 1991). The world class Mount Isa copper deposit is hosted by the Urquhart Shale and sits immediately above

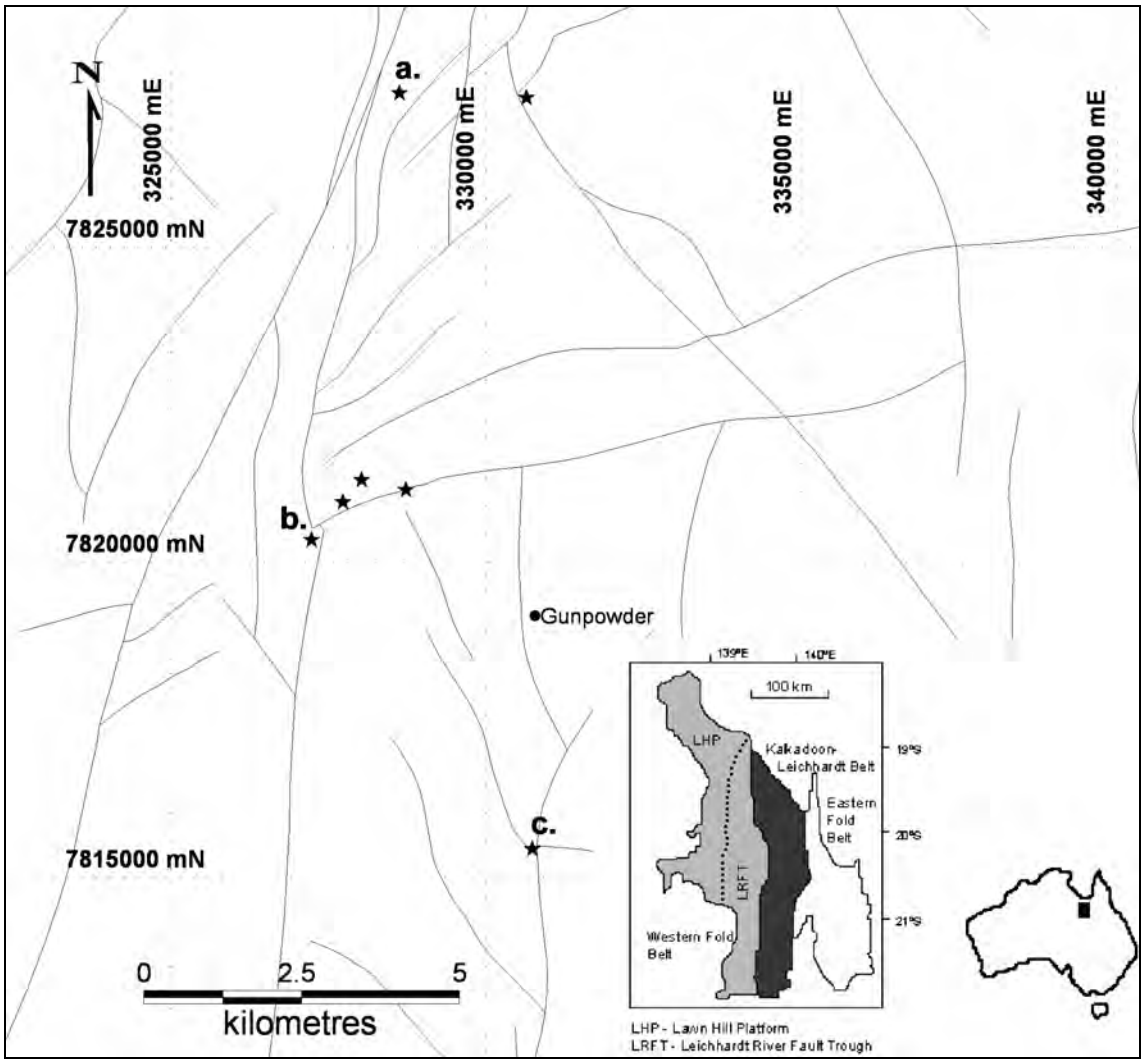

Figure 1: Map illustrating copper deposits (★) in the Gunpowder region of the Western Succession of the Mount Isa Inlier proximal to (a) a fault bend, (b) a fault jog (with a cross-cutting fault), and (c) a fault intersection. Faults are interpreted from the Northwest Queensland Mineral Province Report (Queensland Department of Mines and Energy et al., 2000). Copper deposit locations extracted from the Queensland Mineral Occurrence Database (Queensland Department of Natural Resources and Mines, 2005). Inset illustrates location of the three tectonic divisions of the Mount Isa Inlier with the Western Succession comprising of the Western Fold Belt and the Kalkadoon-Leichhardt Belt (Blake and Stewart, 1992; McDonald et al., 1997).

the Eastern Creek Volcanics (metabasalts) (Wyborn, 1987; Matthäi et al., 2004). The copper deposit lies just to the east of the Mount Isa fault zone, which has been proposed as a fluid and heat conduit in the mineralizing system (Matthäi et al., 2004). The Mammoth and Esperanza copper deposits are both located within the Mount Gordon fault zone north of Mount Isa, near Gunpowder, with Mammoth being hosted by the Myally Subgroup (quartzite, sandstone, and siltstone) and Esperanza hosted by the Esperanza Formation (dolostone and chert) (Scott and Taylor, 1982; Van Dijk, 1991; Nijman et al., 1992).

NUMERICAL MODELLING

This study aims to investigate generic controls on deformation, fluid flow and possible mineralization based on the general Western Succession Mount Isa geology, rather than specific local controls. The effects of different fault geometries, rock types and a combination of the two, are tested in three-dimensional models to determine the most favourable variables in terms of potential for hydrothermal copper mineralization in the Western Succession. Using Fast Lagrangian Analysis of Continua in Three Dimensions (FLAC^{3D} ©) (Itasca Consulting Group, 2002), coupled deformation and fluid flow models were constructed and tested to determine which configurations had the highest mineralization potential. Table 1 summarises the models tested.

A simple fault bend geometry is shown in Fig. 2 with the length of the fault bend/jog (L), dip (D), width of fault (w), and orientation of fault bend/jog relative to North (θ, positive values clockwise from N, negative values anti-clockwise) being varied in the models. Figures 3 and 4 illustrate the basic geometry of the fault jog models and intersecting fault models respectively. The effect of parameter variation was evaluated

Table 1: Summary of model configurations tested.

Model No.	Bend/Jog	Rock Type(s)	θ	L (m)	D	W (m)	X-Cut	Dilation Ratio	IFF Ratio
1	Bend	ECV	-175°	2500	90°	50	N	-0.00046	804.44
2*	Bend	ECV	-165°	2500	90°	50	N	*	*
3	Bend	ECV	-150°	2500	90°	50	N	-0.00048	807.70
4	Bend	ECV	-135°	2500	90°	50	N	-0.00052	793.89
5	Bend	ECV	175°	2500	90°	50	N	-0.00047	803.53
6	Bend	ECV	165°	2500	90°	50	N	-0.00049	800.67
7	Bend	ECV	150°	2500	90°	50	N	-0.00052	793.67
8	Bend	ECV	135°	2500	90°	50	N	-0.00058	782.39
9	Bend	ECV	-150°	2500	90°	25	N	-0.00032	997.17
10	Bend	ECV	-150°	2500	90°	100	N	-0.00075	688.30
11	Bend	ECV	-150°	500	90°	50	N	-0.00048	779.14
12	Bend	ECV	-150°	1000	90°	50	N	-0.00048	783.26
13	Bend	ECV	-150°	5000	90°	50	N	-0.00054	819.67
14	Bend	ECV	-150°	2500	-85°	50	N	-0.00051	823.80
15	Bend	ECV	-150°	2500	85°	50	N	-0.00051	823.76
16	Bend	ECV	-150°	2500	-45°	50	N	-0.01041	1278.8
17	Bend	ECV	-150°	2500	45°	50	N	-0.01041	1278.8
18	Bend	ECV	-150°	2500	90°	50	Y	-0.00062	818.54
19	Jog	ECV	-175°	2500	90°	50	N	-0.00044	872.78
20	Jog	ECV	-165°	2500	90°	50	N	-0.00044	865.79
21	Jog	ECV	-150°	2500	90°	50	N	-0.00044	860.70
22	Jog	ECV	-135°	2500	90°	50	N	-0.00044	851.48
23	Jog	ECV	175°	2500	90°	50	N	-0.00044	865.31
24	Jog	ECV	165°	2500	90°	50	N	-0.00044	857.53
25	Jog	ECV	150°	2500	90°	50	N	-0.00044	855.55
26	Jog	ECV	135°	2500	90°	50	N	-0.00044	855.76
27	Jog	ECV	-150°	2500	90°	25	N	-0.00030	1093.2
28	Jog	ECV	-150°	2500	90°	100	N	-0.00065	738.08
29*	Jog	ECV	-150°	500	90°	50	N	*	*
30	Jog	ECV	-150°	1000	90°	50	N	-0.00044	861.47
31	Jog	ECV	-150°	5000	90°	50	N	-0.00043	897.80
32	Jog	ECV	-150°	2500	-85°	50	N	-0.00046	871.86
33	Jog	ECV	-150°	2500	85°	50	N	-0.00046	872.01
34	Jog	ECV	-150°	2500	-45°	50	N	-0.00543	1000.3
35	Jog	ECV	-150°	2500	45°	50	N	-0.00543	1000.6
36	Jog	ECV	-150°	2500	90°	50	Y	-0.00043	893.43
37	Bend	ECV/Syb	-150°	2500	90°	0	N	-0.00085	53.794
38	Bend	ECV/Syb/Urq	-150°	2500	90°	0	N	-0.00076	64.057
39	Bend	ECV/MSG	-150°	2500	90°	50	N	-0.00057	3504.7
40	Bend	ECV/Syb	-150°	2500	90°	50	N	-0.00055	11326
41	Bend	ECV/MSG	-150°	2500	90°	50	Y	-0.00194	9309.5
42	Bend	ECV/MSG/Urq	-150°	2500	90°	50	Y	-0.00066	6772.1
43	Jog	ECV/MSG/Urq	-150°	2500	90°	50	Y	-0.00065	7818.9
44	Jog	ECV/MSG	-150°	2500	90°	50	Y	-0.00123	8440.1

ECV = Eastern Creek Volcanics (metabasalts); MSG = Myally Subgroup (quartzite); Syb = Sybella Granite; Urq = Urquhart Shale

* Note: Model 2 and Model 29 failed to run to 10% shortening.

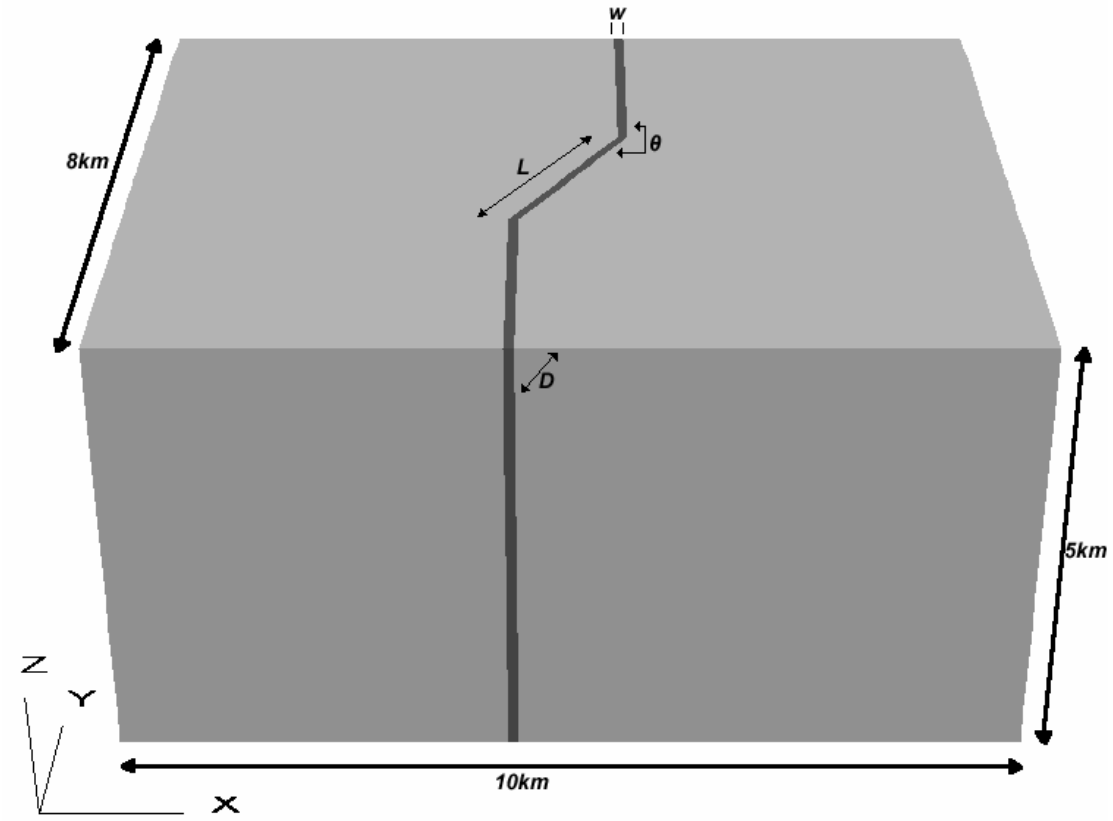

Figure 2: Fault bend geometry (Model 3) indicating values varied during FLAC^{3D} modelling: length of fault bend (*L*), dip (*D*), orientation of fault bend/jog (θ=φ), and width of fault (*w*).

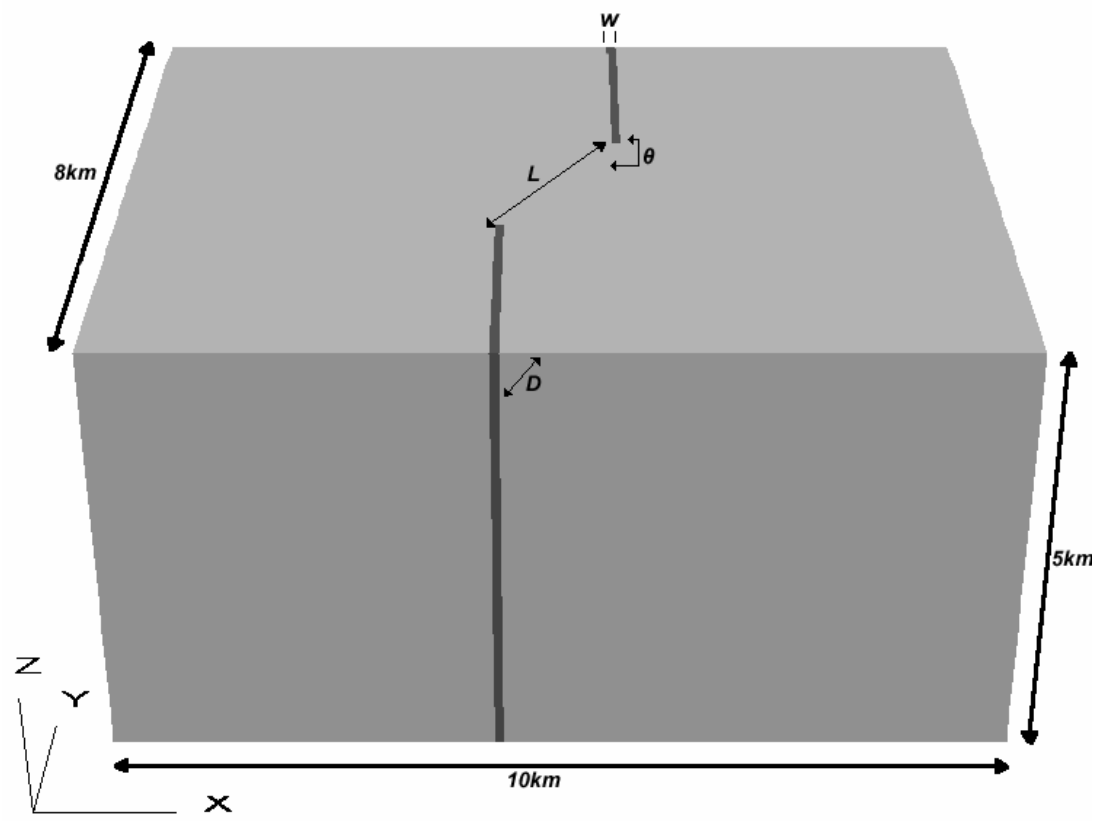

Figure 3: Fault jog geometry (Model 21) indicating values varied during FLAC^{3D} modelling: length of fault bend (L), dip (D), orientation of fault bend/jog (θ=φ), and width of fault (w).

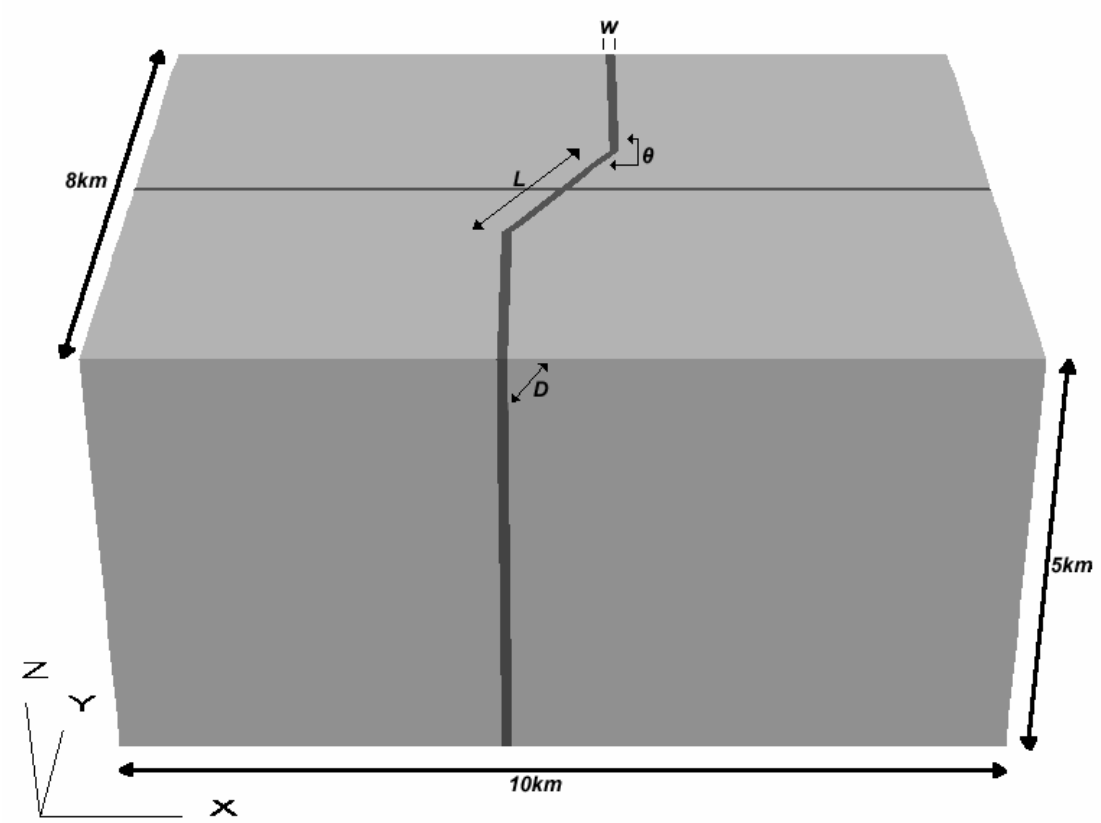

Figure 4: Fault bend geometry with a cross-cutting fault (Model 18) indicating values varied during FLAC^{3D} modelling: length of fault bend (L), dip (D), orientation of fault bend/jog (θ=φ), and width of fault (w).

by varying each parameter from a standard geometry in which L= 2500 m, θ=-150°, D=90 °, and w=50 m.

A Mohr-Coulomb constitutive model was used, which is appropriate for representing the elastic-plastic deformation in the mid to upper crust, with fluid flow obeying Darcy's Law for flow in a porous media (Oliver et al., 2001; McLellan et al., 2004). Vermeer and de Borst (1984) summarize the Mohr-Coulomb constitutive model by defining the elastic moduli, yield functions for shear and tensile failure and the corresponding functions for plastic strain related to yielding. Cohesion, friction angle and tensile strength can be used to define the yield functions. Materials will initially deform elastically up to a yield point, at which point the material will deform plastically (irreversibly). The plastic deformation is associated with shear or tensile failure, which leads to dilatancy in the material. Fluid flux in a system defined by Darcy's Law is governed by the conductivity and hydraulic head, which is related to elevation above a given point, acceleration due to gravity, pore fluid pressure and the fluid density. During plastic deformation, high strain can cause positive dilation, which is governed by the dilation angle. This dilation is associated with a change in pore pressure, which in turn affects the hydraulic head, and thus the fluid flux within the system. The dilation also leads to changes in the effective stress, thus affecting plastic deformation. This feedback loop between the deformation and fluid flow continues in a coupled manner. More comprehensive explanations of the Mohr-Coulomb constitutive model, Darcy's Law, and the coupling of deformation and fluid flow is provided by Vermeer and de Borst (1984), Oliver, et al. (2001) and Ord and Oliver (1997).

The strike of the main faults in the models is N-S, similar the orientations of the Western Border fault zone (N-S), Mount Isa fault zone (N-S) and the Mount Gordon fault zone (NNE), which host the most significant copper orebodies in the Western Succession. Additional geometries considered include an E-W striking fault through the middle of the model, similar to a set of faults in this general orientation in the Western Succession (e.g. Fig. 1). The dimensions of all models were x=10 km, y=8 km, and z=5 km.

Properties of the surrounding host rock were chosen to be representative of the Eastern Creek Volcanics, as this has been suggested as the source of copper at Mount Isa, Mammoth and Esperanza (Scott and Taylor, 1982; Wyborn, 1987; Matthäi et al., 2004). Other rock properties were assigned to be representative of the Mount Isa and Gunpowder regions. In addition to the Eastern Creek Volcanics, models representative of the Mount Isa region included a Sybella Granite unit, an Urquhart Shale unit, and/or a Myally Subgroup (quartzite) unit (Wyborn, 1987). Models representative of the Gunpowder region included a Myally Subgroup unit in addition to the Eastern Creek Volcanics (Scott and Taylor, 1982). Material properties for the Eastern Creek Volcanics, and other rock types used in the models are listed in Table 2. The top of all the models represents a depth of 5 km, consistent with previous studies indicating that the depth of emplacement of the copper orebody at Mount Isa was between 5 km and 10 km with a density of 2700 kg/m^3 for the overburden (Matthäi et al., 2004).

The models were initialized with a hydrostatic fluid pressure, which was allowed to vary from hydrostatic to near lithostatic (cf. Oliver et al., 2001; Zhang et al., 2006). The base of the models remained at a fixed elevation. The left, right, front and back

Table 2: Material Properties for the FLAC^{3D} Models (cf. Oliver et al., 2001; McLellan et al., 2004)

	ECV	MSG	Sybella	Urquhart	Fault
Density (kg/m^3)	2700	2600	2650	2500	2700
Bulk modulus (Pa)	2.7e10	4.0e10	4.95e10	2.8e10	2.7e10
Shear modulus (Pa)	7.0e9	2.5e10	2.9e10	6.7e9	7.0e9
Tensile strength (Pa)	1.0e7	3.5e6	4.0e5	1.2e6	0
Cohesion (Pa)	2.0e7	7.0e7	4.0e6	3.0e6	2.0e2
Dilation Angle (deg)	3	3	3	3	4
Friction Angle (deg)	30	30	30	30	20
Permeability (m^2)	1e-18	1e-19	2e-19	1e-19	1e-16
Porosity (%)	5	5	5	5	5

ECV = Eastern Creek Volcanics (metabasalts); MSG = Myally Subgroup (quartzite); Sybella = Sybella Granite; Urquhart = Urquhart Shale

boundaries were constrained to remain vertical. The top of each model was free to move in any direction (cf. Oliver et al., 2001; Sheldon et al., 2006). Thus the initial rectangular prism was deformed into a parallelepiped with a rhombic base. The models were shortened 10% through the application of velocity boundary conditions (250000 timesteps at 0.002 metres/timestep in the direction of shortening) with the shortening direction set at 112.5º to be consistent previous models of syn-D_3 copper mineralization (McLellan, 2006; McLellan and Oliver, 2007). This boundary condition resulted in dominantly sinistral strike-slip faulting such that the fault bend/jog was releasing with positive θ and restraining with negative θ. Further models were run with contrasts in rock type and no faults, which allowed comparisons to be made with outputs from the different fault geometries. Models containing both contrasting rock types and faults were also tested.

Outputs from the models included pore pressure, mean stress, shear strain increment, volumetric strain, and integrated fluid flux. In this study, focus is placed on the volumetric strain (dilation) and the integrated fluid flux outputs due to their critical importance in ore genesis.

RESULTS

The volumetric strain and integrated fluid flux were evaluated within the fault zone (from the maximum values and 99th percentile values, P99) and in areas proximal to the fault zone (from the 90th percentile values, P90). Detailed examination of several models verifies that the 99th percentile value occurs only within the fault zone, and that at the 90th percentile, the values are proximal to, but outside the fault zone (with the exception of the models with a cross-cutting fault, in which case the P90 values also occur within the fault zone). These criteria were applied to examine the magnitude of dilation and fluid flow in and around the fault, and to determine how well the fault and/or surrounding host rock acted as fluid flow pathways or barriers.

Effect of Fault Dip Variation

Table 3 illustrates that there are approximately two orders of magnitude for fault bend models, and one order of magnitude for fault jog models, between the maximum amount of dilation seen in the 45° dip faults and the maximum dilation seen in the remainder of the fault bend models with vertical dips (Fig. 5a; Fig. 6). Having a lower dip produces much less contrast in integrated fluid. Fault bend models produce higher dilation and integrated fluid flux values than the corresponding fault jog models within the fault zone.

While models with a lower dip fault may have the highest maximum dilation (Fig. 6b, d) and relatively high integrated fluid flux values (Fig. 6f, h), these values are focused entirely along the fault zone. There is a considerable drop in values for the dilation and integrated fluid flux in areas proximal to the fault zone (Table 3).

Table 3: Dilation and integrated fluid flux for each model (parameters defined in Table 1). Min. and Max. are the minimum and maximum values, P99 and P90 are the 99th and 90th percentiles, and results are for 10% deformation with azimuth=112.5°.

	Dilation				Integrated Fluid Flud (m^3/m^2)			
Model	Min.	Max.	P99	P90	Min.	Max.	P99	P90
1	-9.9957	0.0045916	0.003300	0.0011000	0.060835	48.938	31.94540	1.3807
2 *								
3	-9.9881	0.0047777	0.003320	0.0010510	0.0595210	48.075	31.03960	1.3665
4	-9.9986	0.0052442	0.003668	0.0010730	0.0598910	47.547	30.11160	1.3816
5	-9.9978	0.0047066	0.003420	0.0011250	0.0615960	49.494	32.22520	1.3994
6	-9.9474	0.0048596	0.003579	0.0011760	0.0625540	50.085	32.44010	1.4243
7	-9.9608	0.0051560	0.003865	0.0012650	0.0641120	50.884	32.57670	1.4703
8	-9.9742	0.0057495	0.004256	0.0013420	0.0652630	51.061	32.08060	1.5113
9	-9.945	0.0031817	0.001952	0.0008520	0.0211790	21.119	9.33520	0.4249
10	-9.9959	0.0075258	0.005963	0.0013269	0.1348600	92.824	73.87140	3.3814
11	-9.9991	0.0047835	0.003356	0.0010600	0.0533690	41.582	26.42750	1.2003
12	-9.9987	0.0047855	0.003383	0.0010490	0.0599990	46.995	30.94880	1.3680
13	-9.9919	0.0053665	0.003270	0.0010350	0.0593960	48.685	31.16200	1.3578
14	-9.9919	0.0051070	0.003523	0.0010590	0.0585990	48.274	30.95300	1.3683
15	-9.9994	0.0051111	0.003525	0.0010590	0.0586010	48.273	30.95280	1.3682
16	-9.9952	0.1040800	0.052024	0.0013960	0.0572730	73.238	32.05700	1.6376
17	-9.9965	0.1040900	0.052020	0.0013960	0.0572730	73.239	32.05700	1.6376
18	-9.9552	0.0061809	0.004122	0.0013400	0.0382670	31.323	30.30220	9.1121
19	-9.9906	0.0043538	0.002381	0.0011040	0.0628920	54.891	26.67700	1.4139
20	-9.9842	0.0043685	0.002101	0.0010960	0.0627060	54.290	26.53190	1.4148
21	-9.9345	0.0043768	0.002141	0.0010830	0.0627570	54.015	26.51690	1.4161
22	-9.9961	0.0043683	0.002075	0.0010760	0.0633790	53.966	26.54420	1.4169
23	-9.9896	0.0043569	0.002370	0.0011050	0.0635100	54.956	26.73180	1.4143
24	-9.9511	0.0043796	0.002105	0.0010960	0.0634110	54.377	26.63090	1.4159
25	-9.9603	0.0043755	0.002120	0.0010800	0.0631720	54.047	26.62090	1.4183
26	-9.9938	0.0043630	0.002052	0.0010800	0.0630190	53.929	26.64090	1.4199
27	-9.974	0.0030299	0.001630	0.0009010	0.0219310	23.976	7.67004	0.4387
28	-9.9972	0.0065196	0.003397	0.0013920	0.1513800	111.730	73.65290	3.6167
29 *								
30	-9.9765	0.0044328	0.002894	0.0010910	0.0622300	53.609	32.95950	1.4192
31	-9.9598	0.0042553	0.001892	0.0011030	0.0633640	56.888	26.14500	1.3999
32	-9.9795	0.0045570	0.002170	0.0010900	0.0621210	54.161	26.44690	1.4147
33	-9.9701	0.0045587	0.002173	0.0010940	0.0621120	54.162	26.44680	1.4147
34	-9.9995	0.0542770	0.023420	0.0011500	0.0567750	56.790	19.74770	1.4319
35	-9.9916	0.0542670	0.023770	0.0011530	0.0567600	56.795	19.74170	1.4320
36	-9.9948	0.0043140	0.003928	0.0013000	0.0388560	34.715	31.83790	7.6720
37	-9.9378	0.0084830	0.008175	0.0066540	1.5584000	83.833	72.42420	56.0800
38	-9.9745	0.0076240	0.006274	0.0038940	1.3938000	89.283	78.49820	61.9240
39	-9.9978	0.0056916	0.004554	0.0028537	0.0132980	46.605	28.24780	1.3790
40	-9.9858	0.0055398	0.003300	0.0016433	0.0043400	49.155	35.63460	1.4556
41	-9.9989	0.0194200	0.010607	0.0019331	0.0036670	34.138	30.50600	11.8495
42	-9.9953	0.0066363	0.004363	0.0018050	0.0044140	29.892	27.72020	8.1681
43	-9.9102	0.0063940	0.004180	0.0017000	0.0044240	34.591	28.17440	7.2935
44	-9.9822	0.0122850	0.005204	0.0015097	0.0042630	35.980	33.22880	8.8498

* Note: Model 2 and Model 29 failed to run to 10% shortening.

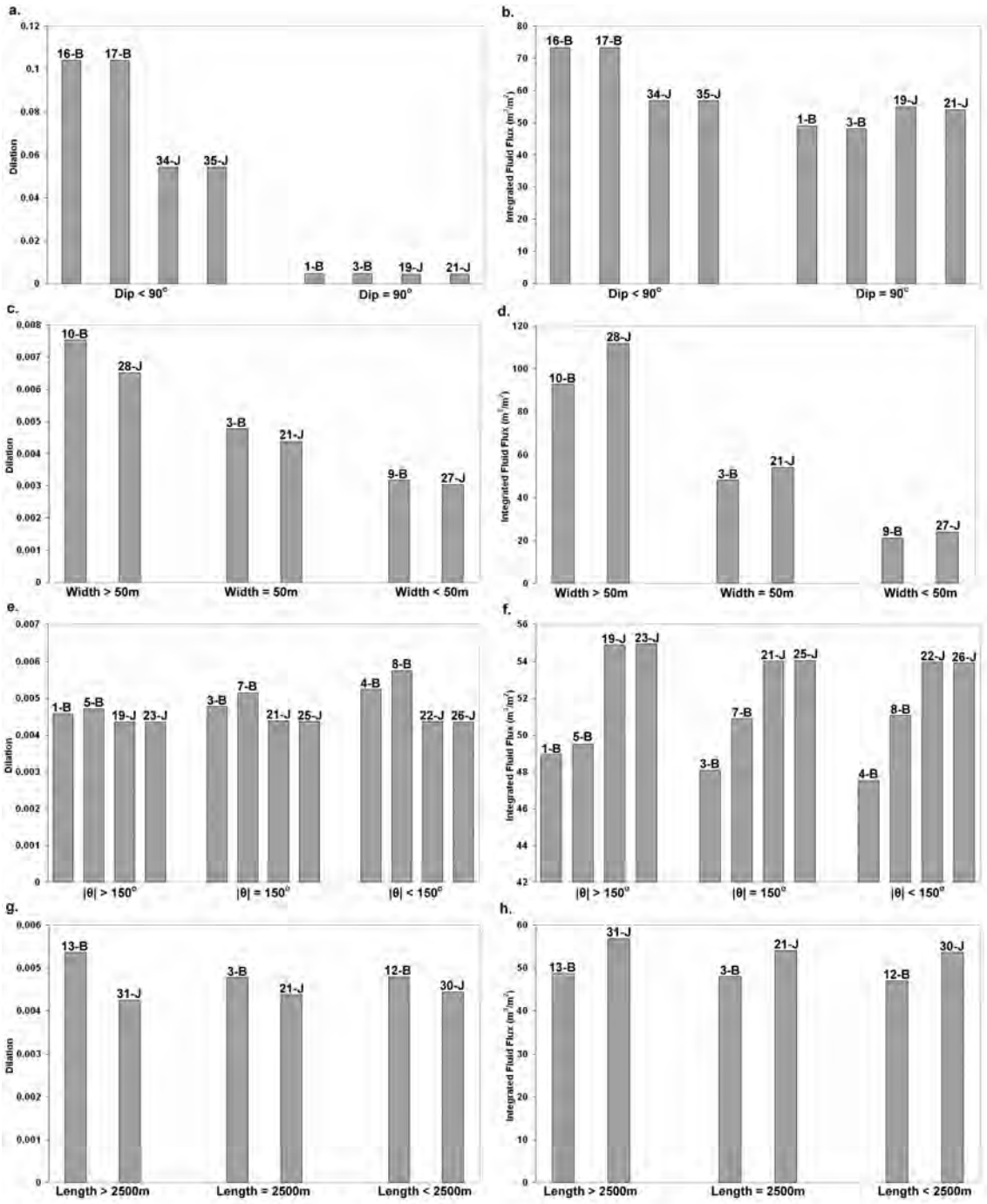

Figure 5: Maximum dilation and integrated fluid flux values for the continuous fault geometry variables from selected fault bend (B) and fault jog (J) models. Illustration of maximum (a) dilation for variation of fault dip, (b) integrated fluid flux for variation of fault dip, (c) dilation for variation of fault width, (d) integrated fluid flux for variation of fault width, (e) dilation for variation of bend/jog angle, (f) integrated fluid flux for variation of bend/jog angle, (g) dilation for variation of bend/jog length, and (h) integrated fluid flux for variation of bend/jog length.

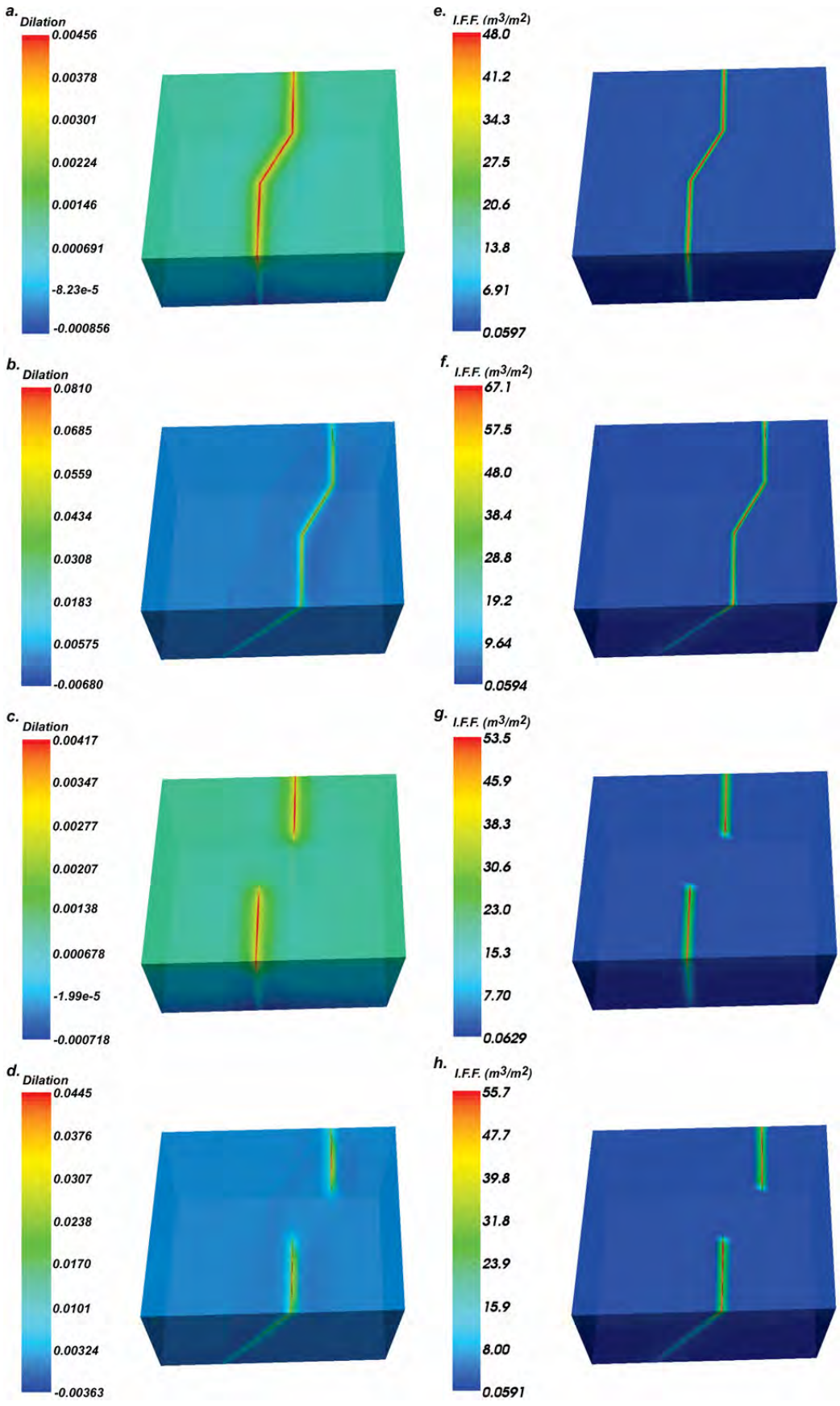

Figure 6: The effect of varying fault dip *D* on dilation (left column, a – d) and integrated fluid flux (right column, e - h).

Effect of Fault Width Variation

Table 3 indicates that wide faults produce comparatively high dilation values within the fault zone when compared to changes in other fault geometry variables, with little difference between the values for the fault bend and fault jog models (Fig. 5c; Fig. 7). The integrated fluid flux was highest in both fault bend and jog models with wider faults, with the fault jog models producing slightly higher values (Fig. 5d; Fig. 7).

Dilation for fault bend models in areas proximal to the fault zone was found to drop considerably (Table 3), and these models also produced lower dilation values when compared to changes in other fault geometry variables. For fault jog models, the dilation was highest when compared to changes in other fault geometry variables for areas proximal to the fault. A wide fault produces higher values of integrated fluid flux proximal to the fault zone than a narrow fault (Fig. 7), though the magnitude drops considerably with distance from the fault.

Effect of Bend/Jog Angle Variation

Fault bends produced higher dilation values within the fault zone as the absolute value of the angle θ of the bend decreased, and the fault jogs had higher dilation as the absolute value of θ increased (Table 3; Fig. 5e). The difference in dilation values within the fault zone as the angle is varied is much greater for the fault bends than the fault jogs, with the maximum values for the fault jogs displaying very minor changes as the angle is varied. Similar results were obtained for the integrated fluid flux values (Fig. 5f; Fig. 8). It is interesting to note that the models with a restraining bend or jog geometry had similar outputs to the releasing fault geometries (Table 3; Fig. 5e, f). In comparison to other geometry variables, having a favorable fault bend or fault jog angle

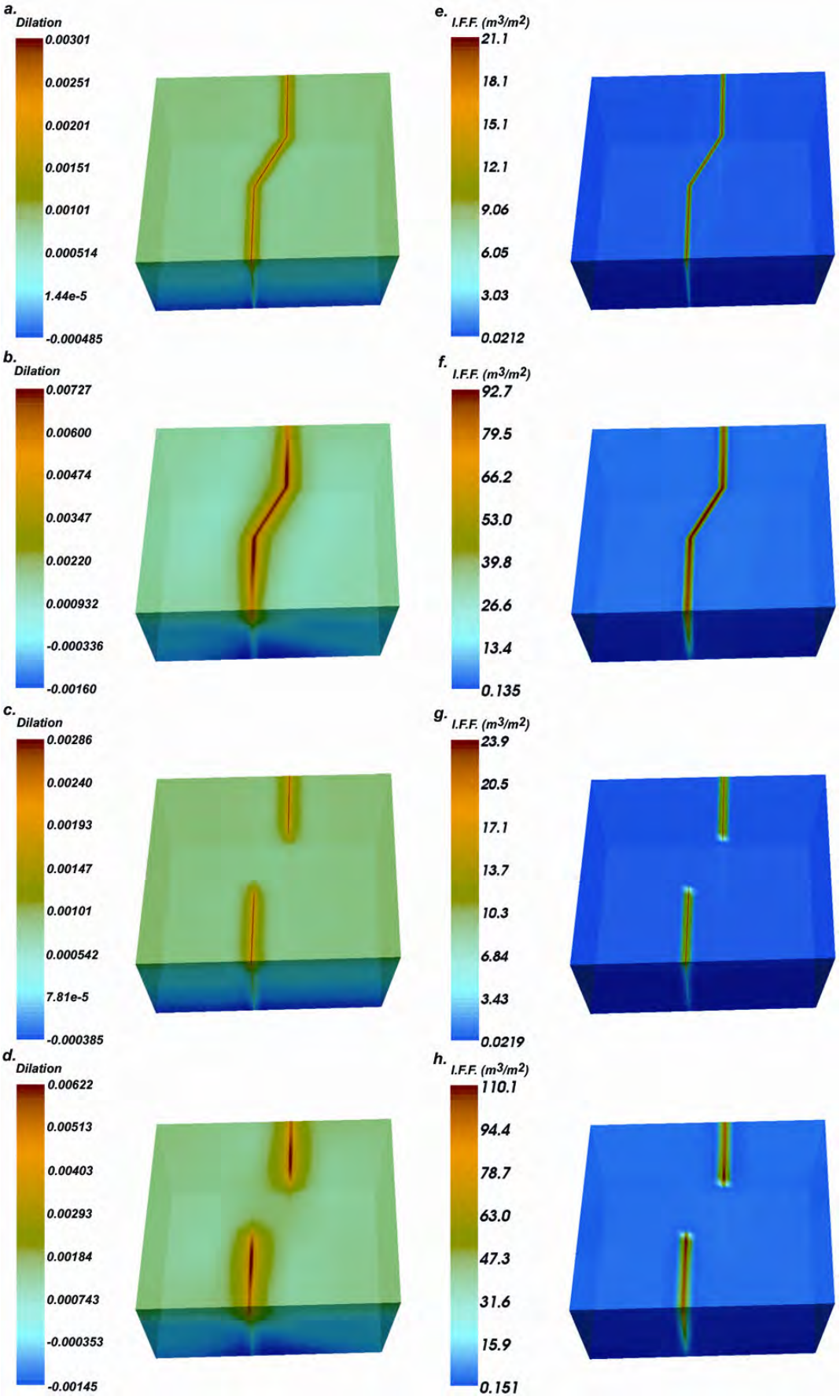

Figure 7: The effect of varying fault width *w* on dilation (left column, a – d) and integrated fluid flux (right column, e - h).

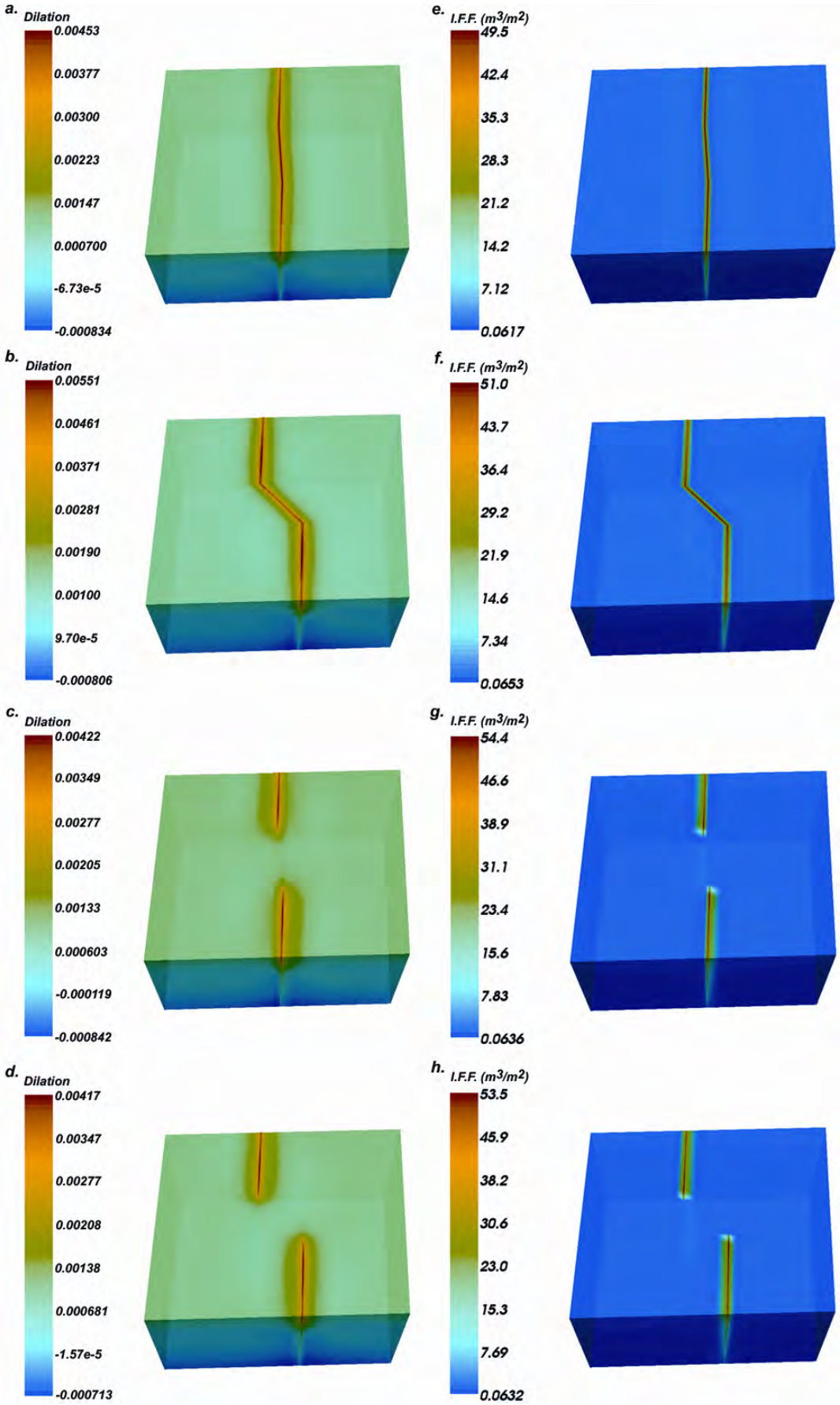

Figure 8: The effect of varying fault bend/jog angle θ on dilation (left column, a – d) and integrated fluid flux (right column, e - h).

did not produce particularly high dilation or integrated fluid flux values within the fault zone.

In areas proximal to the fault zone, decreased absolute values of θ produced higher dilation and integrated fluid flux values for fault bend models (Table 3; Fig. 8). However, fault jog models produce higher dilation values proximal to the fault for larger absolute jog angles, and higher dilation for larger absolute jog angles in areas proximal to the fault zone (Fig. 8). As with values within the fault zone, the variation of θ generates a greater difference in values for the fault bend models than the corresponding fault jog models in areas proximal to the fault zone. The change in integrated fluid flux was not particularly high outside the fault zone in comparison to the changes from variation of other fault geometry parameters. However, the change in dilation for fault bend models outside the fault zone was high in comparison to changes from variation of other parameters.

Effect of Bend/Jog Length Variation

Varying the length of the fault bends showed that models with longer bends had higher dilation within the fault zone (Table 3; Fig. 5g; Fig. 9). However, the fault jog models were found to have higher dilation for shorter fault jog lengths (Fig. 5g; Fig. 9). The integrated fluid flux values in the fault bend models also displayed higher values within the fault zone for longer fault bend lengths. Changes in fault bend length had less effect on integrated fluid flux values than other fault geometry variables. Conversely, changing fault jog length produced high increases in integrated fluid flux values in comparison with changes in other fault geometry variables, and produced higher increases than corresponding fault bend models.

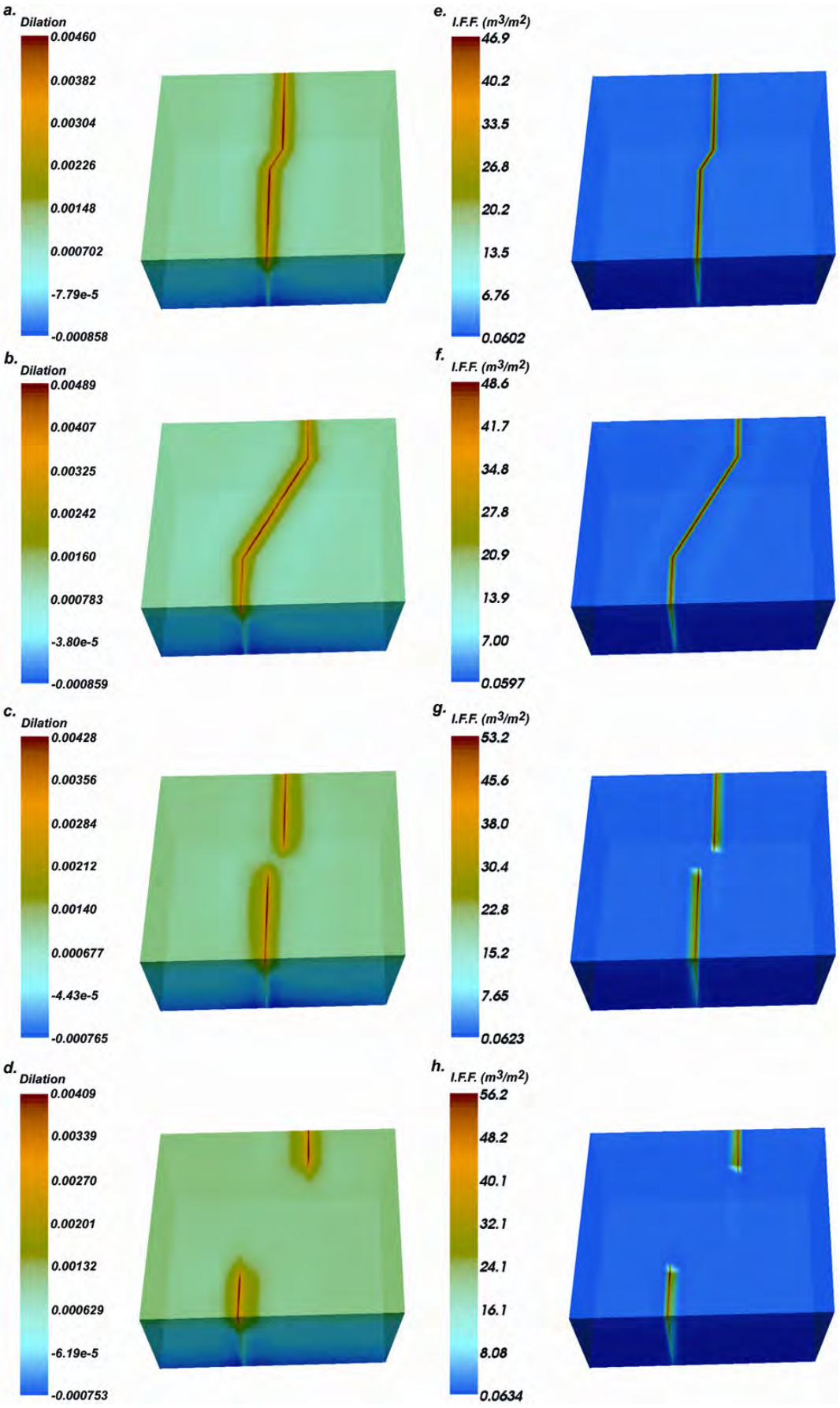

Figure 9: The effect of varying fault bend/jog length *L* on dilation (left column, a – d) and integrated fluid flux (right column, e - h).

In the areas proximal to the fault zone, the length of the fault bend or fault jog produced the lowest effect on dilation and integrated fluid flux values when compared to varying other fault geometry variables. The integrated fluid flux in the area surrounding the fault zone was higher in fault bend models with a longer bend, and in fault jog models with a shorter jog, but the dilation was higher in models with a shorter bend length and in models with a longer jog length (Fig. 9), though these differences are very small.

Effect of a Cross-Cutting Fault

Table 3 demonstrates that including a cross-cutting fault on the fault bend models produced higher dilation within the fault zone than a similar model without the cross-cutting fault (Fig. 10). However the inclusion of the extra fault did not produce as much extra dilation as decreasing the dip of the fault and widening the fault. Within the fault zone, models with a cross-cutting fault generated lower dilation values than other models (Table 3; Fig. 10). The integrated fluid flux within the fault zone was found to be the lowest with the inclusion of a cross-cutting fault compared to the other models for both fault bend and fault jog cases.

The presence of a cross-cutting fault produced considerably higher integrated fluid flux values compared to changes in other fault geometries in areas proximal to the fault zone for both the fault bend and fault jog models (Table 3). However, the dilation values in this area did not vary considerably compared to values from the other models.

Effect of Rock Type Variation

Little difference is seen in the dilation values when the fault is replaced by a contrast in rock type. However an increase is seen in the integrated fluid flux at the lithological

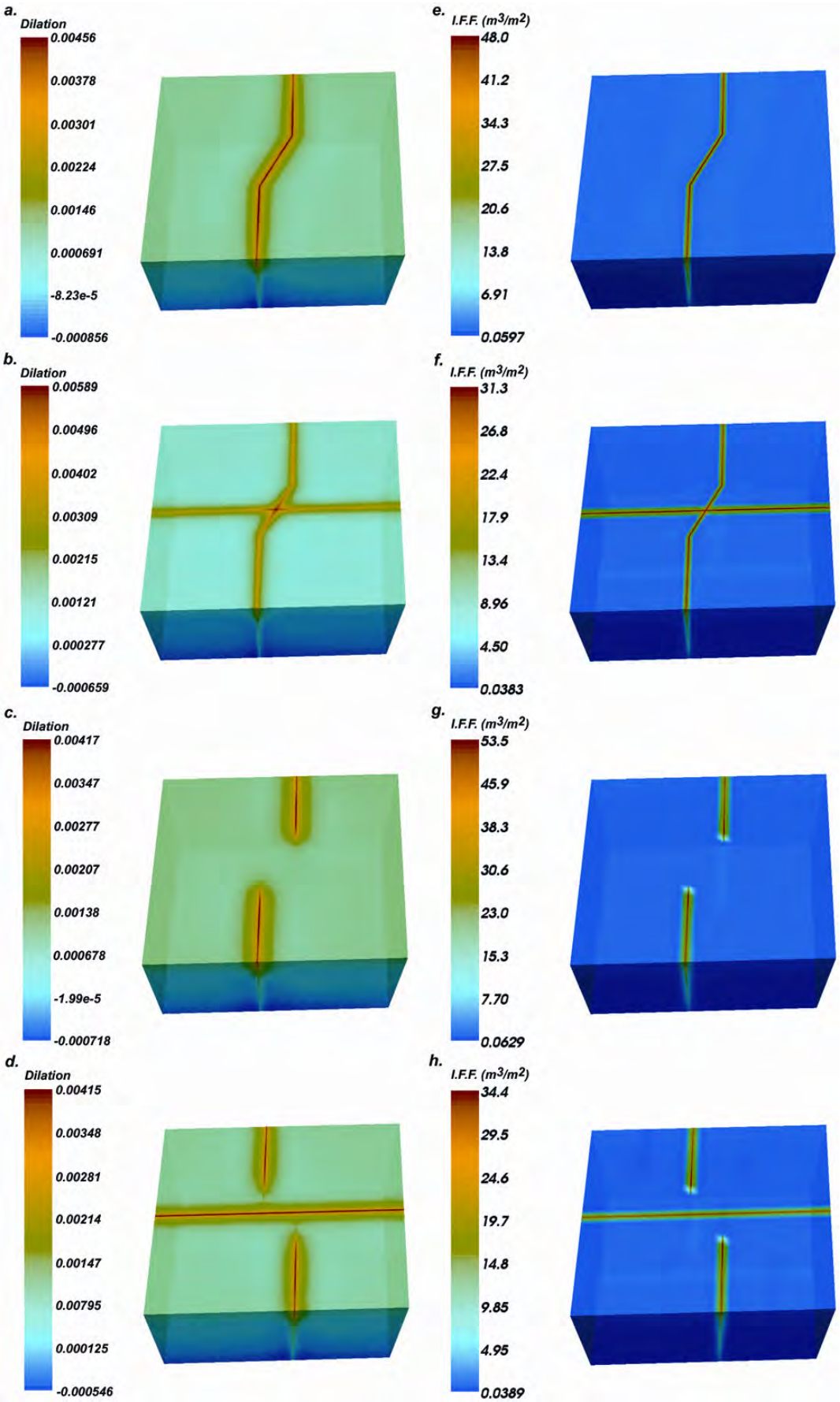

Figure 10: The effect of inclusion of an EW cross-cutting fault on dilation (left column, a – d) and integrated fluid flux (right column, e - h).

boundary (Table 3; Fig. 11a, b, e, f). In areas proximal to the lithological boundaries, the presence of more contrasts in rock types produces lower dilation than in models with fewer different rock types. In contrast, the integrated fluid flux is higher in models with more different rock types. In comparison to the variation of the fault geometry parameters, a contrast in rock types generates relatively high changes in dilation and integrated fluid flux. Integrated fluid flux increases proximal to the lithological boundaries are at least an order of magnitude higher than the increases seen in the same area due to varying the fault geometry parameters.

Reintroducing the fault to the models with a contrast in rock types indicates that it is not simply the presence of a greater number of rock types which produces the highest dilation and integrated fluid flux values, but that the specific rock properties assigned to the rocks have a large effect (Fig. 11c, d, g, h). Higher dilation values (by an order of magnitude) were observed in the models with rock types seen in the Gunpowder region (Eastern Creek Volcanics and Myally Quartzite) as opposed to those models with the rock types seen in the Mount Isa region (Eastern Creek Volcanics, Urquhart Shale, and Sybella Granite). Though the integrated fluid flux values varied much less, slightly higher values were still generated in the Gunpowder rock type models than the Mount Isa rock type models.

Dilation and Integrated Fluid Flux Ratios

The model results were evaluated by the ratios between the highest and lowest values of dilation and integrated fluid flux respectively (referred to as "dilation ratio" and "integrated fluid flux ratio"), which illustrate the extent to which these parameters are focused within the models. All dilation ratios are negative because they contrast a

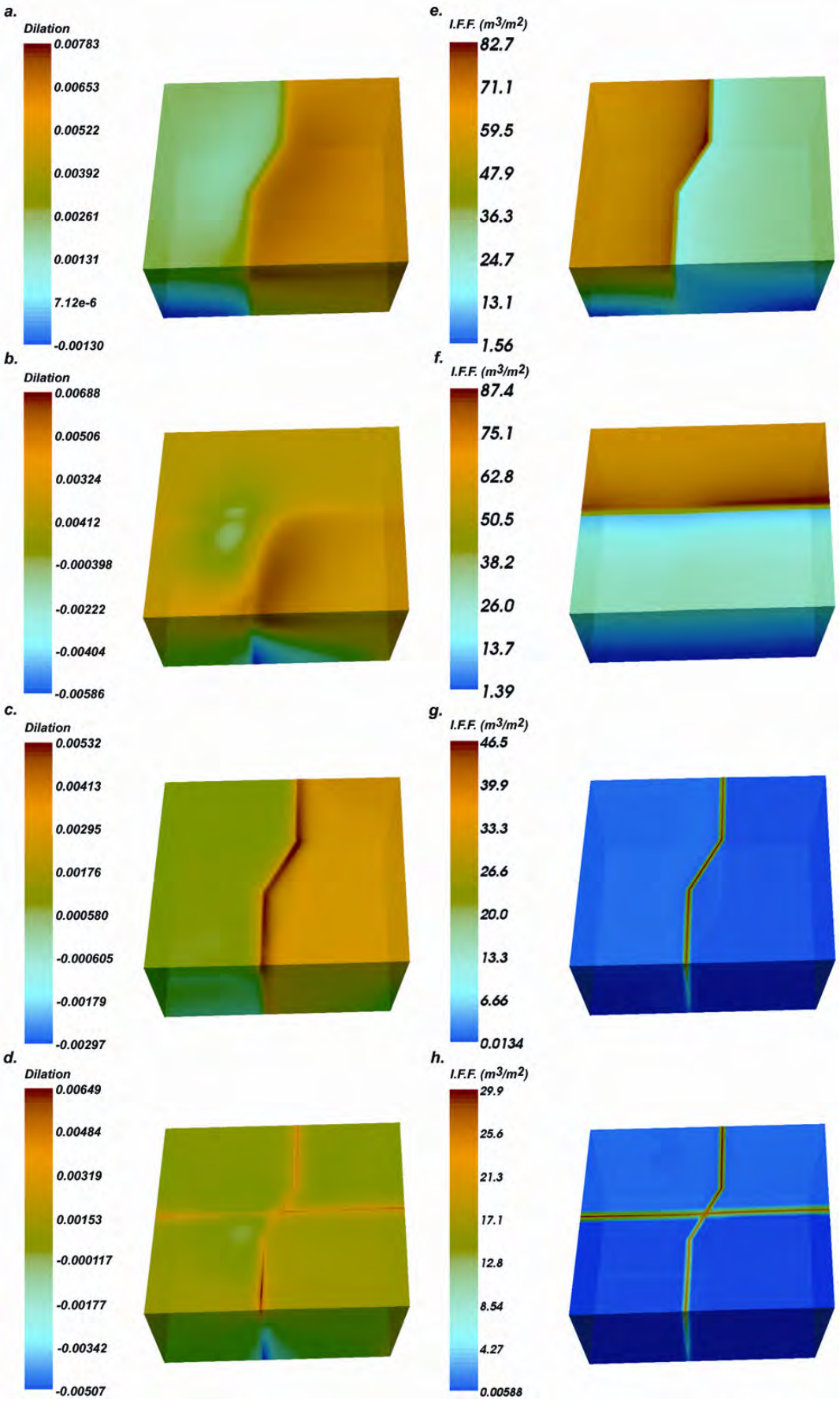

Figure 11: The effect of varying rock types on dilation (left column, a – d) and integrated fluid flux (right column, e - h).

positive maximum value (expansion) with a negative minimum value (contraction) Some general patterns can be observed for the ratios for variation of a particular parameter (Fig. 12). Table 1 shows the dilation ratio in each model is on the order of -0.0005 for the majority of models. Greater differences between the minimum and maximum dilation values (lower dilation ratios) are seen for models with a lower dip (Models 16, 17, 34, and 35), as well as some of the models with a contrast in rock types that represent the Gunpowder region (Models 41 and 44). Figure 12 illustrates that wider fault widths, smaller absolute bend angles, larger absolute jog angles, longer bend lengths and shorter jog lengths show greater differences between the minimum and maximum dilation values. For the majority of models, the integrated fluid flux ratio is on the order of 850 (Table 1). Higher integrated fluid flux ratios are seen in models with a lower dip, and a narrower fault jog. A larger absolute jog angle generates a higher integrated fluid flux ratio (Fig. 12), however the variation of the ratio for the fault bend angle does not show a readily definable pattern. Both fault bend and fault jog geometries show a higher integrated fluid flux ratio for a longer bend or jog length. Considerably higher ratios are seen in models containing a fault and contrast in rock types, in one case by two orders of magnitude (Model 40). However in the models containing a contrast in rock types with no fault, the integrated fluid flux ratio is an order of magnitude lower than in the majority of the models.

Fluid Flow Vectors

Figure 13 shows the fluid flow vectors from the perspective of the front boundary for a selection of models. The top of the models demonstrates downward fluid flow, with greater flow occurring within the fault zone. This is sometimes known to occur as the height of the model increases during deformation

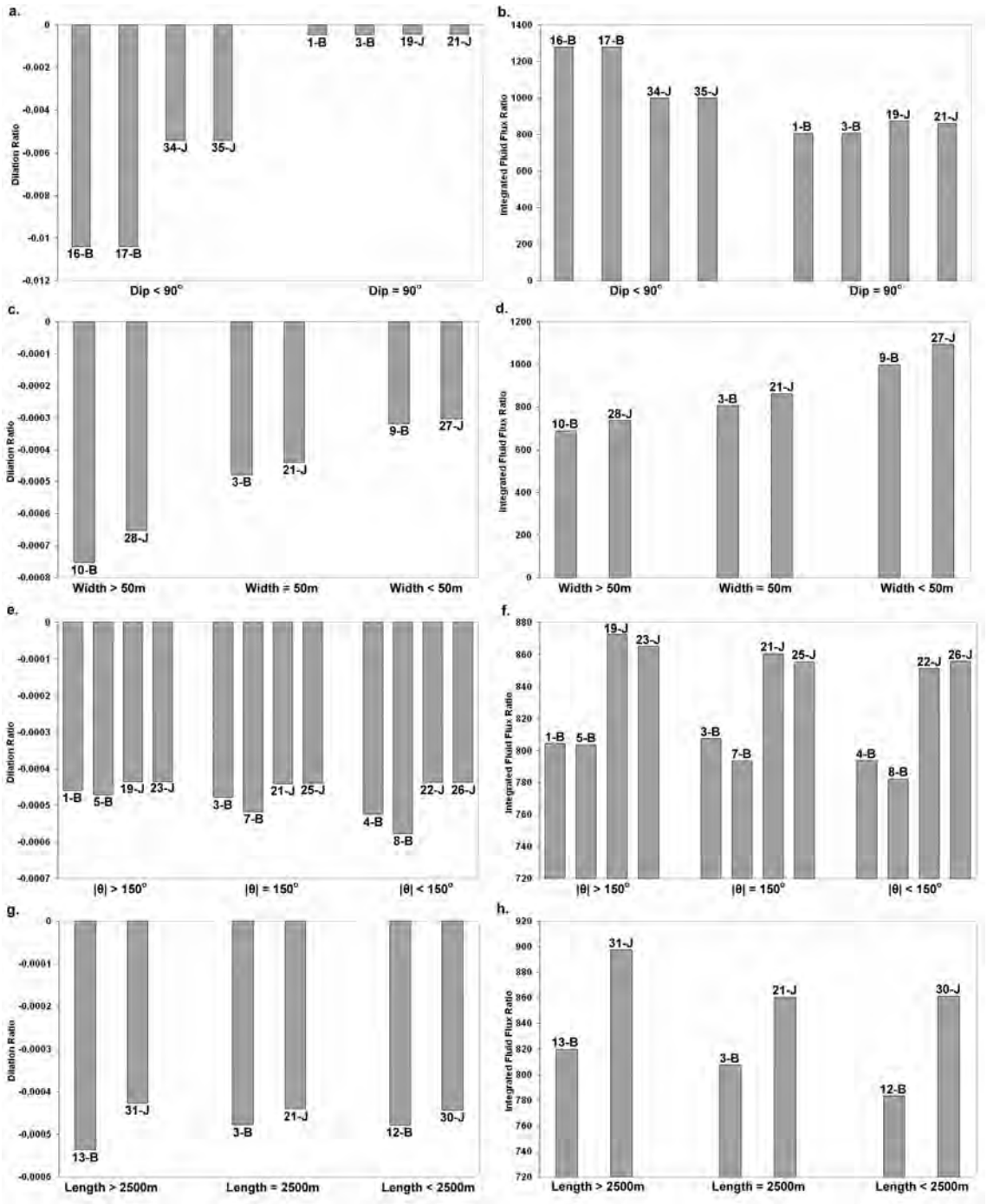

Figure 12: Dilation and integrated fluid flux ratios for the continuous fault geometry variables from selected fault bend (B) and fault jog (J) models. Illustration of (a) dilation ratio for variation of fault dip, (b) integrated fluid flux ratio for variation of fault dip, (c) dilation ratio for variation of fault width, (d) integrated fluid flux ratio for variation of fault width, (e) dilation ratio for variation of bend/jog angle, (f) integrated fluid flux ratio for variation of bend/jog angle, (g) dilation ratio for variation of bend/jog length, and (h) integrated fluid flux ratio for variation of bend/jog length.

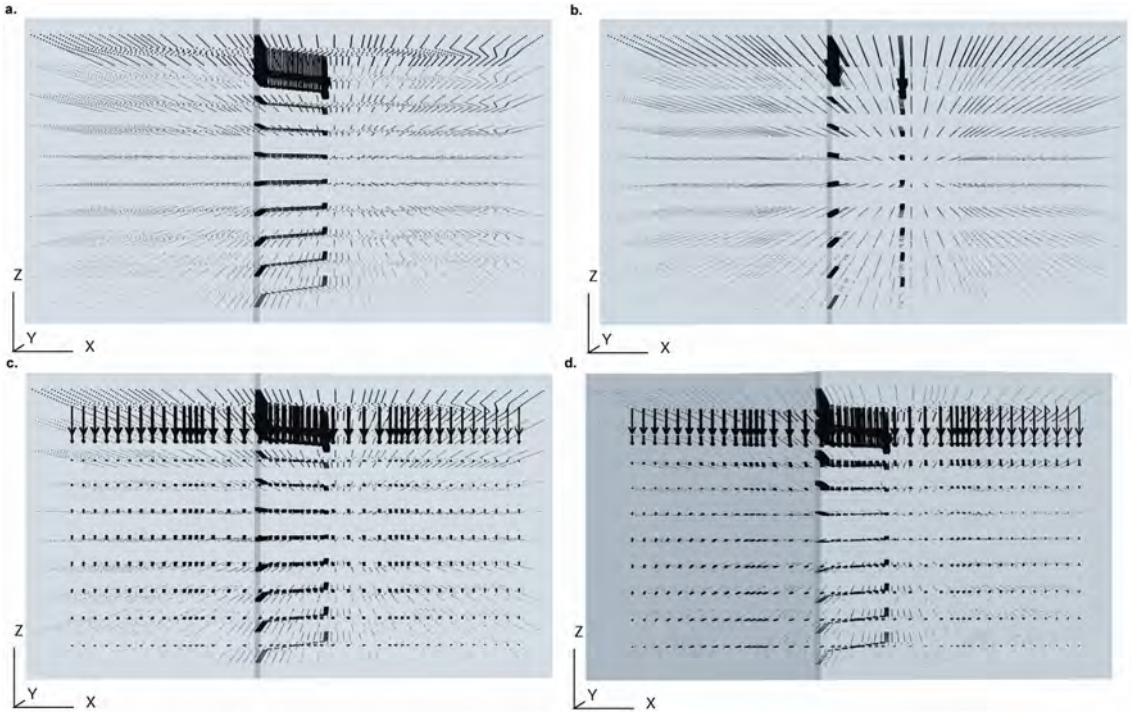

Figure 13: Fluid flow vectors from (a) fault bend model (Model 3), (b) fault jog model (Model 21), (c) fault intersection model (Model 18), and (d) model with contrast in rock types (Model 42).

(cf. Oliver et al., 2001; Gow et al., 2002). Fluid flow below the top of the model is in an upward direction, again with the greatest flow occurring within the fault zone. In the model with contrasting rock types that downward fluid flow is observed for the top half of the model rather than just at the top boundary.

DISCUSSION

The models within this study have explored the effect of varying the geometry on strike-slip deformation and coupled fluid flow. The prospectivity of a variety of geological settings through the use of numerical models has been evaluated in previous studies through the examination of variation in permeability (Ord and Oliver, 1997), and stress orientation and magnitude (Rawling et al., 2006; Robinson et al., 2006; Schaubs et al., 2006; McLellan and Oliver, 2007). While it is critical to recognize how variation of these model parameters affect modelling results in order to understand the model implications for the genesis of ore deposits, it is also critical to understand how small changes in the input geometry can affect results (eg. Schaubs et al., 2006).

Evaluation of the fault geometries by quantifying the dilation and integrated fluid flux both within the fault zone and in areas proximal to the fault zone provides an indication of what type of features are important for increasing the potential for mineralization of simple fault bend and jog geometries. Figure 5 illustrates the variation in maximum dilation and integrated fluid flux from selected models for the continuous parameters investigated in this study (fault dip, fault width, bend/jog angle and bend/jog length). The results suggest that dilation and integrated fluid flux for fault geometries with N-S striking faults containing a fault bend or jog are dominated by lower fault dips, contrasts in rock types, and wide faults. The integrated fluid flux within fault bend models was

dominated by wide faults, followed by a contrast in rock types, and a lower fault dip, whereas fault jog models were dominated by wide faults, a cross cutting fault, and a contrast in rock types.

Lower dips have a dominant effect on the outputs, with steep faults penetrating to the same depth as the low dip faults resulting in less dilation and integrated fluid flux. This could be due to two possible effects: the increased down dip extent of a lower angle fault, or the lower dip faults having less normal stress.

Wider faults can allow larger volumes of fluid through than narrower faults as demonstrated by the larger integrated fluid flux values seen in the models with wider faults. It is suggested that this is due a greater volume of higher permeability within the fault zone in which the fluid can be focused.

An important result of the modelling is that dilation and integrated fluid flux values are similar in restraining and releasing fault bends and jogs (cf. Micklethwaite and Cox, 2004). Dilation can occur in restraining geometries in the model because of the Mohr-Coulomb plastic rheology (or any other non-associated rheology) in which shear induces dilatancy (Vermeer and de Borst, 1984; Ord and Oliver, 1997). To the extent that the Mohr-Coulomb rheology is realistic (eg. Oliver et al., 2001), this result challenges some approaches to prospectivity that focus only on releasing geometries (Allibone et al., 2002a).

The models suggest that similar changes to fault bend and jog geometries have opposite effects on the outputs. Dilation and integrated fluid flux are enhanced by fault bends

that are longer and have smaller absolute bend angles, but by fault jogs that are shorter and have larger absolute jog angles. This interesting result can be explained by the effect of the higher fault permeabilities in the models: the faults are 2 to 3 orders of magnitude more permeable than the adjacent rocks. A decrease in absolute fault jog angle or jog length results in higher dilation and integrated fluid flux due to more continuity along the en echelon fault segments, resulting in less interruption to fluid flow. However, an increase in absolute fault bend angle or an increase in the bend length results in greater dilation and integrated fluid flux. The highest dilation values occur in the bend for the highest absolute bend angles. In the models with a bend angle of ±135°, the highest dilation values occur at the tips of the N-S trending part of the fault directly proximal to the bend. It is possible that higher shear strain on the longer fault bends leads to more dilation. Higher shear strain for the larger absolute bend angles is also possible. Further modelling work in the future is required to verify the reasons for fault bend length and angle producing such results.

The presence of the intersecting fault in both the bend and jog models changed the dilation and integrated fluid flux compared to models without the intersecting fault. However changes in other fault geometry variables, particularly having favorable fault dips and widths, produced even greater changes.

In the models containing a contrast in rock type across the fault (Fig. 11c, d, g, h), the faults act as juxtaposition seals (Knipe, 1992, 1993) rather than conduits for fluid flow, because they juxtapose lower permeability rocks contrasted against higher permeability rocks. Figure 13d shows that the deformation has started to create a fold at the top of the model that is not visible on the models without a contrast in rock type. The

juxtaposition of the lower and higher permeability rocks may a critical factor in the generation of this type of structure. It is also possible that this fold is partly responsible for the increased downward fluid flow seen in Figure 13d.

It is interesting to note that the integrated fluid flux ratios are broadly consistent with the permeability contrast between the fault and the host rocks, such that the variability in ratio can be attributed to geometric factors. The ratios suggest that models with a low fault dip and those with a contrast in lithology across a fault have the greatest capacity for focusing both dilation and integrated fluid flux (Fig. 12). The concentration of dilation and fluid flux in small areas is critical in models for describing the formation of hydrothermal ore deposits (de Wijs, 1951; Turcotte, 1989).

Potential limitations of the numerical modelling performed in this study include the fixed and higher permeabilities used for the fault, and the boundary conditions applied. The use of a fixed permeability for the fault and rock types through the model run was so that the effect of simple fault geometries could be examined rather than the effect of varied permeability due to deformation, which would require a more complex analysis. Fault(s) can be transiently permeable during rupture and the models are effectively integrating this increased permeability over time by assignment of a higher permeability fault. Though the shortening direction of 112.5° is considered to be representative at the time of copper mineralization in the Western Succession of the Mount Isa Inlier (McLellan, 2006), this study did not test other shortening directions which may potentially have produced greater dilation and integrated fluid flux values for the fault geometries under investigation. The boundary conditions imposed on each of the models were set to focus on strike-slip deformation (appropriate to the strike slip

Table 4: Ranking of ingredients for prospectivity analysis in strike slip fault systems in decreasing order of sensitivity.

Fault Bends	Fault Jogs
Low fault dip	Low fault dip
Contrast in rock types	Contrast in rock types
Wide fault	Wide fault
Cross-cutting fault	Cross-cutting fault
Large absolute bend angle	Small absolute jog angle
Long bend	Short jog

kinematics of many major faults in the Western Succession), so that, for example, the effect of transpression was not examined. Further, the results presented were analysed only after a shortening of 10%. Preliminary inspection of the models results at lower values suggests that the same patterns reported here are consistent through the deformation history. Each of these limitations opens up the possibility of further work in the future.

Table 4 summarizes the fault geometry variables which could be used as ingredients for prospectivity analysis. These combinations of fault system variables should therefore produce the most favorable conditions for hydrothermal mineralization which can be applied to copper mineralization in the Western Succession of the Mount Isa Inlier and could feasibly be incorporated into an exploration targeting program.

The majority of the effects seen in the models are consistent with the dominant influence of strain induced dilation on fluid flow, combined with the higher permeabilities ascribed to the faults. These two factors can explain the effects of fault dip, width, and bend and jog length and angle. Some of the results may be challenging to conventional ideas of prospectivity: for example restraining and releasing bends are

equally favourable, and the effects of length and angle are the opposite for bends and jogs.

CONCLUSIONS

Dilation and integrated fluid flux are critical factors in the genesis of ore deposits. This study shows how numerical modelling of three-dimensional strike-slip coupled deformation and fluid flow models can be used to rank fault geometry variables that are important for generating higher dilation and integrated fluid flux values through quantitative analysis of the model outputs.

Analysis of fault system variables indicates which values for these variables produce higher dilation and integrated fluid flux values. In order of priority, dilation is maximized by: a low fault dip, a contrast in rock types, a wide fault, a cross-cutting fault, and for fault bends, a small bend angle and long bend, and for fault jogs, a large jog angle and a short jog. Integrated fluid flux is maximized in order of priority by a wide fault, a contrast in rock types, and a low fault dip; and for fault bends, a small bend angle and long bend, and for fault jogs, a large jog angle and a short jog length, and a cross-cutting fault. Increasing the length or angle of fault bends has opposite effects to those observed for fault jogs. Restraining and releasing fault bend and jog geometries show similar results, indicating the dominant effect of strain-induced dilatancy in these models. These conclusions can be directly extrapolated into the field so that exploration can focus on areas with most favourable fault system parameters.

CONCLUSIONS

Fractal and multifractal analysis of mineralized systems is an expanding discipline within the geosciences. Evaluating the prospectivity of a region using fractal analysis and/or multifractal techniques represents a new direction for the discipline. Exploration for new mineral deposits in brownfields terrains can represent a large financial risk for many exploration companies. Low risk-low cost techniques for reducing terrain scale exploration targets to smaller regional scale targets is an important step in any exploration campaign.

This study has shown that fractal and multifractal analysis can be used to describe various facets of mineralized systems. It has been shown that examining the variation of fractal dimension over a study area provides a method for quantifying spatial relationships between mineral deposits and potential geological controls on mineralization.

Chapter 1 demonstrates that there is a strong linear relationship between the degree of clustering of mineral deposits and clustering of geological features and contrast values as determined from Weights of Evidence analysis using copper occurrences from the Mount Isa Inlier as a case study. This result suggests that the geological features controlling the clustering of the mineral deposits may be the same factors controlling their localization. The combination of fractal analysis and weights of evidence has potential implications for brownfields exploration targeting. Further work in this area should focus on application of the methodology to other commodities and other study areas. A more comprehensive analysis of other potential controls on copper

mineralization in the Mount Isa Inlier should also be undertaken in order to generate a terrain scale copper prospectivity map.

Chapter 2 illustrates that geological complexity rather than complexity gradients has the closer spatial relationship with copper mineralization in the Mount Isa Inlier. Regions of higher geological complexity have a greater capacity to focus the large volumes of fluid and provide the physico-chemical contrasts necessary for the formation of large hydrothermal ore deposits. The high correlations between geological complexity and copper endowment shown by this study suggest that geological complexity could be used as an exploration targeting tool in underexplored regions of the Mount Isa Inlier. Further work should focus on application of the methodology used in this study to the data used in the previous studies of geological complexity as a control on gold mineralization in the Eastern Goldfields of the Yilgarn craton. This further work should clarify potential reasons for the strongly differing conclusions reached in this study and those reached in previous studies.

Chapter 3 presents an expansion of the de Wijs model for describing the distribution of ore tonnage. The relationship between ore grade distributed using the de Wijs model and ore tonnage using the expanded model is shown to be log-normal. Multifractal analysis of ore tonnage values from the expanded model suggests that ore tonnage is not multifractal. Production data from gold deposits in the Zimbabwe craton illustrates a log-normal relationship between ore grade and tonnage, multifractal grade distributions, and the non-multifractal nature of ore tonnage, as predicted by the expanded de Wijs model. Though limited by the availability of comprehensive regional scale production databases, future work should examine production data from other commodities and

study areas and compare the fractal and/or multifractal characteristics of the data to other existing or newly developed theoretical models for element distribution in the crust.

Chapter 4 demonstrates that small variations in fault geometry parameters can greatly affect the results of three-dimensional coupled strike-slip deformation and fluid flow models. Using dilation and integrated fluid flux as proxies for prospectivity, it is shown that dilation is maximized, in order of priority by: a lower fault dip, contrast in rock types, large fault width, a cross-cutting fault, for fault bends – a large bend angle and a longer bend length, and for fault jogs – a small jog angle and a shorter jog length. Whereas integrated fluid flux is maximized in order of priority: a large fault width, a contrast in rock types, a low fault dip, for fault bends – a large bend angle and a longer bend length, for fault jogs – a small jog angle and a shorter jog length, and a cross-cutting fault. It is demonstrated that increasing the length and angle of fault bends has opposite effects to increasing fault jog length and angle. Further, it is shown that contractional and dilational fault bend and jog geometries produce similar results. The fault geometry parameters that generate higher dilation and integrated fluid flux could be incorporated into either brownfields or greenfields exploration targeting. There is scope for a substantial amount of further work in three-dimensional modelling space. Other fault systems including normal and reverse faults could be analysed using the same approach as this study. While this study only varied one fault geometry parameter at a time, future studies could vary multiple fault geometry parameters as well as the boundary conditions or other model parameters in each numerical model.

Given the scale invariance of many geological phenomena, there is scope for investigating the fractal and/or multifractal properties of many other economic geology features (eg. geochemical, geophysical and stratigraphic data) and mineralized systems not addressed in this study (eg. the Eastern Goldfields of the Yilgarn craton or the Victorian goldfields). The methodologies developed and applied within this thesis have shown that there are direct implications for exploration targeting and resource evaluation as a result of quantitative analysis of different facets of mineralized systems. Given the extensive use of fractals in hydrocarbon exploration and production, the time is appropriate for more extensive application to the minerals industry.

REFERENCES

Agterberg, F.P., 1995, Multifractal modeling of the sizes and grades of giant and supergiant deposits: International Geology Review, v. 37, p. 1-8.

—, 2001, Multifractal simulation of geochemical map patterns, *in* Merriam, D.F., and Davis, J.C., eds., Geologic modeling and simulation: Computer Applications in the Earth Sciences: New York, Plenum Press, p. 31-39.

—, 2005, High- and low-value tails of frequency distributions in geochemistry and mineral resource evaluation: Geophysical Research Abstracts, v. 7, p. 03405.

Agterberg, F.P., and Bonham-Carter, G.F., 1990, Deriving weights of evidence from geoscience contour maps for the prediction of discrete events, in: Proceedings 22nd APCOM Symposium, Volume 2: Berlin, Technical University of Berlin, p. 381-395.

—, 2005, Measuring the Performance of Mineral-Potential Maps: Natural Resources Research, v. 14, p. 1-17.

Agterberg, F.P., Bonham-Carter, G.F., Cheng, Q., and Wright, D.F., 1993, Weights of evidence modeling and weighted logistic regression for mineral potential mapping, *in* Davis, J., and Herzfeld, U.C., eds., Computers in Geology - 25 Years of Progress: New York, Oxford Univ. Press, p. 13-32.

Agterberg, F.P., Cheng, Q., and Wright, D.F., 1996, Fractal Modelling of Mineral Deposits, *in* Elbrond, J., and Tang, X., eds., Proceedings of the International Symposium on the Application of Computers and Operations Research in the Minerals Industries: Montreal, p. 43-53.

Allibone, A.H., Teasdale, J., Cameron, G., Etheridge, M., Uttley, P., Soboh, A., Appiah-Kubi, J., Adanu, A., Arthur, R., Mamphey, J., Odoom, B., Zuta, J., Tsikata, A.,

Pataye, F., Famiyeh, S., and Lamb, E., 2002a, Timing and Structural Controls on Gold Mineralization at the Bosogo Gold Mine, Ghana, West Africa: Economic Geology, v. 97, p. 949-969.

Allibone, A.H., McCuaig, T.C., Harris, D., Etheridge, M., Munroe, S., Byrne, D., Amanor, J., and Gyapong, W., 2002b, Structural Controls on Gold Mineralization at the Ashanti Deposit, Obuasi, Ghana, *in* Goldfarb, R.J., and Nielsen, R.L., eds., Integrated Methods for Discovery: Global Exploration in the Twenty-First Century, Volume Special Publication no. 9: Boulder, Society of Economic Geologists, p. 65-93.

Baker, T., and Laing, W.P., 1998, Eloise Cu-Au deposit, East Mt Isa Block: structural environment and structural controls on ore: Australian Journal of Earth Sciences, v. 45, p. 429-444.

Baker, T., Perkins, C., Blake, K.L., and Williams, P.J., 2001, Radiogenic and Stable Isotope Constraints on the Genesis of the Eloise Cu-Au Deposit, Cloncurry District, Northwest Queensland: Economic Geology, v. 96, p. 723-742.

Bardossy, G., and Fodor, J., 2001, Traditional and new ways to handle uncertainty in geology: Natural Resources Research, v. 10, p. 179-187.

Barnsley, M., 1988, Fractals Everywhere: San Diego, Academic Press, Inc.

Bartholomew, D.S., 1990, Gold Deposits in Zimbabwe, Geological Survey of Zimbabwe Mineral Resources Series, 23, 75 p.

Bell, T.H., 1983, Thrusting and Duplex Formation at Mount Isa, Queensland, Australia: Nature, v. 304, p. 493-497.

Bell, T.H., and Hickey, K.A., 1998, Multiple Deformations with Successive Subvertical and Subhorizontal Axial Planes in the Mount Isa Region: Their Impact on Geometric Development and Significance for Mineralization and Exploration: Economic Geology, v. 93, p. 1369-1989.

Bell, T.H., Perkins, W.G., and Swager, C.P., 1988, Structural Controls on Development and Localization of Syntectonic Copper Mineralization at Mount Isa, Queensland: Economic Geology, v. 83, p. 69-85.

Betts, P.G., Giles, D., Mark, G., Lister, G.S., Goleby, B.R., and Ailléres, L., 2006, Synthesis of the Proterozoic evolution of the Mt Isa Inlier: Australian Journal of Earth Sciences, v. 53, p. 187-211.

Billa, M., Cassard, D., Lips, A.L.W., Bouchot, V., Tourliere, B., Stein, G., and Guillou-Frottier, L., 2004, Predicting gold-rich epithermal and porphyry systems in the central Andes with a continental-scale metallogenic GIS: Ore Geology Reviews, v. 25, p. 39-67.

Blake, D.H., 1987, Geology of the Mount Isa Inlier and environs, Queensland and Northern Territory, Bulletin 225, Bureau of Mineral Resources, Australia, p. 83.

Blake, D.H., Etheridge, M.A., Page, R.W., Stewart, A.J., Williams, P.R., and Wyborn, L.A.I., 1990, Mount Isa Inlier - regional geology and mineralization, *in* Hughes, F.E., ed., Geology of the Mineral Deposits of Australia and Papua New Guinea: Melbourne, Australian Institute of Mining and Metallurgy, p. 915-925.

Blake, D.H., and Stewart, A.J., 1992, Stratigraphic and tectonic framework, Mount Isa Inlier, *in* Stewart, A.J., and Blake, D.H., eds., AGSO Bulletin 243: Detailed Studies

of the Mount Isa Inlier: Canberra, Australian Geological Survey Organisation, p. 1-11.

Blenkinsop, T., 2005, I2+3 Total Systems Analysis of the Mt Isa Eastern Succession, pmd*CRC, p. 504.

Blenkinsop, T., and Oliver, N., 2003, Discrimination of Base/Precious Metal Mineralising Systems by Fractal Analysis, Mt Isa, Australia, Geophysical Research Abstracts, Volume 5, European Geophysical Society, p. 14276.

Blenkinsop, T.G., 1994, The fractal distribution of gold deposits: Two examples from the zimbabwe archaean craton, *in* Kruhl, J.H., ed., Fractals and Dynamic Systems in Geosciences: Berlin, Springer, p. 247-258.

—, 1995, Fractal measures for size and spatial distributions of gold mines: Economic applications, *in* Blenkinsop, T.G., and Tromp, P.L., eds., Sub-Saharan Economic Geology, Volume Geological Society of Zimbabwe, Special Publication 3: Rotterdam, Balkema, p. 177-186.

Blenkinsop, T.G., and Sanderson, D.J., 1999, Are gold deposits in the crust fractals? A study of gold mines in the Zimbabwean craton, *in* McCaffrey, K.J.W., Lonergan, L., and Wilkinson, J.J., eds., Fractures, Fluid Flow and Mineralization, Volume Special Publications no. 155: London, Geological Society, p. 141-151.

Block, A., Von Bloh, W., and Schellenhuber, H.J., 1990, Efficient box-counting determination of generalized fractal dimensions: Physical Review A, v. 42, p. 1869-1874.

Boleneus, D.E., Raines, G.L., Causey, J.D., Bookstrom, A.A., Frost, T.P., and Hyndman, P.C., 2002, Assessment Method for Epithermal Gold Deposits in Northeast Washington State using Weights-of-Evidence GIS Modeling: U.S. Geological Survey Open File Report OF01-501.

Bonham-Carter, G., 1994, Geographic Information Systems for Geoscientists: Modelling with GIS: Oxford, Pergamon Press.

Bonham-Carter, G.F., Agterberg, F.P., and Cheng, Q., 1989, Weights of evidence modelling: a new approach to mapping mineral potential, *in* Agterberg, F.P., and Bonham-Carter, G.F., eds., Statistical Applications in the Earth Sciences, Geological Survey of Canada Paper 89-9, p. 171-183.

Bonson, C.G., Childs, C., Walsh, J.J., Schöpfer, M.P.J., and Carboni, V., 2007, Geometric and kinematic controls on the internal structure of a large normal fault in massive limestones: The Maghlaq Fault, Malta: Journal of Structural Geology, v. 29, p. 336-354.

Brankman, C.M., and Aydin, A., 2004, Uplift and contractional deformation along a segmented strike-slip fault system: the Gargano Promontory, southern Italy: Journal of Structural Geology, v. 26, p. 807-824.

Brown, W., Groves, D., and Gedeon, T., 2003, Use of fuzzy membership input layers to combine subjective geological knowledge and empirical data in a neural network method for mineral-potential mapping: Natural Resources Research, v. 12, p. 183-200.

Brown, W.M., Gedeon, T.D., Groves, D., and Barnes, R.G., 2000, Artificial neural networks: a new method for mineral prospectivity mapping: Australian Journal of Earth Sciences, v. 47, p. 757-770.

Butera, K.M., 2004, The role of mafic rocks in the genesis of IOCG and Base Metal deposits, Mount Isa Eastern Succession, NW Queensland, Australia., *in* Barnicoat, A.C., and Korsch, R.J., eds., Predictive Mineral Discovery Cooperative Research Centre - Extended Abstracts from the June 2004 Conference, Volume Record 2004/09: Canberra, Geoscience Australia, p. 21-22.

Butera, K.M., and Blenkinsop, T.G., 2004, Fractal analysis of the spatial distributions of mafic rocks and mineralisation in the Eastern Succession, Mount Isa Inlier, Australia: a possible genetic link, 4th International Conference Fractals and Dynamic Systems in Geoscience: TU München, p. 16-19.

Cannell, D., and Davidson, G.J., 1998, A Carbonate-Dominated Copper-Cobalt Breccia-Vein System at the Great Australia Deposit, Mount Isa Eastern Succession: Economic Geology, v. 93, p. 1406-1421.

Carlson, C.A., 1991, Spatial distribution of ore deposits: Geology, v. 19, p. 111-114.

Carranza, E.J.M., Hale, M., and Mangaoang, J.C., 1999, Application of mineral exploration models and GIS to generate mineral potential maps as input for optimum land-use planning in the Philippines: Natural Resources Research, v. 8, p. 165-173.

Chapman, L.H., and Williams, P.J., 1998, Evolution of Pyroxene-Pyroxenoid-Garnet Alteration at the Cannington Ag-Pb-Zn Deposit, Cloncurry District, Queensland Australia: Economic Geology, v. 93, p. 1390-1405.

Cheng, Q., 1997, Multifractal Modeling and Lacunarity Analysis: Mathematical Geology, v. 29, p. 919-932.

—, 1999a, Spatial and scaling modelling for geochemical anomoly separation: Journal of Geochemical Exploration, v. 65, p. 175-194.

—, 1999b, Markov Processes and Discrete Multifractals: Mathematical Geology, v. 31, p. 455-469.

—, 1999c, Multifractality and spatial statistics: Computers & Geosciences, v. 25, p. 949-961.

—, 1999d, The gliding box method for multifractal modeling: Computers & Geosciences, v. 25, p. 1073-1079.

Cheng, Q., and Agterberg, F.P., 1999, Fuzzy weights of evidence method and its application in mineral potential mapping Natural Resources Research, v. 8, p. 27-35.

Cheng, Q., Agterberg, F.P., and Ballantyne, S.B., 1994, The separation of geochemical anomalies from background by fractal methods: Journal of Geochemical Exploration, v. 51, p. 109-130.

Chester, F.M., and Chester, J.S., 2000, Stress and deformation along wavy frictional faults: Journal of Geophysical Research, v. 105, p. 23421-23430.

Chester, J.S., and Fletcher, R.C., 1997, Stress distribution and failure in anisotropic rock near a bend on a weak fault: Journal of Geophysical Research, v. 102, p. 693-708.

Connors, K.A., and Page, R.W., 1995, Relationships between magmatism, metamorphism and deformation in the western Mount Isa Inlier, Australia: Precambrian Research, v. 71, p. 131-153.

Conover, W.J., 1999, Practical Nonparametric Statistics: New York, John Wiley & Sons.

Cox, S.F., 1999, Deformational controls on the dynamics of fluid flow in mesothermal gold systems, *in* Lonergan, L., Wilkinson, J.J., and McCaffrey, K.J.W., eds., Fractures, Fluid Flow and Mineralization, Volume Special Publication No. 155: London, The Geological Society, p. 123-140.

—, 2005, Coupling between Deformation, Fluid Pressures, and Fluid Flow in Ore-Producing Hydrothermal Systems at Depth in the Crust, *in* Hedenquist, J.W., Thompson, J.F.H., Goldfarb, R.J., and Richards, J.P., eds., Economic Geology One Hundredth Anniversary Volume: Littleton, Society of Economic Geologists, p. 39-75.

Cox, S.F., and Ruming, K., 2004, The St Ives mesothermal gold system, Western Australia-a case of golden aftershocks?: Journal of Structural Geology, v. 26, p. 1109-1125.

Craw, D., 2000, Fluid flow at fault intersections in an active oblique collision zone, Southern Alps, New Zealand: Journal of Geochemical Exploration, v. 69-70, p. 523-526.

de Wijs, H.J., 1951, Statistics of ore distribution: (1) Frequency distribution of assay values: Journal of the Royal Netherlands Geological and Mining Society, v. 13, p. 365-375.

—, 1953, Statistics of ore distribution: (2) Theory of binomial distribution applied to sampling and engineering problems: Journal of the Royal Netherlands Geological and Mining Society, v. 15, p. 12-24.

Drummond, B.J., Goleby, B.R., Goncharov, A.G., Wyborn, L.A.I., Collins, C.D.N., and MacCready, T., 1998, Crustal-scale structures in the Proterozoic Mount Isa Inlier of north Australia: their seismic response and influence on mineralisation: Tectonophysics, v. 288, p. 43-56.

Egan, S.S., Kane, S., Buddin, T.S., Williams, G.D., and Hodgetts, D., 1999, Computer Modelling and Visualisation of the structural deformation caused by movement along geological faults: Computers & Geosciences, v. 25, p. 283-297.

Evertsz, C.J.G., and Mandelbrot, B.B., 1992, Multifractal Measures (Appendix B), *in* Peitgen, H.-O., Jürgens, H., and Saupe, D., eds., Chaos and Fractals: New Frontiers of Science: New York, Springer-Verlag, p. 921-953.

Feltrin, L., Oliver, N.H.S., Kelso, I.J., and King, S., 2003, Basement metal scavenging during basin evolution: Cambrian and Proterozoic interaction at the Century Zn-Pb-Ag Deposit, Northern Australia: Journal of Geochemical Exploration, v. 78-79, p. 159-162.

Ford, A., and Blenkinsop, T.G., 2007a, Combining fractal analysis of mineral deposit clustering with weights of evidence to evaluate patterns of mineralization: Application to copper deposits of the Mount Isa Inlier: Ore Geology Reviews, in press, DOI: 10.1016/j.oregeorev.2007.01.004.

—, 2007b, Evaluating geological complexity and complexity gradients as controls on copper mineralisation, Mt Isa Inlier: Australian Journal of Earth Sciences, in press, DOI: 10.1080/08120090701581364.

Foster, D.R.W., and Austin, J.A., 2005, Revised chronostratigraphy for the Mt Isa Inlier with emphasis on the Eastern Succession, Unpublished I2+3 Final Report, pmdCRC, p. 40.

Foster, D.R.W., and Rubenach, M.J., 2006, Isograd pattern and regional low-pressure, high-temperature metamorphism of pelitic, mafic and calc-silicate rocks along an east-west section through the Mt Isa Inlier: Australian Journal of Earth Sciences, v. 53, p. 167-186.

Gagnon, J.-S., Lovejoy, S., and Schertzer, D., 2003, Multifractal surfaces and terrestrial topography: Europhysics Letters, v. 62, p. 801-807.

Garven, G., Bull, S.W., and Large, R.R., 2001, Hydrothermal fluid flow models of stratiform ore genesis in the McArthur Basin, Northern Territory, Australia: Geofluids, v. 1, p. 289-311.

Giles, D., Betts, P.G., and Lister, G.S., 2002, Far-field continental backarc setting for the 1.80-1.67 Ga basins of northeastern Australia: Geology, v. 30, p. 823-826.

Gow, P.A., Upton, P., Zhao, C., and Hill, K.C., 2002, Copper-gold mineralisation in New Guinea: numerical modelling of collision, fluid flow and intrusion-related hydrothermal systems: Australian Journal of Earth Sciences, v. 49, p. 753-771.

Groves, D.I., Goldfarb, R.J., Knox-Robinson, C.M., Ojala, J., Gardoll, S., Yun, G.Y., and Holyland, P., 2000, Late-kinematic timing of orogenic gold deposits and

significance for computer-based exploration techniques with emphasis on the Yilgarn Block, Western Australia: Ore Geology Reviews, v. 17, p. 1-38.

Håkansson, J., and Russberg, G., 1990, Finite-size effects on the characterization of fractal sets: f(α) construction via box counting on a finite two-scaled Cantor set: Physical Review A, v. 41, p. 1855-1861.

Harris, J.R., Wilkinson, L., and Grunsky, E.C., 2000, Effective use and interpretation of lithogeochemical data in regional mineral exploration programs; application of geographic information systems (GIS) technology: Exploration Geochemistry, v. 16, p. 107-143.

Harris, S.D., McAllister, E., Knipe, R.J., and Odling, N.E., 2003, Predicting the three-dimensional population characteristics of fault zones: a study using stochastic models: Journal of Structural Geology, v. 25, p. 1281-1299.

Hodkiewicz, P., 2003, The interplay between physical and chemical processes in the formation of world-class orogenic gold deposits in the Eastern Goldfields Province, Western Australia [PhD thesis]: Perth, University of Western Australia.

Hodkiewicz, P.F., Weinberg, R.F., Gardoll, S.J., and Groves, D.I., 2005, Complexity gradients in the Yilgarn Craton: Fundamental controls on crustal scale fluid-flow and the formation of world-class orogenic-gold deposits: Australian Journal of Earth Sciences, v. 52, p. 831-841.

Holcombe, R.J., Pearson, P.J., and Oliver, N.H.S., 1991, Geometry of a Middle Proterozoic extensional detachment surface in northeastern Australia: Tectonophysics, v. 191, p. 255-274.

Hronsky, J.M.A., 2004, The science of exploration targeting, *in* Muhling, J., Goldfarb, R., Vielreicher, N., Bierlein, F., Stumpfl, E., Groves, D., and Kenworthy, S., eds., SEG 2004 Predictive Mineral Discovery Under Cover, Volume Publication No. 33: Perth, Centre for Global Metallogeny, University of Western Australia, p. 129-133.

Itasca Consulting Group, 1998, 3DEC: 3-Dimensional Distinct Element Code: Minneapolis, Itasca.

—, 2000, UDEC: Universal Distinct Element Code: Minneapolis, Itasca.

—, 2002, FLAC3D: Fast Lagrangian Analysis of Continua in 3 dimensions: Minneapolis, Itasca.

Johnston, J.D., and McCaffrey, K.J.W., 1996, Fractal geometries of vein systems and the variation of scaling relationships with mechanism: Journal of Structural Geology, v. 18, p. 349-358.

Knipe, R.J., 1992, Faulting processes and fault seal, Volume Special Publication 1, Norwegian Petroleum Society (NPF), p. 325-342.

—, 1993, The influence of fault zone processes and diagenesis on fluid flow: American Association of Petroleum Geologists Studies in Geology, v. 36, p. 135-154.

Knox-Robinson, C.M., 2000, Vectorial fuzzy-logic: a novel technique for enhanced mineral prospectivity mapping, with reference to the orogenic gold mineralisation potential of the Kalgoorlie Terrane, Western Australia: Australian Journal of Earth Sciences, v. 47, p. 929-941.

Kreuzer, O.P., Blenkinsop, T.G., Morrison, R.J., and Peters, S.G., 2007, Ore controls in the Charters Towers goldfield, NE Australia: constraints from geological,

geophysical and numerical analyses, and implications for exploring a 'mature' terrain: Ore Geology Reviews, v. 32, p. 37-80.

Laing, W.P., 1998, Structural-metasomatic environment of the East Mt Isa Block base-metal-gold province: Australian Journal of Earth Sciences, v. 45, p. 413-428.

Liebovitch, L.S., and Toth, T., 1989, A fast algorithm to determine fractal dimensions by box counting: Physics Letters A, v. 141, p. 386-390.

MacCready, T., 2006, Structural cross-section based on the Mt Isa Deep Seismic Transect: Australian Journal of Earth Sciences, v. 53, p. 5-26.

Mandelbrot, B.B., 1983, The Fractal Geometry of Nature: New York, W. H. Freeman and Company.

—, 1985, Self-affine fractals and fractal dimension: Physica Scripta, v. 32, p. 257-260.

Mark, G., Oliver, N.H.S., and Carew, M.J., 2006, Insights into the genesis and diversity of epigenetic Cu-Au mineralisation in the Cloncurry district, Mt Isa Inlier, northwest Queensland: Australian Journal of Earth Sciences, v. 53, p. 109-124.

Mark, G., Williams, P.J., and Boyce, A.J., 2004, Low-latitude meteoric fluid flow along the Cloncurry Fault, Cloncurry District, NW Queensland, Australia: geodynamic and metallogenic implications: Chemical Geology, v. 207, p. 117-132.

Marshall, L.J., 2003, Brecciation within the Mary Kathleen group of the Eastern succession, Mt Isa block, Australia : implications of district-scale structural and metasomatic processes for Fe-oxide-Cu-Au mineralisation [PhD thesis]: Townsville, James Cook University. 323 p.

Matthäi, S.K., Heinrich, C.A., and Driesner, T., 2004, Is the Mount Isa copper deposit the product of forced brine convection in the footwall of a major reverse fault?: Geology, v. 32, p. 357-360.

McDonald, G.D., Collerson, K.D., and Kinny, P.D., 1997, Late Archean and Early Proterozoic crustal evolution of the Mount Isa block, northwest Queensland, Australia: Geology, v. 25, p. 1095-1098.

McLellan, J.G., 2006, Discrete element modelling of the Isa Inlier, Predictive Mineral Discovery: Science at the Sharp End: University of Western Australia, Perth, Predictive Mineral Discovery CRC, p. 25.

McLellan, J.G., and Oliver, N.H.S., 2007, Discrete element modelling applied to copper prospectivity in the eastern Mount Isa Inlier: Precambrian Research, in press.

McLellan, J.G., Oliver, N.H.S., and Schaubs, P.M., 2004, Fluid flow in extensional environments; numerical modelling with an application to Hamersley iron ores: Journal of Structural Geology, v. 26, p. 1157-1171.

Micklethwaite, S., and Cox, S.F., 2004, Fault-segment rupture, aftershock-zone fluid flow, and mineralization: Geology, v. 32, p. 813-816.

Mustard, R., Blenkinsop, T., McKeagney, C., Huddleston-Holmes, C., and Partington, G., 2004, New perspectives on IOCG deposits, Mt Isa Eastern Succession, northwest Queensland, SEG 2004 Predictive Mineral Discovery Under Cover: Extended Abstracts: University of Western Australia, Perth, Centre for Global Metallogeny, p. 281-284.

Nemčok, M., Henk, A., Gayer, R.A., Vandycke, S., and Hathaway, T.M., 2002, Strike-slip fault bridge fluid pumping mechanism: insights from field-based palaeostress analysis and numerical modelling: Journal of Structural Geology, v. 24, p. 1885-1901.

Nie, F.-J., Jiang, S.-H., Su, X.-X., and Wang, X.-L., 2002, Geological features and origin of gold deposits occuring in the Baotao-Bayan Obo district, south-central Inner Mongolia, People's Republic of China: Ore Geology Reviews, v. 20, p. 139-169.

Nijman, W., Mijnlieff, H.F., and Schalkwijk, G., 1992, The Hero Fan delta (Lower Mount Isa Group) and its structural control: deformation in the Hero/Western Fault Zone and Paroo Range compared, Proterozoic, Mount Isa Inlier, Queensland, Australia, *in* Stewart, A.J., and Blake, D.H., eds., AGSO Bulletin 243: Detailed Studies of the Mount Isa Inlier: Canberra, Australian Geological Survey Organisation, p. 75-111.

O'Dea, M.G., Lister, G.S., MacCready, T., Betts, P.G., Oliver, N.H.S., Pound, K.S., Huang, W., and Valenta, R.K., 1997, Geodynamic evolution of the Proterozoic Mount Isa terrain, *in* Burg, J.P., and Ford, M., eds., Orogeny Through Time, Volume Special Publications no. 121: London, Geological Society, p. 99-122.

Oliver, N.H.S., Cleverley, J.S., Mark, G., Pollard, P.J., Rubenach, M.J., Marshall, L.J., Williams, P.J., and Baker, T., 2004, Geochemistry and geochemical modeling of fluid-rock interaction in the eastern Mt Isa Block, Australia: the role of sodic alteration in the genesis of iron oxide-copper-gold deposits: Economic Geology, v. 99, p. 1145-1176.

Oliver, N.H.S., Ord, A., Valenta, R.K., and Upton, P., 2001, Deformation, Fluid Flow, and Ore Genesis in Heterogeneous Rocks, with Examples and Numerical Models from the Mount Isa District, Australia: Society of Economic Geologists Reviews, v. 14, p. 51-74.

Ord, A., 1990, Mechanical controls on dilatant shear zones, *in* Knipe, R.J., and Rutter, E.H., eds., Deformation Mechanisms, Rheology and Tectonics, Volume Special Publication No. 54: London, Geological Society, p. 183-192.

Ord, A., Hobbs, B.E., and Regenauer-Lieb, K., 2007, Shear band emergence in granular materials - A numerical study: International Journal for Numerical and Analytical Methods in Geomechanics v. 31, p. 373-393.

Ord, A., and Oliver, N.H.S., 1997, Mechanical controls on fluid flow during regional metamorphism: some numerical models: Journal of Metamorphic Geology, v. 15, p. 345-359.

Pearson, P.J., Holcombe, R.J., and Page, R.W., 1992, Synkinematic emplacement of the Middle Proterozoic Wonga Batholith into a mid-crustal extensional shear zone, Mount Isa Inlier, Queensland, Australia, *in* Stewart, A.J., and Blake, D.H., eds., AGSO Bulletin 243: Detailed Studies of the Mount Isa Inlier: Canberra, p. 289-328.

Phillips, G.N., Groves, D.I., and Brown, I.J., 1987, Source requirements for the Golden Mile, Kalgoorlie: significance to the metamorphic replacement model for Archean gold deposits: Canadian Journal of Earth Sciences, v. 24, p. 1643-1651.

Phillips, G.N., Groves, D.I., and Kerrich, R., 1996, Factors in the formation of the giant Kalgoorlie gold deposit: Ore Geology Reviews, v. 10, p. 295-317.

Queensland Department of Mines and Energy, Taylor Wall and Associates, SRK Pty Ltd, and ESRI Australia, 2000, North-West Queensland Mineral Province Report (NQMPR), Queensland Department of Mines and Energy.

Queensland Department of Natural Resources and Mines, 2005, Mineral Occurrence and Geological Sites 2005.

—, December 2002, Queensland Mineral Resource Database (MINOCC 2002) - Microsoft Access Database.

Raines, G.L., 1999, Evaluation of weights of evidence to predict epithermal-gold deposits in the Great Basin of the Western United States: Natural Resources Research, v. 8, p. 257-276.

Rawling, T.J., Schaubs, P.M., Dugdale, L.J., Wilson, C.J.L., and Murphy, F.C., 2006, Application of 3D models and numerical simulations as a predictive exploration tool in western Victoria: Australian Journal of Earth Sciences, v. 53, p. 825-839.

Roberts, L.S., 2005, Aspects of Resource Geology in Archaean Orogenic Gold Deposits [PhD thesis]: Townsville, James Cook University, 296 p.

Robinson, J.A., Wilson, C.J.L., and Rawling, T.J., 2006, Numerical modelling of an evolving gold-lode system: structural and lithological controls on ore-shoot formation in the Magdala goldmine, western Victoria: Australian Journal of Earth Sciences, v. 53, p. 799-823.

Rubenach, M.J., 2005, Tectonothermal evolution of the Eastern Fold Belt, Mount Isa Inlier, *in* Blenkinsop, T.G., ed., Total Systems Analysis of the Mount Isa Eastern Succession, pmdCRC Project I2+3 Final Report, p. 99-168.

Rubenach, M.J., and Barker, A.J., 1998, Metamorphic and metasomatic evolution of the Snake Creek Anticline, Eastern Succession, Mount Isa inlier: Australian Journal of Earth Sciences, v. 45, p. 363-372.

Sanderson, D.J., Roberts, S., and Gumiel, P., 1994, A Fractal Relationship between Vein Thickness and Gold Grade in Drill Core from La Codosera, Spain: Economic Geology, v. 89, p. 168-173.

Sanderson, D.J., and Zhang, X., 1999, Critical stress localization of flow associated with deformation of well-fractured rock masses, with implications for mineral deposits, *in* McCaffrey, K.J.W., Lonergan, L., and Wilkinson, J.J., eds., Fractures, Fluid Flow and Mineralization, Volume Special Publications no. 155: London, Geological Society, p. 69-81.

—, 2004, Stress-controlled localization of deformation and fluid flow in fractured rocks, *in* Cosgrove, J.W., and Engelder, T., eds., The Initiation, Propagation, and Arrest of Joints and Other Fractures, Volume Special Publications no. 231: London, Geological Society, p. 299-314.

Schaubs, P.M., Rawling, T.J., Dugdale, L.J., and Wilson, C.J.L., 2006, Factors controlling the location of gold mineralisation around basalt domes in the stawell corridor: insights from coupled 3D deformation-fluid-flow numerical models: Australian Journal of Earth Sciences, v. 53, p. 841-862.

Scott, K.M., and Taylor, G.F., 1982, Eastern Creek Volcanics as the source of copper at the Mammoth mine, Northwest Queensland: BMR Journal of Australian Geology & Geophysics, v. 7, p. 93-98.

Sheldon, H.A., Barnicoat, A.C., and Ord, A., 2006, Numerical modelling of faulting and fluid flow in porous rocks: An approach based on critical state soil mechanics: Journal of Structural Geology, v. 28, p. 1468-1482.

Singer, D.A., and Kouda, R., 1999, Comparison of the weights of evidence method and probabilistic neural networks: Natural Resources Research, v. 8, p. 287-298.

Sorjonen-Ward, P., Zhang, Y., and Zhao, C., 2002, Numerical modelling of orogenic processes and gold mineralisation in the southeastern part of the Yilgarn Craton, Western Australia: Australian Journal of Earth Sciences, v. 49, p. 935-964.

Tripp, G.I., and Vearncombe, J.R., 2004, Fault/fracture density and mineralization: a contouring method for targeting in gold exploration: Journal of Structural Geology, v. 26, p. 1087-1108.

Turcotte, D.L., 1986, A Fractal Approach to the Relationship between Ore Grade and Tonnage: Economic Geology, v. 81, p. 1528-1532.

—, 1989, Fractals in Geology and Geophysics, *in* Scholz, C.H., and Mandelbrot, B.B., eds., Fractals in Geophysics, Birkhauser, p. 171-196.

Twomey, T., and McGibbon, S., 2001, The Geological Setting and Estimation of Gold Grade of the High-grade Zone, Red Lake Mine, Goldcorp Inc.: Exploration and Mining Geology, v. 10, p. 19-34.

Van Dijk, P.M., 1991, Regional Syndeformational Copper Mineralization in the Western Mount Isa Block, Australia: Economic Geology, v. 86, p. 278-301.

Vermeer, P.A., and de Borst, R., 1984, Non-associated plasticity for soils, concrete and rock: Heron, v. 29, p. 1-62.

Wang, H., Cai, G., and Cheng, Q., 2002, Data integration using weights of evidence model: applications in mapping mineral resource potentials, Proceedings (CD) of Int. Society of Photogrammetry and Remote Sensing: Ottawa, p. 9.

Weinberg, R.F., Hodkiewicz, P.F., and Groves, D.I., 2004, What controls gold distribution in Archean terranes?: Geology, v. 32, p. 545-548.

Williams, P.J., 1998, An Introduction to the Metallogeny of the McArthur River-Mount Isa-Cloncurry Minerals Province: Economic Geology, v. 93, p. 1120-1131.

Wyborn, L.A.I., 1987, The petrology and geochemistry of alteration assemblages in the Eastern Creek Volcanics, as a guide to copper and uranium mobility associated with regional metamorphism and deformation, Mount Isa, Queensland, *in* Pharaoh, T.C., Beckinsale, R.D., and Rickard, D., eds., Geochemistry and Mineralization of Proterozoic Volcanic Suites, Volume Special Publications no. 33: London, Geological Society, p. 425-434.

Xie, S., and Bao, Z., 2004, Fractal and Multifractal Properties of Geochemical Fields: Mathematical Geology, v. 36, p. 847-864.

Zhang, X., and Sanderson, D.J., 1996, Numerical modelling of the effects of fault slip on fluid flow around extensional faults: Journal of Structural Geology, v. 18, p. 109-119.

Zhang, Y., Hobbs, B.E., Ord, A., Barnicoat, A., Shao, C., Walshe, J.L., and Lin, G., 2003, The influence of faulting on host-rock permeability, fluid flow and ore genesis of gold deposits: a theoretical 2D numerical model: Journal of Geochemical Exploration, v. 78-79, p. 279-284.

Zhang, Y., Sorjonen-Ward, P., and Ord, A., 2006, Fluid Flow during Deformation Associated with Structural Closure of the Isa Superbasin at 1575 Ma in the Central and Northern Lawn Hill Platform, Northern Australia: Economic Geology, v. 101, p. 1293-1312.

Appendix A-C

Supplementary Data for Section A

Supplementary Data for Section B

Supplementary Data for Section C

Appendix D (Part 1/2)

Supplementary Data for Section D

Appendix D (Part 2/2)

Supplementary Data for Section D

Appendix E

Digital Copy of Thesis Text

CHAPTER 3

Remote mapping of Sodic-Calcic alteration: Application to IOCG exploration in the Eastern Succession, Mount Isa Inlier

ABSTRACT

Proterozoic rocks of the Mount Isa Eastern Succession preserve a history of sodic-calcic metasomatism which is temporally and spatially associated with structurally controlled Cu-Au mineralisation. While such metasomatism is widely recognised throughout the district it is heterogeneously distributed and consists of several stages of development and numerous mineral assemblages and is very difficult to map at a regional scale. Remote sensing technologies have proven to be useful for mapping of mineral-system related alteration, but methods utilising ASTER (the Advanced Spaceborne Thermal Emission and Reflectance Radiometer) data have not been previously applied to the identification of sodic–calcic (Na-Ca) alteration systems. ASTER band ratios (mineral indices) are used to map minerals such as amphiboles and carbonates as a means of identifying sodic-calcic alteration. ASTER data may be used to identify mineral components of sodic-calcic alteration, but there are ambiguities, due to numerous mineral species having similar absorption features. This problem has been overcome by the integration of ASTER band 8 data with magnetic and K-radiometric data to form a new mineral index. The new sodic-calcic mineral index highlights albite-actinolite-magnetite assemblages, many of which are spatially coincident with copper mineralisation. This mineral index may be useful for exploration targeting of IOCG (Iron-Oxide Copper-Gold) deposits in the Mount Isa Inlier and potentially within similar terrains globally.

1. INTRODUCTION

A major advance in remote sensing for geology is the recognition that the spectral properties of minerals within rocks can be used to infer mineralogical assemblages. Remote sensing imagery is used for two purposes in mineral exploration: to map geology and faults / fractures that localize ore deposits and to recognize hydrothermally altered rocks by their spectral signatures (Sabins 1999). Numerous studies (e.g. Rowan and Mars 2003; Rowan et al. 2003; Berger et al. 2003; Van der Wielen et al. 2004; Hewson et al. 2005) have demonstrated that ASTER and recent airborne and hyper-spectral imagery (e.g. AVIRIS and HyMap) can be utilised to assist mapping and mineral exploration. Spectral properties identified by the different band ratios (or Mineral Indices) can be used to map lithological units or alteration patterns related to mineral systems.

Such ASTER processing methods have proven effective for some alteration types and mineral systems (e.g. phyllic, argillic, porphyry copper, epithermal gold), but most require expert knowledge in remote sensing techniques (Bierwirth 2002). ASTER's effectiveness is largely unknown for many other alteration types, including sodic-calcic (Na-Ca) metasomatism. Furthermore ASTER's effectiveness is untested over many terrains.

The Mount Isa Inlier is one of the world's richest mineral provinces, containing Cu, iron oxide–copper-gold (IOCG), Ag-Pb-Zn and U deposits. Na-Ca alteration is spatially and temporally associated with IOCG deposits, such as Ernest Henry (Williams and Pollard 2003; Williams et al. 2005; Marshall et al. 2006). Prospectivity analysis conducted by Mustard et al. (2004) shows that major structures such as the Cloncurry Lineament and Cloncurry Fault act as fluid pathways, and thus structurally

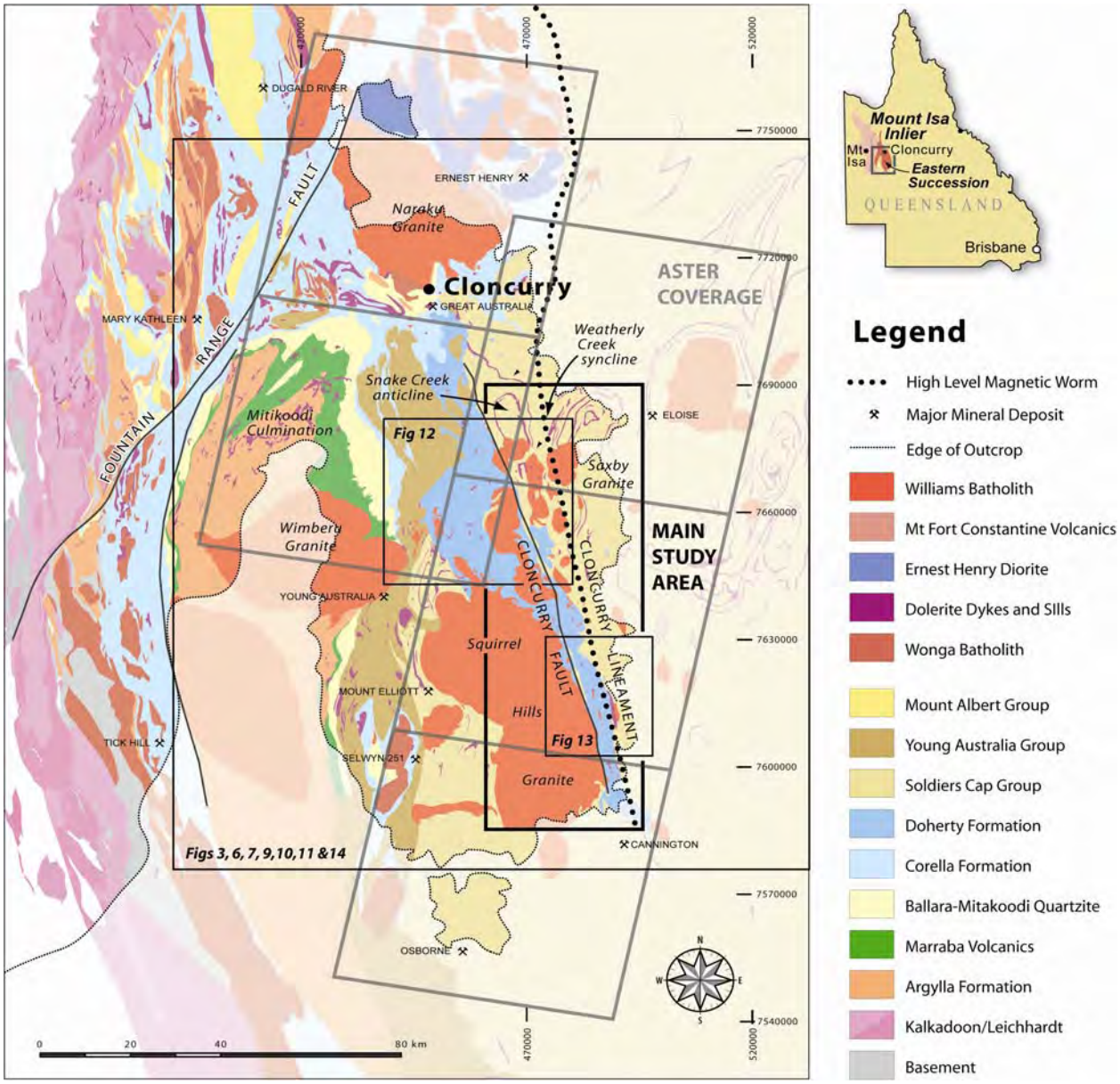

Figure 1: Geology, ASTER coverage of the study area, and locations of other figures. The box marked main study area corresponds to the area that has been investigated in detail and sampled for PIMA analysis. Outcropping geology is in full colour and areas under of Tertiary sediment cover are partially masked out. Map after Foster and Austin (2008); modified from the Queensland Department of Mines and Energy et al. (2000).

control Cu-Au deposits. However, the timing of various alteration stages, their structural controls and relationship to mineralisation is contentious (e.g. Baker 1998; Davidson 1998; Mark et al. 2006)

Regional Na-Ca alteration field mapping (e.g. Marshall 2003) is problematic due to the irregular patterns of alteration, and the difficulty of objectively classifying alteration the field. The aim of this study is to investigate the spatial relationships between ASTER band ratios, PIMA spectra, geochemical, radiometric and magnetic intensity data in order to differentiate the spectral and geophysical definition of Na-Ca alteration from carbonates and amphibolites in the eastern part of the Mount Isa Inlier (Figure 1). The spectral and geophysical expression of Na-Ca alteration and its relationship with major fault systems and mineral occurrences may be useful for exploration targeting of IOCG deposits.

2. BACKGROUND

2.1. ASTER Background

ASTER is a 14 band, high resolution, multispectral imaging devise (Table 1) that records data in Visible Near-InfraRed (VNIR) Short Wave InfraRed (SWIR) and Thermal InfraRed (TIR) spectra. It is mounted on Terra, the Earth Observing System (EOS) satellite (Abrams 2000) which was launched in December 1999 and sits in a polar orbit that repeats on a 16 day cycle (Abrams 2000).

The short wave infrared (SWIR) data consists of 6 bands designated 4 to 9. Bands 5 to 9 cover an area of the short wave infrared where many OH- and carbonate minerals have absorption features. Bands 5 to 8 approximately cover the wavelength limits of

LANDSAT band 7. Minerals of interest to exploration geologists that produce absorption features in SWIR bands are outlined below:

Alunite and kaolinite are significant for mineral exploration because they define advanced argillic alteration (Hemley & Jones 1964), i.e., low pH environments. Alunite has a diagnostic absorption feature near 2.17 μm (Rowan et al. 2006) that is recorded in band 5. Kaolinite is characterised by a twin absorption feature at 2.17 and 2.20 μm (Rowan et al. 2006), which corresponds to asymmetric absorption in ASTER bands 5 and 6. Landsat TM has no capability to define advanced argillic alteration.

Table 1: The three subsystems which make up ASTER, their band numbers, spectral range, radiometric uncertainty and spatial resolution (After Rowan et al. 2003).

Subsystem	Band Number	Spectral Range (μm)	Radiometric Uncertainty	Spatial Resolution
VNIR	1	0.52 - 0.6	< 0.5%	15m
	2	0.63 - 0.69	< 0.5%	15m
	3	0.76 - 0.86	< 0.5%	15m
SWIR	4	1.60 - 1.70	< 0.5%	30m
	5	2.145 - 2.185	<1.3%	30m
	6	2.185 2.225	<1.3%	30m
	7	2.235 - 2.285	<1.3%	30m
	8	2.295 - 2.365	<1.0%	30m
	9	2.36 - 2.43	<1.3%	30m
TIR	10	8.125 - 8.475	<0.3K	90m
	11	8.475 - 8.825	<0.3K	90m
	12	8.925 - 9.275	<0.3K	90m
	13	10.25 - 10.95	<0.3K	90m
	14	10.95 - 11.65	<0.3K	90m

Illite, muscovite and smectite are components of phyllic and argillic alteration. Phyllic alteration of feldspars produces Al-phyllosilicate minerals, such as muscovite, which yield spectra having an intense Al–OH absorption feature near 2.20 μm and secondary features near 2.35 and 2.44 μm, (Rowan et al. 2006). ASTER can not identify the Al-OH bearing minerals (muscovite-illite-Al smectite) specifically, but they can be identified as a group (e.g. Rowan & Mars 2003).

Mg-OH and carbonate are major components of lithological units and ore systems that are not detectable with Landsat TM. Calcite and chlorite have diagnostic absorption feature near 2.350 μm which coincides with a symmetric absorption feature in ASTER band 8 (centred 2.320 μm). Other Mg-OH bearing minerals such as talc and amphibole, which are characterised by absorption features near 2.320 μm and 2.390 μm, have similar ASTER band 8 responses (e.g. Rowan et al. 2004). ASTER can not separate carbonate from Mg-OH bearing minerals (J Mars pers. comm. 2007), but it will identify them as a group which is an advantage over Landsat TM.

The ASTER VNIR and SWIR data show greater discrimination between mineral assemblages than Landsat TM, which has a similar spatial resolution but fewer bands, thus limiting its usefulness for making mineral determinations (Rowan et al. 2003). Apart from airborne systems (e.g. AVRIS) ASTER TIR data is the only multispectral thermal imaging data available, and is very useful for defining surface silicification despite having only 90 m resolution (e.g. Ninomiya and Fu 2002).

2.2. Climate, land cover and topography

Land cover, particularly the amount of vegetation and alluvium, is an important influence on the results obtained from spectral sensors such as ASTER, which are most useful over arid to semi-arid areas. The eastern Mount Isa Inlier has a semi-arid

tropical environment (Slatyer 1964; Donchak et al. 1983) with an average maximum temperature is 32 ºC and minimum of 17 ºC. The area receives 375-500 mm average annual rainfall that decreases to the south and occurs mostly during summer (Donchak et al. 1983).

The study area consists of three major topographic domains, the central of which forms a watershed dividing for the Cloncurry River in the west and the Fullarton and Williams rivers in the east. In the east of the study area, low rolling hills and plains above the Soldiers Cap Group give way east to the Cloncurry and Julia plains. The vegetation cover is dominantly grasslands; Spinifex that gives way eastwards to Mitchell and Flinders grasses. Watercourses are commonly lined by medium to large gum trees. The plains give way westerly to rocky hills and gorges at the contact of the Soldiers Cap Group and Doherty Formation where an escarpment cuts west into the Selwyn Range highlands. The vegetation in the highlands consists of spinifex and low open woodlands, with the watercourses lined by gums and often filled with small acacias. Mesas composed of Jurassic-Cretaceous sedimentary rocks are found throughout the area (Donchak et al. 1983), particularly in the high country, and are often barren or thinly covered by grasses and acacias. The plains and areas of low relief in the west support grasslands similar to those in the east (Donchak et al. 1983).

2.3. Geological Background

2.3.1. STRATIGRAPHY

Rocks outcropping within the study area were laid down during two successive rifting phases, Cover Sequences 2 ($CS_{2;}$ 1.8-1.72 Ga) and 3 ($CS_{3;}$ 1.7-1.6 Ga) (Blake and Stewart 1988; 1992). The main units of interest are described from east to west. The CS_3 Soldiers Cap Group (SCG) consists mostly of psammopelitic rocks, quartzite,

schist, gneiss and migmatite. Mafic metavolcanics (Amphibolites) are commonly sub-concordant to bedding within the SCG (e.g. the Toole Creek Volcanics). The CS_2 Corella and Doherty formations range from intact / minimally altered laminated-massive calc-silicates to a variety of Na-Ca alteration assemblages and massive breccias. The Young Australia Group (Foster and Austin 2008) includes the Marimo Slate, Stavely and Kuridala Formations that consist of slate and arenite to schist and quartzite lithologies. The Ballara-Mitakoodi Quartzite unit consists dominantly of quartzite with minor siltstone, and mafic and felsic volcanics. Further west the Marraba Volcanics comprise mainly metabasalt with minor psammopelitic units. The Argylla Formation, in the core of the Mitakoodi Culmination (Figure 1), comprises mainly felsic volcanics with minor siltstone and metabasalt. Proterozoic tectonostratigraphy is described in detail by Foster and Austin (2008).

Plutons of the Williams-Naraku Batholith intruded large areas of the Eastern Succession from ~1550-1490 Ma. The Maramungee granite and its correlatives (~1550 Ma) occur mostly in the southeast of the study area, the Saxby and Mount Angelay granites, aged ~1540-1520 Ma, occupy the central area and the Squirrel Hills and Naraku granites (1510-1490 Ma) and occupy the southwest and northern parts of the study area. Doleritic dykes and sills of various ages intrude throughout the area. They are commonly extensively folded and metamorphosed to amphibolite facies (Donchak et al. 1983), but some are unaltered (dl of Donchak et al. 1983) and probably correlatives of the Lakeview dolerite (~1116 Ma: Page 1983).

Several Phanerozoic units, which are shown as cover on Figure 1 are also discussed in this paper. The oldest are Cambrian calcareous units sitting to the west of the main study area, above the Wimberu granite and Mitakoodi Quartzite. These include the Thorntonia Limestone, Chatsworth Limestone and the Pomegranite Limestone and

collectively consist of chert, breccia, dolomite and limestone and marl (Blake 1987). Outliers of Cretaceous Toolebuc Formation, which consists of Calcareous Shale and limestone (Blake 1987), crop out east of the main study area. Mesas of the Jurassic Gilbert River Formation, which consist of sandstone and conglomerate at the base and an upper claystone unit, sit unconformably above the Precambrian units (Blake et al. 1983) throughout much of the study area. Various Tertiary sand, gravel, clay and Quaternary alluvial deposits also sit unconformably above the Precambrian, particularly to the east of the main study area.

2.3.2. Tectonics and Metamorphism

The Isan Orogeny, occurring from ~1600-1500 Ma, was the major contractional deformation event in the Mount Isa Inlier, consisting of numerous deformation events termed D_1, D_2 etc. (after Bell and Duncan 1978). D_1 was recognised in the west of the Inlier (Bell, 1983) as a N over S thrusting event. However in the east there remain contrasting views about the existence and structural importance of D_1 (Austin and Blenkinsop 2008). D_2 and D_3 were both roughly E-W shortening events and are thought to have formed the dominant ~N-S structural grain of the Eastern Succession (Beardsmore et al. 1988; Adshead-Bell 1998; Betts 2000; Hatton & Davidson 2004). Both events produced upright folding and numerous shear zones, which acted as pathways for metasomatic fluids, and localised brecciation during D_4. Dextral faulting (Laing 1998) occurred syn- to post-D_4 (<1530 Ma), in conjunction with the later stages of east-west shortening.

Metamorphism in the inlier is high temperature, low pressure and is commonly thought to peak syn-D_2 at 1595-1580 Ma (Rubenach and Barker 1998; Rubenach 2003; Foster & Rubenach 2006, Rubenach et al. 2008). Mechanisms proposed to

explain the high temperature/low pressure metamorphism include mantle under-plating (e.g. Oliver et al. 1998) and large mafic / felsic mid-crustal intrusions (McLaren et al. 1999; Hand and Rubatto 2002, McLaren et al. 2005). The metamorphic grade of the area varies from greenschist facies in the north to upper amphibolite facies in the south (Foster and Rubenach 2006). In the high grade areas, pelitic rocks contain sillimanite and/or K-feldspar and calc-silicate rocks contain diopside (Foster and Rubenach 2006).

2.3.4 METASOMATISM

Metasomatic alteration has long been recognised in the Eastern Succession of the Mount Isa Inlier (e.g. Edwards and Baker 1954; Carter et al 1961) and consists of several stages (Table 2). Primary sodic alteration is widespread throughout the study area, along and adjacent to the Cloncurry Fault (De Jong and Williams 1995; Williams 1998; Mark 1998; Rubenach and Lewthwaite 2002).

The second stage of Na-Ca alteration (Stages 2a-2d: De Jong 1995), which is texturally destructive (Cannell and Davidson 1998), has been recognised as a major component of the alteration assemblages around numerous mineral deposits (e.g. Ernest Henry: Mark 1999; Oliver et al. 2004). Chlorite-epidote alteration, which primarily occurs adjacent to brittle quartz-breccia faults, such as the Cloncurry fault, is thought to have occurred late-post Isan Orogeny (Mark 1998).

Potassic alteration (Stage 6: De Jong 1995), consisting of K-feldspar-hematite (otherwise known as red-rock alteration, Carter et al. 1961) is also widely recognised, but its timing is unclear. Cannell and Davidson (1998) suggest it occurs between the two stages of Na-Ca alteration, whereas De Jong (1995) suggests it occurs after all Na-Ca alteration has ceased. It is possible that potassic alteration may have occurred

Table 2 The stages of Na-Ca alteration observed by De Jong (1995) for the study area, and the minerals that ASTER and PIMA studies could use to identify them. Other than amphibole, carbonate, epidote and chlorite which can not be separated due to their similar absorption features in ASTER band 8, only Quartz and Iron band ratios could potentially be used to differentiate the alteration stages of DeJong (1995). This illustrates the difficulty involved in subdividing various metasomatic events in this study area using ASTER data.

Stage	Mineral Occurrence	ASTER Minerals	PIMA Minerals
1	Oligioclase, actinolite ± diopside	Amphiboles	Actinolite
2a	Actinolite, albite ± magnetite ± titanite ± marialite (± diopside)	Amphiboles, ferrous iron	Actinolite
2b	Actinolite (± diopside) albite ± magnetite	Amphiboles, ferrous iron	Actinolite
2c	Actinolite / tremolite ± diopside veins with rims of albite ± magnetite	Amphiboles, ferrous iron	Actinolite, tremolite
2d	Albite clasts in actinolite / tremolite matrix ± magnetite ± apatite, with haematitedusted albite rim.	Amphiboles, ferrous iron	Actinolite, tremolite, (hematite)
3a	Albitite, quartz, titanite, magnetite ± actinolite ± diopside ± apatite	Quartz, Amphiboles, ferrous iron	Actinolite
3b	Quartz ± titanite ± diopside ± albite	Quartz	
Brittle-ductile transition			
4	Diopside, actinolite, albite ± magnetite ± epidote ± allanite ± calcite ± chlorite	Amphiboles, ferrous iron, epidote ± chlorite, carbonates	Actinolite, epidote, calcite, chlorite
5a	Epidote (in veins) ± prehnite ± quartz ± albite ±chlorite ± talc	Epidote ± chlorite	Epidote, chlorite, ± prehnite ± talc
5b	Tremolite needles, Mg Calcite (Dolomite)	Carbonates	Calcite (± tremolite, dolomite)
6	K-Feldspar ± hematite ± quartz	Quartz, ferrous iron	(goethite, hematite)
7	Quartz ± Sulphides	Quartz	

sporadically throughout the metasomatic history of the region, possibly as a by-product of Na-Ca alteration (Mark et al. 2006). De Jong (1995) analysed the characteristics of pristine to highly Na-Ca altered calc-silicates and breccias in the Doherty Formation using XRF (X-Ray Fluorescence) geochemical analysis. The data have been averaged and the bulk chemical change during each alteration stage has been calculated (Table 3). De Jong's analyses show that the early albitisation caused a relative loss of, SiO_2, K_2O, Al_2O_3 and Fe_2O_3 but relatively large gains in Na_2O and CaO. Such chemical changes would likely result in loss of almost all the quartz present, a major decrease in K-feldspar and a major increase in albitic plagioclase.

Table 3 The relative changes in chemistry during Na-Ca alteration which are shown as the change in weight percent (±Wt%) and the percentage change in weight percent (%Σ). Data from De Jong 1995.

	Pristine calc-silicates			Moderately Altered Calc-Silicates			Highly Altered Calc-Silicates			Breccias
	Average	± Wt %	% Σ	Average	± Wt %	% Σ	Average	± Wt %	% Σ	Average
SiO2	62.70	1.13	1.80	63.83	-4.39	-6.87	59.44	1.08	1.82	60.52
TiO2	0.68	-0.02	-3.51	0.65	0.04	6.05	0.69	-0.12	-17.09	0.57
Al2O3	15.58	-1.10	-7.06	14.48	1.98	13.70	16.46	-3.63	-22.07	12.83
Fe2O3	5.86	0.11	1.84	5.96	-0.33	-5.50	5.64	-0.70	-12.48	4.93
MnO	0.06	-0.02	-42.22	0.03	0.02	66.15	0.05	-0.01	-9.72	0.05
MgO	2.86	0.16	5.55	3.02	0.04	1.30	3.06	1.86	60.73	4.92
CaO	3.22	0.31	9.67	3.53	0.87	24.77	4.41	2.55	57.82	6.95
Na2O	3.27	0.52	15.93	3.79	3.69	97.38	7.47	-0.60	-8.09	6.87
K2O	4.54	-0.47	-10.29	4.07	-2.87	-70.52	1.20	-0.82	-68.46	0.38
P2O5	0.13	0.02	18.66	0.16	-0.02	-12.26	0.14	-0.08	-56.80	0.06
LOI	1.43	0.11	7.34	1.54	-0.34	-21.89	1.20	0.04	3.65	1.24
Total	100.31			101.05			99.76			99.32

The second stage of alteration, which is associated with regional brecciation, produced large relative losses of Al_2O_3, and K_2O, and large increases in CaO and MgO. These chemical changes should result in an increase in diopside / actinolite. Although there is an increase in CaO throughout the alteration sequence, most calcite appears to have formed late, possibly due to CO_2 within the brecciating metasomatic fluids. Magnetite is commonly found within breccias despite an overall loss of Fe, suggesting that the precipitation of magnetite was caused by a shift in the redox conditions.

3. DATA AND METHODS

3.1. ASTER Processing

Five ASTER scenes, covering an area shown in Figure 1, were obtained from Geoscience Australia and processed following Geoscience Australia's ASTER manual (i.e. Kalinowski and Oliver 2004). Level 1B radiance at sensor data was used due to low cost and ready availability, although Level 2 AST07 Surface reflectance-VNIR, SWIR data may provide better constrained results (J Mars pers. comm. 2007). A crosstalk correction was performed using the ERSDAC (Earth Remote Sensing Data Analysis Center) Crosstalk 3 tool (Iwasaki et al. 2001). The tool corrects for signal leakage from band 4 to the adjacent band 5 and 9 detectors. Band 4 is a particular problem because the solar output in that frequency range is significantly higher than for the other SWIR bands. The ASTER data are then imported into ER Mapper as separate VNIR, SWIR and TIR raster datasets. The images are rectified and a radiance calibration is performed to rescale the digital values to the observed top of atmosphere radiance values.

Table 4 The different band ratios used in this study (after Kalinowski and Oliver 2004).

Feature	Band or Ratio	Reference
Iron		
Ferric iron, Fe3+	2 / 1	Rowan et al. 2004
Ferrous iron, Fe2+	5/3 + 1/2	Rowan et al. 2004
Laterite	4 / 5	Bierwith 2002
Gossan	4 / 2	Volesky 2003
Ferrous silicates	5 / 4	Kalinowski and Oliver 2004
Ferric oxides	4 / 3	Kalinowski and Oliver 2004
Carbonates / Mafics		
Calcite / carbonate / chlorite / epidote	(7+9) / 8	Rowan et al. 2003
Epidote / chlorite / amphibole	(6+9) / (7+8)	Kalinowski and Oliver 2004
Amphibole	(6+9) / 8	Hewson et al. 2005
Amphibole	6 / 8	Bierwith 2002
Dolomite	(6+8) / 7	Rowan et al. 2003
Carbonate	13 / 14	Ninomiya and Fu 2002
Silicates		
Sericite / muscovite / illite / smectite	(5+7) / 6	Rowan and Mars 2003
Alunite / kaolinite / pyrophyllite	(4+6) / 5	Rowan
Phengitic	5 / 6	Hewson et al. 2005
Muscovite	7 / 6	Hewson et al. 2005
Kaolinite	7 / 5	Hewson et al. 2005
Clay	(5+7) / 6^2	Bierwith 2002
Alteration	4 / 5	Volesky 2003
Host rock	5 / 6	Volesky 2003
Silica		
Quartz rich rocks	14 / 12	Rowan et al. 2006
Silica	(11x11) / 10/12	Bierwith 2002
SiO2 / basic degree index	12 / 13	Ninomiya and Fu 2002
Siliceous rocks	(11x11) / (10x12)	Ninomiya and Fu 2002

The ASTER scenes are mosaicked, and the mineral components of various alteration assemblages are differentiated by application of various band ratios (see table 4). The band ratios are algorithms applied to the different ASTER bands, using ER Mapper, that have been previously shown (e.g. Ninomiya and Fu 2002; Bierwirth 2002; Volesky 2003; Rowan and Mars 2003; Rowan et al. 2003; 2004; Hewson et al. 2005) to map various lithologies and/or alteration types. The resulting raster images are then imported into MapInfo (www.mapinfo.com) for comparison with mapped geology and PIMA data.

Band ratios that may be useful for mapping Na-Ca alteration are those that discriminate amphiboles, epidote-chlorite-amphibolite, carbonate, calcite-carbonate-chlorite epidote, dolomite and quartz band ratios.

3.2 PIMA Methodology

Portable Infrared Mineral Analyser (PIMA: http://members.ozemail.com.au/~tdc/pima/pima.htm) is a spectral scanning device that is used on hand samples to measure spectral absorption features. Previous workers have used PIMA, (e.g. Sun et al. 2001) or a combination of both PIMA and ASTER (e.g. Van der Wielen et al. 2004) to identify deposit to regional scale alteration.

Approximately 300 samples from the study area (Figure 2) were cut and analysed using PIMA. The resulting spectra were saved as PimaView Spectrum files which were imported into The Spectral Geologist (TSG: www.thespectralgeologist.com) software. The TSG software can distinguish between 49 different minerals and will list up to two dominant minerals (Table 5) by using the wavelengths of characteristic absorption features. The data are sorted by mineralogy and plotted over the ASTER images to compare with the various band ratios.

Because PIMA can detect more minerals with less ambiguity than ASTER, it is a good tool for validation of ASTER data, and can be used to give more detailed information about lithology and alteration at the sample scale. However the difference in scale between PIMA and ASTER datasets may make spatial comparison problematic. Here it used to quantify the mineral components of Na-Ca alteration.

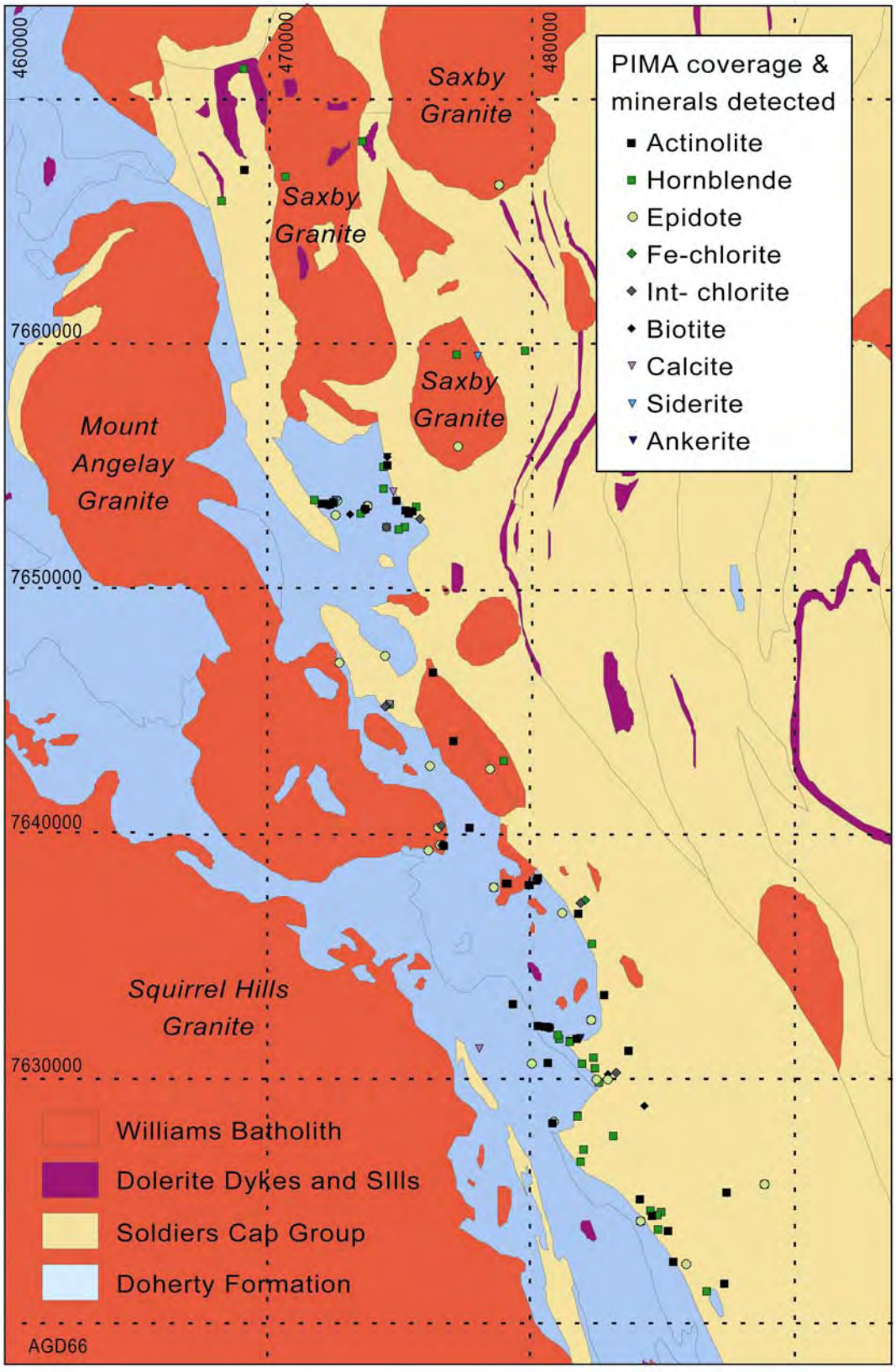

Figure 2 Results from PIMA analyses. Minerals indicative of Sodic Calcic alteration (e.g. actinolite, hornblende and calcite) are distributed widely in the study area while chlorite, and epidote are generally restricted to post-1530 Ma faults.

Table 5 PIMA mineral groups, minerals within each group and total samples with those minerals identified by PIMA. Min1 and Min2 are the primary and secondary minerals detected by PIMA.

Mineral Group	Mineral	Min1	Min2	Mineral Group	Mineral	Min1	Min2
Ambibole	Actinolite	35	9	Mg-rich (misc.)	Antigonite		
	Hornblende	41	7		Brucite		1
	Tremolite	1	1		Serpentinite	1	
	Riebeckite	1			Talc		
Biotite	Biotite (general)	7			Vermiculite		
	Phlogopite	10	6		Magnesium Clays	3	2
	Vermiculite			Silicates (misc.)	Prehnite	3	
Carbonates	Ankerite	1	1		rubellite		
	Aragonite				Topaz		
	Calcite	10	1		Tourmaline	1	
	Dolomite			SiO2	Opaline Silica	2	1
	Magnesite			Smectites	Hectorite		
	Siderite	4			Montmorillonite	8	1
Chlorite	Mg-rich	1			Nontronite	1	
	Fe-rich	3	1		Saponite		
	Int Chlorite	12	2	Sulphates	Alunite		2
Epidote	Clinzoisite				Gypsum		13
	Epidote	17	17		Jarosite		
	Zoisite			White Micas	Illite	25	5
Kaolin	Dickite	4	4		Muscovite	20	6
	Halloysite	13			Paragonite		1
	Kaolinite				Phengite		
Iron Oxides	Goethite			Others	Gibbsite		
	Haematite				Pyrophyllite		

3.3. Geophysical Data

Detailed aeromagnetic and radiometric data over the Mount Isa Inlier were acquired by M.I.M. Holdings Ltd. (now Xstrata) in 1992. The radiometric data was obtained using a 256 channel Exploranium GR800B spectrometer and sampled at 70 m intervals. The survey was flown with a mean terrain clearance of 80 m, flight line spacings of 200 m and tie line spacings 2000 m (Richmond 2000).

The total magnetic intensity data used here are derived from the aeromagnetic survey which was sampled with a split beam Cesium Scintrex V201, which used a 7 m sample interval (Richmond 2000). The survey was flown at a height of 70m with

flight line spacings of 70 m and tie line spacings 400 m (Edmiston et al. 2008). The total magnetic intensity dataset is grided as 50m x 50m cells, providing a high quality dataset that shows good detail (Blenkinsop et al. 2008).

4. RESULTS

4.1 Amphiboles

Three ASTER mineral ratios have been previously used to map Amphiboles (Table 4). The Amphibole (Bierwirth, 2002: Figure 3) and Amphibole ± MgOH ± Carbonate (Rowan et al. 2004) band ratios appear to highlight similar surface lithologies. However, there appears to be far greater contrast in the latter. The Epidote ± Chlorite ± Amphibolite band ratio is virtually identical to the Amphibole (Bierwirth, 2002) band ratio and is discussed later in reference to Epidote-Chlorite alteration.

There is a strong correlation between the Amphibole band ratio and hornblende-bearing granites, such as the Squirrel Hills and Naraku granites (cf. Blake 1987). Another high corresponds to a concentration of doleritic intrusions (unit dl of Donchak et al. 1983) in the hinge and eastern limb of the Mitakoodi Culmination, within Mitakoodi Quartzite and Marraba Volcanics. In this area the dl unit corresponds to metadolerite or amphibolite, which commonly contain hornblende, actinolite and (often partly sericitised) plagioclase (Donchak et al. 1983). In many other cases the dl unit corresponds to dolerites which contain primary pyroxene and thus are not expressed as highs in this band ratio. The most intense high in the band ratio corresponds to metadolerites, metabasalts and amphibolites of the Toole Creek Volcanics, which are interlayered with mainly schistose metasediments (Donchak et al. 1983). Linear traces observed within the high are indicative of layering within the

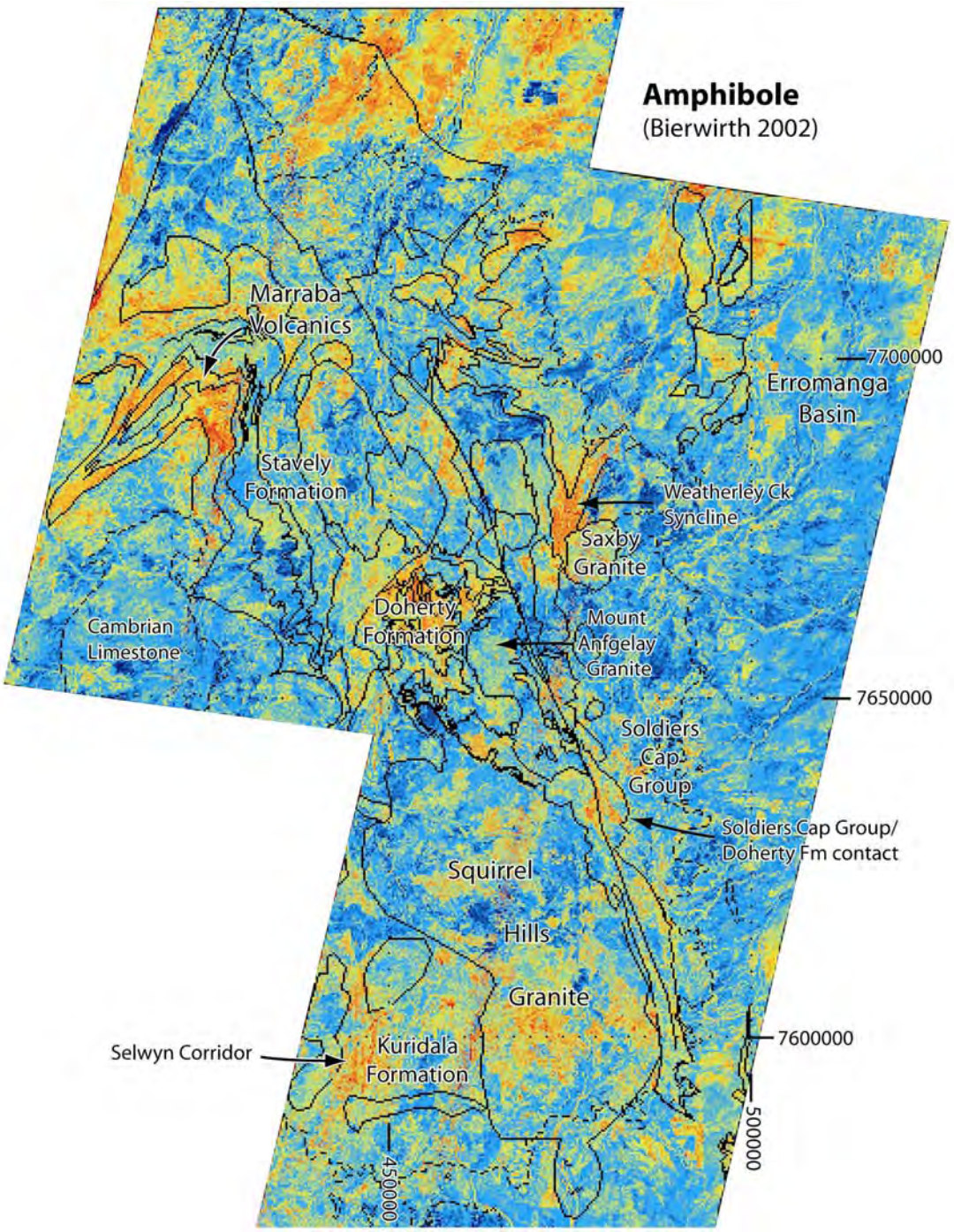

Figure 3 The Amphibole (Bierwirth 2002) index, which is similar to the other amphibole indexes listed in Table 4, highlights amphibolites (e.g. the Marraba and Toole Creek volcanics) but also areas of sodic–calcic alteration (e.g. in the Doherty and Kuridala formations). Numerous other highs may reflect carbonate rich Tertiary sediments. All pseudocolour images are normalised to define a relative scale of intensity, where red is high, yellow intermediate and blue is low.

strata. Moderate highs are also observed in several parts of the Doherty and Kuridala formations. These highs may coincide with actinolite formed during Na-Ca metasomatism, but they may also be due to mafic intrusions (e.g. Figure 4) that are more widespread than mapped by Donchak et al. (1984) and Blake et al. (1984).

Although the amphibole band ratios generally show similar features there are some contrasts between them. The Bierwirth band ratio distinguishes the Cone Creek metabasalt member of the Marraba Volcanics much better than the Amphibole ± MgOH ± Carbonate band ratio. In contrast the Amphibole ± MgOH ± Carbonate band ratio does not show a high for the Wakeful Metabasalt member and shows a high for the Mitakoodi Quartzite. The Mitakoodi Quartzite consists mostly of feldpathic quartzites and arenites, but Blake (1987) does suggest that some calcareous quartzite, calc-silicate rocks and marbles also occur within the unit, which may cause the high.

Hornblende has a major absorption feature at ~2.320 µm detected, by PIMA, in 48 samples and is primarily in black and white foliated and unfoliated Na-Ca altered rocks (Figure 4a) and amphibolites (Figures 4e & f) within the Doherty Formation. Hornblende is also detected as a primary mineral in parts of the Saxby Granite, in marbles, and samples with pink-green alteration. The pink-green alteration probably represents late stage alteration of albite ± actinolite ± tremolite ± hornblende to Calcite ± epidote ± chlorite ± Mg-clays. In figures 4c & d hornbelende occurs with tremolite and epidote respectively.

Actinolite has a major absorption feature at 2.316 µm (Figure 4b) and is detected, by PIMA, in 44 samples in the Doherty Formation. It is primarily found in calc-silicate breccias, mylonites and foliated (e.g., Figure 4b) to unfoliated Na-Ca altered rocks and is commonly associated with epidote and chlorite. Actinolite is also detected in two samples from an unnamed, probably Maramungee type (~1550 Ma) (pg) granite

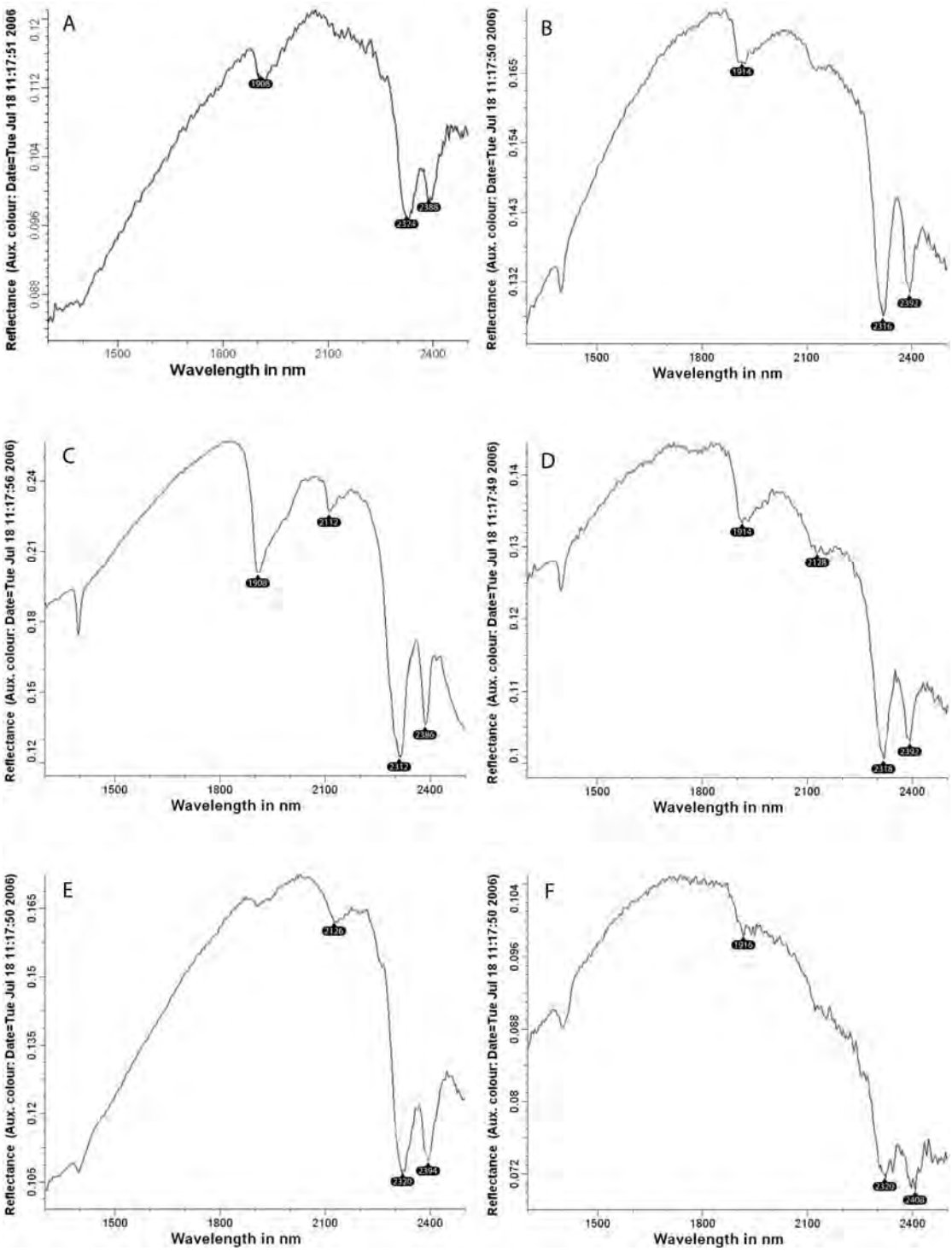

Figure 4 Representative PIMA spectra for amphiboles; a. hornblende and b. actinolite in sodic-calcic altered rocks; c. hornblende and tremolite and d. hornblende and epidote in potassic altered rocks; e. and f. hornblende in amphibolites. Although actinolite and hornblende, the two main amphibole species, have different PIMA spectra, they cannot be differentiated, due to similar absorption features at ~2.320 µm and ~2.400 µm which both correspond to ASTER band 8 and 9 respectively.

at 0477093E 7643734N. No actinolite is detected in the younger granites (Saxby, Mt Angelay and Squirrel Hills granites), which may suggest their intrusion post-dates the major regional Na-Ca alteration phase.

4.2. Chlorite and Epidote

Epidote and chlorite alteration (detected in numerous samples by PIMA) is associated with structurally controlled carbonate hosted copper deposits (e.g. Davidson 1998), but occur over small areas. Although both minerals have absorption features in ASTER bands 7 and 9 (Figures 5a & b) they can not be distinguished from carbonate or amphibolite because the major absorption feature straddle band 8 and 9. Thus there is significant absorption in ASTER band 8.

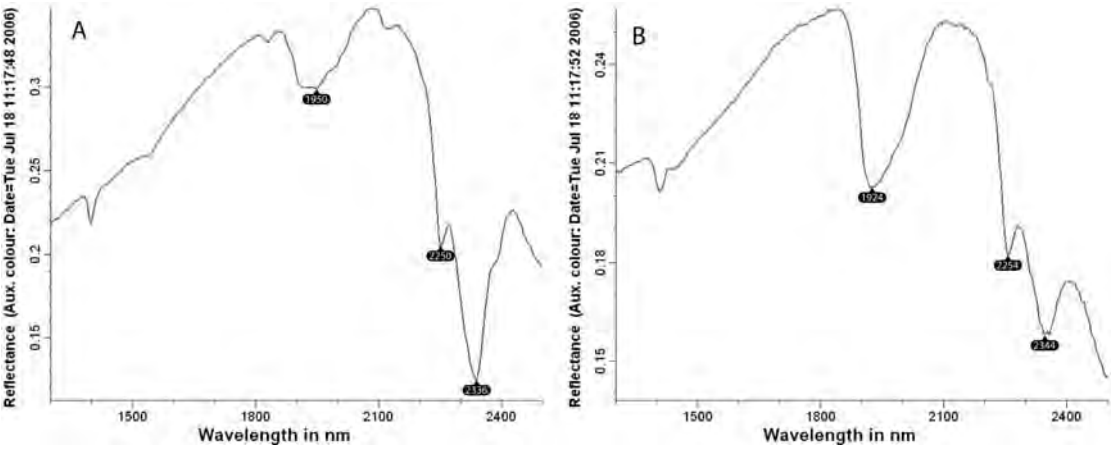

Figure 5 PIMA spectra for: a. Epidote–actinolite alteration of metadolerite showing an asymmetric twin absorption feature at 2.250 and 2.336µm; b. Retrograde mylonite containing Fe- and intermediate chlorite, with an asymmetric twin absorption at 2.250 and 2.344 µm. The major absorption occurs in ASTER bands 8 & 9.

Samples with high epidote and/or chlorite content commonly occur close to late brittle faulting (e.g. the Cloncurry Fault) suggesting that their formation is associated with hydrothermal alteration along such faults. One area (GR: 0480084, 7630555) near a splay of the Cloncurry Fault displays epidote in massive aggregates with amphibole, possibly caused by saussuritisation of Na-Ca altered gabbros. In general, epidote and chlorite tend to occur in mafic and felsic plutonic rocks, many of which are K-feldspar granites or dolerites / gabbros. They also occur in rocks with pink/green (potassic-chloritic) overprinting alteration.

4.3 Carbonates

The Carbonate (Ninomiya and Fu 2002) band ratio (Fig 7) is very grainy due to the poor resolution of the parent bands. However, it is very effective for mapping Cambrian – Cretaceous sediments including the Chatsworth, Pomegranite and Thorntonia limestones and limestone and calcareous sandstones of the Toolebuc Formation (Klo of Ryburn et al. 1988).

The Dolomite band ratio (Figure 7) displays a moderate high over much of the Doherty Formation. However, it also shows a distinct high over the Toole Creek Volcanics in the Weatherly Creek syncline, which is dominated by amphibolites and psammites (cf. Hatton and Davidson 2004). The inability of ASTER SWIT data to differentiate amphiboles from carbonates, epidote and chlorite is a fundamental problem (J. Mars, pers. comm., 2007).

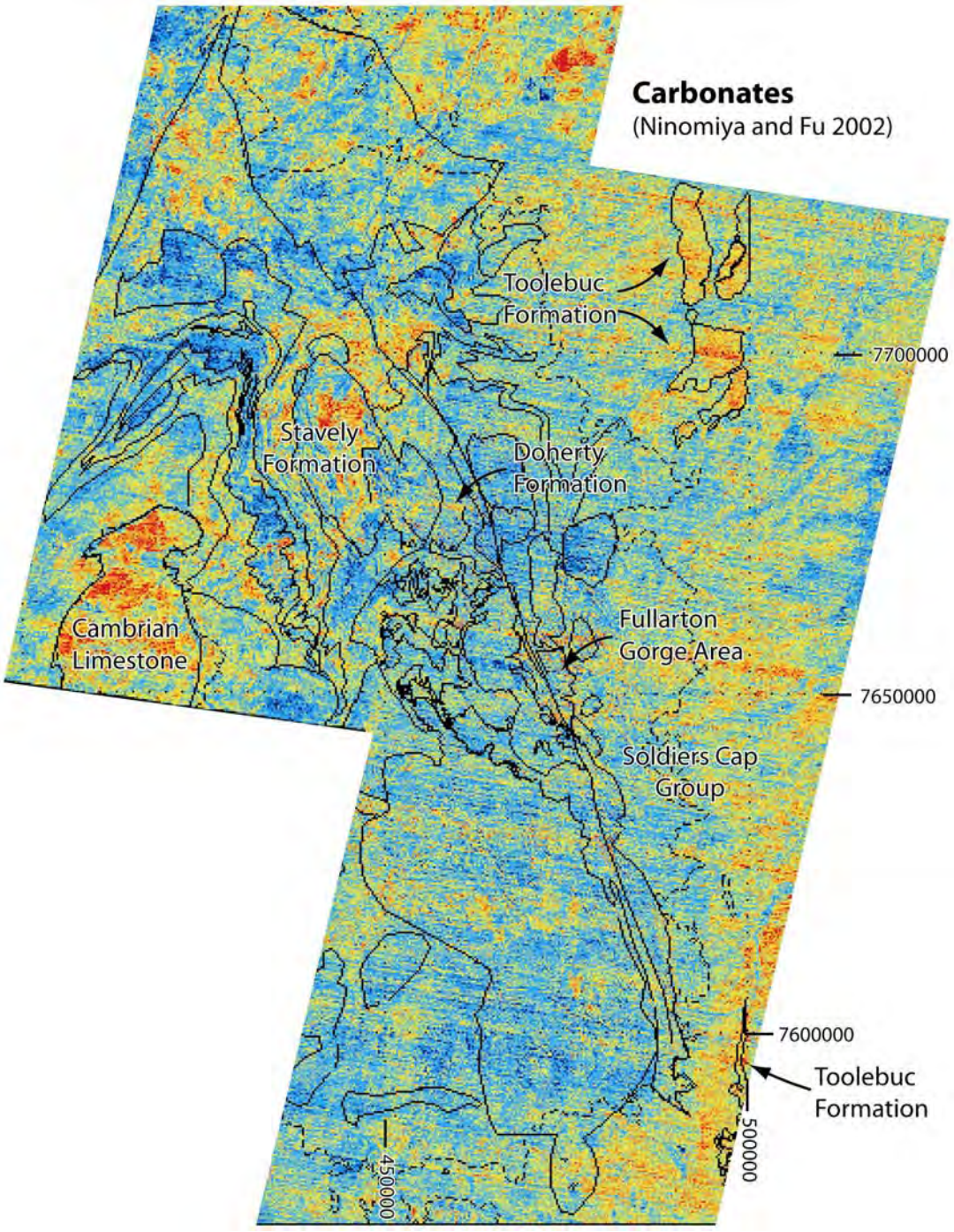

Figure 6 The Carbonate band ratio of Ninomiya and Fu (2002) utilises the ASTER TIR data and best highlights Mesozoic carbonate-rich strata.

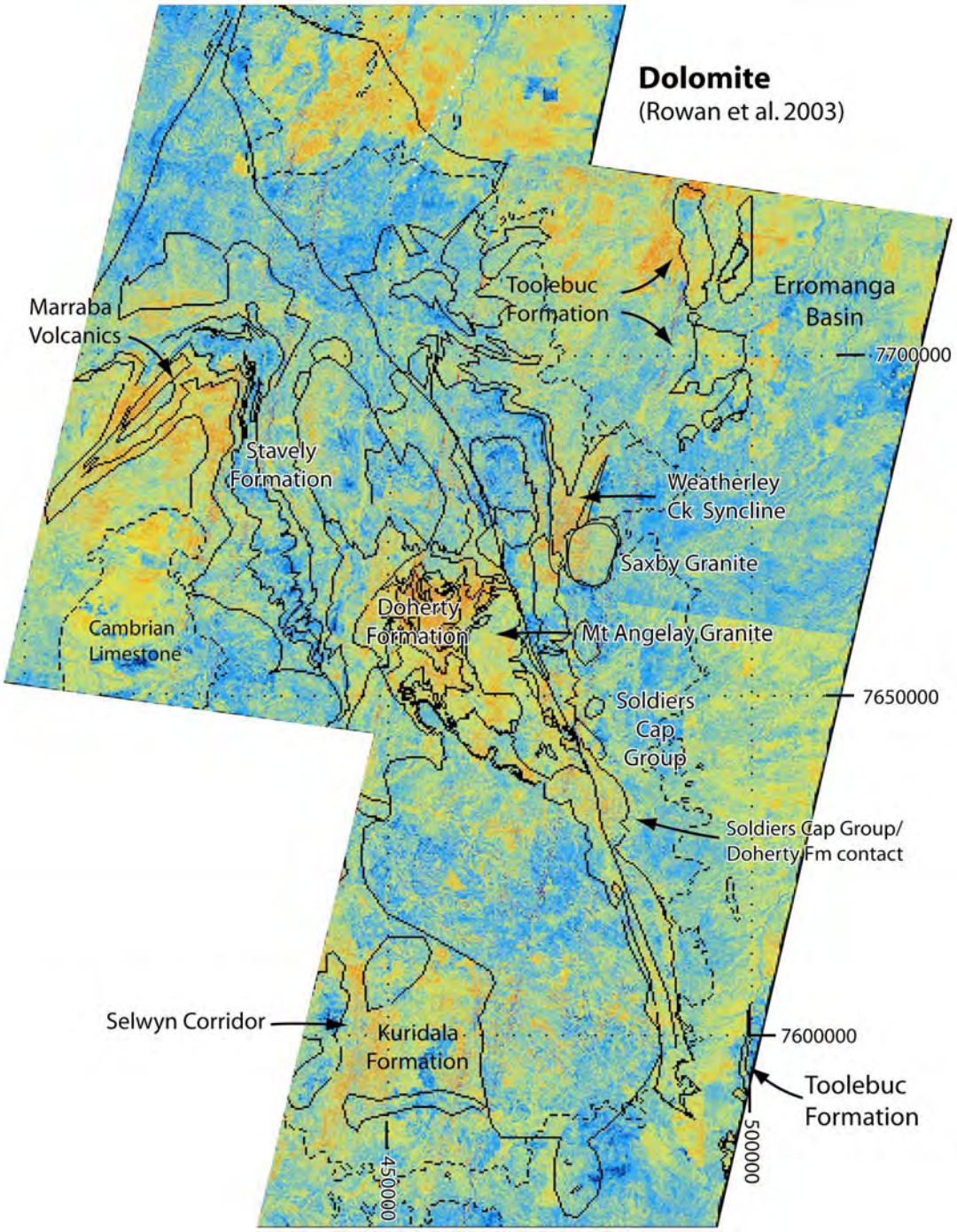

Figure 7 The Dolomite band ratio of Rowan et al. (2003) utilising ASTER SWIR data. It appears to highlight amphibole primarily, associated with amphibolites and with Na-Ca alteration.

Calcite shows diagnostic absorption feature at ~2.340 µm and is detected, by PIMA, in pink-green marbles and calc-silicate breccias (Figure a & b). Most of the samples that contain calcite occur within a small area in the vicinity of the Fullarton River Gorge and commonly occurs with hornblende or epidote. Calcite veins are commonly observed in the field and are associated with siderite, ankerite and gypsum as detected by PIMA. The samples in this area generally coincide with a high in the dolomite band ratio.

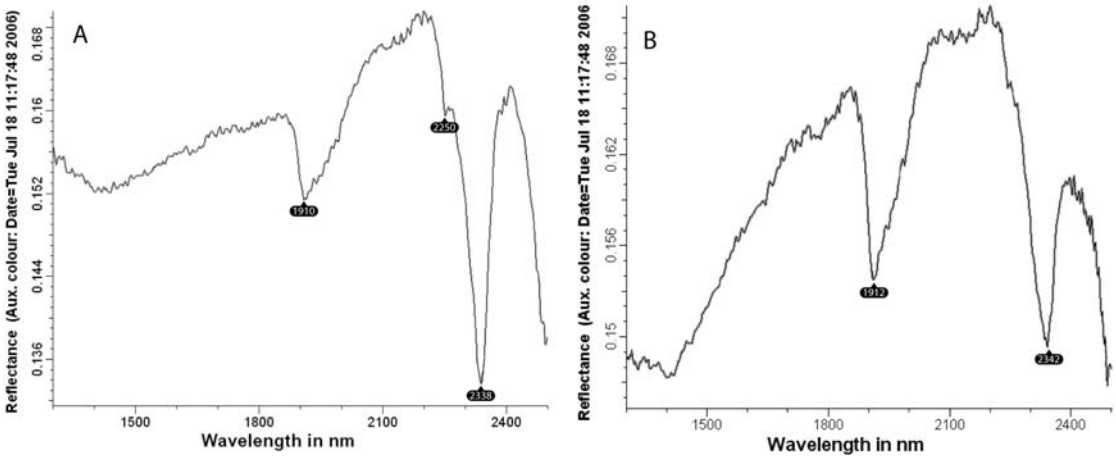

Figure 8 PIMA spectra for a. calcite-epidote breccia/marble and b. a calcite marble from the Doherty Formation both show a pronounced absorption feature at 2.340 µm which corresponds to ASTER band 9.

4.4 Quartz

The quartz band ratio of Rowan et al. (2006) is a highly effective means of identifying relatively quartz rich and poor lithologies in the study area (Figure 9). It shows a clear boundary which coincides with the Cloncurry Lineament. Low amounts of quartz in the Doherty Formation are inferred to the west of the lineament, and high amounts of quartz in the Soldiers Cap Group to the east. This is consistent with the lithological mapping conducted in the area (e.g. Blake 1980; Donchak et al. 1984). In general the quartz band ratio shows lows for areas that are mapped as carbonaceous units. The

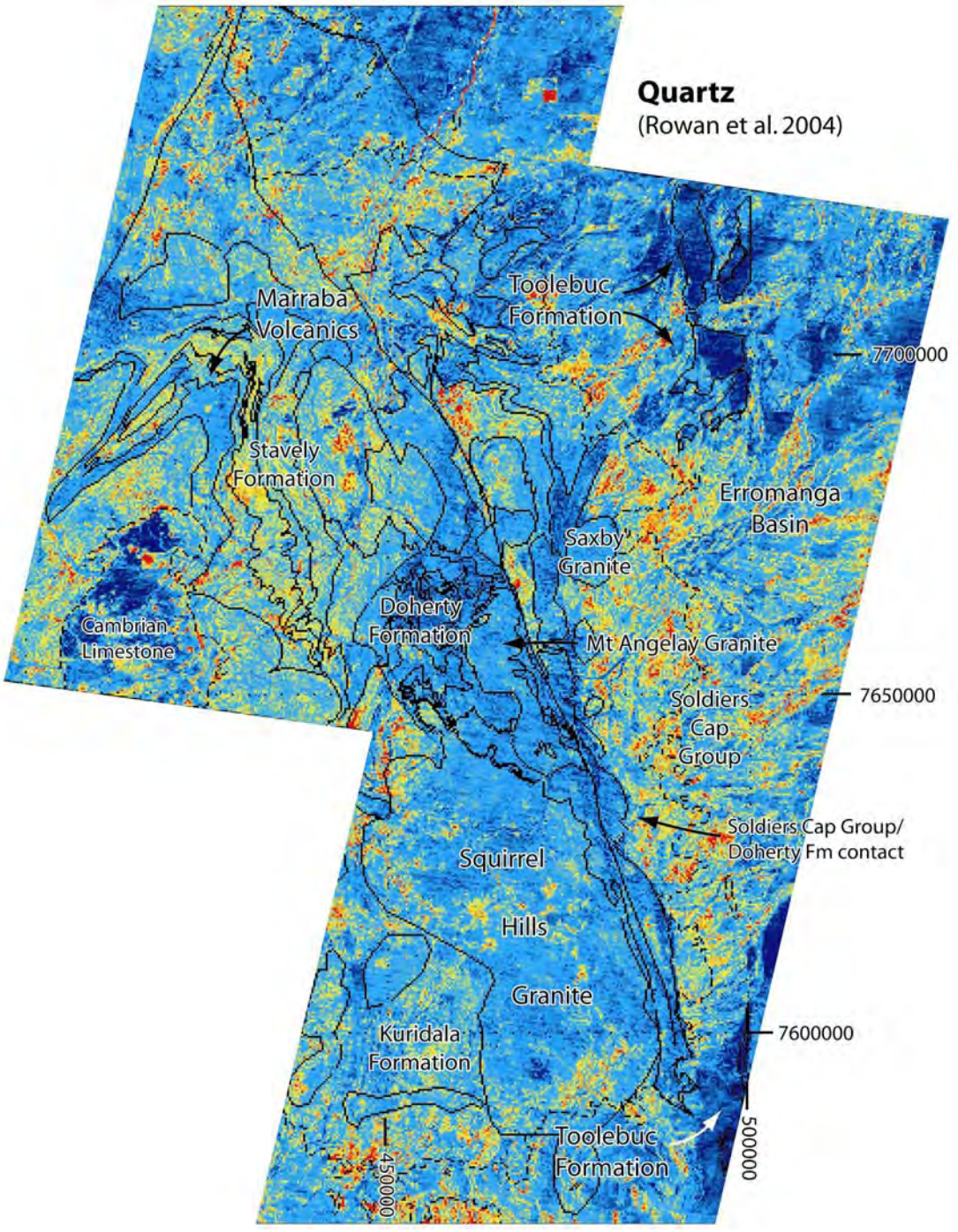

Figure 9 The Quartz band ratio (Ninomiya and Fu 2002) utilises ASTER TIR data and highlights quartz-rich lithologies. In particular it highlights the strong contrast between the quartz-rich Soldiers Cap Group and the quartz-poor Doherty Formation.

quartz ratio band 14/12 is essentially the inverse of the Carbonate band ratio (Ninomiya and Fu 2002) which is band 13/14. The quartz ratio also shows distinct lows for areas of intense Na-Ca alteration, as discussed further in section 4.5.

4.5. Correlations with magnetic and radiometric data

Potassium depletion in Na-Ca altered calc-silicate rocks (Richmond 2000: see Table 3) might be used to map areas of intense sodic-calcic alteration, which should be expressed as lows in K radiometric data (Figure 10). Similarly the high proportion of magnetite within the Na-Ca altered rocks may be utilised for mapping. Highly altered areas correspond to highs in total magnetic intensity data (Figure 11). Figures 12 and 13 show two parts of the Doherty Formation that are highly Na-Ca altered (Oliver 1995; Mark et al. 2004; Kendrick et al. 2008). In both examples there is a clear correlation between the breccias of the Doherty Formation and lows in the K-radiometric data. It is interesting to note that there is a low in the K-radiometric data in the area surrounding the Mount Angelay Granite (Figure 12), which may suggest a link between albitised areas (i.e. Na-rich alteration) and magmatic fluids derived from the granite (e.g. Pollard et al. 1998; Mark et al. 2006). A comparison of the K-radiometrics and Amphibole band ratio also reveals that both data sets have a low adjacent to the NW margin of the Mt Angelay Granite. This may suggest that the breccias adjacent to the pluton retain diopside, possibly precipitated during early Na-Ca alteration stages, that has not been altered to actinolite. Another interesting feature of the K-radiometrics are several highs are spatially associated with late faults and copper mineralisation which is potentially indicative of potassic alteration.

Richmond (2000) states that brecciated and altered rocks have lower U compared with the unaltered calc-silicates. However, this relationship is not observed in Figure 12c

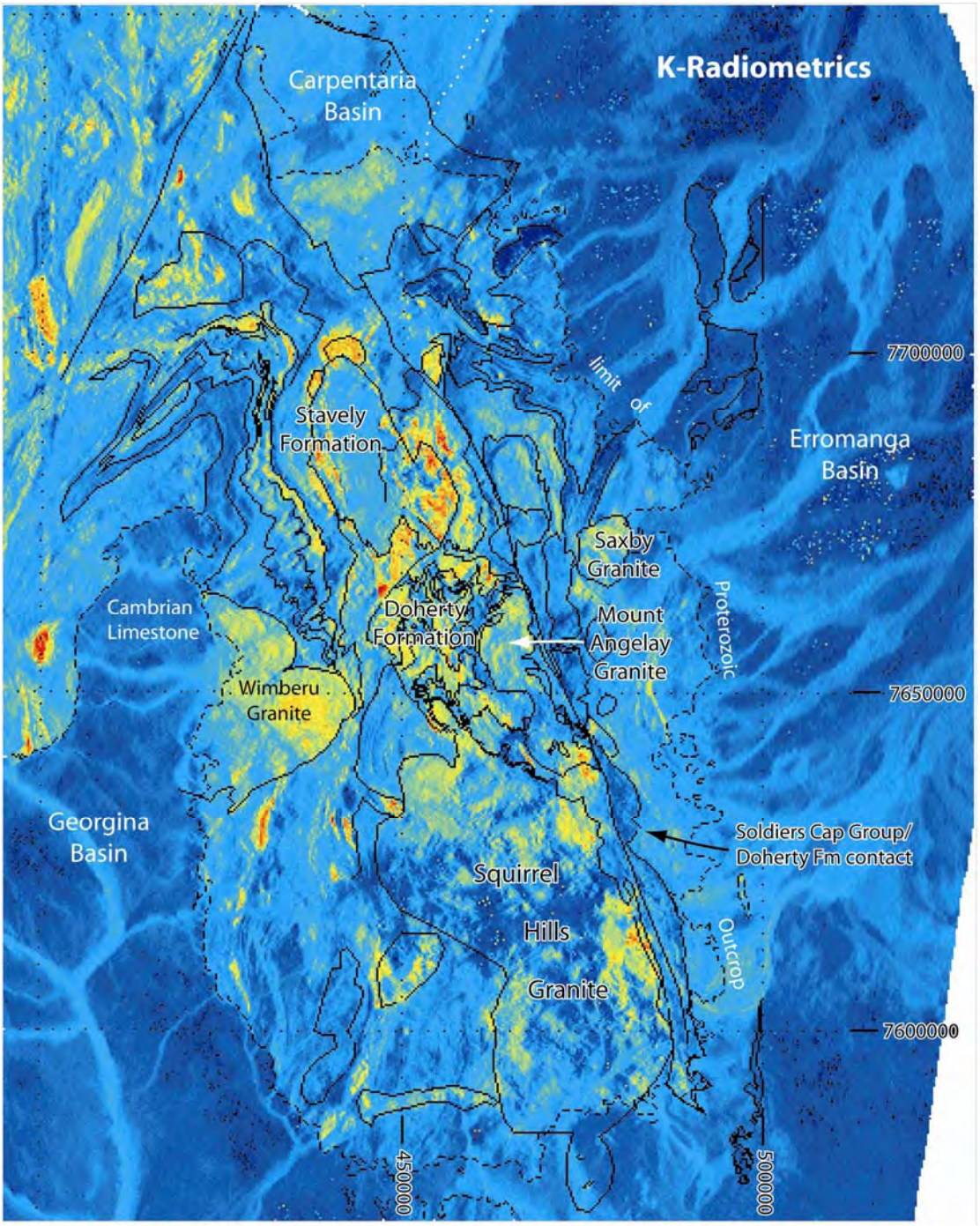

Figure 10 K-radiometric data for the Mt Isa Eastern Succession, showing the limit of Proterozoic outcrop and generalised geology.

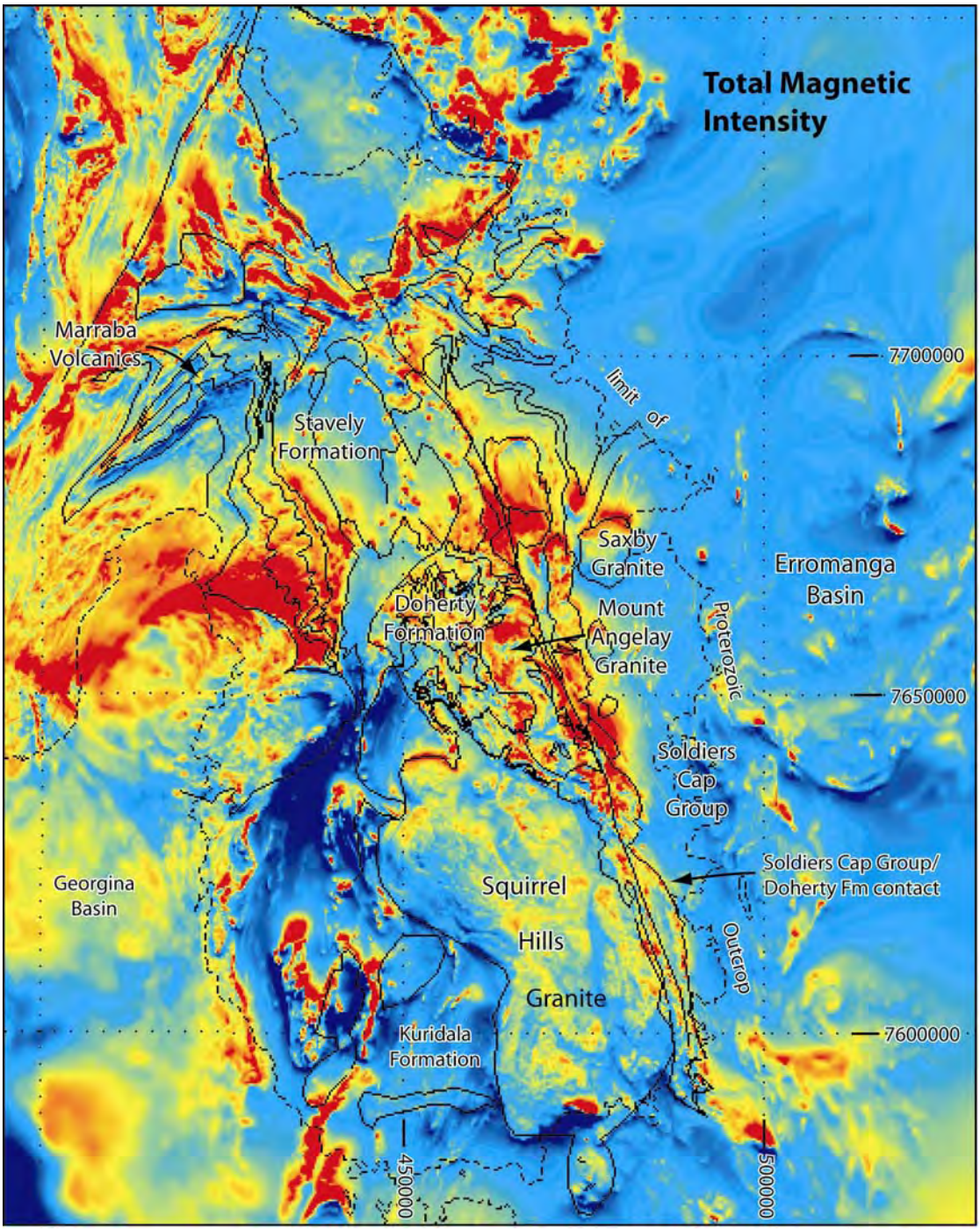

Figure 11 Total magnetic intensity data for the eastern Mount Isa Inlier with geology outlines overlain.

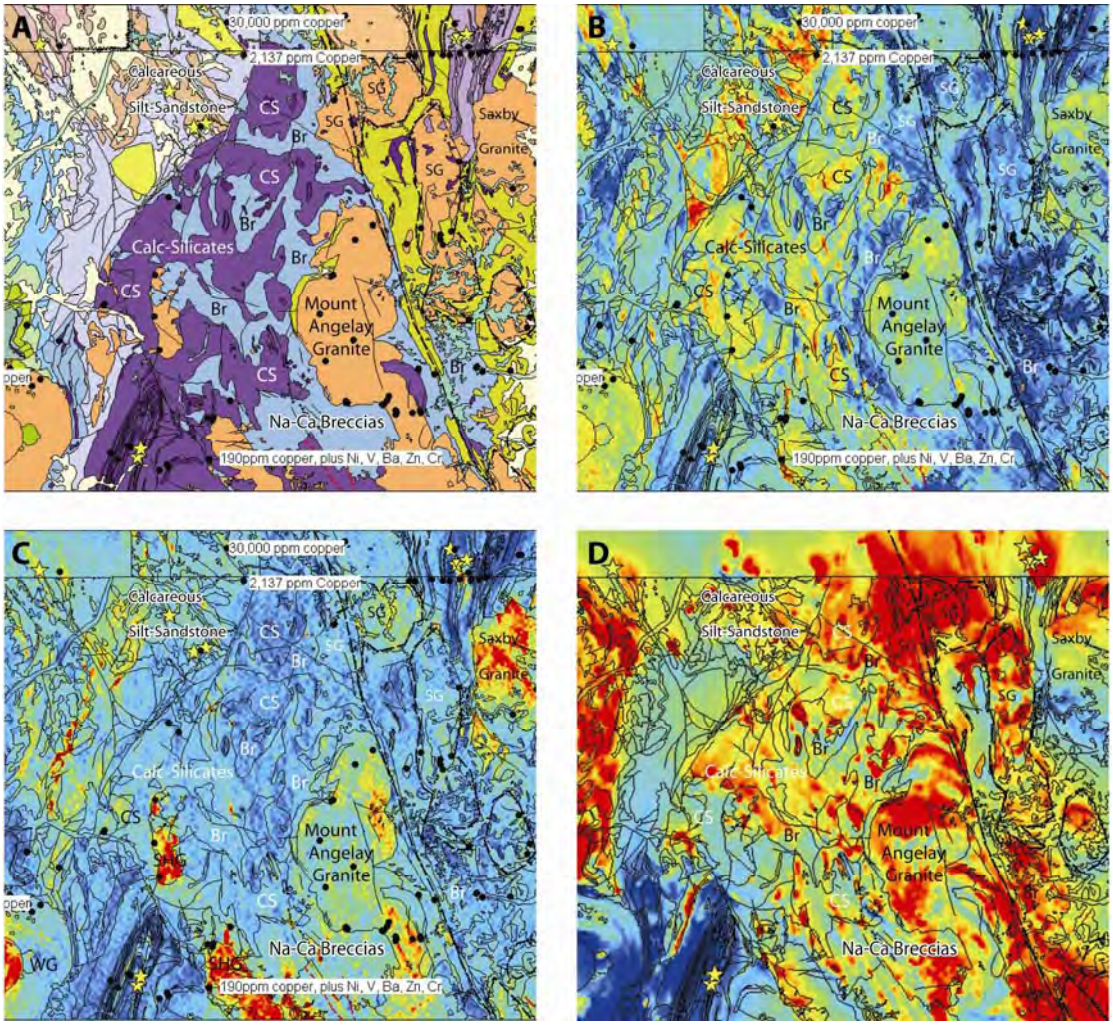

Figure 12 Comparison of the K- and U-radiometric and the magnetic response of different units. A. Geology of the area located in Figure 1, showing the Doherty formation, which is divided into hydrothermal Na-Ca altered breccias (Br), massive to laminated Calc-Silicates (CS), the Saxby (SG) and Mt Angelay granites and sedimentary rocks of the Stavely Formation and the Soldiers Cap Group (in yellow); B. K- radiometric data. Lows correlate with Na-Ca breccias, particularly those haloing the Mt Angelay granite, and east of the Cloncurry Fault. Highs correlate with high copper and heavy metal concentrations in several instances in the Doherty and Stavely formations; C. U-radiometric data. Highs correspond to several granitic intrusions and show internal zoning within the Wimberu Granite (WG); D. Total Magnetic Intensity data. Although the Doherty Formation has high magnetic susceptibility overall, mapped breccias do not directly correspond to elevated magnetic intensity. Small zones within the breccias have high magnetic intensity, which may suggest they are areas of intense oxidation.

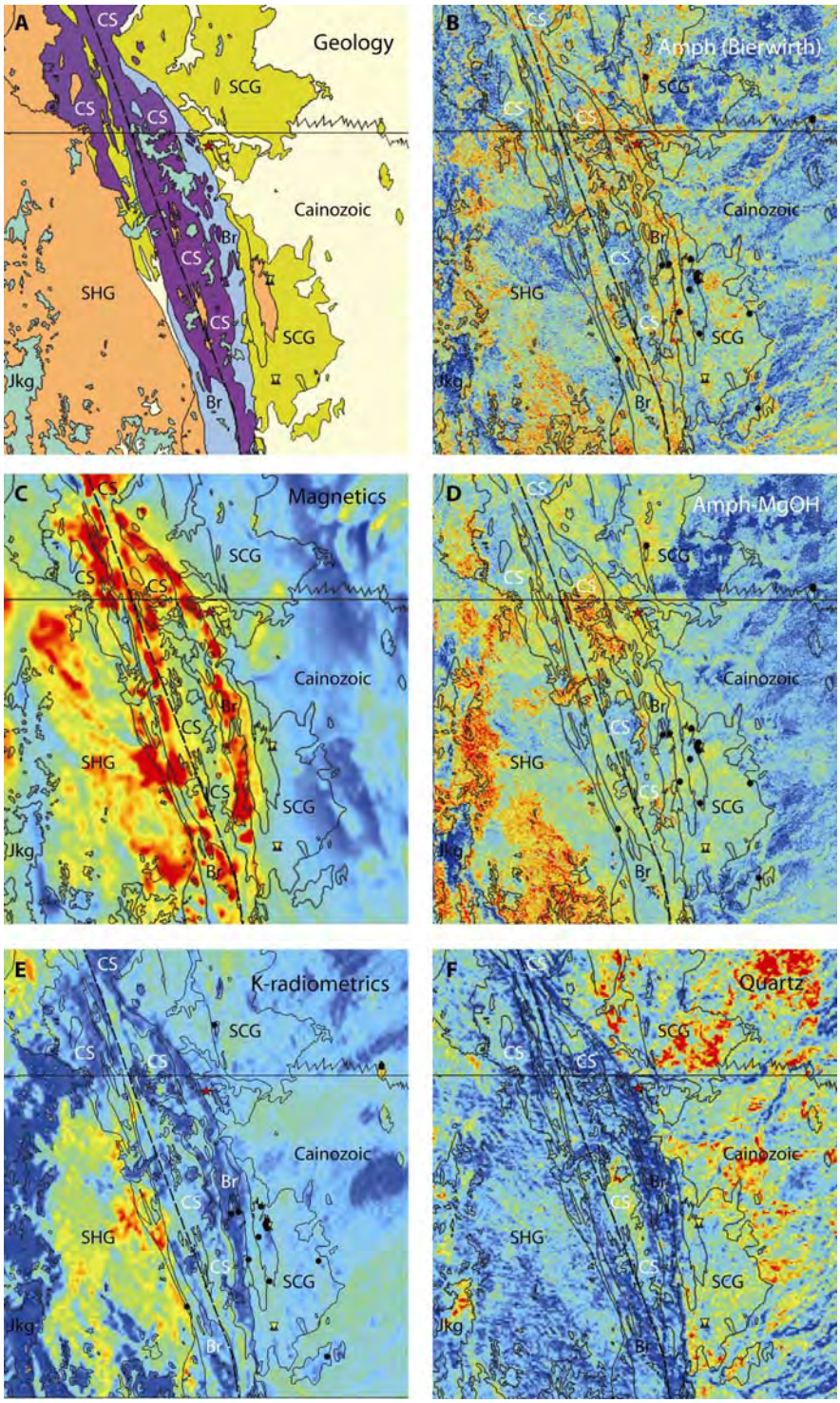

Figure 13 a. Geology of the area located in figure 1; b. the Amphibole (Bierwirth 2002) band ratio; c. total magnetic intensity image; d. the Amphibole-MgOH-Carbonate band ratio (Rowan et al. 2004); e. K-radiometric data; f. Quartz band ratio (Ninomiya and Fu 2002). This figure highlights the relationships between geology, the amphibole band ratios, total magnetic intensity, K-radiometric data, and the Quartz band ratio. The inverse relationship between magnetic intensity data, K-radiometric plus ASTER band 8 data is the basis for the generation of a new band ratio that defines Na-Ca alteration.

Uranium radiometric data highlights several granitic intrusions (NE Saxby, parts of the Mt Angelay, the northern Squirrel Hills Granite (SHG) and the core of the Wimberu Granite (WG)). Although U-Radiometric data was shown (Richmond 2000) to map zonation in granites, it does not appear to be a good proxy for Na-Ca alteration. Figure 13 illustrates the good correlation between the amphibole band ratios (Figs. 13b and d) and the magnetic intensity image (Figure 13c), while there is also a strong inverse correlation between the magnetics and K-radiometric data. The K-radiometrics also have a strong correlation with the quartz band ratio. In this area, all the relationships that are suggested by the chemical analyses of De Jong (1995) and by the findings of Richmond (2000) can be observed. Na-Ca alteration forms a mineralogy that has a high proportion of amphiboles and magnetite, which is detected by the ASTER amphibole band ratios, and can be inferred from the elevated magnetic intensity within the altered zones (Austin and Blenkinsop 2008). The Na-Ca alteration leads to depletion of potassium and quartz that is shown by the lows (blue) in the potassium radiometric data and ASTER quartz band.

4.6. Sodic-Calcic alteration index

Based on the above observations a Na-Ca alteration index has been generated using the magnetic intensity, K-radiometric, and ASTER band 8 data. The Sodic-Calcic alteration index (Figure 14) is calculated by:

$$\text{Sodic Calcic alteration} = \frac{2^{nd} \text{ derivative of Magnetic Intensity}}{\text{K-radiometrics + ASTER band 8}}$$

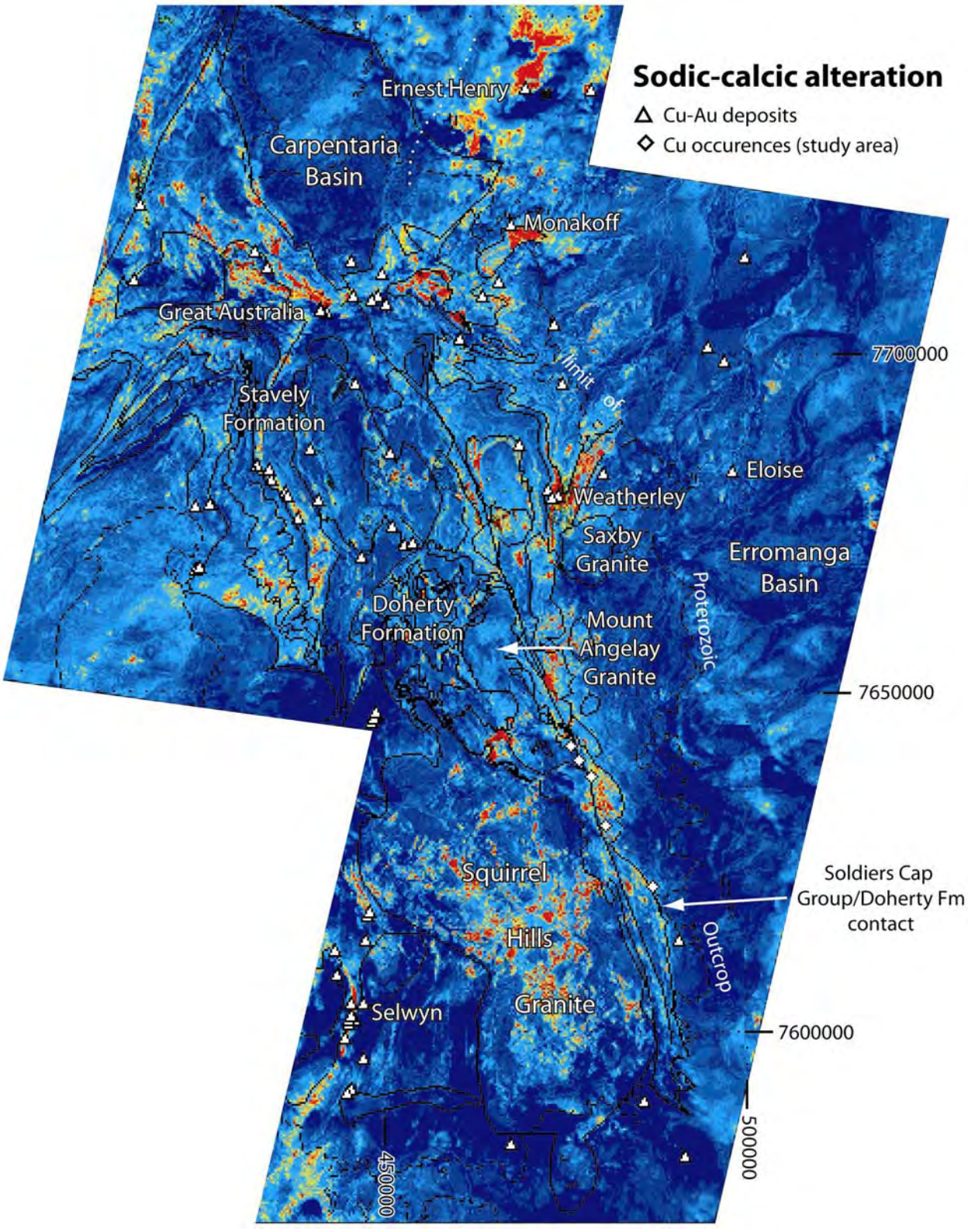

Figure 14 The Sodic-Calcic alteration index was developed to highlight areas of intense sodic-calcic alteration. It identifies several narrow moderate highs that coincide with areas of mineralisation; e.g. Monakoff, Kuridala, the Selwyn Corridor and numerous deposits sitting on faults in the Stavely Formation.

The second derivative magnetic data was used because it offers a simple method of locating geologic anomalies of importance in mineral reconnaissance (Elkins 1951). It emphasises the expression of local features (e.g. faults) and removes the effects of regional anomalies. The resulting alteration index highlights several zones that are known to be highly Na-Ca altered, e.g. the Selwyn Corridor, and the Doherty Formation adjacent to the Cloncurry Fault. In the case of the Doherty Formation, the band ratio highlights the albite-actinolite-magnetite breccias preferentially. Many of these highs spatially coincide with copper mineralisation, e.g. the Selwyn Corridor, Ernest Henry,

Osborne, Kuridala, and deposits that sit along NNW oriented highs (e.g. Southern Cross, Eldorado and Red Sierra) within the Stavely Formation. Several occurrences of massive magnetite (ironstone) or localised copper mineralisation, observed in the main study area, also coincide with a high adjacent to the Cloncurry Lineament. However the band ratio also highlights features that clearly do not coincide with Na-Ca alteration. Obvious examples are the carbonate rich Mesozoic strata which have a low K-radiometric response, and overly relatively magnetic Proterozoic rocks (Doherty Formation and Squirrel Hills Granite). The same is true of the amphibolites in the Toole Creek Volcanics, except that the absorption in band 8 is due to the units being rich in amphibole, and spatially coincident iron formations are highly magnetic.

5. DISCUSSION

ASTER can be used to help define distinct lithologies and alteration, even in complicated terrains such as the Mount Isa Eastern Succession. However, many of the band ratios are not diagnostic for specific minerals, but indicate a wide array of potential mineralogy (e.g. amphibole, carbonate and epidote) which all have a major absorption features in band 8 and comprise the majority of minerals detected by PIMA in rocks from the study area. Although ASTER Amphibole ratios appear to be relatively good at mapping amphibole, particularly within amphibolites and granite, the highs may also correspond to epidote, chlorite or carbonate or combinations thereof. Some alteration types (e.g. potassic and chlorite-epidote alteration) that this study aimed to map with ASTER occur at vein scale along late faults and are too spatially complex to be delineated by the 30m pixel resolution of ASTER SWIR bands (4-9).

The spectral expression of Na-Ca alteration is very complicated because all of the detectable minerals formed have spectral absorption features in ASTER band 8. PIMA analyses in this study commonly detected actinolite, hornblende and calcite in the Doherty Formation breccias which are major products of Na-Ca alteration (De Jong 1995; Chapman and Williams 1998; Cannell and Davidson 1998). This suggests that there is significant Na-Ca alteration associated with brecciation in the Doherty Formation, as mapped by Kendrick (2008; after Oliver et al. 2004; Mark et al. 2006).

Na-Ca alteration assemblages in the study area can not be confidently mapped using ASTER alone because of the poor correlation between amphibole ± carbonate ± epidote band ratios and mapped alteration in the field (cf. Oliver 1995; De Jong 1995; Marshall 2003; Mark et al. 2004; Oliver et al. 2004; Marshal et al. 2006; Kendrick et

al. 2008). Furthermore, it is difficult to separate the amphiboles formed by Na-Ca alteration from amphiboles formed during metamorphism.

Integration of ASTER data with radiometrics and magnetic intensity data can better define areas of intense Na-Ca alteration. Lows in the K-radiometric data correlate with highly altered, usually brecciated, zones within the Doherty Formation, with highs in the magnetics and amphibole ratios, and with lows in the quartz band ratio. However, the correlation between Na-Ca alteration and the amphibole band ratios is inconsistent, possibly due to zonation within the Na-Ca alteration where diopside from earlier alteration phases may be preserved.

The Sodic-Calcic alteration index is an effective means of highlighting areas where strong Na-Ca alteration may exist and can be utilised in conjunction with pre-existing geological knowledge of the area to reveal new target areas for further investigation. Although the Sodic-Calcic alteration index could be better constrained (e.g. by using ASTER level 2 surface reflectance data) the approach taken here shows that ASTER SWIR data can be integrated with geophysical data to better discriminate Na-Ca alteration. Integration of spectral and geophysical data is an approach that has great potential to be used for mapping a wide array of alteration types and lithologies, and may bypass some of inherent problems with ASTER data (e.g. allow amphiboles and carbonates to be better discriminated). Furthermore, a similar approach may be used to map potassic alteration which is also spatially associated with a number of Cu-deposits in the Mount Isa Eastern Succession and other similar terranes worldwide.

REFERENCES

Abrams M. & Hook S. 1995. Simulated ASTER data for geologic studies. *IEEE Transactions on Geoscience and Remote Sensing* 33, 692–699.

Abrams M. 2000. The Advanced Spaceborne Thermal Emission and Reflection Radiometer (ASTER): data products for the high spatial resolution imager on NASA's Terra platform. *International Journal of Remote Sensing* 21, 847-859.

Adshead-Bell N. S. 1998. Evolution of the Starra and Selwyn high-strain zones, Eastern fold belt, Mount Isa Inlier; implications for Au-Cu mineralization. *Economic Geology* 93, 1450 - 1462.

Austin J. R. & Blenkinsop T. G. 2008. The Cloncurry Lineament: Geophysical and geological evidence for a deep crustal structure in the Eastern Succession of the Mount Isa Inlier. *Precambrian Research*, doi:10.1016/j.precamres.2007.08.012

Beardsmore T. J. Newbery S. P. and Laing W. P. (1988), The Maronan Supergroup: An Inferred Early Volcanosedimentary Rift Sequence in the Mount Isa Inlier, and its Implications for Ensialic Rifting in the Middle Proterozoic of Northwest Queensland. *Precambrian Research*, 40/41 487-507

Bell T. H. 1983. Thrusting and duplex formation at Mount Isa, Queensland, Australia. *Nature* 304, 493-497.

Berger B. R., King T. V. V., Morath L.C. & Phillips J. D. 2003. Utility of High-Altitude Infrared Spectral Data in Mineral Exploration: Application to Northern Patagonia Mountains, Arizona. *Economic Geology* 98, 1003–1018

Betts P. 2000. Asymmetric extension of the lithosphere and its influence on Palaeoproterozoic Pb-Zn deposits of the Western fold belt, Mount Isa Terrane. *Journal of the Virtual Explorer 1*.

Bierwirth P. N. 2002. *Evaluation of ASTER satellite data for geological applications*. Consultancy report to Geoscience Australia.

Blake D. H. 1980. The early geological history of the Proterozoic Mount Isa Inlier, northwestern Queensland; an alternative interpretation. *BMR Journal of Australian Geology and Geophysics* 5, 243-256.

Blake D. H., Jaques, A. L., & Donchak, P. J. T. 1983. *Selwyn region, 1:100,000 Geological Map Commentry*, Queensland. Canberra, A.C.T., Australian Government Publishing Service.

Blake D. H., Jaques A. L. & Donchak P. J. T. 1984. *Selwyn region, 1:100,000 Geological Map*, Queensland. Canberra, A.C.T., Australian Government Publishing Service.

Blake D. H. 1987. *Geology of the Mount Isa Inlier and environs, Queensland and Northern Territory.* Canberra, A.C.T., Australian Geological Survey Organization.

Blake D. & Stewart A. 1988. Block and possible terrane boundaries in the Mount Isa Inlier. *BMR Research Newsletter* 9, 2-3.

Blake D. H. & Stewart A. J. 1992. Stratigraphic and tectonic framework, Mount Isa Inlier. In: Stewart A. J. & Blake D. H. eds. *Detailed Studies of the Mount Isa Inlier*. Bureau of Mineral Resources Bulletin 243,

Blenkinsop T. G., Huddlestone-Holmes,C., Foster,D., Mark,G., Austin J. R., Edmiston M., Lepong P., Ford A., Murphy F., Stark M. 2008. Crustal structure and Inversion in the Eastern Succession of the Mt Isa Inlier. *Precambrian Research* – In Press

Cannell J. & Davidson G. J. 1998. A carbonate-dominated copper-cobalt breccia-vein system at the Great Australia Deposit, Mount Isa eastern succession. *Economic Geology* 93, 1406 - 1421.

Carter E. K., Brooks J. H. & Walker, K. R. 1961. *The precambrian mineral belt of northwestern Queensland.* Bureau of Mineral Resources, Australia, Bulletin 51.

Chapman L. H. & Williams P. J. 1998. Evolution of pyroxene-pyroxenoid-garnet alteration at the Cannington Ag-Pb-Zn deposit, Cloncurry District, Queensland, Australia. *Economic Geology* 93, 1390 - 1405.

Davidson G. J. 1998. Variation in copper-gold styles through time in the Proterozoic Cloncurry goldfield, Mt Isa Inlier: a reconnaissance view. *Australian Journal of Earth Science* 45: 445–462.

De Jong G. 1995. Post metamorphic alteration and mineralization in a highly deformed Proterozoic terrain: the eastern Selwyn Range, Cloncurry District NW Queensland. *PhD Thesis, JAMES COOK UNIVERSITY*, unpublished.

De Jong G. & Williams P. J. 1995. Giant metasomatic system formed during exhumation of mid-crustal Proterozoic rocks in the vicinity of the Cloncurry Fault, Northwest Queensland. *Australian Journal of Earth Sciences* 42, 281-290

Donchak P. J. T., Blake D. H., Noon T. A. & Jaques A. L. 1984. *Kuridala region, 1:100,000 Geology*, Queensland. Canberra, A.C.T., Australian Government Publishing Service.

Donchak P. J. T., Blake D. H., Noon T. A. & Jaques, A. L. 1983. *Kuridala region, 1:100,000 Geological Map Commentry*, Queensland. Canberra, A.C.T., Australian Government Publishing Service.

Edmiston M. A., Lepong P. & Blenkinsop T. G. 2008. The hidden Isan Orogeny: revealing crustal structure under cover to the east of the Mount Isa Inlier. *Precambrian Research*, doi:10.1016/j.precamres.2007.08.013.

Edwards A. B. & Baker G. 1954. Scapolitization in the Cloncurry district of northwestern Queensland. *Journal of the Geological Society of Australia*. 1, 1-33

Elkins T. A. 1951. The Second Derivative Method of Gravity Interpretation. *Geophysics* 16, 29-50.

Foster D. R. W. & Austin J. R. 2008. The 1800 to 1610 Ma stratigraphic and magmatic history of the Eastern Succession, Mount Isa Inlier, and correlations with adjacent Paleoproterozoic terranes, *Precambrian Research*, doi:10.1016/ j.precamres.2007.08. 010

Foster D. R. W. & Rubenach M. J. 2006. Isograd pattern and regional low-pressure, high temperature metamorphism of pelitic, mafic and calc-silicate rocks along an east-west section through the Mount Isa Inlier. *Australian Journal of Earth Sciences* 53, 167 – 186.

Giles D., Betts P. G., Aille`Res L., Hulscher B., Hough M. & Lister G. S. 2006. Evolution of the Isan Orogeny at the southeastern margin of the Mt Isa Inlier. *Australian Journal of Earth Sciences* 53, 91 – 108.

Hand M. & Rubatto D. 2002. The scale of the thermal problem in the Mount Isa Inlier (in Geoscience 2002; expanding horizons; abstracts of the 16th Australian geological convention, Preiss,) *Abstracts - Geological Society of Australia* 67, 173

Hatton O.J. & Davidson G. J. 2004. Soldiers Cap Group iron-formations, Mt Isa Inlier, Australia, as windows into the hydrothermal evolution of a base-metal-bearing Proterozoic rift basin. *Australian Journal of Earth Sciences* 51, 85-106.

Hemley J. J. & Jones W. R. 1964. Chemical aspects of hydrothermal alteration with emphasis on hydrogen metasomatism. *Economic Geology* 59, 538−569.

Hewson R. D., Cudahy T. J. & Huntington J. F. 2001. Geologic and alteration mapping at Mt Fitton, South Australia, using ASTER satellite-borne data. *IEEE 2001 International geoscience and remote sensing symposium, 9 – 13 July.*

Hewson R. D., Cudahy T. J., Mizuhiko S., Ueda K. & Mauger A. J. 2005. Seamless geological map generation using ASTER in the Broken Hill-Curnamona province of Australia. *Remote Sensing of Environment* 99, 159 – 172.

Hook S. J., Myers J. J., Thome K. J., Fitzgerald M. & Kahle A. B. 2001. The MODIS/ASTER airborne simulator (MASTER)—a new instrument for earth science studies. *Remote Sensing of Environment* 76, 93–102.

Hubbard B. E. & Crowley J. K. 2005. Mineral mapping on the Chilean-Bolivian Altiplano using co-orbital ALI, ASTER and Hyperion imagery: Data dimensionality issues and solutions, *Remote Sensing of Environment* 99, 173-186.

Iwasaki A., Fujisada H., Akao H., Shindou O. & Akagi S. 2001. Enhancement of spectral separation performance for ASTER/SWIR. *Proceedings of SPIE, The International Society for Optical Engineering* 4486, 42– 50.

Kalinowski A. & Oliver S. 2004. *ASTER Mineral Index Processing Manual. Remote Sensing Applications*. Geoscience Australia. (http://www.ga.gov.au/acres/prod_ser/aster.jsp)

Kendrick M. A., Baker T., Fu B., Phillips D. & Williams P. J. 2008. Noble gas and halogen constraints on regionally extensive midcrustal Na-Ca metasomatism, the Proterozoic Eastern Mount Isa Block, Australia. *Precambrian Research* - In Press

Laing W. P. 1993. Structural-metasomatic controls on ore deposits of the east Mt Isa Block: the key to tonnes and grade. In *symposium on recent advances in the Mt Isa Block, Australian Institute of Geoscientist Bulletin* 13: 17-24

Laing W. P. 1998. Structural-metasomatic environment of the East Mt Isa Block base-metal-gold province. Australia. *Australian Journal of Earth Sciences* 45 p 413-428.

McLaren S., Sandiford M. & Hand M. 1999. High radiogenic heat-producing granites and metamorphism; an example from the western Mount Isa Inlier, Australia. *Geology* 27, 679 - 682

McLaren S., Sandiford M., & Powell R. 2005. Contrasting styles of Proterozoic crustal evolution: A hot-plate tectonic model for Australian terranes. *Geology* 33, 673 – 676.

Marshall L. J. 2003. *Brecciation within the Mary Kathleen Group of the Eastern Succession, Mt Isa Block, Australia: Implications of district-scale structural and metasomatic processes for Fe-oxide-Cu-Au mineralisation.* PhD Thesis, JAMES COOK UNIVERSITY, unpublished.

Marshall L. J., Oliver N. H. S. & Davidson G. J. 2006. Carbon and oxygen isotope constraints on fluid sources and fluid-wallrock interaction in regional alteration and iron-oxide-copper-gold mineralisation, eastern Mt Isa Block, Australia. *Mineralium Deposita* 41, 429-452

Mark G. 1998. *Granites and regional Alteration in the Cloncurry district, NW Queensland*. PhD Thesis, JAMES COOK UNIVERSITY, unpublished.

Mark G. 1999. *Characteristics and Origin of the Ernest Henry Iron Oxode-Copper-Gold hydrothermal system.* Results of the 1999 collaborative SPIRIT research project. Unpublished.

Mark G. 2001. Nd isotope and petrogenetic constraints for the origin of the Mount Angelay igneous complex; implications for the origin of intrusions in the Cloncurry District, NE Australia. *Precambrian Research* 105,17-35.

Mark G., Foster D. R. W., Pollard P. J., Williams P. J., Tolman J., Darvall M. & Blake K. L. 2004. Stable isotope evidence for magmatic fluid input during large-scale Na-Ca alteration in the Cloncurry Fe oxide Cu-Au district, NW Queensland, Australia. *Terra Nova* 16, 54-61.

Mark G., Oliver N. H. S. & Carew M. J. 2006. Insights into the genesis and diversity of epigenetic Cu–Au mineralisation in the Cloncurry district, Mt Isa Inlier, northwest Queensland. *Australian Journal of Earth Sciences* 53, 109-124.

Mustard R., Blenkinsop T., McKeagney C., Huddleston-Holmes C. & Partington G. 2004. New perspectives on IOCG deposits, Mt Isa Eastern Succession, northwest Queensland. *Extended abstracts, SEG2004*, 281-284.

Ninomiya Y. & Fu B. 2002. Quartz Index, Carbonate Index and SiO2 Content Index Defined for ASTER TIR Data. *Journal of Remote Sensing Society of Japan* 22, No.1, 50-61.

Oliver N. H. S. 1995. Hydrothermal history of the Mary Kathleen fold belt, Mt Isa Block, Queensland. *Australian Journal of Earth Sciences*. 42: 267-279.

Oliver N. H. S., Mark G., Marshall L. J., Rubenach M. J., Carew M., Pollard P. J. 1998. *Mineralisation, alteration and magmatism in the Eastern fold belt, Mount Isa Block, Australia*. Geological review and field guide, Geological Society of Australia Specialist Group in Economic Geology.

Oliver N. H. S., Cleverley J. S. Mark G., Pollard P. J., Fu B., Marshall L. J., Rubenach M. J., Williams P.J. & Baker T. 2004. Modeling the role of sodic alteration in the genesis of ion oxide-copper-gold deposits, eastern Mount Isa Block, Australia. *Economic Geology* 99, 1145-1176.

Page R. W. 1983. Chronology of magmatism, skarn formation, and uranium mineralization, Mary Kathleen, Queensland, Australia. *Economic Geology* 78, 838-853.

Pollard P. J., Mark G. & Mitchell L. C. 1998. Geochemistry of post-1540 Ma granites spatially associated with regional sodic-calcic alteration and Cu-Au-Co mineralisation, Cloncurry district, northwest Queensland. *Economic Geology* 93, 1330-1344.

Queensland Department of Mines and Energy, Taylor Wall and Associates, SRK Consulting Pty Ltd & ESRI Australia 2000. *North-west Queensland Mineral Province Report*. Queensland Department of Mines and Energy, Brisbane.

Richmond J. 2000. *Mapping Intrusions using Gamma-ray spectrometry: a case study in the Cloncurry district, Northwest Queensland*. PhD Thesis, JAMES COOK UNIVERSITY, unpublished.

Rowan,L. C. & Mars J. C. 2003. Lithologic mapping in the Mountain Pass, California area using Advanced Spaceborne Thermal Emission and Reflection Radiometer (ASTER) data. *Remote Sensing of Environment* 84, 350–366.

Rowan L. C., Hook S. J., Abrams M. J. & Mars J. C. 2003. Mapping hydrothermally altered rocks at Cuprite, Nevada, using the Advanced Spaceborne Thermal Emission and Reflection radiometer (ASTER), A new satellite-imaging system. *Economic Geology* 98, 1019–1027.

Rowan L. C., Simpson C. J. and Mars J. C. 2004. Hyperspectral analysis of the ultramafic complex and adjacent lithologies at Mordor, NT, Australia. *Remote Sensing of Environment* 91, 419–431.

Rowan L. C., Schmidt R.G. & Mars J.C. 2006. Distribution of hydrothermally altered rocks in the Reko Diq, Pakistan mineralized area based on spectral analysis of ASTER data. *Remote Sensing of Environment* 104, 74–87.

Rubenach M. J. 1993. Petrogenesis of a variety of metasomatic lithologies west of Mount Isa. Mid- to lower-crustal metamorphism and fluids conference, Mount Isa. *Abstracts – Geol. Soc. Aust*. 35, 60

Rubenach M. J. & Barker A. J. 1998. Metamorphic and metasomatic evolution of the Snake Creek Anticline, Eastern Succession, Mt Isa Inlier. *Australian Journal of Earth Sciences* 45, 363-372.

Rubenach M. J. & Lewthwaite K. A. 2002. Metasomatic albitites and related biotite-rich schists from a low-pressure polymetamorphic terrane, Snake Creek Anticline, Mount Isa Inlier, north-eastern Australia; microstructures and P-T-d paths. *Journal of Metamorphic Geology* 20,191-202.

Rubenach M. J. 2003. The use of inclusions in andalusite in distinguishing between early albite/biotite alteration and later Cl-enrichment of biotite, Snake Creek Anticline, Australia. *Program with Abstracts - Geological Association of Canada; Mineralogical Association of Canada: Joint Annual Meeting* 28.

Rubenach M. J., Foster D. R. W., Evins P. M., Blake K. L. & Fanning C. M. 2008. Age constraints on the tectonothermal evolution of the Selwyn Zone, Eastern Fold Belt, Mount Isa Inlier. *Precambrian Research* doi:10.1016/j.precamres. 2007.08.014

Ryburn R. J., Wilson I. H., Grimes K. G. & Hill, R. M. 1988. *Cloncurry, 1:100,000 Geological Map Commentry*. Queensland. Canberra, A.C.T., Australian Government Publishing Service.

Sabins F. F. 1999. Remote sensing for mineral exploration. *Ore Geology Reviews* 14, 157–183.

Sayab M. 2005. Microstructural evidence for N–S shortening in the Mount Isa Inlier (NW Queensland, Australia): the preservation of early W–E-trending foliations in porphyroblasts revealed by independent 3D measurement techniques. *Journal of Structural Geology* 27, 1445–1468.

Slatyer R. O. 1964. Climate of the Leichardt-Gilbert area. In Perry, R. A. et al., *General report on the lands of the Leichardt-Gilbert area*. Queensland, 1953-54. CSIRO, Australia, Land Research Series, 11, 90-104.

Sun Y., Seccombe P.K. & Yang, K. 2001. Application of short-wave infrared spectroscopy to define alteration zones associated with the Elura zinc-lead-silver deposit, NSW, Australia. *Journal of Geochemical Exploration* 73, 11-26.

Twidale C. R. 1966. *Geomorphology of the Leichardt-Gilbert area of northwest Queensland*. CSIRO Land Research Series 16.

Van der Wielen S., Oliver S. & Kalinowski A. 2004. Remote sensing and spectral investigations in the Western Succession, Mount Isa Inlier: Implications for exploration. In *Eds. A.C. Barnicoat and R.J. Korsch, Predictive Mineral Discovery Cooperative Research Centre: Extended abstracts from the June 2004 conference*, Geoscience Australia Record 2004/09

Volesky J. C., Stern R. J. & Johnson P. R. 2003. Geological control of massive sulfide mineralization in the Neoproterozoic Wadi Bidah shear zone, southwestern Saudi Arabia, inferences from orbital remote sensing and field studies; Evolution of the East African and related orogens, and the assembly of Gondwana. *Precambrian Research* 123, 235-247.

Williams P. J. 1998. Metalliferous economic geology of the Mt Isa Eastern Succession, Queensland. *Australian Journal of Earth Sciences* 45, 329-341.

Williams PJ and Pollard PJ (2003) Australian Proterozoic iron oxide– Cu–Au deposits: an overview with new metallogenic and exploration data from the Cloncurry district, northwest Queensland. *Exploration and Mining Geology* 10, 191–213.

Williams P.J., Barton M, D., Johnson D. A., Fontboté L., de Haller A., Mark G., Oliver N. H. S. & Marschik R. 2005. Iron Oxide Copper-Gold Deposits: Geology, Space-Time Distribution, and possible Modes of Origin. *Economic Geology* 100, 371-405.

Yamaguchi Y., Kahle, A.B., Tsu, H., Kawakami, T. & Pniel, M., 1998. Overview of advanced spaceborne thermal emission and reflection radiometer (ASTER). *IEEE Transactions on Geoscience and Remote Sensing* 36 (4), 1062– 1071.

Recognition of hydrothermal footprints in the Eastern Fold Belt of the Mount Isa Inlier using geophysical-geochemical spatial data

C. Laukamp, T. Cudahy, M. Thomas, M. Jones, J. Cleverley, N. Oliver

Abstract

Hyperspectral images from the Eastern Fold Belt of the Mount Isa Inlier, released by the collaborative Queensland NGMM project between GSQ and CSIRO, were validated as new tool for the detection of IOCG related alteration. High resolution of mineral maps derived from hyperspectral imaging (4.5m/pixel) enables the recognition of various types of hydrothermal alteration patterns and the localisation of fluid pathways. Groundtruthing of a suite of mineral maps was conducted in 2007. Though sample analyses in the lab is still in process, but some preliminary results already show some promising features.
Geochemically discrete alteration shells at IOCG deposits (e.g. potassic alteration at Ernest Henry) correspond to distinct mineral distributions. Potassic alteration in mafic rocks of the Cloncurry District was detected by a combination of MgOH and Fe^{2+}-mineral maps ("MgOH content", "MgOH composition", "amphibole/chlorite" and "Fe^{2+} ass. with MgOH") combined with white mica mineral maps ("white mica composition" and "white mica abundance"). The MgOH and Fe^{2+}-mineral maps were also used to distinguish various mafic rocks from amphibolites, which are host rocks for some of the Fe oxide Cu-Au deposits in the Eastern Fold Belt (e.g. Mount Elliott), and calcsilicate breccias pipes (e.g. Suicide Ridge). White mica mineral maps were applied to narrow down the spatial distribution of regional sodic-calcic alteration in metasedimentary successions of the Soldiers Cap Group in the Snake Creek Anticline. Albitised rims of granites, assigned to the Williams-Naraku Granite Suite, show characteristic absorption features in the SWIR-range and can be detected with white mica mineral maps ("white mica composition", "white mica content/water abundance"). Along major fault zones, such as the Mt Dore fault zone in the Selwyn Corridor, which are interpreted as important fluid pathways, gradients reflecting the altered mineral chemistry can be highlighted with mineral maps (e.g. "white mica abundance", "white mica composition", "white mica relative water").
In summary hyperspectral images provide a powerful tool for the recognition of various hydrothermal alteration patterns and could be used in combination with other geophysical remote sensing data, such as radiometrics and magnetics. Limitations of this technique are defined by unsatisfactory coverage of mineral maps, man made features, river systems and distribution and composition of debris. A good knowledge of the local geology is necessary to extract the full information provided by the mineral maps. Calibration of ASTER data with the hyperspectral data can hopefully extend interpretation made from the HyMap data into adjacent areas, which are only covered by ASTER.

1. Introduction

The aim of this study was to apply hyperspectral imaging to the recognition of hydrothermal alteration patterns related to Cu-Au mineralising systems. This study was based on former investigations of hydrothermal and metasomatic altered rocks in the Eastern Fold Belt (EFB) (Marshall et al., 2006; amongst others). Understanding genetic relationships between different alteration patterns and their spatial distribution is a key to successful exploration for IOCG and other styles of mineralisation. The development of spectral and hyperspectral remote sensing technologies over the last decade has significantly advanced capabilities for mapping mineral-system related alteration, particularly by defining phyllic and argillic alteration (Van

der Wielen et al., 2005). Geochemical-geophysical remote sensing data are also a powerful tool for the recognition of IOCG related alteration in the Mount Isa Inlier. In order to evaluate hyperspectral mineral maps as an exploration tool, hydrothermal and metasomatic alteration systems occurring in the EFB have been compared with mineralisation related alteration in Ernest Henry-type deposits. The case study was conducted in specific areas of the EFB, which is part of the Mount Isa Inlier (NW Queensland) (Fig. 1). The key areas occur within the coverage of the HyMap scenes flown in 2006 for the Geological Survey of Queensland.

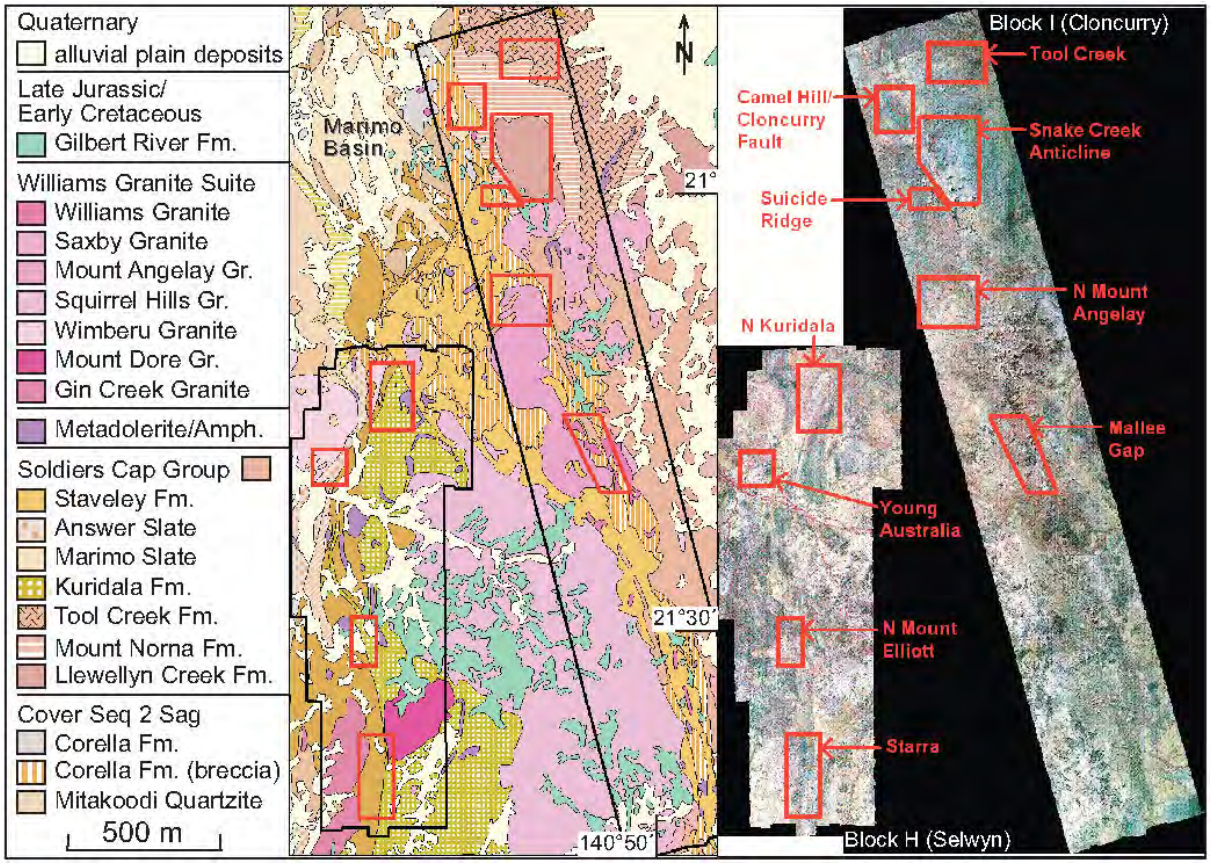

Figure 1: Geological Map (left) and false colour images (right) of the southeastern Mount Isa Inlier with key areas in red. Areas addressed in this report: Camel Hill/Cloncurry Fault, Mallee Gap, Snake Creek Anticline, Starra, Suicide Ridge. Areas selected for further evaluation of hyperspectral mineral maps: N Mount Angelay, N Mount Elliott, N Kuridala, Tool Creek, Young Australia. Black frames in the geological map show the coverage of HyMap scenes flown in the 2006 campaign.

1.1 Regional Geology

The southeastern part of the Mount Isa Inlier consists of metasedimentary successions with interlayered volcanic rocks deposited in the late Paleoproterozoic (Statherian), and are attributed to the Cover Sequences 2 and 3 (here Soldiers Cap Group) (Fig. 1). These formations were intruded by igneous bodies of the Williams (-Naraku) Granite Suite from 1550 - 1500 Ma and altered in several events due to the prolonged tectonothermal evolution of the Mount Isa Inlier (Rubenach, this volume). In the present report, the classification of the deformational events of the Mount Isa Inlier is used according to Rubenach (this volume). Two major fault systems are located in the discussed area: (1) the NNW-trending Cloncurry Fault in the East and (2) a roughly NNW to NE-trending Young Australia Fault system in the

Selwyn Range, extending from the Mount Dore Fault in the South (Starra area) to NE-trending faults in the Kuridala area (Martin Creek Fault southeast of the Marimo Basin).

1.2 Hydrothermal alteration patterns in the EFB

Four different types of hydrothermal alteration patterns were identified:
1) metasomatic 1 - metasediments (e.g. Snake Creek Anticline)
2) metasomatic 2 - igneous bodies (e.g. Camel Hill/Cloncurry Fault gabbros; granites at Mallee Gap)
3) fluid channels 1 - faults (e.g. Cloncurry Fault, Mt Dore Fault and parallel shear zones)
4) fluid channels 2 - breccia pipes (e.g. Suicide Ridge north of the Saxby Granite).

The most prominent metasomatic alteration in the EFB is the pervasive Na(-Ca) alteration, which occurred mainly during D1 and D2 (Rubenach, this volume) synchronously with the intrusion of the Williams-Naraku Batholiths at ca. 1.55 to 1.5o Ga (de Jong and Williams, 1995; Pollard et al., 1998; Rubenach and Lethwaite, 2002; Mark et al., 2004a; Oliver et al., 2004). The mineral assemblage that formed consists mainly of albite and actinolite ± quartz, calcite, magnetite, diopside, scapolite, apatite, biotite, and titanite. Specific mineral alterations in the Cloncurry District comprise: (1) pervasive diopside-rich alteration, (2) albite- and actinolite-rich shear veining and brecciation and (3) large calcite veining (Marshall & Oliver, 2006). Sodic-Calcic alteration in the Cloncurry District typically is associated with fault zones, but is also developed in areas distal to faults that have been affected by intense breccia-related alteration (Williams and Phillips, 1992; de Jong and Williams, 1995; Mark, 1998a,b). The heterogeneous distribution of Na(-Ca) alteration in the EFB could have been generated by several "pulses" of metasomatic alteration during the whole tectonothermal evolution of the Mount Isa Inlier. Even though sodic-calcic alteration is widespread and multiphased in the EFB, a relationship to the development of IOCG's is evident from recent studies (Mark et al., 2006b; Kendrick et al., 2007), suggesting that this complex type of alteration could focus exploration for Cu-Au mineralisation in the EFB. Sodic-calcic alteration commonly occurs distal from ore and predates K-Fe alteration and mineralisation (Williams et al., 2005). Therefore it seems to represent a precondition, but not a direct indicator for IOCGs (Mark et al., 2006b).
The importance of alteration of igneous bodies in the EFB is suggested by the close spatial relationship between IOCGs and intrusions, such as intra-ore intermediate dykes at the Mount Elliott Cu-Au deposit (Wang and Williams, 2001), pre- to syn-ore pegmatites at the Osborne Cu-Au deposit (Gauthier et al., 2001) and magmatic-hydrothermal Magnetite-rich mineralisation within the Squirrel Hills Granite (Perring et al., 2000). As mentioned before sodic-calcic alteration is not solely related to fault zones or breccias. Mark & Foster (2000) pointed out that Na-Ca alteration in metasedimentary rocks around the Roxmere Pluton is not related to faults associated with the Cloncurry Fault, but confined to tens of metres from the contact to the igneous body. Na-rich, K-poor, intermediate granitoids may have influenced localised zones of sodic-calcic alteration (Mark & Foster, 2000).
In the Cloncurry District located in the southeastern Mount Isa Inlier, several occurrences of strata-discordant breccia pipes are known at the contact of the Cloncurry Formation with the Soldiers Cap Group. Oliver et al. (2006) suggest that breccia initiation was triggered by build-up of magmatic-hydrothermal fluid pressure under the contact aureoles of Williams-Naraku Suite granites in the Suicide Ridge area and the Cloncurry Fault in the Camel Hill/Cloncurry Fault area (Fig. 1). The Cloncurry discordant breccias include Corella Formation rocks derived from the contact zone of the Williams Batholith (Oliver et al., 2006). Highly saline brines and abundant CO2 were associated with felsic-mafic magma mixing and mingling

during the crystallization of the Williams Batholith (Perring et al., 2000; Pollard, 2001; Fu et al., 2003) and could have acted as fluidising agents during the brecciation at Cloncurry (Oliver et al., 2006).
The so called "Transitional metasomatic assemblage" (Marshall & Oliver, 2006), is important for the formation of the IOCGs in the EFB, as shown by the well preserved example at the Gilded Rose Breccia Pipe south of Cloncurry. The alteration assemblage comprises calcite, quartz, chlorite ± K-feldspar (and/or subordinate albite), actinolite (and/or Na- to Na-Ca amphibole), biotite, hematite (and/or subordinate magnetite), epidote, muscovite, fluorite, tourmaline, pyrite and chalcopyrite. The relationship between both the potassic and sodic-calcic alteration, and the IOCGs in the EFB is discussed, together with the description of the Ernest Henry deposit, below (1.3 IOCGs in the Eastern Fold Belt).

1.3 IOCGs in the Eastern Fold Belt

Paleoproterozoic successions in the EFB of the Mount Isa Inlier are host to numerous IOCG deposits (Tab. 1). Apart from the Osborne deposit, ages range mainly from 1540 to 1500 Ma, which is contemporaneous with the intrusion of the Williams-Naraku-Suite. The largely structurally controlled deposits can be separated into 3 main types according to their genetic relationship with iron oxide units (Tab. 1). The difference between the Fe oxide hosted Cu-Au deposit of Starra and the Fe oxide Cu-Au deposits such as Ernest Henry, Osborne and Mt Elliott lies in the nature of the Fe oxides. At Ernest Henry for example the Fe oxides associated with the ore-forming hydrothermal system were deposited concurrent with Cu–Au mineralisation. At Starra, the Fe-oxide hosted Cu-Au deposit formed by preferential oxidation of relatively reduced magnetite ironstones by oxidised (hematite-stable) fluids associated with Cu–Au mineralisation.

deposit	age (Ma)	host rocks	structure	type
Ernest Henry	>1510	metaandesites, brecciated	hydrothermal breccia system bound by shear zones	Fe oxide (syn) Cu-Au
Osborne	1600 - 1540	Qtz-Mag and Hem ironstone, ironstone schist within feldspathic arenite and pelite	ductile shear zones in or near tight fold structures	
Mt Elliott	1505	Amphibolite, carbonaceous schist	Veining and breccia in dilational jog: steep-moderate dipping shear zones	
Starra	1505	Mag-Hem-Qtz altered and brecciated, Alb-Act altered biotite-schist	Ductile Shearing and brecciation	Fe oxide-hosted Cu-Au
Eloise	1530 -1514	Siliciclastic metasedimentary rocks and amphibolite	Veining/alteration in jog associated with shear zones	Fe oxide-poor Cu-Au
Lady Clayre	1540 - 1500	Albitised carbonaceous schist and siltstones	Veining, steep-moderate dipping faults	

Tab. 1: A list of some of the major IOCGs in the EFB of the Mount Isa Inlier and their main characteristics (modified from Mark et al., 2006a)

The Cu-Au deposit of Ernest Henry is hosted by a breccia pipe, which has similarities to the breccia pipes south of Cloncurry, such as clast roundness and size distribution and contains

partly milled breccias with calcsilicate clasts (Oliver et al., 2006). The fluid conduits for Ernest Henry might therefore be comparable to the discordant breccia pipes. In figure 2, the alteration assemblages that can be found in and around Ernest Henry are summarised (Oliver et al., 2004; Mark et al., 2006b). The regional sodic alteration is overprinted by two alteration cycles. The first cycle developed prior to mineralisation and comprises Na-Ca alteration as well as potassic alteration with biotite and magnetite as major components. This first cycle was overprinted by the Cu-Au endowment and concurrent potassic alteration with K-feldspar as major component. Spatially these alterations occur as three discrete alteration shells: (1) a distal one, enriched in Mn, K and Ba and depleted in Na, (2) an inner shell, enriched in As, Co and Cu and (3) a proximal shell, enriched in K, Fe, Cu, Au, Mo, Ag, U, Sb and Bi.

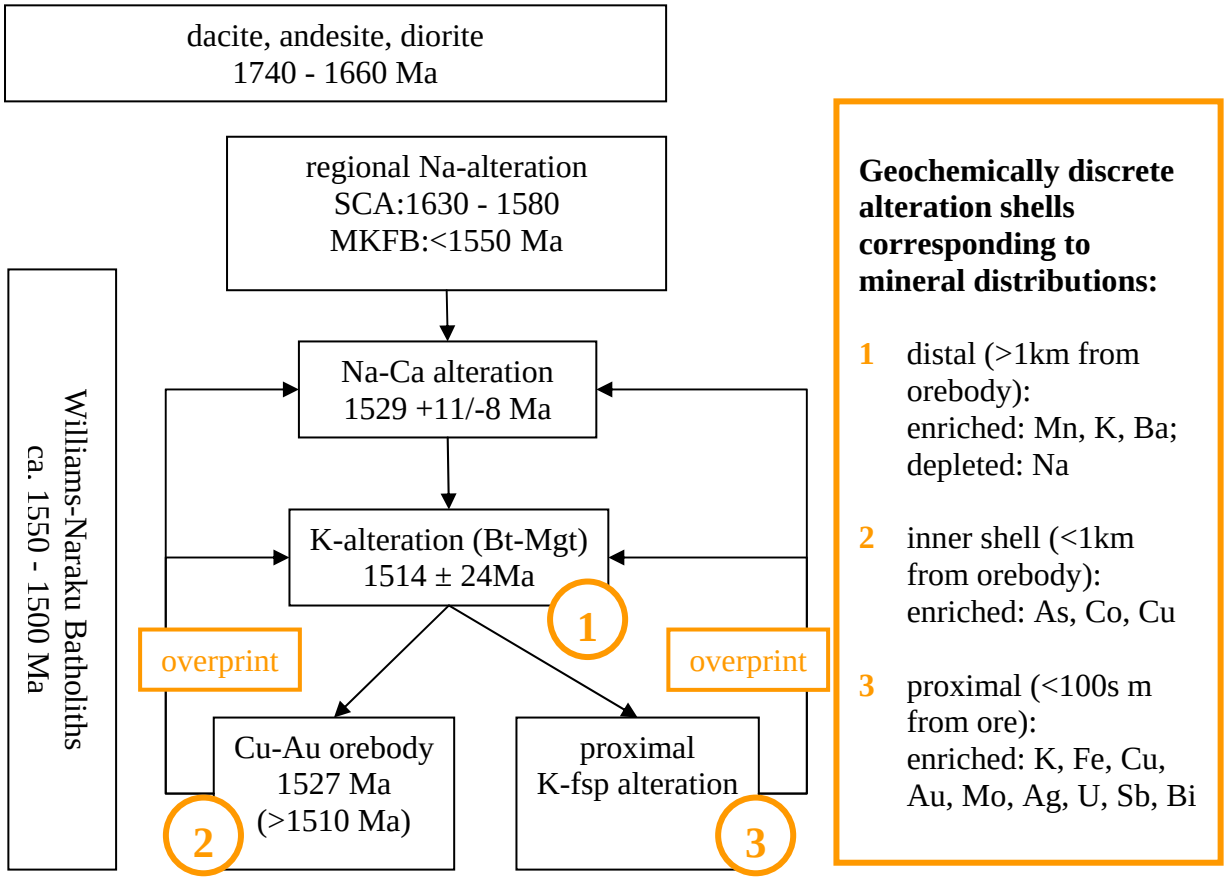

Figure 2: Simplified flow chart showing the main metasomatic and hydrothermal alteration events at the Ernest Henry Deposit, Eastern Fold Bolt. Data from Mark et al. (2006b) and Oliver et al. (2004) and references therein.

3. Methods and Results

Spectral images provided by CSIRO/NGMM

New high-resolution HyMap data were collected by HyVista Corporation in the Mount Isa Inlier for GSQ during 2006. The processing of this data was done by CSIRO as follows: Raw HyMap data were corrected to apparent ground reflectance using HyCORR, which is a radiative transfer program based on ATREM/6S. CSIRO's C-HyperMAP software was used for geoscience information extraction and the generation of image mosaics.

The discussed report focuses on hyperspectral mineral maps (Tab. 2) from the southeastern Mount Isa Inlier, namely Block H (Selwyn South) and Block I (Cloncurry) shown in figure 1. The full suite of the Stage 1 HyMap data is available as an ftp download from the www.em.csiro.au/NGMM webpage.

Product name (in red) JPEG2000 @ high compression	**applicable for the listed minerals**	**base algorithm**	**stretch lower limit**	**stretch upper limit**
HyMap false colour		Reflectance bands: Red: 750nm, Green:650nm Blue:550nm Multiplicative cross track-corrected, 2nd order polynomial	R: 860 DN G: 117 DN B: 304 DN	R: 3120DN G: 2548DN B: 1480DN
HyMap ferrous iron content	in silicates/carbonates (Fe-chlorites, Fe-amphibole, Fe-pyroxene, Fe-olivine, Fe-carbonate)	$(R_{920}+R_{1650})/(R_{1230}+R_{1035})$	0.85 Blue : low content	1.03 Red : high content
HyMap mica abundance	illite, muscovite, Al-smectite, kaolinite	Normalised depth of a fitted 4th order polynomial between 2120 and 2245 nm.	0.005 Blue : low content ~10% Al-mica	0.1 Red : high content ~50% Al-mica
HyMap mica composition	phengite, paragonite/muscovite, illite/brammalite	Wavelength of absorption minimum calculated using the 1st derivative of a fitted 4th order polynomial between 2120 and 2245 nm.	2180 nm Blue is Al-rich mica (muscovite, paragonite, illite, brammalite)	2215 Red is Al-poor mica (~phengite)
HyMap mica relative water	"mica crystallinity"	*(2200D mica) / (1900D)*	0.004 Blue is low crystallinity	0.09 Red is high crystallinity
HyMap MgOH content	incl. calcite, dolomite, chlorite, epidote, amphibole, talc, serpentine	$(R_{2265}+R_{2349})/(R_{2316}+R_{2333})$	1.06 Blue is low content	1.125 Red is high content
HyMap MgOH composition	calcite, dolomite, magnesite, chlorite, epidote, amphibole, talc, serpentine	Wavelength of the absorption minium calculated using the 1st derivative of a fitted 4th order polynomial between 2220 and 2337 nm	2300nm Blue is (magnesite, dolomite, talc,)	2325 nm Red is calcite, siderite, amphibole epidote, chlorite)
HyMap Ferrous iron and MgOH	e.g. amphibole, chlorite	$(R_{920}+R_{1650})/(R_{1230}+R_{1035})$	0.85 Blue: low Fe^{2+} content (typ. in silicates/carb.) ass. with pixels that have MgOH (+carbonate) mineralogy.	1.085 Red: high Fe^{2+} content (typ. in silicates/carb.) ass. with pixels that have MgOH (+carbonate) mineralogy.
HyMap amphibole-chlorite	e.g. amphibole, chlorite	"*MgOH content*" divided by depth of 2260nm absorption $\{(R_{2230}+R_{2228})/(R_{2247}+R_{2265})\}$	0.96 (blue ~ chlorite)	1.05 (red ~ amphibolite)

Tab. 2: HyMap Geoscience products made available by GA and CSIRO (Status: 27th November 2007). For complete table including information about used filters, stretch type, colour chart and accuracy see www.em.csiro.au/NGMM webpage.

PIMA

Spectral analyses were made on field samples using PIMA and ASD spectrometers. About 300 samples were measured following the field validation sampling campaign. Measurements were made on clean, dry rock faces in order to roughly evaluate the hyperspectral images in combination with the observations in the field. An area of ca.15 mm diameter is analysed using PIMA. Only a limited range of minerals can be picked up (SWIR 1300-2500nm wavelengths), such as chlorite, mica, sulphates and carbonate, but not mineral groups without OH molecules such as feldspar and quartz. Interpretation of the spectrometer data was done with "The Spectral Geologist" software from CSIRO (Version 4.10.001). As the spectral analyses are purely qualitative and provide various possible results, only selected spectra are discussed in this report.

XRD/XRF

In order to validate the hyperspectral mineral maps and the PIMA measurements, samples collected during the 2006 field campaigns were prepared and analysed with XRD and XRF at the Advanced Analytical Centre of the James Cook University, Townsville. For XRD, approximately 0.5g of finely crushed rock powder was mixed with water, smeared on to glass slides and inserted into a plastic cavity mount suitable for insertion into the Siemens D5000 X-ray diffractometer. Selected XRD results of the Suicide Ridge area are shown in table 3. For XRF analyses, samples were crushed and then either compressed into a disk or fused to form a glass-like bead. The samples were analysed with a Bruker-AXS S4 Pioneer X-Ray Fluorescence Spectrometer. The results of semiquantitative XRF-analyses that were used for the interpretation of the XRD data are shown in table 4.

locality: Suicide Ridge			quartz	fsp		micas		clinochlore	talc	meionite (scapolite)	amph		carb		opaques	
				K-feldspar	albite	muscovite	Na-muscovite				actinolite	hornblende	calcite	ankerite	hematite	magnetite
sample	rock type	unit														
25582	micaschist	Pon					x	x								
25583	metaquarzite	Pon	x	x	x	x		x								
26381	breccia	breccia pipe	x		x				x		x		x		x	
26382b	breccia	breccia pipe	x		x				x		x		x		x	
26382c	breccia	breccia pipe	x		x				x			x	x		x	
26581	calcsilicate-hornfels	carapace			x			x			x		x			x
26582	calcsilicate-hornfels	carapace		x	x			x			x	x	x			(x)
26681	amphibolite	Pon_d		x				x		x	x			x		

Tab. 3: Qualitative XRD results of samples from the Suicide Ridge area. Minerals in italic are critical in the interpretation of the HyMap data. Rock units: Pon -Mt Norna Quartzite Fm, Pon_d - dolerite. Mineral occurrences: xx - percentage ≥ 80%, x - major component, (x) - minor component. Fsp - feldspas, amph - amphiboles, carb - carbonates.

rock type	micaschist	meta-quarzite	breccia	breccia	breccia	calcsilicate-hornfels	calcsilicate-hornfels	amphibolite
sample	255S2	255S3	263S1	263S2b	263S2c	265S1	265S2	266S1
O	54,593	56,181	54,101	53,098	54,599	48,923	47,764	50,841
Na	0,379	1,410	4,675	5,965	5,526	4,071	2,034	3,280
Mg	1,696	1,236	3,157	1,991	1,392	3,356	3,872	2,632
Al	12,485	6,465	5,558	7,284	6,114	7,648	7,047	7,959
Si	20,874	29,971	24,258	26,866	23,668	22,227	22,078	17,753
P	0,071	0,074	0,131	0,198	0,120	0,063	0,035	0,100
S		0,005	0,006	0,008	0,010	0,069	0,018	0,039
Cl	0,034	0,024	0,032	0,061	0,042	0,059	0,059	1,323
K	5,138	2,110	0,063	0,068	0,049	0,797	3,496	0,637
Ca	0,381	0,251	4,557	1,423	6,156	4,048	4,119	7,407
Ti	0,472	0,253	0,273	0,329	0,252	0,613	0,910	0,589
V	0,012			0,007		0,036	0,036	0,028
Cr	0,004	0,004						0,003
Mn	0,082	0,018	0,039	0,032	0,024	0,088	0,143	0,091
Fe	3,728	1,920	3,128	2,643	2,030	7,985	8,313	7,301
Ni						0,004		
Cu						0,004		
Rb	0,015	0,010					0,013	0,001
Sr						0,013	0,015	0,015
Zr	0,015	0,024	0,020	0,019	0,021	0,007	0,010	0,006
Ba	0,046	0,014					0,042	
W		0,050	0,021	0,025	0,020			
Total	100,0	100,0	100,0	100,0	100,0	100,0	100,0	100,0

Tab. 4: Semi-quantitative XRF analyses of samples from the Suicide Ridge area. All values in weight %. Blanks below detection limit.

4. Discussion

4.1. metasomatic 1 - Regional Na(-Ca)-alteration in the Snake Creek Anticline

The Snake Creek Anticline, located in the northern Cloncurry District (Fig. 1), was chosen for mapping of regional, metasomatic alteration of metasediments. The large scale folding of the metasedimentary successions and interlayered amphibolites of the Soldiers Cap Group is visible in the "white mica abundance" image (Fig. 3). Red to orange colours represent a high mica abundance and therefore the occurrence of white mica-bearing metasediments. On the ground, red areas are characterised by a high content of porphyroblasts and less altered rocks (Rubenach, pers. comm.). Dark layers in the north and the east represent amphibolites, which are faulted in the northeastern part of the Snake Creek Anticline. Northwest trending features in the northern Snake Creek Anticline, perpendicular to the folded bedding, are caused by dolerites. An almost straight N-S striking bedding of the Soldiers Cap Group is evident in the eastern part of the image. The mafic units can be made visible by the "MgOH" and "Fe^{2+} ass. with MgOH" maps (Tab. 2), as shown for other areas described below (e.g. Suicide Ridge).
In the Snake Creek Anticline, sodic alteration is characterised by albitisation mainly of meta-psammite and quartzite layers and albitite veining, which is dominant in some areas (Rubenach & Lethwaite, 2002) (Fig. 3). Albitite veins occur along shear zones parallel to axial planes of mesoscopic F3-folds. For comparison, albitised areas, postulated by Rubenach & Lethwaite (2002), are plotted on top of a hyperspectral mineral map, showing the "white mica abundance" (Fig. 3). Enhanced albitisation is shown in the map by cool colours in the central and southeastern part of the Snake Creek Anticline (Fig. 3), roughly concordant with areas 2 and 3. The decreasing mica abundance could be the result of replacement by albite in quartzites and psammitic schists, as suggested by Rubenach & Lethwaite (2002). In the remaining areas, interpretation of the mineral map is difficult, because of high amounts of mafic units and/or covering Mesozoic to Cenozoic sediments. The triangular shape of the albitised area 2, appearing in the mineral map shown in Figure 3, is partly framed by north and northeast trending faults. Combined with the orientation of albitite veins along shear

zones (Rubenach & Lethwaite, 2002) a structural control of fluid flow is evident in the Snake Creek Anticline.

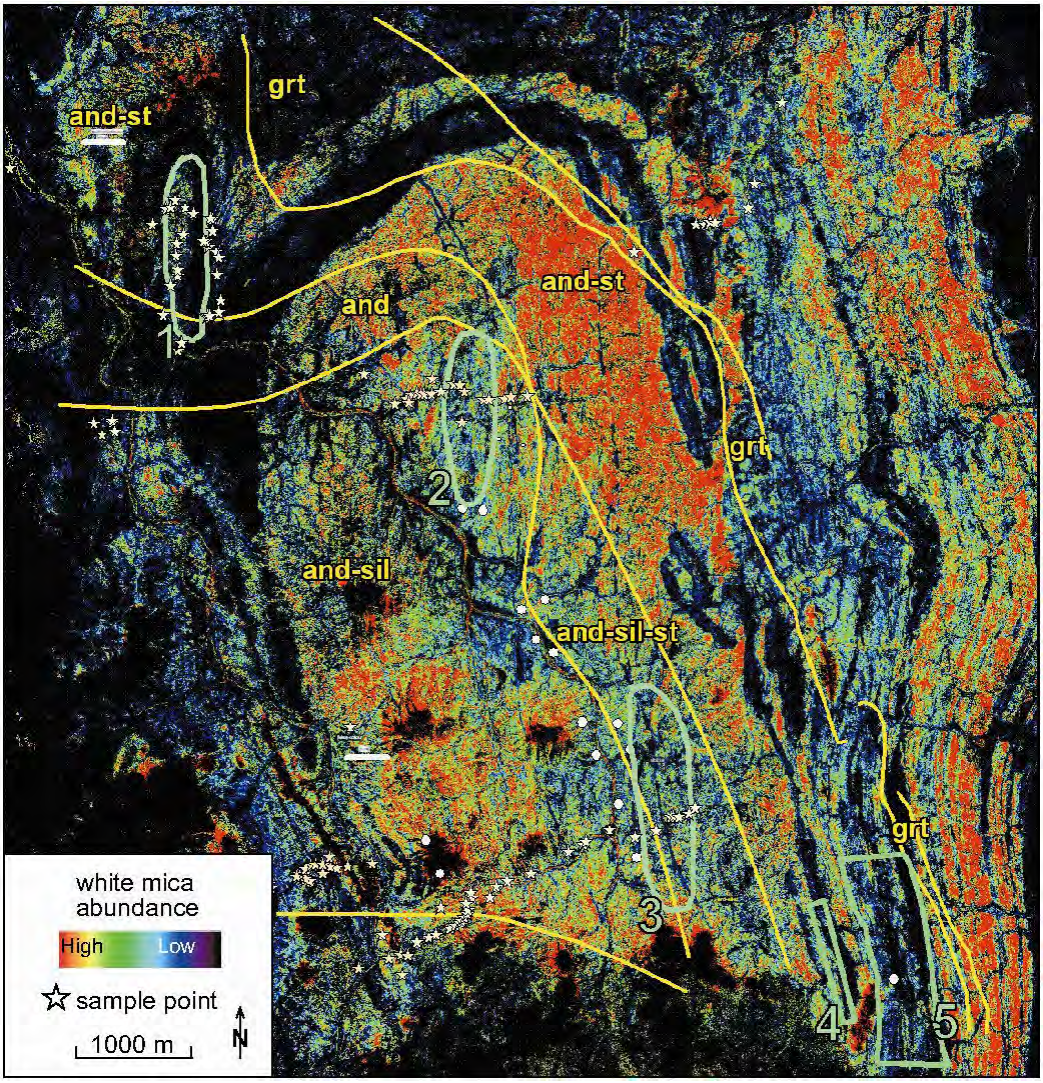

Fig. 3: White mica abundance in the Snake Creek Anticline (black areas: below threshold). Yellow lines show isograde and bright green framed areas indicate major albitisation, white dots show Cordierite occurrences (Rubenach & Lethwaite (2002)).

4.2. metasomatic 2 - igneous bodies - Mallee Gap

Alteration of igneous bodies has been described in many areas in the EFB (Mark & Foster, 2000 and Perring et al., 2000 amongst others). Tonalitic granites in the Mallee Gap area (Fig. 1) have been chosen to evaluate the hyperspectral mineral maps for the detection of alteration. De Jong (1995) described albitisation of granites in the vicinity of the Cloncurry Fault. In the northern Mallee Gap area granites of the Williams Granite Suite have intruded the Corella Fm (Fig. 4). The NNW-trending Cloncurry Fault to the east of the granites offsets metasedimentary successions and amphibolites of the Cover Sequence 3. The hyperspectral Fe^{2+}-content-map (Fig. 4b) shows the extension of the central granite body (called "Mallee Gap Granite" below) very well. Field studies suggest that the southeastern extension of the Mallee Gap Granite is separated from the northern main granite body, as shown on the hyperspectral mineral maps (Fig. 4). Calcsilicate breccias assigned to the Corella Fm. crop out in this area. Figures 4c and 4d showing the white mica composition and the white mica crystallinity ("mica content/water abundance") respectively highlight the rim of the Mallee

Gap Granite, whereas data from the centre of this granite are below the threshold. The "Kaolin content"-map shows a low Kaolin abundance in the central, non-albitised core of the granite and in the outer part of the albitised rim. PIMA analyses on samples from various altered and non-altered granites are shown in Fig. 5. Major differences in the reflectance spectra between the non altered (e.g. 465P1a) and the albitised granites (e.g. 459P1f) occur in the 2100 - 2250 nm wavelength range, suggesting variations in the white mica crystallinity. Further interpretation of the PIMA spectra has to be backed up by XRD/XRF. The various Fe^{2+}-contents of units assigned to Cover Sequence 3 are caused by the high variability of metasedimentary rocks and the occurrence of amphibolites. The ferrous iron content-maps can show the occurrence of a whole suite of Fe^{2+}-bearing silicates and carbonates (Tab. 2). The white mica composition and crystallinity maps reflect the various compositions of the metasedimentary successions. An increasing phengitic component in the white micas towards the Cloncurry Fault is accompanied by a decline of the white mica crystallinity.

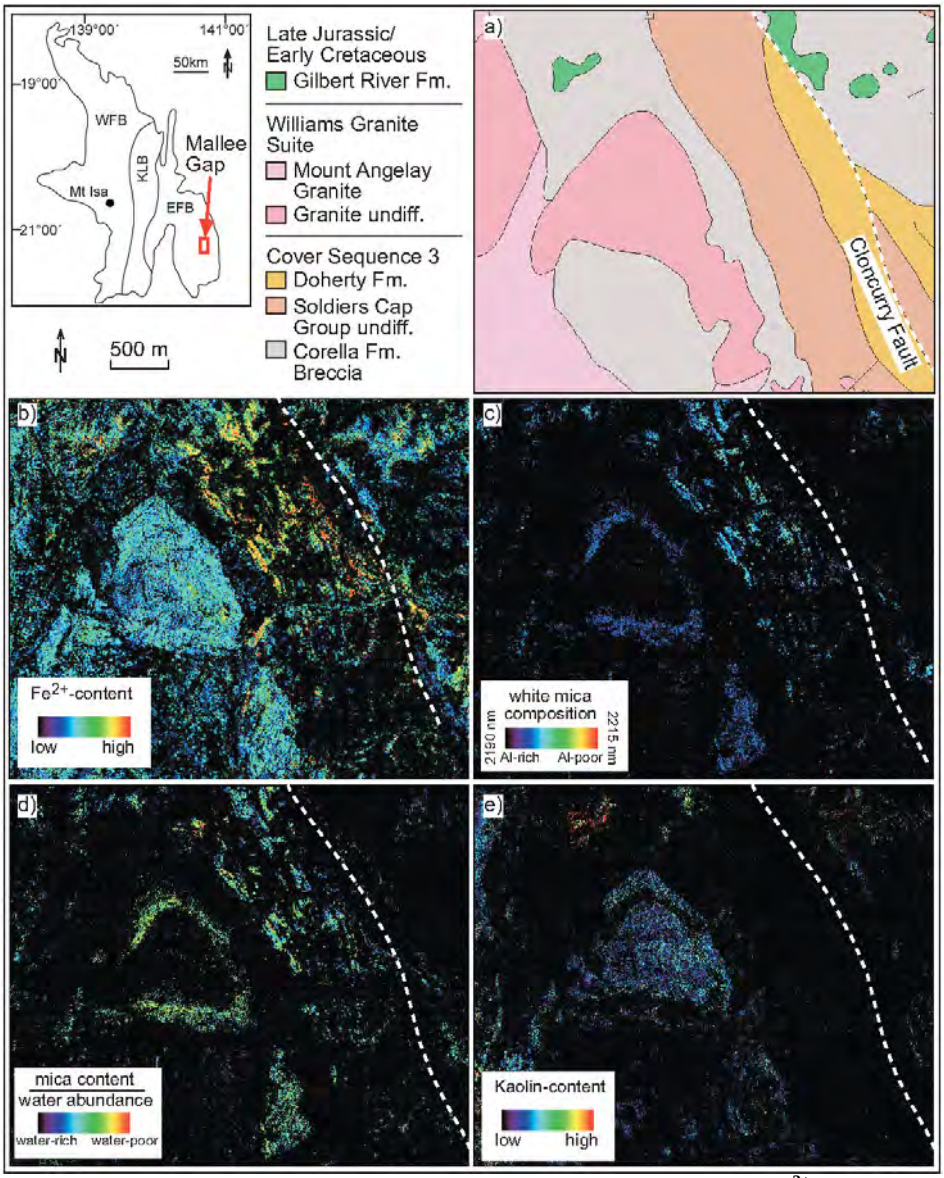

Fig. 4: Mallee Gap area - Alteration rim of a granite. a) Geological map, b) Fe^{2+}-content, c) white mica composition, d) mica content/water abundance, e) Kaolin-content. Black is below threshold.

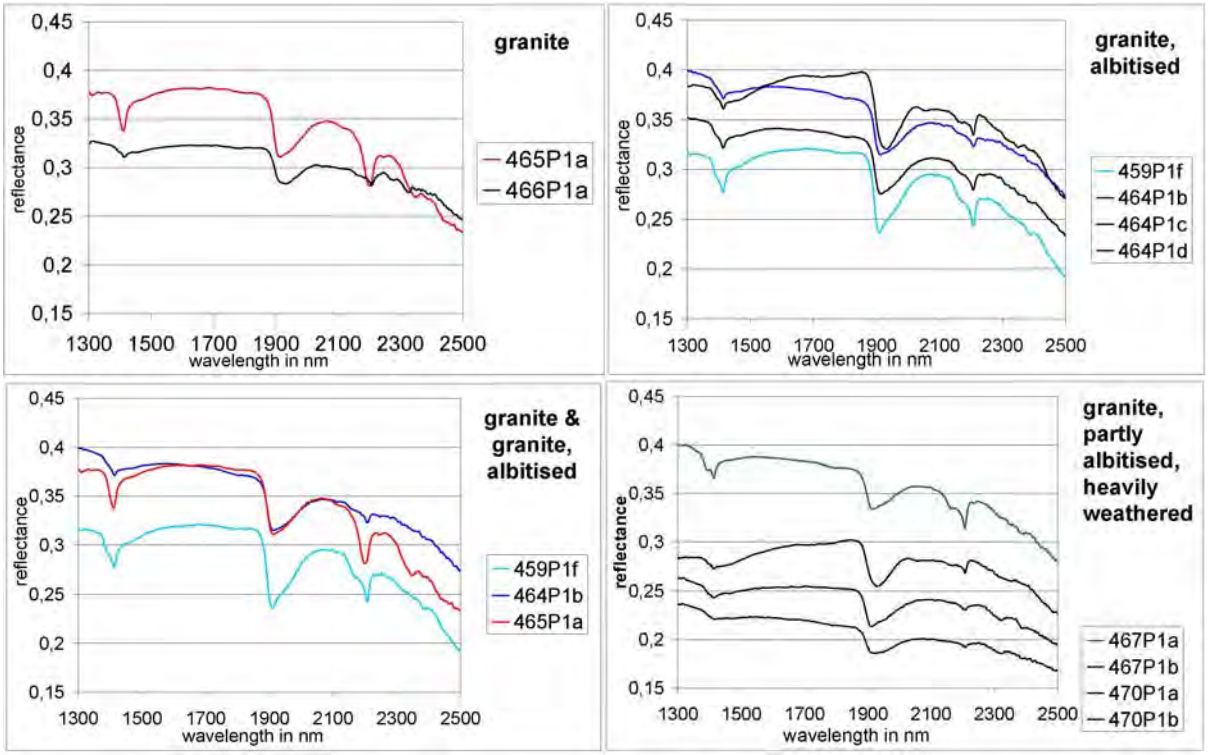

Fig. 5: PIMA spectra of samples from the Mallee Gap Granite.

4.3 fluid channels 1 - Fault related alteration patterns in the Starra area

Many studies on fluid pathways, as well as the results of the numerical modelling during this project (McLellan, this volume; Ford, this volume; Keys et al., this volume), have shown that faults are major pathways for fluid migration. The interaction of migrating fluids with the faulted rocks is very variable. Alteration can extend hundreds of meters from the main shear zone into the surrounding rocks.

An interesting area for the validation of hyperspectral mineral maps in detecting fault zones and related alteration haloes is the Starra area (Fig. 1) in the southern Selwyn Range (HyMap swath Block H). In this highly deformed area east of the Gin Creek Granite ironstones, graphite-rich layers and amphibolites are interlayered in metasedimentary successions of the Kuridala Fm. The Mount Dore Fault (Fig. 6a) is part of a roughly north-south-striking shear zone and spatially closely related to Fe oxide Cu-Au deposits such as Mount Elliott (Tab. 1). Hyperspectral mineral maps showing the white mica abundance (Fig. 6c) and the relative water content of mica (Fig. 6d) highlight the petrographic differences between the Mount Dore Fault and the surrounding lithologies. In the Starra area major Cu-Au deposits are hosted by Fe oxide rich units west of the Mount Dore Fault. On the mineral maps a gradient in the white mica composition is represented by a decreasing Al-content from the Mount Dore Fault towards the Fe oxide units (Fig. 6e). To the west of the Fe oxide units a dominance of Al-rich white micas is evident in the Kuridala Fm. The chemical gradient suggests a close relationship of the Mount Dore Fault to the Fe oxide hosted Cu-Au deposits and its importance as pathway for mineralising fluids. In conclusion the hyperspectral mineral maps can in this area not only be used for the detection of major fault zones, but also the recognition of alteration gradients.

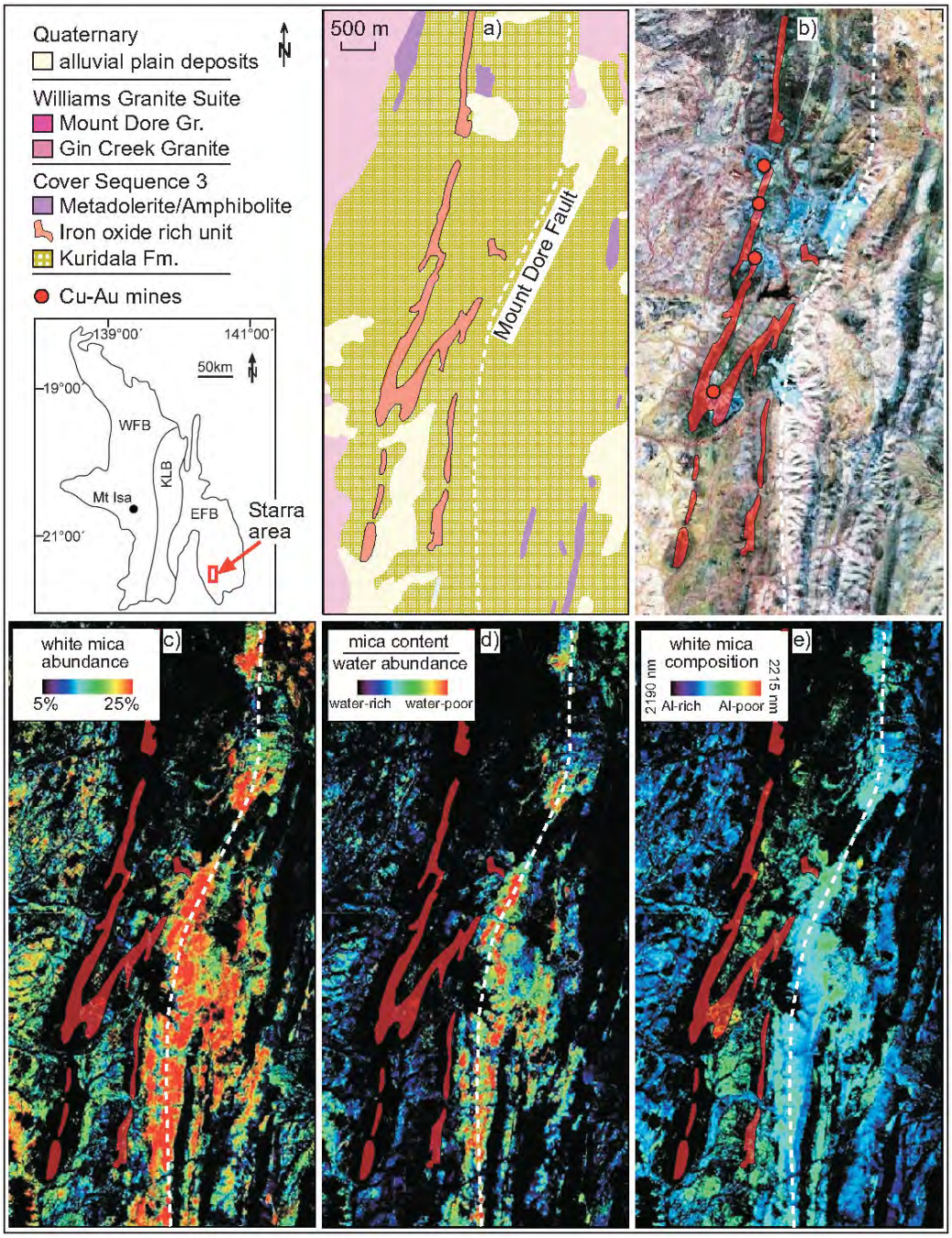

Fig. 6: Starra area - Fault related alteration patterns: a) Geological map, b) false colour map, c) white mica abundance, d) mica content/water abundance, e) white mica composition. Black is below threshold

4.4 fluid channels 2 - The Suicide Ridge breccia pipe

The breccia pipe at Suicide Ridge is a non-linear feature, striking roughly southwest - northeast, discordant to metasedimentary sequences and amphibolites of the Soldiers Cap Group. The western end of the breccia pipe is connected to a carapace of breccia surrounding a granite body northwest to the main body of the Saxby Granite. The eastern part ends in micaschists and metasiltstones of the Mount Norna Quartzites, close to a strata-concordant pegmatite. The age of the breccia pipe is roughly constrained to be post D2, implicated by it's crosscutting with the regional S2 in the Mount Norna Quartzites. The breccia pipe contains clinopyroxene (diopside) and K-feldspar as infill minerals together with albite, magnetite, and quartz (Oliver et al., 2006) and actinolite (Bertelli, 2007). Breccia clasts are dominated by

calcsilicates of the Corella Fm with rare fragments of the hosting Soldiers Cap Group (Bertelli, 2007). Other clast types consist of partly large boulders of granites and gabbros. Throughout the breccia pipe ironstones can be found at various sizes, which change their composition from magnetite-dominated bodies in the soutwestern and central part to hematite-dominated ironstones in the northeastern part, the latter ones accompanied by quartz-hematite ± magnetite veining. indicating a hydrothermal origin of these ironstones (Bertelli, 2007). The carapace surrounding the granite mainly consists of clinopyroxene and albite (Oliver pers. comm.). Intensive sodic alteration affects the breccia pipe, the containing clasts and the adjacent lithologies, shown by pervasive Fe-rich albite alteration (Bertelli, 2007).

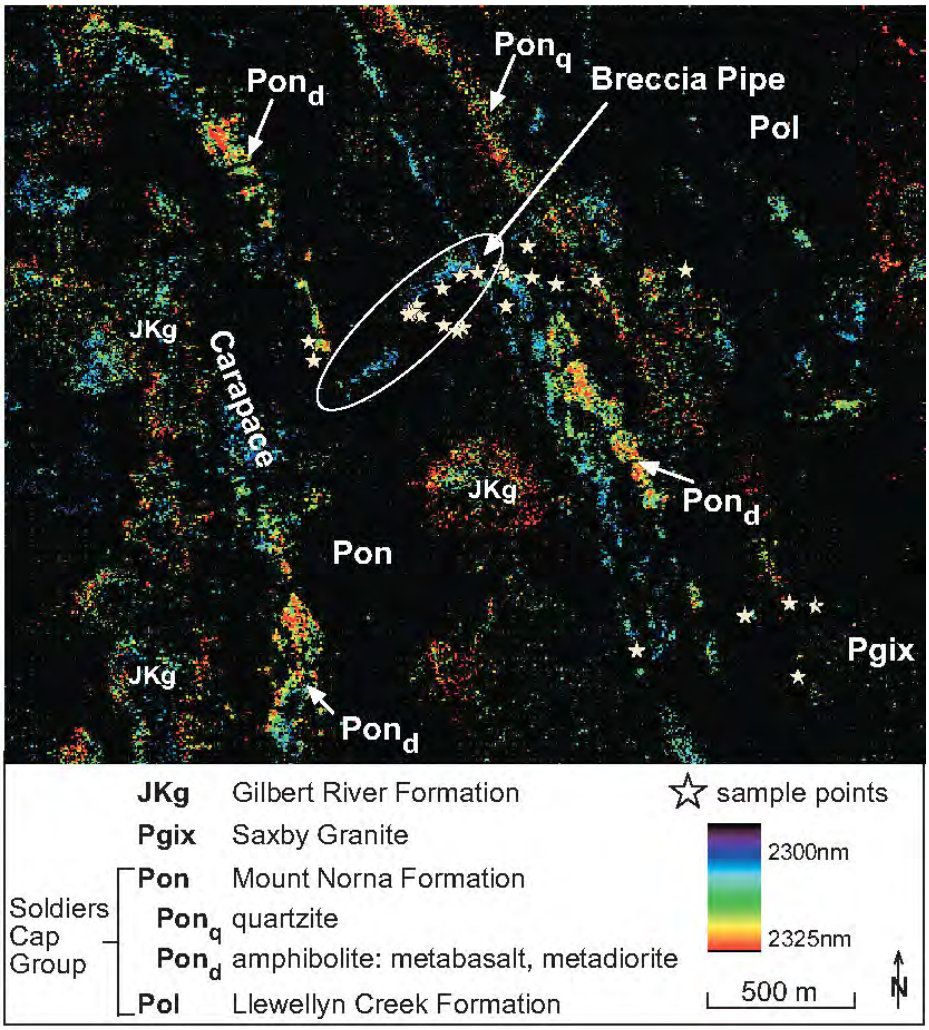

Fig. 7: MgOH composition image of area northwest of the Saxby Granite (see Fig. 1 for location). Breccia Pipe extending from a carapace on the north-eastern rim of a granite body to the NE (white ellipse). For carbonates: blue colours: magnesite, dolomite; red colours: calcite, siderite. For MgOH-bearing rocks: blue colours: e.g. talc; red colours: amphibole, epidote, chlorite. Black is below threshold.

The HyMap geoscience product "MgOH composition" of the Suicide Ridge area is shown in figure 7. The NNW-striking successions of the Soldiers Cap group are characterised by various adsorption features. Amphibolites of the Mount Norna Formation are highlighted by adsorption of higher wavelengths (red patches), presumably caused by a mineral composition containing actinolite, clinochlore and meionite (Ca-scapolite) as major Mg and Ca-bearing minerals (Tab. 3). The Mount Norna quartzites show adsorption in similar wavelengths, which is less pronounced presumably because of a high muscovite-chlorite ratio in the micaschists (Tab. 3). High muscovite contents can disturb the mineral interpretation from the "MgOH-composition"-map, as these minerals absorb in the same range of wavelengths. The

Suicide Ridge Breccia Pipe contains a mineral assemblage similar to the amphibolites plus calcite, but shows adsorption at lower wavelengths in the "MgOH-composition"-map. This could be explained by the talc content (Tab. 3). The stratadiscordant appearance is clearly visible, although most of the surrounding metasedimentary units are masked out. In spite of the high content of MgOH-bearing minerals in the carapace, these rocks are masked out as well on the presented hyperspectral mineral map. Debris of the Jurassic Gilbert River Fm and dense vegetation, observed in this area during the field campaign, may lead to the obliteration of the hyperspectral information on the carapace.

4.5 Camel Hill/Cloncurry Fault area - K-alteration in mafic igneous bodies

In contrast to the postulated similar evolution of the Suicide Ridge and Camel Hill/Cloncurry Fault Breccia Pipes (Oliver et al., 2006), the composition of the breccias is very different. The composition of each of the breccia pipe types is comparable to the rocks they originate from, if the "barrier theory" of Oliver et al. (2006) is followed up. The composition of the Suicide Ridge breccia pipe is similar to the composition of the carapace of the Saxby Granite, whereas the Camel Hill/Cloncurry Fault Breccia Pipes are compositional similar to the breccias of the Corella Fm. However, the high actinolite content should still be visible in the various hyperspectral mineral maps showing absorptions features caused by MgOH-bearing minerals (Tab. 2). The recognition of the Camel Hill/Cloncurry Fault Breccia Pipes with hyperspectral mineral maps is still problematic. In the vicinity of the northern Cloncurry Fault the recognition might be hindered by sparse outcrops and dense vegetation.
Nevertheless some of the HyMap Geoscience products provide information about other rock units, important for the exploration for IOCG's in the EFB. Mineral maps showing ferrous iron content (associated or not with MgOH) and white mica composition detect alteration of igneous bodies. The ferrous iron content is slightly enhanced in the rim of a sampled gabbro (Fig. 8c; sample 388). A mineral map showing the ferrous iron content associated with MgOH bearing minerals indicates a change in the amphibole chemistry of the gabbro (Fig. 8d). This change is confirmed by slight variations in adsorption bands in the 2300 to 2450nm range of PIMA spectra taken from fresh surfaces of representative gabbro samples (Fig. 9). The less altered gabbro (sample 390P1a) shows an additional absorption band at 2327nm compared to an inclined slope in the PIMA spectra of the altered gabbro (sample 388P1a) in this range. The additional absorption band at this wavelength indicates a higher Mg-abundance in amphiboles in the centre of the gabbro. The rim is characterised by Mg-depletion, which coincides with the enrichment of ferrous iron shown in Fig. 8d. The detection of Al-rich white mica in the rim of the gabbro (Fig. 8e) could point to the occurrence of K-feldpar weathering products and therefore be an indicator for potassic alteration. However, the observed band depths are strongly influenced by the amount of contaminants. The HyMap mineral maps and PIMA spectra reflect the mineral assemblages in the whole rocks and characterisation of specific mineral species has still to be undertaken by further analytical studies such as XRD and XRF.

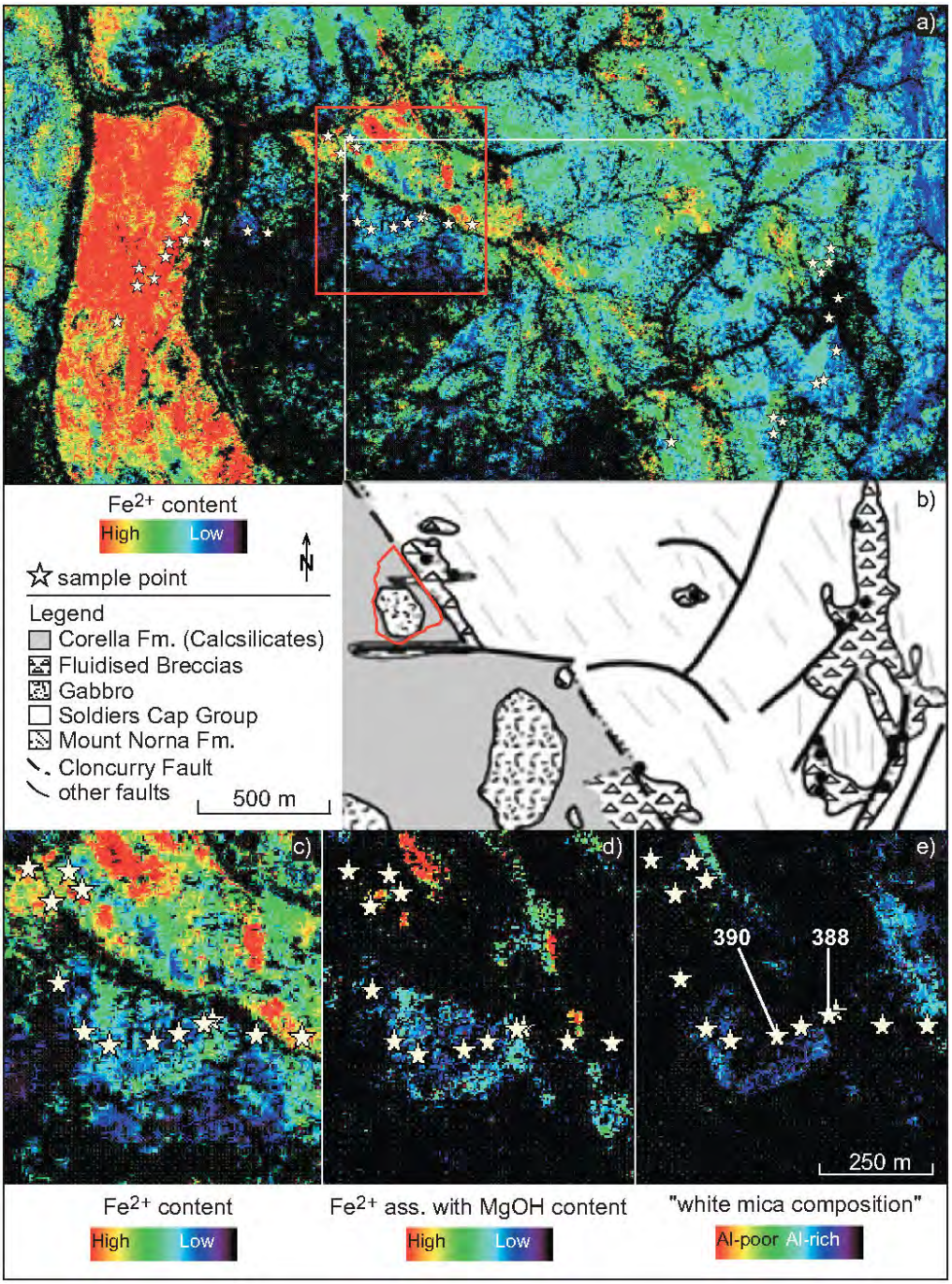

Fig. 8: HyMap derived mineral maps and geology of the Camel Hill/Cloncurry Fault area showing an altered margin of a gabbro body (for location see Fig.1). Black is below threshold.

a: Fe^{2+}-content. High Fe^{2+}-contents in calc-silicates and schists of the Corella Formation in the west and calcsilicate breccias north of the sampled gabbro body. Low Fe^{2+}-contents in the unaltered gabbro, in calcsilicate breccias surrounding the gabbro and in schists of the Mount Norna Fm in the east. Black is below threshold. Red frame: location of Figs. 8c-e. b: excerpt of Fig. 1D of Oliver et al. (2006) showing occurrences of fluidised breccias and gabbros at a stratigraphical contact. The red line shows the extent of this gabbro body, determined by new mapping and comparison of various HyMap derived mineral maps (for loaction see white frame in Fig. 8a). c: Fe^{2+}-content. d: Fe^{2+}-content associated with MgOH. e: white mica composition.

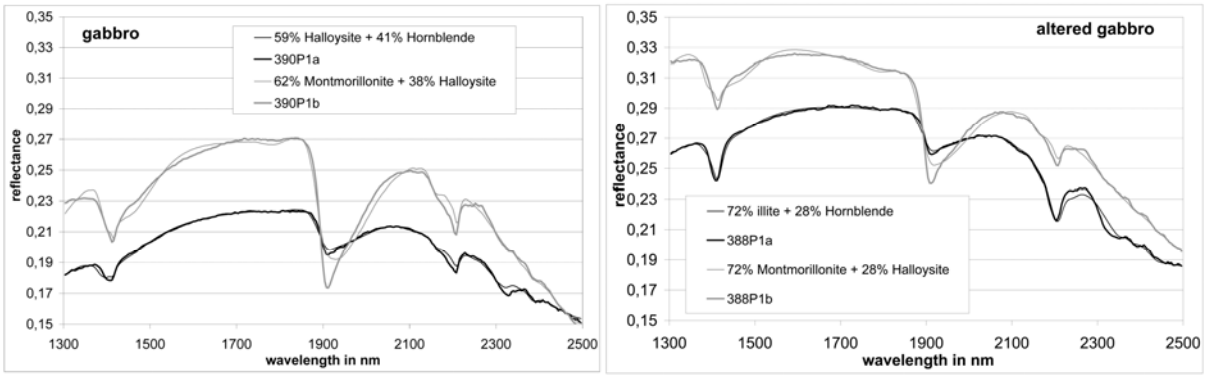

Fig. 9: PIMA spectra of gabbro samples from the Camel Hill/Cloncurry Fault area. 390P1a and 388P1a are spectra from fresh surfaces and 390P1b and 388P1b are spectra from weathered surfaces. For sample localities see Fig. 8e.

5. Conclusions

Hyperspectral mineral maps, alone or in combination with other geophysical data (e.g. magnetics, radiometrics) can be used to detect not only possible host rocks, but also alteration assemblages and their spatial distribution. The extension of regional metasomatic alteration systems (e.g. sodic-calcic alteration in the Snake Creek Anticline: "white mica composition", "white mica abundance") can be narrowed down and hydrothermal alteration along major fault zones can be recognised (e.g. Mt Dore fault zone in the Selwyn Corridor: "white mica abundance", "white mica composition", "white mica relative water"). Spatial relationships of sodic-calcic and potassic alteration are important for the recognition of IOCGs in the EFB and can be detected with mineral maps derived from hyperspectral data (Na(-Ca)-alteration: e.g. "white mica composition", "white mica abundance"; K-alteration in mafics: "MgOH content", "MgOH composition", "amphibole/chlorite" and "Fe^{2+} ass. with MgOH" combined with "white mica composition" and "white mica abundance"). Amphibolites, forming for example host rocks for some of the IOCGs in the EFB (e.g. Mount Elliott, Selwyn Corridor) can be separated from other mafic units (e.g. gabbros, dolerites) using mineral maps derived from hyperspectral data ("MgOH content", "MgOH composition", "amphibole/chlorite" and "Fe^{2+} ass. with MgOH").

For the use of hyperspectral mineral maps for exploration in the EFB a good knowledge of the mineralisation related alteration assemblage and its spatial distribution in combination with a good knowledge of the geology of the investigated area is required. Further limitations comprise unsatisfactory coverage of mineral maps, man made features, river systems and distribution and composition of debris. The latter limitations can be largely eliminated by a good knowledge of the factors mentioned before.

Based on the calibration of the ASTER data with the hyperspectral data and the reprocessing with new techniques (both done by GA and CSIRO), interpretation made from the HyMap data can be hopefully extended into adjacent areas, which are only covered by ASTER. The preliminary studies show that hyperspectral mineral maps can be used as a powerful tool for mapping lithologies and various alteration patterns. However, further validation has to be done using XRD and XRF. In combination with other geophysical remote sensing methods the significance of HyMap data could be possibly improved.

Refererences

Adshead, N.D. (1996): Geology, Alteration and Geochemistry of the Osborne Cu-Au Deposit, Cloncurry District N .W. Queensland, Australia..- Unpublished Ph.D. thesis, Townsville, James Cook University, 360 p.

Adshead, N.D., Voulgaris, P., Muscio, V.N. (1998): Osborne copper-gold deposit.- Monograph Series - Australasian Institute of Mining and Metallurgy, 22, 793-799.
Baker, T. (1998): Alteration, mineralization, and fluid evolution at the Eloise Cu-Au deposit, Cloncurry District, Northwest Queensland, Australia.- Economic Geology, 93, 8, 1213-1236.
Baker, T., Perkins, C., Blake, K.L., Williams, P.J. (2001): Radiogenic and stable isotopic constraints on the genesis of the Eloise Cu-Au deposit, Cloncurry District, Northwest Queensland.- Economic Geology, 96, 4, 723-742.
Bertelli, M. (2007): Application of fluid inclusion microanalytical techniques to reduced IOCG deposits of the Cloncurry district - Unpublished Ph.D. thesis, Townsville, James Cook University of North Queensland, 302 p.
De Jong, G., 1995, Post metamorphic alteration and mineralization in a highly deformed Proterozoic terrain; the eastern Selwyn Range, Cloncurry district, NW Queensland.- Unpublished Ph.D. thesis, Townsville, James Cook University of North Queensland, 302 p.
DeJong, G. & Williams, P.J. (1995): Giant metasomatic system formed during exhumation of mid-crustal Proterozoic rocks in the vicinity of the Cloncurry Fault, northwest Queensland.- Australian Journal of Earth Sciences, 42 281-290.
Ford, A. (2008): Factors affecting fluid flow in strike-slip fault systems: Coupled deformation and fluid flow modelling with an application to the western Mount Isa Inlier, Australia. - this volume
Gauthier, L., Hall, G., Stein, H.J., Schaltegger, U. (2001): The Osborne Deposit, Cloncurry District; a 1595 Ma Cu-Au skarn deposit..- Contributions of the Economic Geology Research Unit, 59, 58-59.
Kendrick, M.A., Baker, T. Fu, B., Phillips, D. Williams, P.J. (2007): Noble gas and halogen constraints on regionally extensive mid-crustal Na-Ca metasomatism, the Proterozoic Eastern Mount Isa Block, Australi, Precambrian Research.
Keys, D., Miller, J., McLellan, J.G. (2008): Structural controls on depositional sites for Cu deposits in the Western Fold Belt, Mount Isa: integration of field observations and UDEC modelling. - this volume
Mark, G., 1998. Albitite formation by selective pervasive sodic alteration of tonalite plutons in the Cloncurry district, NW Queensland. Austr. J. Earth. Sci. 45, 765-774.
Mark, G. & Foster, D.R.W. (2000): Magmatic–hydrothermal albite–actinolite–apatite-rich rocks from the Cloncurry district, NW Queensland, Australia.- Lithos, 51, 223-245.
Mark, G., Oliver, N.H.S., Williams, P.J. (2006b) Mineralogical and chemical evolution of the Ernest Henry Fe oxide-Cu-Au ore system, Cloncurry district, northwest Queensland, Australia.- Mineralium Deposita, 40, 769-801.
Mark, G., Oliver, N.H.S., Carew, M.J. (2006a): Insights into the genesis and diversity of epigenetic Cu–Au mineralisation in the Cloncurry district, Mt Isa Inlier, northwest Queensland.- Australian Journal of Earth Sciences, 53, 109-124.
Marshall, L.J. (2003): Geology, Alteration and Geochemistry of the Osborne Cu-Au Deposit, Cloncurry District, N.W. Queensland, Australia.- Unpublished Ph.D. thesis, Townsville, James Cook University, 314 p.
Marshall, L.J. & Oliver, N.H.S. (2006): Monitoring fluid chemistry in iron oxide–copper–gold-related metasomatic processes, eastern Mt Isa Block, Australia.- Geofluids, 6, 45-66.
McLellan, J.G. (2008): Q4.1.2 Numerical Modelling of the Leichhardt River Fault Trough; insights into the basin development, fluid flow and associated mineralising systems. - this volume
Oliver, N.H.S., Rubenach, M.J., Fu, B., Baker, T., Blenkinsop, T.G., Cleverley, J.S., Marshall, L.J., Ridd, P.J. (2006): Granite-related overpressure and volatile release in the mid crust: fluidized breccias from the Cloncurry District, Australia. Geofluids, 6, 1-13.
Perring, C.S., Pollard, P.J., Dong, G., Nunn, A.J., Blake, K.L. (2000): Metallogeny of the Lightning Creek Cu-Au prospect, Mount Isa Inlier, Australia.- Proceedings of the Biennial SGA Meeting 5, pages 413-416.
Rotherham, J.F., Blake, K.L., Cartwright, I., Williams, P.J. (1998): Stable isotope evidence for the origin of the Mesoproterozoic Starra Au-Cu deposit, Cloncurry District, Northwest Queensland.- Economic Geology, 93, 8, 1435-1449.
Rubenach, M.J. & Lethwaite, K.A. (2002): Metasomatic albitites and related biotite-rich schists from a low-pressure polymetamorphic terrane, Snake Creek Anticline, MOunt Isa Inlier, northe-eastern Australi: microstructures and P-T-d paths.- Journal of metamorphic Geology, 20, 191-202.
Rubenach, M.J. et al. (2008): Tectono-thermal and metasomatic history of the Mt Isa Inlier. - this volume
van der Wielen, S.E., Oliver, S., Kalinowski, A.A., Creasy, J. (2005): Remotely sensed imaging of hydrothermal footprints in Western Succession, Mount Isa Inlier. In: Gibson, G.M. & Hitchman, P. (eds). *pmd**CRC I1 Project Final Report—3D Basin Architecture and Minerals Systems in the Mt Isa Western Succession. Unpublished report, 268.
Wang, S. & Williams, P.J. (2001): Geochemistry and origin of Proterozoic skarns at the Mount Elliott Cu-Au(-Co-Ni) deposit, Cloncurry District, NW Queensland, Australia.- Mineralium Deposita, 36, 2, 109-124.

Williams, P.J. & Phillips, G.N. (1992): Cloncurry Mapping Project 1990; Geology of the Selwyn Range (McKinlay River and Maramungee Creek areas).- Contributions of the Economic Geology Research Unit, 40.

Williams, P.J., Barton, M.D., Fontboté, L., deHaller, A., Johnson, D.A., Mark, G., Oliver, N.H.S. , Marschik, R., 2005. Iron oxide-copper-gold deposits: Geology, space-time distribution and possible modes of origin. Econ. Geol. 100th anniversary volume, 371-405.